

Pengfei Zhao

Yun Ouyang

Min Xu

Li Yang

Yuhui Ren *Editors*

# Advances in Graphic Communication, Printing and Packaging

Proceedings of 2018 9th China  
Academic Conference on Printing and  
Packaging

# Lecture Notes in Electrical Engineering

## Volume 543

### Series Editors

Leopoldo Angrisani, Department of Electrical and Information Technologies Engineering, University of Napoli Federico II, Napoli, Italy

Marco Arteaga, Departament de Control y Robótica, Universidad Nacional Autónoma de México, Coyoacán, Mexico

Bijaya Ketan Panigrahi, Electrical Engineering, Indian Institute of Technology Delhi, New Delhi, Delhi, India  
Samarjit Chakraborty, Fakultät für Elektrotechnik und Informationstechnik, TU München, München, Germany

Jiming Chen, Zhejiang University, Hangzhou, Zhejiang, China

Shanben Chen, Materials Science & Engineering, Shanghai Jiao Tong University, Shanghai, China

Tan Kay Chen, Department of Electrical and Computer Engineering, National University of Singapore, Singapore, Singapore

Rüdiger Dillmann, Humanoids and Intelligent Systems Lab, Karlsruhe Institute for Technology, Karlsruhe, Baden-Württemberg, Germany

Haibin Duan, Beijing University of Aeronautics and Astronautics, Beijing, China

Gianluigi Ferrari, Università di Parma, Parma, Italy

Manuel Ferre, Centre for Automation and Robotics CAR (UPM-CSIC), Universidad Politécnica de Madrid, Madrid, Madrid, Spain

Sandra Hirche, Department of Electrical Engineering and Information Science, Technische Universität München, München, Germany

Faryar Jabbari, Department of Mechanical and Aerospace Engineering, University of California, Irvine, CA, USA

Limin Jia, State Key Laboratory of Rail Traffic Control and Safety, Beijing Jiaotong University, Beijing, China

Janusz Kacprzyk, Systems Research Institute, Polish Academy of Sciences, Warsaw, Poland

Alaa Khamis, German University in Egypt El Tagamoa El Khames, New Cairo City, Egypt

Torsten Kroeger, Stanford University, Stanford, CA, USA

Qilian Liang, Department of Electrical Engineering, University of Texas at Arlington, Arlington, TX, USA

Ferran Martin, Departament d'Enginyeria Electrònica, Universitat Autònoma de Barcelona, Bellaterra, Barcelona, Spain

Tan Cher Ming, College of Engineering, Nanyang Technological University, Singapore, Singapore

Wolfgang Minker, Institute of Information Technology, University of Ulm, Ulm, Germany

Pradeep Misra, Department of Electrical Engineering, Wright State University, Dayton, OH, USA

Sebastian Möller, Quality and Usability Lab, TU Berlin, Berlin, Germany

Subhas Mukhopadhyay, School of Engineering & Advanced Technology, Massey University, Palmerston North, Manawatu-Wanganui, New Zealand

Cun-Zheng Ning, Electrical Engineering, Arizona State University, Tempe, AZ, USA

Toyoaki Nishida, Graduate School of Informatics, Kyoto University, Kyoto, Kyoto, Japan

Federica Pascucci, Dipartimento di Ingegneria, Università degli Studi "Roma Tre", Rome, Italy

Yong Qin, State Key Laboratory of Rail Traffic Control and Safety, Beijing Jiaotong University, Beijing, China

Gan Woon Seng, School of Electrical & Electronic Engineering, Nanyang Technological University, Singapore, Singapore

Joachim Speidel, Institute of Telecommunications, Universität Stuttgart, Stuttgart, Baden-Württemberg, Germany

Germano Veiga, Campus da FEUP, INESC Porto, Porto, Portugal

Haitao Wu, Academy of Opto-electronics, Chinese Academy of Sciences, Beijing, China

Junjie James Zhang, Charlotte, NC, USA

The book series *Lecture Notes in Electrical Engineering* (LNEE) publishes the latest developments in Electrical Engineering - quickly, informally and in high quality. While original research reported in proceedings and monographs has traditionally formed the core of LNEE, we also encourage authors to submit books devoted to supporting student education and professional training in the various fields and applications areas of electrical engineering. The series cover classical and emerging topics concerning:

- Communication Engineering, Information Theory and Networks
- Electronics Engineering and Microelectronics
- Signal, Image and Speech Processing
- Wireless and Mobile Communication
- Circuits and Systems
- Energy Systems, Power Electronics and Electrical Machines
- Electro-optical Engineering
- Instrumentation Engineering
- Avionics Engineering
- Control Systems
- Internet-of-Things and Cybersecurity
- Biomedical Devices, MEMS and NEMS

For general information about this book series, comments or suggestions, please contact [leontina.dicecco@springer.com](mailto:leontina.dicecco@springer.com).

To submit a proposal or request further information, please contact the Publishing Editor in your country:

#### **China**

Jasmine Dou, Associate Editor ([jasmine.dou@springer.com](mailto:jasmine.dou@springer.com))

#### **India**

Swati Meherishi, Executive Editor ([swati.meherishi@springer.com](mailto:swati.meherishi@springer.com))

Aninda Bose, Senior Editor ([aninda.bose@springer.com](mailto:aninda.bose@springer.com))

#### **Japan**

Takeyuki Yonezawa, Editorial Director ([takeyuki.yonezawa@springer.com](mailto:takeyuki.yonezawa@springer.com))

#### **South Korea**

Smith (Ahram) Chae, Editor ([smith.chae@springer.com](mailto:smith.chae@springer.com))

#### **Southeast Asia**

Ramesh Nath Premnath, Editor ([ramesh.premnath@springer.com](mailto:ramesh.premnath@springer.com))

#### **USA, Canada:**

Michael Luby, Senior Editor ([michael.luby@springer.com](mailto:michael.luby@springer.com))

#### **All other Countries:**

Leontina Di Cecco, Senior Editor ([leontina.dicecco@springer.com](mailto:leontina.dicecco@springer.com))

Christoph Baumann, Executive Editor ([christoph.baumann@springer.com](mailto:christoph.baumann@springer.com))

**\*\* Indexing: The books of this series are submitted to ISI Proceedings, EI-Compendex, SCOPUS, MetaPress, Web of Science and Springerlink \*\***

More information about this series at <http://www.springer.com/series/7818>

Pengfei Zhao · Yun Ouyang ·  
Min Xu · Li Yang · Yuhui Ren  
Editors

# Advances in Graphic Communication, Printing and Packaging

Proceedings of 2018 9th China Academic  
Conference on Printing and Packaging

 Springer

*Editors*

Pengfei Zhao  
China Academy of Printing Technology  
Beijing, China

Yun Ouyang  
China Academy of Printing Technology  
Beijing, China

Min Xu  
China Academy of Printing Technology  
Beijing, China

Li Yang  
China Academy of Printing Technology  
Beijing, China

Yuhui Ren  
China Academy of Printing Technology  
Beijing, China

ISSN 1876-1100                      ISSN 1876-1119 (electronic)  
Lecture Notes in Electrical Engineering  
ISBN 978-981-13-3662-1              ISBN 978-981-13-3663-8 (eBook)  
<https://doi.org/10.1007/978-981-13-3663-8>

Library of Congress Control Number: 2019930568

© Springer Nature Singapore Pte Ltd. 2019

This work is subject to copyright. All rights are reserved by the Publisher, whether the whole or part of the material is concerned, specifically the rights of translation, reprinting, reuse of illustrations, recitation, broadcasting, reproduction on microfilms or in any other physical way, and transmission or information storage and retrieval, electronic adaptation, computer software, or by similar or dissimilar methodology now known or hereafter developed.

The use of general descriptive names, registered names, trademarks, service marks, etc. in this publication does not imply, even in the absence of a specific statement, that such names are exempt from the relevant protective laws and regulations and therefore free for general use.

The publisher, the authors and the editors are safe to assume that the advice and information in this book are believed to be true and accurate at the date of publication. Neither the publisher nor the authors or the editors give a warranty, expressed or implied, with respect to the material contained herein or for any errors or omissions that may have been made. The publisher remains neutral with regard to jurisdictional claims in published maps and institutional affiliations.

This Springer imprint is published by the registered company Springer Nature Singapore Pte Ltd. The registered company address is: 152 Beach Road, #21-01/04 Gateway East, Singapore 189721, Singapore

# **2018 9th China Academic Conference on Printing and Packaging and Conference of Scientific Research Innovation**

**Date** November 16–19, 2018

**Location** Jinan, China

## **Sponsors**

China Academy of Printing Technology

Qilu University of Technology (Shandong Academy of Sciences)

## **Support**

Chinese Society for Imaging Science and Technology

## **Organizers**

Beijing Key Laboratory of New Technology of Packaging and Printing, China Academy of Printing Technology

School of Light Industry Science and Engineering, Qilu University of Technology (Shandong Academy of Sciences)

Printing Technology Professional Committee, Chinese Society for Imaging Science and Technology

## **Co-sponsors**

School of Printing and Packaging Engineering, Beijing Institute of Graphic Communication

College of Light Industry and Engineering, South China University of Technology

College of Packaging and Printing Engineering, Tianjin University of Science and Technology

Faculty of Printing, Packaging Engineering and Digital Media Technology, Xi'an University of Technology

School of Media and Design, Hangzhou Dianzi University

School of Printing and Packaging, Wuhan University

Light Industry College, Harbin University of Commerce

College of Communication and Art Design, University of Shanghai for Science and Technology

School of Light Industry and Chemical Engineering, Dalian Polytechnic University

State Key Laboratory of Modern Optical Instrumentation, Zhejiang University

College of Light Industry Science and Engineering, Nanjing Forestry University

College of Bioresources Chemical and Materials Engineering, Shaanxi University of Science and Technology  
School of Biological and Chemical Engineering/School of Light Industry, Zhejiang University of Science and Technology  
College of Engineering, Qufu Normal University  
College of Materials Science and Engineering, Beijing University of Chemical Technology  
School of Packaging and Material Engineering, Hunan University of Technology  
School of Food and Chemical Engineering, Beijing Technology and Business University  
College of Material Science and Engineering, Zhengzhou University  
School of Mechanical Engineering, Tianjin University of Commerce  
Food Science and Engineering College, Beijing University of Agriculture  
School of Materials and Chemical Engineering, Henan University of Engineering  
School of Mechanical Engineering, Jiangnan University  
School of Media and Communication, Shenzhen Polytechnic  
Shanghai Publishing and Printing College  
Department of Graphic Communication Arts, College of Communications, Taiwan University of Arts

## **Conference Executive Committee**

### **Chairman**

Zhao Pengfei (President of China Academy of Printing Technology)

Chen Jiachuan (President of Qilu University of Technology (Shandong Academy of Sciences))

### **Vice Chairman**

Ye Zhuangzhi (Vice President of China Academy of Printing Technology)

Chu Fuqiang (Dean of School of Light Industry Science and Engineering, Qilu University of Technology (Shandong Academy of Sciences))

### **Honorary Chairman**

Qu Desen (Former President of Beijing Institute of Graphic Communication)

Chu Tingliang (Former President of China Academy of Printing Technology, Executive Vice Chairman of the Printing Technology Association of China)

Xu Wencai (Former Vice President of Beijing Institute of Graphic Communication)

Pu Jialing (Chairman of Chinese Society for Imaging Science and Technology)

### **Secretary-General**

Xu Min (Director of Industry Development Research Department, China Academy of Printing Technology)

Lin Maohai (Director of Institute of Printing Engineering, School of Light Industry Science and Engineering, Qilu University of Technology (Shandong Academy of Sciences))

## **Conference Academic Committee**

### **Chairman**

Li Deren (Academician of Chinese Academy of Sciences, Academician of China Engineering Academy, Academician of International Eurasian Academy of Sciences, Academician of New York Academy of Sciences, Academician of International Academy of Astronautics, Professor of Wuhan University, Director of State Key Laboratory of Information Engineering in Surveying, Mapping and Remote)

### **Vice Chairman**

Ni Guangnan (Academician of China Engineering Academy, Researcher of Institute of Computing Technology Chinese Academy of Sciences, Board Chairperson of Chinese Information Processing Society of China)

Chen Kefu (Academician of China Engineering Academy, Professor of South China University of Technology, Director of Academic Committee of State Key Laboratory of Pulp and Paper Engineering)

Zhuang Songlin (Academician of China Engineering Academy, Director and Professor of School of Optical-Electrical and Computer Engineering of University of Shanghai for Science and Technology, Optical Expert)

Lu Bingheng (Academician of Chinese Academy of Engineering, Professor of Xi'an Jiaotong University, Director of the National Engineering Research Center of Rapid Manufacturing)

### **Commissioners**

Andreev Yuri (Head of Moscow State University of Printing Arts)

Bigger Stephen W. (Doctor, Professor, Vice President of Faculty of Engineering and Science of Victoria University)

Cao Congjun (Doctor, Professor of Xi'an University of Technology, Master Student Supervisor)

Cao Guorong (Doctor, Professor of Beijing Institute of Graphic Communication, Master Student Supervisor)

Chen Guangxue (Doctor, Professor of South China University of Technology, Doctoral Supervisor)

Chen Hong (Professor of Beijing Institute of Graphic Communication)

Chen Ping (Doctor, Doctoral Supervisor)

Chen Yunzhi (Doctor, Professor of Tianjin University of Science and Technology, Doctoral Supervisor)

Chopra Kamal (Professor, President of All India Federation of Master Printers)



- Chu Fuqiang (Doctor, Professor of Qilu University of Technology (Shandong Academy of Sciences), Master Student Supervisor)
- Chu Tingliang (Professorial Senior Engineer of China Academy of Printing Technology, Master Student Supervisor)
- Fang Changqing (Doctor, Professor of Xi'an University of Technology, Doctoral Supervisor)
- Gane Patrick (Doctor, Professor of Printing Technology at the School of Chemical Technology, Aalto University)
- Gao De (Professor of Ningbo Institute of Technology, Zhejiang University, Master Student Supervisor)
- Green Phil (Professor of Colour Imaging, London College of Communication)
- Hansuebsai Aran (Doctor, Associate Professor of Chulalongkorn University)
- Hardeberg Jon Yngve (Doctor, Professor of Norwegian University of Science and Technology)
- Hersch Roger D. (Doctor, Professor of Computer Science and Head of the Peripheral Systems Laboratory at the Ecole Polytechnique Fédérale de Lausanne (EPFL))
- Hinkelmann Mathias (Doctor, Professor of Stuttgart Media University)
- Hoffmann-Walbeck Thomas (Professor of the Faculty of Print and Media Technology, Stuttgart Media University)
- Huang Min (Doctor, Professor of Beijing Institute of Graphic Communication)
- Hsieh Yungcheng (Doctor, Professor of Taiwan University of Arts)
- Guinée Jeroen (Doctor, Associate Professor of Leiden University)
- Jin Guobin (Professor of Shanghai University, Vice Director of China Packaging Education Committee)
- Xiao Kaida (Doctor, University Academic Fellow of University of Leeds)
- Kitamura Takashi (Doctor, Professor of Graduate School of Advanced Integration Science, Chiba University)
- Kuang Shijun (Consultant Engineer of China National Pulp and Paper Research Institute, Chief Engineer)
- Lagaron Jose Maria (Doctor, Professor, Leader and Founder of the Group Novel Materials and Nanotechnology for Food Related Applications at the Institute of Agrochemistry and Food Technology of the Spanish Council for Scientific Research)
- Lee Benjamin (Professor, Director of Department of Technology, California State University)
- Li Houbin (Doctor, Professor of Wuhan University, Doctoral Supervisor)
- Li Luhai (Doctor, Professor of Beijing Institute of Graphic Communication, Master Student Supervisor)
- Li Zhijian (Doctor, Professor of Shaanxi University of Science and Technology, Doctoral Supervisor)
- Lin Maohai (Doctor, Associate Professor of Qilu University of Technology (Shandong Academy of Sciences))
- Liu Haoxue (Doctor, Professor of Beijing Institute of Graphic Communication, Master Student Supervisor)

Liu Guodong (Doctor, Associate Professor of Shaanxi University of Science and Technology)

Liu Yanan (Doctor, Engineer of China Academy of Printing Technology)

Liu Zhen (Professor of University of Shanghai for Science and Technology, Doctoral Supervisor)

Lu Dongming (Doctor, Professor of Zhejiang University, Doctoral Supervisor)

Luo M Ronnier (Doctor, Professor of University of Leeds, Director of Color and Image Science Center)

Ma Xiufeng (Professor of Qufu Normal University, Master Student Supervisor)

Pan Zhigeng (Doctor, Professor of Hangzhou Normal University)

Pienaar Pierre (Professor, President of the World Packaging Organization)

Piergiovanni Luciano (Professor of the Department of Food, Environmental and Nutritional Sciences, Faculty of Agricultural and Food Sciences, University of Milan)

Poovarodom Ngamtip (Doctor, Associate Professor of Department of Packaging and Materials Technology of Faculty of Agro-Industry, Kasetsart University)

Pu Jialing (Doctor, Professor of Beijing Institute of Graphic Communication, Doctoral Supervisor)

Ren Penggang (Doctor, Professor of Xi'an University of Technology, Master Student Supervisor)

Roos Alexander (Professor of Stuttgart Media University)

Shi Ruizhi (Doctor, Professor of Zhengzhou Institute of Surveying and Mapping, Doctoral Supervisor)

Sun Jiazhen (Doctor, Vice Professor of Qilu University of Technology (Shandong Academy of Science))

Sun Zhihui (Professor of Harbin University of Commerce, Doctoral Supervisor)

Tang Zhengning (Doctor, Professor of Jiangnan University, Master Student Supervisor)

Teleman Anita (Doctor, Research Manager of Printing Solutions at the Research Institute Innventia, Sweden)

Teng Yuemin (Professor of Shanghai Publishing and Printing College)

Tsyganenko Alexander (Professor of Media Industry Academy)

Urban Philipp (Head of Emmy-Noether Research Group, Institute of Printing Science and Technology, Technische Universität Darmstadt)

Vogl Howard E. (Visiting Professor of Rochester Institute of Technology)

Wan Xiaoxia (Doctor, Professor of Wuhan University, Doctoral Supervisor)

Wang Haiqiao (Doctor, Professor of Beijing University of Chemical Technology, Doctoral Supervisor)

Wang Jianqing (Professor of Tianjin University of Science and Technology, Doctoral Supervisor)

Wang Lijie (Professor of Shenzhen Polytechnic)

Wang Qiang (Doctor, Professor of Hangzhou Dianzi University, Doctoral Supervisor)

Wang Yiqing (Doctor, Professor of Xi'an Jiaotong University)

Wei Xianfu (Doctor, Professor of Beijing Institute of Graphic Communication, Doctoral Supervisor)

Wei Yuchang (Professor of Chinese Culture University)

Wu Jimei (Doctor, Professor of Xi'an University of Technology, Doctoral Supervisor)

Xie Punan (Professor of Beijing Institute of Graphic Communication)

Xin Xiulan (Doctor, Professor of Beijing Technology and Business University, Master Student Supervisor)

Xu Jinlin (Professor of Xi'an University of Technology)

Xu Wencai (Professor of Beijing Institute of Graphic Communication, Doctoral Supervisor)

Yang Bin (Doctor, Researcher of Peking University)

Yao Haigen (Professor of Shanghai Publishing and Printing College)

Yin Yadong (Doctor, Professor of University of California, Riverside)

Zhang Haiyan (Professor of Xi'an University of Technology, Master Student Supervisor)

Zhao Pengfei (Senior Engineer of China Academy of Printing Technology)

Zhao Xiuping (Professor of Tianjin University of Science and Technology, Master Student Supervisor)

Zhou Shisheng (Doctor, Professor of Xi'an University of Technology, Doctoral Supervisor)

Zou Yingquan (Doctor, Professor of Beijing Normal University, Doctoral Supervisor)

### **Reviewers**

An Li (Doctor, Teacher of Beijing Institute of Graphic Communication)

Cao Congjun (Doctor, Professor of Xi'an University of Technology)

Chen Guangxue (Doctor, Professor of South China University of Technology)

Chu Fuqiang (Doctor, Professor of Qilu University of Technology(Shandong Academy of Sciences))

Du Bin (Doctor, Associate Professor of Beijing University of Agriculture)

Fang Yi (Doctor, Teacher of Beijing Institute of Graphic Communication)

Fu Yabo (Doctor, Associate Professor of Beijing Institute of Graphic Communication)

Gao Shanshan (Doctor, Associate Professor of Qingdao University of Science and Technology)

Gu Chong (Doctor, Associate Professor of Tianjin University of Science and Technology)

He Minghui (Doctor, Teacher of South China University of Technology)

Huang Junyan (Master, Professor of Dalian Polytechnic University)

Huang Zhen (Doctor, Professor of Tianjin University of Commerce)

Huo Lijiang (Professor of Dalian Polytechnic University)

Jiang Xiaoshan (Doctor, Associate Professor of Beijing Institute of Graphic Communication)

Jin Yang (Doctor, Professor of Beijing Institute of Graphic Communication)

Li Shi (Doctor, Teacher of Hangzhou Dianzi University)  
Li Shuangyang (Doctor, Teacher of Beijing Technology and Business University)  
Li Xiaozhou (Doctor, Associate Professor of Qilu University of Technology (Shandong Academy of Sciences))  
Li Zhijiang (Doctor, Associate Professor of Wuhan University)  
Liang Jing (Post Doctor, Lecturer of Dalian Polytechnic University)  
Lin Maohai (Doctor, Associate Professor of Qilu University of Technology (Shandong Academy of Sciences))  
Liu Guodong (Doctor, Associate Professor of Shaanxi University of Science and Technology)  
Liu Haoxue (Doctor, Professor of Beijing Institute of Graphic Communication)  
Liu Qiang (Doctor, Associate Professor of Wuhan University)  
Liu Yanan (Doctor, Engineer of China Academy of Printing Technology)  
Liu Zhuang (Doctor, Associate Professor of Harbin University of Commerce)  
Luo Rubai (Post Doctor, Teacher of Xi'an University of Technology)  
Mo Lixin (Doctor, Associate Professor of Beijing Institute of Graphic Communication)  
Mou Xinni (Doctor, Associate Professor of Tianjin Vocational Institute)  
Qi Wenfa (Master, Senior Engineer of Institute of Computer Science and Technology of Peking University)  
Shi Ruizhi (Doctor, Professor of Zhengzhou Institute of Surveying and Mapping)  
Si Zhanjun (Professor of Tianjin University of Science and Technology)  
Sun Zhaonan (Doctor, Teacher of Beijing Information Science and Technology University)  
Wang Haiqiao (Doctor, Professor of Beijing University of Chemical Technology)  
Wang Mengmeng (Post Doctor, Member of International Colour Association)  
Wang Qiang (Doctor, Professor of Hangzhou Dianzi University)  
Wang Yigang (Doctor, Professor of Hangzhou Dianzi University)  
Wei Xianfu (Post Doctor, Professor of Beijing Institute of Graphic Communication)  
Xie Dehong (Doctor, Teacher of Nanjing Forestry University)  
Xin Xiulan (Doctor, Professor of Beijing Technology and Business University)  
Xu Zhuofei (Doctor, Teacher of Xi'an University of Technology)  
Ye Changqing (Doctor, Associate Professor of Suzhou University of Science and Technology)  
Zhang Erhu (Doctor, Professor of Xi'an University of Technology)  
Zhang Fazhong (Doctor, Engineer of China Academy of Printing Technology)  
Zhang Zhengjian (Doctor, Associate Professor of Tianjin University of Science and Technology)  
Zheng Yuanlin (Doctor, Associate Professor of Xi'an University of Technology)  
Zhong Yunfei (Doctor, Professor of Hunan University of Technology)  
Zhu Ming (Doctor, Associate Professor of Henan Institute of Engineering)

# Preface

“2018 9th China Academic Conference on Printing and Packaging and Conference of Scientific Research Innovation”, one of the series “China Academic Conference on Printing and Packaging” which is mainly hosted by China Academy of Printing Technology, was held on 16–19 November 2018, in Jinan, China. The conference was co-hosted by China Academy of Printing Technology and Qilu University of Technology (Shandong Academy of Sciences) and co-organized by Beijing Key Laboratory of New Technology of Packaging and Printing of China Academy of Printing Technology, School of Light Industry Science and Engineering of Qilu University of Technology (Shandong Academy of Sciences) and Printing Technology Professional Committee of Chinese Society for Imaging Science and Technology.

By far, “China Academic Conference on Printing and Packaging (CACPP)” and its series of events have been held for nine sessions since the first session in 2010, and have already become the most influential academic exchange activities in printing and packing fields in China.

Scientific research and innovation is playing a more and more important role in the development of enterprises and the whole country; the technology content is higher and higher in printing and packaging fields. In order to promote the transformation and application of research results in the actual production, the conference also hosted “Conference of Scientific Research Innovation” and set up the exchange session between the enterprise technology demands and scientific results of universities, to explore new ideas and new approaches of industrialization of scientific research application, to widen research channel of the innovation technical teams and the research institutes, to accelerate comprehensive collaborative innovation in production, education, research and application, to create printing and packaging industry innovation chain and to realize comprehensive promotion of innovation capacity building in printing and packaging fields.

In recent years, the printing and packaging industry of China has been keeping a stable growth. In 2017, the total output value of China printing industry has topped to RMB 1205.77 billion, increasing by 4.6%, the speed of development has

bottomed out and rebounded, the trend of controlling quantity and improving quality is obvious, the new kinetic energy keeps growing, and the new window period effect is emerging.

The conference invited Kaida Xiao, Associated Professor from University of Leeds, England, TC 8-17 Technical Chairman from International Light Association; Jeroen Guinée, Associated Professor from Leiden University, the Netherlands; Aran Hansuebsai, Associated Professor from Chulalongkorn University, Thailand; Zhigeng Pan, Professor from Hangzhou Normal University and Vice Chairman from China Society of Image and Graphics (CSIG) to make keynote speeches “Colour Image Reproduction for 3D Printing”, “Life Cycle Assessment of Packaging; Past, Present and Future”, “Printability of an Aqueous Based Nano-Silver Ink for Fabrication of Conductive Lines” and “Research Development of VR/AR and its Application in Publishing”. Moreover, the conference also invited distinguished Vice Prof. Sun Jiazhen from Qilu University of Technology (Shandong Academy of Sciences), Prof. Wei Wu from Wuhan University, Prof. Changqing Fang from Xi’an University of Technology, Prof. Min Huang from Beijing Institute of Graphic Communication, Associate Prof. Guodong Liu from Shaanxi University of Science and Technology, Dr. Yanan Liu from China Academy of Printing Technology as outstanding young scholars to make speeches, respectively. At the same time, the participants had oral presentations, academic exchanges and latest research achievement communication on colour science, image processing, digital media, printing innovation materials, packaging innovation materials, etc., on four panel discussion meetings.

The conference received 236 papers this year, among which 138 were selected to be published on Lecture Notes in Electrical Engineering (LNEE) (ISSN: 1876-1100) by Springer.

Here, we greatly acknowledge all the organizations that offered great support for the conference, and they are: the Printing Technology Association of China, Chinese Society for Imaging Science and Technology, School of Printing and Packaging Engineering of Beijing Institute of Graphic Communication, School of Printing and Packaging of Wuhan University, College of Communication and Art Design of University of Shanghai for Science and Technology, School of Media and Design of Hangzhou Dianzi University, College of Light Industry and Engineering of South China University of Technology, Faculty of Printing, Packaging Engineering and Digital Media Technology of Xi’an University of Technology, Light Industry College of Harbin University of Commerce, College of Packaging and Printing Engineering of Tianjin University of Science and Technology, State Key Laboratory of Modern Optical Instrumentation of Zhejiang University, School of Mechanical Engineering of Jiangnan University, School of Light Industry and Chemical Engineering of Dalian Polytechnic University, School of Packaging and Material Engineering of Hunan University of Technology, School of Biological and Chemical Engineering/School of Light Industry of Zhejiang University of Science and Technology, College of Engineering of Qufu Normal University, School of Mechanical Engineering of Tianjin University of Commerce, Food Science and Engineering College of Beijing University of Agriculture, School

of Materials and Chemical Engineering of Henan University of Engineering, College of Light Industry Science and Engineering of Nanjing Forestry University, College of Bioresources Chemical and Materials Engineering of Shaanxi University of Science and Technology, College of Materials Science and Engineering of Beijing University of Chemical Technology, College of Material Science and Engineering of Zhengzhou University, School of Food and Chemical Engineering of Beijing Technology and Business University, Shenzhen Polytechnic, Shanghai Publishing and Printing College, College of Communications of Taiwan University of Arts.

We would like to express our gratitude to the 40 experts from China, Germany, Britain, American and Japan for reviewing and recommending papers for the conference with strict standards.

We also thank Springer for offering us an international platform for publishing.

We look forward to our reunion at 2019 10th China Academic Conference on Printing and Packaging.

Jinan, China  
October 2018

Edited by  
Beijing Key Laboratory of New Technology  
of Packaging and Printing  
China Academy of Printing Technology

# Contents

<b>Part I Color Science and Technology</b>	
<b>Testing Performance of Whiteness Formulas</b> . . . . .	3
Yuzhao Wang, Xi Lv, and Ming Ronnier Luo	
<b>Spectral Power Distributions with High Gamut-based Metric Values</b> . . . . .	9
Zheng Huang, Hongyu Lin, Bisheng Wu, Weiming Wang, and Qiang Liu	
<b>Effect of Backgrounds with Different Lightness on the Color Appearance of Printed Samples</b> . . . . .	16
Ruili He, Min Huang, Chunli Guo, Yonghui Xi, and Yu Liu	
<b>Reviews on Observer Metamerism and Individual Color Vision Variability</b> . . . . .	23
Qianwen Chen, Lu Feng, Yalin Li, and Shengyan Cai	
<b>Study on the Constancy of Color Vision</b> . . . . .	31
Haiwen Wang, Jie Li, Xiaoxia Wan, Ling Lu, Pengfei Wang, and Yongwei Wang	
<b>Research on Digital Printing Color Prediction Model Based on PSO-BP Neural Network</b> . . . . .	37
Siwei Lu, Qiang Wang, Ping Yang, and Weiyan Zhang	
<b>Research on the Atmosphere and Emotionality of Apparel Stores Under LED Lighting Environment</b> . . . . .	44
Liang Sun, Jing Liang, Ze Liu, and Yuanming Zhang	
<b>Research on the Antagonism Mechanism of Human Color Vision</b> . . . . .	50
Shengwei Yang, Xiangyang Xu, and Lingjun Kong	



**Study on the Faded Model of Painting Substrate Based on Chemical Kinetics** . . . . . 57  
Ling Cai, Guangxue Chen, and Zhen Liu

**Color Prediction Model for Flexographic Prints Based on Spectral Reflectance** . . . . . 66  
Dongwen Tian, Zhonghua Yu, and Jinghuan Ge

**Natural and Preferred White on Displayed Images Under Varying Ambient Illuminants** . . . . . 72  
Mingkai Cao and Ming Ronnier Luo

**Testing Cone-Cell Response of Young and Old Observers by Using Nearly Metameric Samples** . . . . . 80  
Yonghui Xi, Min Huang, Ruili He, Chunli Guo, and Ning Ding

**Effect of Printed Color Sample Separation and Color-Difference Magnitude on Perceived Color Difference** . . . . . 87  
Ting Xu, Guihua Cui, Lan Jiang, Ming Ronnier Luo, Fereshteh Mirjalili, and Jan Morovic

**Objective Colour Quality Assessment for Lighting** . . . . . 93  
Weiming Wang, Shuai Gao, Hongyu Lin, Ying Liu, and Qiang Liu

**The Performance of Different Whiteness Formulas for White Papers** . . . . . 102  
Chunli Guo, Xiaoyan Zuo, Yu Liu, Ruili He, Yonghui Xi, and Min Huang

**Measurement and Evaluation of the Surface Color of 3D Paper Product** . . . . . 108  
Mingming Cui, Xiaozhou Li, Guangyuan Wu, and Qian Cao

**Evaluating the Quality of Color Profiles for Output Devices** . . . . . 114  
Ping Yang, Zizhao Wu, Yong Wang, Siwei Lu, Weiyan Zhang, and Qiang Wang

**Research on the Soft Proofing Technology Based on Substrate-Corrected Colorimetric Aims** . . . . . 120  
Jinghuan Ge, Enyin Fang, and Dongwen Tian

**Quantitative Analysis Method of Color Gamut Difference Between Digital Image Originals** . . . . . 127  
Wenda Jin, Qiang Wang, and Jing Cao

**Analysis on the Basic Color Database of Shaanxi Fengxiang Woodcut New Year Pictures** . . . . . 135  
Jie Du and Wanyi Mu

<b>Analysis of the Color of Qin Qiong and Jing De Door-God Picture of Taohuawu and Fengxiang</b> .....	144
Jie Du and Yawen Wang	
<b>Review of Anti-counterfeiting of Prints Based on Infrared Spectroscopy</b> .....	150
Ge Yang, Zhenxin Guo, Zengqi Bao, Jiawei Zhao, Dongsheng Jiang, and Liang Yan	
<b>Research on Reproduction of Brand Colors Based on Hi-Fi Color Printing</b> .....	157
Yan Liu, Ping Gu, and Songtao Li	
<b>Study of the Morphological Character of Spectral Reflectance of UV Flexpress in Different Conditions</b> .....	163
Quanhui Tian, Bo Zhang, Ping Gu, and Shenwei Yang	
<b>Effect of Lens on Spectral Characteristics of Imaging System</b> .....	170
Lan Jiang, Guihua Cui, and Ting Xu	
<b>Color Correction Method of Digital Printing Based on Local Polynomial</b> .....	178
Ping Dai and Jieyue Yu	
<b>Part II Image Processing Technology</b>	
<b>Dual Anti-counterfeiting of QR Code Based on Information Encryption and Digital Watermarking</b> .....	187
Yijing Xun, Zhijiang Li, Xiaolu Zhong, Sheng Li, Jiawang Su, and Ke Zhang	
<b>A Multi-metrics Integrated FR IQA Method Based on Machine Learning</b> .....	197
Zhenhua Pan, Jinhua Xiao, Liying Sun, and Yehong Chen	
<b>A Printing Image Restoration Method for Multiple Degradation Factors</b> .....	206
Xiaochun Li, Yuanyuan Zhang, and Ming Zhu	
<b>Objective Aesthetic Quality Assessment for Photos</b> .....	211
Qichuang Zeng and Quanxiang Liu	
<b>Design and Analysis of Switch Median Filters for Salt and Pepper Noise</b> .....	220
Ming Zhu, Bowei Liu, Mengfei Wang, and Yu Lu	
<b>Color Transfer Based on Visual Saliency</b> .....	227
Minghua Fan, Zhijiang Li, and Jiaxian Long	

**Small-Scale Image Inpainting on Mobile Platform** . . . . . 233  
Chen Shao, Qiang Wang, and Shi Li

**Multiple Reference Images Color Transfer Based on Improved GMM Model** . . . . . 241  
Zhenshan Tan, Zhijiang Li, Yanhao Li, and Liqin Cao

**Influence of Image Noise on Digital Photo Definition** . . . . . 250  
Jing Geng, Congjun Cao, and Yonghong Qi

**An Improved Image Denoising Algorithm in Wavelet Domain** . . . . . 258  
Zhongmin Jiang and Yingmei Zhou

**Research on Adaptive Face Recognition Algorithm Under Low Illumination Condition** . . . . . 266  
Anning Yang, Qiang Wang, and Jing Cao

**Research on 3D Printing Color Image Processing of Micro-lens Combined with Micrographics** . . . . . 273  
Yaojian Hu, Liyu Liao, Zhaohui Yu, and Yunfei Zhong

**Image Quality Evaluation of Digital-Analog Imaging System** . . . . . 284  
Yuliya Kim, Qiang Wang, and Jing Cao

**Comparison of Grayscale Image Colorization Methods in Different Color Spaces** . . . . . 291  
Liqin Cao, Yongxing Shang, Jianjun Zhao, and Zhijiang Li

**Research on Evaluation Method of Scanner Imaging Quality** . . . . . 301  
Zhuoran Zhang, Qiang Wang, and Weiyan Zhang

**High-Simulation Oil-Painting-Style Images Based on Stroke Characteristics** . . . . . 309  
Jing Geng, Congjun Cao, and Yonghong Qi

**High-Efficiency Image Color Gamut Mapping Based on Spherical Coordinates** . . . . . 318  
Shiwei Liu, Junfeng Li, Quanhui Tian, and Ming Zhu

**Innovative Research on Image Processing Based on Replication of Chinese Painting and Calligraphy** . . . . . 325  
Jinglin Ma

**Part III Digital Media Technology**

**Application of Augmented Reality in Product Package with Quick Response Code** . . . . . 335  
Haoming Li and Zhanjun Si

**Restricted Chinese Natural Language Analysis Based on Dependency Grammar Model** . . . . . 343  
 Yongxing Shang, Zhijiang Li, Liqin Cao, and Tian Song

**HTML5-Based Tools Management Mobile Application the Implementation in the WeChat Public Platform** . . . . . 352  
 Qingjie Lin, Caifeng Liu, and Wei Wang

**Technical Research of Clearing Floating Effect in CSS Cascading Style Sheets** . . . . . 359  
 Jing Wang and Zhanjun Si

**Research on Multithreaded Download and Local File Operation of HTML5 Browser** . . . . . 365  
 Wei Wang, Aibin Huang, and Caifeng Liu

**Application of Multi-target Tracking Technology for Packing Box** . . . . . 370  
 Shenghui Li, Ruizhi Shi, Siyang Liu, and Dongling Zhao

**Research on Mobile Terminal Augmented Reality Application for Cultural Heritage** . . . . . 378  
 Lichan Zhang, Qiang Wang, Jing Cao, and Yan Shi

**Research on Addressing Method in XML File Based on XPointer** . . . . . 384  
 Chanyuan Fan and Zhijiang Li

**Design and Development of Network Printing Exhibition** . . . . . 390  
 Yanxing Liu, Yusheng Lian, Yang Jin, Xiaojie Hu, and Zhuangzhuang Xiong

**Design and Implementation of Salary Management System for Printing Enterprises** . . . . . 396  
 Yuke Huo, Wenjie Yang, Peipei Ran, Chunli Guo, Yanxing Liu, Ge Yang, and Shaozhong Cao

**Design of Instant Messaging Software in Printing Enterprise Based on Web** . . . . . 403  
 Peipei Ran, Wenjie Yang, Yuke Huo, Zhongyue Da, and Shaozhong Cao

**Design and Making of Sudoku Game Based on Unity3D** . . . . . 410  
 Xinhui Xie, Zhanjun Si, and Shan Zhang

**Researching an Effective Interactive E-Book for Programming Courses** . . . . . 416  
 Ying Hu and Huiqiang Lyu

**Research and Design of Mobile Terminal APP for Fengxiang Woodcut New Year Picture Based on the Protection of Intangible Cultural Heritage** ..... 421  
 Jie Du and Yujia Gao

**How Conventional Printers Lead into Customized Web-to-Print** ..... 436  
 Yungcheng Hsieh, Mingchw Wei, and Xinyi Wong

**Study of Cultural Creative Merchandises of Museums and Cultural Heritage** ..... 447  
 Mingchw Wei, Tzuhan Chen, and Yungcheng Hsieh

**Implementation of Responsive Web Page Layout Based on Media Query and Flexible Box Model** ..... 452  
 Jingru Zhang, Caifeng Liu, and Aibin Huang

**Part IV Printing Engineering Technology**

**Effect of Pretreatment Methods to Cotton Fabrics on Printing Conductive Patterns** ..... 461  
 Meijia Yan, Zhiqing Xin, Shouzheng Jiao, Feilong Li, and Luhai Li

**Research on Inkjet Printing Three-Dimensional Electrode Structure of Supercapacitors** ..... 467  
 Bo Cui, Fuqiang Chu, Jiazhen Sun, and Chenghu Yun

**Research of 3D Printing Self-support Technology Based on DFM** ..... 473  
 Meng Li, Linlin Liu, Qiumin Wu, Xiang Liu, and Jie Ma

**Application Research of Nano Silver Conductive Ink in Flexographic Printed RFID Antenna** ..... 480  
 Zhenxin Guo, Ge Yang, Woye Zhang, Qi Liu, Lixin Mo, and Luhai Li

**Research on Load Balancing Algorithm of Flexographic Printing Job-Shop Based on Group Technology** ..... 488  
 Huailin Li, Shisheng Zhou, and Rubai Luo

**Research on Cutting-Bonding Process of Powder Based 3D Printing Model** ..... 495  
 Xiaochun Wang, Guangxue Chen, Jiangping Yuan, and Ling Cai

**Research on Influencing Factors of Conductivity of Screen Printed Circuits** ..... 501  
 Xi Li, Aijing Gao, Lihong Cao, Fan Su, and Luhai Li

**Research on the Factors of 3D Printing Forming Time Based on G-Code File** ..... 507  
 Qian Deng, Qinghui Tang, Siyang Liu, and Ruizhi Shi

**Design and Realization of a Support Bracket for Medical Test Tubes Based on 3D Printing** . . . . . 513  
 Chunmei Li, Ying Xiao, and Liang Zheng

**Research on the Printability of Pearl Inkjet Photo Paper with Nano-copper Flexography Ink** . . . . . 521  
 Jinghan Liu, Lai Peng, and Yi Fang

**Feasibility Study of Flexographic Platemaking Based on SLA 3D Printing Technology** . . . . . 528  
 Liang Zheng, Lingjun Kong, and Chunmei Li

**Study on the Influence of Back Exposure on the Quality of Flexographic Platemaking** . . . . . 535  
 Lingjun Kong, Miao Tan, and Liang Zheng

**Research on the Solid Screening with Microcell Technology in the Flexographic Printing** . . . . . 543  
 Enyin Fang and Jinghuan Ge

**Design and Application of Intelligent Plate Making Process for Box Packaging and Printing** . . . . . 551  
 Yongfa Feng, Lihe Zhu, Zhihui Liu, and Xin Wang

**Application of Situational Awareness Decision in Intelligent Situation Printing System** . . . . . 559  
 Rubai Luo, Shasha Gao, Huailin Li, Shisheng Zhou, Haoran Fang, and Yumeng Liu

**Design of Online Variable Data Printing Jobs Production System Based on Cloud-Platform** . . . . . 564  
 Rubai Luo, Xueying Fan, Shisheng Zhou, Yunjie Shi, Haiying Jiang, and Yuxiang Zhu

**Gravable Printing Plate Surface Defect Intelligent Detection Method** . . . . . 569  
 Yechi Pang, Zhuangzhi Ye, and Zhijie Li

**Research on Fractional Lower Order Feature Extraction of Bearing Vibration Signals Under Alpha Stable Noise Conditions** . . . . . 580  
 Qianqian Xu, Kai Liu, and Zhuofei Xu

**Study on the Operational Characteristics of Offset Press** . . . . . 587  
 Peng Liu, Zhuofei Xu, and Heping Hou

## **Part V Packaging Engineering Technology**

<b>Development and Application Prospect of Functional Packaging Materials</b> .....	597
Hui Liu, Dongli Li, Wencai Xu, and Yunzhi Chen	
<b>Application of Functionally Integrated Modified Atmosphere Packaging Design in Preservation of Nanguo Pears at Room Temperature</b> .....	603
Jiachun Ma, Da Yang, Min Zhang, Dongli Li, and Wencai Xu	
<b>Effects of Edible Chitosan Coating on Postharvest Quality of Zigui Navel Orange</b> .....	609
Jinli Li, Yuye Zhong, Shaoyun Huang, Ting Guo, Li Cheng, and Houbin Li	
<b>Study on the Cold Storage Agent for Food Insulation Packaging</b> .....	620
Fangfang Lu, Baoying Wang, Qingbao Wei, and Jingzhou Wang	
<b>Design and Development of Alcohol Packaging Anti-counterfeiting System Based on Augmented Reality Technology</b> .....	629
Wenjie Yang, Li Liu, Yating Wang, and Yunfei Zhong	
<b>Study on the Cushion Performance of the Cushion Material Composed of EPE and Honeycomb Paperboard</b> .....	636
Xiaoli Song, Gaimei Zhang, Yue Cao, and Qiyang He	
<b>Study on Life Cycle Inventory Analysis of Folding Carton</b> .....	644
Mengting Li, Guorong Cao, and Lizheng Zhang	
<b>A Survey of the Most Acceptable Handle for Express Boxes</b> .....	652
Yingzhe Xiao and Huiwen Meng	
<b>Automated Box Buckling Strength Analyses with Finite Element Modeling</b> .....	660
Shane Johnson, Liping Kang, Haihua Ou, Zeeshan Qaiser, and Jorge Macort	
<b>Experimental Study on Material Matching for Corrugated Board Box of Lithium Battery</b> .....	666
Chenyang Liu, Lijiang Huo, Wanping Zhan, and Yizhe Tian	
<b>Stress Analysis of the Glass Cup in the Process of Falling Based on the Finite Element Method</b> .....	671
Xiaoli Song, Gaimei Zhang, Lizheng Zhang, Yue Cao, and Changhe Li	
<b>Analysis on Stress of Laptop and Cushion During Drop Using Finite Element Method</b> .....	678
Gaimei Zhang, Xiaoli Song, Fan Su, Yue Shi, Yue Cao, Yi Jiang, and Xue Han	

**Part VI Paper and Related Technology**

- Influence of Nano-silica on Inkjet Paper Coating** ..... 689  
Huanmei Wang, Yunzhi Chen, and Zhengjian Zhang
- Study of the Influence of Styrene-Acrylic Emulsion for Advanced Calligraphy Paper Performance** ..... 697  
Xiaoxiu Hao, Ziyu Xing, Tong Wang, and Changhong Liu
- Preparation of a Surface Sizing Agent of Dialdehyde Chitosan/Cationic Starch and Barrier Property** ..... 704  
Yong Lv, Ci Song, Qiuqian Xu, and Yusheng Yu
- Study on the Correlation Between Surface Properties of Paper and Printing Tonal Gradation by Grey Correlation Method** ..... 710  
Li Cheng
- Facile Strategy for the Fabrication of Superhydrophobic Coatings on the Surface of Paper** ..... 717  
Qing Wang, Guangxue Chen, Zhaohui Yu, and Mingguang Yu
- Research on the Influence of Optical Properties of Paper on the Ink-Jet Printing Color** ..... 723  
Yonghong Qi and Boqi Wu
- Standard Test Analysis of Edgewise Crush Resistance and Bursting Strength of Corrugated Board** ..... 730  
Yafang Feng, Guorong Cao, Lizheng Zhang, Meiqi Yang, and Mengting Li

**Part VII Ink and Related Technology**

- Application of Anthracene-Based Fluorescent Materials on Green Fluorescent Inkjet Ink** ..... 739  
Wan Zhang, Hui Kuang, Yingjie Xu, Hui Wang, Beiqing Huang, and Xianfu Wei
- Preparation of Low Temperature Sintered Graphene/Silver Nanocomposite-Based Conductive Ink** ..... 751  
Qingqing Zou, Congjun Cao, Huayang Zhu, and Chengmin Hou
- Research of Inkjet Printing of Water-Based Inkjet Ink for the Curved Surface** ..... 759  
Pengfei Zhao, Pingping Zhang, Xiaoli Liu, Kai Huang, Zhuangzhi Ye, and Yanan Liu
- Preparation and Photopolymerization Kinetics of UV-Curable Fluorescent Inks Doped with Quantum Dots** ..... 769  
Hui Wang, Le Ma, Bin Yang, Wan Zhang, Beiqing Huang, and Xianfu Wei



<b>Preparation and Research of Acrylate Latex</b> .....	778
Yingying Li, Xiulan Xin, and Xitong Mao	
<b>Study on Performance of Nano-silver Conductive Inkjet Printed Circuits</b> .....	783
Kaiyang Sang, Maohai Lin, Chenhang Zhang, Ben Liu, Zhijin Li, and Meiqi Lin	
<b>Research on Electrophoretic Display Ink and Its Microencapsulation</b> .....	788
Aijing Gao, Meijuan Cao, Jia Yan, Luhai Li, Xi Li, Shouzheng Jiao, and Tianshu Zhao	
<b>Preparation and Characterization of Nano-TiO<sub>2</sub>/SiO<sub>2</sub> Composite Particles</b> .....	794
Bin Du, Kenan Yang, Rubai Luo, Qiqi Li, Feng Chen, Haibin Li, Ying Yang, and Shisheng Zhou	
<b>Study on Storage Stability of Waterborne Gravure Ink and Adhesion on PET/BOPP Film Surface</b> .....	800
Wei Sun, Ying Du, Xiaoyu Li, and Haiqiao Wang	
<b>Preparation and Application in Ink of Aromatic Microspheres</b> .....	806
Shouzheng Jiao, Zhicheng Sun, Dongsheng Li, Furong Li, Qian Li, Nan Yang, Xiaoliang Zhang, and Luhai Li	
<b>Effect of 2,2-Bis(Hydroxymethyl) Propionic Acid Content on the Properties of Aqueous Polyurethane</b> .....	813
Nan Song, Xiulan Xin, and Bin Li	
<b>A New Synthesis Method of Hyperbranched Polyurethane Acrylate for Conductive Ink</b> .....	819
Xinya Du, Qifeng Chen, and Guangxue Chen	
<b>Research on Printing and Prototyping Performance of Three-Dimensional Printing Materials for UV-Curing Ink-Jet</b> .....	827
Beiqing Huang, Yueqiu Lü, Le Ma, Xianfu Wei, and Hui Wang	
<b>Preparation of High Performance Poly (3,4-Ethylenedioxythiophene) Nanoparticles Ink and Its Inkjet Printability</b> .....	840
Ting Chen, Linjuan Yan, Rong Liu, Wei Zhong, and Guangxue Chen	
<b>Evaluation of Monomer Performance for UV-LED Inkjet Inks</b> .....	850
Rongxia Bu, Shiyong Luo, and Xiao Liu	
<b>Study on Curing Rate of Color 3D Printing Materials</b> .....	856
Le Ma, Beiqing Huang, Bin Yang, Yidong Zhao, Kangshi Qin, and Xianfu Wei	

<b>Study on Pretreatment of Non-permeable Substrate Used for Printing Conductive-Ink</b> . . . . .	863
Rui Zhou, Zhiqiang Gao, Xintang Liu, and Rui Niu	
<b>Part VIII Film and Related Material Technology</b>	
<b>Preparation and Characterization of Non-woven Blend Membrane from CA and PES in DMAc/LiCl</b> . . . . .	873
Aiai Wang and Zhonghua Sun	
<b>Nanocellulose Prepared from Cassava Residues by Mechanochemical Method and Its Hydrophobic Modification</b> . . . . .	882
Yinghan Shi, Guangxue Chen, Qifeng Chen, and Lijie Huang	
<b>Effects of Lignin on Properties of Hemicellulose/Methyl-Cellulose Composite Films</b> . . . . .	890
Lingxiao Liu, Maohai Lin, Guichun Hu, Meiqi Lin, and Zhengpeng Wu	
<b>A Comparison Study on Thermal Degradation of Two Different Poly (Lactic Acid)/Metal Oxide Hybrids</b> . . . . .	896
Xiaojie Wang and Zhen Huang	
<b>Preparation and Properties of PET/PE Solvent-Free Laminated Packaging Films</b> . . . . .	902
Pengfei Guo, Yabo Fu, Xijin Cui, Jinjin Zuo, Youzhong Zhao, and Wencai Xu	
<b>Transparency Research of Poly(L-lactide) Films and Its Modified Films</b> . . . . .	907
Xiaohui Zhang and Wenjuan Gu	
<b>Study on Physical Properties of Degradable Polylactic Acid Packaging Film</b> . . . . .	914
Yingying Qin and Hongge Guo	
<b>Preparation and Characterization of Conductive Films Based on Nanocrystalline Cellulose</b> . . . . .	920
Hao Zhang and Liang Hong	
<b>Study on Preparation and Properties of Paper Plastic Laminatings Based on PVP and PVA</b> . . . . .	928
Meiqi Yang, Guorong Cao, Peiyu Fu, and Lizheng Zhang	
<b>Research on Migration of Butylated Hydroxytoluene from Polyethylene Packaging Materials</b> . . . . .	935
Yan Zhang, Meng Tao, and Qingbao Wei	

## **Part IX Novel Functional Material Technology**

<b>Synthesis of 6-[3,6,7,10,11-Pentakis(pentyloxy)triphenylen-2-yloxy]-hexyl Methacrylate and Its Mesophases Study</b> .....	943
Yuwen Feng, Jingze Bi, Huanzhi Yang, Zhenhu Zhang, Chunxiu Zhang, and Jialing Pu	
<b>Effect of Lignin Content on the Degradation of the Composite Material Prepared from Thermoplastic Starch and Sugarcane Pith</b> .....	949
Yali Wu, Yanna Lv, Maocheng Deng, and Beihai He	
<b>Fabrication of High Conductivity Polyurethane/Polyaniline Composite Coating Based on In-Situ Polymerization</b> .....	958
Xuekai Gao and Fuqiang Chu	
<b>Study of Extinction Characteristics of Au–Ag Nanosphere Periodic Array</b> .....	964
Jun Wang, Chunyu Chen, Yabin Shao, Jing Han, Xin Zhao, Jijuan Jiang, and Yachen Gao	
<b>Synthesis of 5-3,6,7,10,11-pentakis(pentyloxy)triphenylen-2-yloxy-pentyl Methacrylate and Its Mesomorphism Study</b> .....	973
Jingze Bi, Yuwen Feng, Zhenhu Zhang, Huanzhi Yang, Chunxiu Zhang, and Jialing Pu	
<b>Preparation of Durable Superhydrophobic Surface Material and Its Application in Packaging</b> .....	980
Xiao Liu, Shiyong Luo, and Rongxia Bu	
<b>Surface Structure Design and Performance Test of 3D Printing Microwave Absorbing Material</b> .....	987
Yingjie Xu, Lai Peng, X. Han, You Zhao, Chenyang Yuan, Wan Zhang, Xianfu Wei, Beiqing Huang, and Qi Wang	
<b>Preparation and Study of HA-CS-Mineralized Collagen Gel</b> .....	996
Miaomiao Hu, Kun Hu, Yuzhu Cui, Jia Yan, Guijuan Yang, Lin Zhu, Min Yan, Yen Wei, Luhai Li, and Fan Zhang	
<b>An Integrated Film Sensor for Measuring Force and Temperature for Artificial Skin Applications</b> .....	1003
Xiaoyu Wang, Yue Shi, Fenlan Xu, Ruping Liu, Wei Wang, and Luhai Li	
<b>Application of NIR Analysis Technology in Determining the Freshness Grade of Eggs</b> .....	1008
Liwei Chen, Wenguang Wei, Xiujuan Zhi, and Bin Du	

<b>Study on the Degradation Property of nHAC/PLA Composite Wire Material</b> .....	1016
Yuzhu Cui, Miaomiao Hu, Kun Hu, Jia Yan, Guijuan Yang, Chunyang Zhang, Xinyu Wang, Panpan Xue, Yen Wei, Luhai Li, and Fan Zhang	
<b>Application of NIR Analysis Technology in Quality Control of Tartary Buckwheat Products</b> .....	1022
Yan Cheng, Liang Zhuang, Xiujuan Zhi, and Bin Du	

**Part I**  
**Color Science and Technology**



# Testing Performance of Whiteness Formulas

Yuzhao Wang, Xi Lv, and Ming Ronnier Luo<sup>(✉)</sup>

College of Optical Science and Engineering,  
Zhejiang University, Hangzhou, China  
m. r. luo@leeds. ac. uk

**Abstract.** Whiteness is an important characteristic for surface color, especially in printing and textile industries. The widely used CIE whiteness formula had two shortcomings, i.e. firstly, the formula was only defined under standard D65 illuminant, and secondly, the boundary was found to be too limited. With these in mind, several modified whiteness formulas were developed. In this study, an experiment was conducted to test the performance of whiteness formulas. In the experiment, the whiteness appearance of 88 samples containing FWA (fluorescent whitening agent) were estimated under four lighting conditions with four different correlated color temperatures (3000, 4000, 5000 and 6500 K) at high UV radiation, by 20 observers. The data were used to test the performances of the developed whiteness formulas. The results indicated that generally the CIE whiteness formula with the CAT02 chromatic adaptation transform had good performances when predicting samples under each lighting condition separately. However, when combining all the data including all the lighting conditions, the performance of whiteness formula with the CAT02 chromatic adaptation transform did not perform better than other formulas. It was found that this is due to the incomplete chromatic adaptation under low CCT conditions.

**Keywords:** Whiteness · Chromatic adaptation

## 1 Introduction

Whiteness is an important colorimetric characteristic for surface colors. In some area the white perception is strongly related with the quality of the product, such as paper, plastic, fabric, etc. Fluorescent Whitening Agents (FWAs) is widely used for whiteness enhancement. These materials can absorb Ultra-Violet radiation and re-emit blue radiation. Such an effect can make the appearance of surface color look brighter and become slightly bluish. These two together enhance the whiteness of surface colors.

To characterize the whiteness of surface colors, many efforts have been done. The CIE whiteness formula ( $W_{CIE}$ ) is the one of the most widely used metric [1]. The formulas are given in Eq. (1).

$$W_{CIE} = Y + 800(x_n - x) + 1700(y_n - y) \quad (1)$$

$$T_{CIE} = 1000(x_n - x) - 650(y_n - y) \quad (2)$$

Or

$$T_{10,CIE} = 900(x_{n,10} - x_{10}) - 650(y_{n,10} - y_{10}) \quad (3)$$

where  $Y$ ,  $x$  and  $y$  are the luminance factor and the chromaticity coordinate of a surface color under CIE standard D65 illuminant;  $x_n$  and  $y_n$  are the chromaticity coordinates of CIE standard D65 illuminant.

Equations (2) and (3) calculate the red/green tint value of the surface color under  $2^\circ$  and  $10^\circ$  Color Matching Function (CMF) respectively. It is noted that the  $W_{CIE}$  only make sense when  $40 < W_{CIE} < 5Y - 280$  and  $-4 < T_{CIE}$  (or  $T_{10,CIE}$ )  $< +2$ . These are the defined whiteness limits.

However,  $W_{CIE}$  has its shortcomings, i.e. it can only be applied under D65 illuminant, and the whiteness limits are not too limited. More recently, new formulas were developed. One typical example is the Optimized CIE whiteness formula ( $W_{CIE,Optimized}$ ), which was proposed by Ma et al. [2]. Equation (4) defines the  $W_{CIE,Optimized}$ :

$$W_{CIE,Optimized} = Y_{10} + a'(x_{n,10} - x_{10}) + b'(y_{n,10} - y_{10}) \quad (4)$$

$$a' = -0.1891 \times CCT + 2267.2 \quad (5)$$

$$b' = 0.3202 \times CCT - 493.36 \quad (6)$$

Where  $Y_{10}$ ,  $x_{10}$  and  $y_{10}$  are the luminance factor and the chromaticity coordinate of the test specimen under CIE 1964 ( $10^\circ$ ) and D65 illuminant. The  $x_{n,10}$  and  $y_{n,10}$  are the chromaticity coordinates of the reference white under the same CIE conditions, and  $CCT$  is the Correlated Color Temperature of the lighting condition.

The other proposed method was to use Chromatic Adaptation Transform such as CAT02 [3] to transform surface color from other lighting condition to CIE standard D65 illuminant ( $W_{CIE,CAT02}$ ). The advantage of the method is that it can apply the current  $W_{CIE}$  to any lighting condition using this method.

The purpose of this study is to test the performance of several whiteness formulas using newly collected data, and to develop a new adapted formula.

## 2 Experiment Setup

In order to obtain data to test the performance of several whiteness formulas, a psychophysical experiment was conducted.

A multi-channel LED illumination system (LEDCube) was used for the experiment. The system contained 11 monochromatic LEDs and 3 white phosphor lightings, which allowed user to match any desired illuminants. The system was placed on top of a viewing booth, whose interiors were painted uniformly using matte grey paint. The lighting has a 98% uniformity on the floor of the viewing booth. This study designed 8 different lighting conditions for testing. The 8 lighting conditions included 4 Correlated Color Temperature (CCT) with 2 different UV levels. All the experiments were carried

out with a luminance of  $140 \text{ cd/m}^2$ . Table 1 provides the engineering data for each lighting condition.

**Table 1.** Engineering data for each lighting condition

TargetCCT (K)	Exp. CCT (K)	UV level	Duv	R <sub>a</sub>
6500	6463	Medium	0.001	95.57
5000	4903	Medium	0.004	97.40
4000	3974	Medium	0.002	98.45
3000	2887	Medium	0.001	96.25
6500	6496	High	0.001	95.48
5000	4916	High	0.004	97.46
4000	3974	High	0.001	98.41
3000	2890	High	0.000	96.21

Two UV levels was adopted, as medium and high. The former was adjusted to have the whiteness values of some FWA samples measured by a spectroradiometer to match the measurement results from a typical whiteness calibrated spectrophotometer. The high UV level was made by adjusting the UV level to be 1.5 times as the medium level. Figure 1 shows the Spectral Power Distribution (SPD) of the 8 lighting conditions used in the experiment. UV content can be seen below 400 nm.

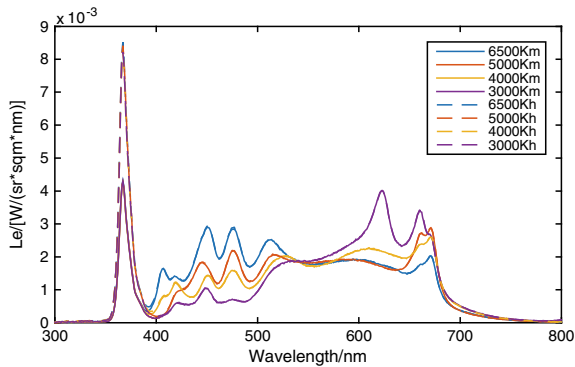


**Fig. 1.** SPD of the 8 lighting conditions

In total, 16 fabric samples were used for the experiment, including one as reference sample. These samples had a size of  $6 \text{ cm} \times 6 \text{ cm}$ , and they were selected to have different amount of FWAs, which allowed them to have different white appearance under the 8 lighting conditions.

During the experiment, each observer was asked to look at the reference sample under D65 illuminant first. Observer was asked to memorize the reference sample having a whiteness value of 100, and then adapted to the testing lighting conditions for



1 min before the whiteness estimation. During the visual assessment, observers were asked to give a whiteness score to each fabric sample compared to the reference in their memory. An  $0^\circ/45^\circ$  illumination/viewing geometry was used.

Twenty observers participated in the experiment, with 7 males and 13 females. The age of the observers was between 19 and 26 with an average age of 20.5. All of the observers had normal color vision, i.e. they all passed the Ishihara color vision test.

### 3 Analysis and Discussion

#### 3.1 Testing Different Whiteness Formulas

The visual results in terms of whiteness rating were used to test the above mentioned whiteness formulae. Figure 2 shows the distribution of the results on “whiteness rating—calculated whiteness” plane. The correlation coefficients ( $R$ ) were calculated as well and are plotted in Fig. 2.

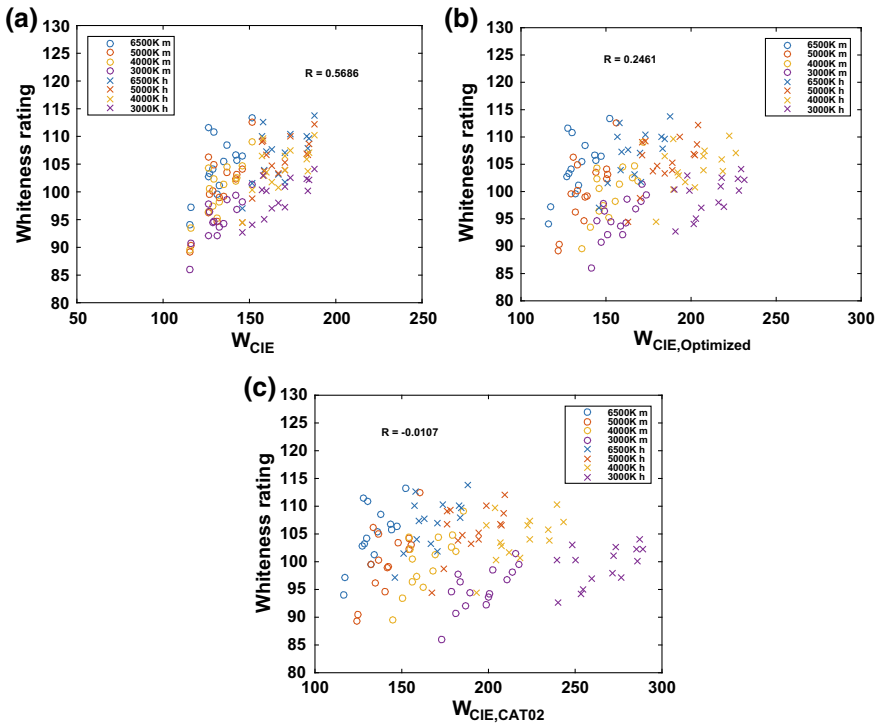


**Fig. 2.** The plots of the visual results against the predictions from 3 whiteness formulas: **a**  $W_{CIE}$ , **b**  $W_{CIE,Optimized}$  and **c**  $W_{CIE,CAT02}$ , respectively

It can be seen that the R values for the 3 methods ( $W_{CIE}$ ,  $W_{CIE,Optimized}$  and  $W_{CIE,CAT02}$ ) were 0.5686, 0.2461 and  $-0.0107$  respectively. Amongst the three methods,  $W_{CIE}$  had the highest R value, while  $W_{CIE,CAT02}$  had the lowest (even negative) R value. Note that the calculation for  $W_{CIE,CAT02}$  was assumed a full chromatic adaptation by setting the chromatic adaptation degree (D) to 1. From the earlier studies, we found *CAT02* performed well with almost full adaptation for viewing surface samples. However, in this study, the FWA samples appeared to be ‘fluoresce’, more like self-luminance colors. This may be the reason *CAT02* transform performed badly.

### 3.2 $W_{CIE,CAT02}$ with Optimized Adaptation Degree

The performance of  $W_{CIE,CAT02}$  was not promising when data from different lighting conditions were combined together. The visual whiteness results indicate that, when under lower CCT lighting conditions the whiteness rating would have lower values compared to those under higher CCT lighting conditions. However, this was found to be opposite for the  $W_{CIE,CAT02}$  predictions. This implies optimizing the incomplete adaptation factor, D, could improve the model’s performance. Recent studies by Zhai and Luo [4] revealed that, the D of CAT could vary, especially under lower CCT lighting conditions. Hence, efforts were first made to find the best general D value for all the lighting conditions to achieve the highest R value.

Figure 3 shows the performance of  $W_{CIE,CAT02}$  with a generally optimized D ( $W_{CIE,CAT02,generalD}$ ). The R value is 0.7224 which is much better than  $W_{CIE}$ ,  $W_{CIE,Optimized}$  and  $W_{CIE,CAT02}$ . This result proves the incomplete adaptation under lighting with different CCTs rather than 6500 K. The most ideal situation is that, different CCTs should had its own adaptation degrees, but a general adaptation degree. More efforts should be paid on this topic.

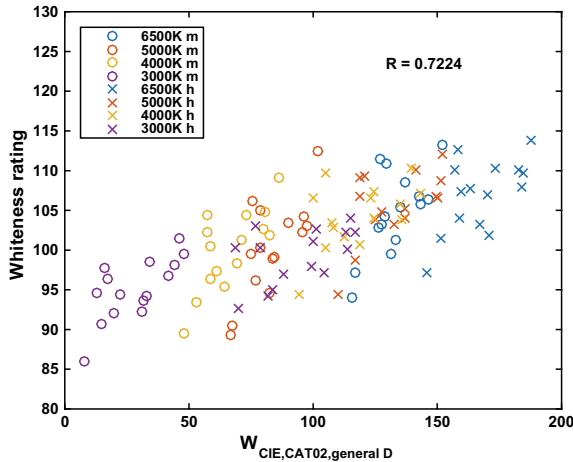


**Fig. 3.** The plots of the visual results against the predictions from 3 whiteness formulas  $W_{CIE,generalD}$

## 4 Conclusions

This study focused on the performance of whiteness formulae. A new psychophysical experiment was conducted to collect testing data for scaling whiteness. The results indicated that, the  $W_{CIE,CAT02}$  and  $W_{CIE,Optimized}$  did not perform better than  $W_{CIE}$  even though they were adapted formulae based on  $W_{CIE}$ . A newly method to calculate whiteness was purposed. The new formula was based on  $W_{CIE,CAT02}$  with an optimized general chromatic adaptation degree. The result showed that, the new formula had the best performance among the four whiteness formulae.

## References

1. Commission Internationale de l'Éclairage (CIE). (2004). *Colorimetry*, CIE No. 15. Vienna, Austria. pp. 1–79.
2. Ma, S., Wei, M., Liang, J., Wang, B., Chen, Y., Pointer, M., et al. (2016). Evaluation of whiteness metrics. *Lighting Research & Technology*, 50(3), 429–445.
3. Li, C., Luo, M. R., Bryan, R., & Hunt, R. W. G. (2002). CMC 2000 chromatic adaptation transform: CMCCAT2000. *Color Research and Application*, 27, 49–58.
4. Zhai, Q., & Luo, M. R. (2018). Study chromatic adaptation via neutral white matches on different viewing mediums. *Optics Express*, 26(6), 7724–7739.



# Spectral Power Distributions with High Gamut-based Metric Values

Zheng Huang<sup>1</sup>, Hongyu Lin<sup>1</sup>, Bisheng Wu<sup>2</sup>, Weiming Wang<sup>1</sup>,  
and Qiang Liu<sup>1,3(✉)</sup>

<sup>1</sup> School of Printing and Packaging, Wuhan University, Wuhan 430079, China  
liuqiang@whu.edu.cn

<sup>2</sup> Guangdong JG Lighting Technology Co., Ltd, Dongguan 523808, China

<sup>3</sup> Shen Zhen Research Institute, Wuhan University, Shenzhen 518000, China

**Abstract.** It is widely acknowledged that gamut-based measures have close relationship with color preference of lighting. In order to explore the characteristics of spectral power distribution of light with high values for gamut-based measures, a large database which contains a lot of spectral power distributions have been established. The values for gamut-based measures of these light sources were calculated and it is found that the light sources with higher values for gamut-based measures always exhibits three energy peaks in the red, green and blue bands, respectively.

**Keywords:** Colour quality · Colour gamut · Spectral power distribution · Colour preference

## 1 Introduction

As lighting technology continues to improve, people's requirements for light quality are increasingly getting higher. Among them, colour preference of lighting is undoubtedly regarded as a very important dimension.

It is showed in existing research that people prefer light sources with higher values of gamut-based measures [1–4]. That is due to the fact that colour preference is correlated with saturation and the increased gamut area is always related to saturation (or chroma) enhancement. In our recent work, an absolute gamut volume based metric (GVI) was developed based on meta-analysis and optimized colour samples [2]. The performance of such a measure was comprehensively compared to 20 typical colour quality measures, in form of the weighted average correlation between metric predictions and preference ratings of 8 psychophysical studies. However, at current stage it is still not known which kind of light source could obtain a better value for gamut-based measures.

Therefore, in this contribution the values for four classical gamut-based measures of 591 typical light sources from relevant research and dataset [3–16] were calculated. The characteristics of spectral power distribution (SPD) of 50 light sources with highest gamut-based values were further analyzed to explore the relationship between the

colour gamut quality of light source and their SPD characteristics. The results show that a SPD with three peaks at certain red, green and blue wavelength regions always exhibits higher scores for gamut-based measures.

## 2 Classical Gamut-based Measures

The four gamut-based measures adopted in this work are Gamut Area Index (GAI) [17], Qg in Color Quality Scale (CQS) [18], Rg in IES-TM30 [19] and Gamut Volume Index (GVI) [2].

### 2.1 Gamut Area Index

The GAI measure was proposed by Mark S. Rea and J. P. Fressinier in 2008. By this measure, the gamut area is defined as the area enclosed by the polygon created by the eight test-color samples used in the CIE colour rendering index calculation within the CIE 1976 UCS diagram ( $u'$ ,  $v'$ ) [17].

### 2.2 Qg

Qg is a measure intended for gamut area quantification by the Color quality Scale approach [18]. The CQS system is optimized in terms of color sample size, color sample saturation and the calculation method of average color difference. The Qg in CQS corresponds to the relative colour gamut area.

### 2.3 Rg

Rg is one of dimensions of the TM-30 (Rf and Rg) lighting color quality evaluation system which proposed by the North American Lighting Engineering Association (IESNA). Such a measure also corresponds to the relative colour gamut area.

### 2.4 Gamut Volume Index

This GVI measure was developed by our team in 2017. It is based on a meta-analysis of 8 psychophysical studies and thus has better performance in preference predicting [2]. It is based on the absolute gamut volume of optimized colour samples which was obtained by optimizing the correlation between the metric predictions and the subjective ratings for a large dataset of psychophysical studies.

## 3 SPD Dataset

The 591 light sources involved in this paper were derived from relevant research [3–16], together with several typical SPD databases (IES-TM-30\CRI-2012\CQS \Memory CRI\CRI-CAM02UCS) in the EXCEL program established by relevant scholars or organizations, as well as 14 typical light sources provided by 7 famous

lighting source suppliers for museum and gallery exhibition in China. Note that this article only introduces these SPDs briefly. For more detailed information, please refer to the relevant citations. In addition, some of the SPD data in this work is available upon request.

To be specific, the 591 SPDs (without repetition) adopted in this paper mainly come from the following work and dataset: Xu et al. (multi-CCT, 2017, 10 SPDs) [3], Wei et al. (metameric lighting, 2014, 2 SPDs) [4], Narendran et al. (multi-CCT, 2002, 7 SPDs) [5], Szabó et al. (metameric lighting, 2016, 20 SPDs) [6], Feltrin et al. (multi-CCT, 2017, 5 SPDs) [7], Royer et al. (50 SPDs), Dangol et al. (metameric lighting, 2013, 8 SPDs) [8], Islam et al. (metameric lighting, 2012, 24 SPDs) [9], Jost-Boissard et al. (metameric lighting, 2009, 14 SPDs) [10], Jost-Boissard et al. (metameric lighting, 2014, 17 SPDs) [11], He et al. (multi-CCT, 2015, 4 SPDs) [12], Dikel et al. (multi-CCT, 2013, 6 SPDs) [13], Liu et al. (multi-CCT, 2017, 9 SPDs) [14], Royer et al. (metameric lighting, 2016, 26 SPDs) [15], Khanh et al. (metameric lighting, 2017, 36 SPDs) [16], typical light sources provided by seven suppliers of lighting source for museum exhibition in China (14 SPDs), CRI2012 excel dataset (36 SPDs) [20], CQS 9.0.3 excel dataset (83 SPDs) [18], MCRI excel dataset (30 SPDs) [21] and TM30-15 excel dataset (190 SPDs) [19].

## 4 Results and Discussion

The 50 light sources with highest values for each measure were selected for further analysis. Obviously, the best case is that a certain light source ranks in the top 50 of all the four measures (GAI [17], Qg [18], Rg [19], and GVI [2]).

Among the 591 light sources, there are 5 light sources that rank four times in the top 50 of these four measures, and 30 light sources that rank three times. The total 35 light sources are shown in Fig. 1.

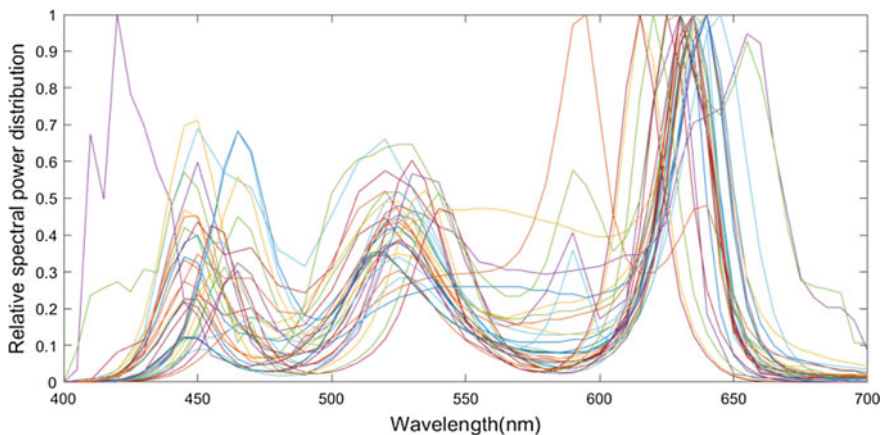


**Fig. 1.** The 35 spectral power distributions with best colour gamut performance

It seems that the light source SPD with three peaks (450–480 nm, around 530 nm, around 620 nm) will have a good objective evaluation for colour gamut and thus colour preference. That is to say, if the energy distribution of the light source in the three bands of R, G and B is relatively uniform, or have peaks in these three bands, the values for these measures tends to be high.

In addition, the SPDs of the 50 light sources with highest values for these measures of GAI [17], Qg [18], Rg [19], and GVI [2] are drawn separately, as shown in Figs. 2, 3, 4 and 5.

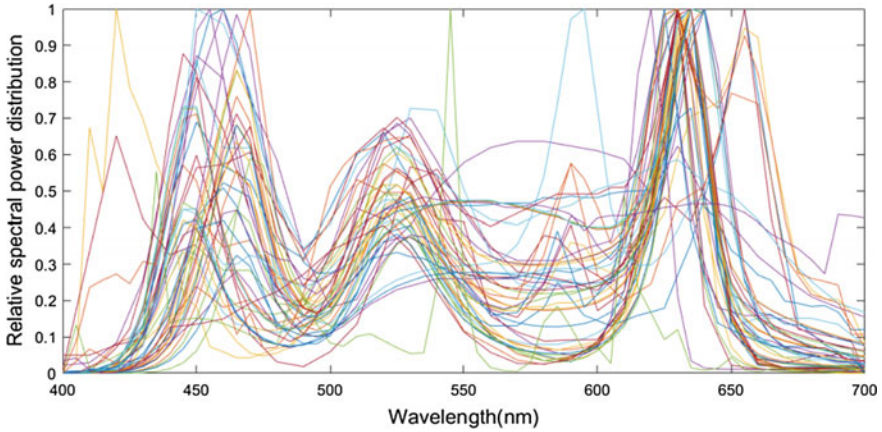


**Fig. 2.** Top 50 SPDs with highest GAI values

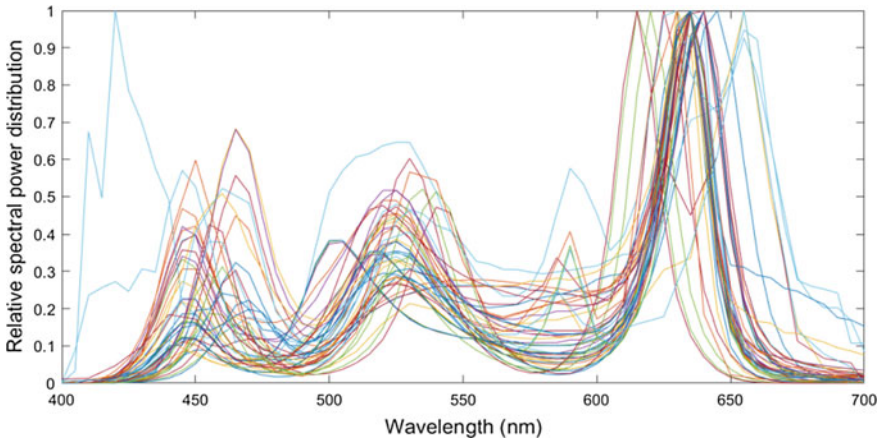


**Fig. 3.** Top 50 SPDs with highest Qg values

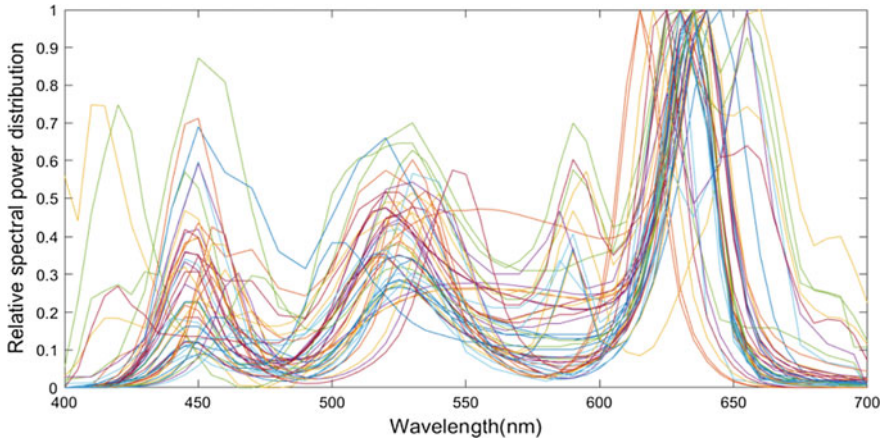


**Fig. 4.** Top 50 SPDs with highest Rg values

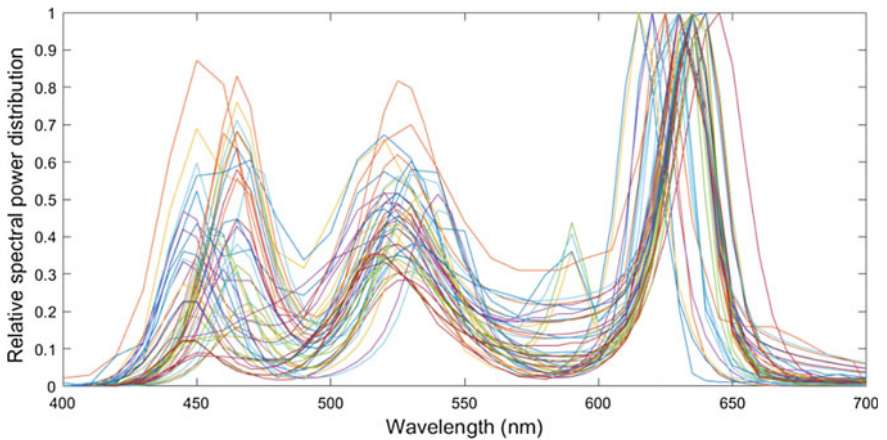


**Fig. 5.** Top 50 SPDs with highest GVI values

It is quite obvious that the drawings in Figs. 2, 3, 4 and 5 correlate quite well with Fig. 1, which to some extent proves a hypothesis—if a SPD possess three peaks at R, G, B bands (450–480 nm, around 530 nm, around 620 nm), such a distribution tends to obtain higher values for gamut-based measures.

In addition, it should be mentioned that there is an obvious difference between GAI, GVI and Rg, Qg. The former two measures are absolute measures while the latter two are relative measures. That is, the computation of GVI does not need any reference source while GAI exclusively takes the equal energy spectrum as reference. However, for Rg and Qg, a reference source of a same Correlated colour Temperature (CCT) with the testing source is always needed. Therefore, according to Figs. 2, 3, 4 and 5, it seems



that the above mention assumption that three RGB peaks generates higher colour gamut could stand no matter under the conditions of a same CCT or of different CCTs.

At last, it must be pointed out that the above objective analysis, together with the conclusions could only serve as a method to choose the SPDs with high values for gamut-based measures. Since the performance of those SPDs has not been tested by psychophysical studies, it is not safe to conclude that those lights will be definitely appreciated by observers, let alone the fact that too saturated a light might also impair colour preference of lighting [1, 2, 18].

## 5 Conclusions

In this paper, to reveal the truth about which light source could obtain a better value for gamut-based measures, the values for four typical gamut-based measures of 591 light sources in a newly-built database were calculated. The 50 light sources with highest values for each gamut-based measure were selected and visualized. Through further discussion, it is concluded that if the energy distribution exhibits three bands of R, G and B in certain wavelength regions, it is easier to obtain higher values for gamut-based measures. The authors believe such a finding could provide a better understanding for light spectrum optimization in future.

**Acknowledgement.** This work is supported by the National Natural Science Foundation of China (Project No. 61505149) and the Young Talent Project of Wuhan City of China (Project No 2016070204010111).

## References

1. Houser, K. W., et al. (2013). Review of measures for light-source color rendition and considerations for a two-measure system for characterizing color rendition. *Optics Express*, 21(8), 10393–10411.
2. Liu, Q., et al. (2017). Gamut volume index: A color preference metric based on meta-analysis and optimized colour samples. *Optics Express*, 25(14), 16378–16391.
3. Wang, Q., et al. (2017). Influence of color temperature on comfort and preference for LED indoor lighting. *Optik—International Journal for Light and Electron Optics*, 129, 21–29.
4. Wei, M., et al. (2014). Color preference under LEDs with diminished yellow emission. *Leukos*, 10(3), 119–131.
5. Narendran, N. (2002). Color rendering properties of LED light sources. *Proceedings of SPIE—The International Society for Optical Engineering*, 4776, 61–67.
6. Szabó, F., et al. (2014). A study of preferred colour rendering of light sources: Home lighting. *Lighting Research & Technology*, 48(2), 103–125.
7. Feltrin, F., et al. (2017). Analysis of painted artworks' color appearance under various lighting settings. In *2017 IEEE International Conference on Environment and Electrical Engineering and 2017 IEEE Industrial and Commercial Power Systems Europe (EEEIC/I&CPS Europe)*.
8. Dangol, R., et al. (2013). User acceptance studies for LED office lighting: Preference, naturalness and colourfulness. *Lighting Research & Technology*, 47(1), 36–53.

9. Islam, M. S., et al. (2013). User preferences for LED lighting in terms of light spectrum. *Lighting Research & Technology*, 45(6), 641–665.
10. JostBoissard, S., Fontoynt, M., & BlancGonnet, J. (2009). Perceived lighting quality of LED sources for the presentation of fruit and vegetables. *Journal of Modern Optics*, 56(13), 1420–1432.
11. Jost-Boissard, S., Avouac, P., & Fontoynt, M. (2014). Assessing the colour quality of LED sources: Naturalness, attractiveness, colourfulness and colour difference. *Lighting Research & Technology*, 47(7), 769–794.
12. He, J., et al. (2015). Preference for appearance of Chinese complexion under different lighting. *Lighting Research & Technology*, 49(2), 228–242.
13. Dikel, E. E., et al. (2014). Preferred chromaticity of color-tunable LED lighting. *Leukos*, 10(2), 101–115.
14. Huang, Z., et al. (2017). Light dominates colour preference when correlated colour temperature differs. *Lighting Research & Technology*, 2017, 1477153517713542.
15. Royer, M. P., et al. (2016). Human perceptions of colour rendition vary with average fidelity, average gamut, and gamut shape. *Lighting Research & Technology*, 49(8), 966–991.
16. Khanh, T. Q., et al. (2017). Colour preference, naturalness, vividness and colour quality metrics, part 4: Experiments with still life arrangements at different correlated colour temperatures. *Lighting Research & Technology*, 2017, 1477153517700705.
17. Freyssinier, J. P., & Rea, M. (2002). A two-metric proposal to specify the color-rendering properties of light sources for retail lighting. *Proceedings of SPIE*, 7784, 7784V.
18. Davis, W., & Ohno, Y. (2010). Color quality scale. *Optical Engineering*, 49(3), 033602.
19. David, A., Fini, P. T., Houser, K. W., Ohno, Y., Royer, M. P., Smet, K. A., et al. (2015). Development of the IES method for evaluating the color rendition of light sources. *Optics Express*, 23(12), 15888–15906.
20. Nickerson, D., & Jerome, C. W. (1965). Color rendering of light sources: CIE method of specification and its application. *Illuminating Engineering*, 60, 262–271.
21. Smet, K. A. G., Ryckaert, W. R., Pointer, M. R., Deconinck, G., & Hanselaer, P. (2010). Memory colours and colour quality evaluation of conventional and solid-state lamps. *Optics Express*, 18(25), 26229–26244.



# Effect of Backgrounds with Different Lightness on the Color Appearance of Printed Samples

Ruili He, Min Huang<sup>(✉)</sup>, Chunli Guo, Yonghui Xi, and Yu Liu

School of Printing and Packaging Engineering, Beijing Institute  
of Graphic Communication, Beijing, China  
huangmin@bigc.edu.cn

**Abstract.** In this paper, the influence of neutral backgrounds with different lightness on color appearance was studied, five color centers and nine neutral backgrounds with different lightness based on printed samples were prepared. 20 observers were organized to carry out visual experiment with the method of paired comparison. The obtained experimental results indicate that the color appearance of color center is more affected by higher lightness backgrounds than the lower, which is quite different with the results computed by color appearance models (CAM). Furthermore, the factor of Standardized Residual Sum of Squares (STRESS) was used to evaluate the performance of CAM16 and CAM02 model. The STRESS values show that CAM16 (37.22) predicted more close to the visual results and performed well comparing with CAM02 (44.00).

**Keywords:** Color appearance · Different lightness · Color difference · Paired comparison

## 1 Introduction

The generation of visual color is a complex psychophysical process which is not only related to the physical properties of the object itself, but also its surroundings, viewing conditions and other psychological factors. Therefore, the same color stimuli can cause different color appearance in different viewing conditions or backgrounds, which makes it difficult to describe, replicate and evaluate accurately on different media. The proposal of color appearance model provides a solution for accurate cross-media reproduction which is based on the human color vision. It mainly solves the problems of color accurate transmission and reproduction under different viewing conditions, backgrounds and different surroundings. Nowadays, the most commonly used color appearance model is CIE CAM02 [1], which has been widely used in scientific research and industrial applications since recommended by CIE in 2002. However, it was reported that in some cases, for example, in cross-media color reproduction applications, computational problems in the calculation of brightness J may result in poor performance of this model. Li et al. [2] established a new color appearance model CAM16 and its uniform color space (CAM16-UCS) by changing the structure of CAM02 and complete the two adaptations in the same space.

In order to study the influence of neutral backgrounds with different lightness on color appearance, 20 observers were organized to carry out the visual evaluated experiment with the method of paired comparison, and the experimental results were also used to test the performance of CAM16 and CAM02 models.

## 2 Experimental

### 2.1 Samples and Illumination

Five color centers (gray, red, yellow, green, blue) recommended by CIE [3] were selected as target colors in our experiments. The target color samples were printed by Epson Stylus Pro7908 Inkjet Printer on Color Long Inkjet web matte paper, with the size of 5 cm × 5 cm. In addition, nine neutral colors with different lightness ( $L_{10}^* \approx 20, 30, 40, 45, 50, 55, 60, 70, 80$ ), were also printed with the size of 20 cm × 20 cm to be the background samples. When all the samples were prepared, each target sample was stuck respectively on the center of nine background samples. The chromatic values of five target color samples and nine neutral background samples measured by x-rite eXact spectrophotometer were shown in Table 1.

**Table 1.** The chromatic values of five target color samples and nine neutral backgrounds

	X	Y	Z	$L_{10}^*$	$a_{10}^*$	$b_{10}^*$	$C_{10}^*$
Gray	28.95	30.01	31.94	61.66	-0.26	0.45	0.52
Red	20.00	13.89	6.97	44.07	36.78	23.22	43.50
Yellow	61.87	67.18	26.63	85.60	-7.03	49.57	50.06
Green	16.89	23.81	25.65	55.90	-30.40	-0.08	30.40
Blue	9.16	8.65	22.88	35.30	6.84	-30.96	31.70
L20	3.04	3.12	3.22	20.53	0.41	0.85	0.94
L30	6.20	6.39	6.96	30.39	0.19	-0.33	0.38
L40	10.49	10.89	11.90	39.39	-0.29	-0.53	0.60
L45	14.02	14.55	15.72	45.01	-0.26	-0.18	0.32
L50	18.29	18.86	20.77	50.53	0.30	-0.91	0.96
L55	22.26	23.00	24.99	55.07	0.15	-0.45	0.47
L60	26.56	27.61	29.44	59.53	-0.53	0.35	0.63
L70	39.61	40.82	44.15	70.05	0.45	-0.30	0.54
L80	54.05	55.95	60.89	79.59	-0.12	-0.68	0.69

Referring to CIE recommended observation conditions, the Gretag Macbeth the Judge II viewing cabinet fitted with D65 simulator was selected in our visual experiment. The correlated color temperature (CCT) and luminance measured by PR655 spectroradiometer was 6223K and 965lx, respectively. The relative spectral power distribution (SPD) of the light source is shown in Fig. 1.

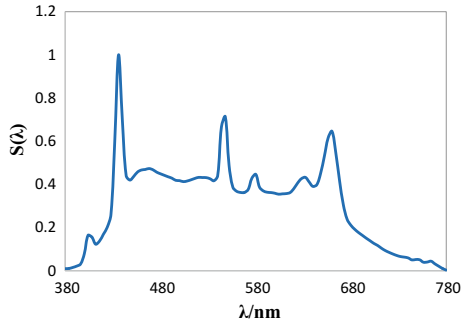


Fig. 1. SPD of the light source

## 2.2 Experimental Procedure

The visual assessments were conducted in a dark room. For each color center, the target color sample on L50 background was placed in the middle of viewing cabinet, other samples on different neutral backgrounds were displayed randomly on the left or right side, as shown in Fig. 2. Observers were asked to sit in front of the cabinet at a distance of approximately 25–30 cm and the viewpoint is  $0/45^\circ$ . In the visual assessment, observers need to compare the color difference between the target color on the left background and the target color on the middle background, named  $\Delta V_1$ , and the color difference between the right and the middle, named  $\Delta V_2$ . Then comparing which color difference was larger,  $\Delta V_1$  or  $\Delta V_2$ . When the judgment was done, the visual results were recorded. For each target color center, 28 judgments ( $8 \times 7/2 = 28$ ) were gathered and there were totally 140 ( $28 \times 5 = 140$ ) judgments for each observer.

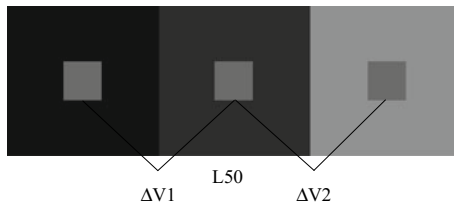


Fig. 2. The scheme of visual assessments

20 observers aged from 22 to 25, involving 10 males and 10 females were organized to conduct the visual experiment. All observers were students from Beijing Institute of Graphic Communication and have theoretical knowledge of color science. In order to evaluate the reliability of judgments made by observers, 5 of the observers were selected to perform the replicated evaluation.

### 3 Results and Discussions

#### 3.1 Observer Variability

Observer variability, including inter and intra observer variability, were evaluated using the method of Wrong Decision (WD) [4]. For investigating inter- observer variability, the number of wrong decision made by each individual against the panel results were computed. For examining intra-observer variability, WD is also used to represent number of wrong decision made by a single observer from two repetitions. For a perfect agreement, WD should equal to zero.

From the obtained results, the inter-observer variability (0.18) is almost two times larger than the intra-observer variability (0.09), which means the observer variability in the visual experiment is reasonable and acceptable [4].

#### 3.2 Visual Color Difference

The experimental results of each target color judged by all observers were used to do probability statistics ( $P\%$ ) and then converted into Z-score using Eq. (1),  $i$  refers to the  $i$ th observer,  $u$  refers to the average value and  $S$  refers to the standard deviation value of the data judged by  $i$ th observer. After eliminating the negative numbers, the visual color difference values [5] between target color in L50 background and other lightness backgrounds judged by all observers were obtained, as shown in Table 2. The visual color differences were drawn into histogram in Fig. 3.

**Table 2.** The obtained visual color differences

$\Delta V$	L20	L30	L40	L45	L55	L60	L70	L80
Gray	1.23	0.93	0.91	0.30	0.46	1.64	2.66	3.87
Red	1.22	0.98	1.00	0.84	0.34	1.03	2.39	4.20
Yellow	2.18	1.87	1.35	1.10	0.55	0.73	1.77	2.44
Green	1.24	0.99	0.77	0.52	0.76	1.36	2.15	4.20
Blue	1.24	1.02	0.53	0.36	0.77	1.48	2.55	4.04

$$Z = (P_i - u)/S \quad (1)$$

From Table 2 and Fig. 3, it can be figured out that the visual color difference of target color samples between L45 or L55 and L50 background is smaller than that of other lightness background. Besides, the more the lightness of the background deviates from that of neutral gray (L50), the higher the visual color difference is. When the background lightness is 20–45, the visual color difference of yellow is larger than that of the other four colors, while when the background lightness is 60–80, the visual color difference of yellow is smaller than that of the other four colors. Because the lightness

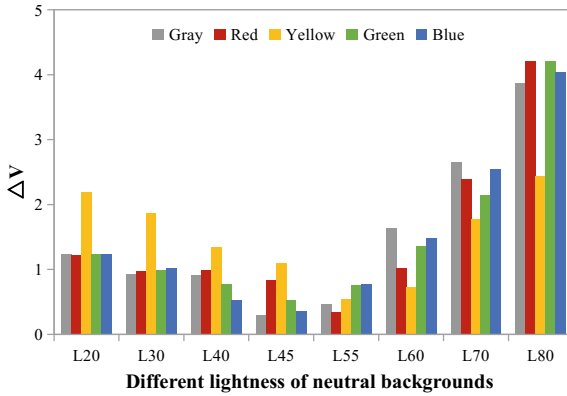


Fig. 3. Visual color difference from different backgrounds

of yellow is higher, its color appearance is more influenced by low lightness background and less by high lightness background. For other colors except for yellow, the visual color difference with higher lightness backgrounds is larger than those with low lightness backgrounds compared with the L50 neutral background.

### 3.3 Performance of CAM16 and CAM16-UCS

The measured XYZ values of five target colors, the lightness of nine neutral backgrounds and other known parameters were put respectively in CAM02 and CAM16 models. Then the color differences of each target color between L50 background and other eight different lightness backgrounds were computed by CAM02-UCS and CAM16-UCS. Further, the power function ( $\Delta E = 1.41(\Delta E')^{0.63}$ ) developed by Huang et al. [6] was applied to the color difference metric associated with CAM02-UCS. The obtained results were shown in Figs. 4 and 5.

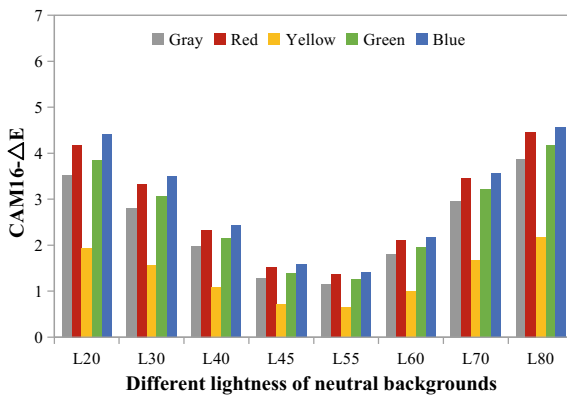
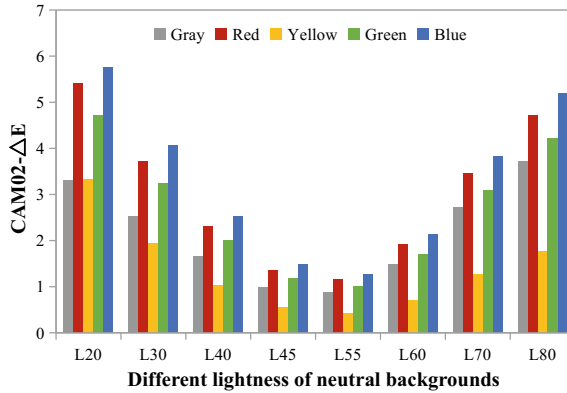


Fig. 4. CAM16-UCS color difference histogram



**Fig. 5.** CAM02-UCS color difference histogram

The color difference histograms computed by color appearance models both form symmetrical V-shape, which is quite different from Fig. 3 that shaped by observers' visual color difference. The computing results indicated that the color difference between the target color on L50 background and the target color on other lightness backgrounds increases with the lightness deviates from L50 neutral background and the color differences computed by CAM02-UCS are larger than the results computed by CAM16-UCS.

In order to compare the performance of CAM16 and CAM02 color appearance model, Standardized Residual Sum of Squares (STRESS) [4] was used to evaluate the correlation between the visual color difference judged by observers and the color difference predicted by color appearance model, the results were shown in Table 3. The range of STRESS value is 0–100, and the smaller the STRESS value is, the better the corresponding color appearance model performs.

**Table 3.** The performance of CAM02-UCS and CAM16-UCS in terms of STRESS

STRESS	Gray	Red	Yellow	Green	Blue	Mean
CAM02-UCS	40.44	49.09	33.22	48.42	48.84	44.00
CAM16-UCS	42.11	43.57	12.31	42.94	45.17	37.22

As shown in Table 3, the STRESS value in gray center computed by CAM02-UCS is smaller than that of CAM16-UCS, while for other four color centers, especially in yellow center, the STRESS value computed by CAM16-UCS is quite smaller than that of CAM02-UCS. Comparing the color difference histograms in Figs. 4 and 5, the variation trend in yellow center is quite different. From the average of five colors' STRESS values, it can be concluded that CAM16 color appearance model has been improved and performed better than the prediction of CAM02.



## 4 Conclusions

In order to study the influence of neutral backgrounds with different lightness on color appearance, five CIE recommended target colors and nine neutral backgrounds were prepared based on printed samples. 20 observers were organized to carry out the visual experiments with the method of paired comparison. The results showed that the color appearance of color center is more affected by the backgrounds with higher lightness than the lower. And The lightness of target samples may also have an impact on the color perception. Furthermore, the experimental results were used to test the performance of CAM16 and CAM02 model. The average STRESS value of five colors predicted by CAM16-UCS is 37.22, while the average value computed by CAM02-UCS is 44.00, which indicated that CAM16 performed better than CAM02.

**Acknowledgements.** This research was supported by National Natural Science Foundation of China (grant 61675029, 61308081). Thanks every observer participating in the experiments.

### Compliance with Ethical Standards

**Conflict of Interest** The authors declare that they have no conflict of interest.

**Ethical Approval** All procedures performed in studies involving human participants were in accordance with the ethical standards of the School of Printing and Packaging Engineering, Beijing Institute of Graphic Communication and with the 1964 Helsinki declaration and its later amendments or comparable ethical standards.

**Informed Consent** Informed consent was obtained from all individual participants included in the study.

## References

1. Moroney, N. (2002). The CIECAM02 color appearance model. In *Color and Imaging Conference* (pp. 23–27).
2. Li, C., Li, Z., Wang, Z., et al. (2017). Comprehensive color solutions: CAM16, CAT16, and CAM16-UCS. *Color Research and Application*, 42(1), 703–718.
3. Witt, K. (1995). CIE guidelines for coordinated future work on industrial color-difference evaluation. *Color Research and Application*, 20(6), 399–403.
4. Wang, H. (2008). *Evaluation of colour difference based on object surface colors*. Zhejiang: Zhejiang University.
5. He, R., Huang, M., Guo, C., et al. (2018). Color-difference discrimination between young and old observers. *Laser and Optoelectronics Progress*, 55(3), 33301.
6. Huang, M., Cui, G., Melgosa, M., et al. (2015). Power functions improving the performance of color-difference formulas. *Optics Express*, 23(1), 597–610.



# Reviews on Observer Metamerism and Individual Color Vision Variability

Qianwen Chen, Lu Feng, Yalin Li, and Shengyan Cai<sup>(✉)</sup>

College of Packaging and Printing Engineering, Tianjin University of Science and Technology, Tianjin 300222, China  
longviews@sina.com

**Abstract.** Significant color discrimination exists among color deficiency observers, while the color vision variability was used to being neglected among ordinary individuals. The standard observer is widely used in the traditional colorimetry for convenience with the observer metamerism phenomenon ignored. While with the contribution of physiology, psychophysics, color science and other areas, the study of color vision variability in individual observers goes further. This paper reviews on the past research works about observer metamerism and individual color vision variability according to its physiological influence factors, significance and quantification.

**Keywords:** Review · Observer metamerism · Physiological · CMFs

## 1 Introduction

Metamerism [1] is the phenomenon exhibited by two color stimuli with the same tristimulus values but different spectral radiant power distributions under certain conditions. It is the core and fundamental theory that the televisions, cameras, projects and printings etc. based on to present thousands of colors with only three or four primaries.

Kuo [1] comprehensively concluded four types of metamerism, which respectively occurs due to the change in illuminant, observer, or the geometry of illumination and viewing. However, the illuminant and observer metamerism (OM) are known more widely. OM was defined by the CIE [2] as variations of color matches (of spectrally different stimuli) among different observers. It is mainly caused by individual variability for quite complex physiological attributions.

In traditional colorimetry, standard observer is used to describe the average observer color characteristic for convenience at the cost of the precision. It has influenced the critical modern color critical applications nowadays, especially, for the newly developed techniques such as LEDs, OLEDs, and lasers. They have spectrally narrow primaries and tend to present the OM effect. It calls for more precise characterization of individual color vision.

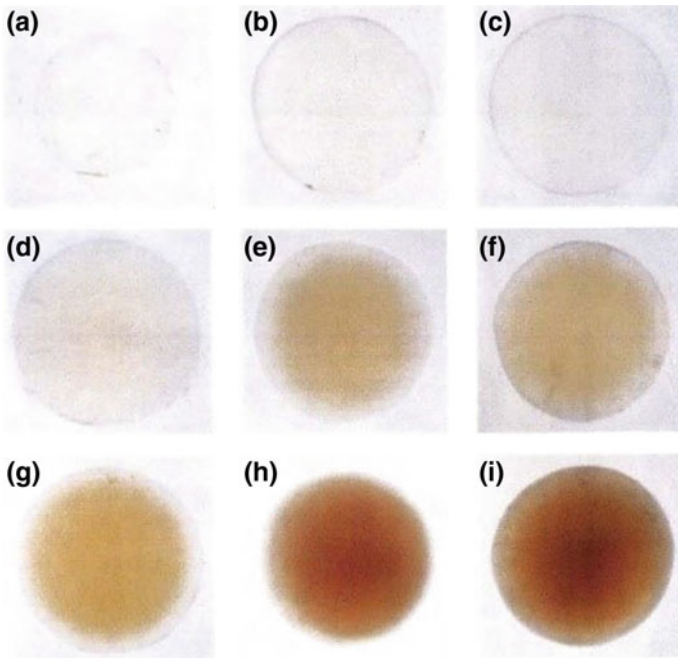
## 2 Physiological Attributions

Physiological factors which contribute to individual visual variability are quite complex. First of all, the genes from parents give a person unique physiological construction. However, it changes as one get older or suffer from certain diseases. It even relates to one's dietary intake, fat percentage and habits like smoking. From a group perspective of view, difference in gender and ethnicity also show individual variability.

### 2.1 Lens and Variable Factors

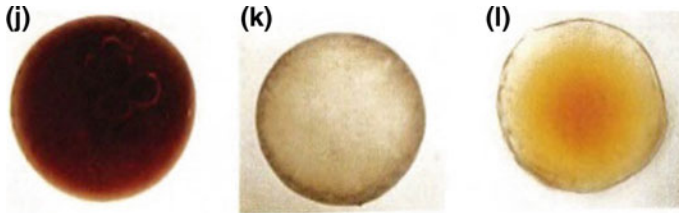
Age is the most important factor for lens variability. According to Artigas et al. [3] age explains 47% variations in lens, or 50% reported by Berendschot [4]. Norren and Vos [5] examined on Crawford's [6] 50 observers aged from 17 to 30, and found the lens optical density (LOD) of these young people mainly varies 25% from the average. After that, Pokorny et al. [7] aimed to investigate the individual variability throughout one's lifelong time, it was shown that the LOD increases by 38% from the age 20 to 60. In addition, Artigas [3] was confirmed greater variability of lens density after the age 60.

Figure 1 [8] shows extracted lenses of people in nine different ages from the new born of six months to the 91-year-old one. The change is obvious from the nearly pure white of the new born gradually turns yellow and then even darker. More related details can be referred in Werner [9], Scheffrin [10], Xu et al. [11] and Berendschot [4].



**Fig. 1.** Extracted lenses of people in different ages: **a** six months, **b** eight years, **c** 12 years, **d** 25 years, **e** 47 years, **f** 60 years, **g** 70 years, **h** 82 years, **i** 91 years

Diabetic's influence on lens was investigated by Lutez and Bresnick [12] in 1991. He affirmed that young diabetic individual has similar yellow lens as normal individuals over 60 years which may cause by age related glycosylation of lens proteins. Other pathological factors such as keratitis or cataracts [13] also have been reported to influence lens. The differences in lenses of three different cataracts patients can be seen from Fig. 2 [8].



**Fig. 2.** Cataract patients: **j** nuclear cataract, age 70, **k** cortical cataract, age 68, **l** mixed nuclear and cortical cataract, age 74

Individual habits related with LOD such as smoking was investigated by Hammond et al. [14]. It was proved that smoking would make LOD increase even after smoking cessation.

To conclude, the age factor which matters most has been well investigated. Pathological factors and individual habits have been proved to have relations with LOD. The general trend was obvious, yet more data are required.

## 2.2 Macular and Variable Factors

Significant differences exist in the macular pigment optical density (MPOD) among observers, even sometimes varies from the right and left eyes of a single observer. The variability occurs mainly between 400 and 525 nm and the peak MPOD varies over 1.2 log units [15]. Estimation variability exists in a range of 40–50% from the average according to recent publications.

To investigate the race factor, researchers took samples from different living areas and found macular variability from different human race. Howell et al. [16] compared samples of south Asian and the white, concluded that the white group has MPOD significantly lower than the Asian group. While Iannaccone et al. [17] reported a 41% below in blacks than in whites from his test group.

Human cannot produce lutein and zeaxanthin which consists in macular pigment (MP) themselves. Therefore, factors that have influence on the efficiency of lutein and zeaxanthin transportation that the retina consumes could affect MPOD. External dietary intake could increase MPOD, which was verified by Ciulla et al. [18] and Bone et al. [19]. In addition, Nolan et al. [20] examined that MPOD drops as the human body fat content climbs, due to the adipose tissue and retina will compete for lutein and zeaxanthin. In addition, the gender factor matters for the reason that men have stronger

ability in lutein and zeaxanthin transportation than women. Related researches have been carried on by Hammond.

In conclusion, besides the race factor, variable factors for MPOD mainly correlate to the content of lutein and zeaxanthin.

### 2.3 Photopigment and Variable Factors

Lens and macular can be seen as pre-receptor in the visual pathway. Light has to reach the photoreceptor layer at the back of the retina. Thomas et al. [21] summarized the underlying optical density variations including the length of the cone outer segment, the concentration at which photopigment is expressed, and quantal efficiency of individual photopigment molecules.

In addition, the genetic sequence is another variable factor. Neitz et al. [22] concluded that a single amino-acid substitution was correlated with trichromacy in the subjects who have photopigments with the same peak wavelength sensitivity but only different in optical density.

Lately, Yuta [23] described two types of variability in photopigment types: (1) variations in the peak optical densities of photopigments; (2) variations in  $\lambda_{\max}$  shifts (overall shifts in spectral sensitivity curves either toward shorter- or longer-wavelength region) of photopigments.

Few researches on photopigment variability were reported compared with lens and macular, perhaps for the difficulty of physiological experiments.

## 3 Quantification of Observer Metamerism

As to quantify observer metamerism, individual variability factors discussed above should be taken into consideration based on the traditional standard observer in colorimetry. Endeavor has been made by many researchers on this topic.

### 3.1 Standard Observer

Color Matching Functions (CMFs) composed by three sets of spectral energy distributions have been applied to represent the visual characteristics of human eyes. Meantime, the standard observer was recommended by CIE to represent the average normal observers.

Researches on color matching can be traced back to Maxwell [24] in 1860. But it wasn't until 1928 that Wright [25] started to collect actual measured observer data. Wright [26] and Guild [27] conducted experiments based on 10 and 7 observers respectively with the same experimental conditions (bipartite field,  $2^\circ$ ). In 1931 CIE defined the 1931 standard observer CMFs based on their data, on behalf of the human vision characteristic, on average.

However, CIE 1931 function calculations show deviation for the field size larger than  $4^\circ$ , due to the rod intrusion. Then in 1964, CIE recommended the 1964 CIE large-field standard observer for colorimetry based on color matching data from the laboratories of Stiles and Burch [28] and Speranskaya [29].

### 3.2 Individual Observer

CIE has paid more attention to OM since 1979. The metamerism subcommittee of CIE TC 1.3, Colorimetry, devoted on how to specify test observers for deriving suitable indices of OM. CIE TC1-07 recommended a Standard Deviate Observer (SDO) which was based on Nayatani et al.'s study in 1989 [30]. However, it was reported that real human observer variability was significantly underestimated.

Fairchild and Heckaman [31] developed a Monte Carlo model of color matching functions that allowed the computational creation of color matching functions for hypothetical individuals with various lens and macula optical densities and cone spectral responsivities.

In 2006 the CIE TC1-36 of Division I published a model named CIE Physiological Observer 2006 (CIEPO06) to predict mean color matching functions for average observers of various ages and field sizes [32].

Recently in 2015, Asano [23] developed an Individual Colorimetric Observer Model as Eq. 1. The proposed model is an extension of the CIEPO06, while it incorporates eight physiological parameters, representing all known significant variables.

$$\text{lms} - \text{CMF}_s = f(\text{age}, \text{fs}, d_{\text{lens}}, d_{\text{macula}}, d_l, d_m, d_s, s_l, s_m, s_s) \quad (1)$$

- (1)  $\text{age}, \text{fs}$ : age and field size as in CIEPO06;
- (2)  $d_{\text{lens}}, d_{\text{macula}}, d_l, d_m, d_s$ : density deviations [%] from average for lens, macula, L-, M-, S-cone;
- (3)  $s_l, s_m, s_s$ : shifts of  $\lambda$  [nm] from average for L-, M-, S-cone;

In summary, growing body of literature has drawn their attention to model and quantify individual observer CMFs. However, it is a tough work for too much variability involved, and more physiological data need to be collected.

### 3.3 Categorical Observer

Sarkar [15] developed a two-step method for deriving a minimal set of colorimetric observer categories. Meantime, eight observer categories and their corresponding CMFs were proposed through this method. Sarkar also developed an experiment to classify observers into nine observer categories.

Asano [23] made improvements on Sarkar's work, and proposed ten categorical observers. He derived categorical observers by two steps too. First 10,000 observer functions were generated from his individual colorimetric observer model using Monte Carlo simulation. After that cluster analysis with a modified k-medoids algorithm was applied.

The method of sorting human into different categories, offered a new way to deal with the problem of vision variability. However sufficient investigations need to be made on the more critical method or the number of categories.

## 4 Conclusions

Color science and technologies are undergoing a revolution, it is time to break through the limitation of traditional colorimetry which use a standard and average color description. Thus, observer vision variability among normal individual shall be taken seriously to promote the industrial applications.

It is recommended that further research should be undertaken in the following areas: (1) Further and in-depth physiological investigation shall never stop for it is the fundamental and root cause which contribute to individual variability and observer metamerism, although it is a tough work. (2) More rigorous observer data should be collected by carefully designed psychophysical experiments with variable control under full consideration. Among the various and complex physiological factors have been discussed above, only very few of them had been quantified. (3) Quantified relationships need to be built through mathematical methods with the support of more verified data. (4) Recognizing the significance of individual visual variability, cooperative investigation shall be taken through areas including physiology, psychophysics, colorimetry.

Potential applications need to be developed with the cutting-edge technologies, such as modern display and illumination industry, especially the LED, OLED and laser technologies. The special customized services will also be a broad and new application area, such as personalized calibration for color devices, or offering specific design for the certain group of consumers.

**Acknowledgments.** Thanks for the laboratory innovation funds of Tianjin University of Science and Technology, No. 1706A201.

## References

1. Kuo, W. G. (1995). Quantification of metamerism and color constancy. Loughborough University of Technology.
2. CIE. (1987). *International lighting vocabulary*. Genève: Bureau Central de la Commission Electrotechnique Internationale.
3. Artigas, J. M., Felipe, A., et al. (2012). Spectral transmission of the human crystalline lens in adult and elderly persons. *Investigative Ophthalmology Visual Science*, 53(7), 4076–4084.
4. Berendschot, T. T. J. M. (2002). Lens aging in relation to nutritional determinants and possible risk factors for age-related cataract. *Archives of Ophthalmology*, 120(12), 1732–1737.
5. Norren, D. V., & Vos, J. J. (1974). Spectral transmission of the human ocular media. *Vision Research*, 14(11), 1237–1244. [https://doi.org/10.1016/0042-6989\(74\)90222-3](https://doi.org/10.1016/0042-6989(74)90222-3).
6. Crawford, B. H. (1949). The scotopic visibility function. *Proceedings of the Physical Society. Section B*, 62(5), 321–334. <https://doi.org/10.1088/0370-1301/62/5/305>.
7. Pokorny, J., Smith, V. C., & Lutze, M. (1987). Aging of the human lens. *Applied Optics*, 26(8), 1437–1440. <https://doi.org/10.1364/AO.26.001437>.
8. Backhaus, W., Kliegl, R., & Werner, J. S. (1998). *Color vision: Perspectives from different disciplines*. Berlin: Walter de Gruyter.

9. Werner, J. S., & Scheffrin, B. E. (1993). Loci of achromatic points throughout the life span. *Journal of the Optical Society of America A*, 10(7), 1509.
10. Scheffrin, B. E., & Werner, J. S. (1993). Age-related changes in the color appearance of broadband surfaces. *Color Research & Application*, 18(6), 380–389.
11. Xu, J., Pokorny, J., & Smith, V. C. (1997). Optical density of the human lens. *Journal of the Optical Society of America A*, 14(5), 953.
12. Lutze, M., & Bresnick, G. H. (1991). Lenses of diabetic patients “yellow” at an accelerated rate similar to older normals. *Investigative Ophthalmology & Visual Science*, 32(1), 194–199.
13. Ambach, W., Blumthaler, M., et al. (1994). Spectral transmission of the optical media of the human eye with respect to keratitis and cataract formation. *Documenta Ophthalmologica*, 88(2), 165–173.
14. Hammond, B. R., Wooten, B. R., et al. (1999). Smoking and lens optical density. *Ophthalmic & Physiological Optics the Journal of the British College of Ophthalmic Opticians*, 19(4), 300–305.
15. Sarkar, A. (2011). Identification and assignment of colorimetric observer categories and their applications in color and vision sciences. School of Computer and Communication.
16. Howells, O., Eperjesi, F., & Bartlett, H. (2013). Macular pigment optical density in young adults of South Asian origin. *Investigative Ophthalmology & Visual Science*, 54(4), 2711–2719.
17. Iannaccone, A., Mura, M., et al. (2007). Macular pigment optical density in the elderly: Findings in a large biracial Midsouth population sample. *Investigative Ophthalmology & Visual Science*, 48(4), 1458–1465.
18. Ciulla, T. A., Curran-Celantano, J., Cooper, D. A., Hammond Jr, B. R., Danis, R. P., Pratt, L. M., Riccardi, K. A., & Filloon, T. G. (2001). Macular pigment optical density in a midwestern sample. *Ophthalmology*, 108(4), 730–737.
19. Bone, R. A., Landrum, J. T., Guerra, L. H., & Ruiz, C. A. (2003). Lutein and zeaxanthin dietary supplements raise macular pigment density and serum concentrations of these carotenoids in humans. *The Journal of Nutrition*, 133(4), 992–998.
20. Nolan, J., O’Donovan, O., Kavanagh, H., et al. (2004). Macular pigment and percentage of body fat. *Investigative Ophthalmology & Visual Science*, 45(11), 3940–3950.
21. Thomas, P. B. M., Formankiewicz, M. A., & Mollon, J. D. (2011). The effect of photopigment optical density on the color vision of the anomalous trichromat. *Vision Research*, 51(20), 2224–2233.
22. Neitz, J., Neitz, M., He, J. C., et al. (1999). Trichromatic color vision with only two spectrally distinct photopigments. *Nature Neuroscience*, 2(10), 884–888. <https://doi.org/10.1038/13185>.
23. Asano, Y. (2015). Individual colorimetric observers for personalized color imaging. Rochester Institute of Technology.
24. Maxwell, J. C. (1860). On the theory of compound colours, and the relations of the colours of the spectrum. *Philosophical Transactions of the Royal Society of London*, 10, 404–409.
25. Wright, W. D. (1928). A trichromatic colorimeter with spectral primaries. *Transactions of the Optical Society*, 29(5), 225–242. <https://doi.org/10.1088/1475-4878/29/5/302>.
26. Wright, W. D. (1929). A re-determination of the trichromatic coefficients of the spectral colours. *Transactions of the Optical Society*, 30(4), 141–164. <https://doi.org/10.1088/1475-4878/30/4/301>.
27. Guild, J. (1932). The colorimetric properties of the spectrum. *Philosophical Transactions of the Royal Society A: Mathematical, Physical and Engineering Sciences*, 230, 149–187.
28. Stiles, W.S., & Burch, J.M. (2010). N.P.L. colour-matching investigation: Final report (1958). *Optica Acta: International Journal of Optics*, 6(1), 1–26.
29. Speranskaya, N. I. (1959). Determination of spectrum color coordinates for 27 normal observers. *Optics and Spectroscopy*, 7, 424.



30. Nayatani, Y., Takahama, K., & Sobagaki, H. (1983). A proposal of new standard deviate observers. *Color Research & Application*, 8(1), 47–56.
31. Fairchild, M. D., & Heckaman, R. L. (2016). Measuring observer metamerism: The Nimeroff approach. *Color Research & Application*, 41(2), 115–124.
32. CIE. (2006). *Fundamental chromaticity diagram with physiological axes*. Vienna: Commission Internationale de l'Éclairage.



# Study on the Constancy of Color Vision

Haiwen Wang<sup>1</sup>(✉), Jie Li<sup>2</sup>, Xiaoxia Wan<sup>3</sup>, Ling Lu<sup>4</sup>, Pengfei Wang<sup>1</sup>,  
and Yongwei Wang<sup>5</sup>

<sup>1</sup> School of Environmental and Natural Resources,  
Zhejiang University of Science and Technology, Zhejiang, China  
wanghaiwen1@126.com

<sup>2</sup> School of Information Engineering, Quzhou College of Technology, Zhejiang,  
China

<sup>3</sup> School of Printing and Packaging, Wuhan University, Hubei, China

<sup>4</sup> Time Publishing and Media Co., Ltd, Anhui, China

<sup>5</sup> Zhejiang Minong Century Group, Zhejiang, China

**Abstract.** The constancy of color vision is referred to as an ability of human eye under different ambient light source illumination conditions to correctly identify and perceive colors of objects. It is of great significance for color recognition and high-fidelity reproduction. Based on measurement of Chroma, three psychophysical experiments of visual color constancy, constancy of the same color under different illuminant, constancy of different colors under different illuminant, instances of color constancy in daily life, were designed. By altering the illumination conditions of external photo-source, the experimenter's visual changes are employed for use of obtaining test conclusions. The results indicate that constancy of color vision includes process of selective extraction of color, automatic correction and compensation. It is affected by external illuminant, contrast between observed objects, as well as precedent memory of color on objects in human brain. This advanced visual feature of human brain makes it enjoy a relatively stable judgment of color between same or similar color, which is conducive for human to acquire, process and express color information.

**Keywords:** Color constancy · Color vision · Automatic correction · Selective extraction · Vision persistence

## 1 Introduction

The constancy of color vision is referred to as an ability of human eye under different ambient light source illumination conditions to correctly identify and perceive color of the object. This attribute diminishes the effect on color of image from illumination change or even hardly to detect the color change [1–3]. The color constancy includes size constancy, color constancy, shape constancy and brightness constancy, studies currently focus on constancy of color [4]. The study of color constancy is vital for color recognition, computer vision, video surveillance, and high-fidelity reproduction [5–8].

Current studies on color constancy mainly focuses on how to eliminate impact from illumination of light source, maintenance of color constancy, the algorithm of color

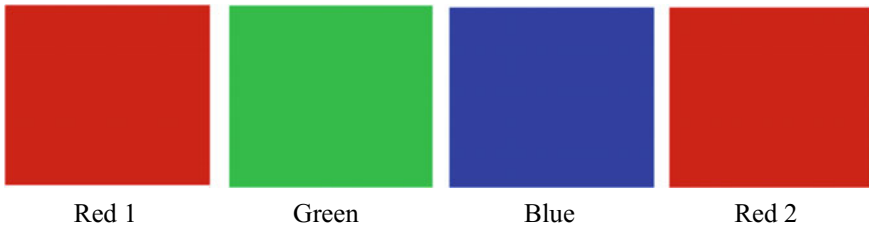
constancy, and ill-posed problem of color constancy under low illumination and complex illumination conditions [9–11]. However, there is a lack of research on psychophysics of color constancy and evaluation index system of color constancy. For this reason, the thesis designed three psychophysical tests of the visual constancy of color (constancy of the same color under different light sources, constancy of different colors under different light sources, examples of color constancy in daily life), by changing the outside illumination conditions. Visual changes of the tester were employed to draw conclusions of the tests (The publication of the paper was approved by all testers.). And, based on the self-compensation theory generated by human brain in order to cope with changes in the external environment, the laws of color visual constancy and cognitive functions of human vision were deeply studied.

## 2 Color Visual Constancy Experiment

The experiment is based on optical color measurement, observing and analyzing the visual persistence of the objects' color by changing the physical observation conditions, so as to study the color constancy laws of different objects. A total of three psychophysical tests were designed and illustrated as follows.

### 2.1 Same Color Constancy Experiment in Different Light Sources

Use software Photoshop to design four color blocks (as shown in Fig. 1, the RGB values of the four color blocks are  $R = 200, G = B = 0$ ;  $G = 200, R = B = 0$ ;  $B = 200, R = G = 0$ ;  $R = 150$  and  $G = B = 0$ ).

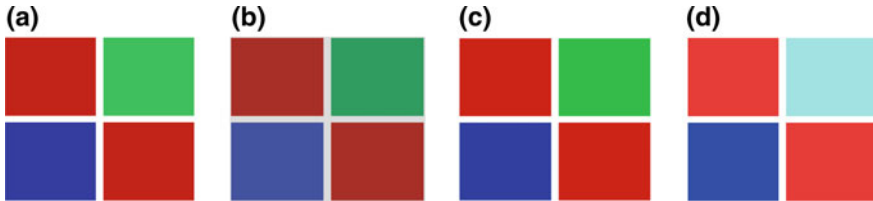


**Fig. 1.** Four color blocks

First of all, in the case of four kinds of light sources (A light source: average daylight D65, B light source: cool white fluorescence, C light source: horizontal sunlight, D light source: incandescent light), diffused through frosted glass, evenly illuminates the color sample's surface. Then, 10 college students (5 males and 5 females) with good color vision and visual acuity of 1.5 or more were selected for observation. Finally, print color blocks in high-fidelity, and then use a digital camera to shoot, a spectrophotometer for colorimetric measurements (measurement values shown in Table 1) and conduct human eye visual evaluation (the visual result of color blocks under four light sources is shown in Fig. 2), compare it, to go further, with original color data criterion to investigate the laws related to the human eye's color constancy.

**Table 1.** RGB value of 4 blocks under A, B, C illuminants

Results	A			B			C		
Red 1	225	59	62	261	26	38	189	23	15
Green	231	48	56	269	36	41	169	10	12
Blue	219	56	36	258	48	18	189	15	21
Red 2	189	38	42	288	59	62	163	12	9

**Fig. 2.** Four blocks' color results under four illuminants (from left to right, under A, B, C, D illuminant)

As the experiments suggest, although the appearance of the above four colors has undergone major changes, the experimenters still hold that they are the same color. In particular, the green color patches have become sky blue under the D light source, however, the testers still insist that they are the same color. This shows that the human visual system can automatically correct and compensate certain colors (especially the memory colors such as sky blue and grass green). In addition, the human eye has a strong adaptability to ambient light, and a strong selective extraction characteristic for visually obtained color information.

## 2.2 Constancy Experiment of Different Colors Under Different Illuminants

Design five red color blocks (as shown in Fig. 3, color block color values  $G = B = 0$ ,  $R$  are 250, 200, 180, 160, 120, respectively) by software Photoshop, then print out and shoot it by digital camera, finally display it on a computer and viewed under standard illuminant and incandescent illuminants.

**Fig. 3.** Five color block samples

It was found that the visual evaluation results of the five color blocks under different light conditions were almost the same, and only one experimenter contended that the color of the fifth color block was dark red. This demonstrates that the color constancy is not only affected by the contrast between the color blocks but also by the implicit cognition of the color. Therefore, so long as the brain is given sufficient environmental information, it will automatically compensate for the color of the environmental object according to the environmental information, such as the external illuminant, the background illuminant, the contrast with the surroundings of measured object, etc. it will automatically compensate for objects' genuine color so that the visual sense perceives the original color of the object.

### 2.3 Instances of Color Constancy in Daily Life

Through the color effect of the colorful Rubik's Cube, easy to find in daily life, under different filters, the color constancy is studied (as shown in Fig. 4). The specific plan is: Place the Rubik's Cube in the daytime outdoor daylight environment, and then observe through the red and the blue filter. As a result, the testers can recognize the red and also the blue blocks well; finally input two pictures to the computer. Although the colors of the color blocks in the image have transformed hugely, we can still recognize it easily. Hence, the brain produces a visual compensation and correction for changes of the ambient light source so that no changes in the color perception of the object can be detected.

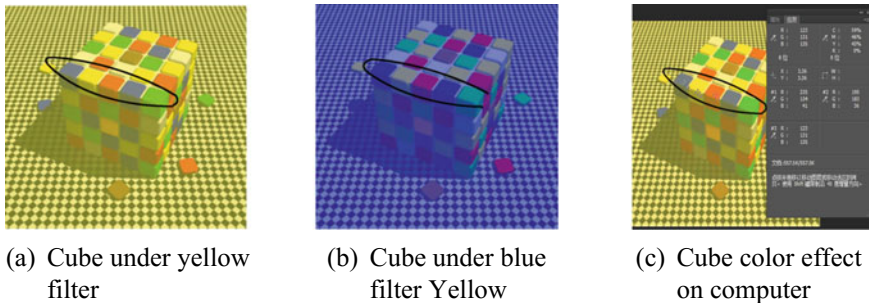


**Fig. 4.** Rubik's Cube under different filters and color effect on computer

## 3 Analysis of Experiment Results

From the above experiments it can be concluded that the constancy of color vision is influenced by the contrast between the colors of the objects as well as the latent impact of the memory colors in the human brain. The constancy of color vision involves the selective extraction to color information, the visual experience compensation from cerebral cortex and the process of surrounding environmental correction, which is a complex physical, physiological and psychological activity.

The human visual system automatically corrects and compensates for physical changes of color vision caused by altering ambient light source, so that the color at the visual level remains intact or changes little. This kind of correction or compensation phenomenon of human color vision allows for a specific adaptation environment for maintaining the constancy of color vision.

The constancy of color vision is not only a kind of visual low-level activity limited to eye cells, but also a judgment through combination of various environmental information so as to complete selective color extraction, automatic correction or automatic compensation to objects. It further confirms that the constancy of color vision is a high-level consciousness activity of human brain's visual information processing.

## 4 Conclusions

The constancy of color vision includes the process of selective extraction, automatic correction and compensation of color objects. It is influenced by the contrast between ambient environment illuminants and observation object, also by the pre-existing color memory of the object itself in human brain. This high-level human brain's visual characteristics makes relatively stable color judgments to same or similar colors available, which is conducive for human to acquire, process, and express color information.

The study of color constancy enriches theoretical theory of color vision, and provides a certain reference for color information processing and high-fidelity reproduction, therefore it is of great significance both on theory and application. In addition, postulated condition of the psychophysics test is the single color external light source in a homogeneous light intensity, but the genuine lighting environment is much more complicated. Hence, it is necessary to carry out research on the color constancy under the multiple light sources and real environment. Meanwhile, there is a lack of an objective evaluation system for color constancy at present, which is a topic to be further studied in the future.

**Acknowledgements.** This work is funded by application research project of Zhejiang Province public technology (2016C31080), key technology innovation special project of Zhejiang Province (2015-422), postdoctoral fund of Anhui Province (2016B125) and interdisciplinary research project of Zhejiang University of Science and Technology (2015JC06Y).

### **Compliance with Ethical Standards**

**Conflict of Interest:** The authors declare that they have no conflict of interest.

**Ethical Approval:** All procedures performed in studies involving human participants were in accordance with the ethical standards of the school of environmental and natural resources, Zhejiang University of Science and Technology and with the 1964 Helsinki declaration and its later amendments or comparable ethical standards.

**Informed Consent:** Informed consent was obtained from all individual participants included in the study.

## References

1. Zhao, Q., Pan, B., & Zheng, S. (2009). Color constancy enhancement in two steps under variable illumination. *Optics and Precision Engineering*, 17(4), 859–866.
2. Liu, Q., Wan, X., Liu, Z., Li, C., & Liang, J. (2013). Research on developing the spectral dataset for dunhuang typical colors based on color constancy. *Spectroscopy and Spectral Analysis*, 33(11), 3071–3074.
3. Jiao, S., Ji, G., & He, H. (1997). The process of human vision system's cognitive operation in keeping color constancy. *Acta Psychologica Sinica*, 29(2), 113–120.
4. Zhang, X. (2016). *The color constancy algorithm research based on computer vision*. China: Tianjin.
5. Rao, X., Zhang, L., & Zhou, H. (2014). Color constancy for scenes of non-uniform spectral power distribution of multiple light sources. *Journal of Yunnan University*, 36(2), 187–192.
6. Cai, X., Meng, X., & Xiang, H. (2004). The study of an illumination & hue color constancy algorithm. *Journal of Image and Graphics*, 9(8), 922–926.
7. Amano, K., Linhares, J. M. M., & Nascimento, S. M. C. (2018). Color constancy of color reproductions in art paintings. *Journal of the Optical Society of America*, 35(4), 324–333.
8. Tang, Z., Liu, H., & Yuan, J. (2016). Advances research on color constancy computation under single illuminant. *Computer Science*, 43(11), 12–18.
9. Liu, Q., Wan, X. X., Liu, Z., & Sun, P. (2014). Spectral separation method for multi-ink printers based on color constancy. *Applied Mechanics and Materials*, 731(1), 18–21.
10. Zhu, J. (2011). *The research on color constancy theory and application in image enhancement*. Hefei, China.
11. Gao, S.-B., Zhang, M., Li, C.-Y., & Li, Y.-J. (2017). Improving color constancy by discounting the variation of camera spectral sensitivity. *Journal of the Optical Society of America*, 34(8), 1448–1462.



# Research on Digital Printing Color Prediction Model Based on PSO-BP Neural Network

Siwei Lu<sup>(✉)</sup>, Qiang Wang, Ping Yang, and Weiyan Zhang

College of Media and Design, Hangzhou Dianzi University, Hangzhou, China  
sweeluu@163.com

**Abstract.** This paper is aimed at the key technology of digital printing in the textile industry. According to the color reproduction characteristics of digital printing, a color prediction model based on Particle Swarm Optimization (PSO) was proposed to optimize the three-layer BP neural network, solving the problem that BP neural network is easy to fall into local minimum value through optimization of weights and thresholds, which effectively improved the digital printing color prediction accuracy. The experimental and industrial application results show that the prediction accuracy of this paper is higher than BP neural network model and the Yule-Nielsen modified Neugebauer model these two mainstream algorithms, which is more in line with the practical needs of digital printing industry applications.

**Keywords:** Digital printing · BP neural network · Particle swarm optimization (PSO) · Color prediction model

## 1 Introduction

Digital printing technology is the application of digital inkjet printing and digital control technology to break through the bottleneck of traditional textile printing production long cycle, high cost, and complex quality control. It is a new technology for the establishment of on-demand printing custom [1]. However, digital ink jet printing still has the problems of large color fluctuation and insufficient accuracy of partial color reproduction, which makes the color prediction model in color reproduction of high-precision digital inkjet printing a key issue and a hotspot.

In recent years, researches on color prediction models mainly focus on the Neugebauer cell model, the spectral Neugebauer models and its modified or optimized models, the polynomial regression models, the table-look up models and the neural network models [2]. However, due to the large number of non-linear factors in digital ink jet printing equipment, the existing models have the disadvantages of low sample size, model complexity, and low model efficiency. Therefore, it is urgent to construct a high-precision color prediction model to break through the bottleneck.

Based on the neural network, this paper proposes a new PSO-BP neural network model for color prediction of ink jet printing by using PSO to optimize the BP neural network and solve the problem that BP neural network has slow convergence rate and it's easy to fall into local minima.



## 2 PSO-BP Neural Network Principle

### 2.1 BP Neural Network

BP neural network is a multi-layer feed-forward neural network trained according to the error reverse propagation algorithm [3]. It adopts the minimum mean square error learning method [4] and the network has the three-layer topology structure of input layer, hidden layer and output layer. Through the hidden layer from the input layer, the signal finally reaches the output layer, and from the output layer to the hidden layer, the error in the input layer is back-propagated to adjust the weight and bias of the hidden layer to the output layer and the input layer to the hidden layer in turn.

### 2.2 PSO Algorithm

Particle swarm optimization (PSO) is a biological evolution algorithm [5] that defines one point as a particle by defining a D-dimensional search space. It first initializes a group of particles and then iteratively finds the optimal solution in a group of particles. In each iteration, the particle updates the position and velocity through their own search for the optimal solution  $P_{best}$  and the global extremum  $G_{best}$  searched by the entire particles. The update formulas for the position and velocity of particles are Eqs. (1) and (2).

$$v_{ij}(t+1) = \omega \times v_{ij}(t) + c_1 \times r_1 \times [p_{ij}(t) - x_{ij}(t)] + c_2 \times r_1 \times [p_{gi}(t) - x_{ij}(t)] \quad (1)$$

$$x_{ij}(t+1) = x_{ij}(t) + v_{ij}(t+1) \quad (2)$$

Among them,  $\omega$  is inertia weight,  $c_1$ ,  $c_2$  are learning factors,  $r_1$ ,  $r_2$  are random numbers between 0 and 1.

If the population particle number is  $n$ , each particle is  $m$ -dimensional, and the position of the  $i$ -th particle is expressed as  $x_i = (x_{i1}, x_{i2}, \dots, x_{im})$ , and the  $i$ -th particle's current optimal position is  $P_{best_i} = (p_{i1}, p_{i2}, \dots, p_{im})$ , the group's current optimal position  $G_{best_i} = (g_1, g_2, \dots, g_m)$ , and the position change of the  $i$ -th particle is  $v_i = (v_{i1}, v_{i2}, \dots, v_{im})$ .

### 2.3 PSO Optimization BP Neural Network

This paper aims at the BP neural network does not have local search optimization method for global search performance. It has slow convergence speed, easily falls into local extremum, and is very sensitive to parameters such as initial weights and learning rates. So we adopt PSO algorithm with fast convergence rate, high robustness, and good global search capability, optimize weights and thresholds of BP neural network by updating the position and rate of particles to obtain the optimal initial weights and thresholds of fitness value, which can make up for the defects of BP neural network, meet the accuracy of the output value. The working principle of PSO-BP neural network is shown in Fig. 1.

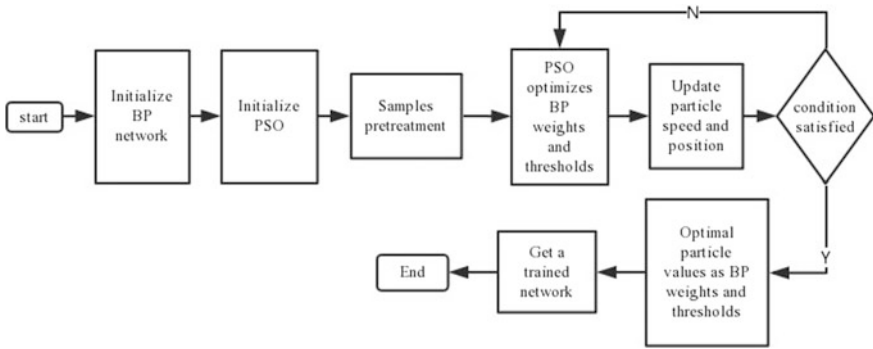


Fig. 1. PSO-BP neural network working principle

### 3 The Construction and Realization of Prediction Model

#### 3.1 PSO-BP Model Establishment

1. The PSO parameters in the PSO-BP algorithm of this paper are based on the better optimization result of the dynamic values, that is, using the linear decrement of the weights, decreasing linearly from 0.9 to 0.4, and selecting the particle dimension H, H is calculated from formula (3):

$$H = h_j + h_i \times h_j + h_j \times h_k + h_k \tag{3}$$

Among them,  $h_i$ ,  $h_j$  and  $h_k$  are the number of nodes in input layer, hidden layer and output layer respectively.

2. When constructing the PSO-BP model and BP network parameter settings, the number of nodes selecting the input layer and the output layer is three. The number of hidden layer nodes is calculated by using empirical formula (4):

$$h_j \leq \sqrt{h_i \times (h_k + 3)} \tag{4}$$

3. The mean square error function of the BP neural network is selected as the fitness function of the particle swarm algorithm. The formula for calculating the fitness value of the particle is formula (5).

$$\text{Fitness} = \frac{1}{N} \sum_{i=1}^N \sum_{j=1}^M (y_{ij} - \bar{y}_{ij})^2 \tag{5}$$

where  $N$  is the number of samples,  $M$  is the particle dimension,  $y_{ij}$  is the theoretical output of the BP neural network corresponding to sample  $i$ , and  $\overline{y_{ij}}$  is the actual output of the BP neural network corresponding to sample  $i$ .

4. If the fitness value of the current particle is better than its historical optimal fitness value  $P_{best}$ , the historic optimal fitness value  $P_{best}$  is changed to the current particle's fitness value; if not, then the global optimal fitness value  $G_{best}$  is changed to the historical optimal fitness value of the current particle.
5. When these two extremums are found, the position and velocity of each particle are iteratively updated according to Eqs. (1) and (2) to reach the optimum. When the stop condition is satisfied, the iteration is stopped and the connection weights and thresholds are output. Use them to train BP neural network.

### 3.2 Layers Partitioning Based on Lightness

In this paper, considering the sensitivity of the human eye to lightness and the maximum ink value of  $K$  (black) in actual production, the color space is divided into six layers  $K_0$ ,  $K_{10}$ ,  $K_{30}$ ,  $K_{50}$ ,  $K_{70}$ , and  $K_{90}$  based on lightness. The prediction of the model is performed separately in six layers.

### 3.3 Experimental Design

The experimental samples of this article used the Honghua 3186S high-speed machine for digital ink jet printing, and the printing fabric was twill silk.  $C$ ,  $M$ , and  $Y$  were arranged according to the dot area percentage [0, 10, 50, 90, 100%] as a training sample,  $3^5 = 243$  in total, and the dot area percentage of  $C$ ,  $M$ , and  $Y$  were arranged as [0, 5, 30, 70, 95, 100%] and combined color patches as test samples,  $3^6 = 729$  in total. The color patch samples are shown in Fig. 2. X-rite's spectrophotometer  $i_1$  was used as a measuring device to measure the  $L$ ,  $a$ , and  $b$  values of the color patches. PSO-BP network training and analysis used MATLAB R2015 software.

The device was tested for constancy before the experiment. The sample was measured three times with  $i_1$  and analyze the result. The average color difference of the three measurements was  $\Delta E_{00} = 0.05$ . To reduce the error, the experimental data was taken as the average of the three groups of sample data.

### 3.4 Prediction Results and Analysis

Figure 4 shows the trend of the color difference statistics obtained from the different layers  $K_0$  to  $K_{90}$ . The horizontal axis is the numbered samples based on statistics, and the vertical axis is the color difference range. It can be seen that the statistical color difference trends in each layer are approximately the same. And the whole model itself can be compared longitudinally. When the lightness decreases, the smaller the color difference is, the less the sample with the color differences above 4 and the higher the precision of the model. Figure 3 shows the variation curve of the individual fitness of particles in the iteration process of the PSO algorithm in the  $K_0$  layers. In the constant iteration process, the fitness value is minimized, that is, the mean square error is

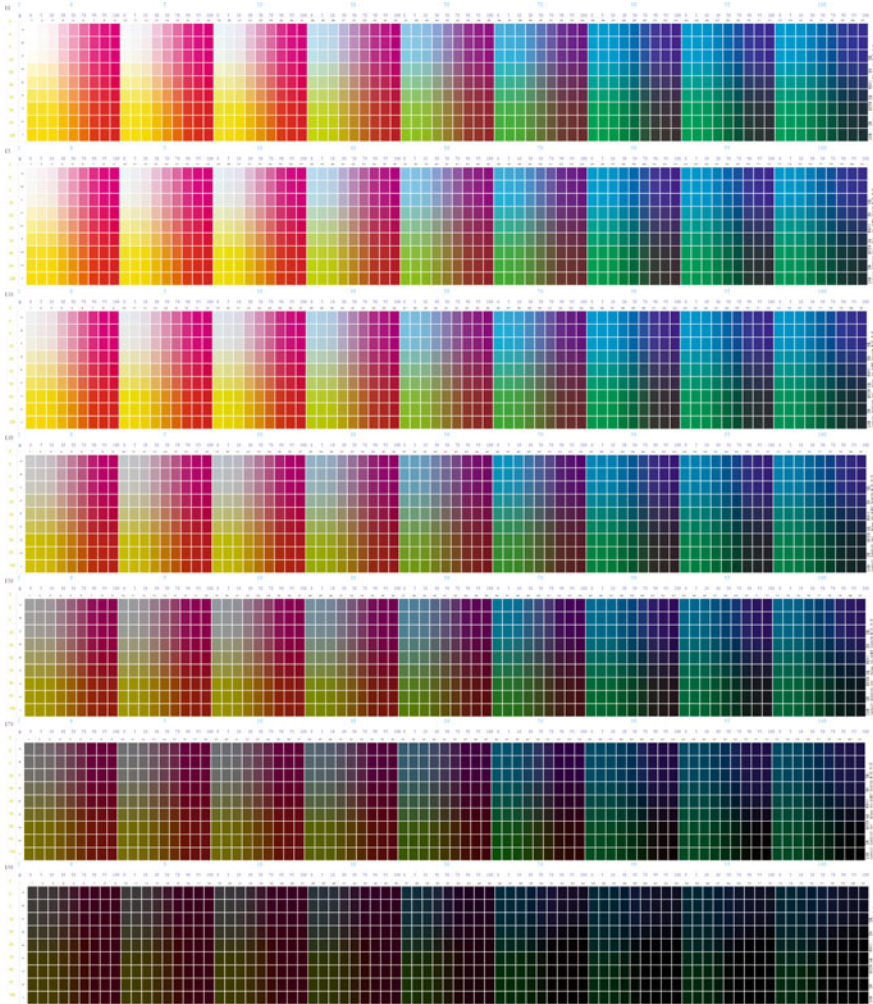


**Fig. 2.** Color patch samples

minimized, and the model is trained at about 40 times. At that time, the model tends to be stable and the model reaches a convergent state, which avoids the problem that the BP neural network easily falls into a minimum value.

With the same number of samples, this paper compares the prediction errors of PSO-BP and BP and Yule-Nielsen modified Neugebauer model, and uses color difference and root mean square error (RMSE) to represent the predicted accuracy. The results are shown in Table 1. we can see that the PSO-BP model has the best indexes, while the Yule-Nielsen modified Neugebauer model has the largest error.

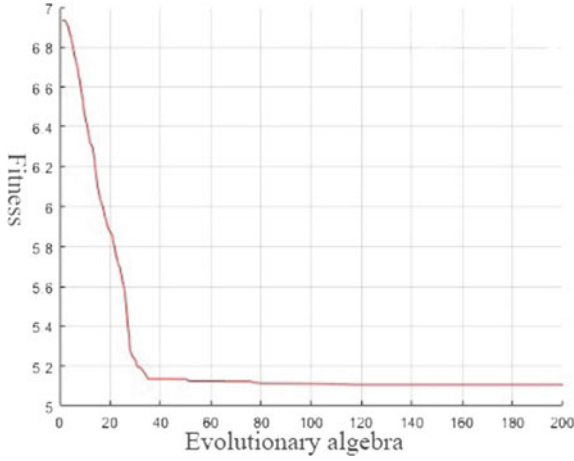


Fig. 3. K0 layer fitness curve

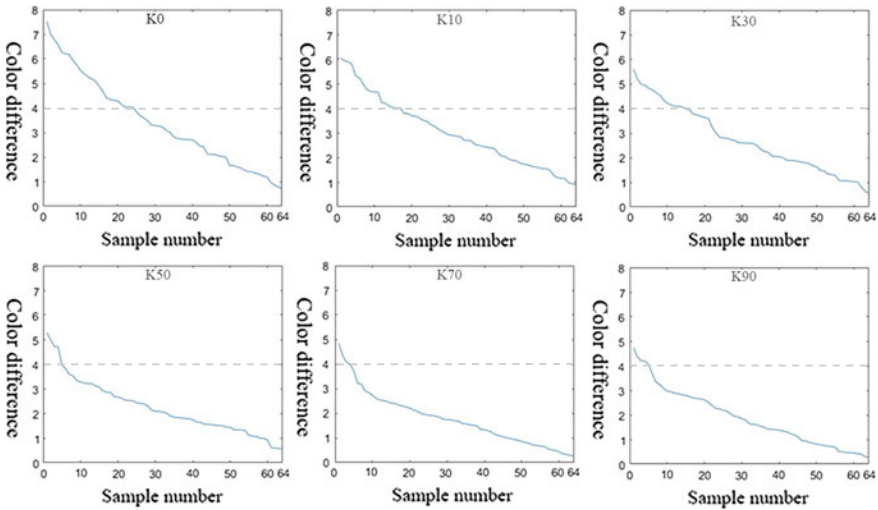


Fig. 4. Color difference trend chart of K0 to K90 layers

## 4 Conclusion

According to the nonlinear characteristics of ink-jet equipment in digital printing, this paper proposes a digital printing color prediction model that optimizes BP neural network weights and thresholds through particle swarm optimization algorithm and compares the prediction accuracy of PSO-BP with BP, Yule-Nielsen modified Neugebauer model. Experimental results show that the PSO-BP algorithm can avoid the occurrence of local extremes, reach the minimum fitness value, significantly

**Table 1.** Comparison of prediction accuracy among PSO-BP, BP and Yule-Nielsen modified Neugebauer

Partition	4 × 4 × 4 PSO-BP		4 × 4 × 4 BP		4 × 4 × 4 Y-N	
	Mean $\Delta E_{ab}^*$	Mean RMSE	Mean $\Delta E_{ab}^*$	Mean RMSE	Mean $\Delta E_{ab}^*$	Mean RMSE
K0	2.997	0.823	11.689	2.697	16.325	27.414
K10	2.7	0.601	10.004	2.402	13.758	25.989
K30	2.296	0.457	8.452	2.328	11.554	20.127
K50	1.899	0.234	8.048	2.179	10.208	15.735
K70	1.759	0.111	7.265	1.934	8.995	10.989
K90	1.88	0.065	6.788	1.69	7.698	10.322
All	2.255	0.382	8.708	2.205	11.423	18.429

improve the model’s prediction accuracy, algorithm stability and portability, and better meet the actual needs of digital printing industry applications.

**Acknowledgements.** This work is funded by National Key Technology Research and Development Program of the Ministry of Science and Technology of China (2012BAH91F03) and Hangzhou Dianzi University Graduate Innovative Research Fund (CXJJ2018017) and Digital Imaging Theory-GK188800299016-054.

## References

1. Yun, Q., & Wang, Q. (2017). Research on spectral prediction model based on textile digital printing. *Journal of Hangzhou Dianzi University*, 37(6), 67–72.
2. Yu, H., Liu, Z., & Tian, Q. (2015). Multi-color prediction model based on BP-NN optimized by GA and PCA. *Chinese Journal of Luminescence*, 36(6), 711–717.
3. Wu, Z., Zhao, Y., Luo, X., & Du, H. (2017). License plate recognition technology based on PSO-BP neural network. *Journal of Sun Yat-sen University*, 56(1), 46–52.
4. Zeng, W., Wei, R., & Chen, H. (2008). Research and application of BP neural network based on improved PSO algorithm. *Computer Technology and Development*, 18(4), 49–51.
5. Suresh, A., Harish, K. V., & Radhika, N. (2015). Particle swarm optimization over back propagation neural network for length of stay prediction. *Procedia Computer Science*, 46, 268–275.



# Research on the Atmosphere and Emotionality of Apparel Stores Under LED Lighting Environment

Liang Sun<sup>2</sup>, Jing Liang<sup>1(✉)</sup>, Ze Liu<sup>2</sup>, and Yuanming Zhang<sup>2</sup>

<sup>1</sup> School of Information Science and Engineering,  
Dalian Polytechnic University, Dalian, China  
ljlove426@163.com

<sup>2</sup> School of Light Industry and Chemical Engineering,  
Dalian Polytechnic University, Dalian, China

**Abstract.** The paper is to study the atmosphere and emotional performance of undergraduate students in simulated clothing store LED lighting environment. By analyzing the basic evaluation indicators in this environment, the influence of color temperature and brightness on the evaluation indicators of atmosphere was discussed. Using psychophysical experiments, 53 undergraduates (aged 19–22 years old) assessed the atmosphere of the four light environments. For each condition, 71 pairs of scales questionnaires were used. Factor analysis determines a basic dimension of the environment: cosiness and liveness. And eighteen scales are established to evaluate the atmosphere of clothing stores. The results of the study show that higher brightness will make the environment livelier. The clothing store uses a warm light of about 3000 K to make people feel comfortable.

**Keywords:** LED lighting · Psychophysical experiment · Factor analysis · Atmosphere · Emotionalization

## 1 Introduction

Many surveys have shown that the lighting environment affects human emotions, behaviors, perceptions and preferences. Therefore, the atmosphere of the clothing store will directly affect the enthusiasm of consumers. Vogels believes that emotion and atmosphere are an experience that human observers have for the surrounding environment [1]. At the same time, research shows that the definition of atmosphere requires at least two dimensions: comfortable and lively [1], but she uses fluorescent lamps and halogen lamps when defining these dimensions. With the increasing popularity of LEDs, traditional light sources (halogen lamps, etc.) are gradually being replaced, and most apparel stores today also use LED lighting combined with traditional lighting (halogen lamps, etc.).

In view of the above problems, this paper, based on the current situation of shopping malls and clothing stores, invites college students to conduct psychophysical experiments by simulating the environment of clothing stores, and obtain psychological

perception data of observers in the atmosphere of simulated clothing stores. Study the atmosphere and emotional performance of college students in the LED lighting environment of simulated clothing stores.

## 2 Psychophysics Experiment

### 2.1 Observer Selection

53 (14 female, 39 male) undergraduate observers from Dalian University of Technology were selected for the experiment. Except for the 14 people in the B1 group, the other three groups were thirteen, and the age range was 19–22 years old. The color blindness test was normal. Before observers entered the experimental environment, it was necessary to adapt to the test adaptation environment for one minute, then walked around the experience and fill out the questionnaire. The 71-scales questionnaires are used by XY. Liu is in the questionnaires [2].

### 2.2 Experimental Environment and Method

The experiment was completed in the Light Environment Simulation Laboratory of Dalian Polytechnic University. The lights are all bright, except for the two halogen lamps, all the lights are brightened, and some of the lights are illuminated, all the lights are extinguished in four cases, divided into A (all lights are bright), B (all lights except two halogen lights) A1 (part lights) B1 (no lights) four groups experiments were carried out, and basic parameters were measured at the center. The observers were divided into four groups to evaluate the atmosphere of the 71 groups of the lights in the four environments, and the lowest score of  $-3$  means no \*\* (like, comfortable, attractive, etc.), the highest score of 3, indicating very \*\* (like, comfortable, attractive, etc.) (Table 1).

**Table 1.** Basic parameters of the light source used in the experiment

Lighting condition	Ambient color temperature/K	Ambient illumination/lx	x	y	Ra
A	3431	1457	0.4090	0.3921	91.9
B	3407	1125	0.4097	0.3909	92.4
A1	3415	1383	0.4096	0.3916	92.2
B1	3632	1.6	0.4247	0.4624	81.8

Experiment process:

- (1) Visual test (testing whether the observer has visual defects or color blindness);
- (2) Introduce the experiment to the observer;
- (3) Adaptation of the lighting environment (about 1 min);



- (4) Subjective evaluation of the atmosphere of the light environment of the simulated clothing store (the experimenter requires the observer to fill in the corresponding score according to the questionnaire);
- (5) Switching light source to change the lighting environment of the simulated clothing store;
- (6) Repeat 3–4 times until the end of the experimental data collection.

### 3 Results and Analysis of This Experiment

#### 3.1 Observer Reliability

The values of reliability  $\alpha$  range from 0.628 to 0.942. It can be seen from Table 2 that the credibility values of the four groups of experiments are within the range of values, so the observers of the experiment have high reliability.

**Table 2.** Reliability analysis of each group of observers

Groups	A	B	A1	B1	Total
Cronbach's alpha	0.930	0.917	0.739	0.927	0.929

#### 3.2 Principal Component Analysis

Using the principal component analysis software SPSS to determine the basic elements of atmosphere perception Principal component. It is designed to generate independent variables called factors. Table 3 lists the distribution of each factor. According to the principal component analysis, the five main factors extracted were 22.964, 8.82, 6.044, 5.473, and 4.716%. For each factor, there is a feature value calculated to correspond to it. The values of factors 3–5 are significantly small, indicating that their differences are small. Figure 1 shows the distribution of various factors. It can be seen from the figure that the distribution of factor 1 is the most dense, according to the theory of confirming the basic dimension according to PJM Custers M.Sc. [3] as shown in Table 4: the basic perceptual dimension of factor 1 is cosiness. And in the factor 1, there are also pairs of words such as depression-inspired, so liveness can therefore also be used. At the same time, 18 scales of factor 1 were also established to evaluate the atmosphere of the clothing store.

#### 3.3 The Relationship Between Brightness, Warmth and Cosiness

In this paper, the bright-dark as the brightness, the cool-warm as the warmth, through the multi-factor analysis of variance, the results are shown in Table 5. The results show that the cosiness is positively correlated with the visual acuity, and it is opposite to Vogels' experiment [4]. At the same time, it was found that cosiness was positively correlated with warmth. The CCT used in this experiment is mostly in a warm yellow

**Table 3.** Load the atmospheric size using a factor of 71 scales

Overall variance: 48.025%	Factor 1	Factor 2	Factor 3	Factor 4	Factor 5
Scales	22.96%	8.82%	6.04%	5.47%	4.71%
Depressed-cheerful	<b>0.789</b>	-0.054	-0.280	0.015	0.087
Dejected-inspiring	<b>0.767</b>	-0.218	-0.119	0.064	0.188
Negative-positive	<b>0.757</b>	-0.119	-0.204	-0.027	0.173
Bright-dark	<b>0.724</b>	-0.018	-0.107	-0.197	0.225
detached-cheerful	<b>0.716</b>	-0.141	-0.100	-0.150	0.154
Safe-dangerous	<b>0.699</b>	-0.010	0.308	-0.021	0.054
Cool-warm	<b>0.698</b>	-0.162	0.006	-0.171	-0.135
Wilted-excited	<b>0.686</b>	-0.091	0.027	0.086	0.043
Lifeless-energetic	<b>0.681</b>	-0.068	0.170	-0.162	0.047
Alienated	<b>0.680</b>	-0.131	-0.187	0.010	0.105
Desolation-radiant	<b>0.679</b>	-0.137	0.085	-0.194	-0.250
Unhappy-happy	<b>0.670</b>	0.047	-0.330	-0.097	-0.074
Hostile-friendly	<b>0.662</b>	-0.333	-0.121	0.144	0.046
Repressed-active	<b>0.639</b>	-0.310	0.034	0.203	0.288
heavy-happy	<b>0.635</b>	-0.127	0.580	-0.108	0.151
Dull-vivid	<b>0.634</b>	-0.044	0.218	-0.298	-0.098
Fearful-close	<b>0.626</b>	-0.305	-0.092	0.279	0.229
Old-fashionable	<b>0.606</b>	0.205	-0.241	-0.263	0.023
Vulgar-noble	0.219	<b>0.817</b>	-0.180	-0.047	-0.041
Feminine-masculine	-0.035	<b>0.643</b>	0.124	-0.205	0.287
Unightly-beautiful	0.531	<b>0.559</b>	0.322	-0.074	-0.126
Cheesy-refined	0.234	<b>0.522</b>	-0.281	0.089	-0.117
Frivolous-serious	-0.091	<b>0.517</b>	0.188	-0.244	-0.036
Impetuous-calm	-0.053	0.416	<b>0.516</b>	0.296	0.098
(In)dependent	-0.240	-0.082	<b>0.504</b>	-0.217	0.057
Classical-modern	0.321	-0.057	<b>0.428</b>	0.237	-0.110
Commercial-literary	0.328	0.195	<b>0.340</b>	-0.151	-0.200
Anxious-calm	0.125	0.169	0.351	<b>0.601</b>	0.139
Casual-formal	0.057	0.428	-0.178	0.019	<b>0.644</b>

light of about 3000 K, so the regional culture difference can be found. Vogels experiment found that the Dutch are more comfortable and active in the case of low CCT [5], and this experiment is contrary to him. The Chinese observers feel more comfortable under a CCT of around 3000 K.

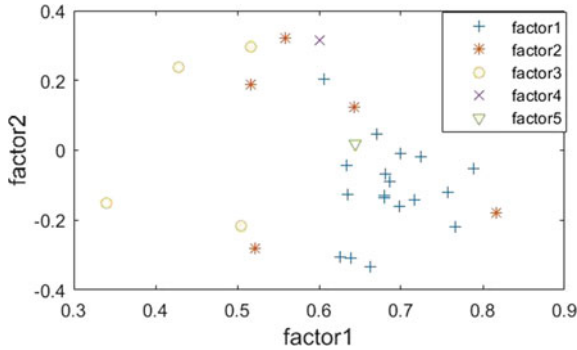


**Fig. 1.** Distribution of five factors

**Table 4.** Four basic atmosphere dimensions

Dimensions	Cosiness	Liveness	Tenseness	Detachment
Items	Cosy	Lively	Tense	Business
	Intimate	Stimulating	Terrifying	Forma
	Pleasant	Inspiring	Oppressive	Cool
	Safe	Cheerful	Uncomfortable	Chilly
			Threatening	

**Table 5.** The effect of brightness and warmth on factor 1 (cosiness)

		Brightness	Warmth
Factor 1 (cosiness)	Person r	0.729 <sup>**</sup>	0.702 <sup>**</sup>
	P value	0.000	0.000

<sup>\*\*</sup> $P < 0.01$

## 4 Conclusions

This research is mainly to study the atmosphere of the clothing store. The research results show that the cosiness is enough to describe the atmosphere of the clothing store. The same liveness can also be used to describe the atmosphere of the clothing store, and the eight scales are established which can be used to study the clothing store. The study also found that higher brightness will make the clothing store more comfortable, about 3000 K. The color temperature makes the environment of the clothing store more comfortable. Finally, cultural differences were discovered.

For cosiness, in the clothing store environment, Chinese people feel warm when the color temperature is about 3000 K.

**Acknowledgements.** This work is supported by QianBaiHui Research Fund Project (2017-228195).

### Compliance with Ethical Standards

**Conflict of Interest:** The authors declare that they have no conflict of interest.

**Ethical Approval:** All procedures performed in studies involving human participants were in accordance with the ethical standards of the school of Information Science and Engineering Dalian Polytechnic University and with the 1964 Helsinki declaration and its later amendments or comparable ethical standards.

**Informed Consent:** Informed consent was obtained from all individual participants included in the study.

## References

1. Vogels, I. (2008). Atmosphere metrics: A tool to quantify perceived atmosphere. In *International Symposium Creating an Atmosphere*. Grenoble, France.
2. Liu, X. Y., Luo, M. R., & Li, H. (2014). A study of atmosphere perceptions in a living room. *Lighting Research & Technology*, 47(5), 581–594.
3. Custers, P. J. M., De Kort, Y. A. W., et al. (2010). Lighting in retail environments: Atmosphere perception in the real world. *Lighting Research & Technology*, 42(3), 331–343.
4. Vogels, I., Sekulovski, D., Clout, R., & Moors, R. (2009). A quantitative study on the impact of light on the atmosphere of an environment. In A. K. Yener & L. D. Ozturk (Eds.), *Lux Europa 2009: 11th European Lighting Congress* (pp. 385–392). Istanbul: Turkish National Committee on Illumination.
5. Vogels, I. (2008). Atmosphere metrics: Development of a tool to quantify experienced atmosphere. In J. M. D. M. Westerink, M. Ouwerkerk, T. J. M. Overbeek, W. F. Pasveer, & B. de Ruyter (Eds.), *Probing Experience: From Assessment of User Emotions and Behaviour to Development of Products* (pp. 25–41). Dordrecht: Springer.



# Research on the Antagonism Mechanism of Human Color Vision

Shengwei Yang<sup>1(✉)</sup>, Xiangyang Xu<sup>2</sup>, and Lingjun Kong<sup>1</sup>

<sup>1</sup> Department of Printing and Packaging Engineering,  
Shanghai Publishing and Printing College, Shanghai, China  
bestysw@qq.com

<sup>2</sup> School of Communication Engineering, Shenzhen Polytechnic,  
Guangdong, China

**Abstract.** The antagonistic mechanism of human color vision is the physiological characteristics of the human visual system. The processing of spatial color information in visual color channels is opposite, which presents that the black-white opposition color channel, the red-green opponent color channel and the yellow-blue opposition color channel are all multi-scale. This paper aims to study the algorithm of the antagonistic mechanism of human color vision. Based on the theory of the visual receptive fields, seven filter operators associated with the human observation condition are designed; the mapping relation between these operators and human visual observation scale is established. The paper put forward to an algorithm for simulating the antagonistic mechanism of human color vision, which is carried out in visual opposite color space. The experiment results show that the algorithm has the ability of color constancy prediction, and the color reduction accuracy is not lower than the automatic white balance processing result of the professional digital SLR camera.

**Keywords:** Color vision · Contrast sensitivity · Color constancy · White balance

## 1 Introduction

Neurophysiological evidence shows that color antagonistic cell exists on the optic nerve pathway of the retina and brain visual cortex area. Color antagonistic cell only responds to color or color contrast. This type of cell has a central-marginal antagonistic organizational structure [1]. Based on the central- marginal antagonism mechanism, researchers have developed algorithms that simulate this mechanism in order to achieve some desired effect. The algorithms have been applied accordingly in digital image enhancement techniques [2], high-dynamic image compression techniques [3], computation of color constancy [4] and other aspects. This type of algorithms only embodies the single-scale or dual-scale nature of spatially complex color stimulation. But in fact, color antagonistic cell is multi-scale in perception of spatial color information.

The purpose of this paper is to simulate the multi-scale processing algorithm of spatial complex color stimulation in human eye color antagonism mechanism. It is expected to solve two problems. Firstly, a quantization method for spatial frequency tuning curve filter operator corresponding to visual opposite color channel is proposed to solve the problem that visually antagonizing color space cannot describe the spatial correlation of spatial complex color stimulation. Secondly, to solve the problem that the current human eye color visual antagonist mechanism simulation algorithm does not realize the multi-scale processing mechanism simulation of human visual field color perception field space.

## 2 Antagonism Mechanism Simulation Algorithms

The center-edge antagonism of the human eye vision is measured by the image of the color contrast changing with the spatial frequency of the sine wave. The measurement result is the human visual contrast sensitivity function (CSF) [5–8].

As shown is Fig. 1, The CSF function can be decomposed into multiple band-pass filter operators in the frequency domain. These operators show that the perception of color information of human eyes is a process of extracting details level by level. If the filter characteristics can be quantified, the human eye can be realized. The antagonism mechanism simulation algorithm of human eye visual system can be developed.

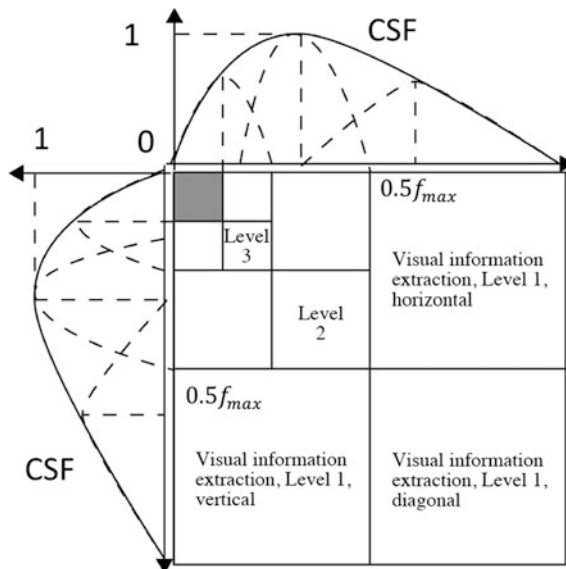


Fig. 1. CSF and spatial multi-scale processing

## 2.1 Visual Spatial Scale Decomposition

Visual spatial scale decomposition is quantified by the size of the perspective. The size of the human eye space scales in different visual attention areas are related to the resolution, image size, and observation distance shown as Formula 1.

$$SpD = 0.01745 \times D \times imR \quad (1)$$

In the formula, SpD indicates the number of sampling points in the  $1^\circ$  viewing angle, imR indicates the resolution of the observed image, and D indicates the visual observation distance. Theoretically, the maximum viewing angle  $V_{\max}$  is known when the observation distance, image size, and image resolution are fixed. If the angle of view changes in 1 step, the image can be decomposed into  $[V_{\max}]$  visual window. If decomposing the image into multiples scales according to the method of half down-sampling, the decomposition form of the image is expressed as Formula 2, where the original size of the image is represented as  $V_0$ .

$$V \stackrel{def}{=} \left\{ V_0, \frac{1}{2} V_0, \frac{1}{4} V_0, \frac{1}{8} V_0, \dots, SpD \right\} \quad (2)$$

## 2.2 CSF Multi-channel Filter Operator

If the CSF model proposed by Johnson and Fairchild [8] is approximated by multiple Gaussian numbers, the multi-band expressions as Formulas 3 and 4 show:

$$csf_{lum} = a_1 \cdot \exp\left(-\frac{(x-b_1)^2}{c_1^2}\right) + a_2 \cdot \exp\left(-\frac{(x-b_2)^2}{c_2^2}\right) + a_3 \cdot \exp\left(-\frac{(x-b_3)^2}{c_3^2}\right) \quad (3)$$

$$csf_{chrom} = a_1 \cdot \exp\left(-\frac{(x-b_1)^2}{c_1^2}\right) + a_2 \cdot \exp\left(-\frac{(x-b_2)^2}{c_2^2}\right) \quad (4)$$

Formulas 3 and 4 are the CSF functions of the luminance and chroma channels in the form of the sum of multiple Gaussian functions. The relevant parameters are shown in Table 1. The  $c_i$  in Table 1 can be used to calculate the half bandwidth FWHM of the Gaussian function to simulate the width of the visual bandpass filter. The calculation of the half bandwidth is expressed by Formula 5.  $a_i$  simulate the telescopic characteristics of the analog bandpass filter. Different filters are mapped to different visual spatial scales, that is, the starting and ending frequencies are different, which can be defined by

**Table 1.** The parameters for CSF multi-channel decomposition model

	a <sub>1</sub>	a <sub>2</sub>	a <sub>3</sub>	b <sub>1</sub>	b <sub>2</sub>	b <sub>3</sub>	c <sub>1</sub>	c <sub>2</sub>	c <sub>3</sub>
L	0.3793	0.5008	0.2815	3.092	6.26	10.11	3.261	6.232	12.42
	a <sub>1</sub>	a <sub>2</sub>	b <sub>1</sub>	b <sub>2</sub>	c <sub>1</sub>	c <sub>2</sub>			
r-g	1.126	0.3415	-7.435	5.467	14.95	5.52			
y-b	1.023	0.1406	-1.184	9.4	5.066	9.118			

defining the size of the filtering window  $Hsize$ . The calculation of the filtering window size is expressed as Formula 6:

$$FWHM = 2 \cdot c_i \cdot \text{sqrt}(2 \ln 2) \quad (5)$$

$$Hsize = FWHM \times SpD \quad (6)$$

Therefore, Gaussian filter operator convolution in the opposite color space of the human visual can be calculated with the sub-images decomposed by the spatial scale of the image and the Formulas 3 to 6. It can realize the simulation of spatial color multi-scale processing algorithm of the human eye color antagonism mechanism:

$$\begin{cases} L_{out}(x, y) = L(x, y) + w_i \sum_{i=1}^3 l_i(x, y) \otimes L_i(x, y) \\ R\_G_{out}(x, y) = R\_G(x, y) + w_i \sum_{i=1}^2 r\_g_i(x, y) \otimes R\_G_i(x, y) \\ Y\_B_{out}(x, y) = Y\_G(x, y) + w_i \sum_{i=1}^2 y\_b_i(x, y) \otimes Y\_B_i(x, y) \end{cases} \quad (7)$$

In Formula 7,  $L(x, y)$ ,  $R\_G(x, y)$  and  $Y\_B(x, y)$  indicate black-and-white, red-green and yellow-blue opposite color channel image separately which are input images.  $l_i(x, y)$ ,  $r\_g(x, y)$  and  $y\_b_i(x, y)$  indicate filter operators corresponding to different frequency bands of each color channel.  $w_i$  indicates weight adjustment factor which is  $a_i$  in Table 1.  $L_i(x, y)$ ,  $R\_G_i(x, y)$  and  $Y\_B_i(x, y)$  indicate sub-images of each color channel after visual image-decomposed.  $L_{out}(x, y)$ ,  $R\_G_{out}(x, y)$  and  $Y\_B_{out}(x, y)$  indicate visual image processed after visual antagonism.

### 3 Experimental Results

The simulation calculation mainly includes the following steps: (1) converting the RGB color mode image to the CIE Lab color mode image which describing color in the opposite color space, (2) performing 3 scale filtering calculations on the L channel, and performing 2 scales on the a and the b channel separately, (3) synthesizing the multi-scale filtering result image in each channel separately (4) converting the Lab color mode image into the RGB color mode image.

In order to verify the performance of the algorithm to predict the color constancy, The Xrite ColorChecker SG (hereinafter referred to as CC) color standard is captured by the Nikon D700 camera in a neutral gray darkroom environment in this experiment. Four kinds of light source which are CIE D50, D65, A, C, and two kinds of luminance



which are 1000 lx and 500 lx are used in this experiment. For each combination of illumination and light source, the experiment gets the images under two kinds of situations. Situation 1, custom shooting situation, turns off all the automatic color correction functions of the camera, and set the camera shooting color temperature which is the closest to the actual measurement value. Situation 2, auto white balance shooting, images with automatically white balance of the camera under corresponding environment. A total of 16 test images are achieved in this experiment.

## 4 Analysis and Discussion

The test images are divided into two groups. The first group of 8 images is obtained by the custom shooting situation and calculated using the algorithm proposed in this paper. The second group of 8 images is obtained by the automatic white balance shooting situation. Taking the measured values of the CC card under the D50 light source as the standard values, the color difference calculations are performed respectively with the CC card values in the two groups of images. The color difference formula adopts the CIE DeltaE00 (hereinafter referred to as DE00) color formula. And the average value and standard deviation of the color difference DE00 of all the color patches in the CC card are used as evaluation indexes. The color difference calculation result is shown in Fig. 2.

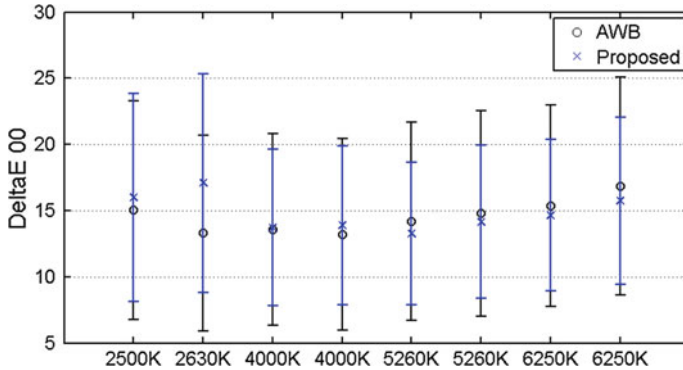


**Fig. 2.** The results of the DE00 color difference

In Fig. 2, the ordinate indicates DE00, the abscissa indicates the shooting color temperature,  $\circ$  AWB indicates the color prediction accuracy of the automatic white balance algorithm, and  $\times$  Proposed indicates the color prediction accuracy of the algorithm proposed in this paper. The vertical line in Fig. 2 expresses two statistical parameters of color reproduction, the average color difference (indicated by the center point position) and the standard deviation (indicated by the length of the line segment). The lower the center point and the shorter the line length is, the higher the prediction accuracy is. Figure 2 shows that when the color temperature is higher than 4000 K, the standard deviation of the prediction results using the algorithm of this paper is

obviously small (the blue line in Fig. 2 is shorter) and the prediction accuracy is higher than the white balance algorithm of the camera. when the color temperature is lower than 4000 K, the algorithm has no obvious advantage compared with the camera automatic white balance algorithm. For the case of 2500 K, the average prediction result is larger than the camera automatic white balance prediction, but the standard deviation is relatively small. It shows that the color difference data is relatively small. For the case of 2630 K, the prediction result of this algorithm is not as good as the camera automatic white balance algorithm and the color difference is large. However, as shown in Table 1, this image is captured under the condition of A source illumination and 1000 lx. The color temperature deviation between ambient light source and setting is also the largest which is greater than 50. Based on the comprehensive comparison results, it can be considered that the prediction performance of the algorithm proposed in this paper is relatively better than that of the professional white SLR automatic white balance algorithm in color constancy.

## 5 Conclusions

The paper argues that the processing of color information by the human eye visual antagonism mechanism is a mapping between spatial scale and spatial frequency tuning curve. In this paper, the CSF model of the opposite color space is used to calculate the isotropic Gaussian filter operator by Gaussian function fitting when simulating the spatial frequency tuning curve of human visual space. Based on this, the simulation algorithm of human eye color visual antagonistic mechanism is proposed. The experimental results show that the prediction performance of the algorithm is not lower than the automatic white balance performance of high-end digital SLR cameras in color constancy of human visual vision. The focus of this paper is on theoretical reasoning and simulation verification. Due to the lack of measurement data of human visual spatial frequency tuning curve, the multi-scale filter operator in the paper only represents the theoretical reasoning characteristics of the visual spatial frequency tuning curve, so the operator characteristic of the instantiation algorithm needs to be supplemented which is the direction for the efforts in the future.

**Acknowledgements.** This research is supported by Lab of Green Platemaking and Standardization for Flexographic Printing (No. ZBKT201705 and No. ZBKT201806).

## References

1. Conway, B. R., Chatterjee, S., Field, G. D., et al. (2010). Advances in color science: From retina to behavior. *The Journal of neuroscience*, 30(45), 14955–14963.
2. Li, J., Zhou, L., & Liu, J. (2014). Algorithm for remote sensing image enhancement based on multiscale retinex theory. *Journal of Xi'an Technological University*, 34(1), 27–33.
3. Xie, D., & Wan, X. (2011). Multi-scale DoG filter based high dynamic range image rendering method. *Geomatics and Information Science of Wuhan University*, 36(1), 1381–1385.

4. Shao, B. (2013). *Visual mechanisms based color constancy model and its application in image processing* (pp. 40–50). Chengdu: University of Electronic Science and Technology of China.
5. McGugin, R. W., Gatenby, J. C., Gore, J. C., & Gauthier, I. (2012). High-resolution imaging of expertise reveals reliable object selectivity in the fusiform face area related to perceptual performance. *Proceedings of the National Academy of Sciences USA*, *109*(42), 10–16.
6. Simpson, W. A., & McFadden, S. M. (2005). Spatial frequency channels derived from individual differences. *Vision Research*, *45*(21), 2723–2727.
7. Cooper, B., Sun, H., & Lee, B. B. (2012). Psychophysical and physiological responses to gratings with luminance and chromatic components of different spatial frequencies. *Journal of the Optical Society of America A*, *29*(2), A314–A323.
8. Fairchild, M. D. (2010). Color appearance models and complex visual stimuli. *Journal of Dentistry*, *38*(s2), e25–e33.



# Study on the Faded Model of Painting Substrate Based on Chemical Kinetics

Ling Cai<sup>1</sup>, Guangxue Chen<sup>1(✉)</sup>, and Zhen Liu<sup>2</sup>

<sup>1</sup> State Key Laboratory of Pulp and Paper Engineering, South China University of Technology, Guangzhou, China  
chengx@scut.edu.cn

<sup>2</sup> Qufu Normal University, Rizhao, China

**Abstract.** Based on the chemical kinetic model, the effect of influencing factors on the rate of change and the reaction mechanism of organic matter in the process of change were recorded. In this paper, 240 h aging simulation of the commonly used color printing materials—untreated Xuan Paper, treated Xuan Paper and the oil painting board was simulated. By analyzing the LCH, X, Y, Z values and spectral reflectance of the same pigment on different substrates, the faded model of the painted substrate can be constructed according to the chemical kinetic model. In this paper, the precision coefficient SSE and the decision coefficient R-square are chosen as the evaluation parameters to construct the model. The precision coefficients SSE of the resulting untreated Xuan Paper, treated Xuan Paper and the oil painting board are respectively 1.1452, 0.4911 and 0.6461; the decision coefficients R-square are 0.3393, 0.3037 and 0.4994. The results show that the faded model built error is small, simulated color fading effect is good. The faded model reflects the rull of fading of different substrates: With the extension of aging time, the chromaticity of untreated Xuan Paper is reduced and the hue becomes yellowish; the tone of treated Xuan Paper is more stable, brightness increased; the chromaticity of the oil painting board increased. This conclusion provides constructive guidance for the high simulation of artwork.

**Keywords:** Dynamic model · Printing materials · Fade model · SSE · R-square

## 1 Introduction

As a treasure of traditional culture, painting depicts the cultural characteristics of various periods in China. However, with the passage of time, the changes of the environment, the protection and restoration of painted calligraphy and painting, also faces enormous difficulties. Focusing on the study of the fading and restoration of painted calligraphy and painting is the primary task of protecting painted painting and calligraphy.

China's painted paintings and foreign oil paintings cannot avoid the problem of fading and discoloration [1]. Therefore, in order to protect cultural heritage, scholars at home and abroad have conducted a lot of research. For example, Soo-Chang adjusts yellowed paper by color correction and adjusts faded pigments by enhancing saturation

[2, 3]; Pan Yunhe, a fellow at Zhejiang University, studies the virtual restoration of Dunhuang frescoes based on the experience of Dunhuang workers [4]; Shanxi History Li Yuhu, the director of the Cultural Heritage Protection Science Research Center, invented the technique of painting and visual restoration to restore the original outline of the painting [5]. Although there have been various advances in the study of the fading and restoration of painted paintings, the ancient painting restoration techniques based on color adjustment and the ancient painting color restoration methods based on multi-spectral images still need to further improve the accuracy [6–8].

In this paper, the aging test is used to explore the law of fading of painting and calligraphy, and the advantages and disadvantages of existing research are combined to restore the aging environment as realistically as possible [9–12]. The chemical kinetic model is used to record the influence of the influencing factors of organic matter on the rate of change of the organic matter, so as to improve the accuracy of the restoration of painting and calligraphy [13–15]. It is of great significance for the protection and restoration of painted calligraphy and painting.

## 2 Substrate and Representative Pigment Aging Model

### 2.1 The Experimental Process

The aging simulation was carried out by selecting untreated Xuan Paper, familiar propaganda and oil painting board [16–18]. Apply solid color blocks and color blocks to the substrate to cover the color of the paper [19, 20]. Through the above method, three experimental samples containing 34 colors were obtained, each of which contained 24 solid colors and ten mixed colors. The prepared sample was air-dried for use, and the tristimulus value and spectral reflectance of the sample were measured.

The prepared color card is aged in a constant temperature and humidity ultraviolet aging box. The temperature is set to 25 °C. Humidity is set to 60. Keep two ultraviolet lamps 20 h per aging. After each aging, it is measured with an integrating sphere spectrophotometer. The Color i control software was used to record the tristimulus values and spectral reflectance of the paper white and color blocks of the three color cards of untreated Xuan Paper, treated Xuan Paper and the oil painting board. A total 240 h of aging, and the aging time for each sample is 240 h. The  $L^*$ ,  $C^*$ ,  $H^*$ ,  $X$ ,  $Y$ ,  $Z$  values and spectral reflectance of each color of each color card are recorded each time.

### 2.2 Aging Models of Printing Materials

The Arrhenius model is a chemical kinetic mode. Chemical kinetics mainly studies the influence of influencing factors on the rate of change and the reaction mechanism in the process of change. It is widely used in all aspects of chemistry. The process of color fading is also a process of organic changes. Therefore, the Arrhenius model of chemical kinetics also applies to the study of color fading.

The Arrhenius model, as shown in Eq. (1), reveals the essence of the effect of temperature on the reaction rate and the more accurate empirical equation for the k-t relationship.

$$k = k_0 e^{-\frac{E_a}{RT}} \tag{1}$$

Among them,  $E^a$  means activation energy,  $k_0$  known as a pre-factor or frequency factor, both  $E^a$  and  $k_0$  are empirical constants.

From the aging experiment, the trends of  $L^*$ ,  $C^*$ , and  $H^*$  of Shengxuan, Shuicuan and oil painting boards are consistent. As the aging time increases, the brightness value of the medium increases and the chromaticity value decreases. From the perspective of the chromaticity angle, untreated Xuan Paper and treated Xuan Paper, are in the direction of yellowish at around  $90^\circ$ ; The oil painting board changed from 304.87 to 66.9, indicating that the oil painting board changes from blue to yellowish; These changes are consistent with the actual aging of paper and oil painting boards, confirming the accuracy of the model.

Because paper is sensitive to ultraviolet light, it usually takes a severe chemical bond break after 10–20 h of irradiation. Untreated Xuan Paper, treated Xuan Paper have a significant change in  $L^*$  and  $C^*$  values before aging until the 20th hour. Therefore, in the establishment of the aging model, the birth and maturity should be analyzed from the 60th hour of aging. The oil painting board has a large reduction after 60 h of aging, and the color change is too large. The model should be selected from the 80th hour of analysis. It can be seen that the aging phenomenon of the oil painting board is not obvious, which is the main reason for the long retention period of the oil painting works (Figs. 1, 2 and 3).

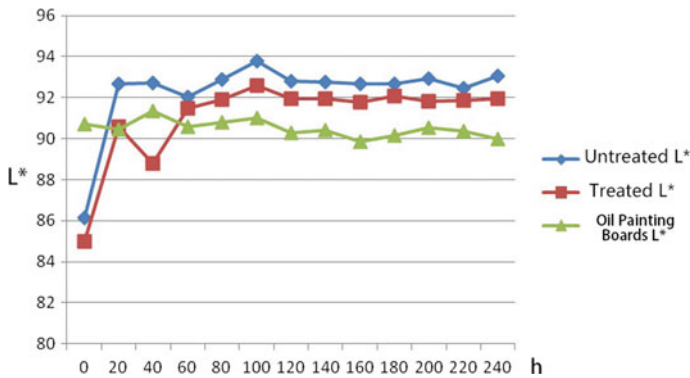


**Fig. 1.** Aging trends table of  $L^*$  values of untreated Xuan paper, treated Xuan paper, and oil painting boards

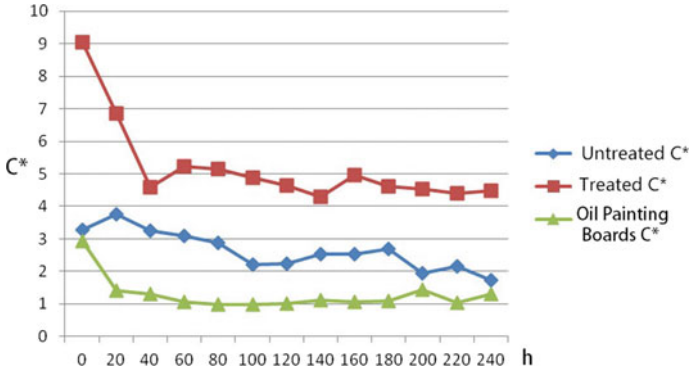


**Fig. 2.** Aging trends of  $C^*$  values of untreated Xuan Paper, treated Xuan Paper, and oil painting boards

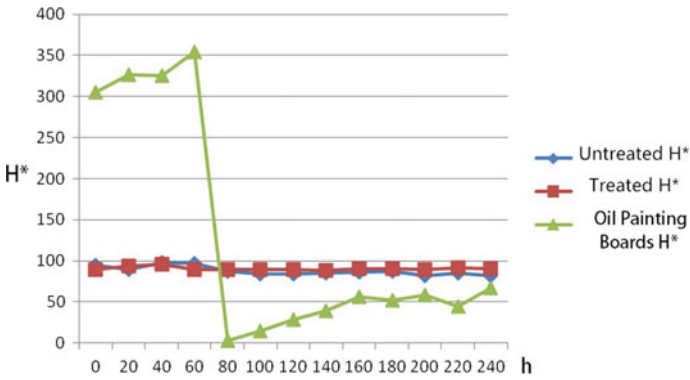


**Fig. 3.** Aging trends of  $H^*$  values of untreated Xuan Paper, treated Xuan Paper, and oil painting boards

Combining the aging trend of untreated Xuan Paper with the Arrhenius model, the aging model function of untreated Xuan Paper can be obtained as Formula (2).

$$\left\{ \begin{array}{l} L^* = 92.74e^{(5.741e-6)t} \\ C^* = 3.304e^{-0.002192t} \\ h^* = 93.66e^{-0.0005643t} \end{array} \right\} \quad (2)$$

Combining the aging trend of treated Xuan Paper with the Arrhenius model, the aging model function of treated Xuan Paper can be obtained as Formula (3).

$$\left\{ \begin{array}{l} L^* = 91.92e^{(9.55e-7)t} \\ C^* = 5.359e^{-0.0008612t} \\ h^* = 88.69e^{(8.766e-5)t} \end{array} \right\} \quad (3)$$

Combining the aging trend of Oil Painting Boards with the Arrhenius model, the aging model function of Oil Painting Boards can be obtained as Formula (4).

$$\begin{cases} L^* = 91.05e^{(-4.643e-5)t} \\ C^* = 0.8509e^{-0.001652t} \\ h^* = 11.7e^{0.007378t} \end{cases} \quad (4)$$

### 3 Results and Discussion

The aging model test image obtained by untreated Xuan Paper's aging function model can be further obtained as Fig. 4.

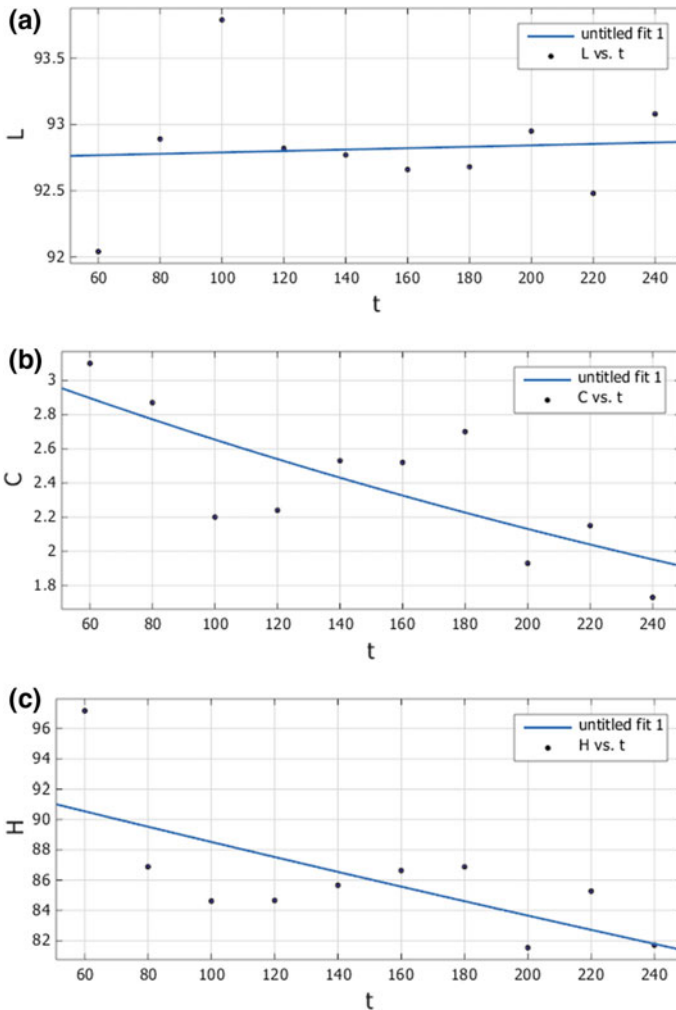


**Fig. 4.** An  $L^*$  (a),  $C^*$  (b),  $H^*$  (c) curve of untreated Xuan Paper aging model



It can be seen from the image that the brightness change of untreated Xuan Paper is relatively small. As the aging progresses, the color of the raw will be biased toward the yellow. The precision coefficients SSE of the  $L^*$ ,  $C^*$ , and  $H^*$  value function models are 1.792, 0.7197, and 0.924, respectively. R-square is 0.005205, 0.5585 and 0.4541, respectively. On the whole, there are certain errors, but constructively apply the aging chemical principles to data.

The aging model test image obtained by treated Xuan Paper's aging function model can be further obtained as Fig. 5.

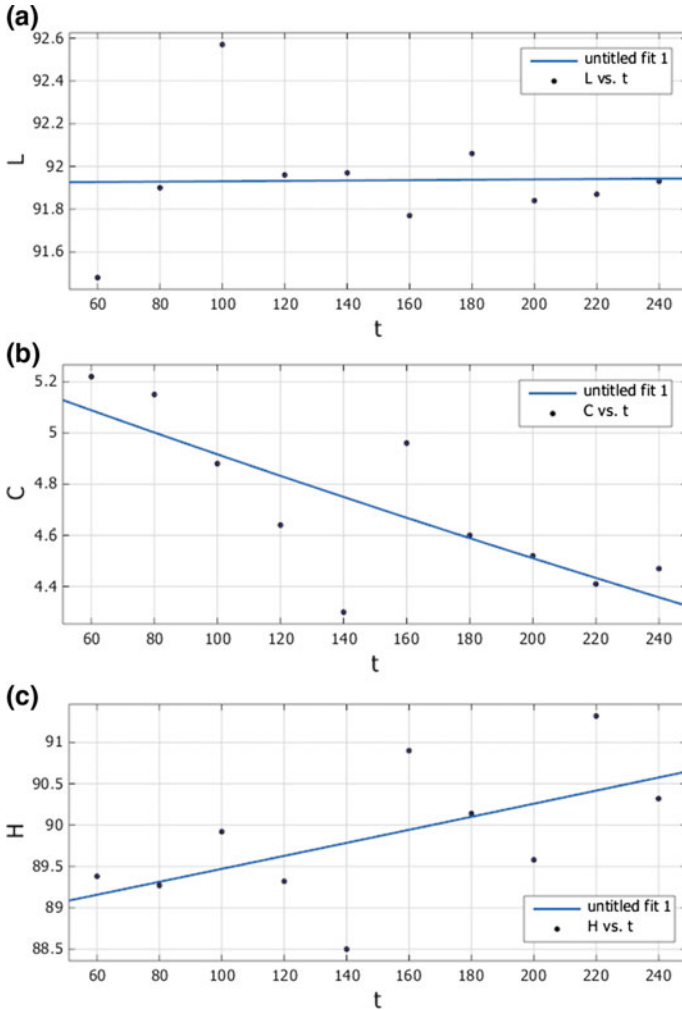


**Fig. 5.** An  $L^*$  (a),  $C^*$  (b),  $H^*$  (c) curve of treated Xuan Paper aging model

It can be seen from the image that the fluctuation of the treated Xuan Paper change is relatively small. As aging progresses, it will continue to shift in the yellow direction. The precision coefficients SSE of  $L^*$ ,  $C^*$  and  $H^*$  value function models are 0.6692, 0.3781 and 0.4259, respectively. R-square is 0.000383, 0.5862, and 0.3245, respectively. Overall, the fitting effect error is small, which improves the high-precision reproduction of painted paintings and paintings.

The aging model test image of the fitted model can be further obtained by the aging function model of the oil painting board as Fig. 6.

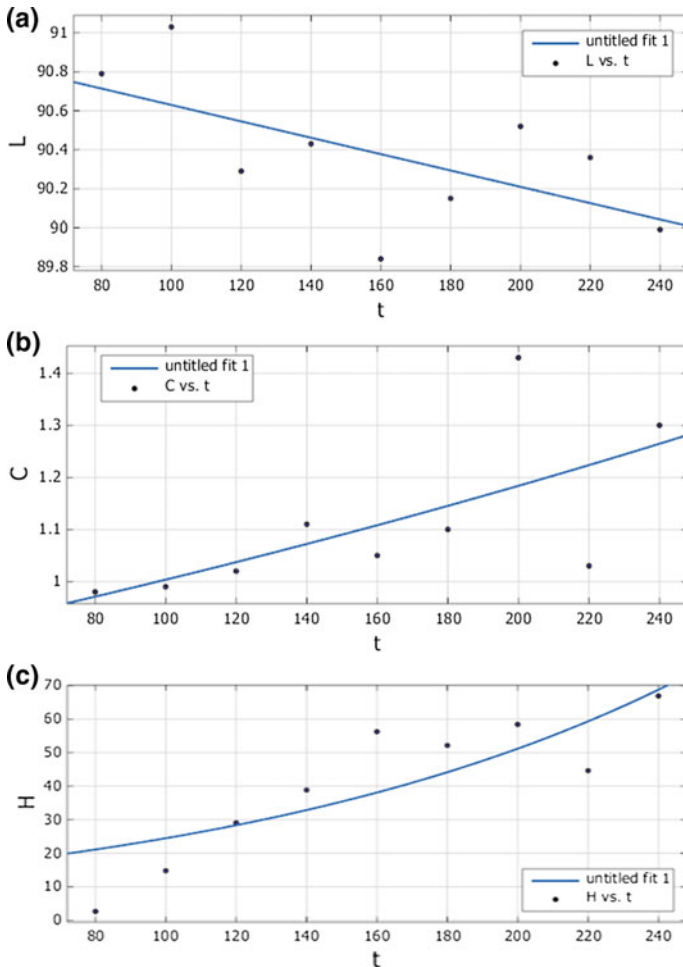


Fig. 6. An  $L^*$  (a),  $C^*$  (b),  $H^*$  (c) curve of oil painting panel aging model

It can be seen from the image that the brightness of the oil painting board is lowered and the chromaticity is increased. As the aging progresses, the oil painting board changes from a reddish to a yellowish direction. The fitting precision coefficients SSE

of the  $L^*$ ,  $c^*$ , and  $h^*$  value function models are 0.6956, 0.1068, and 1.136, respectively. The R-square is 0.3777, 0.432, and 0.6884, respectively. From the fitting effect, the law of color fading based on the chemical kinetic model can accurately reproduce the true color before color fading.

## 4 Conclusions

Painted calligraphy and painting has a very high appreciation and human value. However, as time goes by, it is prone to problems such as yellowing and fading. The restoration of faded color paintings is a difficult technical issue. The use of information technology to protect and restore painted paintings and calligraphy has important significance in the protection of cultural relics.

This paper combines the chemical kinetics Arrhenius model with the actual aging experiment to explore the law of fading of painted paintings. Combine various influencing factors, find out the law of color fading of painted paintings, and establish a fading model of color substrate materials. Through the established model, the state of the color after aging in a certain period under experimental conditions can be successfully introduced. And the model takes the fitting precision coefficient and the fitting variance as the measurement parameters, and the obtained model has high accuracy and close fitting to the actual aging process. This conclusion is of great guiding significance in the replication of art.

**Acknowledgements.** This work is supported by the Science and Technology Planning Project of Guangdong Province (No. 2017B090901064), the Science and Technology Project of Guangzhou City (No. 2016070220045).

## References

1. Soo-Chang, P., & Yi-Mei, C. (2006). Background adjustment and saturation enhancement in ancient Chinese paintings. *IEEE Transactions on Image Processing*, 15(10), 3230–3234.
2. Sverak, T., Bulejko, P., Kristof, O., et al. (2016). Covering ability of aluminum pigments prepared by milling processes. *Powder Technology*, 305, 396–404.
3. Joubert, M., Save, M., Mornet, S., et al. (2014). Surface patterning of micron-sized aluminum flakes by seeded dispersion polymerization: Towards waterborne colored pigments by gold nanoparticles adsorption. *Polymer*, 55(3), 762–771.
4. Tawiah, B., Zhang, L., Tian, A., et al. (2016). Coloration of aluminum pigment using  $\text{SiO}_2$  and  $\gamma$ -glycidoxypropyltrimethoxy-silane with dichlorotriazine reactive dye. *Pigment & Resin Technology*, 45(5), 335–345.
5. Du, B., Zhou, S. S., Li, M., et al. (2014). Material properties and applications of mineral pigments. *Journal of Hebei Institute of Architecture and Technology*, 34(5), 410–418.
6. Chen, X. G., Li, Y. H., & Gao, J. (2013). *Color management handbook* (p. 7). Beijing: Cultural Development Press.
7. Ma, J. X. (2015). Preventive cultural relic protection environmental monitoring and control technology. *Science Press, Beijing*, 35, 46–47.

8. Whitmore, P. M., et al. (2009). The fading of artists' colorants by exposure to atmospheric nitrogen dioxide. *Studies in Conservation*, 34(2), 85–96.
9. Zong, H. (2005). *Analysis of aging color difference of Chinese painting pigments*. Anhui: Anhui University.
10. Wang, X. F., & Yu, L. K. (2005). *Mineral color manual* (pp. 93–94). Beijing: People's Fine Arts Publishing House.
11. Qiu, Q. N. (2014). *Research on traditional Chinese painting pigments* (p. 109). Suzhou: Suzhou University Press.
12. Fan, Y. Q., Li, Z. X., Yu, R. Z., et al. (2012). Reinforcement effect on pigment of wall painting. *Res Dunhuang*, 4, 45–56.
13. Li, S., Li, Y. H., Xiang, X. M., et al. (1993). Illumination weathering experiment on ethanol polyethylene and ...in special circumstance. In *Corpus of Dunhuang research (conservation of rock caves)* (pp. 206–222). Lanzhou: Gansu Nationality Publishing House.
14. Su, B. M., Li, Z. X., & Hu, Z. D. (2006). Research on the stability of the mixing pigment. *Res Dunhuang*, 3, 149–162.
15. Li, Z. X. (1993). General study on the weathering of wall painting adhesive in Dunhuang. In *Corpus of Dunhuang research (conservation of rock caves)* (pp. 236–248). Lanzhou: Gansu Nationality Publishing House.
16. Tie, F. D., Sun, S. Y., & Wang, J. Y. (2004). *Has revealed the damage and protection of the mural*. Lanzhou: Gansu Nationality Publishing House.
17. Li, Z. X. (1993). Influence of light and humidity on red lead, vermilion and hematite. In *Corpus of Dunhuang: Conservation of rock caves* (pp. 219–235). Lanzhou: Gansu Nationality Publishing House.
18. Siegesmund, S., Ullemeyer, K., Weiss, T., & Tschegg, E. K. (2000). Physical weathering of marbles caused by anisotropic thermal expansion. *International Journal of Earth Sciences*, 89, 170–182.
19. Srinivasan, R. (2005). Thermal expansion of calcite from room temperature up to 400 °C. *Proceedings Mathematical Sciences*, 42(5), 81–85.
20. Guo, H., Han, R. B., Zhao, J., et al. (2005). Pigment and the prevention of its fading on petroglyphs of the flower mountain. *Sciences of Conservation and Archaeology*, 17(4), 7–14.



# Color Prediction Model for Flexographic Prints Based on Spectral Reflectance

Dongwen Tian<sup>1,2</sup>(✉), Zhonghua Yu<sup>1</sup>, and Jinghuan Ge<sup>1</sup>

<sup>1</sup> Department of Printing and Packaging Engineering,  
Shanghai Publishing and Printing College, Shanghai, China  
dwtian@sppc.edu.cn

<sup>2</sup> University of Shanghai for Science and Technology, Shanghai, China

**Abstract.** In order to promote the greening of flexographic printing and reduce the waste of consumables such as plates and printing materials. It is necessary to accurately predict the spectral reflectance of flexographic film-type printing and establish a spectral reflectance color prediction model for flexographic film prints. The prediction model of flexographic film prints is based on the theory of multiple internal reflections of photons in a plastic film substrate and horizontal transmission inside the plastic substrate, assume that the film and the ink have the same refractive index and the flexographic print is placed on a standard white background. Finally, we tested our model on a flexographic printing machine. Good agreement was found between the predicted and measured reflectance for the flexographic printed patches. The model could be used in prepress color prediction and virtual color proofing, significantly reduce printing materials and energy consumption.

**Keywords:** Halftone prints · Prediction model · Reflectance model · Flexographic process

## 1 Introduction

As an environmentally friendly printing, flexographic printing is increasingly used in packaging products around the world. Flexographic printing has become the fastest growing printing method in the printing process worldwide. Especially in the field of packaging, flexographic printing has been widely used in various types of packaging printing. With the continuous development of science and technology, the flexographic printing process has been continuously improved, and flexographic printing will have a broader development space with the development of the packaging and printing industry. In order to better save energy and reduce emissions and reduce the waste of printing raw materials, it is necessary to have a good flexographic printing color prediction model to accurately predict the printing color. Printed image color theory can be divided into two categories. One is for halftone prints such as the Neugebauer equation, the Yule-Nielsen model and the classic Clapper-Yule model. The other is the K-M theory based on the principle of continuous color reduction. These theories have made a significant contribution to color control in the printing industry.

In 1937, Neugebauer first used mathematical methods to indicate the propagation of light between paper and ink after it entered the printed matter. Although this is a mathematical relationship obtained under perfectly ideal conditions, and the model can't solve its value by conventional calculation method, it is this way of thinking that promotes the development of later color prediction models. In 1953, based on the Neugebauer equation proposed by Neugebauer, Clapper and Yule considered the interaction of light into the coloring matter and the actual propagation of light inside the printed matter, and came up with the classic Clapper-Yule color prediction model. Later, Williams and Clapper considered the propagation law of light in the ink layer, and obtained the Williams-Clapper color Prediction model [1, 2]. However, Clapper-yule, like the Williams-clapper model, does not consider the effects of paper base, coloring layer and air-coloring boundary on light reflection and transmission. When multicolor ink overprinted, the calculations become complex and error-prone, resulting in unsatisfactory prediction results.

Therefore, it is necessary to establish a color spectrum prediction model for half-tone prints to accurately control the color of printed matter to achieve optimal color reproduction. In the process of color reproduction, accurately predicting the color rendering characteristics of color halftone prints, and establishing a spectral reflection color prediction model for flexographic halftone prints is a topic of printing equipment characterization and printing quality control.

Based on the theory of multiple internal reflections of light in a plastic film substrate and lateral propagation of light inside the plastic film substrate, the paper assumes that the film substrate and the ink have the same refractive index and the film is placed on a standard white substrate. It is consistent with the actual measurement method of the printing industry.

The structure of this paper is as follows: In Sect. 2, spectral reflectance model for flexographic film prints is proposed. Then, in Sect. 3, an experimental and results of the model is given. In Sect. 4, draw conclusions.

## 2 Spectral Reflectance Model for Flexographic Film Prints

The ink penetrates into the paper when it is printed. The printing ink of flexographic film printing can't penetrate to the interior of the substrate, but it is adsorbed on the surface of corona-treated film. Therefore, the color prediction model for plastic film is very different from the paper-based color prediction model [3–5].

In the prediction of the color of paper prints, the ink penetrates to the interior of the paper, so when photons are returned from the plastic base to the upper interface, only the inside reflection of the plastic base and the non-image area needs to be considered, regardless of the colored upper interface reflection. In flexographic of plastic films printing, since the ink is adsorbed on the surface of the film, in addition to considering the internal interface reflection of the plastic and air, the reflection between the image area and the plastic film interface is also considered. Therefore, these situations are to be considered and a new model is built.

In order to create a new color prediction model, first, we consider that only one color is transferred to the plastic film. In the case of the imaged area and the non-imaged area, as shown in Fig. 1.

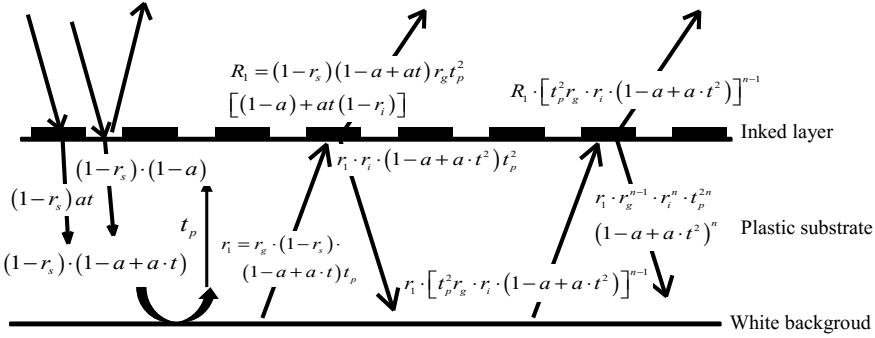


Fig. 1. Multiple internal reflection process of flexographic plastic prints

Assume that the ink dot area coverage on the film substrate is  $a$ , the probability that a light beam enters the film through the ink (as the ink transmittance) is  $t$ , and the probability of directly entering the film substrate of non-image area is  $(1 - a)$ . The index of refraction of the ink and film substrate is approximately equal, the transmission of the film substrate is  $t_p$ , the substrate reflectance is  $r_g$ , and the reflectance between the inked layer and air inside interface is  $r_i$  [6–9].

When a beam of light with unit intensity energy is incident on the air and printed interface, the first surface reflectance between the air and film substrate interface is  $r_s$ . The reflected light reaches the spectrum measuring instrument is  $K$ , the light reflected from the first surface is,

$$R_0 = K r_s \tag{1}$$

Then only  $(1 - r_s)$  parts enter the surface of the print. Therefore, the light that enters the film through the ink is  $(1 - r_s)at$ , and the light that directly through the plastic film is  $(1 - r_s)(1 - a)$ . The sum of the light in these two parts is the light which enters the film substrate at the first time. Its size is  $(1 - r_s)(1 - a + at)$ .

Since the total reflectance of the film substrate to light is  $r_g$ , the light entering the film base is diffusely reflected by the white background, and the light reaching the upper surface of the film base is  $r_i t_p$ .

The other part of the light, reflected by the inside surface of the plastic film, will then be split into two parts, one part out of the surface of the print and the other part back to the film substrate. The light emitted from the surface of the print has two parts, one part directly passes through the surface of the print, the size is  $(1 - r_s)(1 - a + at)r_g t_p^2(1 - a)$ , and the other part passes to the ink area. Since the reflectivity of the inked layer inside layer is  $r_i$ . The light has  $r_i$  part reflected to the film substrate, and only the  $(1 - r_i)$  part emerges from the ink layer. This portion of light

has a size of  $(1 - r_s)(1 - a + at)r_g t_p^2 \cdot at(1 - r_i)$ . The sum of the two parts is the light emitted from the surface of the print product for the first time. Its intensity is,

$$R_1 = (1 - r_s)(1 - a + at)r_g t_p^2 [(1 - a) + at(1 - r_i)] \quad (2)$$

The intensity of the light reflected back to the film substrate is also composed of two parts, one is the size of the part of the light reflected by the blank part back to the film base, and the other part is reflected by the ink from the interface between the ink layer and the non-image area. The intensity of photons emitted from surface of the printed product again is:

$$R_2 = (1 - r_s)(1 - a + at)r_g t_p^4 [(1 - a) + at^2 \cdot r_i] \cdot r_g [(1 - a) + at(1 - r_i)] \quad (3)$$

Similarly, the intensity of the light emitted from the surface of the printed product for the  $n$ th time is:

$$R_n = (1 - r_s)(1 - a + at)t_p^{2n} \{r_g [(1 - a) + r_i \cdot at^2]\}^{n-1} \cdot r_g [(1 - a) + at(1 - r_i)] \quad (4)$$

By considering the photons from all inside reflections, we obtain the spectral reflection model.

$$R = Kr_s + \frac{(1 - r_s)(1 - a + at)r_g [(1 - a) + at(1 - r_i)]}{1 - r_g t_p^2 [(1 - a) + r_i \cdot at^2]} \quad (5)$$

### 3 Experimental and Results

To prove the accuracy of the model, color control bar of flexography prints have been measured. The dot area coverage of cyan, magenta and yellow are 0.25, 0.5, 0.75, 1, respectively. Based on the reflectance between the prediction model calculated and the X-Rite Exact device measured, the CIE L\*a\*b\* value we are calculated through MathWorks MATLAB 2016a. The color difference CIEDE00 of each control bar between measured and predicted is then calculated.

The measuring instrument is X-Rite Exact spectrophotometer. Spectral Range is from 400 to 700 nm. The measurement conditions are D50/2°, M1, Status T. Measurement Geometry is 45°/0° ring illumination optics. The flexographic equipment is TAIYO CI Press, and the screening frequency of printing is 150 LPI.

According to the measurement and Eq. 5, we get  $r_s = 0.05$ ,  $K = 0$ ,  $r_i = 0.65$ ,  $t_p = 0.9$ . The color difference CIEDE00 of test patches between measured and predicted (Eq. 5) are as follows (Table 1).



**Table 1.** Color difference CIEDE00 of control bar between measured and predicted

Test patches (%)	Color difference (CIEDE00)
C25	2.01
C50	0.96
C75	0.72
C100	0.02
M25	1.90
M50	0.75
M75	0.71
M100	0.01
Y25	0.86
Y50	1.74
Y75	0.85
Y100	0.01

## 4 Conclusions

The study assumes that the ink and plastic film are non-scattering media. Based on the theory of multiple internal reflections of light in a plastic film substrate and lateral propagation of light inside the plastic film substrate, assumes that the film substrate and the ink have the same refractive index and the film is placed on a standard white substrate, the reflectance model for flexographic film prints is proposed. In the color difference result, maximum and minimum color differences are 2.01, 0.001. The results show that the predicted reflectivity of the model is very consistent with the measured reflectance. The established model can provide a method for flexographic halftone prints to accurately control the color of printed matter to achieve optimal color reproduction. In the future work, we will test more colors including gray balance patches to improve the model and expand the scope of the model.

**Acknowledgements.** The authors want to thank “Lab of Green Platemaking and Standardization for Flexographic Printing”, project number ZBKT201706.

## References

1. Clapper, F. R., & Yule, J. A. C. (1953). The effect of multiple internal reflections on the densities of halftone prints on paper. *Journal of Optical Society of America*, 43, 600–603.
2. Williams, F. C., & Clapper, F. R. (1953). Multiple internal reflections in photographic color prints. *Journal of Optical Society of America*, 29, 595–599.
3. Hebert, M. (2006). *Compositional model for predicting multilayer reflectances and transmittances in color reproduction*. France: University Jean Monnet.
4. Yixin, Z., & Yanjun, D. (2007). Clapper-yule spectral reflection and transmission of halftone color fluorescent image. *Acta Optica Sinica*, 27(2), 365–370.
5. Zhang, Y., & Zang, D. (2008). Clapper-yule color prediction model for recto-verso halftone images. *Acta Optica Sinica*, 28(1), 200–204.

6. Judd, D. B. (1942). Fresnel reflection of diffusely incident light. *Journal of Research of the National Bureau of Standards*, 29, 329–332.
7. Hébert, M., & Hersch, R. D. (2004). Classical print reflection models: A radiometric approach. *Journal of Imaging Science and Technology*, 48, 363–374.
8. Perkampus, H. H., Grinter, H. C., & Grinter, R. (1995). *Encyclopedia of spectroscopy*. Weinheim: VCH.
9. Hébert, M., & Hersch, R. D. (2006). Reflectance and transmittance model for recto-verso halftone prints. *Journal of the Optical Society of America*, 23(10), 2415–2432.



# Natural and Preferred White on Displayed Images Under Varying Ambient Illuminants

Mingkai Cao and Ming Ronnier Luo<sup>(✉)</sup>

College of Optical Science and Engineering,  
Zhejiang University, Hangzhou, China  
m. r. luo@leeds.ac.uk

**Abstract.** This study is aiming to investigate the adaptive white point of different images on a display in terms of preference and naturalness under a dark condition and five ambient lighting conditions with different correlated color temperature (CCT). Under each ambient lighting, the natural and preferred white points were assessed by eleven observers using a categorical judgment method. The data were analyzed by the weighted average method in term of CCT and the departure from the Planckian locus (Duv) for each ambient light. The results showed a general agreement between the preferred and natural white points, the adapted white also varied according to different images. The white point of the display was also dependent on the CCT of the ambient illuminant. The Duv value for the Preferred and natural white points are both slightly below the Blackbody locus (BBL).

**Keywords:** White point · Chromatic adaptation

## 1 Introduction

Manufacturers for mobile devices are interested to achieve high image quality, for which white balance has been a major issue. The white point is typically specified by CIE  $x$ ,  $y$  chromaticity coordinates, or correlated colour temperature (CCT) and the distance from the Planckian locus (Duv). The experiments to look for pure white have continued since last century [1–8]. Most people did research to find an adaptive white, then moved on to find white locus. They mainly used patches illuminated by light sources. Until recently, electronic products play an increasingly important role in work and life, display white is becoming increasingly interested. Choi and Suk [9] and Huang et al. [10] recently reported their research results.

Choi and Suk investigated [9] the image of black texts against a white paper on a tablet display in a room both under varying ambient lighting condition and in the dark environment. The results showed that CCT of the dark-adapted white was 7300 K, and the Duv value is positive which means the white point is above the BBL. It was also found that the adapted whites were ranged from 6179 to 7479 K in CCT and from  $-0.0038$  to  $0.0144$  in Duv under chromatic-adaptive conditions. Huang et al. [10] investigated the white perception of a white screen on a tablet display under 17 ambient lighting conditions surrounding the BBL including a dark condition. Their results showed that when the CCT of the ambient light higher than 3000 K, the adapted white

also has a higher CCT on the BBL. However, when the CCT of ambient light is lower than 3000 K, the adapted white is lower than the BBL but has a higher CCT. Although Huang et al. [10] conducted their experiments on displays, they used uniform white colour covering the full screen, which was rarely used in the daily life. Choi and Suk [9] only studied one image (black texts on white paper) which was somewhat limited. Besides, they asked observers to judge degree of “optimal” white, which could be difficult to understand. The goal of this study is to identify the most “preferred” and the most “natural” white point for images on a display under a set of ambient lighting conditions in a real room, which can be applied in practical applications.

## 2 Experiment Setup

### 2.1 Lighting Conditions

A psychophysical experiment was conducted to identify the most “preferred” and the most “natural” white point. The experimental room arranged as an office environment illuminated by a spectrum tunable LED system. The system can accurately produce desired sources with CCTs ranged from 2000 to 20,000 K. And many other light parameters could be precisely controlled, including CIE Ra, Duv, luminance and intensity. Five ambient lighting conditions close to zero Duv but varying CCTs at 3000, 4000, 5000, 6000, 7000 K were used in the experiment, which all keep a constant illuminance level of 300 lux at the table top. The dark condition was set an illuminance below 2 lux.

### 2.2 Stimuli

Figure 1 shows the four original images used in the experiment. Image ‘Text’ was made by typing black Chinese calligraphy on white background. The other three images were selected to include contents of memory colours such as variety of fruits and skin colors from the images used in the previous study [11]. They represent the typical image contents used on mobile phone display.

Each original image under 6500 K was rendered by CAT02 chromatic adaptation transform [12]. As a consequence, 96 stimuli images were generated, i.e. 4 original images  $\times$  24 white points. Figure 2 shows the 24 white points varying at 6 CCTs (3000, 4000, 5000, 6500, 8000, 10,000) and 4 Duv levels ( $-0.02$ ,  $-0.01$ , 0 and 0.01). It was designed to cover a large colour gamut uniformly close to BBL.

### 2.3 Experimental Environment

Figure 3a shows the experimental setup. An EIZO CG243W display (24”) was used. For each image, a white border was included, which forced observers to adapt to the image white point. The width of the white border was 1.6 cm on the vertical direction and 1.2 cm on the horizontal direction. A black instead of gray background on the display was used to avoid chromatic adaptation induced by the surrounding environment.

When the ambient lighting is on, the glare was added to the image with a level below  $2 \text{ cd/m}^2$ . In the experiment, observers were asked to be seated in front of the



Fig. 1. The original images a fruit, b party, c lady, d text

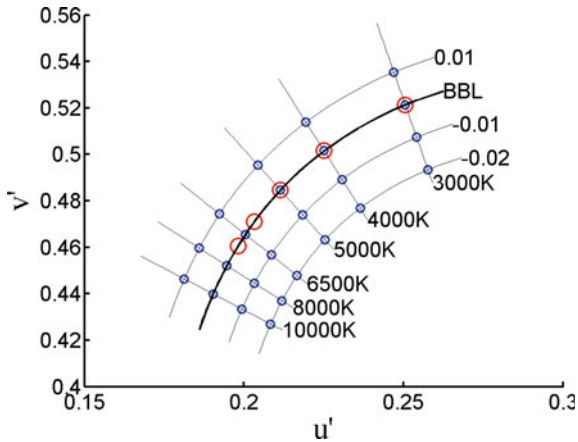
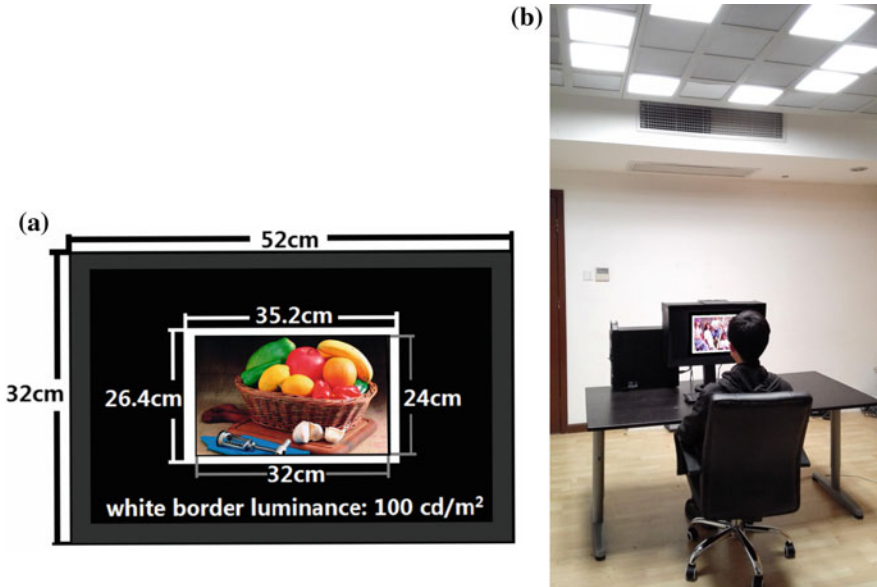


Fig. 2. The blue and red circles showed 24 display white points and 5 ambient light stimuli respectively in CIE 1976  $u'$   $v'$  chromaticity diagram



**Fig. 3.** **a** Experimental environment, **b** real environment

display and were instructed to observe the images on the display. The viewing distance about 60 cm (the distance used in daily work and learning), providing an image stimulus field of view (FOV) of  $30^\circ$ , a display and adaptation white border FOV of  $46^\circ$  and  $3^\circ$ , respectively. Hence, all of the chromaticity values were calculated with the CIE  $10^\circ$  observer. The display was switched on for at least an hour before the visual experiments to ensure a stable luminance output. The size of the room was  $6\text{ m} \times 5\text{ m} \times 3\text{ m}$ , the walls were white and a majority of the furniture were black. Figure 3b shows the experimental environment.

This study involved totally 11 participants (5 males and 6 females) with a mean age of 22 ranged from 21 to 27. They all are the volunteers from ZheJiang University and were agree that the experimental data based on their judgement was used for publication. All participants passed the Ishihara's colour vision test. The participants were asked to assess stimuli in terms of preference and naturalness using a six-point scale, respectively. The scale ranged from  $-3$  (least preferred/natural) to  $+3$  (most preferred/natural). In total, 1152 times of judgment were made in the experiment:  $96$  (display stimulus)  $\times 6$  (illuminants)  $\times 2$  (questions).

### 3 Analysis and Discussion

#### 3.1 Weighted Average Result

A weighted averaged method was used to calculate the most natural and preferred image white point. Each observer's raw data were processed to obtain acceptance percentage which means the proportion of the observers who considered the white

point of the image is natural or preferred. The average scores for each image at each white point were calculated and ranked in a descending order. The most natural and preferred image white points were computed by the tristimulus values of the white points whose acceptance percentage is high enough and taking the acceptance percentage as the weight. Equation (1) explained the operating steps of the weighted average method.

$$T_w = \frac{\sum_{i=1}^5 T_i \cdot W_i}{\sum_{i=1}^5 W_i} \tag{1}$$

where T is one of the tristimulus values (X, Y, Z);  $T_i$  represents the stimuli of the high acceptance white points which had highest total scores among the twenty-four image white points;  $W_i$  is the mean score of all the observers;  $T_w$  are the weighted average tristimulus values of the most natural or preferred white points. The CCT and Duv were obtained from the weighted average tristimulus values. Tables 1 and 2 shows the weight result of the preferred and natural image white point under varying ambient lighting conditions.

**Table 1.** Preferred white for all images under 6 lighting conditions

CCT of the light		Dark	3000 K	4000 K	5000 K	6000 K	7000 K
1. Fruit	CCT (K)	4578	4208	4680	4749	4851	5331
	Duv	-0.0025	-0.0045	-0.0034	-0.0024	-0.0022	-0.0013
2. Kids	CCT (K)	5008	4821	4976	4971	5069	5187
	Duv	-0.0028	-0.0028	-0.0028	-0.0027	-0.0028	-0.0028
3. Lady	CCT (K)	6644	5133	5515	5672	5656	5693
	Duv	-0.0007	-0.0020	-0.0015	-0.0015	-0.0013	-0.0012
4. Text	CCT (K)	7607	5947	6284	7081	7145	7219
	Duv	-0.0003	-0.0015	-0.0007	-0.0007	-0.0001	-0.0006

**Table 2.** Natural white for all images under 6 lighting conditions

CCT of the light		Dark	3000 K	4000 K	5000 K	6000 K	7000 K
1. Fruit	CCT (K)	4599	4197	4596	4623	5175	5319
	Duv	-0.0021	-0.0041	-0.0031	-0.0020	-0.0023	-0.0021
2. Kids	CCT (K)	5220	4943	5005	5105	5119	5138
	Duv	-0.0023	-0.0030	-0.0027	-0.0029	-0.0026	-0.0027
3. Lady	CCT (K)	5894	5444	5470	5561	5689	5803
	Duv	-0.0014	-0.0025	-0.0016	-0.0014	-0.0013	-0.0012
4. Text	CCT (K)	7578	5869	6261	6822	7054	7835
	Duv	-0.0007	-0.0011	-0.0007	-0.0006	-0.0005	-0.0006

The correlation coefficient  $r$  between preference and naturalness scores, from the present study  $r$  as high as 0.912. The values of 0.911, 0.901 and 0.62 were found between naturalness and preference according to individual lighting conditions, individual images and individual observer, respectively. These results confirm the good agreement between naturalness and preference. The white perception take off a rather large region. The CCT of the white point in the dark was higher than that in the varying ambient lighting conditions. While the Duv of the white point under both conditions were found to be below the BBL. The result was found to be image-dependent. For example, the average preferred CCT of the ‘Fruit’ image was only about 5000 K, but that of the preferred CCT of the ‘Text’ image was 7000 K. This implies the natural and preferred white points were dependent on the images. Besides, all images had same tendency, the CCT of image white points increases when the ambient light CCT rises. This indicates that image white point also was highly dependent on the chromaticity of the ambient illuminant.

### 3.2 Compare with Former Studies

For ‘Text’ image, the most natural and preferred image white points were at 7600 K for dark environment, which is close to Choi and Suk’s [9] result 7200 K and Huang et al.’s [10] result 7900 K. The CCT of the image white points under chromatic-adaptation condition were also very similar to Choi and Suk’s result, with the range from 6000 to 7300 K while Huang et al.’s CCT was higher at the range from 6600 to 7300 K. Besides, the natural and preferred Duv of the Text image was slightly below the BBL in the present study while the proposed white point is slightly above the BBL in Choi and Suk’s result. While Huang et al.’s Duv was more negative than that of present study (Table 3).

**Table 3.** Compare results of different study groups

CCT of the light		Dark	3000 K	4000 K	5000 K	6000 K	7000 K
Ours	CCT (K)	7607	5947	6284	7081	7145	7219
	Duv	-0.0003	-0.0015	-0.0007	-0.0007	-0.0001	-0.0006
Huang et al. [10]	CCT (K)	7924	5975	6647	7082	7690	8395
	Duv	-0.0055	-0.0079	-0.0067	-0.0044	-0.0025	-0.0005
Choi et al. [9]	CCT (K)	7246	5769	6124	6723	6970	7326
	Duv	0.0010	0.0019	0.0022	0.0052	0.2259	0.0640

### 3.3 General Discussion

The image white points were investigated both in the dark and under chromatic-adapted ambient lighting conditions on the display. The dark-adapted white region was shifted towards a higher colour temperature and slightly under the BBL. Moreover, the chromatic-adapted white have a lower CCT and negative Duv values. The present study also found that there are well agreement between natural white points and



preferred white points. From the results, it was also found that no matter how the images and illuminant changed, the natural white points were always higher than the preferred white points. This implies that the images viewed under higher CCT would appear more natural and those under slightly lower CCT would be more preferred. The experiment found that image white point was dependent on both the image itself and the chromaticity of the ambient illuminant.

This study was aimed to investigate the effect of the chromaticity of ambient lighting conditions on display images, the effect of illuminance level was not considered, while Smet et al. [7] and Walraven and Werner [13] confirmed that white perception is luminance invariant. Additionally, as mentioned in the introduction, the standards of white points differ substantially depending on the applications and a culture influence. Hence, it would also be valuable to evaluate whether any cultural effects exist on the perception of white. Overall, the present study can be used to enhance image quality on computer and mobile displays. Our wish is to contribute the findings to achieve the preferred or comfort white balance.

## 4 Conclusions

An experiment was conducted to study the naturalness and preference of image white point under varying CCT conditions. Weighted average method was used to allocate the most natural and preferred image white point of four typical indoor images. The results showed that the most natural and preferred image white points were image dependency and the white point was also dependent on the chromaticity of the ambient illuminant. White points with negative Duv ( $-0.0041 \sim -0.0005$  and  $-0.0045 \sim -0.0001$  levels) were seemed natural and preferred. The results of this study can be used to enhance image quality on computer and mobile displays.

**Compliance with Ethical Standards. Conflict of Interest:** The authors stated that they had no conflict of interest with the experimental subjects.

**Ethical Approval:** All the procedures carried out in the research involving human participants were in line with the Academic Rules of Engineering Graduates of Zhejiang University and 1964 Helsinki declaration and its subsequent revisions or similar ethical standards.

**Informed Consent:** All individual participants included in the experiment were informed and agreed that the results of this study were used for academic research and publication of the paper.

## References

1. Kuriki, I. (2006). The loci of achromatic points in a real environment under various illuminant chromaticities. *Vision Research*, 46(19), 3055–3066.
2. Rea, M. S., & Freyssinier, J. P. (2013). White lighting. *Colour Research & Application*, 38(2), 82–92.
3. Li, H., Luo, M. R., Liu, X. Y., Wang, B. Y., & Liu, H. Y. (2016). Evaluation of colour appearance in a real lit room. *Lighting Research & Technology*, 48(4), 412–432.
4. Wang, Q., Xu, H., & Cai, J. (2015). Chromaticity of white sensation for LED lighting. *Chinese Optics Letters*, 13(7), 073301.

5. Ohno, Y., & Oh, S. (2016). Vision experiment II on white light chromaticity for lighting. In *Proceedings of CIE* (pp. 175–184).
6. Smet, K. A. G., Deconinck, G., & Hanselaer, P. (2014). Chromaticity of unique white in object mode. *Optics Express, OE*, 22(21), 25830–25841.
7. Smet, K. A., Deconinck, G., & Hanselaer, P. (2015). Chromaticity of unique white in illumination mode. *Optics Express*, 23(10), 12488–12495.
8. Smet, K. A. (2018). Two neutral white illumination loci based on unique white rating and degree of chromatic adaptation. *Leukos*, 14(2), 55–67.
9. Choi, K., & Suk, H.-J. (2016). Assessment of white for displays under dark-and chromatic-adapted conditions. *Optics Express*, 24(25), 28945–28957.
10. Huang, H. P., Wei, M., & Ou, L.-C. (2018). White appearance of a tablet display under different ambient lighting conditions. *Optics Express*, 26(4), 5018–5030.
11. Zhu, Y. T., Luo, M. R., Fischer, S., Bodrogi, P., & Khanh, T. Q. (2016). The effectiveness of colour appearance attributes for enhancing image preference and naturalness. In *Color and Imaging Conference* (No. 1). Society for Imaging Science and Technology.
12. Fairchild, M. D. (2013). *Colour appearance models* (3rd ed.). Chichester, West Sussex: Wiley.
13. Walraven, J., & Werner, J. S. (1991). The invariance of unique white; a possible implication for normalizing cone action spectra. *Vision Research*, 31(12), 2185–2193.



# Testing Cone-Cell Response of Young and Old Observers by Using Nearly Metameric Samples

Yonghui Xi, Min Huang<sup>(✉)</sup>, Ruili He, Chunli Guo, and Ning Ding

School of Printing and Packaging Engineering, Beijing Institute of Graphic Communication, Beijing, China  
huangmin@bigc.edu.cn

**Abstract.** To compare the color discrimination and then to study the retinal spectral response between young and old observers, 18 pairs of nearly metameric color patches based on 3 target colors (gray, nigger brown and light brown) were prepared, 40 color-normal observers (26 young observers aged from 20 to 25 and 14 old observers aged from 62 to 75) were organized to conduct the color difference experiments by using the method of psychological paired-comparison. The STRESS factor was computed between the visual color difference and CIE DE2000 values calculated from different color matching functions [CIE1931, CIE1964, S2, S6, S7, CIE2006 (age = 22, 68)]. The results show that there are significant differences about the performances of color matching functions (CMFs) between young and old observers. For young observers, CIE2006 (22y) CMFs gets the best performance, attended by S2 and S6 CMFs. For old observers, CIE1931 outperforms others.

**Keywords:** Color matching functions · STRESS · Color discrimination · Nearly metamerism

## 1 Introduction

The CMFs of CIE1931 and CIE1964 only took into account the effect of small field of view ( $1\text{--}4^\circ$ ) and large field of view ( $>4^\circ$ ) on human eye color perception, and did not consider the difference of color vision of observers with different ages. The CIE2006 model was based on a great deal of work of Stockman and Sharpe [1], with the reference of 47 CMFs under the Stiles and Burch [2]  $10^\circ$  view field. The model provided the average cone fundamentals of the observer that can calculate any field size between  $1^\circ$  and  $10^\circ$  and any age between 20 and 80.

In 2011, Sarkar [3] proposed eight different CMFs by using cluster analysis methods to analyze 47 individual CMFs of Stiles-Burch data and 61 CIE2006 CMFs, hereinafter referred to as S1, S2, ..., S8 color matching functions. But the performances of the CMFs are still needed to be tested, especially for individual observers with different ages.

## 2 Experimental

### 2.1 Lighting Source

The viewing cabinet used in this experiment was THOUSLITE LED Cube illumination device, which color temperature could be adjusted to simulate the LED lighting conditions at 5000 K. The spectral power distribution measured by Photo-Research PR655 spectral radiometer is illustrated in Fig. 1. Moreover, the illuminance received at the bottom of the viewing cabinet was 1117 lx. Most importantly, the color rendering index was 98.2. Figure 2 presents the diagram of color samples at 5000 K.

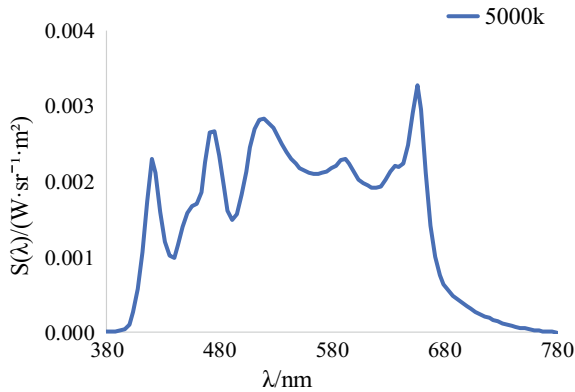


**Fig. 1.** Spectral power distribution of light illumination

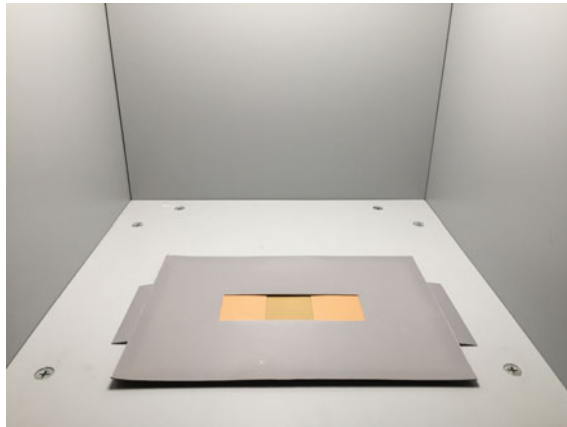


**Fig. 2.** Diagram of color samples

### 2.2 Colors Samples

Three colors (gray, nigger brown and light brown) in the color card (published by China Popular Color Association in 1987) were selected as the target samples in the visual experiment, six comparative colors with different reflectance were chosen from hundreds of color samples around each target sample. Epson Stylus Pro7908 inkjet printer and Color long Inkjet soft proofing paper were used to prepare comparative samples. The size of all samples was both 5 cm × 5 cm. Their spectral reflectance measured by the e-Xact spectrophotometer is shown in Fig. 3.

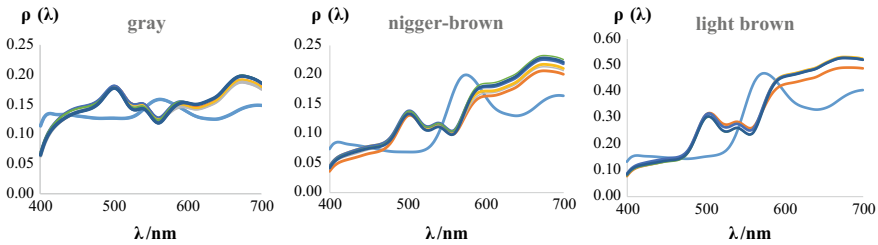


Fig. 3. Spectral reflectance curves of the target and compared color patches

Experimental samples were made according to CIE DE2000 color difference tendencies computed by CIE1931 and CIE1964, which colorimetric values and CIE DE2000 color difference are summarized in Fig. 4 and Table 1. For example, in the gray center, CIE DE2000 color difference increase/decrease from color pairs #1 to #6 using the CIE 1931/1964 standard observers.

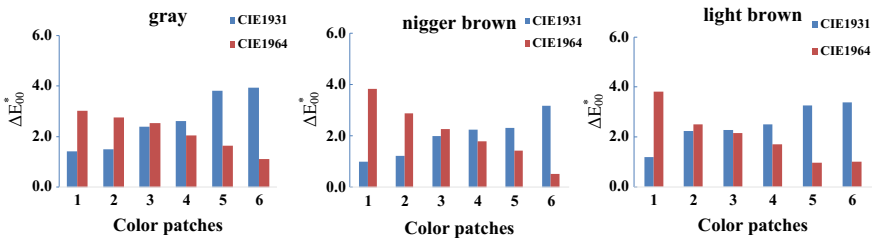


Fig. 4. CIEDE2000 color-difference calculated by CIE1931 and CIE1964

### 2.3 Experimental Process

26 young observers (9 males and 17 females) and 14 old observers (5 males and 9 females) with normal color vision participated in the paired comparison experiment. Young observers’ ages varied from 21 to 24, with the average age of 22. They are both students from Beijing Institute of Graphic Communication with a background of color

**Table 1.** Color samples' colorimetric values and CIEDE2000 color-difference values

	CIE1931				CIE1964			
	L*	a*	b*	$\Delta E_{00}$	L* <sub>10</sub>	a* <sub>10</sub>	b* <sub>10</sub>	$\Delta E_{00}$
Target (gray)	44.31	-1.12	2.76		44.18	-0.27	2.48	
1	45.57	-1.41	2.10	1.41	45.66	-2.21	2.86	3.03
2	44.94	-1.24	1.28	1.50	45.05	-2.12	2.05	2.75
3	45.28	-0.71	0.45	2.39	45.38	-1.58	1.14	2.53
4	45.69	-0.08	0.86	2.62	45.79	-0.99	1.54	2.05
5	45.35	1.00	0.67	3.80	45.45	-0.02	1.33	1.63
6	44.74	1.33	1.11	3.94	44.85	0.20	1.83	1.10
Target (nigger brown)	43.09	8.87	17.55		42.51	10.92	16.38	
7	42.42	8.00	17.18	1.01	42.18	7.45	17.74	3.84
8	42.70	8.63	15.62	1.22	42.48	7.91	16.17	2.88
9	43.17	9.07	14.65	1.99	42.95	8.39	15.07	2.25
10	43.57	9.78	15.01	2.24	43.35	9.06	15.43	1.78
11	43.84	10.76	16.45	2.31	43.59	10.03	16.86	1.42
12	43.28	11.51	15.79	3.17	43.04	10.65	16.20	0.53
Target (light brown)	63.02	12.07	30.25		62.14	15.01	28.83	
13	63.88	10.71	29.29	1.19	63.42	10.55	29.97	3.81
14	64.56	14.84	31.80	2.23	64.04	14.52	32.36	2.51
15	64.53	14.72	30.64	2.27	64.03	14.35	31.18	2.16
16	64.33	14.78	29.39	2.50	63.86	14.32	29.92	1.71
17	63.31	16.43	30.05	3.26	62.82	15.86	30.57	0.97
18	63.63	16.29	29.38	3.38	63.16	15.68	29.89	1.00

science. Meanwhile, old observers' ages varied from 61 to 74, with the average age of 68. All of them are retired people.

The visual experiment was carried out in a dark room. The visual angle of observation was about 45° and each observer about 25–30 cm in visual distance. Each of target samples was placed in the center of the viewing cabinet, while the samples to be compared were randomly placed on both sides of the target sample. Additionally, a gray mask with a window of 5 cm × 15 cm was played on the target and compared samples, whose L\*<sub>10</sub>a\*<sub>10</sub>b\*<sub>10</sub> values were 61.00, -0.76, -0.08. The color pair No. 1 was composed of the target sample and a test sample 1 on the left, and No. 2 was composed of the target sample and a test sample 2 on the right, observers need to judge which color difference appears larger than the other by comparing with the target sample. After that the results will be recorded and then the organizer randomly picks out a test sample 3 to the observers.

All observers did 10 repeated experiments on each target color in the visual experiment at different time intervals. For one observer, there are 15 [= 6 × (6 - 1)/2] judgments about one target color. In total, there are 18,000 (= 15 judgments × 10 repetitions × 3 target colors × 40 observers) data sets.

### 3 Analysis and Discussions

#### 3.1 Visual Color Difference

The experimental data of each observer were recorded to calculate the probability. Then the probability was converted to z-score. Finally, in order to get the visual color difference data, a value of 3 was added to the z-score to eliminate negative values. Thus, the visual color difference  $\Delta V$  was obtained [4].

The mean values of the normalized visual color difference about young and old observers are shown in Fig. 5. It can be seen that under the three target samples, the visual color difference of the older observers show an upward trend, while young observers show a decreasing trend.

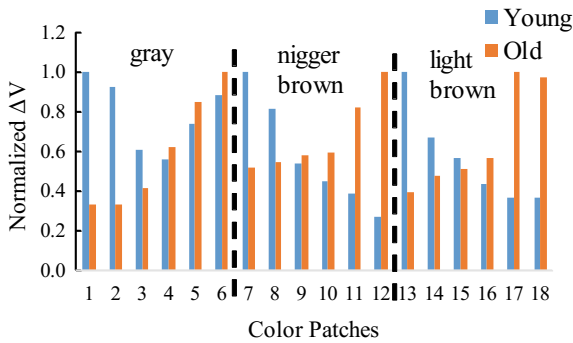


Fig. 5. Distribution of visual color difference for young and old observers

#### 3.2 The Accuracy of the Observers

The root-mean-square error (RMSE) of each observer was computed to verify the accuracy of the observers’ visual evaluation. The maximum values calculated by young and old observers were 1.62 and 1.37, the minimum values were 0.24 and 0.37, and the mean values were 0.75 and 0.67, respectively. The results of accuracy evaluation about young and old observers were similar. Compared with previous experiments by Ou [5], the accuracy of 16 young and old observers was 1.90 and 2.14, respectively. The results of different observers in our experiment were reliable and effective.

#### 3.3 Test Different Color Matching Functions

The CMFs used in this experiment were CIE1931, CIE1964, S2, S6, S7, CIE2006 (age = 22, 68). All color samples were chosen from different CIE DE2000 color difference tendencies calculated by CIE1931 and CIE1964. In our previous study [6], S2, S6 outperformed others between young observers; while for old observers, CIE1931 CMFs had the best performance. The average age of young and old observers in our experiment was 22 and 68 respectively. So 22y and 68y from CIE2006 CMFs were chosen to evaluate the results.

STRESS (Standardized Residual Sum of Squares) was used to determine the consistency between the CIE DE2000 color difference data calculated by different CMFs and the visual color difference data. The variety range of STRESS is 0–100, the smaller the value is, the better the consistency between the two groups of data sets is. In Table 2, the number labeled in bold font is the minimum STRESS value of the three colors in each color matching function.

**Table 2.** Performance of different CMFs for young and old observers in terms of STRESS

CMFs		CIE1931	CIE1964	S2	S6	S7	22y	68y
Young	Max	75.20	62.85	53.17	62.93	55.96	51.05	78.22
	Min	40.43	18.45	15.52	16.63	24.06	14.54	47.41
	Mean	62.71	32.50	31.10	32.14	41.34	<b>27.86</b>	66.68
Old	Max	47.17	75.71	68.00	75.55	44.69	68.30	52.91
	Min	9.63	38.08	27.16	38.75	19.53	25.33	16.80
	Mean	<b>23.84</b>	67.57	59.42	67.59	35.78	58.43	27.45

It can be seen from Table 2 that for young observers, the minimum STRESS value is 27.86 which means CIE2006 (22y) color matching functions has the best performances with the visual results. CIE1964, S2 and S6 CMFs have the better performance. While, for old observers, CIE1931 outperforms others with the minimum STRESS value is 23.84, followed by CIE2006 (68y) and S7 CMFs. This consequence is consistent with Sarkar's conclusion that S7 is suitable for calculating the cone cell response of old observers.

The number of observers with minimum STRESS value among 7 CMFs was counted. For 26 young observers, there were 3, 10, and 8 people were respectively consistent with the results of S2, S6 and CIE2006 (22y) CMFs. About the 14 older observers, 11 people were consistent with the results of CIE1931 and 3 people were in good agreement with S7 CMFs. It is obvious that the individual difference of the observer leads to abnormal spectral response of cone cells at the same age.

## 4 Conclusions

The paired comparison experiments were conducted for 40 color-normal observers by using 18 pairs of nearly metameric samples. The STRESS factor was used to evaluate the performance of different CMFs. The experimental results show that the visual color difference between young and old observers is quite different. On one hand, CIE2006 (22y) color matching functions gets the best performance for young observers. On the other hand, CIE1931 outperforms others in the function evaluation between old observers. Additionally, individual differences among young observers are greater while old observers are more stable.

**Acknowledgements.** This research was supported by National Natural Science Foundation of China (grant 61675029, 61308081). Thanks for all participants in our study.



**Ethical Approval:** All procedures carried out in the study involving human participants comply with the ethical standards of the school of printing and packaging engineering, Beijing Institute of Graphic Communication and with the 1964 Helsinki declaration and its later amendments or comparable ethical standards. Informed consent was obtained from all subjects.

## References

1. Stockman, A., & Sharpe, L. T. (2000). The spectral sensitivities of the middle- and long-wavelength-sensitive cones derived from measurements in observers of known genotype. *Vision Research*, *40*, 1711–1737.
2. Stiles, W. S., & Burch, J. M. (1959). NPL color matching investigation: Final report. *Optica Acta: International Journal of Optics*, *6*(1), 1–26.
3. Sarkar, A., Autrusseau, F., Vienot, F., et al. (2011). Form CIE 2006 physiological model to improved age-development and average colorimetric observers. *Journal of the Optical Society of America A*, *28*(10), 2033–2048.
4. He, R., Huang, M., Guo, G., et al. (2018). A study on the color difference between young and old observers. *Laser & Optoelectronics Progress*, *55*, 033301.
5. Ou, L. C., Luo, M. R., & Sun, P. L. (2012). Age effects on colour emotion, preference, and harmony. *Color Research and Application*, *37*(2), 92–105.
6. Huang, M., He, R., & Guo, C. (2018). Test and optimization of color matching functions for different age observers. *Acta Optica Sinica*, *38*(3), 0333001.



# Effect of Printed Color Sample Separation and Color-Difference Magnitude on Perceived Color Difference

Ting Xu<sup>1</sup>, Guihua Cui<sup>1</sup>(✉), Lan Jiang<sup>1</sup>, Ming Ronnier Luo<sup>2</sup>,  
Fereshteh Mirjalili<sup>2</sup>, and Jan Morovic<sup>3</sup>

<sup>1</sup> College of Mathematics, Physics and Electronic Information Engineering,  
Wenzhou University, Zhejiang, China  
gcui@wzu.edu.cn

<sup>2</sup> State Key Laboratory of Modern Optical Instrumentation,  
Zhejiang University, Zhejiang, China

<sup>3</sup> HP Inc., Barcelona, Catalonia, Spain

**Abstract.** 460 pairs of printed samples, around 5 CIE recommended color centers, with/without gap, and 4 color-difference magnitudes of 1, 2, 4 and 8 in CIELAB units, were employed to study the effects of separation and color-difference magnitude on perceived color difference. All the sample pairs were visually evaluated 20 times, using a gray-scale method, by a panel of 15 observers. The experimental results show that the smaller the color difference is, the larger the uncertainty of perceived color difference will be. Comparing datasets gathered with and without separation, it was found that the smaller the color difference is, the more obvious the influence of the gap between two samples will be. The visual data were also used to test the performance of six color-difference equations: CIELAB, CIEDE2000, CIE94, CMC, CAM02-UCS, and CAM16-UCS, the results show that CAM16-UCS outperformed the remained color-difference formulas.

**Keywords:** Parametric effect · Color difference · Gray scale method · Color-difference formula

## 1 Introduction

The quantitative description of color difference is a prerequisite for color management and accurately control of any color. However, the color-difference evaluation is affected by many viewing conditions, including sample size, sample separation, texture, color background, color-difference magnitude, etc. Manufacturers in industries must provide products with desired colors and control color changes to suit product use and customer expectations. Color-difference assessment is the basic tool to help manufacturers achieve an efficient color production process.

CIE [1] has periodically recommended color-difference assessment methods. CIELAB [2] color-difference formula was recommended in 1976, CIE94 [3] and CIEDE2000 [4] were optimized based on CIELAB color space in 1995 and 2000, respectively. CMC [5], CAM02-UCS [6], CAM16-UCS [7] and a series of color-

difference formulas were all established on the basis of visual data obtained under certain experimental conditions. The models for industrial color-difference evaluation are limited to use under the reference conditions, and correction factors are sometimes used to minimize the parametric effects for various conditions of use. If the viewing conditions change, the sensitivity of the human eye to color difference may change significantly.

Recently, Mirjalili et al. [8] studied the effect of gapless printed sample pairs and color-difference levels on perceived color difference, around 11 CIELAB color centers. For each color center, the samples were uniformly selected around the center, in three vertical planes, namely  $L^*a^*$ ,  $L^*b^*$ , and  $a^*b^*$ . 1012 sample pairs, with average CIE-LAB color difference of 1, 2, 4 and 8, were selected. Each color pair was printed without gap on a HP Latex 365 Printer on an  $8 * 8 \text{ cm}^2$  Avery Self-Adhesive Vinyl substrate with CMYKcm inks. 19 observers with an average age of 27.5 years performed visual color-difference evaluation on the color sample pairs using a gray scale method.

In this study, the 460 (5 centers \* 4 levels \* 23 pairs/per-center) pairs for 5 CIE recommended color centers, including gray, red, yellow, green, and blue [9], with 4 color-difference levels of 1, 2, 4, and 8, used by Mirjalili et al. were selected again. However, the original sample pairs were cut into two patches with a gap of hairline to show the effect of separation on perceived color difference, and visual assessment experiments were performed using the same gray scale as Mirjalili et al. The motivation of the study was to examine the effect of printed samples' separation and color-difference magnitude on the perceived color difference.

## 2 Experimental

An X-Rite SpectroEye spectrophotometer was applied to measure the spectral reflectance of the samples in  $45^\circ:0^\circ$  measuring geometry.

All the gray-scale samples were also prepared using the same inkjet printer on the same substrate with different gray level inks in a  $4 * 8 \text{ cm}^2$  rectangular size. The gray scale contained 8 gray levels and one standard (S). The first grayscale sample had the same gray level as the standard (S). The other grayscale samples had higher gray level than the standard (S), and the gray level gradually increased from the sample 1 to sample 8.

All the visual assessments were carried out inside a viewing cabinet lighted with spectrum tunable LED, under a D65 simulator. The relative spectral power distribution (SPD) as well as the colorimetric characteristics of the D65 simulator including the correlated color temperature (CCT), color rendering index (CRI) and illuminance were measured using a calibrated JETI spectroradiometer. The CCT (K), CRI (Ra) and illuminance (lux) of the lighting system were 6460, 96.5 and 960, respectively.

The experiment was carried out in a very quiet dark room. 15 observers, all of them were graduate students with normal color vision, and average age of 24 years, participated in the experiment. Five of them repeated the experiment twice to investigate the observer repeatability. Before starting the experiment, the observers had been well trained. During the experiment, the sample pair and the gray-scale samples were

situated in the middle of the cabinet's floor, and the left-right position and sequence of sample pair to be presented were randomly selected, as shown in Fig. 1.

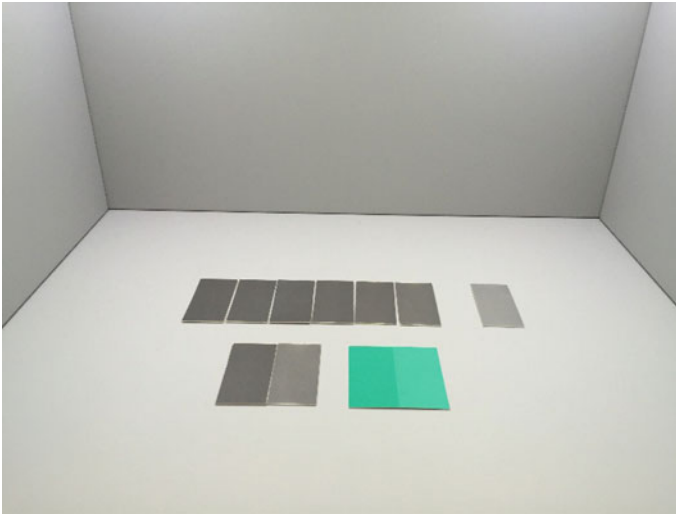


**Fig. 1.** Configuration of the sample pair and grayscale samples inside the viewing cabinet

Before the beginning of experiment, the lights in viewing cabinet were warmed up for at least 5 min. The observer performed light adaptation for about 1 min and then officially started the color discrimination experiment. The gray scale score (GS) for each color-difference pair was collected.

### 3 Results and Discussion

To convert the gray-scale score (GS) into visual color difference ( $\Delta V$ ), a regression (curve fitting) technique was used to find the relationship between the gray level and the corresponding color difference ( $\Delta E^*$ ) of these levels, as shown in Eq. (1). The color difference ( $\Delta E^*$ ) for each gray level is equivalent to the visual color difference ( $\Delta V$ ).

$$\Delta V = 0.0933e^{0.6571GS} \quad (1)$$

#### 3.1 Observer Variability

The STRESS index [10] which been widely used in color-difference evaluation was applied to evaluate the intra-observer's and inter-observer's variations, and in the remained data analysis. The smaller the STRESS is, the better the agreement between two datasets compared will be. The intra-observer variability computed from five observers' repeated experiments ranged from 21.0 to 25.8 with an average of 23.7. The

range of inter-observer variability among 15 observers (including replicated data for five observers) was 16.8 to 37.2 with an average of 23.8. Compared with other related color-difference evaluation experiments [8], this value represents the typical performance of visual evaluation by the observer using the gray-scale method.

### 3.2 Magnitude Effect

To study the effect of one parameter on the perceived color difference, the visual color differences ( $\Delta V$ ) obtained from two experiments with different values of the parameter can be directly compared, i.e., comparing the visual color difference for the color-difference level 1 with levels 2, 4 and 8, respectively, and calculating the corresponding STRESS and/or correlation coefficient  $r$ , to reveal the effect of magnitude between level 1 and level 2, 4, and 8, and so on. The correlation between visual differences of different color-difference magnitudes are listed in Table 1.

**Table 1.** Correlation between visual differences of various color-difference magnitudes

Comparison	STRESS	$r$
$\Delta V - 1$ versus $\Delta V - 2$	24.5	0.68
$\Delta V - 1$ versus $\Delta V - 4$	21.6	0.71
$\Delta V - 1$ versus $\Delta V - 8$	25.5	0.45
$\Delta V - 2$ versus $\Delta V - 4$	20.6	0.78
$\Delta V - 2$ versus $\Delta V - 8$	27.6	0.53
$\Delta V - 4$ versus $\Delta V - 8$	21.5	0.68

From Table 1, it can be observed that the maximum correlation reaches 0.78, and STRESS value is 20.6 for  $\Delta V - 2$  versus  $\Delta V - 4$ . The correlation of  $\Delta V - 1$  and  $\Delta V - 8$  is the smallest (only 0.45) amongst all the comparisons. Those findings are similar to that of Mirjalili et al. Mirjalili et al.'s results with gapless samples show that there is a greater correlation between high color-difference levels, especially the correlation between  $\Delta V - 4$  and  $\Delta V - 8$  is the largest, and the correlation between  $\Delta V - 1$  and  $\Delta V - 8$  is the smallest.

### 3.3 Gap Effect

Comparing with the Mirjalili et al.'s study [8], the only difference between two experiments was that the separation or gap between two color samples in a pair, i.e., without gap in Mirjalili et al.'s study and with hairline gap in this study, so it is more persuasive to see the gap effect on the perceived color difference by comparing two studies. The STRESS values between Mirjalili et al.'s and current studies for each center and each color-difference level were computed, and the results of comparison are enumerated in Table 2.

From the data in Table 2, it can be seen that the samples' gap has a significant effect on the visual color difference, i.e., the STRESS value for each color center decreases as

**Table 2.** Effect of separation on perceived color difference in term of STRESS

Color-difference level	Blue	Green	Gray	Red	Yellow
1	49.1	52.4	49.6	61.7	41.6
2	39.6	44.2	40.3	46.8	55.1
4	31.9	37.8	22.5	28.0	39.5
8	23.5	23.3	15.8	21.8	26.2

the color-difference level increases. That means the smaller the color-difference magnitude is, the more obvious the influence of the gap between the samples will be.

### 3.4 Performance of Color-Difference Equations

The performances of six color-difference equations were tested using STRESS measure and the current experimental data (Table 3).

**Table 3.** Performance of six color-difference formulas in terms of STRESS

	CIELAB	CIEDE2000	CIE94	CMC	CAM02-UCS	CAM16-UCS
Full data set	25.0	24.1	26.7	25.0	23.9	23.0
$\Delta E_M = 1$	38.0	29.2	34.8	31.9	31.1	30.5
$\Delta E_M = 2$	33.2	23.7	31.8	25.8	26.8	26.0
$\Delta E_M = 4$	29.7	23.7	29.7	26.6	26.1	25.2
$\Delta E_M = 8$	20.5	22.7	23.7	23.2	21.5	20.4

From the total data in Table 3, it can be noticed that the STRESS values of all the formulas were ranged from 23.0 to 26.7, and the performances for six tested formulas were very close, with CAM16-UCS performed best, and CIE94 performed the worst. However, they are very close to the average intra-observer and inter-observer variability for the experiment, i.e., 23.7 and 23.8, respectively. That means the tested color-difference formulas performed well in predicting color difference in this study. It can also be seen from Table 3 that in evaluating different color-difference magnitudes for a color-difference equation, the performances of all formulas were gradually improving as the color difference increasing from  $\Delta E_M = 1$  to  $\Delta E_M = 8$ .

## 4 Conclusions

A psychophysical gray-scale experiment was conducted to collect visual color-difference data for printed samples under two sample gaps: gapless and hairline, and four color-difference magnitudes: 1, 2, 4 and 8 in CIELAB units. The effects of sample gap and color-difference magnitude on perception and on the performance of six color-

difference equations were studied. From the experimental results, it can be concluded that the sample gap and color-difference magnitude had an obvious effect on the perceived color difference and on the performance of color-difference equations. The sample gap's effects increased as the color-difference magnitude decreased for printed samples.

**Acknowledgements.** This study is supported by National Science Foundation of China (61775170, 61671329, and 61501331).

**Ethical Approval:** All procedures performed in studies involving human participants were in accordance with the ethical standards of the Wenzhou University and with the 1964 Helsinki declaration and its later amendments or comparable ethical standards. And informed consent was obtained from all individual participants included in the study.

## References

1. Commission Internationale de l'Éclairage (CIE). (1993). *Parametric effects in colour-difference evaluation*. CIE Publication No. 101. Vienna, Austria: Central Bureau of the CIE.
2. Commission Internationale de l'Éclairage (CIE). (2004). *Colorimetry*, CIE Publication No. 15. Vienna, Austria: Central Bureau of the CIE.
3. Commission Internationale de l'Éclairage (CIE). (1995). *Industrial colour-difference evaluation*. CIE Publication No. 116. Vienna, Austria: Central Bureau of the CIE.
4. Luo, M. R., Cui, G., & Rigg, B. (2001). The development of the CIE 2000 colour-difference formula: CIEDE2000. *Color Research and Application*, 26, 340–350.
5. Clarke, F. J. J., McDonald, R., & Rigg, B. (1984). Modification to the JPC79 colour-difference formula. *Journal of the Society of Dyers and Colourists*, 100, 128–132.
6. Luo, M. R., Cui, G., & Li, C. (2006). Uniform colour spaces based on CIECAM02 colour appearance model. *Color Research and Application*, 31, 320–330.
7. Li, C., Li, Z., Wang, Z., et al. (2017). Comprehensive color solutions: CAM16, CAT16, and CAM16-UCS. *Color Research and Application*, 42(6), 703–718.
8. Mirjalili, F., Luo, M. R., Cui G. et al. (2018). A parametric colour-difference equation to evaluate colour-difference magnitude effect for gapless printed stimuli. To be presented in CIC 2018 Conference.
9. Robertson, A. R. (1978). CIE guidelines for coordinated research on Colour-difference evaluation. *Color Research and Application*, 3(3), 149–151.
10. García, P. A., Huertas, R., Melgosa, M., et al. (2007). Measurement of the relationship between perceived and computed color differences. *Journal of the Optical Society of America A. Optics and Image Science*, 24(7), 1823–1829.



# Objective Colour Quality Assessment for Lighting

Weiming Wang<sup>1</sup>, Shuai Gao<sup>2</sup>, Hongyu Lin<sup>1</sup>,  
Ying Liu<sup>1</sup>, and Qiang Liu<sup>1,3</sup>✉

<sup>1</sup> School of Printing and Packaging, Wuhan University,  
Wuhan 430079, China

liuqiang@whu.edu.cn

<sup>2</sup> Tsinghua Holdings Habitat Development Lighting Institute Co., Ltd.,  
Beijing 100085, China

<sup>3</sup> Shen Zhen Research Institute, Wuhan University, Shenzhen 518000, China

**Abstract.** In this contribution, the colour quality of lighting was evaluated with 21 typical objective colour quality metrics. A large dataset of 591 light sources was established. This database includes different kinds of sources including incandescent lamps, LEDs, fluorescent lamps, high intensity lamps as well as theoretical lights. A multidimensional scaling analysis method was adopted to reduce the dimensionality of colour quality evaluation, by which 6 typical measures were obtained for the final assessment. At last, the overall performance of the 591 light sources was comprehensively analyzed, together with a deep discussion on the colour quality of 14 typical sources for gallery lighting in China.

**Keywords:** Colour quality of lighting · Objective evaluation · Multidimensional scaling analysis · Gallery lighting

## 1 Introduction

Nowadays, due to the fact that people always pay much attention to the visual colour perception of lighting conditions, the assessment of colour quality has become the hotspot of current research [1–5]. It is quite clear that subjective evaluation based on psychophysical studies is the most reliable and rigorous evaluation method [2, 5]. However, limited by time, space, and test environment, subjective evaluation is difficult to achieve in most of the applications.

According to previous studies, it is a fast and relatively effective method to evaluate the colour quality of lighting with typical objective metrics [1–5]. Therefore, in this work with the aim of systematically assess the colour quality of lighting, 591 light sources (including 14 typical light sources of gallery), were objectively evaluated with 21 typical color quality metrics. To our knowledge, the objective evaluation of so many of SPDs with so many colour quality measures has not been reported in current literature.

A multidimensional scaling analysis method was adopted to reduce the dimensionality of 21 typical color quality metrics. It is found that six of them in colour



fidelity and colour gamut dimensionalities could be defined as typical measures. Therefore, the corresponding six typical measures were used for the final assessment and their sum of ranking orders was used to represent the overall colour quality of each source.

To be specific, the aims of the study are as follows: (1) To find the optimal Spectral Power Distributions (SPDs) which exhibit best colour quality from the light source dataset. (2) To investigate the impact of Correlated Colour Temperature (CCT) upon the overall colour quality. (3) To compare the performance of 14 typical light sources of the galleries.

## 2 SPD Dataset

A large dataset of 591 light sources was established, the detail information is shown in Table 1. There is no repetition in this dataset and the wavelength ranges were uniformly set to 400–700 nm, with 5 or 10 nm intervals.

**Table 1.** The 591 light sources adopted in this dataset

No.	Psychophysical study or dataset	SPDs adopted
1	Wang et al. (Multi-CCT, 2017) [4]	10
2	Wei et al. (Metameric lighting, 2014) [6]	2
3	Narendran et al. (Multi-CCT, 2002) [5]	7
4	Szabó et al. (Metameric lighting, 2016) [7]	20
5	Feltrin et al. (Multi-CCT, 2017) [8]	5
6	Royer et al. (Metameric lighting, 2016) [9]	50
7	Dangol et al. (Metameric lighting, 2013) [10]	8
8	Islam et al. (Metameric lighting, 2013) [11]	24
9	Jost-Boissard et al. (Metameric lighting, 2009) [12]	14
10	Jost-Boissard et al. (Metameric lighting, 2014) [13]	17
11	He et al. (Multi-CCT, 2015) [14]	4
12	Dikel et al. (Multi-CCT, 2014) [15]	6
13	Huang et al. (Multi-CCT, 2017) [16]	9
14	Royer et al. (Metameric lighting, 2016) [9]	26
15	Khanh et al. (Metameric lighting, 2016–17) [17–20]	36
16	Typical sources for gallery exhibition in China	14
17	CRI2012 excel [21]	36
18	CQS 9.0.3 excel [22]	83
19	MCRI excel [23]	30
20	TM30-15 excel [24]	190
Sum	—	591

### 3 Twenty-One Colour Quality Metrics

Twenty-one typical color quality metrics are used for objective evaluation, including Color Rendering Index [25], Gamut Area Index [26], Color Quality Scale (Qa, Qf, Qg, Qp) [22], Full Spectrum Color Index [27], Color Preference Index [28], Feeling of Contrast Index (CAM02) [29], Color Discrimination Index [30], Cone Surface Area [31], CRI-CAM02UCS [25, 32], CRI2012 [21], Memory Color Rendering Index [33], IES-TM 30 (Rf and Rg) [34],  $\Delta C^*$  [18, 19], Color Quality Index (CQI [19], CQI' [18]), GAI-RA [13] and Gamut Volume Index GVI [2]. Limited by the length of this paper, this section only serves as a short list for the metrics. Please refer to the relevant citations for detailed information.

## 4 Result and Discuss

### 4.1 Multi-dimensional Scaling

Multi-dimensional scaling (MDS) is a visualization method to display high-dimensional multivariate data in low-dimensional space. The method looks similar to plotting scores with principal component or plotting scores. The basic goal of multi-dimensional scaling is to minimize any deformation caused by dimensionality reduction by “fitting” the original data into a low-dimensional coordinate system [35]. The problems involved in multidimensional scaling can be described as: when the similarity (or distances) between each item in  $n$  project is certain, the representation of these items in low-dimensional space is obtained, and the degree of proximity among the projects is “general match” with the original similarity (or distance).

MDS subdivision can be divided into several types. This article only introduces one of the most commonly used requirements of raw data: non-metric MDS. The idea of this method is to create points based on the similarity matrix such that the Euclidean distance between them can represent the original similarity approximately.

Based on the MDS method and the relevant research findings mentioned in the above citations, six typical measures (CRI, Rf, GAI, Qg, MCRI, GVI) were selected, as shown in Fig. 1. In the following, these six measures will be used to analyze the colour quality of 591 SPDs and the overall performance of each candidate could be assessed by the sum of rank orders with regard to each measure.

### 4.2 Overall Analysis of 591 light Sources

The results of overall analysis of 591 light sources indicate that the gamut-based measures and fidelity-based measures could not reach an optimum simultaneously. For instance, among the 591 sources a LED of 6500 K exhibits smallest sum of rank order, whose rank (CRI) = 266, rank (GAI) = 11, rank (Qg) = 116, rank (MCRI) = 5, rank (Rf) = 149, rank (GVI) = 5. Obviously, such a measure exhibits better colour-gamut attribute than that of colour fidelity. As for other SPDs, quite similar results (i.e. the gamut-based metrics and fidelity-based metrics do not vary simultaneously) were obtained.

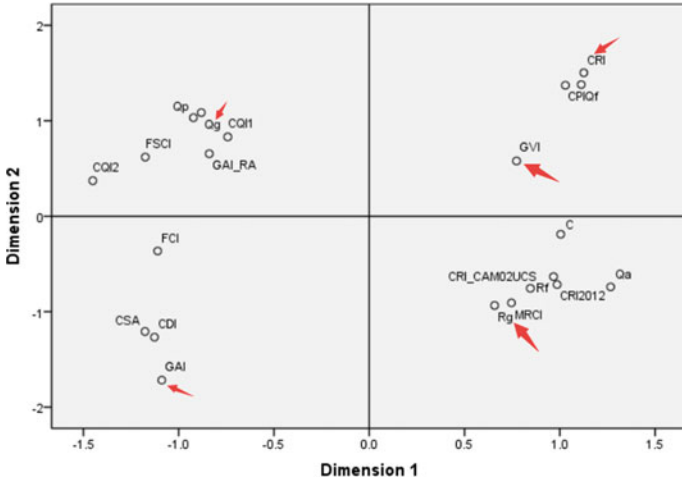


**Fig. 1.** Multidimensional scaling of the 21 colour quality measures based on 591 SPDS

Figure 2 illustrates the correlation between Correlated Colour Temperature and Sum of rank order. From this picture, it is quite clear that although a certain CCT may corresponds to different sum of rank orders, in general there is a trend that a higher CCT correlates with a smaller sum of rank order.

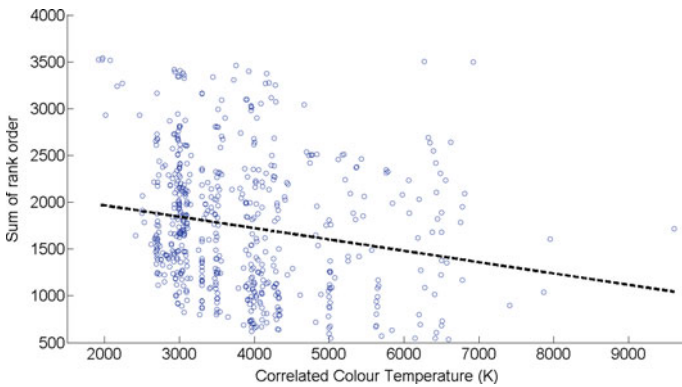


**Fig. 2.** Correlation between Correlated Colour Temperature and sum of rank order

### 4.3 Analysis of 14 Typical Light Sources for Gallery Lighting

The colour quality performance of the 14 typical light sources for gallery was further analyzed. Such light sources were provided by 7 suppliers of gallery lighting in China (each supplier provides two light sources, 3000 and 4000 K). Due to the fact that the

CRI, Qg and Rf measures are relative measures (i.e. their calculation is based on certain reference source of a same CCT), only the sources of similar CCT were grouped and compared together. Therefore, 130 SPDs from the dataset with a CCT between 2900 and 3100 K were adopted to evaluate the performance of 7 gallery lights with a CCT of 3000 K, while 83 SPDs with a CCT between 3800 and 4100 K were adopted to evaluate the performance of seven 4000 K sources.

Tables 2 and 3 summarize the colour quality of the gallery lightings. From these two tables, several conclusions could be drawn. First, the light sources for gallery lighting always exhibit sound performance in colour fidelity (i.e. CRI, Rf) while their performance in colour gamut (GAI, GVI, Qg) is relatively poor. This could be ascribed to the fact that the light sources suppliers actually pay much attention on the colour fidelity attribute while relatively ignore the colour gamut attributes, although many psychophysical studies have revealed that the gamut-based measures are in closer relationship with human visual appreciation [2, 12, 13, 16, 36]. Secondly, interestingly, the light sources of supplier 4 exhibit smallest sum of rank order compared to other suppliers (9/137 for 3000 K, 24/90 for 4000 K), which indicates that such sources tend to perform best, at least from the aspect of overall colour quality.

**Table 2.** The colour quality of light sources for gallery lighting (3000 K-LED) compared with a pool of 137 SPDs

ID	Rank (CRI)	Rank (GAI)	Rank (Qg)	Rank (MRCI)	Rank (Rf)	Rank (GVI)	Rank (Sum)
3000 K-supplier 1	21	83	97	43	24	74	342
3000 K-supplier 2	17	74	67	28	13	72	271
3000 K-supplier 3	23	73	49	28	24	61	258
3000 K-supplier 4	4	61	49	17	6	56	193
3000 K-supplier 5	24	79	88	43	16	68	318
3000 K-supplier 6	22	90	88	43	12	75	330
3000 K-supplier 7	12	84	58	28	7	69	258

**Table 3.** The colour quality of light sources for gallery lighting (4000 K-LED) compared with a pool of 90 SPDs

ID	Rank (CRI)	Rank (GAI)	Rank (Qg)	Rank (MRCI)	Rank (Rf)	Rank (GVI)	Rank (Sum)
4000 K-supplier 1	28	62	57	43	27	45	262
4000 K-supplier 2	11	44	42	29	18	47	191
4000 K-supplier 3	26	58	57	35	30	38	244
4000 K-supplier 4	6	42	38	29	6	37	158
4000 K-supplier 5	15	49	42	35	8	39	188
4000 K-supplier 6	25	69	50	43	14	52	253
4000 K-supplier 7	32	46	42	43	28	46	237

The followings are the metric values for the sources of supplier 4 (T825-CF26-3WB and T825-CF26-4WB): CRI-3000 K = 98; GAI-3000 K = 58; Qg-3000 K = 101; MCRI-3000 K = 91; Rf-3000 K = 95; GVI-3000 K = 81; CRI-4000 K = 96; GAI-4000 K = 76; Qg-4000 K = 100; MCRI-4000 K = 91; Rf-4000 K = 93; GVI-4000 K = 87. At last, it must be mentioned that there are several criterions when judging the lighting quality for gallery, such as glare, UV level and temperature rise. Therefore, for gallery lighting design, those factors should be taken into consideration as well.

## 5 Conclusions

The objective assessment of colour quality for lighting is of crucial importance for lighting design and applications. In this study, the colour quality of lighting was evaluated with 21 typical objective colour quality metrics and the SPD data of 591 light sources. A Multidimensional scaling method is used to get 6 representative measures (CRI, Rf, GAI, Qg, MRCI, GVI) and the sum of rank orders of those 6 measures were used to quantify the colour quality of light sources. At last, the overall performance of the 591 light sources was comprehensively analyzed, together with a deep discussion on the colour quality of 14 typical sources for gallery lighting in China.

**Acknowledgements.** This work is supported by the National Natural Science Foundation of China (Project No. 61505149) and the Young Talent Project of Wuhan City of China (Project No. 2016070204010111).

## References

1. Houser, K. W., Wei, M., David, A., Krames, M. R., & Shen, X. S. (2013). Review of measures for light-source color rendition and considerations for a two-measure system for characterizing color rendition. *Optics Express*, *21*, 10393–10411.
2. Liu, Q., Huang, Z., Xiao, K., Pointer, M. R., Westland, S., & Luo, M. R. (2017). Gamut volume index: A color preference metric based on meta-analysis and optimized colour samples. *Optics Express*, *25*, 16378–16391.
3. Tang, Y., Lu, D., Xun, Y., Liu, Q., Zhang, Y., & Cao, G. (2018). The influence of individual color preference on LED lighting preference. In *49th Conference of the International Circle of Education Institutes for Graphic Arts Technology and Management (IC) and 8th China Academic Conference on Printing and Packaging, 2017* (pp. 77–87). May 14–16, 2017, Lecture Notes in Electrical Engineering.
4. Wang, Q., Xu, H., Zhang, F., & Wang, Z. (2017). Influence of color temperature on comfort and preference for LED indoor lighting. *Optik-International Journal for Light and Electron Optics*, *129*, 21–29.
5. Narendran, N., & Deng, L. (2002). Color rendering properties of LED light sources. In *International Symposium on Optical Science and Technology* (pp. 61–67).
6. Wei, M., Houser, K. W., Allen, G. R., & Beers, W. W. (2014). Color preference under LEDs with diminished yellow emission. *LEUKOS*, *10*, 119–131.
7. Szabó, F., Kéri, R., Schanda, J., Csuti, P., & Mihálykó-Orbán, E. (2016). A study of preferred colour rendering of light sources: Home lighting. *Lighting Research & Technology*, *48*, 103–125.
8. Feltrin, F., Leccese, F., Hanselaer, P., & Smet, K. (2017). Analysis of painted artworks' color appearance under various lighting settings. In *IEEE International Conference on Environment and Electrical Engineering and 2017 IEEE Industrial and Commercial Power Systems Europe* (pp. 1–6).
9. Royer, M., Wilkerson, A., Wei, M., Houser, K., & Davis, R. (2016). Human perceptions of colour rendition vary with average fidelity, average gamut, and gamut shape. *Lighting Research & Technology*, 1477153516663615.
10. Dangol, R., Islam, M., LiSc, M. H., Bhusal, P., Puolakka, M., & Halonen, L. (2013). Subjective preferences and colour quality metrics of LED light sources. *Lighting Research and Technology*, *45*, 666–688.
11. Islam, M., Dangol, R., Hyvärinen, M., Bhusal, P., Puolakka, M., & Halonen, L. (2013). User preferences for LED lighting in terms of light spectrum. *Lighting Research and Technology*, *45*, 641–665.
12. Jost-Boissard, S., Fontoynt, M., & Blanc-Gonnet, J. (2009). Perceived lighting quality of LED sources for the presentation of fruit and vegetables. *Journal of Modern Optics*, *56*, 1420–1432.
13. Jost-Boissard, S., Avouac, P., & Fontoynt, M. (2014). Assessing the colour quality of LED sources: Naturalness, attractiveness, colourfulness and colour difference. *Lighting Research & Technology*, *47*, 769–794.

14. He, J., Lin, Y., Yano, T., Noguchi, H., Yamaguchi, S., & Matsubayashi, Y. (2015). Preference for appearance of Chinese complexion under different lighting. *Lighting Research & Technology*, *49*, 228–242.
15. Dikel, E. E., Burns, G. J., Veitch, J. A., Mancini, S., & Newsham, G. R. (2014). Preferred chromaticity of color-tunable LED lighting. *Leukos*, *10*, 101–115.
16. Huang, Z., Liu, Q., Westland, S., Pointer, M. R., Luo, M. R., & Xiao, K. (2017). Light dominates colour preference when correlated colour temperature differs. *Lighting Research & Technology*, 1477153517713542.
17. Khanh, T., & Bodrogi, P. (2016). Colour preference, naturalness, vividness and colour quality metrics, part 3: Experiments with makeup products and analysis of the complete warm white dataset. *Lighting Research and Technology*, 1477153516669558.
18. Khanh, T., Bodrogi, P., Vinh, Q., & Stojanovic, D. (2016). Colour preference, naturalness, vividness and colour quality metrics, part 2: Experiments in a viewing booth and analysis of the combined dataset. *Lighting Research and Technology*, 1477153516643570.
19. Khanh, T., Bodrogi, P., Vinh, Q., & Stojanovic, D. (2015). Colour preference, naturalness, vividness and colour quality metrics, part 1: Experiments in a room. *Lighting Research & Technology*, 1477153516643359.
20. Zhu, W., Wan, X., Li, J., Li, C., Jin, G., & Liu, Q. (2017). Nondestructive pigment size detection method of mineral paint film based on image texture. *Journal of Electronic Imaging*, *26*, 011002.
21. Smet, K. A., Schanda, J., Whitehead, L., & Luo, R. M. (2013). CRI2012: A proposal for updating the CIE colour rendering index. *Lighting Research & Technology*, *45*, 689–709.
22. Davis, W., & Ohno, Y. (2010). Color quality scale. *Optical Engineering*, *49*, 033602–033616.
23. Smet, K., Ryckaert, W., Pointer, M. R., Deconinck, G., & Hanselaer, P. (2012). A memory colour quality metric for white light sources. *Energy and Buildings*, *49*, 216–225.
24. David, A., Fini, P. T., Houser, K. W., Ohno, Y., Royer, M. P., Smet, K. A., et al. (2015). Development of the IES method for evaluating the color rendition of light sources. *Optics Express*, *23*, 15888–15906.
25. Nickerson, D., & Jerome, C. W. (1965). Color rendering of light sources: CIE method of specification and its application. *Illuminating Engineering*, *60*, 262.
26. Freyssinier, J. P. & Rea, M. (2010). A two-metric proposal to specify the color-rendering properties of light sources for retail lighting. In *SPIE Optical Engineering + Applications* (pp. 77840V–77846V).
27. Rea, M., Deng, L., & Wolsey, R. (2004). *NLPIP lighting answers: Light sources and color*. Troy, NY: Rensselaer Polytechnic Institute.
28. Thornton, W. (1974). A validation of the color-preference index. *Journal of the Illuminating Engineering Society*, *4*, 48–52.
29. Hashimoto, K., Yano, T., Shimizu, M., & Nayatani, Y. (2007). New method for specifying color-rendering properties of light sources based on feeling of contrast. *Color Research & Application*, *32*, 361–371.
30. Thornton, W. A. (1972). Color-discrimination index. *JOSA*, *62*, 191–194.
31. Fotios, S. A., & Levermore, G. J. (1997). The perception of electric light sources of different colour properties. *Lighting Research & Technology*, *29*, 161–171
32. Luo, M. R. (2011). The quality of light sources. *Coloration Technology*, *127*, 75–87.
33. Smet, K. A. G., Ryckaert, W. R., Pointer, M. R., Deconinck, G., & Hanselaer, P. (2010). Memory colours and colour quality evaluation of conventional and solid-state lamps. *Optics Express*, *18*, 26229–26244.

34. Illuminating Engineering Society of North America. (2015). *TM-30-15 IES method for evaluating light source color rendition*. New York.
35. Steyvers, M. (2000). *Multidimensional scaling* (pp. 93–103).
36. Peng, R., Zhang, Y., Liu, Q., Wang, Q., & Cao, G. (2018). Correlation between color quality metric and color preference of light source. In *49th Conference of the International Circle of Education Institutes for Graphic Arts Technology and Management (IC) and 8th China Academic Conference on Printing and Packaging* (pp. 3–11).





# The Performance of Different Whiteness Formulas for White Papers

Chunli Guo, Xiaoyan Zuo, Yu Liu<sup>(✉)</sup>, Ruili He, Yonghui Xi,  
and Min Huang

School of Printing and Packaging Engineering, Beijing Institute of Graphic  
Communication, Beijing, China  
liuyu@bigc.edu.cn

**Abstract.** Whiteness is an important property to characterize the surface color. A lot of whiteness formulas are used to characterize the whiteness of the materials. However, the performance of these formulas for paper samples is unknown. In this paper, 38 paper samples [27 fluorescent whitening agents (FWA) samples and 11 non-FWA] were evaluated under 6 light sources, including 3 levels of CCT (3000, 5000 and 6500 K) and 2 levels of ultraviolet (UV) radiation (with UV and without UV), by 12 observers (6 males and 6 females) with normal color vision. And 7 whiteness formulas were used to evaluate the accuracy of whiteness formulas in predicting the whiteness of paper samples using STRESS factor. The results suggest that  $W_{CIE}$  and  $W_{Uchida}$  can predict the whiteness of paper samples more accurately.

**Keywords:** Whiteness formula · Whiteness appearance · Fluorescent whitening agents · Ultraviolet

## 1 Introduction

Whiteness is one of the most familiar colors in our minds and there are different white in our daily life. With the development of FWAs and UV radiation, the materials contained FWA can absorb the UV light and emit visible blue light subsequently, and then the object can be whiter in vision.

There are various whiteness formulas to character the whiteness of an object. It is well known that the CIE whiteness formula [1] is the most widely used whiteness formula but it can only be defined under CIE illuminant D65. Recently, a new whiteness formula named optimized whiteness formula has been proposed by Ma et al. [2] and this new formula can be used under arbitrary correlated color temperature (CCT). Wei et al. [3] conducted a psychophysical experiment based on textile and paper samples to verify this new formula's performance. Later, Wei et al. [4] collected textile samples, plastic samples, paper samples, NCS and Pantone matt samples to optimize the whiteness boundary. The above studies are based on multiple materials and the amount of paper samples is relative small. This study aims to verify the performance of various whiteness formulas for paper samples.

In this study, 38 paper samples were evaluated under 6 light sources by 12 observers with normal color vision. And 7 whiteness formulas were used to evaluate

the accuracy of whiteness formulas in predicting the whiteness appearance of paper samples using STRESS factor. The results can be used to evaluate the accuracy of different whiteness formulas in predicting whiteness and provide basic data and theoretical support for the optimization of whiteness formula.

## 2 Whiteness Formulas

Many whiteness formulas have been proposed to characterize the whiteness of an object. The CIE whiteness formula ( $W_{CIE}$ ) [1] was proposed in 1986. However, it is only defined for the CIE D65 illuminant. This formula can only be used when  $W_{CIE}$  value is between 40 and 5Y-280. In 1998, the Uchida whiteness formula ( $W_{Uchida}$ ) [5] was proposed.

In this paper,  $W_{CIE(x_n, y_n)}$ ,  $W_{Uchida(x_n, y_n)}$ ,  $W_{CIE, CAT16}$  and  $W_{Uchida, CAT16}$  were also used.  $W_{CIE(x_n, y_n)}$  and  $W_{Uchida(x_n, y_n)}$  are calculated using  $W_{CIE}$  and  $W_{Uchida}$ , respectively. However,  $Y$  and  $(x, y)$  are the chromatic values of a paper under the current light source, and  $(x_n, y_n)$  are the chromaticities of the current light source.  $W_{CIE, CAT16}$  and  $W_{Uchida, CAT16}$  are calculated using  $W_{CIE}$  and  $W_{Uchida}$ , together with CAT16 [6] respectively.  $Y$  and  $(x, y)$  are the chromatic values converted to D65/10° using CAT16.

$W_{Optimized}$  can be defined by Eq. (1).  $Y$  and  $(x_{10}, y_{10})$  are the chromatic values of a sample under the current light source, while  $(x_{n,10}, y_{n,10})$  are the chromatic values of the current light source. The variables of  $a'$  and  $b'$  are defined in Eq. (2).

$$W_{Optimized} = Y + a'(x_n - x) + b'(y_n - y) \quad (1)$$

$$\begin{aligned} a' &= -0.1891 * CCT + 2267.2 \\ b' &= 0.3202 * CCT - 493.36 \end{aligned} \quad (2)$$

## 3 Experimental

### 3.1 Light Sources

The light sources are produced by LED lighting device produced by THOUSLITE company with wavelength ranging from 350 to 800 nm. 6 light sources are selected in this experiment, including 3 CCT levels (i.e., 3000, 5000 and 6500 K) and 2 ultraviolet radiations levels (with UV and without UV). The relative spectral distributions of 6 light sources, measured by FS spectrometer, are shown in Fig. 1 and the colorimetric values are summarized in Table 1.

Note that “1, 2, 3” represent the 3000 K without UV, 5000 K without UV and 6500 K without UV light source, respectively, and “4, 5, 6” represent the 3000 K with UV, 5000 K with UV and 6500 K with UV light source, respectively.

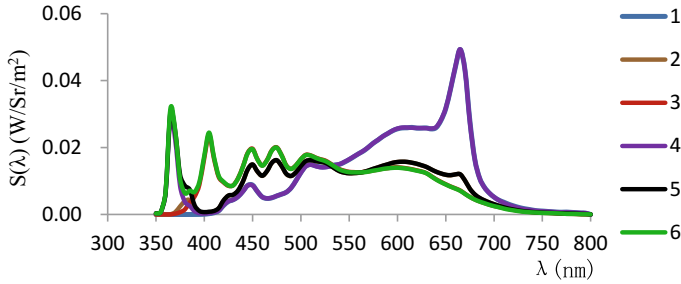


**Fig. 1.** The relative SPDs of the light sources

**Table 1.** Colorimetric characteristic of the illuminants

Light sources	CCT	Lux	$x_n$	$y_n$	$R_a$
1	2833	1379	0.45	0.41	97.0
2	4894	1019	0.35	0.36	93.8
3	6556	1014	0.31	0.33	95.0
4	2827	1379	0.45	0.41	97.0
5	4897	1018	0.35	0.36	93.8
6	6574	1008	0.31	0.33	95.0

### 3.2 White Samples

Thirty-eight white paper samples are carefully prepared, including 27 FWA samples and 11 non-FWA samples. The distribution of 38 paper samples in  $a^* - b^*$  plane is shown in Fig. 2. The red circles represent non-FWA samples while the blue diamond's represent the FWA samples.

### 3.3 Visual Experiment

Twelve observers (6 males and 6 females) with normal color vision are organized to conduct this visual experiment. All of them are student and the average age of these observers is 22. In this experiment, observers were instructed to sort samples from pure white to “feeling of color”. All the samples are evaluated at the center of the cabinet as much as possible. Figure 3 illustrates the process of this visual experiment. Each observer repeats 2 or 3 times under each light source to test the observer variability, 30 datasets are gathered under each light source. In total, 6840 evaluations are collected (i.e., 38 samples  $\times$  6 light sources  $\times$  30 datasets).

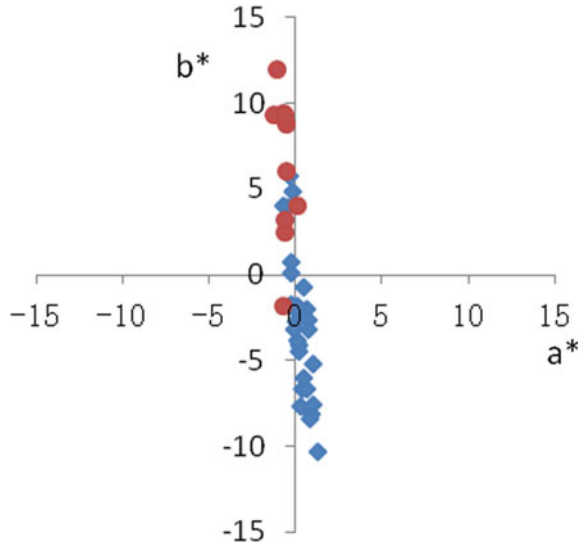


**Fig. 2.** Distribution of the paper samples



**Fig. 3.** Process of visual experiment

## 4 Results and Discussions

### 4.1 The Calculation of Perceived Whiteness

When an observer completes a visual experiment, the experimenter records the order in which the observer arranges the paper samples. The order of arrangement represents the perceived whiteness of each observer. For each sample, the average of 30 assessments

was taken as the perceived whiteness of the paper sample under the current light source. According to the method, the perceived whiteness value under other light sources can be calculated.

## 4.2 Observer Variation

The Standardized Residual Sum of Squares (STRESS) [7] is used to evaluate the inter- and intra-observer variations. The inter-observer variation is calculated between 38 judgements made by each observer and the 38 average judgements. The intra-observer variation is calculated between the repeated judgements and the average judgements of each observer. The average inter- and intra-observer STRESS value is 9.64 and 7.50, respectively, compared with the previous study [3], which indicates that the collected data from this experiment is valid.

## 4.3 The Performance of Whiteness Formulas

The STRESS factors was also used to evaluate the performance of 7 whiteness formulas ( $W_{CIE}$ ,  $W_{Uchida}$ ,  $W_{CIE(xn, yn)}$ ,  $W_{Uchida(xn, yn)}$ ,  $W_{CIE, CAT16}$ ,  $W_{Uchida, CAT16}$  and  $W_{Optimizd}$ ) with the calculated whiteness value and the perceived whiteness. There is a sample (FWA sample) whose value of  $T_w$  is out of range, so the sample is no longer considered in followings. The STRESS values are listed in Table 2.

**Table 2.** The performance of 7 whiteness formulas in terms of STRESS values under different light sources

Light sources	$W_{CIE}$	$W_{CIE(xn, yn)}$	$W_{CIE, CAT16}$	$W_{Uchida}$	$W_{Uchida(xn, yn)}$	$W_{Uchida, CAT16}$	$W_{Optimizd}$
1	21.00	36.67	30.35	21.00	37.67	30.90	35.98
2	20.54	31.25	29.54	20.44	29.68	27.57	31.32
3	19.81	26.92	26.73	19.70	23.79	23.35	26.54
I	21.26	36.15	32.58	21.90	31.90	29.21	35.70
4	21.78	27.74	21.99	22.05	<b>75.35</b>	29.28	28.37
5	21.05	24.64	23.21	21.32	25.68	20.72	25.34
6	21.68	23.79	23.65	21.84	22.27	22.18	23.62
II	22.49	29.25	25.78	23.37	51.46	27.65	29.97
III	21.89	34.49	32.73	22.65	44.70	31.59	34.31

Note that “I”, “II” represent the STRESS value between perceived whiteness of 111 samples (37 samples under 3 light sources) and calculated whiteness of 111 samples, while “III” represents the STRESS value between perceived whiteness of 222 samples (37 samples under 6 light sources) and calculated whiteness of 222 samples.

As shown in Table 2,  $W_{Uchida(xn, yn)}$  cannot predict the whiteness of paper samples under 3000 K with UV radiation (light source 4), as most of the calculated  $T_w$  values of samples under this light source are not between  $-4$  and  $+2$ , and this condition is not considered in the following discussion. The performances of  $W_{CIE}$  and  $W_{Uchida}$  have

been improved after color adaptive transformation, especially under 3000 K light sources. In general, the whiteness formulas have the worst performance under light sources with 3000 K color temperature.  $W_{\text{Uchida}}$  and  $W_{\text{CIE}}$  have better performance in predicting the whiteness of paper samples.

## 5 Conclusions

In order to evaluate the performances of different whiteness formulas, a visual experiment was conducted under 6 different light sources with 38 white papers. Twelve observers were organized to carry out the whiteness assessments. The results indicated that the performance of  $W_{\text{CIE}}$  and  $W_{\text{Uchida}}$  have been improved after CAT16. With the increase of CCT, the performances of whiteness formulas have been improved. Both  $W_{\text{CIE}}$  and  $W_{\text{Uchida}}$  have better performance in predicting the whiteness of all paper samples.

**Acknowledgements.** This research was supported by National Natural Science Foundation of China (grant 61675029, 61308081).

### Compliance with Ethical Standards

**Conflict of Interest:** The authors declare that they have no conflict of interest.

**Ethical Approval:** All procedures performed in studies involving human participants were in accordance with the ethical standards of the school of Printing and Packaging Engineering, Beijing Institute of Graphic Communication and with the 1964 Helsinki declaration and its later amendments or comparable ethical standards.

**Informed Consent:** Informed consent was obtained from all individual participants included in the study.

## References

1. Commission Internationale de l'Eclairage. (2004). *Colorimetry*. CIE Publication 15. Vienna: CIE.
2. Ma, S., Wei, M., Liang, J., Wang, B., Chen, Y., Pointer, M., et al. (2016). Evaluation of whiteness metrics. *Lighting Research & Technology*, 50(3), 429–445.
3. Wei, M., Ma, S., Wang, Y., & Luo, M. R. (2017). Evaluation of whiteness formulas for FWA and non-FWA whites. *Journal of the Optical Society of America A*, 34(4), 640–647.
4. Wei, M., Wang, Y., Ma, S., & Luo, M. R. (2017). Chromaticity and characterization of whiteness for surface colors. *Optics Express*, 13, 27981–27994.
5. Uchida, H. (1998). A new whiteness formula. *Color Research and Application*, 23, 202–209.
6. Li, C., Li, Z., Wang, Z., Xu, Y., Luo, M. R., et al. (2017). Comprehensive color solutions: CAM16, CAT16, and CAM16-UCS. *Color Research and Application*, 42, 703–718.
7. García, P. A., Huertas, R., Melgosa, M., & Cui, G. (2007). Measurement of the relationship between perceived and computed color differences. *Journal of the Optical Society of America A*, 24(7), 1823–1829.



# Measurement and Evaluation of the Surface Color of 3D Paper Product

Mingming Cui<sup>3</sup>, Xiaozhou Li<sup>1,2(✉)</sup>, Guangyuan Wu<sup>3</sup>, and Qian Cao<sup>3</sup>

<sup>1</sup> Key Laboratory of Pulp and Paper Science & Technology of Ministry of Education/Shandong Province, Qilu University of Technology (Shandong Academy of Sciences), Shandong, China

lixiaozhou2000@163.com

<sup>2</sup> State Key Laboratory of Pulp and Paper Engineering, South China University of Technology, Guangzhou, China

<sup>3</sup> School of Printing and Packaging Engineering, Qilu University of Technology (Shandong Academy of Sciences), Shandong, China

**Abstract.** 3D printing surface, a tridimensional surface with varied region color as the angle change, has exhibited an obvious difference compared with that of plane printing which was based on 2D plane in accordance with the existing color reproduction rule of color perception and evaluation. According to the characteristics of 3D printing, an idea was put forward to measure and evaluate the surface color of 3D paper product by using quantities of simple angles to simulate three dimensional angles. A simple angle measurement model and color patches were designed to demonstrate the 3D surface. The surface characteristics of color patches were measured by CS2000 radiometer and spectrophotometer. It showed that the visual perception of the same color and the chromaticity of the 3D surface varied significantly with angle changes. In general, the results provided an useful information for establishing a color measurement and evaluation model of full-color 3D printing products.

**Keywords:** Full-color 3D printing · Viewing angle · Color measurement

## 1 Introduction

Color is one of the main properties to characterize the details and features of the object. The visual perception and color difference calculation are always used to describe the color quality of the printed products.

Color is often demonstrated in CIE1976L\*a\*b\* which is a relative uniform color space [1]. However, there will be color difference for the same color while the visual conditions change. And there are still color differences between the similar color samples. Chromatic shift is the combined result of differences in hue, brightness, and saturation which are the three primitive properties of color [2]. The color difference formula is as follows:

$$\Delta E_{ab}^* = \sqrt{(L_1^* - L_2^*)^2 + (a_1^* - a_2^*)^2 + (b_1^* - b_2^*)^2} \quad (1)$$

where  $L_1^*$ ,  $a_1^*$ ,  $b_1^*$  and  $L_2^*$ ,  $a_2^*$ ,  $b_2^*$  are the coordinate values of the two color samples.

## 2 Color Measurements for 3D Paper Product

Traditionally, 45:0 or 0:45 measurement conditions is used on smooth and flat substrate. However, it is difficult to measure three-dimensional object well. The surface color of 3D printing product is very different according to the direction of the observer [3]. 3D printing is an accumulation of objects made from layer to layer [4]. Because of this feature of 3D printing, color difference formula based on 2D printing can no longer be used directly. An idea was put forward to measure and evaluate the surface color of 3D paper product by using quantities of simple angles to simulate three dimensional angles. Three-dimensional angles can be regarded as quantities of simple angles. Therefore, displace angles for measuring the surface of paper plane were designed according to viewing angles, as shown in Fig. 1.

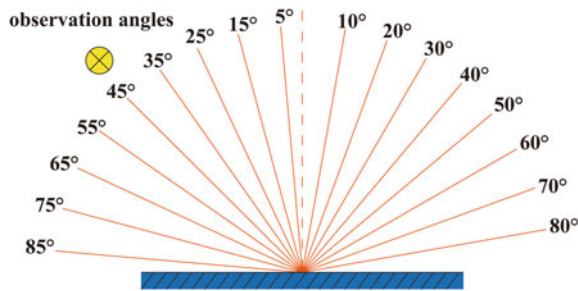


Fig. 1. Measurement angles

## 3 Experiments and Analysis

In this chapter, CS2000 radiometer was used to measure the color patches at different display angles and the effects of different angles on the color measurement and perception were studied.

Konica Minolta color laser printer was used to print the C, M, Y and K color patches which were designed to be 6 cm × 6 cm. The paper was coated art paper. The whole experiment was conducted in a dark room to avoid the influence of external light sources. D65 light source was used. The measuring distance was design as in Fig. 2 according to the principle of CS2000 measurement. Where, L is the distance from paper surface to radiometer, and h is the paper sample height, which is 6 cm in this experiment.



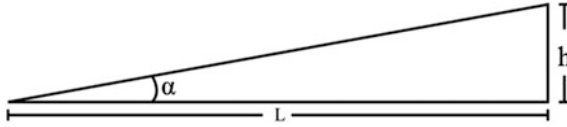


Fig. 2. Viewing angle and the viewing distance

### 3.1 Magnitude Estimation

Standard observation condition: darkroom, color patches placed in the Gretag Macbeth Judge II standard light source observation box under different angles, D65.

Visual evaluation: Binocular Stereo Vision [5]. Adopt 7 grade evaluation methods [6]. Color patch of  $0^\circ$  was set as the standard sample (Table 1).

Table 1. Magnitude estimation scoring table

Observer angle ( $^\circ$ )	5	10	15	20	25	30	35	40	45	50	55	60	65	70	75	80	85
1	2	2	4	3	5	5	6	5	5	4	2	4	5	4	5	4	5
2	2	2	3	2	6	6	7	4	5	4	3	4	4	4	5	4	5
3	2	1	3	2	5	6	6	4	3	3	2	3	5	5	5	6	6
4	3	3	2	5	3	4	4	2	3	4	3	3	5	7	6	7	7
5	1	1	3	3	6	6	6	4	4	5	1	4	3	5	4	4	6
6	1	1	2	2	5	7	5	6	3	3	3	3	4	4	6	5	6
7	2	1	3	2	4	5	5	5	3	4	2	4	5	4	5	5	4
Mean	2	2	3	3	5	6	6	4	4	4	2	4	4	5	5	5	6

The results show that the grade is higher at about  $30^\circ$ , which indicates that the color of this angle is more different from that of  $0^\circ$ , the gloss and color are not as bright as  $0^\circ$ , and the effect of visual evaluation is the worst.

### 3.2 Objective Evaluation

The emissivity of the color patch was measured by CS2000 spectrometer at 18 angles. It can be seen in Fig. 3 that the radiation flux was different from various directions. The radiometric changed corresponding to different angles.

In Fig. 3, the radiation intensity of the four color patches was the highest at  $30^\circ$ , it meant when the angle was at  $30^\circ$ ; the spectrum of radiation to the human eye was maximum, which was consistent with the magnitude estimation results. The relationship between the radiation intensity of the four color patches was  $30^\circ > 60^\circ > 45^\circ > 75^\circ > 15^\circ$ .

In Fig. 4, the chroma was the smallest at  $30^\circ$ . And the chroma decreased with the angle increased from  $0^\circ$  to  $30^\circ$  they showed an upward trend. The chroma of yellow was the biggest while the black was the least.

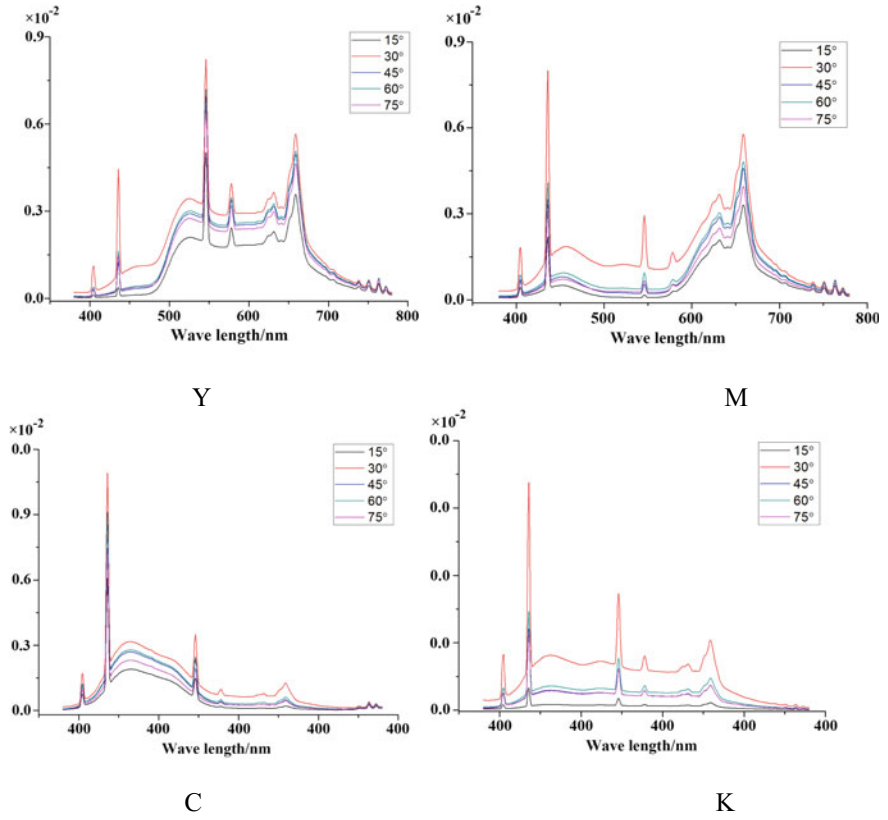


Fig. 3. Radiation intensity of four color patches and different angles

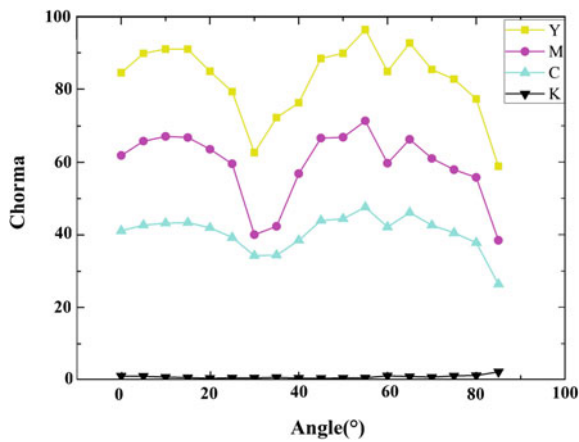


Fig. 4. Viewing angles and chroma of four color patches

The increase of the observation angles were shown in Fig. 5. The brightness gradually increases. When the angle reaches 30° and 35°, the brightness of the four color patches reach the maximum. The yellow patch has the highest brightness in the four colors, and the black has the lowest lightness.

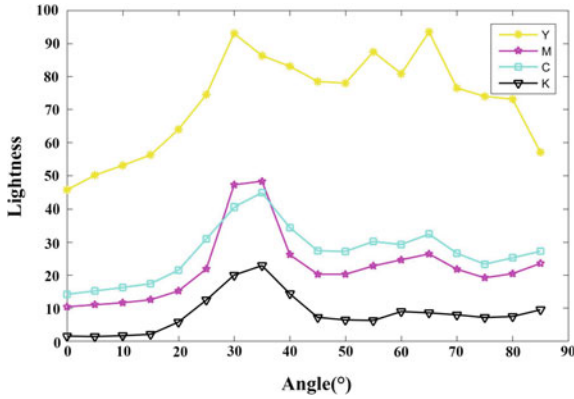


Fig. 5. Different viewing angles and brightness of four color patches

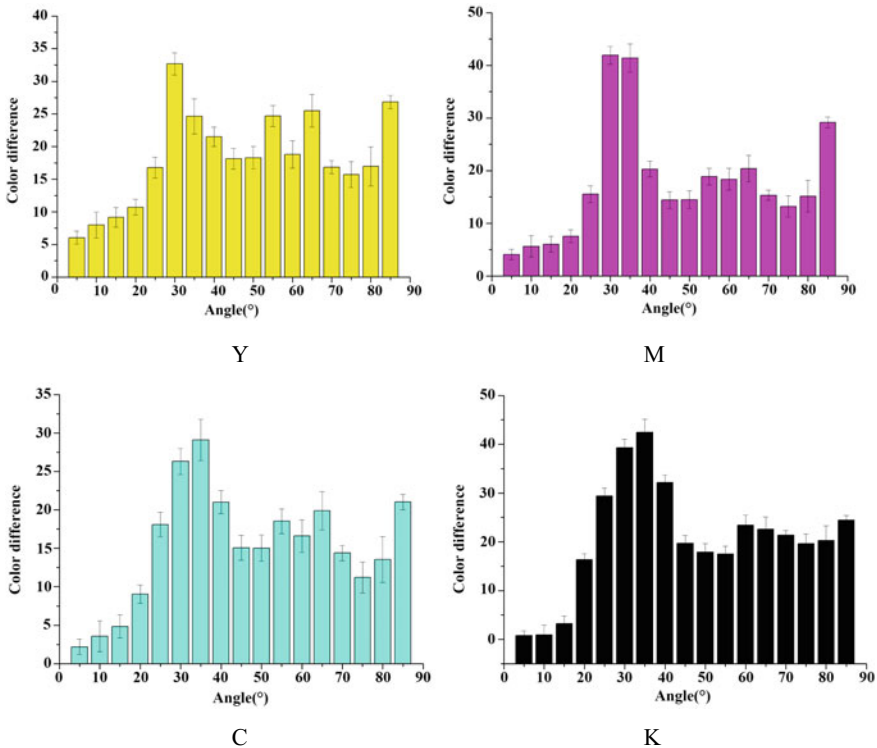


Fig. 6. Viewing angles and color difference of four color patches

The color differences of the four color patches with different viewing angles were shown in Fig. 6. The maximum appeared when the observation angle was at 30° and 35°. It showed that the incidence, reflection and absorption of light had the greatest influence on color appearance.

## 4 Conclusions

Color perception and color properties under different viewing angles were measured and evaluated. Multi-angle measurement is used to simulate the effects of 3D printing. The color differences of yellow, magenta, cyan and black were verified at different angles. It showed that there were obvious differences in color appearance of different angles for the same color sample under standard viewing conditions. The visual perception and color difference of 30° were mostly obvious. These are helpful for color characterization of full color 3D printing.

**Acknowledgements.** This work was supported by State Key Laboratory of Pulp and Paper Engineering (Project Number 201722), the Foundation (No. KF201604) of Key Laboratory of Pulp and Paper Science and Technology of Ministry of Education/Shandong Province of China, Jinan City Colleges and Universities Independent Innovation Project (Grant No. 201311032).

## References

1. Yang, J., Zhen, L., & Wang, P. F. (2013). Research on contrast sensitivity function of hue in CIE 1976 L\*a\*b\* color space. *Transactions of Beijing Institute of Technology*, 33(8), 824–828.
2. Sun, J., Zhou, S., & Zhou, L. (2011). Study on color difference detection of printed matter based on CIEDE2000 color difference formula. *Mechanical Science and Technology*, 30(4), 582–585.
3. Song, L. M., Gao, Y. Y., & Zhu, X. J. (2016). A 3D measurement method based on multi-view fringe projection by using a turntable. *Optoelectronics Letters*, 12(5), 389–394.
4. Matusik, W., Matusik, W., & Matusik, W. (2017). Color contoning for 3D printing. *ACM Transactions on Graphics*, 36(4), 124.
5. Zou, X., Zou, H., & Lu, J. (2012). Virtual manipulator-based binocular stereo vision positioning system and errors modelling. *Machine Vision and Applications*, 23(1), 43–63.
6. Reinhard, E., Stark, M., Shirley, P., & Ferwerda, J. (2002). Photographic tone reproduction for digital images. *ACM Siggraph*, 21(3), 267–276.



# Evaluating the Quality of Color Profiles for Output Devices

Ping Yang, Zizhao Wu, Yong Wang<sup>(✉)</sup>, Siwei Lu, Weiyan Zhang, and Qiang Wang

School of Digital Media & Design, Hangzhou Dianzi University,  
Hangzhou, Zhejiang, China

yangping@hdu.edu.cn, wangyong\_zju@163.com

**Abstract.** This paper focused on the key technology the color profile in the color management. The research analyzed criterion for selecting the feature color and the mechanism of the characterization by taking the output device as research target. And a color profile evaluating model was established based on neutral gray rendering with ICC profile and color difference detection in the experiment. As the results, the evaluation model improved accuracy of the color profile in color management. It can be applied to evaluate color profile and optimize its accuracy.

**Keywords:** Color management · Color profile · ICC profile evaluation

## 1 Introduction

It aims to achieve “3C” in color management, including the calibration, characterization and conversion [1]. In color management, correct device working principles in color application system has to be established. Then the color profiles in the color space in digitized device can be acquired with spectrophotometer as the foundation of series of precise color patches [2, 3]. Finally, the accurate conversion of the color space and color matching are processed with color profile according to industrial purpose and requirement [4, 5]. Therefore, color profile is the technical key to the color management and the foundation to achieve the accuracy of the color management.

## 2 Theory of Establishing Color Profile

Color profile refers to color characterization in the color space that digital devices can present [6]. It simplifies the complexed color reproduction and color rendering as mathematical processing between two color spaces. Thus, modern computer can reach the goal of color management and color control. Establishment of color profile has to be provided with three fundamental elements, including color patches, instrument of color measurement and special software of establishing color profile [7].

## 2.1 Color Patches

Color patches refers to the limited quantity of color samples and their data in the color space of a device. It is on the basis of scientific analysis about color space characterizations that a device can be processed.

Theoretically and practically, color space includes millions of colors so that the color patches have to be established scientifically. That is to say, a number of limited color samples should be extracted to present and control the whole three-dimension color space precisely. They are characterized colors, the key to achieve dot-to-dot color space conversion by computer in color management. As is shown in research findings, there are principles of characterized color selection: (a) selected color can control the key node of the color space according to the color space and color rendering principles, such as white, black, neural gray, three-primary colors, secondary color and some tertiary colors; (b) selected nodes in the color model should accord with characteristics of color space and the quantization accuracy should fix with computer processing system; (c) selected characterized colors should keep isometry in the view or uniform distribution in color solid, which conforms to visual interval distribution rules.

At present, there are some common color patches including IT8.7/3, IT8.7/4 AND ECI2002 to reveal out-put device color features. As is shown in Fig. 1, IT8.7/3 color patches include 928 color units. According to features in geometric distribution, stable angular points on the equilateral triangle (they refer to secondary colors) are selected as color feature units and the key node of computing control in the CMY space.

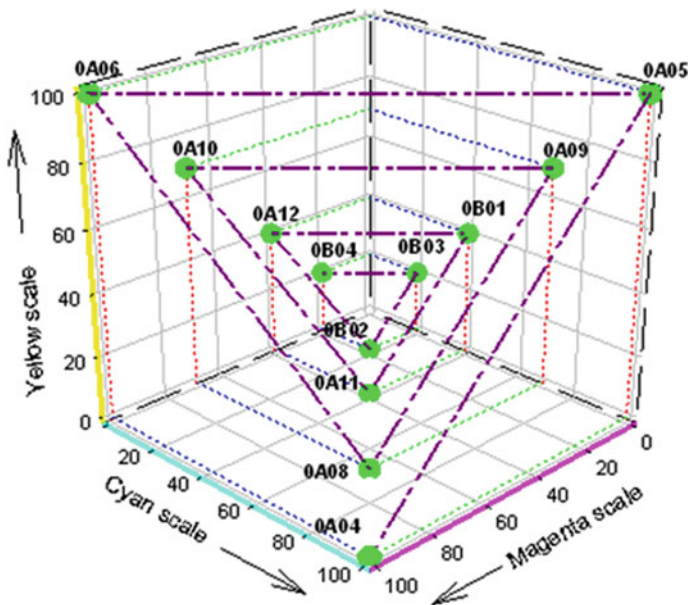


Fig. 1. The distribution of some compound color of IT8.7/3 in CMY space

## 2.2 Instrument of the Color Measurement

A color sample among the color patches need to be used by spectrophotometer to measure value of chroma objectively and precisely. Through spectral measurement, characterized colors are transformed into values, achieving conversion in different color space or color gamut.

Color measurement is the key and the foundation to reach precision of color management. When color is measured, instrument and parameters should be selected based on precision requirement and value errors should be controlled to insure accuracy of the subsequent operation.

## 2.3 Special Software of the Color Profile Establishment

Special software of the color characterization refers that measured chroma values are converted date file in general or special format according to fixed principles. Besides, it can optimize data and revise program.

Measured color value has to be organized as color profiles based on fixed principles to convert and match colors in different color spaces in order to achieve consistency of color transferring. Among these color profiles, ICC profile is a color profile format based on the cross-computer platform by International Color Consortium. ICC profile offers two color conversion processing models used in distinguishing color space, including matrix model and color look-up-table (LUT) model. Color profiles on the output device are based on color LUT model.

# 3 Color Profile Evaluations

Color profile decides the precision of the color management. Therefore, it is vital to estimate color profile in color management. In the research, there are two ways to evaluate color profile. Experiment samples include Jindong coated paper (157 g/m<sup>2</sup>), Toyo ink, SM-CD102 press, IT8.7/3 color patches and EFI Spectrometer ES-1000. And four kinds of color profiles are numbered as B.icm, D.icm, I.icm and F.icm.

## 3.1 Evaluation of Neutral Gray Rendering

Neutral gray balance as the most important norm insures the correct color rendering. In the research, a circumference of the circle test was designed to evaluate ability of neutral gray rendering in the color profile. Firstly, a group of neural gray data based on the LAB was designed in the test. Specifically, lightness (L) was from 0 to 100, interval was 1, and chroma A and B were 0. Then, this group of testing data was made as gray scale with LAB model by Photoshop. Image > Model > Conversion was used as configuration profile option. Configuration profile under the target space was selected as evaluated color profile. Rendering intent was absolute colorimetric rendering intent. Color management module was ACE. Thus, gray scale image was processed in the CMYK color space. Next, image in CMYK model was rendered in the Lab color space. Image > Model > Conversion was used as configuration profile option. Configuration

profile in the target space was selected as Lab color profile. Rendering intent and color management module were chosen as the same as the above. So the gray scale was rendered in LAB color space. And a series of new chroma values were defined as L'A'B'. Finally, compared LAB with L'A'B' by mean of vector, the distance the vector deviated the axis of lightness (vertical axis) revealed neutral gray rendering ability. And the smaller the distance was, the stronger the neutral gray rendering ability was.

The for color profiles (B.icm, D.icm, I.icm and F.icm) as main samples in primary neutral gray testing data, generated four groups of L'A'B' values after circumference of circle test. The compared results were shown as Fig. 2. It can be seen that I.icm neutral gray axis after rendering deviated smallest distance from the primary lightness axis than other three color profile (B.icm, D.icm and F.icm).

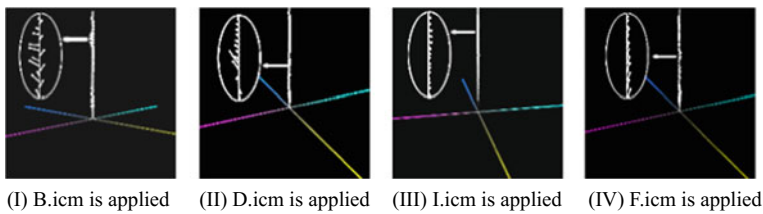


**Fig. 2.** The comparison of neutral behavior of ICC profiles

### 3.2 Evaluation of Color Difference

The Evaluation of color difference indicates the compared degree of the closeness in the real press and general standard or manufacturer's technical index. Hereon, general standard or manufacturer's technical index uses ICC profile which accords with industrial standards or typical production environment in some industries, such as Euroscale coated paper, ICC. In our research, Heidelberg Printopen was used to evaluate color difference prediction.

The evaluation was worked in Printopen's inspection function, the digital test pattern in CMYK model was opened and then color profile B.icm, D.icm, I.icm and F.icm were imported. The USOffset coated.icm as reference foundation, color difference prediction was calculated according to the imported color profile. The CYMK values on the color patches were transformed as LAB value. Then the color difference E was computed respectively. Specifically, they were the color difference value between B.icm, D.icm, I.icm and F.icm, and the correspond color units which were converted through USOffset. Next, color difference distributions were depicted by the compared results, shown in Fig. 3.

According to color difference computing and its statistical data, the result was shown as:

$$E_{B.icm \text{ and } RE.icm} > E_{D.icm \text{ and } RE.icm} > E_{F.icm \text{ and } RE.icm} > E_{I.icm \text{ and } RE.icm}$$



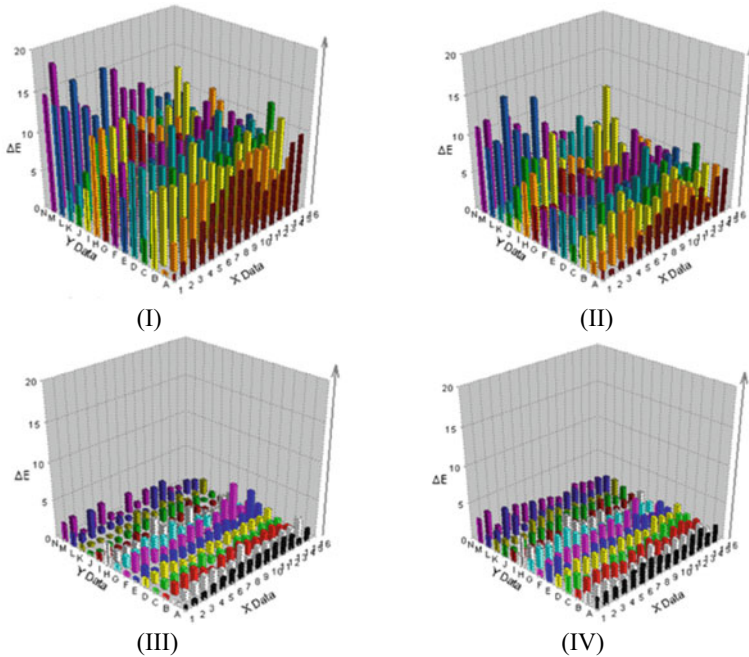


**Fig. 3.** The distribution of color difference. (I) B.icm versus RE.icm color difference distribution Average  $\Delta E = 8.45$ , (II) D.icm versus RE.icm color difference distribution Average  $\Delta E = 5.03$ , (III) I.icm versus RE.icm color difference distribution Average  $\Delta E = 1.42$ , (IV) F.icm versus RE.icm color difference distribution Average  $\Delta E = 1.94$

From the two evaluated results, it can be found that I.icm color profile is more precise than B.icm, D.icm and F.icm. Therefore, I.icm should be applied to present press color profile.

## 4 Conclusions

This paper proposed a color profile evaluation model on the basis of neutral gray rendering and estimation of color difference. Through the experiment, the objectivity and accuracy of the evaluation model was tested. And the results showed that this proposed color profile evaluation model was easy to use with high precision degree. It can solve the difficulty in evaluating the color profile precision in color management. Practically, it is characterized by excellent values of guidance and application in practical industrial process.

**Acknowledgements.** The work is financially supported by National Natural Science Foundation of China (NO. 61605038), and Research start-up fund of HDU (KYS225617053).

## References

1. ICC Profile Format Specification Version 3.2. (1999, November). *International color consortium*.
2. ISO 12647-2. (1996). *Graphic technology—Process control for the manufacture of half-tone color separations, proof and production prints—Part 2: Offset lithographic processes*.
3. ISO 12642. (1996). *Graphic technology—Input data for characterization of 4-color process printing*.
4. McDowell, D. (2004). Process control characterization data color management profiles. In *What, When, & How They Are Related*. NPES/Eastman Kodak Company.
5. Sharma, A., & Fleming, P. D. (2005). Measuring the quality of ICC profiles and color management software. *The Seybold Report*, 4(20), 10–16.
6. Has, M. (1995). FOGRA color management: Current practice and the adoption of a new standard. In *International Color Consortium*.
7. Janjomsuke, W. (2004, June). *Comparison of color gamut and amplitude responses between AM and FM screening*. School of Print Media, Rochester Institute of Technology.



# Research on the Soft Proofing Technology Based on Substrate-Corrected Colorimetric Aims

Jinghuan Ge<sup>(✉)</sup>, Enyin Fang, and Dongwen Tian

Department of Printing and Packaging Engineering,  
Shanghai Publishing and Printing College, Shanghai, China  
sytuprint@126.com

**Abstract.** With the rapid development of display technology and color control technology, as well as the printing industry's strong demand for cost reduction and efficiency, soft proofing will be used more and more in the printing production process. In the traditional soft proofing workflow, the standard ICC profiles of printers are generally used as the target of the display simulation. However, the delta E between the soft proofing and prints is always larger because of the whiteness difference between the actual printing paper and the standard paper. In this paper, the method of substrate-corrected colorimetric aims (SCCA) is used to revise the printing profile. Also, the parameters of the displays are set appropriately according to the experiments. Comparing the results between the prints and soft proofing, the effect of soft proofing is tested by objective evaluation and subjective evaluation. The experimental results show that the effect of soft proofing has been significantly improved by using SCCA method, especially in its accuracy and efficiency. It can also be the guidance in the actual printing process.

**Keywords:** Color management · Soft proofing · Color correction · Paper whiteness

## 1 Introduction

Soft proofing is the viewing on a display that a printed image will look like ahead of time, so that you can make changes or approve the image before it gets printed. This is an incredibly useful feature that most people like to do.

The key technology of soft proofing is based on accurate display calibration and color management of the whole system. Display calibration makes its effect in the best state on the basis of testing and adjusting. Color management is the controlled conversion between the color representations of various devices, such as digital cameras, displays, computer printers and offset presses. The primary goal of color management is to obtain a good match across different color devices [1]. The principle of soft proofing workflow is shown in Fig. 1.

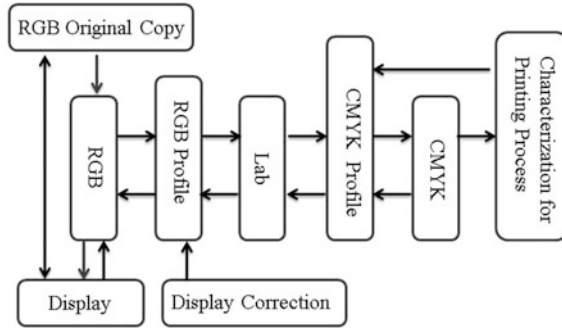


Fig. 1. The principle of soft proofing workflow

## 2 The Soft Proofing Process Based on SCCA

In order to save time and simplify the process, the standard printing profiles is usually used as the target of the display simulation in the traditional soft proofing workflow. In actual printing, the source of the paper is not fixed, and its performance parameters are often unstable. Especially the whiteness of the printed paper is different from the standard one, which will affect the effect of soft proofing to a certain extent. In order to improve the proofing accuracy, it is necessary to print test chart with the specific paper, and then generate the target profile for proofing by using the color data which is measured from the test targets printed in the standard condition. The process is extremely complex and inefficient. Based on the colorimetric data of the substrate, the color dataset in the target profile is corrected by the method of substrate-corrected colorimetric aims (SCCA), then the printing effect is predicted, the applicability of soft proofing is improved, and the process is greatly simplified [2]. The new process is

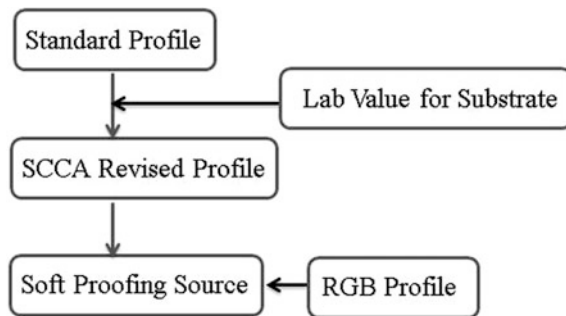


Fig. 2. The soft proofing process based on SCCA

shown in Fig. 2. The SCCA equation is shown as below.

$$x_2 = x_1(1 + C) - x_{\min}C \quad \left[ C = \frac{x_{w2} - x_{w1}}{x_{w1} - x_{\min}} \right]$$

where  $x_1$  and  $x_2$  are the tristimulus values of printed color on Substrate\_1 and Substrate\_2.  $x_{w1}$  and  $x_{w2}$  are the measured tristimulus values of Substrate\_1 and Substrate\_2.  $x_{\min}$  is the minimum (max TAC) tristimulus value of Substrate\_1.

Based on the above equation, substrate-corrected CIEXYZ can be calculated, and then can be converted back to CIELAB space. Finally a substrate-corrected dataset is created that can be used to build a SCCA revised profile.

### 3 Experiments

#### 3.1 Experimental Conditions

Display: EIZO Color Edge CG243 W,  
 Measuring instrument: Spectrophotometer X-Rite i1 Pro2,  
 Standard light source: GTI Viewing Booth MM-4e-CPT,  
 Digital proofing equipment: EPSON Stylus Pro 9908,  
 Software: Color Navigator, CGS ORIS Color Tuner, Profilemaker, Photoshop.

#### 3.2 Display Calibration and Characterization

This experiment uses Color Navigator to automatically calibrate and characterize the display. It is necessary to adjust the color temperature, gamma and brightness of the display in the process. ColorChecker chart is used for testing the accuracy of the soft proofing and then the most reasonable combination of the settings is determined. According to ISO standard, 5000 K is selected as color temperature. Also gammas and brightness levels are selected for testing. As the results shows, when the gamma is 1.8 and the brightness is 100 cd/m<sup>2</sup>, the average color difference for the 24 patches is the smallest between the display and ColorChecker. The profile generated in this state can be used as the source profile for this display.

The color uniformity of the display is also of great importance. In this experiment, the nine-point measurement method is used to detect it. The test results shows when the screen is grey, the maximum difference between the brightness around the display and that in the middle is 4%, which is lower than the standard requirement of 10% in ISO 12646 [3]. In addition, the stability test results of the display show that the average chromatic aberration is only 0.04 after turning on for 30 min. This also shows that the EIZO display performs pretty well and it can be put into practical application.

#### 3.3 Printer Profiles Making and Test Samples Printing

The main purpose of this step is to make the standard printing sample through the printer's correction, and to simulate the printing sample after the substrate replacement.

In this experiment, the printer's target profile is generated from the dataset "CGATS21-2-CRPC6". Then a standard output workflow for simulating the offset

printing is established after cyclic correction. The LAB value of proofing paper should close to (95, 1, -4).

For better evaluation, 46 color patches defined by “Fogra Media Wedge CMYK V2” were selected as objective evaluation indexes, as shown in Fig. 3. Also, the following 9 classical images were selected as test graphs for subjective evaluation [4], as shown in Fig. 4.



**Fig. 3.** The measurement strip for Fogra media wedge CMYK V2



**Fig. 4.** The 9 classical test images for subjective evaluation

Then the standard workflow is used to output the test samples for subjective and objective evaluation respectively. It is theoretically possible to determine that these test samples are ISO compliant prints if the printing conditions and materials conform to the standard. They are defined as the standard printing sample  $P_{St}$ .

After that, replacing the coated proofing paper and printing two kinds of the test images by the same output workflow. It is used to simulate the offset prints with the different paper; it can be regarded as the revised printing sample  $P_{Re}$ .

### 3.4 The Realization of Soft Proofing

Photoshop is selected for soft proofing in this experiment. It is very important to set the parameters properly for color management in Photoshop [5].

The experiment is divided into two steps. In the first step, the ICC profile generated by the dataset “CGATS21-2-CRPC6” is uploaded as the target profile in the CMYK workspace. The purpose of this step is to simulate a standard printed sample. In the second step, measuring the colorimetric values of the replaced paper; and then recalculating the color in the “CGATS21-2-CRPC6” dataset with the SCCA formula; finally, a revised profile generated by the new dataset “CGATS21-2-CRPC6-SCCA” is

obtained. After that, the revised profile is placed in Photoshop as the target profile for soft proofing. This proofing is mainly to simulate the prints with different substrate in printing workshop.

### 3.5 Experimental Evaluation and Analysis

Both subjective and objective evaluations are used for the soft proofing test [6, 7]. Twenty qualified observers who have passed the FM 100 Hue Test participate in the subjective evaluation. The objective evaluation is to calculate the chromatic aberration between the corresponding patches by measuring the 46 patches on the display and print sample respectively, also statistical analysis is necessary.

Firstly, we evaluate the first step of the experiment. For the objective evaluation, 46 color patches on the standard sample  $P_{St}$  and the revised sample  $P_{Re}$  are measured separately, and then these two sets of data are compared with the measured values of the color patches displayed on the screen without SCCA method, the chromatic aberration is calculated. The statistical results are shown in Table 1 (see the data in column 2 to 5).

**Table 1.** Color difference distribution of 46 colors in objective evaluation

Soft proofing $\Delta E$	ICC before revised				ICC after revised	
	Standard sample $P_{St}$		Revised sample $P_{Re}$		Revised sample $P_{Re}$	
	Number	Percentage	Number	Percentage	Number	Percentage
$\Delta E \leq 0.5$	1	2.17	0	0	0	0
$0.5 < \Delta E \leq 1.5$	18	39.13	4	8.70	11	23.91
$1.5 < \Delta E \leq 3$	15	32.61	11	23.91	20	43.48
$3 < \Delta E \leq 6$	9	19.57	16	34.78	10	21.74
$\Delta E > 6$	3	6.52	15	32.61	5	10.87
$\Delta E$ mean	1.97	/	5.94	/	2.81	/
Max $\Delta E$	10.29	/	17.83	/	13.65	/
Min $\Delta E$	0.48	/	1.39	/	0.78	/

For the subjective evaluation, The 9 classical images displayed in the screen without SCCA method are compared with the 9 printed images on the standard prints  $P_{St}$  and the revised prints  $P_{Re}$ , which are evaluated according to the similarity between the soft proofing effect and the actual printing effect, and are rated according to the criteria of Table 2. The results of the subjective evaluation are shown in Table 3 (see the data in row 2 to 3).

**Table 2.** Subjective evaluation scale

Rating	1	2	3	4	5
Level of similarity	Perfect	Similar	Acceptable	Tolerable	Unacceptable

**Table 3.** The result of the subjective evaluation

Image			1	2	3	4	5	6	7	8	9
Average value for rating	ICC before revised	P <sub>St</sub>	2.3	2.2	2.1	2.4	2.4	2.2	2.5	2.8	2.6
		P <sub>Re</sub>	3.5	3.3	3.2	3.3	3.4	3.6	3.8	4.1	3.9
	ICC after revised	P <sub>Re</sub>	2.7	2.5	2.4	2.3	2.2	2.6	2.9	3.0	2.9

According to Tables 1 and 3, standard prints P<sub>St</sub> can meet the requirements of soft proofing. Therefore, if the printing process is properly controlled; ink, paper and other consumables are also in line with the standard, the soft proofing effect can be guaranteed. However, the gap between revised prints P<sub>Re</sub> and soft proofing is large, indicating that the whiteness changing of the paper in printing will affect the proofing effect. In actual printing, the whiteness of the paper cannot be kept consistent.

Therefore, the soft proofing must be corrected according to the whiteness of the paper, that is, the second soft proofing step with SCCA method is adopted, and the modified soft proofing effect is evaluated. Similar to the first step, objective and subjective evaluations are conducted separately, but only for the revised printing sample P<sub>Re</sub>.

The new objective evaluation and subjective evaluation results are also shown in Table 1 (see the data in column 6 and 7) and Table 3 (see the data in row 4) respectively, and it can be seen that the results are greatly improved. The average color difference of the objective evaluation decreased from 5.94 to 2.81, which is dramatically improved; and the average values for rating of the subjective evaluation are between 2.2 to 3.0, which is obviously better than that before the correction. Although the rating values for the highlights and the other three overprints are slightly larger, the average rating values for the subjective ratings are all less than 3. It is between similar and acceptable, indicating that the SCCA-corrected soft proofing effect has been significantly improved.

## 4 Conclusions

In this paper, the color management process of soft proofing is deeply studied, the color matching effect of soft proofing is optimized, and the final optimization effect is objectively and subjectively evaluated. It is proved that the correction method based on SCCA has positive significance in optimizing soft proofing process, especially in predicting the color effect of unprinted products, which will obviously expand the application range of soft proofing. At the same time, it provides a solution for prepress designers to predict the printing effect.

**Acknowledgements.** This research is supported by Lab of Green Platemaking and Standardization for Flexographic Printing (No. ZBKT201701 and No. ZBKT201804).



## References

1. Liu, H. (2009). *Research and realization of soft proofing* (M.S. thesis). Tianjin University of Science & Technology, Tianjin, China.
2. Chung, R., & Tian, Q. (2011). *Substrate correction in ISO 12647-2*. Presented at the TAGA Conference, Pittsburgh, PA.
3. ISO 12646. (2008). *Graphic technology—Displays for color proofing—Characteristics and viewing conditions*. Available from <http://www.iso.org/>
4. Liu, J. (2010). Soft proofing and ISO 12646. *Printing Magazine*, 12(7), 40–42.
5. Yang, L., & Zhao, X. (2008). Method of soft proofing in photoshop. *Package Engineering*, 29(8), 86–88.
6. Zan, G., & Dai, J. (2013). Digital evaluation method of soft proofing and its realization. *Printing Quality & Standardization*, 12(3), 21–25.
7. Liu, H., Huang, M., et al. (2007). Color difference evaluation for printed images. *Journal of Beijing Institute of Graphic Communication*, 15(2), 1–4.



# Quantitative Analysis Method of Color Gamut Difference Between Digital Image Originals

Wenda Jin<sup>(✉)</sup>, Qiang Wang, and Jing Cao

School of Media and Design, Hangzhou Dianzi University,  
Hangzhou, Zhejiang, China  
xxwdd2816@163.com

**Abstract.** Digital imaging is an important means of making image originals in the field of media reproduction and dissemination today. The gamut of digital image original not only restricts the accuracy of color reproduction in the traditional hard copy, but also the quality of the hard copy would be affected directly. In order to scientifically and quantitatively analyze the digital image original gamut, this paper uses unsupervised clustering analysis method. Comparing various imaging environment factors affecting the digital image original gamut through the designed experiment, and some good applications for digital imaging and digital image original evaluation are obtained.

**Keywords:** Digital image original · Quantitative analysis · Clustering · CRF

## 1 Introduction

In the field of modern media reproduction, especially in the printing industry, digital platforms based on mobile Internet and various high-precision digital imaging devices are widely used. Color management and digital production processes are used to achieve high-quality spatial information reproduction and correction is now becoming the mainstream of industrial development. Although, scholars at home and abroad have carried out extensive research in the past 10 years. How to ensure the consistent transfer of color from spatial information to hardcopy, especially to quantitatively analyze and compare the color gamut of digital image originals [1], has become a research hotspot and difficulty in the field of color hardcopy reproduction in the establishment of digital image original evaluation of the standard data and evaluation parameters.

## 2 The Principle of Quantitative Analysis of Digital Original Color Gamut

In this document, the digital image original refers specifically to spatial information data obtained by a digital imaging device and used for color reproduction. Due to the imaging environment, imaging device and exposure restrict the presentation of digital image original color gamut directly, and the production of traditional digital image originals mainly adopts hands-on guidance methods and lacks the use of measuring

instruments and data standards [2], Bring many problems to follow-up hard copy production in terms of inconsistent color or different color gamut. Therefore, the evaluation of digital image originals using color quantitative parameters and methods [3] is becoming a research hotspot in the industry.

### 2.1 Color Gamut Quantitative Evaluation Parameters

In this paper, quantitative analysis is performed using colorimetric analysis. The main evaluation parameters are described as follows:

We use the  $a^*b^*$  coordinate system to analyze the difference in chromaticity between samples, in the color gamut evaluation of colorimetry. The main parameters are  $\Delta E_{ab}^*$ ,  $\Delta C^*$ ,  $\Delta L^*$ ,  $\Delta a^*$  and  $\Delta b^*$ , As shown in Fig. 1.

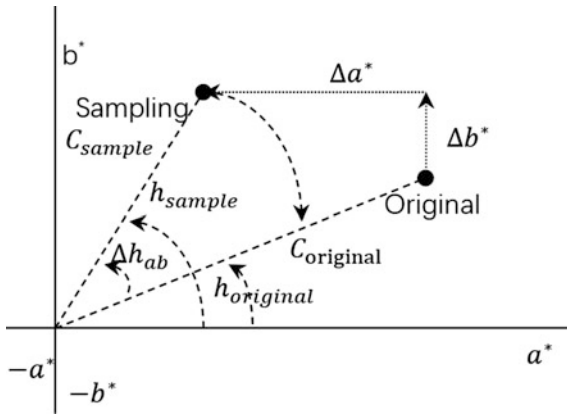


Fig. 1. Schematic diagram of color gamut evaluation parameters

$$\Delta E_{ab}^* = \sqrt{\Delta L^{*2} + \Delta a^{*2} + \Delta b^{*2}} \tag{1}$$

$$\Delta L^* = L_{sample} - L_{original} \tag{2}$$

$$\Delta h_{ab} = \arctan\left(\frac{b^*}{a^*}\right)_{sample} - \arctan\left(\frac{b^*}{a^*}\right)_{original} \tag{3}$$

$$\Delta a^* = a_{sample} - a_{original} \tag{4}$$

$$\Delta b^* = b_{sample} - b_{original} \tag{5}$$

Recent researches have shown that the current mainstream color gamut quantitative analysis methods are density analysis and chroma analysis. The density analysis method uses density as the standard for quantitatively describing the color gamut and quality of an image but has the disadvantage of low evaluation accuracy. The chroma

analysis method [4] uses the spectroscopic spectrum as the standard for quantitatively describing and evaluating the color gamut and quality of the image. The accurate expression of the color features become the main methods for color hard copy quantitative evaluation.

#### 1. Color difference statistics histogram

The color difference statistics histogram is a plane chart drawn after arranging the color difference between the original document and the copied sample. In the plane chart, the X axis represents the position coordinates of the sampling points, and the Y axis represents the color difference parameter values. The color-difference histogram can be used to determine what kind of color difference is needed, and can intuitively express the change of the color-difference parameter value of each sampling point, as shown in Fig. 4.

#### 2. Color distribution probability cumulative curve

The color difference distribution probability accumulation curve refers to the color difference parameter as the abscissa, the probability (percentage) of each color difference value is the ordinate, adding in order and accumulating to obtain each cumulative value (100% maximum), such as Fig. 6 shows. For example, using the color difference  $\Delta E$  as a statistical parameter, the number of sampling points of each color difference value is a numerator, the number of sampling points is a denominator, and the frequency of obtaining each color difference value is calculated, and then a corresponding curve is drawn by connecting each point.

In the quantitative analysis of the color gamut, both the planar histogram and the cumulative probability distribution curve of the color difference distribution can be used to more accurately and completely reflect the color gamut state and the copying result of the digital image original.

#### 3. Cluster analysis

Cluster analysis refers to the process of grouping collections of physical or abstract objects into multiple classes consisting of similar objects. As shown in Fig. 3, each pixel of the digital image original is sampled to obtain the RGB value of each sample. In the RGB color mode, the data set is divided into several clusters so that the similarity of the data points in the same cluster is as large as possible and finally the center point of the cluster is taken out as the characteristic color.

### 3 Experimental Design and Data Analysis

Based on the above theoretical analysis, this study designed an experimental test for quantitative analysis of digital image original gamut. Through the collection processing, analysis and verification of test data, satisfactory results were achieved that met the expected goals.

### 3.1 Experimental Conditions

This study selected Canon EOS 70D digital cameras to capture a set of digital image originals. Use the same aperture and different exposure times (1/4 s, 1/8 s, 1/10 s, 1/15 s, 1/20 s, 1/25 s, 1/30 s, 1/40 s, 1/50 s, 1/60 s, 1/80 s) and 4000 K in the T60 (4) TILO light source box for the objects.

And then three digital image originals with overexposure (1/4 s), normal exposure (1/25 s), and underexposure (1/50 s) were selected. In the experiment, adopt the CIM15BBF display and the sRGB IEC61966-2.1 profile.

### 3.2 Experiment Procedure

1. Use a well-designed program to perform color clustering analysis on the chromaticity values of digital image originals, extracting 7 areas with dense pixel points in the RGB color pattern as target sampling points [5], as shown in Figs. 2 and 3.

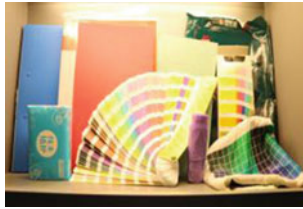


**Fig. 2.** Digital image originals

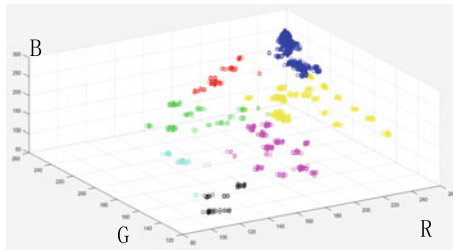


**Fig. 3.** Under exposure image original cluster distribution

2. Samples were taken from digital image originals of  $584 \times 270$  pixels and the k-means clustering was used to obtain RGB chroma scatter plots, as shown in Fig. 3.
3. Using the Lab value of the normal exposure photograph as the reference value, calculate the difference between the normal exposure and the underexposure photo of Lab, as well as the color difference. The same method is used for color difference between over-exposure and normal-exposure photographs.

4. According to the calculation results, in excel software, make the comparison charts required, analyze and compare the elements of interest and their details, as shown in Figs. 4, 5, 6 and 7.

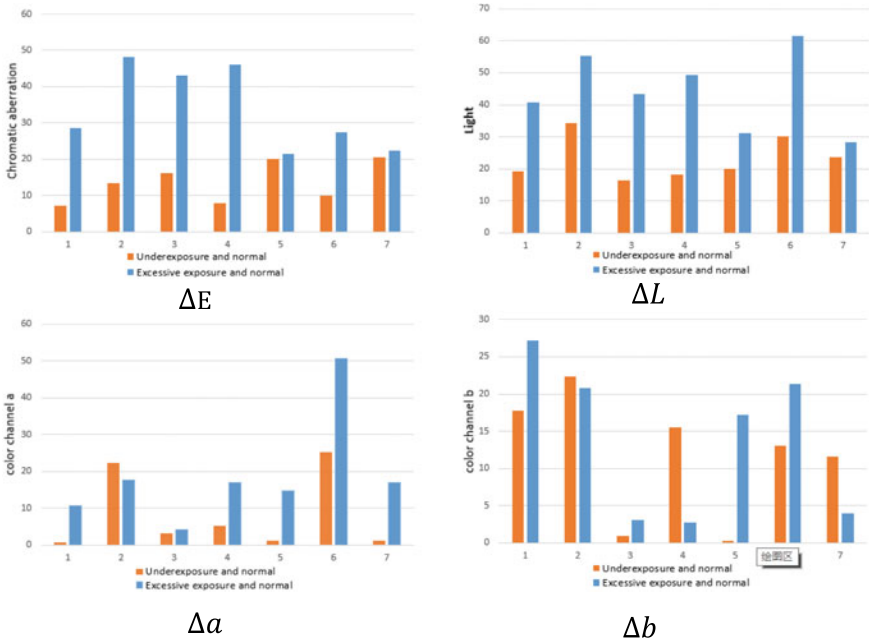


**Fig. 4.** Comparison of the primary color histogram for underexposed and exposed normal digital image originals and the histogram of the dominant color of the digital image original with overexposed and normal exposure

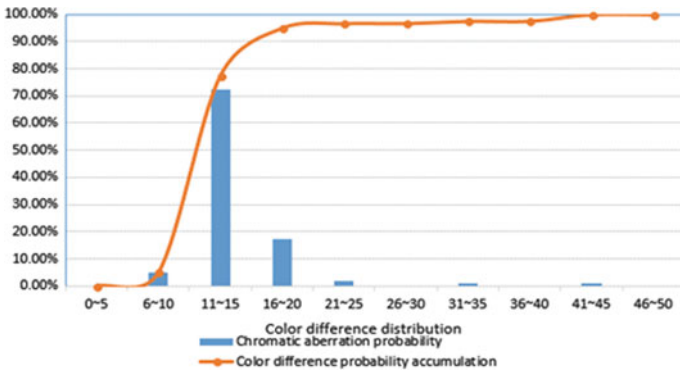


**Fig. 5.** Accumulated color difference distribution curve for underexposure and normal exposure digital image originals

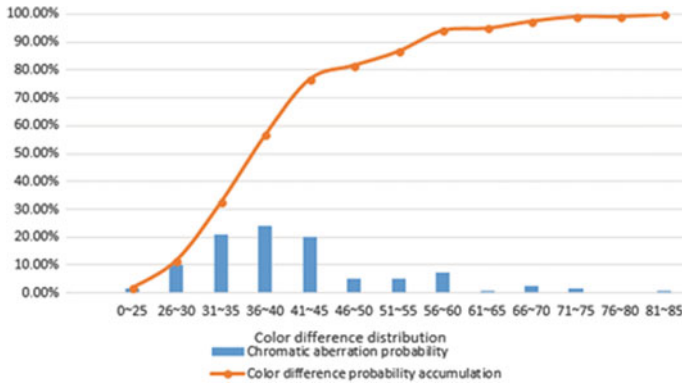


**Fig. 6.** Accumulated color difference distribution curve for exposure overexposure and normal exposure digital image original

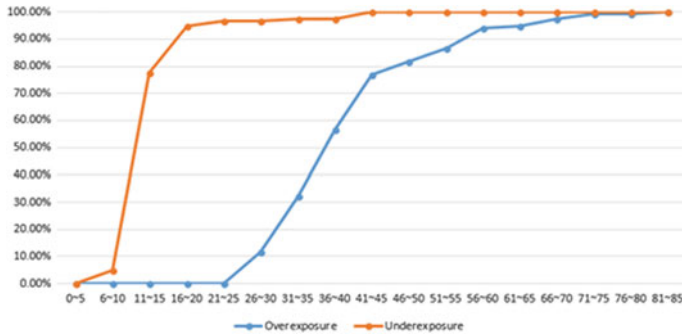


**Fig. 7.** Accumulated color difference distribution curve for exposure overexposed and underexposed digital image originals and normal exposure digital image original

The clustered digital image originals are mainly divided into 7 characteristic colors 1–7, corresponding to beige, brown, light blue, blue, brown, red, and green. From Fig. 4, it can be seen that the colors of brown and red are quite different.

Next, the digital image original of  $584 \times 270$  pixels is pixilated to form a picture composed of  $8 \times 15$  pixel squares as the sampling point. The difference between the normal exposure photograph and the underexposed photograph and the overexposure photograph of chromatic aberration is calculated.

Figure 5 shows the combined graph of the chromatic aberration distribution probability cumulative curve and the color-difference column type of the underexposure and exposure-normal digital image originals, wherein the abscissa indicates the color difference value, and the ordinate indicates the proportion of the sample points under the color difference value. The histogram shows the frequencies of the sample points contained in each color difference range. The graph is accumulated by the frequency of the histogram, which can intuitively reflect the color gamut state and copy

results of the digital image original. As can be seen from Fig. 5, in case of under exposure, the sample with a color difference of about 11–15 accounts for a large proportion. Figure 6 shows that the sample mainly concentrates on a color difference of 26–50 when the exposure is excessive.

Comparing the cumulative distribution curves of the chromatic aberration distributions of the two sets of digital image originals, it is found that the increasing trend of the two sets curves is similar, which proved that the influence of overexposure or underexposure on the color gamut is basically the same.

### 3.3 Data Analysis and Comparison

In this study, quantitative analysis of digital image originals was carried out from two aspects of cluster color comparison and data analysis. It is easy to find that in the comparison of cluster color, underexposure and exposure of normal digital image originals clustered scatter plots on the red items and blue. The color of the item is quite different. Overexposed and properly exposed digital image originals have a large difference between the colors of yellow and red on the cluster scatterplot. From the data analysis, it can be found that the overexposure or lack of exposure has basically the same effect on the color gamut, but the influence on red and green is obvious, especially the effect of brightness on chromatic aberration is greater.

## 4 Conclusions

This paper uses a combination of density and color analysis to analyze and filter out the control and evaluation parameters of the digital image original and its reproduction process comprehensively. And through the designed samples and experiments, the influence of spatial position, lighting conditions and shooting parameters of digital image originals on digital image originals and their control parameters was verified. It provides an effective solution to the problem of color consistency between image originals and digital samples and has a good guiding role and practical value for the digital collection of color images.

**Acknowledgements.** This work is funded by National Key Technology Research and Development Program of the Ministry of Science and Technology of China (2012BAH91F03) and Hangzhou Dianzi University Graduate Innovative Research Fund (CXJJ2018017) and Digital Imaging Theory- GK188800299016-054.

## References

1. Yin, Z., Yongwen, J., & Maohai, L. (2017). A new device color gamut boundary description algorithm based on irregular segmentation. *Color Research & Application*, 42(2).
2. Masaoka, K. (2016). Analysis of standard chromaticity gamut area metrics. *Journal of the Society for Information Display*, 24(12).
3. Jiang, Y. W., & Lin, M. H. (2015). Evaluation of device color gamut description algorithms. *Applied Mechanics and Materials*, 3784(731).



4. Liñero, O., Ciudad, M., Arana, G., Nguyen, C., & De Diego, A. (2017). The use of a standard digital camera as an inexpensive, portable, fast and non-destructive analytical tool to measure colour: Estimation of the ripening stage of tomatoes (*Solanum lycopersicum*) as a case study. *Microchemical Journal*, 134.
5. Yu, J., Liu, F., Wang, Z., & Chu, M. (2014). Camouflage primary color extraction method based on spectral color. *Ordnance Automation*, 33(01).



# Analysis on the Basic Color Database of Shaanxi Fengxiang Woodcut New Year Pictures

Jie Du and Wanyi Mu<sup>(✉)</sup>

School of Art and Design, Xi'an University of Technology,  
Xi An, Shaanxi, China  
919468867@qq.com

**Abstract.** Shaanxi Fengxiang woodcut New Year picture is China's intangible cultural heritage. In order to better inherit and carry forward it, it is necessary to restore and retain the New Year painting in digitized form. Therefore, the method of color collection of the New Year pictures is used, and the color differences of the collected data are compared by using the CIE1976 color difference formula. After analyzing the data, the unique color card and color threshold range of the New Year pictures are obtained, and the color database of Fengxiang woodcut New Year pictures is built to incorporate the data results. The establishment of the color database of Fengxiang woodcut New Year pictures quantifies and digitizes the color of the New Year pictures, providing reliable and detailed data files for subsequent experts and scholars.

**Keywords:** Fengxiang woodcut new year pictures · Color collection · Munsell · Color database

## 1 Introduction

Shaanxi Fengxiang woodcut New Year picture has strong local characteristics and unique artistic style characteristics [1]. They are the true expression of folk art forms. The colors of the New Year paintings are mainly red, green, yellow and purple. The color purity is high with the cross use of color blocks. Because the beauty of vulgar and bold contrast intensely, and it is eye-catching, it is quite aesthetic [2, 3]. This unique color program is a complete, customary, color specification system formed by the local folk artists for many years of oral teaching and inheritance.

However, with the passage of time, the color of Shaanxi Fengxiang woodcut New Year painting will fade to a state that is difficult to repair. It is a typical representative of Shaanxi Guanzhong folk culture, so the study, conservation and reusing is of great necessity. This paper establishes the data repository for color of Fengxiang Woodcut New Year, objectively records and retains the information of Fengxiang woodcut New Year's picture, and realizes the protection and sharing of color resources, which is of great significance to the inheritance and restoration of Fengxiang woodcut New Year pictures [4, 5].

Based on the previous research results of art characteristics and cultural connotation of Fengxiang Woodcut New Year, this paper conducts deeper investigation and research, scientifically collects the original color of Fengxiang woodcut New Year picture, and measures the Munsell color card  $L^*a^*b^*$  by spectrophotometer to compare it with the collected  $L^*a^*b^*$  chromatic value of Fengxiang woodcut New Year sample to build the unique color card and color threshold data for the Fengxiang woodcut New Year color. On this basis, the color data of Fengxiang woodcut New Year picture is organized and scientific and objective color database is established.

## 2 Color Collections

The color collection of the Fengxiang woodcut New Year picture is related to the spectral characteristics of the New Year sample itself, as well as the lighting conditions, observation conditions and the visual characteristics of the observer. Therefore, it is necessary to ensure the same observation conditions such as the surrounding environment, background, sample surface characteristics and lighting conditions at the time of collection.

### 2.1 Acquisition Equipment and Conditions

This paper collects the color of Fengxiang woodcut New Year's painting by X-Rite, a color measuring instrument, and scans it into an electronic document under the condition that the Fengxiang woodcut New Year's picture is not damaged. Then the author modulates the X-Rite color photometer to the natural light with the  $2^\circ$  of viewing angle without a filter (M0, D50,  $2^\circ$ ), and the  $L^*a^*b^*$  chromatic value of the desired color can be obtained to ensure that each collection is in the same state as above.

### 2.2 Acquisition Process

This paper selects 12 samples of Chinese New Year pictures from the six subject categories of Fengxiang woodcut New Year picture for color collection research (Fig. 1). Each color in a New Year picture is collected five times, and the average value of the  $L^*a^*b^*$  chrominance of the five colors is obtained. Thereby the  $L^*a^*b^*$  value corresponding to each color accurately can be obtained. In the collection process, there are 9 colors in the 12 samples of New Year pictures: red, green, blue-green, grass green, yellow, orange, pink, purple and black, and there are at least 3–7 colors in each New Year pictures, so a total of 59 color samples are obtained. For example, there are four colors in sample 1, which are named ①-1 for red, ①-2 for green, ①-3 for yellow and ①-4 for black, and so on (Fig. 2).

### 2.3 Comparison with Munsell Color System

First, the author uses the spectrophotometer to collect the  $L^*a^*b^*$  chromatic value of the Munsell color card (standard color), then compare it with the  $L^*a^*b^*$  chromaticity value data of the Fengxiang woodcut New Year picture sample collected in "Table 1",



Fig. 1. 12 collection samples of Fengxiang woodcut New year pictures

Name	Color Block	L	a	b	Name	Color Block	L	a	b
①-1	Red	45.11	59.95	28.49	⑦-3	Pink	51.58	62.44	-13.77
①-2	Teal	38.91	-33.90	-18.09	⑦-4	Teal	59.35	-27.30	-17.62
①-3	Yellow	85.90	-7.38	68.47	⑦-5	Purple	31.63	31.52	-37.16
①-4	Grey	46.21	0.64	2.96	⑧-1	Red	51.23	49.49	23.00
②-1	Red	44.17	58.18	27.51	⑧-2	Green	58.80	-38.61	22.43
②-2	Teal	31.10	-20.48	-14.61	⑧-3	Yellow	86.03	-8.33	62.73
②-3	Yellow	85.03	-6.38	76.26	⑧-4	Pink	53.34	59.14	-22.08
②-4	Grey	45.76	-0.46	8.58	⑧-5	Teal	62.06	-29.87	-12.37
③-1	Red	44.57	58.19	34.82	⑧-6	Purple	28.33	31.64	-37
③-2	Green	63.59	-19.92	20.43	⑨-1	Red	49.89	50.91	22.20
③-3	Yellow	78.02	3.21	72.38	⑨-2	Green	39.11	-34.76	-16.14
③-4	Red	50.26	59.53	-20.47	⑨-3	Yellow	85.43	-10.30	63.67
③-5	Grey	47.62	0.19	2.48	⑨-4	Pink	55.76	50.23	-19.36
③-6	Orange	61.97	41.79	47.53	⑨-5	Teal	45.86	0.55	2.64
④-1	Red	44.57	58.19	34.52	⑨-6	Purple	71.59	30.79	54.25
④-2	Green	70.76	-17.40	13.46	⑩-1	Red	41.23	55.65	32.17
④-3	Yellow	81.72	0.01	68.26	⑩-2	Teal	45.03	-36.86	-17.24
④-4	Pink	51.29	60.19	-18.63	⑩-3	Yellow	85.40	-9.2	62.88
④-5	Grey	49.00	0.48	3.06	⑩-4	Pink	61.09	49.16	-16.04
④-6	Orange	65.24	41.59	47.30	⑩-5	Grey	52.88	0.77	3.08
⑤-1	Red	50.27	55.58	24.00	⑩-6	Orange	54.94	40.29	34.37
⑤-2	Teal	61.67	-22.37	-6.63	⑪-1	Red	48.67	52.46	13.52
⑤-3	Yellow	85.80	-5.48	36.41	⑪-2	Teal	68.47	-20.15	0.24
⑥-1	Red	48.51	57.97	30.64	⑪-3	Yellow	84.22	-5.23	63.67
⑥-2	Teal	51.86	-24.57	-4.94	⑪-4	Pink	51.69	62.61	-19.20
⑥-3	Light Yellow	84.30	-3.21	20.81	⑪-5	Grey	45.38	0.34	2.31
⑥-4	Grey	27.42	0.49	3.97	⑫-1	Red	66.56	-18.52	1.72
⑦-1	Green	54.70	-37.28	30.52	⑫-2	Teal	86.30	-5.52	45.48
⑦-2	Dark Green	86.48	-6.90	81.26	⑫-3	Yellow	59.45	51.22	-16.10
					⑫-4	Pink	58.46	0.36	3.76

Fig. 2. The lab values of all samples after the five mean

and then use the CIE1976 color difference formula  $\Delta E = \sqrt{(L_1 - L_2)^2 + (a_1 - a_2)^2 + (b_1 - b_2)^2}$  [6] to collect the data to put it into the color difference formula. "Figure 3" is the color difference calculation flow chart.

Then the author randomly selected a number of sample colors collected from the New Year pictures, and interviewed the craftsmen of Fengxiang woodcut New Year

**Table 1.** Nine colors of Fengxiang woodblock New Year pictures

Color phase	Red	Green	Blue and green
Color number	5R4/12	7.5BG6/4	10BG6/6
Color phase	Grass green	Yellow	Orange
Color number	5BG7/4	10Y8.5/10	5YR7/10
Color phase	Peach red	Purple	Black
Color number	2.5RP6/12	2.5P3/10	N4.5

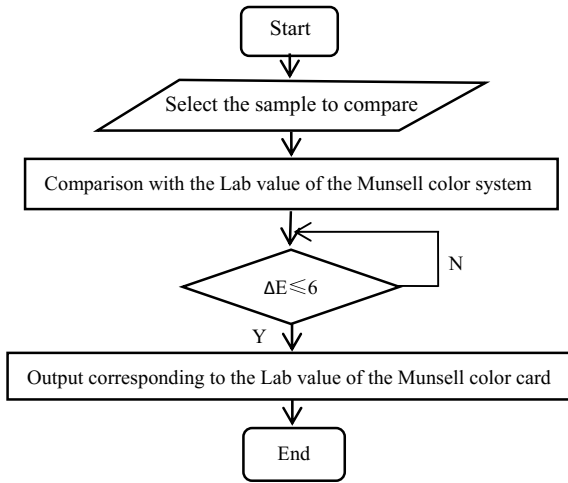


**Fig. 3.** Flow chart of chromatic aberration

pictures. Within the same field range, the craftsmen of Fengxiang woodcut New Year pictures recognized the color that best matched the color of the New Year pictures, and then made the color difference comparing. It is found that when the color difference  $\Delta E \leq 6$ , the color of the sample collected at this time is closest to the color of the New Year pictures, then all the sample colors of  $\Delta E \leq 6$  can be objectively considered as the color satisfying the condition. The color difference between the sample color and the Munsell standard color is compared, the color with the smallest color difference value in the color difference  $\Delta E \leq 6$  color us selected (Fig. 4), and the color with the smallest color difference value in the data of the color difference  $\Delta E \leq 6$  is found. The corresponding color is a proprietary standard color card for nine colors in Fengxiang woodcut New Year pictures (Table 1).

### 2.4 Color Threshold Analysis

After analyzing the 12 samples in “Fig. 4”, which are divided into nine colors, percentage of each color in a hue region can be obtained (Fig. 5).

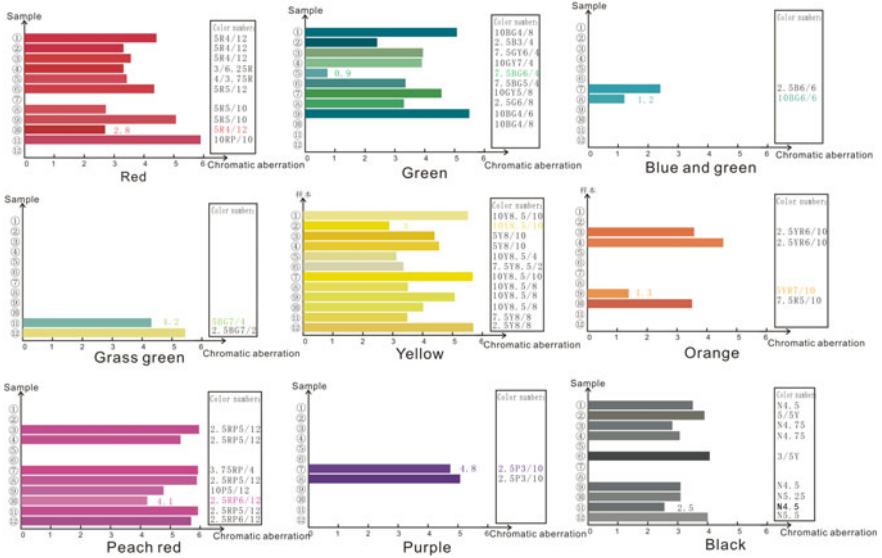


Fig. 4. Munsell color cards corresponding to Fengxiang woodcut New year pictures

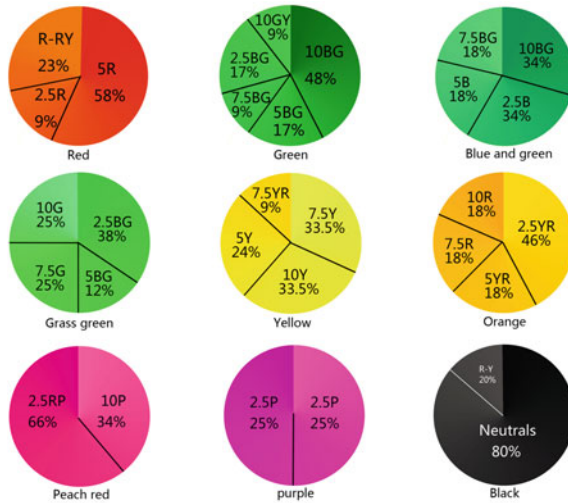


Fig. 5. The nine color threshold frequency maps of the Fengxiang woodcut New Year pictures

From the analysis of “Fig. 5”, it can be found that the highest color threshold of the nine colors of the Fengxiang woodcut New Year picture sample appear in the color card of the Munsell color system is: the red has the highest frequency within the 5R color threshold of the Munsell color card, and the green color is within the 10BG color

threshold, yellow is within the 7.5Y and 10Y color thresholds, blue-green is within the 2.5B color threshold, grass green is within the 2.5BG color threshold, orange is within the 2.5YR color threshold, pink is within the 2.5RP color threshold, purple is within the 2.5P color threshold and black is within the Munsell color card Neutrals color threshold. And the color difference in the color threshold with the highest frequency of occurrence of the nine colors is  $\Delta E \leq 6$ , which is difficult for the human eye to recognize the difference in color, so the color within the color threshold can be determined as the color threshold range of Fengxiang woodcut New Year pictures in the sample of text.

### 3 Establishment of Color Database

As an electronic medium, the database plays a considerable role in the recording and dissemination of intangible cultural heritage. In this paper, the  $L^*a^*b^*$  chromatic value of Munsell color card is collected by spectrophotometer to convert the color of Fengxiang woodcut New Year picture into accurate numerical value and then it is quantified. Then this paper accurately stores data and establishes color database of Fengxiang woodcut New Year pictures. In the color database, the relevant data information of the unique color card in the sample of the New Year pictures and the color threshold of all the colors can be retrieved. The system is based on the Windows 7 operating system platform, using My SQL database, and relying on the Java EE technology system, and uses the mainstream MVC pattern to design and develop the Web application system. The application server is Apache Tomcat 7.0, and the integrated development tool is My Eclipse 8.0.

Fengxiang Woodcut New Year Color Database provides digital protection from multiple angles and all dimension. It is a macroscopic, comprehensive, stereoscopic, and multi-angle information record, as well as microscopic, in-depth classification and more detailed classification and protection of color folk resources. The function module of the color database mainly includes a homepage exclusive color card module, a theme color information module and a color threshold information module.

- 1 The collection of the unique color card information of Fengxiang woodcut New Year picture color database has changed the visual classification method based on perceptual cognition in the past, and accurately visualized and digitized the painting characteristics of Fengxiang woodcut New Year picture, which recorded the exclusive color card belonging to Fengxiang woodcut New Year picture (Fig. 6).
- 2 The theme color module of the database collects the colors in each piece in a single piece. A single Fengxiang woodcut New Year picture contains at least 3 to 7 colors. After color collection, the  $L^*a^*b^*$  chromatic value corresponding to a single New Year picture is obtained, so that the color data is digitalized, and each New Year picture color of Fengxiang woodcut New Year picture can be stored. Fengxiang woodcut New Year pictures all use a single color for offset printing. The same type of color has a difference in hue in each New Year picture, so the original color information of each Fengxiang woodcut New Year picture is recorded in detail. This module also has a color matching information function, which consists of a

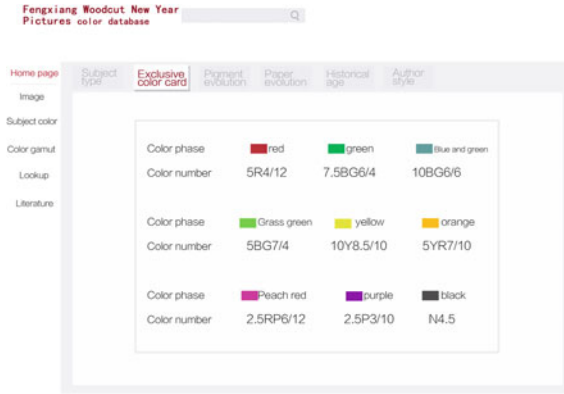


Fig. 6. Special color card module in the home page of Fengxiang woodcut New year pictures

color matching picture and color matching text information. The picture information is used to display the color matching block of New Year picture. The text information is used for the description of the digital color, including the number of times of color registering during printing and the main color RGB value and the Lab value, the RGB value of the secondary color, and the Lab value, where the number of secondary colors can be displayed according to the specific color registration in the color matching of the pattern (Fig. 7).

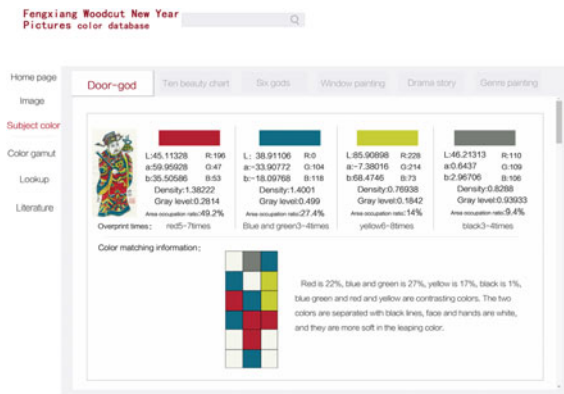


Fig. 7. Color information module of Fengxiang woodcut year pictures

3. The color threshold function module of the color database of Fengxiang woodcut New Year picture is to sort out the color threshold range of the nine New Year picture colors obtained above, and to realize the search and threshold reference of the color of Fengxiang woodcut New Year picture. The color threshold data is introduced into the color database of Fengxiang woodcut New Year picture, which



can protect the color status of the existing New Year pictures at the utmost, and ensure the integrity and latitude of the collected color data information in time, so that the system can accurately retrieve the color information of the New Year pictures. This played a key role in promoting the continuation and retention of Fengxiang woodcut New Year picture (Fig. 8). Taking the yellow color in the Fengxiang woodcut New Year painting as an example, the yellow color is distributed within the color thresholds of 10Y, 7.5Y, 5Y, and 7.5YR, respectively, and the frequency is highest within the 10 and 7.5Y color thresholds.

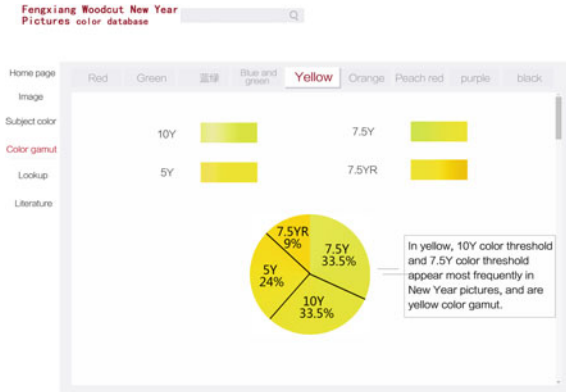


Fig. 8. Color and color threshold information module of Fengxiang woodcut Year pictures

#### 4 Summaries

This paper uses the color card of Munsell color system to represent the color of Fengxiang woodcut New Year picture by objective data, and enter the information of New Year pictures into the digital information platform with the function of displaying, color data, query and retrieval through the establishment of color database. The data information such as the color selection of each New Year picture is classified in the library, and the color of the New Year picture can be more intuitively understood.

We introduced the color data into the field of color protection of Fengxiang woodcut New Year picture, collected the color data information in time, and quantified the parameter information of the database, which can accurately reflect the true characteristics of Fengxiang woodcut New Year picture and the color law relationship. It has important theoretical and practical significance for protecting and spreading the color of Fengxiang woodcut New Year picture and stimulating its development vitality in the new period. It not only provides reliable and comprehensive color information for scholars who study Fengxiang woodcut New Year picture, but also builds a detailed and three-dimensional archive for Fengxiang woodcut New Year picture.

**Acknowledgements.** Project Fund: Humanities and Social Sciences Project of Shaanxi Provincial Education Department (17JK0527); General Project of Humanities and Social Sciences of the Ministry of Education (17YJC760007).

## References

1. Fang, L. (2015). Research on the artistic characteristics of Fengxiang woodcut New year pictures. *Stage*, 1–2.
2. Zhu, J. (2011). Color analysis of Fengxiang woodcut New Year pictures. *Fine Arts Education Research*, 32–43.
3. Chen, P. The artistic characteristics of Baoji Fengxiang woodcut New Year pictures. *Mass Art (Folk Custom)*.
4. Zhang, S. (2006). Folk custom and humanistic spirit of Chinese traditional woodcut New Year pictures. *Shandong Social Sciences*, 53–58.
5. Xue Feng (2015). Analysis of the current situation and protection of contemporary Chinese wood plank New Year pictures. *stage*, 99–100.
6. Zheng, Y. L., Zhou, S. S. (2013, March). *Printing color science [M]*. Culture Development Press.



# Analysis of the Color of Qin Qiong and Jing De Door-God Picture of Taohuawu and Fengxiang

Jie Du and Yawen Wang<sup>(✉)</sup>

School of Art & Design, Xi'an University of Technology, Xi'an, Shaanxi, China  
349831949@qq.com

**Abstract.** The military door-god Qin Qiong and Jing De in the representative Suzhou Taohuawu woodcut New Year pictures in the south and the Shaanxi Fengxiang woodcut New Year pictures in the northwest are selected as the research objects. The color of door-god pictures and its area ratio can be obtained through the color picking tools in Photoshop and MatLab color clustering method. Through the color results obtained, the color application and color matching of the door-god pictures in the two places are compared and analyzed. Finally, the color matching characteristics of Taohuawu and Fengxiang door-god woodblock New Year pictures are summarized.

**Keywords:** Taohuawu · Fengxiang · Qin Qiong and Jing De · Door-God pictures · Color

## 1 Introduction

The door-god picture is the earliest and most important category in Chinese woodcut New Year pictures, and it occupies a very important position in the folk woodcut art of China. People think that gods exist in everything related to daily life, and the door is guarded by the door-gods, which can make the house peaceful [1]. The door-god New Year picture was born in Yuan and Ming Dynasties, the custom of taking Qin Qiong and Jing De as the door-gods has been formed [2]. With the improvement of people's cognitive level, the function of the door-god pictures has been gradually changed from the original driving evils and gradually enriched to be the exorcism and blessing, which also satisfied the decoration of the door. The color in the door-god picture reflects the creation idea and emotional orientation of the local folk artists and the elegant aesthetic taste and rich cultural connotation of the Chinese nation.

Contrast effect and its classification is an appropriate starting point for studying color aesthetics [3]. In order to clarify the color characteristics of the door paintings, this paper selects the general door-gods "Qin Qiong" and "Jing De" in Taohuawu and Shaanxi Fengxiang woodcut New Year picture as the research objects for comparative analysis. The works and artistic styles of door-god pictures of Qin Qiong and Jing De are relatively mature, of which the colors include oriental color concepts and folk custom [4]. In this paper, color picking tool in Photoshop is used to extract the colors of door-god picture of Qin Qiong and Jing De and MatLab color clustering method is used to obtain the colors in the door-god pictures. Then the area ratio of the colors is calculated. The color matching is analyzed and the colors area that occupies the top two

colors is selected. Analysis is made based on the Eden twelve-color hue circle and the contrast of light and dark, and contrast between cold and warm. Using modern color theory and methods, we study the color characteristics from different angles, and more accurately grasp the coloring rules in color configuration, which is very important for the research system of the door-god New Year pictures and its inheritance and protection.

## 2 Analysis of the Color of Qin Qiong and Jing De Door-God Pictures

### 2.1 The Analysis of the Color of Qin Qiong and Jing De Door-God Pictures of Taohuawu

Through the MatLab clustering method, three pairs of Taohuawu door-god pictures of Qin Qiong and Jing De were processed, and sorted according to the color area. The color spectrum was extracted, and the following three figures were obtained.

The color of first pair of Qin Qiong and Jing De door-god picture in Fig. 1 is mainly purple and red, with a yellow face and red embellishment. Qin Qiong's costumes are mainly red, supplemented by purple, while the color of Jing De's costumes is the opposite. The five dots under the two gods are red with pink, and purple with dark green, with yellow embellishment. Highly saturated color matching is warm and vivid.



**Fig. 1.** Taohuawu Qin Qiong and Jing De clustering diagram and chromatography

The color of second pair of Qin Qiong and Jing De door-god picture in Fig. 1 is pink, which run through the entire picture. The colors of Qin Qiong's costumes are mainly composed of red and peach, while that of Jing De's costumes is mainly composed of purple and peach. Then details are decorated with dark green and yellow. Due to the high color purity of this pair of door-god pictures, in addition to the beard and the ink line draft, black appears at the edge of the character costume, thereby weakening the bouncy feeling of the picture.

The color of third pair of Qin Qiong and Jing De door-god picture in Fig. 1 that Qin Qiong is mainly red with dark green, and the details are presented with pink, purple and

yellow. The color of Jing De is mainly composed of purple and yellow, and the details are presented with red, pink and dark green. The color of costumes of these two military door-gods are full and warm, with obvious warm colors of pink, purple, and red, and there is the cold color dark green blending in it, making the picture calm and pretty.

Qin Qiong and Jing De door-god pictures of Taohuawu are neat rather than trivial, and the color blocks in character’s costumes are elegant and cheerful. The color is elegant, with the colors such as red, pink, purple and light ink interlacing. It is both elegant and distinctive, with national characteristics and gentleness, and is full of decorative beauty and rhythm, showing a distinct local flavor.

### 2.2 Analysis of the Color of Qin Qiong and Jing De Door-God Picture of Feng Xiang

The color of first pair of Qin Qiong and Jing De door-god picture in Fig. 2, the headwear of the two gods are yellow and orange, embellished with dark green and orange. Qin Qiong’s costumes are mainly red with yellow, and the details of the armor are decorated with purple. Jing De’s costumes are mainly purple with yellow and red. The color of the door-god painting is gorgeous, with more details and overall color matching is integrated.



Fig. 2. Fengxiang Qin Qiong and Jing De clustering diagram and chromatography

The color of second pair of Qin Qiong and Jing De door-god picture in Fig. 2, the characters are surrounded by a circle of yellow tiger hair and tiger stripes with red and black crossing. Qin Qiong’s accessories are painted with yellow, red and dark green. The official clothes are mainly orange and embellished with dark green. Jing De’s accessories are painted with purple, yellow, red and dark green. The official clothes are mainly purple, with red as embellishment.

The color of third pair of Qin Qiong and Jing De door-god picture in Fig. 2, the overall skeleton of Qin Qiong is outlined with dark green and red lines, with a large area of yellow as the main color. Jing De’s costumes are mainly purple and yellow,

supplemented by red and black. The horses are mainly red and embellished with black patterns. This pair of door-god pictures uses a large area of primary colors, with bright and beautiful tone.

Qin Qiong and Jing De door-god pictures of Fengxiang use simple color, and tend to paint on a large area with a single color. It uses the red and yellow in large color blocks, with dark green in small area to make the New Year pictures appear bright color and strong contrast effect. With cheerful and lively visual impact, it is very decorative. It also fully reflects the pleasant folk atmosphere of the New Year pictures, and strengthens its agrestic flavor.

### 3 Comparative Analysis Based on the Modern Color Theory

#### 3.1 The Main Color Extraction and Analysis of Qin Qiong and Jing De Door-God Pictures of Taohuawu

By comparing the main color samples of Taohuawu Qin Qiong door-god pictures, it is found that the three pictures all use red; comparing the main color samples of Jing Demen door-god pictures, the three all use purple. It can be said that in the Qin Qiong and Jing De door-god pictures of Taohuawu, red is the specific color of Qin Qiong while purple is the specific color of Jing De. Qin Qiong and Jing De door-god pictures pay attention to the unique symbolism of each character’s color, use fixed colors matching to design characters. The same character’s color has the same attributes and the color matching is stylized (Table 1).

**Table 1.** Principal Colors of Qin Qiong and Jing De Door-god Pictures

		Qin Qiong	Jing De
Figure 1	I	Purple—red	red—purple
Figure 1	II	red—peach	peach—purple
Figure 1	III	red—green	purple—yellow
Figure 2	I	yellow—green	yellow—purple
Figure 2	II	yellow—green	yellow—green
Figure 2	III	yellow—red	red—purple

By comparing the main color samples of Feng Xiang Qin Qiong door-god picture, it is found that Qin Qiong door-god pictures all use yellow, and the color matching is basically the same. For the sample of Jing De, the main color of most Jing De door-god pictures is purple. Feng Xiang Qin Qiong and Jing De door-god pictures pay attention to the interrelationship between the color matching of the two characters in a pair of door-god pictures. There is same color in both pictures and the color matching has an intrinsic relevance.

The color matching of Qin Qiong and Jing De door-god pictures is mainly based on primary colors, supplemented by secondary color, without complex color and gray.

The color contrast is strong, conspicuous, and the contrast is obvious, reflecting the strong and masculine spirit of folk color, with very strong decoration effects and pure folk art features.

### 3.2 Color Contrast

Contrast between light and shade: Qin Qiong and Jing De door-god pictures of Taohuawu and Fengxiang have higher color brightness, and the contrast between light and shade is weaker. The overall feeling will be more lively and gorgeous.

Contrast between cold and warm: The door-god pictures of the two places are dominated by a large area of adjacent color to form a warm tone. Taohuawu tends to use two warm colors of the same hue, such as red and peach. Fengxiang tends to use two warm colors that differ in hue, such as yellow and dark green. Therefore, Qin Qiong and Jing De door-god pictures of Taohuawu are warm and vivid, while the color of Fengxiang Qin Qiong and Jing De door-god pictures contrast strongly.

## 4 The Influence of the Cultural Background of the Two Places on the Color of Qin Qiong and Jing De Door-God Pictures

### 4.1 Differences in Artistic and Cultural Background

The visual features presented by the color scheme of the two places show rich and strong regional styles. The artistic style of Suzhou Taohuawu woodcut New Year pictures inherited the essence of the traditional culture of the Southern Song Dynasty, integrated the delicate and fine culture of Jiangnan culture. The color of the door-god pictures has the beauty and elegance of Jiangnan, which is light and lively with rich layers. Fengxiang is located in the central Shaanxi plain, and it retains the artistic techniques of murals, stone carvings and social fires in the Han and Tang Dynasties. The bold and unrestrained folk style gives Fengxiang woodcut New Year pictures a warm, unrestrained color, with simple and bright colors, strong contrast and expressiveness.

### 4.2 Differences in the Materials

The earliest Taohuawu and Fengxiang woodcut New Year picture use traditional hand-boiled water-based botanical pigments and stone mineral pigments. Over time, the color of this pigment will become more stable. Beginning in the Qianlong period, the Taohuawu woodcut New Year pictures used the paints produced by “Suzhou Jiangsixu”, which have been used until now [5]. The color does not fade for a long time, and the color saturation is not high, so the color is light with rich layer. Fengxiang woodcut New Year pictures are made from “Mali” pigment for Chinese painting, water and bone glue. The papers currently used for New Year pictures of the two places are all Xuan papers of Jiang County, Anhui Province, which are tough enough and can't be easily damaged. The printed New Year pictures are bright and long-lasting.

## 5 Conclusions

Through the use of MatLab color clustering method, this paper analyzes the color of Taohuawu and Fengxiang Qin Qiong and Jing De door-god pictures, and gets a new understanding of the color of the Southern and Northern Woodcut New Year paintings from another angle, which provides a certain reference for deeper understanding of the color of the woodcut New Year pictures in the future and has certain value for a comprehensive understanding of the color characteristics of woodcut pictures in different regions.

**Acknowledgements.** This study is funded by a Humanities and Social Sciences Project of Shaanxi Provincial Education Department (17JK0527). This work is also supported by the General Project of Humanities and Social Sciences of the Ministry of Education (17YJC760007).

## References

1. Zhong, X. (2005). Origin classification and characteristics of folk door-god new year pictures. *Journal of Shaoyang University*, 4, 33–34.
2. Wu, W., Shan, H. (2007). Qin Shubao, Yuchi Gong—The exploration of the military door-god paintings. *Furniture and Interior Decoration*, 3, 64–67.
3. Johannes, E. (1999). *Color art*, Du Dingyu tr., Beijing: World Publishing Corporation, 79.
4. Luo, L. (2007). The folk characteristics of the door-god New Year painting. *Journal of Literature and History*, 02, 38–42.
5. Zhang, N. (2016). *Modern design performance of the elements of Taohuawu New Year painting*. Shanghai University, 11.





# Review of Anti-counterfeiting of Prints Based on Infrared Spectroscopy

Ge Yang<sup>1</sup>(✉), Zhenxin Guo<sup>1</sup>, Zengqi Bao<sup>1</sup>, Jiawei Zhao<sup>1</sup>,  
Dongsheng Jiang<sup>1</sup>, and Liang Yan<sup>2</sup>

<sup>1</sup> Beijing Institute of Graphic Communication, Beijing, China  
306246253@qq.com

<sup>2</sup> Artron Art Group, Beijing, China

**Abstract.** Infrared spectroscopy is a molecular selective absorption of certain wavelengths of infrared rays. So the infrared spectrum will show information about certain groups. The detection of the surface molecular information of printed matter based on infrared spectroscopy can effectively detect the authenticity of printed matter. This paper briefly describes the application of near-infrared spectroscopy, Fourier transform infrared (FTIR) spectroscopy; Fourier transform attenuated total reflection infrared (FTIR-ATR) spectroscopy for anti-counterfeiting detection of printed matter. Through the inductive analysis of some application examples to compare the advantages and disadvantages of the three techniques, the application of spectral analysis technology to the anti-counterfeiting detection of printed matter put forward some ideas and suggestions.

**Keywords:** Printed matter · Spectral analysis technique

## 1 Introduction

Now the anti-counterfeiting technology of banknotes, bills, and high-end goods is very mature, but there are still many cases of imitation. The infrared spectroscopy method is applied to the anti-counterfeiting detection of printed materials, and the subtle differences in the composition of the materials can be expressed by the spectral information. The printed matter consists of paper and ink. Paper anti-counterfeiting is effective in preventing fraud by making specialty paper, but it also increases the anti-counterfeiting effect and increases the cost. The prints of many imitations don't seem to make any difference, but there are big differences in the spectrum, because the composition of the inks is different. The study centered on ink because they are the most important part of printed matter.

Ink is a very complex mixture consisting mainly of resins, pigments (dye), solvents and small amounts of additives. Pigments are pigmented in particulate form and do not dissolve. They are the most commonly used pigments in inks. The dye is formulated into a solution when used, and is colored in a molecular state, and the effect is not as good as that of the pigment. Pigments can be classified into inorganic pigments and organic pigments by type. Inorganic pigments such as titanium white, cadmium red, chrome green, ultramarine blue, and the like. Organic pigments such as azo, indigo, etc.

Now it has many advantages using spectrometers: the technology is well-rounded, ordinary laboratories can carry out experiments, and there are many ready-made pigment database can effectively analyze the content of its components.

## 2 Near Infrared Spectroscopy

Near infrared spectroscopy refers to the 780–2500 nm band, which is mainly the characteristic information of the organic molecules containing hydrogen group (C–H, O–H, N–H, P–H, S–H, etc.). It can be used to analyze complex samples quickly, batch and nondestructive, so it can be widely used in agriculture, food, petrochemical and pharmaceutical analysis and other fields. The ink information on the printed matter is mainly some inorganic trace elements, the signal of near infrared spectroscopy is weak, the sensitivity is low, and so its application and research in inorganic trace elements is very little. It is shown in Table 1.

**Table 1.** NIRS content brief

NIRS	Principle	Purpose	Advantage	Disadvantage
Shao Xueguang of Nankai University used near infrared spectroscopy to analyze inorganic trace element components [1]	Indirect method for measuring trace elements	Detection of the content of trace elements	Improve analysis speed and greatly improve measurement sensitivity	A large number of experiments are needed to establish the model. The near-infrared diffuse reflectance spectrum is poorly interpreted and the detection limit is high
Li Yan, Beijing Institute of Graphic Communication, analyzes the spectrum of printed matter based on near-infrared spectroscopy data [2]	Spectral absorption feature matching method and spectral global similarity matching method	Identify the authenticity of printed matter	Fast, non-destructive, no sample processing required	A lot of algorithm research is needed in the later stage to improve the accuracy of the identification

Shao Xueguang from the School of Chemistry, Nankai University uses near-infrared spectroscopy to analyze inorganic trace element components [1]. The inorganic ions generally do not respond in the near-infrared spectrum, but inorganic trace

elements can form chelates or complexes with organic or non-metallic substances in the measured substances. By detecting the content of these compounds, the content of inorganic micro-elements can be detected, so that the rapid determination of inorganic elements can be realized indirectly.

Li Yan from Beijing Institute of Graphic Communication analyzed the spectrum of printed matter based on near-infrared spectroscopy data [2]. The instrument used in the experiment was ASD Field Spec 3 portable spectrometer manufactured by American ASD Company. The wavelength range was 350–2500 nm. The experimental sample was McDonald's fries box. Taking into account the variability of the ink's origin, the French fries samples were purchased from seven cities. The collected data are processed by a spectral absorption feature matching method and a spectral overall similarity matching method. The results of spectral matching show that for the three types of prints with different spectral similarity, the methods of matching the absorption peak distribution and the characteristic parameters matching the absorption peak can effectively distinguish the spectral data. The accuracy of the characteristic parameter matching method is high, and the accuracy rate reaches 88.9–100%. The results show that the analytical techniques of printed spectral data can be used for spectral difference analysis of printed matter.

Analysis of the above two examples, the use of near-infrared can achieve the purpose of distinguishing the authenticity of printed matter, but limited by the characteristics of near-infrared itself, cannot display the information of inorganic elements well, it has caused great difficulties in data analysis. Moreover, the spectral characteristics are not obvious enough, and it is easy to bring a large error to the experiment. Therefore, it is not recommended to use the method for anti-counterfeiting detection of printed matter.

### 3 Fourier Transform Infrared Spectroscopy

Fourier transform infrared spectroscopy is abbreviated as FTIR. In the late 1960s, a Fourier transform infrared spectrometer based on interferometer frequency modulation was introduced, which was mainly composed of a Michelson interferometer and a computer [3]. Fourier transform red spectrum has high detection sensitivity, high measurement accuracy, high resolution, fast measurement speed, low astigmatism and wide band. Fourier transform infrared spectroscopy can change some elements to study the spectrum of the whole near-infrared, mid-infrared and far-infrared  $10,000\text{--}10\text{ cm}^{-1}$ . This has a great effect on the determination of inorganic compounds and organ metallic compounds. It is shown in Table 2.

Zhang Xuan, a medical student at Henan University, used Fourier transform infrared spectroscopy to identify ink types of signature pens [4]. It is also fully applicable to the identification of inks on printed materials. Their principles are completely compatible. The signature pen ink is detected by Fourier transform infrared spectroscopy. The ball pen ink is mainly composed of dye, resin and solvent lubricant. The dyes in the blue pen oil mainly include copper titanium cyanide and triaryl methane. Different ratios of dyes will cause changes in the infrared spectrum. According to the difference in the number of characteristic peaks in the infrared

**Table 2.** FTIR content brief

FTIR	Principle	Purpose	Advantage	Disadvantage
Zhang Xuan of Henan University uses Fourier transform infrared spectroscopy to identify the types of ink for signature pen [4]	Infrared spectral curve feature difference	Identify the type and ratio of dyes in the mixed spectrum	Non-destructive analysis can visually identify the structural composition of the dye	The preparation of samples by KBr pressing method is difficult and heavy workload
Zhang Jinzhuang of Liaoning Police Officer School identifies laser printer samples based on FTIR single point mode method [5]	Single point mode detection	Differentiate samples from different brands of laser printers	Perform a second-order reciprocal operation on the spectrum to make the fine structure of the spectrum more prominent	The selection of sample sampling points has a greater impact on the experimental results

spectrum, the peak position and peak area ratio or peak-to-height ratio of the absorption peak are further distinguished. The purpose of distinguishing between different manufacturers and different types of inks is achieved.

Zhang Jinzhuang, Cui Lianyi, etc. of Liaoning Police Officer School based on FTIR single-point mode method for non-destructive identification of different brands of laser printer ink pink marks [5]. At present, the most common laser printer toners can be divided into two categories. One type is two-component toner; the other type is one-component toner, but the two types of toner are composed of resin, dye, magnet powder, etc. [6]. Different brands of laser printer toners have differences in the composition or distribution ratio of each group. Using the Fourier infrared image system, the collected eight brands of samples are scanned in infrared by a single point mode, and the infrared spectrum is collected. The infrared spectra of the two samples were subjected to a second derivative operation to obtain a corresponding second derivative spectrum. The experimental results show that this method can effectively distinguish different brands of laser printing samples, no special preparation of samples, easy to operate, fast, and non-destructive testing, in line with the requirements of current inspection and identification.

From the above examples, the data of the spectral range of  $4000\text{--}400\text{ cm}^{-1}$  collected by Fourier transform infrared spectrometer can reflect some trace evidence, which is good in characteristics and suitable for qualitative identification. The purpose of this study can be better achieved, and the technology is stable and the resolution is high. A complete data acquisition takes only a few seconds, and the experiment can be completed in many laboratories.

## 4 Fourier Transform Attenuated Total Reflection Infrared Spectroscopy

Attenuated total reflection infrared accessories appeared in the early 1960s, but due to the performance limitations of dispersion-type infrared spectrometers, ATR technology application research field is not extensive. In the early 1980s, microscopic technology was applied to the Fourier transform infrared spectrometer, and the Fourier transform attenuated total reflection infrared spectrometer was born, which makes the analysis of the micro-area components convenient and fast, measuring the microscopic area diameter up to several microns [7]. With the application of Fourier transform infrared spectrometer and the development of chemo metrics, Fourier transform attenuated total reflection infrared spectroscopy (ATR-FTIR) is an advantageous tool for surface structure analysis. It is shown in Table 3.

**Table 3.** ART-FTIR content brief

ART-FTIR	Principle	Purpose	Advantage	Disadvantage
South China University of Technology Jiangshan uses attenuated total reflection infrared spectroscopy to detect true and false RMB [8]	Infrared spectral curve feature difference	Distinguish between true and false RMB	The spectral characteristics of the ink part can be effectively distinguished	The infrared spectrum of the white part of the paper is not much different
Meng Chaoyang of Liaoning Police Officer School uses attenuated total reflection technology in Fourier transform infrared spectroscopy to detect inkjet printed samples [9]	Difference of peak shape and peak position in infrared spectrum	Differentiate between different brands of printing inks	The sample demand is small, the analysis speed is fast, and there is no damage to the sample	Different printed paper materials will have a certain impact on the experiment

South China University of Technology Jiangshan, Yin Shiheng, Tang Min, etc. used attenuated total reflection infrared spectroscopy to determine the true and false banknotes of the fifth set of RMB Chinese Yuan [8], and selected several more characteristic areas as sampling points of the spectrum: paper white Part, serial number printing ink, Intaglio printing ink, light-changing ink printing pattern, safety line. The comparison of the difference peaks and the common peaks in the infrared spectrum shows that the infrared spectroscopy can clearly distinguish the paper and ink selected

by the counterfeit currency and the real coin. By analyzing the results of the experiment, the common banknotes can be identified.

Meng Chaoyang of Liaoning Police Officer School used Fourier transform infrared attenuated total reflection spectroscopy technology to non-destructively determine the three major inks of Hp, Canon and Epson commonly used in ink jet printing documents and their corresponding alternative inks [9]. According to the characteristic absorption of the infrared spectrum, these three kinds of inks and their substitute inks can be distinguished and identified. The method can perform non-destructive testing on samples, and provides a fast, accurate and applicable identification method for the identification of ink jet printing inks.

The information on the surface of the sample is more easily analyzed by the above-described example Fourier transform attenuated total reflection infrared spectroscopy technique. It is very suitable for prints, which only require surface information detection. Eliminating the complicated sample preparation process and directly measuring the surface of the sample, the experimental purpose can be achieved.

## 5 Conclusions

This article collects relevant literature and summarizes it. For the near-infrared spectroscopy, Fourier transform infrared spectroscopy, Fourier transforms attenuated total reflection infrared spectroscopy for the anti-counterfeiting detection of printed matter to make a summary analysis. Compared with near-infrared spectroscopy and Fourier transform infrared spectroscopy, the latter has a wider spectral range, and can better qualitatively distinguish inorganic trace elements in the mid-infrared part, which can better analyze the anti-counterfeiting identification of printed materials. The Fourier transform attenuated total reflection infrared spectroscopy technique is an upgrade in the Fourier transform infrared spectroscopy technique. Fourier transform attenuated total reflection infrared spectroscopy is mainly used to analyze the surface structure of samples. After comprehensive analysis, the best solution is to use Fourier transform attenuated total reflection infrared spectrometer for information collection to achieve the best results.

**Acknowledgements.** The project of Beijing Municipal Education Committee.

## References

1. Shao, X., Ning, Y., Liu, F., et al. (2012). Application of near infrared spectroscopy in the analysis of inorganic trace components. *Acta Chimica Sinica*, 70(20), 2109–2114.
2. Li, Y. (2018). *Research on spectral analysis method of prints based on visible-short wave infrared spectroscopy data*. Beijing Institute of Graphic Communication.
3. Feng, J. (2010). *Application of infrared spectroscopy in trace material evidence analysis*. Chemical Industry Press.
4. Zhang, X., Sun, S., Wang, W., & Luo, G. (2001). The nondestructive identification of blue ballpoint pen ink dye components by fourier transform infrared spectroscopy. *Chinese Journal of Analytical Chemistry*, (02), 242.

5. Zhang, J., Cui, L., Xiu, M., Xu, X., et al. (2012). Nondestructive determination of laser printer ink powder mark by FTIR image-single point mode. *Journal of Liaoning Police Academy*.
6. Wang, P., Gao, Y., Chen Li, Z., et al. (2006). Research progress of toners for copiers and laser printers. *Information Recording Materials*, 7(2), 55–58.
7. Cai, B., Cai, X., & Zhang, F. (2004). Development and application of attenuated total reflection-fourier transform infrared spectroscopy. *Wuyi Science*, 20, 192–194.
8. Jiang, S., Yin, S., & Tang, M. (2010). Analysis and comparison of spectrum and energy spectrum of true and false banknotes. *Modern Instruments*, 16(04), 59–61+68.
9. Meng, C. (2009). Attenuation of ink jet printed documents by attenuated total reflection infrared spectroscopy. *Chinese Journal of Spectroscopy Laboratory*, 26(06), 1583–1586.



# Research on Reproduction of Brand Colors Based on Hi-Fi Color Printing

Yan Liu<sup>1</sup>(✉), Ping Gu<sup>1</sup>, and Songtao Li<sup>2</sup>

<sup>1</sup> Printing and Packaging Engineering Department,  
Shanghai Publishing and Printing College, Shanghai, China  
sppcply@163.com

<sup>2</sup> Prepress Department, Shanghai Zidan Printing Co. LTD, Shanghai, China

**Abstract.** To study the reproducibility of brand color in Hi-Fi colorprinting. The paper begins from the ICC color management process. Through the comparison of the color gamut between seven colors Hi-Fi printing and four-color printing, the color conversion variation and by measuring the reproducibility of Hi-Fi color printing reproduction, the feasibility of the brand color reproduction in Hi-Fi printing was analyzed and evaluated. The color gamut of Hi-Fi color printing is larger than four-color printing. The 95% cumulative relative frequency (CRF) value of the color conversion variation is 5.1  $\Delta E_{00}$  in Hi-Fi color printing. The Reproducible Pantone colors in Hi-Fi color printing are 81.3%. Both are better than four-color printing. The average color difference of Hi-Fi color printing is 2.6  $\Delta E_{00}$ . This paper analyzed the feasibility of the reproducing brand colors in Hi-Fi color printing with data analysis and provides a reference on the brand colors reproduction for printing enterprise.

**Keywords:** Brand color · Hi-Fi colorprinting ·  $\Delta E_{00}$  · CRF

## 1 Introduction

Brand colors are special colors, specified as a part of the design process, to enhance the product appearance [1]. In printing, brand colors are also known as spot colors. Designer uses Pantone color books to select brand colors and build job files. They are printed by three methods: (1) Specially formulated inks and dedicated printing units; (2) Standard four-color (CMYK) inks without additional printing units [2–4]; (3) More than four-color inks for printing and copying. E.g. CMYKO (Orange) G (Green) V (Violet). This method of printing brand colors is called Hi-Fi color printing [5].

With the continuous improvement of people's pursuit for a better life, the print quality is also increased. At present, Hi-Fi color printing has been increasingly applied by printing enterprises. This paper compared the color gamut between seven color Hi-Fi color printing and four-color printing, the color conversion variation and analyzed the reproducibility of Hi-Fi color printing reproduction by measuring the  $\Delta E_{00}$ , and provided a reference on the brand colors reproduction for printing enterprise.



## 2 Experiments

### 2.1 Resources

Pantone (Coated) CIELAB list (the databases are from Pantone company), representing 1755 brand colors (a\*b\*plot) [6]; Exact spectrophotometers; ICC profiles: CRPC5/CRPC6/CRPC7 (present CMYK printing) [7] and ALWAN-CMYKOGV.icc (presents Hi-Fi color printing); ColorThink Pro 3, a color management utility; Excel (.xls) with  $\Delta E_{00}$  macro.

### 2.2 Methodology

This paper studied three aspects of the reproduction of brand colors in Hi-Fi color printing. They are the color gamut comparison, color conversion variation and printing replication variation. The color gamut is compared from two dimensions and three dimensions by ColorThink Pro 3.0.3. Color conversion variation is determined by the ICC workflow. Pantone colors are defined calorimetrically. They can be reproduced using ICC color management and Pantone licensed software. Using A-to-B tags and B-to-A tags inside a printer ICC profile for color conversion purposes. A represents the device space. B represents the profile connection space or CIELAB value [8]. Method for determining printing replication variation is selecting 97 Pantone colors, representing different hue, chroma, and lightness. Print these Pantone colors in Hi-Fi color printing and measure these Pantone colors using Exact. Compare color differences ( $\Delta E_{00}$ ) between the measured values and the theoretical values. The average  $\Delta E_{00}$  is used to represent the color replication variation.

## 3 Results

### 3.1 The Color Gamut Comparison

Open the CRPC5/CRPC6/CRPC7 and ALWAN-CMYKORG.icc in ColorThink Pro 3. We can compare the color gamut in 2-D (see Fig. 1) and 3-D (see Fig. 2).

It can be seen from the figures that the gamut of seven color Hi-Fi color printing is somewhere larger and somewhere is smaller than that of four-color printing (CRPC5/CRPC6/CRPC7). So the key factor is the location of brand colors in CIELAB color space.

### 3.2 Color Conversion Variation

For each ICC profile (CRPC5/CRPC6/CRPC7/ALWAN-CMYKOGV.icc), Open the Pantone Solid Coated 1755 LAB list in ColorThink Pro 3. Convert the LAB list to the CMYK list via the B-to-A tag of an ICC profile using the absolute colorimetric rendering intent. Convert the CMYK list back to the LAB list via A-to-B tag of the same ICC profile using the absolute colorimetric rendering intent [9].  $\Delta E_{00}$  is calculated by the two group LAB values. The 95th percentile  $\Delta E_{00}$  is used to specify the color conversion variation as a single number (see Fig. 3) [10].

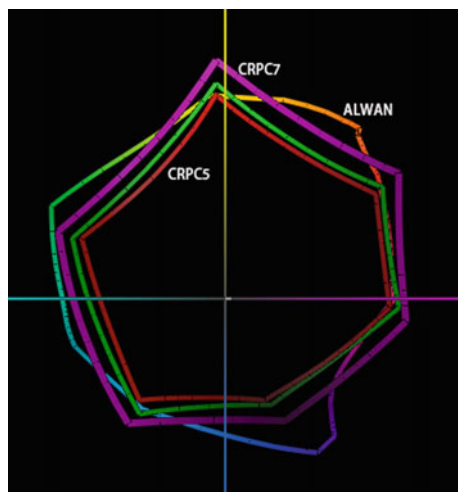


**Fig. 1.** 2-D gamut of ALWAN and CRPC5-7

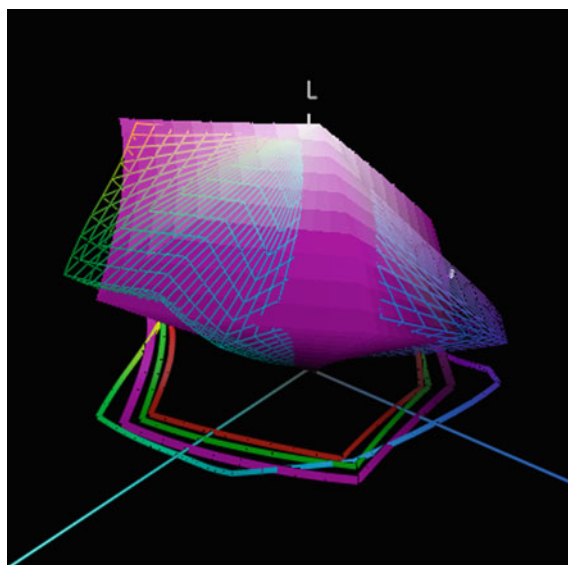


**Fig. 2.** 3-D gamut of ALWAN and CRPC5-7

Seen from the Table 1, It can be concluded that the color difference value converted by the Hi-Fi color printing color conversion profile is much lower than four-color printing profiles (CRPC5/CRPC6/CRPC7). It shows that the color reproduction in Hi-Fi color printing is better than four-color printing.

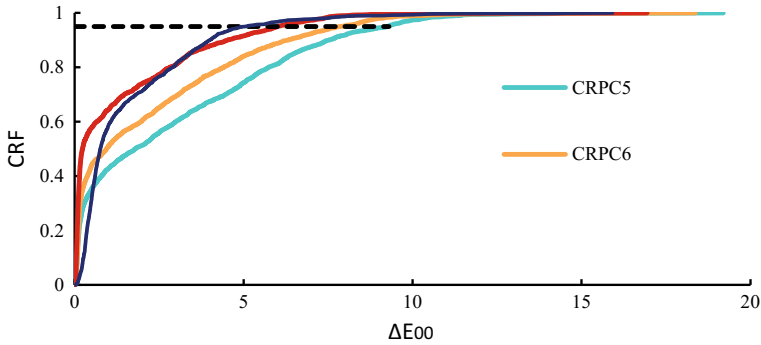


Fig. 3. CRF distribution of color conversion variation

Table 1. The database of color conversion variation

Printing condition	95th percentile $\Delta E_{00}$
CRPC5	9.3
CRPC6	7.8
CRPC7	6.1
ALWAN	5.1

Based on the visual acceptable color difference 3.0 [11], Reproducible Pantone colors in CRPC5, CRPC6, and CRPC7 printing conditions are 60.1, 69.4, and 80.9% respectively. The reproducible Pantone color in ALWAN-CMYK0GV is 81.3% (see Fig. 4).

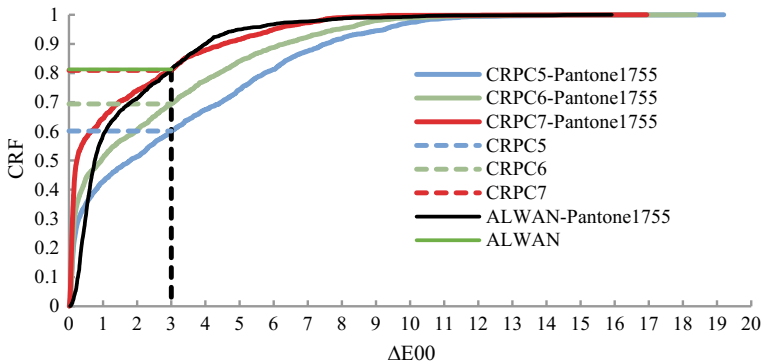


Fig. 4. CRF distribution of Pantone color 1755 by ALWAN and CRPC5–7

### 3.3 Printing Replication Variation

To further study the reproduction of Hi-Fi color printing on brand colors, 97 Pantone colors were printed on the white cardboard of Jiaoyang brand with DIC ink by KBA printing machine. The printing process was sampled every 20 min to measure the LAB data of the sample, and compared the measured data with the original LAB values, and calculated the color difference between the printed color and the theoretical color. The color difference distribution is as follows (see Fig. 5).

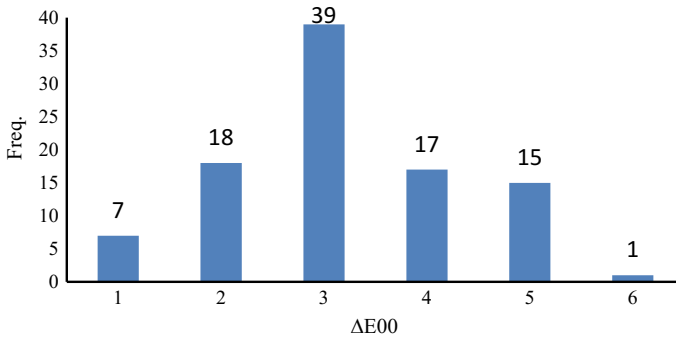


Fig. 5. Frequency distribution of Pantone color difference

It can be seen from the graphic data that the color difference of Hi-Fi color printing is mainly distributed to 2–3  $\Delta E_{00}$ . The average color difference of 97 Pantone colors is 2.6  $\Delta E_{00}$ .

## 4 Conclusion

Brand color aims are specified by Pantone color books and their CIELAB values. But how brand color replicability in Hi-Fi color printing is usually unknown. This paper studied the reproducing brand colors in Hi-Fi color printing based on the color gamut comparison, color conversion variation and printing replication variation. Through the experimental study, we have the following conclusions:

1. Reproducible brand colors is proportional to gamut size. The gamut range of ICC Profile used for Hi-Fi color printing is much larger than that of four-color printing. The number of colors that can be accurately reproduced is also more. Therefore, using Hi-Fi color printing to reproduce brand colors has a better reproduction and reproduction possibility.
2. From the print copy color difference, the average color difference of the seven colors Hi-Fi color printing is 2.6  $\Delta E_{00}$ , which is within the range of visual perception. Therefore, it is feasible to reproduce the brand color in Hi-Fi color printing.

3. This paper analyzed the feasibility of reproducing brand colors in Hi-Fi color printing on the basis of a series of experimental data and analysis in color-managed printing workflows. It can provide reference for the practical application of brand color reproduction.

**Acknowledgements.** This study is funded by Green Platemaking and Standardization Laboratory for Flexography Printing (ZBKT201805).

## References

1. Heath, L. (2015). Brand color, predictability from design to production. In *Printing Industry of America Color Management Conference*, Phoenix, AZ.
2. Hao, W. (2010). *Study on flexible printed version of the computer color matching system*. Tianjin: Tianjin University of Science & Technology.
3. Wang, C. (2006). How to judge the color repeatability of spot color printing. *Printing Field*, 7, 45–47.
4. Tian, Q. (2015). Unconventional spot color copy of decoration image. *Printing Field*, 4, 44–47.
5. Sun, T. (2011). Research progress of Hi-Fi color printing technology. *Guangdong Printing*, (3), 18–19.
6. Liu, J. (2005). Some points of prepress process in spot color printing. *Guangdong Printing*, 2, 25–26.
7. <http://www.color.org/registry/index.xalter>. Accessed May 21, 2018.
8. Fraser, B., Murphy, C., & Bunting, F. (2005). *Color management* (H. Liu & Xue, et al., Trans.). Beijing: Publishing House of Electronics Industry (pp. 476–477).
9. Fraser, B., Murphy, C., & Bunting, F. (2005). *Color management* (H. Liu & Xue, et al., Trans.). Beijing: Publishing House of Electronics Industry (pp. 80–83).
10. Zhang, L., Zhang, M., & Xu, Y. (2010). Research on color difference in spot color printing. *Packing Engineering*, 10(19), 84–86.
11. Cheng, J., Liang, Z., & Liu, Y. (2016). *Color principle and application*. Culture Development Press, 51.



# Study of the Morphological Character of Spectral Reflectance of UV Flexopress in Different Conditions

Quanhui Tian<sup>1</sup>(✉), Bo Zhang<sup>2</sup>, Ping Gu<sup>1</sup>, and Shenwei Yang<sup>1</sup>

<sup>1</sup> Lab of Green Platemaking and Standardization for Flexographic Printing, Department of Print and Package, Shanghai Publishing and Printing College, Shanghai 200093, China

{tqh0509, press27}@163.com, 115187733@qq.com

<sup>2</sup> Shanghai Value Tech Co., LTD, Shanghai 201108, China  
bob.zhang@163.com

**Abstract.** Under the different experimental condition, different combinations of halftone samples were printed out with UV flexopress. More than 100 groups from different substrates, print speed and photoinitiator of reflectance spectra of the samples were measured. The morphological character indices (spectral area, perimeter, depth, width of shoulder) are selected and the variations of sample of different printing conditions are analyzed. The conclusions are that, the correlation between these morphological indexes was obvious; 4 chosen morphological indices were removed, whose  $R^2$  was greater than 0.9 ( $R$  is correlation coefficient) and confidence level was greater than 0.05, the best morphological index was chosen for different character wavelength of different primary color; the variation of different morphological indices in different wavelength was distinct; the relationship between morphological character and the printing conditions was fitted by linear and polynomial curves,  $R^2$  is greater than 0.9.

**Keywords:** Spectral analyses · Spectral character · Spectral morphological · Spectral reflectance · UV flexopress

## 1 Introduction

Spectroscopy and spectral analysis are widely used in many fields, such as matter analysis, detection, etc. Recently with the development of color science, color spectral research has become a hot topic. UV ink is a kind of ink which uses ultraviolet light of different wavelengths and energy to polymerize the monomer in the ink connector to form ink film and dry. Flexopress is a kind of green printing method with UV ink because UV ink is a solvent-free and its pollutant emission is almost zero. There were some studies about the components and performance of UV ink used in flexopress, such as the ink film—forming properties after UV curing [1]. The research focus on ink viscosity, granularity, flexibility [2–6], etc. However, there is a lack of research on spectral characteristics of UV ink printing production, especially the morphological character of spectral reflectance of UV Flexopress printing in different conditions.

Therefore, more than 100 groups of reflectance spectra of the samples from different substrates, print speed and brand ink, were measured. By analyzing the morphological characteristics of spectral reflectance curves of these UV Flexopress samples, the variation of spectral reflectance morphological characteristics in different substrates, print speed and photoinitiator is discussed to investigate the impact of UV ink performance in different condition to improve ink performance.

## 2 Experiment

### 2.1 Output and Measurement

Print out 10, 25, 50, 75 and 100% of halftone samples of C, M, Y and K with flexopress machine, 600lines anilox roller and different brand of UV ink as UFM, SUPER, BIT.

The measurement instrument used in the experiment include X-Rite's i1 (holographic diffraction grating with 128-pixel diode array and built-in wavelength check) portable spectrophotometer 0.38–0.73 mm, spectral resolution 0.01 mm, spot size 0.035 mm, measuring light source A and UV-LED, measuring geometric equipment 45°/0°. Measure the output sample. In order to prevent the influence of external light on the result of color sample measurement, the measurement is carried out in the dark room and the color sample is placed on the white backing. The substrate is paper sticker and polyester (PE) sticker from PULSE roll label production.

During the test, the press correction is carried out. In the normal operation of the equipment, the output printed out the test form. The output samples were measured with i1 spectrophotometer, and the average value was taken as 5 times measurement.

### 2.2 Spectral Data Preprocessing

In order to facilitate the selection of spectral bands, spectral reflectivity of each group is derived by spectral differentiation, and the characteristic bands of each group color are extracted as shown in Table 1. The spectral analysis of spectral reflectance data of different groups of colors was carried out. Different characteristic bands were selected and morphological indexes were extracted.

**Table 1.** The Proper wavelength of cyan magenta yellow and black

Color	Proper wavelength I (um)	Proper wavelength II (um)	Proper wavelength III (um)	Proper wavelength IV (um)
Cyan	0.40–0.58	0.64–0.72	0.52–0.66	0.68–0.72
Magenta	0.39–0.53	0.56–0.73	0.43–0.61	–
Yellow	0.39–0.45	0.42–0.52	0.47–0.58	–
Black	0.39–0.46	0.46–0.56	0.42–0.68	0.64–0.71

### 2.3 Selection and Calculation of Spectral Index

The spectral perimeter, wave depth, total area and shoulder width are compared and analyzed. The area is solved by trapezoidal area integral, and the circumference, wave depth and shoulder width are calculated by Euclidean distance formula [7–12]. At first,  $\lambda$  is the wavelength vector  $r$  as the reflectivity vector, corresponding to the wavelength and spectral reflectivity of each output mixed pixel, respectively.

- (1) Spectral length (L): Total length of the curve of the spectral absorption trough or reflected wave peak, using Eq. (1) [7–12].

$$L = \sum_{\lambda_1}^{\lambda_2} \sqrt{(r_{\lambda_i} - r_{\lambda_{i+1}})^2 + (\lambda_i - \lambda_{i+1})^2} \quad (1)$$

Among them,  $\lambda_2$  and  $\lambda_1$  is the initial value and truncation value of characteristic wavelength,  $\lambda_i$  is the component of wavelength vector, and  $r_{\lambda_i}$  is the component of reflectivity vector.

- (2) Depth of wave (Depth): The distance between the minimum value of the spectral characteristic absorption peak or the maximum point of the reflection peak relative to the 100% line, indicating the ability of the color sample to absorb or reflect in the trough or the peak  $\lambda_i$ , as Eq. (2) [7–12].

$$\text{Depth}_{\lambda_i} = \left| 1 - r_{\lambda_{i\min/\max}} \right| \quad (2)$$

$r_{\lambda_{i\min/\max}}$  is the minimum or maximum reflectivity vector in  $\lambda_i$  characteristic band, the minimum value in absorption band and the maximum value in reflection band.

- (3) Area (S): The area of the wave depth of the absorption trough or reflection peak of the spectral characteristic and its spectral curve, as Eq. (3) [7–12].

$$S = \sum_{\lambda_1}^{\lambda_2} r_{\lambda_i} \Delta\lambda \quad (3)$$

$\lambda_2$  and  $\lambda_1$  is the initial value and truncation value of characteristic wavelength,  $\Delta\lambda$  is the interval of characteristic wavelength, and  $r_{\lambda_i}$  is the component of reflectivity vector.

- (4) Shoulder width (D): it indicates the opening degree of the absorption peak and the reflected trough as Eq. (3) [7–12].

$$D_{\lambda_i} = \sqrt{(r_{\lambda_1} - r_{\lambda_2})^2 + \Delta\lambda} \quad (4)$$

$\lambda_2$  and  $\lambda_1$  is the initial value and truncation value of characteristic wavelength,  $\Delta\lambda$  is the interval of characteristic wavelength, and  $r_{\lambda_i}$  is the component of reflectivity vector.



### 3 Results

#### 3.1 Qualitative Analysis of Spectral Morphological Indexes

By using Eqs. (1)–(4), the variation law of spectral morphological indexes in each characteristic band is calculated, as shown in Fig. 1.

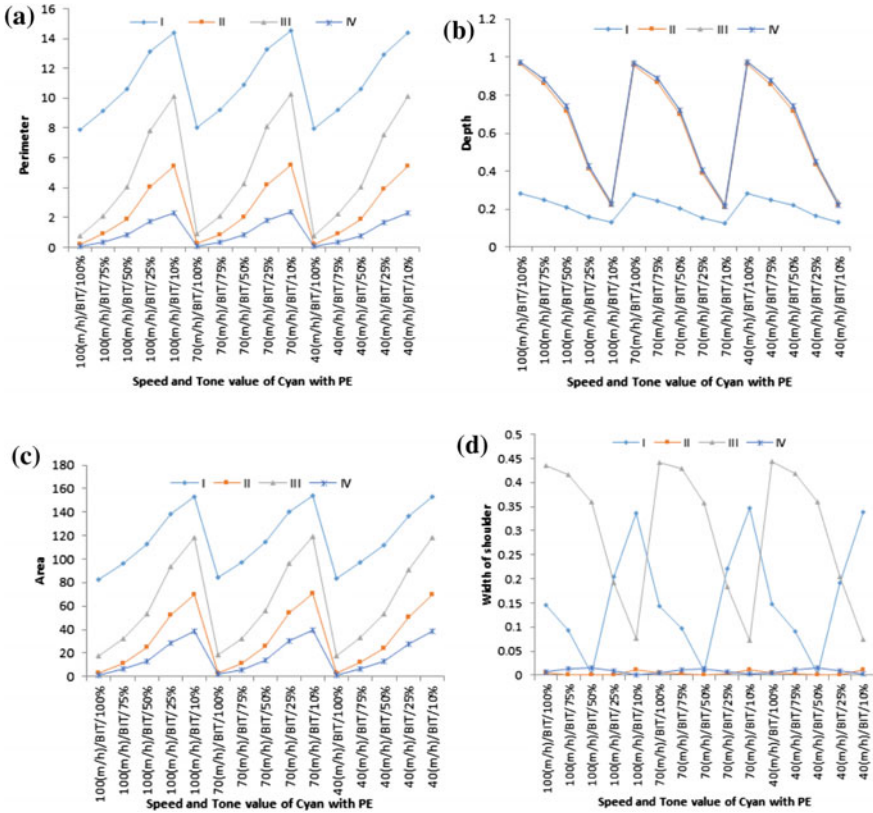


Fig. 1. Different spectral morphological indexes of cyan with BIT ink and PE substrate

#### 3.2 Quantitative Statistics of Spectral Morphological Indexes

Furthermore, the spectral reflectance of different conditions of print sample was quantitatively analyzed by correlation coefficient and significance test.

According to level 0.01 significant, correlation coefficient on different characteristic bands. From the correlation coefficient, we can find that there are obvious differences in the correlation of four indexes, namely perimeter, wave depth, area and shoulder width, and the correlation of each index in different characteristic bands. The spectral perimeter and spectral area is high similar, and the correlation coefficient is larger than 0.9. Therefore, two morphological indexes can be removed as one index.

In order to reduce the amount of data, according to the correlation analysis between different characteristic bands and different indexes, and synthesizing the above qualitative and quantitative analysis, the corresponding morphological indexes of each characteristic band are determined as shown in Table 2.

**Table 2.** The spectral forms in different special wavelength

	Cyan	Magenta	Yellow	Black
Perimeter	I <sub>C</sub>	I <sub>M</sub> , II <sub>M</sub> , III <sub>M</sub>	III <sub>Y</sub>	–
Depth	II <sub>C</sub> , III <sub>C</sub> , IV <sub>C</sub>	I <sub>M</sub> , II <sub>M</sub> , III <sub>M</sub>	I <sub>Y</sub> , II <sub>Y</sub> , III <sub>Y</sub>	I <sub>K</sub> , II <sub>K</sub> , III <sub>K</sub> , IV <sub>K</sub>
Area	–	–	–	–
Width of Shoulder	I <sub>C</sub> , II <sub>C</sub> , IV <sub>C</sub>	I <sub>M</sub> , II <sub>M</sub> , III <sub>M</sub>	III <sub>Y</sub>	II <sub>K</sub> , IV <sub>K</sub>

### 3.3 Correlation Analysis of Characteristic Index and Different Condition

According to the qualitative and quantitative analysis, the correlation analysis of the spectral reflectance curves of each color in different characteristic bands is shown in Table 3.

The morphological indices of most feature bands are linearly correlated with the proportion of halftone and different printing condition, but there are some nonlinear characteristic bands ( $R^2 < 0.5$ ). With regression analysis [12], the relation of quadratic polynomial can fit the nonlinear region well ( $R^2 > 0.95$ ).

## 4 Conclusion

By measuring and calculating the spectral reflectance of flexo printing samples in different substrate with different UV ink, it is found that different primary colors have different responses to different morphological indexes in different characteristic bands. The characteristic bands of different primary colors are determined by spectral differential technique. Through qualitative analysis, the relationship between spectral morphological indexes of different characteristic bands and spectral perimeter, depth, area and width of shoulder is analyzed. The response states of these morphological indices to different characteristic bands are analyzed.

Through the analysis of correlation and significance, it was found that the spectral reflectance morphology of flexo printing samples under different printing conditions was not related to printing speed, and nonlinear to ink formula of different printing materials and dot area ratio.

The characteristics of dot ratio and spectral reflectance of printing samples can be obtained by using spectral curve. The research results are helpful to improve the efficiency of spectral prediction algorithm of printing color under different control states of flexo printing.

**Table 3.** The correlation of cyan, magenta, yellow and black between the spectral forms and different printing condition

Cyan	I <sub>C</sub>		II <sub>C</sub>		III <sub>C</sub>		IV <sub>C</sub>	
	R <sup>2</sup>	Sig.	R <sup>2</sup>	Sig.	R <sup>2</sup>	Sig.	R <sup>2</sup>	Sig.
Perimeter	0.9834	$4.21 \times 10^{-32}$	-	-	-	-	-	-
Depth	0.1214	0.0611	0.9971	$2.1 \times 10^{-32}$	-	-	0.9904	$2.79 \times 10^{-27}$
Width of shoulder	0.9847	$7.1 \times 10^{-24}$	0.1496	0.0313	0.9790	$4.29 \times 10^{-27}$	0.5881	$7.06 \times 10^{-7}$
Magenta	I <sub>M</sub>		II <sub>M</sub>		III <sub>M</sub>		IV <sub>M</sub>	
	R <sup>2</sup>	Sig.	R <sup>2</sup>	Sig.	R <sup>2</sup>	Sig.	R <sup>2</sup>	Sig.
Perimeter	0.9678	$1.96 \times 10^{-22}$	0.9384	$1.75 \times 10^{-18}$	0.9874	$3.85 \times 10^{-28}$	-	-
Depth	0.5924	$6.62 \times 10^{-7}$	0.9096	$3.81 \times 10^{-16}$	0.9990	$8.98 \times 10^{-44}$	-	-
Width of shoulder	0.9755	$4.22 \times 10^{-24}$	0.9996	$1.32 \times 10^{-48}$	0.2934	0.002	-	-
Yellow	I <sub>Y</sub>		II <sub>Y</sub>		III <sub>Y</sub>		IV <sub>Y</sub>	
	R <sup>2</sup>	Sig.	R <sup>2</sup>	Sig.	R <sup>2</sup>	Sig.	R <sup>2</sup>	Sig.
Perimeter	-	-	-	-	0.9772	$1.55 \times 10^{-24}$	-	-
Depth	0.9668	$3.00 \times 10^{-22}$	0.9680	$1.77 \times 10^{-22}$	0.6846	$1.71 \times 10^{-8}$	-	-
Width of Shoulder	-	-	-	-	0.9800	$2.41 \times 10^{-25}$	-	-
Black	I <sub>K</sub>		II <sub>K</sub>		III <sub>K</sub>		IV <sub>K</sub>	
	R <sup>2</sup>	Sig.	R <sup>2</sup>	Sig.	R <sup>2</sup>	Sig.	R <sup>2</sup>	Sig.
Perimeter	-	-	-	-	0.9064	$3.16 \times 10^{-15}$	0.9056	$1.18 \times 10^{-16}$
Depth	0.7973	$8.36 \times 10^{-14}$	0.9097	$2.68 \times 10^{-16}$	0.7922	$4.92 \times 10^{-14}$	0.9220	$4.99 \times 10^{-17}$
Width of Shoulder	-	-	-	-	0.1394	0.037	0.8610	$2.90 \times 10^{-13}$

**Acknowledgements.** This study is funded by Green Platemaking and Standardization laboratory for Flexographic Printing (ZBKT201703).

## References

1. Pu, R., & Gong, P. (2008). *Hyperspectral remote sensing and its application* (p. 8). Beijing: Higher Education Press.
2. Wan, J. H., Han, Z. Z., Song, X. X., & Liu, J. (2016). Oil spills identification using hyperspectral imaging based on multi-pattern method. *Chinese Journal of Luminescence*, 4, 473–480.
3. Gullem, C., & Yolanda, S. (2007). The multi-angle view of MISR detects oil slicks under sun glitter conditions. *Remote Sensing of Environment*, 107, 232–239.
4. Suo-Anttila, J. M., Blanchat, T. K., Ricks, A. J., et al. (2009). Characterization of thermal radiation spectra in 2 m pool fires. *Proceedings of the Combustion Institute*, 32(2), 2567–2574.
5. Li, J., Gai, J., et al. (2016). Mycoplasma suis biological and morphological character. *Jilin Animal Science and Veterinary Medicine*, 37, 13–15.
6. Dai, H., Mao, W., Gao, H., & Lian, H. (2016). Lian Huayao, analysis on the leaf shape morphological characters of fine individual plants of *Syzygium grijsii*. *Jiangxi Forestry Science and Technology*, 44, 20–23.
7. Zhu, F., Gong, H., Sun, T., et al. (2013). Study on reflectance spectra morphological character of the hyperspectral mixed pixels at different component proportion. *Spectroscopy and Spectral Analysis*, 33(7), 1897–1902.
8. Liu, Q., Wan, X., et al. (2013). Research on developing the spectral dataset for dunhuang typical colors based on color constancy. *Spectroscopy and Spectral Analysis*, 33(11), 3071–3074.
9. Masahiro, Y., et al. (2002). Color image reproduction based on the multispectral and multi-primary imaging: Experimental evaluation. *Proceedings of the SPIE*, 4663.
10. Wang, L., Zhuo, L., He, Y., et al. (2004). Oil spill identification by near-infrared spectroscopy. *Spectroscopy and Spectral Analysis*, 24(12), 1537–1539.
11. Cobel, P. G. (2007). Marine optical biogeochemistry: The chemistry of ocean color [J]. *Chemical Reviews*, 107(2), 402–418.
12. Tzeng, D. Y., Berns, R. S. (2005). A review of principal component analysis and its applications to color technology [J]. *Color Research & Application*, 2005, 30(2), 84–98.



# Effect of Lens on Spectral Characteristics of Imaging System

Lan Jiang, Guihua Cui<sup>(✉)</sup>, and Ting Xu

College of Mathematics, Physics and Electronic Information Engineering,  
Wenzhou University, Wenzhou, China  
gcui@wzu.edu.cn

**Abstract.** Spectral sensitivity is an important parameter reflecting spectral response for an imaging system. In order to study the effect of different types of optical lenses on the spectral characteristics of an imaging system, a monochromator was used to measure the spectral sensitivity function of a black-and-white industrial camera under three different lenses. The experimental results show that spectral sensitivity curves for a digital camera with three different lenses are different, and the average root-mean-square error between spectral sensitivity curves with different lenses was 0.061, which was about 7.7 times larger than that of the measurement error. This shows that the optical lens had a significant effect on the spectral characteristics of an imaging system.

**Keywords:** Imaging sensor · Spectral sensitivity function · Lens · Digital camera

## 1 Introduction

Imaging Systems are widely used for observation or capturing image in a variety of applications including inspection, machine vision, etc. An imaging system usually consists of a camera, an optical lens, and an illumination source. In general, the performance of an imaging system is greatly affected by its optical transmission characteristics or spectral sensitivity. If the total spectral response of an imaging system is available, it can be used for a variety of applications, such as machine vision, color reproduction, video signal processing, and so on. However, the spectral sensitivity of an imaging system is a comprehensive result of many factors, such as imaging sensor, optical filter, optical lens and image processing algorithm in the system. In those factors, optical lenses are made from different optical materials such as glass or plastic, and usually coated with different optical coatings. Different optical materials or different optical coatings have different spectral characteristics, so different optical lenses have different spectral characteristics as well. Even if the same camera with different optical lenses or different filters, the spectral sensitivity of the imaging system may be different due to the difference in optical system structure, optical material transmittance, and optical coatings. Therefore, the manufacturers of camera usually do not provide accurate spectral sensitivity data for their digital camera.

The methods for measuring or estimating the spectral sensitivity of a digital imaging system [1–5] are also being developed in order to facilitate the application of commercial digital camera in the research of color information. At present, there are mainly two kinds of method, direct measurement [1–3] and indirect estimation [4, 5], for obtaining spectral sensitivity data of an imaging system. The former uses a monochromator to produce monochromatic light and a standard diffuse white to reflect the monochromatic light, which is measured by a spectroradiometer and captured by a camera, respectively. Then the camera spectral sensitivity function can be calculated from the camera response and the relative spectral power distribution (SPD) measured by the spectroradiometer. The latter is a generally mathematic method. Firstly, a color image for a standard color chart is captured by the camera, and then the spectral sensitivity curve of the digital camera is optimized from the sensor responses and the known color reflectance.

In this paper, the spectral sensitivity functions of a black-and-white digital camera under three different lenses were measured by a monochromator, and the effect of optical lens on the spectral sensitivity function was studied based on the measurements.

## 2 Experimental

The instruments used in this experiment are listed as follows: an 7ISW301 double grating scanning monochromator, an JETI Specbos 1211 UV spectroradiometer, a black-and-white industrial camera MER-231-41U3 M kindly provided by Daheng Imaging, a standard diffuse white produced by Shanghai Fusion Optical Co Ltd., three types of camera lenses: CHIOPT HC1205A ( $f = 12$  mm), CHIOPT HC1605A ( $f = 16$  mm), and Kowa LM16JC5M2 ( $f = 16$  mm).

The data acquisition method using a monochromator is shown in Fig. 1. In order to prevent environment lights from interfering with the experimental results, the experiment was performed in a darkroom. The parameters of the camera under test, such as the exposure time, aperture etc., were set to that suitable for responding both the weakest and the strongest monochromatic light in the range of 0 to 255. The data acquisition process can be divided into the following five steps:

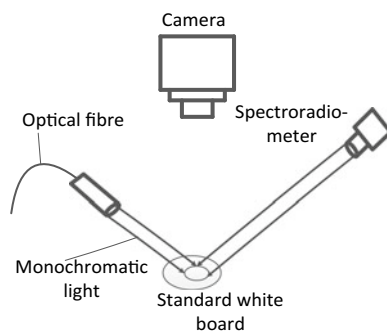


Fig. 1. Monochromator measurement method



**Fig. 2.** Image of a standard whiteboard captured by a black-and-white camera

- (1) The monochromatic light with wavelength  $\lambda_i$  was generated by the monochromator, and projected onto the standard whiteboard;
- (2) A standard whiteboard image as shown in Fig. 2 was captured with the black-and-white camera to obtain the camera response value  $I(\lambda_i)$ ;
- (3) The diffused monochromatic light from the standard whiteboard was measured by the spectroradiometer, and the output was the product of relative spectral power distribution (SPD)  $E(\lambda_i)$  of the monochromatic light and reflectance  $S(\lambda_i)$  of the standard whiteboard;
- (4) A different wavelength of monochromatic light was produced and the above three steps were repeated;
- (5) The different lenses were used and the above four steps were repeated.

During the experiment, the monochromator generated monochromatic lights starting from 380–740 nm at an interval of 10 nm. Therefore, 37 images were captured, and 37 products of  $E(\lambda_i)S(\lambda_i)$  were measured for each tested lens.

### 3 Calculation of Camera Spectral Sensitivity Function

After data acquisition, the camera's spectral sensitivity function can be calculated. According to the definition of tristimulus, the camera response can be expressed by the following formula:

$$\begin{aligned}
 R &= k \sum_a^b E(\lambda)S(\lambda)r(\lambda)\Delta\lambda \\
 G &= k \sum_a^b E(\lambda)S(\lambda)g(\lambda)\Delta\lambda \\
 B &= k \sum_a^b E(\lambda)S(\lambda)b(\lambda)\Delta\lambda
 \end{aligned} \tag{1}$$

where  $a$  and  $b$  are the spectrum range,  $E(\lambda)$  denotes the relative spectral power distribution of the light source,  $S(\lambda)$  denotes the spectral reflectance of the standard whiteboard,  $r(\lambda)g(\lambda)b(\lambda)$  denote the spectral sensitivity function of the camera for red, green and blue channel, respectively, and  $k$  denotes the normalization coefficient. Since a black-and-white camera was used in this study, its response values for the RGB channels are the same. If  $I$  is used to represent the response of a black-and-white camera, and  $Q(\lambda)$  to represent the spectral sensitivity function of the imaging system, then

$$I = k \sum_a^b E(\lambda)S(\lambda)Q(\lambda)\Delta\lambda \quad (2)$$

In this experiment, the sampling wavelength was starting from 380 nm to 740 nm with  $\Delta\lambda = 10$  nm, then

$$\lambda_i = 380 + (i - 1)\Delta\lambda, \quad i = 1, 2, \dots, 37 \quad (3)$$

A total of 37 wavelengths were sampled. The light source  $E(\lambda_i)$  was narrow-band monochromatic at wavelength  $\lambda_i$  for each sampling, so  $E(\lambda_i)S(\lambda_i)$  at most wavelengths other than  $\lambda_i$  are close to zero, then approximately

$$I_i = k \left[ \sum E(\lambda_i)S(\lambda_i) \right] Q(\lambda_i) \quad (4)$$

Here the camera response value  $I_i$  at the  $i$ th sampling can be read out from captured image. Therefor the spectral sensitivity at the wavelength  $\lambda_i$  was obtained as:

$$Q(\lambda_i) = \frac{I_i}{\{k[\sum E(\lambda_i)S(\lambda_i)]\}}, \quad i = 1, 2, \dots, 37 \quad (5)$$

According to Eq. (5), the spectral sensitivity of the camera at 37 sampling wavelengths can be calculated to obtain the camera's spectral sensitivity curve.

In order to eliminate systematic error as much as possible, the camera for each lens was measured twice and then a root-mean-square error (RMSE) of the two measurements was calculated as shown in Eq. (6). The smaller the error between the first measured spectral sensitivity  $Q_1(\lambda_i)$  and the second measured spectral sensitivity  $Q_2(\lambda_i)$  is, the more stable the measured camera spectral sensitivity  $Q(\lambda_i)$  will be.

$$RMSE = \sqrt{\frac{1}{37} \sum_{i=1}^{37} [Q_1(\lambda_i) - Q_2(\lambda_i)]^2} \quad (6)$$

In order to study the effect of different lenses on the spectral characteristics of the imaging system, the average of the spectral sensitivity from repeated measurements for each lens was used as the spectral sensitivity of the imaging system corresponding to



the lens, and the RMSE errors between them were calculated using Eq. (6) again to show the effect of lens on the spectral sensitivity function. At this moment,  $Q_1(\lambda_i)$  and  $Q_2(\lambda_i)$  are the spectral sensitivities of the camera system with two different lenses.

## 4 Results and Discussion

The results of repeated measurements for each of three lenses are shown in Figs. 3, 4 and 5, respectively. Table 1 shows the RMSEs of camera spectral sensitivities for the three lenses. It can be seen from Table 1 that the RMSEs of the camera spectral sensitivities for three lenses measured were very small with an average measurement error of 0.0079 for three lenses. From Figs. 3, 4 and 5, it can also be seen that the curves of CHIOPT HC1605A, CHIOPT HC1205A, and Kowa LM16JC5M2 were basically consistent in two repeated experiments. That means the method and equipment for measuring spectral sensitivity are reasonable stable.

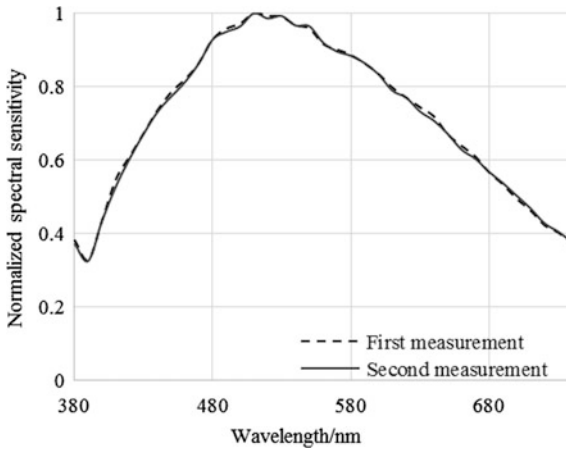


**Fig. 3.** Camera spectral sensitivity function measured twice for Kowa LM16JC5M2 lens

Table 2 lists the RMSEs of the camera spectral sensitivities between three lenses. Comparing the RMSEs in Tables 1 and 2, it can be seen that the measurement error in Table 1 was much smaller than the difference between lenses, which shows that the influence of different lenses on the spectral characteristics of an imaging system is significant, i.e., the average difference of the spectral sensitivity curves for three lenses reaches 0.061, which is about 7.7 times of the measurement error. This difference can also be clearly seen in Fig. 6. For example, at the wavelength of 390 nm, the spectral sensitivity for Kowa lens had an obvious drop, which may be caused by the optical glass or coating used in the lens. Among the three different lenses, the RMSE between Kowa LM16JC5M2 and CHIOPT HC1205A is the smallest, and the RMSE between CHIOPT HC1605A and Kowa LM16JC5M2 is the largest.

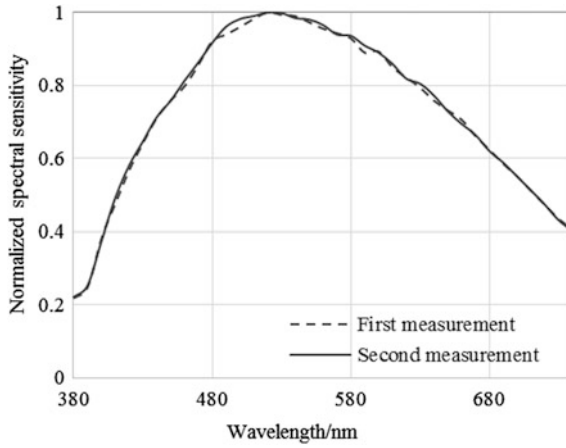


**Fig. 4.** Camera spectral sensitivity function measured twice for CHIOPT HC1205A lens

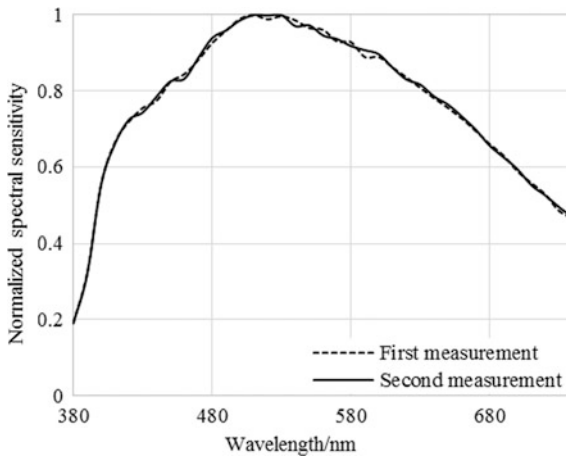


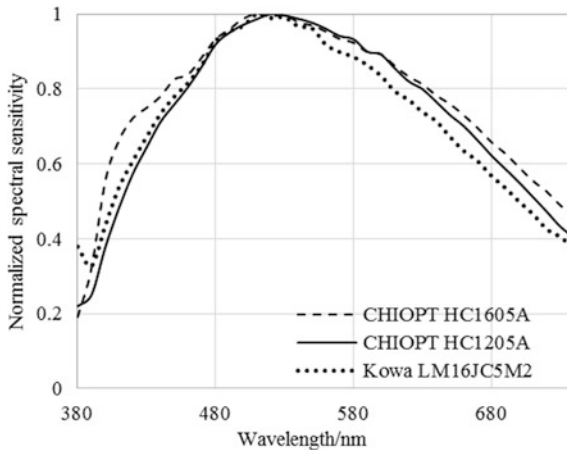
**Fig. 5.** Camera spectral sensitivity function measured twice for CHIOPT HC1605A

**Table 1.** The RMSE of the camera spectral sensitivity function of three lenses

Lens	HC1205A	HC1605A	LM16JC5M2
RMSE	0.0092	0.0079	0.0067

**Table 2.** The effect of different lenses on the spectral sensitivity function

Lens	HC1205A versus HC1605A	HC1605A versus LM16JC5M2	LM16JC5M2 versus HC1205A
RMSE	0.0604	0.0735	0.0492

**Fig. 6.** Average spectral sensitivity function of camera for three kinds of lenses

## 5 Conclusions

To investigate the effect of optical lens on the spectral sensitivity function of imaging system, a direct measurement method was used to measure the spectral sensitivity of a black-and-white camera with three different lenses by means of a monochromator and a spectroradiometer. The experimental results show that different camera lenses had a significant effect on the spectral sensitivity of imaging system, even for lenses from the same manufacturer with different optical system. Among three lenses tested, the difference in terms of RMSE ranged from 0.0492 to 0.0735.

**Acknowledgements.** This study is funded by National Science Foundation of China (61775170, 61671329, and 61501331).

## References

1. Vora, P., Farrell, J. E., Tietz, J. D., et al. (1997). *Digital color cameras-1-response models*. Hewlett Packard Co. HPL, 97–53.
2. Chang, G. W., Chen, Y. C. (1999). Automatic spectral measurement system for color video cameras. *IEEE Transactions on Consumer Electronics*, 45(1), 225–235.
3. Sharma, G., Sharma, G., Bala, R. (2002). *Digital colorimaging handbook*. Boca Raton: CRC Press, 51–56.

4. Alsam, A.. & Lenz, R. (2007). Calibrating color cameras using metameric blacks. *Journal of the Optical Society of America A*, 24(1), 11–17.
5. Barnard, K., Funt, B. (2002). Camera characterization for color research. *Color Research and Application*, 27(3), 152–163.



# Color Correction Method of Digital Printing Based on Local Polynomial

Ping Dai and Jieyue Yu<sup>(✉)</sup>

School of Digital & Design, Hangzhou Dianzi University,  
Hangzhou, Zhejiang, China  
{569291795, 416115323}@qq.com

**Abstract.** In the process of digital printing, due to the change of the performance of the printer, the targeted color space of the traditional printer and the color gamut differences of the output devices, the actual printing colors may deviate from the allowable range of the target color. Therefore, in order to solve this problem, this paper proposes a method of using local nine-item polynomial to set up the mapping relation to modify the color, and realizes the color correction of digital printing by modifying the specific file. The method can control the chromatic aberration to the lowest, more accord with the color correction, and make the digital printing color approximate to the target color in the gamut space of the whole digital printing press.

**Keywords:** ICC profile · Local polynomial · Color correction

## 1 Introduction

Digital printing refers to use the computer to read digital files, complete the image reproduction directly without the need to make a printing plate [1]. In the digital printing process, when the digital printer reads RGB mode or CMYK mode source files, requires the operator for the source file color information to specify a feature file [2]. The digital printer converts the device-related color information in the source file to the device-independent color information according to the specified source specific file, then converts the color information of the digital printer according to the device specific file of the digital printer, then prints out the hard copy.

Because of the change in the performance of the digital printer, the actual print color may deviate from the allowable range for the traditional printer's source digital file or analog color space and the color gamut difference of the output device. This paper proposes a method based on test graph detection results, using local polynomial to fit data to modify specific files and achieve color correction, which has the characteristics of high correction precision and independent of subjectivity.

## 2 Color Correction Method Based on Local Polynomial

### 2.1 The Color Correction Based on Calculation

First, find out the mapping relationship between the source specific file and the specific files for images after printout, then the specific file of the target file is brought into the mapping relation as the independent variable, and the correction value of the source specific file is deduced. Finally, the source specific file corrected to the final target file with positive value.

At the same time, the number should take into account the impact of the cost of calculation [3]. Considering that when the method of polynomial regression is used to establish the mapping relationship, the number of items is less, the mapping relation is lower [4, 5]; the number of items is more, the mapping relation is easy to be in oscillation, this paper chooses 5 items, 9 items, 11 items and 18 items as the experimental group and selects the best experimental group [6].

The lab value in the source specific file is represented by Vector R [7], the lab value of the target specific file is represented in Vector H, and the mapping relation between the source specific file and the target specific file can be represented by a formula (1):

$$H = MR \tag{1}$$

If the vector R value Only has L, a, b, then the transformation between vector R and Vector p is simply a linear transformation; If you increase the number of items in R, such as:  $L^2, A^2, B^2, Lab$ , the transformation is non-linear, and the results are closer to the target value. In this paper 5, 9, 11 and 18 these items are used as experimental groups, and the error test method is adopted to verify the relevant conclusions.

If 11 items are selected for conversion of the feature file, utilize the value of  $L_{P1L1}^* a_{P1L1}^* b_{P1L1}^* L_{P1L2}^* a_{P1L2}^* b_{P1L2}^*, \dots, L_{P1L30}^* a_{P1L30}^* b_{P1L30}^*$  to build 30 row 11 column input matrix, the value, and select 30 as the number of samples in the experiment, get the input matrix R:

$$R = \begin{bmatrix} 1 & L_{P1L1}^* \cdot a_{P1L1}^* \cdot b_{P1L1}^* & L_{P1L1}^* \cdot a_{P1L1}^* & b_{P1L1}^* & L_{P1L1}^* \cdot a_{P1L1}^* & L_{P1L1}^* \cdot b_{P1L1}^* & a_{P1L1}^* \cdot b_{P1L1}^* & L_{P1L1}^2 & a_{P1L1}^2 & b_{P1L1}^2 \\ 1 & L_{P1L2}^* \cdot a_{P1L2}^* \cdot b_{P1L2}^* & L_{P1L2}^* \cdot a_{P1L2}^* & b_{P1L2}^* & L_{P1L2}^* \cdot a_{P1L2}^* & L_{P1L2}^* \cdot b_{P1L2}^* & a_{P1L2}^* \cdot b_{P1L2}^* & L_{P1L2}^2 & a_{P1L2}^2 & b_{P1L2}^2 \\ \vdots & \vdots & \vdots & \vdots & \vdots & \vdots & \vdots & \vdots & \vdots & \vdots \\ \vdots & \vdots & \vdots & \vdots & \vdots & \vdots & \vdots & \vdots & \vdots & \vdots \\ 1 & L_{P1L30}^* \cdot a_{P1L30}^* \cdot b_{P1L30}^* & L_{P1L30}^* \cdot a_{P1L30}^* & b_{P1L30}^* & L_{P1L30}^* \cdot a_{P1L30}^* & L_{P1L30}^* \cdot b_{P1L30}^* & a_{P1L30}^* \cdot b_{P1L30}^* & L_{P1L30}^2 & a_{P1L30}^2 & b_{P1L30}^2 \end{bmatrix} \tag{2}$$

Using the  $L_{SL1}^* a_{SL1}^* b_{SL1}^* L_{SL2}^* a_{SL2}^* b_{SL2}^*, \dots, L_{SL30}^* a_{SL30}^* b_{SL30}^*$  value of  $L^*, a^*, b^*$ , build the output matrix of 30 rows 3 columns by Type (3) H:

$$H = \begin{bmatrix} L_{SL1}^* & a_{SL1}^* & b_{SL1}^* \\ L_{SL2}^* & a_{SL2}^* & b_{SL2}^* \\ \vdots & \vdots & \vdots \\ L_{SL30}^* & a_{SL30}^* & b_{SL30}^* \end{bmatrix} \tag{3}$$

The formula (3) utilizes the least squares method, the mapping relation matrix  $M$  is derived according to the formula (4) [8]:

$$M = (R^T R)^{-1} (R^T H) \quad (4)$$

The formula (4) uses the target value  $L_{T1}^* a_{T1}^* b_{T1}^*$  of the 1th color block of the characteristic color mark image, according to the formula (5) [9], calculates the correction positive value of the 1th color block of the characteristic file as  $L_{C1}^* a_{C1}^* b_{C1}^*$ , which is taken into account:

$$[L_{Cn}^* \ a_{Cn}^* \ b_{Cn}^*] = [L_{Tn}^* \ a_{Tn}^* \ b_{Tn}^*] M \quad (5)$$

This thesis adopts the comparison error method to analyze the experimental data, the so-called comparison error is the European distance between the data  $L^* a^* b^*$  and the target  $L^* a^* b^*$  in the paper, where  $n$  is the color block order. The differences between the two data sets can be expressed in terms of visual values, which are analyzed objectively [10]. In this paper, the target space is CIElab space, then the corresponding Euclidean distance formula is as follows (6):

$$\Delta E_{ab}^* = \sqrt{(L^* - L^{*'})^2 + (a^* - a^{*'})^2 + (b^* - b^{*'})^2} \quad (6)$$

In the formula (6),  $L^*$ ,  $a^*$ ,  $b^*$  is the actual measured value of the original manuscript,  $L^{*'}$ ,  $a^{*'}$ ,  $b^{*'}$  is the value calculated by the model,  $\Delta E_{ab}^*$  is the chromatic aberration.

### 3 Experimental Design and Results Analysis

#### 3.1 The Specific Process of the Experimental Process

The specific operation can be divided into four steps:

- (1) Specifies that the attribute file A is the source specific file of the characteristic color mark image, prints the characteristic color standard image, measures the LAB value of each color block and the target LAB value of each color block.
- (2) The chromatic aberration value between the target value and the 1st color block of the characteristic color mark image is calculated respectively. According to the principle of small chromatic aberration, the measurement value of first 30 color blocks is taken out from all color blocks, make the relevant records and marked as the first set of data, and then the value of 30 color blocks in the corresponding position is found out from the data recorded in the characteristic data file, make the relevant records and marked as the second set of data.
- (3) Take the measured value first group of 30 color blocks as the independent variable and the second group of measured value as the dependent variable, the mapping relation  $M$  is established by the method of polynomial least squares regression. Taking the target of the 1st color block of the characteristic color mark image as the independent variable, the modified value of the 1th color block of the

characteristic file is computed by using the obtained mapping relation, calculate it in the same way and get some correction values of the characteristic file. Replace the value recorded in the characteristic data file described in step (3) with the obtained correction value, and then make the modified characteristic file B with the revised characteristic data file.

- (4) In the condition of specifying the characteristic file B is the source characteristic file for the characteristic color label image, printing the characteristic color standard image again, measuring the  $L^*a^*b^*$  value of each color block, making the record according to the order separately, calculating the chromatic aberration value from the target value separately and then calculate the average chromatic aberration and maximum chromatic aberration, if average chromatic aberration and maximum chromatic aberration is less than set expectation, specify the modified characteristic file as the to be printed source file for the digital file and print. If the expectation is not met, the characteristic file is revised same as step (3) and (4) again until the requirement is met by the same method (Fig. 1).

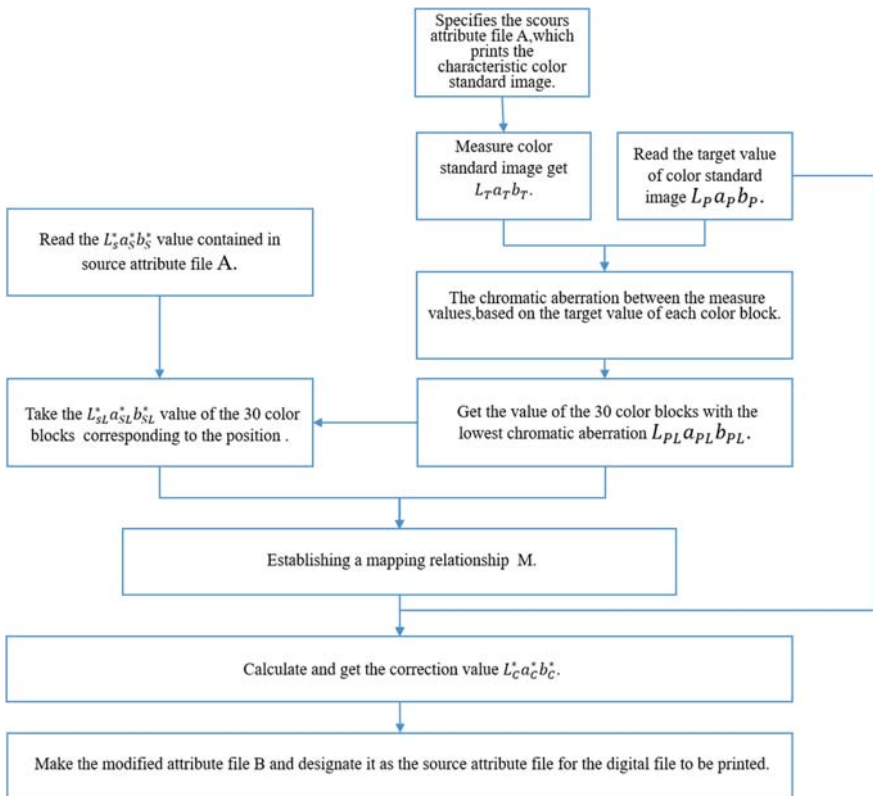


Fig. 1. The specific process of the experimental process



### 3.2 Experimental Results Analysis

After the experiment, 5 items, 9 items, 11 items and 18 polynomials were fitted by using the formula (2). Using the formulas (3), (4) input to revise and deduce a set of correction value respectively, and then using the error Eq. (5) to calculate the error between the correction value and the target test chart, and obtain the following experimental results, The chromatic aberration results are shown in the Table 1.

**Table 1.** Error analysis of color under different item numbers

Polynomial	Minimum error	Maximum error	Average error
5 Items	0.07	5.5693	2.8197
9 Items	0.19	3.3905	1.7902
11 Items	0.48	4.5693	2.5247
18 Items	0.89	4.5563	2.7232

From the above data, we can conclude that the 9-item polynomial and the 11-item polynomial are smaller than the 5-item polynomial on the average error data. Compared with 9 polynomial and 11 polynomial, the error of the 9 polynomial is slightly smaller than that of the 11 polynomial and it is concluded that the results of local color correction using 9 polynomial fitting are more ideal and more accurate than 5 polynomial, 11 polynomial and 18 polynomial.

In practical application, we should choose the number of polynomial in the local polynomial, the choice of the number of items will directly affect the efficiency of the conversion, usually the higher the number of items the lower the conversion efficiency; In addition, if the number of tests selected is small, you should reduce the number of items, Otherwise, the conversion efficiency and conversion accuracy will be reduced, which results in unsatisfactory experimental data.

## 4 Conclusion

Color correction is a hotspot in image processing, it is also an important means to ensure the quality of printing. This paper proposes to use local polynomial fitting to modify the characteristics of the file to achieve the purpose of color correction. At the same time, this paper proves through experiments that, in a certain range, the increase of polynomial item number can improve the precision of experiment but the number of items will cause oscillation, which leads to the decrease of conversion precision, in this experiment, we choose 9 items as local polynomial to achieve good color correction effect.

## References

1. Zhehong, W., & Haisong, X. (2006). Lightness threshold evaluate on visual color matching. *Acta Optica Sinica*, 26(8), 1274–1278 (in Chinese).
2. Wang, Y., & Xu, H. (2006). Spectral characterization of a flat panel color scanner using PCA method. In *proceedings of the SPIE*, 6003, (144–148).
3. Liang, H., & Gaoli, C. (2013). Characterization of display based on polynomial regression mode. *Packaging Engineering*, 34(19), 83–86.
4. Son, C. H., & Park, H. M. (2011). Improved color separation based on dot-visibility modeling and color mixing rule for six-color printers. *Imaging Science and Technology*, 55 (1), 16.
5. Liu, H. (2008). *Printing chromatology*. Beijing: China Light Industry Press.
6. Liang, H., & Ming, Z. (2013). The application of BP neural network in the display of color space conversion. *Packaging Engineering*, 34(19), 83–86.
7. Gao, Y., & Chen, G. (2012). Precision evaluation of polynomial regression algorithm for color space conversion based on printed data sets. *China Printing and Packing research*, 3.
8. Zhen, Y., & Zhou, S. (2010). Evaluation of CIELAB series color difference formula based on printed data set. *China Printing and Packing Research*, SI, 63–66.
9. Wang, Y., & Xu, H. (2007). Color characteristic of scanner based on polynomial regression model. *Journal of Optics*, 27(6), 1135–1138.
10. National Printing Standardization Technical Committee. (2005). *Interpretation of common printing standards*. Beijing: Printing Industry Publishing House.

**Part II**  
**Image Processing Technology**



# Dual Anti-counterfeiting of QR Code Based on Information Encryption and Digital Watermarking

Yijing Xun<sup>1</sup>, Zhijiang Li<sup>2</sup>(✉), Xiaolu Zhong<sup>2</sup>, Sheng Li<sup>2</sup>,  
Jiawang Su<sup>2</sup>, and Ke Zhang<sup>2</sup>

<sup>1</sup> School of Management, University of Science and Technology of China,  
Anhui, China

<sup>2</sup> School of Printing and Packaging, Wuhan University, Hubei, China  
lizhijiang@whu.edu.cn

**Abstract.** The QR code is widely used in modern internet life as its fast speed of response, large capacity of information and the wide range of coding. Therefore, it's an important means to improve the anti-counterfeiting performance of QR code and prevent QR code from being copied and tampered in order to improve the security of information. Based on the coding principle and identification method of two-dimensional codes, this paper proposes a dual anti-counterfeiting method with information encryption and digital watermarking for QR code. Firstly, an encryption algorithm based on RSA is used to encrypt authorization information. Then, a corresponding watermark image is generated based on the encrypted information. Finally, an anti-print embedding and extraction image watermarking method combined with discrete wavelet transform (DWT) and singular value decomposition (SVD) is introduced. The extracted watermark and decrypted information are compared and verified to achieve the dual security of QR code. The result of the attack experiment shows that the digital watermark has strong robustness and invisibility. The anti-counterfeit test results verified the feasibility of the proposed method.

**Keywords:** QR code · Anti-counterfeiting · Information encryption · Digital watermarking

## 1 Introduction

The two-dimensional bar code technology combines the technology of information coding, image processing and data transmission. It is the latest and most widely used bar code technology which overcomes the capacity limitation and low fault tolerance. QR code is a typical two-dimensional barcode which is composed of simple repeating black and white modules. The omni-directional literacy, fast recognition speed, large information capacity and other advantages make it visible everywhere, such as media communication, commodity trading, transportation and other places [1]. But the technology in encoding and decoding process of QR code is open, it is almost impossible to be a strict anti-counterfeiting technology only depends on its' coding regulations [2].

Digital watermarking in QR code is a usual consideration [3], which include spatial domain watermarking and frequency domain watermarking. Previous research proves that the performance of embedding watermark in the spatial domain is poor while embedding a watermark in transform domain which mainly includes discrete cosine transform (DCT), discrete Fourier transform (DFT) and discrete wavelet transform (DWT) is more robust.

Based on the coding characteristics and digital watermarking theory, this paper proposed a dual anti-counterfeit scheme for QR code combined with RSA information encryption technology and DWT-SVD digital watermark technology.

## 2 Dual Anti-counterfeiting Framework

The proposed dual anti-counterfeiting method includes three steps. Firstly, adding encrypted user information into the data during the encoding process. Then, a digital watermark is embedded into the QR image. Finally, compares the encrypted information with the embedded watermark information to verify the legitimacy of users and copyrights. The frame is shown as Fig. 1.

### 2.1 RSA Encryption

RSA encryption is one of the asymmetric encryption algorithms which require two different keys to encrypt (public key) and decrypt (private key) [4]. The RSA algorithm is highly encrypted because it relies on the decomposition of large numbers. From the algorithm principal, the longer of the key, the more security of the encryption information [5].

In the QR code decoding process, the final output data does not contain functional graphics, location graphics, version information, and format information. Then extract the encrypted text from the output data according to the special sign bits, and use the private key to decrypt it. The whole process is shown in Fig. 2.

### 2.2 Digital Watermarking Algorithm

#### 2.2.1 Digital Watermark Embedding

The watermark embedding process takes the encrypted  $690 * 690$  pixel size QR image as the carrier image, and the authenticate image of the  $345 * 345$  pixel size as the digital watermark image. Through the watermarking algorithm to hide the watermark information in the QR image [6–11]. The watermark embedding steps are as follows:

- (1) Decomposing the QR image using DWT to divide into four frequency bands. Then choose the low-frequency sub-band marked as  $cA_I$  and use SVD for the matrix of  $cA_I$  to get the singular value marked as  $S_{qr}$ .
- (2) Using SVD to get the singular value  $S_w$  of the watermark image.
- (3) Selecting the watermark embedding intensity coefficient  $k$  according to the practical need, and use the add algorithm to embed the watermark into QR image information:  $S_{wqr} = S_{qr} + k * S_w$ ;

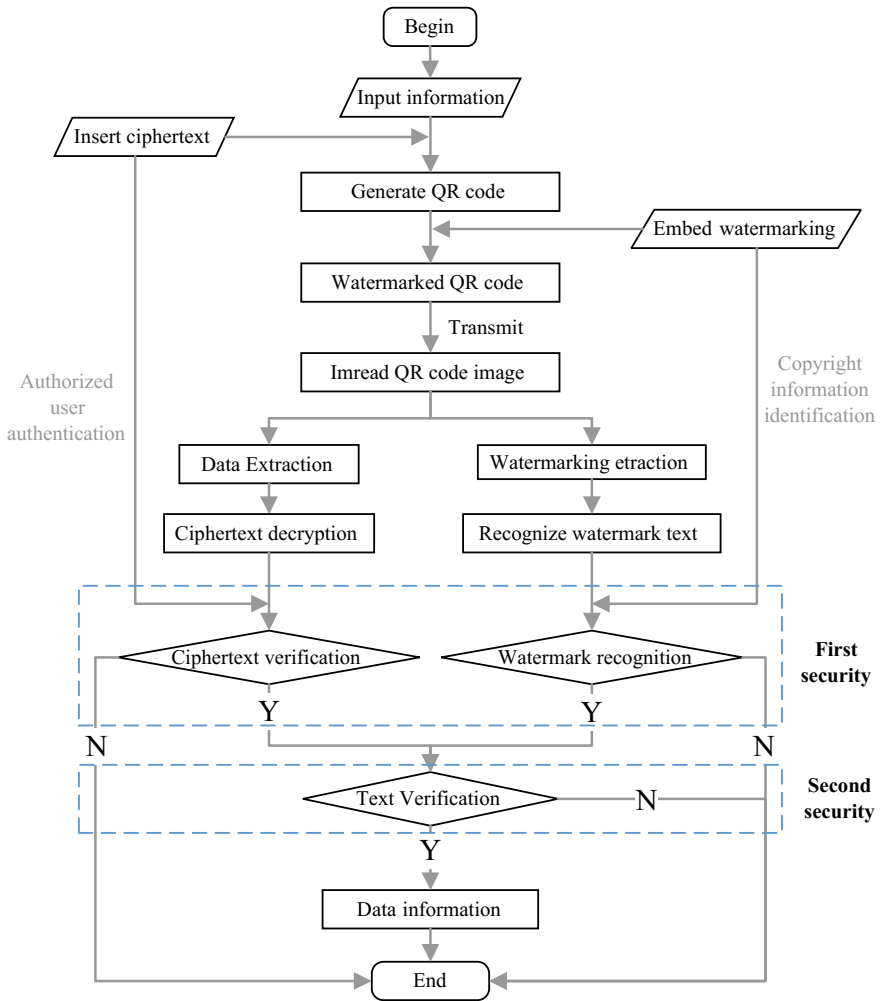


Fig. 1. Dual anti-counterfeiting scheme

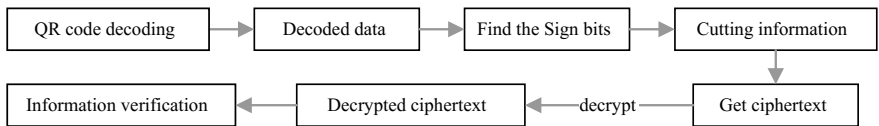


Fig. 2. RSA decrypt process

- (4) Reconstructing the singular value of  $S_{wqr}$ ,  $cA_2 = U_{qr} * S_{wqr} * V_{qr}$ , and get the low-frequency signal of the watermarked QR image.
- (5) Combining the high-frequency part of the original QR image with the discrete wavelet inverse transform of  $cA_2$ , and the watermarked QR image is obtained.

### 2.2.2 Digital Watermark Extraction

The extraction process is the reverse process of the watermark embedding process. It needs to use some information of the original QR image and watermark image. The specific steps of extraction are as follows:

- (1) Using DWT to get the low-frequency sub-band of watermarked QR image.
- (2) Using SVD to get the singular value  $S_{eqr}$  of the low-frequency part of the watermarked QR image.
- (3) According to the coefficient  $k$  in the embedding process, using the inverse formula,  $S_2 = (S_{eqr} - S_{qr})/k$ , to get singular value  $S_2$  of extracted watermark image.
- (4) Reconstructing the singular value  $S_2$ ,  $W \neq U_w * S_2 * V_w$ , to get the extracted watermark image matrix  $W$ , and restoring the extracted watermark image.

## 2.3 Cross-Validation

### 2.3.1 Recognition of Watermark Texts

The paper proposed a method, hit or not processing, based on binary morphology to evaluate the correlation coefficient between the template and input image. The definition of hit or not is as shown in Formula (1), in which  $X$  is the extracted image and  $S$  is the template image composed of text part  $S_1$  and blank part  $S_2$ . The hitting part is the text part after processing. Considering that the transmission attack, it allows tolerance in the hitting process. Then set an NC threshold for hitting judgment. When the NC value exceeds the experimental threshold, it can be considered that the input image is hit successfully. Then the template text is used as the watermark text for cross-validation.

$$X \otimes S = \{x|S_1 + x \subseteq X, S_2 + x \subseteq X^c\} \quad (1)$$

### 2.3.2 Cross Verification

The ciphertext, marked as *text A*, is obtained from QR code decryption by RSA private key. The *text A* and the *watermark template text* are compared to judge whether it is consistent or not. If the text matches successfully, it proves that the QR code is authorized and the content of the QR code is legitimate. If the RSA cipher cannot be successfully decrypted or the ciphertext is inconsistent with the watermark text, it proves that the QR code is not authorized and the security of QR code is not guaranteed.

## 3 Experiment and Analysis

### 3.1 Experimental Environment

Python2.7 and Pycharm are used to develop the experiment system. Digital composite printer with  $2400 \times 600$  dpi print resolution and 300 dpi scan resolution are used to test the function of the proposed method.

## 3.2 Experimental Workflow

### 3.2.1 Encryption and QR Image Generation

The QR image generation process is shown as Fig. 3. The final watermarked QR image is generated in three steps: generate encrypted data and insert it to the final data, generate QR code based on the final data, generate watermarking image and embed it into the QR image. The experimental input data of the QR code is “<http://www.whu.edu.cn/>” and recorded as  $D1$ . The copyright information text is “WUHAN UNIVERSITY ALL RIGHTS RESERVED”, and the encrypted information recorded as  $D2$ . Using the “0000” character as identifiers to distinguish ciphertext and plaintext is recorded as  $D3$ . All data are made up of  $D1$ ,  $D3$ , and  $D2$ , then encode all data according to the coding standard to generated QR image shown in Fig. 4 (left).

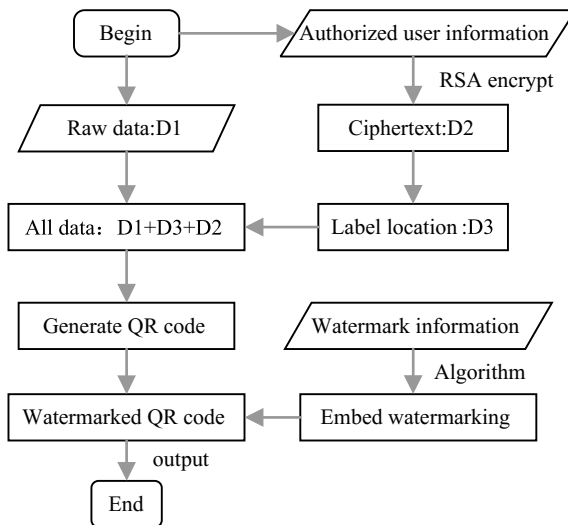


Fig. 3. Generate QR image



Fig. 4. The final watermarked QR image

The watermark image used in the experiment is an image with copyright data shown as Fig. 4 (middle). When embedding the digital watermark, the DWT takes the Haar wavelet basis because that the Haar wavelet is the only discontinuous wavelet with tight support and strictly orthogonal. It also preserves 97.75% of the energy while removing 75% of the amount of data, and the maximum degree can effectively restore



the original map through the low-frequency part [12]. The watermark embedding strength is selected as 0.05 according to the experimental test, that is  $k$  equals 0.05. After embedding watermark information, the final watermarked QR image is shown in Fig. 4 (right).

### 3.2.2 Decode and Information Verification

After the electronic document or print and scan transmission, decode the QR code information and extract the watermark image. The extracted watermark images are shown in Fig. 5. The left one is from the electronic document and the right one is obtained after print and scan. The extracted images can match to the original watermark text template. It proves that the transmission information of the QR code is safe and reliable.



The electronic document    Image after print and scan

**Fig. 5.** The extracted watermark images

### 3.2.3 Attack Test

Considered actual using scenarios, noise, resampling, blur, printing and scanning attack is simulated respectively. As Fig. 6 shows, the Image (1) is adding Gauss noise, Image (2) is Gauss blurred, Image (3) is printed and scanned, Image (4) is printed and take picture by mobile camera, Image (5) is cut by 5% ratio and image (6) is cut by 10% ratio. The extracted watermark images are as shown in Fig. 7.



(1) Noise    (2) Blurred    (3) Scanned    (4) Camera    (5) 5% Sheared    (6) 10% Sheared

**Fig. 6.** Simulate attacked QR images

## 3.3 Experimental Results

### 3.3.1 Evaluation Indicator

The experimental results use PSNR and SSIM to evaluate the difference between the original QR image and the watermarked QR image under attack [13], and use NC to judge whether the text can be matched correctly. Formula (2) is the calculation method of PSNR and SSIM, in which  $x$  and  $y$  are the original and watermarked images,  $MAX$  represents the maximum number of color,  $\mu_x$  and  $\mu_y$  are the mean values of  $x$  and

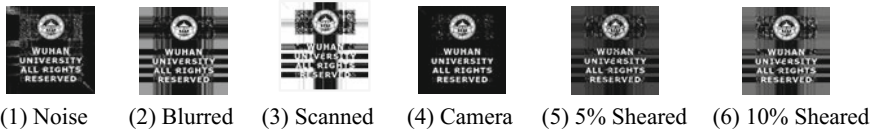


Fig. 7. Extracted watermarked images

y respectively,  $\sigma_x^2$  and  $\sigma_y^2$  are the variance and  $\sigma_{xy}$  is the covariance of x and y. Formula 3 is the calculation method of NC, in which  $W(i, j)$  and  $W'(i, j)$  are the original watermark image text and the extracted watermark image text respectively. If the value of SSIM and NC equals 1, it indicates that the two pictures are the same.

$$\left\{ \begin{aligned} PSNR &= 10\log_{10} \left( \frac{MAX^2}{\frac{1}{mn} \sum_{i=1}^n \sum_{j=1}^m |x(i,j) - y(i,j)|^2} \right) \\ SSIM(x, y) &= \frac{(2\mu_x\mu_y + c_1)(2\sigma_{xy} + c_2)}{(\mu_x^2 + \mu_y^2 + c_1)(\sigma_x^2 + \sigma_y^2 + c_2)} \end{aligned} \right. \quad (2)$$

$$NC = \frac{\sum_{i=1}^n \sum_{j=1}^m W(i, j) * W'(i, j)}{\sqrt{\sum_{i=1}^n \sum_{j=1}^m [W(i, j)]^2} \sqrt{\sum_{i=1}^n \sum_{j=1}^m [W'(i, j)]^2}} \quad (3)$$

3.3.2 Experimental Results

Table 1 presents the PSNR and SSIM values, while values without any attack is as the control group. Table 2 exhibits the NC values of the extracted watermark image text and the original watermark image template text.

Table 1. The experimental values of PSNR and SSIM

Attack Image	Signal		Print and scan		Sheared		Non-attack
	Noise	Blur	Scan	Camera	5%	10%	
PSNR	21.2794	17.5868	6.8878	6.4685	20.0788	17.1080	39.5409
SSIM	0.5116	0.7009	0.3280	0.2787	0.8530	0.8277	0.8814

Table 2. The experimental values of NC

Processing	Noise	Blur	Scan	Camera	5% sheared	10% sheared
NC	0.9634	0.9795	0.9627	0.9548	0.9463	0.9432

In Table 1, the PSNR and SSIM are 39.5 dB and 0.88 in the control group. It proves that the embedded watermark in the absence of attack has good invisibility, which indicates that the watermark algorithm used in the experiment makes the watermark better hidden and ensure the original QR image with high fidelity. The PSNR of the attack is below 30, indicating that a human-visible difference has occurred. This is in line with true visual perception. When analyzing the values of different attack types, the value of signal attack is less than shear attack, and the print and scan attack have the lowest values. This is due to the complexity and diversity of the attack types that encountered during the transmission process.

The values in Table 1 show obvious differences in human eyes, but the watermark extraction process is successful. It proves that the watermark under attack is very robust and maintains the main information. Table 2 is the correlation coefficient value of extracted watermark text and template text. The whole NC values are greater than 0.9, so set 90% threshold to judge whether the text is consistent. When NC value exceeds 0.9 that the template text and the watermark text are equal, and the purpose of authentication and text verification in QR code anti-counterfeiting process is completed.

### 3.4 Anti-counterfeiting Test

#### 3.4.1 Objective Indicator

The process of the anti-counterfeiting test is shown as Fig. 8. When the match process in step one is successful, get *text A* to verify the authentication of users and go to step three. When the decryption is not successful or the text is different from the original text, output message: *unauthorized user*. The extracted watermark image is matched with the original watermark image and get *text B* in step two. When the watermark image cannot be extracted in step two or the matching process is unsuccessful, output message: *unrecognized copyright*. Comparing *text A* with *text B* to verify the security of QR information in step three. When the verification is successful, the dual anti-counterfeiting security is completed and output QR code information.

#### 3.4.2 Analysis

Experiments are carried out following the process mentioned above. Table 3 exhibits the test results. In step one, the unauthorized user information that encrypted by RSA cannot be deciphered successfully. In step two, the non-copyright watermark information is extracted but the matching result is unsuccessful. In step three, unauthorized user information and non-copyright information are used to test together. The text matching is unsuccessful.

For the first anti-counterfeiting, the RSA algorithm is based on a random number operation that the keys can be formulated for each user. When embedding the non-copyright watermark, the extracted watermark cannot match the template successfully. The only verification ensures the reliability of the first anti-counterfeiting in the system. For the second anti-counterfeiting, the content of the watermark is only consistent with the previous user information. The cross-validation can guarantee the authenticity of the transmission data.

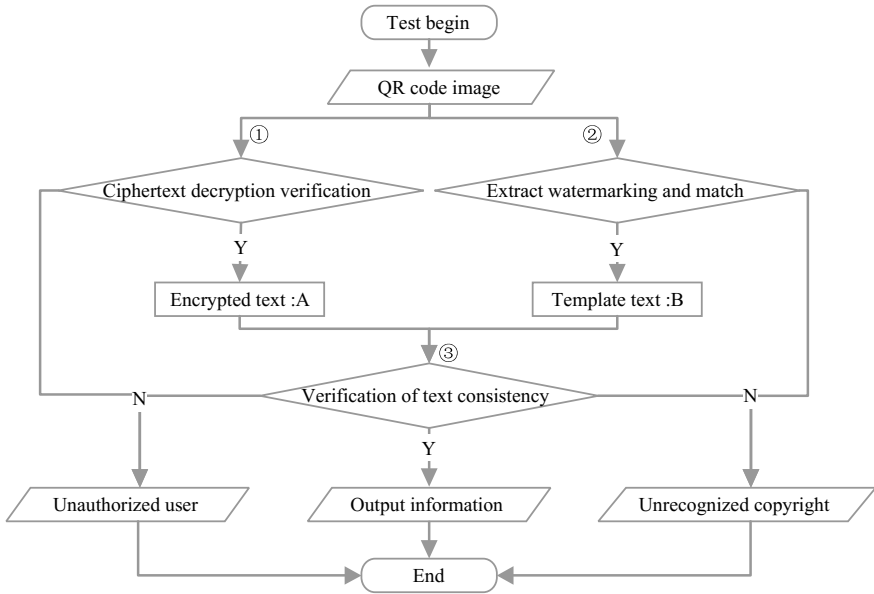


Fig. 8. Test process

Table 3. Anti-counterfeit contrast test

Test	Results	Analysis
User authentication	Unauthorized user	Illegal user
Non-copyright watermark	Unrecognized copyright	Copyright error
Abnormal text	Unauthorized user and copyright	Text matching failure
Dual anti-counterfeiting	Output QR information	Success

The test results show that QR code data cannot be transferred as long as any one of the verification in all steps is not successfully transmitted. Only the dual anti-counterfeiting scheme can get the QR code information. In a comprehensive analysis, dual verification can fully prove the safety and reliability of the QR code of the transmission. It proves that the users with this QR code are authorized users and have authorized user rights in the system.

## 4 Conclusions

This research proposed an anti-counterfeiting method combining the coding characteristics of the two-dimensional code and the digital watermark to enhance the security of the QR code. The method uses RSA encryption algorithm in the encoding process and DWT-SVD algorithm in digital watermark process. The embedding watermark is very good in invisibility and robustness, and it can implement cross verification

successfully through the attack test experiment. The experimental results can strongly confirm that the proposed anti-counterfeiting method is effective in the aspect of QR code security.

## References

1. Shuhua, X. (2011). DES and RSA encryption algorithm based on the data security transmission technology research. *Manufacturing Automation*, 02, 180–182.
2. Sun, B., & Gao, M. (2010). Applications of quick response code in anticounterfeiting technology. *Computer Security*, 09, 6–9.
3. Gupta, V., et al. (2014). Robust and secured image watermarking using dwt and encryption with qr codes. *International Journal of Computer Applications*, 100(14), 33–37.
4. Mohammad, A. A., Alhaj, A., & Shaltaf, S. (2008). An improved SVD-based watermarking scheme for protecting rightful ownership. *Signal Processing*, 88(9), 2158–2180. <https://doi.org/10.1016/j.sigpro.2008.02.015>.
5. Zhu, Y., & Li, Y. (2011). Application of hybrid encryption algorithm in software anti-piracy. *Computer Programming Skills & Maintenance*, 16, 125–126.
6. Panyavaraporn J., Horkaew P., & Wongtrairat W. (2013). QR code watermarking algorithm based on wavelet transform. *International Symposium on Communications & Information Technologies IEEE*, Surat Thani, Thailand. <https://doi.org/10.1109/ISCIT.2013.6645969>.
7. Agreste, S., et al. (2007). An image adaptive, wavelet-based watermarking of digital images. *Journal of Computational and Applied Mathematics*, 210(1–2), 13–21. <https://doi.org/10.1016/j.cam.2006.10.087>.
8. Chow, Y., et al. (2017). A QR Code watermarking approach based on the dwt-dct technique. *Lecture Notes in Computer Science*, 10343, 314–335. <https://doi.org/10.1007/978-3-319-59870-3>.
9. Xie, R., et al. (2015). Anti-counterfeiting digital watermarking algorithm for printed QR barcode. *Neurocomputing*, 167, 625–635. <https://doi.org/10.1016/j.neucom.2015.04.026>.
10. Xue, Q. C., et al. (2016). Geometrical attack resistant digital watermarking technology based on DWT-SVD and QR code. *Packaging Engineering*, 11, 158–163.
11. Andrews, H., & Patterson, C. I. (1976). Singular value decomposition(SVD)image coding. *IEEE Transactions on Communications*, 24(4), 425–432.
12. Cho, D. J. (2014). A study on effective digital watermarking method suitable for QR code. *Advanced Science and Technology Letters*, 51, 94–97. <https://doi.org/10.14257/astl.2014.51.22>.
13. Tong, Y., Zhang, Q., & Qi, Y. (2006). Image quality assessing by combining PSNR with SSIM. *Journal of Image and Graphics*, 12, 1758–1763.



# A Multi-metrics Integrated FR IQA Method Based on Machine Learning

Zhenhua Pan<sup>1</sup>, Jinhua Xiao<sup>1</sup>, Liying Sun<sup>1</sup>, and Yehong Chen<sup>2</sup>(✉)

<sup>1</sup> School of Printing & Packaging, Qilu University of Technology, Jinan, China

<sup>2</sup> Key Lab of Pulp and Paper Science & Technology, Ministry of Education  
(Shandong Province), School of Printing & Packaging, Qilu University of  
Technology, Jinan, China  
chenyh@qlu.edu.cn

**Abstract.** In this paper, a FR (full reference) image quality prediction model learned by AdaBoost BP neural network is proposed by using a bag of features. Firstly some FR image quality assessment methods to improve metrics by considering human visual system are summarized. Further, a group of FR IQA (image quality assessment) metrics are extracted as the candidates of the representation of images. AdaBoost algorithm is finally used to enhance BP network built on a bag of features (9 chosen metrics) for image quality prediction. Then the learned prediction model can map a bag of features into an image quality score as MOS or DMOS. Our experiments are executed on TID2008, TID2013 and LIVE Dataset. Experimental results show that our proposed multi-metrics integrated prediction model works well and get better results than any single metric under complex situations.

**Keywords:** Full reference image quality assessment · AdaBoost BP network · Phase congruency · A bag of features

## 1 Introduction

The objective IQA (image quality assessment) metrics which are computed by computer is crucial for modern image processing. The current IQA methods fall into two main categories. The early developed is FR (Full Reference) method which interpret image quality as similarity with a “reference” or “perfect” image. NR (No Reference) evaluation methods are urgent in situations without a given reference; however only get better evaluation results on some specific situations.

MSE and PSNR are two widely used FR IQA metrics, however have been discovered do not correlate well with human perception. People had explored to develop new metrics with consideration of human visual nature characteristics through building HVS (human visual system) [1, 2]. In order to make HVS simple and feasible, the majority of it simply consist of a CSF (Contrast sensitivity function). In 1993, an IQA metric was implemented which weighted images errors in frequency domain by CSF [3]. Besides, gradient based edge detection such as those developed by Sobel, Marr and Hildreth, Canny and others all can be considered as the energy supplements of IQA models [4]. In 2004, Zhou wang and A.C. Bovik proposed image quality assessment

method based on structural distortion, referred to SSIM, which is the important landmark of IQA [5–7]. In 1986, M. concetta et al. [8] claimed that phase relationships between Fourier components are important to the structure people perceive. In 1995, a fast PC (phase congruency) extraction algorithm was presented through the use of wavelets, this made PC feature more popular in image processing [9]. Some paper also introduce Pyramid structural PC features, which can extract contour information very well, and that is good for solving the FR IQA problem [10]. In 2006, researchers in [11] presented an information fidelity criterion VIFP (Visual information feature) for IQA problem that related the quality with the amount of information shared between a reference and a distorted image.

In the past decade, new IQA metrics and new testing datasets are continuously emerging (<http://sse.tongji.edu.cn/linzhang/IQA/IQA.htm>). Lots of objective and subjective measurements can be found on the internet. Some researchers are giving a systematic evaluation of all the popular IQA metrics on all the available datasets [12–16]. However, the FR IQA problem is still not very clear for understanding. By our considerations, most of above metrics are independently developed, faced with different problems, and often more effective in addressing special issues. Intuitively, to combine all those independently developed IQA metrics working together should results in a better prediction results than before. The goal of this paper is to build a comprehensive model based on accumulations of FR IQA resources. The learned prediction model can map the FR IQA metric vector to an image quality score MOS/DMOS. AdaBoost is used algorithm to enhance BP network for a implement of automatic feature selection. Finally, we trained an IQA prediction model on TID2013, and the evaluation of this model is got on LIVE Dataset. From experiments, our proposed data driven model based on a bag of features come into better performance than all prior FR IQA algorithms.

## 2 Data and Metrics

TID2008 is a color image database for evaluation of full-reference visual quality assessment metrics. It contains 1700 test images (25 reference images, 17 type of distortions for each reference image, 4 different levels of each type of distortion). Reference images are obtained by cropping from Kodak Lossless True Color Image Suite([r0.k.us/graphics/kodak/](http://r0.k.us/graphics/kodak/)). Mean Opinion Scores (MOS) for this database have been obtained as a result of more than 800 experiments. Any details of the dataset information are expressed in paper [12]. With respect to TID 2008, TID 2013 contains a larger number (3000) of test images obtained from 25 reference images, 24 types of distortions for each reference, and 5 levels for each type of distortion. LIVE ([live.ece.utexas.edu/research/quality/subjective.htm](http://live.ece.utexas.edu/research/quality/subjective.htm)) database is proposed for evaluation the performance of FR IQA algorithms, the “ground truth” image quality data is obtained from about 25,000 individual human quality judgments. Further more, metrics download in this paper mainly are from the webset of Zhou Wang (<https://ece.uwaterloo.ca/~z70wang/research/>).

### 3 Related Works

SSIM only considers the structure of an image, while the PC (phase congruency) map of an image can be used not only a feature to calculate local similarity mapping, but also a weighting function in pooling strategy of quality assessment, since PC extraction mechanism conforms to the human visual system. PC map can be accepted as a way of defining structure and structural distortion in a perceptual manner. It is a dimensionless quantity invariant to changes in image brightness or contrast; hence it provides an absolute measure of the significance of feature points (Fig. 1). Values of phase congruency vary from a maximum of 1, indicating a very significant feature, down to 0 indicating no significance.

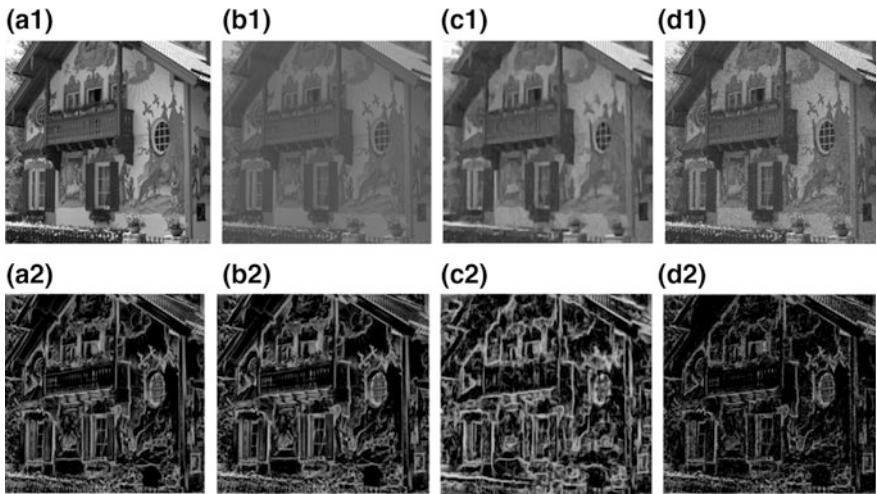


**Fig. 1.** Comparisons of 4 distortion images from one reference image. The first row is the gray scale channel of these images. The second row is PC maps of the first row images

From Fig. 1, we can come to two conclusions. Firstly, PC maps recover the structural information from different illumination conditions. Look at (a1) and (b1), they are under different illumination conditions, however their PC maps of (a2) and (b2) are very similar to each other. Secondly, PC maps of images response the structural distortion. Look at (c1), it is a blurring image, its' PC map (c2) looks like a result of a dilatation operation, revealing the eyes' focus dispersed and information of image becomes blurring now. Look at (d1), it is an image added with Gaussian noise, and the PC map (d2) looks like a result of an erosion operation, revealing the loss of some fine details and information becomes attenuation, (d2) also can be thought as a result after a band pass filter as CSF.

To compute the PC of a two-dimensional (2D) gray scale image, a group of 2D Log-Gabor filters is optimized to produce a filter with a minimal spatial extent. These 2D Log-Gabor filters are constructed with an arbitrary bandwidth by using the



Gaussian filter as the spreading function. By modulating the bandwidth and direction, we obtain a set of responses at each point  $I(x,y)$ . The 2D PC at point  $I(x,y)$  is related to the local amplitude on a scale and the local energy along orientations. The 2D PC at point  $I(x,y)$  is defined as.

$$PC_{2D}(x, y) = \frac{\sum_j E_{\theta_j}(x, y)}{\varepsilon + \sum_n \sum_j A_{n,\theta_j}(x, y)} \quad (1)$$

where  $A_n, \theta_j(x, y)$  is the local amplitude on a scale  $n$  and  $E_{\theta_j}$  is the local energy along orientation  $\theta_j$ . Finally, the calculated  $PC_{2D}(x,y)$  is a real number within 0–1.

A group of collected IQA algorithms from internet are executed on different datasets to get a group of metrics and related evaluation results. Except those download algorithms, we also modify some metrics by considering phase consistency as a kind of visual weights. Firstly the original and the distorted color images after normalization are projected to the illuminant channel. Then the phase congruency map is calculated by using Gabor wavelets in a faster way. Finally, the PC map is used as a weighting function in pooling strategy of quality assessment. Experiments show that PC is very powerful for IQA, however, the running speed of PC calculation is a little bit slow. In this paper, PC enhanced metrics are named after p-, for example, we use PC to weight local MSE and PSNR, then getting PMSE and PPSNR, both improving the performance than before.

## 4 Our Constructive Works

Our task is to build an automatic model without knowledge of distortion type which works well under complex distortion situations. After comparison and analysis of previous got metrics, we select a group of metrics as the bag of features for image quality representations. A learning model using an AdaBoost-BP neural network is constructed. We choice BP network to build this fuzzy model on distorted images based on multi-metrics as a bag of features to map the subjective score MOS. AdaBoost algorithm is combined to enhance BP network, for an automatic feature selection. The key benefit of the AdaBoost algorithm is that it boosts many weak models to build a strong model, which is more robust to the distribution of the training set. In this study, the BP neural network is used as the weak learning model of the AdaBoost main frame. The training of this network is based on iterations. Every iteration results in a weak learner. During every iteration, this algorithm adaptively adjusts the errors of the weak hypotheses online depending on the evaluation of all weak learners. Finally, a linear combination of weak hypotheses can build a strong learner as the finally trained quality metric. The design details can be found in the literature [17–19]. There are two hidden layers containing  $n$  nodes, similar to the input layer, as same as the number of metrics used. The output layer is formed by one linear neural cell for prediction outcomes of the image quality. Our whole work frame can be described in Fig. 2.

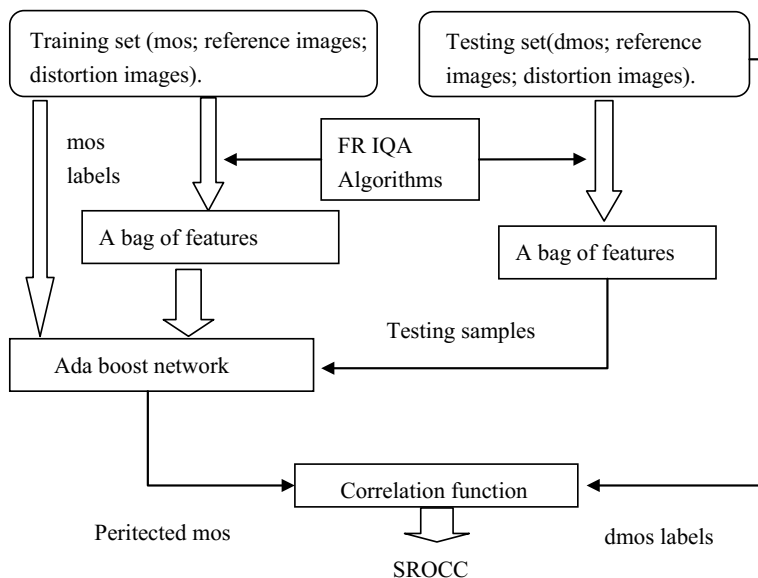


Fig. 2. Work frame of data driven IQA prediction model proposed in this paper

## 5 Experiments and Discussions

We collect a group of metrics among art of the state with related paper on the internet (<https://ece.uwaterloo.ca/~z70wang/research/>), and use these previous works as a start point of our work. The evaluation of IQA model usually is expressed by some correlation coefficients: Spearman rank correlation coefficient (SROCC), Kendall rank correlation coefficient (KROCC), Pearson correlation coefficient (PLCC). The better the performance of objective algorithm is, the closer to 1 the value of the above three correlation coefficients are. Together with RMSE (Root—mean—square error), the smaller the RMSE value is, the better the performance of the algorithm is. We evaluated those metrics (download algorithms as well as a few new PC enhanced algorithms) in indexed of SROCC. Evaluation results calculated on Datasets of TID 2013, TID 2008 and LIVE are recorded in following Table 1. Our proposed multi-metrics integrated model is also recorded in it. All above selected 9 metrics will be used as input features feed into AdaBoost BP networks for IQA prediction modeling. Image data and MOS/DMOS labels are slipped into three partitions for every database, two partitions are used as training data, and the left one is for testing. Our proposed model are trained and tested respectively on Datasets TID 2008, LIVE and TID 2013. Partitions are executed randomly, and all experimental results are got from 5 time executions. AdaBoost BP network have three parameters as the input layer neuron number, the second layer neuron number and the iteration numbers. In our experiments we fix these parameters as: iteration is 15, the input neuron number is 9 and the second layer neuron number is also 9. Our experimental results are recorded in Table 2 in four kinds of correlation indexes of SROCC, KROCC, PLCC and RMSE.

**Table 1.** Evaluation of metrics by download algorithms, a few of modified ones and our proposed multi-metrics integrated model

Metrics	SROCC		
	TID2013	TID2008	LIVE
vifp	0.7738	0.8506	0.9220
Mssim	0.6208	0.7874	0.8957
Essim	0.8035	0.8800	0.9242
Mse	0.6320	0.5531	0.8197
Pmse (MSE combining PC)	0.6779	0.7534	0.8758
Hvpsnr (PSNR combining CSF)	0.6534	0.5944	0.8754
Hvsmprnr (multi-scale hvpsnr)	0.6247	0.5612	0.8878
Psnr	0.6387	0.5514	0.8194
Ppsnr (PSNR combining PC)	0.6798	0.7576	0.8758
Multi-metrics integrated model	0.9234	0.9325	0.9499

**Table 2.** Evaluation results on different datasets of the multi-metrics integrated model

Database	SRCOO	KROCC	PLCC	RMSE
ID2008	0.9325	0.7786	0.9383	0.4260
TID2013	0.9234	0.7690	0.943	0.3770
LIVE	0.9499	0.7994	0.9631	3.8512

From Table 1, we find all metrics we considered usually work better on simple Dataset like LIVE than more complex ones like TID 2013. From Table 1, we can see MSE and PSNR are around 0.5 of SROCC in TID 2008, a litter bit better (around 0.6) in TID 2013, and the best(around 0.8) in LIVE. PPSNR and PMSE are metrics using PC map as local error weighting for global score, and both show their contribution to prior metrics in Table 1. On these three datasets, our trained model using a bag of 9 features improve the prediction performance evaluation on all these three datasets as recorded in Tables 1 and 2. From Table 2, we come to some conclusions: (1) Prediction model built on LIVE get the best perception performance; it means LIVE database is the most ease one for IQA problem. AS an independently developed dataset, LIVE is more suitable to be used as a test dataset for evaluation rather as a training dataset. (2) TID 2013 is the most challenge database, so TID 2013 is more suitable to be used as a training dataset for complex IQA problem modeling. Figure 3 shows the fit curve drawings from the same experiments as in Table 2, which also agreed with above conclusions.

In order to evaluate the generic property of our proposed model, we train and test the model on different datasets. Before evaluation, there is a problem need to be solved: the subjective measurement recorded in LIVE is DMOS rather than MOS. DMOS is from 0 to 100, and 0 is stand for reference images. The bigger the DMOS is, the worse the quality level is. However, MOS is from 0 to 9, the bigger the MOS is, the better the

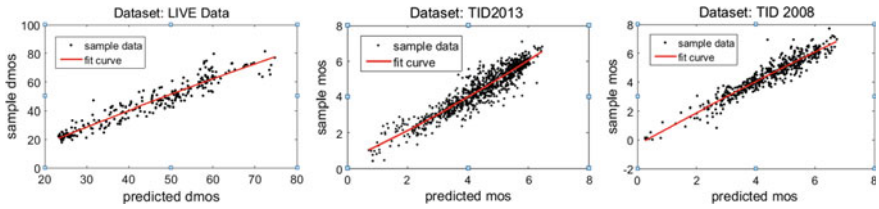


**Fig. 3.** Fit curve drawings for learned IQA model in cross over experiments on single datasets including LIVE, TID2013 and TID2008 from left to right. A bag of features (9 metrics) was used as the presentation of images

quality level is. From the literature, DMOS can be thought as the strength of MOS, so we use (100-dmos). \*0.09 to transform DMOS from 0 to 100 into 9 to 0 to map MOS value. After this transformation, we can build our model on either MOS or DMOS. There are only 5 kinds of distortion in LIVE, as well as 17 for TID 2008 and 25 for TID2013. Because that LIVE dataset is too simple to cover the distortion issues involved in TID 2008 or TID 2013, LIVE only used as test set in our crossover experiments and the evaluation results are recorded in Table 3. All records are got by the mean of 5 times running.

**Table 3.** The cross over evaluation results of our proposed multi-metrics integrated prediction model between different datasets

Train data	Test data	SROCC	KROCC	PLCC	RMSE
TID2008	TID2013	0.8294	0.6446	0.8385	0.5114
TID2013	TID2008	0.9037	0.7329	0.9156	0.4564
TID2008	LIVE	0.8456	0.6533	0.8418	0.6015
TID2013	LIVE	0.9001	0.7132	0.8798	0.6814

From Table 3, we come to some conclusions: (1) Our proposed model trained on TID 2013 work better than TID 2008. Our proposed model trained on TID 2013 got performance as 0.9037 of SROCC testing on TID 2008 and 0.9001 of SROCC testing on LIVE. Table 2 showed prediction model training and testing on partitions inside TID 2013 get 0.9234 of SROCC, this is a little bit lower than cross over inside TID 2013. So we can say TID 2013 is a good choice for training machine learning IQA model than others. Although simple dataset like LIVE could get better performance through some proper metrics, for example ESSIM or VIFP as in table, any single metrics could not perform better than our learned model on complex dataset like TID 2013 or TID 2008. So for real word complex IQA problem without clear distortion knowledge, our proposed multi-metrics integrated model is a benefit resolution option.

Figure 4 shows the fit curve drawings of experimental results from our proposed prediction model trained on TID 2103 and tested on TID 2008 and LIVE. To sum up, our proposed IAQ prediction model is a useful method to meet the requirement of real world applications.

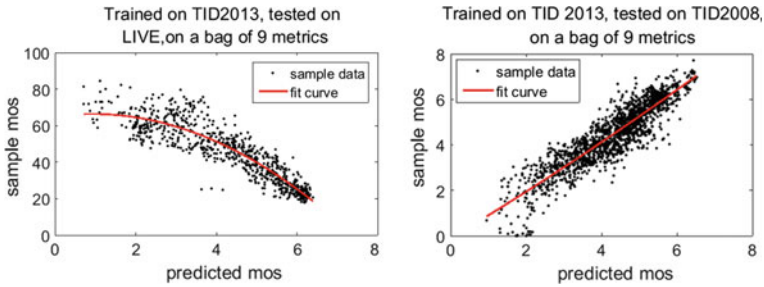


**Fig. 4.** Comparison of experiments on different Dataset. Model trained on TID 2013 get good performance when test on both LIVE dataset and TID 2008

## 6 Conclusions and Future Works

In this paper, some methods are summarized to improve image quality assessment metrics by considering human visual system. The proposed model considers some existed FR IQA methods and chooses part of them as the bag of features. A full reference image quality prediction model is proposed by using a bag of features learned by AdaBoost BP neural network. The learned prediction model can map the full reference image quality assessment presentation into an image quality score MOS/DMOS. The evaluation of the learned prediction model show up that it is better than what learned from any single metric inside the feature bag. This suggests that metrics in feature bag complement each other, and instead of thinking out more complicated metrics, we got better performance through this bag of metrics modeling. In the next step, more recent methods will be included in our comparison experiments as feature standards used in the feature bag.

**Acknowledgements.** The authors would like to thank Dr. Zhou Wang for open their precious works and collected rich resources with no restriction. This study is supported by a foundation of Key Lab of Pulp and Paper Science & technology, Ministry of Education (Shandong Province) in 2017–2018, China (0308250502).

## References

1. Barten, P. G. J. (1990). Evaluation of subjective image quality with the square-root integral method. *Journal of Optical Society of America A*, 7(10), 2024–2031.
2. Mitsa, T., & Varkur, K. L. (1993). Evaluation of contrast sensitivity functions for the formulation of quality measures incorporated in halftoning algorithms. In *IEEE International Conference on Acoustics, Speech, and Signal Processing* (Vol. 5, pp. 301–304).

3. Teo, P. C., & Heeger, D. J. (1994). Perceptual image distortion. In *IEEE International Conference on Proceedings of the Icip* (Vol. 2179, pp. 127–141).
4. Cui, L. (2012). An image quality metric based on corner, edge, and symmetry maps. In *Proceedings of the British Machine Vision Conference*.
5. Wang, Z., Bovik, A. C., Sheikh, H. R., & Simoncelli, E. P. (2004). Image quality assessment: from error visibility to structural similarity. *IEEE Transactions on Image Processing*, 13(4), 600–612.
6. Wang, Z., Simoncelli, E. P., & Bovik, A. C. (2003). Multiscale structural similarity for image quality assessment. In *Proceedings of the IEEE Asilomar Conference on Signals, Systems and Computers* (Vol. 2, pp. 1398–1402).
7. Wang, Z., & Li, Q. (2011). Information content weighting for perceptual image quality assessment. *IEEE Transactions on Image Processing A Publication of the IEEE Signal Processing Society*, 20(5), 1185–1198.
8. Morrone, M. C., Ross, J., Burr, D. C., & Owens, R. (1986). Mach bands are phase dependent. *Nature*, 324(6094), 250–253.
9. Kovsi, P.(1999). Image features from phase congruency. *Videre: Journal of Computer Vision Research*, 1(3), 1–26.
10. Huang, L., & Zou, H. (2015). Image feature extraction algorithm of multi-scale pyramid based on phase congruency. *Computer Technology & Development*, 25(3).
11. Sheikh, H. R., Bovik, A. C., & Cormack, L. (2005). No-reference quality assessment using natural scene statistics: jpeg2000. *IEEE Transactions on Image Processing*, 14(11), 1918–1927.
12. Ponomarenko, N., Lukin, V., Zelensky, A., Egiazarian, K., Carli, M., & Battisti, F. (2009). Tid 2008—A database for evaluation of full-reference visual quality assessment metrics. *Advances of Modern Radioelectron*, 10, 30–45.
13. Ponomarenko, N., Jin, L., Jeremeiev, O., Lukin, V., Egiazarian, K., Astola, J., et al. (2015). Image database tid2013: Peculiarities, results and perspectives. *Signal Processing: Image Communication*, 30, 57–77.
14. Zhang, L., Zhang, L., Mou, X., & Zhang, D. (2013). A comprehensive evaluation of full reference image quality assessment algorithms. In *IEEE International Conference on Image Processing* (pp. 1477–1480).
15. Salberg, A. B., Hardeberg, J. Y., & Jenssen, R. (2009). A hybrid image quality measure for automatic image quality assessment (Vol. 5575, pp. 91–98).
16. Ghadiyaram, D., & Bovik, A. C. (2017). Perceptual quality prediction on authentically distorted images using a bag of features approach. *Journal of Vision*, 17(1).
17. Gomezverdejo, V., Arenasgarcia, J., & Figueirasvidal, A. R. (2008). A dynamically adjusted mixed emphasis method for building boosting ensembles. *IEEE Transactions on Neural Networks*, 19(1), 3–17.
18. Korytkowski, M., Rutkowski, L., & Scherer, R. (2009). On Combining Backpropagation with Boosting. In *IEEE International Joint Conference on Neural Network Proceedings* (Vol. 33, pp. 1274–1277).
19. Liu, L., Hua, Y., Zhao, Q., Huang, H. & Bovik, A. C. (2016). Blind image quality assessment by relative gradient statistics and adaboosting neural network. *Signal Processing: Image Communication*, 40, 1–15.



# A Printing Image Restoration Method for Multiple Degradation Factors

Xiaochun Li, Yuanyuan Zhang, and Ming Zhu<sup>(✉)</sup>

Department of Material and Chemical Engineering,  
Henan University of Engineering, Zhengzhou, China  
zhuming\_printing@haue.edu.cn

**Abstract.** A printing image restoration method for multiple degradation factors which includes Salt & Pepper noise, Gaussian noise and blur is proposed in this paper. First, considering the noise density of printing image is not very high, a two-step algorithm based on gray-scale range criterion and local difference criterion are used for detecting and removing Salt & Pepper noise. The test results show that the proposed algorithm can achieve good results for restoration of most test images. For the purpose of removing Gaussian noise and image blurring, considering the principle of the edge-reserving smoothing filter, the bilateral filter and guided filter are applied to the image restoration, and on this basis, the second-time guided filter for detail-enhancement is designed and applied. The superiority of the second-time guided filter is verified by evaluating the five image restoration approaches.

**Keywords:** Image restoration · Salt & pepper noise · Gaussian noise · Guided filter

## 1 Introduction

In the process of acquisition and recording, images are usually disturbed by multiple degradation factors. The degradation occurred in image acquisition is called blur, and the one occurred in recording process is called noise [1]. To obtain higher printing quality, image restoration must be carried out in pre-press stage. At present, most of the researches on image restoration are limited to the restoration for a certain degradation factor, such as the typical image restoration methods for Salt & pepper noise [2–6]. Typical restoration methods for Gaussian noise and blurring of image include: Wiener filter, least square filter [7]. Considering the printing images are usually disturbed by multiple degradation factors, an image restoration algorithm should be designed to deal with the above degradation problems before output.

## 2 Basic Principles and Methods

### 2.1 Framework

Figure 1 shows that the workflow of the proposed image restoration approach for multiple degradation factors. In an image, the Salt & pepper noise with the extreme signal values are often independent, so the proposed image restoration framework can be divided into two main parts: The first one is responsible for the detection and removal of Salt & pepper noise. Compared with Salt & pepper noise, Gauss noise and blur are not easy to distinguish at the micro level. So in the second part, both of them are dealt with simultaneously. There are five approaches (Wiener filter, least square filter, the bilateral filter, guided filter, the second-time guided filter for detail-enhancement) for removing Gaussian noise and image blurring, the effects of them are compared and analyzed.

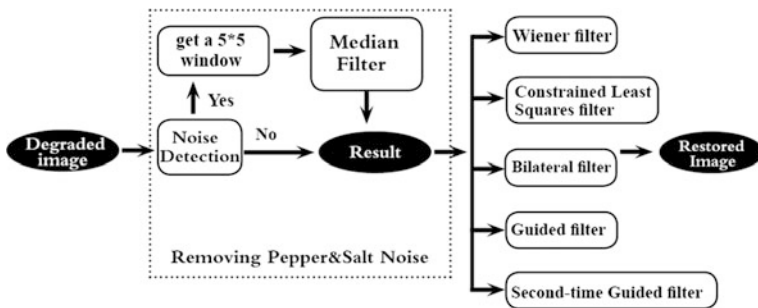


**Fig. 1.** The workflow of the proposed image restoration approach for multiple degradation factors

### 2.2 Removal of Gaussian Noise and Blurring

In this article, an algorithm based on gray-scale range criterion and local difference criterion are used for detecting and removing Salt & Pepper noise [6]. The test results show that the proposed algorithm can achieve good results for restoration of most test images. Conventional restoration methods for Gaussian noise and blurring of images include: Wiener filter, least square filter. Considering the principle of the edge-reserving smoothing filter, the bilateral filter [8] and guided filter are applied to the image restoration, and on this basis, the second-time guided filter for detail-enhancement is designed and applied.

Guided filter is one of the edge-preserving smoothing filters, it can remove halo-artifacts more effectively. As shown in Eq. (1),  $I_{input}$  represents input pixel,  $I_{output}$  represents output pixel,  $I_{guide}$  represents guidance image which can be same as  $I_{input}$ , “r” is the window radius of the guided filter. The function of parameter “eps” is similar to range filter parameter “sigma2” that in the Bilateral filter. The value of “eps” is used to control the high-variance image-edge area. Therefore, if the “eps” value is too small, the Gauss noise can not be effectively removed, but if the value is set too large,



although the Gauss noise can be removed, the edge of image is more likely to be blurred [9].

$$I_{\text{output}} = \text{guidedfilter}(I_{\text{input}}, I_{\text{guide}}, r, \text{eps}); \quad (1)$$

To protect image-details effectively in denoising, the second-time guided filter for detail-enhancement is designed and applied. The procedure is shown in Eq. (2): first, the first-time guided filter is performed on the original image to get the basic layer image  $I_{\text{base}}$ . In order to enhance image-details, the difference between  $I_{\text{base}}$  and  $I_{\text{input}}$  is multiplied by the enhancement coefficient “ $n$ ”. The result is added to  $I_{\text{base}}$  to obtain  $I_{\text{enhanced}}$ .  $I_{\text{enhanced}}$  represents the detail-enhanced image. Finally, the second-time guided filter is applied, and get the final output image  $I_{\text{output}}$ .

$$\begin{aligned} I_{\text{base}} &= \text{guidedfilter}(I_{\text{input}}, I_{\text{input}}, r, \text{eps}); \\ I_{\text{enhanced}} &= I_{\text{base}} + (I_{\text{input}} - I_{\text{base}}) * n; \\ I_{\text{output}} &= \text{guidedfilter}(I_{\text{enhanced}}, I_{\text{enhanced}}, r, \text{eps}); \end{aligned} \quad (2)$$

### 3 Assessment

This article uses the following filters to deal with the two degradation factors (Gaussian noise and blurring): Wiener filter, constrained least square filter, bilateral filter, guided filter for preserving image edge, the second-time guided filter for detail-enhancement. The test images are shown in Fig. 2. To enhance the persuasiveness of the evaluating experiment, the degradation degree of each test image is divided into 4 levels. Table 1 shows the PSNR values for the four degradation levels. From the table, we can know that for all test images, with the enhancement of degradation degree, the PSNR gradually decreases and the image distortion gradually increases.

**Table 1.** The PSNR values for the four degradation levels

Degradation degrees	Test images				
	101	102	103	104	105
Gaussian blur: 5*5 window; Gaussian noise mean: 0, variance: 0.0003	22.73	34.37	33.84	28.03	30.17
Gaussian blur: 5*5 window; Gaussian noise mean: 0, variance: 0.0006	22.50	31.78	31.48	27.28	28.99
Gaussian blur: 9*9 window; Gaussian noise mean: 0, variance: 0.0006	21.07	29.88	28.69	25.59	26.69
Gaussian blur: 9*9 window; Gaussian noise mean: 0, variance: 0.0010	20.85	28.47	27.57	25.01	25.94



Fig. 2. The thumbnails of test images used in evaluating experiments

The PSNR values between the original images and restored images with four filters are listed in Fig. 3. Wiener filtering has the worst restoration effects for all test images, the PSNR values for the restored image are even lower than the degraded image. If using Wiener filter, the noise power spectrum needs to be known in advance. The constrained least square filter and guided filter is better than Wiener, the PSNR for the corresponding restored images are higher than the degraded images. The second-time guided filter has the greatest results, especially for the test image “I03” and “I04”, their PSNR can be up to 40. This is mainly because in the case of proper threshold parameters, the second-time guided filter not only can remove Gaussian noise but also can preserve image edges. Besides, it can also enhance the image details. For the five test images, the restoration effects of “I01”, “I03” and “I04” are more obvious, and the restoration results for “I02” and “I05” are poor. It indicates that no matter what image restoration method is used, the effect is not very obvious for images with more fine edges.

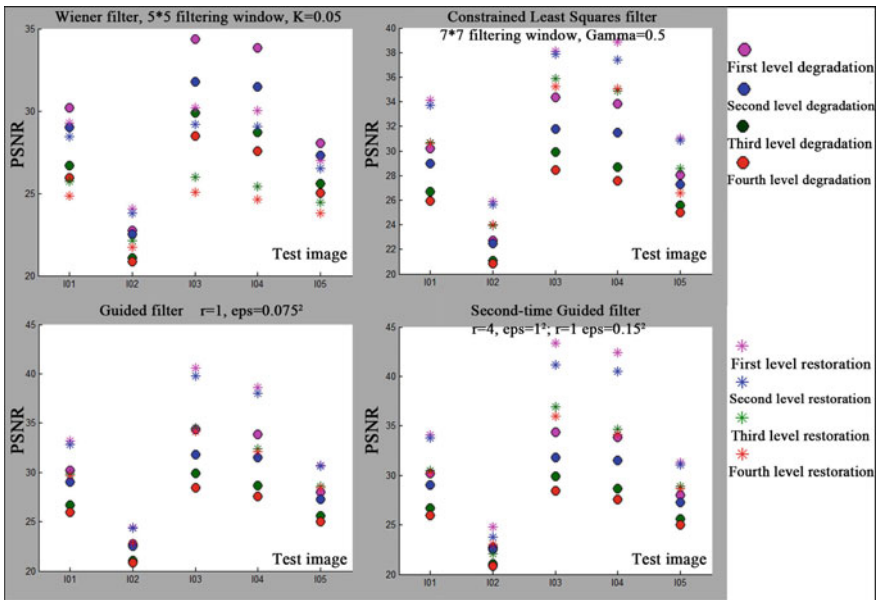


Fig. 3. The PSNR values between the original images and restored images with different filters

## 4 Conclusions

A printing image restoration method for multiple degradation factors which includes Salt & Pepper noise, Gaussian noise and blur is proposed in this paper. The method is divided into two main parts, the first part is used to detect and remove Salt & pepper noise, the second one is used to remove Gaussian noise and image blurring. The first module uses a two-step algorithm based on gray-scale range criterion and local difference criterion. In the second one, the bilateral filter and guided filter are applied to the image restoration, and on this basis, the second-time guided filter for detail-enhancement is designed and applied. The superiority of the second-time guided filter is verified by evaluating the five image restoration approaches.

## References

1. Zhang, Y. (2012). *Image engineering* (3rd ed.). Beijing: Tsinghua University Press.
2. Brownrigg, D. (1984). The weighted median filter. *Communications of the ACM*, (8), 807–818. <https://doi.org/10.1145/358198.358222/27>.
3. Hwang, H., & Haddad, R. (1995). Adaptive median filters: New algorithms and results. In *IEEE Transactions on Image Processing A Publication of the IEEE Signal Processing Society*, (4), (pp. 499–502). <https://doi.org/10.1109/83.370679/4>.
4. Wang, H., Li, Y., & Zhang, K. (2007). An image filtering algorithm based on extremum detection. *Laser & Infrared*, (10), 1117–1119. <https://doi.org/10.3969/j.issn.1001-5078.2007.10.026/37>.
5. Qiao, K., Guo, C., & Mao, D. (2011). An adaptive switch median filtering algorithm for salt and pepper noise. *Computer Applications and Software*. (10), 253–256. <https://doi.org/10.3969/j.issn.1000-386x.2011.10.073/28>.
6. Chen, J., & Zheng, S. (2012). Salt and pepper noise detection algorithm based on directional median. *Journal of Computer Applications*, (10), 2790–2792. <https://doi.org/10.3724/sp.j.1087.2012.02790/32>.
7. Wang, Z., Sun, L., Shao, X., et al. (2012). An image denoising algorithm combined with wavelet transform and wiener filtering. *Packaging Engineering*, (13), 173–178. <https://doi.org/10.19554/j.cnki.1001-3563.2016.13.031/37>.
8. Wang, N., Zhu, M., & Chen, G. (2016). A spatial gamut mapping algorithm based on bilateral filter. *Acta Electronica Sinica*, (8), 1924–1931. <https://doi.org/10.3969/j.issn.0372-2112.2016.08.022/44>.
9. He, K., Sun, J., & Tang, X. (2013). Guided image filtering. In *IEEE Transactions on Pattern Analysis and Machine Intelligence*, (6), (pp. 1397–1409). <https://doi.org/10.1109/tpami.2012.213/35>.



# Objective Aesthetic Quality Assessment for Photos

Qichuang Zeng and Quanxiang Liu (✉)

School of Printing and Package, Wuhan University, Wuhan, China  
{zengqichuang, lqx}@whu.edu.cn

**Abstract.** Nowadays, the acquisition of digital photos is becoming easier and easier, and the demand for objective assessment of the aesthetic quality of photos is growing, with the development of computer vision and pattern recognition technology, this demand is gradually being explored. After studying the effect of gray interval distribution on the aesthetic quality of photos, an objective assessment method for the aesthetic quality of photographs which considers both global and local features is proposed. For the whole features, the gray interval and line angles features are extracted. The subject areas are extracted from the photos through clarity detection method, then calculate the clarity, lighting and the calculation of rule of thirds in the subject area, as to extract the local features. A total of 18 features including the whole and the local features, using LIBSVM to calculate and train, and to test this method on CUHKPQ image dataset, then we get a good performance. It can be concluded that the combination of 18 features in the objective assessment of photos aesthetic quality can meet the demand of practical application.

**Keywords:** Aesthetic quality · Objective assessment · Features extraction · Natural photos

## 1 Introduction

With the development of computer science, it is hoped to achieve objective aesthetic quality assessment for the photos with the aid of computer science, helping people to automatically complete work, such as automatic arrangement for a large number of photos according to the aesthetic quality of high and low, automatically screening out high aesthetic quality photos, etc. As a result, the objective aesthetic quality assessment method based on computer vision and pattern recognition techniques arises at the historic moment.

Since Hoernig [1] proposed the computable direction of photos aesthetic quality assessment, relevant work such as Tang et al. [2] extracted global and local features for aesthetic quality assessment and achieved good results. Datta et al. [3] proposed 56 low-level and high-level features for the aesthetic quality assessment, and used SVM and classification tree to automatically classify photos of high and low aesthetic quality. Ke et al. [4] designed high-level aesthetic features. Wong et al. [5] used a significantly enhanced method to classify photos with high or low aesthetic quality. Yao et al. [6] discovered the important influence of composition on the aesthetic quality of photos.

Xiao et al. [7] built an online rating system for the aesthetic quality of photos. Due to the strong subjectivity in the process of photos aesthetic quality assessment, factors that affect the aesthetic quality of subjective assessment with composition, light, clarity, and various aspects of factors, and these factors is hard to quantify by the right way, so the features of the calculation according to different ways have different degree of impact, so the focus of the research is how to find out the features which are most closely related to the aesthetic quality, how to make a better quantitation on these features, and thus to make a better objective photos aesthetic quality assessment. This paper considers local and global features of photos to put forward 18 features to the assessment of aesthetic quality, and high accuracy was obtained.

## 2 The Whole Features

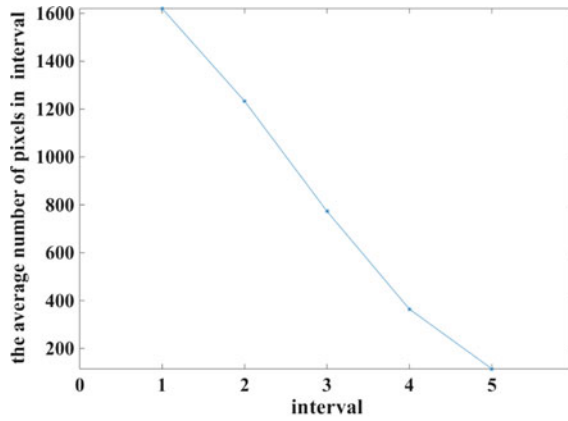
### 2.1 Gray Interval

When taking a photo, if the lighting distribution of the photo is properly controlled, so that the light of the photo is smooth and natural, it is conducive to improving the aesthetic quality of the photo. If ignoring the control of the light, such as the distribution of the light is not natural, then the aesthetic quality of the photos will inevitably decline.

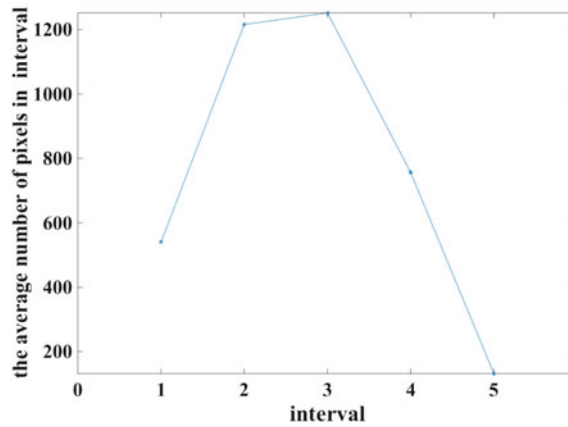
Converting the color photos to gray photos, then dividing the grey value into five intervals  $I_i = [v_{i-1}, v_i]$ , with  $1 \leq i \leq 5$ , the five intervals are black interval  $I_1$ , shadows interval  $I_2$ , midtone interval  $I_3$ , highlight interval  $I_4$ , and white interval  $I_5$ . There is  $v_0 = 0$ ,  $v_1 = 19$ ,  $v_2 = 58$ ,  $v_3 = 187$ ,  $v_4 = 237$ ,  $v_5 = 255$ . Counted the number of pixels in each interval of the photo, and then calculated the average pixel number of each grayscale interval [8]:

$$p_i = \frac{n_i}{v_i - v_{i-1}}, i = 1, \dots, 5 \quad (1)$$

On the basis of reference [8], we did a further work with statistical calculation and optimization in photos dataset CUHKPQ [2] and got the statistical figure as shown in Fig. 1, namely the gray distribution of high and low aesthetic quality photos. This shows great difference between these two kind of gray interval, in the high aesthetic quality photo gallery, the average number of pixels in  $I_1$  is the largest, and then in turn with  $I_2$ ,  $I_3$ ,  $I_4$ , and  $I_5$ . We analyzed that it was because that the high aesthetic quality photo's grayscale range was generally larger and evenly, and dark tone information was more likely to attracted people. In the low aesthetic quality photo gallery, the average number of pixels in  $I_3$  and  $I_2$  are the largest, next in turn are  $I_4$ ,  $I_1$ , and  $I_5$ . We analyzed that shadow and midtone were relatively larger than other interval, but the average sizes were larger too, it can easily be seen that the most grayscale of pixels concentrated in these two interval, means that the range of grayscale obtained by the photo was relatively small and concentrated, other intervals had relatively few pixels and contained relatively little information, leading to the lower aesthetic quality. Therefore, the features used to distinguish two types of photos can be obtained from the grayscale intervals.



(a) High aesthetic quality photos



(b) Low aesthetic quality photos

**Fig. 1.** The gray distribution of high and low aesthetic quality photos

As Fig. 1 shown that normally the average number size of each gray scale interval in high aesthetic quality photos are  $p_1 > p_2 > p_3 > p_4 > p_5$ , but that of low aesthetic quality photos are  $p_3 > p_2 > p_4 > p_1 > p_5$ , so we define the features with  $F_1 = p_1 - p_2$ ,  $F_2 = p_2 - p_3$ ,  $F_3 = p_1 - p_3$ ,  $F_4 = p_1 - p_4$ , to distinguish these two kinds of different photos. We can easily know that the ideal situation should be  $F_1 > 0$ ,  $F_2 > 0$ ,  $F_3 > 0$ ,  $F_4 > 0$  in the high aesthetic quality photos, and  $F_1 < 0$ ,  $F_2 < 0$ ,  $F_3 < 0$ ,  $F_4 < 0$  in the low aesthetic quality photos. This is often difficult in practice, but we know that the larger the four  $F_1$ ,  $F_2$ ,  $F_3$ ,  $F_4$  are, the higher the aesthetic quality of the photos are.

## 2.2 Line Angle

When taking a high aesthetic quality photo, the treatment of lines should not be careless. The use of lines can highlight the subject of a photo and increase the

attractiveness of it. Generally, the lines are orderly, that is, the line angles are concentrated in a certain range. Given photo  $I$ , calculate the horizontal gradient map  $G_x(x, y)$  and vertical gradient map  $G_y(x, y)$ , and calculate the gradient direction of each pixel in the photo [9]:

$$\theta(x, y) = \arctan\left(\frac{G_y(x, y)}{G_x(x, y)}\right), \theta(x, y) \in [0, 360^\circ) \quad (2)$$

Dividing the gradient direction  $\theta(x, y)$  into 9 equal intervals so we can get the histogram of gradient direction  $\text{hist}(i)$ , namely the features  $F_{4+i} = \text{hist}(i)$ ,  $i \in 1, 2, \dots, 9$ . It can be seen that when the gradient direction is concentrated in a certain direction range, the aesthetic quality of the photo is higher.

### 3 Local Features

#### 3.1 Extraction of the Subject Area

It is called as the subject area where the observers notice in the photo. When taking a photo, photographer will basically keep the subject area clear, because it is the most important area in a photo, while other areas (that is, the background area) are often blurred, to reduce the interference of the subject area. When assessing the aesthetic quality of photos by human eyes, subject area is where the eyes concentrated most, so the assessment results of photo is affected most by this area, when making objective assessment of aesthetic quality in a photo, we should focus on this area.

Since subject area was usually clear, and background area was often blurred, so we calculated the subject area of photos with clarity in this paper, and then calculated some of the features with the subject area. In this paper, the Clarity-Based Subject Area Extraction method [2] was used to extract the photo's subject area because it's good performance.

We defined a kernel of  $f_k(k = 1, 2, \dots, 50)$  with size  $k \times k$  to calculate the convolution of the original photo respectively, and got 50 images with different degree of blur. Set  $d_x = [1, -1]$ ,  $d_y = [1, -1]^T$  to calculate the horizontal and vertical gradient of each blurred images, and got:

$$p_{xk} \propto \text{hist}(\mathbf{I} * f_k * d_x), p_{yk} \propto \text{hist}(\mathbf{I} * f_k * d_y) \quad (3)$$

For each pixel in the original photo, the likelihood of the rectangle region containing the pixel in each blurred image was calculated, that was:

$$L_k(i, j) = \sum_{(i', j') \in \Omega(i, j)} (\ln p_{xk}(I_x(i', j')) + \ln p_{yk}(I_y(i', j'))) \quad (4)$$

where  $I_x(i', j')$  and  $I_y(i', j')$  was the horizontal and vertical gradient of pixels in the rectangular area  $\Omega(i, j)$  of the original photo pixel  $(i, j)$ .

Set

$$k^*(i,j) = \arg \max_k L_k(i,j) \quad (5)$$

When  $k^*(i,j) = 1$ , denoted that the pixel was a clear pixel, otherwise it was a blurred pixel, and thus the subject area of the photo was extracted. The subject area of the photo was optimized by convex hull and super pixel processing.

As shown in Fig. 2, the left is the original photo, and the right is the extracted subject area map.



**Fig. 2.** The left is the original photo, the right is the extracted subject area map

### 3.2 Clarity

The subject area which extracted with clarity is relatively clearer than the photo's background area, but different photo's subject area have different degree of clarity. Generally, the subject area is very clear in high aesthetic quality photo, and often the aesthetic quality may decline if it is not clear. So the clarity of the subject area of photo can distinguish the aesthetic quality of photo.

For the obtained subject area, calculated the clarity with [8]:

$$A = \frac{\sum_{(i,j) \in R \wedge M(i,j) > T} M(i,j)}{|R|} \quad (6)$$

where  $T$  is a given threshold,  $|R|$  is the number of pixels in the subject area  $R$ , and  $M(i,j)$  is:

$$M(i,j) = \sqrt{G_x^2(i,j) + G_y^2(i,j)} \quad (7)$$

where  $M(i,j)$  is Tenengrad gradient,  $G_x$  and  $G_y$  is the  $x$  and  $y$  direction gradient calculated by Sobel operator. Finally, the clarity features of the photos are obtained with  $F_{14} = A$ .



### 3.3 Lighting

Most high aesthetic quality photos tend to stress the subject area of the photos, the performance is that the brightness in the subject area is brighter than the background area, or else the photos' aesthetic quality will fall, so the using of light is often not the same in different aesthetic quality photos, which can be defined as feature  $F_5$ . The ratio between the average brightness of the subject area and the average brightness of the background area is taken as one of the features to judge the beauty of photos [10], that is:

$$F_{15} = \ln\left(\frac{B_f}{B_b}\right) \quad (8)$$

where  $B_f$  is the average brightness of the subject area, and  $B_b$  is the average brightness of the background area. Statistically, the  $F_5$  in high and low aesthetic quality photos are distributed in the range of [0.03, 0.20] and [0.00, 0.06] respectively.

### 3.4 Rule of Thirds

Using good method of composition can take a photo with high aesthetic quality, the most popular composition method is rule of thirds. As shown in Fig. 3, dividing the height and width of a photo into three equal parts, then the four intersection points are the most beautiful point on vision, photographer usually locate the subject area in one of the four intersection points.

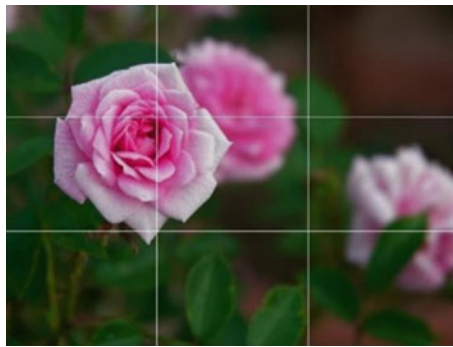
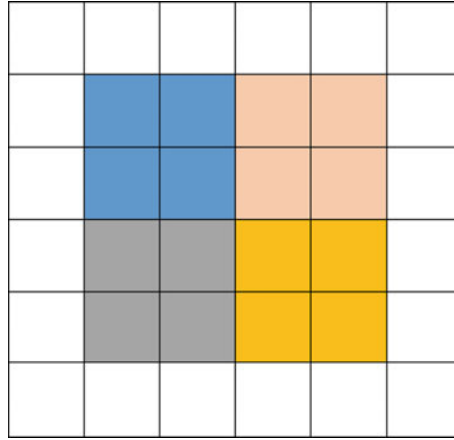


Fig. 3. Rule of thirds

By calculating the relationship between the subject area in the photo and the four intersections, the aesthetic quality of the photo can be distinguished. The method in this paper was to divide the height and width of the photo into six equal parts, as shown in Fig. 4, so that the four intersections were at the center of the four same color areas. The features were obtained by calculating the ratio of the area of the subject area in the four regions to the area of the region:



**Fig. 4.** The calculation of rule of thirds

$$F_{16} = \max_{i=1,2,3,4} a_i \quad (9)$$

It can be seen that the larger  $F_{16}$  is, which means the more concentrated the subject area is at a certain intersection area, and the more conform the photo is with the rule of thirds, then the higher the aesthetic quality of the photo is. It can be seen that the subtraction between the maximum ratio and the minimum ratio is also an important feature:

$$F_{17} = \max_{i=1,2,3,4} a_i - \min_{i=1,2,3,4} a_i \quad (10)$$

Because the bigger  $F_{17}$  is, the more concentrated the subject area is, and the less scattered it is. When taking photos with close-up objects, the subject area accounts for a larger area, causing  $F_{17}$  less than a certain value, the composition method does not comply with the rule of thirds, but if the more the subject area in the middle of the photo, the higher aesthetic quality the photo is. Therefore, we have feature:

$$F_{18} = \frac{1}{4} \sum_{i=1,2,3,4} a_i \quad (11)$$

That is, the ratio of the total area of the subject area in the four color areas to the area of the four areas. The higher the ratio is, the more concentrated the subject area is in the center of the photo, and the higher the aesthetic quality of the photo is. It can be seen that when shooting a non-near object, feature  $F_{18}$  is less than a certain value, and the better the photo should be in accordance with the rule of thirds.

## 4 Experiment and Analysis

LIBSVM [11] is a simple, easy to use and efficient software for SVM classification and regression, which is used in this paper for data training and testing. CUHKPQ [2] dataset contains 17673 photos with manually labeled ground truth as two categories of aesthetic quality as “high” and “low”, these two kind of photos are subdivided into seven categories, that are “animal”, “architecture”, “human”, “landscape”, “night”, “plant”, and “static”.

Randomly selected half of the high and low aesthetic quality photos of each category of the photo dataset CUHKPQ as training group, the other half as test group, and did the same selection on all photos. Calculated the all 18 features in the training group, and trained the data in LIBSVM, to verify the accuracy of this method in the test group. In order to ensure the accurate of the experiment, we repeated this experiment 10 times, and calculated the average of the results of these 10 times experiment as a final assessment accuracy of this method.

When compared with other methods, in order to ensure the objectiveness and accuracies of the comparing results, reducing the interference of other factors, we took the methods which proposed by Datta et al. [3], Ke et al. [4] and Luo et al. [10], with the completely same experimental conditions as our one, to test in the photo dataset CUHKPQ, results were obtained as shown in Table 1. In the aesthetic assessment of all categories of photos, the accuracies of our method were higher than 80%, in six categories namely “animal”, “human”, “landscape”, “night”, “plants” and “static”, as well as for all the photos, the accuracies of our method was the highest, only in the category of “architecture”, our method’s accuracy was lower than Ke et al. but this category had the highest accuracy in Ke et al. and lowest accuracy in our method. Our method focused on the assessment of all photos, and Ke et al. was more targeted in this category so it had a better performance than ours. Our method had the highest accuracy of 86.54% in “static”, and accuracy of 81.62% for the lowest in “animals”, suspecting that maybe something such as animal hair causing the low accuracy, while the extraction of subject area is consistent with the actual situation in “static”, making a higher accuracy.

**Table 1.** Comparison with other methods

Categories	Animal (%)	Architecture (%)	Human (%)	Landscape (%)	Night (%)	Plant (%)	Static (%)	All (%)
Datta et al. [3]	78.61	73.86	76.94	77.53	64.21	76.38	71.74	77.92
Ke et al. [4]	77.51	<b>85.26</b>	79.08	81.70%	73.21	80.93	78.29	79.44
Luo et al. [10]	81.61	73.86	77.94	77.53	64.21	82.38	81.74	77.92
Our proposed	<b>81.62</b>	81.84	<b>84.79</b>	<b>81.81</b>	<b>84.06</b>	<b>85.65</b>	<b>86.54</b>	<b>82.45</b>

## 5 Conclusions

Owing to the photos aesthetic quality assessment has a very strong subjectivity, even if is a subjective assessment of the human eye, different people due to reasons such as personality, knowledge, the aesthetic quality assessment with the same photo will be different, so it can't distinguish the absolute aesthetic quality of high or low. Therefore, the screening and sorting of a large number of photos is not the same as the appreciation of photographic works, and the high accuracy can meet the requirements. The experimental results showed that the combination of 18 features proposed in this paper can be used for the objective assessment of the aesthetic quality of photos, which has achieved a high accuracy and can meet the needs of practical application.

## References

1. Hoenig, F. (2005). Defining computational aesthetics. In *Computational Aesthetics 2005: Eurographics Workshop on Computational Aesthetics in Graphics, Visualization and Imaging 2005*, Girona, Spain, May. DBLP: 13–18.
2. Tang, X., Luo, W., & Wang, X. (2013). Content-based photo quality assessment. *IEEE Transactions on Multimedia*, 15(8), 1930–1943.
3. Datta, R., Joshi, D., Li, J., et al. (2006). Studying aesthetics in photographic images using a computational approach. In *European Conference on Computer Vision* (pp. 288–301). Berlin, Heidelberg: Springer.
4. Ke, Y., Tang, X., & Jing, F. (2006). The design of high-level features for photo quality assessment. In *2006 IEEE Computer Society Conference on Computer Vision and Pattern Recognition* (Vol. 1, pp. 419–426). IEEE.
5. Wong, L. K., & Low, K. L. (2009). Saliency-enhanced image aesthetics class prediction. *IEEE International Conference on Image Processing* (pp. 993–996). IEEE Press.
6. Yao, L., Suryanarayan, P., Qiao, M., et al. (2012). OSCAR: On-site composition and aesthetics feedback through exemplars for photographers. *International Journal of Computer Vision*, 96(3), 353–383.
7. Xiao, H., Xiao, H., & Eckert, C. (2013). OPARS: Objective photo aesthetics ranking system. In *European Conference on Information Retrieval* (pp. 861–864). Springer Berlin Heidelberg.
8. Song, C., Zhou, B., & Guo, W. (2016). Aesthetic quality assessment of photographic images. In *2016 12th World Congress on Intelligent Control and Automation (WCICA)* (3088–3093). IEEE.
9. Xie, Y., Chen, Z., & Ye, D. (2017). Image aesthetic quality scoring method based on feature complementation. *Pattern Recognition and Artificial Intelligence*, 30(10), 865–874.
10. Luo, Y., & Tang, X. (2008). Photo and video quality evaluation: Focusing on the subject. *Computer Vision–ECCV* 386–399.
11. Chang, C. C., & Lin, C. J. (2011). LIBSVM: A library for support vector machines. ACM.



# Design and Analysis of Switch Median Filters for Salt and Pepper Noise

Ming Zhu<sup>(✉)</sup>, Bowei Liu, Mengfei Wang, and Yu Lu

Department of Material and Chemical Engineering,  
Henan University of Engineering, Zhengzhou, China  
zhuming\_printing@haue.edu.cn

**Abstract.** An algorithm based on signal local difference and an algorithm based on signal directional difference for detecting salt and pepper noise are designed in this article. Both of them belong to two-stage noise detection algorithms, and the first-stage detection for both is based on gray-scale range criterion. The difference between the two algorithms embodies in the second-stage detection. The former is based on local difference criterion, and the later is based on directional difference criterion. In the section of algorithm evaluation, first, the optimal parameter settings for the two algorithms are determined through analysis and experiments. Then, the denoising effects of the two algorithms are evaluated by denoising the test images with different noise density. The evaluation results show that the algorithm based on directional difference has better performance than the algorithm based on local difference. For both of the two algorithms, the denoising effects are inversely proportional to noise density. But more importantly, the two algorithms may be prone to misjudge the image-edge pixels or detail pixels as noise points. This will be the main improvement direction of the switch median filtering algorithm in the future.

**Keywords:** Image denoising · Salt and pepper noise · Median filter · Image edge · Image detail

## 1 Introduction

The generation of salt and pepper noise is usually caused by the faults and defects of image sensors, transmission channels or decoding systems [1]. Because the salt and pepper noise pixels often have the similar characteristics as the normal pixels at the edges of image, in order to protect image-details and edges, the nonlinear median filtering algorithm is first used to detect and remove the salt and pepper noise. Then on this basis, weighted median filtering algorithm [2, 3] and adaptive median filtering algorithm are proposed [4, 5]. These algorithms above also modify the normal pixels when filtering noise points. It may results in blurring. For the problem, in recent years, the idea of switch median filtering is proposed and studied [6–9]. Such approaches first need to determine whether each pixel is a noise point or a normal pixel, and only noise points need to be filtered. It can avoid blurring of image-edges to the greatest extent [10]. This idea has been widely adopted.

In this article, considering the idea of signal local difference, an algorithm based on gray-scale range criterion and local difference criterion for detecting salt and pepper noise is designed. Considering the idea of signal directional difference, another one based on gray-scale range criterion and directional difference criterion is designed. Both of them belong to two-stage noise detection algorithms, and the first-stage detection for both is based on gray-scale range criterion, which is a simple method of extreme value judgment. The difference between the both embodies in the second-stage detection. The optimal parameter settings for the two algorithms are determined through analysis and experiments. In the assessment, by means of the test images with different noise density, the denoising effects of the two algorithms are evaluated and analyzed.

## 2 The First Algorithm

### 2.1 Gray-Scale Range Criterion

Salt & Pepper noise is a kind of impulse noise. The values of pixels contaminated by Salt & pepper noise are often near the extremum value 0 or 255. If all the extremum pixels are considered to be noise points, some normal extreme points like edges may be misjudged as noise points. It will greatly increase the detection error rate, and destroy image-edge. It is not reliable to judge whether a pixel is noise point by extremum. The extreme pixels can only be seen as suspicious noise point. So, it is necessary to detect the noise point for the second level. In this article, the first-level detection is based on gray-scale range criterion. Suppose the gray-scale range of image is  $[L_{\min}, L_{\max}]$ , when a pixel's value is within  $[L_{\min}, T_g]$  or  $[L_{\max}-T_g, L_{\max}]$ , it just can just be seen as a suspicious noise point.  $T_g$  represents the threshold, the larger the value is, the more likely the extreme pixel is judged as a suspicious noise point.

### 2.2 Local Difference Criterion

In order to reduce detection error rate and preserve image-edges, the second-level detection is based on local difference criterion. The Salt & Pepper noise point tends to be isolated, and there is great gray difference between it and most of the other pixels in its neighborhood. Therefore, the threshold parameter  $T_v$  is used for determining whether the gray difference between the suspicious noise point and its neighborhood pixel is large enough, and another threshold  $T_n$  is set up to determine whether the number of neighborhood pixels which can satisfy the above condition are large enough. If the value of a suspicious noise pixel satisfies Eq. (1), it can be determined that the pixel is a Salt & pepper noise point.

$$\frac{\#[|f(x, y) - f(s, t)| > T_v]}{\#[N(x, y)]} > T_n \quad (1)$$

The above two criteria can be expressed in Eq. (1). The neighborhood of a suspicious noise point at coordinate position  $(x, y)$  can be represented as  $N(x, y)$  in  $5 * 5$

window, and its adjacent pixel at (s, t) is f(s, t). The symbol #[.] represents the number of pixels satisfied the condition. If a pixel is judged to be a noise point, in order to reserve the image-details, we use the median filter to remove it. Considering a large-size filtering window may cause a large amount of calculation, and a small filtering window can protect image-details better. So, a 5 \* 5 filtering window is proposed in this article.

### 3 The Second Algorithm

The second algorithm designed in this article is based on signal directional difference. Its first-stage detection is also based on gray-scale range criterion, which is same as the way in Sect. 2.1. But its second-stage detection is based on directional difference.

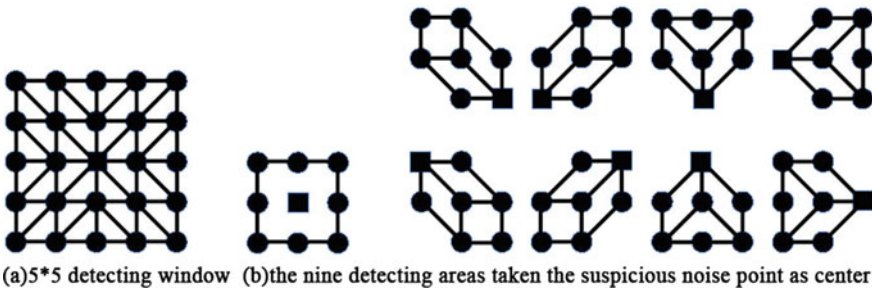


Fig. 1. A filtering window for 5 \* 5 size and the nine detecting areas

First, we set up 9 detection areas in a 5 \* 5 noise detection window (as shown in Fig. 1a), including a 3 \* 3 detecting area (8 pixels in total) centered at the suspicious noise point and 8 other detecting areas (6 pixels in each area) with the vertex of the suspicious noise point, as shown in Fig. 1b. Then, the gray median for each detecting area (exclude the suspicious noise point) needs to be calculated, as expressed in Eq. (2). “median[.]” represents the median calculation for a detection area, “f<sub>k</sub>” represents the set of gray values (exclude the suspicious noise point) in the k th detection area (k = 1 ~ 9). “A<sub>k</sub>” is the gray median for the k th detection area. In a detecting area, if the number of pixels participated in median calculation is even, its median can be set to the gray mean of the two middle pixels after sorting.

$$A_k = median[f_k] \tag{2}$$

The last step is determination of noise point: ① The absolute difference between the gray values of the suspicious noise point “suspicious\_gray” and “A<sub>k</sub>” are calculated and represented as “d<sub>k</sub>”; ② The value of “d<sub>k</sub>” related to each detecting area needs to be compared with a threshold “T”, and we can get the number of “d<sub>k</sub>” greater than “T”, it is represented as “num”; ③ If the “num” is bigger than another specified threshold



**Fig. 2.** The thumbnails of test images used in evaluating experiments

“ $T_{num}$ ”, the suspicious noise point will be determined as noise pixel “noise\_signal”, otherwise it will be seen as a normal pixel “normal\_signal”.

## 4 Assessment and Analysis

### 4.1 Evaluation of the First Algorithm

The proposed algorithms are simulated by means of Matlab7.11 for evaluation. This article selects 4 test images as shown in Fig. 2, and adds the salt and pepper noise with different noise densities “0.01, 0.03, 0.05 and 0.07”. The MATLAB command for adding the salt and pepper noise with noise density “0.01”: “imnoise (image, ‘salt & pepper’, 0.01)”. In the first-stage of the noise detection, based on the extreme characteristic, we can set the value of the threshold “ $T_g$ ” to 25.

The analysis shows that the value of “ $T_v$ ” should not be set too large when “ $T_n$ ” is constant. This is because there are some Salt noise points with extremely high luminance in bright area. And there are also Pepper noise points with extremely low luminance in dark area. Although there is a little visual difference between the noise points and the normal signal points in the same area, if  $T_v$  is large enough, these noise points cannot be detected. If  $T_v$  is too small, the number of pixels which have larger difference between the center pixel and its neighborhood than  $T_v$  will increase. Some normal extreme points like image-edge pixels may be misjudged as noise points. This will enhance the false detection rate and destroy the image-edge. Therefore, based on a large number of tests, the parameters “ $T_n$ ” and “ $T_v$ ” are limited in the range of [0.5, 0.7] and [20, 30] respectively in this article.

In Fig. 3a, first, when “ $T_g = 25$ ,  $T_v = 20$ ,  $T_n = 0.5$ ”, with the increase of noise density, for any test images, PSNR before and after denoising gradually decreases. It indicates the denoising effect also gradually decreases. But with the increase of noise



density, the running time of the algorithm (not listed in the article for saving space) gradually increases. It verifies that the increase of noise points will also increase the time for detecting and filtering noise pixels; Second, it can be found that the denoising effect for test image “I01” is best according to the distribution of PSNR values as shown in Fig. 3a. Its PSNR value for each noise density can reach more than 40, It indicates that images before and after denoising can hardly be distinguished visually. The denoising effect for test image “I04” is worst. The analysis shows that the normal points at tiny image-edge and detail are easily to be misjudged as noise points, as shown in the two areas of Fig. 4. Taken a tiny detail pixel (gray value: 6) in area 1 as center, in this detecting window, the percentage of neighboring pixels have gray difference of more than 20 from the central pixel has exceeded 50%. As a result, the normal pixel is misjudged as noise point. In like manner, the tiny edge pixel with gray value of 22 is also detected as noise point mistakenly.

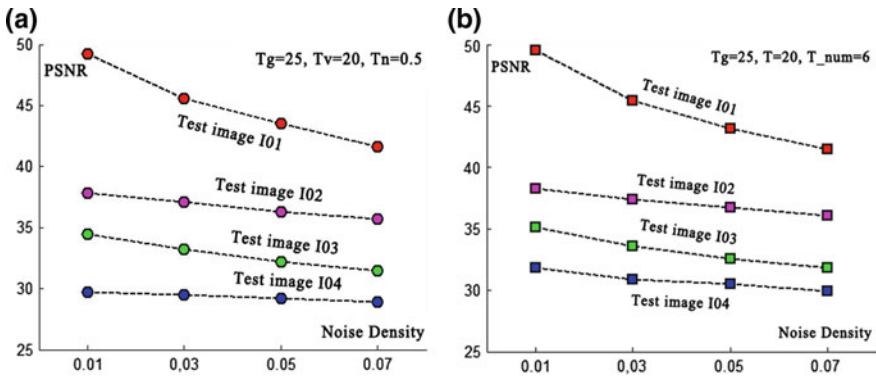


Fig. 3. The noise-removing effects based on local signal difference (a) and directional difference (b)

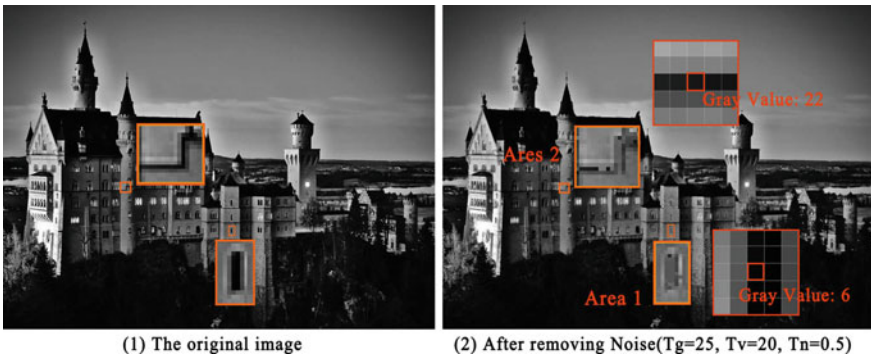


Fig. 4. The case for detecting salt & pepper noise at image-edge and detail (“I04”)

## 4.2 Evaluation of the Second Algorithm

The second algorithm is based on signal directional difference. Its first-stage detection is also based on gray-scale range criterion, which is same as the way in Sect. 2.1. So the threshold parameter “ $T_g$ ” is also set to 25. The key of the second algorithm is the setting of threshold parameters “ $T$ ” and “ $T_{num}$ ”. By analysis, we can find the parameter “ $T$ ” can control the difference threshold between the central pixel and its neighborhood. Its function is similar to “ $T_v$ ” in Sect. 2.1. This article proposes “ $T = 20$ ”. The parameter “ $T_{num}$ ” can control the percentage threshold of pixels which have large local gray difference in detecting window. Its function is similar to “ $T_n$ ” in Sect. 2.1. Through a large number of experiments, it can be found that PSNR gradually increases with the increase of “ $T_{num}$ ”. When “ $T_{num}$ ” reaches 6, PSNR will vary a little (maybe decrease), even if it continues to increase the “ $T_{num}$ ”. In this article, we proposes  $T_{num} = 6$ .

Figure 3b shows that the noise-removing effects based on directional difference. The threshold parameters are set as following:  $T_g = 25$ ,  $T = 20$ ,  $T_{num} = 6$ . The PSNR distribution is similar to that in Fig. 3a. For any test images, with the increase of noise density, the PSNR before and after denoising gradually decreases. It indicates the denoising effect also gets weaker. Through careful observation and comparison, we can find the PSNR values in Fig. 3b are slightly higher generally than that in Fig. 3a. It indicates that the algorithm based on directional difference is better than the other one based on local difference. For the test images “I03” and “I04”, there will still be misjudgment of edges and detail pixels. It will be main improving direction of the algorithm in the future.

## 5 Conclusions

Switch median filters are very suitable for detection and removal of the salt and pepper noise. An algorithm based on signal local difference and an algorithm based on signal directional difference for detecting salt and pepper noise are designed in this paper. Both of them belong to two-stage noise detection algorithms, and the first-stage detection for both is based on gray-scale range criterion. The difference between the two algorithms embodies in the second-stage detection. The former is based on local difference criterion, and the later is based on directional difference criterion. In the section of algorithm evaluation, first, the optimal parameter settings for the two algorithms are determined through analysis and experiments. Then, the denoising effects of the two algorithms are evaluated by denoising the test images with different noise density. The evaluation results show that the algorithm based on directional difference has better performance than the algorithm based on local difference. For both of the two algorithms, the denoising effects are inversely proportional to noise density. But more importantly, the two algorithms may be prone to misjudge the image-edge pixels or detail pixels as noise points. This will be the main improvement direction of the switch median filtering algorithm in the future. It verifies the structural similarity between them.

**Acknowledgements.** This article is founded by the National Natural Science Foundation of China (project number: 61301231) and the Young Backbone Teachers Training Program of Henan Province in China (project number: 2017GGJS154).

## References

1. Zhang, Y. (2012). *Image engineering* (3rd ed.). Beijing: Tsinghua University Press.
2. Brownrigg, D. (1984). The weighted median filter. *Communications of the Acm*, 807–818. [https://doi.org/10.1145/358198.358222/27\(8\)](https://doi.org/10.1145/358198.358222/27(8)).
3. Yang, R., Lin, Y., Gabbouj, M., et al. (1995). Optimal weighted median filtering under structural constraints. *IEEE Transactions on Signal Processing*, 591–604. [https://doi.org/10.1109/78.3706151995/43\(3\)](https://doi.org/10.1109/78.3706151995/43(3)).
4. Hwang, H., & Haddad, R (1995). Adaptive median filters: New algorithms and results. In *IEEE Transactions on Image Processing A Publication of the IEEE Signal Processing Society* (pp. 499–502). [https://doi.org/10.1109/83.370679/4\(4\)](https://doi.org/10.1109/83.370679/4(4)).
5. Ni, C., Ye, M., & Chen, X. (2006). An improved adaptive median filter Algorithm. *Journal of Image and Graphics*, 672–678. [https://doi.org/10.3969/j.issn.1006-8961.2006.05.011/11\(5\)](https://doi.org/10.3969/j.issn.1006-8961.2006.05.011/11(5)).
6. Qiao, K., Guo, C., & Mao, D. (2011). An adaptive switch median filtering algorithm for salt and pepper noise. *Computer Applications and Software* (pp. 253–256). [https://doi.org/10.3969/j.issn.1000-386x.2011.10.073/28\(10\)](https://doi.org/10.3969/j.issn.1000-386x.2011.10.073/28(10)).
7. Chen, J., Zheng, S., Yu, L., et al. (2013). Improved Algorithm for adaptive median filter with multi-threshold based on directional information. *Journal of Electronic Measurement and Instrument*, 156–161. [https://doi.org/10.3724/sp.j.1187.2013.00156/27\(2\)](https://doi.org/10.3724/sp.j.1187.2013.00156/27(2)).
8. Chang, D., Yang, F., & Zhao, G., et al. (2012). Salt and pepper noise filtering algorithm based on two stage noise detection. *Laser & Infrared*, 100–104. [https://doi.org/10.3969/j.issn.1001-5078.2012.01.022/42\(1\)](https://doi.org/10.3969/j.issn.1001-5078.2012.01.022/42(1)).
9. Chen, J., & Zheng, S. (2012). Salt and pepper noise detection algorithm based on directional median. *Journal of Computer Applications*, 2790–2792. [https://doi.org/10.3724/sp.j.1087.2012.02790/32\(10\)](https://doi.org/10.3724/sp.j.1087.2012.02790/32(10)).
10. Zhang, C., Chi, J., Zhang, Z., et al. (2010). Removing noise of color images based on edge detection and bilateral filter. *Acta Electronica Sinica*, 38(8), 1776–1783.



# Color Transfer Based on Visual Saliency

Minghua Fan<sup>1</sup>, Zhijiang Li<sup>1(✉)</sup>, and Jiaxian Long<sup>2</sup>

<sup>1</sup> School of Printing and Packaging, Wuhan University, Wuhan, China  
lizhijiang@whu.edu.cn

<sup>2</sup> The Company of H3C, Hangzhou, China

**Abstract.** Color transfer is usually used to match the color between input images and reference images to change the global color performance or local color of some specified object. The technology had been widely used in digital media, photography industry, culture and art, remote sensing, biomedicine and other relative fields. Automatically construction of the color mapping relationship between the reference image and the input image had become a key problem of color transfer. The paper proposed a color transfer intention construction model with the subjective perception prior to predicate background and saliency regions based on the Simple Linear Iterative Clustering (SLIC) color clustering of input image and reference image. In the model, a novel visual saliency algorithm is presented. Firstly, a boundary assumption is introduced to compare the contrast between different color clustering and boundaries. Then, the chromaticity distance of color clustering is defined. Finally, visual attention model is introduced to simulate the visual perception process to generate a feature map with different visual saliency factors to construct a color transfer intention based on subjective prior. 20 images are selected from ASD-1000 dataset as experiment samples to verify the model proposed in the paper. A new image quality evaluation method based on visual attention model is suggested to compare the proposed model and typical algorithms. The experimental results demonstrate that the method proposed in this paper can construct the color transfer intention effectively and obtain reasonable color transfer results.

**Keywords:** Color transfer · Visual attention model · Visual saliency

## 1 Introduction

Color transfer is a practical method to change the appearance of a source image according to the color pattern of a target image [1]. The current color transfer field can be divided into two major research directions. One is global algorithm based on statistical characteristics such as [2–8], which is effective for the typical dominant color images or images with similar structure. In many case, traditional global algorithm is easy to lose details and transfer wrongly. The other is local algorithm based on image segmentation such as [1, 9–11], which separates image into a number of color clusters and set a target color for each color cluster in the image. However, it is not stable when the number of the dominate color between the source and target image is obviously different, due to it has not clear description for the extra-color. Hence, some manual interaction is still necessary in the process of color transfer intention construction.

To tackle this problem, a color transfer method based on visual weighted histograms is proposed in this paper to make the method work for images with obvious difference in color performance or texture. In the method, a color mapping between the salient region and background region of the source image and the target image is established. Then, a new weighted color histogram considered the spatial distribution of all colors in the image is used to obtain images with more visually coherence.

The remaining of the paper is organized as follows. Section 2 reviews related work. Section 3 shows the experiments and results. Section 4 states the conclusion of the system.

## 2 Related Work

Many global transfer algorithms has been proposed to achieve the overall color transfer. In 2001, Reinhard et al. [2] proposed a linear transformation for the target image and the source image to have the same mean value and variance. Lee et al. [3] established a color mapping relationship by cluster similarity for color transfer. Huang et al. [4] utilized an image quality factor measurement technique to obtain an automatic color selection algorithm between images. Pitie et al. [6] proposed an original algorithm for transferring N-dimensional pdfs. However, as shown in Figs. 1 and 2, The transfer of the overall style of the image color can cause the image detail to be lost or the entire image to be overlaid with a special color, resulting in an unrealistic visual effect.

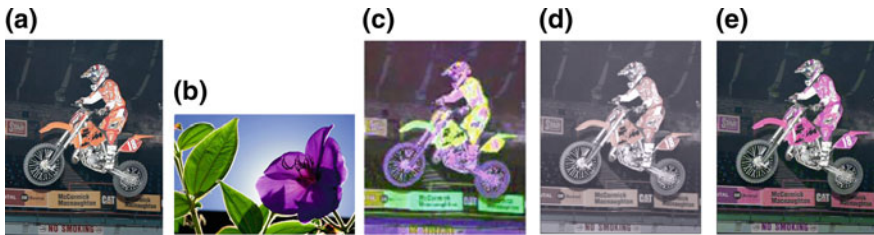


Fig. 1. Comparing with the visual consistency produced from three areas (people, motorcycle body and tire)

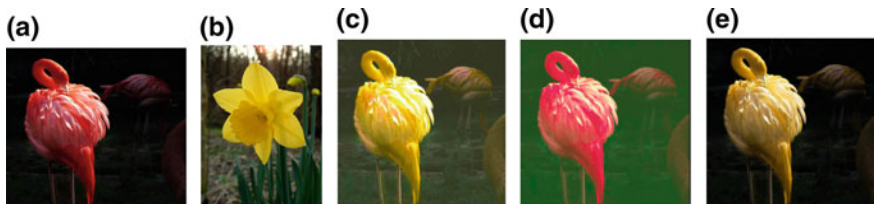


Fig. 2. Comparing the details of the image from the feathers of the flamingos and their backs

The local algorithm implements color transfer by dividing the image into several local sub-regions. Li et al. [9] formulated colorization of target superpixels as a dictionary-based sparse reconstruction problem. Recently, Yang et al. [1] presented a color transfer method for portraits by exploring their high level semantic information. Tai et al. [10] proposed a probability segmentation method and modeled this region as a Gaussian mixture model. Wu et al. [11] presented a local color transfer algorithm that integrates spatial distribution of target dominant colors in an optimization framework.

The algorithms above can work in a lot of occasions. But experiments indicate that they are more suitable for images with similar or consistent color styles. When the color style between source image and reference image is obvious, there are usually some defects in visually coherence of image contents. Hence, the paper focuses on the method of automatically color transfer intention construction.

### 3 Image Semantic Content Analysis

Different image content represent different semantic information. The color mapping should be constructed between similar semantic content of images. Image segmentation based on SLIC is used to obtain sub-regions. Then the foreground and background region are obtained by sub-region reunion based on the weighted saliency calculation. Finally, according to the range of color saturation in the color histogram and the corresponding number of pixels, a color mapping intention can be established automatically.

#### 3.1 Saliency Region Detection

Target-based background priors is introduced to detect the saliency regions.

##### 3.1.1 Image Segmentation

SLIC segment methods [12] is used to convert pixel value into regional superpixel. Firstly, initializing cluster center, also called the seed point. The distance between cluster centers in adjacent ranges can be calculated by the superpixel size. The formula is as follows:

$$S = Ns = \text{sqrt}(N/K) \quad (1)$$

where K denotes superpixel pre-division quantity, and N means the total number of image pixels.

Secondly, calculating the similarity between each pixel in the image and the cluster center closest to it.

Finally, calculating the superpixel segmentation result of the complete edge. The formula is as follows.

$$D' = \sqrt{\left(\frac{d_c}{m}\right)^2 + \left(\frac{d_s}{S}\right)^2} \quad (2)$$

where  $d_c$  represents the Euclidean distance measure between pixels,  $d_s$  represents the distance measure at the spatial coordinates.

### 3.1.2 Underlying Feature Calculation

Lab color space is more suitable for the representation of the colour difference. The Lab values of all pixels in the superpixel are averaged as Lab values  $L_i$ ,  $a_i$ ,  $b_i$  of the superpixel, and then the colour difference is calculated with all other superpixels  $D_{color}$ :

$$D_{color} = \sqrt{(L_i - L_j)^2 + (a_i - a_j)^2 + (b_i - b_j)^2} \quad (3)$$

By combining spatial information ( $X_i$ ,  $Y_i$  is the center coordinate of the  $i$ -th superpixel) and the center weight between the superpixels, we can obtain the saliency map in the Lab space. The main calculations are as follows:

$$D_{dis} = \sqrt{\left(X_i - \frac{W}{2}\right)^2 + \left(Y_i - \frac{h}{2}\right)^2} \quad (4)$$

$$S_{Lab}(i) = \frac{e^{-D_{dis}} \times \sum_{j=1, j \neq i}^n D_{Lab}(i)}{n} \quad (5)$$

where  $D_{dis}$  is the spatial coordinate position of superpixel  $i$ , and  $S_{Lab}(i)$  is the normalized result of significance value.

## 3.2 Bidirectional Mapping Construction

The visual weight calculation in [13] is adopted to calculate the color histogram for each sub-block. The visual weight of each pixel point can be calculated according to the Formula (6).

$$w(i, j) = k \cdot \exp \left[ -\frac{1}{2\sigma^2} \left[ \frac{\varphi(i, j)}{\iint_{x, y \in I} \varphi(x, y) dx dy} \right] \right] \quad (6)$$

where  $w(i, j)$  is visual weight of pixel  $(i, j)$ , which has been normalized to the  $[0, 1]$  range. And  $\varphi(i, j)$  is the color complexity measure (CCM),  $I$  represents the entire image area.

The total sum  $W_k$  of the visual weights of image sub-block  $B_k$  in the foreground and background are calculated as Formula (7).

$$w_k = \sum_{(i, j) \in B_k} w(i, j) \quad (7)$$

where  $W_k$  is the visual weight of image block  $B_k$ , and  $w(i, j)$  is the visual weight of pixel  $(i, j)$ .

## 4 Experiment and Analysis

The experiments are implemented using python on a computer with an Intel Xeon E5-2620 v4 2.1 GHZ \* 16 processor and 64 G memory. The experiment images and reference images are selected from ASD saliency database, which consists of 1998 images with 999 ground truth images and 999 processed images (all of them are manually segmented).

The following three sets of experiments show comparisons between the color transfer methods of [2, 6] which is typically represented by global color transfer, where (a) represents source image, (b) represents target image, and (c) represents Pitie et al.'s resultant image, (d) represents Reinhard et al.'s resultant image and (f) represents the resultant image of the proposed method in the paper.

Experimental results show that our method has better color transfer effect. Figure 1 shows the results of different regional processing. It is obvious that a incorrect color transfer occurred in the connection area between the person and the motorcycle in (c) and the whole image produces an unreal color in (d). Our method performs a more accurate transfer in (f), according to the image structure of the source image.

Figure 2 shows the different methods of color transfer. The resultant image of [1] haven incorrect transfer in the target image (d), and the highlight part of the back feathers of flamingos in (c) is lost while it can be convert better apparently in our method.

Figure 3 shows the comparison of results when the number of major colors is inconsistent. The two women and forest separately present the color-style of the butterfly in (b). The color spatial information is lost in (c), while the yellow style is disappeared in (d). Our result better preserves the brightness and contrast of the scene.

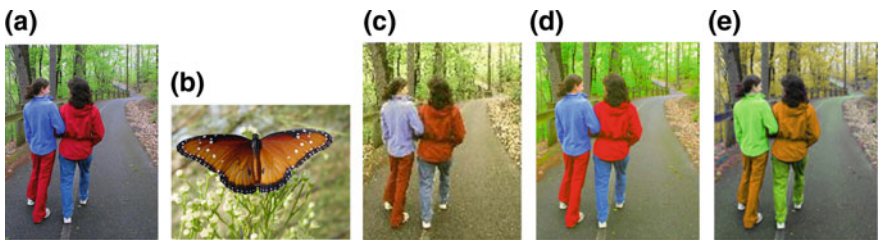


**Fig. 3.** Comparison of results when the number of major colors is inconsistent

## 5 Conclusions

In this paper, we have proposed a new image color transfer method to efficiently convert the color style of an image. Considered the human visual salience attention mechanism, a reasonable color transfer method is generated by analyzing the image semantically.



In the future, we expect to generate image region matching colors automatically by further grading the combination of visual saliency so as to obtain a method more consistent with human visual perception.

## References

1. Yang, Y., Zhao, H., You, L., et al. (2017). Semantic portrait color transfer with internet images. *Multimedia Tools & Applications*, 76(1), 523–541.
2. Reinhard, E., Ashikhmin, M., Gooch, B., & Shirley, P. (2001). Color transfer between images. *IEEE Computer Graphics and Applications*, 21(5), 34–41.
3. Lee, J. Y., Sunkavalli, K., Lin, Z., et al. (2015). Automatic content-aware color and tone stylization, 2470–2478.
4. Huang, Y. H., Wang, P. C., Chou, C. C., et al. (2011). An automatic selective color transfer algorithm for images. *ACM Symposium on Applied Computing*. *ACM*, 66–71.
5. Welsh, T., Ashikhmin, M., & Mueller, K. (2002). Transferring color to greyscale images. *Conference on computer graphics and interactive techniques*. *ACM*, 277–280.
6. Pitie, F., Kokaram A. C., & Dahyot, R. (2005). N-dimensional probability density function transfer and its application to colour transfer, (2)2, 1434–1439.
7. Hacoheh, Y., Shechtman, E., Dan, B. G., et al. (2011). Non-rigid dense correspondence with applications for image enhancement. *ACM*, 1–10.
8. Frigo, O., Sabater, N., Demoulin, V., et al. (2014). Optimal transportation for example-guided color transfer. In *Asian Conference on Computer Vision* (pp. 655–670). Cham: Springer.
9. Li, B., Zhao, F., Su, Z., et al. (2017). Example-based image colorization using locality consistent sparse representation. *IEEE Transactions on Image Processing*, 26(11), 5188–5202.
10. Tai, Y. W., Jia, J., & Tang, C. K. (2005). Local color transfer via probabilistic segmentation by expectation-maximization. In *IEEE Computer Society Conference on Computer Vision and Pattern Recognition*. *IEEE Computer Society* (pp. 747–754).
11. Wu, F., Dong, W., Yan, K., et al. (2014). Content-based colour transfer. In *Computer Graphics Forum* (pp. 190–203). Blackwell Publishing Ltd.
12. Achanta, R., Estrada, F., Wils, P., et al. (2008). *Salient region detection and segmentation* (pp. 66–75). Berlin Heidelberg: Computer Vision Systems. Springer.
13. Yoon, K. J., & Kweon, I. S. (2001). Color image segmentation considering human sensitivity for color pattern variations. *Proc Spie*, 4572(4572), 269–278.



# Small-Scale Image Inpainting on Mobile Platform

Chen Shao, Qiang Wang<sup>(✉)</sup>, and Shi Li

School of Media and Design, Hangzhou Dianzi University, Zhejiang, China  
profwq@hdu.edu.cn

**Abstract.** In the digitization of literature, especially in the electronic storage of library books, the remake of documents and the repair of defects are increasingly important. In this paper, based on the needs of library remake, a JavaScript algorithm is used to design and develop a repair algorithm for retrieving image information using a digital camera on a mobile platform. It achieves the repair of damaged books, improves readers' reading experience and reaches the application goal of cross-platform, low equipment cost, and low algorithm complexity.

**Keywords:** Image inpainting · Document remake · Small scale

## 1 Introduction

In recent years, the use of remaking or scanning technology to realize the digitization and application of paper documents is the main means to manage innovative files and improve the level of file services [1]. Now, it is constantly adapting and meeting the needs of current digital management, storage and utilization, and it makes use of digital means to repair the damage, flaws and other defects of the paper files become the key technology of digitalization of paper files and research hot spots.

At present, the international and domestic digital image inpainting techniques mainly include inpainting for repairing small-scale defects and completion for filling large pieces of lost information in images [2]. Based on the above two methods, it has derived more algorithms that work better and faster through the optimization and improvement of the algorithms. For example, the Criminis algorithm for improving the priority credibility [3], fast image inpainting algorithm based on watershed segmentation [4] and the inpainting algorithm based on partial differential equations.

According to the principle of FMM image restoration algorithm, this paper proposes a small-scale image restoration algorithm for the problem of insufficient efficiency of mobile platform image restoration algorithm. The problem of efficiency of small-scale image restoration on mobile platforms is better solved.

## 2 Related Algorithm Principle

As we all know, the goal of image inpainting technology is to remove defects, scratches in the image. The principle of the related algorithm is described as follows:

(1) The principle of an image inpainting technology based on fast marching method [5, 6].

The FMM uses the arrival time function  $T(x, y)$  to simulate the evolution of the curve, it pushes the patching area from the edge to the interior and completes the repair of the image point by point. As it shows in Fig. 1, if  $\Omega$  is the area of the image to be repaired,  $\partial\Omega$  is the boundary of the area. Assume that  $p$  is a point on  $B_\epsilon(p)$  and take a small neighborhood around  $p$ , The repair of point  $p$  should be determined by the neighboring pixels  $B_\epsilon(p)$ . The known point  $q$  in the neighborhood can be first-order approximation to point  $p$  according to the Formula (1).

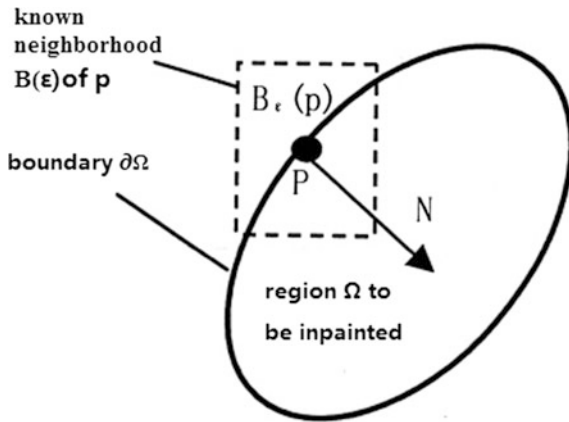


Fig. 1. Repair principle

$$I_q(p) = I(q) + \nabla I(q)(p - q) \tag{1}$$

Then treat the point  $p$  as a function of all points  $q$  in  $B_\epsilon(p)$  and use a weighting function  $w(p, q)$  to accumulate. The weighting function  $w(p, q)$  here must be able to transmit image gray values as well as maintain edge details in  $B_\epsilon(p)$ .

$$\frac{\sum_{q \in B_\epsilon(p)} w(p, q)[I(q) + \nabla I(q)(p - q)]}{\sum_{q \in B_\epsilon(p)} w(p, q)} \tag{2}$$

(2) Image quality assessment algorithm

For the repaired image, this paper uses the peak signal-to-noise ratio (PSNR) and structural similarity (SSIM) parameters for quality assessment. The formula for calculating quality assessment parameters is as follows:

$$MSE = \frac{1}{mn} \sum_{i=0}^{m-1} \sum_{j=0}^{n-1} \|I(i, j) - K(i, j)\|^2 \tag{3}$$

$$PSNR = 10 \times \log_{10} \left( \frac{(2^n - 1)^2}{MSE} \right) \quad (4)$$

$$SSIM(x, y) = \frac{(2\mu_x\mu_y + c1)(2\sigma_{xy} + c2)}{(\mu_x^2 + \mu_y^2 + c1)(\sigma_x^2 + \sigma_y^2 + c2)} \quad (5)$$

The algorithm needs to pay attention to the fact that PSNR is not completely consistent with the human visual quality. The level of PSNR is not linearly related to human visual sensitivity error, and the perceived result changes due to other factors. As a perceptual-based computational model, SSIM considers the fuzzy changes of human perception caused by structural information between pixels in the image, especially the structural information between pixels in the vicinity of the space.

### 3 Image Inpainting Algorithm on Mobile Platform

This paper proposes a small-scale image inpainting algorithm that combines scanning edge pixel information and linear-filled image inpainting technology aiming at eliminating the defects of digital image information such as missing, flaws and scratches in image remake. The flow chart of the repair algorithm is shown in Fig. 2.

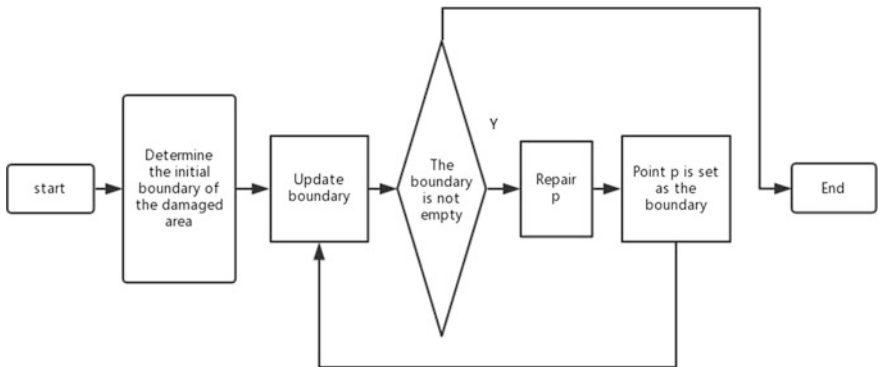
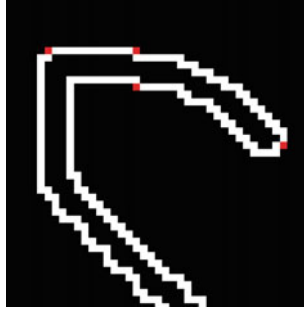


Fig. 2. Repair flowchart

The repair algorithm in this paper firstly finds the area to be repaired and its boundary by traversing the image, and establishes a boundary band linked list. Pre-processing boundary, when the boundary point  $p$  (as shown in Fig. 3) is in a certain corner, the pixel value of point  $p$  is the average of the known pixels of the image in 4 neighborhoods, remove the point  $p$  from band list at this time. Figure 4 shows the preprocessed boundary. Then start the repair operation. When the image is traversed to the first boundary point  $p$ , the grayscale gradient values for each pixel in the eight neighborhoods of  $p$  are calculated. The pixel points in the area to be repaired are

linearly filled according to the gradient value along the gradient direction. Add the repaired point information to the boundary list, update the boundary value of point  $p$  and loop repair operations until the boundary list is empty.



**Fig. 3.** Points at the corner



**Fig. 4.** Boundary after preprocessing

In the image inpainting application of the book remake, at first, use a digital camera to capture a sample of the book image, and then import the collected samples into the mobile platform. Image defects are interactively repaired by marking the area to be repaired with the touch screen and repairing the marked image area.

## 4 Repair Results

### 4.1 Subjective Comparison of Image Inpainting

Figures 5, 6 and 7 are the color continuous tone images to be repaired, Figs. 8 and 9 are the comparison between the algorithm repair image and the repair effect of the FMM.

Figures 10, 11 and 12 shows the comparisons between the repair effect of this paper and FMM for the image to be repaired.



**Fig. 5.** Image to be repaired



**Fig. 6.** Result of FMM



**Fig. 7.** Results of this article



Fig. 8. Repair details of FMM



Fig. 9. Repair details of this article

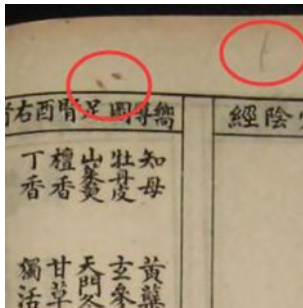


Fig. 10. Book to be repaired

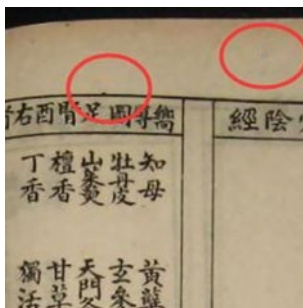
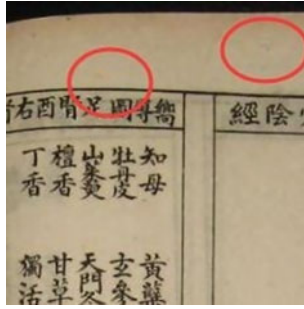


Fig. 11. Result of FMM



**Fig. 12.** Results of this article

## 4.2 Objective Comparison of Image Inpainting

This article uses PSNR and SSIM quality evaluation parameters to compare the repair results objectively. The results are shown in Table 1.

**Table 1.** Comparison of PSNR and SSIM Values

Repair algorithm	PSNR	SSIM-R	SSIM-G	SSIM-B
FMM	32.4518	86.989928	90.100821	88.987948
This article's algorithm	32.5228	86.917236	90.051046	88.953280

From two kinds of image quality evaluation experimental data, it is known that the algorithm proposed in this paper has maintained the visual integrity after image inpainting. On the other hand, in terms of efficiency, the FMM takes 929 ms while the algorithm of this paper takes 616 ms. The algorithm maintains the integrity of the restored image information and is superior to the FMM in terms of repair efficiency.

## 5 Conclusions

In this paper, through the design of the image repair algorithm by using JavaScript, it is convenient and quick to repair the image damage and defects in the mobile terminal. It also reduces the complexity of the algorithm and causes little damage to the reproduction of the document. It provides a solution that is simple in equipment and low in cost. However, the algorithm needs further improvement when repairing complex texture image quality.

**Acknowledgements.** This work is funded by National Key Technology Research and Development Program of the Ministry of Science and Technology of China (2012BAH91F03) and Digital Imaging Theory-GK188800299016-054 and Hangzhou Dianzi University Graduate Research Innovation Fund-CXJJ2018017.



## References

1. Qiao, C. (2014). An analysis of the content and standards of the digitalization of paper archives. *File Space-Time*, 10, 32–33.
2. Hongying, Z., & Qiyu, P. (2007). A review of digital image inpainting techniques. *Journal of Image and Graphics*, 12(1), 1–10.
3. Zun, L., Jin, W., & Jin, L. (2016). Target removal of criminisi image inpainting algorithm. *Infrared technology*, 38(1), 28–32.
4. Tu, Y., Shengqi, N., Gengsheng, C., & Wei, X. (2017). A fast image inpainting algorithm based on watershed segmentation. *Journal of Fudan University (Natural Science)*, 56(1), 57–70.
5. Fan, Q., Huang, X., & Zhang, L. (2014). Image inpainting based FMM algorithm by a direction selection method. *International Conference on Industrial Application Engineering* 12–15.
6. Jialun, K., Xianghong, T., & Shu, R. (2012). A direction-based image inpainting algorithm based on FMM. *Proceedings of Zhejiang Institute of Electronics Annual Conference, 2012*, 147–150.



# Multiple Reference Images Color Transfer Based on Improved GMM Model

Zhenshan Tan<sup>1</sup>, Zhijiang Li<sup>1</sup>(✉), Yanhao Li<sup>2</sup>, and Liqin Cao<sup>1</sup>

<sup>1</sup> School of Printing and Packaging, Wuhan University, Wuhan, China  
lizhijiang@whu.edu.cn

<sup>2</sup> China Merchants Bank Network Technology Co., Ltd., Hangzhou, China

**Abstract.** Color transfer is to change the image color according to one or more reference images to match people's cognition. Usually, there are two problems deserved to be researched further. One is to find suitable reference colors for a complex image. The other is to lessen the details loss in the process. In the paper, GMM model is improved by considering the geometric position relation of the color clustering to construct color transfer intentions between source image and multiple reference images. The geometric coordinate smoothing parameter is introduced to improve EM algorithm to reduce the details loss. Based on Baidu data set and the reference paper data sets, a comparison experiment between typical color transfer algorithms and our method was presented. The experimental results can demonstrate that the algorithm proposed in the paper is reasonable and effective.

**Keywords:** Color transfer · GMM model · EM algorithm · Multi-example-based

## 1 Introduction

Color transfer plays an important role in image processing such as image color stylization and image colorization. However, color transfer usually suffers from color distortion and detail loss [1], which mainly caused by misleading color mapping and inadequate colors of reference image. An ideal color transfer model should provide enough reference colors to ensure the correct mapping. However, it is usually difficult in the single example-based color transfer.

Color mapping is to construct corresponding relationships between the source and the reference image. Many representative approaches, such as 3-Dimensional histogram matching [2], correlated color space mapping [3], N-Dimensional probability distribution [4], probabilistic moving least square [5], foreground and background separation based on image analysis [6], dominant color [7] and CNN convolutional neural network [8, 9], have been verified in the past. They attempted to construct the correct mapping between images but limited into the inadequate colors of the reference. Therefore, this paper adopted multiple reference images instead of single example-based. To solve the problem of detail loss, Chang et al. [10] used sigmoid function to find the pseudo contour areas. Kong et al. [6] used super-pixel method and Su et al. [1] used a self-learning filtering scheme to preserve the details. Moreover, Tai et al. [11]

modeled the color distribution as GMM models and used expectation maximization to avoid detail loss. Mairéad et al. [12] used  $\mathcal{L}_2$  distance to minimize the similarity between images and simplified the scalar product to process the details. The advantage of GMM models is that it can fit any type of distribution, which is very useful in color clustering.

This paper suggested a method based on improved GMM models to construct the correct mapping relationships and suppress pseudo contours based on the smoothing parameter. The paper is organized as follows. Section 2 presents a color transfer method based on the improved GMM models and EM algorithm. Section 3 shows some results and its' quality analysis. Conclusions are drawn in Sect. 4.

## 2 Multiple Reference Images Color Transfer Model

Traditional GMM models have three disadvantages. Firstly, the models only regarded pixels as independent variables but neglected the neighborhood relations in the pixel coordinates space, which might lower the accuracy of color clustering. Secondly, the details of the image might be lost because of wrong color division. Finally, in the M-step, transitivity of judgment conditions in traditional algorithm misled the result of cluster merging. The improved GMM models and EM algorithm in the paper are proposed to solve these problems.

In this paper, we proposed several additional improvements to address the above issues. Firstly, taking multiple reference images instead of single reference images enriched the colors of reference. Secondly, our frame was extended to improve the neighborhood relations in the pixel coordinates space to preserve the details. Thirdly, this paper improved the merging parameters in M step to avoid wrong color division. Finally, we added the step of luminance normalization of the images to confirm correct color mapping.

### 2.1 Improved GMM Model and EM Algorithm

#### 2.1.1 Construct GMM Models

Given a source image  $I_s$  and  $n$  reference images  $I_r^n$ , GMM models construct color clusters  $r_i$  in each of them. The  $k$  color clustering in the image can be expressed by the  $k$  component of the GMM models, which is determined by the color distribution of the pixels in the clustering. Generally, the probability function of each  $r_i$  is the same, and the parameters are different. The  $r_i$  to be divided can be represented by some statistical features, such as pixel value, mean, standard deviation, location, texture and so on, which can reflect the differences between  $r_i$ .

GMM model is used in color clustering for the input image  $I$ , the color distribution of each color clustering  $r_i$  ( $i = 1, 2, \dots, K$ ) can be approximately represented as a Gauss component  $G(\rho_i)$ .  $K$  is the number of color clusters. So the probability density of pixels  $I(p)$  belonging to Gauss components  $G(\rho_i)$  can be expressed as the Formula (1).

$$p(I(p)|\rho_i) = \frac{1}{(2\pi)^{3/2}|\sum_i|^{1/2}} \exp\left(-\frac{1}{2}(I(p) - \mu_i)^T \sum_i^{-1} (I(p) - \mu_i)\right) \quad (1)$$

where,  $\mu_i$  is the mean of  $r_i$ ,  $\sum_i$  is the covariance matrix of  $r_i$ ,  $\rho_i = \{\mu_i, \sum_i\}$ . Generally,  $\mu_i$  and  $\sum_i$  are calculated by K-means algorithm.

Therefore, the fitting model  $G(\rho)$  of the color distribution of the image can be described as Formula (2).

$$G(\rho) = \sum_{i=1}^K a_i p(I(p)|\rho_i) \quad (2)$$

Here,  $a_i$  is the weight of  $r_i$ ,  $a_i = N_i/N_{total}$ ,  $N_i$  is the number of pixels of  $r_i$ ,  $N_{total}$  is the number of pixels of the image. The value of Formula (2) is calculated by EM algorithm.

### 2.1.2 Improved EM Algorithm

Firstly, taking neighborhood relations in the pixel coordinates space and preserving the details, a smoothing parameter in the E-step is suggested in the paper.

The smoothing parameter in E-step is expressed as Formula (3).

$$p^{i,\Omega_\varepsilon} = \frac{1}{W_i} \sum_{I_\varepsilon(p) \in \Omega_\varepsilon} D(I(p), I_\varepsilon(p)) p(I(p)|\rho_i) \quad (3)$$

where,  $I_\varepsilon(p) \in \Omega_\varepsilon$  is the pixels of the neighborhood areas.

$W_i = \sum_i \sum_{I_\varepsilon(p) \in \Omega_\varepsilon} D(I(p), I_\varepsilon(p)) p(I(p)|\rho_i)$  is the normalization parameter.

$D(I(p), I_\varepsilon(p))$  is the smoothing parameter, which is represented as Formula (4)

$$D(I(p), I_\varepsilon(p)) = \exp\left(-\frac{(x - x_\varepsilon)^2 + (y - y_\varepsilon)^2}{\delta_d}\right) \exp\left(-\frac{|I(p) - I_\varepsilon(p)|^2}{\delta_g}\right) \quad (4)$$

Here,  $(x, y)$  is the situation of  $I(p)$ .  $(x_\varepsilon, y_\varepsilon)$  is the situation of  $I_\varepsilon(p)$ .  $\delta_d$  and  $\delta_g$  are the smoothing factors.

Therefore, the modified probability is described as Formula (5).

$$p^{i,I(p)} = \frac{a_i p(I(p)|\rho_i)}{G(\rho)} + p^{i,\Omega_\varepsilon} \quad (5)$$

Secondly, taking the transitivity of judgment conditions, which means that if  $|\mu_i - \mu_k| < \delta$  and  $|\mu_k - \mu_j| < \delta$ , but the value of  $|\mu_i - \mu_j|$  may larger than  $\delta$ . Therefore, this paper changes the merging condition.

The improved M-step is calculated as Formula (6).

$$\mu_i = \frac{\sum_i p^{i,I(p)} I(p)}{\sum_i p^{i,I(p)}} \quad (6)$$

$$\sum_i = \frac{\sum_i p^{i,I(p)} (I(p) - \mu_i)(I(p) - \mu_i)^T}{\sum_i p^{i,I(p)}}$$

Then, change the merging parameters. And the progress is described as followed.

- (1) Calculate the distance  $|\mu_i - \mu_j|$  of each color clustering  $r_i$  and  $r_j$ .
- (2) Find the most similar color clustering  $r_j$  to the  $r_i$ , the  $j$  is relabeled as  $k$ .
- (3) If  $|\mu_i - \mu_k| < \delta$ , then merge them and recalculate the parameters.

The progress is ended when any value of  $|\mu_i - \mu_j|$  is larger than  $\delta$ .

## 2.2 Color Transfer

### 2.2.1 Luminance Normalization

Luminance is an important parameter in color matching. The source and the reference images should have the analogous luminance, which means the luminance histogram between images should be similar, however, it is usually difficult. Therefore, luminance normalizes every image to ensure the correct color mapping. The formula is in Formula (7).

$$l'_{ref(n)} = \frac{\sigma^l_{src}}{\sigma^l_{ref(n)}} \left( l_{ref(n)} - \mu^l_{ref(n)} \right) + \mu^l_{src} \quad (7)$$

Here,  $l_{ref(n)}$  is the reference pixel's luminance.  $\mu^l_{src}$  and  $\mu^l_{ref(n)}$  are the mean luminance values of the source and the reference image.  $\sigma^l_{src}$  and  $\sigma^l_{ref(n)}$  are the covariance luminance values of the source and the reference image.

### 2.2.2 Construct Color Mapping

If the two color clusters are able to establish color mapping, they will have the same color distribution. Therefore, the color distribution model  $G(\rho_{src})$  is used as the initial parameter. Then color clustering for each reference image. The Formula (8) is similar to Formula (5)

$$p^{i,I(p)}_{ref(n)} = \frac{a_i p \left( I(p) | \rho_{ref_i(n)} \right)}{G \left( \rho_{ref_i(n)} \right)} + p^{i,\Omega_c}_{ref(n)} \quad (8)$$

Here, the initial value of  $\rho_{ref_i(n)}$  is  $\rho_{src}$ ,  $p^{i,I(p)}_{ref(n)}$  is the probability of the neighborhood area of  $I(p)$  belonging to  $r_i$ . Moreover,  $p^{i,I(p)}_{ref(n)}$  is similarity of the pixel between the source and the reference image.

Formula (8) may construct the mapping that many color clustering areas of the reference to the same area of the source. Then construct the best color mapping between the source and reference images as Formula (9)

$$f(src_i, ref_i(n)) = \frac{1}{p_{ref(k)}^i} \left| \mu_{ref_i(n)} - \mu_{src_i} \right| \quad (9)$$

Here,  $1 \leq i \leq K$ ,  $1 \leq n \leq N$ ,  $N$  is the number of reference images.  $\mu_{ref_i(n)}$  and  $\mu_{src_i}$  are the weighting means of the reference  $ref_i(n)$  and the source  $src_i$ . The smaller the value of  $\left| \mu_{ref_i(n)} - \mu_{src_i} \right|$  is, the more similar between the two areas.  $p_{ref(k)}^i$  is the probability density of pixels  $I(p)$  belonging to the reference.

$$p_{ref(k)}^i = \frac{1}{T} \sum_{I(p)} p_{ref(n)}^{i,I(p)} \quad (10)$$

Here,  $T$  is the number of  $r_i$  of reference.

So, according to Formula (11) can get the best mapping relationship between the source and the reference.

$$(src_i, ref_i) \leftarrow \min\{f(src_i, ref_i(n)) | 1 \leq i \leq K, 1 \leq n \leq N\} \quad (11)$$

### 2.2.3 Pixels Color Transfer

Before pixels color transferring, we should transfer the RGB color space to the  $l\alpha\beta$  color space [13]. That's because the three components of  $l\alpha\beta$  color space have little correlation.

The gray image only offers the luminance information and the color image offers the luminance information and the hue information. Therefore, different transfer and synthesis methods are used for grayscale and color images respectively.

#### (1) Gray image

Normalize the source and the reference images to  $M$  level as Formula (12).

$$l' = \text{ceil} \left( M \times \frac{l - l_{\min}}{l_{\max} - l_{\min}} \right) \quad (12)$$

Then calculate the color  $\alpha_{ref_{i,k}}, \beta_{ref_{i,k}}$  and mean value  $\mu_{ref_{i,k}}^\alpha, \mu_{ref_{i,k}}^\beta$  in  $m(m = 1, 2, \dots, M)$  level of the reference, and calculate the mean value  $\mu_{src_{i,k}}^l$ . Pixels based color transfer of gray image is in Formula (13).

$$l_{res} = l_{src}$$

$$\alpha_{ref_{i,k}} = p^{i,I(p)} \times \mu_{ref_{i,k}}^\alpha \times \frac{l_{src}}{\mu_{src_{i,k}}^l}$$

$$\beta_{ref_{i,k}} = p^{i,I(p)} \times \mu_{ref_{i,k}}^\beta \times \frac{l_{src}}{\mu_{src_{i,k}}^l} \tag{13}$$

Here,  $p^{i,I(p)}$  is the probability of  $I(p)$  belonging to  $src_i$ .

(2) Color image

Transferring the color components  $\alpha\beta$  first. Then transferring the  $l$  component globally to achieve the luminance consistency. The formula is shown as Formula (14).

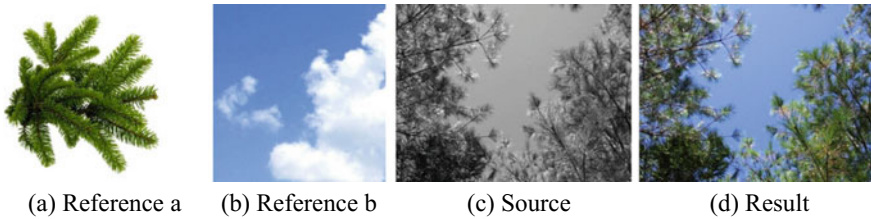
$$\begin{aligned} \alpha_{res} &= \sum_{i=1}^K p^{i,I(p)} \left( \frac{\sigma_{ref_i}^\alpha}{\sigma_{src_i}^\alpha} (\alpha_{src} - \mu_{src_i}^\alpha) + \mu_{ref_i}^\alpha \right) \\ \beta_{res} &= \sum_{i=1}^K p^{i,I(p)} \left( \frac{\sigma_{ref_i}^\beta}{\sigma_{src_i}^\beta} (\beta_{src} - \mu_{src_i}^\beta) + \mu_{ref_i}^\beta \right) \\ l_{res} &= \frac{\sigma_{ref}^l}{\sigma_{src}^l} (l_{src} - \mu_{src}^l) + \mu_{ref}^l \end{aligned} \tag{14}$$

Here,  $\sigma$  is the covariance.

### 3 Result and Analysis

#### 3.1 Results

Figure 1 shows the result of experiments of colorization based on multiple reference images.



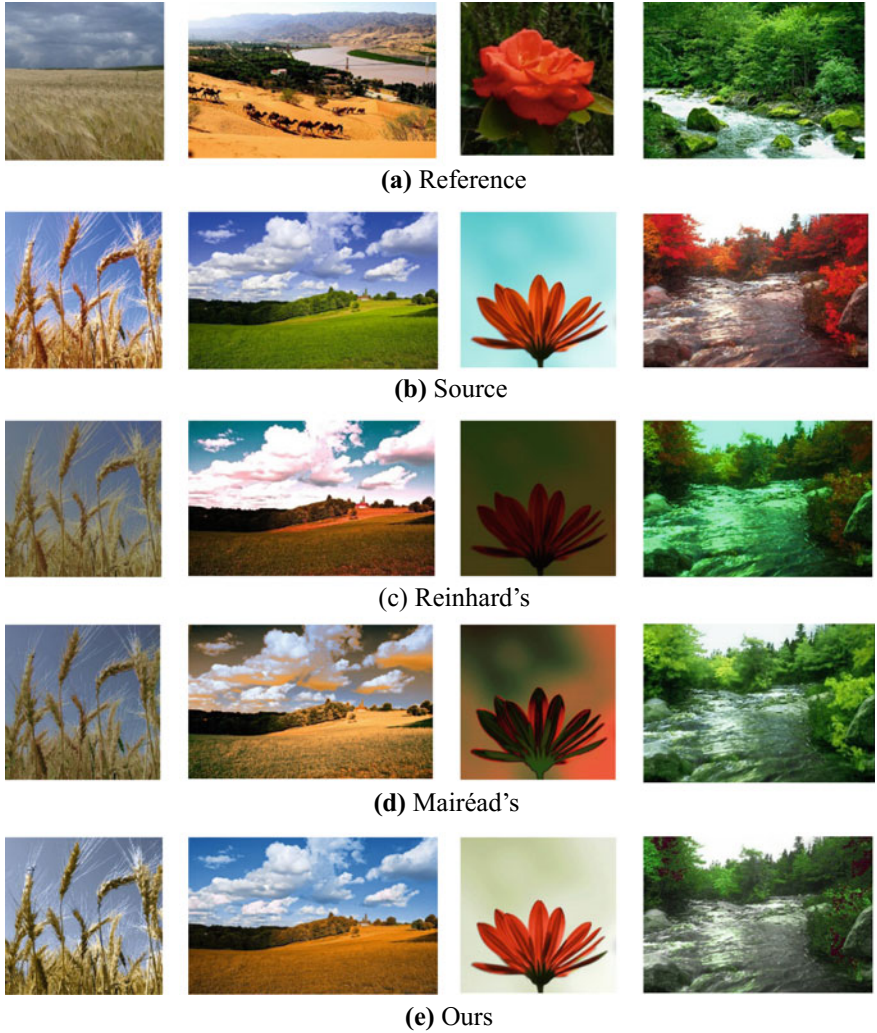
**Fig. 1.** Result of experiments of colorization based on multiple reference images

Figure 2 shows the result of experiments of color image transfer based on multiple reference images.

In color image transfer, this paper compared our result with Reinhard [13] and Mairéad [12]. The result is shown in Fig. 3 and the data comes from Mairéad [12] and baidu data.



**Fig. 2.** Result of experiments of color image transfer based on multiple reference images



**Fig. 3.** Result with Reinhard and Mairéad



### 3.2 Image Quality Assessment

This paper evaluated the image from the subjective and objective quality.

To the subjective quality, 10 groups of images were selected, and 40 people (20 males and 20 females) ages ranging from 17 to 40 years old were evaluated. The results of each group were divided into two approaches, one was to evaluate the similarity between the result and the source image on the structure (*ss*), and the other was the similarity between the result and the reference image in the color (*cs*). The degree was scored from 1.0 (not pleasing) to 5.0 (very pleasing). Then calculated the average of the two approaches.

To the objective quality, we chose the classic algorithms including SSIM [14] (*SS*) and color similarity [15] (*CS*). Then, this paper defined the comprehensive objective assessment as Formula (15).

$$Q(I_{res}) = \left( \text{sigmoid}'(SS(res, src)) + \text{sigmoid}'(CS(res, ref)) \right) / 2 \quad (15)$$

Here,  $\text{sigmoid}'$  function can be calculated in Formula (16).

$$\text{sigmoid}'(x) = \left( \frac{1}{1 + e^{-x}} - 0.5 \right) \times 2 \quad (16)$$

The data of comparing assessment with Reinhard [13] and Tai [11] is in Table 1.

**Table 1.** The data of quality assessment

Methods	Subjective index			Objective index		
	ss	cs	$q(I_{res})$	SS	CS	$Q(I_{res})$
Reinhard	2.8	2.4	2.6	0.84	2.48	0.6212
Mairéad	4.0	3.4	3.7	0.92	3.15	0.6739
Ours	4.3	4.1	4.15	0.97	3.90	0.7053

According to the data of Table 1, our subjective index has a better values than others. Moreover, we can see that the values of structure similarity (SS) and color similarity(CS) of the proposed method are larger than others, which means the structure and the color are more similar to the source. The value of  $Q(I_{res})$  denotes the comprehensive index of structure and color, our value of  $Q(I_{res})$  is larger than others, which means our results loss less details and keep more colors.

## 4 Conclusions

Compared with traditional color transfer methods, multiple reference images enrich the colors of reference. Simultaneously, richer color references will produce less detail losing. The paper proposed a multiple reference images color transfer method by

adding a smoothing parameter and changing the merging condition in GMM model and EM algorithm. Experiments has proved that our results performed better than traditional methods. However, GMM models cannot fit any kind of color distribution. Therefore, generalized Gauss model, which can substitute the GMM models, should be researched further to improve the adaptability of the method.

**Acknowledgements.** This work was supported by National Natural Science Foundation of China under Grant Nos. 41671441.

## References

1. Su, Z., Zeng, K., Liu, L., et al. (2014). Corruptive artifacts suppression for example-based color transfer. *IEEE Transactions on Multimedia*, 16(4), 988–999.
2. Neumann, A. (2005). Color style transfer techniques using hue, lightness and saturation histogram matching. In *Eurographics Conference on Computational Aesthetics in Graphics, Visualization and Imaging*. Eurographics Association (pp. 111–122).
3. Xiao, X., & Ma, L. (2006). Color transfer in correlated color space, 305–309.
4. Pitie, F., Kokaram, A. C., & Dahyot, R. (2005). N-dimensional probability density function transfer and its application to color transfer. In *Tenth IEEE International Conference on Computer Vision* (pp. 1434–1439). IEEE.
5. Hwang, Y., Lee, J. Y., Kweon, I. S., et al. (2014). Color transfer using probabilistic moving least squares. In *IEEE Computer Society IEEE Conference on Computer Vision and Pattern Recognition* (pp. 3342–3349).
6. Kong, Y., Dong, W., Zhang, X., et al. (2013). Content-based color transfer. *Computer Graphics Forum*, 32(1), 190–203.
7. Dong, W., Bao, G., Zhang, X., et al. (2010). Fast local color transfer via dominant colors mapping. *Acm Siggraph Asia Sketches*, 1–2.
8. Gatys, L. A., Ecker, A. S., & Bethge, M., (2015). A neural algorithm of artistic style. *Computer Science*.
9. Yijun, L., Ming-Yu, L., et al. (2018). A closed-form solution to photorealistic image stylization. In *IEEE Conference on Computer Vision and Pattern Recognition*. *IEEE Computer Society*, 19(2).
10. Chang, Y., Saito, S., Uchikawa, K., et al. (2005). Example-based color stylization of images. *Acm Transactions on Applied Perception*, 2(3), 322–345.
11. Tai, Y. W., Jia, J., & Tang, C. K. (2005). Local color transfer via probabilistic segmentation by expectation-maximization. In *IEEE Computer Society Conference on Computer Vision and Pattern Recognition*. *IEEE Computer Society*, (pp. 747–754).
12. Mairéad, G., & Rozenn, D. (2017). Robust registration of Gaussian mixtures for colour transfer. *IEEE Conference on Computer Vision and Pattern Recognition*. *IEEE Computer Society*, 17(5).
13. Reinhard, E., Adhikhmin, M., Gooch, B., et al. (2002). Color transfer between images. *IEEE Computer Graphics and Applications*, 21(5), 34–41.
14. Wang, Z., Bovik, A. C., Sheikh, H. R., et al. (2004). Image quality assessment: from error visibility to structural similarity. *IEEE Transactions on Image Processing*, 13(4), 600–612.
15. Hasler, D., & Suesstrunk, S. E. (2003). Measuring colorfulness in natural images. *Human Vision and Electronic Imaging VIII*, 87–95.



# Influence of Image Noise on Digital Photo Definition

Jing Geng<sup>(✉)</sup>, Congjun Cao, and Yonghong Qi

Faculty of Printing, Packaging Engineering and Digital Media Technology,  
Xi'an University of Technology, Xi'an, China  
gengjing\_qianye@163.com

**Abstract.** This study aimed to investigate the cognition of object texture formation and subjective preference in image evaluation. The relationship between the addition of noise and the definition of natural objects in digital photos was studied. Two experiments were designed on the basis of the psychophysical experimental and objective evaluation methods. Psychological scales were used to quantify the relationship between noise level and image definition. The results of objective evaluation indicated that the definition of the digital image gradually deteriorated as noise levels increased. The results of subjective evaluation revealed that not all observers perceived an improvement in image definition with the addition of noise.

**Keywords:** Image noise · Image definition · White Gaussian noise

## 1 Introduction

Digital photos are comparable with silver halide photographs because the former contains particle noise that is similar to defects in silver halide film. Some professional photographers improve the textural quality of digital photos through the deliberate addition of granular noise. The addition of noise increases the sharpness of rectangular grating and checkerboard pattern images. Digital image definition deteriorates as the level of noise added through high-frequency stimulation increases and increases to the maximum value when noise is added at a certain level through low-frequency stimulation [1].

The feasibility of noise addition to enhance image definition was investigated in this work. In addition, the type of natural images that can be improved through noise addition was identified, the noise level that provided the optimal image definition was obtained and the difference between the objective and subjective evaluation of images was determined.

White Gaussian noise was used in all experiments. MATLAB was used to add noise to test images. Then, the mean squared error (MSE) and peak signal-to-noise ratio (PSNR) of the images were calculated through the traditional objective evaluation method. Finally, the experimental results were analysed and classified, and the relationship between image noise and image sharpness was identified.

## 2 Experiment

### 2.1 Selection of Experimental Materials

Two digital photos were selected as experimental materials. Given that most images taken in actual situations, such as highway images acquired by monitoring cameras, are blurry, therefore, two blurred images were selected in the experiment (Figs. 1 and 2).



**Fig. 1.** Landscape image



**Fig. 2.** Bench surface image

Both images were converted to greyscale. Greyscale conversion is a basic and direct spatial image processing method that involves changing the greyscale value of each pixel in the original image point by point in accordance with a specific transformation relation to improve image quality and clarity. It is also conducted to avoid the influence of image colour on human vision given that interference from image colour may reduce the accuracy of experimental results and affect post experimental analysis. Two images were used in the experiment: a highly detailed image of a landscape, and a poorly detailed image of the surface of a bench. The landscape and bench images were classified as high-frequency and low-frequency images, respectively.

## 2.2 Applicability of Noise to Images

Common image noises, such as white Gaussian noise, speckle noise, and salt-and-pepper noise, have specific characteristics. The effects and applicability of various types of noise on natural images should be considered. The addition of salt-and-pepper noise to images is unsuitable for enhancing image definition because the appearance of various light and dark granular dots in the image reduces image quality. Given its unsuitability, salt-and-pepper noise (shown in Fig. 3) was not applied in the following experiments.



**Fig. 3.** Salt-and-pepper noise image

The addition of white Gaussian noise or speckle noise to images has negligible effects. Thus, these noise types can be used as experimental noise. White Gaussian noise was selected for this experiment. White Gaussian noise with standard deviation values of 5, 10, 15, 20 and 25 were added to the images. These values were selected because numerous experiments on noise addition have shown that the addition of low levels of noise did not result in visually discernible differences between two images,

whereas the addition of high levels of noise affected the accuracy of experimental results. The optimal standard deviation was determined as 5 through numerous experiments.

The five landscape and bench surface images enhanced using white Gaussian noise with standard deviation values of 5, 10, 15, 20 and 25 are shown below (Figs. 4 and 5).

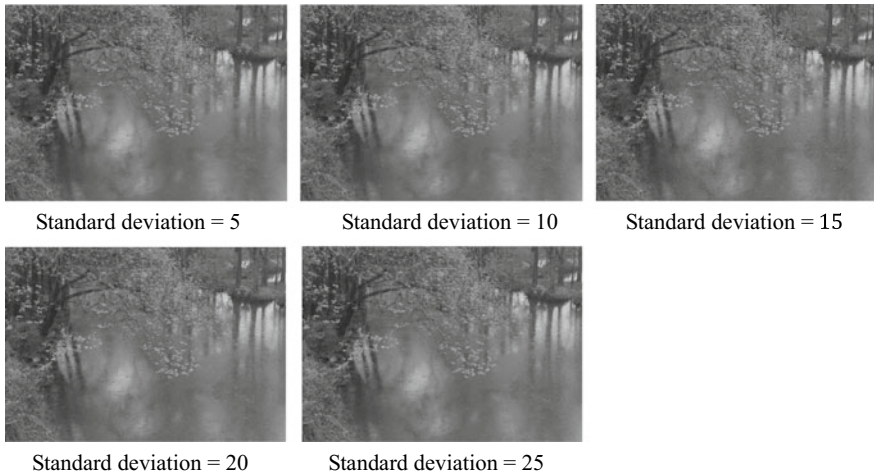


**Fig. 4.** Landscape images enhanced using white Gaussian noise with standard deviations of 5, 10, 15, 20 and 25

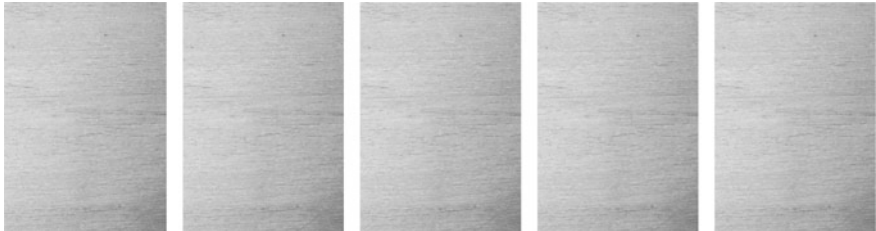


**Fig. 5.** Bench surface images enhanced using white Gaussian noise with standard deviations of 5, 10, 15, 20 and 25 (from left to right)

### 2.3 Evaluation Conditions

The images for evaluation were printed on matte photo paper with sizes of 12 cm  $\times$  16 cm using an ink jet printer (EPSON L1800). A total of 50 students aged 18–30 years old were recruited as evaluators. At least 30 of the evaluators should provide valid responses to reduce error and avoid erroneous conclusions. The images were observed under a fluorescent lamp (D50) with high colour-rendering properties of up to 700 lx and unlimited observation distance.

## 2.4 Psychometric Scaling Method for Scale Ranking

The psychometric scaling method is a scalar constitution method because it comprises a sequence of scales [3]. This evaluation method is based on scaling order.

## 2.5 Evaluation of Image Definition

Methods for the evaluation of image definition include subjective and objective methods. In subjective evaluation, firstly, some original images are used as the standard image. Then, the sharpness level of the evaluated image is determined through observation and comparison with the standard image.

Objective evaluation is a mathematical model based on the subjective system of human vision. This method mainly involves MSE and PSNR, which represent the comprehensive analytical error of a whole image.

### 2.5.1 Subjective Evaluation

To ensure the accuracy of the experiment, the original image of the landscape was mixed with five images enhanced using different noise levels and presented in a random sequence.

When the observer could not differentiate the original image from the processed images, the six images were sorted by sharpness. Then, the sensory order of each observer was recorded, and the evaluator was asked to state their observations.

### 2.5.2 Objective Evaluation

In this work, the traditional method, which is based on MSE and PSNR, was selected to evaluate image sharpness [2].

## 3 Results and Discussion

### 3.1 Results

#### 3.1.1 Results for Landscape Images

To facilitate data processing, 1 was used to represent the original image, and 2, 3, 4, 5 and 6 were used to represent the images enhanced using white Gaussian noise with standard deviations of 5, 10, 15, 20 and 25. Data were plotted as histograms as shown in Fig. 6. The abscissa represents images 1 to 6, and the ordinate indicates the scores obtained by the images (Table 1).

Images 5/0, 10/0, 15/0, 20/0 and 25/0 are images that had been enhanced using noise with standard deviations of 5, 10, 15, 20 and 25. The latter data are the PSNR values.

#### 3.1.2 Results for Bench Surface Images

See Fig. 7 and Table 2.

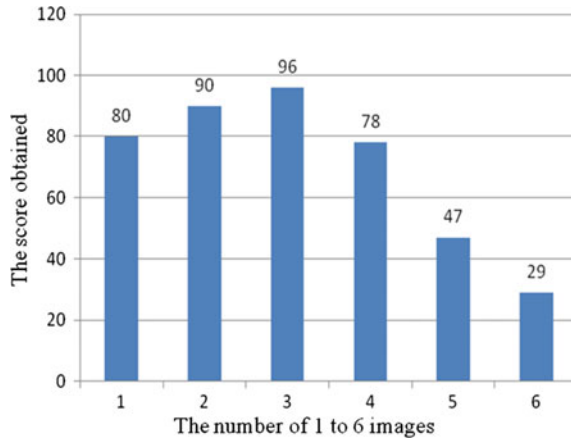


Fig. 6. Scores for landscape images

Table 1. Results for the objective evaluation of landscape images

Noise-added image/original image	PSNR value
5/0	35.6748
10/0	28.5491
15/0	24.0886
20/0	21.4701
25/0	19.6649

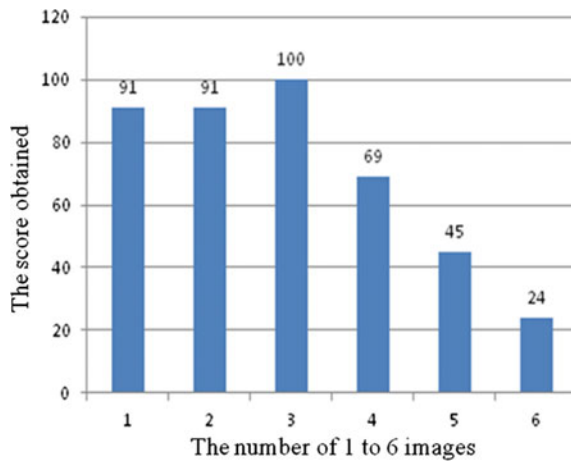


Fig. 7. Scores for bench surface images



**Table 2.** Results for the objective evaluation of bench surface images

Noise-added image/original image	PSNR value
5/0	36.8758
10/0	28.5452
15/0	24.0706
20/0	21.5010
25/0	19.7668

### 3.1.3 Analysis of Experimental Data

The landscape and bench surface images represent two types of images. The landscape images represent images with high frequency and detail. The bench surface images represent images with low frequency and detail. The small difference between the two experimental results indicates that the image enhancement approach studied in this work is applicable to high- and low-frequency images. Therefore, only the data for the landscape images were analysed.

The weighted average for the subjective evaluation scores shows that images 2 and 3 images are clearer than the original image. Most of the evaluators stated that they could distinguish object outlines from other details. The other evaluators stated that when viewed from a distance, images with added noise were more discernible than images without added noise. Some evaluators were unable to identify differences between the images.

The results of objective evaluation show that as the noise level increases, the severity of image distortion increases. Specifically, image definition deteriorates as noise level increases. This result shows that the subjective and objective evaluation methods provide different results.

The results of subjective evaluation are highly valuable and suitable for representing human visual experience. The results of this method, however, are dependent on the state of the observer, the type of the image and the conditions of the observation environment. Thus, it provides highly variable results with poor stability and requires a complex evaluation process. Although the objective method is simple and convenient, its results fail to represent human visual experience. This characteristic differentiates objective evaluation from subjective evaluation.

## 3.2 Effect of Image Noise on Image Sharpness

White Gaussian noise was added to high- and low-frequency images, and image sharpness was then evaluated through combined subjective and objective evaluation methods. The results of objective evaluation show that increased noise can reduce image sharpness, whereas those of subjective evaluation indicate that the human eye mainly focuses on regions with deep shading. Therefore, the addition of noise is equivalent to deepening the shading of image outlines and improves image clarity. Increasing noise levels sharpens image texture but decreases image sharpness. The

addition of noise with the standard deviation of 10 provides the optimal result and the ideal visually observable effect. Image sharpness appears to have improved when noise is applied to image texture.

## 4 Conclusions

This study aimed to investigate the effect of image noise on the definition of digital images. Representative natural images were selected as research materials. White Gaussian noise was added to the test images through various methods by using MATLAB. Then, the processed images were printed for subjective and objective evaluation.

The following conclusions were drawn:

- (1) The results of objective evaluation show that the addition of high noise levels decreased image definition.
- (2) The results of subjective evaluation indicate that most evaluators believed that images enhanced using noise with the standard deviation of 10 are clearer than the original image.
- (3) The comparison of the subjective and objective evaluation results indicates that increasing image noise increased the clarity of the image outline or texture. Evaluators stated that the sharpness of the image appears to have increased when they focused on the outlines of the whole image.
- (4) Traditional objective evaluation methods for image quality depend on MSE and PSNR and can only be used to evaluate the distortion of an image relative to that of the original image. It is not a professional evaluation method for image sharpness and provides results that differ from those provided by subjective evaluation.

**Acknowledgements.** This study is funded by the Science and Technology Innovation Project of Xi'an University of Technology (2016CX032).

## References

1. Kurihara, T., Manabe, Y., Aoki, N., & Kobayashi, H. (2008). Digital image improvement by adding noise: an example by a professional photographer. *Journal of Imaging Science and Technology*, 55(3), 30503-1–30503-9.
2. Yu, Q. (2011). *Study on image denoising and sharpening based on bilateral filtering*. Chongqing University (12).
3. Engeldrum, P. (2000). *Psychometric scaling: a toolkit for imaging systems development* (Chap. 6). Imcotek Press, Winchester.



# An Improved Image Denoising Algorithm in Wavelet Domain

Zhongmin Jiang<sup>1</sup> and Yingmei Zhou<sup>2(✉)</sup>

<sup>1</sup> Shanghai University of Science and Technology, Shanghai, China

<sup>2</sup> Shanghai Publishing and Printing College, Shanghai, China

47131532@qq.com

**Abstract.** In order to effectively eliminate the random noise in the noise image, based on the principle of Canny operator, an adaptive median filter is used to optimize, and an improved wavelet domain image denoising algorithm is proposed. The algorithm divides the noise image by wavelet decomposition into an approximate component for adaptive Wiener filtering, the detail component is extracted by the Canny operator based on the adaptive median filter, and the processed components are reconstructed to obtain the denoised image. The simulation results show that the proposed algorithm performs well in the random noise, and the PSNR value is greater than 24 dB. In this paper, the PSNR of the noise of the random noise is higher than that of other algorithms, and the maximum is about 12 dB, which verifies the effectiveness of the algorithm. The improved wavelet domain image denoising algorithm can remove the random noise of the image, which is a kind of excellent denoising algorithm.

**Keywords:** Wavelet transform · Wiener filter canny operator · Image denoising

## 1 Introduction

With the development of the denoising technology in images, lots of algorithms rose, which brings prepress profits? Imaging process was influenced by such as environment, device quality and signal interference, etc. [1–3]. The noising pollution is very random that cannot be defined by the single-model [4, 5]. Li [6] put forward a blind source separation denoising algorithm based on convex hull optimization. However, this algorithm cannot remove the multiplicative noise. Zhou [7] mentioned the definition of special packet filter, which can denoise by groups with  $3\sigma$  theory to aim to delete the Gaussian noise and impulse noise. But the time complexity is too high, and there is no way to delete the other noise.

The test showed this was better than other traditional algorithm, still existed impulse noise. In this paper, an improved wavelet domain image denoising algorithm is proposed by optimizing the adaptive median filter based on the principle of Canny operator.

## 1.1 Improved Canny Operator

In the traditional canny operator, the variance sigma  $\sigma$  of 2D Gauss function  $G(x, y)$  need to be set by manual. By Gauss filtering template and image convolution operator, smooth image noise achieved denoising, but the convolution operation is easy to damage the image edge information, which caused image distortion by fuzzy. And Gauss filter is applied to eliminate. In this paper, an adaptive median filter is used to improve the Canny operator, which can automatically eliminate the random noise and extract the edge of the image under the premise of protecting the edge information of the image.

## 1.2 Adaptive Median Filter Algorithm

Adaptive median filter algorithm is adaptive to two points. First, the filter window changes dynamically with the different noise density. Secondly, different processing strategies are adopted for image noise and real information, that is, keeping the real information unchanged, and filtering the noise. (1) Assuming that the size of the image is  $M * N$ , the pixel points at  $(x, y)$  are  $f(x, y)$ , and the current window size is  $W(x, y)$ , and  $W_{max}$  is the maximum allowed window. The gray value of all pixels in the current window size  $W(x, y)$  can be sorted by size ascending order, and the minimum gray value  $F_{min}$ , median  $f_{med}$  and maximum  $F_{max}$  can be easily obtained. The specific implementation steps of adaptive median filtering algorithm is as follows: if  $F_{min} < f_{med} < F_{max}$ , transfer to the third steps above, then jump, otherwise it will increase the window  $W(x, y)$  size; (2) if  $W(x, y) < W_{max}$ , jump to the above first steps, otherwise, output  $f(x, y)$ ; (3) if  $F_{min}(x, y) < f(x, y) < f_{max}$ , output  $f(x, y)$ , or  $f_{med}$  is the result. The specific flow chart of the adaptive median filtering algorithm is as Fig. 1.

# 2 An Improved Wavelet Image Denoising Algorithm

## 2.1 Enhanced Wavelet Imaging Denoising Algorithm

The approximate components obtained from image wavelet decomposition occupying a relatively large percentage of the original image information and have good robustness, while the detail component occupies less percentage of the original image information which showed the edge information and poor robustness of the image. Therefore, Wiener filtering for approximate components can not only remove noise but also protect low-frequency information effectively. However, filter details components directly will destroy image texture information due to convolution and cause edge information distortion. The improved Canny operator can automatically eliminate the random noise of images, and can extract edges under the premise of protecting the edge information of images. The improved Canny operator is used to extract the edge of the detail component after wavelet decomposition, and to eliminate the random noise distributed at high frequency. Finally, the wavelet reconstruction of the approximate component and the detail component after processing is reconstructed to restore the image to complete the image denoising. The improved wavelet domain image denoising algorithm flow as shown in the following Fig. 2.

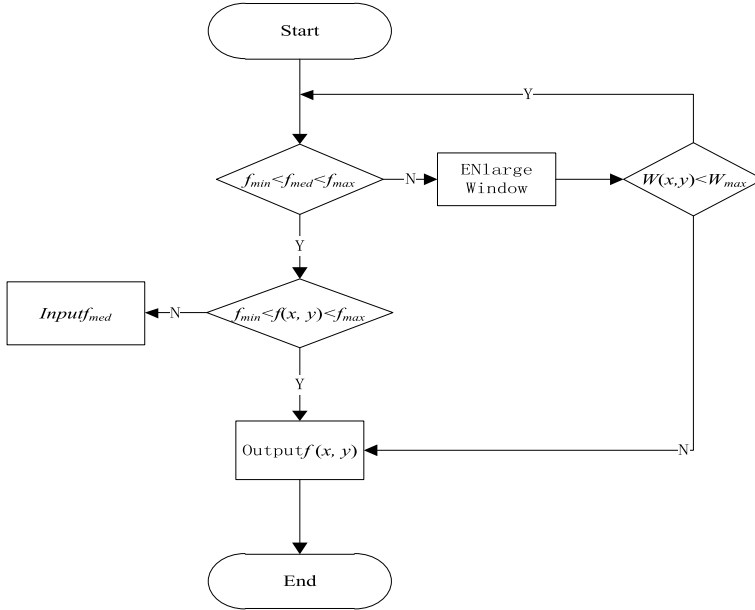


Fig. 1. Flow chart of adaptive median filter

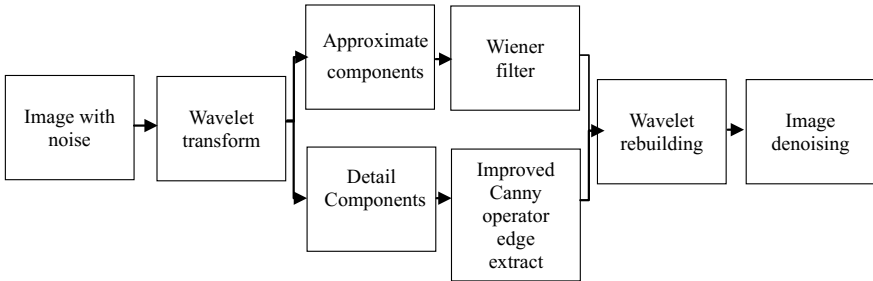


Fig. 2. Algorithm flow chart

### 3 Experimental and Analysis

This experiment selects the Matlab2009a software platform and simulates on the 32 bit Windows 7 operating system. The image with JPG format is chosen, and the pixel as the standard Lena images of 512 \* 512. PSNR [8–10] is selected as the evaluation index of de-noising effect (Fig. 3).

- (1) Gauss noise, salt and pepper noise, multiplicative noise and Poisson noise are common random noises in digital images. Simulation experiments will be designed based on these four kinds of noise. The experimental image with random noise of



**Fig. 3.** Test image

variance 0.01 is added to control variable. The algorithm is used to de-noising the noisy image to get the denoising result, as shown in the Fig. 4.

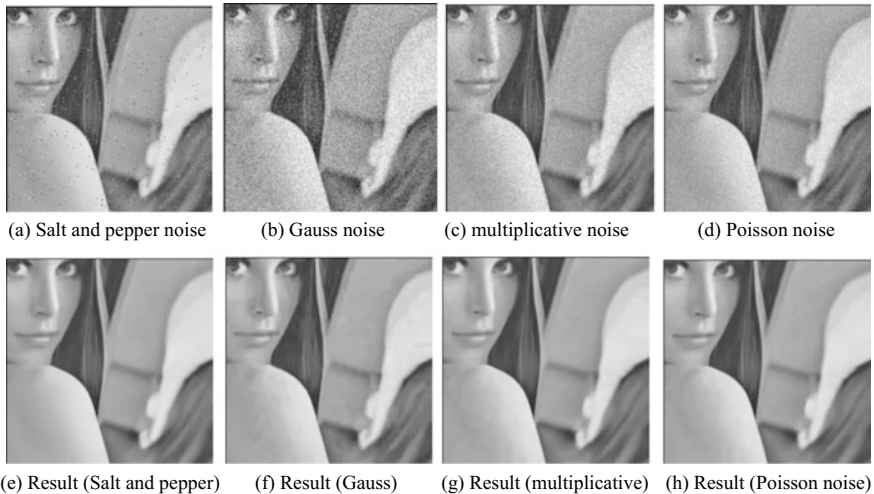


**Fig. 4.** Comparison of images before and after random noise pollution

Under the same variables, Wiener filtering algorithm, soft threshold, hard threshold filtering algorithm, document and literature [11] denoising algorithm, five groups of denoising algorithms were established to contrast group, and then compare the denoised data with the algorithm in this paper. The PSNR results are shown in the following Table 1.

**Table 1.** Comparative experimental results

	Salt and pepper noise	Gauss noise	Multiplicative noise	Poisson
Wiener filtering	25.8402	27.6568	30.4640	30.9075
Soft threshold filtering	26.2593	29.8420	29.5665	29.9814
Hard threshold filtering	25.6106	20.0711	25.7180	27.2990
Ref. [12]	26.5006	23.8749	28.7145	30.7219
Ref. [11]	32.8345	30.6295	31.6750	31.8362
Improved algorithm	34.5306	32.2654	33.6597	34.5303

According to the experimental data, the algorithm is used to denoise the experimental images with random noises. The PSNR values of denoising results are all less than 32.2654 dB, which satisfies the visual quality requirements of digital images. The experimental results showed that the PSNR value of the algorithm was 32.2654–34.5306 dB, the maximum value was higher than 12.1943 dB, and the effect is better.

- (2) The randomness of noise in practical applications is also reflected in the situation that random noise probably mixed together. The random noise of the variance 0.01 is mixed with control variable, the algorithm and the contrast algorithm are used to carry out the denoising experiment. The PSNR results are shown as shown in Table 2.

According to the experimental data, the algorithm performs denoising on experimental images containing random mixed noise, and the PSNR values of denoising results are all less than 29.1434 dB, which satisfies the visual quality requirements of digital images. The experimental results showed that the PSNR value of the algorithm was 29.4134–31.4486 dB, the maximum value was higher than 12.2237 dB, and the effect was better.

- (3) In the real applications, the random noise of the noise is also reflected in the variance of the random noise. Adding random noise of 0.01, 0.03, 0.05, 0.10, 0.30, 0.50 to the experimental images to control variables respectively. The algorithm is applied to the experiment, and the PSNR results are shown in the following Table 3.

From the experimental data, we can see that using this algorithm to remove the random variance in the image, the random result is better. The PSNR value of the objective index is not less than 24.2561 dB, the range is 24.2561–34.5306 dB, which achieves the visual quality requirement, and the denoising effect is obvious and effective.

Table 2. Comparative experimental results

	Wiener filtering	Soft threshold filtering	Hard threshold filtering	Ref. [12]	Ref. [11]	Improved algorithm
Salt and pepper + Gauss	24.7753	28.1385	19.0219	22.5915	29.9795	31.2456
Salt and pepper + multiplicative	25.9212	28.5589	22.7895	22.4480	29.0755	31.2078
Salt and pepper + Poisson	25.8200	28.6095	23.3010	23.0038	29.1645	31.4486
Gauss + multiplicative	26.0859	27.1807	19.0558	22.7218	28.8997	30.2145
Gauss + Poisson	26.4022	27.2726	19.3311	22.9697	28.9749	30.7845
Multiplicative + Poisson	29.4436	28.7918	23.4001	26.5709	29.3270	31.4421
Salt and pepper + Gauss + Multiplicative	24.1678	26.7799	18.2325	21.7057	28.1658	29.8854
Salt and pepper + Gauss + poisson	24.2437	26.8759	18.4434	21.9387	28.5605	30.1124
Gauss + Multiplicative + poisson	25.5430	26.9005	18.4941	22.1252	27.7046	29.8457
Four hybrid	23.8751	26.5035	17.7835	21.2995	27.2849	29.4134



**Table 3.** Results of random noise denoising with different variances

Variance	Salt and pepper noise	Gauss noise	Multiplicative noise	Passion noise
0.01	34.5306	32.2654	33.6597	34.5303
0.03	32.9847	31.2017	32.1476	32.5547
0.05	31.7841	29.5429	30.5514	31.5546
0.10	28.5532	26.3345	29.0643	29.5203
0.30	26.8512	25.4410	27.9124	27.9651
0.50	25.1463	24.2561	26.8912	27.0145

## 4 Conclusions

Based on the randomness of digital image of noise pollution and, single model cannot define the characteristics. we propose an improved image denoising algorithm in wavelet domain by using adaptive median filter to optimize with the principle of Canny operator. The comparison experiment results of different control variables showed that the algorithm was superior to the common random noise removal effect, the objective evaluation index PSNR is also greater than 24 dB, and the denoising effect is efficient. Compared to Wiener filter algorithm, soft threshold and hard threshold filtering algorithm, this algorithm in this paper to random noise values results PSNR were higher than the other algorithms with the highest 12 dB, verify the validity and superiority of this algorithm.

**Acknowledgements.** The paper is supported by Key Laboratory of National Press and Publication Administration: Green Platemaking and Standardization for Flexography Printing.

## References

1. Shi, R. Z., Fan, K. B., Zhou X., et al. (2013). Study on the model of chromaticity closed-loop control for print online detection. In *Applied Mechanics and Materials* (Vol. 262, pp. 291–296).
2. Xu, M., & Zheng, Y.-L. (2012). Research of printed image quality based on SSIM. *Packaging Engineering*, 33(5), 98–101.
3. Ma, S., Cao, C.-P., & Sun, Y. (2014). Online detection of the ink film thickness of metal sheet printing based on CCD method. *Packaging Engineering*, 35(23), 120–125.
4. Wang, Z.-H., Sun, L.-J., & Shao, X. (2016). An improved block matching 3D filtering image denoising algorithm. *Packaging Engineering*, 37(21), 198–203.
5. Liu, S.-Y., & Tang, W.-Y. (2014). Application of image denoising in print quality detection. *Packaging Engineering*, 35(15), 83–86.
6. Li, C.-H., Xie, D.-H., & Chen, M.-Z. (2016). Image denoising with blind source separation based on convex hull optimization. *Packaging Engineering*, 37(21), 204–210.
7. Zhou, Y., Lin, M., Xu, S., et al. (2016). An image denoising algorithm for mixed noise combining nonlocal means filter and sparse representation technique. *Journal of Visual Communication & Image Representatio*, 41(11), 74–86.

8. Li, M., Xiao, D., Liu, H., et al. (2016). A recoverable chaos-based fragile watermarking with high PSNR preservation. *Security & Communication Networks*, 9(14), 2371–2386.
9. Sun, L.-J., Bao, G.-X., Wang, Z.-H., et al. (2016). Holographic watermarking for anti-image processing based on spatial and frequency domains. *Journal of Optoelectronics Laser*, 27(1), 61–66.
10. Zhang, L.-H., Tang, B., Li, B.-C., et al. (2013). Strong robustness holographic watermarking algorithm based on DWT-SVD. *Packaging Engineering*, 21, 105–109.
11. Wang, Z.-H., Sun, L.-J., Shao, X., et al. (2016). An image denoising algorithm combined with wavelet transform and Wiener filtering. *Packaging Engineering*, 37(13), 173–178.
12. Zhao, Y.-M., & Quan, Z.-Y. (2004). An efficient Wavelet-Wiener Denoising algorithm. *Journal of Beijing University of Posts and Telecommunications*, 27(4), 41–45.



# Research on Adaptive Face Recognition Algorithm Under Low Illumination Condition

Anning Yang<sup>(✉)</sup>, Qiang Wang, and Jing Cao

School of Media and Design, Hangzhou Dianzi University, Zhejiang, China  
604843381@qq.com

**Abstract.** With the popularization of face recognition technology, the demand for the accuracy of face recognition has greatly increased. In the face image acquisition, the low illumination environment has a significant effect on the quality of human face images. Face images are susceptible to many factors such as image background, brightness, and image noise. This leads to many problems such as low detection rate of face recognition and the decline of recognition accuracy. In this paper, we take the face images under low illumination condition as a sample and present an adaptive algorithm based on the OTSU segmentation algorithm, which realizes the self-adaptation image acquisition under low illumination condition. By using the Adaboost classification detector to verify low-light face images before and after processing, the model we used in this paper successfully improved the accuracy of face detection.

**Keywords:** Low illumination condition · Self-adaptation · Face recognition · OTSU segmentation algorithm · Adaboost classification detector

## 1 Introduction

Since the 1970s, face recognition technology has evolved from initial face recognition and video coding system development, face detection applications based on image features, to face change descriptions based on principal component analysis (PCA) [1], hidden Markov model (HMM) [2]. Recently, new face recognition technologies such as classifier design and training based on neural networks (NN), support vector machines (SVM), and Boosting [3] methods have emerged. However, face recognition accuracy and detection rate are still not high under low illumination.

The low illumination image has the characteristics of narrow grayscale range, fuzzy gray level change, and high spatial correlation of adjacent pixels, which restricts image recognition. These characteristics lead to low efficiency on face recognition in a low illumination environment. In this paper, an improved face recognition algorithm based on OTSU segmentation is proposed. The proposed algorithm effectively solved the problem of incomplete information on low-illumination face images, and effectively improved the accuracy of face recognition under low illumination.

## 2 Related Algorithm

### 2.1 OTSU

The OTSU algorithm [4] is an optimal algorithm for threshold selection of image segmentation, which is simple in calculation, free from the effects of image brightness and contrast, and widely used. It divides the threshold parameters by measuring the variance of gray distribution uniformity, and splits the image into two parts, background and foreground, according to the gray characteristic of image. If the variance between background and foreground is large, the probability of misclassification is low.

### 2.2 Adaboost

AdaBoost [5] (Adaptive Boosting) algorithm learnt a series of weak classifiers from training data, and it combines them into a strong classifier. It uses the matrix feature of learning the input image through weak classifier training, called Haar [6] feature, to find out the feature number and the feature value. And then it generates a strong classifier to identify face samples by iterating. A training data set of binary classification is defined as follow:

$$T = \{(x_1, y_1), (x_2, y_2), \dots, (x_N, y_N)\} \tag{1}$$

Each sample point consists of instances  $\chi$  and labels  $\mathcal{Y}$ , where the range of  $x$  is  $x_i \in \chi \subseteq R^n$  and the range of  $y$  is  $y_i \in \mathcal{Y} = \{-1, +1\}$ .  $\chi$  is the instance space and  $\mathcal{Y}$  is the label set. When a strong classifier detects an image, all weak classifiers will vote for instance  $x_i$  and the error rate is weighted by the label  $y_i$  to calculate the sample confidence.

## 3 Face Grayscale Correction Based on OTSU Segmentation

In this paper, to solve the poor correction effects of traditional methods in low illumination image processing, a preprocessing algorithm is proposed to calculate the threshold value  $t$  of the image brightness and darkness interval using the OTSU segmentation algorithm, where the value of  $t$  is determined by the gray distribution. The image preprocessing process is shown in Fig. 1.

### 3.1 Face Gray Segmentation Based on OTSU Algorithm

The grayscale range of the input image  $f$  is  $[0, 255]$ .  $n_i$  is the number of pixels when the grayscale is  $i$ .  $N = \sum_{i=0}^{255} n_i$  is the sum of all pixels.  $p_i = n_i/N$  is the probability of each grayscale and  $\sum_{i=0}^{255} p_i = 1$ . The grayscale range is divided into two parts (denoted as  $c_0$  and  $c_1$ ), light and dark, with the gray value  $t$  as a threshold where the range of  $c_0$  is  $[0, t]$  and the range of  $c_1$  is  $[t, 255]$ . The average grayscale of  $c_0$  and  $c_1$  are calculated as follows:

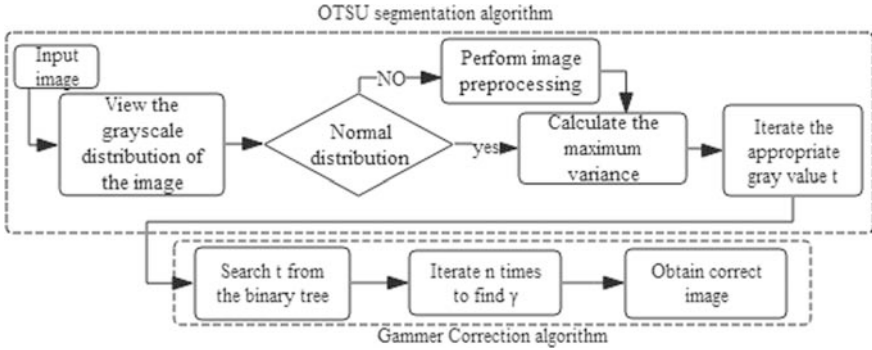


Fig. 1. Image preprocessing process

$$u_0 = \frac{\sum_{i=0}^{t-1} ip_i}{p_0} = \frac{u(T)}{p_0} \tag{2}$$

$$u_1 = \frac{\sum_{i=t}^{255} ip_i}{p_0} = \frac{u - u(T)}{p_0} \tag{3}$$

$u$  is the average grayscale of image  $f$ :

$$u = \sum_{i=t}^{255} ip_i = p_0u_0 + p_1u_1 \tag{4}$$

The total variance of  $c_0$  and  $c_1$  is defined as:

$$\sigma^2 = p_0 * (u_0 - u)^2 + p_1 * (u_1 - u)^2 \tag{5}$$

The OTSU segmentation algorithm is used for recursive operations  $n$  times, where  $t_i$  are the different thresholds obtained each time, and  $t$  is taken from  $[0, 255]$  in order. When the value of  $\sigma$  is the largest,  $t_i$  is the most suitable segmentation threshold.

Because the difference value of the gray level of the image captured in the low illumination environment is lower than the image captured in the normal environment, while using the OUST method to perform the gray division, the storage method of the binary sort tree is used in this paper to optimize the storage of the threshold  $t_i$ . A binary-ordered tree can traverse to a possibly appropriate  $t_i$ , to obtain a suitable  $t_i$  value by comparing the left and the right subtrees, thereby reducing more than half traversal time  $t_i$  and improving the calculation query speed.

### 3.2 Adaptive Gamma Correction Algorithm

This paper presents an adaptive gamma correction algorithm for the characteristics of the images captured in the low illumination environment. The algorithm is implemented through two steps of sample training and feature matching. The sample training is assign different gamma values to the images in the standard library, then block

training, extract their light characteristics. Feature matching is match the illumination characteristics of each block of the image to be processed with the illumination characteristics obtained from the training of the sample, so as to determine the optimal gamma value of each block in the image, and then carry out gamma correction in each region. The  $\gamma$  value is initialized as follows:

$$\gamma = \frac{t_{i+1}}{t_i} \tag{6}$$

where  $t_i$  denotes the corresponding threshold stored in the leftmost leaf node of the binary tree, and  $t_{i+1}$  denotes the corresponding threshold stored by the sibling node of the leftmost leaf node in the binary tree. After finding the optimal  $\gamma$  value of the region by iterating, the mean-value filtering of the Gamma matrix is used to reduce the difference of grayscale in different regions, so that the final image has better visual effects after correction.

## 4 Adaboost Face Detection Based on Haar-Like Features

### 4.1 Classifier Model

After using adaptive gamma values to preprocess low-illumination images, Adaboost face detection [5] based on Haar-like features [6] is used to perform feature selection, training and classifier construction for low-illumination images. Haar-like features mainly have some features such as borders, thin lines, and diagonal lines. The Adaboost training classifier model is shown as follow (Fig. 2):

### 4.2 Adaboost Training Classifier Process

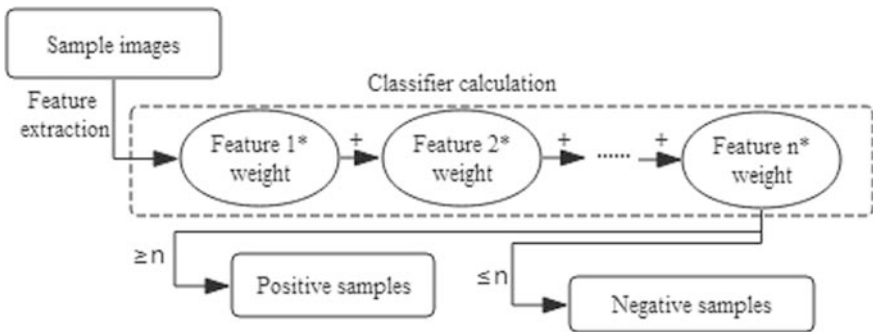


Fig. 2. A diagram showing the outline of the algorithm of classifier

The classifier and Haar-like spatial features are used to calculate the eigenvalues and the latest classification thresholds of the Haar-like features on the positive and negative

samples to obtain the weight values of the best recognition effect. The Adaboost process is shown as follows:

- (1) Acquire the sample image  $(x_1, y_1), \dots, (x_n, y_n)$  where  $y_i = 0$  denotes negative samples and  $y_i = 1$  denotes positive samples.
- (2) Weights  $w_t$  and  $w_j$  are initialized as  $w_{t,j} = 1/2m, 1/2l$  where  $m$  and  $l$  are the number of positive and negative samples.
- (3) When  $t = 1, \dots, T$ , the steps of training are summarized in the following:

- ① Update weight  $w_{t,j} \leftarrow \frac{w_{t,j}}{\sum_{j=1}^n w_{t,j}}$ .
- ② Calculate the classifier error by  $\varepsilon_j = \sum_i w_i |h_j(x_i) - y_i|$  where  $j$  is the feature index and  $h_j$  is the corresponding classifier.
- ③ Select the smallest  $j$  for obtaining the optimal classifier  $h_t$  and smallest  $\varepsilon_t$ .
- ④ When  $x_i$  is correctly classified by  $h_t$ , the weight  $w_{t+1,i}$  is updated by  $w_{t+1,i} = w_{t,i} \beta_t^{1-e_i}$ ,  $e_i = 0$ . Otherwise, update  $\beta_t$  using  $\beta_t = \frac{\varepsilon_t}{1-\varepsilon_t}$ .
- ⑤ Final strong classifier  $h(x)$  is defined as follow:

$$h(x) \begin{cases} 1 & \sum_{t=1}^T \log \frac{1}{\beta_t} h_t(x) \geq \frac{1}{2} \sum_{t=1}^T \alpha_t \\ 0 & otherwise \end{cases} \quad (7)$$

## 5 Experimental Results and Analysis

### 5.1 Comparison of Visual Effects of Images

In order to verify the effectiveness of face gray Segmentation based on OTSU algorithm in low illumination, the experiments were carried out using low illumination images of different light levels in the Yale B face database (image size: 168 \* 192) and the CMU-PIE face database (image size: 64 \* 64) and the face images collected in this study. Each light image was processed using the original Gamma correction and the modified OUST-based Gamma correction. The comparison test results are shown in Fig. 3.

From Fig. 3 we can see that the image preprocessing method proposed in this paper has better recognition performance. The experimental results obtained by the Gamma correction method in the literature [4] are overall bright, the accuracy of the face recognition is not high. The improved gamma algorithm proposed in this paper significantly improved the lighting effect of the image and retains the contrast information of the image, thereby improving the effectiveness of face detection.

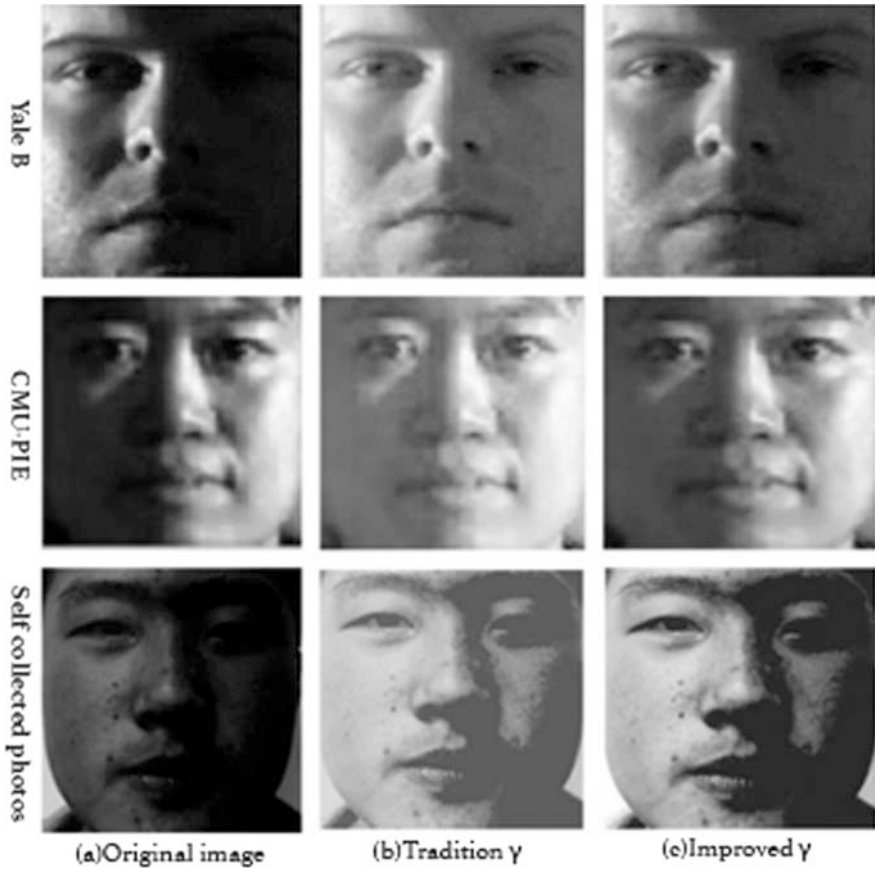


Fig. 3. Comparison of different image processing effects

## 5.2 Comparison of Image Quality Parameters

The image's signal-to-noise ratio (SNR), mean squared error (MSE) and gray average gradient (GMG) are used to compare the visual effects and the image quality. The accuracy of face detection is tested by Adaboost (Table 1).

From Table 1, we can see that the OTSU segmentation gamma correction algorithm proposed in this paper has better performance than the traditional gamma correction algorithm. It not only effectively improved the image quality under low illumination, but also preserved the image information as much as possible, which also avoided the local distortion of the image. After Adaboost feature detecting, it has been proved that the matching of image feature points processed by this algorithm is more accurate.



**Table 1.** Image quality parameter comparison

Image source	Approach	Image quality evaluation			Feature points
		SNR	MSE	GMG	Windows 24 * 24
Yale B	Tradition $\gamma$	8.389	3.147e+03	2.539	164,567
	Improved $\gamma$	21.744	57.821	3.006	176,543
CMU-PIE	Tradition $\gamma$	7.137	3.399e+03	6.167	85,356
	Improved $\gamma$	19.746	64.712	5.504	91,234
Shoot by self	Tradition $\gamma$	12.563	3.564e+03	2.846	123,345
	Improved $\gamma$	20.100	71.993	3.403	134,568

## 6 Conclusions

Experimental results show that the OTSU segmentation algorithm proposed in this paper solved the problems of traditional segmentation, improved image illumination, enhanced image quality, image visual effects and face recognition accuracy. Verification was performed using the Adaboost classifier to detect feature points. However, there are still some problems that need to be further improved in terms of memory resource usage and calculation time.

**Acknowledgements.** This work is funded by National Key Technology Research and Development Program of the Ministry of Science and Technology of China (2012BAH91F03) and Digital Imaging Theory-GK188800299016-054 and Hangzhou Dianzi University Graduate Innovative Research Fund-CXJJ2018017.

## References

1. Niu, S., Chen, Q., de Sisternes, L., Ji, Z., Zhou, Z., & Rubin, D. L. (2017). Robust noise region-based active contour model via local similarity factor for image segmentation. *Pattern Recognition*, 61, 104–119.
2. Sarkar, S., Bhairannawar, S. S., KB, R., & Venugopal, K. R. (2015). FPGA implementation of moving object and face detection using adaptive threshold. *International Journal of VLSI design & Communication Systems*, 6(5), 15–35.
3. Sharifara, A., Rahim, M. S. M., & Anisi, Y. (2014). A general review of human face detection including a study of neural networks and Haar feature-based cascade classifier in face detection. In *2014 International Symposium on Biometrics and Security Technologies (ISBAST)* (pp. 73–78). IEEE.
4. Lv, Z., Wang, K., Zou, G., & Yuan, L. (2013). Illumination compensation method for face image based on improved gamma correction. In *2013 32nd Chinese Control Conference (CCC)* (pp. 3733–3737). IEEE.
5. Kuo, S. C., Lin, C. J., & Peng, C. C. (2014). Using Adaboost method for face detection and pedestrian-flow evaluation of digital signage. In *2014 International Symposium on Computer, Consumer and Control (IS3C)* (pp. 90–93). IEEE.
6. Cimpoi, M., Maji, S., & Vedaldi, A. (2015). Deep filter banks for texture recognition and segmentation. In *2015 IEEE Conference on Computer Vision and Pattern Recognition (CVPR)* (pp. 3828–3836). IEEE.



# Research on 3D Printing Color Image Processing of Micro-lens Combined with Micrographics

Yaojian Hu<sup>1</sup>, Liyu Liao<sup>1</sup>, Zhaohui Yu<sup>1(✉)</sup>, and Yunfei Zhong<sup>2(✉)</sup>

<sup>1</sup> YUTO R&D Institute, Shenzhen YUTO Packaging Technology Co., Ltd.,  
Shenzhen, China

Alex.yu@szyuto.com

<sup>2</sup> School of Packaging and Materials Engineering,  
Hunan University of Technology, Hunan, China  
maczone@163.com

**Abstract.** Under the condition of naked eye observation, the micro-lens array could achieve 3D image effect with 360° panoramic depth, which made them an important developing direction of 3D printing technology. Currently, the original images of micro-lens 3D printing technology, designed by micrographics array and printed with spot-color, had the characteristics of poor 3D imaging effect, single color as well as gradation. In order to obtain excellent imaging effect, rich gradation, and colorful image, the method of 3D printing color image processing combined with micrographics arrays was proposed based on the micrographics array processing technology. Specifically, both of SPMG model and MG4CP model were constructed with combination of micrographics and color images, and the experimental scheme and process were designed. Then the original color images were screened with ordinary process, SPMG model and MG4CP model, respectively. The effects of original images were compared, and the feasibility of the two models was verified. The results showed that the MG4CP model had more advantages in image processing, effects reproduction, and printing.

**Keywords:** Micrographics array · Micro-lens array · 3D printing · Image processing · Moire

## 1 Introduction

Micro-lens arrays have both horizontal and vertical parallax in stereo display and can present 3D image effect in the range of 360° under the condition of naked eye observation, which avoids the image jumping and vertigo caused in the process of cylindrical grating 3D imaging. At present, the original stereo images of micro-lens array 3D printing are mainly carried out through spot-color printing or monochromatic micrographic arrays, which have the shortcoming of poor 3D imaging effects, toneless color and single form after imaging. Furthermore, in conjunction with the abundant gradual color images, the reproduction effect of the original images is not soft. According to the situation, the color separation and combination modes with

micrographics were studied through the integration of processing technologies of micrographics with color image separation and screening technologies. Two kinds of color separation and screening models (SPMG and MG4CP) were put forward and to be used in the original color images of micro-lens 3D printing, by which the color micrographics arrays were achieved and the quality of micrographic arrays in combination with color image was promoted obviously [1, 2].

## 2 Micro-lens and Micrographics Array Technologies

### 2.1 Micro-lens Arrays

Micro-lens array refers to the lens array formed by periodic arrangement of tiny lenses between 10 and 1000 um in diameter on a plane. The micro-lens units mainly consist of square lens, circular lens or regular hexagon lens. The lens array is formed by orthogonal or cellular arrangement during periodic arrangement. The arrangement period of lens array will directly determine the arrangement period of micrographics array with 3D printing [3, 4] (Fig. 1).

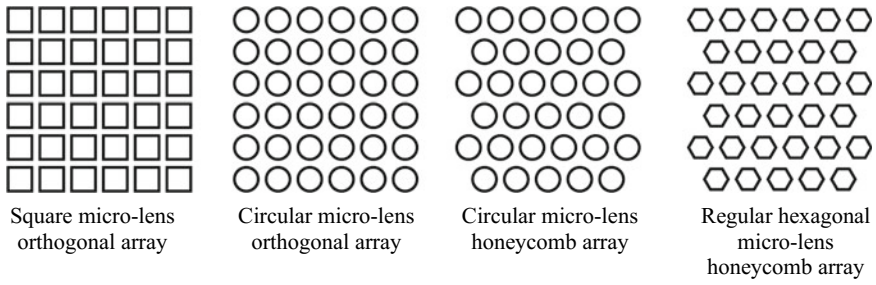


Fig. 1. Schematic diagram of micro-lens arrays with different shapes

### 2.2 Micrographics Arrays

Micrographics, the smallest units of 3D images in the 3D printing of micro-lens, are usually in the form of letters, numbers, figures, symbols, etc. According to the arrangements, cycles, and sizes of the micro-lens arrays, the parameters of micrographics units including size, arrangements, and cycles are designed. And the files of micrographics arrays for 3D printing are made by graphic design soft-wares [5] (Fig. 2).

### 2.3 3D Imaging Principle of Micro-lens Arrays

3D printing of micro-lens arrays, one of the important 3D display technologies with naked eye, is based on the integrated imaging technology and Moire magnification theories. Through the superposition of micro-lens arrays and micrographics, the enlarged Moire patterns in combination with micrographics arrays are formed. And



Fig. 2. Schematic diagram of micrographics array A

then the 3D image effect with 360° panoramic depth is obtained based on the integrated imaging theory of micro-lens arrays [6].

The paper mainly pays attention to the design and production of micrographics arrays when the angle between the micro-lens array and the micrographics array is zero. At this point, the period  $T$  of the enlarged Moire pattern is [7]:

$$T = \frac{T_1 T_2}{|T_1 - T_2|} \quad (1)$$

where  $T_1$  is the permutation period of the micro-lens array, and  $T_2$  is the permutation period of the micrographics array.

### 3 Modeling of Color Image Processing About Micro-lens 3D Printing

#### 3.1 Micro-lens 3D Printing

The imaging graphic of micro-lens 3D printing, that is the micrographics arrays and printed on the soffit of the transparent substrate, can present the 3D effect through the micro-lens array on the upper surface of the substrate. In combination with color images which are mainly printed on the upper surface of the transparent substrate, namely the color images are printed on the top of the micro-lens array. The visual effects with multiple depths of field and abundant gradation are formed. In order to print the micro-lens array on the soffit of the substrate together with the color images, parts of the color images need to be hollowed out and filled with micro-lens array to form the color images with micro-lens array.

In order not to destroy the design effect of color images, it is of great significant to combine the micrographics array into color separation files in processes of the color separation and screening. Two main ways of combination are existed. One is to overprint the micrographics array directly in the full or part areas of the color images in the printing process, and the other is to integrate the micrographics array into the color separation files by the microstructure screening technology before printing in processes

of the color separation and screening. The color separation models of the micro-lens 3D printing color image processing were studied and established taking the letter A as the micrographics unit based on the above methods.

### 3.2 Spot-Color Process Micrographics Model (SPMG)

SPMG model refers to the color images with the micrographics are created by overprinting the color images with the micrographics array which acts as a spot-color. In order to get a real color reproduction, a similar color with color image is specified based on the effect of color images. Subsequently, the Neugebauer model is used for color separation of the images. Then five color separations consisting of the CMYK four-colors and the spot-color are obtained following the extraction of the spot-color channel.

The Neugebauer model indicates that the color in each region is the weighted average of all the base colors in the region, and the weight is the percentage of the area covered by the base colors. Micrographics units are equal to the dots in printing. The size of micrographics units has an effect on the dot coverage of the spot-color, further affects the specified color value and the extraction of the spot-color information. The theoretical dot coverage areas or dot coverages need to be calculated to get a more accurate extracted color value of the spot-color according to the micro-pattern array [8].

### 3.3 Micrographics Four-Color Process Model (MG4CP)

In the MG4CP model, the micrographics unit acts as the dot and the period of micrographics arrays is equal to the dot spacing in the screening process of the four-color separation based on conventional four-color separation of the color images. Each color separation plate is composed of a micrographic array and then half-tone color separation plates with the micrographic arrays are formed, which can be called microstructure screen processing. Finally, the color images with the micrographic arrays are obtained after overprinting [9, 10].

In the process of microstructure screening, the halftone screening of the images can be carried out by constructing a threshold matrix. The setting and arrangement of matrix elements is of great importance. After constructing a matrix template capable of 0–256 grayscales, the dot shape of the micrographic elements is taken as the arrangement baseline, the matrix elements are set along the baseline trend, and the perimeter of the dot boundary is controlled to reduce dot expansion [11]. The grid design of  $m * n$  threshold matrix, the minimum unit in the micrographics array, is shown in Fig. 3.

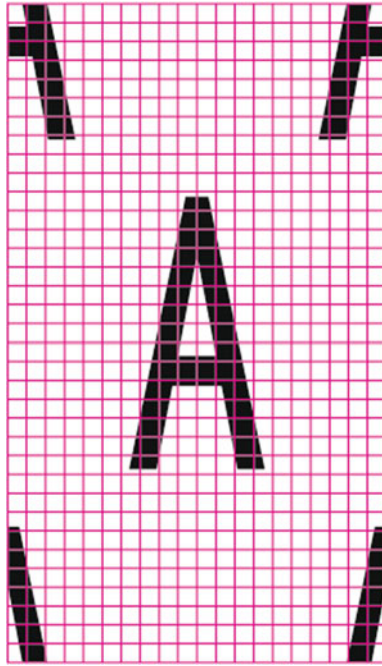


Fig. 3. Schematic diagram of the grid design of  $m * n$  threshold matrix

## 4 Simulation Sampling Experiment and Quality Evaluation

### 4.1 Experimental Scheme and Procedure

In order to compare the color reproduction effects of the color images, an original color image is screened with ordinary process (the control group), SPMG model and MG4CP model, respectively. The experimental process is shown in Fig. 4.

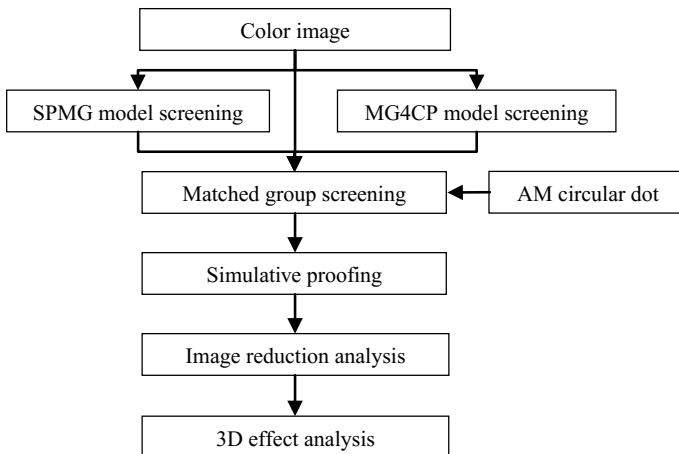


Fig. 4. The experimental flow chart

### 4.2 Screening Processing of Color Images

Lena, a classical digital image, is selected as the experimental object for screening and is shown in Fig. 5. The size of the image is 40 \* 40 mm and the resolution is 300 dpi.

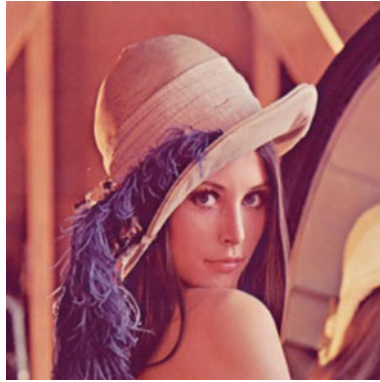


Fig. 5. The original color image (Lena)

In the paper, the micro-lens array material with a period of  $T_1 = 0.12$  mm and a radius of  $r = 0.04$  mm are used as experimental data sources. The arrangement structure and parameters of the material are shown in Fig. 6. The distance  $d$  between two virtual lines can be equivalent to the distance between two adjacent dots in printing and screening in the figure. According to the Pythagorean Theorem,  $d$  is equivalent to 244 lpi. The letter A is selected as a micrographics element and the array is conducted according to 0.117 mm ( $T_2$ ) of the period. Similarly, it can be seen that the equivalent screening lines in A micrographics array is 251 lpi. In order to minimize the effect of the screening lines on the image reproduction, 250 lpi are used for four-color plates (CMYK) in the control group and the SPMG model.

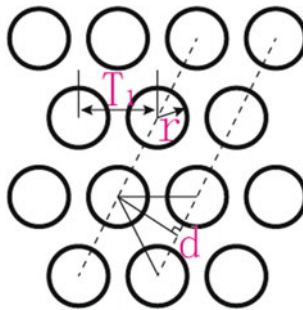
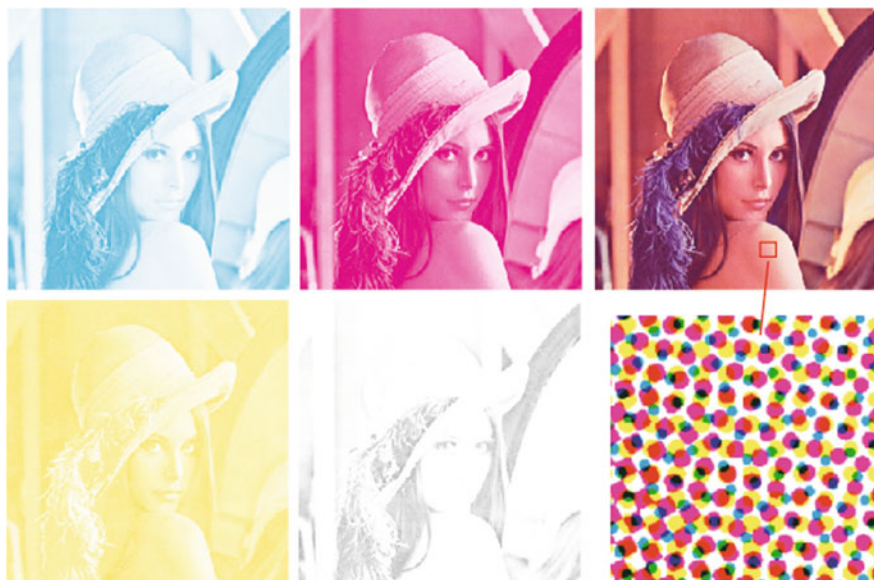


Fig. 6. Structure and parameters of the micro-lens array

In the control group, the 5080 dpi of output precision and the 250 lpi of amplitude modulation (AM) screening are adopted. The screening angles including  $18^\circ$ ,  $72^\circ$ ,  $90^\circ$ , and  $45^\circ$  are applied for the C, M, Y, and K plates, respectively. The size of the image is consistent with the original image after screening. The screening effect in the control group is shown in Fig. 7.



**Fig. 7.** The effect of normal four-color separation and screening

In the SPMG model, the 5080 dpi of output precision and the 250 lpi of amplitude modulation screening are adopted. The screening angles including  $18^\circ$ ,  $72^\circ$ ,  $90^\circ$ , and  $45^\circ$  are applied for the C, M, Y, and K plates, respectively. The spot-color plate with the micrographics array is full point printing, and the screening angle can be arbitrary because that it has no obvious influence on the pattern effects. The micrographics array consisting of letter A is conducted based on 0.117 mm of the period and  $45^\circ$  of the screening angle. The size of the image is consistent with the original image after screening. The screening effect in the SPMG model is shown in Fig. 8.

In the MG4CP model, the 5080 dpi of output precision is adopted. The four-color plates adopt the same micrographics array consisting of letter A which is conducted based on 0.117 mm of the period and  $45^\circ$  of the screening angle. The size of the image is consistent with the original image after screening. The screening effect in the MG4CP model is shown in Fig. 9.





**Fig. 8.** The color separation and screening effect with SPMG model



**Fig. 9.** The color separation and screening effect with MG4CP model

### 4.3 Performance Comparison of Image Processing Between the Two Models

The corresponding halftone images are obtained after screening with ordinary process, SPMG model and MG4CP model, respectively. The original image as well as the screening effects with MG4CP, AM, and SPMG model are shown in Fig. 10. It can be seen that the half-tone image effect with the MG4CP model is closer to the original image than others.



**Fig. 10.** Comparison of the image processing effect with different models

The SPMG model takes up less memory in the processes of color separation and screening, and can easily generate uniform 3D patterns. The spot-color information in the color image can be extracted following the determination of the micrographics elements and array. However, the color image with the 3D micrographics array is heavier than the original image, and the color reproduction difference between the two images is obvious. Therefore, the model is not applicable for the products with high requirements in reproduction. Furthermore, the five-color printing inevitably raises costs. Comparatively, MG4CP model, with a complicated process, takes up more memory in the processes of color separation and screening, and the threshold matrix cannot be changed after determination. But the obtained color image with excellent

color reproduction is close to the original image. The 3D patterns can present different effects in size, color, depth, etc. What's more, four-color printing can meet the requirement, which hardly increases the costs.

Both of SPMG model and MG4CP model can be used to realize the combination of 3D micrographics arrays with full-page or local color images in the processes of color images, and the effects are flexible and changeable.

## 5 Conclusions

In the 3D printing color image processing of micro-lens, the excellent color separation was carried out by adopting the spot-color separation and microstructure screening technology. The color image effects with micro-lens 3D printing, large depth of field, and 360° stereo effect have been achieved. Furthermore, the feasibility of the two models was verified. Finally, the image after color separation and screening could present the features of the original image well and achieve the expected effect.

**Acknowledgements.** Project is supported by Natural Science Foundation of Hunan Province (Grant No. 2016JJ6034), Training Project of Hunan Industrial Application of Higher Education Institutions (Grant No. 15CY003), Hunan Province Higher Education Institutions Demonstration Base of Production, Education and Research (Grant No. 2014-117).

## References

1. Yang, C. (2015). *The micro-mirror array technology in anti-counterfeiting design of high-fidelity printing*. Wuxi: Jiangnan University.
2. Li, M. (2016). *Research on stereo image rendering based on microlens array*. Guangzhou: South China University of Technology.
3. Lin, V., Wei, H.-C., Hsieh, H.-T., & Su, G.-D. J. (2011). An optical wavefront sensor based on a double layer microlens array. *Sensors*, *11*, 10293–10307.
4. Joo, B.-Y., & Ko, J.-H. (2014). Simulation study on the minimization of moiré patterns caused by microlens array films for backlight applications. *Journal of the Optical Society of Korea*, *18*(5), 538–545.
5. Zheng, W., Shen, S., Gao, Y., Liu, N., & Liu, Y. (2017). Design methodology for moiré magnifier based on micro-focusing elements. *Optics express*, *25*(25), 31746–31757.
6. Athineos, S. S., Sgouros, N. P., Papageorgas, P. G., Maroulis, D. E., Sangriotis, M. S., & Theofanous, N. G. (2005). Physical modeling of a microlens array setup for use in computer generated IP. In *Stereoscopic Displays and Virtual Reality Systems XII*. SPIE (Vol. 5664, pp. 472–479) © 2005 SPIE and IS&T.
7. Gabrielyan, E. (2007) The basics of line moiré patterns and optical speedup. [arXiv:physics/0703098](https://arxiv.org/abs/physics/0703098) [physics. optics]. April.
8. Yang, L., Zhong, Y., & Wang, B. (2012). Spot color separation of printing images based on fuzzy rules. *Journal of Computer Applications*, *32*(6), 1598–1600.
9. Ostromoukhov, V., & Hersch, R. D. (1995). Artistic screening. In *Computer Graphics Proceedings, Annual Conference Series* (pp. 219–228).

10. Ostromoukhov, V., & Hersch, R. D. (1999). Multi-color and artistic dithering. In *Computer Graphics Proceedings, Annual Conference Series* (pp. 1–9).
11. Zhou, X., Shi, R., Su, Q., Pang, Y., & Lin, D. (2014). A new anti-counterfeiting technology based on artistic dot screening. *Journal of Geomatics Science and Technology*, 31(2), 203–207.



# Image Quality Evaluation of Digital-Analog Imaging System

Yuliya Kim<sup>(✉)</sup>, Qiang Wang, and Jing Cao

School of Media and Design, Hangzhou Dianzi University, Zhejiang, China  
molitea@yandex.ru

**Abstract.** Digital-analog imaging system which integrate digital imaging and AgX photographic imaging system are the best means to reproduce and simulate digital images. The adaptation of digital imaging and photography of AgX is key to optimizing the image quality of the digital-analog imaging system output. This paper will use image quality parameters such as MTF (Modulation Transfer Function), the Wiener spectrum and Gamut. These parameters have been based on the developed digital image test chart, which includes quality elements such as density step wedges, color chart, edges in different AgX photosensitive material. This paper will use these parameters to objectively evaluate the modulation transfer characteristics, noise, and color reproduction of the digital-analog imaging system by micro-density measurement methods.

**Keywords:** Image quality · Digital analog system · MTF · Wienur spectrum

## 1 Introduction

Still photography has a rich history of technological innovations which date back to the early 19th century. While digital images have grown in popularity, digital imaging technology does not replace silver halide (AgX) photography. Digital imaging technology and AgX photography have mutually integrated to form an advanced-imaging system—the digital-analog imaging system.

Digital imaging technology has many benefits and is useful for contrast control, color adjustment, image sharpening, the combination of text, graphic and image, image defects removal and image masking. Being able to copy, store and transfer digital images on the internet is also a very convenient feature of the digital system [1].

AgX photography performs better than the digital display of CRT and LED on many key points such as tone, color reproduction, high-resolution display and a lower price. Therefore, a combination of the advantages of digital imaging technology and AgX technology—more specifically, the integration of digital front-end processing and analog AgX imaging output module of the digital-analog imaging system, is the key to satisfactory image quality [2].

## 2 Description of the Imaging Process of Digital-Analog Imaging System

To compare the input and output image features, it is good practice to use test patterns consisting of special image information (such as step wedge, edges and color patches etc.) as shown in Fig. 1. In short, first expose test patterns of a digital-analog imaging system on AgX materials, and obtain the photographic visual images after this treatment. In this process, it is necessary to consider the spectral features of imaging equipment, and the number of pixels and the resolution carefully. It is also important to consider the image processing speed, storage capacity, file format and the impact of image compression method [3]. Only by establishing scientific and rational input and output linkages, and evaluating image quality parameters of each imaging module, can we get the best image quality evaluation methods and standards.

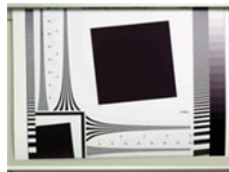


**Fig. 1.** Slant edge was used for input and output image features

In this study Konica qd21 image recorder, and digital image were used in conjunction with one another. The performance of imaging process can be described by a series of independent physical parameters, such as MTF, Wiener spectrum, the color gamut and characteristic curve. The most appropriate measure characteristics are chosen scientifically.

### 2.1 Modulation Transfer Function

MTF is one of the best ways to evaluate system imaging capability comprehensively. MTF curves show resolution and contrast information simultaneously allowing a lens to be evaluated based on the requirements for a specific application. This can be used to compare the performance of multiple lenses. Used correctly, MTF curves can help determine if an application is actually feasible [4]. That is in image chain the all links in the chain are linear processes, MTF of the imaging systems  $M_s(T)$  is the product of all links MTF  $M_i(T)$ :

$$M_s(T) = \pi M_i(T) \quad (1)$$

Therefore,  $M_s(T)$  of the entire process of imaging chain is the product of a video recorder  $M_f(T)$  and AgX materials  $M_p(T)$ . Therefore,  $M_f(T)$  calculated from  $M_s(T)$  and  $M_p(T)$ :

$$M_f(T) = M_s(T)/M_p(T) \quad (2)$$

Typically, modulation transfer of imaging recorder and the overall AgX materials are non-linear, and MTF is related with the density. This requires to consider the use of linear curve of the region in the MTF calculation, use lower input modulation parameters ( $M_s = 0.26\text{--}0.62$ ), to reduce the impact of nonlinear aspect.

## 2.2 Wiener Spectrum

In Wiener spectrum analysis, the Wiener spectrum of the ultimate image  $N_s(T)$  is the sum of the Wiener spectrum of an image recorder  $N_f(T)$  and the Wiener spectrum of AgX materials  $N_p(T)$  [5]. The main noise of the image recorder is the electronic noise, the electronic noise transmit to AgX materials converts to scale changes of AgX material characteristics curve  $\gamma_p$  and MTF  $M_p(T)$ .

$$N_s(T) = \gamma p^2 M_{p^2}(T) N_f(T) + N_p(T) \quad (3)$$

Therefore, the Wiener spectrum of the image recorder should be:

$$N_f(T) = (N_s(T) - N_p(T)) / \gamma p^2 M_{p^2}(T) \quad (4)$$

The scale value and shape of Wiener spectrum vary with the AgX material density. The graininess of AgX materials  $\sigma D$  refers to the root-mean-square (RMS) of the density change, can be calculated from the scale value of the Wiener space frequency spectrum  $N(0)$ . RMS value is relative to its area  $A$ .

$$RMS = 103\sigma D = (N(0)/A)^{1/2} \quad (5)$$

## 2.3 Color Gamut

In a digital-analog imaging system, an image recorder will record RGB in AgX materials, and uses a spread of a dye-based CMYK hybrid system to reproduce color. The hue, saturation and brightness of generated color based on this AgX material system are formed and controlled by computer system. This determines hue, saturation and brightness of the color imaging in AgX materials, and is also affected by the photographic processing on ultimate color imaging. The CIE1931 x y system is a very useful tool and method to reflect the scope of color imaging system.

Gamut refers to the color range the color imaging system can reproduce. This describes the ability of an imaging system to express the number of colors in color space under certain conditions [6]. As gamut is not exclusively used in one specific imaging system (CRT or photo paper), it is suited to comparing the color reproduction capacity of different imaging systems.

## 2.4 Characteristic Curve

In a digital-analog imaging system, there are input and output non-linear features, when digital information is translated to analog information, and when AgX materials convert optical image information to visual image information. Such nonlinear transformation relations are characteristic curves [7]. Characteristic curves usually include linear and nonlinear parts and it is very important to use the linear part of characteristics curve to ensure correct information transfer of the greatest extent, and to reduce the impact of nonlinear functions in the transmission of information the imaging system.

## 3 Experimental Results and Analysis

### 3.1 Experiment

This study used a Konica qd21 imaging recorder, used in accordance with manufacturer's recommended standards to set film sensitivity, gradient and neutral gray balance of AgX materials. There was a focus on controlling technical parameters impacting image quality, including the color reproduction benchmarks determined by the DAC and exposure controller, the sharpness benchmark determined by resolution, the focusing system and lens, the noise elimination from the DAC and electron gun, and color reproduction controlled by exposure spectral characteristics and color filters (RGB).

We used the Konica qd21 to output at different speeds for color, and black-and-white test patterns, and compared this with the standard exposure samples (edge MTF in 0.26–0.62), considering density and graininess, to assess the image quality of the image recorder. We used the CCD scan-micro-densimeter to measure the micro-density of two copies using the same treatment conditions, and implements flat field correction and noise removal and other digital image analysis and corrections. At the same time, under the higher S/N ratio, we measured the MTF and the Wiener spectrum, and used the exposure table to get  $MP(T)$  and  $NP(T)$ . To get  $Ms(T)$  and  $Ns(T)$  from image recorder exposure, we can get the  $Mf(T)$  and  $Nf(T)$  that has not been calculated by formula 2 and 4, and calculate the RMS of the density changes value  $\sigma D$  and system resolution using Wiener spectrum measured from the different densities.

### 3.2 Results Analysis

Based on the above experiment and calculation, we can get a number of image evaluation parameters for Konica qd21, the main parameters are as follows.

#### 3.2.1 MTF

The  $Mf(T)$  of the highest resolution of Konica qd21 are smaller than the  $MP(T)$  of photosensitive materials, the resolution on  $Mf(T) = 0$  is 29 L/mm, that is, pixel size is 17  $\mu\text{m}$ . When the edge density is about 1.0, the contrast is about 0.26–0.62, the measure does not impact the  $Mf(T)$  of the contrast and density, as shown in Fig. 2. The high resolution testing image is sharper and close to the quality of photographic film, but the resolution is 50% lower, the sharpness would be significantly reduced.



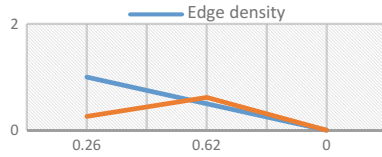


**Fig. 2.** Modulation transfer function

**3.2.2 Graininess**

In each measuring density, the RMS of density changes of image generated by Konica qd21 exposure is higher about 15–25% than images generated by the standard exposure table, as shown in Fig. 3. By comparing Wiener spectrum shapes of two different exposure methods, found that the reason of the higher RMS is that the Konica qd21 exposure samples have excess noise that the space below the frequency of 30 L/mm, and has dramatic reduction at  $T > 10$  L/mm and can't be measured after  $T > 30$  L/mm, and the noise and frequency space are as same as the MTF.

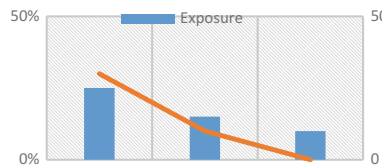


**Fig. 3.** Changes generated by Konica qd21

**3.2.3 Gamut**

According to analysis of the color gamut the in CIE1931 x y, the key parameters of the Konica qd21's system was set, including the brightness, gamma, and gray balance [8]. The only way to maximize the elimination of gamut difference between electronic media generated images and the actual images, and to reduce the color difference of main color, was by adjusting the parameters according to the characteristics of different AgX materials. This was the only way to get an acceptable color reproduction.

**4 Conclusions**

In this study objective image quality evaluation methods, such as MTF and Wiener spectrum measurement, have applied to digital-analog imaging system which combines AgX imaging and electronic imaging successfully. This study used the imaging quality parameters of each module of the digital-analog imaging system by comparing these two different methods of imaging functions between the standard model and digital-analog imaging system. The study used an analysis of the constraint relationship of the Konica qd21 image resolution and pixel size to construct the testing method of photosensitive materials color characteristics using the control method of color reproduction.

Experimental results show that the application of MTF, Wiener spectrum and color gamut can be used to evaluate the characteristics of a digital-analog imaging system, which can help to optimize the match between the associated system components, in order to get the best quality image.

**Acknowledgements.** This work is funded by National Key Technology Research and Development Program of the Ministry of Science and Technology of China (2012BAH91F03) and Digital Imaging Theory—GK188800299016-054.

## References

1. Liu, M., Zhao, X., Aoki, N., & Kobayashi, H. (2010). *Digital imaging giving a feeling of the silver halide photography*. ITE Technical Report.
2. Li, M., Min, L., & Wang, M. (2015). Dynamic analysis of coupled gray cow patches and checkerboards coexist cellular neural networks. In *Proceedings of 2015 IEEE 16th International Conference on Communication Technology (ICCT)*.
3. Zhao, Y. (2016). Control method of image quality in digital printing. *Journal of Simulation*, 4(1).
4. Wu, Z., Luo, Z., Zhang, Y., Guo, F., & He, L. (2018). Image quality assessment of high-resolution satellite images with MTF-based Fuzzy comprehensive evaluation method. In *Proceedings Midterm Symposium on Developments, Technologies and Applications in Remote Sensing*.
5. Pedersen, M., Bonnier, N., Hardeberg, J. Y., & Halbregesten, F. (2010). Attributes of image quality for color prints. *Journal of Electronic Imaging*, 19, 011016-1-13.
6. Li, Y., Po, L.-M., Xu, X., & Feng, L. (2014). No-reference image quality assessment using statistical characterization in the shearlet domain. *Signal Processing: Image Communication*, 29(7), 748–759.
7. Guo, M.W., Zhang, C.B., & Chen, Z. H. (2014). A novel method of image quality assessment. In *Applied mechanics and materials*.
8. Ruikar, J., Sinha, A., & Chaudhury, S. (2017). Image quality assessment using edge correlation. *International Journal of Electronics and Telecommunications*, 63(1), 99–107.



# Comparison of Grayscale Image Colorization Methods in Different Color Spaces

Liqin Cao, Yongxing Shang, Jianjun Zhao<sup>(✉)</sup>, and Zhijiang Li

School of Printing and Packaging, Wuhan University, Wuhan, China  
whpps2018@126.com

**Abstract.** With the aim of coloring old black and white photos, medical image illustrations, and classic movies, the gray-scale image colorization methods are used to assign color information to grayscale image. Color space, as the basis of quantitative color information, plays an important role in the gray-scale image colorization. In this paper, the different color spaces—Lab, Luv, YCrCb, YIQ used in the grayscale image colorization are analyzed. Two classical automatic colorization methods, Welsh approach and Gupta approach, are carried out in those color spaces. Different performances are observed in such color spaces when using the two colorization methods. In Welsh approach, the transfer result depends on the luminance information of reference image. Since the process of Gupta approach is on the purpose of propagating color information using the least-squares optimization method, the result shows limited relevance to the reference image luminance. The experimental results demonstrate that YCrCb and YIQ have better performance in texture similarity than Lab and LUV at both color transfer methods. LUV presents the worst performance for most of the images when applying color migration. The optimal results are obtained based on YCrCb and YIQ in Welsh approach. While, it is observed that Gupta method has limited effect on the colorization results.

**Keywords:** Colorization · Color space · Grayscale image

## 1 Introduction

Color is defined as a subjective feeling of human, which is produced by the visual nervous system when the retina perceives a variety of wavelengths of light. Color space, as a model of quantitative representation of color, is widely used in various fields of image processing, including image clustering and segmentation. Reinhard summarized the color space currently used in color processing [1, 2], including Lab, LUV, YUV, PCA-specific color space, RGB, and XYZ. Variety of color transfer methods have been proposed, targeting at the color space applications. As a special case of color transfer, grayscale image colorization has gained significant attentions in the literature.

Grayscale image colorization is applied in many fields such as image processing in medical (colorization of medical imaging and X-ray scanning), industrial, and movie fields. The purpose of colorization is to obtain the color information from the original image which only has luminance information and generate the result image with a

certain degree of confidence. To achieve this goal, the process of color transfers often chooses color space that the luminance and chrominance can be coordinated without interfering each other. Welsh proposed a method based on Lab color space [3], by changing the value of a, b of grayscale image to achieve colorization. In addition, other color spaces are applied to the existing colorization methods. Levin's method based on human intervention uses YUV color space [4], and Cheng uses neural network implementation under LUV color space [5]. All of them have the same characteristic, that is, in such a luminance-chrominance opposite color space.

Although such color spaces have been widely used in all kinds of color processing work, few researchers have analyzed the effect of color spaces for colorization. According to the CIE standards, the luminance-chrominance independent color space has great difference in all aspects. The purpose of this paper is to analyze the influence of different color spaces in the colorization. In this paper, Welsh's and Gupta's [6] methods are selected to compare the performance under lab, LUV, YCrCb and YIQ color spaces, and the quality evaluation method is used to evaluate the effect of colorization. The results show that Welsh's and Gupta's methods based on reference image adjusts the color components of the initial false color image with a uniform conversion, in linear or non-linear ways respectively. This process can benefit from the correlation between the channels, which is much higher in YCrCb and YIQ space. Therefore, YCrCb and YIQ have better performance in texture similarity than Lab and LUV for both color transfer methods. LUV presents the worst performance for most of the images at color migration. The optimal results are obtained using YCrCb and YIQ spaces in Welsh approach. The choice of color space has limited effect on the colorization results at Gupta method, because this approach is based on the least-squares optimization, which is used to propagate color information not for point color transfer method such as Welsh method.

The remaining of this paper is organized as follows. Section 2 describes the related color space and colorization techniques in detail. Experimental results and analysis are shown in Sect. 3 before conclusions are given in Sect. 4.

## 2 Color Spaces and Colorization Methods

### 2.1 Color Space Transformation

In the process of colorization, the color image is called the reference/source image, and the grayscale image to be colorized is called the target image. The process of the grayscale image colorization is based on keeping the target image's luminance information and borrowing the color information from the reference image. Therefore, researches usually select the luminance—chrominance color space, such as Lab, LUV, YCrCb and YIQ. The three channels in Lab and LUV color spaces are independent, while and channels in YCrCb and YIQ are linear correlated.

#### (1) Lab

Lab color space is a model developed by the International Commission on Illumination for industrial use in 1976. L represents luminance, ab value represents chrominance

information. Where  $a$  represents the position between magenta and green and  $b$  represents the position between yellow and green. It is obtained from the RGB color space through the XYZ color space by non-linear transformation. It's a uniform color space which means that when the value changes uniformly, the sense of the human visual is also uniformly changed. Therefore, the purpose of formulating this color space is to obtain a color expression consistent with human visual perception [7].

## (2) LUV

LUV color space is derived from a simple transformation of the XYZ color space, just as visually as Lab. Similarly, L represents the luminance, U-V value represents the chroma information. This color space is designed to be perceptually uniform, which means a given change in value corresponds roughly to the same perceptual difference over any part of the space. It is a color space, which is independent of the display device.

## (3) YCrCb

YCrCb color space, a sampling of YUV, is used primarily to optimize the transmission of video signals' color. It is a simplified representation of RGB color space by linear transformation, to reduce the bandwidth used during transmission. Y indicates the luminance, Cr indicates the difference between red and luminance, and Cb indicates the difference between the blue and the luminance.

## (4) YIQ

YIQ is similar to YCrCb and is also utilized for television signal transmission. Y is the luminance, I indicates the change from orange to cyan, and Q indicates the change from purple to yellow-green. YIQ color space has the advantage of separating the luminance components in the image, and the relationship between the YIQ color space and the RGB color space is a linear transformation. Therefore, the calculation amount is small and the clustering characteristic is relatively good. The YIQ color space can adapt to the change of light intensity, and be effectively used for color image processing and identified the moving objects in complex background collected under natural conditions.

## 2.2 Grayscale Image Colorization Methods

There are two main categories of colorization methods: user-assisted colorization methods and automatic colorization methods. User-assisted colorization methods [4, 8, 9] require users manually define layer mask or mark color scribbles on grayscale image. Manual colorization is time-consuming and it cannot provide sufficient and desirable color scribbles. Automatic colorization methods can reduce the extent of user effort, which transfer color from an exemplar color image. The color transferring is usually performed from the luminance channel of both images and the final color is computed with methods such as machine learning and statistics approaches [6, 10–13]. In our work, two classical methods are selected, Welsh method and Gupta method. Both of them are based on Lab space.

### (1) Welsh method

Welsh et al. [3] proposed an automatic colorization technique, which relies only on matching the luminance values in small neighborhoods of each pixel in the target grayscale image to those in the reference color image, and transfers color accordingly.

There are three steps in the colorization producer. First, each image is converted into the lab color space. Next, for each pixel in grayscale image in scan-line order, the best matching sample in color image using neighborhood statistics are found. The best match is determined by using a weighted average of pixel luminance and the neighborhood statistics. Finally, the chromaticity values of the best match pixel are transferred to the pixel in grayscale image to form the final image. Here, the neighborhood size is  $5 \times 5$ , and the statistics consist of the mean and standard deviation of luminance values of the neighborhood.

### (2) Gupta method

Gupta et al. adopted a fast cascade feature matching scheme to automatically colorize grayscale image. This method is an example-based automatic method in colorization. It works at the resolution of superpixels and attains a strong extent of spatial consistency in colorization.

During the colorization process, the features from the target and reference images are extracted, and then the corresponding superpixels between the images are found. Each correspondence is identified by voting paradigm leveraging on spatial information. Each correspondence is assigned a confidence based on the feature matching costs and high confidence correspondences are assigned an initial set of chromatic values to the target superpixels. To enforce the spatial coherence of these initial color assignments, Gupta et al. proposed an image space voting framework to identify and correct invalid color assignments. Finally the color assignments are propagated to the entire grayscale image by Levin's algorithm, and the final colorization image is obtained.

## 3 Experiment and Analysis

In order to compare the performance of those methods mentioned above in different color space, four images (Fig. 1) in different lightness tone are selected. Welsh method and Gupta method have been carried out in Lab, LUV, YCrCb and YIQ for colorization. The structural similar index and color similarity are utilized to evaluate the colorization results.

### 3.1 Evaluation Methods

#### (1) Structural similar index

In our work, we implement PSNR, SSIM and GSSIM to measure the structural similarity between the target image and colorization result image [14–16]. The main purpose is to show whether the structure information of the original image has been



**Fig. 1.** **a** The target images. **b** Reference images

changed in the process of colorization. According to the experimental results, we use a weighted combination to express the above three indicators.

$$NMS = \alpha_1 PSNR + \alpha_2 SSIM + \alpha_3 GSSIM. \tag{1}$$

Here,  $\alpha_1$  is 0.2,  $\alpha_2$  and  $\alpha_3$  are 0.4. Higher value of NMS results smaller change of structure information.

(2) Color similarity

Bhattacharyya distance, cosine similarity and histogram cross-core are leveraged to measure the color similarity between the reference image and generated image. The different distances between them are calculated in RGB color space.

The formula of Bhattacharyya distance is as follow:

$$BD = \sqrt{1 - \frac{\sqrt{\mathcal{A} * \mathcal{B}}}{(3 * N)^2 * \overline{\mathcal{A}} * \overline{\mathcal{B}}}} \tag{2}$$

Here,  $\mathcal{A}, \mathcal{B}$  indicate the color vectors of the reference image and the generated image,  $N$  means color digit, we set  $N$  as 8.  $\overline{\mathcal{A}}$  and  $\overline{\mathcal{B}}$  indicate the average of the two-color vectors corresponding to the two images respectively.

Calculating the cosine similarity, we regard the R, G, B combination of each pixel in the RGB color space as a vector to represent the color, then the calculation of the cosine similarity between two-color vector can be regarded as a measure of the similarity of color information. In this paper,  $1 - \cos(\theta)$  is utilized to measure cosine similarity.

$$\cos(\theta) = \frac{\sum_{k=1}^3 x_{1k}x_{2k}}{\sqrt{\sum_{k=1}^3 x_{1k}^2}\sqrt{\sum_{k=1}^3 x_{2k}^2}}. \tag{3}$$

Histogram intersection is calculated by comparing the degree of overlap of the various levels in the histogram of the two images:

$$\mathcal{J}(H(X), H(Y)) = \sum_{j=1}^r \min(H(X)_j, H(Y)_j). \tag{4}$$

where  $X$  and  $Y$  represent histograms of the reference and colorization result images.  $H(X)_j$  is the  $j$ th bin in the  $X$  histogram and  $r$  is the number of the bin in the histogram. Histogram information values are normalized in the calculation.

The smaller the Bhattacharyya distance, cosine similarity and histogram intersection result more similar color information between reference image and colorization image.

### 3.2 Colorization Results and Analysis

Most of example-based color transfer methods depend on the color information of reference image. In Welsh and Gupta methods, the color channel information is determined by reference images. While, the lightness channel is significant basis for finding the matching color information between target and reference images. In our work, two categories images are selected, ①  $L_t \in L_r$ , ②  $L_t \notin L_r$ .  $L_t$  and  $L_r$  are the range of luminance of target image and reference image respectively. The second category images can be divide into three cases: ①  $L_{t,min} \langle L_{r,min} \&\& L_{t,max} \rangle L_{r,max}$ , ②  $L_{t,min} > L_{r,min} \&\& L_{t,max} > L_{r,max}$ , ③  $L_{t,min} < L_{r,min} \&\& L_{t,max} < L_{r,max}$ . Images in columns 2–4 in Fig. 1 correspond to above three cases.

Figure 2 shows the colorization images based on Welsh method. The process of color information migration depends on luminance matching. When the value of luminance exceeds the range of the reference image, the color transfer will be abnormal. When  $L_t \in L_r$ , the color range of the generated images is nearly consistent with that of the reference image. The transfer algorithm has a good performance in each color space. When  $L_t \notin L_r$ , there are obvious color noise, especially in  $L_{t,min} < L_{r,min} \&\& L_{t,max} < L_{r,max}$  case. Comparing four spaces, the results based on Lab and LUV spaces are displeased. While the colorization results in YCrCb and YIQ spaces are relatively insensitive. The reason is that the results can be benefit from the correlation between the channels of YCrCb and YIQ.

Figure 3 shows the colorization results of Gupta methods. Compared with Welsh method, the colorization images based on Gupta method has better consistency in color space. Since the color transfer depends on the optimization of the global image, the influence of the difference between the ranges of luminance is not obvious. The results demonstrate that there is stability process in different color spaces and the generated images are similar. In some cases, the LUV color space obtains anomaly results in Fig. 3b.



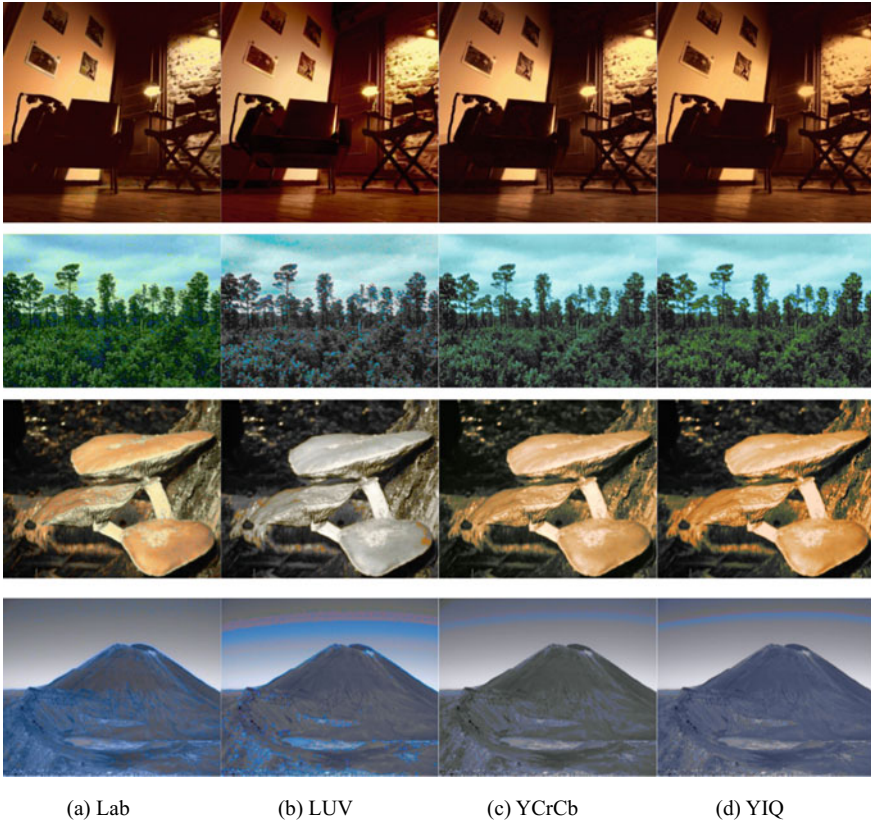


**Fig. 2.** The colorization results of Welsh method in different color spaces

Figure 3 shows the colorization results of Gupta methods. Compared with Welsh method, the colorization images based on Gupta method has better consistency in color space. Since the color transfer depends on the optimization of the global image, the influence of the difference between the ranges of luminance is not obvious. The results demonstrate that there is stability process in different color spaces and the generated images are similar. In some cases, the LUV color space obtains anomaly results in Fig. 3b.

To further analysis the colorization result, the texture and color similarity are statistics analyzed in Tables 1 and 2. For the texture similarity, the value of NMS in YIQ and YCrCb spaces are larger than that in Lab and LUV, which indicates the texture results between the target image and the colorization image are much similar. In Gupta method, LUV performance is the worst, and texture structure based on YCrCb space keeps best.

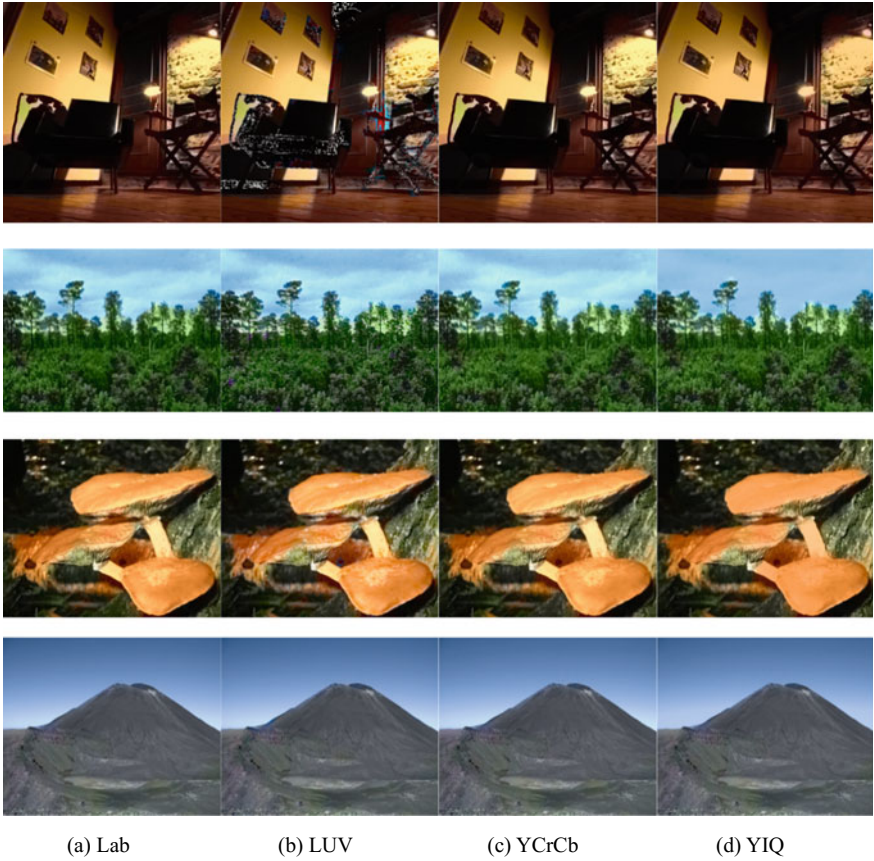


**Fig. 3.** The colorization results of Gupta method in different color spaces

Table 2 shows the color similarity between the reference image and the colorization result in different color spaces. It demonstrates that LUV spaces lead to the worst result. For Welsh algorithm, the colorization images based on YCrCb and YIQ spaces achieves better results than those images based on the other spaces. For Gupta method, the generated results have little difference in Lab, YCrCb and YIQ spaces. The conclusion is consistent with the visual display in Fig. 3.

**Table 1.** Texture similarity between the target image and the colorization result in different color spaces

No.	Color spaces	Welsh				Gupta			
		SSIM	GSSIM	PSNR	NMS	SSIM	GSSIM	PSNR	NMS
1	Lab	0.89	0.97	18.01	<b>4.34</b>	0.97	0.96	18.65	4.50
	LUV	0.91	0.96	18.35	4.42	0.84	0.80	15.15	<b>3.68</b>
	YCrCb	0.90	0.97	18.86	<b>4.52</b>	0.97	0.97	19.07	<b>4.59</b>
	YIQ	0.90	0.97	18.02	4.35	0.96	0.97	18.56	4.48
2	Lab	0.97	0.80	15.97	<b>3.70</b>	0.98	0.88	16.77	<b>4.10</b>
	LUV	0.90	0.80	18.14	4.31	0.98	0.89	17.03	4.15
	YCrCb	0.97	0.97	19.55	<b>4.69</b>	0.99	0.97	17.40	<b>4.27</b>
	YIQ	0.98	0.97	19.11	4.60	0.95	0.97	16.70	4.11
3	Lab	0.97	0.92	16.49	4.05	0.99	0.95	18.02	4.38
	LUV	0.98	0.92	14.66	<b>3.69</b>	0.99	0.94	17.88	<b>4.35</b>
	YCrCb	0.99	0.97	17.05	4.20	0.99	0.96	18.40	<b>4.46</b>
	YIQ	0.99	0.97	17.35	<b>4.25</b>	0.95	0.95	18.09	4.38
4	Lab	0.97	0.92	13.51	<b>3.45</b>	0.99	0.94	16.62	4.10
	LUV	0.94	0.85	14.47	3.61	0.99	0.94	16.58	<b>4.09</b>
	YCrCb	0.99	0.96	14.45	3.67	0.99	0.97	16.90	<b>4.16</b>
	YIQ	0.99	0.97	14.48	<b>3.68</b>	0.98	0.97	16.85	4.15

Bold indicates the maximum and minimum value of texture/color similarity between each reference image and the colorization result in difference color space

## 4 Conclusions

In this study, the influence of different color spaces on grayscale image color transfer methods have been studied, and the performance of the two approaches in Lab, LUV, YCrCb and YIQ space have been compared. Since the correlation between the channels of YCrCb and YIQ spaces is higher than those of Lab and LUV, the first two color spaces can achieve better results for Welsh algorithm, especially when the luminance range of target image is outside that of reference image. For Gupta method, as this method is a global color transfer using optimization processing, all color spaces have similar performance, except for LUV.

**Acknowledgements.** This work was supported by National Key Research and Development Program of China under Grant No. 2017YFB0504202, the Fundamental Research Funds for the Central Universities under Grant No. 2042018kf0229, National Natural Science Foundation of China under Grant No. 41671441 and Natural Science Foundation of Hubei Province in China under Grant No. 2016CFA029.

**Table 2.** Color similarity between the reference image and the colorization result in different color spaces

No.	Color spaces	Welsh				Gupta				No.	Welsh				Gupta						
		DB	CC	HI	DB	DB	CC	HI	DB		DB	CC	HI	DB	CC	HI	DB	CC	HI		
1	Lab	0.86	<b>0.22</b>	0.47	0.87	0.27	0.51	2	Lab	<b>0.88</b>	<b>0.59</b>	<b>0.55</b>	0.88	4	Lab	<b>0.88</b>	<b>0.61</b>	<b>0.61</b>	0.88	<b>0.64</b>	
	LUV	<b>0.87</b>	<b>0.56</b>	<b>0.64</b>	<b>0.88</b>	<b>0.29</b>	<b>0.53</b>		LUV	<b>0.94</b>	<b>0.92</b>	<b>0.84</b>	<b>0.89</b>		LUV	<b>0.88</b>	<b>0.61</b>	<b>0.61</b>	0.88	0.61	0.63
	YCrCb	<b>0.86</b>	0.24	<b>0.47</b>	<b>0.86</b>	<b>0.23</b>	<b>0.47</b>	YCrCb	0.90	0.82	0.73	<b>0.88</b>	YCrCb		0.90	0.70	0.67	<b>0.88</b>	0.60	0.63	
	YIQ	0.87	0.35	0.51	0.87	0.27	0.51	YIQ	0.89	0.78	0.69	0.89	YIQ		0.89	<b>0.72</b>	<b>0.70</b>	<b>0.88</b>	<b>0.59</b>	<b>0.63</b>	
3	Lab	0.86	<b>0.17</b>	0.51	0.85	0.18	0.46	4	Lab	0.89	0.62	0.64	<b>0.88</b>	4	Lab	0.89	0.62	0.64	<b>0.88</b>	<b>0.61</b>	0.62
	LUV	<b>0.90</b>	<b>0.33</b>	<b>0.65</b>	<b>0.86</b>	<b>0.21</b>	<b>0.51</b>		LUV	<b>0.88</b>	<b>0.61</b>	<b>0.61</b>	0.88		LUV	<b>0.88</b>	<b>0.61</b>	<b>0.61</b>	0.61	0.63	
	YCrCb	<b>0.86</b>	0.24	0.51	0.85	<b>0.17</b>	<b>0.45</b>		YCrCb	0.90	0.70	0.67	0.88		YCrCb	0.90	0.70	0.67	0.88	0.60	0.63
	YIQ	0.87	0.28	<b>0.49</b>	<b>0.85</b>	0.19	0.46		YIQ	<b>0.90</b>	<b>0.72</b>	<b>0.70</b>	<b>0.88</b>		YIQ	<b>0.90</b>	<b>0.72</b>	<b>0.70</b>	<b>0.88</b>	<b>0.59</b>	<b>0.63</b>

Bold indicates the maximum and minimum value of texture/color similarity between each reference image and the colorization result in difference color space

## References

1. Reinhard, E., & Pouli, T. (2011). Colour spaces for colour transfer. In R. Schettini, S. Tominaga, & A. Trémeau (Eds.), *Computational Color Imaging. CCIW 2011. Lecture Notes in Computer Science*. Berlin, Heidelberg: Springer.
2. Faridul, H. S., Pouli, T., Chamaret, C., Stauder, J., Reinhard, E., Kuzovkin, D., et al. (2016). Colour mapping: A review of recent methods, extensions and applications. *Computer Graphics Forum*, 35, 59–88.
3. Deshpande, A., Rock, J., & Forsyth, D. (2015). Learning large-scale automatic image colorization. In *The IEEE International Conference on Computer Vision (ICCV)*. Santiago, Chile: IEEE Computer Society.
4. Levin, A., Lischinski, D., & Weiss, Y. (2004). Colorization using optimization. In *SIGGRAPH '04*. Los Angeles, USA: ACM.
5. Cheng, Z., Yang, Q., & Sheng, B. (2015). Deep colorization. In *The IEEE International Conference on Computer Vision (ICCV)*, Santiago, Chile.
6. Gupta, R. K., Chia, A. Y. S., Rajan, D., Ng, E. S., & Huang, Z. Y. (2012). Image colorization using similar images. In *Proceedings of the 20th ACM International Conference on Multimedia*, Nara, Japan. ACM.
7. Hernández-Hernández, J. L., García-Mateos, G. J., & González-Esquivia, M. (2016). Optimal color space selection method for plant/soil segmentation in agriculture. *Computers and Electronics in Agriculture*, 122, 124–132.
8. Huang, Y.-C., Tung, Y.-S., Chen, J.-C., Wang, S.-W., & Wu, J.-L. (2005). An adaptive edge detection based colorization algorithm and its applications. In *Proceeding of the 13th Annual ACM International Conference on Multimedia*, ACM, Singapore.
9. Liu, B.-B., Lee, H.-K., & Hu, Y. (2009). Source camera identification from significant noise residual regions. In *IEEE International Conference on Image Processing* (vol. 119, pp. 1749–1752).
10. Bugeau, A., Ta, V. T., & Papadakis, N. (2014). Variational exemplar-based image colorization. *IEEE Transaction on Image Processing*, 23(1), 298–307.
11. Liu, S., & Zhang, X. (2012). Automatic grayscale image colorization using histogram regression. *Pattern Recognition Letter*, 33(13), 1673–1681.
12. Zhang, R., Isola, P., & Efros, A. A. (2016). Colorful image colorization. In arXiv preprint [arXiv:1603.08511](https://arxiv.org/abs/1603.08511).
13. Cao, L. Q., Jiao, L., Li, Z. J., Liu, T. T., & Zhong, Y. F. (2017). Grayscale Image colorization using an adaptive weighted average method. *Journal Imaging Science and Technology*, 6(61), 60502-1–60502-10(10).
14. Antonini, M., Barlaud, M., Mathieu, P., & Daubechies, I. (1992). Image coding using wavelet transform. *IEEE Transaction on Image Processing*, 1(2), 205–220.
15. Wang, Z., Bovik, A. C., Sheikh, H. R., & Simoncelli, E. P. (2004). Image quality assessment: From error visibility to structural similarity. *IEEE Transaction on Image Processing*, 13(4), 600–612.
16. Chen, G. H., Yang, C. L., & Xie, S. L. (2006). Gradient-based structural similarity for image quality assessment. *Journal of South China University of Technology*, 2(9), II–II.



# Research on Evaluation Method of Scanner Imaging Quality

Zhuoran Zhang<sup>(✉)</sup>, Qiang Wang, and Weiyan Zhang

School of Media and Design, Hangzhou Dianzi University, Zhejiang, China  
1543404712@qq.com

**Abstract.** Scanner is an important tool for digitizing color graphics, and the imaging quality directly determines the accuracy and quality of digital image digitization. This article addressed the need for color image reproduction, and also developed and designed a set of scanner imaging quality evaluation process and their evaluation parameters. And it established a scanner imaging quality evaluation method, and achieved a scientific accurate quantitative assessment of the scanner. The results of research have played a very important guiding role in the evaluation and application of scanners.

**Keywords:** Scanner · Resolution · Dynamic range · Quantitative evaluation

## 1 Introduction

A scanner is an image digitizing device that converts various original information into digital information which is more suitable for computer processing. With the popularization and development of computers, networks, and multimedia technologies, it has become the key to computer-based image input, just like the computer's "eyes". The evaluation of the scanner is very important for the selection and application of the scanner.

This article is based on systematic analysis of the research methods of scanner imaging quality by domestic and foreign scholars in the past 10 years, targeting the objective evaluation of imaging quality, and filtering out the key parameter "scanner resolution and dynamic density range" that reflects the quality of the digitized image captured by the scanner. This article sets up a set of scanning image quality evaluation process and data processing methods. The obtained results can be applied to scanner quality evaluation and equipment selection.

## 2 Scanner Quality Evaluation Principle

Currently, the scanner is mainly used in digital color content of the original graphic attribute and the location attribute of information [1]. Among them the digitization of content attributes mainly includes: the resolution of the scanner, the dynamic range of imaging, the ability of color reproduction, and the definition of graphics and texts. The digitization of position attributes mainly includes: size scaling and geometric deformation.

## 2.1 Image Digitization Principle

Image digitization refers to the process of converting analog image information into digital image information by using digital imaging devices (such as scanners, digital cameras). Sampling theorem is the theoretical basis for image digitization. In 1928, it was officially quoted as a theorem by H. Nyquist, C. E. Shannon, the founder of Information Theory in 1948. As shown in formula 1, the expression is as follows: If a certain time function  $s(t)$  does not contain greater frequency components than  $W$ ,  $s(t)$  is uniquely determined by these given function values within the time domain  $T = 1/2 W$  time interval.

$$s(t) = \sum_{k=-\infty}^{\infty} s(kT) \frac{\sin^c(2Wt - k)}{C(2Wt - k)} \quad (1)$$

In this formula,  $s(t)$  represents the time function,  $s(k)$  represents the frequency,  $W$  represents the highest frequency and  $T$  is a function of time.

The  $s(t)$  value when  $s(\frac{k}{2W})$  is  $\frac{k}{2W} - k$  is also the sample value  $s(kT)$  [2].

If the relationship between the spatial frequency response and the maximum visual resolution is determined, it based on the Nyquist frequency limit of the sampling theorem. The spatial frequency corresponding to the spatial frequency response 0.1 is taken as the maximum visual resolution [3]. When using Imatest Master 4.4.8 analysis software to analyze spatial frequency response (SFR), the SFR value is calculated by Formula (2):

$$\text{SFR}(k) = \frac{\left| \sum_{j=1}^N \overline{LSF'_w(j)} e^{-t^2 \pi k j / (N-1)} \right|}{\sum_{j=1}^N \overline{LST'_w(j)}} \quad (2)$$

where  $\overline{LSF(j)}$  is the line spread function.

## 2.2 Main Parameters of the Scanner Evaluation

The performance of the scanner is mainly reflected by the quality of the digitized image obtained by scanning the simulated image [4]. From the digitization of content attributes, the main parameters include: resolution, color reproduction range, imaging dynamic density range and sharpness. Among them, the resolution and imaging dynamic density range are the most critical. From the digitization of position attributes, the main parameters include: scaling and geometric deformation. Among them, geometric deformation is the most important.

### 2.2.1 Resolution

Resolution refers to the scanner's ability to express the details of an image. It is usually expressed in pixels per inch (ppi). The resolution of the scanner is divided into optical resolution, interpolation resolution and maximum resolution. The resolution in this paper only refers to the optical resolution.

### 2.2.2 Dynamic Density Range

The dynamic density range, also called scan density range, refers to the scanner's ability to reproduce subtle changes in hue, that is, the range of tones that the scanner can record from white to black or the difference between the brightest and darkest colors that can be measured. The better the dynamic range is more layers that correctly capture the various shades will have, and more image can be directly output.

### 2.2.3 Geometric Deformation

Image distortion includes lateral deformation and longitudinal deformation, which means that the scanned image can't be ignored in the deformation error [5]. The deformation error is reflected by the contrast of the image feature points before and after scanning. If the vertical and horizontal deformation coefficients are different, a change in the coordinates of the characteristic point occurs in a certain direction, and then geometric distortion correction is required.

## 3 Scanner Evaluation Test Chart

In this paper, based on the scanner's ability to scan and reflect originals, according to the resolution and dynamic density range evaluation requirements, a reflective resolution test chart and a dynamic density range evaluation chart are adopted [6, 7].

### 3.1 Resolution Test Chart

In this study, it is a commercial version of the standard resolution test. As shown in Fig. 1. The resolution of the scanner is tested by testing the test patterns of the different composition setting parameters in the template, and the distribution of the test pattern is shown in Fig. 2. The reflective resolution test chart is made of monochrome paper-based light-sensitive material. The plate background is not easy to fade uniform neutral gray material. The effective size of the test chart is  $\geq 100$  mm. The resolution test chart design has 14 pattern areas [8].

Zone 1 is an edge-edge pattern with a  $5^\circ$  angle to the vertical, and it is used to test horizontal sampling.

Zone 2 is the Center Focusing Area—two concentric circles of different frequencies to assist in focusing.

Zone 3 is an edge-edge pattern with a  $5^\circ$  angle to the horizontal, and it is used to test the vertical sampling capability.

Zone 4 is the Contrast Indicator—it is used to show the contrast conditions under different spatial frequencies.

Zone 5 and Zone 6 are Diagonal Res— $45^\circ$  diagonal resolving power strips. It is used to measure the viewing resolution of  $45^\circ$  and has a test range of 100–1000 LW/PH.

Zone 7 and Zone 8 are Vertical Res—the ability to visualize the camera's resolution of vertical images.

Zone 9 is a combination of the 1st and 2nd zone patterns. The MTF curve and the horizontal MTF curve can be tested on both sides of the edge.



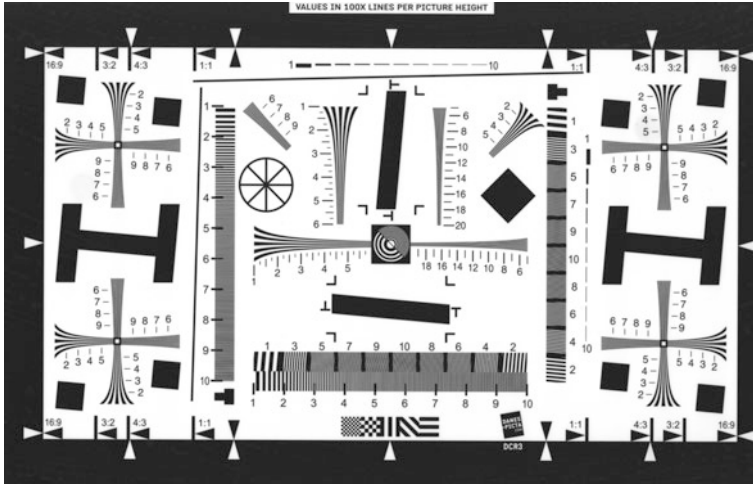


Fig. 1. Resolution test chart

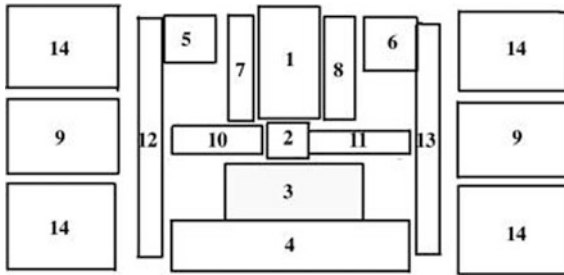


Fig. 2. Distribution of components of the resolution test chart

Zone 10 and Zone 11 are Horizontal Res—the ability to visualize the camera’s resolution of horizontal images.

Zone 12 is used to visually determine the maximum resolution of the scanner, consisting of horizontal and vertical lines. In the reflective test chart, the spatial frequency of the lines are 6, 8, 12, 24, and 40 l/mm, i.e. 300, 400, 600, 1200, and 2000 ppi. In the transmissive test chart, the spatial frequencies are 25, 33.350, 100, and 166.7 l/mm, i.e. 1200, 1600, 2400, 5000, and 8400 ppi.

Zone 13 is an approximately horizontal and approximately vertical line with an angle of about 5° to the vertical, and the spatial frequency setting is the same as in zone 12.

Zone 14 is a quad cross-type test unit for measuring the horizontal and vertical viewing resolution of the four corners and has a test range of 100–1000 LW/PH.

### 3.2 Dynamic Density Range Test Chart

This article uses Kodak’s dynamic density range test chart to conduct experiments, which is reflective. As shown in Fig. 3. Among them, the reflective dynamic density range test chart is made of non-fading uniform neutral gray material, the effective size should be  $\geq 100$  mm, the minimum density value of 20 gray blocks is  $\leq 0.01$ , and the maximum density value is  $\geq 1.80$ , as shown in Table 1.

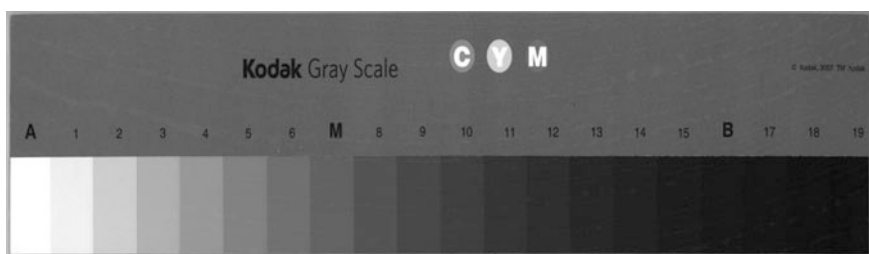


Fig. 3. Dynamic density range test chart

Table 1. Density values of reflective dynamic density range test chart

A	1	2	3	4	5	6	M	8	9
0.01	0.1	0.21	0.31	0.41	0.51	0.61	0.7	0.81	0.91
10	11	12	13	14	15	B	16	17	18
1.00	1.10	1.20	1.29	1.39	1.48	1.58	1.64	1.75	1.82

#### 3.2.1 Benchmark Mark

In the test chart, a fiducial mark was also designed to verify the scanner’s sampling frequency. Among them, the horizontal spacing of the reflective test chart reference marks is 12.5 mm, and the vertical distance is 83.3 mm.

## 4 Scanner Imaging Quality Evaluation

### 4.1 Scanner Resolution Evaluation

In this paper, binary lines of the test chart area 4, 11 and 12 are used for evaluating the maximum visual resolution of the scanner and the linear and periodic scan artifacts of the calibration scan. Among them, the maximum visual resolution is determined by visually reading the scanned test chart image reproduced on the display and the hard copy material. The resolution of the vertical line is used for determining the resolution of the fast scan, and the resolution of the horizontal line is used for determining the resolution of the slow scan.

Using the test chart area 1, 2, 9 to objectively evaluate the resolution of the scanner, that is, through the software Imatest Master 4.4.8 to analyze the spatial frequency response curve of the scan test chart, fast scan and slow scan, as shown in Fig. 4.

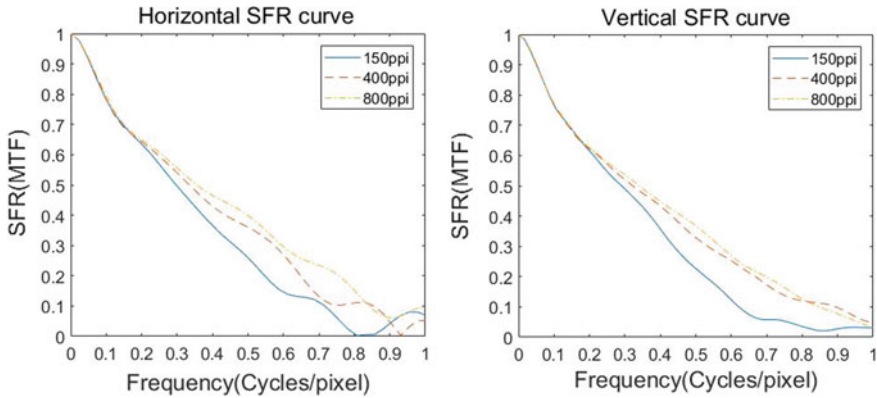


Fig. 4. SFR curves for fast and slow scanning at different resolutions

From the experimental results and analysis, it can be seen that the higher the image resolution, especially the resolution of the high-key and low-key regions of the image, the better the performance of the scanner and more suitable for high-quality image digitization.

## 4.2 Scanner Dynamic Density Range Evaluation

A gray scale is composed by different gray scales. It means that the dynamic density range test chart can obtain the difference between the maximum density and the minimum density of the linearly reproduced gray scale, and then evaluate the dynamic density range of the scanner. As shown in Fig. 5.

By measuring the density and gray level of the dynamic density range test plate multiple times, finally, 150, 400 and 800 ppi experimental data were taken for comparison. By the dynamic range of the scanner the graph was obtained. And in the experiment, it was found that the gray level of the same density was similar in the resolution range before 150 ppi and after 400 ppi. Between 150 and 400 ppi, the higher the density, the greater the difference in gray levels. The experimental comparison shows that when the dynamic range of the scanner is larger, especially the linear dynamic range, the practicality of the scanner is stronger, and the ability to express the details of the image, the higher the digital quality of the image is also stronger.

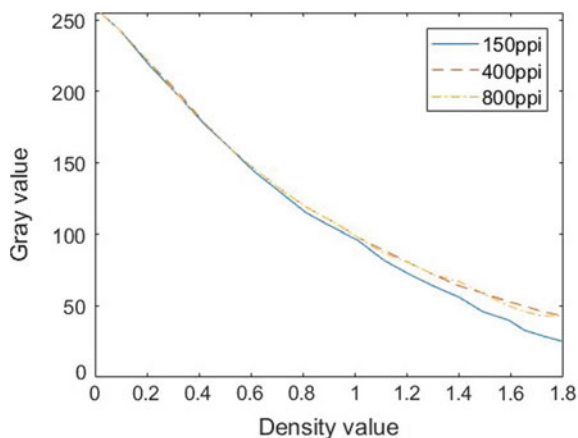


Fig. 5. Scanner dynamic range curve

## 5 Conclusions

In the application scenario where the scanner becomes an important tool for image digitization, this article proposes a set of evaluation methods to correctly evaluate the image quality of the scanner. It provides users with a better understanding of the scanner's performance indicators, also provides scientific scanners with correct evaluation parameters and methods, and reasonably selects and screens the scanner's specific performance parameters. And the acquisition method provides scientific basis and guidance method for the correct selection and reasonable use of the scanner, and has guiding significance for the scientific evaluation of image quality.

**Acknowledgements.** This work is funded by National Key Technology Research and Development Program of the Ministry of Science and Technology of China (2012BAH91F03) and Digital Imaging Theory—GK188800299016-054.

## References

1. Cheng, C., Yi, X., Su, H., et al. (2014). Scanner Imaging quality evaluation method based on MTF and MSSIM. *China Printing and Packaging Research*, 6(3), 31–36.
2. Hao, J. (1998). Research on sampling theorem and nyquist criterion. *Telemetry and Telecontrol*, 2, 12–20.
3. Yao, H. (2013). An attempt to measure the effective resolution of digital printing machine based on spatial frequency response. *China Printing and Packaging Research*, 5(5), 31–36.
4. Zhang, G. (1999). Main performance index of platform scanner. *Printing Technology*, 11, 28–31.
5. Luo, Y., Wu, Z., & Nie, X. (1999). Correction of geometric distortion in computer map image scanning. *China Education Informatization*, (12), 61–64.
6. Simone, G., Pedersen, M., & Hardeberg, J. Y. (2012). Measuring perceptual contrast in digital images. *Journal of Visual Communication and Image Representation*, 23(3), 491–506.

7. Li, G., & Ma, J. (1996). Principles of scanner technology. *Journal of Ningxia Institute of Technology: Natural Science Edition*, 2, 67–69.
8. Qi, F. (2012). Digital printing technology and equipment (vi) Part I: Overview–comparison and comparison of digital printing and traditional printing. *Today's Printing*, 1, 69–71.



# High-Simulation Oil-Painting-Style Images Based on Stroke Characteristics

Jing Geng<sup>(✉)</sup>, Congjun Cao, and Yonghong Qi

Faculty of Printing, Packaging Engineering and Digital Media Technology,  
Xi'an University of Technology, Xi'an, China  
gengjing\_qianye@163.com

**Abstract.** Stylised rendering is a research field that combines computer technology and painting art. It simulates an artist's effect via a computer simulation to generate different artistic styles rapidly. Two methods based on graphic image processing can be used for the computer simulation of oil painting style, and these two are simulation of art media, such as oil painting canvas and brush, and simulation of the art creation process to produce oil paintings automatically. This study aims to combine these two methods and fully consider the image tone reproduction of original oil paintings and the representative colours of each painter's oil painting to simulate the effect of the artist's creation. The brush texture of a painter is applied to generate stylised images through a non-realistic rendering algorithm. The tone reproduction (greyscale histogram) of digital photos is adjusted to fit the tone reproduction of the target oil painting (grayscale histogram) and make the produced oil painting style image approximate the artist's creation. Then, the hue of the digital photos is adjusted, and the colour and appearance of the painter's oil painting are imitated from the hue. Through these steps, the final rendering effect of the stylisation treatment of oil paintings and the similarity with the target image are improved. The overall effect on landscape painting is better than that on portrait painting.

**Keywords:** Image stylisation · Color transfer · Visual information · Quality assessment

## 1 Introduction

### 1.1 Purpose of This Study

Brush stroke refers to the trace of certain texture features left by a painter when the brush touches the picture in the process of painting. Although brush stroke is a technical factor related to a painter's painting techniques, it conveys the painter's emotion, personality and cultivation. Thus, the oil paintings of different painters vary. This study is based on the stroke texture feature of image oil painting styles. Digital photos are created through non-photorealistic rendering (NPR) to produce images with the stroke texture features of Monet, Seurat, van Gogh, and other artists. By adjusting the gradation and tone of the original photograph, the style used in the produced image approximates the style of the original oil painting.

### 1.2 Related Work and Prospects in Image Stylisation

Computer simulation of various artistic styles of drawing is a major research content of computer NPR technology. NPR was introduced in the 1980s. Early studies on this technology include those of Steve [1] and Sasada [2]. Saito and Takahashi [3] and Haerberli [4] published two influential papers in the Siggraph Conference in 1990. In 1997, Siggraph considered NPR a category, and NPR technology entered a period of steady development.

Image style transformation is an emerging technology based on deep learning, and it adopts the convolutional neural network (CNN). Image style migration based on neural network was proposed by Gatys et al. [5] in 2015. They developed a texture modelling method that uses deep learning to separate picture content from picture style, and the content of one picture was combined with the style of another picture. In the study, a project applicant created several pictures by using Gatys' open source code and performed a simple analysis. The good results of landscape painting show people. In facial style migration, the greater the similarity to the style image is, the better the migration effect is. Therefore, in the results, the eyes are coloured black and the character style of migration exhibits a slight deformation, causing a serious effect and large deviation (Figs. 1 and 2).

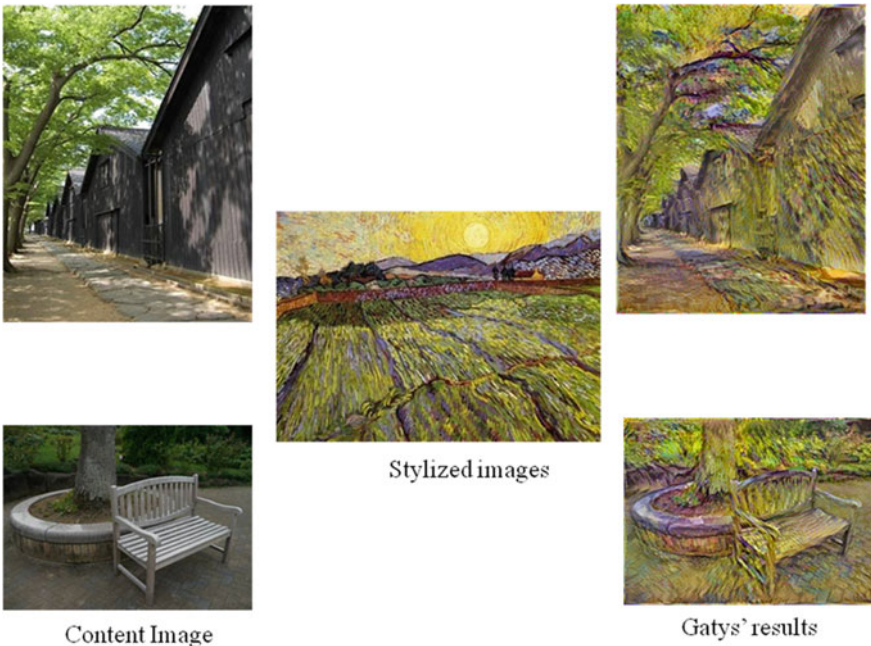


Fig. 1. Result of landscape



Fig. 2. Result of portrait

To sum up, current research on high-simulation painting style images has the following problems. Firstly, the practical application of traditional style transfer is limited, and the program only can do a certain style or scene. Secondly, the neural style should be improved, and the influence on the face of the portrait should be considered.

## 2 Study Contents

### 2.1 Overall Conception

The unique visual features of oil painting are associated with many factors, such as brush stroke. Different painters have different painting techniques and stylistic features. Therefore, a digital photo of a painting stylised treatment requires the following procedures. Firstly, the stylistic features of the target painter should be extracted. Secondly, based on the painter's brush stroke feature, stylised treatment of digital photos endows these photos with the stylistic features of the target painter. To make the current study universal, the oil paintings of three masters, namely, Monet, Seurat and



van Gogh, were selected. The brush strokes obtained from each artist's painting make up the basic material of the research. Unlike the long stripes that van Gogh used, Monet used short strokes to describe objects, and this usage is related to his objectives. Seurat used stacked point-like strokes to express the shape of an object. The differences between paintings are not only observed in the characteristics of the brush style, but also in the composition or conventional colours. To treat photos as similar regardless of the styles of different painters, the characteristics of the brush strokes used by each target painter must be understood and studied. To imitate the artist's painting style in stylised image processing, not only the painter's brush strokes, but also the paintings' hue, saturation and so on are used as references.

## 2.2 Experiment

### 2.2.1 Selection of Experimental Images

Taking into account the proportion of different subjects, two landscape photographs and two Portraits of characters photographs were used in this study (The images of "Portrait1 and Portrait2" in the manuscript are the pictures of the author's former colleagues in Japan. We have sought and obtained their consent to publish as a research paper). Use D65 Kodak camera to get original digital photos. Considering the different scenes, the tone reproduction of the images after shooting is different. For example, in the case of insufficient exposure, tone reproduction is adjusted to a uniform standard to find the best tone reproduction [6] (Fig. 3).



**Fig. 3.** Original digital photos for stylized migration

### 2.2.2 Experimental Method

#### Method One

- (1) For the lightness of the produced oil painting style image to be as close to that of the original oil painting as possible, the lightness of the original digital photo is adjusted to fit the lightness of the oil painting. A digital photograph's tone reproduction is affected by shooting conditions and other factors. Therefore, an idea is considered in this study. This idea is the use of the grayscale histogram in Photoshop for fitting. Three parameters can be seen on the lightness histogram

panel, i.e. average value, standard deviation and intermediate value, which reflect the lightness characteristics of the image to some extent. The tone of the digital photos is adjusted to change their brightness and darkness. Thus, the average value, standard deviation and median value of the lightness histogram of digital photos are close to the lightness histogram of the target oil painting. The original photograph's tone is matched with that of the painter's oil painting. In the process, the colour of the original photograph remains the same (Fig. 4).

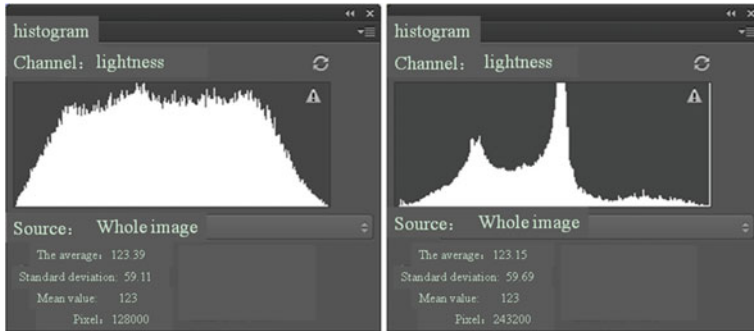


Fig. 4. Fitting histogram parameters

- (2) To better mimic painting, the use of colour kinds should be understood, and the representation colour of the target painting must be extracted. The extraction of the representation colour is divided into two steps. Firstly, the oil painting colour space is converted. Secondly, through two-step clustering, the representative colours of the oil paintings can be extracted. The representative colours are applied to the digital photos.

### Method Two

- (1) The digital photos can also be matched to the shape of the histogram of the original oil. That is, the shape of the histogram of the digital photo is adjusted to be close to the histogram of the target oil painting.
- (2) Colour matching can also be achieved by using the fitting histogram method. When the three RGB channels of the oil painting are read separately and the histogram is drawn, histograms in red, green and blue can be obtained.

## 3 Evaluation and Analysis of Results

'Starry night' is one of the most well-known paintings by van Gogh. Two representative colours are extracted from the painting. The strong spectral energy of the brush stroke is a typical characteristic of a van Gogh painting. Three colour paints are used: sky blue, yellow and white. Blue accounts for 58% of the painting. All  $a^*$  values of the

representative colour are less than 10. The results obtained by Method Two are similar to the original target oil painting. However, the orange moon and the cluster of starlight depicted in the painting are not reflected in both results. This means that this method can only imitate the general tone, and the less dominant colours are ignored. The texture applied to the digital photo is disordered in the direction of the texture (Figs. 5 and 6).



**Fig. 5.** Brush strokes cut from van Gogh

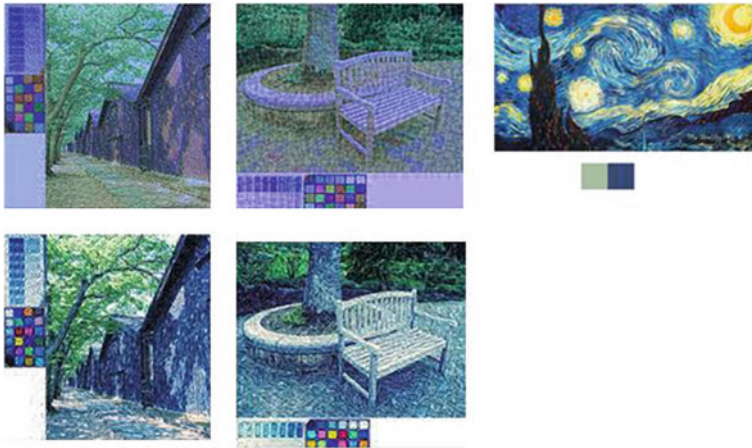


**Fig. 6.** Van Gogh's work and the imitation of van Gogh's oil paintings

Then, the imitation of Monet's works. We use the Monet heap series. Three representative colours are extracted from it: the colour of  $L^*$  values greater than 50 represent more than 35%, the colours of  $a^*$  and  $b^*$  values less than 10 represent more than 26% and the entire image has a brown tone. In terms of visual perception, the result of Method One is similar to the oil painting of a dry grass pile (Figs. 7 and 8).

Next, we evaluate Seurat's artworks and the imitation of Seurat's artworks. 'Big Bowl Island Sunday Afternoon' is a representative work of Neo-Impressionism. Two representative colours are extracted from the image. The proportion of colours with  $L^*$  value greater than 50 is more than 40%. This painting uses the point painting method, and the entire picture is composed of millions of colour points. Although only two representative colours are extracted, the distribution of colours is relatively dispersed,

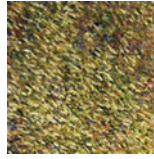


**Fig. 7.** Brush strokes cut from Monet



**Fig. 8.** Monet's work and the imitation of Monet's oil paintings

and imitation is difficult. The image content of the result obtained by Method Two is clear (Figs. 9 and 10).

Four digital photos are selected: two for landscape and two for portrait. A total of 57 original paintings are studied, including 10 of van Gogh's landscapes, 16 of Monet's landscapes, 10 of Seurat's landscapes, 13 of Monet's portraits and 10 of Seurat's portraits.



**Fig. 9.** Brush strokes cut from Seurat

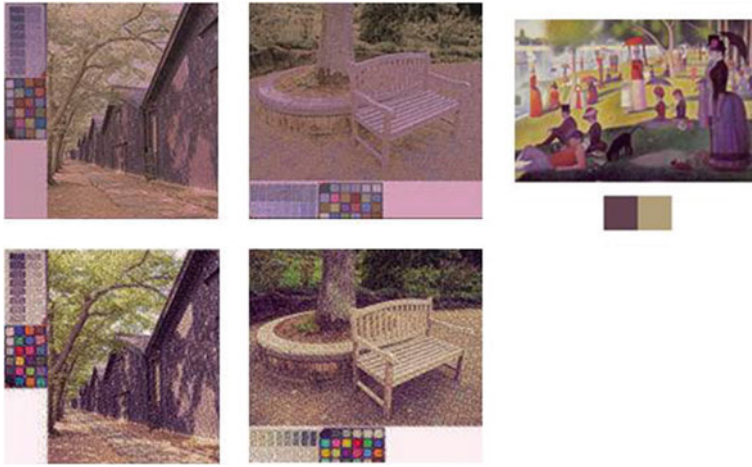


**Fig. 10.** Seurat's work and the imitation of Seurat's oil paintings

## 4 Conclusions

In cases where a clear sense of the stroke direction can be seen in the original painting, these methods are unsuitable for simulating stroke texture features because the processed image semantic content cannot be identified. Thus, applying texture direction is messy. Therefore, these methods should be applied to works of point painters with relatively uniform strokes and a weak sense of direction.

Two methods that involve the use of histogram shape fitting for image tone adjustment perform well. The information contained in the image content is protected to a great extent. However, these two methods have a limited range of application. For oil paintings with clear but few primary colours, the simulation effect is good. Method One performs slightly than Method Two when the main tone is clear and a few representative colours exist.

When the large colour distribution is clear and represents the case of less colour, Method Two performs better than Method One.

**Acknowledgements.** This study is funded by the Xi'an University of technology high level scientific research fund.

### **Compliance with Ethical Standards**

**Conflict of Interest:** The authors declare that they have no conflict of interest.

**Ethical Approval:** All procedures performed in studies involving human participants were in accordance with the ethical standards of Faculty of Printing, Packaging Engineering and Digital Media Technology, Xi'an University of Technology and with the 1964 Helsinki declaration and its later amendments or comparable ethical standards.

**Informed Consent:** Informed consent was obtained from all individual participants included in the study.

## References

1. Steve, S. (1986). Hairy brushes. In *Proceedings of ACM SIGGRAPH* (pp. 225–232).
2. Sasada, T. T. (1987). Drawing natural scenery by computer graphics. *Computer-Aided Design*, 19(4), 212–218.
3. Saito, T., & Takahashi, T. (1990). Comprehensible rendering of 3D shapes. In *Proceedings of ACM SIGGRAPH* (pp. 197–206).
4. Haeberli, P. (1990). Paint by numbers: Abstract image representations. In *Proceedings of ACM SIGGRAPH* (pp. 207–214).
5. Gatys, L. A., Ecker, A. S., & Bethge, M. (2016). Image style transfer using convolutional neural networks. In *Proceedings of the IEEE Conference on Computer Vision and Pattern Recognition* (pp. 2414–2423).
6. James, T. H. (1977). *The theory of photographic process* (p. 557). Macmillan: New York.



# High-Efficiency Image Color Gamut Mapping Based on Spherical Coordinates

Shiwei Liu<sup>1(✉)</sup>, Junfeng Li<sup>1</sup>, Quanhui Tian<sup>2</sup>, and Ming Zhu<sup>3</sup>

<sup>1</sup> Department of Printing and Packaging Engineering, Henan University of Animal Husbandry and Economy, Zhengzhou, China

hnzzlsw@163.com

<sup>2</sup> Department of Printing and Packaging Engineering, Shanghai Publishing and Printing College, Shanghai, China

<sup>3</sup> Department of Materials and Chemical Engineering, Henan Institute of Engineering, Zhengzhou, China

**Abstract.** Color gamut mapping technology includes two parts: color gamut boundary description and specific mapping algorithm. To improve the accuracy of mapping calculation, so far, there have been hundreds of specific mapping algorithm has been proposed, but most of these algorithm is mapped from device to device, but the algorithm from image to device is relatively lack. The error can't be eliminated when image color gamut boundary is described by the existing algorithms, and calculation efficiency is low. This paper present a precise, fast, and zero error methods to extract image color gamut boundary (we call it IGBAD), combining IGBAD method, fast color gamut mapping method is put forward. The redundant calculation is eliminated in the process of mapping; the efficiency of map calculation is high.

**Keywords:** IGBAD · Spherical coordinates · Image color gamut mapping

## 1 Introduction

Color gamut mapping algorithm can be divided into “device to device” and “image to device” color gamut mapping according to the color reproduction process [1–4].

In the “device to device” color gamut mapping algorithm, source device gamut is mapped to the target device according to the specific color gamut mapping algorithm, the characteristics of copied image isn't considered. So in the process of mapping, color images are often overly compressed even it's color gamut is less than the target device boundary. This is not conducive to accurate image replication and can't make full use of the color gamut of the target device.

In the “image to the device” color gamut mapping algorithm, specific image gamut is mapped to a target device gamut. The image can reproduced better because the target device color gamut is best used. Therefore, the “image to the device” color gamut mapping algorithm is favored by more researchers [5–8].

Color gamut mapping includes two steps, First, the color gamut boundary of the image and the color gamut boundary of the target device are described, and then the specific mapping calculation is performed [9, 10].

In the color gamut mapping process of “image to device”, the calculation process is described as follows: First the device-independence color space is determined, the color values of the input image and the target device are transformed to the space, and the target device color gamut boundary points and image color gamut boundary points are calculated after point by point in the image pixels, and then according to the mapping algorithm adopted the image color within the gamut mapping to a target device, after finish all the color in the image mapping, mapping the image conversion to images of a target device color space on the target device.

## 2 Image Gamut Boundary Description Algorithm

Image gamut boundary accurately descriptor (IGBAD) using spherical coordinates description is inspired by SMGBD (segment maxima gamut boundary descriptor) color gamut description algorithm. But in SMGBD method, color space is divided into multiple partitions, an extremum point is extracted from each partition as a boundary point and constitute GBD matrix. For the image, the pixels are distributed in a certain scope of color gamut space, not evenly distributed in the whole color space, this feature may lead to SMGBD description of image color gamut boundary error is bigger, it is difficult to meet the needs of high precision replication.

Steps of IGBAD method are introduced as:

First all pixels of image are converted into the spherical coordinates through Formula (1), expressed by hue angle  $\alpha$ , elevation  $\theta$  and the radius of sphere  $r$ , and record the original position.

$$\begin{cases} r = \sqrt{(L^* - L_E^*)^2 + (a^* - a_E^*)^2 + (b^* - b_E^*)^2} \\ \alpha = \tan^{-1} \left[ \frac{b^* - b_E^*}{a^* - a_E^*} \right] \\ \theta = \tan^{-1} \left\{ \frac{L^* - L_E^*}{[(a^* - a_E^*)^2 + (b^* - b_E^*)^2]^{0.5}} \right\} \end{cases} \quad (1)$$

Formula (1),  $L^*$ ,  $a^*$ ,  $b^*$  is the value in rectangular coordinate system,  $L_E^*$ ,  $a_E^*$ ,  $b_E^*$  is the value of sphere center in rectangular coordinate system, the value is (50,0,0).

$r$  is the distance between sampling points to the sphere center  $E$ , hue angle  $\alpha$  is and the positive half coordinate axis of  $a^*$ , the range is  $0^\circ$ – $360^\circ$ , elevation  $\theta$  is the angle between  $r$  and the  $a^*b^*$  plane, values range from  $90$  to  $-90$ . As shown in Fig. 1.

Second, all pixels in the image are ranked according to the value of  $\alpha$ , elevation  $\theta$  and  $r$ .

Third, the biggest sphere  $r$  point is the boundary point in all the points which hue angle and elevation is same, all the points of boundary make a set  $\psi$  in which the boundary point is recorded by  $\alpha$ ,  $\theta$ ,  $r$  value.



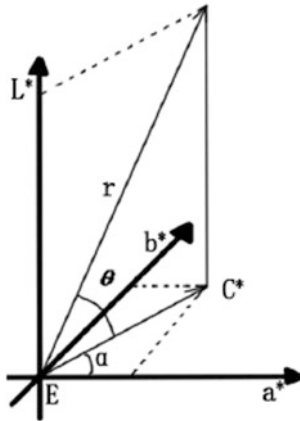


Fig. 1. The spherical coordinates

### 3 High-Efficiency Image Gamut Mapping Method

Conventional color gamut mapping is done point by point from image to the target device, so it caused a large number of redundant calculation lots, and wastes a lot of time.

In order to solve the problems above, a high-efficiency image gamut mapping method is proposed in this paper.

The process of high-efficiency image gamut mapping method is shown in Fig. 2. This method is divided into the following steps:

- (1) the pixel in the image is denoted by  $\alpha$ , elevation  $\theta$  and the radius of sphere  $r$ , and the original position of each pixel is recorded.
- (2) all pixels in the image are ranked according to the value of  $\alpha$ , elevation  $\theta$  and  $r$ . calculate the boundary point of image make a set  $\psi$ .
- (3) calculate target device boundary points (according to the SMGBD algorithm).
- (4) according to the gamut mapping scheme selected, all the pixels mapping from image to device is completed, and the pixel point of the image is replaced after the mapping.

### 4 Experiments and Analysis

In order to evaluate the performance of IGBAD algorithm, three images were selected as test image shown in Figs. 3, 4 and 5. SMGBD algorithm and IGBAD algorithm were respectively adopted to extract the gamut boundary points of the images.

First image gamut boundary points are calculated by IGBAD algorithm, and made a data set  $\psi$ , then  $\alpha$  and elevation  $\theta$  as known information, the  $r$  of image gamut boundary points is calculated by  $9 * 9$  SMGBD method. Then calculate the Lab color difference between the boundary point extracted by IGBAD algorithm and the

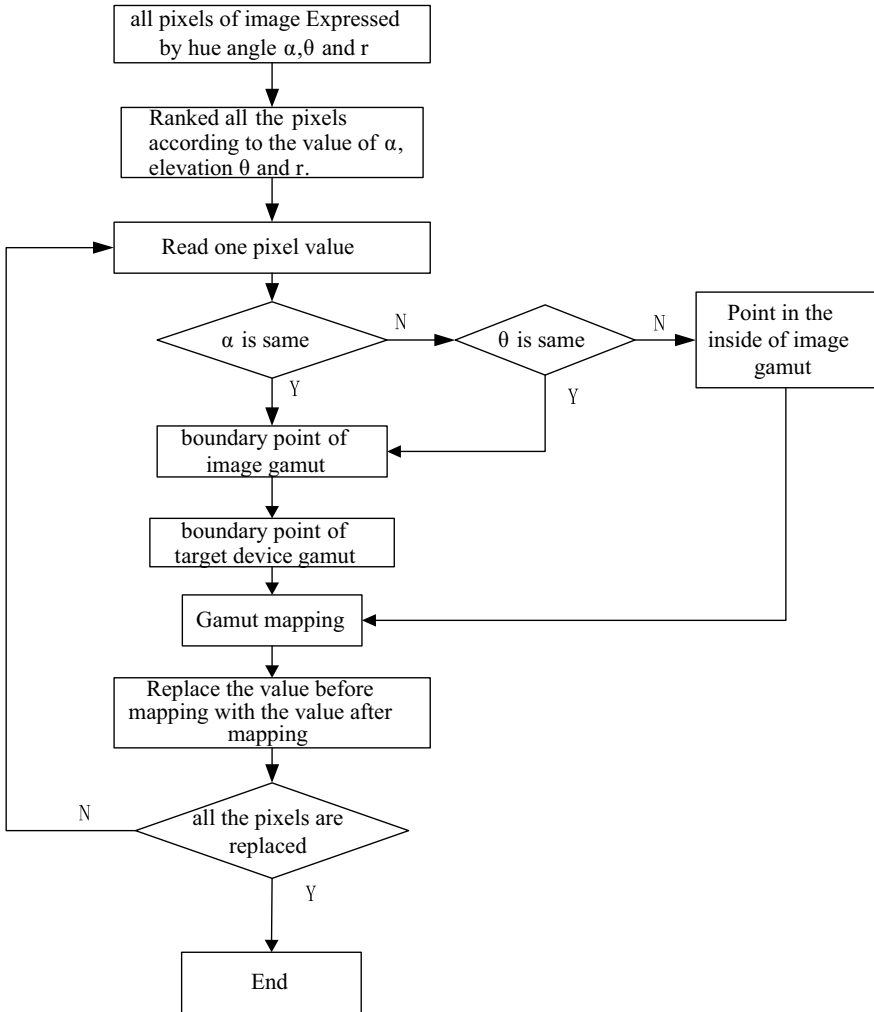


**Fig. 2.** High-efficiency image gamut mapping method

boundary point calculated by SMGBD algorithm, Color error is in  $\Delta E_{ab}^*$ . We can compare efficiency and precision between the two algorithms according to the result of experiments, the date is show in Table 1.

According to the data in Table 1, there is no error in the edge points of the image extracted by IGBAD algorithm, and the calculation time is short. There is an error between the edge points of the image calculated by SMGBD and the actual boundary points, and it takes a long time to calculate. Therefore, IGBAD algorithm is more suitable to extract the boundary points of the image than SMGBD algorithm.



**Fig. 3.** Test image 1



**Fig. 4.** Test image 2



**Fig. 5.** Test image 3

**Table 1.** Efficiency and precision between the two algorithms

	IGBAD					SMGBD	
	Total pixels	Boundary points	Percent of boundary points (%)	Calculate time (s)	Color error ( $\Delta E_{ab}^*$ )	Calculate time (s)	Mean/max error ( $\Delta E_{ab}^*$ )
Figure 3	376,479	35,387	9.4	4.04	0	170	6.31/50.38
Figure 4	376,479	58,731	15.6	6.75	0	165	3.88/45.71
Figure 5	376,479	31,248	8.3	3.02	0	168	8.6/55.14

## 5 Conclusions

On the basis of analyzing the shortcomings of SMGBD algorithm, this paper proposes an algorithm IGBAD which can quickly and accurately extract image boundary points. On the basis of IGBAD method, an optimized fast color gamut mapping algorithm is proposed. Results show that the research of image high-efficiency border extraction method is efficient and without error.

Compared with the conventional mapping algorithm, IGBAD method reduce about 90% of the image point to be calculated to target color gamut, three times its computation efficiency is improved, the computational efficiency has been improved remarkably.

**Acknowledgements.** This study was supported by the National Natural Science Foundation of China (no. 61301231).

## References

1. Zhu, M., Liu, Z., & Chen, G. (2011). Research on six-color separation model based on subarea neugebauer equations. *Acta Optica Sinica*, 31(7), 288–297.
2. Guo, J. (2010). Novel spectral characterization method for color printer based on the cellular Neugebauer model. *Chinese Optics Letters*, 8(11), 1106–1109.
3. Sun, B., Liu, H., Zhou, S., et al. (2015). Modified spectral neugebauer model for printer characterization. *Spectroscopy Letters*, 48(9), 660–668.
4. Wang, B. (2012). Color separation criteria for spectral multi-ink printer characterization. *Chinese Optics Letters*, 10(1), 013301.
5. Jin, C.-C., Shen, H.-L., Shao, S.-J., et al. (2011). Color characterization method for colorful inkjet printers. *Acta Optica Sinica*, 31(12), 316–320.
6. Xu, X.-Y., Zhu, Y.-H., & Sang, F.-X. (2012). Image-dependent gamut mapping algorithm. *Geometrics and Information Science of Wuhan University*, 37(5), 626–629.
7. Tian, Q., Liu, Z., Yu, H., et al. (2015). The spectral radiance piecewise partition model for characterizing liquid crystal displays. *Displays*, 39, 133–138.
8. Zhang, J. Q., Cai, F., Shen, X. Y., et al. (2016). Backward spectral characterization of liquid crystal display based on forward spectral characterization. *Journal of Spectroscopy*, 2016(4), 1–8.

9. Lu, Y., & Zhen, L. (2013). Application research of least squares with interpolation in printer's gamut boundary description. *Packaging Engineering*, 34(11), 80–84.
10. Zhang, J. Q., Liu, Z., Lu, L., et al. (2014). Research on the color performance changes of iPad affected by brightness settings. In *Applied Mechanics & Materials* (Vol. 513–517, pp. 4319–4322).



# Innovative Research on Image Processing Based on Replication of Chinese Painting and Calligraphy

Jinglin Ma<sup>(✉)</sup>

Shandong Communication and Media College, Shandong, China  
371725079@qq.com

**Abstract.** The purpose of this dissertation is, by adjusting the digital files of calligraphy and painting using digital image processing software, to establish a systematic method to completely retain the artistic features of calligraphy and painting, reproduce the original features of the paintings and the author's personal characteristics perfectly, and obtain highly restored replicas. The research method is an experimental one, in which the color difference of the replica obtained by the software under different parameter conditions are compared, and the best solution by adjusting the software parameters is obtained. The result of the study is that small and medium-sized printing companies that are not equipped with a color management system can obtain a set of mature processes and supporting parameters suitable for copying Chinese calligraphy and painting using relevant equipment and software. The important conclusion is that the innovative use of digital technology and equipment to replicate Chinese classical painting and calligraphy is of vital importance to inherit and promote excellent Chinese culture.

**Keywords:** Color correction · Color mode · GCR · Color reference points · Curve

## 1 Introduction

Calligraphy is the art of writing, and painting is the combination of imagination and creation. Calligraphy and painting are among the greatest achievements in the development of human civilization and an important carrier for the dissemination of culture and knowledge. The Chinese painting and calligraphy, which are the exemplification in this respect, date back to the ancient times of the oracle bone scripts and painted pottery paintings and last thousands of years, making great contributions to the succession of Chinese civilization. Today, Chinese painting and calligraphy are one of the most important sectors in arts market, and have conquered the arts-loving people around the world with its unique style and charm.

For ordinary arts lovers, expensive paintings are sometimes beyond their affordability, and consequently, high-quality replicas have become an ideal alternative. At present, the relatively mature Replication techniques of painting and calligraphy arts mainly refer to woodblock printings and high-definition micro-injection. Woodblock printing technology, whose techniques are relatively complex, with long production

cycle and high cost, is less popular among ordinary customers. High-definition micro-injection, on the other hand, is a kind of replication technology emerging with the development of science and technology, boasting its all-digital operations. It relies on high-precision scanning, color correction, and high-precision inkjet printing as the technical means to replicate the artworks on rice paper with a diffusion-resistant coating.

The Replication technology of calligraphy and painting art has been quite mature in countries and regions such as Europe, America and Japan. In particular, Japan's Nigensha Publishing started very early and has made great achievements in using large-format photo-engraving technology. Due to the differences in cultural traditions, the Replication techniques of European and American countries are concentrated in the category of oil canvas as the carrier, and the copying on rice paper and silkworm is mainly deployed in Japanese companies and some emerging enterprises in China. These companies typically rely on complex data acquisition systems and complete color management systems to deliver high-quality replicas on digital micro-jet special rice paper or other materials. This technology, although highly efficient and of good quality, costs highly due to the expensive equipment. The sales price of the resulting replica is not particularly favorable.

This article aims to explore a technique which is suitable for small and medium-sized printing companies that are not equipped with a color management system. Firstly, technicians can use Photoshop to calibrate the scanned digital image, compare the color sample with the original using a spectrodensitometer, gradually reduce the comparison error by adjusting the color calibration curve, and finally obtain a calibration curve that is basically the same as the original one, laying the foundation for subsequent copying under the same conditions. That is also the novelty point of this dissertation.

## 2 Image Color Correction

The experimental conditions in this paper are shown in Table 1.

**Table 1.** Experimental conditions

Software	Equipment		Rice paper
Photoshop CS4	Scanner	Microtek Phantom 9900XL	65 g Jimoxuan coated rice paper (with large porosity silica coating)
	Printer	Epson 9800	
	Spectral densitometer	Minolta FD-5BT	

The copy object chosen in this article is Guoliang Shi's *Dance of the Tianshan*, as shown in Fig. 1.



**Fig. 1.** Dance of the Tianshan, by Guoliang Shi

Guoliang Shi, who is a famous Chinese modern painter, is good at character painting and has been highly recognized in the market, giving research on copying his paintings a representative significance.

## 2.1 Color Mode Conversion

The scanned image is in RGB mode and must be converted to CMYK mode before being calibrated. The conversion rules must be defined before converting the color mode. The color separation type is: GCR, and the black version is: More. Because for Chinese painting, the use of black ink is an important expression technique, thus called the skeleton of the painting. Correctly reproducing the black elements in the original painting is a key step in successfully replicating Chinese painting. The custom CMYK conversion rules are shown in Fig. 2.

GCR (Gray Component Replacement) is an important method for making long-tone black prints. According to the parameters generated in the black prints set in Fig. 2, the gray component in the color part of the original from the bright tone to the dark tone is replaced with black to generate different types of long tone black prints. For paintings, the parameters of black version can be set “More”. For a calligraphy work, it is necessary to replace all the gray components in the color part of the original with black.



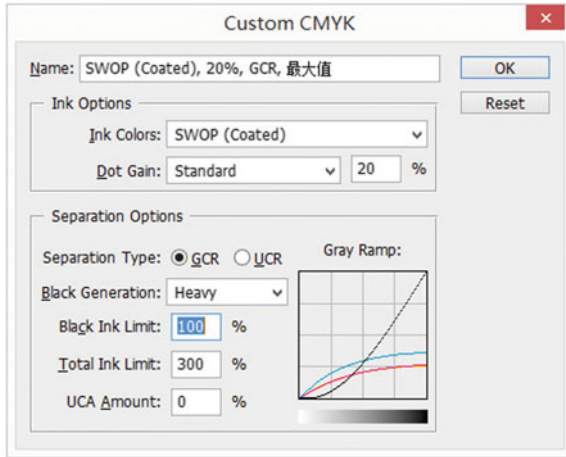


Fig. 2. Custom CMYK

### 2.2 Select the Color Reference Points

Five representative points are selected as the reference point for the color correction in the manuscript. According to the original color characteristics, the reference points are selected as shown in Fig. 3.

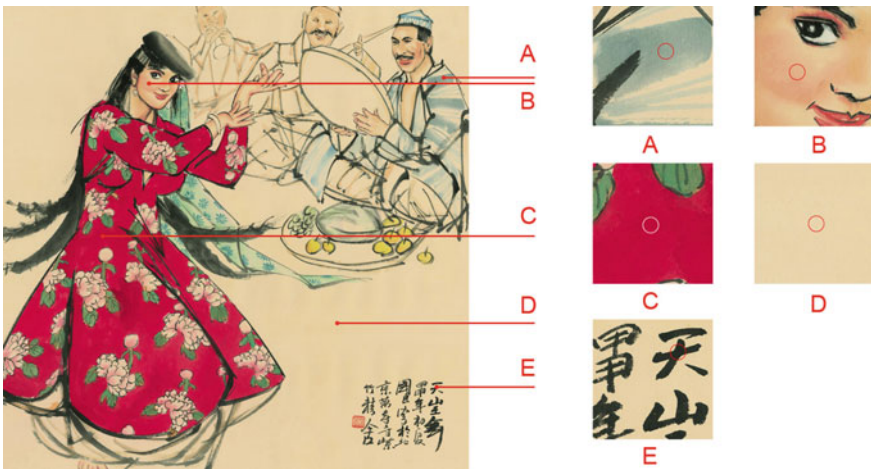


Fig. 3. Color correction reference points

The five color correction reference points cover the most important areas of the manuscript. If the color of the reference point can be copied with high precision, the entire picture can be reproduced to perfection.

When collecting the color data at the reference points in the manuscript, the spectrodensitometer is used to collect the CMYK color separation color density value of the reference point, and the data collected is used as the reference data, and a comparison between the CMYK color density value of the comparison point at the same position of the replica with the reference data is made.

Data collected using the spectrodensitometer for the 5 reference points of the original are shown in Table 2.

**Table 2.** Separation color density values at reference points

Reference point	Separation color density values			
	C	M	Y	K
A	0.46	0.41	0.52	0.44
B	0.24	0.39	0.58	0.33
C	0.44	0.99	0.98	0.70
D	0.20	0.27	0.45	0.24
E	1.10	1.13	1.19	1.12

The data in Table 2 is the original data collected in the manuscript. Other data in the experiment thereafter are compared against this data.

**2.3 Correction of Image Color via Measuring Color Error of Reference Points in Printed Copy**

A color sample (1:1) was printed on the coated rice paper, and the CMYK color separation color density values of the comparison points in the figure were collected using a spectrodensitometer as shown in Table 3.

**Table 3.** CMYK separation color density value (No. 1)

Reference point	Separation color density values			
	C	M	Y	K
A	0.65	0.34	0.69	0.20
B	0.44	0.28	0.70	0.14
C	0.57	0.87	1.13	0.52
D	0.38	0.25	0.62	0.14
E	1.35	0.98	1.35	0.97

By comparing the data gaps between Tables 3 and 2, it was found that for the first printing, the color C and Y were heavier than the original, and M and K were lighter, requiring color correction of the image.

According to the conclusion obtained in the previous step, the “curve” tool in Photoshop is used to perform image correction on the original and set the calibration curve as shown in Fig. 4.

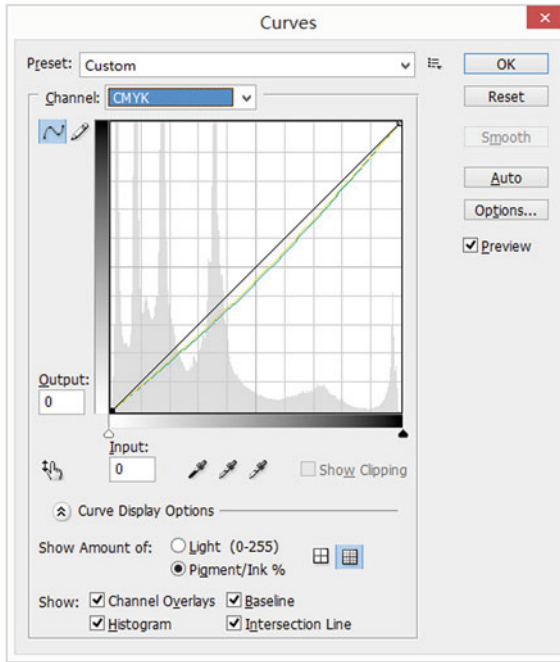


**Fig. 4.** First correction curve

In the calibration curve shown in Fig. 4, the two color curves of C and Y are bent downwards, and the correction parameters are set as:

C: input 50 → Output 46

Y: input 50 → output 44

After the initial color correction is complete, a color sample (1:1) is printed. The color density values of the CMYK color separation points are collected using the spectrodensitometer, as is shown in Table 4.

Comparing the data in Tables 4 with 2, the color density of the C component has been found to have decreased, but to the extent of less than the color density of the C component in the original. The Y component is basically similar to the original. M and K have not been adjusted and the data has not changed significantly. According to the data comparison, a second color correction is performed.

According to the conclusion obtained in the previous step, the “curve” tool in Photoshop is used to perform image correction on the original and the calibration curve is set as in Fig. 5.

**Table 4.** CMYK separation color density value (No. 2)

Reference point	Separation color density values			
	C	M	Y	K
A	0.40	0.43	0.55	0.40
B	0.23	0.42	0.62	0.32
C	0.41	0.96	1.06	0.70
D	0.18	0.33	0.61	0.21
E	1.01	1.17	1.40	1.13

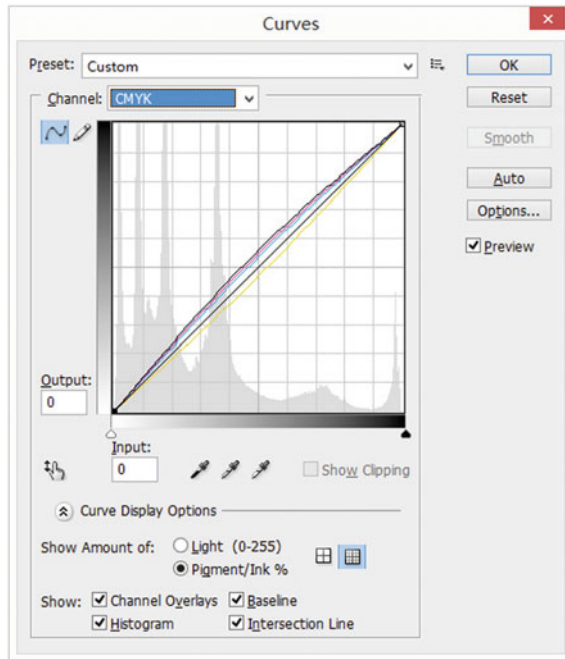


**Fig. 5.** Second correction curve

In the calibration curve, based on the data comparison gap, C, M, Y, and K have all been adjusted, and the correction parameters are set as:

- C: input 50 → output 53
- M: input 50 → output 55
- Y: input 50 → output 47
- K: input 50 → output 57

After the second color correction is complete, a 1:1 color sample is printed. The color density values of the CMYK color separation points are collected using the spectrodensitometer, as is shown in Table 5.

**Table 5.** CMYK separation color density value (No. 3)

Reference point	Separation color density values			
	C	M	Y	K
A	0.45	0.41	0.52	0.45
B	0.23	0.40	0.59	0.35
C	0.44	0.98	0.99	0.69
D	0.19	0.27	0.45	0.23
E	1.11	1.14	1.20	1.13

Through comparison, it is found that the color density value obtained by the third collection of the printed color sample is basically the same as the original, the data gap is within a reasonable error range, and the visual inspection result of the copy color is hardly distinguishable by human eyes from the original.

Through the operation process above, a color calibration curve that can be reused under the same operating environment has been obtained. The equivalent operating environment refers to using the same scanner and printer in the experiment, and the same brand of coated rice paper and ink are used. The two calibration curves in the experiment are set as a layer group in Photoshop, and the curve layer group digitization file is the final result of the experiment. By using the curve layer, the subsequent copying process of calligraphy and painting can be optimized, improving the overall efficiency and quality.

### 3 Conclusions

In this paper, by using the spectrodensitometer to collect and compare the original and replica color samples, the image processing software to multi-calibrate the electronic images of the calligraphy and painting, a set of reusable calibration color data is obtained as the same copying condition. The color correction process is improved and efficiency increased. It provides a method worthy of reference for small and medium-sized painting and calligraphy Replication enterprises that do not have a color management system, and innovatively uses digital technology and equipment to replicate the art of Chinese classical painting and calligraphy, contributing to the replication of Chinese classical painting and calligraphy arts and communication of traditional Chinese culture.

**Part III**  
**Digital Media Technology**



# Application of Augmented Reality in Product Package with Quick Response Code

Haoming Li and Zhanjun Si<sup>(✉)</sup>

Packaging and Printing Engineering Institute, Tianjin University  
of Science and Technology, Tianjin, China  
Szj@tust.edu.cn

**Abstract.** Users understand a product usually need to open its packaging, control product manuals to understand the function and usage of the product. However, through the use of Augmented Reality (AR) technology and some computer 3D modelling techniques into Quick Response Code (QR Code) on product packaging, a virtual product model can be constructed by scanning a QR Code with a mobile phone without disassembling the package can understand the appearance, function and use of the product. This article aims to study the market value of the technology and its technical means. Meanwhile, its advantages are discussed in packing.

**Keywords:** Augmented reality · 3D modelling techniques · QR Code · Virtual product

## 1 Introduction

Augmented reality (AR) is a technology that combines virtual information with the real world, overlaying virtual images onto reality through electronic devices [1]. Nowadays, with the popularization of smart phones and tablet computers, mobile augmented reality (MAR) has gradually become the main direction of AR technology development. And the Quick Response Code (QR Code) has the characteristics of large amount of information, fast reading speed, and full readability, and has a good development prospect [2, 3].

Nowadays, most of the QR Codes on the packaging have only simple product information, store less information, and cannot intuitively understand the product [4, 5]. In order to solve this problem, this paper proposes a method of applying augmented reality on QR Code, designs this method, and verifies its feasibility.

## 2 Methods

This article uses 3D software to model the product, uses c# code to design the interaction of the virtual product, and finally completes the design.

### 2.1 Modelling and Animation

This article uses 3ds Max to model the cup of the experimental sample. 3ds Max is a comprehensive three-dimensional animation rendering and production software that can effectively improve the modelling efficiency and can also better restore the structure of the product itself.

The modeling steps are as follows. First, build a cylinder as the bottom of the cup. Then, create a new ring on the cylinder and form the cup body by “squeezing” the ring. Finally, dividing the lid into three parts, and built a frustum of a cone on the top of the lid. The original cup is shown in Fig. 1, and the built model is shown in Fig. 2.

The purpose of animation production is to visualize the internal structure of the product and the detachable area of the product. It can also be used to demonstrate the use of the product.



**Fig. 1.** Plastic cup



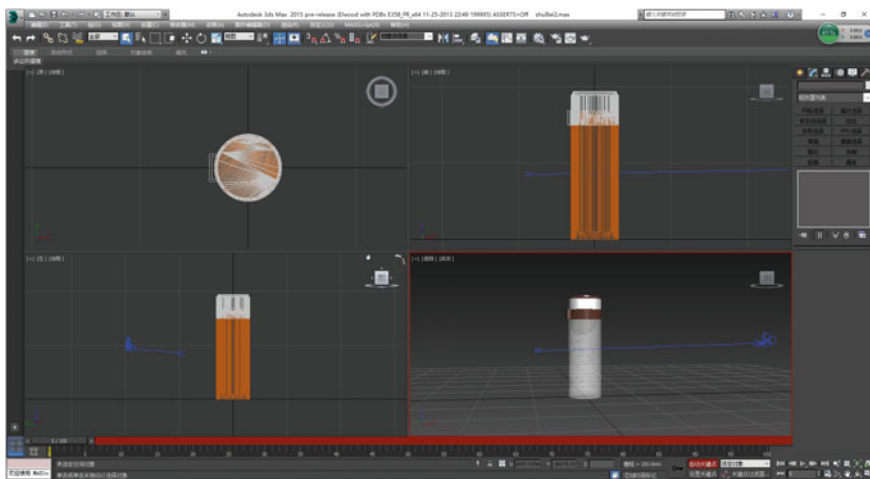


**Fig. 2.** The built model

The animation uses “frame animation” to complete. Set the current state of the cup in each keyframe so that it can form a continuous animation. Figure 3 is an animation designed for the cup. The animation is the process that the cup lid of the cup rotates and moves sideways.

## 2.2 Control Algorithm and App Production

Unity 3D is used to edit the 2.1 cups. Unity 3D is a multi-platform integrated development tool that can be used in the game area, 3D virtual simulation, 3D display of large products, 3D scene navigation, and demonstration of the use of some precision instruments. And so on, the application area is very extensive. First, import the model into Unity 3D and use the QR Code in Fig. 4 as the image for recognition.

Then, set up the animation state machine and write the code for the animation controller (Fig. 5), and attach the code to the model. When you click on the cap, an animation of cap opening is played.

Finally, import the Qualcomm AR resource package, set the necessary parameters, adjust the coordinate location of the ARCamera, and activate the ImageTarget database. The completed project interface is shown in Fig. 6.

## 3 Results and Discussion

### 3.1 Test Results

The completed project is tested and the test results are shown in Fig. 7. Use the computer’s front camera to simulate the phone’s camera and scan the QR Code image.

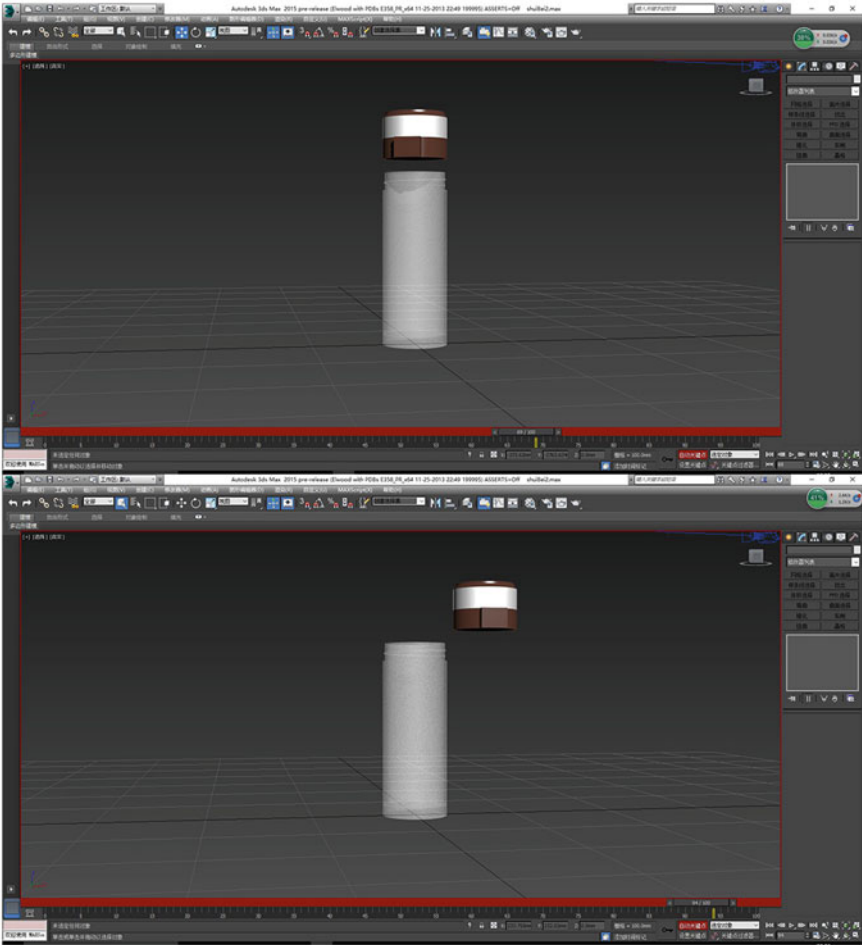


**Fig. 3.** The animation of this cup

It can be seen from the figure that the experiment successfully identifies the QR Code and allows the virtual water glass to display in reality. When you click on the lid of the cup, it will automatically open and move to the side. At this time, the mobile camera will be able to observe the style and structure of the cup from all directions.



Fig. 4. QR Code

```
4
5 #public class Controller : MonoBehaviour {
6     Animator takeTop;
7
8     private Ray ra;
9     RaycastHit hitInfo;
10    RaycastHit hit;
11
12    // Use this for initialization
13    void Start () {
14        takeTop = GetComponent<Animator>();
15    }
16
17    // Update is called once per frame
18    void Update () {
19
20        if(Physics.Raycast(Camera.main.ScreenPointToRay(Input.mousePosition), out hitInfo, Mathf.Infinity))
21        {
22            if (Input.GetMouseButtonDown(0))
23            {
24                takeTop.SetBool("isTake", true);
25            }
26        }
27    }
28
29
30
31
```

Fig. 5. Code for the animation controller

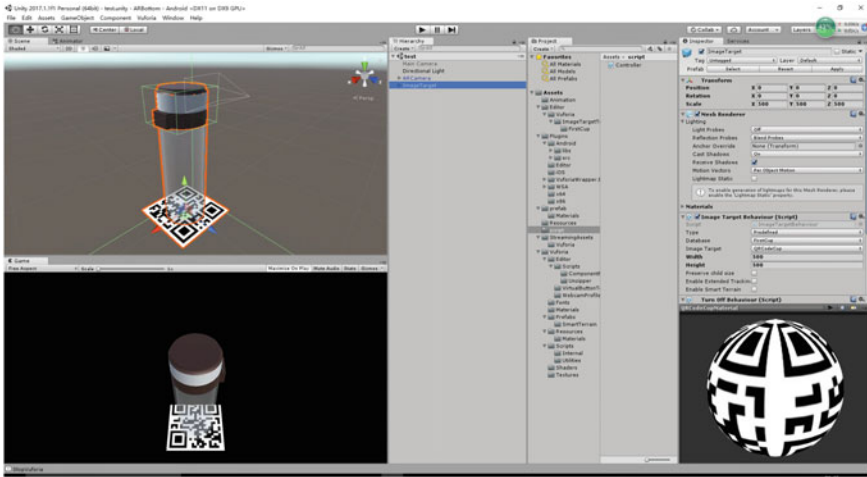


Fig. 6. The completed Unity project

### 3.2 Application on Packaged Products

Applying AR technology to the QR Code on the package can provide consumers with a lot of convenience. First, it achieves a one-and-two-purpose function. The QR Code recognizes the image as AR while still retaining its own stored text information. It can be used as a QR Code to scan text information with common scan code software, or through the App designed for AR recognition. Second, consumers can understand the appearance, function and usage of products without opening the package, which greatly facilitates consumers. The consumer's understanding of the product's functionality is enhanced and the actual presentation is easier and more understandable than the textual description. Third, it provides a certain degree of interactivity for product packaging [6, 7]. Through interactions between consumers and products, consumers' interest is increased, and consumers' impression of products is enhanced, thereby attracting consumers to purchase the product.

## 4 Conclusions

This article proposes a method of applying AR technology to the QR Code of product packaging, and successfully implements the idea, enriching the function of QR Code. Using this app, the QR Code on the package can be used to display the model of the internal product, so that the appearance, function, and usage of the product can be understood without having to open the package. It improves the lack of information on the current packaging and lacks interactivity. In today's digital environment, people are increasingly interested in information technology. With the development of AR technology in the future, this technology will be more intelligent and widely used.



Fig. 7. Final result

## References

1. Haydar, M., Roussel, D., Otmame, S., & Mallem, M. (2011). Virtual and augmented reality for cultural computing and heritage: A case study of virtual exploration of underwater archaeological sites. *Virtual Reality*, 15(4), 311–327.
2. Zhai, L.-L., Wang, Y.-T., Yang, J., & Liu, Y. (2012). Research on mobile augmented reality system based on ARcode. *Computer Engineering*, 38(10), 247–249.

3. Gui, Z.-W., Wang, Y.-T., Liu, Y., & Chen, J. (2014). Study on the application of two-dimensional code in mobile augmented reality. *Journal of Computer-Aided Design & Computer Graphics*, 26(1), 34–39.
4. Gammer, N., Cherrett, T., & Gutteridge, C. (2013). Disseminating real-time bus arrival information via QRcode tagged bus stops: A case study of user take-up and reaction in Southampton, UK. *Journal of Transport Geography*, 34, 254–261.
5. Yang, Y.-X. (2013). Applications of two-dimensional code in academic journals. *Acta Editologica*, 25(4), 374–376.
6. Guo, J., & Du, W.-C. (2017). Packaging information design based on AR technology. *Packaging Engineering*, 38(6), 26–29.
7. Xie, Q. (2017). Modern brand design packaging innovation based on AR technology. *Packaging Engineering*, 38(2), 60–63.



# Restricted Chinese Natural Language Analysis Based on Dependency Grammar Model

Yongxing Shang, Zhijiang Li<sup>(✉)</sup>, Liqin Cao, and Tian Song

School of Printing and Packaging, Wuhan University, Wuhan, China  
lizhijiang@whu.edu.cn

**Abstract.** Chinese natural language analysis is an important interface between humans and computers. During the analysis, unstructured natural languages were usually input, while a generating structured query language is needed for computer understanding. The paper proposes a method for natural language analysis in some restricted modes based on domain knowledge database, lexical analysis and syntactic analysis. In our approach, a semantic dependency tree is treated as an intermediate language, and semantic dependency analysis model and grammar recognition were used to re-present the input sentence as a structural sentence. An experiment system has been developed based on traffic information database. The experiment results and examples demonstrate that our method can effectively understand various common natural query statements with good usability in restricted situations.

**Keywords:** Natural language processing · Dependency grammar analysis · Domain knowledge database

## 1 Introduction

Natural language processing (NLP) transforms natural languages in text into structured data that can be resolved by computers. The natural language is the communication language in peoples' daily life, while the structured data is the structured query language (SQL) in most cases. The natural language processing relates to artificial intelligence and information processing, which is applied in man-machine dialogs, machine translation, text categorization, information retrieval [1]. It's the most critical technology for computers to understand user's intentions.

The Natural language interface is an effective application for NLP, which allows people to communicate with computer in restricted fields by using a subset of natural language [2]. However, users must comprehend the SQL in traditional interface, while it's not feasible for most non-professional users. To fix this problem, researchers put forward the natural language query interface. The advantage of the query interface can be summarized into three parts: (1) Users search the information by relevant concepts instead of specific data. (2) It's friendlier for users, because the SQL is not necessary. (3) Users can make clear and simple query requests [3].

In recent decades, Natural Language Interface to Database has been studied by many institutions. The earliest and most representative in 1960s is the Green's BASEBALL system, that was used for information search in National Baseball League [4].

The system analyzed the English text by using keyword matching technology [5–7]. In 1970s, the LUNAR system designed by W. A. Woods was the most representative specific query interface system, which first implemented the Augmented Transition Network in syntax analysis [8–10]. However, the portability of these specific systems is poor because they were only designed for specific tasks. Since then, people have started to design the general interface that could satisfy different fields' need, such as Themis, Intellect and ASK [11, 12].

Recently, the interface systems have been more reliable and feasible. Many new technologies are implemented in this area like Annual Neural Network [13]. The mainstream methods can be divided into two categories. The first is the methods based on rules, such as Finite State Transition Network, Recursive Transition Network, Dependency Grammar Model. The other one is the methods based on statistics like Hidden Markov Model, Maximum Entropy Model [14], Viterbi algorithm and Support Vector Machine.

Based on the background presented above, a natural language query interface based on the combination of statistics and rules has been designed in this paper. We have proposed a dependency analysis and grammar identification method based on database semantics. In this framework, the transitional language is a semantic dependency tree. In general, the algorithm obtains the query targets and conditions by separating the sentences into patches and parsing them by grammar rules. Finally, the targets and conditions are combined into the structured language as the parsing result.

## 2 Approaches

The core of query interface is the understanding of natural language. Because of the complexity and diversity of Chinese, it's difficult to find a general model to describe Chinese language, which can fix the problems such as semantic ambiguity or sentence segmentation. It will be easier to decrease the probability of ambiguity if the query target belongs to a specific field. The problem can be reduced to the parsing procedure of a subset of Chinese language.

In this paper, to achieve the restricted Chinese natural language analysis, two qualifications for the query statement have been established. The first one is Query Target which indicates the table's name in database, such as Human, Building and so on. The Target is an entity that the algorithm needs to process. The other one is Query Condition which means the limitation factors of user intent like Human's name, age or Building's address.

The system can be divided into three parts: The Database, Lexical Analysis and Semantic Syntax Analysis.

### 2.1 Database

The support database module consisted of two databases. The General Corpus for lexical analysis applies to various fields. It's the basis of word segmentation. The words in Corpus are not associated with database's field, while it's necessary for analyzing Chinese sentences. It contains the common words and phrases of Modern Chinese. The



General Corpus used in this paper is segmented from the public news content of People's Daily in 2014 to get a professional Chinese vocabulary data set. The property of the general corpus is shown in Table 1. The Standard Word means the entity of the word. The standard word can have multiple vocabularies like noun, verb. Frequency refers to the frequency of occurrence of each vocabulary during the training.

**Table 1.** Structure of general corpus

Standard word	Vocabulary A	Frequency of A	Vocabulary B	Frequency of B
---------------	--------------	----------------	--------------	----------------

The Special Corpus for semantic syntax analysis is an additional complement for General Corpus. It consists of several tables that storage the knowledge of specific field. The function of these tables includes dedicated segmentation, entities and dimensions' relationship, vocabulary template. Table 2 shows the structure of dedicated segmentation table. The other tables all store the description and standard statement in binary pairs.

**Table 2.** The structure of dedicated table

Field name	Field type	Explanation
Name	String type	Word
POS	String type	Vocabulary
FQ	Integer type	Frequency
NE	String type	Entity name
NE type	String type	Entity type

## 2.2 Lexical Analysis

In this paper, an improved Shortest Path segmentation method based on database semantics is proposed [15]. As the reality that there is redundant information in query statement like particle or preposition is concerned. They may lead to semantics ambiguity if the algorithm segments these words at first. So, the pre-process step has been added in the Shortest Path Segmentation algorithm. In this step, the algorithm segments words according to the Special Corpus at first, then uses General Corpus to segment other phrases. The remaining part of segmentation is to calculate the shortest path of the Directed Acyclic Graph. The Graph consists of the patches from the previous step. The length  $L$  of path can be calculated by Formula 1.

$$L = -\log\{a * P(C_{i-1}) + (1 - a)P(C_i|C_{i-1})\} \quad (1)$$

$\alpha$  is a coefficient between 0 and 1.  $C_{i-1}$  is the current word and  $C_i$  is the next one.  $P(C_{i-1})$  indicates the probability of current word.  $P(C_i|C_{i-1})$  is the probability of the next word  $C_i$  while the previous word is  $C_{i-1}$ . Figure 1 shows the Directed Acyclic Graph of a query statement in this system for which searching the age of a person.

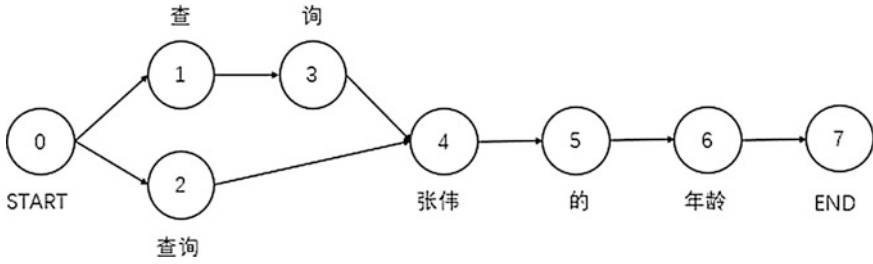


Fig. 1. Directed acyclic graph of an example of query statement

The next step of lexical analysis is labeling. Hidden Markov Model and Viterbi Algorithm are applied to label the segmented patches. In general, the purpose is to find the most possible vocabulary term  $S = \{s_1, s_2, s_3, \dots, s_n\}$  to match the segmented term  $K = \{k_1, k_2, k_3, \dots, k_n\}$ , and the maximum probability is  $P(s_1, s_2, \dots, s_n | k_1, k_2, \dots, k_n)$ .

Formula (2) can be available from Bayesian formula.  $P(s_1, \dots, s_n)$  is the probability of the most possible vocabulary term S.

$$P(s_1, s_2, \dots, s_n) = P(k_1, k_2, \dots, k_n | s_1, s_2, \dots, s_n) / P(k_1, k_2, \dots, k_n) \tag{2}$$

Then, the independence assumption is adopted while the  $P(k_1, k_2, \dots, k_n)$  is ignored as shown in Formula (3).

$$P(s_1, s_2, \dots, s_n) = \prod_{i=1}^n P(s_i | s_{i-1}) \tag{3}$$

According to Binary Combination Model, the formula of labeling the vocabulary can be summarized by Formula (2) and (3) in Formula (4).

$$P(s_1, s_2, \dots, s_n) * P(k_1, k_2, \dots, k_n | s_1, s_2, \dots, s_n) = \prod_{i=1}^n P(s_i | s_{i-1}) * P(k_i | s_i) \tag{4}$$

The Hidden Markov Model is implemented to solve the problem [16]. The possible observation indicates the segmented term K. The state is the vocabulary term S. The state transition probability is  $P(s_i | s_{i-1})$  and the output probability is  $P(k_i | s_i)$ . At last, Viterbi algorithm is implemented to solve the Maximum Probability's term S.

### 2.3 Semantic Syntax Analysis

To parse the labeled term from previous steps, the improved Nivre's Dependency Grammar Analysis method based on database semantics is proposed. The dependency grammar is the description of the relationship between the words in sentence [17]. Dependency here means the status of domination between words. The dependency analysis based on decision is applied in this paper, which means processing a sentence

word by word in a specific direction. Every step needs to make decision according to status.

In this paper, we construct a dependency grammar model, which transforms the sentence processed by lexical analysis into semantic dependency tree. The model can be represented as a Quintet Vector in Formula (5).

$$DRAM: (PQ, DRD, DRR, DRAP, T) \tag{5}$$

*PQ* means the query statement after segmentation and labeling. *DRD* is the dependency that summarized in Table 3. *DRR* is the method for judging the dependency by Formula (6). *DRAP* is the dependency grammar analysis algorithm and the improved Nivre algorithm was adopted in this paper [18]. *T* is the semantic dependency tree.

**Table 3.** Dependency types

Dependency	Instructions
Value and comparing dependencies	Operators like >, <, =
Quantifier dependencies	All, Any, Every, Some, Only, Not
Verb lattice component dependencies	The verbs between entities
Connection dependencies	Modified relationship between entities

$$DRR = ([O1, O2], Condition, DRelation) \tag{6}$$

*O1, O2* are the objects that are needed to judge the dependency. *DRelation* is the DRD between *O1, O2*.

The strategy based on database semantics is applied to overcome the ambiguity of words in query statement. The algorithm locates the ambiguous words in the dependency tree, according to the related words which have the modifications or contact with the ambiguous words. Then, it analyzes whether the ambiguous words and related words can constitute a complete database semantics or not. The complete semantics demonstrate that it is a correct query statement.

However, there is uncertainty whether the algorithm only determines the query target by semantics dependency tree because the target may exist in any part of the tree. To overcome this problem, The Maximum Reverse Matching method is utilized to decide the target. While the query target is determined, the query condition can be obtained from the semantics dependency tree. Finally, the system outputs the structured language that consist of query target and condition.

### 3 Experiments and Analysis

To validate the reliability and feasibility of the method presented above. A query system for traffic information was designed as the experiment.

### 3.1 System Framework

In this paper, we have constructed a Chinese Language Query Interface to apply in the experiment. The system framework is shown in Fig. 2.

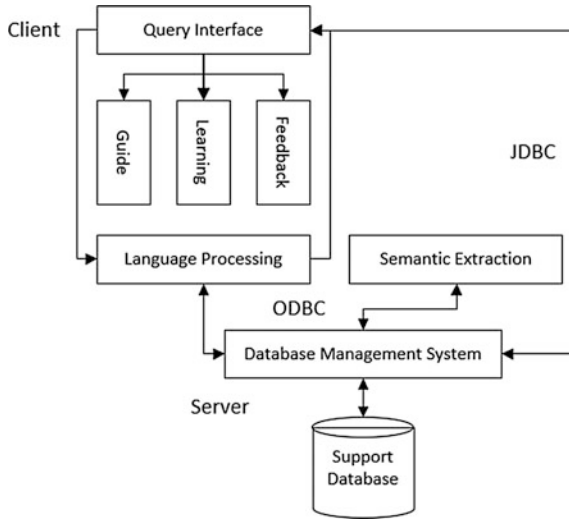


Fig. 2. System framework

In Fig. 2, Client is the Query Interface and Server is responsible for processing client requests. In this framework, the system accesses database by applying the Java Database Connectivity for processing query statement and knowledge extraction. In addition, the server’s database is an Oracle database and the client’s database is a MySQL database, and therefore the connection between Local Client and Server is the Open Database Connectivity.

### 3.2 Experiment

The system was designed and deployed in Web Service as a part of constructing Smart City in Wuhan. Therefore, the data set contains information about human, building, administrative division and road as the Table 4 shows.

Table 4. The content of testing data set

Entity type	Property
Human	Name, Sex, Age, Height, Identity number, Salary, Taxes and so on
Administrative Division (Community, Village, Town, County)	Name

This interface is for processing Chinese language, and the norm has five components. The Main target and condition indicate the primary entity in statement. The Correlative target and condition indicate the other entity occurs in statement. There are two Type of the results: Statistics and List. The procedure of system can be shown in Fig. 3. The Output parsing result will be reorganized to Json format data for transmitting in Web server as the final output in Fig. 4.

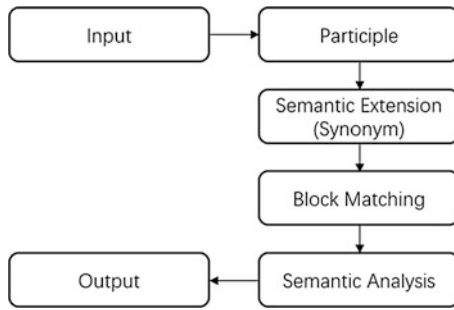


Fig. 3. The procedure of system



Fig. 4. The Json result of an input example

Then, 150 testing examples were adopted to validate the reliability of the interface system in local client and server. There are three test data sets, corresponding to three kinds of query conditions.

**1. Single Query Target and Multiple Query Conditions**

In this case, the statement only contains one entity and the process that belongs to single-table query.

**2. Multiple Query Targets and Query Conditions**

The statement contains plural entities and the process belongs to cross-table query. The interface needs to judge the primary and secondary relationship of the entities.

### 3. Redundancy and Fuzzy search in natural language processing

This is the most difficult case. There is an uncertain or wrong description about the entity. The algorithm needs to find out the most approximate result from the data set.

#### 3.3 Analysis

Among the results shown in Table 5, results of the test set 1 and 2 demonstrate that the interface can effectively process single table query and cross table query, while set 3 shows the worst result. There are two reasons for it. The first reason is that the corpus is not perfect. The database lacks necessary prior knowledge for some information. The second reason is that the interface has less intelligence so that it can't process the dependencies in some complex patterns. In addition, the grammar in this paper may be not suit for any patterns.

**Table 5.** The experiment statistics

Result	Number of failures			Number of success	Total	Accuracy (%)
	Complete failure	Partially failure	Subtotal			
Test set 1	1	0	1	59	60	98.3
Test set 2	2	2	4	46	50	92.0
Test set 3	4	3	7	33	40	82.5
Total	7	5	12	138	150	92.0

## 4 Conclusions

The natural language interface is a combination of artificial intelligence and database technology. Its direct purpose is to transform the natural description into structure query language. The natural language query interface designed in this paper has good portability and it operates independently by database management system.

The major contribution of this paper consisted of corpus and Chinese natural query language processing. To achieve the accurate analysis of query statement, the method based on the combination of rules and statistics was implemented. The results demonstrated that the interface effectively understood various Chinese language query statements in restricted situations.

## References

1. Xu, L. (1997). A study on natural language query technology in database. *Computer Science*, 24(5), 50–54.
2. Zheng, F. (2001). *On the study of natural query language understanding in computer*. Southwest Jiaotong University.

3. Hu, X. (2006). *The study on database query based on natural Chinese language*. University of Electronic Science and Technology.
4. Chang, Y., Xu, H., & Bai, S. (2004). TREC 2003 question answering track at CAS-ICT. In *The Twelfth Text Retrieval Conference* (pp. 65–68).
5. Bonnie, M. O. K., & Meng, H. M. (2002). *Improvements on a belief network framework for natural language understanding of domain-specific Chinese queries*. TaiPeiS: ISCSLP.
6. Guan, D., Chu, M., Zhang, Q., Liu, J., & Zhang, X. (1998). *The research project of man-computer dialogue system in Chinese*. Singapore: ISCSLP.
7. Lu, C. (2001). *Syntactic network of Chinese grammar*. Commercial Press.
8. Ammicht, E., & Fosler-Lussier, E. (2001). *Ambiguity representation and resolution in spoken dialogue system*. Eurospeech.
9. Burton, R. R. (1976). *Semantic grammar: An engineering technique for constructing natural language understanding system*.
10. Li, B., & Zhou, X. (1999). The study on natural language interface system based on database. *Computer Systems and Applications*, 1999(12), 31–34.
11. Brandt-Pook, H., Finlc, G. A., Hilderbrandt, B., & Kummert, F. (1996). *A robust dialogue system for making an appointment*. ICSLP.
12. Wu, H., Huang, T., & Xu, B. (2000). *A generation system for Chinese tests*. China: ICSLP.
13. Glass, J., & Weinstern, E. (2000). *Facilitating spoken dialogue system development*. Eurospeech.
14. Deepthi, S., Rejimoan, R., & Vinod Chandra, S. S. (2014). Maximum entropy based natural language interface for relational database. *International Journal of Engineering*, 7(1), 69–77.
15. Zhang, H., & Liu, Q. (2002). Models of Chinese words rough segmentation based on N-shortest-paths method. *Journal of Chinese Information Processing*, 2002-9, 16(5), 1–7.
16. Luo, G. (2001). *The research on decrypt search engine technology*.
17. Rao, G., Agarwal, C., Chaudhry, S., et al. (2010). Natural language query processing using semantic grammar. *International Journal on Computer Science and Engineering*, 2(2), 219–223.
18. Nivre, J., & Schlz, M. (2004). Deterministic dependency parsing of english text. In *Proceedings of COLING04* (pp. 64–70), Geneva, Switzerland.



# HTML5-Based Tools Management Mobile Application the Implementation in the WeChat Public Platform

Qingjie Lin<sup>(✉)</sup>, Caifeng Liu, and Wei Wang

School of Media and Design, Hangzhou Dianzi University, Hangzhou, China  
linqingjie@live.cn

**Abstract.** At present, for the popularity of cross-platform development technology used in mobile application development, and the prevalence of enterprise and individual use of WeChat public platform. This paper adopts hybrid mobile application development model, analyze cross-platform mobile application development technology and use the functions and features of the WeChat public platform to propose building cross-platform mobile applications based on HTML5, JavaScript and other languages, then, practices on this scheme, using the WeChat public platform native browser kernel designs and implements a tool management system for power station company and optimize the speed of loading application webpages, then, to verify the feasibility and reality of the solution.

**Keywords:** HTML5 · Mobile applications · WeChat public platform

## 1 Introduction

With the rapidly development of mobile Internet in recent years, smart phones and other mobile terminals have become indispensable products in people's daily life. Among them, the WeChat public platform has brought more convenient services to people. The WeChat public platform is a service added by WeChat. Apart from the communication functions of social networks, there are some unique features, such as information push and menu settings, which make it easy for users to build their own personalized platform [1].

At present, two mobile operating systems, Android and iOS, account for most of the market share of smart mobile platforms. Mobile applications developed for different mobile operating systems and it require different development languages and development platforms. This development model is called the native mobile development model. This kind of development mode is complicated to transplant. For example, on the Android platform, due to different mobile phone screen size and other issues, development needs to be adapted to various mobile phone models, but the hybrid mobile development model solves the cross-platform migration problem of mobile applications. The current hybrid mobile development model mainly includes PhoneGap, Appcan and other frameworks. The open source PhoneGap [2] framework provides a full range of plug-ins, abstracting and simplifying the complex plug-ins API



provided by mobile devices itself, and uses HTML, JavaScript, CSS and other technologies to migrate mobile applications to different mobile operating systems.

This article mainly uses HTML5, PhoneGap and GZip to implement the WeChat public platform. The hybrid mobile application on the WeChat public platform uses the built-in browser kernel of WeChat. GZip compresses the content of the webpage and sends it to the visiting browser to display it, that solve the problem of slow access to large data pages in web technology.

## **2 Hybrid Mobile Application Development Model Overview**

### **2.1 Hybrid Mobile Application Development Model**

Currently mobile applications are widely used in various industries. There are three modes for implementing these APPs [3]: native mobile applications, web mobile applications, and hybrid mobile applications. Native mobile applications can directly call hardware devices and various sensors of mobile devices, but its development costs are high, complex maintenance and can't be cross-platform, web mobile applications can achieve cross-platform and short development cycle, but can't call mobile device hardware, Hybrid mobile applications improve the advantages and disadvantages of the two development modes mentioned above, making applications using the hybrid mobile development model [4] closer to native apps.

### **2.2 Hybrid Mobile Application Development Model Architecture**

This article mainly uses the PhoneGap framework to implement mobile applications. The essence of the PhoneGap framework is to allow developers to build localized mobile applications using only Web technologies, and to integrate native features to the maximum extent, and use JS to invoke native functions. PhoneGap provides plenty API, including Accelerometer mobile sensor, Compass device pointing and Notification. PhoneGap provides hardware access control. Compared with the traditional Web applications, through the JS classes provided by PhoneGap can access the mobile device hardware described above to make up for the inadequacies of traditional Web applications.

The principle structure of the hybrid mobile application using the PhoneGap framework is shown in Fig. 1. First, using Web technology such as HTML, JavaScript and CSS to support cross-platform, and then packaged into an independent mobile application using the mobile development framework PhoneGap, and uses the native APIs provided by PhoneGap to access the mobile device APIs, the mobile application is placed in the native program framework, the client can access it through WebView.

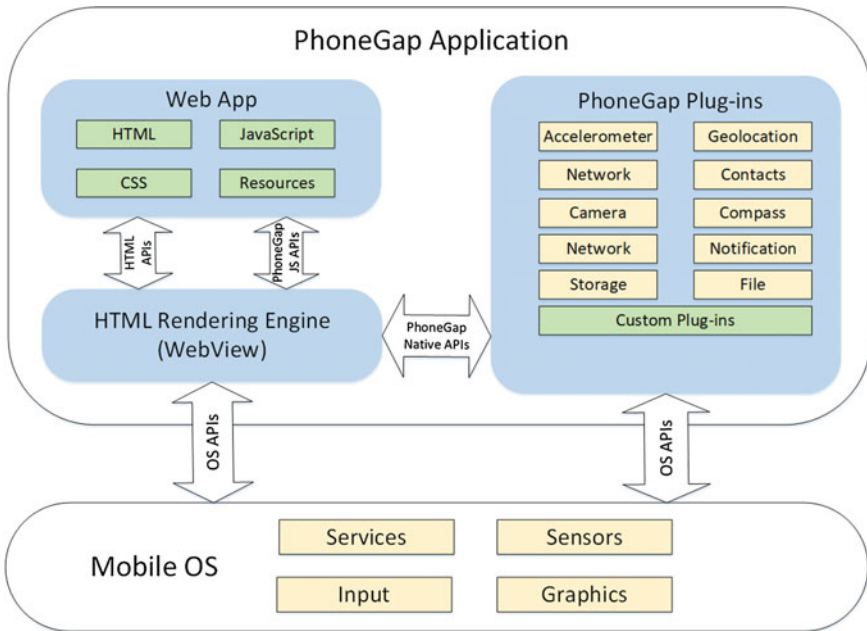


Fig. 1. The principle structure diagram of the hybrid mobile application scheme using PhoneGap

### 3 Implementation of Hybrid Mobile Application on WeChat Public Platform

#### 3.1 System Requirements Analysis

The tool management system is a simple and quickly way to manage all kinds of tools. This article uses the PhoneGap framework to develop a cross-platform mobile application tool management system for a hydropower station. Considering the variety of tools needed in the maintenance of the hydropower station, there are many inconveniences in manual management, and because the hydropower station workers need the faster information feedback, it is a necessary requirement to increase the website access speed. Then, due to the differences in the types of employees' mobile devices, there is a WeChat application installed in each employee's devices. So, considering the above situation, using the PhoneGap framework to implement a cross-platform tool management system running on WeChat is the best choice.

#### 3.2 System Development Environment and Platform Construction

System development and operating environment construction is divided into the following steps:

1. NPM is responsible for the management of the PhoneGap application package, so Node.js should already be installed in the development environment.
2. PhoneGap's core Cordova is installed with the following command: "Npm install—g cordova" After Cordova is installed, you can create an engineering application.
3. Database installation and use. The system uses SQL Server as a database management system.
4. Building PHP environment.

### 3.3 WeChat Public Platform Development

WeChat public platform as a new media, can obtain service number or subscribe number by applying in the Tencent. Fill in the server address in the developer center of the public platform management page, which is limited to port 80. After obtaining the public platform [5], the link of the system is embedded in the public platform. The Web version of this system shares a background program on the WeChat public platform.

### 3.4 Key Technologies

GZip compression is a key technology that used on the server side of the system, because when the user uses the system, such as query a tool, the query result needs to return quickly, so the user experience will feel better. GZip compression efficiency is very high, usually can achieve 70% compression rate, so the server uses GZip compression function that main idea is to compress the page requested by users, to save network bandwidth, improve the access speed of the website. The key configuration code to use GZip function in IIS is as follows:

```

/ **
* Modify the file suffix that needs to be compressed, where HcFileExtensions is the
extension of the static file and HcScriptFileExtensions is the extension of the
dynamic file
* /
HcCreateFlags="1"
HcDoDynamicCompression="TRUE"
HcDoOnDemandCompression="TRUE"
HcDoStaticCompression="TRUE"
HcDynamicCompressionLevel="9"
HcFileExtensions="htm, html, txt, js, css"
HcOnDemandCompLevel="10"
HcPriority="1"
HcScriptFileExtensions="asp
aspx
dll
exe"

```

## 4 System Test and Performance Analysis

### 4.1 System Test

The tool management system implements more than 10 functions, such as search tools, scan code to borrow, and so on. Each function is clearly displayed to the user, and the specific interface is shown in Figs. 2 and 3.

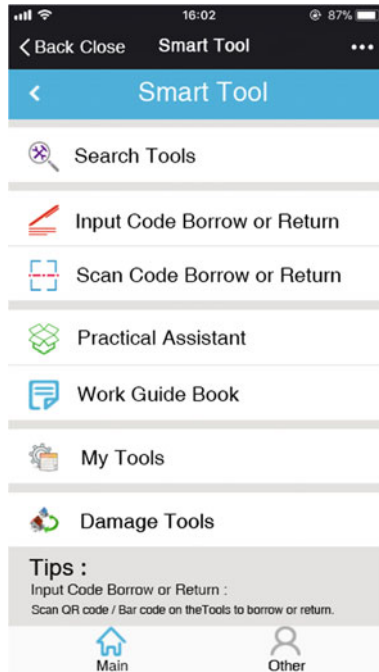


**Fig. 2.** Application index

### 4.2 Performance Analysis

The performance of this application is greatly affected by the network, because it will load the server-side pages. If the loading time is too long, the user experience will be very bad, so it is necessary to increase the loading speed of the web pages.

The idea of compressing the interface data by GZip compression function improves the loading time of the front page. Analyze the effects of Gzip compression on application performance, it's uses hybrid mobile applications that use Gzip compression and hybrid mobile application that do not use Gzip compression to test. Among them, the average load time of the hybrid mobile application using the Gzip compression function is 0.115 s, and the average load time of the hybrid mobile application without using the Gzip compression function is 0.176 s. The average page load

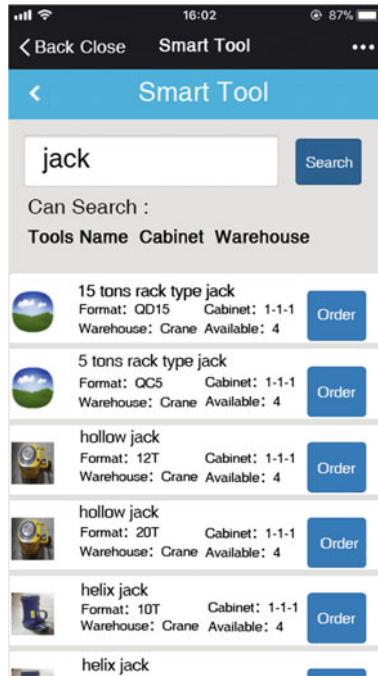


**Fig. 3.** Search tool details page

efficiency difference between the two modes is quietly obvious. So, hybrid mobile applications using Gzip compression can achieve a better user experience.

## 5 Conclusions

With the continuous development of the mobile Internet, more and more cross—platform applications will be developed based on HTML5. In this paper, the WeChat public platform for tools management mobile application after testing, it's shows perfect function, and good loading speed during use. The use of the WeChat public platform simplifies the development model compared to the use of native application development, and do not have to remember the domain name, convenient for the user to use.

## References

1. Yan, L., & Wang, D. (2016). Application of WeChat public platform in university scientific research management by taking Communication University of China as an example. *Science Research Management*, *SI*, 301–308.
2. Wu, J. (2012). The cross platform phonegap research. *Information Technology*, *3*(12), 71–72.

3. Gu, C. (2014). Research on development model of APP application program. *Silicon Valley*, 5, 35–36.
4. Shuai, D. U., Haihong, E., & Ke, X. (2015). New development model for hybrid mobile applications. *Computer Engineering & Software*, 36(6), 12–17.
5. Bei, Z., Tianfang, D., & Chengyu, Z. (2014). Design and implementation of library WeChat public platform service in development mode. *New Technology of Library and Information Service*, 30(1), 87–91.



# Technical Research of Clearing Floating Effect in CSS Cascading Style Sheets

Jing Wang and Zhanjun Si<sup>(✉)</sup>

College of Packaging and Printing Engineering,  
Tianjin University of Science and Technology, Tianjin, China  
Szj@tust.edu.cn

**Abstract.** The addition of CSS cascading style sheets completes the layout of the interactive web page in the interactive web page layout technology HTML5+CSS3. The effect of web page optimization is very obvious, and it is also very important to float and clear floating in the web page layout. The four methods of clearing floating has been introduced mainly, in order to achieve the effect of further optimization to compare the advantages and disadvantages of each method from all aspects, and ultimately to make the overall layout of the page optimal. But floating can cause many problems, and it is especially significant to clear the float. There are many ways to clear float, but each method has more or less limitations. And other methods must be found to eliminate these limitations. In contrast, the method of removing floats by pseudo-elements is the most perfect.

**Keywords:** CSS cascading styles · Clearing float · Page layout · Methods

## 1 Introduction

The mobile smart devices have penetrated the all corners of people's lives at a very fast speed because of the rapid development of mobile Internet technology has made. The use of web pages as an information carrier has made the interactive demands on web pages among the people increasingly demanding [1]. The most popular interactive web page layout technology, HTML+CSS, is quickly and widely used with its unique advantages. HTML5 hypertext markup language production webpages, combining with CSS3 cascading stylesheet language, can improve the layout of interactive web pages [2]. Floating is indispensable in the layout of a web page, but it will also have many unnecessary effects. This requires us to clear away some of the floats and optimize the pages.

## 2 Characteristics and Impacts of Float

### 2.1 Characteristics of Float

There are four values for the Float element. Left: the element floats to the left. Right: the element floats to the right. None: it is the default value, and the element does not

float. It will appear where it appears in the text. Inherit: the value of the float value should be inherited from the parent element [3]. The first two attributes are the most frequently used codes. Floating is one of the indispensable codes in a web page layout. It can make the page element away from the limitations of the document flow and move the target element to the specified position in the parent element so that re-publish the page. At last, it can change the default arrangement order of the elements in the original page. The characteristics of the floating element itself have certain advantages, as shown below.

- (1) The floating element is displayed on one line.
- (2) When the property value 'left' is set, the floating elements will be arranged from the left side of the parent box to the right side. When the property value 'right' is set, the floating elements will be arranged from the right side of the parent box to the left [4].
- (3) The floating elements automatically have the properties of block-level elements. After adding a floating element to an inline element, there is no need to add the code 'display:block', otherwise it is a waste code.
- (4) The floating elements are out of the document flow.
- (5) Child elements within floating elements do not inherit floating attributes.
- (6) The following elements of the floating element do not recognize the height and position of the floating element.
- (7) All elements can use floating attributes.

## 2.2 Impact of Float

### 2.2.1 Parent Element to Set the Background Color Does not Work

When setting a float for block-level elements, block-level elements can be implemented out of the document flow and display on one line. But the float will make the background color of the parent element not display because the height of the parent element is zero.

### 2.2.2 Parent Element Setting Border Properties Will not Be Opened

When the parent element is set to a border value, the border property is not expanded and the block-level element is not wrapped. The four sides of the border line are grouped together.

### 2.2.3 Parent Element Setting Padding Properties Will not Be Opened

The padding value does not work when the padding attribute is set for the parent element.

## 3 Methods of Clearing Float

Method one, the Adding a fixed height to the floating element's parent element is very important. Because the height of the parent element is zero, the floating side effects can be eliminated by manually adding the same height as the floating element when writing



the code. As shown in Fig. 1, you can clear the float by adding the same height as the child element to the parent element. Figure 2 are renderings.

```

3  <head>
4    <meta charset="UTF-8">
5    <title>Title</title>
6    <style type="text/css">
7      .wrap {
8        background: blue;
9        border: 10px solid #11c900;
10       padding: 10px; /*四个方向10px的内间距*/
11       height: 200px;
12     }
13
14     .left {
15       float: left;
16       width: 200px;
17       height: 200px;
18       background: lightcoral;
19     }
20
21     .right {
22       float: left;
23       width: 200px;

```

Fig. 1. Program code

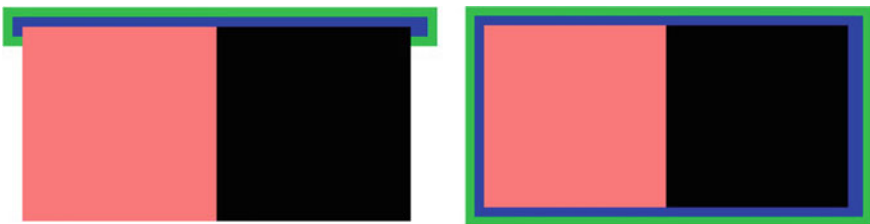


Fig. 2. Effect of not adding height attribute (left) and effect of adding height attribute (right)

Although this method is simple and effective, it is not recommended for everyone to use. Because manually adding heights is a matter of fixing the scope, and adding new elements is not possible unless you create a fixed-height webpage.

Method two, setting the code ‘overflow: hidden/auto;’ to the floating element’s parent element is a very simple method, as shown in Fig 3.



**Fig. 3.** Effect of not adding the “overflow:hidden/auto;” attribute (left) and the effect of adding the “overflow:hidden/auto;” attribute (right)

```
<style>
    .box{width:300px;border:1px solid #000;overflow:hidden;}
    .div1{ width:260px;height:400px;background:Red;float:left;}
</style>
<body>
    <div class="box"></div>
    <div class="div1"></div>
</body>
```

Method three, in order to add an empty label with the characteristics of block-level elements to the parent element of the float element before the end of the label, we will use div, add a ‘clear: both;’ to the element under normal circumstances. As shown in Fig. 4, the results are shown in Fig. 2.

The biggest disadvantage of this method is that the margin is invalid, especially in the case of a large number of floating layouts of the page. Adding too many empty divs to clear the floating is inconvenient to optimize.

Method four, the clearfix pseudo-element to clear the float is the most important method. This method uses the attribute ‘:after’ to clear the float in the clearfix pseudo-element, which is the most commonly used method in the project. First of all, we should ensure that it is a block-level element by setting the ‘display: block;’, and then there is no floating object left and right, so you must apply the style ‘clear: both;’ to the element. Special attention should be paid to the pseudo-element ‘:after’, it comes with an attribute ‘content:“ ”;’. This attribute must be written. If it is not written, the pseudo-element will have no effect. The above three conditions are necessary and indispensable.

```

20
21 .right {
22     float: left;
23     width: 200px;
24     height: 200px;
25     background: black;
26 }
27 .clear{
28     clear:both;
29 }
30 </style>
31 </head>
32 <body>
33 <div class="wrap">
34     <div class="left"></div>
35     <div class="right"></div>
36     <div class="clear"></div>
37 </div>

```

Fig. 4. Program code

This method also has four attributes that are not required:

- (1) 'height: 0;': To prevent the default 'height: 1px;' in low-level browsers, we could use 'height: 0;' to override.
- (2) 'font-size: 0;': We could set the font size to 0.
- (3) 'overflow: hidden;': We could make the element overflow hidden.
- (4) 'visibility: hidden;': We could hide all visibility elements.

Here, we will notice that 'overflow: hidden;' and 'visibility: hidden;' are similar, but there are a few differences between the two.

'overflow: hidden;' is to hide the excess elements, that is, when setting the property, the extra part will be cut off according to the set width and height. And 'visibility: hidden;' hides that layer, which means that you cannot see its contents but the space it occupies still exist [5]. (It is invisible but touched).

That is, using the pseudo-element ':after' to clear floating fixed code, it is only necessary to add '.clearfix' to the parent element of the floating element.

```

.clearfix {
    display:block;
    clear:both;
    content:" ";
    height:0;
    font-size:0;
    overflow:hidden;
    visibility:hidden;
}

```

To make all browsers compatible, we can add  
 .clearfix {\*zoom:1;}

## 4 Conclusions

The optimization of the web page cannot be separated from the setting of the floating property, but clearing the float is indispensable. This article first introduced the characteristics of floating elements in web pages and the impact of floating, and then introduced four methods for clearing float. Although there are many methods for clearing float, each method has certain disadvantages. In contrast, the elimination of floating pseudo-elements is the best solution.

## References

1. Nashun, M. (2007). *Research and implementation of mongolian web production template in the distance education platform*. Fudan University.
2. Du, L. (2016). Static web design—Using CSS to control hypertext text styles. In *Computer knowledge and technology* (pp. 215–216).
3. Zhang, L., & Yue, S. (2014). Project five corporate website design. Web design and production. Chongqing University Press.
4. Dong, G. (2016). Research on web page layout based on DIV + CSS box model. *Information and Computer*, 22, 87–88.
5. Bubuko Knowledgebase. (2015). The area between display:none, overflow:hidden, visibility:hidden, Anonymous. <http://www.bubuko.com/infodetail-1128650.html>. Accessed March, 30 2017.



# Research on Multithreaded Download and Local File Operation of HTML5 Browser

Wei Wang, Aibin Huang, and Caifeng Liu<sup>(✉)</sup>

Hangzhou Dianzi University, Hangzhou, China  
lcf88089135@126.com

**Abstract.** Traditional browsers are inefficient in single-threaded download and rely too heavily on target servers. In order to improve download speed and stability, multithreaded download tools are urgently needed. However, current multithreaded download tools, such as Thunder and Free Download Manager, cannot meet the convenience and versatility of browser download process. Aiming at the above problems, this paper proposes a method that use Web Workers to implement multithreaded download of browser-side. Multiple sub-threads are created by the main thread of the browser, and these sub-threads request file data from the server at the same time, thereby improving file download efficiency and download speed. This article demonstrates the feasibility of this technique and verifies the integrity of the downloaded file using the File System API provided by HTML5.

**Keywords:** Multithreaded download · Web worker · File system API · Thread

## 1 Introduction

As the new features of HTML5, Web Workers creates a new running mode for JavaScript of browser-side and enables JavaScript to create a new running environment in another thread, which allows JavaScript to be processed in the background [1]. Based on this feature, this paper innovatively proposes that using Web Workers to achieve browser side multithreaded download technology. In addition, HTML 5 provides an interface to access the local file system from the browser, that is the File System API which can verify the integrity of the downloaded file [2].

## 2 Browser-Side Multithreaded Download System Overview

### 2.1 Multithreaded Download Steps

The overall design workflow of the system is as follows:

1. After the user clicks the download button, the browser sends requests to the original download point and downloads some resource fragments.
2. The browser submits the original download URL to the resource index server and queries the server addresses of other available download sites.

3. The resource indexing server returns a list of available resources and the size of these resource files to the browser.
4. The browser side segments the files, and creates the sub-threads, then merge these sub-threads. Each sub-thread downloads the resource fragments from their specific target server respectively.
5. The download site server returns the resource fragments to the browser.
6. The browser side combines the resource fragments and writes them to the local file system, and then the download ends [3].

## 2.2 Resource Index Server

The main functions of the resource index server are accomplished by the resource analysis module, including querying the available resource addresses and dynamically updating the resource index server. The workflow of resource analysis module:

1. After receiving the query request, it queries address content mapping table according to the original URL.
2. If this address exists, the resource hash value and resource size corresponding to the address will be obtained, the content address mapping table is queried according to the resource hash value, and the list of available addresses corresponding to the resource hash value is obtained, then the multithread download module is returned to the browser.
3. If this address does not exist, it will be updated to the resource index server after the download is completed [3].

## 2.3 Resource Download Module

Using the characteristics of Web Workers to design a browser-side multithreaded download module. The main thread is responsible for interacting with the user, splitting the target resources, creating multiple concurrent sub-threads, monitoring and managing the sub-threads. The sub-thread only needs to receive the download request from the main thread to download the corresponding resource fragment and return the downloaded resource fragment to the main thread. During the download process, multiple sub-threads are running simultaneously, requesting the resource fragment what they need from multiple servers, thereby implementing the multithreaded download function of the browser [4].

The main thread uses Web Workers to create sub-thread, sends the file information and the target URL to the sub-thread through the `PostMessage` function, and monitor to the message of the sub-thread through the `onMessage` function to obtain the downloaded resource fragments by the sub-thread.

After the sub-thread is created, the `onMessage` function is used to acquire and analyze the downloaded information sent by the main thread, then, construct an `xml-httprequest` object based on that information, and send the object to the server. The server can obtain the resource fragments information requested by the user by analyzing the header information of the request object, and then return the corresponding resource fragments to the web front end.

Since each sub-thread is independent of each other, they communicate with each other through the main thread, so the download between the sub-threads is concurrent.

## 2.4 Write Operation Model

The multithreaded download module needs to transfer the data to the write file module after download the data. In order to solve the conflict problem of multithreaded write operations, the system uses `ArrayBuffer` array in the write operation module [5].

- (1) When the main thread segments the resource, each resource fragment needs to be numbered, and file fragment order number is one-to-one corresponding to the starting offset order of the file fragment. For example, if starting offset equal to 0, the resource fragment is numbered 0, the next resource fragment is numbered 1, and so on.
- (2) After the sub-thread downloads the resource fragment, it first returns to the main thread, and sends the resource fragment starting offset and the resource fragment number to the main thread.
- (3) Before creating the sub-thread, the main thread needs to save an `ArrayBuffer` array for storing the file fragment. When the main thread receives the resource fragment that sent by the sub-thread, it will place them in the `ArrayBuffer` according to the number of the resource fragment.
- (4) After all the sub-threads have finished downloading, the main thread writes the resources to the local through the `BLOB` object, then complete the download [3].

## 3 Experiment and Application

### 3.1 Browser Multithreaded Download File Experiment

It can be seen from Figure that in the case of normal smooth network and network delay, in the file downloading process less than 10 M, the download efficiency of multithread and single-thread is similar, and the download efficiency of single-thread is slightly better than multithread. However, in the process of downloading files larger than 10 M, the download efficiency of multithreading is significantly better than single thread (Figs. 1 and 2).

### 3.2 Browser Multithreaded Download Technology Application Scenario

Author of this article has designed and developed an online training system for cross-platform mobile applications of hydropower stations. And the specific interface is shown in Fig. 3. Due to the special nature of hydropower station work, network fluctuations often occur, so browser multithreaded download technology play a very important role in this work environment.

After the file is downloaded using multithreaded download technology, using File System API to retrieve the document from a specified cache folder on the local SD

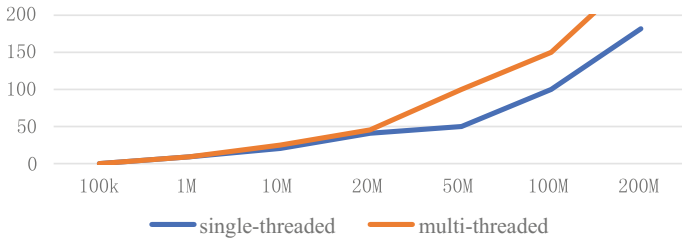


**Fig. 1.** Comparison of single-threaded and multithreaded download efficiency in unblocked and no delay, no high packet loss rate network environment

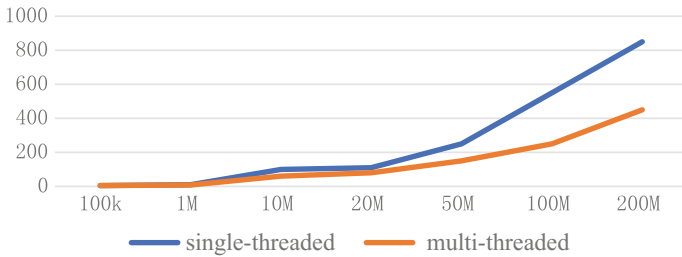


**Fig. 2.** Comparison of single-threaded and multithreaded download efficiency in high-latency network environment that network delay 100 ms



**Fig. 3.** Read and download document pages



card. It can verify the integrity of document through multithreaded download technology [2]. The key code to determine the document type and open it is as follows:

```
@ Suppress Lint(" Default Locale")
public static Intent open File(String file Path) {
File file = new File(file Path);
if ((file == null) || ! file.exists( ) || file.is Directory( ))
return null;}
```

## 4 Summary

In order to solve the problem that the traditional browser needs to install the client or plug-in so that can use multithread download, this paper proposes to use resource content as the core, then extend user single-threaded downloads to multithreaded downloads. During the download process, the resource index server is updated to dynamically obtain the resource distribution in the network. Due to the limitations of JavaScript itself, in the multithreaded download process on the browser side, the resource fragments need to be merged into the ArrayBuffer array before the file can be written into the local, so the efficiency of multithreaded download is not particularly ideal for small files [2]. For very large files, all file fragments cannot be placed directly into the array. At present, the document segmentation strategy used in the work is relatively simple. Therefore, further optimization is needed for multithread download.

## References

1. Mozilla Developer Network. (2017). *Using Web workers*. [https://developer.mozilla.org/enUS/docs/Web/API/Web\\_Workers\\_API/Using\\_web\\_workers](https://developer.mozilla.org/enUS/docs/Web/API/Web_Workers_API/Using_web_workers).
2. Freeman, A. (2014). *The definitive guide to HTML5* (K. Chang, J. Hu, J. Zhao, Trans.). Post & Telecom Press.
3. Ren, S.-J., Zhou, X., Ren, Y.-M., & Li, L.-L. (2017). (Computer Network Information Center, Chinese Academy and Sciences, Beijing 100190, China) (University of Chinese Academy of Sciences, Beijing 100049, China) Multi-Thread Downloading Technology Based on HTML5.
4. QUIC and TCP—why multi-threaded downloads are faster than single threads? (2014). <http://henrystark.blog.chinaunix.net/>.
5. Mozilla Developer Network. (2016). ArrayBuffer. [https://developer.mozilla.org/en-US/docs/Web/JavaScript/Reference/Global\\_Objects/ArrayBuffer](https://developer.mozilla.org/en-US/docs/Web/JavaScript/Reference/Global_Objects/ArrayBuffer).



# Application of Multi-target Tracking Technology for Packing Box

Shenghui Li<sup>1</sup>(✉), Ruizhi Shi<sup>2</sup>, Siyang Liu<sup>3</sup>, and Dongling Zhao<sup>1</sup>

<sup>1</sup> Henan Mechanical and Electrical Vocational College, Zhengzhou, China  
lishenghui2006@126.com, l291zhao@163.com

<sup>2</sup> Information Engineering University, Zhengzhou, China  
ruizhishi@sina.com

<sup>3</sup> Zhengzhou Institute of Surveying and Mapping, Zhengzhou, China  
875128290@qq.com

**Abstract.** Product information is usually printed on the packaging of products in the form of graphics, images or text during the packing process. But the information printed on the packing boxes is difficult to change and cannot provide multiple kinds of data presentation for consumer. With the development of augmented reality technology, we have a new solution for this problem. Based on the analysis of augmented-reality technology and the characteristic of packing box, we adopt a technique that can identify and track multiple target faces at the same time. Thus, the augmented reality based on multi-target tracking technology can be applied to the expression of product information printed on the packing box. The new approach can be used to identify and track six target faces in real time to determine the packing box's coordinate and rotation angle, then calculate the spatial relationship between virtual information and real packing box. The approach proposed in this paper can provide multiple kinds of presentation for information, which ultimately improve the user experience.

**Keywords:** Intelligent packaging · Augmented reality · Multi-target tracking · Image recognition

## 1 Introduction

Augmented reality technology, also known as AR (Augmented Reality) technology, is a new technology that can superimpose virtual information with real scenes. This technology not only can provide multiple kinds of presentation for data, but also enables people to obtain more effective information. The product information of the box packaging is generally printed on the product packaging box in the form of graphics, images or text. But the information printed on the packing boxes is difficult to change and cannot provide multiple kinds of data presentation for consumer. Therefore, how to convey the product information to consumers by information processing technology while not changing the structure and internal materials of the traditional packaging has gradually become an important research direction. The development and

maturity of augmented reality technology provide a new option for solving this problem.

Based on the analyzing of the principle of image recognition and tracking in augmented reality technology, this paper proposed a multi-target tracking technology that can simultaneously identify and track multiple images. The technology can identify and track the product packaging, determine the coordinate position and rotation angle of the packaging box in real time, and then calculate the positional relationship between the virtual information and the real product packaging, so that the virtual information can not only be displayed on the outside of the packaging box, but also on the inside of the box, creating a “perspective” effect.

## **2 Implementation Process of Multi-target Tracking Technology**

### **2.1 Image Recognition and Tracking Principle**

Augmented reality technology based on image recognition and tracking can be mainly divided into two types, Marker-based Augmented Reality and Marker-less Augmented Reality, and this paper mainly discusses the marker-less augmented reality technology [1]. As shown in Fig. 1, the principle of image detection and recognition in the mark-less augmented reality technology mainly includes three steps: the first is feature detection, the second is feature description, and the third is feature recognition. Feature detection is based on a certain algorithm and calculation rules, using the camera to detect the point where the gray value in the image changes significantly, such as the corners, the edges of the image, and so on. The feature description is to describe the detected feature points with binary data. Compared with the original image data, the binary data is only a few tenths or even a few hundredths of the original image, which greatly reduces the image recognition. Feature recognition is based on the feature data generated after feature description to determine whether the recognition is successful. If the recognition is successful, the recognition is completed.

### **2.2 Multi-target Tracking Technology Implementation Process**

Augmented reality technology uses the form of image feature recognition to achieve seamless integration of virtual information with the real environment [2]. In general, image feature detection and recognition are mainly for a single image, but a packaging box may have many faces, such as a three-dimensional packaging box generally has six faces, the images on each face are different, which greatly increases the difficulty of image recognition and tracking. The augmented reality multi-target tracking technology can simultaneously recognize and track multiple images in real time, calculates the relative positions and relative angles of different images. The real-time adjustment of the virtual information’s coordinate position and display angle make the virtual information looks very realistic, the implementation process of multi-target tracking technology is generally shown in Fig. 2.

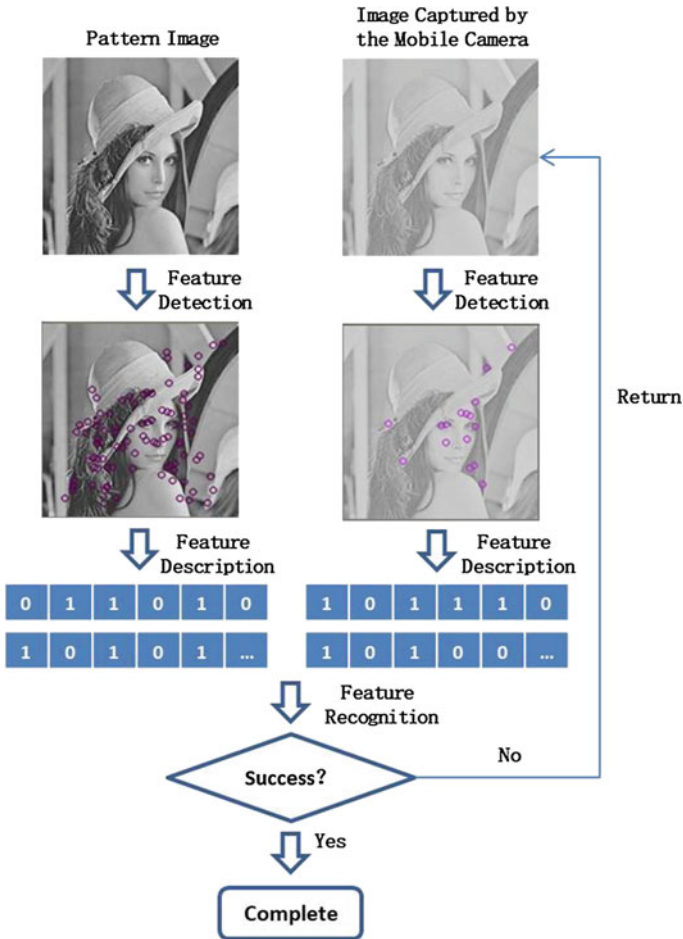


Fig. 1. Principle of image detection and identification

Multi-target tracking technology can be roughly divided into two parts: Firstly, the technology should track and identify multiple target images in real time. Compared with traditional image recognition and tracking technologies, multi-target tracking technology is no longer a single image recognition or tracking. Instead, it recognizes and tracks multiple images captured by the camera. An image data set is formed from multiple images, and then it is calculated in real time through image feature detection and recognition algorithm. The coordinate position, direction angle, and the coordinate relationship between the image and each image in the data set are obtained. Secondly, multi-target tracking technology should realize the superposition of virtual information with real environment. The key to augmented reality technology lies in the ability to ensure the seamless integration of virtual information with the real environment or real objects, and the coordinate information, location information and relation information between different images must be calculated in real time according to the algorithm [3].

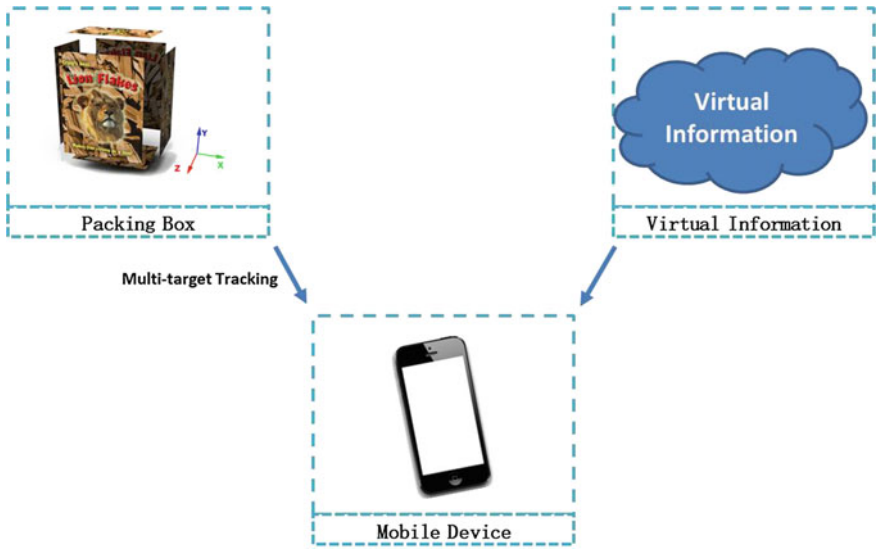


Fig. 2. Multi-target tracking technology implementation process

### 3 Application of Multi-target Tracking Technology in Box Packaging

#### 3.1 Implementation Process of Multi-target Tracking Technology

The multi-target tracking technology used in this paper is mainly based on the Vuforia SDK. The Vuforia SDK is an augmented reality tool development kit that can track and identify plane images, three-dimensional packages, etc. [4]. The multi-targets function of Vuforia is applied to the identification and tracking process of a three-dimensional packaging box. The technical implementation process mainly includes five steps, as shown in Fig. 3 [5].

1. Select the three-dimensional box. Vuforia SDK can identify and track multiple types of images, such as flat images, two-dimensional code images, three-dimensional packaging, etc. If you want to realize the identification and tracking of three-dimensional packaging, you need to select the “three-dimensional packaging box” and download the appropriate development tools.
2. Upload the image. Since the three-dimensional packaging box generally has six faces, the multi-target tracking technology performs corresponding recognition and tracking on all six faces of the packaging box, so six images need to be uploaded, that is, each face has a corresponding image texture to identify and track the three-dimensional packaging box.
3. Download image data. After uploading an image, the Vuforia SDK server generates a set of image data sets based on the image content uploaded by the developer. This set of data includes the size of the uploaded image, the feature data, and the

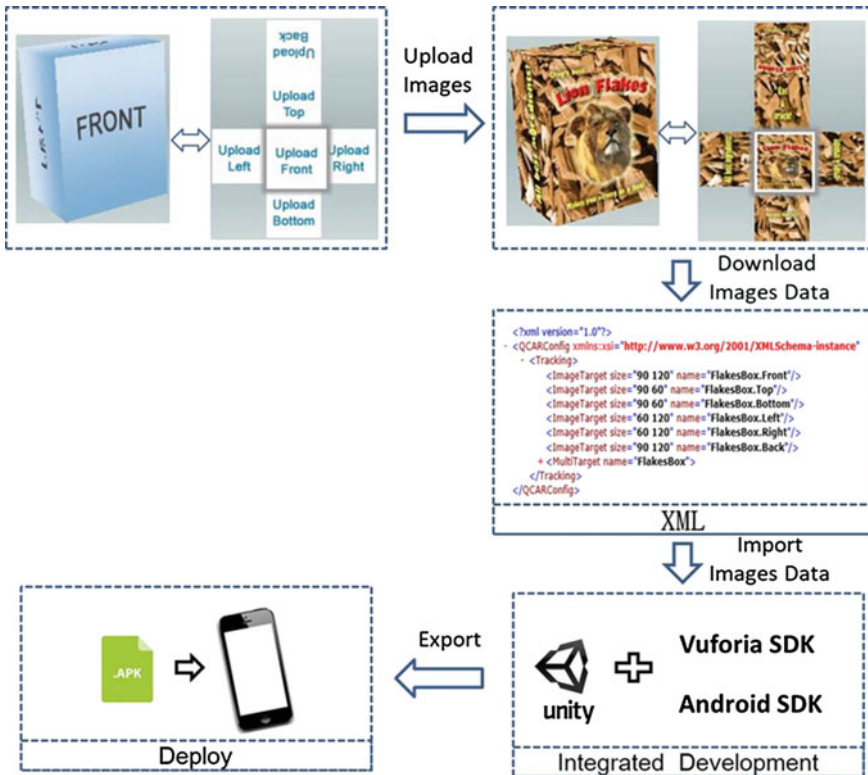


Fig. 3. Implementation process of multi-target tracking technology

relationship among the images. The developer downloads this image data set for the identification and tracking of the three-dimensional box.

4. Integrated development. The developer imports the downloaded image data into the Unity development environment and combines it with the augmented reality development tools provided by the Vuforia SDK and the mobile development tools provided by the Android SDK to complete the development and implementation of the software system. Eventually, the software is exported in .apk format.
5. Install the software to your phone. The software installed in the fourth step is deployed in a mobile phone to realize the identification and tracking of the three-dimensional packaging. However, the six faces of this three-dimensional box must be consistent with the six images uploaded in the second step in terms of image content, positional relationship among images [6].

### 3.2 Development and Operating Environment

In this paper, we verify the feasibility and practicality of multi-target tracking technology applied to three-dimensional box packaging used Vuforia SDK, Android SDK and other development kits. Finally, the developed software is exported and installed in

an Android mobile phone so as to realize the application of the multi-target tracking technology in the box packaging. The environment involved in this experiment mainly includes two parts, one is the hardware environment, and the other is the software environment, as shown in Table 1.

**Table 1.** Development and operating environment

Category	Hardware environment			Software environment	
Development environment	Computer	Processor	i5-4590, 3.30 GHz	System	Windows 10 Professional
		Video card	AMD R5 340X	Development	Unity 2017
		RAM	8 G	Toolkit	Android SDK 6.0 Vuforia 7 SDK
Operating environment	Android phone		HuaweiP10 Plus (128 G)	System version	Android 8.0.0

### 3.3 Realization of Multi-target Tracking Technology in Box Packaging

After the completion of software development, then the software can be exported in the form of .apk and installed on an Android phone. The software developed in this paper can use the camera of Android mobile phone to capture the images on the three-dimensional packaging box in real time, and calculate the coordinate position, orientation angle, and the relationship of the captured images, then superimpose the virtual information on the three-dimensional packaging box. Figure 4 shows the three-dimensional box image captured by the camera and no virtual information is superimposed on it at this time.

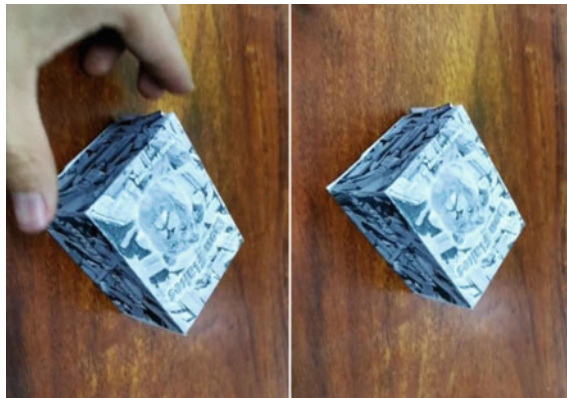


**Fig. 4.** Three-dimensional package captured by the camera

Figure 5 shows the effect of superimposing the virtual information on the interior of the three-dimensional packaging box. It can be seen from the figure that the three-dimensional packaging box becomes a “transparent” state and can display the model of a red car inside the packaging box. In fact, the car is a virtual model and does not really exist, but it can change synchronously with the change of the coordinate position and orientation angle of the box, as if there is a real car inside the box.



Fig. 5. Box for superimposing virtual information

## 4 Conclusions

In 2016, according to the Technical Forecast Report released by the International Institute of Electrical and Electronics Engineers and Gartner Inc., the most authoritative information technology research and consulting company in the United States, augmented reality technology has been ranked as one of the most promising technologies [7]. This paper applies the multi-target tracking technology in augmented reality technology to the three-dimensional packaging box. It has certain significance for



enriching the traditional expression of packaging information and improving the user experience. However, during the process of software running, the virtual information jitter occurs occasionally. This is generally due to the lack of accuracy in the image recognition and tracking algorithm. Therefore, improving the accuracy of the relevant algorithms still need further analysis and research.

## References

1. Lee, T., & Hollerer, T. (2007). Handy AR: Markerless inspection of augmented reality objects using fingertip tracking. In *IEEE International Symposium on Wearable Computers* (pp. 83–90). IEEE.
2. Kasahara, G., Matsuyama, K., Konno, K., et al. (2014). Augmented reality system using package design on mobile devices: Case of Yamada-Chou. *Ite Technical Report*, 38, 179–180.
3. Li, S., & Shi, R. (2016). The comparison of two image matching algorithms based on real-time image acquisition. In *Advanced Graphic Communications, Packaging Technology and Materials* (Vol. 369, pp. 241–248). [https://doi.org/10.1007/978-981-10-0072-0\\_31](https://doi.org/10.1007/978-981-10-0072-0_31).
4. Li, S., Shi, R., & Ye, H. (2016). An efficient approach of color image matching by combining color invariant and ORB feature. In *China Academic Conference on Printing & Packaging and Media Technology* (pp. 195–203). Springer, Singapore.
5. Santos, A. B. D., Dourado, J. B., & Bezerra, A. (2016). ARToolkit and Qualcomm Vuforia: An analytical collation. In *Virtual & Augmented Reality* (pp. 229–233). IEEE Computer Society.
6. Gelšvartas, J., Simutis, R., & Maskeliūnas, R. (2018). Augmented reality object selection user interface for people with severe disabilities. In *International Conference on Information and Communication Technologies for Ageing Well and E-Health* (pp. 156–160).
7. Li, S., Shi, R., & Ye, H. (2018). The applied research of mobile augmented reality in prints. In *Advanced Graphic Communications, Packaging Technology and Materials* (Vol. 477, pp. 309–316).



# Research on Mobile Terminal Augmented Reality Application for Cultural Heritage

Lichan Zhang, Qiang Wang, Jing Cao, and Yan Shi<sup>(✉)</sup>

College of Media and Design, Hangzhou Dianzi University, Hangzhou, China  
hzshiyang@gmail.com

**Abstract.** The development of intelligent technology continuously promotes the application of augmented reality (AR) technology in the field of mobile Interconnection. This article uses the Unity3D engine and Vuforia SDK as development tools, and takes the world cultural heritage West Lake as the research sample, through researching the development model of the mobile AR cultural experience platform, this paper constructs an innovative App model for multivariate display of West Lake attractions. The app is designed to apply AR technology features to enhance the user's audio-visual experience, as well as the protection, display and interaction of the cultural heritage through the combination of virtual reality and reality. In this paper, a new technical means for the multi-dimensional display, multi-modal interaction and multi-scene applications of cultural heritage information is provided.

**Keywords:** Augmented reality · Mobile terminal · Cultural heritage

## 1 Introduction

Augmented Reality is a technology that combines real-world with virtual information such as images, videos, and 3D models which can be perceived by human to generate real-time interactions, thereby enhancing a person's realistic sensory experience [1]. In recent years, AR technology has begun to be used in the digitalization of cultural heritage.

This article uses the Unity3D engine and the Vuforia AR development kit, takes the world cultural heritage West Lake as the sample, constructs a multivariate display model of West Lake attractions based on the characteristics of cultural exchange and communication, develops a mobile terminal augmented reality application to increase the interest and interactivity of West Lake attractions, and to meet the new needs of cultural heritage protection and sharing.

## 2 Related Technologies and Principles

A complete mobile AR system can be divided into three parts: video input, tracker registration, and rendering output, the most critical of which is tracker registration part.

## 2.1 Key Technologies

Augmented reality tracker registration technology is one of the most important research direction in AR field, it refers to capturing the position and posture of a camera in real time, calculating the spatial projection relationship between the virtual object and the real environment, superimposing the computer-generated digital content into the real scene, and achieving dynamic and accurate integration.

In the whole process, image matching is the key point [2], that is, after the system detects the outline of the recognition object, the correlation coefficient matching algorithm is used to match the template. When the correlation coefficient of the image and the template corresponding position reaches the maximum, the template matching is realized. The correlation coefficient matching algorithm flow is as follows:

1. Selecting the image contours in the identified image, normalizing the image to obtain an image  $S(x, y)$  of the same size as the template image  $T(x, y)$ .
2. Calculating the correlation coefficient between the template image  $T(x, y)$  and the image  $S(x, y)$ . Assuming that after the specification, the size of the template  $T$  and  $S$  is  $M \times N$ , the correlation coefficient is used to solve the problem. The solution formula is expressed as:

$$\rho(x, y) = \frac{\sum_N^M \sum_N^M [S(x, y) - \bar{S}] [T(x, y) - \bar{T}]}{\left\{ \sum_N^M \sum_N^M [S(x, y) - \bar{S}]^2 \sum_N^M \sum_N^M [T(x, y) - \bar{T}]^2 \right\}^{\frac{1}{2}}} \quad (1)$$

where  $x = 0, 1, 2, \dots, M$ ,  $\bar{T}$  is the average value of pixels in  $T$ ,  $\bar{S}$  is the average value of pixels in  $S$ , and  $\rho(x, y)$  is the correlation coefficient between image  $S$  and template  $T$ ,  $0 < \rho(x, y) < 1$ ,  $\rho(x, y)$  takes the maximum value of 1 when  $S(x, y)/T(x, y)$  is constant. After calculating the correlation coefficient value, rotate the image  $S$  by  $90^\circ$  and repeat steps 2 to 3 for a total of four iterations.

3. After calculating the correlation coefficient value, rotate the image  $S$  by  $90^\circ$  and repeat steps 2 to 3 for a total of four iterations.
4. Comparing the four correlation coefficient values and take the maximum value. When the correlation coefficient is close to 1, the image is the detected mark image, and the mark matches the template.

## 2.2 Software Development Kit

Based on a systematic comparison of ARToolKit at Washington University, ARKit and ARCore at Apple and Google, this experiment uses the Qualcomm Vuforia AR Development Kit. It uses computer vision technology to identify and capture planar images or simple 3D objects in real time, supports multi-platform augmented reality application development such as Android, iOS and PC, and provides C#, Java, Object-C and .NET languages through Unity game engine extensions. The application editing interface can simultaneously support the native development of iOS and Android, and facilitates the porting of augmented reality applications developed in the Unity game engine to the iOS and Android platforms.

### 3 System Design and Implementation

#### 3.1 System Design

In this paper, aiming at the application of mobile augmented reality, an AR system based on image feature recognition is designed and developed on iOS mobile devices using Unity3D engine, Vuforia SDK and Xcode platform development tools. The system mainly includes five modules: video acquisition module, tracker registration module, virtual integration module, rendering display module and real-time interaction module. The system workflow is shown in Fig. 1:

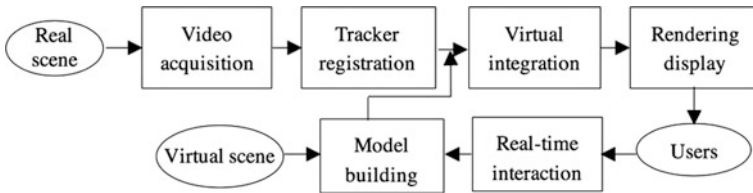


Fig. 1. Mobile terminal AR system workflow diagram

1. Video acquisition module: It is mainly responsible for initializing video capture of cameras and real scenes;
2. Tracker registration module: It is used to track the position and posture of the camera and calculate the transformation matrix between the target and the camera;
3. Virtual Integration Module: It is responsible for registering virtual information with real-world information to achieve virtual integration;
4. Rendering display module: It is responsible for the display after the virtual integration;
5. Real-time interaction module: It is mainly responsible for the interaction between the user and the system, including gesture interaction, virtual menus, and so on.

According to the different characteristics of the West Lake attractions, this article uses multimedia software such as PS, 3ds Max, and Final Cut Pro X to construct a multi-dimensional display model from 2D to 3D. For example, in the effect display of “Winery Yard and Lotus Pond”, a 3D animated media format was adopted. When the camera captures the target image, a lotus pond model will be displayed, the opening lotus in the model will fluctuate slowly with the breeze, giving people stunning visual effects. In addition, there are 15 interactive three-dimensional models, animated short films, hand-drawn maps, text pictures, special effects videos, etc., additional text videos introducing the West Lake attractions, showing the depth of history and culture.

#### 3.2 Feature Matching

According to Vuforia’s recognition principle, this paper completes feature matching by detecting natural feature points of planar images. That is, in the database, the image detection feature points detected in the defined target set are stored first, and then the

feature points in the real image are detected in real time, so that they match the feature point data of the template image in the database.

In order to improve the recognizability of the target image and prevent the superimposed virtual information from being dithered or difficult to be identified, this paper enhances the image contrast, reduces the repetition features, enriches the image information to increase the number of feature points of the identified image, improves the recognition stability, and optimizes the recognition. The feature matching of the image is shown in Fig. 2.

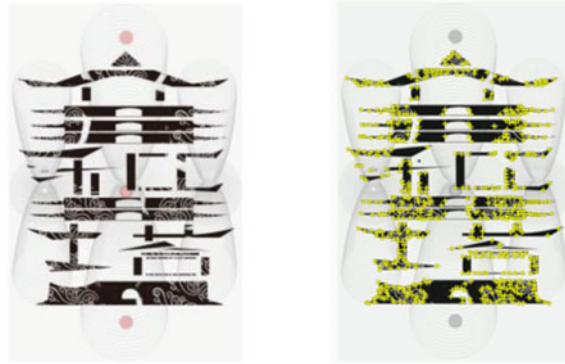


**Fig. 2.** Target image's feature point extraction

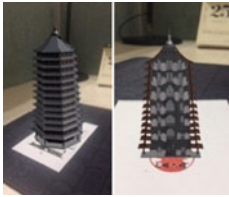




### 3.3 Effect Display

This article uses a variety of effects and methods for the AR display of the West Lake attractions, as shown in Table 1.

### 3.4 Result Analysis

By testing the availability of experimental samples, this paper verifies that the mobile AR app satisfies the need of users to obtain information in the experimental environment, and investigates 5 aspects, such as the experience novelty, the content interest, the recognition stability, the function integrity and the overall satisfaction of the application, the results are shown in Table 2. Among them, the user scored higher on experience novelty and content interest, obtained the second in recognition stability, scored slightly lower on the function integrity, and the user's overall satisfaction with the app was good. From the data analysis, we can see that the mobile AR technology of this paper has better interaction novelty and can meet people's demand for digital experience of cultural information, but it still needs to be improved in terms of functional integrity.

**Table 1.** West Lake attractions AR effect display

No.	Attraction name	Display content	Presentation form	Final effect
1	Six harmony pagoda	The Origin of “Seven Bright and Six Dark”	Interactive 3D model	
2	Nanping Evening Bell	The meaning of the southern screen bell	Interactive video introduction	
3	Two Peaks Piercing the Clouds	Mountain map	Interactive hand-drawn map	
4	Winery Yard and Lotus Pond	Ancient rhyme	3D model animation	
5	Lingyin Temple	Why Lingyin’s door does not open	Hand-painted commentary animation	

**Table 2.** Comparison of mobile AR application scores

Title/value	1	2	3	4	5	Average
Experience novelty	0	0(0%)	0(0%)	5(38.46%)	8(61.54%)	4.62
Recognition stability	0	0(0%)	4(30.77%)	6(46.15%)	3(23.08%)	3.92
Content interest	0	0(0%)	2(15.38%)	5(38.46%)	6(46.15%)	4.31
Functional integrity	0	2(15.38%)	7(53.85%)	4(30.77%)	0(0%)	3.15
Overall satisfaction	0	0(0%)	2(15.38%)	8(61.54%)	3(23.08%)	4.08

## 4 Conclusions

In this paper, according to the needs of the mobile AR cultural platform, a multivariate display of West Lake attractions based on image recognition is designed and implemented. The digital cultural content of different attractions in the West Lake is realized on the material media carrier. The digital experience of the culture can provide users with the display and interactive experience of the digital content of the West Lake attractions in the real environment, and at the same time provide referenceable technical solutions for diversified cultural heritage display models.

**Acknowledgements.** The authors acknowledge the design work from students of Teacher Shi. This work is funded by National Key Technology Research and Development Program of the Ministry of Science and Technology of China (2012BAH91F03) and Digital Imaging Theory (GK188800299016-054), and the Social Science and Humanity on Young Fund of the Ministry of Education (Grant No. 16YJC760047).

## References

1. Van Krevelen, D. W. F., & Poelman, R. (2010). A survey of augmented reality technologies. *International Journal of Virtual Reality*, 9(2), 1.
2. Azuma, R. T. (1997). A survey of augmented reality. *Presence: Teleoperators & Virtual Environments*, 6(4), 355–385.
3. Dos Santos, A. B., Dourado, J. B., & Bezerra, A. (2016, June). ARToolkit and Qualcomm Vuforia: An analytical collation. In *2016 XVIII Symposium on Virtual and Augmented Reality (SVR)* (pp. 229–233). IEEE.
4. Peng, F., & Zhai, J. (2017, June). A mobile augmented reality system for exhibition hall based on Vuforia. In *2017 2nd International Conference on Image, Vision and Computing (ICIVC)*, (pp. 1049–1052). IEEE.



# Research on Addressing Method in XML File Based on XPointer

Chanyuan Fan<sup>1,2</sup> and Zhijiang Li<sup>1</sup>✉

<sup>1</sup> School of Printing and Packaging, Wuhan University, Wuhan, China  
lizhijiang@whu.edu.cn

<sup>2</sup> School of Electrical, Information and Media Engineering, University of Wuppertal, Wuhan, China

**Abstract.** XML is a markup language that describes data and is widely used to exchange data across platforms. Currently, there are three main tools for addressing XML document: XLink, XPath, and XPointer. Among them, XPointer is an advanced addressing tool, which can not only address elements, but also can address specific data such as strings, points and ranges in XML documents. However, for the positioning based on XPointer, how to extract the non-well-formed data content in XML document is still a problem. This paper focuses on the extraction of non-well-formed data content in XML documents. Based on XPath 3.0, extracting and filtering nodes was analyzed. Based on XSLT template, the content of XML documents was selectively output. Finally, a location system based on XPointer was derived, and ultimately achieved advanced addressing for XML documents. 20 XML files were selected as experiment samples to verify the model proposed in the paper. The experimental results demonstrate that the proposed method can locate and represent non-well-formed as well as well-formed data content in XML documents.

**Keywords:** XML addressing · XPointer · XPath 3.0 · Non-well-formed data

## 1 Introduction

With the continuous development of network technology, database technology and informationization, how to store, transfer and display data has become an issue. XML (eXtensible Markup Language) is a user-definable semi-structured data standard, with tremendous scalability and flexibility. XML has become the current trend to describe and record data and played an important role in many areas of information exchange, such as e-commerce, web services, and digital libraries. In the era of Industry 4.0, for example, printing industry is highly mechanized and XML-based format JDF files are used to record and transfer data [1].

Therefore, how to address data in XML document is an essential issue. XML uses the following three main tools for linking, accessing, and addressing data [2]: XLink (XML Linking Language), XPath (XML Path Language), and XPointer (XML Point Language). XLink is intended to link two or more resources [3]. XPath is a query



language providing for XSLT and XPointer to access node-sets from XML document. XPointer is an advanced address language which can address a specific data fragment in XML documents.

Existing methods such as XPath 2.0 can only extract complete node-set information, which must be well-formed [4]. Using XPointer, the range between any two position can be represented, whether the range is well-formed or non-well-formed. However, how to extract such non-well-formed range is still a problem.

XPath version 3.0 was published by W3C working group in April 2014 [5], which provides a new expression “let” to define inline function and create higher-order function in XPath expression. Therefore, this paper attempted to select necessary nodes of the non-well-formed data content by using expression “let”. In addition, XSLT (Extensible Stylesheet Language Transformations) [6] was used to construct the location system by converting XML source tree to an HTML result tree for selectively outputting non-well-formed data information.

## 2 XPointer

XML Pointer Language is used with XLink to identify specific data fragment in XML document in the URI of the XLink [7].

XPointer includes an xpointer() scheme, which is able to make examination of a document’s hierarchical structure and can address the internal structure of an XML document [8]. Xpointer() scheme provides two new locations types: point and range, and 8 functions: “start-point”, “end-point”, “range-to”, “range-inside”, “covering-range”, “string-range”, “here”, “origin”. It has the ability to address almost any information in XML document, such as attribute, comment, processing-instruction, the specific characters in these nodes and non-well-formed data content.

### 2.1 Point and Range

Point is a location in an XML information set with no content or children. It is dimensionless and represents the position between two adjacent nodes or characters. A range represents all the XML structure and content between two points: start point and end point. It means that range contains the start/end-tag, attribute and other XML information. A range can be well-formed as well as non-well-formed XML data content, for example, it can contain only end-tag of a node but no start-tag and vice versa.

In general, a non-well-formed range is produced by function “range-to” in xpointer() scheme. As mentioned before, there is no way to get a range directly from the XPath expression so far, so how to realize function “range-to” is the core issues of extraction non-well-formed data.

### 2.2 Function “range-to”

Function “range-to” is intended to get all the XML content information between start point and end point acquired by two arguments. Its syntax is:

```

<?xml version="1.0" encoding="utf-8"?>
  <persons>
    <person xml:id="person1">
      <firstname>Joy</firstname>
      <lastname>Smith</lastname>
    </person>
  </persons>

```

**Fig. 1.** XML document example

location-set range-to(location-set)

Take an XML document as an example (Fig. 1), if the XPath expression is: `xpointer(//firstname/range-to(//lastname))`

It means to address a range from the start point of element “firstname” to the end point of element “lastname”. The start point of element “firstname” is the position before character “J”, the end point of “lastname” is the position after “h”. So the result range is:

```

  Joy</firstname>
<lastname>Smith

```

The following sections mainly explained the method proposed in this paper to implement function “range-to” to get a range of non-well-formed data information. Firstly, a well-formed node-set which exactly cover the target range was obtained. XPath 3.0 was used to get this node-set by selecting and deleting nodes from target XML file. And then XSLT 3.0 was used to selectively and explicitly output the node-set to get non-well-formed data content.

### 3 Node-Set Extraction Based on XPath 3.0

Expression “let” in XPath 3.0 was used in this paper to extract node-sets from target XML file. A series variables were defined by expression “let”, which represented related node-sets. After deleting nodes by operating such related node-sets, all the necessary nodes between start and end point was obtained, which can just cover the target range.

Firstly, all the nodes between start and end node in document order were sequentially set to \$all. Node comparison expressions “<<”, “>>” and “is” were used here to determine the position of each node.

```

let $all := for $s in document($doc)//*
  return if ($s >>> $start and $s <<< $end
    or $s is $start or $s is $end)
  then $s else (),

```

But \$all was composed of a large number of duplicate nodes with redundant child nodes. So the second step was to eliminate duplicate child nodes. Under the same expression “let”, “intersect” was used to compare two sets of sequences. Combined with expression “if”, a sequence of unique nodes was obtained eventually. The

principle of the entire statement was, for each node in \$all, if its ancestor node is also in \$all sequence, then the node is not output, otherwise the node is output to the sequence \$every.

```
$every := for $node in $all
  return if ($node/ancestor::node() intersect $all)
    then () else $node,
```

Compared with the target range, node-set \$every still missed data content of previous nodes. Therefore, \$startnode was defined to get necessary ancestor node of the start node. The principle was to find all the ancestor of the first node of sequence \$every, and then determine these nodes as following respectively: if the node is previous sibling of the nodes in \$every, then the node is set to sequence \$startnode.

```
$startnode := for $a in $every[1]/ancestor-or-self::node()
  return
  if ($a intersect $every/preceding-sibling::element()[1])
  then $a else (),
```

At last, \$startnode and \$every sequences were took as a union and the redundant nodes were removed again. In this way, all the necessary nodes from target XML file can be obtained.

## 4 Address System Construction Based on XSLT 3.0

In this paper XSLT 3.0 was used to construct the experimental system. Three steps were required. Firstly, extract the necessary two XPath expressions from function “range-to” inside the XPointer expression. After evaluate the XPath expressions, start node, start character, end node and end character of result range were obtained. Then expression “let”, as explained before, was used to get a well-formed node-set, which can just cover the target range. Secondly, all the XML information of the node-set was copied in order to display. At last, regular expression was used to match the characters between the start character and end character combined with XSLT template to output a non-well-formed data content in HTML.

### 4.1 Extract XPath Expressions

The two strings before and after “range-to” in the function expression can be just an XPath expression or a nesting function. Therefore the regular expression “\([^\)]+\)” was used to get the characters in the innermost parentheses of these two strings and set the result in different cases. For each case, XPath expression was evaluated by using XSLT 3.0 function “xsl:evaluate” setting different parameters. In this way, the corresponding start and end node as well as start and end character from target document were obtained.

### 4.2 Copy Node Information

For all the XML data information of all the node types, start-tag, end-tag, text content as well as attribute information should be contained. In order to explicitly output XML

data information in HTML, “<”, “/”, “>” and other necessary characters were added to the output sequence.

Expression “instance of” was used to determine the node type. For different node types different character should be copied. Here, the new operator “[|]” in XPath 3.0 was used to connect all characters and strings. When the node-set is composed of multiple nodes, expression “for” was used to perform self recursion on each node.

### 4.3 Output Non-well-Formed Data

Regular expression was used here to match the string obtained from last step into the string of result range. The result string is the characters between the start character of start node and the end character of end node. It is worth to notice that because the string extracted by regular expression is greedy by default, the node-set obtained in Sect. 3 must be the smallest range that can just cover the target range to avoid matching needless characters.

Combining with XSLT template, the required data information was selectively output on HTML.

### 4.4 System Verification

20 XML files were selected as experiment samples to verify the model proposed in the paper.

In this system, different XPointer expressions were designed to test function “range-to”, all of them got the correct results, regardless of whether the result range is well-formed or non-well-formed. But functions with parentheses can not appear inside the XPointer expression, such as “text()” or “last()”. In addition, if there are a large number of similar nodes in the XML file, more nodes need to be further removed depending on the particular situation.

## 5 Conclusions

With the development of XML technology, query and extraction of data from XML documents should be more refined, and the function of XPointer is likely to be greatly utilized. XPointer provides advanced positioning query function for XML documents especially location type “range”, which can represent non-well-formed data content. XPath 3.0 and XSLT 3.0 was used in this paper to implement an xpointer-based query system, which makes it possible to extract and output non-well-formed as well as well-formed data content. Although there are lacks in the experiment of this paper, it makes some helpful attempts to extract non-well-formed XML data and provides ideas for follow-up researchers.

## References

1. Kühn, W., Grell, M., & Robinson, D. (2005). *Jdf: Process integration, technology, product description* (p. 46) (x.media.publishing).
2. Liu, Q., & Zhang, Y. (2005). Analysis and research of XPath, XLink and XPointer. In *Microcomputer Development, 2000* (Vol. 15, no. 10, pp. 19–22).
3. DeRose, S., & Maler, E. (2010, May 6). *XML Linking Language (XLink) Version 1.1—W3C recommendation*. [EB/OL]. <https://www.w3.org/TR/xlink/>. Accessed May 10, 2018.
4. Jia, M. (2008). Application of XPath in XML query. *Journal of Chongqing Three Gorges University, 24*(3), 51–53.
5. Robie, J., & Chamberlin, D. (2004, April 8). *XML Path Language (XPath) 3.0—W3C recommendation*. [EB/OL]. <https://www.w3.org/TR/xpath-30/>. Accessed May 10, 2018.
6. Kay, M. (2017, June 8). *XSL Transformations (XSLT) Version 3.0—W3C recommendation*. [EB/OL]. <https://www.w3.org/TR/xslt-30/>. Accessed May 10, 2018.
7. Derose, S. (2002, August 16). *XML XPointer Language (XPointer) [EB/OL]*. <http://www.w3.org/TR/xptr/>. Accessed May 10, 2018.
8. DeRose, S., & Maler, E. (2002 December, 19). *XPointer xpointer() Scheme—W3C working draft*. [EB/OL]. <https://www.w3.org/TR/xptr-xpointer/>. Accessed May 10, 2018.



# Design and Development of Network Printing Exhibition

Yanxing Liu, Yusheng Lian<sup>(✉)</sup>, Yang Jin, Xiaojie Hu,  
and Zhuangzhuang Xiong

School of Printing & Packaging Engineering, Beijing Institute of Graphic  
Communication, Beijing, China  
lianyusheng@126.com

**Abstract.** Based on the analyzing of the requirement of exhibition industry for printing field, a system framework of network printing exhibition is proposed. By using the new coding technology, webpage design and background programs for network printing exhibition are developed and achieved. The new coding technology HTML5, CSS3, and JS are used for the development of network program and the design of the interaction functions. By making use of ASP development language, webpage and ACCESS databases are connected and bound, which realize interactivity of the website data. Users can enjoy better interactive experience. Ultimately, test and optimization are carried out to the website.

**Keywords:** Network printing exhibition · Interactivity · HTML5

## 1 Introduction

As the quick development of computer network technology, network exhibition becomes an efficient and low-cost alternative approach for commodities fair; It has also become a concentrated research area [1]. At present, most of the network exhibition-websites are mainly based on exhibition information platform, but their functions are still incomplete. Especially, web-exhibitions for printing are very few. The design of the website for printing exhibition is outmoded, the interactivity is also low.

Some international printing exhibitions have begun to adopt network form, the interactive technology of their network exhibitions are outstanding [2]. Therefore, it is feasible to design and implement a network exhibition for printing field.

## 2 Demand Analysis

### 2.1 User's Requirements

The users of the network printing exhibition are enterprise and participants. For enterprise, website should strengthen the corporate brands and promote the corporate culture. For participants, website should use a variety of interactive technologies to

make the tedious information of resources into interactive exchanges of information to meet the browsing requirements of the participants.

## 2.2 Interactivity Analysis

By increasing the webpage's interactivity, the resource information could be displayed in an ordinal and interesting way, the difficulty in obtaining information for the user is reduced.

By the analysis of information demand from the user's point of view, the interactive element is not the more the better, but has a limitation. Therefore, the basic design of interactivity for the network printing exhibition website is very important.

## 2.3 Function Analysis

The demand of network printing exhibition website and the influencing factors of the web access are analyzed, in order to meet the user's requirements. A modularization framework and application of the technical platform for network printing exhibition was recommended. It contains four functional modules: Exhibits Display, Enterprise Information, Exhibition News, and Offline Exhibition information.

- (1) Exhibits Display: the exhibits are classified by type, process technology, latest products and interaction design, and it could be commented by users on the webpage.
- (2) Enterprise Information: this webpage displays publicity pages, products and the latest techniques of the enterprises.
- (3) Exhibition News: this webpage releases the latest news of printing exhibition and information of development in print industry.
- (4) Offline Exhibition Information: module of offline exhibition publishes the latest information of offline printing exhibition, and collects information of on-line registration for offline exhibition.

## 3 System Architectures

As shown in Fig. 1, the working principle of the website system is as follows: when a user requests ASP webpage by browser, the web server responds the requisition, executes ASP file by calling ASP jet and interprets its script languages [3]. By connecting database with ODBC (Open Database Connectivity), ADO (ActiveX Data Objects), the system completes the database operation. And then ASP generates the HTML webpage with query result. Finally, the webpage is returned to the user by CSS3 and JS control [4].

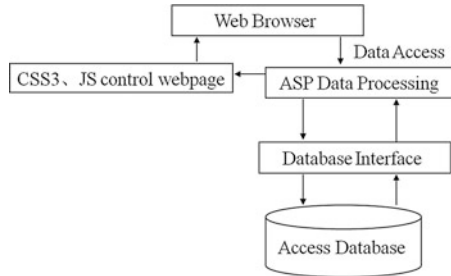


**Fig. 1.** System frame diagram

## 4 Website Building

### 4.1 Webpage-Making

The webpage framework is created by using HTML5 and CSS3 coding technology. The website uses JavaScript to realize HTML document manipulation, animation and dynamic events. As a fast, small, and feature-rich JavaScript library, JQuery [5] makes these operations much simpler. The database is built by Access and the active website is made by using the ASP coding language.

### 4.2 Interactivity Design

- (1) The banner of the home page is made with CSS3 and JS coding technology. It has a function of time second counter, so that users can refer to the time when the image is switched (the switching time is 2 s). When the mouse is put on the banner, the timer stops. Then, it continues timing when the mouse is removed. It avoids switching images when users read information about banner.
- (2) The enterprise recommendation module uses CSS3 and JS coding technology. Each image is set up with a transparent layer to display the information of the enterprise. And the transparent layer is displayed from bottom to top as the mouse passes through the image.
- (3) The recommendation of offline exhibition is displayed like a folding fan. The information of the exhibition is hidden. The image displays the hidden information when the mouse is putting on the image. The telescopic effect is triggered by the mouse. The CSS3 coding technology is used to realize the effect of scaling by using the CSS3 translation and the unique animation execution time curve “ease”.
- (4) As shown in Fig. 2, the exhibits display module by use of CSS3 and JS for layout and setting. Each product is set up with a transparent layer to display the information about the product. When the mouse is put on the image of the product, the transparent layer is displayed from bottom to top.



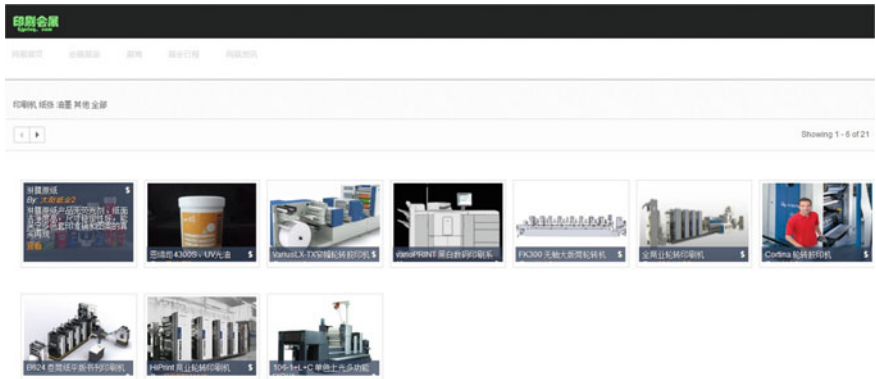


Fig. 2. Exhibits display module

## 5 Running of Website

The running of website is to find various types of errors in the process of system design and programming, and to modify the mistakes. The website passes the functional test and the performance test successfully, and achieves the design requirements. The test results are as follows.

### 5.1 Web Front-End

As shown in Fig. 3, the front-end of the website is divided into five parts: homepage, exhibits display, enterprise information, exhibition news, offline exhibition information.



Fig. 3. Front-end of the website

## 5.2 Web Background

As shown in Fig. 4, it contains homepage, news management, enterprise management, and product management altogether four functional modules.

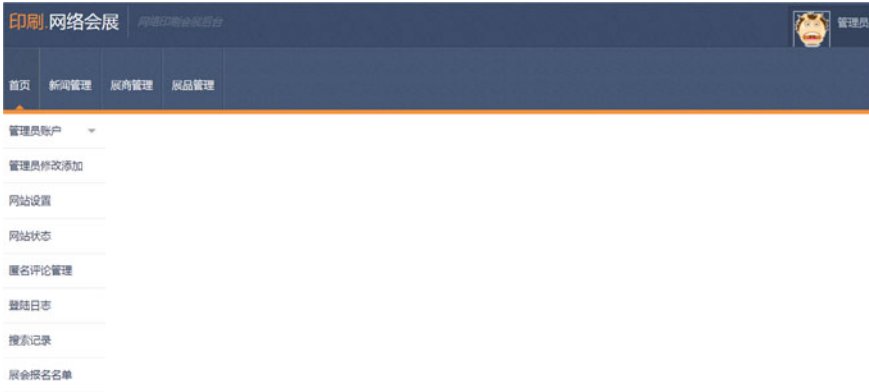


Fig. 4. Background of the website

## 6 Conclusions

The network printing exhibition is designed and developed. The whole frameworks of the website include front-end, background programs, and databases. The new coding technology HTML5, CSS3, and JS are used to build front-end of network printing exhibition and develop interaction design. The ASP and ACCESS databases are used to develop dynamic webpage of the website, whose server is based on windows platform. The running results of the printing exhibition website show that it can realize the functions of network printing exhibition, which include exhibits display, enterprise information recommendation, exhibition information recommendation and exhibition news. Moreover, the interactivity design of the website can make the tedious resources information into interactive exchanges of information to meet the browsing requirements of the users.

**Acknowledgements.** This work was supported by the National Natural Science Foundation of China (Grant No. 61605012), the Project funded by China Postdoctoral Science Foundation (Grant No. 2016M600052), the Science and Technology Project of Beijing Educational Committee of China (Grant No. SQKM201610015005), and the BIGC Project (Grant No. Ea201808, Ec201805).

## References

1. Wang, X. X (2011). The design and implementation of virtual exhibition based on virtual reality technology. In *IEEE 12th International Conference on Computer-Aided Industrial Design & Conceptual Design* (pp. 180–183) [https://doi.org/10.16182/j.cnki.joss.2011.s1.048/\(23\)](https://doi.org/10.16182/j.cnki.joss.2011.s1.048/(23)).

2. Jiang, M. (2011). China exhibition will develop six trends in the future. *Business Times*, (B08), 1–3.
3. Feng, Y. (2006). Website construction of online store. In *Shopping Malls Modernization* (pp. 106–107) [https://doi.org/10.3969/j.issn.1006-3102.2006.19.071\(19\)](https://doi.org/10.3969/j.issn.1006-3102.2006.19.071(19)).
4. Liu, L. (2013). The design and implementation of warehouse MIS based on ASP. *Jilin University*, 9–53.
5. Zheng, J. Research on special effects of web page layout based on Div + CSS + JavaScript. *Computer Knowledge and Technology*, (17), 1556–1558.



# Design and Implementation of Salary Management System for Printing Enterprises

Yuke Huo<sup>1</sup>(✉), Wenjie Yang<sup>1</sup>, Peipei Ran<sup>1</sup>, Chunli Guo<sup>1</sup>,  
Yanxing Liu<sup>1</sup>, Ge Yang<sup>1</sup>, and Shaozhong Cao<sup>2</sup>

<sup>1</sup> School of Printing and Packing Engineering, Beijing Institute of Graphic Communication, Beijing, China

584767862@qq.com

<sup>2</sup> Beijing Key Laboratory of Signal and Information Processing for High-End Printing Equipment, Beijing Institute of Graphic Communication, Beijing, China

**Abstract.** In order to make staff salary management more standardized, this paper designs a salary management platform for employees of printing company, which is based on the Asp.Net framework and uses C# language and SQL Server database to store data, with manage data information and staff attendance, assessment, performance, welfare, rewards and punishments and other functional modules, to achieve full management of the remuneration of printing enterprises employees and promote the fairness of the printing enterprises.

**Keywords:** Employee salary · Printing company · C#

## 1 Introduction

Printing companies are greatly affected by the impact of rising raw materials such as paper prices, environmental pressure and cross-media publishing. There are more than 100 thousand printing companies in China but mostly small and medium-sized enterprises. The fierce market competition has made the profits of printing companies very low. Realizing enterprise information technology is an effective way for companies to improve their competitiveness and reduce their costs. It is of great significance to design a personnel management system suitable for printing companies, because the production and management models of individual orders and complex and trivial processing technologies of printing companies require a high level of assessment for personnel and their capabilities. Salary management, as an important part of personnel management, can assist enterprises to record employees' salaries, evaluate and manage their performance. Based on this, this paper combines the characteristics of the printing company's salary management, designing an employee salary management system based on Web, aiming at the fair and effective management of employees' remuneration and improving the company's Work efficiency and core competitiveness [1, 2].

## 2 System Demand Analysis

### 2.1 Functional Requirement Analysis

The purpose of the printing company’s salary management system is to realize the classification management of the employees’ work situation in each department through the analysis of the content of each employees’ remuneration. Based on this, it should have the functions of inquiring, maintaining and storing information about the basic information of the Department, the basic information of the staff, the staff assessment, attendance, performance and salary.

The use case diagram of the system is shown in Fig. 1. It describes the service provided by the system to the users, and realizes the requirement analysis to the perfection of the system function.

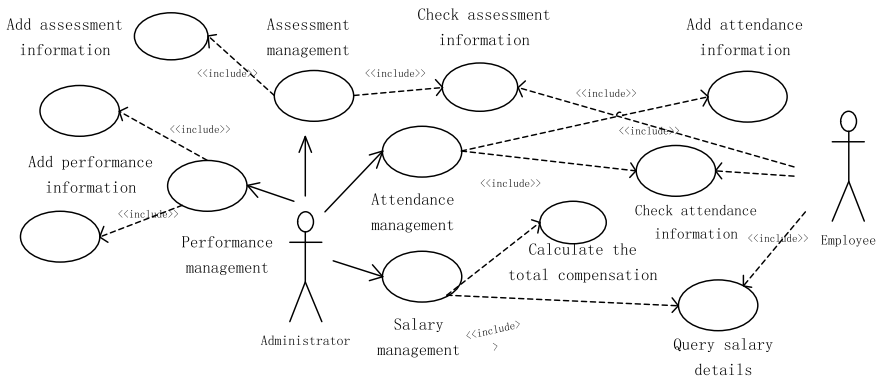


Fig. 1. Use case diagram

### 2.2 User Role Analysis

The printing company’s salary management system requires administrators of information entry and system maintenance, as well as employees to query information.

The business flow chart of user roles is shown in Fig. 2. The administrator performs maintenance of basic information. Through the administrator account into the main page of the system, carry out attendance, assessment, performance, salary input, to realize the maintenance of the basic information of the salary of the entire enterprise staff. Ordinary employees check their own salary information and system can transfer information from the backstage database to the home page according to the account number.

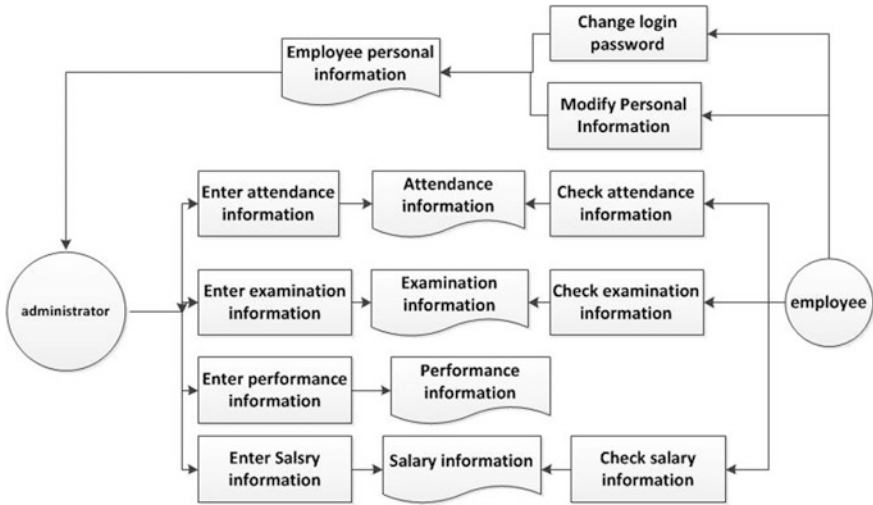


Fig. 2. System business flowchart

### 3 System Design

#### 3.1 Functional Module Design

This article is the management system developed by combining the computer technology with the management of human resources. The purpose is to master the work of each employee and is a comprehensive analysis of employee performance. We should have the following modules:

- (1) Basic data management module: Information management is the basis of enterprise management and mainly includes departmental basic information, such as department name, number, responsibility and contact information. Add administrator account, such as staff number, name, login password and other information.
- (2) Employee information management module: The maintenance of employee's basic information, including account number, photo, name, gender, contact information, department and other detailed information.
- (3) Attendance, assessment, and performance management modules: The contents of these three modules are part of the employees' compensation and are linked directly to the employees' salaries. The realization is based on the personal conditions of the employees for classification management. The attendance module includes the date of the attendance, the type of attendance, and the result. The assessment module includes assessment scores, assessment progress, and assessment content. The performance module includes performance type, amount, month, and content and so on. The common point is that the process of attendance and assessment of employees, the amount and type of performance are recorded through text input, and then updated to the database.

- (4) Compensation Management Module: Realize salary calculations for employees. This module supports the direct reference of attendance, assessment, and performance modules to record the results of staff salaries. In addition to the entry of tax, basic wages, benefits, allowances, awards and penalties paid by employees of enterprises.

This paper designed the user class, login class, attendance class, assessment class, performance class, and compensation class. The login module is used to verify whether the input data matches the corresponding information of the database. The assessment, attendance, performance and compensation modules provide a full selection, modification and deletion methods to achieve system function operation. The class diagram is shown in the Fig. 3.

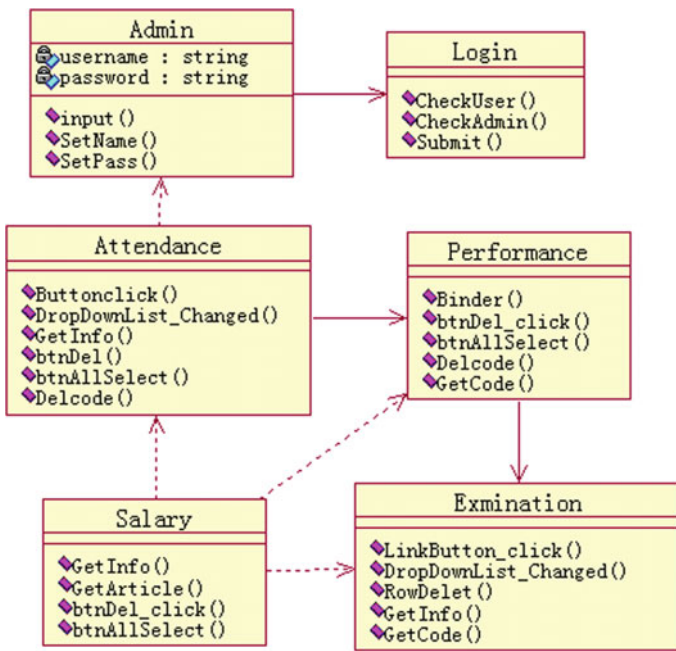


Fig. 3. System class diagram

### 3.2 Database Design

The database uses the SQL Server database as a platform for storing data tables, to increase the relative independence of the data organization as much as possible and to simplify its structure [3]. The database needs the following main table data support:

Department information: department number, department name. Attendance sheet: attendance type, attendance content. Assessment form: examination results, assessment progress. Performance table: performance amount, performance type, month, performance content.

Employee information table: employee number, name, gender, education, e-mail, department number, department name and position.

Employee salary table: number, name, month, basic salary, welfare, allowance, performance, award, penalty and personal tax.

The overall entity contact diagram of each data table is shown in Fig. 4.

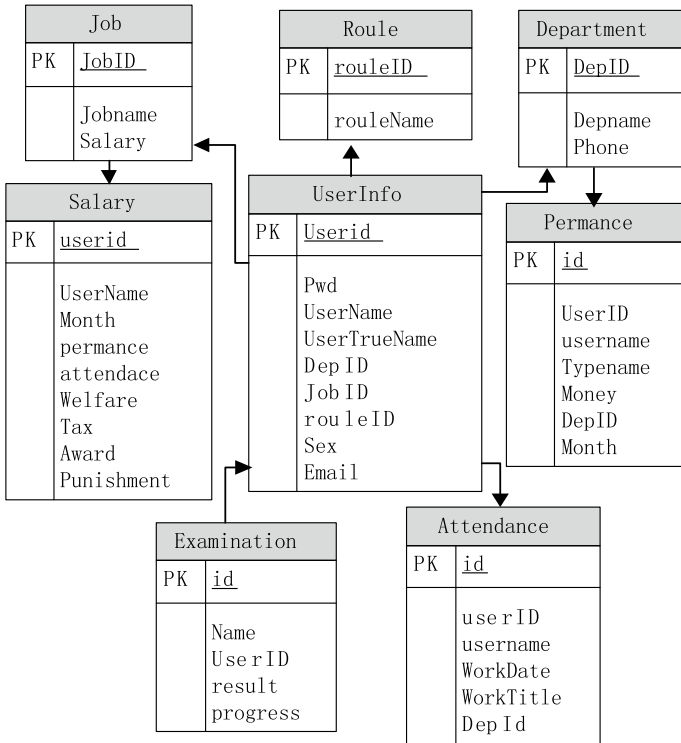


Fig. 4. Overall entity contact diagram of the system

### 3.3 Business Process Design

The salary management system of printing enterprises is suitable for small and medium enterprises. The realization of this system enables enterprises to classify and manage the components of employees’ salaries and the employees can view the detailed information of the remuneration of the employees, which increases the transparency of employees’ salary. The main process is that the administrator first logs into the main page of the system and maintains the information required for the operation. The salary information is calculated through the data information entered in the previous period. Employees can log into the user’s home page to view details of their pay content.

The sequence diagram of the system is shown as shown in the diagram (Fig. 5).



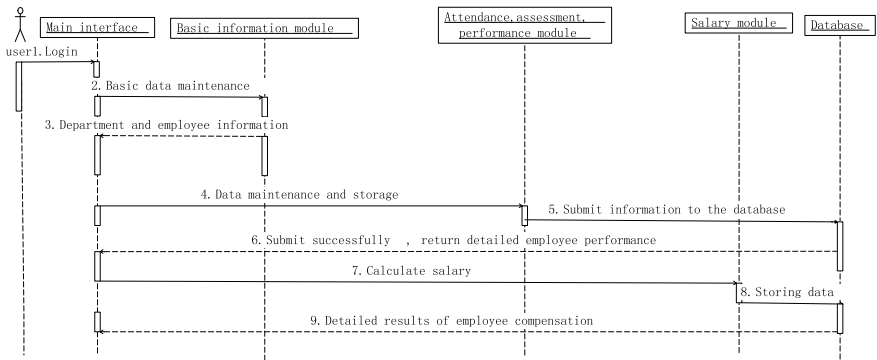


Fig. 5. The sequence diagram of system

## 4 Implementation of the System

### 4.1 Implementation Scheme

Operating system: Windows Server;

Platform and language: Microsoft Visual Studio, Asp.Net, C#;

Database: SQL Server.

The salary management system of the employees of the printing enterprise is an Internet application based on the four layer architecture of the browser/server (B/S) interactive mode. It refers to the information management system using the browser as the client. It is a way of realizing the application structure of the three layers in the C/S layer [4]. The data layer uses SQL Server as a database, and interacts with the Web and server through the database server to complete data requests.

### 4.2 Realization of the Main Interface

The interface of administrator, the basic data management module includes detailed information about the department, salary level information, adding an administrator account and modifying the login password. The assessment information module includes adding examination information and examination management and the examination management is specifically the realization of the functional module design. Attendance information module includes adding employee attendance and attendance management, mainly the type and date of attendance. The performance module includes adding performance and performance management. The compensation module includes the addition of compensation and compensation management. Take the compensation module of the salary module as an example. After entering the employee's name, trigger the function to add the basic salary, performance, benefits, benefits, incentives and fines.

Employees page, to achieve their own basic data management, review the assessment, attendance, performance, remuneration.

The main page of the system is shown in the following diagram (Fig. 6).

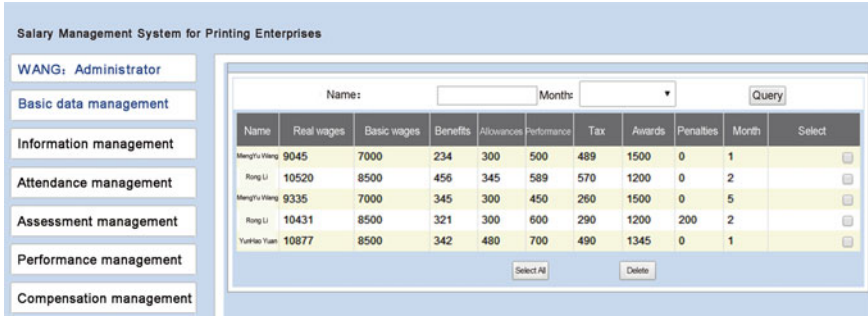


Fig. 6. Administrator main interface

## 5 Conclusions

The salary management of the printing enterprise makes it quick and easy to retrieval staff information. Because the Asp.Net framework is used to design a simple front-end Web interface and C# language is used to implement the functions of each module of the system and SQL Server as the database of data storage, can be maintained and stored at any time. On the basis of the records of the basic information of the Department and staff, the system manages the staff under various departments to increase the transparency of employees' salary and provides a platform for the record, evaluation and management of employees' salary.

**Acknowledgements.** The paper is supported by National Natural Science “Nonlinear Dynamics model and Analysis of Gear Systems for Offset Press” (No. 61472461).

## References

1. Shang, H. (2016). *Design and implement of human resource management system base on B/S*. Tianjin: Tianjin University.
2. Li, A. (2016). .NET binding of human resources information management system design and development. *Electronic Design Engineering*, 24(14), 44–48.
3. Chen, Z. (2016). Design and implementation of enterprise salary management system based on ACCESS. *Enterprise reform and Management*.
4. Guan, C. (2013). *Analysis and design of human resource management system for small and medium sized enterprises*. Fujian: Xiamen University.



# Design of Instant Messaging Software in Printing Enterprise Based on Web

Peipei Ran<sup>1</sup>(✉), Wenjie Yang<sup>1</sup>, Yuke Huo<sup>1</sup>, Zhongyue Da<sup>1</sup>,  
and Shaozhong Cao<sup>2</sup>

<sup>1</sup> School of Printing and Packing Engineering, Beijing Institute of Graphic Communication, Beijing, China

376007414@qq.com

<sup>2</sup> Beijing Key Laboratory of Signal and Information Processing for High-End Printing Equipment, Beijing Institute of Graphic Communication, Beijing, China

**Abstract.** In order to improve efficiency of employees and ensure information security, the computer within the printing enterprise generally does not allow access to the external network, which greatly hinders the exchange of information and data sharing among the personnel. Therefore in order to solve this problem, the instant messaging software based on the small and medium-sized printing enterprises is designed and implemented, which adopts the Java network communication technology and web interface technology to realize instant chat, user login, password modification and other related functions. It not only facilitates information exchange within enterprises, but also safeguards the information security.

**Keywords:** Internetwork communication · Printing enterprise · Java

## 1 Introduction

The application of Instant messaging technology is usually in the form of instant messaging software in printing enterprise, it is a solution, including server, client and database, which provides instant messaging services within the scope of internal network [1]. With the development of internet era and network communication technology, more services are provided by instant messaging, which has become an integrated network communication software. The chat function in LAN is generally not contained in printing enterprise, and in order to improve efficiency of employees and ensure information security, the computer within enterprise generally does not allow access to the external network, that is to say the chat software QQ is not used, which greatly hinders the exchange of information and data sharing among the personnel, so the instant messaging software based on web in LAN is designed.

## 2 Demand Analysis

The instant messaging software, designed and realized in this paper, is mainly applied in small and medium-sized printing enterprise, so the implementation of instant messaging within enterprise is the main functions. It is necessary to realize the exchange of information in LAN without connecting WAN, which can ensure the security of information. The implementation of functions are as follows.

- (1) User registration. Users fill in personal information and set up login password.
- (2) User login. After filling in the username and password, the user authenticates the identity information and verifies the login successfully.
- (3) Information management. Users can modify their personal data or password, and the information of their friends can be checked.
- (4) Chat communication. The functions of information editing, sending and receiving can be realized in chat interface.

This paper introduces UML use case on the function analysis, shown in Fig. 1.

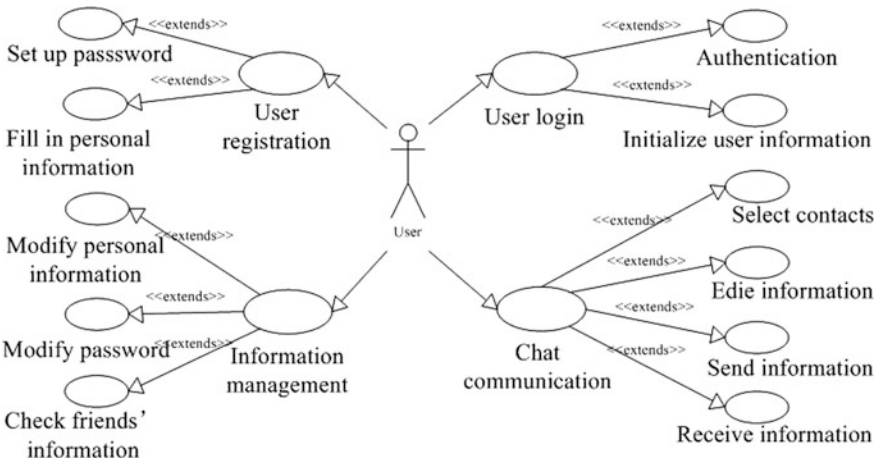


Fig. 1. Use case diagram of instant messaging software

## 3 System Design

### 3.1 Overall Design

The instant messaging software designed in this paper is based on the development of B/S, which adopts Java programming language and MVC design pattern, and data is stored in MySQL database. The user exchange data through the browser and the server, and at the same time the server and the database exchange data. Users can enter the contact interface after the data matching of the login interface, the user can choose the chat object, which can be a certain point to point chat, also can be a group chat. After

the chat, closing the chat interface can exit [2]. The design of overall framework is shown in Fig. 2.

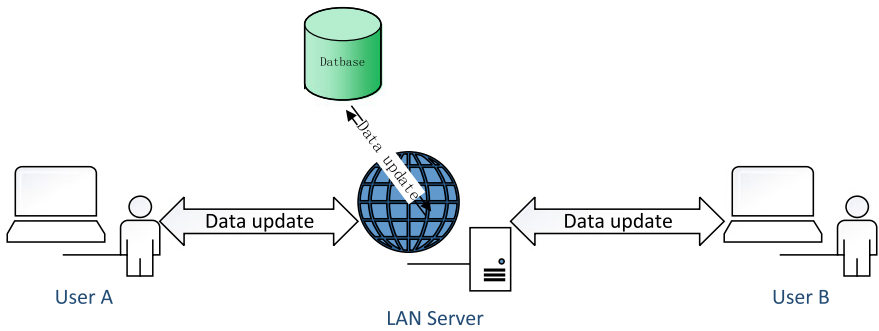


Fig. 2. Overall framework of instant messaging software

## 3.2 Design of Functions

### 3.2.1 Design of Login Function

When the server is started, the connection with database is established at first, then the main thread enters listening state and waiting for the connection of client. After filling in username and password, the connection with server is established, and the personal information is authenticated, login is successful after verification. The friends' information is obtained from database and shown in user interface, and the offline message from other users can be acquired when the user is offline. The design of the user landing activity diagram is shown in Fig. 3.

### 3.2.2 Design of Chat Function

The main function of the instant messaging software is to realize the information exchange between the employees. The interface is divided into columns, and a container is placed on each side. The left side of the column is used to display the list information of the contacts, and the chat window is displayed on the right side. The contact is selected to chat by user, then chat window is popped out on the right, which can instantly send or receive the message that sent by the other user. In order to complete the real-time user message transmitting, the server socket is used to transmit the message packet. The data packet which was sent by the server is composed of data packet types and data content. The sender, receiver and content are contained in data content. The data packet which sent by client is composed of the type and content of the data. The sender, receiver, transmission time and text content are contained in data content. The time of the database record is the time that the server receives the packets [3]. The chat process design is shown in Fig. 4.

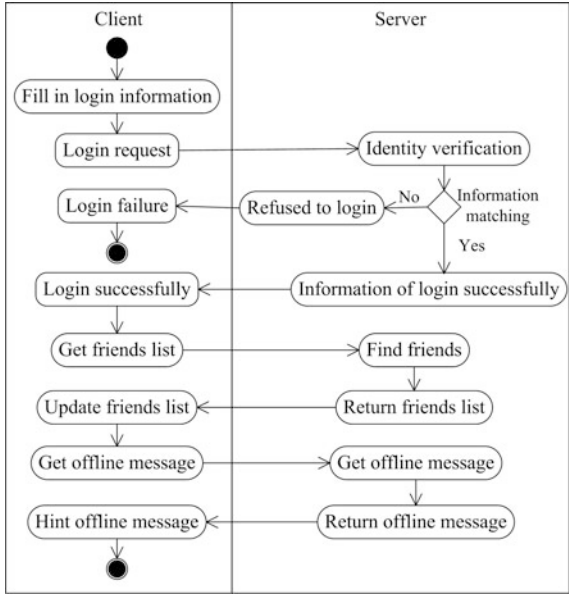


Fig. 3. Design of user landing activity diagram

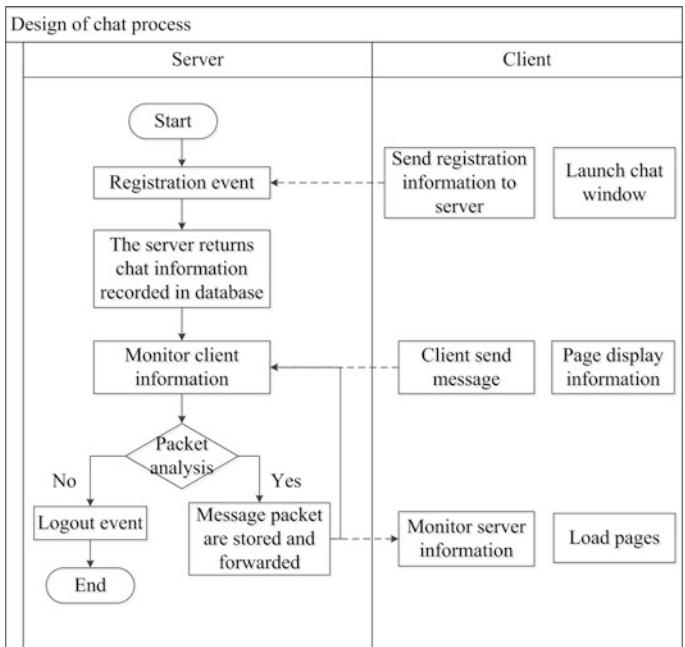


Fig. 4. Design of chat process

### 3.3 Design of Database

The user information and message record are stored in database, so tables with different names and fields are designed according to different requirements. The user information is stored in user table and chat information is stored in message table. The database used in this system is MySQL. We mainly designed the following two data tables. The first table is a table of user information. The second table is the instant messages (Tables 1 and 2).

**Table 1.** User table

User properties	Data type	Meaning	Data source
USER_NAME	VARCHAR(20)	User ID	System or other table
PASSWORD	VARCHAR(45)	Password	System or user
EMPLOYEE_NAME	VARCHAR(16)	Username	System or user

**Table 2.** Message record table

Message properties	Data type	Meaning	Data source
User	VARCHAR(20)	Sender	User
Target user	VARCHAR(20)	Receiver	User
Time	DATETIME	Message time	System
Text	VARCHAR(512)	Message content	User

## 4 System Implementation

### 4.1 System Implementation Environment and Technology

Three-tier structure of browser/server (B/S) is used in system development, including the interface layer, application layer and data layer. During the development process, the financial accounting module is developed on the Eclipse platform using the Java language, and the software can be implemented on different platforms such as Windows, UNIX and Linux. The data information is managed in MySQL, which is a small relational database management system and the data is stored in different tables. SQL language, used to access the database, is the most common table conversion language, which is widely applied in development of the small and medium-sized website due to its small size, fast speed and low cost [4].

### 4.2 Implementation of Chat Function

The interface is divided into columns, and a container is placed on each side. The left side is used to display the contacts information by the way of DataGrid, and the chat window is displayed on the right side, which adopts a HTML Container to show chat information.

The script is written in JavaScript, when the object on the left is clicked, the client sends a chat request to server, then establishes a connection with the server and exchanges data. The server sends messages to the whole online users in the form of a broadcast. After the client received, data packet is parsed and the useless packets will be discarded. If the offline users on line, the server will download the chat log and client information to initialize chat interface. The design of user chat interface is shown in Fig. 5.

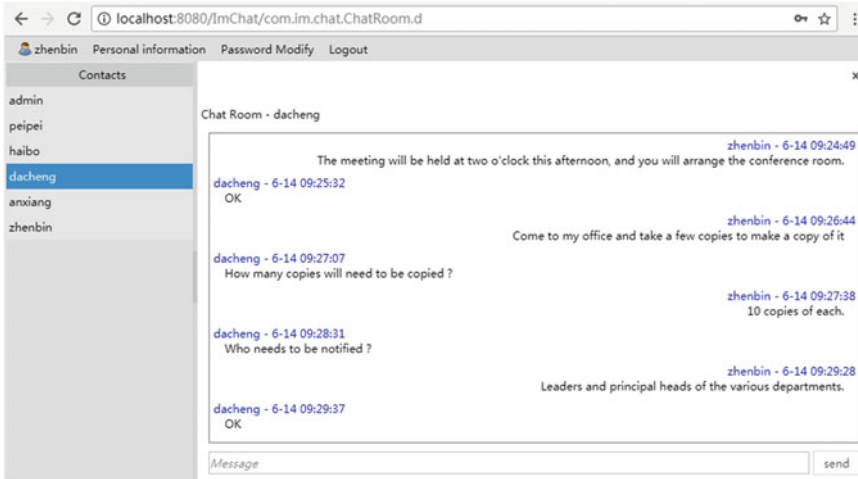


Fig. 5. The design of user chat interface

## 5 Conclusions

The instant messaging software based on web is designed and realized in this paper, which is suitable for the simple local network environment, realizes the functions of user registration, user landing, password modification and instant chat, and it can meet the basic needs of office communication within the enterprise. Because it can run without access to the external network, the low work efficiency as result of the use of personal instant messaging software into non-working chatting or disclosure of enterprise information are effectively avoided, thus the difficulty of information security management is reduced, which not only satisfies the communication needs between employees, but also solves the problem of company system and network security.

**Acknowledgements.** The paper is supported by National Natural Science “Nonlinear Dynamics model and Analysis of Gear Systems for Offset Press” (No. 2018049).



## References

1. Wu, H. (2013). *Design and realization of instant messaging software for enterprise*. University of Electronic Science and Technology.
2. Fei, W. Z. (2016). Design and implementation of network instant messaging software. *Communication Design and Application*, 4(on), 82–84.
3. Yansong, L., & Suihuai, Y., Bo, W., et al. (2010). Engineering Science and Technology. *Design of Socket Security Instant Messaging Software*, 7(12), 2974–2977.
4. Tang, H., Zhai, Z., Guan, B., & Huang, X. (2008). *Easy to understand MySQL*. People's Posts and Telecommunications Press.



# Design and Making of Sudoku Game Based on Unity3D

Xinhui Xie, Zhanjun Si<sup>(✉)</sup>, and Shan Zhang

College of Packaging and Printing Engineering, Tianjin University of Science and Technology, Tianjin, China  
Szj@tust.edu.cn

**Abstract.** Objective Based on the Unity3D game engine development, a 2D casual puzzle Sudoku was designed and production. Methods The game is developed through Unity3D game engine. Material is made and edited in Adobe Photoshop, and Adobe Audition is used to edit and process the audio material. Then set material parameters in Unity3D, and finally use C# script language to write game logic. Results This research made a complete Sudoku game design and completed the test and release of the game. Conclusion Sudoku game is a very popular game developed by Unity3D. It doesn't have a lot of knowledge reserves and the game logic is also very simple, which makes the Sudoku game easily accepted by children and beginners.

**Keywords:** Unity3D · C# · Sudoku game

## 1 Introduction

Unity3D, developed by Unity Technologies, has become a very professional engine for game development in the current market [1]. Before the emergence of Unity3D, the game often encountered in the development process due to different plug-ins, models, programming languages, etc., there will be incompatible situations on different platforms, and even will not open the file [2]. Thanks to Unity's powerful cross-platform features, this is a perfect solution for developers. It evolved from the original development of WEB projects and virtual reality to today's platforms that can span Windows, Mac, Android, etc. From the development of only 3D games to the development of today's 2D and 3D, it can be developed mature step by step. Based on the Android mobile phone operating system, using Unity3D as a game engine to develop games, due to its open source and free features, has rapidly become a popular trend for the development of mobile device games [3]. The Sudoku game is considered by many educational experts to be one of the best games to exercise brainpower. It has always a lot of supporters, and its proportion has been increasing [4]. However, there are few precedents for the development of Sudoku or similar games using Unity3D. Therefore, the design and production of Sudoku based on Unity3D is very meaningful.

## 2 Design of Sudoku Game

### 2.1 Design Ideas

Figure 1 shows the designing framework of this paper. First of all, the picture material and audio material needed for game production were prepared. The picture material is produced in Adobe Photoshop. The audio material is collected and downloaded on the Internet and then imported into Adobe Audition for secondary processing. Then, Unity's plug-in NGUI is used for the game interface. The UI is designed and produced, a C# scripting language is created, and the logic of the game is programmed; finally, the game is run and tested.

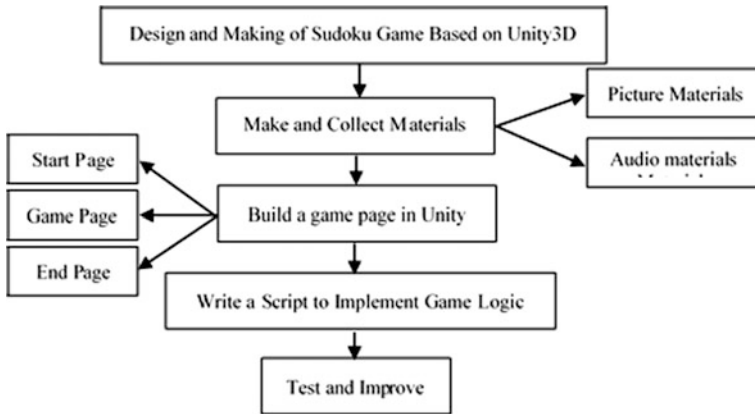


Fig. 1. Flow chart

### 2.2 Production Software and Development Environment

Modeling environment: Windows7, Intel<sup>®</sup> Core<sup>™</sup> i5CPU, 4G memory, 64-bit operating system.

Production software: Unity3D 5.5.1f1, Photoshop CS6, Visual Studio 2010 and Adobe Audition CS6. Use Adobe Audition CS6 to create image material. Then use Adobe Audition CS6 to process the audio material. Next, design the game scene in Unity. Finally, the game logic script is written in Visual Studio.

## 3 Design and Production of Sudoku Game

### 3.1 Preparation and Production of Materials

All image materials required for the game were produced by Adobe Photoshop, including the  $9 \times 9$  grand nine-squared game background board, start the game and exit the game button, three difficulty level buttons, nine numbers of 1–9 Button, blank button, clear button, close game interface button. Figure 2 shows the final effect of the game background. The required audio material was downloaded online and the audio

material was clipped and processed using audio processing software Adobe Audition. After considering a unified compatibility issue, it was eventually exported to the .MP3 format.

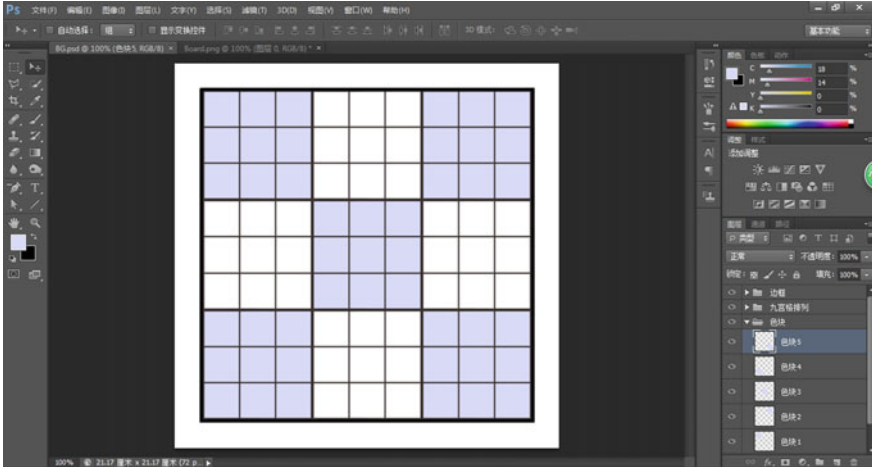


Fig. 2. Final effect of the game background

### 3.2 Construction of Game UI Interface

#### 3.2.1 Construction of the Game Start Interface

First NGUI plug-in is imported into Unity to implement the design of the game interface. Game background image was dragged into the scene panel, and the start game button and exit game button are added to the scene. The effect of starting the interface is shown in Fig. 3. After the button layout of the start interface was designed,

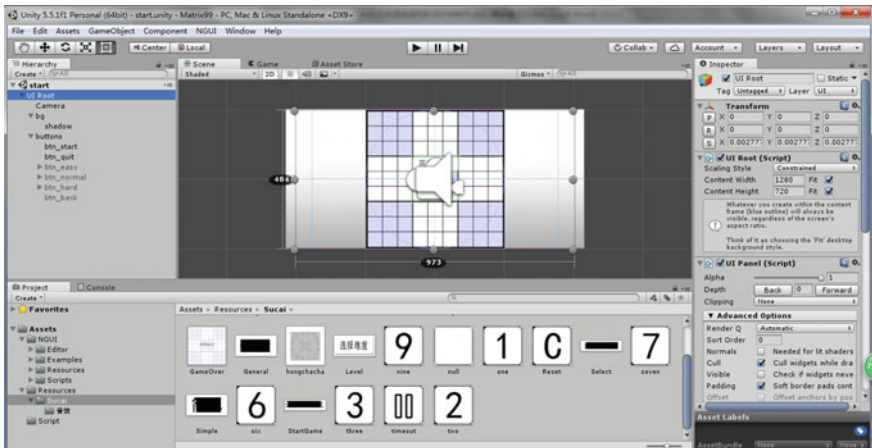


Fig. 3. Start interface creation

we need to add a small animation of the Sudoku game to the start interface, which is to add animation to the Label. Then Tween Rotation and Tween Scale effects are added to Label by clicking Add Component in the Inspector panel.

### 3.2.2 Construction of Game Scene Interface

When the player enters the game menu, there will be three difficulty options: “simple”, “general” and “difficult”. The difference is that the numbers appear on the game interface are different. The more difficult the game is, the less the number appears when the game starts. Players can choose levels of different difficulty according to their own preferences [5]. As shown in Fig. 4, the difficulty selection interface in the operation mode is shown. Then when designing the game scene interface, the most important thing is to write a script to fill in the numbers in the blank squares and determine if the filled numbers are correct. If the number is correct, it will be filled in a blank square, and if the number does not match, an error is displayed and the wrong sound is triggered. The simple level game scene and the keypad effect interface after the number is filled in are shown in Fig. 5.



Fig. 4. Select difficulty level interface



Fig. 5. Keypad effect after filling in the numbers

### 3.2.3 Construction of Game End Interface

When all the blank grids are filled, the game end interface will pop up and the words “You have cleared!” will be displayed, as shown in Fig. 6.

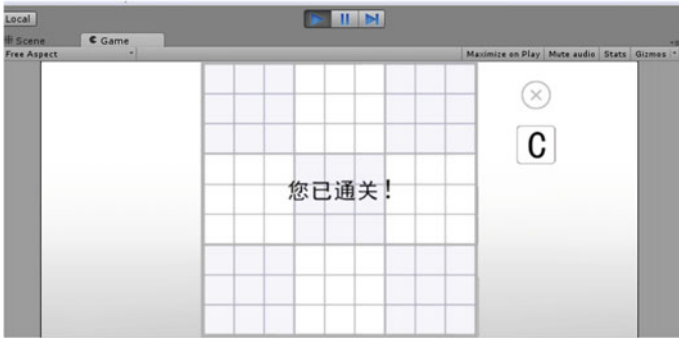


Fig. 6. Game end interface

## 4 Test and Release of the Game

After the game is finished, we will post the project to the PC, click the generated exe. program to test the game, check whether the button click is effective and whether the UI conversion is smooth. Once the test is complete, click on the File menu bar and select the Build Settings option. All scenes are dragged to the Scenes In Build window. Then select the Android publishing platform and set the parameters in the Player Settings. The parameter settings are shown in Fig. 7. Click the Build option and select

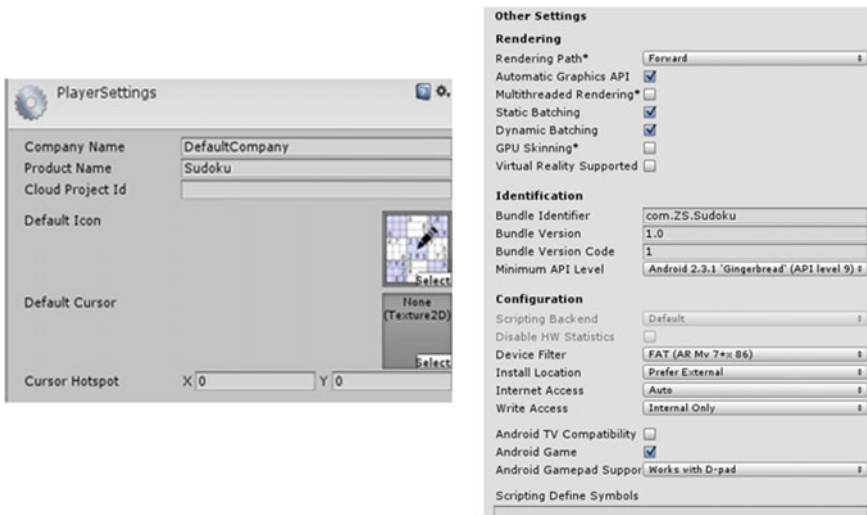


Fig. 7. Android platform publishing settings

the specified path to store the generated .APK file. Finally, the .APK file is downloaded to the Android phone, and the Sudoku game is successfully installed on the mobile phone.

## 5 Conclusions

With the rapid development of embedded technologies and embedded systems, the proportion of people using mobile devices has surpassed that of PCs. This has also increased the odds of people using mobile devices such as mobile phones for entertainment. Sudoku based on Unity design and production, to a large extent, improve the user's user experience, make it easier to play and fill in the numbers faster for Sudoku fans. It is important to move the Sudoku game from the paper to the smart phone, making the game logic more intuitive and adding more fun to the game.

## References

1. Xuemei, C. (2016). Mobile game development based on Unity3D. *Electronic Technology and Software Engineering*, 23, 71–72.
2. Yanjun, L., & Jiayu, Y. (2012). Research on version control in Unity3D game development. *Software Guide*, 11(11), 12–13.
3. Donghan, Z., & Zhanjun, S. (2017). Game design and production based on WebGL technology. *Computer Knowledge and Technology*, 13(09), 193–194.
4. Linbo, W. (2012). Study on the circle-in-difference method of Sudoku's difficulties level. *Computer Engineering*, 38(10), 161–167.
5. Dongbo, H., Hongjiang, W., et al. (2015). Design and implementation of mobile game based on Unity3D. *RTVU Polytechnic*, 01, 22–23.



# Researching an Effective Interactive E-Book for Programming Courses

Ying Hu<sup>1(✉)</sup> and Huiqiang Lyu<sup>2(✉)</sup>

<sup>1</sup> School of Media and Design, Hangzhou Dianzi University, Hangzhou, China  
hdhy@hdu.edu.cn

<sup>2</sup> Computer Science and Technology College, Zhejiang University  
of Technology, Hangzhou, China  
lhq@zjut.edu.cn

**Abstract.** China needs to develop a large number of computer science teachers now. With the failure of massive open online courses, various kinds of interactive e-books for distance learning are becoming more and more urgent. This research primary mission is to determine what makes for good usability in a computer science e-book and measuring if teachers learn using them. The study investigates participants' preferences for interactive computer science e-book designs and usability, in an attempt to review and develop guidelines for educational e-book creation. Comparisons and preferences were made between three interactive educational computer science e-books and specific multimedia widgets within them. Based on the reported findings, some general guidelines were suggested for increasing usability within interactive e-books and ways to enhance their educational value. The results of the study suggest that interactive educational e-books in Runestone Interactive<sup>®</sup>, Zybook<sup>®</sup> and CS Circles<sup>®</sup> are an effective alternative to current distance learning methods for teaching computer science.

**Keywords:** Interactive e-book · Multimedia widgets · Usability for e-book · Learnability for e-book

## 1 Introduction

For an interactive educational e-book to serve as an effective digital teaching platform, the users must be able to efficiently learn from using the e-book. The usage of the e-book should contribute to the user's content knowledge on the subject. Content knowledge generally refers to the facts, concepts, theories, and principles that are taught and learned. Traditional textbooks are limited to immobile images and text on the pages to communicate the knowledge they contain. However, interactive educational e-books have the capability of using multimedia technologies to enhance the teaching of content knowledge. The design and usability of the multimedia technologies within these interactive educational e-books largely influences their ability to serve as an effective teaching platform.

Campbell et al. found that the use of e-books could improve learned content knowledge due to the active learning and portability the e-books provide [1]. In



contrast to this study, a study on web-based learning that analyzed educational websites and resources determined that these tools were an advancement for technology, but a setback for pedagogy [2]. They found that the educational websites took advantage of technology's abilities to enhance communication and provide better information representation. However, the sites were not developed with beneficial pedagogical approaches, such as active involvement and scaffolding, as a basis. While these two studies have contrasting results, it is clear that e-books have a crucial impact on content knowledge and how it is learned. One study, which merged the concepts of e-book usability and content knowledge, intended to determine the characteristics of e-book creation that afford learning and educating [3]. The results found that a combination of several characteristics, such as feedback, creativity, and productivity, could ultimately be used in the creation of an e-book that properly affords learning.

## **2 Usability of Interactive E-Book Research**

### **2.1 Participants of Interactive E-Book**

Subjects consisted of 5 male and 7 female teachers that had half a year or more of experience of coding and related knowledge. Additionally, All participants were undergraduates or above degree and had used interactive e-books.

Participants feedback for Active Code never involved it providing beneficial feedback for errors the user encountered when editing the code. In fact, many participants stated the design of the Active Code widget is presently straightforward and maintains a clear appearance, yet lacks helpful feedback when they encountered an error. Similar to Wasecka's study, much of the provided participant responses indicated a need to improve feedback [3].

### **2.2 Materials of Interactive E-Book**

Three interactive educational computer science e-books that are accessible through a user's web browser were used for this study. All e-books are designed to teach the Python programming language and concepts at an introductory level. While the overarching concept of the e-books is similar, their design and layout are different. To conceal the e-books' identities they will be addressed by the platforms on which they were created on. The first e-book will be referred to as Runestone, the second ZyBook, and the third CS Circles.

Code Lens lacked many suggestions that requested its design or functionality be changed, but mostly had participant feedback regarding how useful and well-designed it currently is. Design suggestions regarding this widget in particular should be taken from Runestone or Zyante, depending on what Code Lens style is appropriate for the e-book. A mixture of the two types of Code Lens widgets could offer an educational benefit that affords learning while maintain a high level of usability. Participant feedback for Parsons Problems also suggested increased feedback for correct and incorrect code block ordering, such as showing the code's output if it was able to be run.

The common theme for providing more feedback for these widgets potentially suggests the widgets didn't always function as the participants thought, indicating a lower level of usability. The last widget, Multiple Choice, was mostly deemed unfavorable or suggested that it should only be used for specific type of questions. This unfavorable attitude toward Multiple Choice may be attributed to the widget not being as innovative or new as the other three widgets.

The Multiple Choice widget is comparable to multiple choice questions seen in printed textbooks, but offers dynamically provided feedback that printed works cannot. Interactivity within the Multiple Choice widget, regardless of platform implementation, is much more limited in comparison to the three other widgets. This limited interactivity and normalcy makes it not surprising that participants were generally not in favor of the Multiple Choice widget, despite their lack of negative usability feedback for the widget or a distaste for Multiple Choice over coding for learning computer science. The dislike for the widget is not due to participants distaste for the widget's design, just for the concept of the widget as a whole.

### **2.3 Instrumentation of Interactive E-Book**

An online questionnaire approach was employed to study the participants' preferences on the varying usability and the three e-books and their interactive widgets. The four-part questionnaire began with asking basic demographic information of the participants. In this section, participants also reported their prior e-book and coding experience.

The second part uses Likert 5-point scale to evaluate the overall design preference of three e-books. They were to rate the three e-book designs on the following key factors: navigation, web information, media arrangement, page layout, font, legibility, white space, and color contrast between background and content. Additionally, they were asked to provide any feedback they had toward the design choices of the e-book via a free response question. In this section, participants are provided with a URL and asked to first evaluate the Runestone e-book, then the ZyBook e-book, and finally the e-book of CS circle.

The third part determines participants' preferences for usability and learnability of the four interactive widgets in each e-book. Attendees were invited to give feedback on the four widgets and their corresponding e-book platforms. For this section the Active Code widget was inquired about first, followed by Code Lens, then Parsons Problems, and finally Multiple Choice. The corresponding e-book platforms went in the same order for each of the four widgets, with Runestone being first, followed by ZyBook, and then CS Circles. For example, Active Code implemented on Runestone was inquired about first, then Active Code on ZyBook, and finally Active Code on CS Circles. For each component-platform combination, a URL is provided to the participant that contains specific widgets implemented on a particular platform, such as Runestone, ZyBook, or CS Circles. After interacting with the widget, they are asked to state the purpose of the widget. They were then asked to describe what they thought each button and widget functioned. Finally, they are always asked to report any widget they find confusing or undesirable.

## **2.4 Procedure of Interactive E-Book**

The survey contained clear written instructions prompting the user to complete the first part of the questionnaire gathering background information. Next, participants were provided links to the three different e-books and told to view and interact with them to their preference. Following this, the participants were to complete the second part of the survey where they answered questions regarding their design preferences of the three e-books as a whole. They were then provided links to the individual interactive widgets contained in each of the e-books. Once again, the participants were instructed to interact with the widgets to their desire. Participants were then asked a series of usability questions corresponding to the particular widget they had just interacted with. For the final part of the survey, they were asked to compare the widgets to one another, report which was the most useful to them, and explain why.

## **3 Learnability of Interactive E-Book Research**

### **3.1 Participants of Interactive E-Book**

Participants were asked to provide suggestions and ways to improve each of the four interactive widgets. Suggestions for the Active Code widget were primarily themed around providing more feedback, such as a detailed error message when the code fails to run. The majority of the suggestions for the Code Lens widget weren't suggested improvement, but rather statements of how useful the widget is currently. For Parsons Problems, several participants suggested showing the code's output, assuming it can be compiled and ran, regardless of it being in the correct order or not. Finally, suggestions for Multiple Choice revolved around them being used sparingly and for testing specific concepts.

### **3.2 Materials of Interactive E-Book**

An interactive educational computer science e-book that's accessible through a user's web browser was used for this study. It was developed using the Runestone Interactive platform and is intended to teach the Python programming language and concepts at an introductory level to teachers. Only chapters one through eight of the e-book were used for this study. These sections cover basic computing concepts in Python, such as define variables and iterate code in while and for loops statements. A pretest was used to gauge the participants' prior programming knowledge. Four posttests were also used to test how much the participants learned from using the e-book.

This study had several limitations, the first being that it is primarily limited to its small sample size. Both studies are targeted toward teachers, who are quite busy during the school year, so enlisting their participation was quite difficult. The sequence for displaying the e-books and widgets to the participant always went in the same order of Runestone, ZyBook, and then CS Circles. This repeated order could have caused a sequencing confound, particularly when identifying the purpose of the widgets. Finally, a few technical errors due to web servers occurred for participants when accessing the various e-books and widgets. Encountering such an error is likely to cause the participant to become frustrated or skip interacting with the widget, thus influencing their response.

### 3.3 Instrumentation of Interactive E-Book

An online questionnaire approach consisting of five different surveys was employed to study the users' acquisition of knowledge after using the e-book. The first of the online questionnaires was a two part pretest, with the first part soliciting the participants for basic demographic information and to report their prior experience with any programming languages. The second part consisted of nine free response questions based on five programming problems. These questions were intended to further gauge the participants' prior programming knowledge and establish a baseline of programming knowledge. For instance, a block of code would be presented to the participant and they'd answer what values would be printed out when that block of code was executed.

## 4 Conclusions

The results of research indicate that for these three e-books platforms, the navigation and amount of information on the page need improvement, yet their use of color and font is well executed. While the context and topic of the question and topic are dependent, all four of the interactive widgets are uniquely beneficial and their use is suggested. Additionally, the use of all three e-book platforms is suggested, with an equal preference toward Runestone and ZyBook.

**Acknowledgements.** This paper is funded by the College of Media and Design, Hangzhou Dianzi University.

#### **Compliance with Ethical Standards**

**Conflict of Interest** The authors declare that they have no any conflict of interest, The paper only discuss how to review and select e-book development platform for programming courses.

**Ethical Approval** All procedures performed in studies involving human participants were in accordance with the ethical standards of the School of Media and Design, Hangzhou Dianzi University, and with the 1964 Helsinki declaration and its later amendments or comparable ethical standards.

**Informed Consent** Informed consent was obtained from all individual participants included in the study.

## References

1. Campbell, A., Callaghan, G., McGarvie, D. W., & Hynd, M. Do students study and learn differently using e-Readers? A cross-discipline research investigation into the pedagogical implications of using e-Readers to study university level texts.
2. Mioduser, D., Nachmias, R., Lahav, O., & Oren, A. (2000). Web-based learning environments: Current pedagogical and technological state. *Journal of Research on Computing in Education*, 33(1), 55–76.
3. Wasecka, J. J. (2013). *Creating an E-book*. Doctoral dissertation, State University of New York Institute of Technology.



# Research and Design of Mobile Terminal APP for Fengxiang Woodcut New Year Picture Based on the Protection of Intangible Cultural Heritage

Jie Du and Yujia Gao<sup>(✉)</sup>

School of Art and Design, Xi'an University of Technology, Xi'an  
Shaanxi, China  
905409167@qq.com

**Abstract.** The design of mobile terminal APP for Fengxiang woodcut New Year picture integrates traditional culture with digital media technology to enhance the user's new experience and expand the social influence and inheritance of Fengxiang woodcut New Year picture by digital inheritance. The information architecture combines the knowledge narrative structure with the user interaction experience, and divides the block functions for different audiences to meet the needs of different groups of people, thereby giving full play to the user's self-creation experience to realize the redesign of traditional cultural heritage. APP design for Fengxiang woodcut New Year picture facing intangible cultural heritage innovation integrates the advantages of traditional media and new media, fully combines product function and user experience, and inherits and protects Fengxiang woodcut New Year picture through digital media technology, thus contributing to the protection and inheritance of intangible cultural heritage.

**Keywords:** Fengxiang woodcut New Year picture · APP design · Digital media technology · Intangible cultural heritage

## 1 Introduction

Fengxiang woodcut New Year picture is listed as China's first batch of intangible cultural heritage, and the research value is stressed by the academic community. Over time, Fengxiang Woodcut New Year Pictures faces the current situation of sharp decline in varieties, loss of ancient engravings, and no technical successor. Against the background of the continuous development of digital multimedia technology and the continuous spread of emerging cultural forms, Fengxiang woodcut New Year picture have encountered new opportunities for protection, rescue, organization and development.

## 2 Research Status

At present, there are several problems in the inheritance and protection of intangible cultural heritage in China: (1) the lack of relatively reasonable development and utilization carriers in the intangible cultural heritage protection mechanism; (2) the protection of intangibles is mainly the protection of form rather than the protection for its content; (3) intangible cultural heritage protection is often limited in the ontology itself, lacking derivatives and practical application innovation [1]. In combination with the problem, the author selected Fengxiang woodcut New Year picture as the prototype of APP design, and studied the design of Fengxiang woodcut New Year picture APP based on intangible cultural heritage protection from three aspects.

Researches during the nearly 20 years, in order to record and protect the Fengxiang woodcut New Year pictures, mainly adopt the form of text printing, photography and video. These forms play a positive role in its theoretical research and inheritance, but due to the limitations of the media itself, there are inevitable drawbacks, such as: long update period of information content, late preservation and inconvenient circulation, passive acceptance of information, and weak demand for appeals, etc. APP has great advantages in making up for these media limitations. Firstly, it can be updated at any time and the information is comprehensive. Secondly, the post preservation and promotion is convenient and the display form is rich. Thirdly, users' demands are strong in the process of actively accepting information, and two-way communication increases the effective interaction with users.

The new information dissemination model has interactive and immediate information transmission and more efficient and multi-dimensional communication effects in terms of information form and communication status. The integration of interactive digital media and traditional media makes traditional cultural communication more vivid [2]. The APP uses digital media as a carrier to interactively connect users, and inherits and protects Fengxiang woodcut New Year picture resources in many aspects. While deepening the user's understanding of Fengxiang woodcut New Year picture culture, we will carry out independent acceptance and independent innovation of traditional culture, and effectively improve user's loyalty and satisfaction.

## 3 Design of Mobile Terminal APP for Fengxiang Woodcut New Year Picture Based on Intangible Cultural Heritage

From the basic perspective of the UCI of Fengxiang woodcut New Year picture, the structure of APP was determined through preliminary research (Fig. 1). Information framework is the organic organization of information, which focuses on the content structure: how to organize and label the content so that users can easily find the information they need [3]. The APP information structure is composed of knowledge module, function module and promotion platform. The knowledge module is divided into basic knowledge and scholar research block. The function module is divided into three types of interactive mini games and folk artist works promotion platform (Fig. 2), and are distinguished in the initial interface (Fig. 3). Different functional areas not only

connect people through APP, but also make the presentation of overall structure more rational according to different modules.

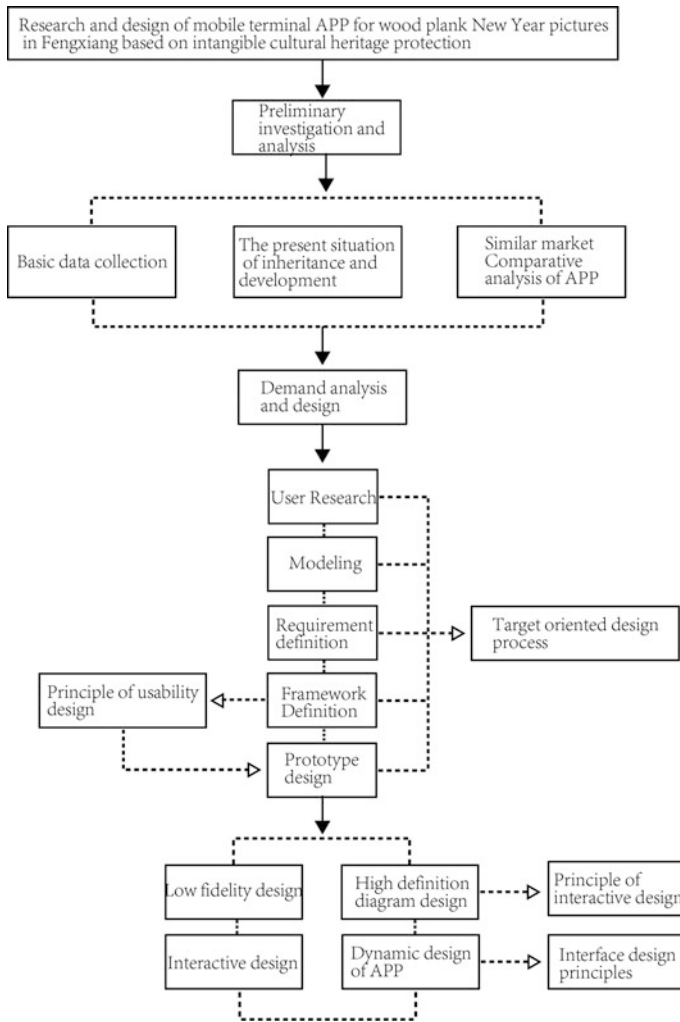


Fig. 1. Design flow

In addition to collecting Fengxiang woodcut New Year picture information resources, this APP also adds purchase and collection labels to the tab bar. It is the trading platform that can support users as seller or buyer to realize the exchange and interaction of buying and selling. The collect labels can allow users to mark the article information they need, so that the information between the APP and the user can be transferred in both directions, and two-way communication between the users can also be reached.

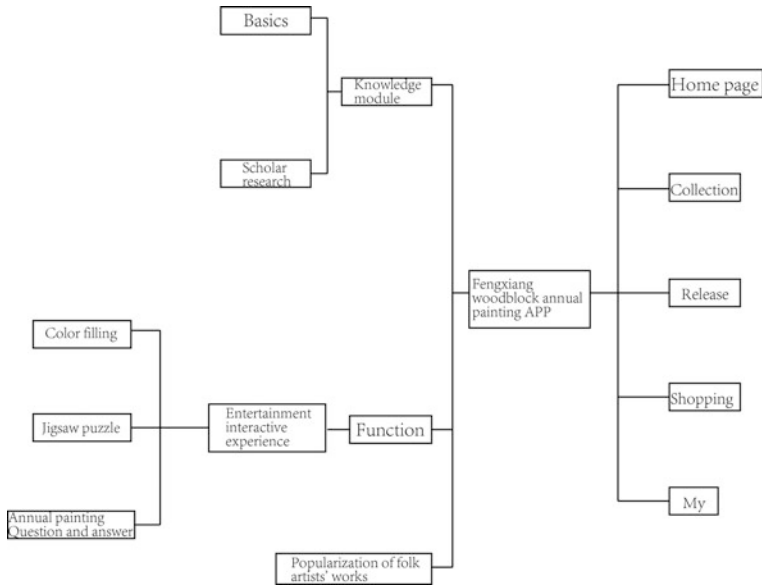


Fig. 2. Information architecture of APP for Fengxiang woodcut New Year pictures

### 3.1 Analysis of the Knowledge Module Design of APP for Fengxiang Woodcut New Year Picture

#### 3.1.1 Design of Basic Knowledge Module

In the basic knowledge block, the research contents and materials of Fengxiang woodcut New Year picture are classified and the basic information content is classified into five categories according to development process, theme works, production process, artistic features, and inheritance and development (Figs. 4 and 5). The establishment of the basic knowledge block makes it possible to: (1) establish a bridge of information between users and the APP, and the required content is presented quickly and efficiently, so that the APP is recognized by users. In the development history block, development history is systematically introduced. (2) The theme works block is divided into six categories: door painting, ten beauty picture, custom painting, drama story, window flower, and six gods for home according to the theme of Fengxiang woodcut New Year picture. (3) The production process is shown in graphic form in the production process block, and the media advantage of APP is used to match the narration and music to enhance the visual display of the folk art creation of Fengxiang woodcut New Year picture.

#### 3.1.2 Design of Scholars Study Module

Aiming at the appeal of research scholars of Fengxiang woodcut New Year picture, focusing on investigation and research and attaching importance to information replacement and scientific reliability, this module provides a professional information platform for them. Based on the information of the basic knowledge block, it concentrates the news, research results and related links of Fengxiang woodcut New Year



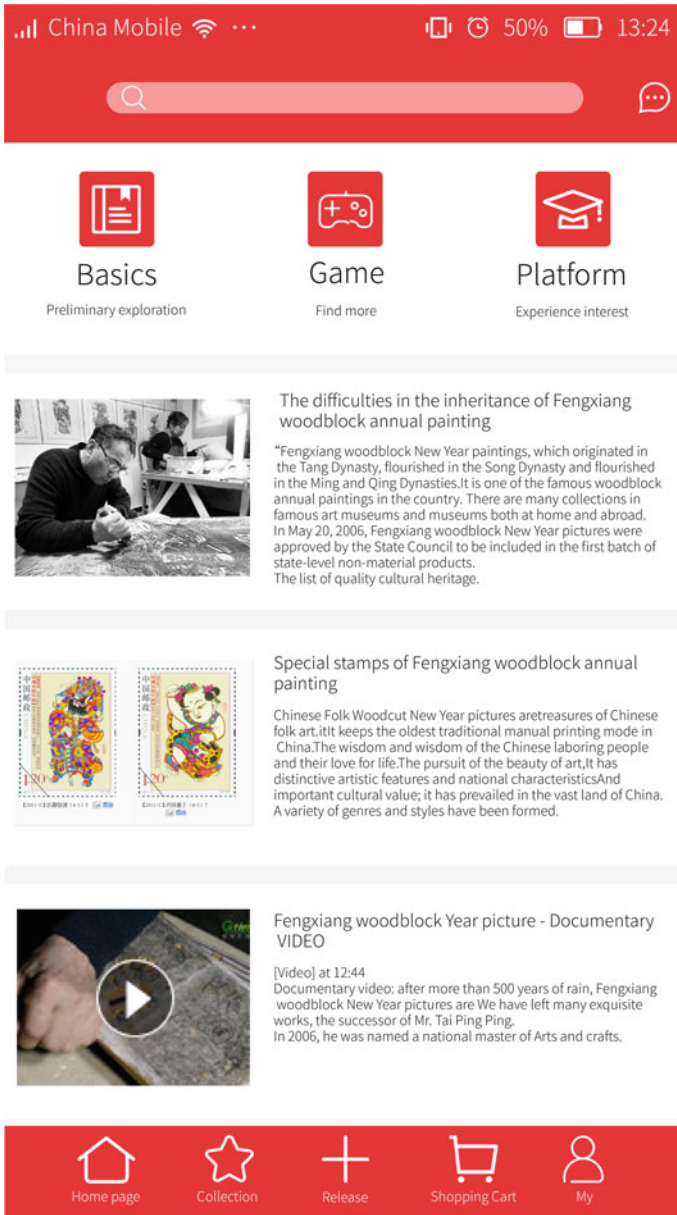


Fig. 3. Home page interface the APP

picture and the original painting database of Fengxiang woodcut New Year picture (Fig. 6). By taking advantage of the timeliness of new media technologies, it solves the problem of the focus of this group and updating and disseminating. In the high-fidelity display of the original painting, it is divided into three parts: original painting sorting,



Fig. 4. Information architecture of basic knowledge

line draft data, and color numericalization. The numerical value of multiple colors Lab, RGB, and CMYK are quantified recorded and saved, which facilitates downloading and conversion of various channels.

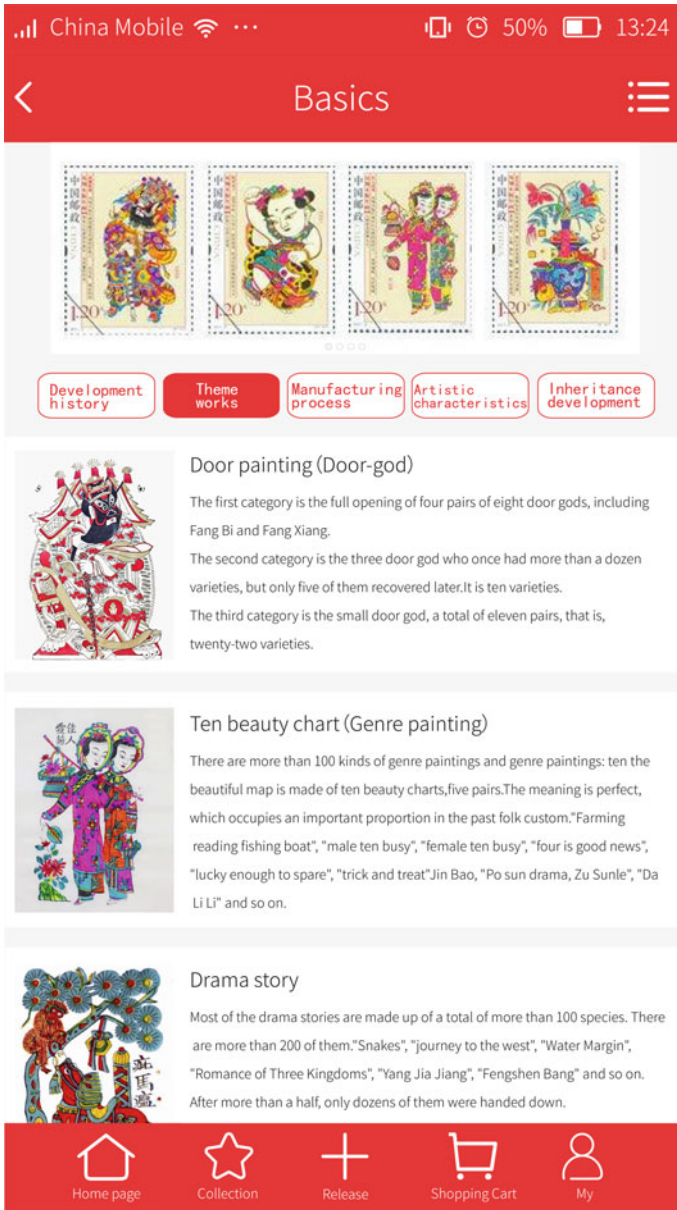


Fig. 5. Basic knowledge interface

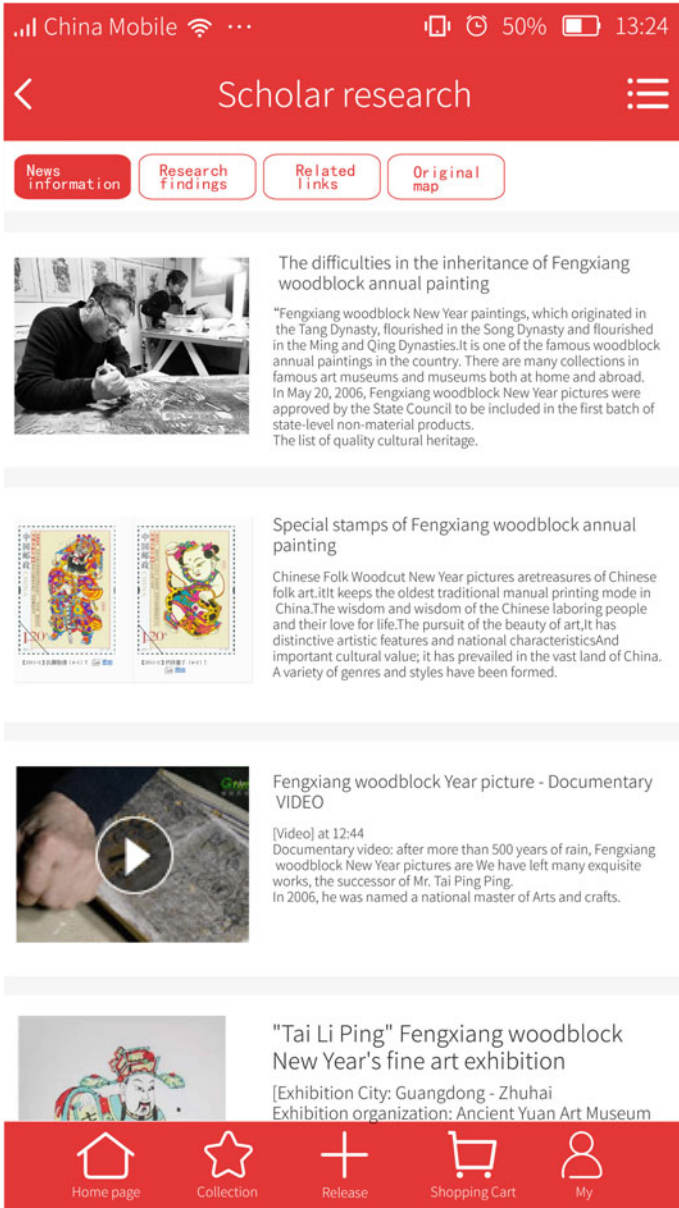


Fig. 6. Interface of scholar research module

### 3.2 Research on the Design of Function Module of APP for Fengxiang Woodcut New Year Picture

In the overall information architecture, only the combination of narrative content and user interaction experience can improve its usability and growth [4]. Integration of traditional culture and creative design can enhance the connotation of design objects [5]. In the design of entertainment experience module of Fengxiang woodcut New Year picture APP (Fig. 7), user interactive experience is added, enabling users to accept culture in the process of experiencing entertainment, which further improves user viscosity and enhancing the breadth and intensity of communication. This module consists of three parts, and the positioning of the three interactive games is all handy, without increasing the burden of the loop game.

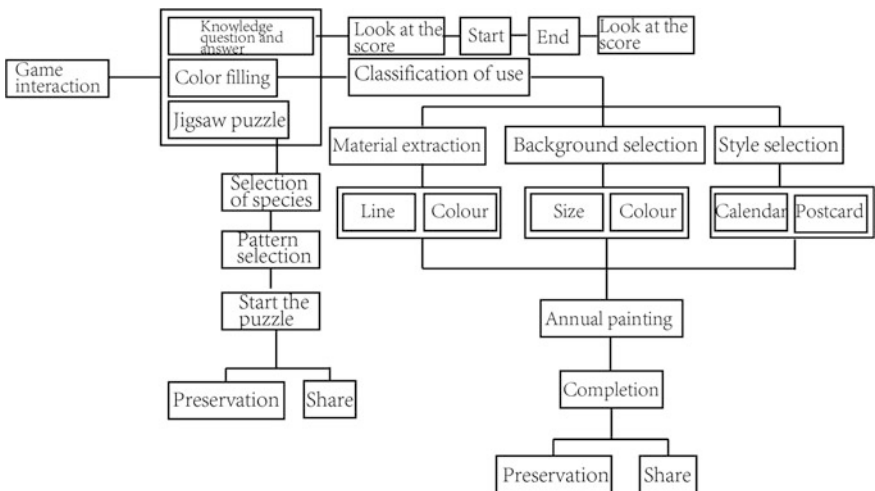


Fig. 7. Architecture diagram of functional module

#### 3.2.1 Color Filling Interaction

Taking the door gods Qinqiong and Jingde as examples, in the color filling interaction module of the APP, the traditional Chinese painting material and the virtual tool in the digital interface are replaced (Fig. 8). In addition to the original painting color, a variety of auxiliary colors are added for the user to select (Fig. 9), so that users can play the color filling interaction game of color matching of Fengxiang woodcut New Year picture according to their own preferences. This block design allows the user to further understand the “big and full” and “High Purity Colors” of Fengxiang woodcut New Year picture, and feel the charm of color in several times matching, so that users can create and design new color match in the process of interactive experience and thus activate traditional culture.

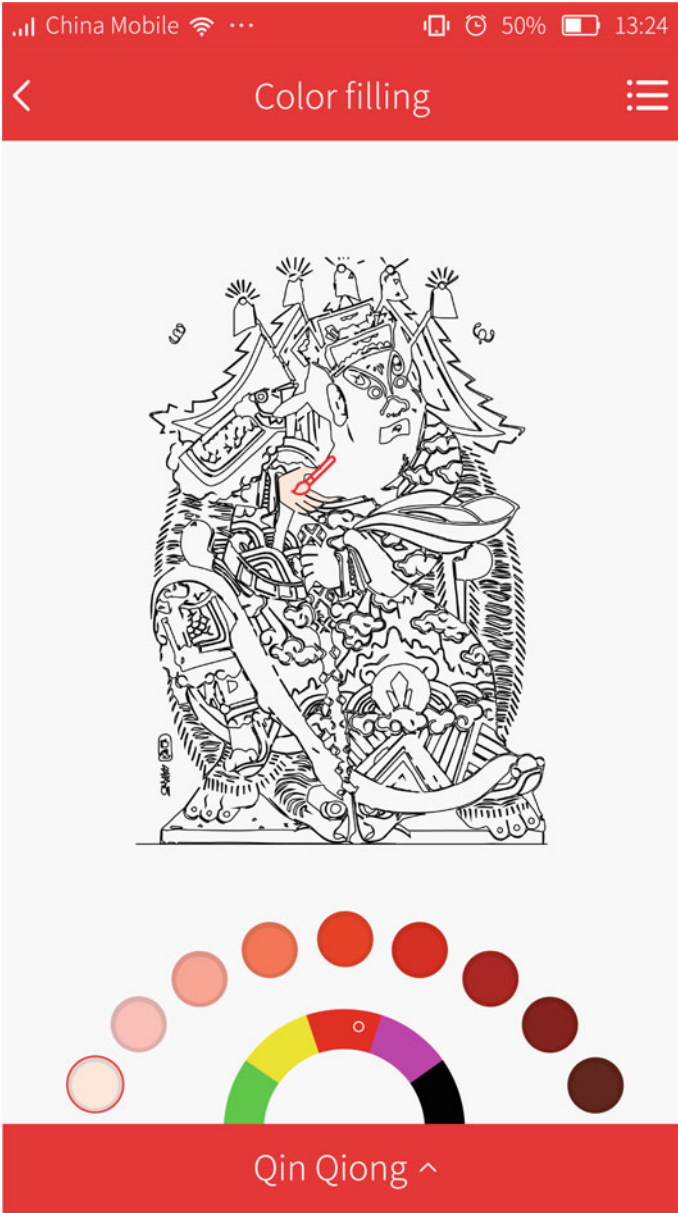


Fig. 8. Color filling game



**Fig. 9.** Color extraction

### 3.2.2 Jigsaw Puzzle

The jigsaw interaction design disrupts the original image block (Fig. 10) and the user restores the pattern of New Year picture. The user can unlock the next jigsaw after completing a jigsaw and scores is decided based on the game time. This block setting restores the original appearance of Fengxiang woodcut New Year picture in a fun and vivid way, analyzes the theme and content of the New Year picture, and pays attention to the participation and interaction of cultural disseminator and cultural recipients.

### 3.2.3 Questions and Answers on New Year Pictures

In this app, the Knowledge Q&A Block of New Year picture is set up to effectively combine Fengxiang woodcut New Year picture knowledge and user experience (Fig. 11). The answer to the question comes from the content in the other modules, so that the three modules are connected and not isolated. Questions of questionnaire related to New Year picture are hidden in the problem to provide reliable big data for the background, and guide the later update. In order to motivate users to participate in the New Year knowledge quiz, the higher the score they get, the more game material can be unlocked. In this way, the three games are connected in series, thereby forming a mechanism stimulating user experience that can grow, and thus improving APP user viscosity.

## 4 Exchange and Promotion Platform for Fengxiang Woodcut New Year Picture

The folk artist promotion platform is a platform for APP users to disseminate Fengxiang woodcut New Year picture. It carries out the promotion of traditional Chinese New Year pictures online and offline at the same time, which is convenient for



Fig. 10. Jigsaw puzzle

maintaining the statistics of sales channels (Fig. 12). The Fengxiang woodcut New Year picture has been handed down from generation to generation by Tai family. According to the inheritance of Tai picture bureau in recent years, classification and fillings are made. A large number of works with personal characteristics are included in



China Mobile 50% 13:24

## Problem of the year painting

1.Fngxiang woodblock annual paintings are classified according to the subject matter?

a.Ink line painting, color painting

b.Fairy tales, auspicious celebrations, and custom sketches

c.Door god painting, window flower, wall painting, middle school painting, etc.

2.Which material is the engraving material of the Fengxiang woodblock annual painting?

a.Woodblock

b.Mud

c.Iron plate

3.The form of Fengxiang woodblock annual painting?

Submission

**Fig. 11.** Q&A on New Year picture knowledge

the inheritance liking with personal websites and related personal news, and the inheritors and new product are updated in real time. Through the background data of the innovative New Year pictures produced by the color filing game, users can customize the derivative of Fengxiang woodcut New Year picture and order the New Year

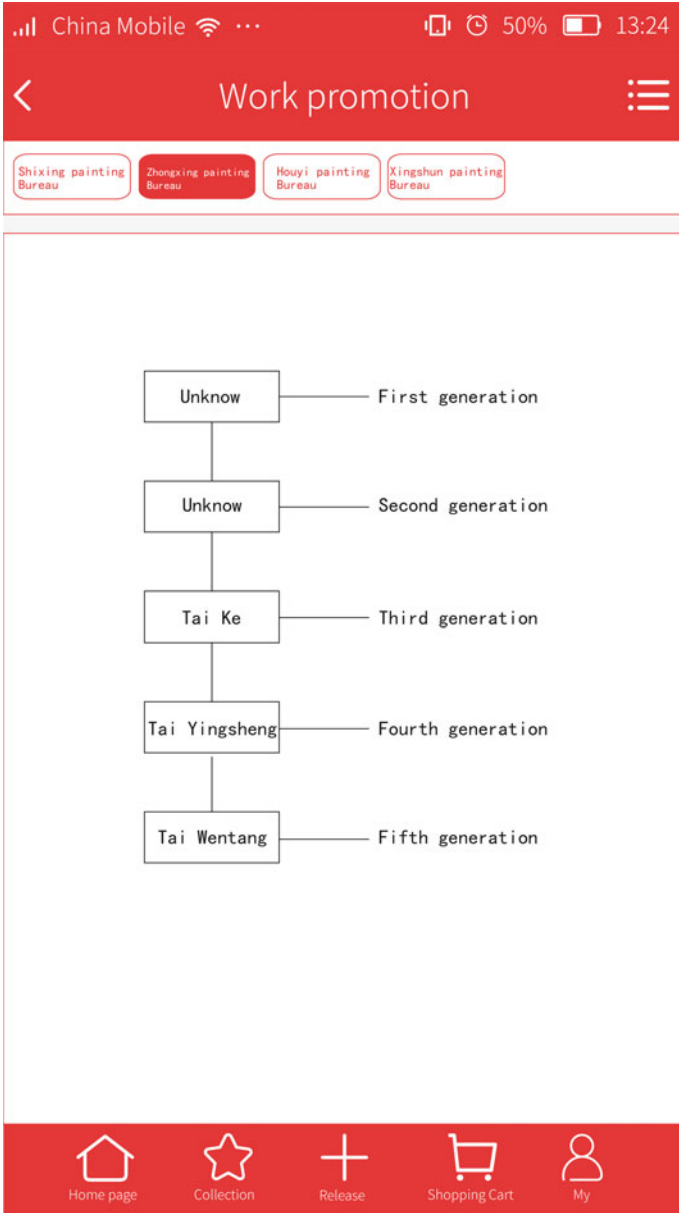


Fig. 12. Promotion interface of Folk artist work

pictures. The inheritance and redesign of traditional culture can be realized, the promotion of Fengxiang woodcut New Year pictures is promoted and the resource sharing system with folk artists is established.

## 5 Conclusions

Design of mobile terminal APP for Fengxiang woodcut New Year picture based on the protection of intangible cultural heritage determines the presentation mode, interaction goals and user experience according to the content and carries out information architecture and visual content design according to the core functions. It conveys its connotation in the design, rather than simply splicing and listing cultural content. The APP function is divided into three parts. The knowledge module as the introduction of the whole knowledge comprehensively elaborates the connotation of Fengxiang woodcut New Year picture for research. The function module is aimed at the entertainment interactive experience, which gives full play to the user's self-creation experience. The platform for exchange and communication of Fengxiang woodcut New Year pictures provides redesign and re-creation platform to get more promotion channels on the online ports. The design of mobile terminal APP for intangible cultural heritage protection uses the current digital media APP technology to protect the intangible cultural heritage culture, integrates the advantages of both sides to inherit and protect the cultural resources of Fengxiang woodcut New Year pictures, and spreads them in an interactive experience way, so as to allow users to get rid of the boring knowledge information instillation. The New Year picture can be spread more creatively in entertainment and get more development opportunities through online platforms, which is a new opportunity for the inheritance and protection of Fengxiang woodcut New Year pictures.

**Acknowledgements.** This study is funded by a Humanities and Social Sciences Project of Shaanxi Provincial Education Department (17JK0527). This work is also supported by the General Project of Humanities and Social Sciences of the Ministry of Education (17YJC760007).

## References

1. Kun, T., Zhenghong, L., & Ying, L. (2015). Study on the design of APP Interface in the context of "intangible cultural heritage" innovation. *Packaging Engineering*, 4.
2. Meiyi, Z., Yang, Z., & Jingyan, Q. (2015). APP user experience design of "virtual new year picture shop". *Packaging Engineering*, 12(24), 52–56.
3. Saffer, D. (2010). *Guide for interactive design*. Beijing: China Machine Press (Chen Junliang, tr.).
4. Xuelin, H., & Xiao, J. (2014). Study on the strategy for the enhancement of website user viscosity based on incentive theory. *Packaging Engineering*, 35(12), 134–138.
5. Weiwei, W. (2014). Research and application of traditional culture design element extraction model. *Packaging Engineering*, 35(6), 73.



# How Conventional Printers Lead into Customized Web-to-Print

Yungcheng Hsieh<sup>1(✉)</sup>, Mingchw Wei<sup>2</sup>, and Xinyi Wong<sup>1</sup>

<sup>1</sup> Department of Graphic Communication Arts, National Taiwan University of Arts, New Taipei, Taiwan

y.ch@ntua.edu.tw

<sup>2</sup> Graduate School of Creative Industry Design, National Taiwan University of Arts, New Taipei, Taiwan

**Abstract.** “Web-to-Print (W2P)” has become a new trend of printing industry. A widely definition of W2P is commercial activities for trading of printing services through the internet. Most of Asian printers still use traditional processes to print orders. Comparing to the printers in the U.S. or European countries, Asian printers seem not so active in the development. Under the influence of digitalization, it will be very important to consider how to provide W2P services. The development of W2P in Asia is on the stage of cloud printing for paper-related product. In the meantime, printers in North America and Europe have elevated their services from W2P to customized W2P due to the great need of personalization. The study carried out in-depth interviews of experienced printers, educators and content analyses of many W2P platforms not only to explore how Taiwanese printers view the requirements and obstacles but also to comprehend the web structure of a customized W2P platform. This study disclosed the essential functionalities and obstacles of a successful customized W2P platform. We hope that this study will elevate competitiveness of conventional printing enterprise.

**Keywords:** Customization · Web-to-Print · Me-commerce · Taiwanese · Printing industry

## 1 Introduction

The combination of Web to Print (W2P) and me-commerce (custom-made e-commerce), so called customized W2P, is the key trend of the digital printing industry worldwide. Customized W2P has been well established in the US and is developing rapidly in Taiwan and China, especially under the pressure of paperless and green policy. Compared with the W2P market in the US and Western Europe, the market in Taiwan and China is facing a stage of transformation from traditional business model to me-commerce model. The customized W2P has brought a new business opportunity and challenge for conventional printers.

In Taiwan, although many printers have introduced some kind of W2P into their workflow, only a few of them offer custom-made services of online design [1]. The demand of personalized merchandises has been increased. Consumers need more

diverse printing products with high quality and personalized creativity. The request of custom-made design has become the main stream of W2P. Moreover, some of advanced W2P printers have even provided smart phone applications (Apps) for users to do the online estimation, order, design, editing, and job tracking anytime. In Taiwan, most of conventional printers own high quality facility and equipment with capability of performing W2P, but it is a pity that not many of them invest on customized W2P due to the lack of online service. This study conducted content analyses on major successful W2P service websites in Europe, North America, and China, and Taiwan to understand the needs, criteria, and necessity of a cost-effective customized W2P platform to explore how conventional Taiwanese printers view the requirements and obstacles. The study also employed in-depth interviews to carry out the research to comprehend the web structure and process of establishing, implementing, and maintaining a customized W2P platform.

## 2 Research Methods and Findings

This research employed the content analysis method to examine the internationally known W2P platforms and their related web structure. The study aims to identify the trend of customized W2P printing and to provide suggestions to conventional printers that wish to develop customized W2P platforms in the future. This research analyzed 69 websites of W2P transactions and services, including 22 US companies, 22 Taiwanese companies, 22 China Mainland companies, 4 UK companies, and 1 Hong Kong printer. Most of the companies provide both conventional mass-production printing and customized printing services. Customers can select their favorite photos from Facebook or Instagram for design and then print. Photos and designs can be even stored in the cloud. Among the 22 US companies, five of them, such as “Shutterfly” and “CafePress” allow customers to buy products made by designers and even encourage customers to sell their own design. These platforms provide a variety of customized products and also cooperate with a multitude of brands to provide high quality licensed photos. The rest of companies specialize a certain type of printing services such as book/paper printing, fabric printing, material printing, and so on. The 22 companies in Taiwan and 20 companies in China of W2P are still at a budding stage. Only 11 of them provide online editing tools to allow customers design their own products and sell their own design currently. The content analysis result indicates that the number of website providing customized W2P services is increasing.

The research also conducted comprehensive interviews of 13 experts including experienced high level printing manager, stakeholders, and educators. The interviews discussed the requirements of leading into customized W2P service from a conventional printing business. All interviews were conducted from March 29 to May 25, 2017. The agendas of the interviews are as follows.

1. Understanding online printing services in Taiwan: Does your company provide customized W2P services? If yes, can you share with us the bottlenecks that your companies have faced? If not, please explain why the company decides not to provide such services.

2. Currently most conventional printers are faced with difficulties caused by business transformation and customized W2P services. What are they?
3. The prerequisites of developing customized W2P platforms in Taiwan.
4. Requirements of internal development: Evaluate and align company's capabilities such as logistics, cash flow, information flow and online editing functions with the requirements of the customized W2P platforms.
5. What are the major considerations of conventional printers while investing customized W2P platforms and suggestions about website structures?

The summary of the opinions collected from the expert interviews is as follows.

### **2.1 Change Conventional Mindset and Learn New Concepts**

Most conventional printers and employees still adopt a traditional mindset towards printing. A customized W2P system should include cloud platforms, information systems, online marketing, website design and more. The system provides customers less expensive, more efficient and custom-made online experiences.

### **2.2 Improve the UI and UX of Online Editing Tools**

There are existing sets of software available on the market that printers can either rent or buy. However, there is a lack of creativity in these templates. One way to improve this is to differentiate the platform by designing the functions based on the custom-made features for customers to use on-line freely. In addition, the UI should also look modern and UX should be easy to use to improve the editing tools [2].

### **2.3 Use Big Data to Analyze the Customers' Preferences**

Businesses can maximize the use of big data collected from their platforms to explore customers' shopping habits and to predict their shopping behaviors in the future. Also, do target marketing accordingly. The personalized marketing tactic of announcing discount codes and sales can boost customer spending. In addition to attract new customers, businesses should change in transaction processes to increase their loyalty by understanding current consumers' buying behaviors and preferences.

### **2.4 Tap into Overseas Markets and Improve Quality and Services**

Since Taiwan's print market is limited, most business owners believe the W2P industry should also tap into overseas markets, especially Southeast Asia. Nonetheless, customized W2P is not only the goal of business transformation, but also the key to continuously strengthen product quality and services.

### **2.5 Cooperate with IT Specialists to Construct a Better Customized W2P System**

Most successful W2P platforms are partner with business owners with IT background. The key to construct a better customized W2P system is to keep the communication

between customers and the website. A successful customized W2P platform should have an operating system that runs smoothly in the back end. IT specialists are necessary to maximize the readability and user friendliness of customized W2P platforms.

## **2.6 Online Marketing and Offline Promotion**

Businesses can draw attention from the target audience by using keyword ads, social media and hot searches. Big data analyses reports can be very useful in personalized marketing, specifically for special event products. As to offline promotion, word-of-mouth is very critical tool for marketing. Consumers nowadays see the CP value of a product as an important influence of purchase. Businesses should pursue continual improvement in pre-sale and post-sale activities, as well as in the product itself, which translates into word-of-mouth marketing in the long term.

## **2.7 Collaborate with Cloud and Platform Economy**

Printing companies can outsource different tasks such as designing, printing, packaging, and delivering to other business partners and share the profits. Companies can make the best use of the platform to learn about users' preferences and improve their services accordingly [3].

## **2.8 Adopt a Customer-Oriented Approach to Sell a Lifestyle to Consumers**

Nowadays most consumers pay more attention to the personalized quality of a product. Companies should put more efforts in developing DIY (Design It Yourself) gifts for consumer. The design and package of these custom-made products should be emphasized to look presentable to customers. Custom-made gifts are not only a good way to surprise loved ones, they can also be an effective way to promote a brand especially when these products are offered during special events.

# **3 Results and Discussion**

This research takes reference from the Top Ten Reviews in the United States that rate the performance of different W2P services in 2016 and evaluate the top ten service providers based on their overall performance. The rating criteria are: Price Competitiveness, Product Choices, Degree of Customization, User Interface, Trading mode, Shipping, Customer Service; Help & Support.

The business flow refers to the pricing and trading modes during the time the information flow refers to printing product options and customer services. The research has concluded the results in Table 1.

Table 1 shows that the top W2P platforms that provide digital content added-value applications on their websites generally put great emphases on five areas: online editing functions, free online digital content sharing, unlimited online storage, customized products and 100% customer happiness service. In addition to online editing functions,

**Table 1.** 2016 US top ten online printing service platforms

Platform/items	1	2	3	4	5	6	7	8	9	10	
	Price (US dollars)										
Business cards (500 sheets)	\$21	\$33	\$40	\$24	\$55	\$54	\$25	\$23	\$19	\$18	
DM (500 sheets)	\$113	\$99	\$325	\$96	\$91	\$95	\$211	–	\$58	\$170	
Postcards (500 sheet)	\$65	\$47	–	\$46	\$129	\$300	\$284	\$43	\$58	\$63	
Quality score		95	90	85	80	60	80	65	70	70	65
<i>Product category</i>											
Brochures & business cards	●	●	●	●	●	●	●	●	●	●	
Event cards & postcard	●	●	●	●	●	●	●	●	●	●	
Flyers& banners/poster	●	●	●	●	●	●	●	–	●	●	
Stickers/labels	●	●	●	–	–	●	–	–	●	●	
Magnets	●	●	●	–	–	●	●	●	●	●	
Menus/table tents	●	●	–	●	●	●	●	–	●	●	
Booklets/bookmarks	●	●	–	●	●	●	●	●	–	●	
Hang tags	●	●	–	●	●	●	●	–	–	●	
Calendars	●	●	●	–	–	●	●	●	●	●	
Mugs	–	●	–	–	–	●	–	–	●	–	
Phone case	–	–	–	–	–	●	–	–	●	–	
T-shirt and fabric	–	●	–	–	–	●	–	–	●	–	
Stationary	–	–	–	–	–	●	–	–	●	–	
Puzzle	–	●	–	–	–	●	–	–	–	–	
Electronic-USB/speakers	–	–	–	–	–	●	–	–	–	–	
Food package	–	–	–	–	–	●	–	–	–	–	
<i>Online design service and customization</i>											
Many choices of size/page etc.	●	●	●	●	●	●	●	●	●	●	
Upload design/photos	●	●	●	●	●	●	●	●	●	●	
Select template and online editing	●	–	●	–	●	●	●	●	●	–	
Download template	–	●	–	●	●	–	–	●	–	●	
Many choices of images	–	–	–	–	●	●	–	●	●	–	
Online file saving space	●	–	–	–	●	●	●	●	●	–	
Online preview and editing	●	–	–	–	●	●	●	●	●	–	
<i>User interface design (information flow)</i>											
Product search	●	●	●	●	●	●	●	●	●	●	
List of price and quantity	●	●	●	●	●	●	●	●	●	●	
Simplicity of site operation	●	●	–	●	●	●	●	●	●	●	
Q&As	●	●	●	●	●	●	●	●	●	●	
Online estimation	●	●	●	●	●	●	●	●	●	●	
App for download	–	–	●	–	–	●	–	–	–	–	
<i>Trade model (capital/cash flow)</i>											
Visa	●	●	●	●	●	●	●	●	●	●	
MasterCard	●	●	●	●	●	●	●	●	●	●	
PayPal	●	●	●	–	●	●	●	●	●	–	

(continued)



**Table 1.** (continued)

Quality score	95	90	85	80	60	80	65	70	70	65
American express	●	●	●	●	●	●	●	●	●	●
Discover/others	●	●	●	●	–	–	–	–	–	–
Online order tracking	●	●	●	●	●	●	●	●	●	●
<i>Shipping (logistics)</i>										
Post mail	●	●	●	●	●	●	●	●	●	●
Rush delivery	●	●	●	●	●	●	●	●	●	●
Ship to customer	●	●	●	●	●	●	●	●	●	●
Shipping within 24 h	●	●	●	●	●	●	●	●	–	●
Shipping tracking	●	●	●	●	●	●	●	–	–	–
Refund/reprint	●	●	●	●	●	●	●	●	●	–
<i>Customer service/help and support</i>										
Overall rating	100	85	85	70	85	60	90	75	70	90
Email inquiry	●	●	●	●	●	●	●	●	–	●
Phone inquiry	●	●	●	●	●	●	●	●	●	●
Live chat	●	●	–	●	●	●	●	–	–	●

Source <https://www.toptenreviews.com/services/internet/best-online-printing-services> [6] summarizing data by author

some international companies also provide a variety of customizable products (including phone cases, T-shirts, stationery, interior decoration or even pet products). Some international companies provide trading services to creators, designers, and artists which allow them to sell their creativity on the platforms. Taiwanese W2P platforms, on the other hand, rarely provide the five aforementioned services. In regard to product customization, the Taiwan market is still in the process of development. Generally, the product types are not as varied as those of international companies. Regarding the content editing process, consumers generally design their files offline before uploading them to a W2P platform. Few provide personalized content editing software to consumers on line or free download services. To date, this research has yet to find any Taiwanese customized W2P platform that offers consignment services for designers and/or artists.

Chinese enterprises invest heavily in e-commerce and digital content industry. These financial figures are massive. In the publication of the top 20 W2P companies in 2017, the concept of “brand” is emphasized. PEK (Printing Industry E-commerce Data Key Indicators) created by Keyin. Media, China is a ranking mechanism which evaluates the overall performance of the W2P service in China (excluding Hong Kong, Macau and Taiwan) using criteria such as content quality, volumes and website security, etc. 20 companies have been selected on the basis of PEK index as shown in Table 2.

**Table 2.** Top 20 web-to-print companies in China in 2017

Company	Web site	Company	Web site
36588.com	<a href="http://www.36588.com.cn/">www.36588.com.cn/</a>	ininin.com	<a href="http://www.ininin.com/">www.ininin.com/</a>
Easy Print	<a href="http://www.98ep.com/">www.98ep.com/</a>	pptake.com	<a href="http://www.pptake.com/">www.pptake.com/</a>
EP365.com	<a href="http://www.ep365.com/">www.ep365.com/</a>	CYT	<a href="http://www.0757p.com/sq.kiy.cn/">www.0757p.com/sq.kiy.cn/</a>
Namex	<a href="http://www.namex.cn/">www.namex.cn/</a>	Yi Si De	<a href="http://www.yiside.com/">www.yiside.com/</a>
Yifutu	<a href="http://www.yifutu.com/">www.yifutu.com/</a>	Zhi Xiang Ge	<a href="http://www.zhixiangge.com/">www.zhixiangge.com/</a>
Yofus	<a href="http://www.yofus.com/">www.yofus.com/</a>	eheyin.com	<a href="http://www.eheyin.com/">www.eheyin.com/</a>
Hucais	<a href="http://www.hucais.com/">www.hucais.com/</a>	ZhonghaoZiyun	<a href="http://www.11ziyun.com/">www.11ziyun.com/</a>
kaixinyin	<a href="http://www.kaixinyin.com/">www.kaixinyin.com/</a>	Xuan Cai	<a href="http://www.xuancai2008.com/">www.xuancai2008.com/</a>
FastPrint	<a href="http://www.92mp.com/">www.92mp.com/</a>	Duoduoyin	<a href="http://www.duoduoyin.com/">www.duoduoyin.com/</a>
wdxc.cn	<a href="http://www.wodexiangce.cn/">www.wodexiangce.cn/</a>	Xiangin	<a href="http://www.xiangin.cn/">www.xiangin.cn/</a>
Boxdiy	<a href="http://www.boxdiy.cn/">www.boxdiy.cn/</a>	Xiao Mei Ji	<a href="http://www.xiaomeij.com/">www.xiaomeij.com/</a>
art2print.cn	<a href="http://www.art2print.cn/scene">www.art2print.cn/scene</a>	huluwa360	<a href="http://www.huluwa360.com/">www.huluwa360.com/</a>
LVAI	<a href="http://lvaifood.1688.com">lvaifood.1688.com</a>	suyinw.cn	<a href="http://www.cailuan.cc/">www.cailuan.cc/</a>

Source Keyin.cn (<http://www.keyin.cn>), top 20 online digital printing companies in China in 2017

This research analyzed 69 websites involved in some degree of W2P transactions and services, including 22 US companies, 22 Taiwanese companies, 20 China mainland companies, 4 UK companies, and 1 Hong Kong printer. The study evaluated the most well-known 10 websites in all regions and shows their major functions and services in regards to customized W2P services in Table 3.

**Table 3.** Evaluation and comparison of the platform functions and services offered by top 10 W2P companies

Platform/items	1	2	3	4	5	6	7	8	9	10
<i>A: Main page</i>										
Search	●	●	●	●	●	●	●	●	●	●
Language	●	-	-	-	-	●	●	●	-	-
Free shipping on order	-	●	●	-	-	-	●	-	●	-
Live chat	●	●	●	●	-	●	●	-	-	●
Email inquiry	●	●	-	●	-	●	●	●	●	●
Customer hotline	●	●	●	●	●	●	●	●	●	●
Consignment	-	-	-	●	-	-	-	-	-	-
Shopping cart	●	●	●	●	●	-	●	●	-	●
Promote code	●	●	-	-	●	-	●	-	-	-
News	●	●	●	●	●	●	●	●	●	●
Best seller	-	●	●	●	●	-	-	-	●	●
Season promotion	●	●	●	-	-	●	-	●	●	●
Feature product	●	●	●	●	●	●	●	-	●	●

(continued)

**Table 3.** (continued)

Platform/items	1	2	3	4	5	6	7	8	9	10
Customized products for event	●	●	-	●	●	-	●	-	-	-
Office supplies/clothing/bags etc.	●	●	●	●	●	-	●	-	-	●
Upload your design	●	●	●	●	●	●	●	●	●	●
Design service	●	-	●	●	-	-	-	-	-	●
Customer reviews	●	●	●	-	-	-	-	-	●	●
Contact us	●	●	●	-	●	-	●	●	-	●
Artist/celebrity endorsement	-	●	-	-	-	-	-	-	-	-
Refer a friend	●	●	-	-	-	-	-	-	-	-
Mobile App	-	●	-	●	●	●	●	-	-	-
Average customer ratings	●	●	●	-	-	-	-	-	-	●
Customer product photos	●	●	●	-	●	-	●	●	-	-
<i>B: Member account/services</i>										
Account tools	●	●	●	●	●	●	●	●	●	●
View order history	●	●	●	●	●	●	●	●	●	●
Reorder	●	-	-	-	-	-	-	-	-	-
Update account settings	●	●	●	●	●	●	●	●	●	●
Stored payments	●	-	-	-	●	-	-	-	-	-
View recent communications	●	-	-	-	-	-	-	-	-	-
My images and logos	●	●	-	●	●	●	●	●	-	●
My favorites	●	●	●	●	-	-	-	-	-	-
Business e-mail	●	-	-	-	-	-	-	-	-	-
Domain names	●	●	-	-	-	-	-	-	-	-
<i>C: Products/services</i>										
Postcard mailing	●	●	-	-	-	-	-	-	-	-
Design re-creation service	●	-	-	●	-	-	-	-	-	-
Graphic design services for customers	●	-	●	●	-	-	-	-	-	●
Product and package design service	●	-	●	●	-	-	-	-	-	-
Email marketing	●	-	-	-	-	-	-	-	-	-
Local listing	●	-	●	●	-	-	-	-	-	-
Social media marketing	●	-	-	-	-	-	-	-	-	-
Browse our designs	●	●	●	●	●	-	●	-	-	●
Upload your own complete design	●	●	●	●	●	●	●	●	●	●
Design yourself	●	●	●	●	●	-	●	-	-	●
Gift certificates	●	-	-	-	-	-	-	-	●	-
<i>C: Products/services</i>										
Personalized mugs	●	●	●	●	●	-	●	-	-	●
Holiday cards	●	●	●	●	●	●	●	●	●	●
Canvas prints	●	●	-	●	●	-	●	●	-	●
Phone cases	●	●	●	-	●	-	●	-	-	-
Clothes (e.g. T-shirt)	●	-	●	-	●	-	-	●	-	●
Puzzles	●	●	●	-	-	-	●	-	-	-

(continued)



### 4 Conclusions

The data analyses showed that customized W2P became a hotly debated topic in the industry 10 years ago. Nevertheless, only about 11 printing companies in Taiwan that started to provide W2P services; the market share is relatively low. The expert interviews revealed that many print business owners hold a pessimistic view toward customized W2P services. The overall results show that the technologies of traditional plate-making and ink-paper printing are highly mature among conventional printers while information flow, human resources, marketing and management, and software and hardware are relatively lacking. However, the integration of the front-end information flow design and the back-end database are inextricably intertwined to me-commerce in W2P platforms. Companies interested in developing such services can focus on improving the three aspects: information flow, human resources and marketing management. During the interviews, it was found that there is an absence of IT engineers and data analysts in the majority of W2P businesses. But it is not easy to train and recruit these professional talents. The study suggests that printers cooperate with IT specialists and designers/artists to develop a partnership model that is beneficial to all and makes resource and profit sharing possible.

Figure 1 provides suggestions to conventional printers, front-end designers, and IT specialists to cooperate together and share a business model.

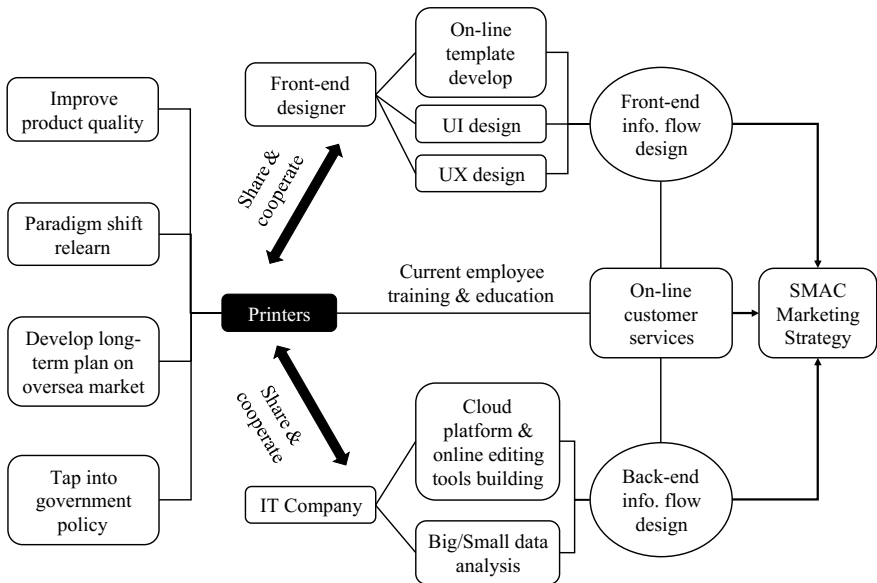


Fig. 1. Suggestions to printing businesses (by authors)

**Acknowledgements.** The study wishes to express a great amount of gratitude to the printing experts and educators who participated in the study and provided valuable opinions and suggestions.

## References

1. Hsieh, Y. C. (2017). The new blue sea for printing media—From online printing to cloud customization e-commerce. In *2017 IC Annual World. Congress & 8th China Academic Conference on Printing and Packaging*.
2. Business.com. (2015). Business card printing review: Make a lasting impression. <http://www.toptenreviews.com/services/internet/best-online-printing-services>. Accessed November 02, 2015.
3. Keyin.cn. (2017). 2017 Top 20 e-commerce printing companies in China. <http://www.keyin.cn/special/spcexp/201703/07-1103050.html>. Accessed March 07, 2017.
4. Hsieh, Y. C., & Lin, H. S. (2011). The functions of online printing tools and workflow. *China Packaging and Printing Magazine*.



# Study of Cultural Creative Merchandises of Museums and Cultural Heritage

Mingchw Wei<sup>1</sup>(✉), Tzuhan Chen<sup>2</sup>, and Yungcheng Hsieh<sup>2</sup>

<sup>1</sup> Graduate School of Creative Industry Design, National Taiwan University of Arts, New Taipei, Taiwan  
ntua10070801@gmail.com

<sup>2</sup> Department of Graphic Communication Arts, National Taiwan University of Arts, New Taipei, Taiwan

**Abstract.** The promotion of sustainable culture heritage, the increasing need of aesthetics, knowledge, and economic growth are all direct contributors to the fact that Museums have become a viral trend not only in Taiwan but also in China in recent years. However, many museums host Cultural Creative Merchandises without proper adjustments to their targeted audience. The priority of quantity over quality is noticeable, leaving visitors unsatisfied. This thesis uses questionnaires to analyze the visitor's consuming patterns in museums, including questions about environmental design, product design and service design in order to understand the preferences of customers. It is hard for consumers to acknowledge the cultural meanings of the merchandises, leading to possible dissatisfaction. However, the consumers tend to approve with the arrangements made within the exhibited space, visiting route and lighting. Therefore, museums should emphasize on promoting culture and combining historical facts with interactive and intuitive elements when designing Cultural Creative Merchandises to maximize the effects of learning through entertainment.

**Keywords:** Museum · Cultural creative merchandise · Consumer behavior · Cultural heritage

## 1 Introduction

### 1.1 General Background Information

Museums enjoy rising popularity in China and Taiwan, partly due to the governments. The government's interest stems from the growing economy and cultural awareness of preserving intangible cultural heritage, knowledge, aesthetics surrounding the museums. Being the main group investing in cultural artwork, middle class is eager raising their cultural and aesthetic knowledge. Therefore, visiting museums is a way of learning through entertainment. The souvenir shops in museums in western countries usually name themselves "The last exhibition hall", which suggests that Cultural Creative Merchandises are ongoing and continue to expand the topic at hand even after the exhibition. As a result, Cultural Creative Merchandises can act as products to preserve and continue culture.

## 2 Literature Review

### 2.1 Cultural and Creative Industry

According to a report “The Globalization of Cultural Trade: A Shift in Consumption” and a survey “Cultural times”. The First Global Map of Cultural and Creative Industries” [1] done by United Nations Educational, Scientific and Cultural Organization (UNESCO) [2], in 2013, Cultural and Creative Industries have created 2250 billion US dollar revenues which is about 3% of World GDP and the industries have created 29.5 million jobs worldwide. It shows that the contribution of Cultural and Creative Industries (CCI) have made them become the backbone of the world economy; the CCI are major economic assets in developed and emerging countries.

The definition of Culture Industry by UNESCO is “the combination of creation, production and distribution of goods and services that are cultural in nature and usually protected by intellectual property rights” [2]; Cultural and Creative Industries can be seemed as creative industries that include music, textual, television and film production and cultural tourism that adds value to content and generates values for people and the societies [3].

### 2.2 Museum Cultural Creative Merchandise

The definition of Cultural Creative Merchandises by UNESCO is: Cultural Creative Merchandises include the goods and services; Cultural Creative Merchandises are defined as consumer goods that convey ideas, symbols and lifestyles. Cultural services are activities that satisfy cultural interests or needs. It does not represent the actual product itself.

### 2.3 Cultural Heritage

Cultural heritage demands cooperation between a government and its people. Through language, art, history and literature, it's possible to spread culture as people get together and socialize. Museums play an important role of carrying and continuing culture by offering cultural collections. Museums also offer customers to purchase merchandise of the exhibition and blend into their daily life at home. Interactive design is essentially the best medium for cultural heritage.

## 3 Method

### 3.1 Research Method

This research paper is using content analysis method to compile information about Cultural Creative Merchandises and continuing cultural meaning as research topic. We further developed questionnaires based on the information that we gathered. The questionnaires were targeting tourists who have been to the National Palace Museum in either China or Taiwan. The questionnaires were sent out between May 1st to May 15th



2018; we have gotten 112 sets of feedbacks from Chinese tourists and 99 sets from Taiwanese tourists.

### 3.2 Research Analysis

The willingness of customers to purchase things at souvenir store has a lot to do with the design of space, the environment of the store, the design and the presentation of the products, the lightings, the flow, and the service. This research contains surveys about the design of the space, product design, and marketing management to determine whether Cultural Creative Merchandises can continue the culture by analyzing the purchasing behaviour of customers.

#### 3.2.1 Descriptive Statistics

Customers' age is ranging from 19–25 years old, 42 people in total; 46–55 years old have 19 people in total; 26–35 years old have 17 people in total; 36.45 years old have 16 people in total; 56–65 years old have 2 people in total; and there's one person who is under 18.

Occupational wise, the major consumers are students, 32 students in total; the rest being service sector for 13 people; other for 12 people; government employees for 10 people; manufacturer and freelancer for 8 people; information industry for 5 people; advertising design for 3 people; art industry for 2 people; financial industry and medical professional for one person.

Monthly income: 45 of the participants have 5500 RMB income; 17 of the participants have 22,001–35,000 RMB income; 16 of the participants have 35,001–50,000 RMB income; 11 of the participants have 50,001–65,000 RMB income; 8 of the participants have 65,001–10,000 RMB income; 1 of the participants has above 10,000 RMB income.

#### 3.2.2 Reliability Analysis

Upon 210 questionnaires of reliability analysis, the value of Cronbach's Alpha is 0.983 which is high in three aspects in general.

#### 3.2.3 Design of Space

A product is seemed as something that can be provided to the market and satisfies the needs of consumers [3]. Products can include the actual objects, services, people, locations, experiences, information, organizations and thoughts. When it comes to Cultural Creative Merchandises, many focuses on selling and developing; they ignore the design of space. The place where products are being presented is equally important to the design of the products; it influences the customers' decision making and their satisfaction. The souvenir shops have the nickname of "the last exhibition of the museum" which means that it is not just a place to sell goods but also a place for people to relive what they just experienced from the museum. The design and the flow of the space play a crucial part of making the last exhibition complete.

1. I believe that the space of souvenir shop is comfortable
2. I believe that the flow of souvenir shop is smooth and clear

3. I believe that the environment of souvenir shop is too loud
4. I believe that the souvenir shop has clear and reasonable price tags.

### 3.2.4 Product Design

Cultural Creative Merchandises need to stand out among all the products in a museum souvenir shop. A well-designed product, first of all, needs to fit the image of the museum it is in so that it can be distinguished from other museums out in the world [4]. Then it needs to contain cultural meaning which is what we have been talking about. Cultural Creative Merchandises should be all about conveying and continuing cultural meaning even after customers leave the museum [5]. Moreover, in order to boost the purchase, products need to be unique to attract people. At current market, products are similar, nothing really stand out to people which reduce the possibility of purchasing. Making a practical and unique product is not easy; as people values quality more, they expect a product to contain not only historical and cultural meaning but also the design has to be at certain level.

1. I believe that souvenir shops in museums convey the traits of the museums
2. I believe that Cultural Creative Merchandises have decent packaging
3. I believe that Cultural Creative Merchandises have contemporary design
4. The design of Cultural Creative Merchandises fits my preferences
5. I believe that Cultural Creative Merchandises cannot relate to the original objects that they are trying to replicate
6. Most people believe that souvenir shops represent and deepen the image of a museum, however the design of its Cultural Creative
7. Merchandises do not necessarily represent the same way which makes consumers being reluctant on purchasing products from the souvenir shop.

### 3.2.5 Marketing Management

According to American Marketing Science Institute, customers' satisfaction depends on not only products but also service quality [6]. In other words, product and service quality, customer satisfaction and company profitability are intertwined; higher level of quality leads to higher level of customer satisfaction. Some people believe that service quality is about whether or not customers would want to revisit based on how they are being served; however, in customers' point of view, service quality is about what they presume they would get from a service and what actually happens. Therefore, it is crucial to know what customers really want in order to provide a higher quality of service. To apply this concept in Cultural Creative Merchandises, having a clerk who knows product's design, meaning and what a product is supposed to convey is what I would consider as high quality of service. In some surveys show what in terms of giving information about Cultural Creative Merchandises; clerks in museum souvenir shops are doing a good job based on the positive feedbacks from the customers.

## 4 Result and Recommendation

One of the responsibilities for modern museums nowadays is to promote Cultural Creative Merchandises. A modern museum is no longer just about education but more of an entertaining educational process. Cultural Creative Merchandises not only carry historical value but also continue the culture. As recent surveys show, consumers generally lack interest in Cultural Creative Merchandises as the meaning and need of said product is unclear. However, the surveys also featured some feedback regarding the space, flow and lighting of a souvenir shop to improve it. We generated some recommendations according to the received feedback.

### 4.1 Presentation of Cultural Meaning

Cultural Creative Merchandise represent a museum and they reflect certain period of history in a museum. In order to represent the theme at hand, products need to be specifically designed to appeal to the target customers to see the value in it. While the production process isn't difficult, the creative development is rather complex and needs consideration for historical meaning and creativity.

### 4.2 Design of Cultural Creative Products

Cultural Creative Merchandise in a museum are mostly replicas or slightly reskinned versions due to lack of thoughtful design and originality, leading to a product that barely stands out and isn't anywhere unique. Therefore, museums need to improve their use of creativity in design, development and promotion of their merchandise.

### 4.3 Usability of Products

Other than the design, the practical usability is another thing designer need to pay attention to when developing their Cultural Creative Merchandise. Products with high usability receive higher satisfactory feedback and customers are therefore more willing to make a purchase, resulting in an educational and cultural souvenir which also has a practical aspect.

## References

1. EY. (2015). *Culture times—The first global map of culture & creativity industries*. United State: CISAC.
2. *The globalization of culture trade: A shift in consumption, 2004–2013*. United State: UNESCO Institute for Statistics.
3. Lee, C.-F., Lan, C.-C., & Wang, S.-H. (2016). Exploring the effects of cultural creative product quality toward perceived value and purchase intention, pp 210–219.
4. Li, J. C. (2016). What is a good museum product? *Museum Studies*, 35(4), 132. Accessed December 2009, Taipei.
5. Li, J. C., & Ho, M. C. (2009). Rethinking about the cultural products of a museum: Perspectives across disciplines.
6. Philip, K., & Kevin, L. K. (2013). *Marketing management*. Pearson.



# Implementation of Responsive Web Page Layout Based on Media Query and Flexible Box Model

Jingru Zhang<sup>(✉)</sup>, Caifeng Liu<sup>(✉)</sup>, and Aibin Huang

School of Media and Design, Hangzhou Dianzi University, Hangzhou, China  
1204451958@qq.com, lcf88089135@126.com

**Abstract.** At present, there are various types of mobile terminal devices on the market, and their screen resolutions also vary widely. How to make web pages adapt to different screen resolutions and provide users with a better browsing experience is a problem of web page layout which is urgent to be solved. This paper analyzes and elaborates the current commonly used methods to solve the problem of web page adaptation and their existing deficiencies. Then, aiming at these deficiencies, we put forward a novel mode of responsive web page layout, which uses the media query technology and flexible box model to solve the problem of web page self-adaptation and verify its feasibility and effectiveness through the practice based on this mode.

**Keywords:** Media query · Flexible box model · CSS3 · Responsive web page layout

## 1 Introduction

By December 2017, the number of mobile phone users in China reached 753 million, accounting for 97.5% [1]. Mobile devices have gradually exceeded desktop devices and become the most common terminal for accessing the Internet. But the screen resolution of mobile devices varies widely, which makes the PC-based fixed layout web pages once migrated to the mobile, the pages tend to be messy. It brings bad browsing experience to users.

Previously, there are two main solutions to this problem. First, different website versions are designed for different devices. This scheme can guarantee the browsing effects on different terminals, but maintaining multiple website versions greatly increases the costs. Second, mobile phone browser's automatic transcoding function is used to transcode web pages, enlarging the texts and reducing the size of pictures. But it lacks flexibility and is not suitable for all web pages.

Today, the new CSS3 standard provides a better solution for responsive web page layouts. With media query technology and flexible box model of CSS3, web pages can automatically adjust the layout according to the screen resolution, showing satisfactory results on various devices.

## 2 Key Technologies

The concept of responsive web design was first proposed by Ethan Marcotte. It is an intelligent method that can be used to adjust web page layouts based on user behavior and the device environment used. Media query and flexible box model are two key technologies of implementing responsive web page layout in this paper.

### 2.1 Media Query Technology

Media query Technology allows us to set different CSS styles according to the characteristics of device monitor (such as window width, device orientation, etc.) [2]. Media query consists of a media type and one or more conditional expressions that detect the characteristics of the media. The syntax structure is as follows:

```
@media [only | not] media type and (media characteristics) {style code}
```

Currently available media types include: all (for all devices), screen (for computer, tablets, smartphones, etc.), print (for printers and print previews), and speech (for screen readers, etc.).

The media characteristics include width, height, color, etc. And using max/min as the logical judgment. For example, “max-width: 800px” means that the style codes are valid when the width of media type is less than or equal to 800px.

### 2.2 Flexible Box Model

Flex box is a new layout mode introduced by CSS3. The traditional layout method is based on the box model, it has some limitations in realizing some special layout [3]. Flexible box model can easily and responsively realize various page layouts, and may become the preferred scheme of responsive web page layout in the future.

Flexible box model consists of flexible containers and flexible items. The main idea of the flexible box model is to allow the container to have the ability to change the width, height, or even order of its child elements, and fill the available space in an optimal way to adapt to all types of display devices and screen sizes.

## 3 Implement Ideas of Response Web Page Layout

### 3.1 Resolution Adaptation of Terminal Devices

The resolution adaptation of terminal devices means let the web pages maintain a consistent or more coordinated browsing effect which closest to the user experience at different resolutions. The core is to choose a font size that is closest to the intuitive comfort of humans as the reference for different resolution devices, and the size of other elements (such as line height, text spacing, etc.) are defined by the relative ratio

(em) of this reference. This paper uses media query technology to set font size references for devices with different resolutions, for example:

```
@media only screen and (max-width: 667px) {html {font-size: 14px}}
```

### 3.2 Prototyping of Web Page Layout

This paper uses a news web page for hydropower station website as an example to make an overall layout prototype.

First of all, determine device types that need to be compatible. And then, make prototypes based on the first step.

Figure 1 shows the webpage layout prototypes, which used in this paper, for PC, tablet and smart phone respectively. In the process of making prototypes, it is necessary to pay attention to the changes of page layouts and the scaling of contents for different device terminals and screen sizes [4].

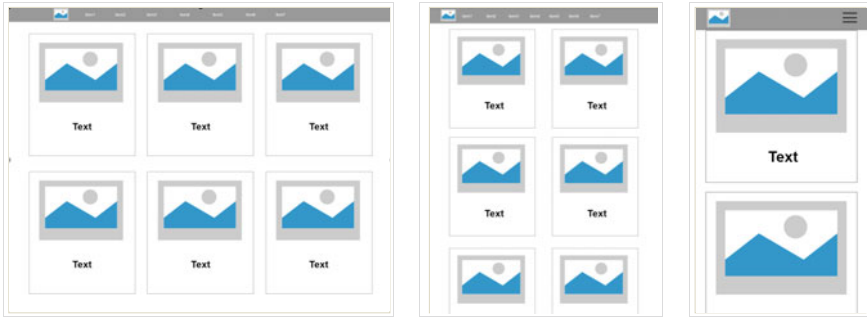


**Fig. 1.** The layout prototypes of a news web page for PC, tablet and smart phone

### 3.3 Implementation

After finishing the overall layout prototypes, we use flexible box model and media query technology to layout elements in each area of the webpage.

Firstly, adding the “viewport” meta tag. It is added to the <head> tag of the HTML document to be compatible with mobile devices. The commonly used “viewport” meta tag for mobile web page is as follows:

```
<meta name=“viewport” content=“width=device-width, initial-scale=1.0”>
```

Using “width=device-width” to set the width of the visible area to the physical width of the terminal device’s screen, “initial-scale” sets the scaling ratio of the page for the first load, the default setting is 1.

Secondly, designing HTML structure. According to the prototypes designed above, the page layout used in this paper is a common two-column layout, which is divided into navigation area and information display area. The codes are as follows:

```

<body>
  <div id="navigation" class="navbar">
    <ul>
      <li>...</li>
      .....
    </ul>
  </div>
  <div id="content" class="container">
    <section id="one" class="item"> ...</section>
    .....
  </div>
</body>

```

Here only shows a simple HTML structure, in the actual development, we need to add image and text tags between <section> and </section> tags.

Thirdly, setting up the flex container. Setting the element's (class name is "container") display attribute to "flex" to make it a flexible container. The codes are as follows:

```

.container {
  display: -webkit-flex; /* Safari, Chrome */
  flex-flow: row wrap;
}

```

"flex-flow: row wrap" indicates that the flexible items are arranged from left to right and when the items cannot be displayed in a single row, they will be arranged in another line.

Fourthly, processing images. Generally, an image in a web page has a fixed width and height. When scaling the browser window, the image don't scale with the window, it may cross other content of the page and affects reading. In this paper, the width of the picture is set by percentage to achieve flexible scaling to adapt to the pages with different widths. The codes are as follows:

```

img {
  width: 100%;
  height: auto;
  max-width: 100%;
}

```

Finally, setting Media Query Conditions. We need to judge the type of terminal devices through the media query conditions, according to the different width of terminals to run the corresponding CSS codes, so that the corresponding layout mode is

transmitted to different terminal devices, and finally implement the responsive layout. The codes are as follows:

```

@media only screen and (max-width: 667px) { /* Smart phone */
@media only screen and (min-width: 668px) and (max-width: 1024px) { /*
Tablet */
@media only screen and (min-width: 1025px) { /* PC */
    
```

Three breakpoints are set here. Each breakpoint has a maximum screen width or a minimum screen width. The specific values can be determined by the developer.

### 4 Application Example

This paper uses the scheme which combine media query technology and flexible box model to realize the responsive layout of a news web page for hydropower station website, and use Window Resizer, an extension program carried by Google Chrome, to simulate different screen resolutions for online testing. The test results are shown in following figures.

As Figs. 2 and 3 shows, compared with the traditional fixed layout, using our scheme can implement the free switching and smooth transition between different terminals of the web page, and provide users with more comfortable presentation interface and better browsing experience [5].

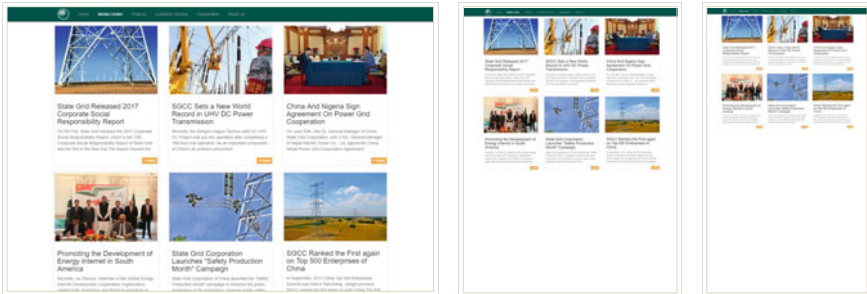


Fig. 2. Test results of PC-based fixed layout page on PC, tablet and mobile phone

And in Fig. 4, we can see that when the horizontal and vertical screens are switched, the page also exhibit good effects. In summary, this scheme based on media query technology and flexible box model is feasible and effective.



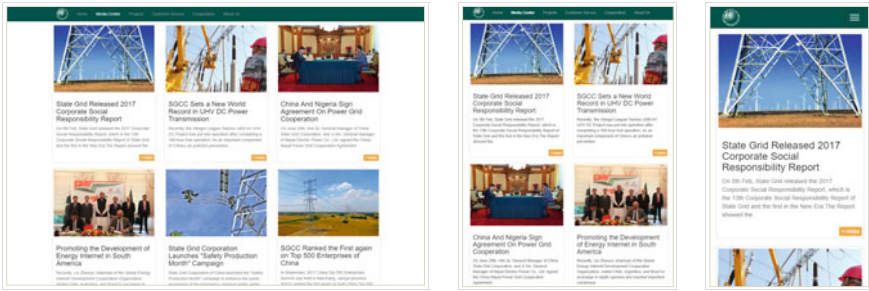


Fig. 3. Test results of responsive layout web pages on PC, tablet PC and mobile phone

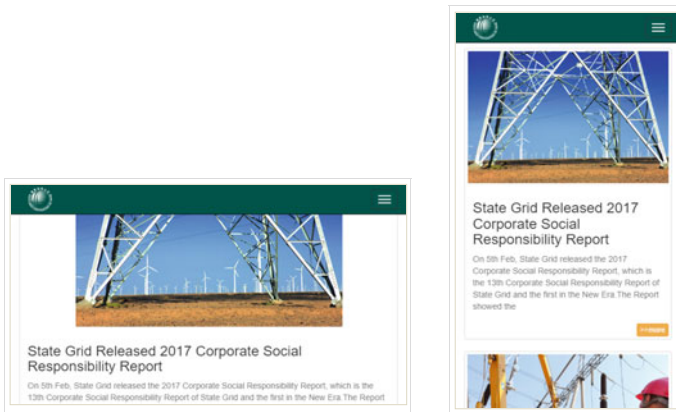


Fig. 4. Test results of horizontal/vertical screen

## 5 Summary

With the development of mobile network technology, terminal devices are continuously updated. And user experience occupies an increasingly important position in website design. This paper propose a new responsive web page layout model, and verify its feasibility and effectiveness through the implementation of the responsive layout of a news web page for hydropower station website. The example shows that this model can load web content flexibly, make full use of webpage space, enhance the readability of the page content, and have better user experience.

## References

1. CNNIC. (2018). The 41th statistical report on internet development in china. [http://www.cnnic.net.cn/hlwfzyj/hlwxzbg/hlwtjbg/201803/t20180305\\_70249.htm](http://www.cnnic.net.cn/hlwfzyj/hlwxzbg/hlwtjbg/201803/t20180305_70249.htm).
2. Feng, X., Hong, D., Luo, J., & Suo, Z. (2016). Key technologies of responsive web design. *Journal of Computer Applications*, 36(S1), 249–251, 256.

3. Lin, W., Lin, W., & Liu, L. (2012). Cross-platform mobile application interface layout based on flexible box model. *Journal of Soochow University*, 32(05), 22–26. (Engineering Science Edition).
4. Yang, Y., Chen, L., & Dong, Q. (2013). The design and technical implementation of responsive web mobile learning resources. *Modern Educational Technology*, 23(06), 107–111.
5. Ye, C., & Ma, L. (2018). Design of responsive layout web page based on HTML 5+CSS3 +jQuery. *Journal of Wuzhou University*, 28(03), 22–35.

**Part IV**  
**Printing Engineering Technology**



# Effect of Pretreatment Methods to Cotton Fabrics on Printing Conductive Patterns

Meijia Yan, Zhiqing Xin<sup>(✉)</sup>, Shouzheng Jiao, Feilong Li,  
and Luhai Li

Beijing Institute of Graphic Communication (BIGC), Beijing 102600, People's  
Republic of China  
zhiqingxin@iccas.ac.cn

**Abstract.** E-textiles have been paid wide attention due of popularization of wearable devices, and its core is the preparation of conductive lines on the fabric surface. In this paper, conductive lines are quickly formed on the surface of cotton fabrics by means of screen-printed conductive inks. The effects of pretreatment methods such as alkali soaking of cotton fabrics, plasma and transparent slurry on the penetration of ink on fabric surface are studied. And the conductivity, water resistance of the patterns printed on the cotton fabric substrate are tested. The results show that the conductive pattern printed after the plasma treatment has the best conductivity, sheet resistance is 120.8 m $\Omega$ /square; the conductive pattern printed after the transparent slurry treatment is 134.8 m $\Omega$ /square; the conductivity after alkali soaking treatment is the worst, and its sheet resistance is 253.8 m $\Omega$ /square, which is even lower than the conductivity of the untreated conductive pattern. This study provides a new direction for the flexible integration of electronic components and textiles in electronic smart textiles.

**Keywords:** Cotton fabrics · Pretreatment · Smart textiles · Fabric properties

## 1 Introduction

Smart textiles can sense the changes that occur in the external environment or internal state, respond to the material itself or some external feedback mechanism, and can adjust itself to adapt to changes in the external environment [1]. Electronic smart textiles are a special class of smart textiles. They are not only electronic components and electronic circuits combined with textiles, but they are based on electronic technology and apply high-tech means such as sensing, communication, and artificial intelligence to textiles. Conductive fabrics can be used as a capacitor, sensor, heater, etc. [2]. Electronic textiles have been applied to medical, military, sports and entertainment. The key of electronic textiles is the preparation of the conductive line on the surface of the fabric. The methods reported at present are usually realized by the method of weaving or covering conductive silver paste to modify the fabric [3].

Conductive silver paste can quickly form conductive patterns on the surface of cotton fabrics by screen printing, which provides a new direction for solving the problem of flexible integration of electronic components and textiles in electronic smart textiles. However, the fabric belongs to flexible material with a porous structure and a

high rough surface, which causes the conductive silver paste penetrate and diffuse in the fabric, thus seriously affect the printing quality [4, 5]. This topic explores the effects of pretreatment on the penetration of micron silver conductive ink on the surface of fabrics by pretreating different methods of cotton fabric substrates, including alkali soaking of cotton fabrics, plasma and transparent slurry. The conductivity, water resistance and other properties of printing patterns are tested.

## 2 Experimental

The ink used is obtained by liquid phase chemical reduction of PVP, hydrazine hydrate and silver nitrate. Cotton fabrics are pretreated with A.R. NaOH (Beijing Chemical Reagents Co), ZY-8200B transparent slurry (Dongguan Zhongyin Printing Materials Co) and DT-025 plasma processor (Suzhou Opus Plasma Technology Co). Morphology is characterized using UCMOS05100KPA optical microscope (Suzhou Jingtong Instrument Co). Conductivity is characterized using an RTS-9 Square resistance tester. Screen plate used for the experiment is 250 mesh (Beijing Yingmai Wire Mesh Equipment Co).

### 2.1 Pretreatment

#### 2.1.1 Alkaline Treatment

3 pieces of 20 cm × 5 cm cotton fabric (plain weave) are taken, then invaded into 3 groups completely immersed in 100 mL NaOH solution with a concentration of 60 g/L, and soaked for 1, 2 and 3 h respectively. Removed, rinsed repeatedly with deionized water and dried by high temperature.

#### 2.1.2 Plasma Treatment

Nine pieces of cotton fabric are treated with plasma at 100, 200, and 300 w different powers for 60, 180, and 300 s.

#### 2.1.3 Transparent Pulp Treatment

The transparent slurry is applied to the screen plate, and the transparent slurry is printed on the cotton fabric with a squeegee knife. It is dried in an oven at a temperature of 130 °C for 180 s.

### 2.2 Screen Printing Conductive Pattern

The printed materials are pure cotton flat woven fabrics (20 cm × 5 cm), which are subjected to test printing before the official printing. The printing condition parameters of all samples are determined, in other words, all pretreated cotton fabrics are screen printed under the same conditions. The printing pattern is dried for 30 min in an oven at a temperature of 60 °C.

## 2.3 Performance Testing

### 2.3.1 Surface Resistance

Make sure the sample is connected to the probe. Record the measured value and repeat at least 3 times, we all think that the average is more accurate. Sheet resistance is only related to the thickness of the conductive film layer.

### 2.3.2 Morphology Test

A low-power microscope under the magnification of 5 times is used, randomly measure the width of the line at the 5 positions of the sample and compare the average values. Surface structure of conductive patterns printed on cotton fabrics was observed and studied by optical microscope. The change of surface morphology of cotton fabrics after different pretreatment modification methods and the bonding state between conductive silver paste and cotton fibers were analyzed.

### 2.3.3 Water Resistance Test

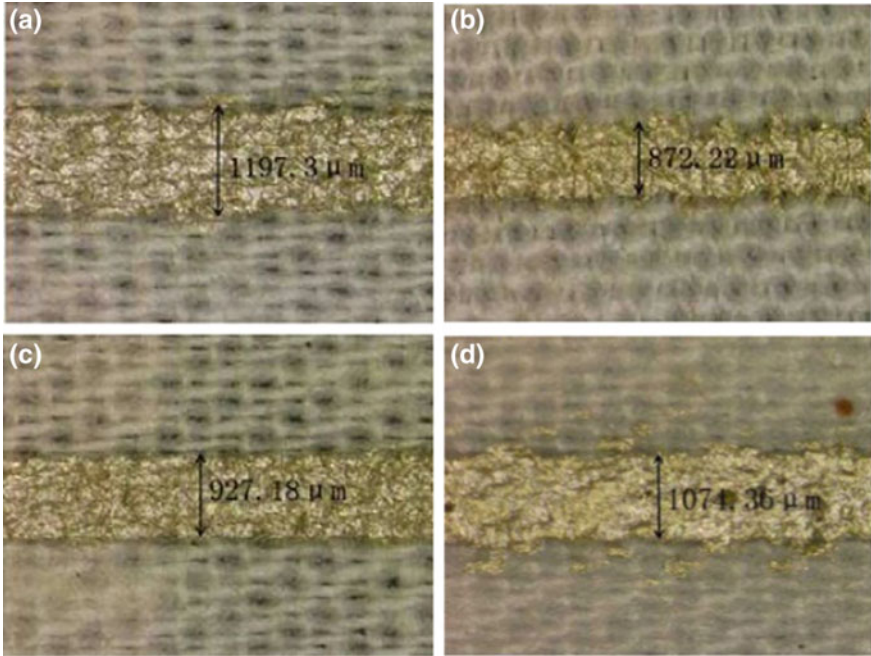
Samples of the conductive pattern are taken, one surface is coated with liquid which the main component is fluorosilane, and the other is untreated. They are continuously soaked by water all a day, dried, and then compare the difference of their conductivity [6].

## 3 Analysis

### 3.1 Pattern Morphology Due to Different Pretreatment Methods

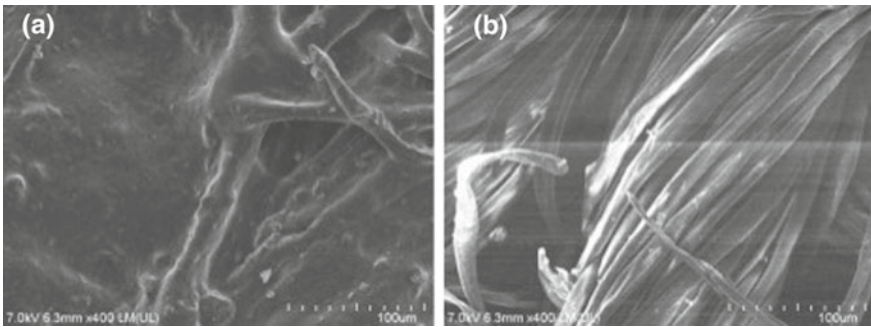
Printing plate is set as 800  $\mu\text{m}$  line width, and under the same conditions, conductive ink is printed on differently treated cotton fabrics, and the width of the lines is tested. As shown in Fig. 1, the diffusion of the conductive pattern without pre-treatment is the most serious, the line width is 1197.3  $\mu\text{m}$ , which is 49.7% higher than the line width of the printing plate; the alkali-treated conductive pattern has the smallest penetration diffusion, and the best soaking time is 2 h, the line width is 872.22  $\mu\text{m}$ , which is 9% higher than that of the printing plate; the diffusion and infiltration by plasma treatment is the second highest. Through Fig. 2, it can be seen that the optimal power for plasma treatment is 200 W and the time is 60 s. The width is 927.18  $\mu\text{m}$ , which is 15.9% higher than that of the printing plate. The diffusion phenomenon caused by the transparent slurry is more serious. The line width is 1074.36  $\mu\text{m}$ , which is 34.3% higher than the plate width.

According to the width of the measured line, the growth rate curve of the width of the pattern line is wider than the line width of the printing plate. The growth rate of the line width of the pattern printed after pretreatment compared with the line width of the printing plate, the growth of the alkali treatment is the smallest, and the growth of the transparent slurry treatment is the largest. After the immersion of the cotton fabric, the voids between the fibers are reduced, which reduces the penetration and diffusion of the ink. The plasma treatment leads to polymerization graft reaction which increasing adhesion of silver paste to substrate; The cotton fabric gap is filled with transparent slurry and a smooth transparent film is formed on the surface of the cotton fabric. Under the effect of pressure, the ink cannot penetrate and spread to both sides, resulting



(a) raw cotton fabric (b) alkali treatment (c) plasma treatment (d) transparent glue primer

**Fig. 1.** Patterned lines printed after pretreatment by different methods



(a)Before

(b)After

**Fig. 2.** Optical microscopy images of fabric with transparent slurry pretreatment

in the largest change rate of the line width. Figure 2 shows the SEM of the fabric surface before and after transparent slurry treatment.

### 3.2 Conductivity Due to Different Pretreatment Methods

Conductive pattern covering on the surface of the original fabric measured sheet resistance is 209.4 mΩ/square, which is reflected by the different methods. The

conductive pattern after plasma treatment has the best conductivity, and its sheet resistance is 120.8 mΩ/square. The plasma treatment etches the surface of cotton, increases adhesion of silver paste to substrate, thus forming a thick ink layer. Conductive pattern printed after the transparent slurry treatment is not bad, and the sheet resistance is 134.8 mΩ/square. The transparent slurry grinds the surface of the cotton fabric, the pores between the fabric fibers are filled with the transparent slurry, and the conductive ink is not easily penetrated fabric, a compact protective film generates. The conductivity after immersion treatment is the worst, and the sheet resistance is 253.8 mΩ/square, which is even lower than that of the untreated conductive pattern. The surface of the cotton fabric after soaking in the alkali solution has a fluffing phenomenon, and the conductive micro-silver particles are doped with fibers to prevent a good continuous conductive path from being formed.

### 3.3 Water Resistance Analysis

It is found that the conductive pattern coated with the liquid which the main component is fluorosilane has certain hydrophobic properties after immersion, and it is also found that the metal layer on the fluorosilane-coated conductive pattern is significantly more than uncoated, so the conductive pattern under these conditions has good mechanical fastness and good water resistance. Conductive performance test of the immersed conductive pattern shows that the conductive pattern coated with the fluorosilane coating liquid after being immersioned has little difference in conductivity from the no immersioned, and the conductivity is hardly affected. Table 1 shows the conductivity comparison of the conductive patterns treated by fluorosilane coating liquid.

**Table 1.** Conductivity of conductive patterns treated by fluorosilane coating

Treatment	Immersioned	No immersioned
Resistance (Unit: mΩ/square)	205.52	196.8

## 4 Conclusions

The alkali-treated conductive pattern has the smallest osmotic diffusion phenomenon, the diffusion phenomenon of transparent slurry treatment is relatively serious, and the diffusion phenomenon without pretreatment is the most serious. The conductive pattern printed after the plasma treatment has the best conductivity, and the processing condition is power 300 W, time 180 s, sheet resistance is 120.8 mΩ/square; the transparent slurry treatment is secondarily followed by conductivity, the sheet resistance is 134.8 mΩ/square; the conductivity after alkali soaking treatment is the worst, and its sheet resistance is 253.8 mΩ/square, which is even lower than the conductivity of the untreated conductive pattern; the conductive pattern coated with the liquid which the main component is fluorosilane has good water resistance and rub resistance.



**Acknowledgements.** This work has been financed by BIGC through Project: (04190118002/064), Course Construction Project (22150118005/003) and College Student Research Training Project (22150118022/077).

## References

1. Cherenack, K., Zysset, C., Kinkeldei, T., et al. (2010). Woven electronic fibers with sensing and display functions for smart textiles. *Advanced Materials*, 22(45), 5178–5182.
2. Yanping, W., & Weiguo, D. (2012). Application and development trend of electronic smart textiles. *Shandong Textile Science & Technology*, 53(3), 38–41.
3. Rossi, D. D., Carpi, F., Lorussi, F., et al. (2003). Electroactive fabrics and wearable biomonitoring devices. *Autex Research Journal*, 3(4), 180.
4. Periolatto, M., Ferrero, F., Montarsolo, A., et al. (2013). Hydro repellent finishing of cotton fabrics by chemically modified TEOS based nanosol. *Cellulose*, 20(1), 355–364.
5. Dahou, W., Ghemati, D., Oudia, A., et al. (2010). Preparation and biological characterization of cellulose graft copolymers. *Biochemical Engineering Journal*, 48(2), 187–194.
6. Yang, K., Torah, R., Wei, Y., et al. (2013). Waterproof and durable screen printed silver conductive tracks on textiles. *Textile Research Journal*, 83(19), 2023–2031.



# Research on Inkjet Printing Three-Dimensional Electrode Structure of Supercapacitors

Bo Cui, Fuqiang Chu<sup>(✉)</sup>, Jiazhen Sun, and Chenghu Yun

Key Laboratory of Green Printing & Packaging Materials and Technology in  
Universities of Shandong, School of Light Industry and Engineering, Qilu  
University of Technology, Jinan, Shandong, China  
fqchu@126.com

**Abstract.** Inkjet printing, as a flexible high-precision functional material deposition method, has been widely used in the preparation of supercapacitors. However, the inkjet printed electrode is usually a planar structure, which greatly reduces the applying performance of the prepared supercapacitor. In this research, the graphene oxide was composited with  $\text{AgNO}_3$  and dispersed ultrasonically in an aqueous solution to obtain an inkjet printing ink. By controlling the substrate temperature and the printing interval, layer-by-layer inkjet printing was performed on the substrate, and then three-dimensional electrode structures were prepared by vapor phase hydrazine reduction. Experiments show that when the substrate temperature is  $55^\circ\text{C}$  and the printing interval is 60 s, a uniform three-dimensional electrode is printed. The conductivity of the three-dimensional electrode is measured as  $2.9 \times 10^5$  S/m, and the specific capacitance is 89.6 F/g, the areal capacitance is 36 mF/cm<sup>2</sup>. The prepared three-dimensional electrode in this research can be applied to supercapacitors, which will have great significance for improving the applying performance of supercapacitors.

**Keywords:** Inkjet printing · Graphene composite materials · Three-dimensional electrodes · Supercapacitors

## 1 Introduction

Supercapacitors are electrochemical devices used to store electrical energy. Unlike secondary batteries and capacitors, supercapacitors can maintain high energy density at high power density, and they also have the advantages of rapid charge and discharge, long cycle life, and a wide range of operating temperatures. Therefore, supercapacitors are considered to be one of the energy storage devices that can be widely used in the future.

According to the energy storage mechanism, supercapacitors can be divided into double-layer supercapacitors that perform electrostatic adsorption on the surface of the double-layer electrodes, and pseudocapacitors that perform redox reactions on the surface of the electrodes [1]. This requires that the electrode has a large specific surface area to provide sufficient electrostatic adsorption or redox reaction points for the supercapacitor to store electrical energy. Graphene is a two-dimensional carbon

material of monoatomic thickness with a honeycomb lattice structure. And graphene has high conductivity, high theoretical surface area ( $2620 \text{ m}^2/\text{g}$ ), high theoretical specific capacitance ( $550 \text{ F/g}$ ) [2]. It is a very ideal electrode material for supercapacitors. However, graphene is difficult to disperse in water and easy to agglomerate. It is necessary to compound graphene with other materials in order to better exert the characteristics of graphene.

Supercapacitor electrode preparation methods include inkjet printing [3], photolithography [4], and electrochemical deposition [5], etc. Different from other preparation methods, inkjet printing is an additive manufacturing technology. By using inkjet printing, functional materials can be quickly deposited on a substrate to complete the patterning and assembly of the supercapacitor electrode. There is no material waste problem and the cost is low. However, the inkjet printed electrode is usually a planar structure, which greatly limits the application performance of the prepared supercapacitors.

In this work, we prepared inkjet inks by combining graphene oxide (GO) with  $\text{AgNO}_3$ , and then prepared a three-dimensional electrode by layer-by-layer inkjet printing. Finally, the three-dimensional electrode was reduced by hydrazine hydrate steam. The effect of print temperature, print interval, and print layer count on the print electrode was analyzed. At the same time, the compound situation of graphene/silver and the properties of printed three-dimensional electrodes were tested and characterized.

## 2 Experiment

### 2.1 Experimental Materials

Potassium permanganate, graphite powder, sulfuric acid ( $\text{H}_2\text{SO}_4$ ), hydrogen peroxide, silver nitrate ( $\text{AgNO}_3$ ), and hydrazine hydrate were purchased from Sigma Aldrich and used without further purification.

### 2.2 Preparation of GO/ $\text{AgNO}_3$ Composite Ink

GO was prepared by modified Hummer method. A  $3 \text{ mg/ml}$  aqueous solution of GO was sonicated for 30 min. Then  $\text{AgNO}_3$  was added to the GO aqueous solution and stirred. After the  $\text{AgNO}_3$  was completely dissolved, it was subjected to ultrasonic treatment for a period of time to obtain GO/ $\text{AgNO}_3$  composite ink.

### 2.3 Inkjet Printing Three-Dimensional Electrodes

The prepared GO/ $\text{AgNO}_3$  composite ink was put into an ink cartridge, and the composite ink was printed using a commercial Dimatix material printer DMP 2800 inkjet printer (Fujifilm Dimatix). In the printing process, three-dimensional electrodes were constructed by controlling the substrate temperature, printing interval time, and number of print layers, by layer-by-layer inkjet printing. Finally, the printed electrode was placed in the hydrated hydrazine vapor to be reduced.

## 2.4 Characterization

The crystal structure of the product was characterized by an automated X-ray powder diffractometer (XRD). The structural characteristics of the as-synthesized product were determined by transmission electron microscopy (TEM). Use a polarizing microscope to observe the uniformity of the printed electrode. Electrochemical performance of the electrodes was tested by a CHI 660 electrochemical workstation and a digital four-probe tester.

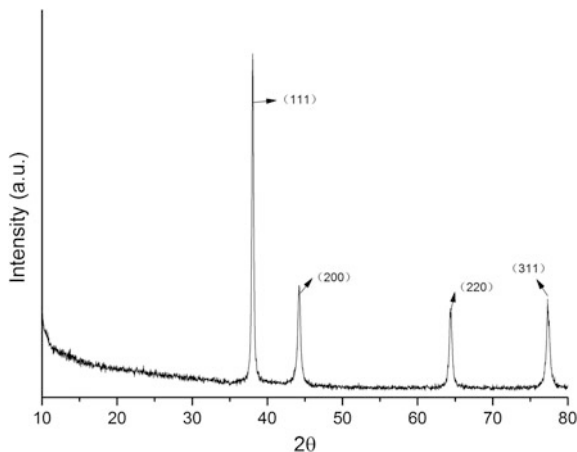
## 3 Results and Discussion

It is known that GO exhibits negative charge in the aqueous solution state due to numerous oxygen-containing groups on the sheet of GO, whereas silver ions exhibit positive charge in the silver nitrate solution. Therefore, the silver ions can be adsorbed on the GO sheet by electrostatic action. In the reduction process, since silver ions have strong oxidizability, silver ions are first reduced to nano silver, and then GO is reduced to graphene. The nano-silver particles can be evenly loaded onto the graphene sheets to prevent graphene from agglomerating.

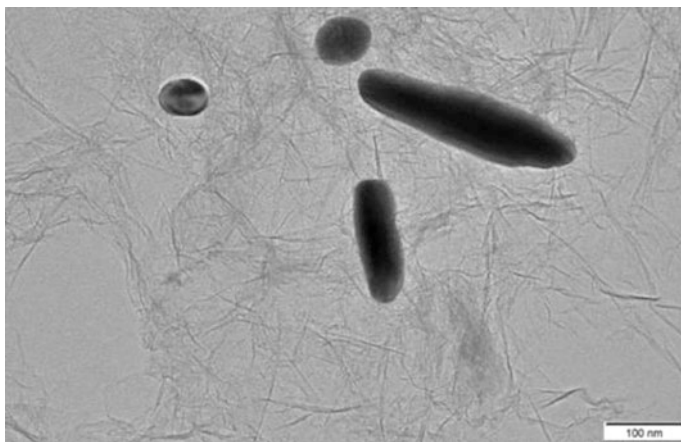
Figure 1 shows X-ray diffraction (XRD) analysis of graphene/silver composites. In the XRD, there are four distinct diffraction peaks at  $2\theta$  of  $38^\circ$ ,  $44.2^\circ$ ,  $64.4^\circ$ , and  $77.3^\circ$ . This corresponds to the face-centered cubic (111), (200), (220), (311) crystal planes of Ag, respectively, indicating that GO/AgNO<sub>3</sub> is successfully reduced to graphene/silver composite by hydrated hydrazine steam [6]. In addition, the appearance of high intensity peaks of the (111) surface indicates that non-spherical nanosilver particles may be present in the synthesized graphene/silver composite [7]. And the diffraction peaks of graphite or graphene do not appear in the XRD pattern of graphene/silver composites. This shows that in the prepared graphene/silver composite material, the silver particles are successfully loaded between the sheets of the graphene, preventing the agglomeration of the graphene [8].

Figure 2 shows a TEM image of a graphene/silver composite. From Fig. 2, it can be observed that the surface of the graphene has obvious wrinkles, which is beneficial to expand the specific surface area of the composite material. And the graph shows that the nanosilver is uniformly loaded on the graphene sheet. Those silvers are composed mainly of spherical particles of 60 nm and rod-like particles having a width of 50 nm and a length of 200–300 nm.

GO/Ag<sup>+</sup> aqueous solution was used as an ink to prepare a thin film electrode by layer-by-layer inkjet printing. In the experiment, the influence of printing temperature and printing interval on printed electrodes was analyzed. Experiments found that when the printing temperature is lower than  $55^\circ\text{C}$  or the printing interval is less than 60 s, the printed electrode are not uniform (Fig. 3a). This may be due to the print temperature being too low or the print interval being too short during the printing process. When the printing temperature is too low or the printing interval is too short, the ink droplets cannot dry completely. The undried ink droplets collect toward the center under the effect of surface tension. Then, the impact and surface tension of the newly printed ink droplets spread the undried ink droplets to the surroundings. Accumulated



**Fig. 1.** XRD patterns of rGO/Ag



**Fig. 2.** TEM images of rGO/Ag

in this way, the ink layer in the middle of the electrode will be thinner than the surrounding ink layer. When the printing temperature is 55 °C and the printing interval is 60 s, the ink droplets in each layer can be perfectly dried, and the printed electrodes will have good uniformity (Fig. 3b). Using this parameter, 40 layers were printed as electrodes, and the conductivity of the electrode was measured to be  $2.9 \times 10^5$  S/m.

On the basis of the thin-film electrode, three-dimensional cylindrical electrode was printed by layer-by-layer inkjet printing. Figure 4 shows the CV curves of three-dimensional electrodes measured in 1 M H<sub>2</sub>SO<sub>4</sub> electrolyte. As shown in Fig. 4, the graphene in the three-dimensional electrode provides double-layer capacitance, and the silver in the electrode provides a large number of tantalum capacitors through redox reactions. The specific capacitances of the electrodes are determined by CV using the following Eq. (1) [9]

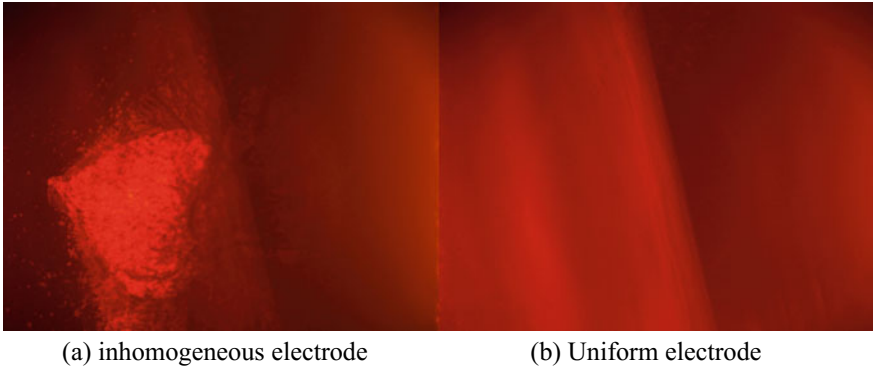


**Fig. 3.** Polarized light microscope images of printed electrode

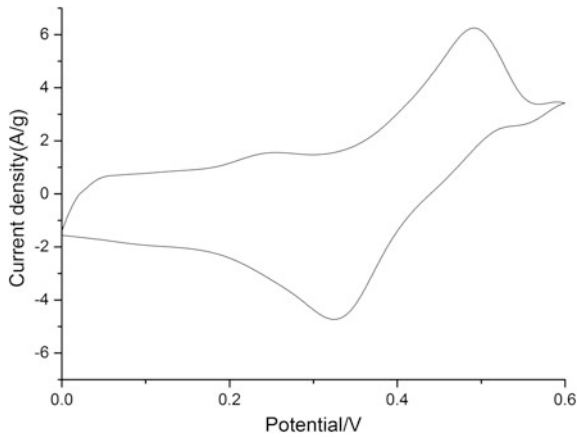


**Fig. 4.** CV curve of three-dimensional electrode

$$C_s = \frac{\int idv}{2m\Delta VS} \tag{1}$$

where  $C_s$  is the specific capacitance,  $\int idV$  is the integrated area of the CV curve,  $m$  is the mass of the electrode material in grams,  $\Delta V$  is the scanned potential window in volts, and  $S$  is the scan rate in volts per second. Based on the equation, the specific capacitance of the three-dimensional electrode is calculated as 89.6 F/g (at 10 mV/s). The value is greater than the specific capacitance of the pure graphene electrode (63 F/g at 10 mV/s) mentioned in the literature [9]. And the area capacitance of the three-dimensional electrode is 36 mF/cm<sup>2</sup> (at 10 mV/s), which is also greater than 13.6 mF/cm<sup>2</sup> (at 10 mV/s) in the literature [10].

## 4 Conclusions

In this work, GO/AgNO<sub>3</sub> aqueous solution is used as the ink, and hydrazine hydrate is used as a reducing agent. A three-dimensional electrode of a supercapacitor is prepared by a layer-by-layer inkjet printing method using a gas phase reduction method. The results show that a uniform electrode can be obtained when the printing temperature is above 55 °C and the printing interval is above 60 s. Next, it is confirmed that in the reduced rod-like and spherical nanosilver particles are loaded onto the graphene sheet by XRD and TEM, which successfully prevent the graphene from agglomerating. And the conductivity of the printed three-dimensional electrode is  $2.9 \times 10^5$  S/m, the specific capacitance is 89.6 F/g, and the areal capacitance is 36 mF/cm<sup>2</sup>.

**Acknowledgements.** This work is financially supported by the Government of Shandong Province (No. 2017GGX80105), which is gratefully acknowledged.

## References

1. Xu, J., Zhang, R., Wu, C., et al. (2014). Electrochemical performance of graphitized carbide-derived-carbon with hierarchical micro- and meso-pores in alkaline electrolyte. *Carbon*, *74* (10), 226–236.
2. Li, Y., Li, Z., & Shen, P. K. (2013). Simultaneous formation of ultrahigh surface area and three-dimensional hierarchical porous graphene-like networks for fast and highly stable supercapacitors. *Advanced Materials*, *25*(17), 2474–2480.
3. Choi, K. H., Yoo, J. T., Chang, K. L., et al. (2016). All-inkjet-printed, solid-state flexible supercapacitors on paper. *Energy & Environmental Science*, *9*(9), 1–9.
4. Wu, Z. S., Parvez, K., Feng, X., et al. (2014). Photolithographic fabrication of high-performance all-solid-state graphene-based planar micro-supercapacitors with different interdigital fingers. *Journal of Materials Chemistry A*, *2*(22), 8288–8293.
5. Grote, F., Yu, Z. Y., Wang, J. L., et al. (2015). Self-stacked reduced graphene oxide nanosheets coated with cobalt-nickel hydroxide by one-step electrochemical deposition toward flexible electrochromic supercapacitors. *Small (Weinheim an der Bergstrasse, Germany)*, *11*(36), 4666–4672.
6. Khamlich, S., Khamliche, T., Dhlamini, M. S., et al. (2017). Rapid microwave-assisted growth of silver nanoparticles on 3D graphene networks for supercapacitor application. *Journal of Colloid and Interface Science*, *493*, 130–137.
7. Tajabadi, M. T., Basirun, W. J., Lorestani, F., et al. (2015). Nitrogen-doped graphene-silver nanodendrites for the non-enzymatic detection of hydrogen peroxide. *Electrochimica Acta*, *151*, 126–133.
8. Tien, H. W., Hsiao, S. T., Liao, W. H., et al. (2013). Using self-assembly to prepare a graphene-silver nanowire hybrid film that is transparent and electrically conductive. *Carbon*, *58*(3), 198–207.
9. Davies, A., Audette, P., Farrow, B., et al. (2011). Graphene-based flexible supercapacitors: Pulse-electropolymerization of polypyrrole on free-standing graphene films. *Journal of Physical Chemistry C*, *115*(35), 17612–17620.
10. Liu, J., Jiang, T., Duan, F., et al. (2018). Electrophoresis deposition of flexible and transparent silver nanowire/graphene composite film and its electrochemical properties. *Journal of Alloys and Compounds*, *745*(2018), 370–377.



# Research of 3D Printing Self-support Technology Based on DFM

Meng Li, Linlin Liu (✉), Qiumin Wu, Xiang Liu, and Jie Ma

Faculty of Printing, Packaging Engineering and Digital Media Technology,  
Xi'an University of Technology, Xi'an, China  
liulinlin1978@qq.com

**Abstract.** Compared with the traditional processing molding, 3D printing (Additive Manufacturing) is a technology for the near-net shape of complex three-dimensional components and FDM (fused deposition modeling) is one of the widely used additive manufacturing technologies. The auxiliary supporting structure is needed to position and support the cantilever structure in the forming process of the cantilever structure in FDM. The traditional complete supports forming process needs more time, has high consumables and low efficiency, and limits the application of the FDM. The paper analyzes forming characteristics in the forming process and designing cantilever supports structural based on DFM (design for manufacturability). Confirming critical state of FDM process with analyzing FDM support characteristics by establishing mathematical model, analyzing cantilever structural of the different angles in FDM, and changing support structure of cantilever model of different angles. Designing and manufacturing the corresponding self-supporting cantilever in FDM. The research provides a design method for cantilever support, improving sprinting efficiency and develops researches of DFM.

**Keywords:** FDM · DFM · Cantilever structure · Self-supporting

## 1 Introduction

Additive manufacturing technology is also called 3D printing technology [1]. Fused deposition modeling (FDM) has certain advantages in complex parts manufacturing and as an additive manufacturing (AM) technology, based on the principle of digital model-discretion-accumulation, fused deposition modeling (FDM) allow for quick and clean development of prototypes and functional components. Although as a printing technology FDM is very flexible, FDM generally has some restrictions on the slope of the overhang, in this process, the nozzle extrudes small flattened strings of molten material to form layers as the material hardens immediately after extrusion from the nozzle on platform or other assisted supports.

The traditional auxiliary support adopts full support and local support and the excessive number of support structures increases the consumption of printing materials. Huang et al. modified the column support structure into a vertebral body to reduce the volume of the support structure [2]. Jin et al. provided an algorithm of automatic assisted supports generation based on sliced data to increase generation efficiency [3].



Masood et al. proposed an expert FDM support designer (EFS) system aiming at the optimization of the assisted supports generation process [4]. Luc et al. introduced a method of adaptive direct slicing of a complex solid model applied to rapid prototyping [5].

Xiaoran Wei uses a tree-like support to reduce the trumpet of the material, but the support structure is complex to generate and the resulting support structure has poor stability in printing [6]. Wang et al. Optimized a support generation method in the way of building hinges [7]. Kritchman et al. considered using a dissolvable material to print the support and required a separate print head to print the support structure [8].

This paper analyzes forming characteristics in the forming process and confirms critical state of FDM process with analyzing FDM support characteristics by establishing mathematical model, changes structure of cantilever model of different angles to be self-supported based on DFM.

## 2 Process Analysis

Whether to add auxiliary support structure is determined by whether the cross-sectional profile of the product has changed. In the molding process, when the linear molding is used as the support structure, as shown in Fig. 1, the following relationship exists between the support structure and the cantilever structure,  $h$  is layer height,  $B$  is line width, and  $w$  is gap width between the support and model entity and  $\theta$  is the angle of the supported surface.

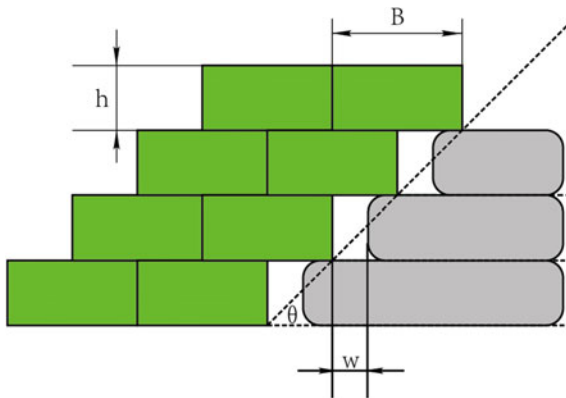


Fig. 1. Support model FDM

$$\tan\theta = \frac{h}{l_1} \tag{1}$$

where  $l_1$  is outside the length of the profiled outside contour

$$\theta = \arctan \frac{2h}{B} \quad (2)$$

When the angle of inclination is less than  $\theta$  in FDM, it is necessary to add assisted supports to meet the FDM process printing requirements, studies on the viscoelastic material with temperature in FDM, it is allowed that  $\theta$  is reduced by  $1^{\circ}$ – $10^{\circ}$ .

### 3 Archassisted Supports

In traditional Chinese architecture, the most primitive armpit beam bridges and bridges have been widely used, but inspired by the construction technology of arched structures, arches were used as the main supporting structure in the main bridges. As shown in Fig. 2, the construction method of arch bridges filled with arches as the supporting structure is similar to the molding process of the new FDM process: the lowest face is used as the construction face for stacking and construction. When the profile shape changes, the support structure is provided for the structure of the upper filling and deck face Support and positioning.

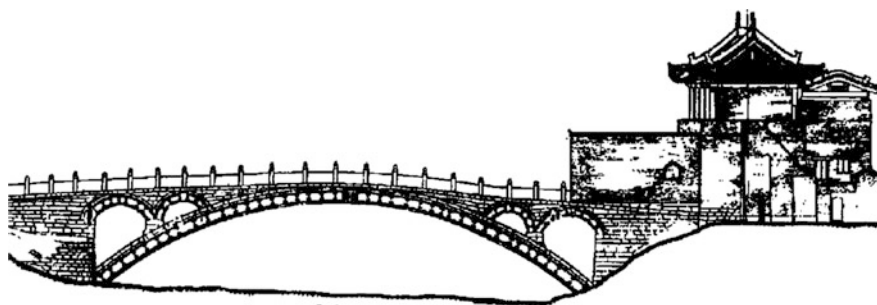
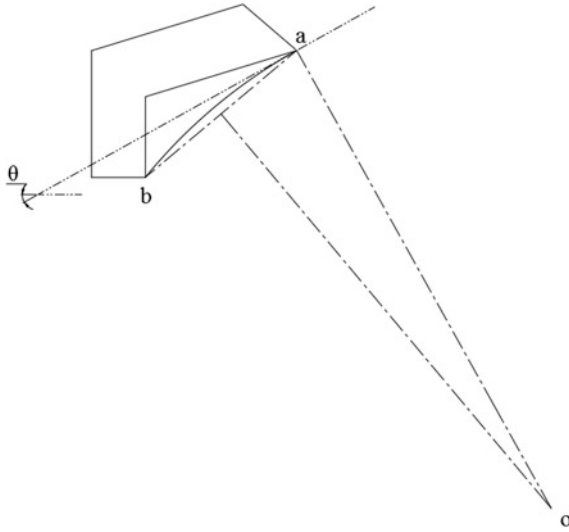


Fig. 2. Bridge model with arch assisted supports

In order to facilitate the molding of parts, a design method for cantilever structure supports that is different from the traditional support structure from the platform to the bottom of the cantilever structure is proposed. As shown in Fig. 3, making a straight line with an inclination of  $\theta$  at point a and a vertical line with point a based on the straight line, it intersects the vertical centerline of ab at point o. Draw the circle with center at o and radius equal to oa and the ab is the self-support.

### 4 Experimental and Results

As shown in Fig. 4, in this paper three-dimensional model of parts is established and saved as STL file. Then the data information of each layer generates the corresponding control code to control the operation of the printer. According to the orthogonal design, nine groups of experimental data were obtained, the Scheme 1–3 is printed without



**Fig. 3.** Design model of self-support

supports in FDM, the Scheme 4–6 is printed with traditional complete supports and the Scheme 7–9 is printed by changing the structure of cantilever model to meet process requirements of FDM based on DFM.

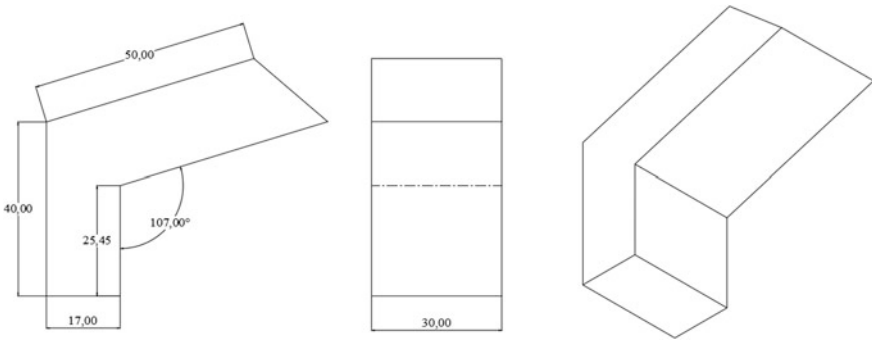


**Fig. 4.** Schematic diagram of 3D model

Process parameters of the nine groups is shown in Table 1. Each group had three samples, and a total of forty-five samples were obtained.

As shown in Fig. 5, nine groups of experimental samples were prepared, and the experimental data of the models is shown in Fig. 5.

As shown in Fig. 6, in the Scheme 1, 2 and 3, the surface forming quality of the piece without supports is poor, there are cracks and breaks on the surface of experimental models. The surface quality of Scheme 4, 5 and 6 is better, but the surface

**Table 1.** Process parameters of test molding

Scheme	Filling density (%)	Layout angle (°)	Extrusion width (mm)	Layer thickness	Support
1	10	45	0.4	0.10	N
2	10	45	0.4	0.15	N
3	10	45	0.4	0.20	N
4	10	45	0.4	0.10	Y
5	10	45	0.4	0.15	Y
6	10	45 </td <td>0.4</td> <td>0.20</td> <td>Y</td>	0.4	0.20	Y
7	10	45	0.4	0.10	Self-support
8	10	45	0.4	0.15	Self-support
9	10	45	0.4	0.20	Self-support



**Fig. 5.** Experimental model

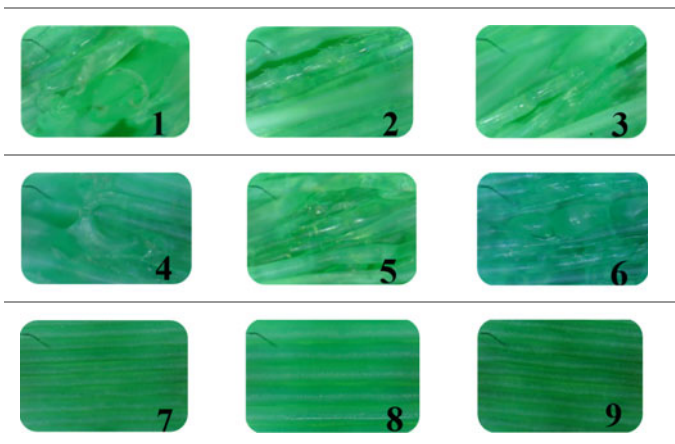


**Fig. 6.** 4× micrograph measurement chart of molding surface

quality is reduced when the support is removed from the experimental model. The Scheme 7, 8 and 9 of experimental models printing by the method are best and the surface have fine and clear textures.

Experiments have proved that the FDM piece surface forming quality optimization method used in this study can meet the user's design requirements. It is a method that changing the structure of cantilever model to meet process requirements of FDM based on DFM.

## 5 Conclusions

In this paper, analyzes forming characteristics in the forming process and designing cantilever supports structural based on DFM to meet process requirements of FDM. The model surface quality of designing and manufacturing the corresponding self-supporting cantilever in FDM is better. The research provides a design method for cantilever support to meet process requirements of FDM based on DFM, improves printing efficiency and develops researches of DFM. Also, it would be improve the development of 3D printing process design system that by changing the structural based on DFM to meet process requirements for manufacturing functional parts.

**Acknowledgements.** The author gratefully acknowledges the support of the science technology plan project of Xi'an (2017080CG/RC043(XALG006); 201805037YD15CG21(29); 20180537YD15CG21(26)), the key research and development program (general project) of Sha'anxi provincial (2018GY-162); the flexographic printing green plate making and standardization laboratory open project (ZBKT201811).

## References

1. Kai, C. C., Fai, L. K., & Chu-Sing, L. (2003). *Rapid prototyping: Principles and applications in manufacturing*. World Scientific Publishing Co, Inc.
2. Huang, X. M., Ye, C. S., Wu, S. Y., Guo, K. B., & Mo, J. H. (2009). Sloping wall structure support generation for fused deposition modeling. *The International Journal of Advanced Manufacturing Technology*, 42(11–12), 1074–1081.
3. Jin, Y. A., He, Y., & Fu, J. Z. (2015). Support generation for additive manufacturing based on sliced data. *International Journal of Advanced Manufacturing Technology*, 80, 1–12. <https://doi.org/10.1007/s00170-015-7190-3>.
4. Masood, S. H. (1996). Intelligent rapid prototyping with fused deposition modelling. *Rapid Prototyping Journal*, 2, 24–33. <https://doi.org/10.1108/13552549610109054>.
5. Zhao, Z., & Luc, Z. (2000). Adaptive direct slicing of the solid model for rapid prototyping. *International Journal of Production Research*, 38, 69–83. <https://doi.org/10.1080/002075400189581>.
6. Wei, X. (2016). Steady and low consuming supporting for fused deposition modeling. *Acta Automatica Sinica*, 42(1), 98–106.

7. Wang, W. M., Wang, T. Y., Yang, Z. W., Liu, L. G., Tong, X., Tong, W. H., et al. (2013). Cost-effective printing of 3D objects with skin-frame structures. *ACM Transactions on Graphics*, 32(5), 177.
8. Kritchman, E., Gothait, H., & Miller, G. (2008, April). System and method for printing and supporting three dimensional objects. U. S. Patent 20080211124.



# Application Research of Nano Silver Conductive Ink in Flexographic Printed RFID Antenna

Zhenxin Guo, Ge Yang, Woye Zhang, Qi Liu, Lixin Mo<sup>(✉)</sup>,  
and Luhai Li

Beijing Engineering Research Center of Printed Electronics,  
Beijing Institute of Graphic Communication, Beijing, China  
molixin@bigc.edu.cn

**Abstract.** In recent years, RFID has received widespread attention and has been widely used in the fields of logistics, transportation, pharmaceutical and other industries. In order to reduce the production cost of RFID and broaden the scope of RFID applications, the influence of flexographic process parameters on the performance of RFID tags has been studied. In this experiment, the effects of nano-silver conductive ink viscosity, printing speed, printing pressure and drying time of conductive ink on the conductive properties of printed RFID, line expansion, ink layer thickness and bending resistance were investigated by orthogonal test. We found that when the nano silver conductive ink viscosity is 1100 cp, the printing pressure gap is 200  $\mu\text{m}$ , the printing speed is 20 m/min, and the drying time is 1 min, the RFID resistance value is 388  $\Omega$ , the line width is 861  $\mu\text{m}$ , and the ink layer thickness is 4.05  $\mu\text{m}$ , the RFID has good bending resistance and optimum performance.

**Keywords:** RFID · Nano silver · Conductive ink · Flexographic printing

## 1 Introduction

Recently, radio frequency identification (RFID) tags, as one of the most important flexible electronic devices in the Internet of Things technology, have been widely used in pharmaceutical products, logistics and transportation, contactless payment and other industries [1]. The traditional RFID manufacturing process is an etching method, which has lots of disadvantages. The printing and the RFID performance of screen printing is comparable to that of RFID produced by traditional methods [2–4]. The thickness of the RFID ink layer is large in screen printing [5]. Đokić et al. [6] compared screen printing and flexible printing method is to directly print the conductive ink on the substrate. The printing speed is fast, the preparation can be not only the large-area preparing but be flexible, and the production cost are low [7]. The most used method of printing is screen printing, and the RFID performance of screen printing is comparable to that of RFID produced by traditional methods [2–4]. The thickness of the RFID ink layer is large in screen printing [5]. Đokić et al. [6] compared screen printing and flexible printing.

RFID, and found that the two printing methods produce UHF antennas with similar performance, flexographic printing is faster and has lower production costs. Nano-silver conductive ink is an important raw material for printing RFID, with excellent electrical conductivity and stable properties [8–10]. However, the influence of flexographic process parameters on RFID performance is still unclear. This study will study the viscosity, printing speed, printing pressure and conductive ink of nano-silver conductive ink through orthogonal experiment. The influence of four factors on the performance of printed RFID, explore the optimal process conditions, and lay the foundation for further reducing the cost of RFID production and improving RFID performance.

## 2 Experimental

### 2.1 Materials

Nano silver conductive ink is self-made in the laboratory, Ethanol and nitric acid were purchased from Beijing Chemical Works, ethylene glycol, ethylene and glycol monobutyl were purchased from Tianjin Guangfu Fine Chemical Research Institute.

### 2.2 Preparation of RFID

In this study, a laboratory-made nano-silver conductive ink and a polyethylene terephthalate (PET) film were used as the substrate. The four-factor and five-level orthogonal experiment method was used to print the conductive ink using a flexographic printing press (FLEXIPROOF100, RK). The plate resolution is 200 lpi. In this experiment, the ink viscosity, printing speed, printing pressure and the time required for drying of the conductive ink were the four influencing factors. The printing pressure is adjusted by adjusting the printing gap. The larger the printing pressure gap is, the smaller the printing pressure is. Adjust printing pressure gap to 120, 160, 200, 240, 300  $\mu\text{m}$  respectively, the printing speed to 10, 20, 30, 40, 50 m/min respectively, the ink viscosity to 312.5, 1100, 1550, 2100, 2800 cp, and the drying time to 8, 6, 4, 2, 1 min respectively. 12 samples were printed for each printing condition. After drying, it was heated in an oven at 120 °C for 10 min.

### 2.3 Characterization and Measurements

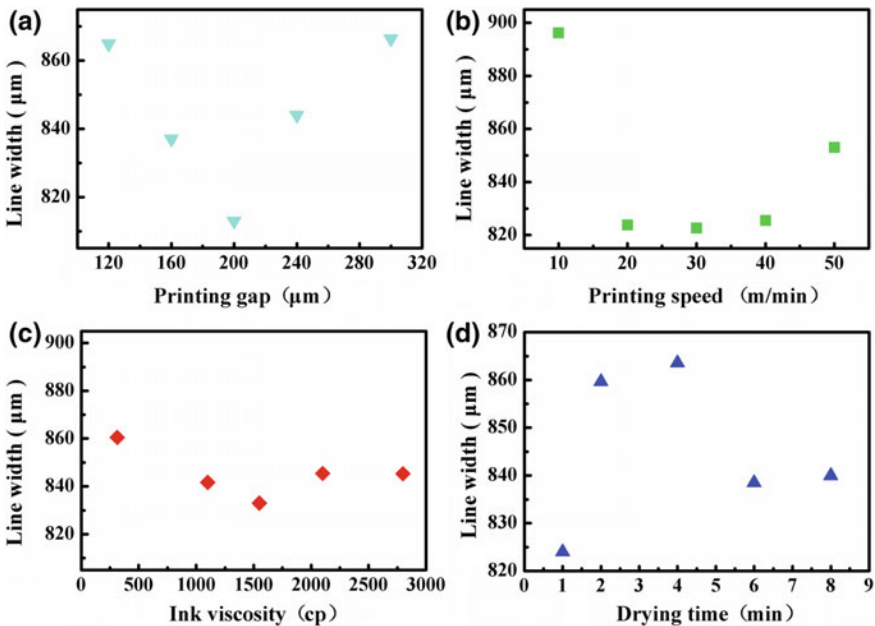
The viscosity of the conductive ink was measured using a viscometer (DV-II+ Pro, BROOKFIELD). The RFID line width and the thickness of the ink layer were measured using a laser confocal microscope (VK-X200, KEYENCE), and six samples were averaged for each printing condition. The resistance of the RFID antenna was tested using a multimeter (8808A, FLUKE), and six samples were tested for each printing condition and averaged. The line of the RFID antenna to be tested is closely attached to the wire rod with a diameter of 10 mm, and the bending is repeated 20 times at  $\pm 90^\circ$  to test the change of the resistance, and the bending resistance of the RFID antenna is characterized.



### 3 Results and Discussion

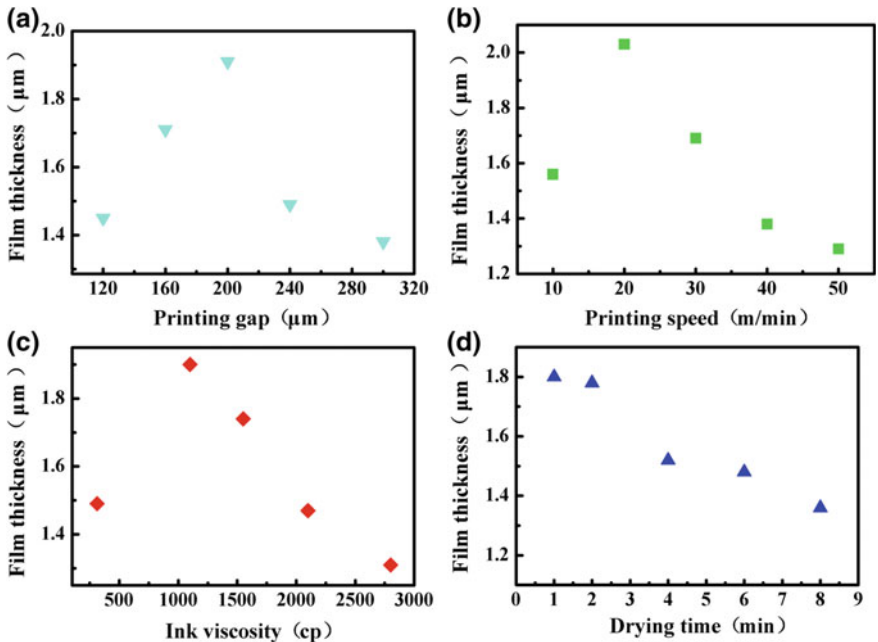
#### 3.1 Impact of Printing Process on the Appearance of RFID

Figure 1a shows as the printing pressure gap increases, the RFID line width first increases, and the line expansion is minimized when the printing pressure gap is 200  $\mu\text{m}$ , and then the line width is gradually increased. Figures 1b and 2b show that the RFID line width first decreases as the printing speed increases, and increases as the printing speed increases as the printing speed reaches a minimum at 30 m/min. Figure 1c shows that the RFID line width first decreases with increasing ink viscosity, reaches a minimum at 1550 cp, and then gradually increases. Figure 1d shows as the drying time becomes longer, the line width becomes larger. Figure 2 shows that the film thickness trend is basically opposite to the trend of line width variation. When the printing pressure is large, the diffusion of ink is severe, the line is enlarged, and the thickness of the ink layer is reduced. The printing pressure is small, resulting in a large line width and a reduced thickness of the ink layer. When the printing speed is slow, the longer the pressing time between the printing plate and the substrate, the larger the line width, and the smaller the thickness. When the printing speed is fast, the force by which the ink is pressed is also increased, so the line width becomes large and the thickness is reduced. When the viscosity of the ink is low, the ink has strong fluidity, the line is enlarged, and the thickness of the film is reduced; the viscosity of the ink is



(a) effect of printing gap on line width, (b) effect of printing speed on line width, (c) effect of ink viscosity on line width; (d) effect of drying time on line width

Fig. 1. Line width effect curve of RFID ink layer



(a) effect of printing gap on thickness of ink layer, (b) effect of printing speed on thickness of ink layer, (c) effect of viscosity of ink on thickness of ink layer; (d) effect of drying time on thickness of ink layer

**Fig. 2.** Thickness effect curve of RFID ink layer

high, the fluidity of the ink is poor, and the amount of transfer is small, so that the thickness of the ink layer becomes low and the line width becomes large. The shorter the drying time, the less easily the ink spreads, the smaller the line, and the larger the thickness. It was found that the optimum print reproducibility at the printing pressure gap 200  $\mu\text{m}$ , printing speed 20 m/min, ink viscosity 1100 cp, and drying time 1 min. The RFID digital photos printed under optimal conditions are shown in Fig. 3.

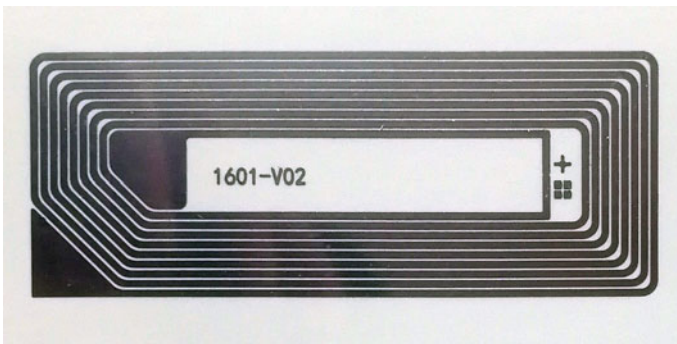
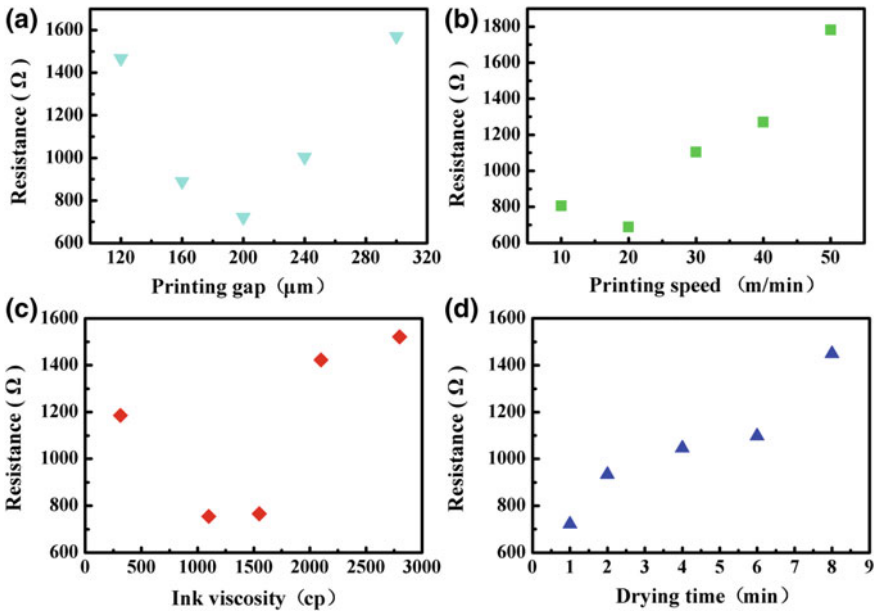


**Fig. 3.** RFID digital photos printed under optimal conditions

### 3.2 Impact of Printing Process on RFID Resistance

Figure 4a shows that the RFID resistor first decreases as the printing pressure gap increases, and reaches a maximum value after the printing pressure gap is 200  $\mu\text{m}$ , and then gradually decreases. Figure 4b shows that the RFID resistor first decreases as the printing speed increases, and reaches a maximum value after the printing speed is 20 m/min. Figure 4c shows that the RFID resistance first decreases as the viscosity of the ink increases, and then reaches a maximum value when the viscosity of the ink reaches 1100 cp, and then gradually decreases. Figure 4d shows that as the drying time becomes longer, the RFID resistance gradually becomes larger. The trend of resistance change is opposite to the trend of film thickness change. The printing process changes, the thickness becomes larger, the conductive path becomes more, the resistance decreases, and vice versa, the resistance increases. It was found that the RFID resistance was 388  $\Omega$  at the printing pressure gap 200  $\mu\text{m}$ , printing speed 20 m/min, ink viscosity 1100 cp, and drying time 1 min.

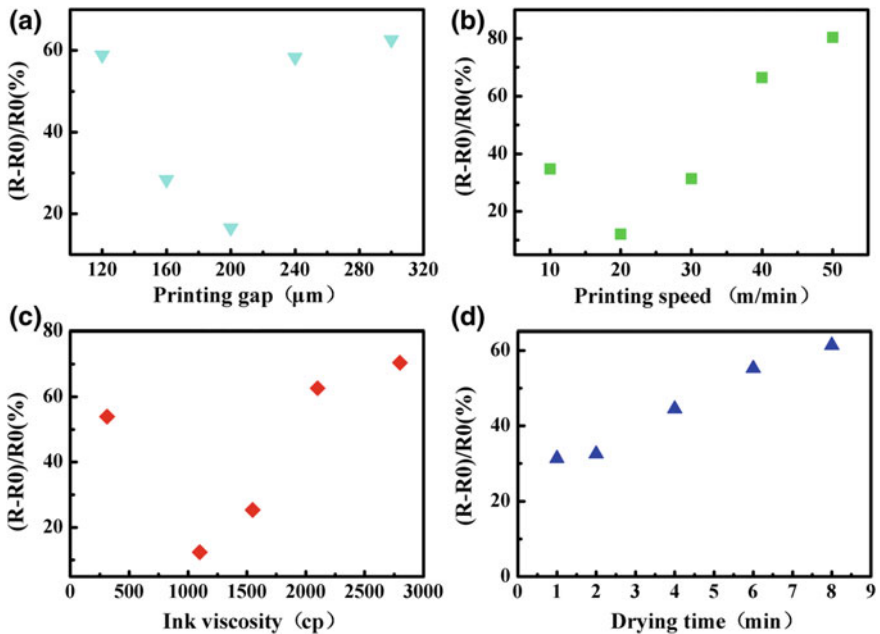


(a) The effect of printing pressure gap on resistance, (b) The effect of printing speed on resistance, (c) The effect of ink viscosity on resistance, (d) The effect of drying time on resistance

**Fig. 4.** Resistance effect curve of RFID

### 3.3 Impact of Printing Process on Bending Resistance of RFID

The resistance change rate of RFID ( $\Delta R$ ) is used to characterize the bending resistance of RFID. The formula of the resistance change rate of RFID is as follows:  $\Delta R = (R - R_0)/R_0$ , which  $R$  is the resistance after bending and  $R_0$  is the resistance before bending. The smaller the resistance change rate of RFID, the better the bending resistance. Figure 5a shows that the change rate of the RFID resistance first decreases as the printing pressure gap increases, and reaches a maximum value after the printing pressure gap is 200  $\mu\text{m}$ , and then gradually decreases. Figure 5b shows that the change rate of the RFID resistance first decreases as the printing speed increases, and reaches a maximum value after the printing speed is 20 m/min. Figure 5c shows that the change rate of the RFID resistance first decreases as the viscosity of the ink increases, and then reaches a maximum value when the viscosity of the ink reaches 1100 cp, and then gradually decreases. Figure 5d shows that as the drying time becomes longer, the rate of change of the RFID resistance gradually becomes larger. This is because when the thickness of the ink layer is small after printing, the passage of the nano silver particles after thermal sintering is thin, and some of the conductive paths are broken after being



(a) effect of printing pressure gap on resistance change rate, (b) effect of printing speed on resistance change rate, (c) effect of ink viscosity on resistance change rate, (d) effect of drying time on resistance change rate

Fig. 5. Resistance change rate effect curve of RFID

bent, resulting in a large rate of change in resistance; and when the ink layer is thick, although part Breaking, there are still many channels, and the conductivity can be well maintained.

## 4 Conclusions

In summary, orthogonal experiments were conducted to investigate the effects of printing pressure, printing speed, ink viscosity and drying time on RFID performance. We found that the RFID line width, resistance and resistance change rate before and after bending showed a first decreasing and then increasing change with printing pressure, ink viscosity, printing speed and drying time. The longer the drying time, the wider the RFID line width, and the higher the resistance change rate before and after the resistance and bending. The trend of the thickness of the RFID ink layer is opposite to that of the RFID line width, and the resistance and the resistance change before and after the bending. Finally, the optimal conditions were as follows: the ink viscosity is 1100 cp, printing gap is 200  $\mu\text{m}$ , the printing speed is 20 m/min, the drying time is 4 min. At the optimal printing conditions, the resistance of RFID is 388  $\Omega$ , the line width is 861  $\mu\text{m}$ , the thickness of the ink layer is 4.05  $\mu\text{m}$ , the ink layer is flat, the adhesion is strong, and the bending resistance is good.

**Acknowledgements.** This work is supported by the fund from Beijing Municipal Commission of Education (KM201810015004), 2017 Outstanding young scholars (CIT&TCD201704051), 2018 Innovation training program (22150118022/071).

## References

1. Dhaouadi, M., Mabrouk, M., Vuong, T. P., Souza, A. C. D., & Ghazel, A. (2014). UHF tag antenna for near-field and far-field RFID applications. In *Wireless and Microwave Technology Conference* (Vol. 5, pp. 1–4). New York: IEEE.
2. Godlinski, D., Zichner, R., Zöllmer, V., et al. (2017). Printing technologies for the manufacturing of passive microwave components: Antennas. *IET Microwaves, Antennas and Propagation*, 11(14), 2010–2015.
3. Xiao, G., Aflaki, P., Lang, S., Zhang, Z., Tao, Y., Py, C., et al. (2018). Printed UHF RFID reader antennas for potential retail applications. *IEEE Journal of Radio Frequency Identification*, (99), 1–1.
4. Liu, W., Chen, G., & Zhang, Y. (2016). Study of the screen printing technology on RFID tag antenna. In *China Academic Conference on Printing & Packaging and Media Technology* (pp. 539–545). Singapore: Springer.
5. Tang, B. (2007). Printing technology of electronic tag (RFID) antenna. *Printed Circuit Information*, 6, 24–27.
6. Đokić, M., Muck, T., Radonić, V., Pleteršek, A., Kavčič, U., & Crnojević-Bengin, V. (2015). Comparison of the characteristics of screen and flexographic printing for RFID applications. *Informacije MIDEM (Ljubljana)*, 45(1), 3–11.
7. Li, L., Mo, L., Ran, J., & Xin, Z. (2014). Progress in conductive inks and their application technology. *Imaging Science and Photochemistry*, 32(4), 393–401.

8. Li, J., Jianhui, L., Wang, Y., Xiao, J., Wang, T., & Shanqun, G. (2014). Research progress of metallic silver conductive inks. *Electronic Components and Materials*, 11, 14–17.
9. He, H., Tajima, J., Sydänheimo, L., Nishikawa, H., Ukkonen, L., & Virkki, J. (2017). Inkjet-printed antenna-electronics interconnections in passive UHF RFID tags. In *Microwave Symposium* (pp. 598–601). New York: IEEE.
10. Salmerón, J. F., Molina-Lopez, F., Briand, D., Ruan, J. J., Rivadeneyra, A., Carvajal, M. A., et al. (2014). Properties and printability of inkjet and screen-printed silver patterns for RFID antennas. *Journal of Electronic Materials*, 43(2), 604–617.



# Research on Load Balancing Algorithm of Flexographic Printing Job-Shop Based on Group Technology

Huailin Li<sup>1(✉)</sup>, Shisheng Zhou<sup>2(✉)</sup>, and Rubai Luo<sup>2</sup>

<sup>1</sup> School of Mechanical and Precision Instrument Engineering, Shaanxi Key Laboratory of Printing and Packing Engineering, Xi'an University of Technology, Xi'an, China  
lihuailin6666@sina.com

<sup>2</sup> Faculty of Printing, Packing Engineering and Digital Media Technology, Shaanxi Key Laboratory of Printing and Packing Engineering, Xi'an University of Technology, Xi'an, China  
zhoushisheng@xaut.edu.cn

**Abstract.** In flexographic printing production, it takes a lot of time to clean the reticle roll and change ink, which results in the waiting time increase. Therefore, based on the analysis of characteristics of the flexographic press and its jobs, the color sequence group technology and the flexographic printing Job-shop of load balancing algorithm are proposed in the paper. A scientific production scheduling is established by introducing the management of the group technology to the flexographic printing production management. The job load balancing algorithm makes the production scheduling becomes fast and reasonable.

**Keywords:** Job-shop scheduling · Load balancing algorithm · Group technology · Color sequence job group

## 1 Introduction

With the continuous pursuit of people's quality of life, personalized and high quality of the printing requirement has been reflected in different consumption areas [1]. The demand for personalized printing not only makes the small batch order increase, but also makes the complexity of the printing jobs raise and the delivery time shorter. Therefore, the proportion of the equipment debugging preparation time to the total printing production time in the printing production process increases so that the final production cost is added. For these reasons, many printing enterprises have used the Enterprise Resource Planning (ERP) system [2]. The printing production scheduling based on ERP system production management platform make a rapid progress. However, ERP system not only can not automatically arrange the production plan and implement dynamic scheduling, but also cannot optimize the actual production. Therefore, we focus on flexographic printing Job-shop of load balancing in this paper. Firstly, the key factors that affect the production capacity of flexographic printing are achieved by combining theoretical research with actual production. Secondly, based on

enterprise specific production, the load balancing algorithm about printing production is proposed after discussing the feasibility of the advanced production management theory in flexographic printing production and exploring an optimization method suitable for flexographic printing production management. Finally, the load balancing algorithm is used to realize the intellectualization and digitalization of flexographic printing job-shop [3–5].

## 2 Definitions of Load Balancing

Load balancing [6] is distributing the task to multiple operation units so that the flexibility and availability of devices can be improved. The load balancing of flexographic printing Job-shop is distributing the printing jobs to multiple printing presses to print respectively, so as to reduce the waiting time and to improve production efficiency. In the flexographic printing Job-shop, the goal of load balancing can be achieved by improving production scheduling that is the key aspects of production management.

## 3 Device and Job Group Technology

Group technology (GT) is a manufacturing technology science that reveals and exploits the similarities between things. According to certain constraints, the same group of things can be processed in the same way, thus improving the efficiency of the technology [7]. It has been involved in the frontier areas of all kinds of engineering technology, computer technology, systems engineering, management science, psychology, sociology and so on. Group technology is the basis of computer aided manufacturing in the manufacturing engineering. It can achieve the most economic benefits by applying group technology philosophy into the design, manufacture and management of the entire production system to change the production method of the multi-species and small batch.

It needs to be explained here that in the application of group technology, too many constraint conditions lead to a group of things, and fewer constraint conditions lead to a poor similarity in the same group of things. Therefore, when selecting constraints, the actual production situation should be considered appropriately.

For the processing and sorting of multiple operations on multiple devices, the complexity of scheduling problems increases with the number of devices. If  $n$  jobs are arranged in the  $m$  devices, there will be  $(n!)^m$  schemes [2]. Because of the limitation of production conditions, some scheduling schemes are not feasible. Even if there are a considerable number of feasible solutions, it is difficult to choose the best scheme. Therefore, the production schemes can be reduced by corresponding the device and the jobs into groups so that it is the easiest to get the optimal solution by the establishment of the model.



(1) Device group technology

First, printing devices are processed in groups. The basic condition of group technology is that devices of the same device group can print all jobs. The main considerations are the material of printing stock, the maximum printing width, the length of repeated printing and so on, which are regarded as the constraint conditions of the device group technology. In the specific application, constraint conditions can be changed according to the actual types and quantities of devices purchased by enterprises, so that the device groups can be obtained. Device group technology is show in Fig. 1.

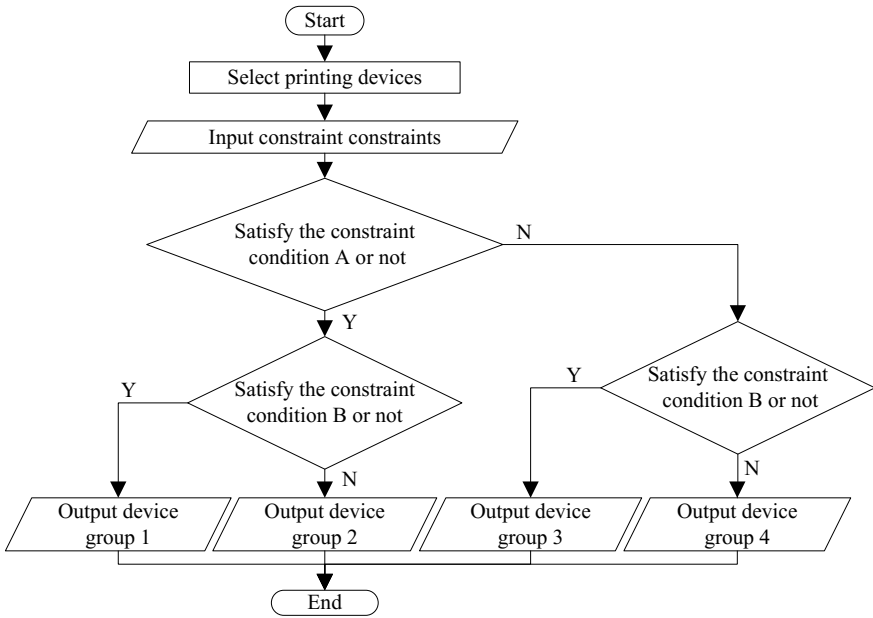


Fig. 1. Flow chart of device group technology

(2) Job group technology

The basic condition of job group technology is that the job can be printed with the same device group. Therefore, when the jobs are grouped, the constraint constraints of the job group technology are the same with the constraint conditions of the device group technology. Then the jobs of job group can be printed with the same devices of device group. Since the parameters of device in the device group may not be exactly the same, it would lead to a part of jobs can only be printed on a certain device. Therefore, there must be a special job group, called *independent job group*. The job group technology is shown as Fig. 2.

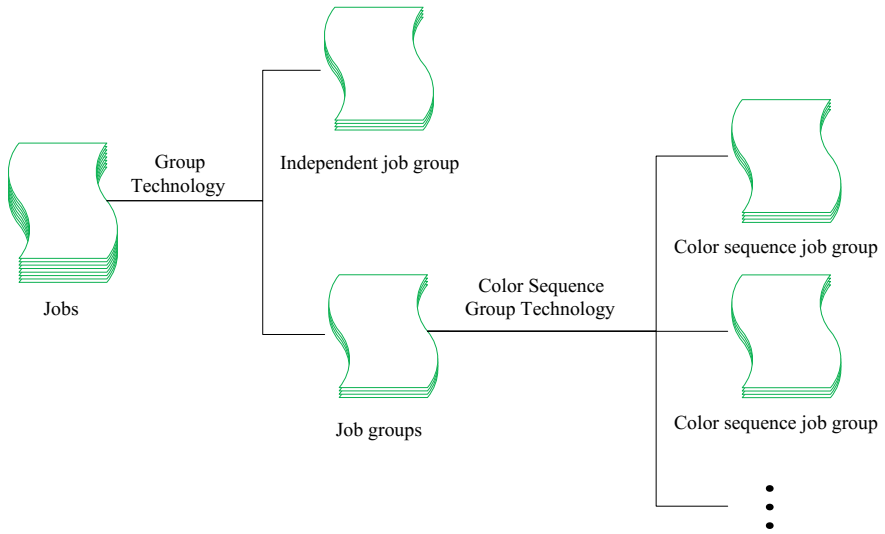


Fig. 2. Flow chart of job group technology

## 4 Job Load Balancing Algorithm

Job load balancing algorithm includes two parts, which are color sequence group technology and assignment method of job groups.

### 4.1 Color Sequence Group Technology

In flexographic printing production, it takes a lot of time to clean anilox rolls and replace ink. In order to reduce the times of replacing the ink and cleaning anilox rolls, the printing workers should try their best to print continuously jobs with the same color sequence, then the waiting time is shortened, and the effective utilization of the device is improved. In this paper, the color sequence group technology is a method that jobs with the high similarity or the same color sequence are distributed to the same group. The implementation steps of the color sequence group technology are as follows:

**Step 1.** A job with the most color number is selected among jobs of the job group as a sample job. The remaining jobs of the job group are called comparative jobs. The number of colors  $N_0$  and the color sequence of the sample job are extracted in the database.

**Step 2.** The number of colors  $N_i$  and the color sequence of the comparative job are extracted in turn. And then the color sequence of the comparative job compared with the color sequence of the sample job as shown in Fig. 3. First, the color sequence of the comparative job and the sample job are marked by  $1, 2, \dots, 8$  and are compared in accordance with  $123, 234, \dots, 567, 78$  in turn. If the same colors are existed, the next three colors are compared. If there isn't the same color, insert value of 0 before the current three colors and the next three colors are compared. The maximum number of 0

inserted in the contrast process is  $N_0 - N_i$ . When the number of 0 is reached the upper limit ( $N_0 - N_i$ ), the color sequence of the sample job the comparative job that has been inserted value of 0 are compared according to the colors 1, 2, ..., 8. The number of the

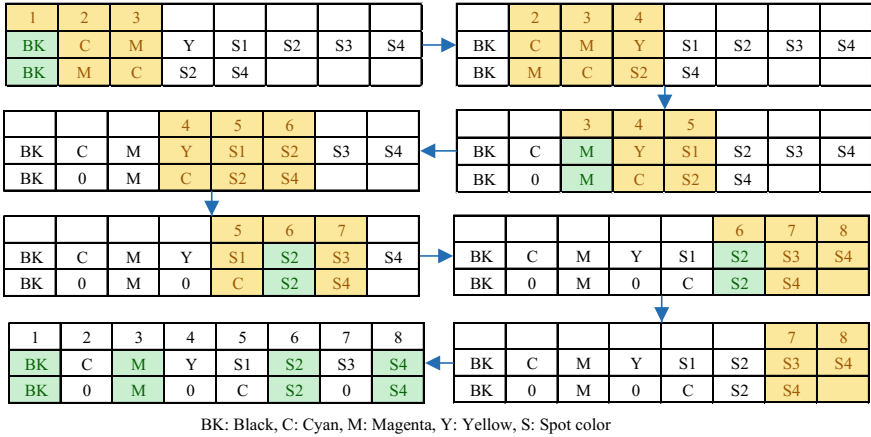


**Fig. 3.** Flow chart of color sequence comparison

same color is denoted as  $R_i$ .

**Step 3.**  $Y_i$  is defined as the *Difference Degree*. There is a  $Y_i$  in all the comparative jobs. The sample and the job jobs with  $Y_i = 0$  are assigned to one group Which is denoted as  $J_i$ .

$$Y_i = N_i - R_i \tag{1}$$

**Step 4.** The remaining jobs are repeated from **Step 1 to Step 3** until the number of remaining jobs is zero.

**Step 5.** The group  $J_i$  that is arranged by using *color sequence group technology* is called *color sequence job group*. In the same color sequence job group, jobs are arranged in the order of delivery date.

Finally, jobs can be assigned to printing devices by group, when all jobs are arranged by *independent job group* or *color sequence job group*.

### 4.2 Assignment Method of Job Groups

When assigning job groups, the independent job groups are allocated firstly, and then the color sequence job groups are assigned.

(1) Assignment method of independent job groups

The jobs of the independent job group are assigned to the corresponding printing devices, according to the parameters of printing devices. If there are all more than 1

jobs and devices in the independent job group, the assignment method should be referred to the assignment method of the color sequence job group.

(2) Assignment method of color sequence job groups

The  $m$  color sequence job groups are assigned to the  $n$  devices as follows:

**Step 1.** The color sequence job groups are arranged according to printing quantity of the order from more to less. The color sequence job group is recorded as  $J_1, J_2, \dots, J_m$ .

**Step 2.** The cumulative net working time within 24 h of the device is recorded as  $T_1, T_2, \dots, T_n$ .

**Step 3.**  $J_1, J_2, \dots, J_m$  are assigned to devices from  $J_1$  to  $J_m$  in turn follow the principle that  $J_i$  is assigned to the device with minimum cumulative printing time until all assignments are allocated. The assignment method of job groups is shown in Fig. 4. When the color sequence job group is assigned, the Eq. (2) enable us to calculate the cumulative working time of the  $i$ th printing device.

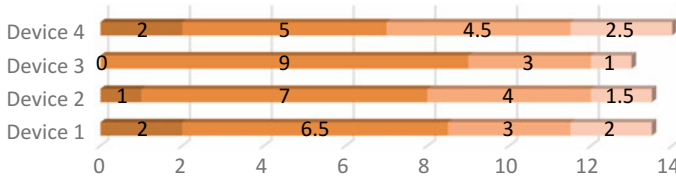


Fig. 4. The job assignment within a device group

$$\begin{aligned}
 T_i &= T_i + T_{J_i} \\
 T_{J_i} &= \frac{M_{J_i}}{v_i}
 \end{aligned}
 \tag{2}$$

with

$T_i$  represents the cumulative working time of the  $i$ th printing device.

$T_{J_i}$  represents the cumulative working time of the color sequence job group  $J_i$ .

$M_{J_i}$  represents the printing quantity of the color sequence job group  $J_i$ .

$v_i$  represents speed of the  $i$ th printing device.

In Fig. 4, it describes the assignment of a device group. First, the independent job group (the deepest color) is allocated to the corresponding printing device. Then the color sequence job groups (the lighter color) are assigned to all devices of the device group.

### 4.3 Adjust the Job Queue According to the Delivery Date

Judge the difference between the delivery date and the complete date of the job plan. If the delivery date is later than the complete date, the job queue is not adjusted. Otherwise, this job has to be adjusted and to be printed ahead of time.

## 5 Conclusions

In this paper, Group Technology is introduced to the production management of flexographic printing. The job load balancing algorithm is given by analyzing the printing characteristics of satellite flexographic press. The color sequence group technology is proposed according to the color sequence of the job. A scientific Job-shop scheduling is established to achieve the goal of load balancing, in which the production costs are cut down, the waiting time is reduced, the effective utilization rate of device is improved, and the malpractice relying on experience is avoided in the production scheduling. The job load balancing algorithm makes the production scheduling becomes fast and reasonable.

**Acknowledgements.** The project is supported by Natural Science Foundation of the Science and Technology Department of Shaanxi Province (Grant no. 15JS075, 2016JM5068 and 2018JQ5100). The project is also supported by Shaanxi Collaborative Innovation Center of Green Intelligent Printing and Packaging.

## References

1. Ben, L., Maohai, L., et al. (2017). Digital printing in the application of personalized packaging. *Today's Printing*, 10, 29–31.
2. Ziyou, X. (2005). *Research about the production planning and scheduling in newspaper printing*. Wuhan: Wuhan University.
3. Kui, Z., & Genke, Y. (2003). Design of single job-shop scheduling system. *Computer Application*, 23(S2), 283–285.
4. Kun, Y., & Jianying, Z. (2007). Improved genetic algorithm for the flexible job-shop scheduling with multi-object. *China Mechanical Engineering*, 18(2), 156–160.
5. Baker, K. R. (1990). Scheduling groups of jobs in the two machine flow shop. *Mathematical and Computer Modelling*, 13(3), 29–36. [https://doi.org/10.1016/0895-7177\(90\)90368-W](https://doi.org/10.1016/0895-7177(90)90368-W).
6. Mitzenmacher, M. (2001). The power of two choices in randomized load balancing. *IEEE Transactions on Parallel & Distributed Systems*, 12(10), 1094–1104. <https://doi.org/10.1109/71.963420>.
7. Yan, L., & Shujuan, L. (2000). *Advanced manufacturing technology and system*. Xian: Shaanxi Science and Technology Press.



# Research on Cutting-Bonding Process of Powder Based 3D Printing Model

Xiaochun Wang, Guangxue Chen<sup>(✉)</sup>, Jiangping Yuan, and Ling Cai

South China University of Technology, Guangzhou, China  
chengx@scut.edu.cn

**Abstract.** Powder based 3D printing technology is one of the few full color 3D printing technologies, which is widely used in customized model and packaging industry, and has been gradually applied in the manufacturing industry of medical model. In the process of printing large-size model and repairing damaged model, cutting-bonding is an essential step. In this paper, the maximum tension of standard model, the cutting angle of test model, the type of adhesive and the effect of temperature on the properties of the adhesive were studied. It was found that the bonding effect was positively related to the smoothness of cut surface. The adhesive with strong stickiness and transparent color was more suitable for powder based model. The bonding strength increased with the increase of the adhesive temperature and 45 °C was the best bonding temperature of powder based model.

**Keywords:** 3D printing · Cutting-bonding process · Adhesive bond strength

## 1 Introduction

As a digital molding and solid manufacturing technology, 3D printing has attracted much attention in recent years due to its advanced technology and wide application. One of the key technologies that will trigger the third industrial revolution is considered. With the development of several remarkable printing materials, the creative functions of 3D printing have attracted attention of the public in the recent decade [1]. Color 3D printing is a remarkable technology for customized manufacture and integrated production in different industries [2]. There are two kinds of 3D printing technology based on color printing principle, powder based 3D printing and paper based 3D printing. Powder based 3D printing process was developed by the Massachusetts Institute of Technology [3]. This process uses powder and different color binders to build each layer according to the sliced two-dimension profile of the model data [4]. Compared with paper based 3D printing, powder based 3D printing is more widely used and model strength is higher.

ProJet CJP 860 Pro is a top-level powder based 3D printer that can print full color models quickly, however the capacity still could not fit all large models (508 \* 381 \* 229 cm). Cutting-Bonding Frame (CBF) is proposed by Yuan et al. [5] to print an oversize color model by dividing whole one into two or more sub-parts. And in the process of printing and the preservation of the model after printing, the powder

based 3D printing model will break due to its own properties, so it is very necessary to study the cutting-bonding process.

## 2 Experiments

### 2.1 Experimental Instruments and Materials

ProJet CJP 860 Pro (3D SYSTEMS Ltd.), ordinary glue (poval solution, deli Ltd.), vegetable gelatin (WingArt Ltd.), 502 adhesive (ethyl  $\alpha$ -cyanoacrylate, deli Ltd.), ceramic repair adhesive (LIDRGON Ltd.), ergo5800 (cyanoacrylate, ergo Ltd.), water-bath, spring dynamometer, computer.

### 2.2 Experimental Procedure

#### 2.2.1 Maximum Tension Test of Powder Based 3D Printing Model

Before cutting-bonding experiment of powder based model, maximum tension test that the model can withstand should be tested, so as to avoid the damage to the model due to the excessive bonding strength of the adhesive, so it is important to test the true bonding effect.

The laboratory humidity was measured as 79%, and the temperature was measured as 25 °C. The standard model of the experiment was a cuboid with a side length of 3 cm. The tension force in parallel and perpendicular of model forming direction was tested by spring dynamometer respectively. The tensile force of fracture was recorded in computer. Each direction was tested three times, and the minimum value in each direction was obtained.

#### 2.2.2 Cutting-Bonding Experiment of Powder Based 3D Model

According to Cutting-Bonding Frame (CBF), as seen in Fig. 1, the standard model was cut in the direction of 0°, 45°, 90° severally. The cutting angle is defined as the angle deviating from the unilaminar plane.

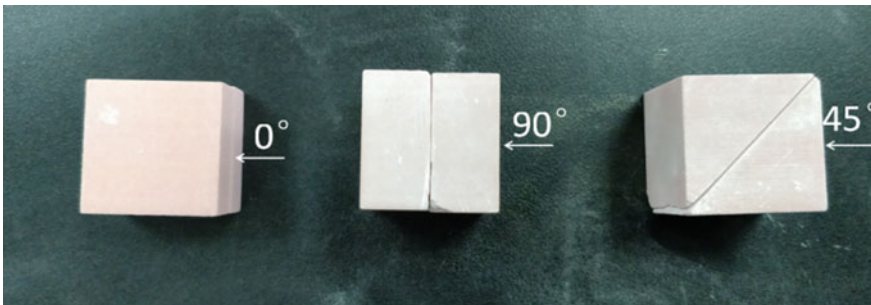
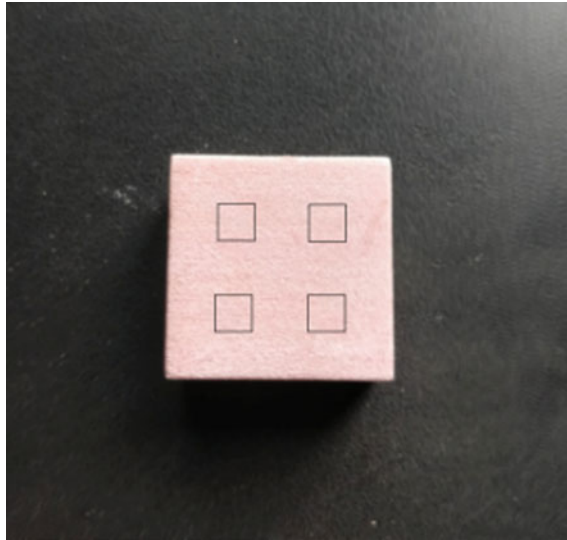


Fig. 1. Three cutting angles

In the pre test, sizing on the whole cutting surface will make the tension force exceed the maximum bearing force of the model and lead to damage the model. Therefore, four square areas with the length of 0.5 cm at the four angles of the cutting surface were selected for sizing, as shown in Fig. 2. Three cutting models were bonded with five kinds of adhesives. Since most adhesives are instant adhesive, we set a bonding time of 15 min. The bonding model was tested with spring dynamometer respectively. Then recording the tensile force of fracture in computer and calculating the bond strength per unit area.



**Fig. 2.** Sizing area

### 2.2.3 Effect of Temperature on Bonding Effect

Based on cutting-bonding experiment of powder based 3D model, the adhesive with the highest strength and the best performance was selected and heated to 30°, 35°, 40°, 40°, 45° and 50° in water bath respectively. The cutting-bonding model with the highest bond strength was selected for bonding experiment. Then recording the tensile force of fracture in computer and calculating the bond strength per unit area.

## 3 Results and Discussion

### 3.1 Maximum Tension of Powder Based 3D Printing Model

The experimental results of the maximum tensile force of the powder based model measured by three times are shown in Table 1.

It can be seen from the table that if the bond strength of the adhesive is more than 285 N, the powder based model will break, and the measured results will not be able to



**Table 1.** Maximum tension of powder based 3D printing model

Direction	Tension (N)		
	1	2	3
Parallel	285	338	322
Perpendicular	382	365	343

express the true bond strength. Moreover, the tensile force perpendicular to the molding direction is larger than the parallel direction, which may be due to the fact that the bonding strength of one layer is greater than that between the layers.

### 3.2 Bond Strength Analysis of Different Cutting Angle Models and Adhesives

The standard model was cut and manually bonded after five kinds of adhesives were coated in the area respectively. After 15 min, the tension in 15 groups were tested as shown in Table 2 and the calculated bond strength per square millimeter is shown in Table 3 and Fig. 3a–e denote ordinary glue, vegetable gelatin, 502 adhesive, ceramic repair adhesive and ergo5800 respectively.

**Table 2.** Bond strength of models cut at three angles

Cutting angle (°)	Bond strength (N)				
	a	b	c	d	e
0	31.0	8.8	120.0	130.3	201.7
45	21.5	7.0	80.6	57.5	171.3
90	26.5	6.3	74.1	78.4	155.0

**Table 3.** Bond strength per square millimeter of models cut at three angles

Cutting angle (°)	Bond strength per square millimeter (N)				
	a	b	c	d	e
0	0.31	0.09	1.20	1.30	2.02
45	0.22	0.07	0.81	0.58	1.71
90	0.27	0.06	0.74	0.78	1.55

It can be seen from Fig. 3 that the bond strength of the 0° cutting model is higher than that of the other models under the test of the five adhesive agents, the bond strength of the 45° cutting model and the 90° cutting model is similar. This result may be related to the roughness of the cutting surface. Because of the forming characteristics of the powder 3D model, the cutting surface of the 0° cutting model is smoother and the bonding effect is better.

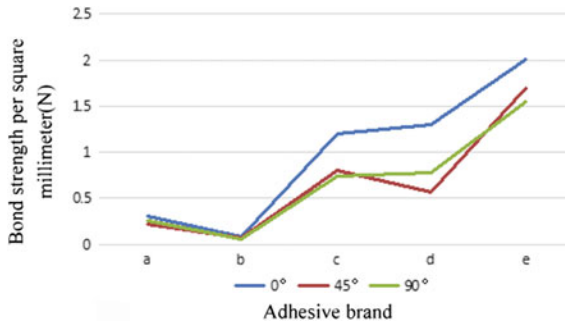


Fig. 3. Measurements of bond strength at three cutting angles

With the comparison of the bonding strength of five kinds of adhesives, The adhesive strength of a and b is too small, and the color of b is white, which will affect the color near the model notch after sizing. So it is necessary to further study the environmental protection glue for powder based 3D printing model. The bond strength of c, d and e meet the bonding standard, but the smell of c is too strong (Table 4) and the adhesive principle of the d is to form rubber solids at the cutting place, which will increase the gap in the adhesive joint. The bond strength of e is the strongest of the five adhesives, and its properties meet the requirements, so it is the best choice to agglutinate powder based model.

Table 4. Properties of five adhesives

Adhesive brand	a	b	c	d	e
Smell of adhesive	M	N	L	N	M
The color of the adhesive	Transparent	White	Transparent	Transparent	Transparent

N is for odourless, M is for faint smells, L is for strong smells

### 3.3 Effect of Temperature on Bond Strength

Experimenting was done with 0° cutting angle model. The ergo5800 adhesive was heated to different temperatures in a water bath pot. After 15 min of bonding, the bond strength was measured at various temperatures.

The bonding strength increases with the increase of temperature as shown in Table 5. When the temperature rises to 50 °C, the bonding strength has exceeded the maximum tension of the powder based model. Therefore, when the powder based model is bonded, the adhesive can be heated to 45 °C to obtain the best bonding effect and energy will not be wasted.

Table 5. Bond strength at different temperatures

Temperature (°C)	25	30	35	40	45	50
Bond strength (N)	201.7	239.5	242.0	264.7	277.3	315.1

## 4 Conclusions

In this paper, the maximum tension force of the powder based standard model was investigated, the bonding strength of three cutting angles and five kinds of adhesives was compared, and the effect of adhesive temperature on the bonding effect was investigated. The following conclusion was drawn that the standard model will break when the tension force is greater than 285 N, the bond strength of the adhesive is the largest at the cutting angle of 0°, and the ergo5800 adhesive is most suitable for bonding process of the powder based 3D printing model. The bonding effect increases with the increase of the adhesive temperature and 45 °C is the best bonding temperature of powder based model.

**Acknowledgements.** This work was funded by the Guangdong Provincial Science and Technology Project [Grant No. 2017B090901064].

## References

1. Schubert, C., van Langeveld, M. C., & Donoso, L. A. (2014). Innovations in 3D printing: A 3D overview from optics to organs. *British Journal of Ophthalmology*, 98(2), 159–161.
2. Yuan, J., Zhu, M., Xu, B., & Chen, G. (2017). Review on processes and color quality evaluation of color 3D printing. *Rapid Prototyping Journal*, 24(11).
3. Sachs, E., Cima, M., Williams, P., Brancazio, D., & Cornie, J. (1992). Three-dimensional printing: Rapid tooling and prototypes directly from a cad model. *Journal of Engineering for Industry*, 39(1), 201–204.
4. Yuan, J., Liu, Y., Chen, G., & He, L. (2016). Process analysis of seamless adhesion for cutting model printed by color paper-based 3D printing.
5. Yuan, J., Zhaohui, Y. U., Chen, G., Zhu, M., & Gao, Y. (2016). Large-size color models visualization under 3D paper-based printing. *Rapid Prototyping Journal*, 23(3).



# Research on Influencing Factors of Conductivity of Screen Printed Circuits

Xi Li<sup>(✉)</sup>, Aijing Gao, Lihong Cao, Fan Su, and Luhai Li

School of Printing and Packing Engineering, Beijing Institute of Graphic Communication, Beijing, China  
1461730959@qq.com

**Abstract.** With the development of printed electronics industry, in order to obtain good printed circuit, it is necessary to ensure the high transfer rate of conductive ink in the printing process. The printing process, the viscosity of the conductive ink, and the post-treatment conditions are important factors affecting the ink transfer. Therefore, the conductive properties of the conductive ink printed circuit were studied by changing the printing speed, the printing pressure, the viscosity of the conductive ink, and the post-processing conditions for the screen printing method. Studies have shown that the viscosity of the conductive ink is 6000 mPa s, the printing pressure is the gear position 4, the printing speed is the gear position 1, and the post processing condition is 120 °C, and the drying time is 10 min, the square resistance of the printed circuit is the smallest.

**Keywords:** Conductive ink · Screen printing · Printing speed · Printing pressure · Electrical conductivity

## 1 Introduction

With the development of printed electronics industry technology, the acquisition of high-conductivity and high-precision printed circuits has become a key technology. The transfer of conductive inks in the printing process has become a key factor affecting the performance of printed electronic devices. There are many factors that affect the ink transfer, such as the ink viscosity, surface tension, solvent volatility, plate composition and surface properties, printing pressure, printing speed [1, 2].

In the conductive ink system, there are countless conductive particles evenly dispersed in the binder, forming a slurry containing a solvent in an insulated state. After curing and drying, the solvent is volatilized, and the conductive material and the binder are solidified and tightly integrated with each other. The distance between the conductive particles becomes smaller, and the free electrons move along the direction of the applied electric field to form an electric current [3, 4]. It can be seen that curing drying is a key factor in achieving electrical conductivity in printed circuits.

In the process of printing using silver conductive ink, if the drying is not complete, the ink layer thickness of the printed sample is too thin to meet the requirements, resulting in the distance between the silver particles is too large, so that the resistance of the sample after printing is large [5, 6]. Therefore, it is very meaningful to study the

effect of post-printing processing conditions on the conductive ink printed circuit. At the same time, Lee et al. showed that the flake-shaped silver has a relatively good electrical conductivity due to the large contact area between the upper and lower overlap [7]. Therefore, this experiment uses a sheet of silver conductive ink. Generally, for any ink, the greater the amount of transfer, the better the printed circuit's conductivity [5].

This paper studied the effect of conductive ink transfer from the aspects of printing pressure, printing speed, ink viscosity, and post-processing conditions through screen printing, i.e. the influence on the conductivity of printed conductive lines.

## 2 Experimental

### 2.1 Experimental Equipment and Materials

The circuits were printed by OLAT semi-automatic screen printing machine, 350-mesh screen printing plate, PET film and Shenzhen sunflower 8000C conductive ink. And then the circuits were dried by DHG-9070A drying oven. DVII+PRO viscometer was used to measure viscosity. The viscosity of ink can be adjusted by ink transfer knife, IKA RW20 stirrer and Propyl acetate (AR, 99.0%, Aladdin). Electronic analytical balance was used to measure the amount of ink that transferred to the substrate.

### 2.2 Experimental Process

In this experiment, OLAT semi-automatic screen printing machine and Shenzhen Sunflower 8000 conductive ink were used to print conductive lines on the PET film, cured and dried, and then using a laser confocal scanning microscope and four-probe tester to measure the printing samples layer thickness and square resistance were studied. The effects of printing speed, ink viscosity, printing pressure, and post-processing conditions on the transfer effect of the conductive ink, i.e. the electrical conductivity of the printed circuit were studied.

## 3 Results and Discussion

### 3.1 Effect of Printing Speed on Printed Circuit Conductivity

In the transfer process, screen printing conductive ink, in addition to the need for a certain pressure, but also take some time. Therefore, the longer the time taken from the start of the squeegee to the end of the squeegee, the higher the ink transfer rate, i.e. the other conditions remain the same, the slower the printing speed, and the higher the humor transfer rate. The thicker the ink layer, the lower the square resistance of the printed product, the better the conductivity [4]. In this experiment, six different speeds were set for printing. The square resistance was measured at five points in the printing direction of the sample and the average value was calculated. The data was fitted with Origin software and obtained Fig. 1. The results showed that the semi-automatic screen printing used in this experiment, the machine has little effect on the transfer of ink,

therefore, in combination with the actual printing conditions, the printing speed can be appropriately controlled to ensure the high conductivity of the printed circuit.

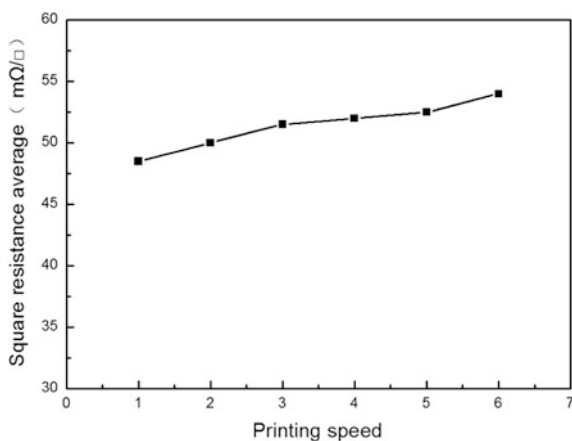


Fig. 1. Square resistance with speed curve

### 3.2 Effect of Ink Viscosity on Printed Circuit Conductivity

In general, ink viscosity is inversely proportional to its transfer rate, ink viscosity is low, the transfer rate is high; ink viscosity is high, its transfer rate is low. Each of the inks was subjected to six treatments as shown in Table 1. Three different proportions of solvent (in this case, n-propyl acetate used as the test diluent) were used to adjust the viscosity of the ink. The ink and diluent ratios were 10:3, 10:1, 20:1, the other two groups were stirred with the original ink for one hour and ten minutes respectively. The last group was the reference group without any treatment. Table 1 shows the adjusted viscosity and printed samples, the average of the square resistance .

Table 1. Viscosity and average square resistance of samples after conductive ink treatment

Processing conditions	Ink viscosity (mPa s)	Square resistance average (mΩ/sq.) value
(ink: diluent) 10:3	500	79
(ink: diluent) 10:1	2500	79.4
(ink: diluent) 20:1	4000	67
Stirring 1 h	6000	52.8
Stirring 10 min	8000	58.92
None	10,000	62.56

As can be seen from Fig. 2, when the ink viscosity is 6000 mPa s, the square resistance of the sample is the minimum. In the printing process, when the viscosity is 500 mPa s, the conductive ink will directly leak from the printing plate to the substrate

without stress, causing the sample to be dirty. When the viscosity of the ink is 10,000 mPa s, the ink transfer is difficult, and the ink layer of the printed product is thin, resulting in a large square resistance of the printed circuit and poor electrical conductivity.

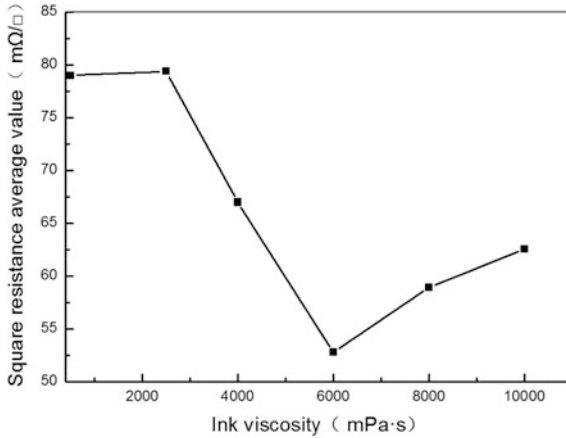


Fig. 2. Square resistance with ink viscosity curve

### 3.3 Effect of Printing Pressure on Printed Circuit Conductivity

In the printing process, the ink is transferred to the substrate by the pressure between the squeegee and the substrate. The pressure depends on the material of the plate and the type of the substrate. Due to the different pressure per unit area, the ink transfer rate is also different [8].

In this experiment, seven pressure were set, and the pressure of No. 1–7 gradually increased.

As can be seen from Fig. 3, when the printing pressure exceeds stage 4, the thickness of the ink layer decreases, resulting in increased square resistance of the sample, because the conductive ink of the printing plate is reduced, the ink transfer rate is reduced, the thickness of the ink layer is thinned, and the square resistance of the printed sample is increased. The red curve of Fig. 3 is the relationship between the ink layer thickness and the printing pressure, which coincides with the black line relationship between the square resistance and the printing pressure. Therefore, in the printing process, the printing pressure cannot be selected to be too small, the ink transfer rate will be too low, the ink layer thickness is too thin, so that the square resistance of the printing sample is too high; likewise, the printing pressure should not be too high, if the printing pressure is too high, the printed circuit will have poor electrical conductivity.

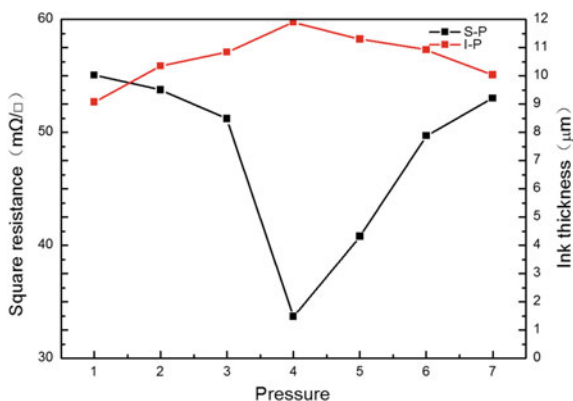


**Fig. 3.** The square resistance and ink layer thickness varies with the printing pressure curve (S-P: the square resistance varies with the printing pressure; I-P: the ink layer thickness varies the printing pressure)

### 3.4 Effect of Post-processing Conditions on the Conductivity of the Printed Circuit

In the experiment, a series of drying conditions as shown in Table 2 were set, and the square resistance at 5 points in the printing direction of the sample under different drying conditions was tested. Table 2 shows that the samples that have not been thoroughly dried have a large resistance. After drying, the square resistance of the printed sample is significantly reduced. It can be seen from the experiment, drying conditions have a great influence on the conductivity of printed samples. Therefore, a higher drying temperature is selected without affecting the print quality.

**Table 2.** Post-processing conditions and the corresponding sample average square resistance

Dry conditions (25 °C)	Square resistance average (mΩ/sq.)	Min (mΩ/sq.)	Max (mΩ/sq.)
Natural drying 10 min	671.3	621.5	814.9
Natural drying 24 h	122.9	114.6	136.1
Drying oven drying 10 min (80 °C)	75.1	69.5	84.4
Drying oven drying 10 min (100 °C)	68.4	62.5	76.3
Drying oven drying 10 min (120 °C)	51.2	42.7	55.3

## 4 Conclusions

According to the experimental research, it was found that for the OLAT semi-automatic screen printing machine, the printing speed has little effect on the transfer of conductive ink. When the viscosity is 6000 mPa s and printing pressure at stage 4, the amount of ink transfer is the most, and the printed product has the best conductivity. And the drying conditions selected 120 °C drying for 10 min, the square resistance of the sample is the lowest, and the conductivity is the best.



**Acknowledgements.** This work was supported by the Beijing Municipal Education Commission (No. SQKM201710015005). Research on Key Common Technologies of Thin Film Printing Electronics (No. PXM2017\_014223\_000041). Flexible printed electronic materials and technical innovation team building (No. Ed201801).

## References

1. Luhai, L., Zhiqing, X., et al. (2017). Research progress of print transfer rate and influencing factors of conductive ink. *Technology Review*, 35(17), 46–52. <https://doi.org/10.3981/j.issn.1000-7857.2017.17.005>.
2. Du, Y., Yu, C., & Wang, Z. (2016). Screen printing suitability and rheology of conductive silver paste. *Precious Metals*, 37(2), 82–90.
3. Cheng, Q. (2008). Problems to be noticed in conductive ink silk screen printing. *Printed Circuit Information*, 12, 65–69.
4. Lei, X., Shuai, Y., & Lu, L. (2017). Current technical status and future development direction of conductive ink. *Marine Electric & Electronic Engineering*, 37(9), 29–33.
5. Ying, W., & Junhao, Q. (2011). Study on influencing factors of ink thickness by RFID screen printing. *Packaging Engineering*, 19, 97–100.
6. Wang, Y., Qian, J., & Li, J. (2008). Research on print quality forecast model of based on ink transfer and penetration, 29(7), 69–72.
7. Lee, C. L., Chang, K. C., et al. (2011). Silver nanoplates as inkjet ink particles for metallization at a low baking temperature of 100 °C. *Colloids & Surfaces A Physicochemical & Engineering Aspects*, 381(1–3), 85–91.
8. Qiuchen, Z. (2011). Common factors that affect ink transfer rate. *Printing Field*, 3, 48–50.



# Research on the Factors of 3D Printing Forming Time Based on G-Code File

Qian Deng<sup>1,2(✉)</sup>, Qinghui Tang<sup>3</sup>, Siyang Liu<sup>1</sup>, and Ruizhi Shi<sup>1(✉)</sup>

<sup>1</sup> Information Engineering University, Zhengzhou, China  
dengqian1717@126.com, ruizhishi@sina.com

<sup>2</sup> Henan University of Engineering, Zhengzhou, China

<sup>3</sup> Beijing Satellite Navigation Center, Beijing, China

**Abstract.** FDM is one of the most widely used 3D printing techniques. This paper mainly studies the impact of different ways of placement, different cross-sectional areas and different molding angles on the molding time of 3D printing models. Using cuboids as the research models, cuboids with three different ways of placement, cuboids with different cross-sectional areas and cuboids with different molding angles were printed respectively by using HORI Z300 fused deposition modeling 3D printer. By analyzing G-code file, the effects of the above three factors on the 3D printing forming time were studied. The results showed that the model was placed horizontally, and the model with a larger cross-sectional area be placed parallel to the x-y surface, avoiding 30 and 60 molding Angle, which could shorten the forming time of the model and improve the printing efficiency.

**Keywords:** G-code file · Way of placement · Cross sectional area · Pattern angle

## 1 Introduction

FDM is a current technique used for three-dimensional (3D) printers and has become one of the most widely used rapid prototyping (RP) techniques in the past decades [1]. Products of FDM are applied to home appliances, office supplies, building modes, medical models as new product development [2]. The materials used in FDM process are generally thermoplastic materials, whose melting points are between 100 and 300 ° C, such as PLA and ABS or Nylon. Materials are fed by conveying mechanism, melt and extruded through the print heads. When the nozzle work along the trajectory of cross-section contour and internal filling inside and outside of work piece, materials extruded are rapidly solidified, and bonded with cured material, step by step accumulation, form physical artifacts. Compared with other 3D printings, FDM uses industrial-grade hot plastic as material manufacturing. Products made in this process have heat resistance corrosion, good antimicrobial properties and small internal mechanical stress [3].

There are several deficiencies in FDM, such as molding speed, formation consistency, integrity of prototyping, quality and function. In view of these shortcomings, it is necessary to study the mechanism and corresponding improvement measures [4]. Due

to a variety of reasons, such as limitations of forming mechanism, forming process, forming materials and other factors, many defects about FDM technology have been caused. This paper focuses on the following three molding factors of FDM: cross sectional area, way of placement and pattern angle to study the effects on the forming time [5]. Through analyzing the G-code file of products with different parameters, which can determine the shortest forming time. This is of theoretical significance to the FDM forming efficiency and the best forming process arrangement for the high quality prototype and even functional parts [6].

## 2 Experiments

### 2.1 Equipments and Materials

- HORI Z300 FDM 3D Printer:
  - Working temperature of printing head: 210 °C;
  - Working temperature of printing plate: 30 °C;
- Software: 3D ONE; HORI 3D Print Software;
- Filament: Type: PLA; Density: 2.983 g/m<sup>3</sup>; Diameter: 1.75 mm;

### 2.2 Samples

Draw one cuboids with size of 10 \* 20 \* 30 (mm<sup>3</sup>) and draw another 18 cuboids with different cross sectional areas showed in Fig. 3 by using 3D ONE software.

### 2.3 Methods

- (1) Draw cuboids which were mentioned in 2.2.
- (2) Load the cuboids into HORI 3D Print Software and put the cuboids in three different ways of placement showed in Fig. 1: horizontal placement (model A for short), sidelong placement (model B for short), vertical placement (model C for short).

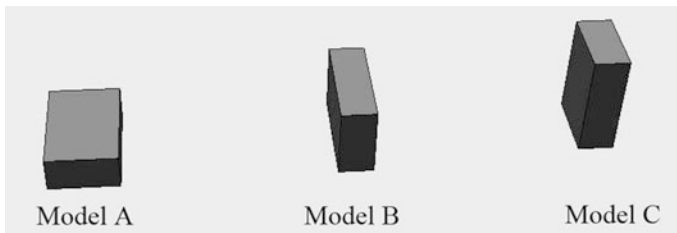


**Fig. 1.** Ways of placement

(3) The parameters of 3D printer are set as following:

Type of support structure: tree form; Model support type: base support;  
 Interior fill pattern: grid; Filling rate: 20%;

- (4) Print model A, B, C with the layer heights of 0.1 mm and 0.2 mm.
- (5) Print cuboids with different cross sectional areas.
- (6) Print model A, B, C with different pattern angles respectively: 0°, 5°, 10°, 15°, 20°, 25°, 30°, 35°, 40°, 45°, 50°, 55°, 60°, 65°, 70°, 75°, 80°, 85°, 90°.

### 3 Results and Discussion

#### 3.1 Effect of Way of Placement on Forming Time

Figure 2 showed the effect of different way of placement on forming time: no matter the layer height was 0.1 or 0.2 mm, the forming time of model A was longest, and model C was shortest. The less layer height was, the more forming time was.

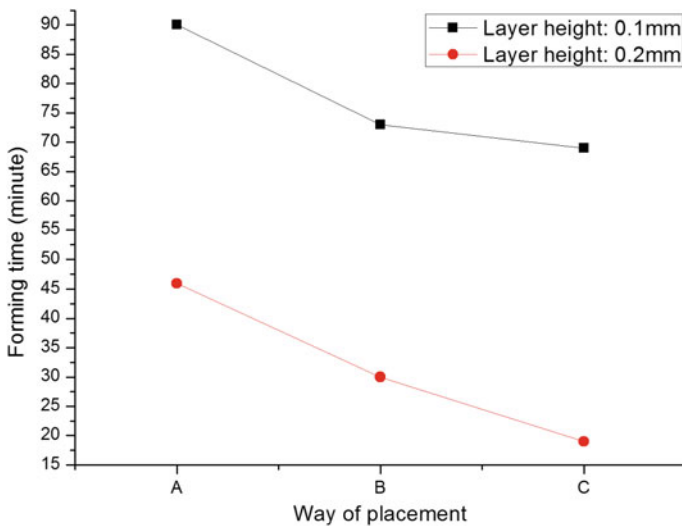


Fig. 2. Effect of different ways of placement on forming time

Table 1 showed the printing content and forming time of A, B, C. Layer 1 to layer 4 were combined into the bottom of cuboids, which were entity and contained the parts of inset and surface. In this period, the speed of G1 of model A was lower than the speed of model B and model C. Layer 5 to layer 145, layer 5 to layer 95, layer 5 to layer 45 were combined into the main body of cuboids model A, B, C respectively. In these periods, the speed of G1 of model A was lowest, the speed of G1 of model C was fastest, the speed of G1 of model B was between them. Layer 146 to layer 149, layer 96

to layer 99, layer 46 to layer 49 were combined into the top of cuboids A, B, C respectively. In these periods, the speed of G1 of model A was lower than the speed of model B and model C. Although Model A, B, C had the same bulk, due to the different forming speed above, the forming time of model C was shortest, and the forming time of model A was longest.

**Table 1.** G-code file of model A, B, C

Layer No.	Way of placement	Printing content	F of G0 (mm/min)	F of G1 (mm/min)	Forming time (min)
Layer 1	A	Inset, Surface	3600	960	32.331858
	B			1200	38.218857
	C			1200	75.718857
Layer 2	A	Inset, Surface	3600	1260	24.854034
	B			1500	31.307058
	C			1500	60.333793
Layer 3	A	Inset, Surface	3600	1500	20.669163
	B			1800	25.495350
	C			1800	50.498086
Layer 4	A	Inset, Surface	3600	1800	17.448261
	B			2100	22.411005
	C			2100	43.190891
L5-L145	A	Inset, Surface, Infill	3600	720	16.16
L5-L95	B			1080	15.64
L5-L45	C			1800	15.73
Layer146	A	Inset, Surface	3600	2040	15.416785
Layer96	B			2400	19.651489
Layer46	C			2400	37.832461
Layer147	A	Inset, Surface	3600	1980	15.739660
Layer97	B			2400	19.245942
Layer47	C			2400	37.998677
Layer148	A	Inset, Surface	3600	2040	15.415320
Layer98	B			2400	19.631005
Layer48	C			2400	37.833748
Layer149	A	Inset, Surface	3600	1980	15.739624
Layer99	B			2400	19.245889
Layer49	C			2400	37.998633

In addition, the speed of the printing equipment on the x-y plane was faster than that along the z-axis, in another word, the production efficiency of the model on the z-axis height was lower than that of the x-y plane. At last, the more layers, the more forming time were needed.

### 3.2 Effect of Cross Sectional Area on Forming Time

Figure 3 showed the effect of cross sectional area on forming time. All the cuboids had the same height. The length and width of cuboids showed in Fig. 3 were from  $10 * 20 \text{ mm}^2$  to  $46 * 20 \text{ mm}^2$ . The general tendency was that the bigger the area was, the faster the speed was. The speeds of forming bottom and top of the cuboids were almost the same among different size of cuboids. For main body, the speeds increased from 720 to 2400 mm/min as the cross sectional area increased. When the size of cross sectional area was up to  $42 * 20 \text{ mm}^2$ , the speed stayed at 2400 mm/min.

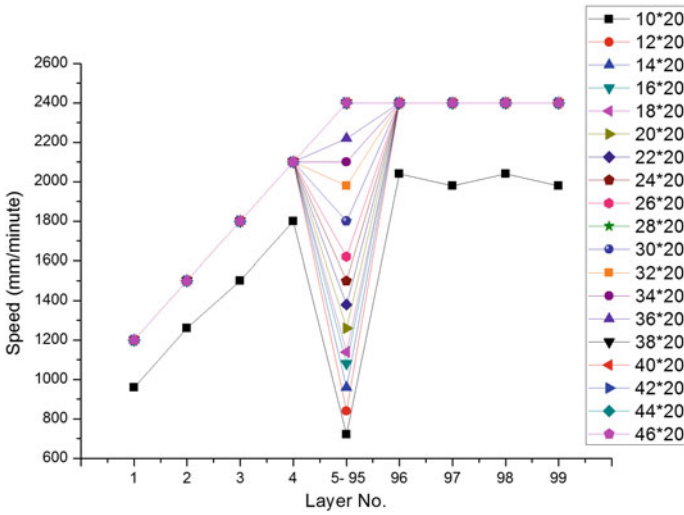


Fig. 3. Effect of cross sectional area on forming time

### 3.3 Effect of Pattern Angle on Forming Time

Figure 4 showed the effect of pattern angle on forming time. The general tendency was like a letter M. The extreme values were corresponding to the pattern angles of 30° and 60° for model A. The extreme values were corresponding to the pattern angles of 30° and 60° for model B. The extreme values were corresponding to the pattern angles of 30° and 80° for model C. The cases of producing extreme values was that it needed more layers and more support to complete the product in these angles. If support was removed, the forming time would reduce 5–10 min in this experiment.

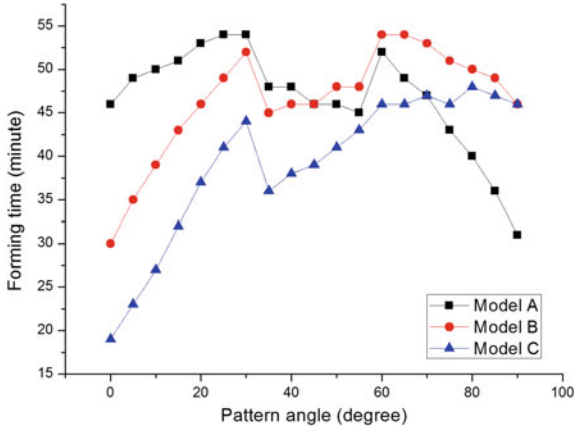


Fig. 4. Effect of pattern angle on forming time

## 4 Conclusions

It could obtain many data from G-code file, like forming time, temperature, forming speed, support type and so on. This paper studied the effect of way of placement, cross sectional area and pattern angle on forming time through studying G-code file. The speed of the printing equipment on the x-y plane was faster than the speed along the z-axis. The best way of placement was horizontal placement if it was possible. The bigger the cross sectional area was, the faster the speed was. It was better to choose bigger cross sectional area parallel with x-y plane. When choosing pattern angles, 30° and 60° or too close to these angles should be avoided.

## References

1. Cantrell, F. T., Rohde, S., Damiani, D., et al. (2017). Experimental characterization of the mechanical properties of 3D-printed ABS and polycarbonate parts. *Rapid Prototyping*, 23, 811–824.
2. Weller, C., Kleer, R., & Piller, F. T. (2015). Economic implications of 3D printing: Market structure models in light of additive manufacturing revisited. *International Journal of Production Economics*, 164, 43–56.
3. Jian, H., Yikan, W., & Tian, X., et al. (2016). Design and study of fused deposition modeling (FDM) 3D printing process parameters optimization. *Technology and Test*, 06, 139–142, 146.
4. Tianming, W. (2006). Research on high speed extrusion device and rapid forming process theory based on melt and accumulation of particles. Ph.D. thesis, Shanghai Jiaotong University, China.
5. Farzadia, W., Solati-Hashjin, M., et al. (2015). Effect of layer printing delay on mechanical properties and dimensional accuracy of 3D printed porous prototypes in bone tissue engineering. *Ceramics International*, 41(7), 8320–8330.
6. Dan, H., Xiaoxun, Z., Xi, W., et al. (2016). The research of the printing time and mechanical properties of the printout based on FDM process. *China Plastics Industry*, 44(03), 89–93.



# Design and Realization of a Support Bracket for Medical Test Tubes Based on 3D Printing

Chunmei Li<sup>(✉)</sup>, Ying Xiao, and Liang Zheng

Department of Graphic Communication, Shanghai Publishing  
and Printing College, Shanghai, China  
lichunmeil206@sina.com

**Abstract.** Design and produce a support bracket according to the special requirements of medical test tubes based on 3D printing methods in this paper. First a suitable 3-dimension model of the support bracket is established based on the requirements. Then the model is sliced into a .STL or .OBJ file. Different 3D printing methods and material were used to print the model. And the material, size accuracy, surface profile and cost were analyzed among the different 3D printing methods. It was found that material, dimensional accuracy and surface profile of SLS process was completely meet the requirements although it was expensive. Industrial FDM method can satisfied the demands and the cost was endurable. Although 3DP process using gypsum powder can just meet the demands of material and dimensional accuracy and the cost was the lowest, the surface of the bracket was too rough. So a suitable 3D printing process should be chosen to satisfy the requirements according to the material, dimensional accuracy, surface profile and the cost.

**Keywords:** 3D printing · FDM · SLS · 3DP

## 1 Introduction

Recently rapid prototyping and additive manufacturing technology has been widely adopted by engineers and designers. Compare to conventional mechanical processing ways such as turning, planning, and milling those will be very costly and time consuming 3D printing has so many advantages: to manufacture complex structure products without assembly; to shorten the processing cycle; saving material; the accurate replication; personalization and lower costs, etc. Based on its versatility 3D printing has been used in dentistry [1], electrochemical [2], strain sensing [3], automotive [4], robot designs [5], medicine [6] and biochemistry [7], etc.

Many different 3D printing processes have been created since 1970s. All those printing machines were large, costly, and restricted in what they could manufactured without exception [8]. Now a lot of 3D printing processes are arisen. The main distinctions among those processes are that how the layers are deposited and what kind of the material can be used. The most widely used processes include fused deposition modelling (FDM), stereo lithography (SLA), selective laser melting (SLM), selective laser sintering (SLS), 3-dimension printing (3DP) and laminated object manufacturing (LOM). Each process has its own advantages and disadvantages. Printing process and



printing material are the two important factors restricting the development of 3d printing technology. Polymer and powder are the main material to print an object.

There are many subjects that lots of researchers studied. These were stated in [9] that printing direction, printing density and supported pattern affected the models printed in FDM. An optimized scheme to generating support structure for 3D printing was studied in [10]. In [11] it was discussed that how printing the hollow objects without infill via fused deposition modeling. An efficient path generating algorithm for 3D printing was established in [12]. In [13] it was proposed that dimensional accuracy and surface finish should be both taken into account to measure quality of affordable 3D Printing. In fact the most common application is to design some personalized and unique parts by using 3D printing process. In this paper a suitable model was designed and printed by 3D printing process according to the user's demands.

## 2 Case Study

### 2.1 Requirements of the Bracket

A support bracket for medical test tubes was put forward by a company. 16 tubes should be hung on the brackets. The cap of a tube is made of plastic and the material used by the bottle is glass. Figure 1 shows the picture of the tube. The size of the tube is shown in Fig. 2. Requirements are listed:



**Fig. 1.** The picture of the tube

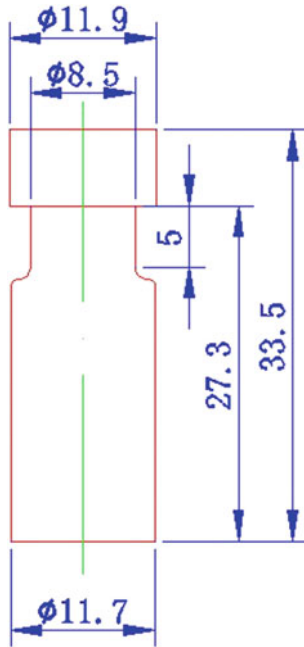


**Fig. 2.** The size of the tube

- (1) Tubes can be picked up and put down without blocking.
- (2) Tubes can be hung by the caps on the Brackets.
- (3) Ensure each tube can accept to the special lights in an experiment box.
- (4) The bracket should not be deformed in the experiment box where the temperature is 80 °C.
- (5) Size accuracy is 0.2 mm.
- (6) Delivery time is 24 h.

An original bracket was manufactured by traditional mechanical processing. There are several problems as following:

- (1) It was expensive to custom single one product.
- (2) Material waste is very serious.
- (3) Several parts need to assemble.
- (4) It can't be produced in 24 h.

According to the requirements and characteristics of the bracket, 3D printing process can be used to solve these problems.

## 2.2 CAD Modeling

A suitable 3D model should be prepared before manufacturing products by 3D printing. There are two ways to get the model. The models can be printed by 3D printing machines should be designed with a computer aided design package and this is

forward modeling. UG, Pro/e, Solidworks, 3dsMax are engineering software. ZBrush, Rhino, Silo, Alias are the creative software. When you want to replicate works or products the 3D scanners or digital cameras should be used. The later method is always used in archaeology or medical fields.

Figure 3 shows the size of upper surface.  $\Phi 11.8$  mm is smaller than the diameter of the tube caps  $\Phi 11.9$  mm and larger than the diameter of bottle  $\Phi 11.7$  mm. So the tube can be hung on the upper surface. The size of the gap 8.4 mm is smaller than the diameter of bottle neck  $\Phi 8.5$  mm. when the bracket is rotating slowly with 16 tubes, the tubes will not be thrown out. Figure 4 shows the 3D model of the bracket. The height of 4 poles to support the upper surface is 38.5 mm, bigger than the height of a tube 33.5 mm to ensure all the tubes can accept to sufficient lights in the experiment box. So the model can satisfy the requirements (1)–(3).

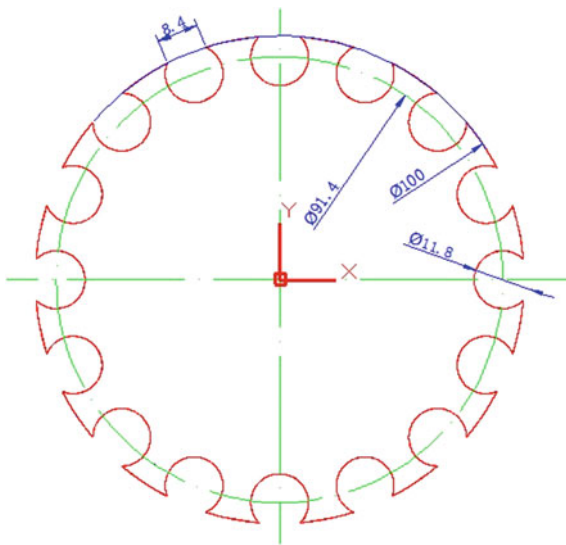


**Fig. 3.** The size of upper surface

### 2.3 Different Process and Material of 3D Printing

The suitable 3D printing process and material should be chosen for printing the bracket. A FDM 3D printer (desktop and industrial) is taken into account firstly because it is cheaper than other 3D printing processes.

The differences between desktop FDM printers and industrial FDM printers are listed as following:

- (1) Temperature control system. Generally there has no temperature control in a desktop FDM printer. Without temperature control system would lead to plug in nozzles, wire drawing unevenly, warped edge and poor stability. Most of industrial FDM printers have temperature control system.

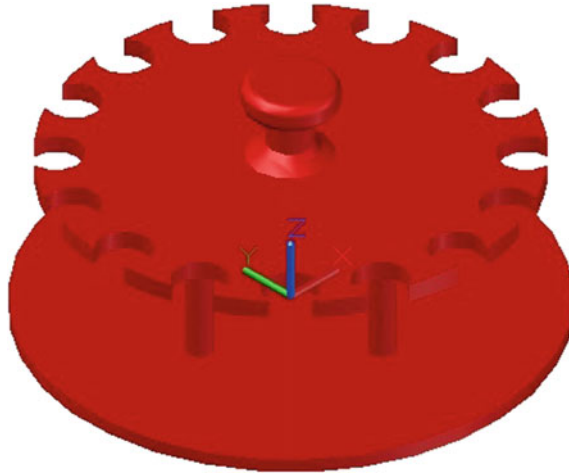


**Fig. 4.** 3D model of a bracket

- (2) Support. The desktop FDM printer has generally only one printing nozzle. And support material is always the same as model material. So the surface where there needs supports will be rough and also easy to deformation. An industrial FDM printer has more than one printed nozzle and different material can be used as supports especially water dissolvable material.
- (3) Material. Most material used by desktop FDM printers are PLA and ABS which can't endure high temperature. A test was done to put a product made by PLA into the oven which was heated to 60 °C, then the product turned soften. We should review the requirements listed in 2.1. No. 4 is that the bracket should resistant 80 °C. Material used in industrial FDM printers is called engineering plastics. Most of them can resistant high temperature up to 80 °C. And its mechanical properties are excellent.

The principle of SLS 3D printing process is that the computer controls laser to move to the accurate position where the powder material was sintering under high temperature of laser and then step by step sintering to finish the model. The powder used in SLS usually is polyamide (PA) also named as nylon which has many advantages such as non-toxic, light weight, higher hardness, high temperature resistance, good wear resistance and good corrosion resistance. SLS needn't to design support structure like FDM process. Because the powder hasn't been sintering can be part of the cavity and cantilever in the model so even very complicated prototypes can be directly produced.

3DP process is similar to SLS process. The difference between them is that 3DP is binding powder by spray adhesive and SLS is to use the infrared laser sintering powder. Gypsum powder is a kind of material that commonly used in 3DP.

The SLA 3D printing process is abandoned for that the material—photosensitive resin will change its nature under high temperature and strong light irradiation.

Finally we choose industrial FDM, SLS, 3DP processes to print the bracket.

## 2.4 Slice the Model

Regardless which kind of the 3D modeling software was used, the file of 3D model should be saved as STL or OBJ file firstly. STL or OBJ file is the general format that can be read by different 3D printers produced by different manufacturing enterprises. Then the model will be sliced into a succession of thin layers by the program build-in different 3D printers. Finally a file including instructions that could be read by a specified 3D printer is generated.

## 3 Experiments

Industrial FDM, SLS, 3DP process are used to print the bracket. Table 1 shows the parameters of 3D printers, model material and support material we used, build time and cost. Figure 5 shows the pictures of Stratasys FORTUS 450mc, FS403P and Spectrum Z<sup>TM</sup>510. Figure 6 shows the three brackets printed by three 3D printers. Especially dimensional accuracy of the key size and surface finish quality are compared among three products printed by three 3D printers.

**Table 1.** Parameters of 3D printers and quality of the brackets

	Industrial FDM	SLS	3DP
3D Printer	Stratasys FORTUS 450mc	FS403P	Spectrum Z <sup>TM</sup> 510
Machine dimension	406 × 355 × 406 mm	375 × 375 × 430 mm	254 × 356 × 203 mm
Layer thickness	0.178 mm	0.12 mm	0.102 mm
Print precision	±0.2 mm	±0.1 mm	600 × 540 dpi
Model material	ABS-M30i	Φ10–Φ30 μm Polyamide	Φ38 μm Gypsum
Support material	SR-30 (water dissolvable)	Φ10–Φ30 μm Polyamide	Φ38 μm Gypsum
High temperature resistance	82 °C	120 °C	80 °C
Build time	3 h	Preheating 3 h, printing 3 h, cooling 3 h	3 h
Cost (RMB)	400	780	300
Key size Φ11.8 mm	Φ11.76 mm	Φ11.82 mm	Φ11.72 mm
Surface profile	189 μm	115 μm	322 μm

Material, dimensional accuracy and surface profile of SLS process was completely meet the requirements although it was expensive. Industrial FDM method can satisfied the demands and the cost was endurable. Although 3DP process using gypsum powder can just meet the demands of material and dimensional accuracy and the cost was the lowest, the surface of the bracket was too rough. If the surface finishing quality is not



**Fig. 5.** The pictures of printers. **a** Stratasys FORTUS 450mc. **b** FS403P. **c** Spectrum Z<sup>TM</sup>510

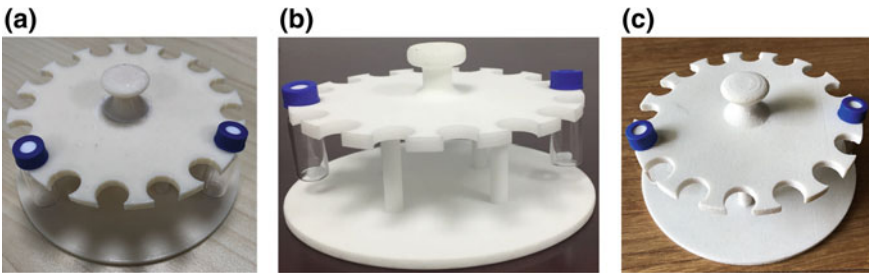


**Fig. 6.** The bracket printed by **a** Stratasys FORTUS 450mc. **b** FS403P. **c** Spectrum Z<sup>TM</sup>510

so good the friction between the bracket and the medical test tube would be increased. So the bracket printed by SLS process was accepted by the company.

## 4 Conclusions

According to the results of the experiments, we can conclude that a suitable 3D printing process should be chosen according to the material, dimensional accuracy, surface profile and the cost. If the cost is the most important factor we can chose 3DP process. If the quality is the most important factor we can chose SLS process. We always choose industrial FDM process because of its high function-price ratio.

**Acknowledgements.** This study is supported Lab of Green Platemaking and Standardization for Flexographic Printing, which is belonged to Key Laboratory of science and stander press and publication, State Administration of Press, Publication, Radio, Film and Television of the People's Republic of China.

## References

1. Bose, S., Vahabzadeh, S., & Bandyopadhyay, A. (2013). Bone tissue engineering using 3D printing. *Materials Today*, *16*(12), 496–504.
2. Ambrosi, A., & Pumera, M. (2016). 3D-printing technologies for electrochemical applications. *Chemical Society Reviews*, *45*(10), 2740–2755.
3. Muth, J. T., Vogt, D. M., Truby, R. L., Mengüç, Y., Kolesky, D. B., Wood, R. J., & Lewis, J. A. (2014). Embedded 3D printing of strain sensors within highly stretchable elastomers. *Advanced Materials*, *26*(36), 6307–6312.
4. Savastano, M., Amendola, C., D’Ascenzo, F., Massaroni E. (2016). 3-D printing in the spare parts supply chain: an explorative study in the automotive industry. In: L. Caporarello, F. Cesaroni, R. Giesecke, & M. Missikoff (Eds.), *Digitally supported innovation* (pp. 153–170). Cham: Springer.
5. Ceccarelli, M., Carbone, G., Cafolla, D., & Wang, M. (2016). How to use 3D printing for feasibility check of mechanism design. In *Advances in robot design and intelligent control. advances in intelligent systems and computing* (Vol. 371). [https://doi.org/10.1007/978-3-319-21290-6\\_31](https://doi.org/10.1007/978-3-319-21290-6_31).
6. Xiao, Jianhua, & Gao, Yanfeng. (2017). The manufacture of 3D printing of medical grade TPU. *Progress in Additive Manufacturing*, *2*, 117–123. <https://doi.org/10.1007/s40964-017-0023-1>.
7. Gross, B. C., Erkal, J. L., Lockwood, S. Y., Chen, C., & Spence, D. M. (2014). Evaluation of 3D printing and its potential impact on biotechnology and the chemical sciences. *Analytical Chemistry*, *86*(7), 3240–3253.
8. Amon, C. H., Beuth, J. L., Weiss, L. E., Merz, R., & Prinz, F. B. (2014). Shape deposition manufacturing with microcasting: processing, thermal and mechanical issues. *Journal of Manufacturing Science and Engineering*, *120*(3).
9. Domínguez-Rodríguez, G., Ku-Herrera, J. J., & Hernández-Pérez, A. (2017). An assessment of the effect of printing orientation, density, and filler pattern on the compressive performance of 3D printed ABS structures by fuse deposition. *The International Journal of Advanced Manufacturing Technology*, *95*, 1685. <https://doi.org/10.1007/s00170-017-1314-x>.
10. Yu-xin, M., Li-fang, W., Jian-kang, Q., & Runyu, W. (2015). *An optimized scheme to generating support structure for 3D printing* (pp. 571–578). Springer International Publishing Switzerland.
11. Wei, X.-R., Zhang, Y.-H., Geng, G.-H. (2016). No-infill 3D Printing. *3D Research Center*, *7*, 24. <https://doi.org/10.1007/s13319-016-0098-3> (Berlin: Kwangwoon University and Springer).
12. Wojcik, M., Pozniak-Koszalka, I., Koszalka, L., & Kasprzak, A. (2017). Experimentation system for path planning applied to 3D printing. In *Advances in applied digital human modeling and simulation. Advances in Intelligent Systems and Computing* (pp. 291–301).
13. Ko, M., Kang, H., ulrim Kim, J., Lee, Y., & Hwang, J.-E. (2016). *How to measure quality of affordable 3D printing: Cultivating quantitative index in the user community* (pp. 116–121). Springer International Publishing Switzerland. [https://doi.org/10.1007/978-3-319-40548-3\\_19](https://doi.org/10.1007/978-3-319-40548-3_19).



# Research on the Printability of Pearl Inkjet Photo Paper with Nano-copper Flexography Ink

Jinghan Liu, Lai Peng, and Yi Fang<sup>(✉)</sup>

School of Printing and Packaging Engineering, Beijing Engineering Research Center of Printed Electronics, Beijing Institute of Graphic Communication, Beijing, China  
fangyi@bigc.edu.cn

**Abstract.** With the fast development of information science and technology, printed electronics technology obtains great potential for application on flexible electronics. Printing electronics has many advantages, such as low cost, low energy consumption, green environmental protection and other features. Printed electronics abandoned conventional “subtraction” etching process and applied “additive” printing process, thereby reducing the waste of materials and pollution. The rise of printing electronics has also contributed to the development of conductive ink. This research aimed to the printability of nanoscale copper ink on pearl inkjet photo paper. By using the nano-copper conductive ink which is fabricated on our lab, the conductive layer was coated and printed on the photo paper. Then the microscopic characterization of the pearl inkjet photo paper was carried out to reveal the surface topography. At last, the microscopic characterization of the pearl inkjet photo paper with copper layer was conducted to analyze the printability, including the testing of adhesion and drying speed. This work could be beneficial for the development of flexible electronic devices.

**Keywords:** Printability · Pearl inkjet photo paper · Nanoscale copper ink

## 1 Background

With the fast development of electronics technology, the huge demand on the electronic product is increasing. More precise requirements of the electronic product have been raised. The manufacturing process of high-precision circuit boards has ushered in a new era of nano-copper conductive ink [1]. The materials of printed electronic has become a key factor in this field. Compare to nano-silver conductive inks in the past several years, nano-copper conductive ink is an emerging technology [2]. As a key material in printed electronics, nanoscale copper ink is important in the electronics industry. It has also been widely researched in universities and institutes [3]. Paper substrate can greatly reduce the weight of electronic devices with conductive ink [4, 5]. Paper substrate with printed electronics can replace the traditional printed circuit board manufacturing process with plastic substrates. It can reduce manufacturing costs and reduce environmental pollution [6]. Photo paper has several unique advantages, such as waterproof, sun protection, long-term preservation, versatile and suitable for pigment



and dye ink printing in a variety of printer types. Among them, the pearl inkjet photo paper is a common product in the paper market. It has good performance and potential to reach the demand on printed electronic device manufacturing and application. In the manufacturing, the complexity on the manufacturing process could be reduced, due to the characteristics of the additive process. It can also realize partial replacement and on-demand production processing [7–9]. Weight of the product makes modern industrial products lighter and thinner, and raises the progress on modern industry. On the environmental side, the use of paper material and nano-copper conductive ink can greatly reduce heavy metal pollution and water pollution during electronic device manufacturing. It could also be used as a substrate for more flexible electronic devices.

Therefore, the research on the printability of nano-copper conductive ink on paper substrate has great significance. It can open up the market after leaving the laboratory stage. In this research, the pearl inkjet photo paper is used as the substrates. The nanoscale copper ink was printed on the pearl inkjet photo paper by flexography. The surface topography of the pearl photo paper was characterized by the laser scanning confocal microscope. The relationship between the topography of the photographic paper and the conductivity of the pattern was investigated.

## 2 Experimental

The nanoscale copper ink based on flexography printing has been prepared on the lab. The nano-copper weight content of the ink is 70%. The main solvent of the nanoscale copper ink is glycerol and water. The viscosity of the nanoscale copper ink is about 3000–4000 cp. The fluidity is about 10–15 mm/s. The pearl inkjet photo paper was purchased from the IMACOLOR. Copper layer on the photo paper was printed by applying a printability tester (IGT-F1) with flexographic plate or coated by a wire rod. 150 N of printing pressure and 0.3 m/s of printing speed were applied. The coated copper layer was analyzed by the laser scanning confocal microscope. The experiment used 3 M tape to conduct the adhesion testing of the copper pattern. 3 M tape method is suitable to test adhesion of ink and substrate. It is widely used in ink adhesion detection in flexographic printing and other printing processes. It is a standard test method. The specific operation method is as follows: (1) Use a knife to cut the top of the sample, and the grid is a square of 1 mm × 1 mm to complete the cutting of the ink film layer. (2) Stick the tape on the surface of the photopaper and keep it for 2–5 min. (3) Strip the tape quickly at an angle of 60°. (4) Observe the peeling results (Table 1).

## 3 Results and Discussion

According to the introduction of the manufacturer and visual observation, the feature of the pearl photo paper is clear texture, crystalline and sparkling. Combined with the CLSM characterization in Fig. 1, it can find that the pearl photo paper was coated with a thin film. The thin layer on the surface can prevent the ink from penetrating and spreading into the paper. The surface smoothness of the pearl photo paper is relatively low. There are large fluctuations on the surface. The paper is firm enough to avoid damage caused by mechanical forces during printing or coating process.

**Table 1.** Adhesion level judgment

Adhesion level	Peeling effect
5B	The cutting edge is very smooth and there is no shedding in the square
4B	There is fine powder falling off at the intersection of the cutting lines, and the affected surface is less than 5%
3B	At the edges and intersections of the cut lines, fine powder falls off, and the affected mesh is between 5 and 15%
2B	In the edges and squares of the cutting line, there are flakes falling off, and the affected grid is between 15 and 35%
1B	At the edge of the cutting line, the strip coating peels off and the entire square falls off, and the affected grid is between 35 and 65%
0B	More serious layer shedding than 1B

**Fig. 1.** Surface topography of the pearl photo paper

It can be seen that the pearl photo paper has a low whiteness in Table 2. The smoothness is also relatively low. The roughness measured by the air leakage method is higher than that of the coated paper. It might be due to the influence of the waterproof layer and the coating layer of the pearl photo paper. However, the air leakage rate is slow, which affects the experimentally measured data. Therefore, the pearl photo paper has better printability than the ordinary coated paper from this experiment.

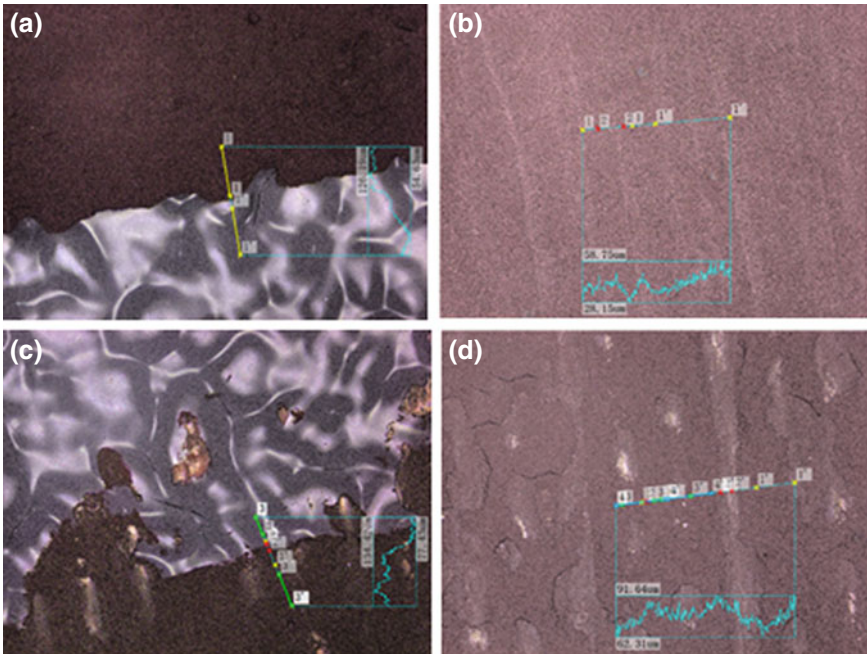
By comparing the printed ink layer at different thicknesses, it can be found that when the printed copper layer is thin, the topography of the photo paper can still be seen; when the copper layer is thick, the original topography of the photo paper cannot be seen. In printing applications, we should prefer the thick printed ink layers in order

**Table 2.** Performance characterization of the pearl inkjet photo paper

Paper performance	Pearl inkjet photo paper	128 g coated paper (comparative)
Whiteness	106.0	143.5
Smoothness	6.55	270 (first surface) 255.6 (second surface)
Roughness	9.35	1.77

to ensure the integrity. Therefore, it could ensure the electrical conductivity and stability of the conductive lines.

It can be seen from Fig. 2 that the edge of the printed area is smooth and the ink layer is thick. It is indicated that flexographic printing can form a regular track on the pearl photo paper. There is a good printing performance between the nanoscale copper ink and the pearl photo paper. Moreover, it is possible to prepare a regular electrical circuit in future applications (Table 3).



(a) is the edge of the thick ink layer; (b) is the solid area of the printed photo paper; (c) is the edge of the thin ink layer; (d) is the solid area of the printed photo paper

**Fig. 2.** CLSM characterization of the nanoscale copper inks on the pearl photo paper

**Table 3.** Adhesion level judgment table

Ink type	Thickness ( $\mu\text{m}$ )	
	Nano-copper flexographic ink	47.36

It has been observed that, in this experiment, the adhesion of the nanoscale copper ink to the pearl area is approximately 1B. According to the relevant experiments, we

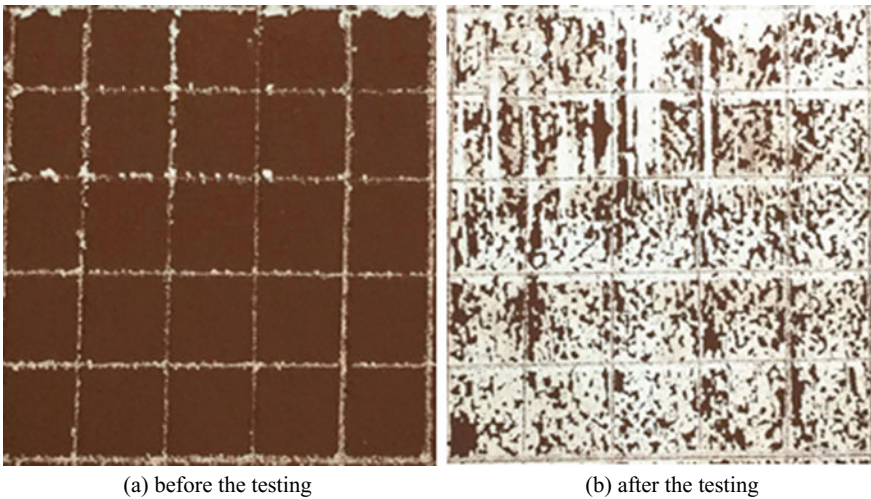


**Fig. 3.** Adhesion test of the flexographic nanoscale copper ink on the pearl photo paper

can find that the adhesion of the dried ink layer is poor. It might cause undesirable phenomena such as smudging after printing. In the further research, it is necessary to improve the adhesion of the nanoscale copper ink (Fig. 3).

In the drying test, the flexographic nanoscale copper ink exhibited a slow drying speed and formed a thick film layer. The printed ink layer was not completely dried even after ten minutes. After a long time, the ink layer is substantially dried because the ink is oxidized and dried. Then, an external force is applied to the ink layer by a doctor blade. Under the action of external force, the ink film is separated from the photo paper, and only a small amount of ink layer remains (Fig. 4).

## 4 Conclusions

The printability of the flexographic nanoscale copper ink on the pearl inkjet photo paper is good, although there is a long drying time. The surface topography of the pearl photo paper was analyzed. The adhesion between the printed ink layer and photo paper



**Fig. 4.** Drying test of the nanoscale copper ink on the pearl photo paper

is poor. The pearl photo paper can absorb the solvent in the nanoscale copper ink well. The nanoscale copper ink can form a uniform conductive layer on the surface of the photopaper. Generally, the pearl photo paper has the potential to become a suitable electronic device substrate. It will be significant to the development of flexible electronic devices.

**Acknowledgements.** This work is supported by Beijing Municipal Commission of Education Foundation for Ability Construction of Scientific and Technological Innovation Service through the projects: Research on Nanoscale Copper Conductive Ink (PXM2017\_014223\_000036), National Natural Science Foundation of China (NSFC) through the projects: printing dynamics for high-definition printed electronics (61474144).

## References

1. Mott, D., et al. (2007). Synthesis of size controlled and shaped copper nanoparticles. *Langmuir*, 23, 5740–5745.
2. Hung, C. (2008). Decomposition kinetics of ammonia in gaseous steam by a nanoscale copper-cerium bimetallic catalyst. *Journal of Hazardous Materials*, 150(1), 53–61.
3. Boccuzzi, F., Chiorino, A., Manzoli, M., et al. (2002). Gold, silver and copper catalysts supported on TiO<sub>2</sub> for pure hydrogen production. *Catalysis Today*, 75(1–4), 169–175.
4. Lee, B., Kim, Y., Yang, S., et al. (2009). A low-cue-temperature copper nano ink for highly conductive printed electrodes. *Current Applied Physics*, 9(2 supplement 1), e157–e160.
5. Songping, W., Li, J., Jing, N., et al. (2007). Preparation of ultra-fine copper-nickel bimetallic powders for conductive thick film. *Intermetallics*, 15(10), 1316–1321.
6. Joshi, S. S., Patil, S. F., Iyer, V., et al. (1998). Radiation induced synthesis and characterization of copper nanoparticles. *Nanostructured Materials*, 10(7), 1135–1144.
7. Cheng, Xiaonong, Zhang, Xifeng, Yin, Hengbo, et al. (2006). Modifier effects on chemical reduction synthesis of nanostructured copper. *Applied Surface Science*, 253(5), 2727–2732.

8. Ihalainen, P., Maattanen, A., Jarnstrom, J., et al. (2012). Influence of surface properties of coated papers on printed electronics. *Industrial and Engineering Chemistry Research*, 51(17), 6025–6036.
9. Li, W., et al. (2013). Preparation of water-based nano-silver gravure conductive ink used for printed electronics. *Applied Mechanics and Materials*, 262, 523–526.



# Feasibility Study of Flexographic Platemaking Based on SLA 3D Printing Technology

Liang Zheng<sup>(✉)</sup>, Lingjun Kong, and Chunmei Li

Printing and Packaging Engineering Department, Shanghai Publishing  
and Printing College, Shanghai, China  
zg\_zg@163.com

**Abstract.** The technology of additive manufacturing, represented by 3D printing, has changed traditional manufacturing, and it can also be applied to platemaking for flexographic printing in principle. The purpose of paper is to study the feasibility of platemaking for flexographic printing by Stereo Lithography Apparatus 3D printing technology. We designed and completed the experiment to detect the line width error and line edge straightness of the results of Stereo Lithography Apparatus 3D printing technology. The detection results are compared with the results of flexographic platemaking in the mainstream market. The results confirm that the Stereo Lithography Apparatus 3D printing technology can be applied to platemaking for flexographic printing, and provide the basis for the flexographic platemaking using the technology of additive manufacturing.

**Keywords:** Flexographic printing forme · SLA 3D printing · Line width · Line edge straightness

## 1 Introduction

At present, there are several flexographic platemaking technologies, such as film imaging technology, laser direct imaging technology (CDI, Cyrel Digital Imager technology), and flexographic direct engraving technology [1], and the former two technologies are the current mainstream technologies. All these technologies are reducing material process. The technology of additive manufacturing, represented by 3D printing, can be applied to platemaking for flexographic printing in principle [2].

Several patents have been issued, and several methods and equipment for flexographic platemaking by 3D printing have been made public [3–5]. They all use 3DP (Three Dimension Printing) technology, which sprays the material onto the substrate with nozzles, and then solidifies the plate. In these technologies, blockage of spray nozzles, cross-linking and solidification under illumination or heating at 80–200 °C after each spraying may lead to uncertainty in the quality of platemaking results. The Stereo Lithography Apparatus (SLA) 3D printing technology selected in this paper can avoid the above problems and help to form a stable flexographic platemaking process based on augmented material manufacturing technology. This paper designed an experiment to analyze the feasibility of using SLA 3D printing equipment to complete flexographic platemaking.

## 2 Detecting Elements and Detecting Methods

Printing elements mainly include images, graphics, and text, and they are dots, lines and areas in the plates. Lines and areas make up most of the graphics and text, and they are the most common page elements in print products, which are easy to be rendered with the current SLA 3D printing equipment. This paper mainly aims at lines, and determines the imaging quality of SLA 3D printing technology.

The detection process is to digitize the 3D print molding results to obtain digital images, and the image processing technology is used to detect the data of the molding results.

### 2.1 Line Width

The line width is defined as the average width of the line along the direction perpendicular to the centerline of the line, which is the width from the edge threshold of one side to the edge threshold of the other side of the line, where edge threshold is defined as 60% of the reflection coefficient [6].

When calculating the line width, first convert the pixel value of the digital image to the brightness value and calculate the reflection coefficient. Then connect the points where the reflection coefficient is equal to 60% to form the threshold contour line. At last, each position perpendicular to the centerline of the line has two points with reflectance equal to 60%, denoted  $A_{60i}$ ,  $B_{60i}$ . If the number of the measurement point is  $n$ , the formula for the line width is:

$$W = \frac{1}{n} \sum_{i=1}^n |A_{60i} - B_{60i}| \quad (1)$$

### 2.2 Line Edge Straightness

The edge of the line may be geometrically distorted from its ideal position, showing a zigzag or wavy shape, deviates from the smooth edge of the ideal straight line shape. This paper evaluate the line edge straightness with the line edge raggedness according to ISO 13660 standard. The line edge raggedness is defined as the standard deviation of the remainder formed after fitting to the edge threshold [6].

When the raggedness value is determined, as in the measurement of line width, the threshold contour line is formed first. Then all the points that constitute the threshold contour line are fitted to the line by the least squares method. The distance between the point on each threshold contour line and the fitted line is the remaining part after fitting [7]. Finally, the Line edge raggedness can be obtained by calculating the standard deviation of the remaining parts. Set  $n$ ,  $m$  for the number of measurement points which is on both sides of the line. Since the measurement points on both sides of the line are generally symmetrically distributed, i.e.,  $n = m$ . The formula for the line edge raggedness is:



$$\sigma = \sqrt{\frac{\sum_{i=1}^n (D_{60i} - D_{60})^2}{2n - 1}} \quad (2)$$

where  $D_{60}$  is the average distance of all 60% reflection coefficient measurement points to the fitted straight line.  $D_{60i}$  is the distance from the 60% reflection coefficient measurement point to the fitted straight line at contour position number  $i$ .  $D_{60i}$  should be calculated from both sides of the line to the center, and the values are all positive.

Line width and line edge raggedness measurement principle shown in Fig. 1.

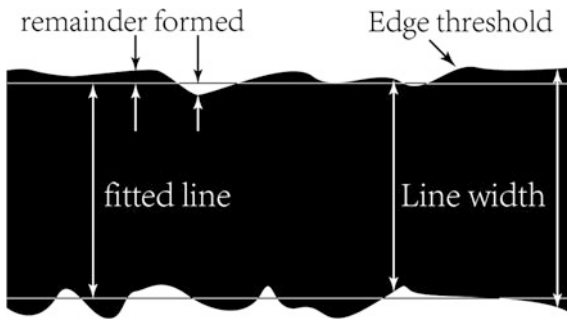


Fig. 1. Line width and line edge raggedness measurement principle

### 3 Experimental Design

Use Adobe Illustrator software to create horizontal lines and vertical lines of different thicknesses, and use the mainstream technology of the market to make flexographic printing forme for comparison. Using an image digitizing device, the forme was captured as a digital image with 600 dpi accuracy [8]. The image was processed according to the algorithm described above, and the line width and line edge raggedness data were calculated and were used as comparison benchmarks.

Convert the two-dimensional line data to a three-dimensional model and use a SLA 3D printing device to output the simulation forme. The 3D printing equipment used in the experiment was laser-scanned with an accuracy of 0.001 mm and a spot diameter of 0.1 mm. Considering that the spot size of the existing SLA 3D printing equipment is larger than the precision requirements of platemaking, the minimum line width is set to 0.4 mm on the test plate. The line width and line edge raggedness data were analyzed and calculated using the above method, and compared with the flexographic printing forme data, the feasibility of using an additive manufacturing technique to complete the flexographic platemaking was evaluated.

## 4 Result Analysis

### 4.1 Line Width

The 3D printing results are processed by the image processing described above, the measured line width data is shown in Table 1, in which the line width and line width errors are the average of the horizontal and vertical lines of the 3D printing result. Previous measurements show that the average linewidth error of flexographic forme made by mainstream technology is 0.01 mm, and the standard deviation of linewidth is 0.01. Comparing the average error of the 3D printing line width with the data of flexographic printing forme, it can be seen that the line width errors of the two are basically the same.

**Table 1.** Data of line width (*unit mm*)

Ideal line width	Molding line width	Line width error
0.40	0.47	0.07
0.50	0.53	0.03
0.60	0.61	0.01
0.70	0.68	-0.02
0.80	0.77	-0.03
0.90	0.87	-0.03
1.00	0.96	-0.04
1.10	1.08	-0.02
1.20	1.17	-0.03
Average of Line width error		-0.01
Standard deviation of line width error		0.03

Figure 2 shows the line widths of the horizontal and vertical lines of the 3D printing results. As can be seen from the figure, there is no significant difference in the line widths between the horizontal line and the vertical line. This shows that the SLA

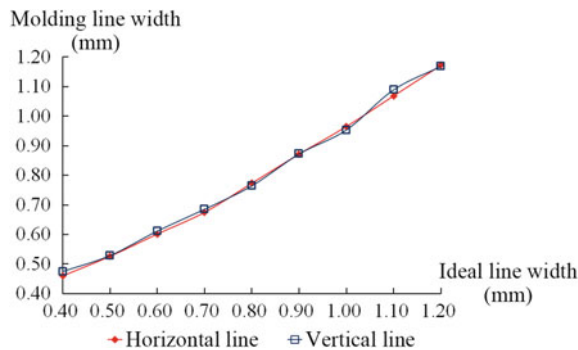


**Fig. 2.** Line width of 3D printing molding

3D printing has no obvious directionality, and the molding results will not be significantly different due to the difference in the direction of the graphics.

As can be seen from the Table 1, in the 9 lines on the simulation forme, except for the line width error of the ideal line width of 0.4 mm, the line width errors of other lines are relatively small, and they are distributed in a relatively small range. Table 1 shows that the standard deviation of the line width error is 0.03, which is not much different from the flexographic printing forme data of 0.01. This also shows that it is feasible and convenient to reduce the error of molding line width through the linearization correction of the output device.

## 4.2 Line Straightness

As described above, the line straightness of the SLA 3D printing results is evaluated by the line edge raggedness. The edge raggedness data obtained by image processing, analysis and calculation is shown in Table 2, in which the line edge raggedness is the average of the horizontal and vertical lines of the 3D printing result. Previous measurements show that the average of edge raggedness of flexographic forme made by mainstream technology is 1.10, and the standard deviation of edge raggedness is 0.20. It can be known that the line edge raggedness of the 3D printing result is relatively close to that of the flexographic printing forme, indicating that the line straightness formed by the two technologies is approximately the same. The line edge raggedness of the 3D printing result is slightly larger than that of the flexographic printing forme, and the reason for this result is that the laser spot diameter of the SLA 3D printing device used in the experiment is large.

**Table 2.** Data of line edge raggedness

Ideal line width (unit: mm)	Molding line edge raggedness
0.40	1.58
0.50	1.48
0.60	0.99
0.70	1.65
0.80	1.53
0.90	1.37
1.00	1.13
1.10	1.97
1.20	1.44
Average of edge raggedness	1.46
Standard deviation of edge raggedness	0.27

In Table 2, most of the line edge raggedness remains around 1.5, that is, the line edge raggedness does not have a direct relationship with the line width. If the laser light spot of a SLA 3D printing device is reduced and the 3D printing accuracy is improved, the line edge raggedness obtained should be smaller and closer to the data of flexographic printing forme.

Figure 3 shows the line edge raggedness of the horizontal and vertical lines of the 3D printing results. It can be seen from the figure that there is no obvious regularity in the line edge raggedness of the horizontal line and the vertical line. This also shows that the 3D printing has no obvious directionality, and the 3D printing results will not be significantly different because of the different direction of the picture.

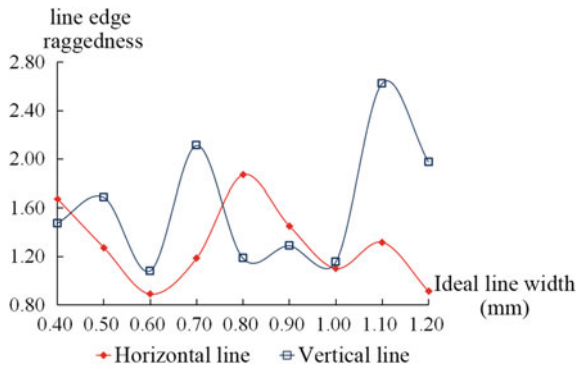


Fig. 3. Line edge raggedness of the 3D printing molding

## 5 Conclusions

Based on the above experimental results, the following conclusions can be drawn:

- (1) In terms of line width and line edge straightness, the results of SLA 3D printing are roughly equivalent to those of mainstream flexographic platemaking technology in the market. It can be concluded that it is feasible to use a SLA 3D printing technology to complete the preparation of a flexographic printing forme.
- (2) SLA 3D printing has no obvious directionality, and the 3D printing results will not be significantly different when directions of the graphics are different.
- (3) There is no direct relationship not only between the line width error and the line width, but also between the line edge straightness and the line width of SLA 3D printing results, which facilitates the linearization correction in the process of making a forme model and outputting a forme.
- (4) The laser spot diameter of existing SLA 3D printing equipment on the market cannot meet the needs of high-precision flexographic platemaking. If an additive manufacturing technology is used to complete the preparation of the flexographic printing forme, the equipment must be reformed.

This paper mainly studies the line quality of the printing forme produced by SLA 3D printing technology, further research on the quality of image dots, text and areas of the printing forme produced by SLA 3D printing technology will be conducted later.

**Acknowledgements.** This study is funded by Green Platemaking and Standardization laboratory for Flexographic Printing (ZBKT201705).

## References

1. Pollard, B., & Smdrel, A. (2017). Details on dle: Direct laser engraving basics, benefits, future business. *Flexo*, 42(10), 96–102.
2. Zhao, C. F., & Wu, D. H. (2015). Discussion on application of 3D printing technology in package printing. *Applied Mechanics and Materials*, 731, 300–303.
3. Zhao, C., Han, Q., & Wu, D. (2013). *Method of platemaking using 3D printing*. CN103448349A.
4. Li, Z., An, L., Qi, Y., & Pu, J. (2014). *Flexographic printing forme CTP direct platemaking method and equipment using 3D rapid prototyping printing principle*. CN 103121323 B.
5. Zhou, H., & Song, Y. (2014). *A 3D manufacturing method and its application in flexographic platemaking*. CN103640219A.
6. ISO/IEC 13660. (2001). Information technology—Office equipment—Measurement of image quality attributes for hardcopy output—Binary monochrome text and graphic images.
7. Yao, H. (2012). *Quality inspection and evaluation of digital printing*. Beijing, China: Graphic Communication Press.
8. Yao, H. (2012). *Line edge quality and its measurement method*. *Publishing & Printing*, 2012 (3).



# Study on the Influence of Back Exposure on the Quality of Flexographic Platemaking

Lingjun Kong<sup>1</sup>(✉), Miao Tan<sup>2</sup>, and Liang Zheng<sup>1</sup>

<sup>1</sup> Printing and Packaging Engineering Department, Shanghai Publishing and Printing College, Shanghai, China  
908641376@qq.com

<sup>2</sup> Sinwa Printech (Shanghai) Co., Ltd, Shanghai, China

**Abstract.** With the increasing demand for green printing and environmental protection, the application of flexographic printing is ever-growing. The purpose of this paper is to study the possibility of the standardization for the quality of flexographic platemaking, and provide basic data and reference for the platemaking process control related standard. Experiments on back exposure control and analysis of printing forme quality through four mainly used brand plates with two different thickness were conducted, the relationships between the relief height and the back exposure time, and the related imaging quality of flexographic printing forme, including small dots, fine lines, small characters, tone reproduction were studied. The results show that it is possible to specify a set of standardized imaging quality indexes for flexographic printing forme to control platemaking process which are suitable for diverse platemaking technology and plates.

**Keywords:** Flexographic printing forme · Platemaking · Process control · Forme quality · Standardization

## 1 Introduction

Flexographic printing is known as the most environment friendly printing process because of the use of water-based ink, which increased rapidly in label printing, food packaging printing, cosmetic printing and other environmental protection demanding industries [1]. Platemaking is an important part of the flexographic printing process, and now there are diverse brands and models of plate and different platemaking equipment involved in the process of flexographic platemaking. The quality control of the flexographic platemaking is the key to the print quality [2].

In recent years, the flexographic platemaking technology has made great progress in print quality, production efficiency and sustainability with the development of flat top screen and solid area screening technology [3]. However, there is still lack of relevant standards for flexographic platemaking process control in China.

Through the study of the relationship between the back exposure time of the flexographic platemaking process and the relief height and the imaging quality of the printing forme, the paper aims to find out the possible specifications for the quality of flexographic forme, and provide the basic data and reference for the platemaking

process control related standard, and further to promote the standardization work for flexographic industry.

## 2 Experiment Preparation and Process

### 2.1 Selection of Plates and Platemaking Equipment

Four brand plates including Flint, DuPont, Kodak and Huaguang, which are commonly used in the domestic flexographic printing industry, were used in the experiment. Two models of each brand were selected, with the thickness of 1.70 and 1.14 mm. The plates are named as FAH114D, FAH170D, DPU45, DPU67, NXH114, NXH170, DR114LS, DR170LS.

The following equipment are used in the experiment.

- (1) Laser imaging system: ESKO CDI Spark4260 and Kodak Flexcel NX
- (2) Back and main exposure system: Dupont Cyrel 3000EC
- (3) Washout processor: Dupont Cyrel 3000PS
- (4) Drying oven: EVO 5D Oven
- (5) Post processor: Sinwa2000
- (6) Laminator: Kodak Flexcel NX Wide laminator.

### 2.2 Test Target Preparation

In order to carry out the experimental research, the test target was prepared on the basis of the quality control experience in the actual production. The size of the test target is 30.5 cm \* 26 cm, which contains the following test contents.

- (1) Independent lines: consisting of two sets of positive lines and reverse lines, with the line width from 0.05 to 0.3 mm and a step length of 0.01 mm.
- (2) Text: contains Chinese and English characters, positive and reverse, the font size varies from 2 to 12 pt with the step of 1 pt, and the Chinese font is Song style and English font is Times New Roman.
- (3) Independent dots: the diameters of dots differ from 0.1 to 0.8 mm, with the step of 0.1 mm.
- (4) Tone graduation scale: the tone value varies from 0.5 to 100%, and the color patch size is 1 cm \* 1 cm. There are four groups, each has different screen ruling of 110, 133, 150 and 175 lpi respectively, as shown in Fig. 1.

### 2.3 Platemaking Process and Related Parameter Settings

There are a little difference between Kodak plates and the other brand plates in the platemaking process, which is mainly reflected in the imaging and lamination process, the platemaking based on Kodak plate has one more process step of film-laminating than other brand plates, and the other steps are the same.

In order to find out the influence of back exposure time on relief height and imaging quality of the printing forme, the experiment kept the platemaking process parameters

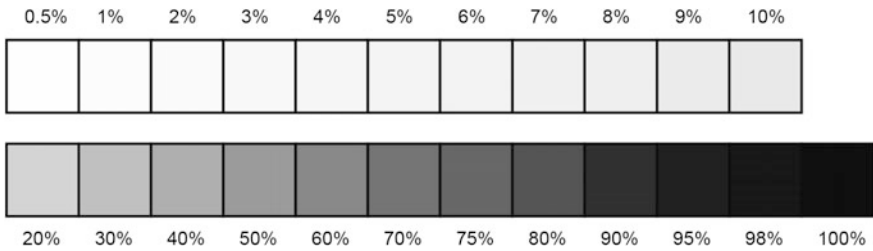


**Fig. 1.** Graduation scale

except the back exposure time as constant as possible, and set the main exposure time, washout time, drying time and other control parameters based on the experience of actual production in the platemaking factory.

The main exposure time for DuPont, Flint, and Huaguang plates was 720 s, and the light finishing time was 4 min; the main exposure time for Kodak 1.14 mm plates and 1.70 mm plates was 1700 and 900 s separately, and the light finishing time for Kodak plates was 8 min. All plates were dried at 60 °C and the drying time was 3 h, and the post-processing time was 6 min. The washout solution rinsing speeds vary slightly with plate thickness, the speed for plates of 1.14 mm thickness and 1.70 mm thickness was 190 and 180 mm/min respectively.

Meanwhile, considering the influence of ambient temperature on back exposure is obvious [4], the platemaking ambient temperature of the experiment was maintained at 20–25 °C.

### 3 Experimental Data and Analysis

The back exposure experiments were carried out on the plates of different thickness and different brands. Each platemaking step during the experiment was sampled and the production time of each step was recorded, and the relief height, fine lines, independent dots, text and tone reproduction effects were measured and analyzed.

#### 3.1 Relationship Between Back Exposure Time and Relief Height

The main purpose of back exposure is to determine the thickness of the plate base and the relief height of the printing forme [5]. The back exposure experiments were performed for each plate at a different time. Figure 2 shows the relief heights resulting from each platemaking process and their corresponding back exposure times.

According to Fig. 2, we can see that the shorter the back exposure time, the higher the relief height of the printing forme for the same plate. Though back exposure time is the same, the relief height obtained from different brands is different, and the relief height obtained from the same brand with different thickness is also significantly different.



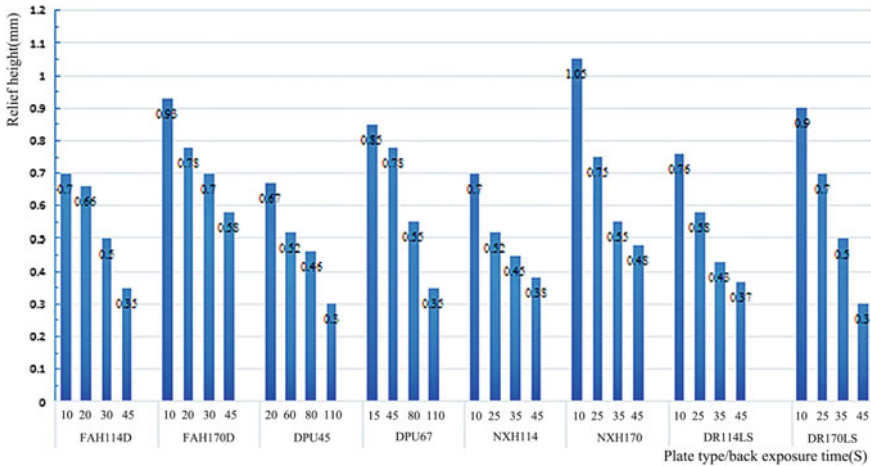


**Fig. 2.** Relief height and its corresponding back exposure time

During the experiment, it was also found that the back exposure time required to obtain a certain relief height for the same plate still varied slightly with the room temperature condition, etc.

The experimental results show that the back exposure time required to obtain a flexographic printing forme with a certain relief height is not only related to the thickness of the plate, but also related to the brand and model of the plate, and the ambient temperature, etc. For the plates of the same thickness, the back exposure time for the different brand plates is quite different so as to obtain the same relief height. Therefore, for the standardization of the platemaking process, it is impossible to give definite back exposure time specification.

### 3.2 Analysis of Imaging Quality of Printing Formes

The positive and reverse lines, independent dots, and Chinese and English characters in the formes obtained by the experiment were measured by a magnifying glass with a scale of 50 times and a microscope with analysis software. It can be found that:

- (1) If the relief height is controlled reasonably, the lines with 0.08 mm width are well reproduced in all formes, and the line edges are straight, but the finer lines may bend (see Fig. 3); the 2 pt English characters and 3 pt Chinese characters of are also well reproduced in all formes, but the 2 pt positive Chinese characters may appear missed strokes or strokes are not straight due to the process parameter used in the experiment, as shown in Fig. 4.
- (2) If the relief height is too high, it will lead to the phenomenon that the edge of graphics of the printing forme is not washed cleanly, and the fine lines are bent or the small positive characters are smeared (see Fig. 5). When the relief height is too low, it will cause the small reverse characters to be smeared.



**Fig. 3.** Bending in fine line



**Fig. 4.** Missed stroke in Chinese character



**Fig. 5.** Pasting of Chinese characters

- (3) If the relief height was controlled in the appropriate range, the 0.1 mm independent dots were well reproduced for most formes, but if the relief height was too high, it will result in the smallest 0.1 mm independent dot cannot be reproduced. The experiment also found that the 0.1 mm independent dots on the forme obtained from one of four brands of plate with a thickness of 1.7 mm cannot be presented regardless of the reasonable relief height (see Fig. 6), and the minimum diameter of the independent dot can only reach 0.2 mm, which may be related to the hardness of the plate itself, and its quality may be improved by adjust other process parameters.

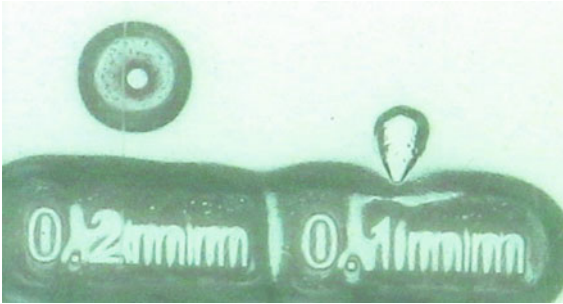


**Fig. 6.** Independent dot failed to reproduce

- (4) If the relief height is reasonable, 1–95% tone values can be well reproduced with the screen ruling of 175 lpi or 150 lpi, and the tone reproduction range on most printing formes can also reach 1–98% under the condition of 150 lpi screen ruling, but several printing formes can only reproduce the gradation range of 1–90% when screen ruling reaches 175 lpi whenever the relief height is reasonable or not, it may be due to the other process control parameters which are not the most appropriate. At the same time, if the relief height is too high or too low, the halftone screen reproduction ability of the printing forme will be reduced. It was also found that the formes made by plates except the NXH series were not able to reproduce the halftone screen of 0.5% tone value, see Fig. 7.

The above experimental results show that the relief height of the flexographic printing forme directly affects its imaging quality. Too high relief height may cause the loss of fine dots in the printing forme, reducing the range of tonal reproduction and the maximum screen ruling that can be achieved. Therefore, in the platemaking process, the relief height should be well controlled.

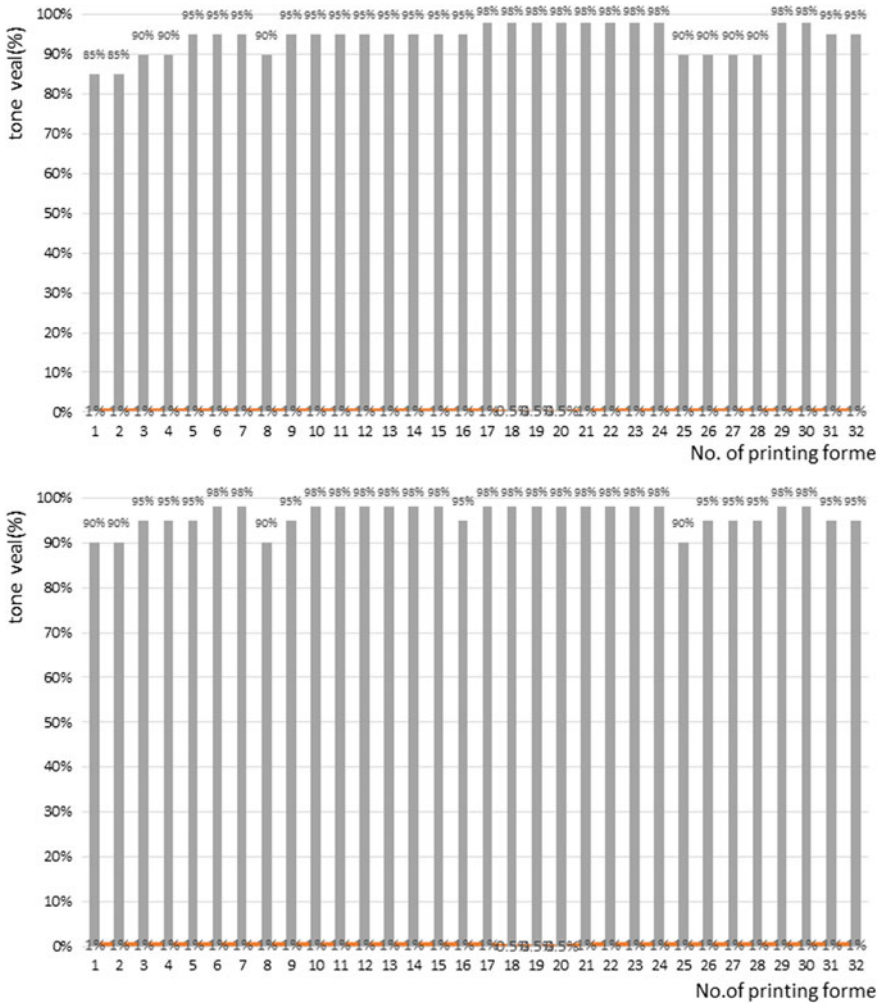


Fig. 7. Tone reproduction range on forms (above: 175 lpi, below: 150 lpi)

### 4 Conclusions

In this paper, the influence of the back exposure time on the relief height of the 1.14 and 1.70 mm plates were studied by using flexographic plates with four mainstream brands as the experimental materials, and the imaging quality of the formes was measured and analyzed through various test elements. The process control parameters such as the back exposure time of the flexographic platemaking is related to the platemaking process technology, the plate brand and model. Therefore, a process control related standard cannot specify the definite and unified back exposure time and main exposure time of process parameters.

The plates with the same thickness, regardless of its brand and model, can obtain effective relief height as long as the platemaking process control is correct and reasonable, and enabling small dots, fine lines, and small characters to be imaged and reproduced with high quality. Therefore, It is possible to specify the reasonable range of relief height and the clear requirements on the reproducible minimum independent dot, the finest line, the smallest characters and tonal reproduction range for flexographic platemaking process control effectively, and develop a standard that is applicable to the process control and quality requirements of flexographic platemaking.

For the flexographic plate with a thickness of 1.14 and 1.7 mm involved in this experimental study, the finest width of positive line and reverse line of the printing forme should be not less than 0.08 mm, and the English characters and Chinese characters of the smallest font should not be less than 2 and 3 pt respectively, and the minimum diameter of independent dots should not be less than 0.2 mm. When the screen ruling is 150 lpi, the range of tone values that the flexographic printing forme can reproduce should reach 1–98%. Moreover, it is also possible to further refine these imaging quality requirement of the two thickness formes.

This paper mainly focuses on the study of the relief height and the imaging quality of the printing forme influenced by back exposure time, and the influence of the main exposure time and other factors on the imaging quality needs to be researched through further experiments. Furthermore, the study of relief height can be further deepened to obtain the exact control range of the effective relief height. In addition, this paper only studied two thicknesses of the plates, and the process control and imaging quality requirements of the plates with other thickness need to be studied by corresponding test experiments.

**Acknowledgements.** The study is funded by Key Laboratory of National Press and Publication Administration: Green Platemaking and Standardization for Flexographic Printing (Project: ZBKT201707). The test target design and platemaking experiments were fully involved and supported by Sinwa Printech (Shanghai) Co., Ltd.

## References

1. Gao, Y., & Li, Z., et al. (2009). A study on making printing plate using 1.70 mm flexographic resin plate. *Imaging Technology*, 45–47.
2. Zhang, J., Li, B., Ceng, Z., et al. (2017). A survey of the flexible platemaking quality based on CDI platemaking equipment parameters. *Journal of Beijing Institute of Graphic Communication*, 6–9.
3. Zhao, S. (2017). Photosensitive resin flexo development and the latest technology. *Printing Field*, 48–53.
4. Zhang, Y., Liu, S., & Li, Y. (2012). Study of digital quality control method of plate making of flexographic printing. *Packaging Engineering*, 99–103.
5. Gu, P., & Qi, S. (2012). Study on platemaking of digital water-washed flexographic plate. *Packaging Engineering*, 122–126.



# Research on the Solid Screening with Microcell Technology in the Flexographic Printing

Enyin Fang<sup>(✉)</sup> and Jinghuan Ge

Department of Printing and Packaging Engineering,  
Shanghai Publishing and Printing College, Shanghai, China  
fensarying@163.com

**Abstract.** Based on different types of printing materials, the paper discusses the influence on solid density with microcell technology in flexographic printing. A kind of testing chart, which consisted of two kinds of solid fields, is designed. The one is un-screened solid area; others are special using four kinds of screening methods, which are MG25, MG34, MG45, and MCWSI, called microcell technology. Then, using different laser energy to expose the testing chart on DuPont plate and printing based on different types of printing materials. Through software, called Image-quality and X-rite 528 spectrophotometer, the evenness and density between un-screened solid area and special solid filed with screened can be analyzed. The experiment shows that solid screening with Microcell technology can not only solve the density deficiency, but also can improve the evenness of the color block used PE as printing material in the flexographic printing. In addition, with the coated paper as the printing material, the effect of solid screening is not very different as that un-screened solid area.

**Keywords:** Solid screening · Flexographic printing · Microcell technology · Solid density

## 1 Introduction

As the pronoun of environmental protection printing, People pay much more attention on flexographic printing. Looking back upon the development process of flexography, the appearance of laser plate making technology has contributed to a leap forward in the quality of flexography, which also makes it possible to catch up with the quality of offset and intaglio printing. However, some problems can not be solved in the actual production process, such as the tone merging, the problem of gradient, and the durability of highlight dots [1, 2], white pin-pole appeared in solid area and so on. Most of these problems are directly or indirectly related to the flexographic plate. In particular, the flexographic printing's ability to transfer ink in the field is often challenged by the packaging industry.

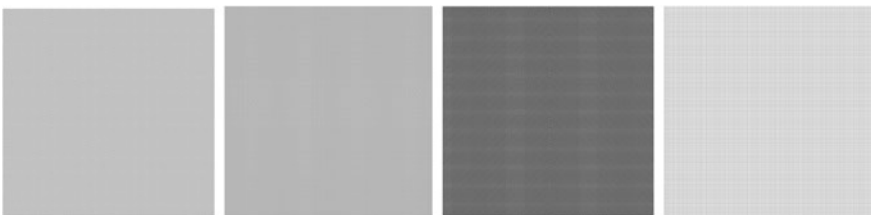
Especially in Soft packaging field, the ability transferring ink to the solid area, which has a low density, have been challenged for a long time, comparing to gravure printing. In addition, the characters, lines and the edge of the solid area can easily have obvious ink expansion phenomenon as the graphic and text part on the flexographic

plate is higher than the non-graphic part, which has also become a major obstacle to the quality of the flexographic printing.

The concept of microcell technology is to add microcell on the top of the dot or solid area, using the ductility of ink to make the solid area look more uniformity. The theoretical research showed that the microcell technology could better solve phenomenon of non-uniform, which used PE film as substrate in flexographic printing [3], but there are few tests for the value of solid density increasing. It requires further discussion about how the results appear under different substrate, such as PE film, coated paper and whether microcell technology is available in flexographic printing or not. This paper designed a kind of testing chart, which consisted of two kinds of solid areas. The one is un-screened solid area; others are special using four kinds of screening methods, which are MG25, MG34, MG45, and MCWSI, called microcell technology. Then, using different laser energy to expose the testing chart on DuPont plate and printing based on different types of printing materials (PE film, coated paper). At last, through printing test, exploring the influence of microcell technology on the solid density based on different substrates in flexographic printing.

## 2 Detection Factors of Flexographic Plate

The MG45 dot shape has four empty pixels between each two dots, and each five pixels as a unit, regularly arranged in a horizontal and vertical direction. The MG34 dot shape has three empty pixels between each two dots, and every four pixels as a unit, regularly arranged in a horizontal and vertical direction. The MG25 dot shape has three empty pixels between each two dots, and every five pixels as a unit, regularly arranged in vertical direction. MCWSI dot shape has three empty pixels between each two dots in horizontal directions, regularly arranged in horizontal direction. Four kinds of Microcell used screened in solid area are shown in Fig. 1.



**Fig. 1.** Four kinds of Microcell form left to right are MG45, MG34, MG25, and MCWS

In the process of designing the original, four kinds of solid screening above-mentioned and the un-screened solid arranged in line, as shown in Fig. 2. In the process of plate making, different laser booster values (from 150 to 285, step length of 15; the higher the value, the greater the instantaneous laser energy) are used to engrave the mask film on the plate. The plate is exposed to harden the printing graphics parts and then the un-hardened resin are removed after rinsing, thus the relief layer on plate is

formed. Then the plate is mounted on the press for printing after drying. The ZiQuan PE film and the ZiXing 90gsm paper coated on both sides are used for Monochrome printing (Cyan). Plate with the mask after Laser engraving under different laser boost value is shown in Fig. 3. Monochrome printing (cyan) using 90gsm coated Paper, which is printed under Test conditions of the printing in Table 1, is shown in Fig. 4.

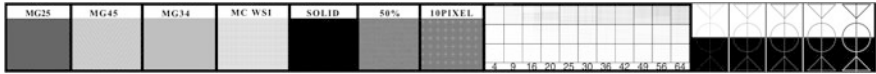


Fig. 2. Digital test manuscript of solid screening

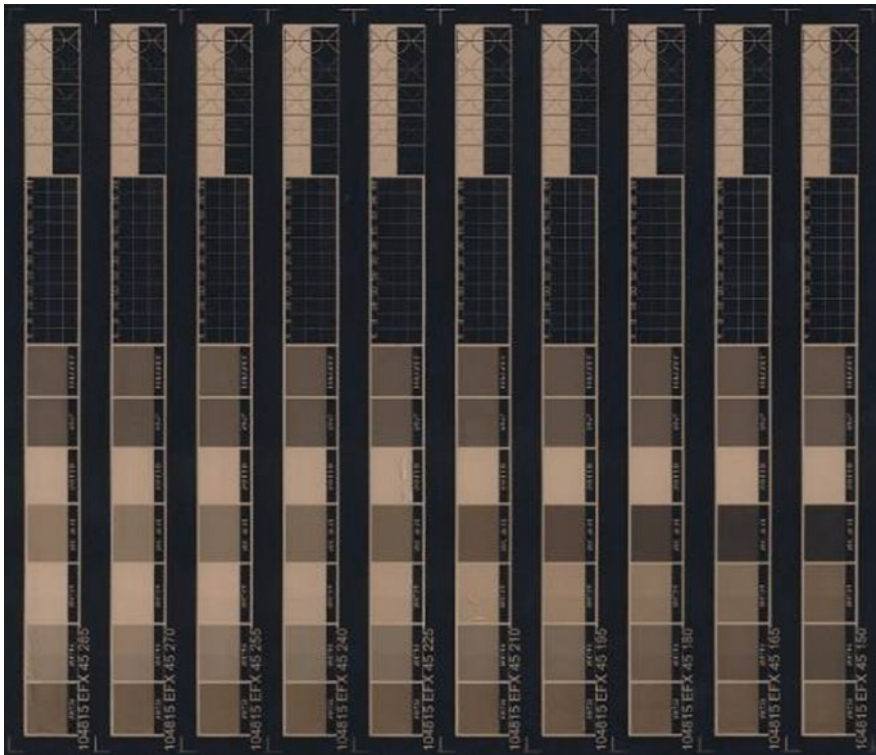
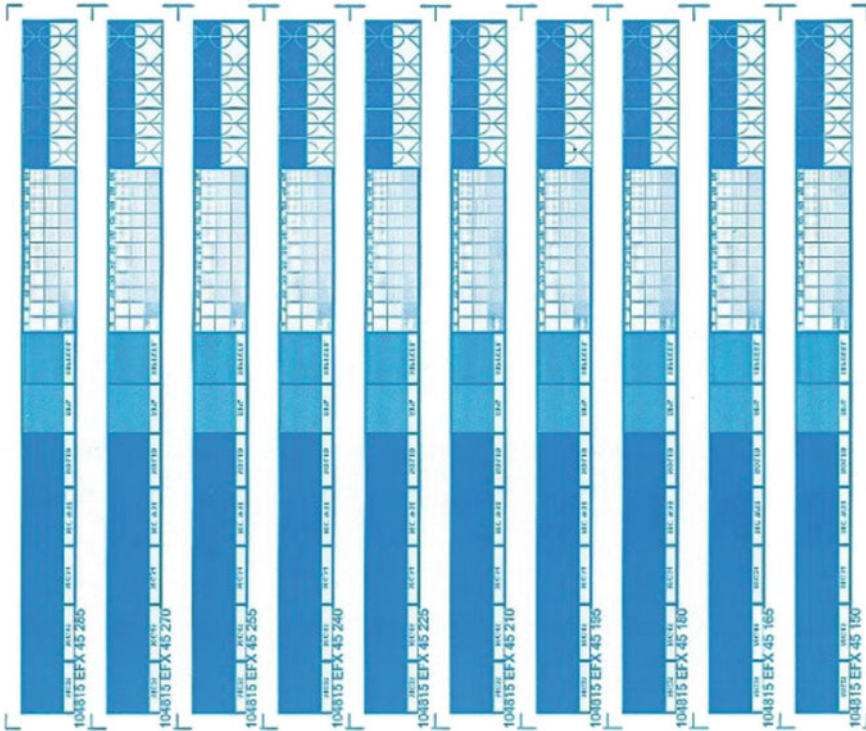


Fig. 3. Plate with the mask after Laser engraving under different laser boost value



**Table 1.** Test conditions of the printing

Projects	Main test conditions	Brand and state
Press	Flexographic press (full color), Speed 200 m/min	TAIYO stf-340-4f+1C +1D
Plate	Thickness 1.14 mm, width 250 mm, perimeter 254 mm, 150 line/inch	DuPont Flexography
Inks	UV alcohol-based ink (cyan)	Bright
Carriers	PE film, Coated paper (90gsm)	ZiQuan blown film, ZiXing coated paper
Anilox roll	800 line/inch, 60°, hexagon cell	BCM2.1
Double sided tape	Scapa 43240	Neutrality
Sampling requirements	Using cyan ink to print, Simple speed 40 m/min, Ink viscosity is 25S, Same pressure, sampling under the same anilox roll	



**Fig. 4.** Monochrome printing (cyan) using 90gsm coated Paper

### 3 Test Conditions of the Printing

In order to test the results, the printing conditions are shown in Table 1.

## 4 Analysis and Evaluation of Measurement Results

### 4.1 Measuring Instruments and Software

Currently, people often widely use density meter, spectrophotometer to measure and evaluate the quality of objects [4, 5]. According to the ISO13660, the measuring instrument should meet the following requirements. First, the pixel of the image capture device should be described by 8-bit depth. second, the resolution is more than 600DPI; In this paper, we use EPSON GTX970 scanner as image capture device, which have properties mentioned above. The software called Image-quality which can be used to measure and evaluate the quality of testing graph. Before used scanner to get digital marks by Image-quality software, we should do space calibration and density calibration for the scanner first [6–8].

### 4.2 Analysis of Measurement Results

In order to test the result, the density value should be measured at the same time using X-rite 528 spectrophotometer. Considering the measurement error of X-rite 528 spectrophotometer, each group of data should be measured for five times and get the average value, the result is shown in Fig. 5. The horizontal axis of the chart is solid density and the vertical axis is laser booster value.

Objective evaluation: According to Fig. 5a, it can be seen that the density value of the solid screening is not constant when PE is adopted as the carrier for printing. When the laser boost value is greater than 225, the density values of the four kinds of solid screening methods are all higher than that of the un-screened solid area, and present good regularity. The density value of the four kinds of solid screening methods is fluctuated when the laser booster value is less than 225. When the laser booster value is less than 180, the solid density values of MG45 and MCWSI are abnormal. It can be seen from Fig. 5b that the density value of only MCWSI method is slightly higher than that of un-screened solid area. Moreover, the density of other methods, MG25, MG45 and MG34, is close to or below that of the un-screened area. In addition, with the same exposure parameters and screening modes, the effect of the solid screening and value of solid density for coated paper are better than that of PE film.

Subjective evaluation: Since the value of density for solid screening is fluctuated when the laser booster value is less than 225, so the anomaly is removed and the value of the laser boost that is greater than 225 can be adopted. The test sample is collected by Image-quality software to judge the uniformity of the solid density. The results are shown in Tables 2 and 3. According to Tables 2 and 3, with PE film as the substrate, the method of solid screening in a certain laser boost value can effectively avoid the deficiency and unevenness of solid area in flexographic printing, and can improve the

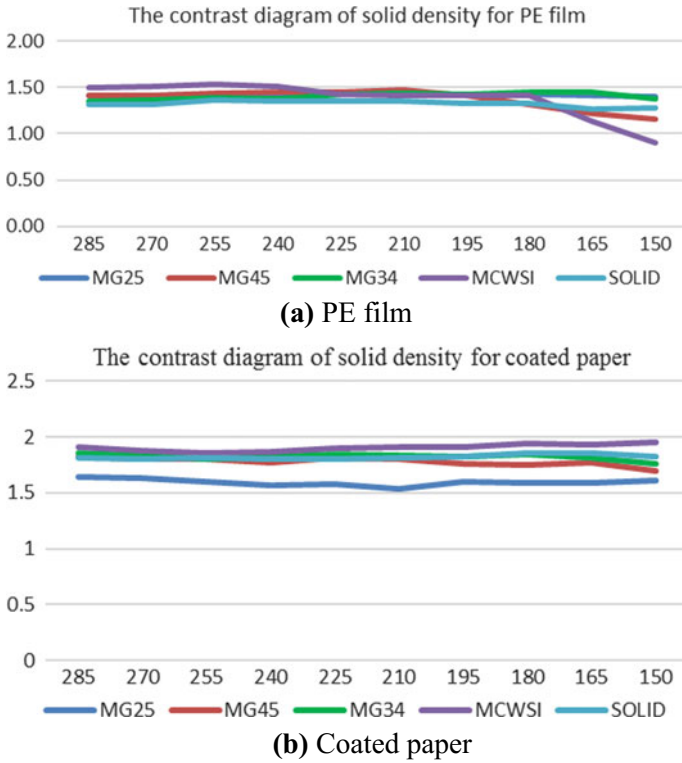


Fig. 5. Solid density for samples under different laser boost value

Table 2. The comparison of solid screening on the PE film

The kinds of Microcell technology	MG25	MG45	MG34	MCWSI	Un-screened solid
Visual evaluation	White spots weaken, no twill, solid area uniformity	Non White spots, no twill, Solid area uniformity	White spots, slight twill, unevenness in the solid area	Non White spots, no twill, uniformity in the solid area is better	White spots, twill, unevenness in the solid area
Comprehensive evaluation	Better	Good	Normal	Great	Worse

value of solid density. With the coated paper as the substrate, the effect of solid screening is the same as that un-screened solid area.

**Table 3.** The comparison of solid screening on the coated paper

The kinds of microcell technology	MG25	MG45	MG34	MCWSI	Un-screened solid
Visual evaluation	Non White spots, no twill, Solid area uniformity	Non White spots, no twill, Solid area uniformity	Non White spots, no twill, Solid area uniformity	Non White spots, no twill, Solid area uniformity	Non White spots, no twill, Solid area uniformity
Comprehensive evaluation	Good	Good	Good	Good	Good

## 5 Conclusions

The paper discusses that the Microcell technology, under different laser booster values and substrates, can effectively improve the solid density and uniformity in the solid area. It can be seen that the solid screening with PE as the substrate can effectively improve the uniformity and value of solid density for the flexographic printing. With or without Microcell technology, it is equivalent to the subjective and objective performance using coated paper as the carrier, but from another point of view, not only it will increase the investment of technology, but also the cost of production. There are some limitations in this experiment. It need to be further verified when the inks and other substrates are changed, Microcell technology whether or not can be used and the duplication of plate making, at the same time, the pressrun of the printing plate in this technology is stability or not.

**Acknowledgements.** This research is supported by Lab of Green Platemaking and Standardization for Flexographic Printing (No. ZBKT201804 and No. ZBKT201701).

## References

1. Zhang, H., & Xu, W. (2008). Study on the Dot Gain of Flexo Printing. *Packaging Engineering*, 18(1), 41–42.
2. Zhao, S. (2017). Review and latest development about flexible technology using flat top dot. *Printing Technology*, 9, 28–31.
3. Huang, P., & Jin, Y. (2006). Tones and color reproduction of color flexography. *Packaging Engineering*, 27(6), 9–11.
4. Yang, H. (2016). Printing control in flexophotographic printing. *Packaging Engineering*, (3), 45–47.
5. Huang, Y. (2006). Analysis of tone and gradation reappearance performance in flexography printing. *Packaging Engineering*, 24(5), 297–298.
6. Fang, E. Y., & Yang, S. (2018). Study on the registration testing of color digital printing machine. In *8th China Academic Conference on Printing and Packaging* (Vol. 1, pp. 158–165).

7. Jin, Z., Zheng, L., & Guan, W. (2012). Line quality analysis and evaluation of digital printing based on ISO13660. *Packaging Engineering*, 15(33), 97–103.
8. Zheng, L., & Jin, Z. (2011). Quality analysis of xerographic printing based on CCD. *Packaging Engineering*, 32(7), 112–116.



# Design and Application of Intelligent Plate Making Process for Box Packaging and Printing

Yongfa Feng<sup>1</sup>(✉), Lihe Zhu<sup>1</sup>, Zhihui Liu<sup>1</sup>, and Xin Wang<sup>2</sup>

<sup>1</sup> Shandong Lu Xin Tianyi Printing Co., Ltd., Jinan, China  
{fengyongfa, zhulihe, liuzhihui}@lxtyyw.com

<sup>2</sup> Qilu University of Technology, Jinan, China  
wangxin2709@163.com

**Abstract.** In order to closely following the “Industry 4.0” strategy, and realized the transformation and upgrading of the printing and packaging industry to digital, automated and intelligent. Based on the deficiencies of the traditional plate making process, The Luxin Tianyi printing Co. Ltd established the intelligent plate-making process through technology exploration, and abandoned the traditional plate-making process. This paper described the new process detailed in combination with the flow diagram of the plate making procession. Through the comparison between the old and new processes, the great value of the new plate making process was appeared. The author also shared how to build the standardized, automated plate making process based on the ESKO software platform, and the technical difficulties in establishing the process.

**Keywords:** Automation Engine (AE) · Web center · SOP · ERP

## 1 Traditional Plate Making Procession

### 1.1 Traditional Plate Making Process

The traditional plate making procession included the following steps. Firstly, the sample was designed according to the customer’s requirements. Secondly the sample was approved by the customers. After the final confirmation, the printing plate was produced by the plate making machine [1].

### 1.2 Problems About the Traditional Plate Making Procession

The major problems of the traditional plate making process were list. The customer cannot accurately expressed his intention through the traditional communication way which by the telephone call or the email. Maybe because of understanding differences, mistakes were made and it was not easy to trace back afterwards. The approval cycle of customers was long.

ERP, office software, design software, production software, output software and color management software were the commonly used in printing production [2]. In fact each process used different application software during the produce process. All

software worked independently rather than together, causing the files conversion error or color chromatic aberration problems [3].

Each process of the traditional plate making process was manually operated with poor precision. For example, the producer made an imposition, manually placed the imposition position and manually rotated the imposition file [4].

During the proofreading process, it was difficult for the naked eye to notice subtle changes in the file, resulting in quality hazards.

## **2 Introduction of ESKO Software**

In order to solve the problems in the traditional plate making procession, ESKO's box packaging software suits were introduced to Lu Xin Tianyi printing Co. Ltd. The software suits mainly including ArtiosCAD, DeskPack, PackEdge, Plato, Automation Engine (AE), WebCenter, Imaging Engine, FlexProof E and Color Engine.

## **3 Two Important Working Platforms**

### **3.1 AE Was the Core Working Platform for ProceSSION Operation**

AE serves as the core platform of any scale pre-press production operation, which can increase the efficiency of the operation. AE serves enabled unparalleled workflow automation with rock-solid quality control. The characteristic of AE was highly scalability and extensive business system integration. According to the AE serves standards, contributed to reducing error and cost during the printing process.

### **3.2 WebCenter Is an Internet-Based Communication Platform**

WebCenter is a powerful and user-friendly web-based platform. It manages packaging preproduction specification, approval and project life cycle for brands and converters alike [5]. Customers can log in to the WebCenter network communication platform to approve the designed documents, and automatically track the progress of the project through PC, iPhone and other tools. After completing customer approval, the system can automatically create an approval report as an archive. A network platform built on a database, which can retrieve and check the contents of approvals at any time, and bring convenience to companies and customers. The network platform was established based on the database can retrieve the approval at any time, bringing convenience to the customers.

### **3.3 Intelligent Plate-Making Workflow**

The intelligent plate-making workflow was showed in the Fig. 1.

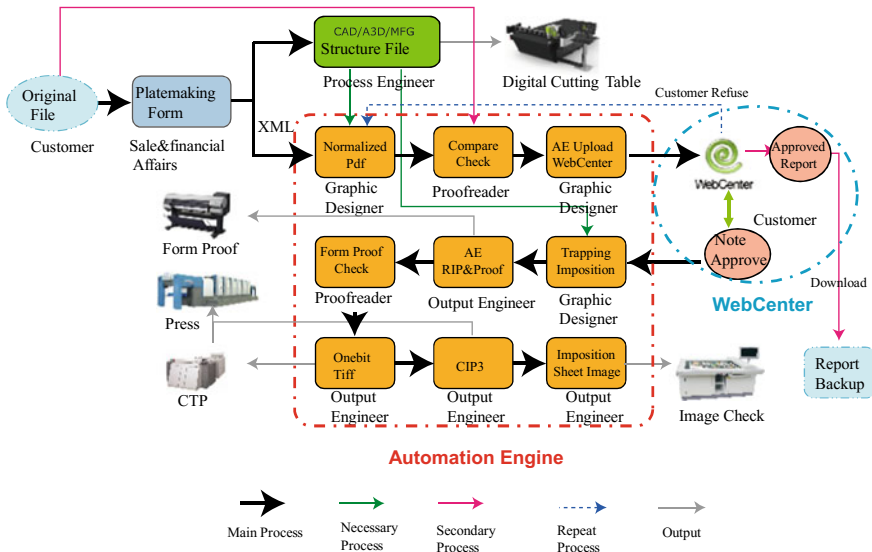


Fig. 1. Intelligent plate-making workflow

### 3.4 Instructions of the Intelligent Plate Flow Chart Operation

The whole workflow started with the plate-making process, and the output of the CTP plate, CIP3, and the large-sheet inspection file. AE has always been the core platform for automated workflows. The customers were automatically reviewing the cloud platform as a supplement. A main line of the full set of processes was automatically executed without excessive manual intervention. The following described the process in detail.

#### 3.4.1 Release a Single-Phased

Firstly, according to the customer’s printing requirements, a production schedule was issued by the printing company. There are two main working routes.

Route 1 (main), the plate-making information was transmitted to the AE folder as an XML file. A standard workflow was created by AE. The printing procession parameters and the working file directory was created according to the standard workflow by AE.

Route 2 (Auxiliary): according to the information of the plate, the single-mold structure file (ARD file) and the imposition structure file (MFG file) were created by ArtoCAD. These structure files not only can be called by the AE but also can be used for making the die-cutting plate.

#### 3.4.2 Stage of Production

The Single Station file (Normalized PDF) was created by DeskPack that under the Illustrator, and then the Single Station file was imported into the AE. In the AE work, the customer manuscript was compared with the produced single-mode file. After



confirming, the production staff uploads the WebCenter through the workflow and waiting for the customer to review and confirm.

### 3.4.3 Stage of Customer Review

The customer received the information that need to be reviewed and confirmed by the e-mail sent by WebCenter, and accessed the web server using an account through a web browser of a computer or smartphone. On the WebCenter cloud platform, customers can review flat box images and virtual 3D display boxes.

When the customer needs to approve in stages, WebCenter automatically initiated the next stage of approval work and completed the approval process. Clients can make important instructions for approval documents on the WebCenter with annotation tools. After the confirmation of the customer was completed, AE automatically created a customer confirmation report to upload the WebCenter for customers to archive.

### 3.4.4 Stage of Make-up

In the imposition process, firstly, PDF optimization was performed on single-mode files. Secondly, the trapping process was performed on the files through the Easy Process Trapping module. Finally, the imposition structure file (MFG file) and imposition information were automatically transferred for automatic imposition process (Fig. 2).

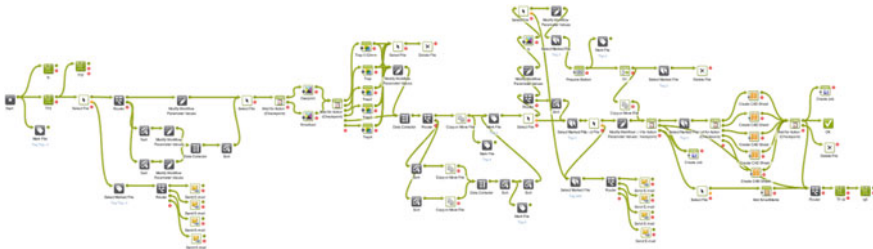


Fig. 2. Flow chart of imposition

### 3.4.5 Stage of Output Proofing

The RIP (rasterization) process of the layout file was performed by the Imaging Engine according to the preset output parameters. After the RIP was completed, the layout proof was automatically performed to ensure the consistency of the proof publishing data. Digital simulation samples processed by Color Management can be automatically output to track color samples during printing. Color Engine played a crucial role in this process.

### 3.4.6 Stage of Layout Proofing

The main job was to check if there was an error in the large version of the proof. If the job has an old version, the process will automatically retrieve the previous version of the file into the current work, easy to proofread the comparison of the old and new documents. In this way, the efficiency of proofreading was improved.

### **3.4.7 Stage of Output CTP**

During the production process of the plate, the AE automation output process was started. The one bit tiff file was produced and exported to the CTP device. The CIP3 data was produced and exported to the printer server. The large inspection files was produced and exported to the sheet inspection equipment for the quality control of the printing process. In addition, the plate making process report can be automatically generated to form a product file.

## **3.5 Necessary Auxiliary Workflow**

### **3.5.1 Management of File Version**

AE intelligent workflow can automatically managed the version of working files. For example, if the current circulation version of the file was the C version, then the B version file needed to be archived separately, and the A version file needed to be deleted automatically.

### **3.5.2 Create a Register Plate**

AE can automatically create positioning plates to meet specific process needs. For example: partial glazing, local UV, bronzing, electronic supervision code, etc. need to be transparent positioning film for precise positioning.

### **3.5.3 Create Ink-Absorbing Area**

During the imposition process, we can complete the production of the ink-absorbing area according to the process requirements. The ink-absorbing area was mainly used to make up for a small amount of ink on the individual swatches of the layout, and it was easy to pile up ink during printing. In order to solve this problem, an ink-absorbing area was added in the imposition space. Increasing the ink-absorbing area also prevents ghosting (a vague pattern in the absence of graphics).

## **3.6 There Is a Big Difference Between the New Automated Process and the Traditional Process**

It was mainly a new process of smart operation, with logical judgment ability, intelligent selection ability, involved a wide production phase, data processing capabilities and other powerful (Table 1).

## **4 Implementation Project**

### **4.1 Project Team Established**

In the process of establishing an automated standard process, a project working group was established composed of technical personnel, related departments, and customer personnel. The project working group mainly focused on the overall planning, technology development, training, standardization and implementation of all process flows. The customers mainly cooperated with the implementation of the website.

**Table 1.** Comparison between the new automated process and the traditional workflow

	New automated process	Traditional workflow
Stage of automated work	Implementing the process flow	Digital proofing, RIP output only
Database docking	AE, WebCenter, External database	Single database
Database backup and recovery	Regular automatic backup, one-click recovery	Manual backup, manual recovery
Work file backup and restore	Automatic backup, intelligent management, one-click recovery	Manual backup, manual recovery
Smart Property	Smart Marks, Dynamic Barcodes, SmartNames (Database Query, String Extract System Value, Script, Xpath Query etc.) Workflow Modules, Workflow Controls, File Type Conversion, Workflow Embedded, Error Handling, Sendmail etc.	Few Smart Property
Work efficiency	High work efficiency, greatly reduce product production cycle	Low efficiency and long production cycle
Work quality	Few errors and errors are controllable	Unpredictable errors, no good preventive measures

## 4.2 Establish a Standardized System

### 4.2.1 SOP (Standard Operating Procedure)

The responsibility of each job was defined and the detailed description of the job was made. The formulation of the SOP was a part of the ISO9001 document, which can avoid the loss of technology due to the flow of technicians. Operators can master advanced and reasonable operating techniques after short-term training.

### 4.2.2 Document Coding Rules

The formulation method of each company may result in different coding due to different classifications. Take Russell Tianyi as an example to illustrate: The plate number code 18A-05-066. 18 Represents 2018, A represents business area, 05 represents May of this year, 066 represents the 66th work order of this month. Product Code: Reasonable coding of the company's products; Material code: Code of customer's product.

### 4.2.3 Put Higher and Stricter Requirements on Operating Specifications

File naming must be standardized and illegal characters cannot appear. The file storage location must be stored as specified, otherwise the system may not find the file. Normalized PDF was the standard usage file and so on.

### **4.3 Steps to Establish an Intelligent Workflow**

#### **4.3.1 Demand**

The traditional work flow was combined, and the best flow structure chart was designed. Technical Difficulties: The process must be logically reasoned and the flow diagrams simple and smooth.

#### **4.3.2 Master Process Module Functions**

Familiar with the function of working modules in the process, especially the input data type and output data type of each module.

#### **4.3.3 Design Flow**

Create an actual workflow based on the process workflow diagram. Technical difficulties: designing reasonable intelligent variables, a wide variety of intelligent variables, you must master the effectiveness of each variable, in particular, use XML language, Script language.

#### **4.3.4 Process Error Correction Capability Design**

When there was an error or warning in the process running, there must be corresponding error handling capability. The process can notify the process user of the cause of the error and the corrective action so that the process will not restart similarly without similar errors.

#### **4.3.5 Process Test**

The running test process was to make sure that there were no obvious errors. After the new design process was put on the line, it was necessary to track it regularly, and find that it was unreasonable or the operation was not smooth.

#### **4.3.6 Data Backup**

Make a backup of the database file, and if there was an abnormal situation, there must be an emergency plan to avoid affecting the production progress.

## **5 Set Up Problems Encountered in the Intelligent Process**

### **5.1 AE with ERP Database**

The backup of the database file was made, and if there was an abnormal situation, there must be an emergency plan to avoid affecting the production progress.

### **5.2 Maximize the Development and Use of Software Features**

How to deeply tap the potential function of the software to achieve the maximum utilization of the software, and to use the software's maximum use value was a problem of software attributes.

### **5.3 Easy Operation of the Process Was an Important Manifestation of the Practicality of ESKO**

Design the intelligent processes, and ordinary employees can get on the job with simple training. For the ease of use of the process, the design process must be carefully logically considered, taking into account all aspects of the process.

## **6 Generated Benefits**

Through the implementation of automated standard process, the product delivery cycle was shortened, the product quality was improved, the human loss was reduced, the work efficiency was improved, the labor intensity of the worker was reduced, and the customer was provided without increasing the production cost.

## **7 Conclusion**

ESKO software was a powerful prepress process management software. If you can achieve the maximum value of the application, you need to continuously explore, research, deep excavation, clever combination, flexible use, you can produce greater fission capabilities.

## **References**

1. Zhu, L. (2016, November). Established a pre-press automation standard process for carton packaging. *Printing Technology*.
2. Jiao, J. (2014, October). 3D online packaging design in cloud era. *Printing Industry*.
3. Yao, H. (2001, February). System engineering and color management. *Print Magazine*.
4. Yao, H. (2001). *Digital printing technology*. Shanghai Science Press.
5. <http://www.esko.com>.



# Application of Situational Awareness Decision in Intelligent Situation Printing System

Rubai Luo<sup>1</sup>(✉), Shasha Gao<sup>1</sup>, Huailin Li<sup>2</sup>, Shisheng Zhou<sup>1</sup>,  
Haoran Fang<sup>1</sup>, and Yumeng Liu<sup>1</sup>

<sup>1</sup> The Faculty of Printing and Packing Engineering, and Digital Media  
Technology, Xi'an University of Technology, Xi'an, China  
luorubai@xaut.edu.cn

<sup>2</sup> School of Mechanical and Precision Instrument Engineering, Xi'an University  
of Technology, Xi'an, China

**Abstract.** In this article, the concept of context-aware is integrated into the design of decision agents. This makes intelligent printing system can intelligently and quickly configure all kinds of manufacturing resources based on different printed product features. Firstly, this paper introduces the current situation of the application of context-aware technology, and the corresponding context information is classified in the printing process. Then, the general framework of decision agent in intelligent situation printing system is given. The function of each component is introduced in detail. Finally, a particular step of that decision agent in preprocess context information is described. The system can meet the needs of scenario printing.

**Keywords:** Context awareness · Decision agent · Intelligent situation printing system

## 1 Introduction

As customer demand becomes increasingly varied, the demand for product customization and pressure for the rapid introduction of new products are increasing [1]. Traditional manufacturing systems, such as dedicated and flexible systems, cannot provide an adequate response at a reasonable cost and have significant shortcomings in meeting these requirements [2]. In the production process, the intelligent application of the printing industry has also become a new idea for many companies to explore.

In the intelligent control system, the context-aware decision module is set up, according to the environment of the workshop and the specific state of the machine, the “personalized decision” is made for different production jobs. In addition, you can also use the JDF (Job Definition Format) and JMF (Job Messaging Format) to implement the internal description of the Job sheet and the information exchange between the parts. JDF standard is based on XML to describe the production control information and management information about the full cycle of printed manufacturing statements, and to track and control the printing operation using the JMF standard.

## 2 Application of Context Awareness

Context can be used to characterize the properties of an entity. Literature [3] defines context as any information that can be used to describe an entity environment. Context awareness in intelligent spaces makes decisions and automatically provides appropriate responses or services by automatically perceiving and computing context changes [4].

Context awareness is widely used as a recommendation system or human-computer interaction study in computer science. It is developed from a number of computing scenarios [5]. At present, the application of context-aware in intelligent space focuses on recommendations, queries, decisions, etc. For example, literature [6] establishes the model of intelligent controller using relevant contextual information in the intelligent space, and provides solutions for solving the uncertain factors in space. Literature [7] classifies the contextual information in the intelligent space and introduces the functions of each component in the model in detail.

## 3 Establishment of Situational Awareness Decision Agent

It is necessary to classify that contextual information before establishing a context aware decision agent model. According to the context information obtained from the classification, a corresponding context-aware strategy is established and a decision base is formed. The context-aware decision library is the core of the situational awareness decision Agent.

The description of situation information in printing production is mainly divided into three aspects: materials, equipment and environment. As shown in Fig. 1, the materials means all material information concerning the printing of the production process, such as base material, printing ink, etc. The equipment should contain the relevant operation of the machine and relevant parameter information. The environment mainly refers to the temperature and humidity information of the workshop during printing. In addition to basic classification as shown in Fig. 1, it should also include printing eligibility, such as paper moisture content, viscosity, etc. JDF's

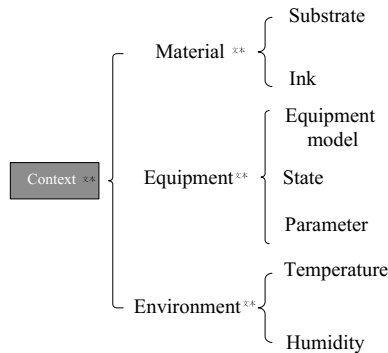


Fig. 1. Classification of context information

description of job and job production is a JDF tree structure, and the logical unit is the JDF node [8]. When describing with JDF, these resources can correspond to the child elements of the resource pool element in the JDF document as input resources, which are fully described according to the definition specification of resources in JDF [9]. For related attributes that are not involved in the JDF standard, a user-defined private data can be used for the description.

### 3.1 Framework of Situational Awareness Decision Agent

Decision agents include context manager, scenario manager, decision manager, operational variant library, and communication module. The internal structure of Agent is shown in Fig. 2. Context manager is used to uniformly manage context information. It can obtain context information through sensors or other means such as calling historical data to form a situational snapshot. The set of situational snapshots in the context manager is  $A = \sum_{i=1}^n \sum_{j=1}^m \langle s_i, v_j \rangle$ , in which  $s_i$  refers to a situational factor, and  $v_j$  refers to the value of the situational element. All kinds of information are stored in internal documents, agenda and log manager. The scenario manager is used to store the context protocol, which defines the standard situation when the operation is performed. The scenario model is  $C = \sum_{i=1}^n S_i$  and  $S_i = \sum_{j=1}^m \langle s_i, v_j \rangle$ : in which, C refers to all possible events in the workshop;  $S_i$  is the situational factor related to the event;  $v_j$  represents the value of an environmental element. Decision manager is a decision library used for storing relevant context-aware policies. Context-aware strategy is a specific measure to adjust the acquired context elements. A context-aware strategy contains corresponding real-time situations and operational variants. The operational variant library is used to store the relevant content of the action. Operational variant refers to the changes that should be made when a situation element does not meet production requirements. Communication module realizes communication with other agents. In the system, scene manager, decision manager, operating variable library should have some extension function. For example, users can add or remove awareness policies in the background.

The decision-making process includes data extraction, event formation, scenario snapshot establishment, scenario authenticity decision, decision chain generation, call operation variables, and output decision. Taking the printing workshop as an example, the order information is analyzed and extracted to form events. Then context managers get context information related to the event. This information includes machine state, material state, and other order-related information. Based on the obtained context information, the situation snapshot  $s = \{\langle a, v \rangle | a \in A, v \in Dom(a)\}$ , where  $A$  represents the set of situational factors related to the printing operation. The  $a$  represents one of the situational factors;  $v$  is the value of the situation element. The scenario manager determines the authenticity of the scenario snapshot. The result is represented by a Boolean function,  $F(b_1, b_2, \dots, b_n)$ ,  $b_i \in \{0, 1\}$ ; 0 indicates that the result of the situation is unqualified, whereas 1 is qualified. Finally, the relevant context-aware strategy in the decision manager is called according to the judgment result. The context-aware



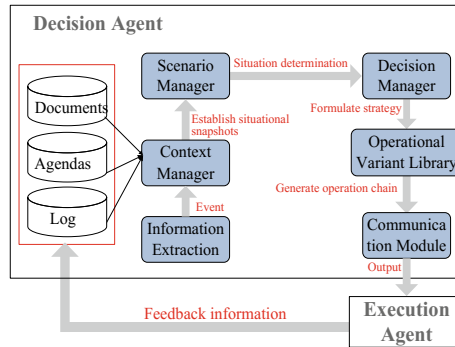


Fig. 2. Framework of decision gent

strategy include the corresponding operation variation, which is the relevant adjustments that should be made if the current situation is not suitable for printing. The operation variant library performs the corresponding operation variation and finally sends the decision information to other agents via the communication module.

JDF can be used to describe event related information during the decision process. Includes basic information, relevant process requirements, and production-related resource parameters. At the same time, JMF can not only complete the communication between various components in the agent, but also complete the communication between the decision agent and other agents. Query can be used to obtain news status, material usage, etc. Decision information can be sent to the appropriate execution agent in the form of command information.

## 4 Conclusions

In this paper, context awareness is integrated into the design of decision agent to obtain a printing system that can rapidly configure manufacturing resources according to different order requirements. The general framework of context-aware decision broker is given. The function and decision process of each component are described in detail. The application of context-aware decision will greatly improve the intellectualization and reconfiguration of the printing system. In addition, we will further integrate the context-aware decision and the design of the printing reconfigurable system to complete the construction of the whole intelligent context reconfigurable printing system.

**Acknowledgements.** This work was supported in part by NSF of the Science and Technology Department of Shaanxi Province under Grant Nos. 2016JM5068, NSF of the Key Laboratory of Shaanxi Provincial Department of Education under Grant Nos. 15JS075 and Shaanxi Province green smart printing and packaging collaborative innovation center.

## References

1. Andersen, A. L., Bejlegaard, M., Brunoe, T. D., et al. (2017). Investigating the impact of product volume and variety on production ramp-up.
2. Koren, Y. (2006). General RMS characteristics. Comparison with dedicated and flexible systems. In H. A. ElMaraghy (Ed.), *Reconfigurable manufacturing systems and transformable factories* (pp. 27–45). Berlin: Springer.
3. Dey, A. K., Kortuem, G., Morse, D. R., et al. (2001). Situated interaction and context-aware computing. *Personal and Ubiquitous Computing*, 5(1), 1–3.
4. Abowd, G. D., Ebling, M., Hung, G., et al. (2002). Context-aware computing. *IEEE Pervasive Computing*, 1(3), 22–23.
5. Maran, V., Machado, G. M., Machado, A., et al. (2018). UPCaD: A methodology of integration between ontology-based context-awareness modeling and relational domain data. *Information*, 9(2), 30.
6. Chahuara, P., Portet, F., & Vacher, M. (2012). Context aware decision system in a smart home: Knowledge representation and decision making using uncertain contextual information. In *The 4th International Workshop on Acquisition, Representation and Reasoning with Contextualized Knowledge (ARCOE-12)* (pp. 52–64).
7. Feng, L., Apers, P. M. G., & Jonker, W. (2017). Towards context-aware data management for ambient intelligence. In *Database and Expert Systems Applications, International Conference, DEXA 2004 Zaragoza, Spain, August 30–September 3, 2004, Proceedings. DBLP* (pp. 422–431).
8. Luo, R., Zhou, S., Li, H., et al. (2013). Computer integrated printing system. *Packaging Engineering*, 11, 23–26.
9. Luo, R., Zhou, S., Li, H., et al. (2016). Layered printing process planning based on polychromatic set theory. *Packaging Engineering*, 15, 189–193.



# Design of Online Variable Data Printing Jobs Production System Based on Cloud-Platform

Rubai Luo<sup>1(✉)</sup>, Xueying Fan<sup>1</sup>, Shisheng Zhou<sup>2</sup>, Yunjie Shi<sup>1</sup>,  
Haiying Jiang<sup>1</sup>, and Yuxiang Zhu<sup>1</sup>

<sup>1</sup> The Faculty of Printing and Packing Engineering, and Digital Media Technology, Xi'an University of Technology, Xi'an, China  
luorubai@xaut.edu.cn

<sup>2</sup> The Faculty of Printing and Packing Engineering, and Digital Media Technology, Xi'an University of Technology, Xi'an, Shaanxi, China

**Abstract.** According to the basic principle of variable data printing and the common production methods of variable data printing, an innovative technical solution for network service platform based on XML technology to realize multi-data format file creation of variable data printing jobs is proposed. The XML format input file is synchronously converted into a PPML format and a PDF format output file by the XML parsing technology DOM4J and the formatting object processor XML-FO. Tencent cloud platform, J2EE development platform to build B/S network architecture and SSM integration framework, MySQL database for data storage and management is used to design and implement cloud-based online variable data print job production system.

**Keywords:** Variable data printing · PPML · System design

## 1 Introduction

Under the premise of the continuous development of the personalized service market, the variable data printing customized according to customer needs has become the main development trend of the printing industry in the future. As a new digital printing mode, variable data printing can meet the needs of customers in small batches and personalized printing. It also enables zero inventory and instant printing, effectively reducing the storage costs of printing companies.

With the wide application of variable data printing, in order to meet the needs of customers, many printers have developed application software of variable data printing. Kloosterman et al. proposed a method for creating the template required for variable data printing by analyzing the variable print job files used to produce relevant parameters [1]. Gimenez et al. developed a variable data printing engine based on PPML/T [2]. Many experts and scholars at home and abroad have proposed different solutions and ideas for the above problems [3–5].

## 2 Establishment of Variable Data Print Job Production System

### 2.1 PPML Introduction

PPML is a kind of XML-based personalized printing markup language, which is one of the applications of XML in the printing field [6]. As a Meta language, PPML itself does not describe page content, but uses various “object units” to describe the structure, pages, and content of printed materials. PPML uses a hierarchical and structured approach to describe the information in the print. <PPML> contains all resource information for the job as the highest hierarchy. This element can only appear as the root element of the PPML data set. Second, it is divided into document hierarchy <DOCUMENT SET> (or <JOB>), document <DOCUMENT>, page <PAGE>, and tag <MARK>.

### 2.2 Variable Data Printing Process

Variable data printing means that each adjacent printed page can contain unique information to produce an unrestricted, unique and targeted personalized product. The most popular production method at present is using the layout design software to create a fixed page template content, using the database to store variable data information, and then combining the two parts of the content and outputting them together on a digital press [7].

The variable data print job file format conversion process is shown in Fig. 1. The conversion process for implementing multi-format output of a single format file can be divided into two parts: conversion from an XML format file to a PPML format file and conversion from an XML format file to a PDF format file.

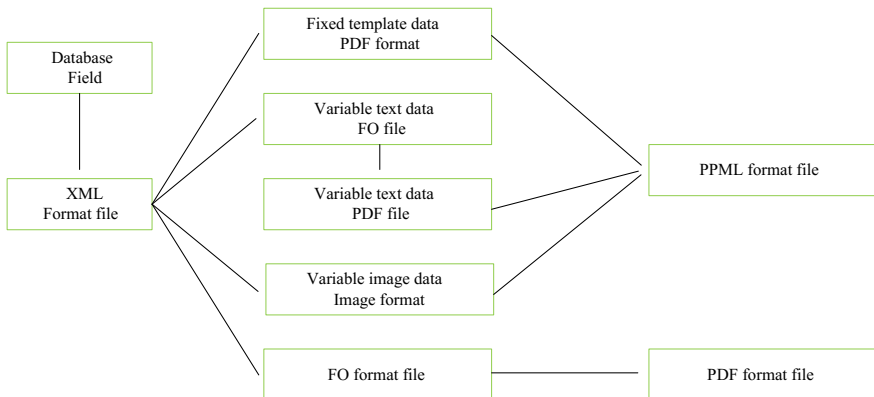


Fig. 1. Manufacture workflow of variable data printing jobs

### 2.3 Modeling of Variable Data Printing System

In this system, it is roughly divided into two categories of users: ordinary users and administrators. Through the research and analysis of the variable data printing process, the system function modules are divided into two parts: the front-end module for ordinary users and the background module for system administrators.

The function of the system foreground include: registration, login, shopping cart, photographer's page, my account and help center and other modules.

System background functions include: personnel management, product management, order management, and website content management modules.

Combined with the database design principles and the actual needs of the system, a database table structure with less redundancy and a reasonable structure is created. So we use MySQL as a database system. The system uses HTML and CSS technology to complete the writing and style design of static pages [8]. Use MyEclipse2016 as a development tool based on the SSM integration framework. Among them, the SSM framework is composed of three open source frameworks: Spring, SpringMVC, and MyBatis.

## 3 Implementation of Online Variable Data Printing Production System Based on Cloud Platform

According to the analysis of the production of variable data printing jobs, the product production module of the platform is divided into four sub-modules: registration login, product selection, variable data printing product production, product ordering. This chapter will briefly show the implementation of several modules in the system.

### 3.1 Variable Data Printing Product Production Function

After the user enters the product details page, click the button on the page to enter the product creation page. The system automatically creates a corresponding number of blank templates based on the number of pages selected by the user. The template can be reused and a preview of the page can be viewed. A question about whether the information is complete before the last save. The user can view the work in the order module under the personal account section. The production interface of the album product is shown in Fig. 2. Click on the template selected on the left and the blank template on the right is replaced, as shown in the Fig. 1 in the figure. The user automatically opens the local file by clicking the sample photo on the template, selects the uploaded photo, and completes the input of the image information, as shown by the number 2 in the figure.

### 3.2 Background Product Management Functions

There is a product series management module and a list of product series is displayed the page when the administrator enters the background management system. A new series can be added and the page will jump to the series add interface. When adding a series, you need to enter the product number, name, price, and select the product type.



Fig. 2. Website of photo album making

After the save operation, the product series is added successfully. When you delete a series, all the template information under the series will be deleted.

## 4 Conclusions

In this paper, XML data format conversion technology is used to realize the production of multiple data format files for variable data printing operations. The cloud platform online photo album production system is designed by analyzing customer needs and finally realizes the functions of single format input and multi-format output. The use of new technology for variable data printing makes personalized printing more convenient and user experience more comfortable. Since the focus of this topic is on making variable data print jobs and converting between different formats, other minor features of the site are not fully implemented. The system will be further upgraded and maintained in the future.

**Acknowledgements.** This work was supported in part by NSF of the Science and Technology Department of Shaanxi Province under Grant Nos. 2016JM5068, NSF of the Key Laboratory of Shaanxi Provincial Department of Education under Grant Nos. 15JS075 and Shaanxi Province green smart printing and packaging collaborative innovation center.

## References

1. Kloosterman, D., & Donahue, T. F. (2003). Variable data printing dynamic imposition template: US, US20030189726[P].
2. Gimenez, G., & Chiarabini, L. (2004). A PPML/T based variable data printing engine. In *Nip & Digital Fabrication Conference* (pp. 347–350(4)).

3. Dyson, P. E. (2002). Variable-data printing adopts PPML and the web. Seybold Report on Publishing Systems.
4. Drennan, B. (1997). Variable-data printing comes of age: Capabilities & market demand converge. Seybold Report on Publishing Systems.
5. Liu, Z., Zhu, M., & Mao, Z. (2009). Research on variable data printing for cross-media digital publishing. In *International Conference on Computer Sciences and Convergence Information Technology* (pp. 723–727). IEEE.
6. Wang, P. (2012). *Variable data printing file analyzing and screening technology base on PPML*. Zhejiang University of Technology.
7. Mao, Z. (2011). *The construction and realization of web service platform of variable data printing*. Nanjing Forestry University.
8. Bao-Wen, W. U. (2012). CSS style sheet implementation in several common page layout structures. *Journal of Wenshan University*.



# Gravable Printing Plate Surface Defect Intelligent Detection Method

Yechi Pang<sup>(✉)</sup>, Zhuangzhi Ye, and Zhijie Li

Beijing Key Laboratory of New Technology of Packaging and Printing, China  
Academy of Printing Technology, Beijing, China  
pangyechi@keyin.cn

**Abstract.** The author visited many gravure printing plate-making enterprises in China and found that in the fierce market competition environment, enterprises have gradually changed their approaches to improving their competitiveness. They used to upgrade their competitiveness by purchasing high-value automation equipment and other heavy assets, and they gradually changed to purchase or upgrade enterprise operation management system software and improve employees' abilities. The core competitiveness has been improved by improving the soft power of knowledge structure, or by continuously optimizing the technology and carrying out the "equipment substitution program". In such a case, the development and productization of "gravity plate surface defect intelligent detection system" has attracted the attention of many gravure printing companies domestically and overseas, and has great market prospects. The detection system is divided into five modules, namely the plate roller bearing module, the plate roller wiping module, the scanning detection module, the coding mark module, and the system control module. The plated roll is loaded onto the inspection device, and every module are at the working state from the initial state. The surface wipe module starts working, after which the scan detection module starts the first scan. By software calculation, non-defects are excluded from suspected defects, and true defects are confirmed. The coding mark module marks the real defects, and after the detection and coding process are finished, every module returns to the initial position. The plate roller is removed from the inspection device to complete the inspection task.

**Keywords:** Gravure printing · Printing plates · Defects · Machine vision · Testing

## 1 Defect Detection System

### 1.1 Gravure Plate Making [1]

Gravure printing process mainly refers to steel roller material selection, metal processing, surface grinding, surface copper plating, grinding and polishing, electronic engraving, chrome polishing, proofing, quality control, and hair plate. Equipment automation has been achieved in all of the above operations. Among them, between the multiple links, it is necessary to check the surface of plate roller for a number of flaws, such as material damage, blisters, bubbles, scratches, and the like. It is found that it



needs to be repaired after boring to ensure that the surface of the plate roll is clean and free of defects, otherwise it will affect the quality of plate making.

The quality standard of the plate after copper plating is [2] no scratches, bumps, ramps, sand holes, large traces of grinding lines, and the surface of the copper layer is smooth, no oxidation, no corrosion points, fingerprints, twill, horizontal stripes, no repair traces, dents. At present, the defects are checked, mainly relying on manual visual inspection. Generally, checking a plate roll of 1200 mm long and 300–400 mm in diameter will cost for 3–5 min. There are dozens to hundreds of plate rolls in one class to be inspected, and the labor intensity is very large. Due to human factors, missing defects are inevitable. If there is flaw on the surface of the plate roll, when the laser engraving plate roll, the engraving head will be damaged, causing dirty plate, which will cause unnecessary economic loss and time loss due to rework, worse yet, customers may be lost as a result. Therefore, the development of an automatic roll detecting device capable of replacing manual rolls is an urgent need for gravure printing companies.

## 1.2 System Composition

Based on the above-mentioned enterprise needs and in accordance with the direction of the national 2025 strategy, China Institute of Printing Science and Technology researched the automated and intelligent methods for surface defect detection of gravure plates, and developed an intelligent detection system for surface defects of gravure plates, using smart devices. Instead of manual, the surface defects of the gravure plate are detected. Among the many suspected defects, the non-defects are eliminated, and the real defects are marked to facilitate the repair of the defects in the subsequent process.

The system is divided into a hardware mechanical part and a software control part.

### 1.2.1 Hardware Mechanical Part

It consists of a plate roller bearing module, a surface wiping module, a scanning detection module, and a code marking module. See Fig. 1.

#### Plate Roller Bearing Module

The module is used for loading the gravure plate roller, and the other end is fixed, so that it can rotate at a constant speed according to the required rotation speed, so as to facilitate the detection of the surface of the plate roller and the marking of the crucible. See Fig. 2.

#### Surface Wiping Module

Before the defect detection on the surface of the plate roller, the surface of the plate roller is wiped at all times to remove dust, which lays a foundation for the elimination of non-defects. See Fig. 3.

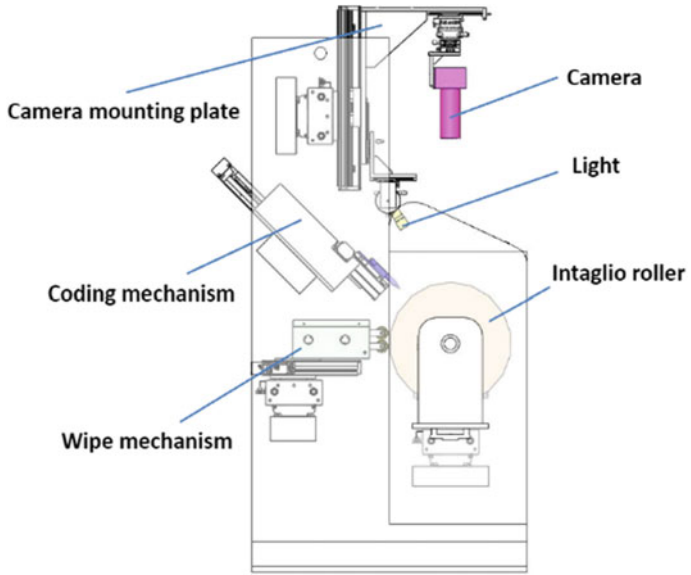


**Fig. 1.** Schematic diagram of the hardware composition of the gravure roll surface defect detection system

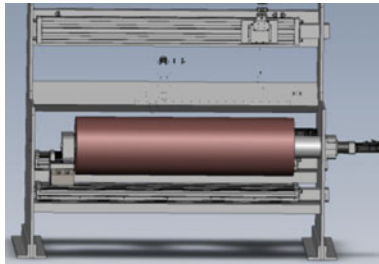


**Fig. 2.** Schematic diagram of the roll bearing module

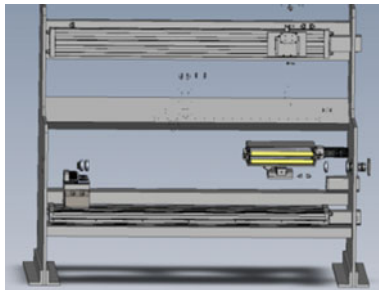


**Fig. 3.** Schematic diagram of the roll surface wiping module

### Scanning Detection Module

The image is illuminated by an angle-adjustable linear source, and the surface of the plate is scanned with a camera capture a complete image of the surface of the plate [3]. The normal plate roll surface should be smooth and free of any flaws, and the flaws (i.e., defects) that appear are of shape and area, and circumference. According to the threshold set by the software for the perimeter, area and shape of the defect, all defects found on the image are judged. The threshold greater than or equal to the threshold is defined as a suspect defect on the map, which is less than the threshold and can be calibrated on the map. All suspected defects are laid out, which lays a foundation for next step to eliminate non-defective interference, see Fig. 4.

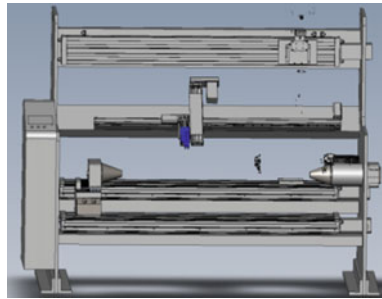


**Fig. 4.** Schematic diagram of the suspected scan detection module

### Code Marking Module [4]

By identifying the suspected defects on the surface of the plate and eliminating the defects, real defects are marked around the defect points on the surface of the plate by coding, which is convenient for repairing the defects, see Fig. 5.

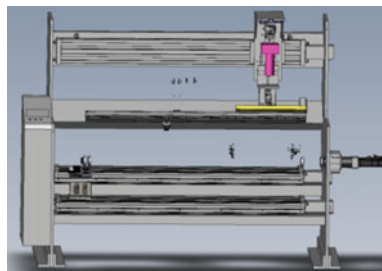


**Fig. 5.** Schematic diagram of the code marking module

### 1.2.2 Software Control Part

A software control part includes a plate roll loading operation control subsystem, an image acquisition subsystem, a plate roll surface wiping control subsystem, a code mark control subsystem, and the like.

#### Plate Roll Loading Operation Control Subsystem

- a. By controlling the clamping motor of the left and right movable top cones, the plate roller is clamped on the detecting device according to the length of the plate roller.
- b. Through the control of the spindle rotating motor, the plate roller can be rotated at a constant speed and the speed can be adjusted.

Image acquisition subsystem

- a. According to the diameter of the plate roller, the distance between the scanning detection module and the surface of the plate roller is adjusted by the control motor to reach the set value.
- b. According to the length of the plate roller, the motor is driven to translate the detection module to the second working position, and the above work is repeated until the end.

#### Plate Roll Surface Wiping Control Subsystem

- a. According to the diameter of the plate roller, adjust the distance between the surface wiping module and the surface of the plate roller by controlling the motor to reach the set value.
- b. Control the motor so that the wiping head contacts the surface of the plate roller under a certain pressure and is wiped by the rotation of the plate roller.
- c. According to the length of the plate roller, the surface wiping module is translated to the second working position by motor drive, and the above work is repeated until the end.

#### Coding Mark Control Subsystem

- a. According to the diameter of the plate roller, adjust the distance between the print head and the surface of the plate roller by controlling the motor to reach the set value.
- b. On the basis of the suspected defects detected by the scanning detection module, the final confirmed defects are marked on the surface of the plate roll by non-defect elimination algorithm and real defect confirmation algorithm.

### 1.3 Process Route

Load a copper plated roll having a surface roughness  $R_a$  between 0.04 and 0.08 onto the detecting device, and adjust the working distance between the surface wiping module, the scanning detecting module and the code marking module and the plate

roller according to the diameter change of the plate roller. To the initial working state, the surface wiping module starts to work. The scanning detection module starts the first inspection. The scanning detection module starts the second detection. According to the length of the plate roller, the surface wiping module and the scanning detection module are moved to the second working position, and the above wiping and repeating are repeated. The inspection work is calculated by software, and the non-defects are eliminated in the suspected defects and the real defect code marking module is coded to mark the real defects found in the first working position, and so on. After the defects of each section of the plate roll are detected, the code mark module moves to the last working segment, and after finishing the defect, all the work is completed. Each module is restored to the initial position, and the plate roller is removed from the detecting device to complete the detection.

## 2 Defect Confirmation Method

The system has developed a set of intelligent equipment using industrial controllers and sensors, linear modules and control software to detect surface defects of gravure plates. The core of the technology is to accurately eliminate non-defects among all the suspected defects detected, achieving a defect recognition rate of 100% and a non-defect elimination rate of approximately 100%.

### 2.1 Non-defective Elimination Method

This method mainly excludes debris that can be moved on the surface of the plate roll such as dust and dust particles. The technical solution is as follows.

#### 2.1.1 First Defect Scan

The first scan of the surface of the plate is performed, and the suspected defect information (the defect has a certain shape) is collected, and record the coordinates of the suspected defects.

#### 2.1.2 Second Defect Scan

While scanning the defect, the plate surface wiping module always wipes the scanned area on the surface of the plate roll to displace the non-defects. At the same time, start the second scan, and the coordinates of the suspected defects are recorded again.

#### 2.1.3 Exclude Non-defects

Compared the suspected defect detected at the second scan with the suspected defect at the first in the same coordinate origin, and the abscissa displacement  $\Delta X$  and the ordinate displacement  $\Delta Y$  are obtained. The abscissa displacement is set as first threshold ( $1 \leq A \leq 10$  ppi) and the ordinate displacement as second threshold ( $1 \leq B \leq 100$  ppi).

If  $\Delta X \geq A$  or  $\Delta Y \geq B$ , then the suspected defect is confirmed as a non-defect.

If  $\Delta X < A$  and  $\Delta Y < B$ , then the suspected defect is confirmed as a suspected defect. And record the coordinate position.

## 2.2 Method of Confirming the True Defect

On the basis of the first suspected defects, the suspected defects are successively judged by the gray value, the area, and the circumference and the real defects are finally defined. The flowchart of the judgment method is shown in Fig. 6.

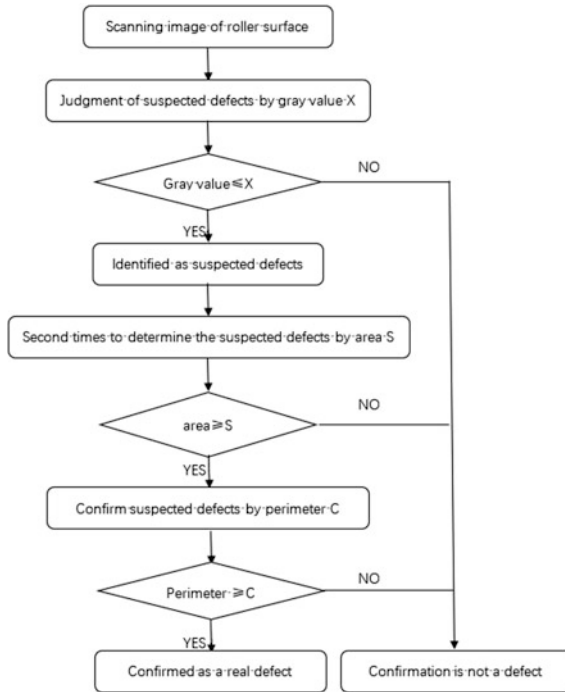


Fig. 6. Flow chart of the method for judging the true defect

### 2.2.1 Determine Whether It Is a Suspected Defect by the Gray Value X for the Second Time

Scan the surface of the plate roll, use the gray value to distinguish the pixel level of the scanned images, and set a gray limit value  $X$  ( $20 \leq X \leq 200$ ).

If the gray value of the suspected defect  $\leq X$ , then it is considered as a suspected defect.

### 2.2.2 Through the Area S for the Third Time to Determine Whether It Is a Suspected Defect

Calculate the suspected defect for the second time, calculate the area for the graph with a certain area of suspected defect, and set an area limit value  $S$  ( $1 \leq S \leq 5 \text{ ppi}^2$ ).

If the area of suspected defects  $\geq S$ , then it was confirmed to be a suspected defect.

### 2.2.3 Through the Perimeter $C$ to Finally Determine Whether It Is a Real Defect

For the third suspected defect that has been confirmed to be recalculated, the perimeter is calculated for the graph of the suspected defect having a certain area. Set a perimeter limit  $C$  ( $10 \leq C \leq 60$  ppi).

If the area of suspected defect  $\geq C$ , then confirm that it is a real defects.

The coordinates corresponding to all the real defects after confirmation are statistically listed for the use of the code marking module.

## 2.3 Intelligent Classification of Defects

The detection system uses a deep learning algorithm to achieve intelligent classification of defects [5].

### 2.3.1 Accumulate Scan Files and Build Training Samples

The defects in the image are intercepted, and then manually classified according to the characteristics of the defects to establish a basic database of training images. According to the characteristics of the image data, the CNN neural network model is constructed, and the pre-stored training database is imported into the model for training. The project passed the defect system test, and obtained more than 8000 defect samples as the basic data, which were manually divided into 8 categories, then removed the data that is difficult to classify and eliminated too much data of some single-class data, and finally selected 4866 data as the data. Basic data. See Figs. 7, 8, 9, 10, 11, 12, 13 and 14 for a list of 8 typical defect images.

### 2.3.2 Form Test Data Based on the Test Information

Among the 15,694 samples stored and intercepted in the factory late roll detection, 268 data were selected as experimental test samples, and 8 types of manual classification were also performed. The training data and test data information table are shown in Table 1.

As can be seen from Table 1, some experimental test data is too small, which will directly affect the classification conclusion.

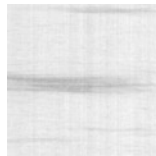


Fig. 7. Traces



**Fig. 8.** Scratches



**Fig. 9.** Sand holes

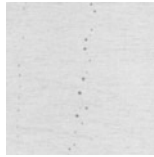


**Fig. 10.** Water drops

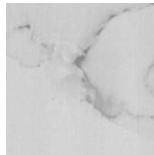


**Fig. 11.** Water stain

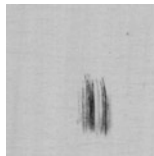


**Fig. 12.** Thread mark

### 2.3.3 Defect Intelligent Classification Based on Deep Learning [6]

Load the experimental test data into the trained model and predict the defect classification. See Table 2 for the test results.

Through the intelligent classification of defects, it can provide guidance for the production status of the enterprise. For example, in a period of time, certain types of



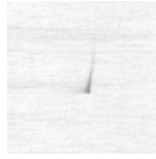


**Fig. 13.** Trailing

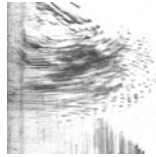


**Fig. 14.** Smudge

**Table 1.** Training data and test data information

No.	Defect type	Training data	Percentage (%)	Test data	Percentage (%)
1	Traces	1356	27.87	46	16.08
2	Scratches	84	1.73	9	3.15
3	Sand holes	392	8.06	68	23.78
4	Water drops	1540	31.65	54	18.88
5	Water stain	353	7.25	17	5.94
6	Thread mark	127	2.61	1	0.35
7	Trailing	75	1.54	2	0.70
8	Smudge	939	19.30	89	31.12
	Total	4866		286	

**Table 2.** Defect classification

Manual classification	Test conclusion							
	Traces	Thread mark	Scratches	Sand holes	Trailing	Smudge	Water stain	Water drops
Traces	45	0	0	0	0	2	0	0
Thread mar	0	1	0	0	0	5	0	0
Scratches	0	0	3	1	1	2	7	1
Sand holes	0	0	1	37	1	3	0	5
Trailing	0	0	1	6	0	1	0	0
Smudge	0	0	0	1	0	63	5	2
Water stain	1	0	4	8	0	6	4	0
Water drops	0	0	0	15	0	7	1	46
Single precision	97.8%	100.0%	33.3%	54.4%	0.0%	70.8%	23.5%	85.2%
Total precision	69.58%							

defects appear frequently, indicating that some problems occur in the early production process. This needs to be rectified. This information help to improve the scientific and intelligent management of factory production.

### 2.3.4 Problems

Data fluctuations change, in the process of detection, as time goes by, new types of defects continue to appear, and some defects will not appear for a long time. If the number of classifications is increased, the classification accuracy will be reduced. The specific classification direction needs to further accumulate data for statistics.

The data is not balanced. When training, the amount of data in each category is inconsistent, this will affect the accuracy of training. Some defects have a particularly low frequency, requiring long-term accumulation of data.

There are various reasons for the occurrence of defects. In the later stage, there may be no statistics on the types of defects in the early stage, which may affect the prediction accuracy.

## References

1. Xu, W., & Zuo, G. (2005). Current situation and development trend of China's gravure printing industry. *Printing Technology*, (12), 69–71.
2. Dong, X. Z. (2008, July 7). Surface treatment of gravure plate making. *China Packaging*, (003).
3. Yang, J., Li, Z., Fan, L., & Huang, Q. (2016). Weld surface defect detection system based on line laser scanning. *Welding*, 2, 19–23+70.
4. Cai, Y. (2015). Construction of cigarette traceability system based on precision coding technology. *Computer Knowledge and Technology*, 11(35), 113–114.
5. Nora. (2015). *FPGA implementation of AQM algorithm based on dSPACE network model*. Jilin University.
6. Sun, C. (2016). *Research on defect detection and intelligent classification of color steel plates based on machine vision*. Tianjin University of Science and Technology.



# Research on Fractional Lower Order Feature Extraction of Bearing Vibration Signals Under Alpha Stable Noise Conditions

Qianqian Xu<sup>(✉)</sup>, Kai Liu, and Zhuofei Xu

Faculty of Mechanical and Precision Instrument Engineering, Xi'an University of Technology, Xi'an, China  
18700197780@163.com

**Abstract.** According to the performance degradation problem of feature extraction from higher-order statistics in the Alpha stable distribution noise, a new feature extraction method of rolling bearings under Alpha Stable Noise Conditions is proposed. Firstly, the non-stationary vibration signal of rolling bearings is decomposed into several product functions by Local Mean Decomposition (LMD) to realize signal stability. Then, the distribution properties of product functions in time domain is discussed by the comparison of heavy tails and characteristic exponent estimation. Fractional lower order p-function optimization is achieved by the calculation of the distance ratio based on K-means algorithms. Finally, faulty feature dataset is created by the optimal FLOS and lower dimensional mapping matrix to accurately and intuitively describe various faulty bearings. Since the Alpha stable noise is effectively suppressed, the presented method has shown nicer performance than the traditional methods in bearing experiments. Inking roller's bearings are described precisely by fractional lower order feature extraction.

**Keywords:** Alpha stable distribution · Fractional lower order statistics · Co-variation · Feature extraction

## 1 Introduction

The existing feature extraction methods of vibration signals are built on second order or higher order statistics to realize signal filtering and decomposition, assuming that the noise is yielding a Gaussian distribution [1]. However, those statistics are not existed under Alpha stable distribution noise conditions [2, 3]. Based on this finite statistics, features of time domain, frequency domain and time-frequency domain would show degradation performance of state description [4–7]. In order to process the bearing vibration signals under Alpha stable noise conditions effectively, a new feature extraction method in fractional lower order is proposed in this paper.

## 2 Time-Domain Distribution Characteristics Analysis

LMD decomposes an arbitrary detection signal  $x(t)$  into a series of components  $PF_i(t)$  and remainders  $u_i(t)$  [8, 9]. However, when the noise is impulsive and modeled as a non-Gaussian  $\alpha$  process, variance, second order and higher order statistical characteristics of  $PF_1(t)$  are infinite. That may reduce the accuracy and reliability of above statistics for the description of equipment states.

$$x(t) = \sum PF_i(t) + u_i(t) \tag{1}$$

Suppose SKF6205-2RS bearing faulty database is  $X = \{A, M . n\}$ , where fault types  $M \in \{B, C, D\}$  and fault sizes  $n \in \{a, b, c\}$ . The faulty samples are grouped in Table 1.

**Table 1.** Grouped faulty samples

No.	Groups	Description
1	$X = \{M . n   M = B, C, D, n = a\}$	Three fault types in fault size a
2	$X = \{M . n   M = B, C, D, n = b\}$	Three fault types in fault size b
3	$X = \{M . n   M = B, C, D, n = c\}$	Three fault types in fault size c
4	$X = \{M . n   M = B, n = a, b, c\}$	Rolling fault in different fault sizes
5	$X = \{M . n   M = C, n = a, b, c\}$	Inner race fault in different fault sizes
6	$X = \{M . n   M = D, n = a, b, c\}$	Outer race fault in different fault sizes

The most striking characteristic of the Alpha stable distributed signals is more peak pulses in time domain and thicker algebraic tails of probability density PDF. Figure 1 is the heavier tails of signal components  $PF_1(t)$ . Then, the mean values of characteristic exponents  $\alpha$  [10] of PF components are shown in Table 2.

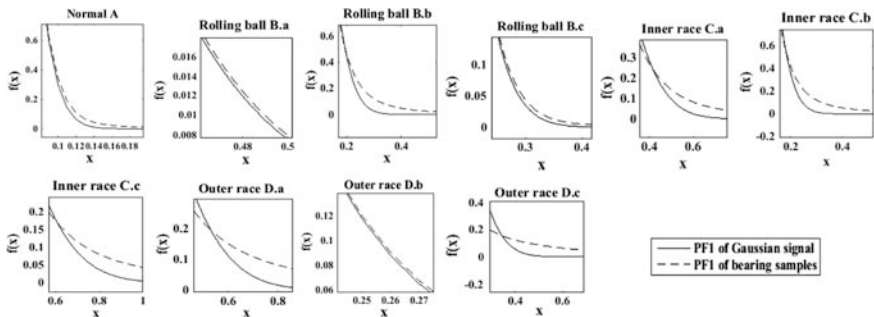


**Fig. 1.** PDF curves comparison of PF1 of faulty bearings and Gaussian signals with the same parameters except  $\alpha$

**Table 2.** Mean values of bearing samples (SKF6205-2RS)

Samples	A	B.a	B.b	B.c	C.a	C.b	C.c	D.a	D.b	D.c
Mean values	1.897	1.997	1.619	1.968	1.522	1.536	1.433	1.170	1.990	1.008

It is proved from Fig. 1 and Table 2: (1) there is no doubt that the alpha distributed noise is existed in the vibration signals under both normal and faulty conditions. (2) When the noise is impulsive and modeled as a non-Gaussian process, PF components are failed to describe the vibration signals accurately, which has been a major drawback to the use of LMD.

Therefore, using fractional lower order features is more adaptive than the conventional second-order and higher-order statistical moments to describe the signal components, avoiding the conventional hypothesis errors effectively.

### 3 Fractional Lower Order Characteristics of Bearing Vibration Signals

This new method constructs the feature matrix of the optimal FLOS and lower dimensional mapping matrix to effectively suppress the impulsive noise and accurately describe the equipment operational condition. The algorithm flow is shown in Fig. 2.

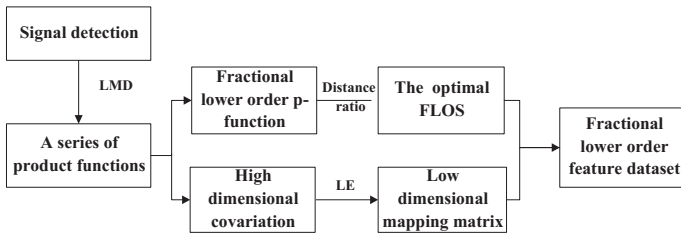


**Fig. 2.** A fractional lower order features extraction method

#### 3.1 Optimal FLOS

The formula of fractional lower order statistics (FLOS) is [11]:

$$E[|X|^p] = \begin{cases} C(p, \alpha)\gamma^{p/\alpha}, & 0 < p < \alpha \\ \infty, & p \geq \alpha \end{cases} \quad (2)$$

where  $C(p, \alpha) = \frac{2^{p+1}\Gamma(\frac{p+1}{2})\Gamma(-p/\alpha)}{\alpha\sqrt{\pi}\Gamma(-p/2)}$  and  $\Gamma(\cdot)$  is Gamma function.

This paper introduces an optimization algorithm of optimal value  $p_{opt}$ . First, we calculate FLOS with different p values as the eigenvalue of each sample, described as  $E_p^{i,j}$ . Then, the best clustering center  $(x^1, x^2, \dots, x^j)$  of each state type is obtained by K-

means clustering algorithm. Finally, we could calculate the distance between  $E_p^{ij}$  and  $(x^1, x^2, \dots, x^l)$  in order to obtain the class separation distance  $D_b$  and intra-class distance  $D_i$  of each sample. At last, the optimal order  $p_{opt}$  of FLOS could be selected by the mean distance ratio of  $\bar{D}_b/\bar{D}_i$ .

### 3.2 Lower Dimensional Mapping Matrix of Co-variation

According to the infinite variance of Alpha stable signals, Miller put forward the concept of co-variation in 1978. For random variables  $X$  and  $Y$  of simultaneous distribution, the co-variation of variables  $X$  and  $Y$  is given by formula (3), with characteristic exponents  $1 < \partial \leq 2$  and dispersion coefficient  $\gamma_y$ .

$$[X, Y]_\alpha = \frac{E(XY^{<p-1>})}{E(|Y|^p)} \gamma_y, \quad 1 \leq p < \partial \tag{3}$$

For the high dimensional covariant matrix, Laplacian Eigenmaps algorithm is used to carry out lower dimensional mapping matrix. Finally, realize the optimal embedding of high dimensional manifolds in the mapping theory.

## 4 Feature Accuracy Comparisons

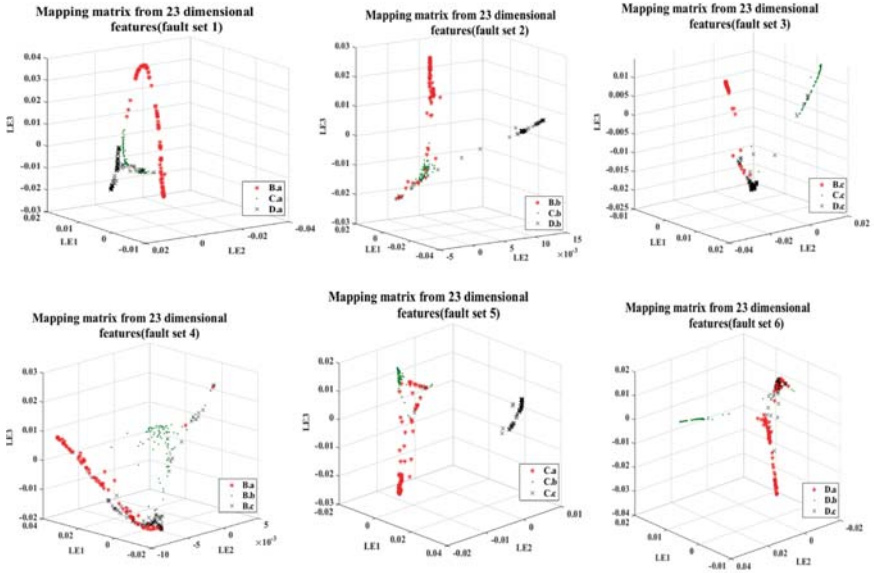
In Sect. 4, we analyze the characteristics of multi-dimensional features and the fractional lower order features proposed in this paper. The range of parameter  $p$  is determined according to the minimum value of characteristic exponents  $\partial$ . Taking the variation of  $p$  as 0.1 and calculating the ratio value of  $\bar{D}_b/\bar{D}_i$ .

As shown in Table 3, the maximum ratio is 319.68 when the value is  $p = 0.1$ . Calculate the co-variation matrixes of component  $PF_1(t)$  and co-variation matrices  $C_{N \times N}$ . Making  $C_{N \times N}$  to be the input matrix, we construct the Laplace characteristic matrix to enhance the faulty components in each type of samples. Thus, we could obtain the lower dimensional mapping matrix  $MC_{N \times 2}$  of each type of samples.

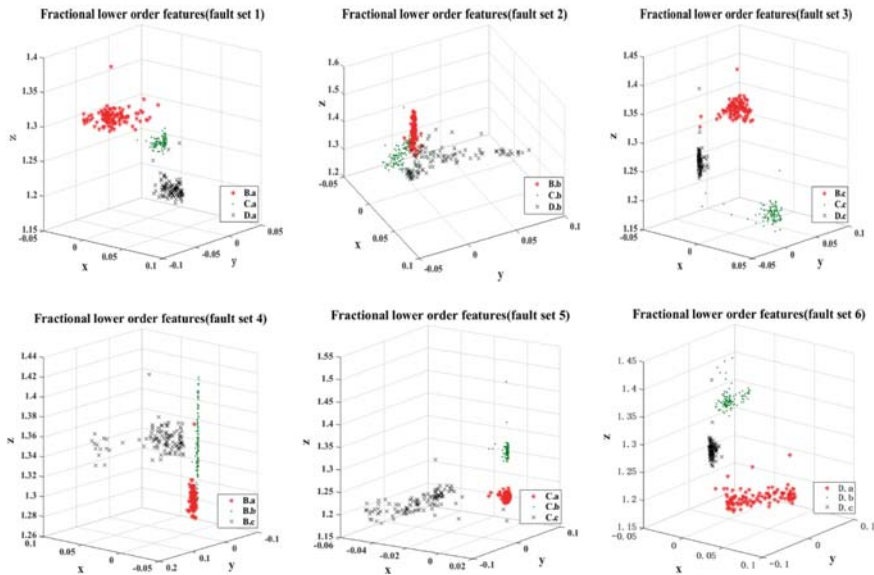
**Table 3.** Ratio of different faulty sets

p	0.1	0.2	0.3	0.4	0.5	0.6	0.7
Ratio	319.68	288.63	85.61	253.99	195.63	126.25	205.08

The characteristic 3D matrix  $FC_{N \times 3}$  of bearing integrates  $MC_{N \times 2}$  and  $E_p$  matrices. Draw scattered plots with this 3D feature of matrix as the x, y and z coordinate. Figure 3 is the comparisons with the mapping features in Ref. [6], which was obtained from 23 dimensional features (Table 4).



(a) Mapping matrix from 23 dimensional features of 1-6 faulty sets



(b) Fractional lower order features of 1-6 faulty sets

Fig. 3. 3D scattered plots comparisons

**Table 4.** Comparisons of the correct classification rates

No.		The correct classification rate (%)						Mean
		1	2	3	4	5	6	
Reference [6]	23	93.87	90.42	98.85	93.49	96.55	96.17	94.89
New	2	99.62	86.59	99.62	96.94	99.62	99.62	97.00

## 5 Conclusions

- (1) The Alpha distributed noise exists in the vibration signals under both normal and faulty conditions.
- (2) When the noise is impulsive and modeled as a non-Gaussian  $\alpha$  process, LMD algorithm does not process the vibration signals effectively for impulsive noise still exists in PF components.
- (3) The improved performance is clearly demonstrated both theoretically and experimentally. In the comparisons with traditional methods, fractional lower order features make the classification accuracy of bearings in servile states up to 97.00%, providing a certain theoretical basis for the intelligent diagnosis of the whole machine.

**Acknowledgements.** This study is funded by the National Natural Science Foundation of China (No. 51275406), the Natural Science Basic Research Plan in Shaanxi Province of China (No. 2017JQ5012) and the Natural science project of Shaanxi Provincial Department of Education (No.17JK0545).

## References

1. Lei, Y., Jia, F., Kong, D., et al. (2018). Opportunities and challenges of machinery intelligent faulty diagnosis in big data era. *Journal of Mechanical Engineering*, 54(5), 94–104.
2. Shao, M., & Nikias, C. L. (1993). Signal-processing with fractional lower order moments—Stable processes and their applications. *Proceedings of the IEEE*, 81(7), 986–1010.
3. Qiu, T., et al. (2004). *Statistical signal processing (processing and application of non-Gaussian signals)* (p. 06). Beijing: Publishing House of Electronics Industry.
4. Yu, G., Li, C., Zhang, J., et al. (2013). A new statistical modeling and detection method for rolling element bearing faults based on alpha-stable distribution. *Mechanical Systems and Signal Processing*, 41(1–2), 155–175.
5. Nolan, J. P. (2005). Stable distributions: Models for heavy-tailed data. Progress Chapter Online at Academic2.american.edu/jpnolan.
6. Qiu, T., Yang, Z., Li, X., et al. (2007). A weighted average least p-norm algorithm under Alpha stable noise conditions. *Journal of Electronics & Information Technology*, 02, 410–413.
7. Zheng, Z., & Wang, S. (2016). Radar target detection method of fractional lower order matched filter in complex sea clutter background. *Acta Electronica Sinica*, 44(02), 319–326.
8. Xu, Q., Liu, K., Hou, H., et al. (2016). Diagnosis method of faulty bearings based on LMD and LE. *China Mechanical Engineering*, 27(22), 3075–3081.



9. He, Q. (2013). Vibration signal classification by wavelet packet energy flow manifold learning. *Journal of Sound and Vibration*, 332(7), 1881–1894.
10. Koutrovelis, I. A. (1980). Regression type estimation of the parameters of stable laws. *JASA*, 75(4), 918–928.
11. Ma, X., & Nikias, C. L. (1996). Joint estimation of time delay and frequency delay in impulsive noise using fractional lower order statistics. *IEEE Transactions on Signal Process*, 44(11), 2669–2687.



# Study on the Operational Characteristics of Offset Press

Peng Liu<sup>(✉)</sup>, Zhuofei Xu, and Heping Hou

School of Printing Packaging and Digital Media, Xi'an University of  
Technology, Xi'an, China  
liupeng@xaut.edu.cn

**Abstract.** The operational characteristic of offset press is studied to provide the theoretical basis for the design and manipulation of the offset press. The theoretical model between blanket cylinder and impression cylinder is built based on elastic hydrodynamic lubrication (EHL) theory. Then numerical calculation method is applied to solve the theoretical model. Results: The universal characteristic curve of the offset press is obtained, which demonstrates the changed rule of the thickness of the ink film under the common influence of the printing load and the printing speed. And the rule is significant to the design and manipulation on the offset press. When the printing load of the offset press is limited to a specific range, the offset press has the best maneuverability. This means that the thickness of the ink film is less sensitive to the change of printing speed.

**Keywords:** Offset press · Operational characteristics · EHL · Universal characteristics

## 1 Introduction

The offset printing is currently the most widely used and leads printing method in the printing field. In the global printing market, the offset printing method occupies 65–70% of market share [1]. Figure 1 shows a schematic diagram of the offset printing press. In offset printing, the graphic-text part and the blank part on the plate are almost on the same plane. Offset printing plate utilizes the principle of “oil-water mutual exclusion” to form the layout. The image area is oily and hydrophobic, and the blank area is hydrophilic and lip phobic. The thin plate is wrapped and installed on the plate cylinder, and the blanket cylinder is covered with a printed rubber blanket. In printing, the dampening unit transfers the fountain solution to the printing plate first, makes the blank region form ink repellent film. Then the inking unit passes the ink to the plate, and the region of graphic and text captures the ink, thus forming the printing sheet plate. The plate cylinder passes the ink to the blanket cylinder through the cylinder contact. When the paper passes between the blanket cylinder and the impression cylinder, the ink is transferred to the surface of the paper from the blanket cylinder under the contact pressure between the two cylinders [2].

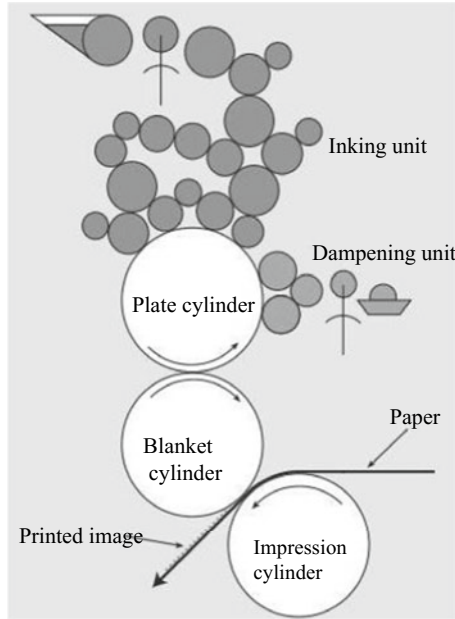


**Fig. 1.** Schematic diagram of offset press

Although the offset press is considered as highly automated device, it must be operated by an experienced operator. When the equipment is printing, the operator needs to constantly extract the printed products, observe the printing quality and adjust the ink supply. In particular, when the printing speed is changed, the offset press cannot change the amount of ink automatically. It is necessary to observe and adjust the input of the ink constantly by the operator until a relatively stable state is reached. Such operation mode not only produces a lot of waste products, increases cost, but also affects printing efficiency. Although several leading printing equipment manufacturers have made some progress in the “speed tracking curve”, they used the experimental fitting method to obtain the relationship of the ink amount and the equipment speed in a type of the offset press [3]. This method is indeed a similar approach because of not involving accurate model. As far as “speed tracking curve”, there are still some severe drawbacks, such as poor precision and still need manual intervention.

At present, there are two kinds of research methods for the mechanism of roll printing: one is facing to ink system. They use graph theory to simulate the ink flow distribution, ink transfer, ink route optimization and other problems. However, the exact theoretical contact model is not involved [4]. Another method is to study the dry contact problem of two rollers. The contact mechanics model does not involve fluid ink. For example, Wang and Knothe used a numerical algorithm to analyze the stress distribution of two viscoelastic roller contacts [5]. Elsharkawy proposed a numerical algorithm for dry contact of two viscoelastic rollers [6]. Some scholars have also studied the roll contact problem of roller with viscoelastic surface cladding. Brant and Kalker demonstrated the use of theoretical calculation and experimental analysis to

study the dry contact problem of two rollers [7]. Goryacheva and Sadeghi have studied the problem of rolling contact and sliding contact between an elastic roller and an elastic plane bonded with viscoelastic rubber [8].

The first method does not incorporate the precise theoretical contact model, so it cannot consider the key factors such as contact pressure, material properties, material deformation, and ink flow splitting position. The second method does not get the mechanical behavior of ink because of no ink considered in the contact model. Therefore, the ink transfer mechanism of offset press is still in the stage of qualitative description at present, and the precise model of roller rolling contact is not established, and the accurate prediction of the amount of ink on the printed material cannot be made.

The thickness of the printing ink layer is one of the core objectives for the printing machine control. There are many factors affecting the thickness of the printing ink layer such as printing load (printing pressure), printing speed, ink property, and ambient temperature. However, the ink property can be determined by choice of specific ink, and the stable environmental temperature can also be achieved by a workshop with central air conditioning. From the view of the equipment, the printing load and printing speed are more important factors for they are routine control action of operators. The change law of ink thickness under the common influence of the printing load and the printing speed has been a puzzle to machine study and machine operation.

Based on the elasto-hydrodynamic lubrication theory (EHL), the rolling contact model of offset press is set up in this paper. The operating characteristics of offset press are studied by numerical calculation, and the changed law of ink thickness under the common influence of printing load and printing speed is obtained.

## 2 Theoretical Analysis

Elasto-hydrodynamic lubrication theory is an important field of tribology research. The object of EHL is classified into two types: line contact and point contact. Most of the research objects of EHL are heavy load lubrication such as the tooth surface of the gear, the rolling body of the rolling bearing, and the high strength contact of the cam. With the development of this theory, low load lubrication between high elastic contacts is studied, which is called soft elasto-hydrodynamic lubrication (SEHL).

The contact form of offset printing ink transfer belongs to linear contact in rolling form. The rotation of cylinders in the offset press is driven by gears. But the rotary movement of ink rollers is transmitted by friction. As the adhesion of the ink is high, it can be considered as a rolling form on the whole. As an example of the offset press for sheet size  $570 \times 840$  mm, the length of the ink rollers and cylinders of the offset press is about 1000 mm, and the contact width is usually 2–5 mm, so the contact length is 2–3 orders of magnitude higher than the contact width, which is a typical line contact. In the printing ink transfer process of offset press, the ink is attached to the ink roller, the ink is passed through the rolling contact area between the two ink rollers, the ink roller and the plate cylinder, the plate cylinder and the blanket cylinder or the blanket cylinder and impression cylinder, and the two contact surfaces are separated from the ink, so it belongs to the EHL research category.

The solution result of EHL theory is the lubrication film thickness and pressure distribution in the lubrication contact area. The solution means of EHL is to equip the contact object as an equivalent elastic cylinder and an equivalent rigid plane.

On the basis of hypothesis conditions, Reynolds equation, deformation equation, load equation, film thickness equations and so on are established. Then the intensity of pressure is calculated according to the assumed deformation function. And the deformation is calculated after the intensity of pressure is obtained. Then the intensity of pressure is calculated according to the modified deformation function. So the thickness distribution of the film is obtained until the satisfactory precision is obtained.

There are many researches on EHL, which are of some reference value to the ink transfer mechanism of the offset press. Ge Peiqi gave the line contact Reynolds equation under the four parameter non Newtonian rheological model, and used the multi-grid method to get the complete numerical solution on the isotherm contact of EHL [9]. Mongkol studied the transient contact analysis of non-Newtonian lubricants in parallel rolling of two rollers [10]. Stakenborg and others analyzed the contact pressure of the radial lip seal and the lubricating oil, the deformation of the radial lip seal and the thickness of the oil film when the radial lip seal is in contact with the shaft [11, 12].

### 3 Theoretical Modeling

On the basis of elasto-hydrodynamic lubrication theory, the roller contact model of ink transfer is established based on the roller contact between the blanket cylinder and the impression cylinder. The necessary idealization assumption is made assuming that the ink is Newton fluid, only making laminar movement and no turbulent flow; in an isothermal condition (ink's temperature is working environment temperature). The Reynolds equation of the contact model is established as follows

$$\frac{d}{dx} \left( \frac{\rho h^3}{\eta} \cdot \frac{dp}{dx} \right) = 12U \frac{d(\rho h)}{dx}, \quad (1)$$

where  $p$  represents ink film pressure,  $h$  represents ink film thickness,  $x$  is the coordinate of contact area,  $\eta$  represents fluid viscosity,  $\rho$  represents fluid density,  $U$  is constant [13].

The load balance equation of the contact model is established as follows

$$w = \int_{x_{in}}^{x_{out}} p dx, \quad (2)$$

where  $x_{in}$  and  $x_{out}$  are the horizontal ordinate of the inlet and outlet position of the ink flow in the rolling contact area respectively.

The ink film thickness equation is set up as follows

$$h = h_0 + \frac{x^2}{2R} - \frac{2}{\pi E'} \int_{-\infty}^{x_{out}} p(x) \ln(x - s)^2 ds, \tag{3}$$

where  $h_0$  is the initial clearance of the two cylinders,  $R$  is the equivalent radius of the cylinder, and the  $E'$  is the equivalent elastic modulus of the cylinder [14].

Under the condition of isothermal condition, the ink density equation is as follows

$$\frac{\rho}{\rho_0} = 1 + \frac{Ap}{1 + Bp}, \tag{4}$$

where  $\rho_0$  is the environment density,  $A$  and  $B$  both are constants.

The ink viscosity equation was established as follows

$$\eta = \eta_0 \exp\left\{(\ln \eta_0 + 9.67) \left[ (1 + 5.1 \times 10^{-9} p)^z - 1 \right]\right\} \tag{5}$$

where  $\eta_0$  is environmental viscosity, and  $z$  is pressure-viscosity coefficient [15].

### 4 Numerical Calculations and Analysis

The offset press for sheet size  $570 \times 840$  mm is selected as example to demonstrate. The viscosity value of offset ink at room temperature is taken as the calculation parameter, which is 35 Pa s [16], and the change of printing speed is set in the range of (0–6) m/s, and the change of printing unit length load is set in the range of  $(0-6) \times 10^4$  N/m. All the relevant calculation parameters are shown in Table 1.

**Table 1.** Calculation parameters

Parameter name	Value
Radius of blanket cylinder	$R_1 = 0.15$ m
Radius of impression cylinder	$R_2 = 0.15$ m
Elastic modulus/Poisson’s ratio of rubber blanket	$E_1 = 1.8 \times 10^6$ Pa/ $\mu_1 = 0.47$
Elastic modulus/Poisson’s ratio of impression cylinder	$E_2 = 7.5 \times 10^{10}$ Pa/ $\mu_2 = 0.3$
Temperature	$T = 293.15$ K (20 °C)
Ink viscosity at room temperature	$\eta_0 = 35$ Pa s
Pressure-viscosity coefficient	$\alpha = 2.2 \times 10^{-8}$ m <sup>2</sup> /N
Unit length load	$w = (0-6) \times 10^4$ N/m
Printing speed (roller rotation speed)	$v = (0-6)$ m/s

In the process of solving the equations, the equations are written into dimensionless form, and then the multi-grid method is used to discretize the models and solve them numerically. The 3D view of outlet ink thickness of the offset press is shown in Fig. 2,

that is, the curved surface of ink thickness under the common influence of printing load and printing speed.

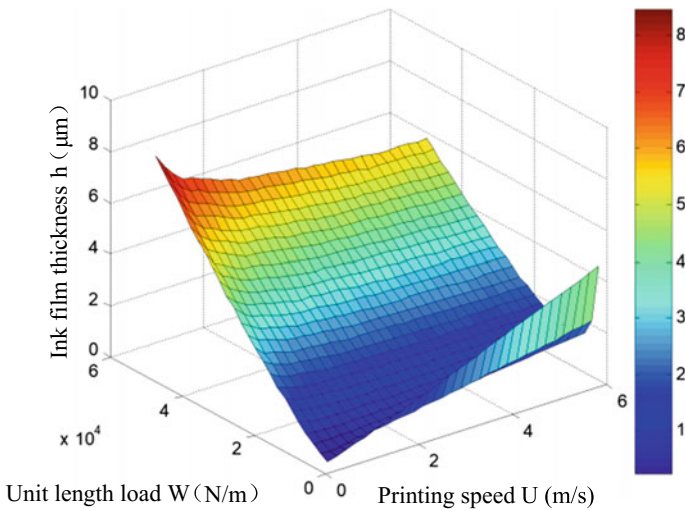


**Fig. 2.** 3D view of outlet ink thickness under the printing load and printing speed

In order to facilitate to analyze the problem, we get the universal characteristic curve of the offset press by changing the exhibition form of the data. The contour map of ink film thickness at the outlet of contact region is shown in Fig. 3: the printing speed is used as the horizontal coordinate; the printing unit length load is used as the ordinate.

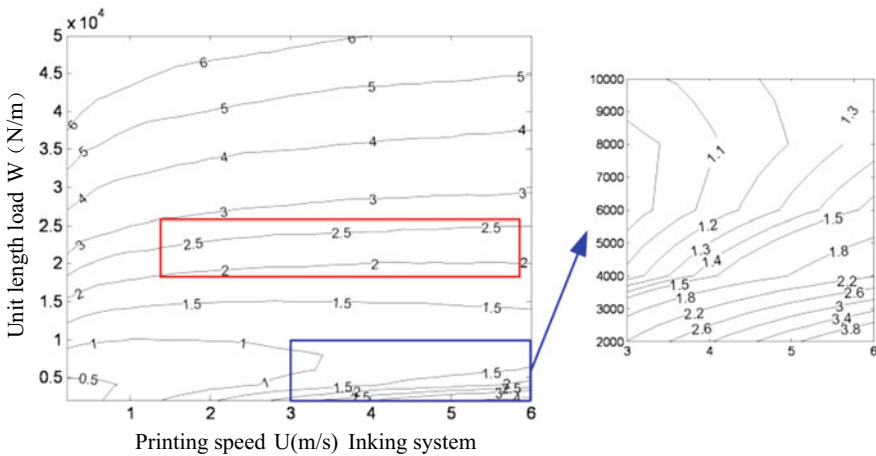


**Fig. 3.** Contour map of ink film thickness at the outlet of contact region

Figure 3 shows that the thickness of the outlet ink under the combined action of load and speed is a series of turning arcs. It is self-evident that the ideal offset printing ink thickness curve is a straight line with a smaller slope or a slowly changing curve. In order to control the ink layer thickness of the offset press effectively, the printing load must be limited to a certain range (the ideal load range), such as the area in the rectangle frame marked in red color in Fig. 3. If the printing pressure is in the ideal load range, the thickness variation of ink layer is relatively small when the printing speed changes. If the printing pressure is out of the ideal load range, the thickness variation of ink layer will be severer and less controlled when the printing speed is changed. Under the same working conditions, the influence of the lower load on the ink layer thickness is more intense than that of the higher load, and the manipulation is poor. This is the inspiration from the universal characteristic curve of offset presses.

## 5 Conclusions

Based on the elasto-hydrodynamic lubrication theory, the ink transfer rolling model of the offset press is established. The changed law of the thickness of the ink layer under the common influence of load and speed is studied by numerical calculation. Moreover the universal characteristic curve of the offset press is obtained, and the offset press puzzle that have been solved theoretically.

The results show that the thickness of the outlet ink under the common influence of printing load and printing speed is a series of arc lines. For the specific kind offset press, as long as the ideal load range is determined, the thickness of the printing ink layer is less sensitive to the change of printing speed, so the difficulty of equipment operation will become easier. The manipulation effectiveness of offset press can also be greatly improved.

**Acknowledgements.** The authors acknowledge the financial support from the Natural Science Basic Research Program of Shaanxi (Grant No. 2018JM5014) and the Scientific Research Program of Education Department of Shaanxi province (Grant No. 14JK1528).

## References

1. Heidelberger Druckmaschinen AG. (2013). *100 years of offset printing: Innovations, markets, technology*. <http://www.docstoc.com/docs/159679082/Years-of-Offset-Printing-Heidelberg>. Cited 5 July 2013.
2. Kipphan, H. (2006). *Handbook of print media: Technologies and production methods*. New York: Springer.
3. Caifeng, L. (2008). Research on printing speed and printing quantity. *Packaging Engineering.*, 29(5), 193–194.
4. Ying, X. I., Congjun, C. A. O., & Weimin, X. I. A. (2013). Simulation of ink spreading process of offset printing by Fluent. *Journal of Xi'an University of Technology.*, 29(3), 343–346.
5. Wang, G., & Knothe, K. (1993). Stress analysis for roiling contact between two viscoelastic cylinders. *Transactions of ASME Journal of Applied Mechanics*, 60(1993), 310–317.



6. Elsherknwy, A. A. (1995). A numerical solution for dry contact between two viscoelastic rollers. In *1995 STLE/ASME Tribology Conference*.
7. Braat, G. F. M., & Kalker, J. (1993). Theoretical and experimental analysis of the rolling contact between two cylinders coated with multilayered viscoelastic rubber. *Contact Mechanics*, 1993, 119–126.
8. Goryacheva, I., & Sadeghi, F. (1995). Contact characteristics of a roiling/sliding cylinder and a viscoelastic layer bonded to an elastic substrate. *Wear*, 184, 125–132.
9. Ge, P. (2000). Numerical analysis of rheological elastohydrodynamic lubrication based on four parameter model. *Transactions of the Chinese Society for Agricultural Machinery*, 31 (6), 91–94.
10. Mongkolwongrojn, M., Wongseedakaew, K., & Kennedy, F. E. (2008). Elastohydrodynamic lubrication of rough surfaces under oscillatory line contact with non-newtonian lubricant. *Tribology Transactions*, 51(2008), 552–561.
11. Slakenborg, M. J. L., van Leeuwen, H. J., & ten Hagen, E. A. M. (1990). Visco-elastohydrodynamic (VEHD) lubrication in radial lip seals: Part 1—Steady-state dynamic viscoelastic seal behavior. *ASME Tribology*, 112, 578–583.
12. van Leeuwen, H. J., & Slakenborg, M. J. L. (1990). Visco-elastohydrodynamic (VEHD) lubrication in radial lip seals: Part 2—Fluid film formation. *ASME Tribology*, 112, 584–592.
13. Wen, S., & Huang, P. (2002). *The principle of tribology*. Beijing: Tsinghua University Press.
14. Peiran, Yang. (1998). *Numerical analysis of fluid lubrication*. Beijing: National Defence Industry Press.
15. Wen, S., & Yang, P. (1992). *Elastic hydrodynamic lubrication*. Beijing: Tsinghua University Press.
16. Yuan, Y., Ding, F., & Fan, Y. R. (2008). Theoretical analysis and measurement of printing ink viscosity. *Chinese Journal of Sensors and Actuators*, 21(10), 1812–1816.

**Part V**  
**Packaging Engineering Technology**



# Development and Application Prospect of Functional Packaging Materials

Hui Liu<sup>1,2</sup>, Dongli Li<sup>2</sup>(✉), Wencai Xu<sup>2</sup>, and Yunzhi Chen<sup>1</sup>

<sup>1</sup> Institute of Packaging and Printing Engineering, Tianjin University of Science and Technology, Tianjin, China

<sup>2</sup> Beijing Key Laboratory of Printing & Packaging Materials and Technology, Beijing Institute of Graphic Communication, Beijing, China  
lidongli6666@126.com

**Abstract.** In order to better understand the development and application of functional packaging materials, four types of functional packaging materials (high barrier packaging materials, anti-static packaging materials, antimicrobial packaging materials, nano packaging materials) were selected for the study. The results showed that the research and development of functional packaging materials had been relatively mature, and some excellent materials had been put into use, but there were still some problems to be solved, such as safety problems, environmental problems, industrial production, etc.

**Keywords:** Functional packaging material · Summarize

## 1 Introduction

Functional packaging materials refer to materials that can meet certain functions of the packaged items. For example, packaging materials with high barrier properties can effectively separate the gas exchange between the packaged goods and the environment so as to achieve the function of protecting products. Antistatic packaging can protect electronic products from static damage. Antimicrobial packaging can inhibit the growth of bacteria and fungi inside the packaging, thus ensuring the quality of products. Nano packaging material is new technology that combines nanotechnology with packaging materials, especially in fruits and vegetables preservation. In this paper, the research status of the above functional packaging materials is reviewed, and the latest research and application progress at home and abroad in this field are introduced, and the development trend of functional packaging materials is prospected.

## 2 Development and Application of Functional Packaging Materials and Technology

### 2.1 High Barrier Packing Materials

Barrier properties are important properties of packaging materials. The stability of the packaging environment can be maintained by the barrier property of the material, so

that the shelf-life of the product can be extended. In particular, food and medicine have higher requirements on barrier properties of packaging materials [1, 2]. At present, the polymer materials with better barrier properties are polyvinylidene chloride, ethylene vinyl alcohol copolymer, polyamide and polyester. Such materials are simple in preparation process and low in economic costs, but polymers are difficult to degrade and cause some environmental pollution [3, 4]. With the continuous development of barrier packaging materials, new technologies and materials with better properties are emerging. It includes composite material, inorganic material filling and blends, MFC composites and steamed materials.

Yang and others prepared the ethylene/vinyl alcohol copolymer/graphene composite by solution blending. The oxygen permeability of the material was 0.5% of the single EVOH film [5]. Liu Xiwei used the solution polymerization method to prepare the vinylidene chloride-methyl acrylate copolymer. The vapor permeation rate of the film was  $5.42 \text{ g}/(\text{m}^2 \cdot 24 \text{ h})$  [6]. Cabedo L. prepared EVOH-kaolin nanocomposites by melting blend method. The results showed that when the clay content was less than 8 wt%, the heat insulation and oxygen resistance properties are improved [7]. The cellulose/BN nanocomposite films has certain barrier properties to the acid and alkali substances such as dilute hydrochloric acid and sodium hydroxide. With the increase of BN nano filler, its barrier ability to acid and alkali is enhanced, its minimum oxygen permeability is  $0.5 \text{ Lit}/\text{cm}^2/\text{min}$ , and has a good barrier property to oxygen [8]. 20–50 nm thick alumina or silicon oxide film was prepared by plasma assisted atomic layer deposition as a barrier layer. The vapor permeability of the material can reach 10 to  $5 \text{ g}/(\text{m}^2 \text{ D})$ , but the deposition rate of the high barrier film by ALD was slow and the cost is high [9].

## 2.2 Anti-static Packaging Materials

The electrostatic protection packaging has the functions of low electrification rate, electrostatic shielding, proper resistivity and charge decay besides the general packaging function. It is possible to avoid the electrostatic discharge of the electrified object or the human body causing the product to damage [10]. Antistatic packaging is mainly used in the packaging of electrostatic sensitive products, such as electrical products, photoelectric products, optical and electronic integration products, missiles, ammunition, explosive and so on [11]. Antistatic packaging materials can be divided into antistatic agent treatment type, surface modified antistatic packaging material, conductive material filling type, structure conductive polymer and nano antistatic packaging material [12]. Antistatic agent treatment is the most commonly used method to improve the antistatic properties of polymer materials [13]. At present, many domestic scientific research institutions have made significant progress in developing polymer permanent antistatic agents by using polymer alloying technology [14].

Jiang Shangjie found that all the strength properties of the coated antistatic corrugated board are better than the printed corrugated board [15]. Radiation is used to irradiate methacrylic acid or acrylic acid and then grafted onto polypropylene or polyethylene can significantly improve the antistatic properties of these materials [12]. The nano  $\text{Fe}_3\text{O}_4$ /cellulose composite packaging film was prepared by situ co precipitation method. The film has good antistatic properties, and its antistatic performance is

more stable in low humidity environment [16]. Carbon black and polyethylene resin are mixed to make high surface antistatic polyethylene film by three layers coextrusion blowing process and corona treatment. It can be applied to the packaging of electronic, chemical and military products sensitive to electrostatic and electromagnetic radiation [17, 18]. Graphene based composite prepared by Wang Zhenting can meet the requirements of antistatic electricity and improve the tensile strength of matrix material [19]. Dong Qingfeng gets PLA/PBAT/CNTs-COOH composites by melting blend, which can effectively lift the impact strength and reduce the surface resistivity, and can be used for antistatic packaging for electrostatic sensitive products [20].

### 2.3 Antimicrobial Packaging Materials

Antimicrobial packaging is a packaging technology that can preserve commodity for a long time by adding antibacterial agents to the internal or surface of the packaging material or using antibacterial polymer materials to kill or inhibit the bacteria and pathogenic bacteria in packaging [21]. The use of antibacterial agents is the key material for antimicrobial packaging. Its main types include inorganic antibacterial agents, organic antibacterial agents, and natural antimicrobial agents [22]. The ways to realize the food antimicrobial packaging can be divided into 5 types: the volatile antibacterial package, the packing material directly adding the antibacterial agent, the coated or adsorbed antibacterial package, the chemical bond type antibacterial package, and the packaging material with antibacterial effects.

Ethanol gas generator is a very mature antibacterial materia, it can inhibit the growth of microorganisms such as mould and prevent the food hardening by inhibiting the evaporation of water and aging of starch [23]. The antimicrobial packaging film of thymus oil can inhibit the respiration, microbial growth and polyphenol oxidase activity of fresh cut lettuce [24]. The antibacterial membrane of thymol/polylactic acid was prepared by the solution blending method. It was found that the bacteriostat with a mass fraction of 7% had a good inhibitory effect on *Staphylococcus aureus*, *Escherichia coli* and *Candida albicans* [25]. Chemical modification of sodium alginate could increase the entrapment rate of active substances to a certain extent, and increase the stability time of bacteriostasis [26]. Kuang Hengfeng and others have found that the particle size, morphology, dispersion, activation and addition of nano ZnO have a great influence on the antibacterial effect in different packaging substrate systems [27]. UZ. M. and others prepared single and three layers of cellulose acetate antibacterial film containing potassium sorbate by dry phase inversion technique [28].

### 2.4 Nano Packaging Materials

Nano packaging material is a new material that improves the performance of packaging materials through nanotechnology, and makes it a new material with nanostructures, nanoscale and special functions (antibacterial, low oxygen permeability, low moisture permeability and carbon dioxide barrier). It has broad application prospects in food industry, especially for fruits and vegetables. According to the packaging requirements of different foods, there are a variety of nanomaterials used for food packaging, such as nano Ag/PE, nano TiO<sub>2</sub>/PP, nanomontmorillonite powder/PA and so on. Their

physical, chemical and biological properties have been greatly improved [29]. These excellent properties of nanoscale packaging materials make new materials, such as nanoscale antibacterial materials, fresh-keeping materials and barrier materials, have been greatly developed in the field of food packaging [30].

By studying the film with nano  $\text{TiO}_2$ , it found that the film can effectively inhibit the growth of *Escherichia coli* and *Staphylococcus aureus* [31, 32]. Yao Yaming used 1-MCP treatment combined with nanoscale packaging to keep fresh and storage of *flammulina velutipes*. The results showed that the fresh-keeping effect of 1-MCP treatment combined with nanoscale packaging was the best [33]. A polythene packaging film containing nano Ag, nano  $\text{TiO}_2$  and attapulgite was prepared by Yang Wenjian. The results showed that the nano packaging materials could effectively improve the storage quality of *Agaricusbisporus* [34]. Yin Xiaoting used ultrasonic cleaning and nano packaging technology to preserve fresh cut lettuce. The results showed that ultrasonic treatment combined with nano packaging had the best effect on the fresh-keeping of lettuce [35]. Qie Bingyu found that nanoscale cellulose as an enhanced component of degradable packaging materials can improve the mechanical properties and barrier properties of the composites and give special functions to the materials [36].

### 3 Prospect of Functional Packaging Materials

In recent years, people pay more attention to the safety performance of packaging. How to ensure the safety performance of product packaging has become a hot spot of research. It can not only guarantee the good performance of packaging materials, but also ensure the safety performance of materials. Secondly, the environmental performance of functional packaging materials is another research hotspot. For example, some technologies are used to solve the problem of material degradation, recycling and reuse. Thirdly, the development and production of new functional packaging materials lack the corresponding national standards or industry standards, so the performance of materials cannot be a unified measurement rule, which is also a problem to be solved in the future.

**Acknowledgements.** This work was supported by the National Natural Science Foundation of China (31471653); the Natural Science Foundation of Beijing, China (2182018); the Coordinative Innovation Project of Beijing Municipal Education Commission (PXM2017\_014223\_000034); the Science & Technology Project of Beijing Municipal Education Commission (KM20161005004, KM201710015011); the Science and Technology Foundation of Beijing Daxing District (KT201806095); and the Science & Technology Project of Beijing Institute of Graphic Communication.

## References

1. Yue, Q. (2011). Application status and development trend of barrier packaging materials. *Plastic Packaging*, 21(3), 19–21.
2. Liu, D. (2014). Research progress of high barrier packaging materials. *Journal of Packaging*, 4(6), 24–30.
3. Chen, X., Zhao, J., Yuan, Y., et al. (2013). Synthesis, properties and application of sulfonyl polymer special engineering plastics. *Guangdong Chemical Industry*, 40(18), 66–67.
4. Hu, M., Xiang, X., Tan, J., & Liu, Y. (2015). The development status of high barrier polymer packaging materials. *Guangzhou Chemical Industry*, 43(9), 10–12.
5. Yang, J., Bai, L., Feng, G., et al. (2013). Thermal reduced graphene based poly(ethylene vinyl alcohol) nanocomposites: Enhanced mechanical properties, gas barrier, water resistance, and thermal stability. *Industrial & Engineering Chemistry Research*, 52(47), 16745–16754.
6. Liu, X., Zhou, Y., Wang, S., et al. (2013). Preparation and properties of PVDC-MA water vapor barrier coatings. *Journal of Wuhan University of Technology*, 35(1), 22–26.
7. Cabedo, L., Giménez, E., Lagaron, J. M., et al. (2004). Development of Evoh-kaolinite nanocomposites. *Polymer*, 45(15), 5233–5238.
8. Swain, S. K., Dash, S., Behera, C., et al. (2013). Cellulose nanobiocomposites with reinforcement of boron nitride: Study of thermal, oxygen barrier and chemical resistant properties. *Carbohydrate Polymers*, 95(2), 728–732.
9. Xu, F., Zhou, M., & Chen, Q. (2017). Research status of flexible high barrier films. *Packaging Engineering*, 38(17), 70–77.
10. Li, Y., & Sun, Y. (2011). Antistatic design of packaging materials. *Packaging Engineering*, 32(19), 73–76.
11. Zhang, S., Li, Z., Liu, X., et al. (2014). Progress in antistatic research of explosive packaging process. *Packaging Engineering*, 35(13), 155–161.
12. Ma, Y. (2014). Classification and development of antistatic packaging materials. *Printing Quality and Standardization*, 11, 23–26.
13. Yong, G., & Zhang, Z. (2012). On the antistatic technology of polymer materials. *China Chemical Trade*, (4), 83.
14. Zheng, A., et al. (2012). Antistatic modification of polypropylene by incorporating Tween/modified Tween. *Applied Surface Science*, 258(22), 8861–8866.
15. Jiang, S. (2016). *Antistatic corrugated board coating process and properties of coated paperboard*. Dalian: Dalian Polytechnic University.
16. Zhang, X., Li, J., & Ma, X. (2016). Study on nano Fe<sub>3</sub>O<sub>4</sub>/cellulose antistatic composite packaging film. *Packaging Engineering*, 37(7), 23–29.
17. Li, J., Li, M., Da, H., et al. (2012). Preparation of Nylon-6/flake graphite derivatives composites with antistatic property and thermal stability. *Composites*, 43(7), 1038–1043.
18. Ji, Z., Sun, H., & Shi, J. (2011). Research on antistatic composite technology of new soft plastic material. *Plastic Industry*, 39(1), 120–124.
19. Wang, Z., Yin, J. Y., Li, Y., & Dai, D. Y. (2017). Preparation and properties of graphene based antistatic materials. *Journal of Heilongjiang University of Science and Technology*, 27(4), 429–432.
20. Dong, Q., Li, H., Zhang, L., & Wang, Y. (2014). PLA/PBAT/CNTs-COOH antistatic packaging material preparation and performance research. *China Printing and Packaging Research*, 6(2), 54–60.
21. Zhao, J., Luo, S., & Xu, W. (2012). Research progress in antimicrobial packaging. *Packaging Engineering*, 33(5), 132–138.

22. Shu, H., Pan, L., Tu, K., et al. (2015). Research progress of antibacterial materials in food packaging. *Food Science*, 36(5), 260–266.
23. Ma, X., Wang, L., Liu, J., et al. (2012). Research progress of ethanol gas generating agent in antimicrobial packaging. *Packaging Engineering*, 33(23), 144–150.
24. Deng, W., Jiang, W., Chen, A., et al. (2016). Effects of packaging of thyme essential oil antimicrobial coating on physical and chemical properties and microorganisms of fresh cut lettuce during shelf life. *Storage, Transportation and Preservation*, 42(7), 247–254.
25. Qian, H., Mu, H., Gao, H., et al. (2017). Study on migration of thymol in food simulants in antimicrobial packaging of polylactic acid. *Food Science*, 6, 1–12.
26. You, L., Wang, L., Fan, S., et al. (2015). Research progress of sodium alginate based antimicrobial packaging materials. *Packaging Engineering*, 36(21), 11–17.
27. Kuang, H., Hu, C., Liu, F., et al. (2015). Research progress of nanoZnO composite food antimicrobial packaging film. *Packaging Engineering*, 36(11), 16–25.
28. Uz, M., & Altinkaya, S. A. (2011). Development of mono and multilayer antimicrobial food packaging materials for controlled release of potassium sorbate. *LWT-Food Science and Technology*, 44(10), 2302–2309.
29. Huang, Y., Wang, L., & Hu, Q. (2005). Application of nano packaging in food preservation and its safety evaluation. *Food Science*, 26(8), 442–446.
30. Guo, X., Ding, L., Li, J., et al. (2013). Research progress of nano packaging materials and their safety evaluation. *Food and Machinery*, 29(5), 249–252.
31. Xing, Y., Li, X., Zhang, L., et al. (2012). Effect of TiO<sub>2</sub> nanoparticles on the antibacterial and physical properties of polyethylene-based film. *Progress in Organic Coatings*, 73(2–3), 219–224.
32. Qing, T., Su, H., & Tan, T. (2011). The bactericidal and mildew-proof activity of a TiO<sub>2</sub>-chitosan composite. *Journal of Photochemistry and Photobiology A: Chemistry*, 218(1), 130–136.
33. Yao, Y., Ren, Y., Liu, R., et al. (2016). 1-MCP combined with nano packaging on the storage quality of *Flammulina velutipes*. *Food Science*, 37(22), 295–301.
34. Yang, W., Shan, N., Yang, Q., et al. (2012). Nanomaterials prolong the storage quality of *agaricusbisporus*. *Agricultural Science in China*, 45(24), 5065–5072.
35. Yin, X., Zhao, K., Jiang, X., et al. (2015). Effects of ultrasonic treatment combined with nano packaging on the quality of fresh cut lettuce. *Food Science*, 36(2), 250–255.
36. Qie, B., Tang, Y., Lu, L., et al. (2017). Application of nanoscale cellulose in degradable packaging materials. *Packaging Engineering*, 38(1), 19–26.





# Application of Functionally Integrated Modified Atmosphere Packaging Design in Preservation of Nanguo Pears at Room Temperature

Jiachun Ma, Da Yang, Min Zhang, Dongli Li<sup>(✉)</sup>, and Wencai Xu

Beijing Institute of Graphic Communication, Beijing, China  
lidongli@bigc.edu.cn

**Abstract.** In order to prolong the shelf life of Nanguo pears at room temperature (25 °C), we made two types of functionally integrated modified atmosphere packaging (MAP), OA and OB. OA integrated self-made high oxygen permeable film (film O) and high moisture permeable film (film A). OB integrated film O and another type of high moisture permeable film (film B). The headspace components in the packaging, and vitamin C (VC) contents, titratable acid (TA) contents and market value of Nanguo pears were monitored during the storage to evaluate the two types of MAP. Results show that OA and OB can effectively reduce the nutrient loss of Nanguo pears during storage, thus maintaining their good commercial value. OA and OB respectively extended the shelf life of Nanguo pears at room temperature from less than 8 days to less than 12 days and more than 14 days.

**Keywords:** Nanguo pears · Headspace · Titratable acid · Vitamin C · Commercial value

## 1 Introduction

Nanguo pears are specialty of Liaonan. They are known as the king of pears and rich in a variety of amino acids necessary for the human body and have a high nutritional value. Nanguo pears are perishable after ripening, and their shelf life are only 2–3 days at room temperature [1]. Therefore, Nanguo pears are generally picked during the stage of green mature to extend their shelf life. The effect of low temperature storage is good, but the cost is high, and it may cause cold damage to Nanguo pears and reduce their market value. Although 1-methylcyclopropene (1-MCP) can delay the ripening of Nanguo pears, the treatment will reduce the aroma of Nanguo pears [2]. Atmosphere storage is an economical and effective preservation method. It can reduce the activity of catalase and polyphenol oxidase in Nanguo pears and the browning index of the fruit [3]. So it has been widely used in the preservation of Nanguo pears.

The functions of film used in conventional MAP are relatively simple, and it is technically difficult to simultaneously achieve high oxygen permeability and high moisture permeability on a kind of film. In order to solve this problem, two types of MAP integrating high-oxygen permeability and high-moisture permeability functions

were made. Our work is purpose to provide new ideas and technical references for the preservation of Nanguo pears and other fruits at room temperature.

## 2 Materials and Methods

### 2.1 Preparation of Modified Atmosphere Packaging and Nanguo Pears

We used a kind of high oxygen permeability film (film O) and two kinds of high moisture permeability film (film A and film B). O film is a kind of polyethylene modified film, its manufacturing process is referred to the patent of CN102863685A [4]. A film and B film are polypropylene modified film, and their manufacturing process is referred to the patent of CN104017243A [5]. The choice of film material and the determination of its dimensions were based on our previous research [6]. Three sides of the two pieces of the film (O and A, O and B) were bonded by hot melt adhesive to make bags (mark as OA, OB). The film parameters are shown in Table 1.

**Table 1.** Film parameters of OA and OB

Packaging	Film material	OTR [mL/(m <sup>2</sup> day atm)]	WVTR [g/(m <sup>2</sup> day)]	Size (m)	Area (m <sup>2</sup> )
OA	O	$1.2 \times 10^5$	<5	$0.30 \times 0.20$	0.06
	A	<5	60	$0.30 \times 0.20$	0.06
OB	O	$1.2 \times 10^5$	<5	$0.30 \times 0.20$	0.06
	B	1000	100	$0.30 \times 0.20$	0.06

Nanguo pears of a mature degree of 70–80% were purchased from the Xinfadi fruit market in Beijing, without any chemical treatment. Nanguo pears were selected according to the same weight and appearance criteria. These pears were divided into three groups, OA, OB and control group (unpacked). Each bag of the OA and OB group contains 6 Nanguo pears (0.5 kg) groups, and 6 Nanguo pears were randomly selected from the control group.

### 2.2 Measurement of the Headspace Component of the Packaging and Nutrient Analysis

CO<sub>2</sub> and O<sub>2</sub> concentrations in the headspace of each packaging were tested using an O<sub>2</sub>/CO<sub>2</sub> handheld gas analyzer (Check Point). The determination of TA content was based on the method of Sivakumar and Korsten [7]. The VC content of pears was determined according to the method given by Li et al. [8].

### 2.3 Commercial Value Evaluation and Data Processing and Analysis

The commercial value of Nanguo pears fruit was evaluated by examining its exterior and taste. This evaluation was conducted by 10 trained people, adopting a 10-point

evaluation method. The evaluation criteria are shown in Table 2. When the score is less than 5 points, it can be considered that the shelf life of Nanguo pears is reached.

**Table 2.** Commercial value evaluation standards of Nanguo pears

Score	Exterior quality	Taste
$8 < X \leq 10$	Peels don't shrink, the color is bright yellow	The flesh is delicate, sour and sweet, without softening
$6 < X \leq 8$	Peels don't shrink, the color of bright yellow fade	The flesh is delicate, sour and sweet, without softening
$5 < X \leq 6$	Peels shrink slightly, turn black	The flesh soften slightly and its sweetness is reduced
$X \leq 5$	Peels shrink obviously, individual rot	The flesh is obviously soft and its sweetness is very light

Using SPSS9.0 for experimental data analysis and drawing with Origin 8.5.

### 3 Results and Discussion

#### 3.1 Changes in Composition of the Headspace

Nanguo pears belong to climacteric fruit, their respiratory intensity will suddenly rise during the maturation process and then enter the aging stage. In order to meet the needs of Nanguo pear's breathing, we used a piece of high oxygen permeability film, film O, to provide sufficient oxygen in the packaging. It can be seen from Fig. 1a, the oxygen content in the packaging had been maintained at more than 20%, which avoided the anaerobic respiration of Nanguo pears and the production of any toxic effects. We used two kinds of high moisture permeable films, film A and B, to eliminate the water vapor produced by Nanguo pears in a timely manner. No water vapor condensation occurred in the packaging during the entire experiment, which verified the rationality of the packaging design. It can be seen from Fig. 1a that the OA group reached the peak of respiration on the 7th day, while the OB reached the peak of respiration on the 9th day. The result shows that the OB can delay the maturation of Nanguo pears. This is because the moisture permeability of the A film was lower than that of the B film, resulting in the excessive relative humidity in the OA. The position of the CO<sub>2</sub> concentration peak in Fig. 1b corresponds exactly to the position of the respiratory peak in Fig. 1a. Thus validating the previous inference.

#### 3.2 Loss of Nutrients

Titrateable acid is an important nutrient in Nanguo pears, and it is also an important factor affecting Nanguo pears's flavor. From Fig. 2a, it can be seen that the total acidity of the three groups of Nanguo pears showed a downward trend during the storage period. The total acid reduction in the OA and OB groups was significantly lower than in the control group. The TA content of the control group decreased to 0.284% on the

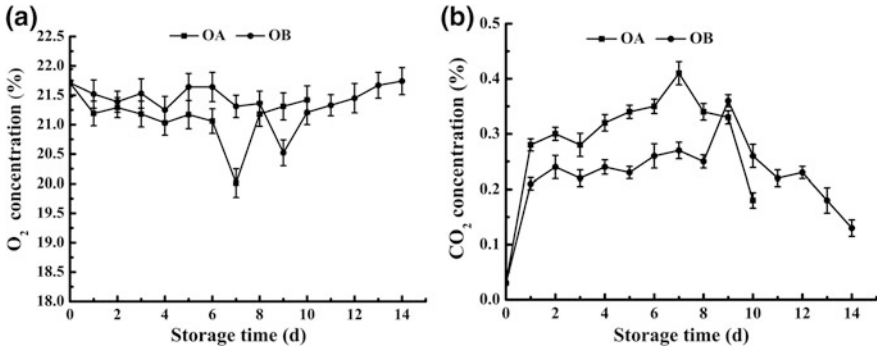


**Fig. 1.** **a** Changes of O<sub>2</sub> concentration in the headspace of packaging. **b** Changes of CO<sub>2</sub> concentration in the headspace of packaging

sixth day, which was only 51% of the initial value. However, the TA content of the OA and OB groups were always higher than this value throughout the storage period. This is because the higher relative humidity environment in the two sets of packaging, which weakened the transpiration of Nanguo pears. It reduced the metabolism of the acid substances.

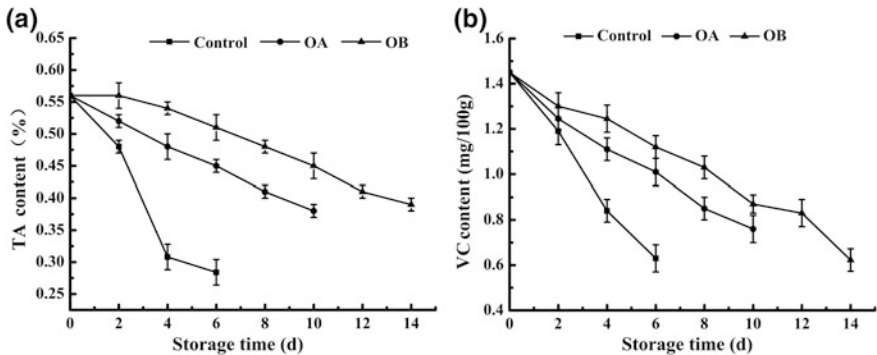


**Fig. 2.** **a** Changes of titratable acid content in Nanguo pears. **b** Changes of VC content in Nanguo pears

Vitamin C is the essential nutrient needed by the human body, and it protects cell tissue from damage and delays spoilage. Our test found that VC content in Nanguo pears was relatively small, and the initial test value was 1.45 mg/100 g. It can be seen from the Fig. 2b that the decrease in the content of the control group during storage was significantly higher than that of OA and OB. On the one hand, the oxygen concentration in the atmosphere of the control group was higher, their respiratory intensity was higher. On the other hand, Nanguo pears in the control group matured

faster than the OA and OB groups. These resulted in a higher oxidation rate of VC in the control group than in the OA and OB groups.

### 3.3 Commercial Value

From Fig. 3, it can be seen that the commercial score of the control group during the storage period was significantly lower than that of the OA and OB groups. Its commercial score was less than 5 on the 8th day, indicating that the shelf life was less than 8 days. The OA group had a commercial score of less than 5 on the 12th day, indicating that the shelf life of the OA group was less than 12 days. The overall score of the OB group on the 14th day was still higher than 5, indicating that its shelf life was more than 14 days. Compared with the control group, the Nanguo pears in the OA and OB groups showed less change in appearance and less nutrient loss, which resulted in a higher commercial value score.

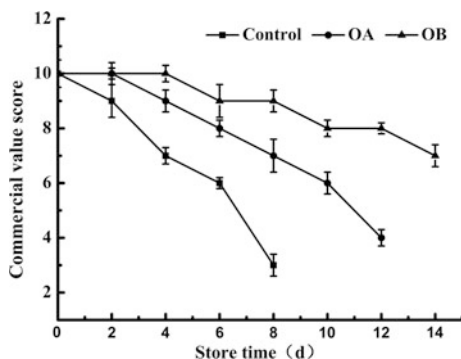


Fig. 3. Changes of commercial value score of Nanguo pears during storage

## 4 Conclusions

In order to adjust the oxygen and humidity inside the MAP at the same time, this experiment proposes two kinds of functional integrated MAP design. The high oxygen permeable film provides the packaging with sufficient oxygen. The high moisture permeable films, A and B, promptly eliminated the water vapor generated by Nanguo pear's respiration. Compared with the control group, both modified atmosphere packaging designs can significantly reduce the loss of VC contents, TA contents and commercial value of Nanguo pears during the storage period. OA and OB respectively extended the shelf life of Nanguo pears from less than 8 days to less than 12 days and more than 14 days at room temperature. This integrated modified atmosphere packaging can also be further expanded to add other functions. Compared with the traditional MAP using single film, it has more features and better flexibility.

**Acknowledgements.** This work was supported by National Natural Science Foundation of China (31471653); Natural Science Foundation of Beijing, China (2182018); Coordinative Innovation Project of Beijing Municipal Education Commission (PXM2017\_014223\_000034); Science & Technology Project of Beijing Municipal Education Commission (KM20161005004, KM201710015011); and Science & Technology Project of Beijing Institute of Graphic Communication.

## References

1. Hu, J. Y., Yang, F. F., Hou, X. F., You, J. Z., Gao, Y., Fang, Z. G., et al. (2014). Effects of storage temperature on the freshness retaining of fresh-cut ‘Nanguo’ pear. *Food Research & Development*, 35(2), 107–108.
2. Ji, S. J., Bu, Q. Z., Li, J. K., & Zhang, P. (2012). Effects of 1-MCP treatment on aroma components of “Nanguo” pear during shelf life after cold storage. *Journal of Fruit Science*, 2012(4), 656–660.
3. Guo, D., Hao, Y., & Han, Y. Q. (2015). Effects of plastic box modified atmosphere storage on physiology and quality of the ‘Nanguo’ pear. *Food Research & Development*, 2015(16), 148–151.
4. Xu, W.C., Li, D.L., Fu, Y. B., et al. (2013). A Kind of Tomato Preservation Packaging Material: China. CN102863685A.
5. Xu, W. C., Li, D. L., Fu, Y. B., et al. (2011). Polyolefin processing aid for food soft packaging, preparation method and use thereof, and polyolefin modified by using the processing aid: China. CN101724176A.
6. Yang, D., Li, D. L., Xu, W. C., Liao, R. J., Shi, J. Z., Fu, Y. B., et al. (2018). Design and application of a passive modified atmosphere packaging for maintaining the freshness of Chinese cabbage. *LTW-Food Science and Technology*, 94, 136–141.
7. Sivakumar, D., & Korsten, L. (2006). Influence of modified atmosphere packaging and postharvest treatments on quality retention of litchi cv. Mauritius. *Postharvest Biology & Technology*, 41(2), 135–142.
8. Li, J. P., Cao, Y., Li, D. L., et al. (2018). Application of design of function integrated fresh-keeping packaging in preservation of Chinese cabbage. *Packaging Engineering*, 3, 1–6.



# Effects of Edible Chitosan Coating on Postharvest Quality of Zigui Navel Orange

Jinli Li<sup>1</sup>, Yuye Zhong<sup>2</sup>, Shaoyun Huang<sup>1,2</sup>, Ting Guo<sup>1</sup>, Li Cheng<sup>1</sup>,  
and Houbin Li<sup>2</sup>✉

<sup>1</sup> Department of Printing Engineering, Jingchu University of Technology,  
Jingmen, China

<sup>2</sup> School of Printing and Packaging, Wuhan University, Wuhan, China  
lhb@whu.edu.cn

**Abstract.** In order to study the preservation effect of chitosan coating on Zigui navel orange at room temperature ( $20 \pm 5$  °C), the coating solution was prepared by using chitosan as film-forming agent and citric acid and glacial acetic acid as solvents. The existing wax coating solution was used as the control. The experimental navel oranges were coated on the surface by impregnation method and stored at room temperature ( $20 \pm 5$  °C) for 35 days. Changes of physical, chemical and sensory quality indexes were determined periodically during storage time. The results were compared and analyzed. The experimental results showed that the coating effect of citric acid as the solvent is better than that of glacial acetic acid and the control treatments. In addition, the quality of navel oranges in 1.5%w/v citric acid treatment was the best in the three different concentrations treatments. After 35 days, the decay rate, total soluble solid and vitamin C content were detected in this treatment. The results suggested that 1.5% w/v citric acid had better potential in prolonging the shelf-life of Zigui navel orange.

**Keywords:** Chitosan coating · Packaging navel orange · Postharvest quality

## 1 Introduction

Lane Late navel orange, which is a late maturing bud sport of Washington navel orange, was successfully bred in Australia in 1950, and was introduced into Zigui of China from New South Wales of Australia in 1990s. Zigui County, located in the Three Gorges valley area of the Yangtze River, warm and humid climate, plentiful rainfall and fertile soil, has made navel oranges grown in this area with special quality of succulent crisp, bright orange-red and rich flavor [1]. However, it is vulnerable to mold because it is harvested in rainy and humid season [2, 3]. Some chemical antimicrobial and fungicides, such as imidazole has been applied in postharvest preservation of navel orange [4]. But, these synthetic chemical compounds have been used under limited circumstances because of their possible toxicity and potential risk to human health.

Chitosan, one of the most abundant amino polysaccharides in nature, is the product of chemical deacetylation of the chitin found in arthropod exoskeletons. It has been generally used in food, cosmetics, medicine, and health care fields for its good

biocompatibility, biodegradability and antimicrobial activity [5–7]. The antibacterial properties of chitosan coating on fruits have been reported in previous researches [8, 9]. The antifungal activity of chitosan on *Penicillium italicum* in ‘Newhall’ navel orange fruits was studied by Liu [10].

In this study, the chitosan coating solution was prepared and used for navel orange preservation. The preservation effect was studied during storage time at room temperature ( $20 \pm 5$  °C), and existing wax coating solution was served as the control group. In addition, comparison researches of two different solvents and three different concentrations were carried out by testing.

## 2 Materials and Methods

### 2.1 Materials

Fresh navel oranges (*Lane late*) were harvested from a local base in Zigui, Yichang, China, and transported to the laboratory in 8 h. navel oranges of uniform size and color that were free from visual defects and mechanical damage were selected for this experiment.

Commercial food grade chitosan with deacetylation degree of 90% was purchased from Regal Biological Technology Development Co., Ltd. (Shanghai, China). Citrus fruit wax 402D was acquired from Licheng Biological Technology Co., Ltd. (Yichang, China). Citric acid, glacial acetic acid, oxalic acid, ascorbic acid and sodium bicarbonate were all purchased from Sinopharm Chemical Reagent Co, Ltd (Shanghai, China). 2, 6-dichlorophenolindophenol sodium was obtained from MP Biomedicals, LLC (California, USA).

### 2.2 Treatments

Five treatments of navel oranges were prepared. Citric acid were used as solvent with 1.0, 1.5 and 2.0% w/v chitosan coating as solute (CA-1.0%CS, CA-1.5%CS, CA-2.0%CS), glacial acetic acid were used as solvent with 1.5% w/v chitosan coating as solute (AA-1.5%CS), and the existing wax coating solution, Citrus fruit wax 402D, was used as the control (CK). The navel oranges were naturally air dried for about 10 h after coating process and moved into PE bags with forearmed holes when the stable dry coating was formed, and stored in a ventilated place without sunshine at ambient temperature ( $20 \pm 5$  °C). There were 25 orange samples for each treatment, 10 samples for weight loss and decay rate, and 15 samples for other indexes. The experiments were carried out every 7 day, and the total test time was 35 days. The original data after harvest were obtained, and three replicates were made.

### 2.3 Methods

#### 2.3.1 Weight Loss

The weight loss rates of the treatments were calculated according to the formula as follows:



$$ML(t)\% = \frac{M_0 - M_t}{M_0} \times 100\% \quad (1)$$

where  $ML(t)\%$  is the percent of mass loss when the time is  $t$ ,  $M_0$  is the sample mass when the test started and  $M_t$  is the sample mass when the time was  $t$ . The sample weight was measured by a digital balance (PTF A600, Fuzhou, China).

### 2.3.2 Decay Rate

We weighed the good fruit and calculated the weight percentage of decayed fruit. Decay rate was calculated by using the following formula:

$$D(t)\% = \frac{M_0 - M_g}{M_0} \times 100\% \quad (2)$$

where  $D(t)\%$  is the decay rate at time  $t$ , and  $M_0$  represents the initial sample mass.  $M_g$  is the good sample mass at time  $t$ .

### 2.3.3 Total Soluble Solids

Total soluble solids (TSS) were measured in the juice obtained from three oranges using a handheld refractometer (LH-T32, Luheng Biological Technology Co. Ltd., Hangzhou, China) at room temperature.

### 2.3.4 Titratable Acidity

Titratable acidities (TA) were measured by acid-base neutralization titration method according to the Chinese national standard GB/T 12456-2008 and expressed as the percentage content of citric acid.

### 2.3.5 Vitamin C

The Vitamin C content was determined by reference to China's national standard GB 5009.86-2016. The juice sample was diluted 10 times with 2% (w/v) oxalic acid solution, and the diluted samples were titrated with 2,6-dichlorophenolindophenol sodium. A 2% (w/v) oxalic acid solution was used as blank titration.

### 2.3.6 Sensory Evaluation

Sensory evaluation was conducted by a nine-member panel with specific training on completing the tests. All panelists were evaluated using a scoring system with three factors (color, odor and flavor) of navel oranges at 7-, 14-, 21-, 28-, and 35-day. Prior to the whole sensory evaluation, all estimators were given sorted oranges of varying degree of quality from three aspects. All raters executed "difference from control" discrimination sensory test for degree of color, odor and flavor on a scoring scale of 0–9, 0 means "no difference" and 9 expresses "extremely different" from the initial fresh sample.

### 2.3.7 Statistical Analysis

Statistical analyses were carried out to determine whether significant differences ( $P < 0.05$ ) existed among physical, chemical and sensory quality indexes. The mean differences were determined by analysis of variance (ANOVA) and Duncan's multiple-range test, with the option of homogeneous groups, using SPSS 13.0 statistics software (IBM, Armonk, NY, USA).

## 3 Results and Discussion

### 3.1 Weight Loss and Decay Rate

The water content of the fruit lost and the weight decreased gradually with storage time because of the respiration metabolism and transpiration of fruits after harvesting [11]. The change of weight loss rate of navel oranges during the storage time is shown in Fig. 1. From Fig. 1, we can see that five treatments showed similar changing trends, namely the weight loss rate increased gradually with storage time and jumped abruptly on the 21st day. The weight loss rate of CK treatment achieved 8.88% while other treatments were below 8% after 21 days, although there still have commercial value, but the tastes of navel orange had changed. On the 35th day, the weight loss rate of CK treatment has reached 13.6% while 11.79% for CA-1.0%CS treatment, 12.72% for CA-2.0%CS treatment and 11.13% for AA-1.5%CS treatment, respectively. The lowest weight loss rate, the CA-1.5%CS treatment, is 10.26%. These results indicated that edible chitosan coating was benefit for the water keeping of navel orange after harvesting and the CA-1.5%CS treatment was the best.

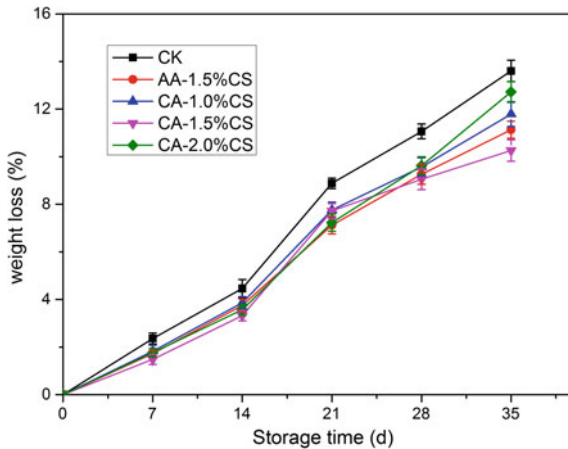


**Fig. 1.** Change of weight loss rate with storage time

Citrus fruits such as navel orange are susceptible to infection by *Penicillium italicum* and *Penicillium digitatum* after the harvest [4]. The fruits which infected by

mould would turn soft, brown, watery-like and shrinking sunken circular spots would appear on the surface of the fruits until they decay. These all would affect the commercial value of navel oranges vastly. Change of decay rate of navel oranges in storage period is shown in Fig. 2. As shown in Fig. 2, the apparent decay occurred in all the experience treatments on the 14th day. The decay rate of CA-1.0%CS treatment was the largest and no longer increase after the 14th day. The decay rates of CK treatment and CA-2.0%CS treatment increased on the 28th day, while, the decay rates of AA-1.5%CS treatment and CA-1.5%CS treatment kept the same. Until the 35th day, the decay rate of CK treatment reached 32.24% while that of AA-1.5%CS treatment and CA-1.5%CS treatment were 10.6 and 9.12%, respectively. These results indicated that AA-1.5%CS treatment and CA-1.5%CS treatment inhibited the breed of *Penicillium italicum* and *Penicillium digitatum* on the navel oranges.

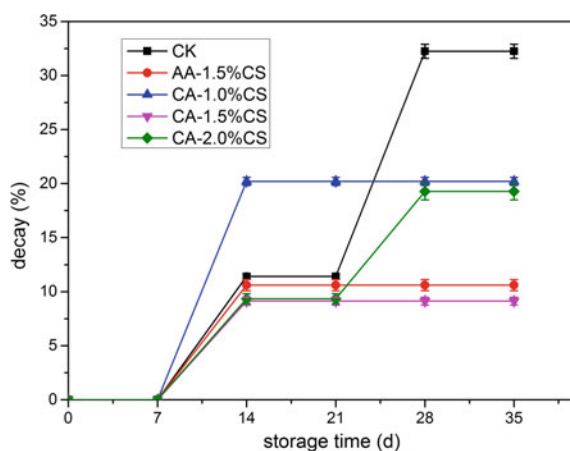


Fig. 2. Change of decay rate with storage time

### 3.2 Total Soluble Solids

Total soluble solids (TSS) content reflects the percentage of soluble sugars in fruit tissue and is one of the most important indexes to evaluate preservation quality of navel oranges [12, 13]. From Fig. 3, on the 7th day, the TSS values of all the treatments distinctly decreased compared with the initial value, and these behaviors are due to sugars decomposition reactions. The TSS values of all the treatments arrived relatively highest value at the 21st day, it is caused by the various reasons, on one hand, the water loss could cause the increase of soluble sugar concentration, and on the other hand, the degradation of polysaccharides to monosaccharide would lead to increasing soluble sugar content. But in the later period of storage, as the fruit turned soft, the respiratory material has been further consumed and the TSS value decreased steadily. The TSS value of CA-1.5%CS treatment changed steadily, while the value of CK treatment dropped sharply, which indicated that the fruits of this treatment were deteriorated.

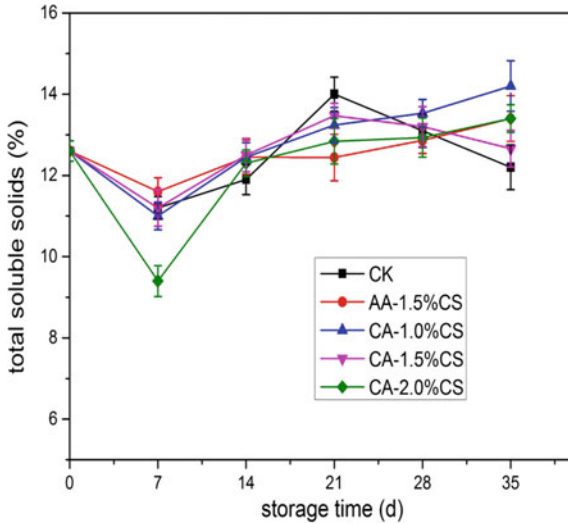


Fig. 3. Change of total soluble solids content with storage time

In the later period, the TSS values of CA-1.0%CS, CA-2.0%CS and AA-1.5%CS treatments maintained high levels because of more water loss.

### 3.3 Titratable Acidity

Titrateable acidity (TA) content can reflect the flavor and taste of fruit. The content of titrateable acidity, which would be preferentially consumed as respiration substrate, showed a general downward trend during the respiratory process [14]. The change of TA values of navel oranges during storage time is shown in Fig. 4. As shown in Fig. 4, in the early storage period, TA values of all five treatments decreased clearly. In the later storage period, TA values of all treatments increased gradually due to the generation of organic acid with sugar decomposition. In the experiment, the TA value of CK treatment started to increase at the 7th day, while that of CA-1.0%CS treatment and CA-2.0%CS treatment at the 14th day and AA-1.5%CS treatment and CA-1.5%CS treatment at the 21st day. These suggested that the respiration of the fruits of CK treatment was more active than other treatments, while the respiration of the fruits of AA-1.5%CS treatment and CA-1.5%CS treatment were inhibited ( $P < 0.05$ ). The TA value of the fruits of CA-1.5%CS treatment did not experience significant change during the whole storage period, at the 35th day, the TA value still kept at 5.10 g/kg, and CA-1.5%CS treatment is good for keeping the postharvest quality of navel oranges.

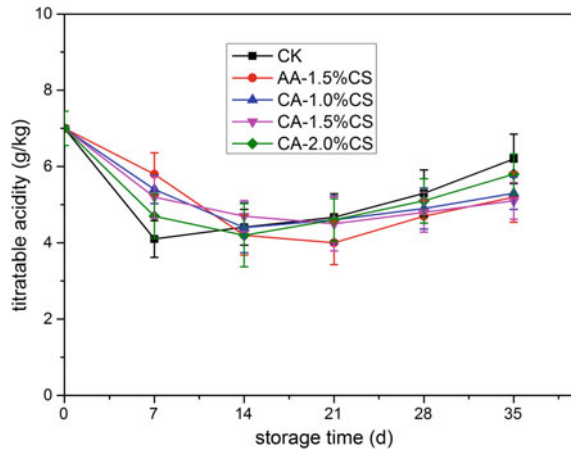


Fig. 4. Change of titratable acidity with storage time

### 3.4 Vitamin C

Vitamin C is one of the main nutrient substances of navel orange. As shown in Fig. 5, the Vc content of all the treatments represents the overall trend of fluctuations during the storage time at room temperature. The fluctuant changes of Vc content during storage period are determined by many factors, for one thing, respiration depletion would lead to the decrease of Vc content, for the other, water loss in turn cause the increase of relative concentration and Vc content in fruit tissue [15]. At the early storage period, the Vc content of all the treatments increased owing to the maturity of the fruits. At the middle and late storage period, with the exhaustion of sugar and acid and accelerating respiration because of dehydration, the Vc content decreased

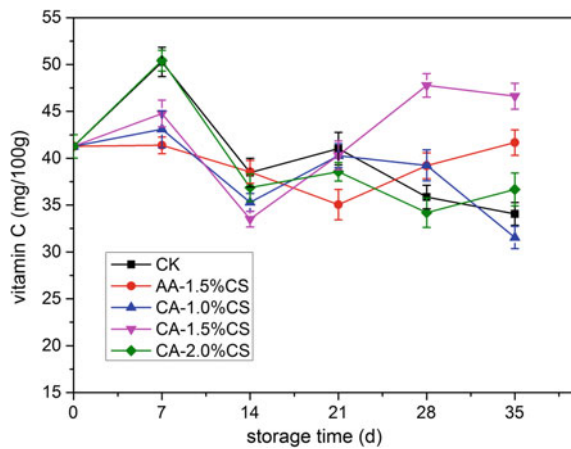


Fig. 5. Change of vitamin C content with storage time

**Table 1.** Sensory evaluation score of color, odor and flavor of navel oranges with storage time

Treatment	Storage time (days)					
	0	7	14	21	28	35
<i>Color</i>						
CK	0 ± 0.00 <sup>a</sup>	1.33 ± 0.50 <sup>a</sup>	1.56 ± 0.53 <sup>a</sup>	3.22 ± 0.67 <sup>a</sup>	4.11 ± 0.78 <sup>a</sup>	5.44 ± 0.53 <sup>a</sup>
AA-1.5%CS	0 ± 0.00 <sup>a</sup>	0.67 ± 0.50 <sup>b</sup>	1.33 ± 0.50 <sup>ab</sup>	1.89 ± 0.60 <sup>b,c</sup>	2.78 ± 0.67 <sup>b</sup>	3.44 ± 0.53 <sup>b</sup>
AC-1.0%CS	0 ± 0.00 <sup>a</sup>	0.56 ± 0.53 <sup>b</sup>	0.89 ± 0.60 <sup>b</sup>	1.78 ± 0.67 <sup>b,c</sup>	2.44 ± 0.53 <sup>b,c</sup>	3.00 ± 0.50 <sup>b,c</sup>
AC-1.5%CS	0 ± 0.00 <sup>a</sup>	0.44 ± 0.53 <sup>b</sup>	0.89 ± 0.60 <sup>b</sup>	1.44 ± 0.53 <sup>c</sup>	2.11 ± 0.33 <sup>c</sup>	2.56 ± 0.55 <sup>c</sup>
AC-2.0%CS	0 ± 0.00 <sup>a</sup>	0.89 ± 0.33 <sup>ab</sup>	1.33 ± 0.50 <sup>ab</sup>	2.11 ± 0.60 <sup>b</sup>	2.89 ± 0.60 <sup>b</sup>	3.44 ± 0.88 <sup>b</sup>
<i>Odor</i>						
CK	0 ± 0.00 <sup>a</sup>	1.00 ± 0.71 <sup>a</sup>	2.00 ± 0.50 <sup>a</sup>	2.89 ± 0.60 <sup>a</sup>	4.33 ± 0.71 <sup>a</sup>	5.44 ± 0.53 <sup>a</sup>
AA-1.5%CS	0 ± 0.00 <sup>a</sup>	1.00 ± 0.50 <sup>a</sup>	1.67 ± 0.50 <sup>ab</sup>	2.44 ± 0.53 <sup>ab</sup>	3.44 ± 0.73 <sup>b</sup>	4.11 ± 0.78 <sup>b</sup>
AC-1.0%CS	0 ± 0.00 <sup>a</sup>	0.67 ± 0.50 <sup>a</sup>	1.44 ± 0.53 <sup>b</sup>	2.00 ± 0.50 <sup>b,c</sup>	3.33 ± 0.50 <sup>b</sup>	3.44 ± 0.73 <sup>b,c</sup>
AC-1.5%CS	0 ± 0.00 <sup>a</sup>	0.56 ± 0.53 <sup>a</sup>	1.22 ± 0.44 <sup>b</sup>	1.67 ± 0.50 <sup>c</sup>	3.22 ± 0.44 <sup>b</sup>	3.33 ± 0.50 <sup>c</sup>
AC-2.0%CS	0 ± 0.00 <sup>a</sup>	1.11 ± 0.33 <sup>a</sup>	1.44 ± 0.53 <sup>b</sup>	2.33 ± 0.50 <sup>b</sup>	3.44 ± 0.73 <sup>b</sup>	4.11 ± 0.78 <sup>b</sup>
<i>Flavor</i>						
CK	0 ± 0.00 <sup>a</sup>	1.22 ± 0.44 <sup>a</sup>	2.11 ± 0.60 <sup>a</sup>	2.67 ± 0.50 <sup>a</sup>	4.00 ± 0.71 <sup>a</sup>	5.33 ± 0.50 <sup>a</sup>
AA-1.5%CS	0 ± 0.00 <sup>a</sup>	1.11 ± 0.33 <sup>a</sup>	1.67 ± 0.50 <sup>ab</sup>	2.56 ± 0.53 <sup>a</sup>	3.33 ± 0.50 <sup>b</sup>	4.33 ± 0.71 <sup>b</sup>
AC-1.0%CS	0 ± 0.00 <sup>a</sup>	0.89 ± 0.33 <sup>ab</sup>	1.67 ± 0.50 <sup>ab</sup>	2.22 ± 0.44 <sup>ab</sup>	3.33 ± 0.50 <sup>b</sup>	3.56 ± 0.73 <sup>c</sup>
AC-1.5%CS	0 ± 0.00 <sup>a</sup>	0.67 ± 0.50 <sup>b</sup>	1.44 ± 0.53 <sup>b</sup>	1.89 ± 0.33 <sup>b</sup>	3.11 ± 0.33 <sup>b</sup>	3.44 ± 0.53 <sup>c</sup>
AC-2.0%CS	0 ± 0.00 <sup>a</sup>	1.22 ± 0.45 <sup>a</sup>	1.56 ± 0.53 <sup>b</sup>	2.44 ± 0.53 <sup>a</sup>	3.33 ± 0.71 <sup>b</sup>	4.00 ± 0.71 <sup>b,c</sup>

Sensory evaluation scores are mean ± standard deviation of nine panelists

<sup>a-c</sup>Means in the same column with different superscripts differ significantly ( $p \leq 0.05$ ) according to Duncan's test

persistently. For the obvious inhibitory effect on respiration of AA-1.5%CS treatment and CA-1.5%CS treatment, the Vc content of these two treatments showed obvious upward trend and the value stayed at a higher level at the late period. These were because that the increase of Vc content for the water loss was more than the decrease of it for the respiration consumption. This result indicated that the treatments of AA-1.5%CS and CA-1.5%CS had a certain effect on maintaining the nutritional components of the fruits.

### 3.5 Sensory Evaluation

Sensory quality is an important index to evaluate the commercial value of navel orange. The scores of sensory quality evaluations are shown in Table 1. With the extension of storage time, the score of three sensory quality evaluations all increased. At the 14th day of storage, the navel oranges of all the treatments kept the characteristics of bright color and rich aroma. At the 21st day, the score of the sensory quality evaluations of navel orange of CK treatment were more than 3 and the brightness of the color decreased obviously ( $P < 0.05$ ), but for the odor and flavor, there was no significant difference between the fruits of CK treatment and other treatments ( $P > 0.05$ ). At the 28th day, the sensory evaluation scores of CK treatment increased obviously and were significantly higher than the treatments coated by edible chitosan ( $P < 0.05$ ), the scores of CA-2.0%CS and AA-1.5%CS treatments were less than the CK treatment and the scores of CA-1.0%CS and CA-1.5%CS were the lest. At the 35th day, the color, odor and flavor scores of CA-1.5%CS were the best, but at that time, the flavor of the fruits of CK treatment was very weak and the color began to darken and there was hardly odor from the fruits. Need of special note is that the score of AA-1.5%CS treatment was higher after 35 days because of the residual of acetic acid, this result is consistent with some previous researches by Tunc et al. [16].

## 4 Conclusion

Navel orange is vulnerable to mold after harvest because it becomes mature in rainy and humid season. Chitosan coating was used for navel orange preservation in this work. Through the experimental results, the preservation effect of the fruits coated by chitosan coating solution of citric acid as the solvent is better than that of glacial acetic acid and the existing wax. The acetic acid remained on the surface of the fruits partly affected the sensory quality of navel orange. When the citric acid was used as solvent, the best concentration was 1.5%w/v, when the concentration was too low, the antiseptic effect was not ideal, and when the concentration was too high, the microspores on the surface of the fruits would be blocked and aerobic respiration of the fruits could be inhibited. After 35 days, the good fruit rate, total soluble solids and vitamin C content of the navel oranges of CA-1.5%CS treatment can be obtained, at the same time, the water loss rate is less and the sensory qualities maintain good. The general results confirmed that CA-1.5%CS treatment can inhibit the respiration and the reproduction of mould, and is benefit for the storage of navel orange and prolong its shelf life.

**Acknowledgements.** This study is funded by a Key Project of Science and Technology Plan of Jingmen (YFZD2017013) and Research project of Hubei province for young talent (Q20184301).

**Ethics Compliance Comments** The methodology used in this paper does not require institutional ethical approval. The reason is that there were no animals involved in the experiments, and all the chemical reagents applied to the fruits were metabolizable. Informed consent was obtained from all subjects.

## References

1. Zeng, R., Zhang, A., Chen, J., & Fu, Y. (2012). Postharvest quality and physiological responses of clove bud extract dip on 'Newhall' navel orange. *Scientia Horticulturae*, *138*, 253–258.
2. Kouassiab, K. H. S., & Jijakli, H. (2012). The control of postharvest blue and green molds of citrus in relation with essential oil-wax formulations, adherence and viscosity. *Postharvest Biology and Technology*, *73*, 122–128.
3. Arpaia, M. L., Kader, A. A. (2013). *Orange: Recommendations for maintaining postharvest quality*. <http://postharvest.ucdavis.edu/PFfruits/Orange/>. Accessed 30 June 2013.
4. Ladaniya, M. S. (2008). *Citrus fruit, biology, technology and evaluation* (p. 455). London, UK: Academic Press.
5. Cooksy, K. (2005). Effectiveness of antimicrobial food packaging materials. *Food Additives & Contaminants*, *22*, 980–987.
6. Srinivasa, P. C., & Tharnathan, R. N. (2007). Chitin/chitosan-safe, ecofriendly packaging materials with multiple potential uses. *Food Reviews International*, *23*, 53–72.
7. Wang, X., Du, Y., Luo, J., Lin, B., & Kennedy, J. F. (2007). Chitosan/organic rectorite nanocomposite films: Structure, characteristic and drug delivery behaviour. *Carbohydrate Polymers*, *69*, 41–49.
8. Sebastien, F., Stephane, G., Copinet, A., & Coma, V. (2006). Novel biodegradable films made from chitosan and poly (lactic acid) with antifungal properties against mycotoxinogen strains. *Carbohydrate Polymers*, *65*, 185–193.
9. Rabea, E. I., Badawy, M. E. I., Steurbaut, W., & Stevens, C. V. (2009). In vitro assessment of N-(benzyl) chitosan derivatives against some plant pathogenic bacteria and fungi. *European Polymer Journal*, *45*, 237–245.
10. Liu, F., Chen, M., & Chen, J. Y. (2010). Antifungal activity of chitosan on *Penicillium italicum* in postharvest 'Newhall' navel orange fruits. *Acta Agriculturae Universitatis Jiangxiensis*, *121*, 51–58.
11. Arnon, H., Granit, R., Porat, R., & Poverenov, E. (2015). Development of polysaccharidesbased edible coatings for citrus fruits: A layer-by-layer approach. *Food Chemistry*, *166*, 465–472.
12. Hussain, S. B., Shi, C. Y., Guo, L. X., Kamran, H. M., Sadka, A., & Liu, Y. Z. (2017). Recent advances in the regulation of citric acid metabolism in citrus fruit. *Critical Reviews in Plant Sciences*, *36*, 1–16.
13. Yu, T., Yu, C., Chen, F., Sheng, K., Zhou, T., Zunun, M., et al. (2012). Integrated control of blue mold in pear fruit by combined application of chitosan, a biocontrol yeast and calcium chloride. *Postharvest Biology and Technology*, *69*, 49–53.



14. Chen, M., Xie, X., Lin, Q., Chen, J., Grierson, D., Yin, X., et al. (2013). Differential expression of organic acid degradation-related genes during fruit development of navel oranges (*Citrus sinensis*) in two habitats. *Plant Molecular Biology Reporter*, *31*, 1131–1140.
15. Ye, M. Z., Chen, Q. X., Xu, J. Z., Xu, X. Z., Zhao, M., & Xia, K. S. (2000). Some physiological changes and storability of citrus fruits during storage. *Plant Physiology Communications*, *36*, 125–127.
16. Tunc, S., Chollet, E., Chalier, P., Preziosi-Belloy, L., & Gontard, N. (2007). Combined effect of volatile antimicrobial agents on the growth of *Penicillium notatum*. *International Journal of Food Microbiology*, *113*, 263–270.



# Study on the Cold Storage Agent for Food Insulation Packaging

Fangfang Lu<sup>(✉)</sup>, Baoying Wang, Qingbao Wei, and Jingzhou Wang

Packaging and Printing Department, Henan University of Animal Husbandry,  
Zhengzhou, China  
hnmyleff@163.com

**Abstract.** The purpose of the research is to study the thermal insulation properties of NaCl, KCl, propanetriol, C<sub>2</sub>H<sub>5</sub>OH and saccharose, which are as the non-toxic primary energy storage agent. In order to obtain the optimum proportion, the rising and cooling curve is tested to find which can preserve heat for longer time. Finally, it obtains the results that the proportion of 6% saccharose + 6% propanetriol + 6% C<sub>2</sub>H<sub>5</sub>OH is cooling faster and rising slower, and the stable performance make it suitable for fruit and vegetable storage coolant. Further more, the effect of cooling and keeping fresh fruits and vegetables is more outstanding in the way of interval placing in the incubator.

**Keywords:** Insulation packaging · Cold storage agent · Energy storage agent

## 1 Introduction

Since the end of the twentieth century, our country has been lead in the world of total fruit and vegetable production. At the same time, however, the loss rate of harvested fruits and vegetables in the storage and transportation process is up to about 28% just because of the backward cold chain transportation system and the slow development of fruits and vegetables [1].

Temperature has a great impact on the quality of the product. Some products are sensitive to temperature changes, such as food, medicine, etc. The function of thermal insulation package is to maintain the temperature range required for the product and effectively extend the preservation time of the product. Cold storage agent is the first choice for the cold chain logistics development. Storage technology will become the main mode of refrigeration in the future [2].

Gao Kai's research on the development of storage agent shows that saccharose and propanetriol cool down rapidly, fluctuate little and more stable, so it is suitable for the main energy storage agent material used as the coolant for fruits and vegetables. One investigator points out that different placement methods of the storage agent in the packaging have different effects on the temperature distribution [3, 4].

## 2 Experiment

### 2.1 Materials and Equipment

NaCl, C<sub>2</sub>H<sub>5</sub>OH, Propanetriol, Yongda chemical reagent Co., Ltd. KCl, Saccharose, Comio chemical reagent Co., Ltd. Deep freezer, BCD-235TGZM(E), Meidi refrigerator Co., Ltd. Probe thermometer, -50- +300 °C, Odyssey technology co., Ltd. Electronic balance, 0–200 g, Youke instrument Co., Ltd. Heat sealing machine, Fengquan packing Machinery Co., Ltd. Colorimeter. CR-400, Rongdong trading co, Ltd.

### 2.2 Single Main Energy Storage Agent

Firstly, do cooling test. Five main energy storage agents, including NaCl, KCl, propanetriol, C<sub>2</sub>H<sub>5</sub>OH and saccharose were prepared into different concentration solutions at room temperature according to a certain concentration gradient (4, 6, 8, 10, 12, 14, 16%). Each solution 40 ml was put into the test tube, and then placed the tube containing the solution in the freezer with a set temperature of -16 °C. The temperature was measured every 40 min [5].

Then, do elevated temperature test. After the measurement of the cooling stage, the solution was moved into a freezer with a pre-set temperature of -5 °C to raise the reagent temperature to the appropriate temperature for the preservation of fruits and vegetables, after a few hours, the solution was placed at room temperature to measure the warming process of the reagent with a probe thermometer. This process was measured every ten minutes.

### 2.3 Two-Component Reagent

Firstly, did cooling test. After comparing and analyzing the cooling and warming data of different concentration solutions of a single reagent, this experiment preliminarily selected 6%, 8% saccharose and propanetriol, and 6%, 8% NaCl and KCl as the compound object.

When the two reagents were mixed, the mixture was prepared at 1:1. The 40 ml solution was taken and put into the test tube and put into the same low-temperature environment, and the experiment was measured every 40 min.

Then did elevated temperature test, the experimental operation of the mixed solution was same as that of the single main energy storage agent.

### 2.4 Three-Component Reagent

Through the analysis and comparison of the experimental data of single reagent and three-component reagent, 6%, 8% saccharose, propanetriol and C<sub>2</sub>H<sub>5</sub>OH were mixed at 1:1:1. Each tube was filled with 45 ml solution, and the temperature changes of cooling and warming were measured.

## 2.5 Packing of Refrigerant

The mixture of saccharose, propanetriol and  $C_2H_5OH$  was selected for packing, and the coolant was filled with PE bags, with 300 ml mixed solution in each bag, and sealed with a small heat sealing machine.

At room temperature, the prepared cold storage agent and fresh fruit were placed in PS incubator at 1:4 mass ratio, that is, 300 g cold storage agent and 1200 g little tomato were placed in each incubator. The cold storage agent was arranged in five ways: diagonal mode, side mode, interval mode, top and bottom mode, stereoscopic center mode, as well as a blank control heat preservation box, a total of six groups of experiments [6] (Fig. 1).

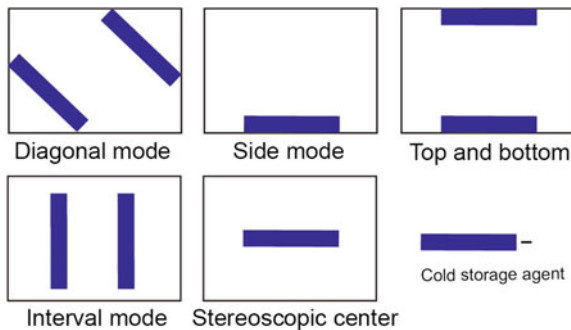


Fig. 1. Placement mode of cold storage agent

## 2.6 Chromaticity and Weight Loss Rate

Three small sized tomatoes were selected in the incubator with different placement mode, and then placed them in the incubator with appropriate distance. Lab value and weight of the sample are detected every day.

## 3 Experimental Data Analysis

### 3.1 Temperature Variation of Single Main Energy Storage Agent

#### 3.1.1 Cooling Test Result

We can see from Fig. 2a, the temperature of NaCl begins to show obvious difference between 40 and 80 min. The cooling rate of 14 and 16% of the solution is the fastest, but the range of cooling became slower in the last period.

From Fig. 2b we can see that the temperature of 14%, 16% KCl reaches  $6^\circ C$  at 40 min, which is obviously lower than that of other concentrations. However, the temperature of 4, 6, 8% KCl has rebounded during at 40–80 min.

From Fig. 2c, it can be seen that there is no smooth cooling curve between different concentrations of  $C_2H_5OH$  before 80 min. The cooling trend slowed after 80 min, with

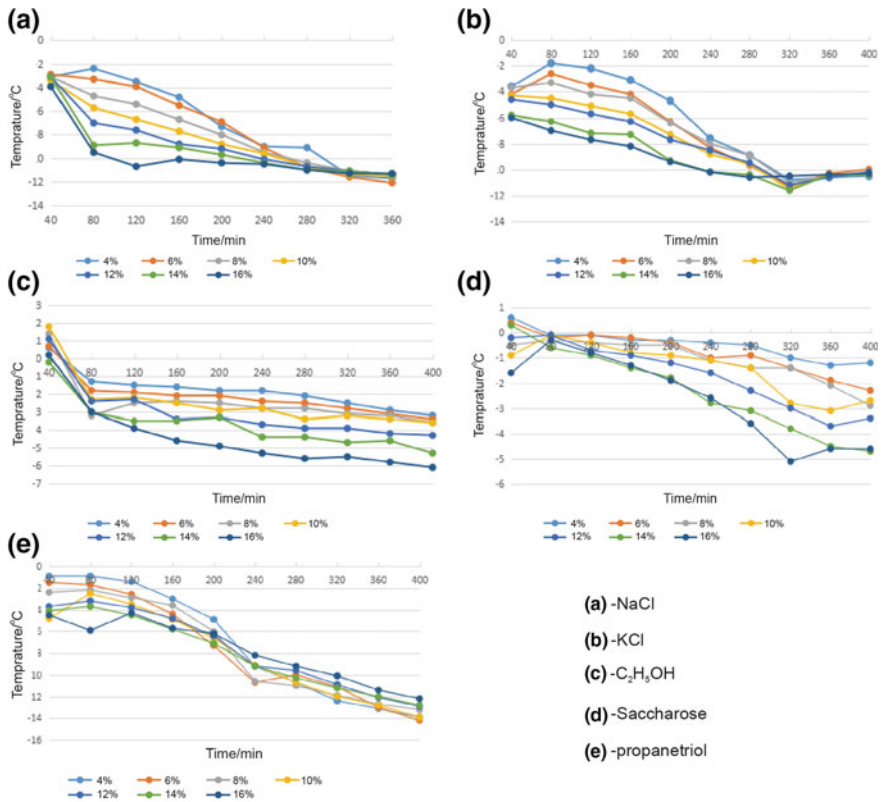


Fig. 2. Cooling curve of single main energy storage agent

16% of ethanol solution cooling faster than other concentrations. It can be seen that the concentration has a certain effect on the temperature change.

It can be seen from Fig. 2d that the cooling trend of 14%, 16% saccharose is faster.

As can be seen from Fig. 2e, the cooling curves of various concentrations of propanetriol overlap with each other between 160 and 240 min. Therefore, the difference of concentration of propanetriol has little effect on temperature change.

### 3.1.2 Elevated Temperature Test Result

From Fig. 3a we can see that the temperature fluctuations of 4 and 6% sodium chloride solutions between 0 and 10 min were not significant, and the temperature of both solutions is lower than that of other NaCl until 50 min.

It can be seen from Fig. 3b that the temperature of 4%, 6% KCl is obviously lower when the temperature is between  $-5$  and  $10$  °C, while the other concentration of KCl shows a steady warming trend and more and more slowly.

It can be seen from Fig. 3c that the temperature rise rate of 4%, 6% C<sub>2</sub>H<sub>5</sub>OH is very slow at the beginning 30 min, and then increases steadily, but the temperature is lower than that of other concentration.

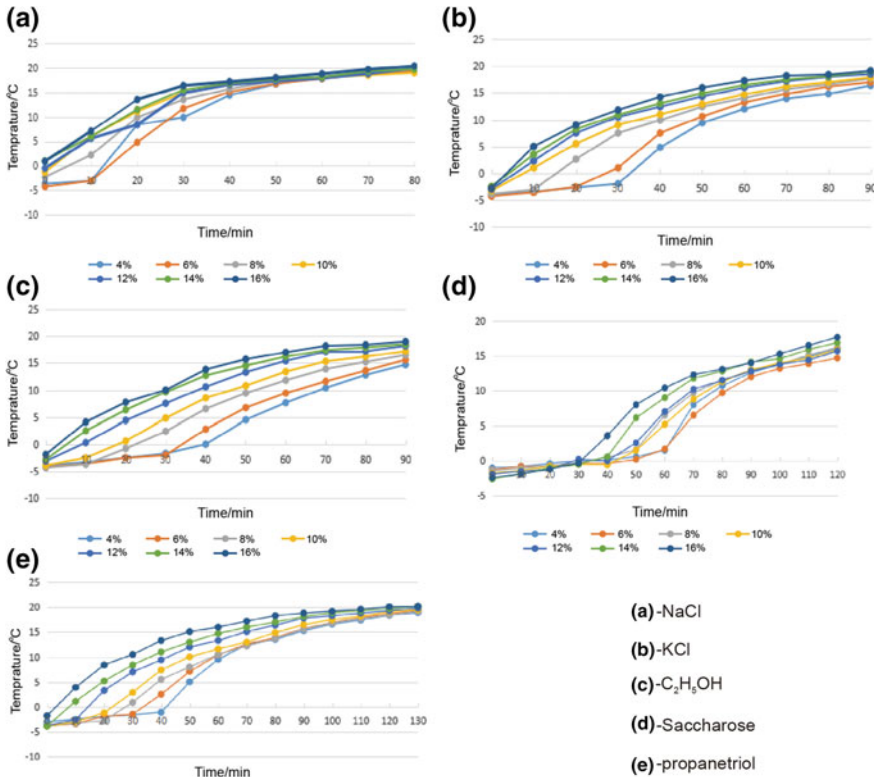


**Fig. 3.** Elevated temperature curve of single main energy storage agent

From Fig. 3d, it can be seen that the temperature rise of 16% saccharose is the fastest and 6% saccharose rises slowly after 30 min.

It can be seen from Fig. 3e that the warming curves of 4, 6, 8, 10% propanetriol are almost overlap in the first 20 min, but 4%, 6% propanetriol remain at a low temperature after 20 min.

Combined with the above experimental results, we can know that the cooling rate and warming rate of NaCl, KCl are both relatively faster, it can't store cold longer. However, the temperature fluctuation of saccharose and propanetriol is relatively small, and the temperature is more stable. Therefore, saccharose and propanetriol are selected as the materials of the main energy storage agent.

### 3.2 Temperature Variation of Two-Component Reagent

#### 3.2.1 Cooling Test Result

It can be seen from Fig. 4 that the cooling curves of the four kinds of mixed solutions are stable, but 6% saccharose + 6% propanetriol and 6% saccharose + 6% C<sub>2</sub>H<sub>5</sub>OH

have a large cooling range and good stability. The cooling range of 8% saccharose + 6% CH<sub>3</sub>CH<sub>2</sub>OH and 8% saccharose + 8% propanetriol mixed solution have relatively larger cooling range.

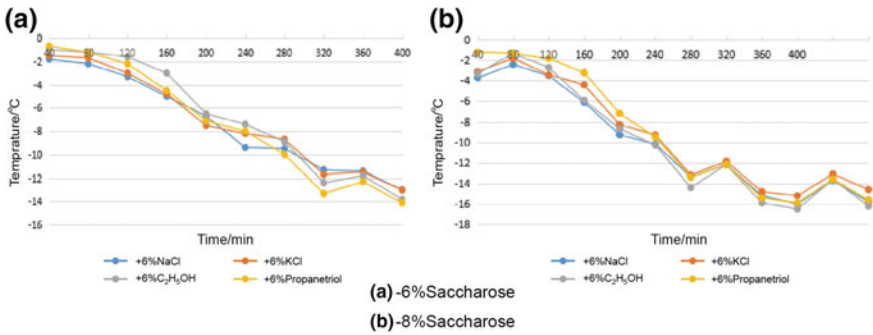


Fig. 4. Cooling curve of two-component reagent

**3.2.2 Elevated Temperature Test Result**

It can be seen from Fig. 5 that the temperature curves of various compound solutions overlap basically in the first 100 min, but only 6% saccharose + 6% propanetriol, 6% saccharose + 6% C<sub>2</sub>H<sub>5</sub>OH, 8% saccharose + 6% C<sub>2</sub>H<sub>5</sub>OH, 8% saccharose + 8% propanetriol have long time of low temperature, which is more suitable to be the main energy storage agent.

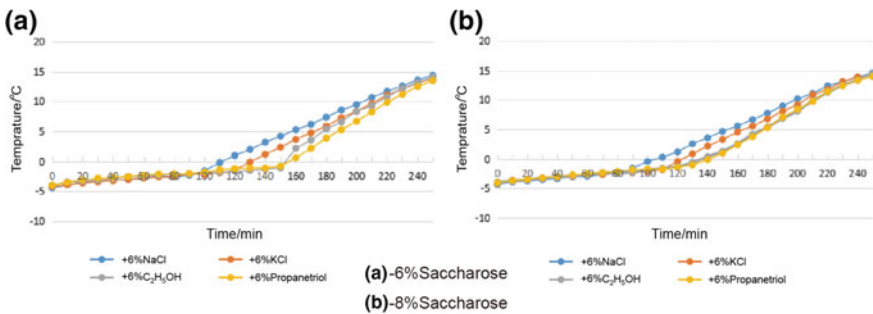


Fig. 5. Elevated temperature curve of two-component reagent

From Figs. 2, 3, 4 and 5 we can see, two-component reagent is cooling down faster and rising up slower than single main energy storage agent.

**3.3 Temperature Variation of Three-Component Reagent**

From Fig. 6 and 7, it can be seen that the 6% saccharose + 6% propanetriol + 6% C<sub>2</sub>H<sub>5</sub>OH compound solution is lower in temperature during the temperature reduction

stage, maintaining at a low temperature during the warming phase. Finally, this experiment is used as the main energy storage agent for making the cold storage agent.

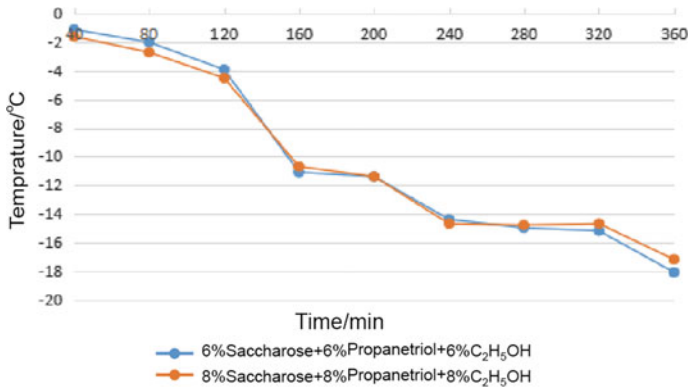


Fig. 6. Cooling curve of three-component reagent

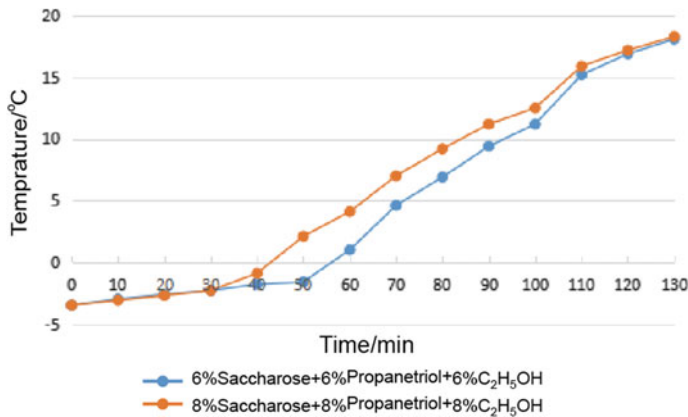


Fig. 7. Elevated temperature curve of three-component reagent

From Figs. 4, 5, 6 and 7 we can see, three-component reagent is cooling down faster and rising up slower than two-component reagent.

### 3.4 Chromatic Aberration Analysis

It can be seen from Fig. 8a that the value of  $\Delta a$  in all space placement modes shows a trend of first increasing and then decreasing, that is to say, it tends to red first and then to green. This is because fresh fruits enter a mature period, accompanied by the ripe holy fruits will become more bright red, when reached physiological maturity with the loss of moisture gradually decay, resulting in a dim color. According to the diagram,



the fluctuation of the curve of the interval and the top and bottom mode is relatively small, which shows that the effect of keeping fresh is more outstanding.

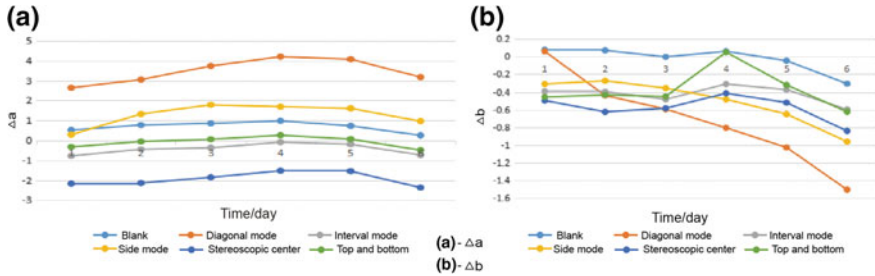


Fig. 8. Value of  $\Delta a$  and  $\Delta b$

It can be seen from Fig. 8b that the maximum variation of the diagonal  $\Delta b$  value is not suitable for the storage of cold storage; the trend of the curve of the first three days is relatively gentle and the change is not significant. In the following three days, the change of  $\Delta b$  value in the interval mode is the least.

### 3.5 Weightlessness Rate

As we can see from Fig. 9, the fruit lost water gradually in each mode, and it was most obvious that the weight lost in the blank mode. The curves shows that the weightlessness rate is the least when the cold storage agent is placed at interval mode, and the effect of keeping fresh at interval mode is the best.

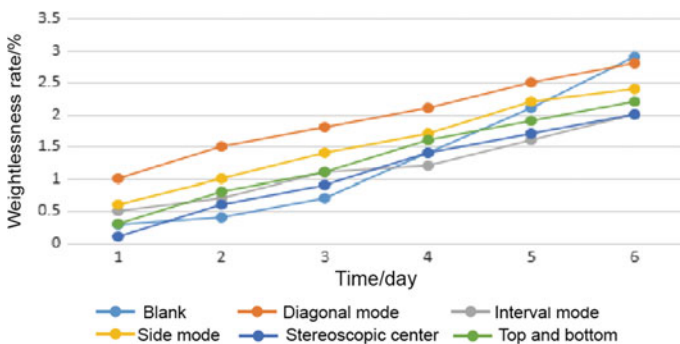


Fig. 9. Weightlessness curve

## 4 Conclusions

NaCl, KCl, propanetriol, C<sub>2</sub>H<sub>5</sub>OH and saccharose, five kinds of salt are selected as the main energy storage agents in this experiment. By studying the temperature variation of the five main energy storage agents in the process of cooling and warming, it is found that the change rule of saccharose, propanetriol, C<sub>2</sub>H<sub>5</sub>OH and anhydrous ethanol solution is suitable for as the main energy storage of fruit and vegetable storage agent.

- a. The cold storage agent prepared by the mixture of 6% propanetriol, C<sub>2</sub>H<sub>5</sub>OH and saccharose at 1:1:1 has the advantages of fast cooling, slow warming and good stability.
- b. The space mode of the cold storage agent has a certain influence on the quality of fruits and vegetables in the heat PS box. The results of color and weight loss showed that the best storage effect of fruits and vegetables is the mode of interval.

## References

1. Mostafavi, H. A., & Mirmajlessi, S. M. (2013). Integrated effect of gamma radiation and biocontrol agent on quality parameters of apple fruit: An innovative commercial preservation method. *Radiation Physics and Chemistry*, *91*, 193–199.
2. Lu, W., & Tassou, S. A. (2013). Characterization and experimental investigation of phase change materials for chilled food refrigerated cabinet applications. *Applied Energy*, *112*, 1376–1382.
3. Gao, K. (2010). Development of fresh Storage Agent for Transport of fruits and vegetables. *Preservation and Processing*, 20–23.
4. Moureh, J., & Derens, E. (2000). Numerical modeling of the temperature increase in frozen food packaged in pallets in the distribution chain. *International Journal of Refrigeration*, *23*, 540–552.
5. Morales, H., & Marín, S. (2009). Influence of post-harvest technologies applied during cold storage of apples in *Penicillium expansum* growth and patulin accumulation. *Food Control*, *21*, 953–962.
6. Ye, J. (2012). Effects of Active Modified Atmosphere Packaging on Postharvest Quality of Shiitake Mushrooms (*Lentinula edodes*) Stored at Cold Storage. *Journal of Integrative Agriculture*, *11*, 474–482.



# Design and Development of Alcohol Packaging Anti-counterfeiting System Based on Augmented Reality Technology

Wenjie Yang, Li Liu, Yating Wang, and Yunfei Zhong<sup>(✉)</sup>

School of Packaging and Materials Engineering,  
Hunan University of Technology, Zhuzhou, China  
yfzhong@hut.edu.cn

**Abstract.** With the rapid development of science and technology, alcohol packaging anti-counterfeiting technology tends to diversify. Because AR (Augmented Reality) technology has the characteristics of real-time interaction and pattern recognition, this paper puts forward an alcohol packaging anti-counterfeiting system based on AR technology. The whole frame structure, interface conception, function realization, user experience and information feedback of the system are designed. The interface design and function development of the system APP are carried out by using HTML5 tools, and the model identification, verification and video playback are realized by AR development tools. This system has cross-platform and good compatibility and can be used in both Android and IOS systems. The experimental results show that the system has excellent recognition performance and anti-counterfeiting performance, and the user can understand the commodity information in all directions in the process of identification.

**Keywords:** Augmented reality · Pattern recognition · Security system · 3D model · Verification code

## 1 Introduction

People's anti-counterfeiting consciousness is more and more intense on the 21st century. The shortcomings of the traditional anti-counterfeiting methods begin to show up and the incidents of counterfeit products emerge one after another, which has caused double losses to businesses in terms of both economy and reputation. Therefore, people begin to apply new information technology to anti-counterfeiting. It can play a crucial role in improving the security and traceability of products, which brings good news to businesses and consumers [1]. The solution of alcohol anti-counterfeiting system based on AR technology makes the product more three-dimensional, vivid and omnidirectional presentation, and truly realizes the information tracing and commodity anti-counterfeiting in the circulation process of alcohol and other articles [2].

## 2 Overview of AR

### 2.1 Introduction to AR

AR is an interactive experience of a real-world environment whereby the objects that reside in the real-world are “augmented” by computer-generated. The formation of interactive three-dimensional image screen gives users a more real experience and feelings [3]. AR technology includes multimedia, 3D modeling, real-time video display and control, multi-sensor fusion, real-time tracking and registration, scene fusion and other new technologies and methods.

### 2.2 Basic Principle of AR Used in Alcohol Anti-counterfeiting

Through the alcohol anti-counterfeiting system solution based on AR technology, the information acquisition and processing of production and circulation are completed. An alcohol anti-counterfeiting information system was established with reasonable management flow, extensible function, random information code and automatic identification of data. The real realization of alcohol and other goods in the circulation of goods in the process of anti-counterfeiting and information tracing, so as to bring immeasurable value to the management of enterprises and product credibility [4, 5].

## 3 Development of Alcohol Packaging Anti-counterfeiting System Based on AR Technology

### 3.1 Overall Design Framework and Model

The recognition graphic is extracted by the camera scanning, and the identification graphic is transmitted to the background server to match the stored graphic. If the matching is successful, the mobile terminal displays the times of the bottle scanned and send the verification code by the background server. If the matching fails, the bottle alcohol is reminded to be a fake alcohol. A verification code is input on the display interface of the mobile terminal to display an opening animation of the bottle; after exiting the display interface, the background server automatically deletes the verification code. As shown in the following Fig. 1.

### 3.2 System Structure

1. Mobile terminal with camera and special APP: mainly responsible for running special APP. Extracting and pattern recognition of images scanned by camera. And transmit the extracted and recognized information to the back-end server [6].
2. Box recognition graphics: mainly responsible for the mobile terminal image extraction and pattern recognition provide material [7].
3. Background server: mainly responsible for storing the relevant identification information of the identified image prepared in advance. Then it will receive and match the information transmitted by the mobile terminal.

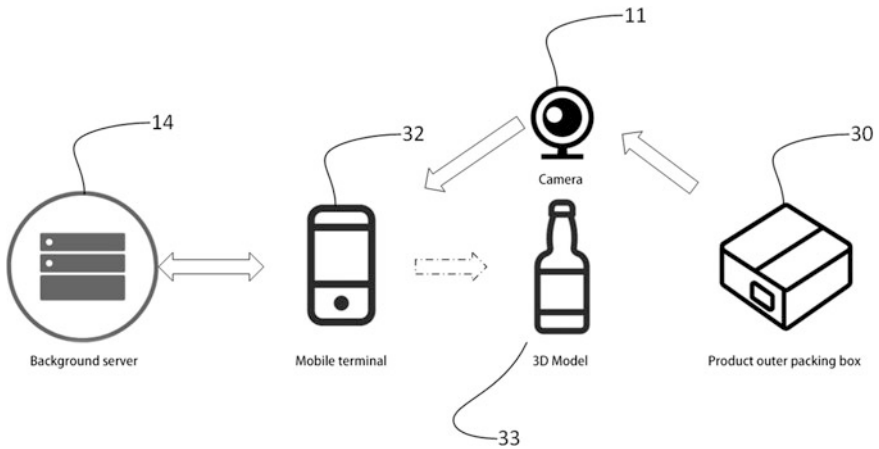


Fig. 1. Overall design framework

### 3.3 Research and Development of APP with HTML5

#### 3.3.1 Development of HTML5 APP

With the diversification of mobile devices, the process of mobile applications compatible with each device become more complicated. HTML5, which can span multiple platforms is a good choice for developers.

#### 3.3.2 Main Module of APP

1. Home page: The home page is the core window of the app. In order to improve the user experience, the preloading technology is used in the portal page (index.html) [8, 9]. As shown in the following Fig. 2.

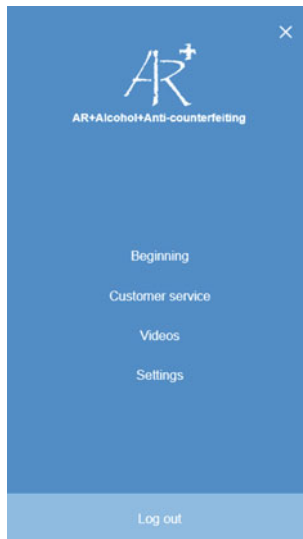


Fig. 2. Home page

2. Verification interface: It mainly includes initial anti-counterfeiting verification, secondary anti-counterfeiting verification and ultimate anti-counterfeiting verification. The ultimate anti-counterfeiting verification interface is shown in the following Fig. 3.
3. AR package: The AR package is the most important implementation component of

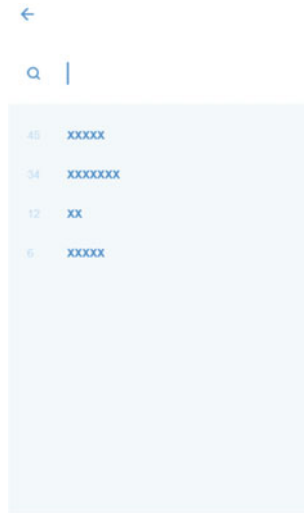


Fig. 3. Verification interface

the system. It can perform pattern recognition based on the recognition pictures provided in advance, and add animation, video, audio, etc. to the augmented reality [10, 11]. Video interface is shown in the following Fig. 4.

### 3.4 System Implementation Flow

The alcohol packaging anti-counterfeiting system based on AR technology mainly runs on the mobile terminal based on Android system. Research and development of the corresponding APP based on HTML5. The main functions of the implementation process as follows:

1. Initial anti-counterfeiting verification of alcohol by scanning the box. As shown in the following Fig. 5 [12].
2. Secondary anti-counterfeiting verification of alcohol by scanning the bottle. As shown in the following Fig. 6.
3. Ultimate anti-counterfeiting verification of alcohol by matching verification code. As shown in the following Fig. 7.



Fig. 4. Video interface

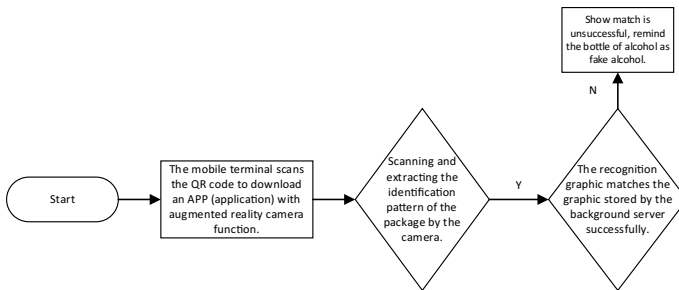


Fig. 5. Initial security verification

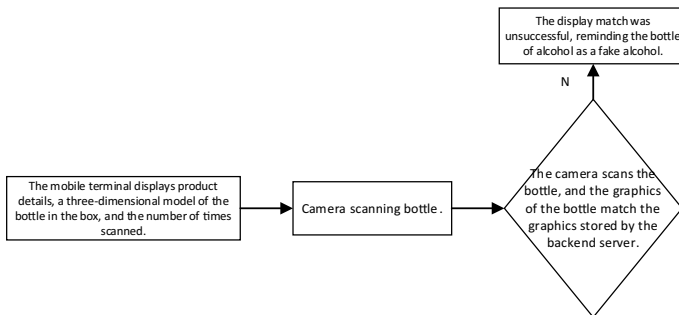


Fig. 6. Secondary anti-counterfeiting verification

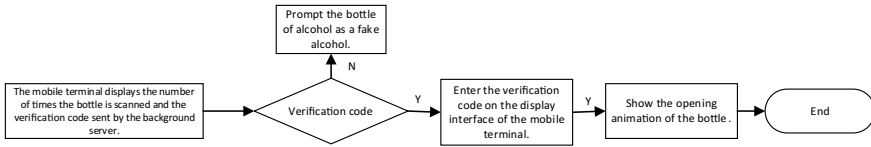


Fig. 7. Ultimate anti-counterfeiting verification

## 4 Conclusion

With the rapid development of AR technology, it will become a way of anti-counterfeiting. Alcohol anti-counterfeiting platform system is mainly used in the alcohol industry with high economic benefits. The AR technology is applied to alcohol anti-counterfeiting system which has cross-platform and good compatibility. It can be applied to both Android and iOS systems. The experimental results show that the system has good identification performance, anti-counterfeiting performance, and the user can know the information of the commodity in the process of identification.

**Acknowledgements.** Project is supported by Natural Science Foundation of Hunan Province (Grant No. 2016JJ6034), Training Project of Hunan Industrial Application of Higher Education Institutions (Grant No. 15CY003), Hunan Province Higher Education Institutions Demonstration Base of Production, Education and Research (Grant No. 2014-117), Project of Innovative Entrepreneurship Training Program for National College Students (Grant No. 40 [2017]), Project Research and Innovative Experimental Program for College Students in Hunan Province (Grant No. 205 [2017]), College Students Research Learning and Innovative Experiment Plan Project of Hunan University of Technology (Grant No. 1 [2017]).

## References

1. Zhang, P., & Zhang, H. (2016). Talking about the current packaging anti-counterfeiting. *Chinese Packaging*, 36(10), 58–59.
2. Wu, W. N., Hsiao, P. C., & Wang, H. C. (2013). Application of augmented reality to anti-counterfeiting technology. [Classification] 55.
3. Jiao, J. (2011). Six technologies affecting education over the next five years-horizon report. *Information Technology Education in China*, 5, 67–68.
4. Su, H., Li, J., & Xu, X. (2015). Augmented Reality Virtual Scenic Spot Information System. *Journal of Overseas Chinese University (Nature Edition)*, 36(4), 432–436.
5. Song, Y., Cao, X., & Zhou, L. (2016). Research on the application of mobile augmented reality in interactive presentation. *Computer Technology and Development*, 26(9), 83–86.
6. Harasaki, S., & Saito, H. (2010). Virtual object overlay onto uncalibrated camera images for augmented reality. *Systems & Computers in Japan*, 34(5), 47–55.
7. Corporation, N. (2015). Augmented Reality (AR) annotation computer system and computer-readable medium and method for creating an annotated 3d graphics model.
8. Gu, X., Hu, M., Jiang, H., & Wang, J. (2016). Development of hybrid mobile application based on HTML5. *Computer Systems Applications*, 25(5), 236–239.
9. Huang, H. (2016). App rapid development and analysis based on HTML5 web technology. *Wireless Interconnection Technology*, 8, 69–70.



10. Chen, M., Su, C., & Gao, F. (2018). Application of HTML5 in web interface design. *Computer Knowledge and Technology*, 14(5), 214–217.
11. Larsen, K. B., Siver, T., & Jones, D. (2012). Mobile augmented reality in advertising: The Tine Melk AR App—A case study. In *ACM SIGGRAPH* (p. 1). ACM.
12. Wei, Y., Yuan, Y., & Cao, L. (2014). Liquor product anti-counterfeiting system based on RFID and two-dimensional barcode technology. *China Science and Technology Expo*, 13, 53.



# Study on the Cushion Performance of the Cushion Material Composed of EPE and Honeycomb Paperboard

Xiaoli Song<sup>(✉)</sup>, Gaimei Zhang, Yue Cao, and Qiyang He

School of Printing & Packaging Engineering, Beijing Institute of Graphic Communication, Beijing, China  
songxiaol109@163.com

**Abstract.** This paper analyzes the static compression performance of the cushion material which is composed of EPE and honeycomb paperboard. The cushioning coefficient and the stress-strain curve are investigated under different thickness of EPE and different honeycomb paperboard and in the way of overlapping. The results show that the way of overlapping does affect the cushioning performance of the material composed of EPE and honeycomb cardboard. In usual case, the cushioning performance appears to be better when the cardboard is placed below. No linear relationship is found between the thickness of honeycomb cardboard and the cushioning performance. When  $\varepsilon = 55.200\%$ , EPE thickness can't affect the cushioning performance of the material. Under other shape changes, the thickness of EPE is not in a linear relationship with the cushioning performance of the material.

**Keywords:** Finite element method · Honeycomb paperboard stress

## 1 Introduction

Packed products are susceptible to be affected by mechanical shock and vibration during the transportation. When improperly packed, the products can be easily damaged, resulting in huge loss for the customers. Under mechanical effect, cushion packaging materials can absorb the energy resulting from the shock so as to effectively protect the commodities from any damage [1–3]. Therefore, to reduce the damage on commodities during transportation and handling, cushion materials such as EPE and honeycomb cardboard are now widely used. But they differ from each other in respect of cushion effect mechanism and performance. For instance, the cushion performance of honeycomb cardboard is mainly displayed in the compression fracture stages of honeycomb core structure, namely elastic-plastic stage and collapse stage. At this time, the yield platform is quite long and cushion coefficient remains low so that the impact-induced energy can be better absorbed. EPE is a kind of foam-rich polyethylene products made of low-density polyethylene (LDPE) through extruding processing. As all the auxiliary materials added form some independent and fine bubble structures in the polyethylene, EPE features light weight, high elasticity, and better absorbing effect on the low load. That accounts for why this material is more suitable to be used as an

anti-vibration material. Nevertheless, it is usually hard to predict about It is unpredictable what kind of shock or vibration is received during transportation. The buffering area of a single cushion material is always limited [4–7]. To better apply the cushion materials, improve the cushion package design, and bring down the economic loss caused by vibration and shock during circulation, this paper tests the stress-strain of serial cushion system composed of EPE and honeycomb cardboard, drafts the static cushion coefficient-strain curves, and analyzes the effect of overlapping method as well as the thicknesses of honeycomb cardboard and EPE thickness on the cushion performance of serial cushion system.

## 2 Experiment

### 2.1 Sample

The density of EPE is  $18.869 \text{ kg/m}^3$ . The size of EPE is  $100 \text{ mm} \times 100 \text{ mm}$  and the thickness is 20, 40 and 50 mm respectively. The thickness of honeycomb board is 15, 20 and 25 mm respectively. The density of honeycomb board's face paper is  $250 \text{ g/m}^2$ . The density of honeycomb board's inside paper is  $170 \text{ g/m}^2$ . The density of core paper is  $170 \text{ g/m}^2$ . The size of honeycomb board is  $100 \text{ mm} \times 100 \text{ mm}$ . All the experimental samples were pretreated according to GB4857.2. The environmental conditions are as follows: temperature in  $23 \text{ }^\circ\text{C}$ , relative humidity of 55%, and treated for more than 24 h.

### 2.2 Equipment

Microcomputer control electronic universal testing machine is used.

### 2.3 Method

- (1) EPE and honeycomb cardboard are combined in a certain form, which is shown in Fig. 1.



Fig. 1. Combination picture of EPE and honeycomb paperboard

- (2) The static compression test was based on GB/T 8168-2008 Static Compression Test Method for Packaging Buffer Material [8]. The compression speed of  $12 \text{ mm/min}$  is used. Finally, the stress-strain curve is recorded.
- (3) Applying the data to calculate the static cushion coefficient, draw the static buffer coefficient—strain curve.

### 3 Results and Analysis

#### 3.1 Effect of the Way of Overlapping on the Cushioning Performance of the Material

The honeycomb cardboard and EPE were kept being 20 and 30 mm, respectively, but their overlapping order was changed to accept a Static compression test. Finally the stress-strain curves are gained, which are shown in Fig. 2.

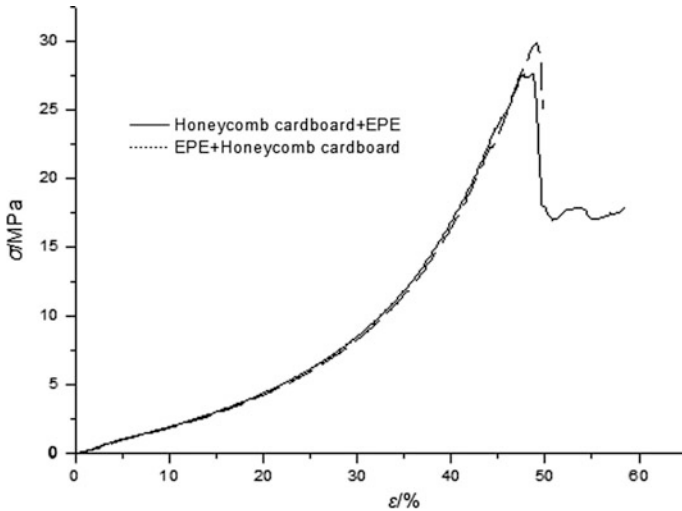


Fig. 2. The stress-strain curve of the material composed of EPE with thickness of 30 mm and honeycomb cardboard with thickness of 20 mm

It can be discovered from Fig. 2 that during the compression, no matter how EPE and honeycomb cardboard are overlapped, the compression process can be roughly divided into linear elastic stage, yield stage, and densification stage. In the first stage, two curves almost coincide with each other, differing only in the yielding point. When  $\epsilon = 48.000\%$  and honeycomb cardboard is below, the yielding point is lower. It means that the cushioning effect of this way of overlapping proves to be better.

According to the measured data, the cushion coefficient can be calculated by Eq. (1) [9, 10]. The cushioning coefficient-strain curve can be obtained, as shown in Fig. 3.

$$C = \frac{\sigma}{\int_0^\epsilon \sigma d\epsilon} \tag{1}$$

It can be discovered from Fig. 3 that when  $\epsilon = 50.060\%$ , two ways of overlapping acquire the minimum cushioning coefficient at the same time. When the cardboard is below, the minimum buffer coefficient is 2.570. And when the cardboard is below, the minimum buffer coefficient is 2.660. This testifies that the cushioning effect of the

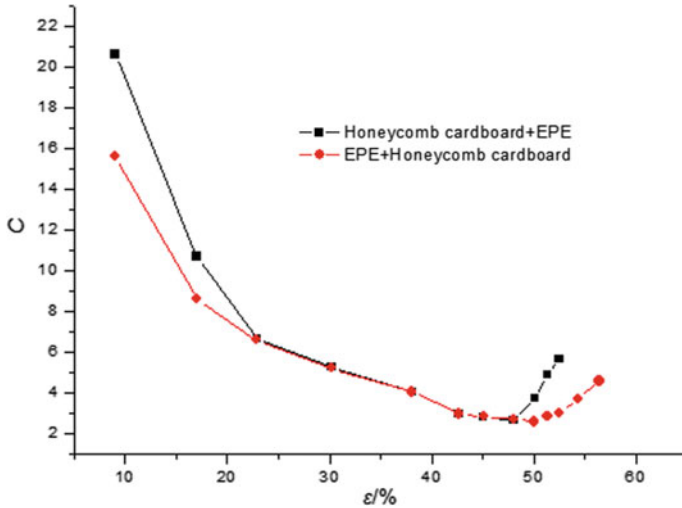


**Fig. 3.** Static cushioning coefficient-strain curve of the material composed of EPE with thickness of 30 mm and honeycomb cardboard with thickness of 20 mm

material composed of EPE and honeycomb cardboard is best when the cardboard is below. Two curves coincide with each other when  $38.080\% \leq \varepsilon \leq 47.080\%$ , which means their cushioning performance are same at this time. When  $47.080\% \leq \varepsilon$  and  $\varepsilon \leq 38.080\%$ , the serial structure with cardboard placed below has a good cushioning performance. When the honeycomb cardboard is placed below, the yielding point is lower. It means the cushioning effect is better for this way of overlapping.

### 3.2 Effect of Honeycomb Cardboard's Thickness on the Cushioning Performance of the Material

The thickness of EPE is 30 mm, but the thickness of honeycomb cardboard take respectively 15, 20 and 25 mm in this experiment. Finally the stress-strain curves are gained, which are shown in Fig. 4.

It can be discovered from Fig. 4 that the shape of the three curves is basically the same. However, there is a certain difference in the yield value. In the figure, the yield value is 15.829, 29.906 and 30.716 when the honeycomb cardboard thickness is 15, 20 and 25 mm, respectively. When the thickness of the honeycomb cardboard is 15 mm, the yield value is lowest. It means the cushioning effect of the material is best. The yield value rises gradually with thickening cardboard. It means the more rigid the serial system is, the lower its cushioning effect will be.

After some computation, the cushioning coefficient-strain curve is formed as shown in Fig. 5.

It can be discovered from Fig. 5 that during the whole compression process, when the cardboard thickness is 20 mm, its curve is below other curves, indicating that regardless of the strain, the buffer coefficient is the smallest. At this time, the absorbed energy is the highest, and the buffering effect is the best.

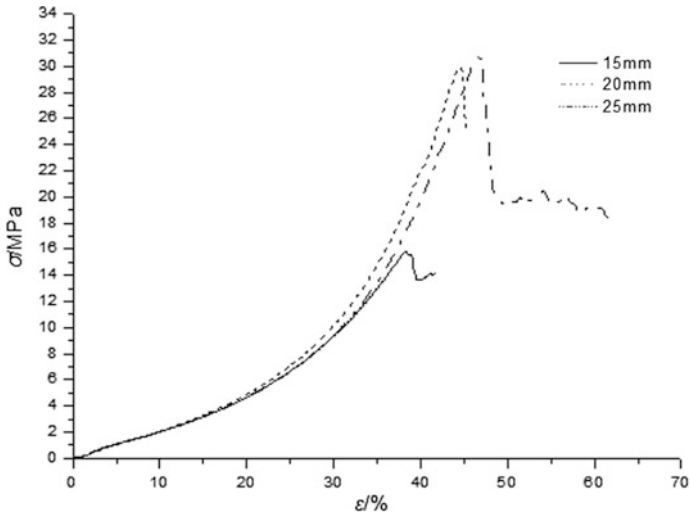


Fig. 4. Stress-strain curve of the material composed of EPE with thickness of 30 mm and honeycomb cardboard with different thickness

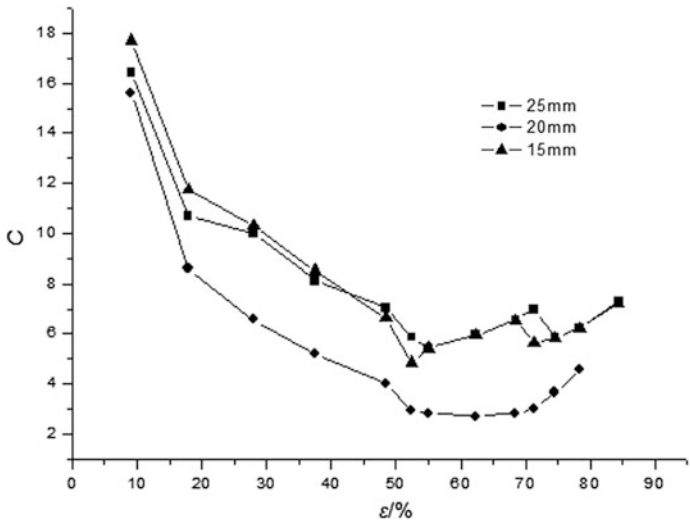
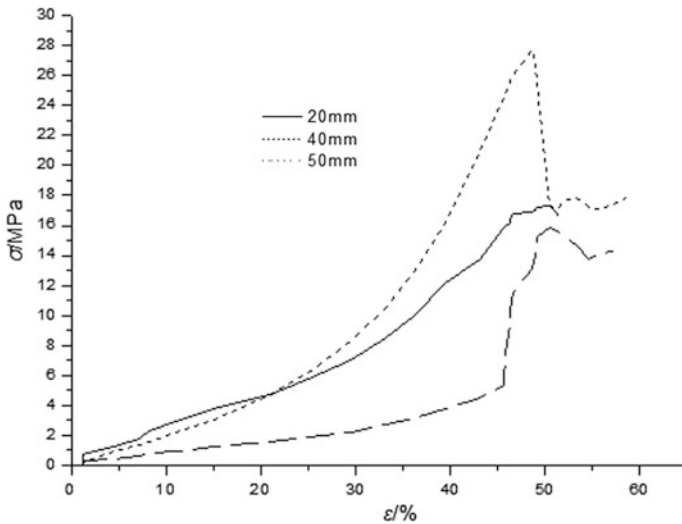


Fig. 5. Static cushioning coefficient-strain curve of the material composed of with thickness of 30 mm and honeycomb cardboard with different thickness

### 3.3 Effect of EPE's Thickness on the Cushioning Performance of the Material

The thickness of honeycomb cardboard is 20 mm, but the thickness of EPE take respectively 20, 40 and 50 mm in this experiment. Finally the stress-strain curves are gained, which are shown in Fig. 6.



**Fig. 6.** Stress-strain curve of the material composed of EPE with different thickness and honeycomb cardboard with thickness of 20 mm

It can be discovered from Fig. 6 that when the EPE thickness changes, the resulting curves display almost same patterns and differ only in the yielding point. The yield value is 17.280, 15.611 and 27.671 when the EPE thickness is 20, 40 and 50 mm, respectively. The lowest yield value and best cushioning performance appear when the thickness of EPE is 40 mm. The yield value and the thickness of EPE are in a non-linear relationship.

The experimental data were computed and processed. Finally the cushioning coefficient-strain curve is formed as shown in Fig. 7.

It can be discovered from Fig. 7 that three curves reach the lowest point at the same time when  $\varepsilon = 55.200\%$ , proving that they have the same cushioning coefficient and performance. This also indicates with rising EPE thickness, the cushioning performance of the material is not in a positive proportion to the thickness of EPE. When  $\varepsilon \leq 55.200\%$ , the material composed of 20 mm-thick EPE and honeycomb cardboard and 50 mm-thick EPE and honeycomb cardboard have almost coinciding cushioning curves. They have lower cushioning coefficient and better cushioning performance than the material composed of 40 mm-thick EPE and honeycomb cardboard. When  $55.200\% < \varepsilon \leq 68.460\%$ , the three curves almost coincide, which means they have equivalent cushioning coefficient and performance. When  $68.460\% < \varepsilon \leq 74.450\%$ ,

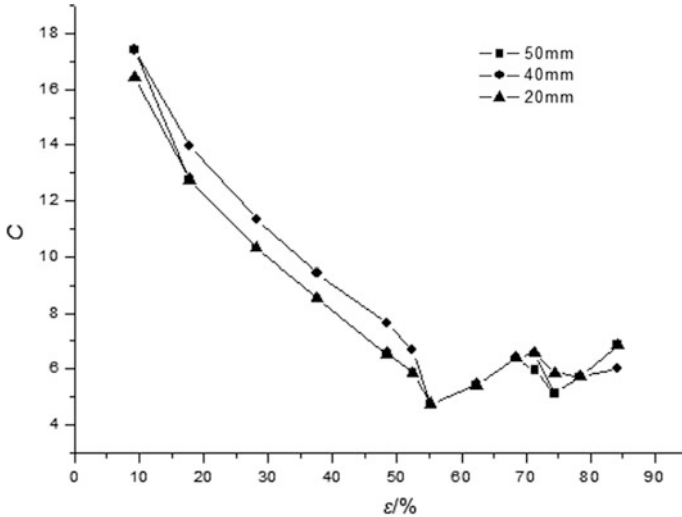


**Fig. 7.** Static cushioning coefficient-strain curve of the material composed of EPE with different thickness and honeycomb cardboard with thickness of 20 mm

the material composed of 50 mm-thick EPE and honeycomb cardboard reveals the lowest cushioning coefficient and best cushioning performance. When  $\epsilon \geq 74.450\%$ , the material made up of 40 mm-thick EPE and honeycomb cardboard have the lowest cushioning coefficient and best cushioning performance.

### 4 Conclusions

Comparing the results, the conclusion can be obtained:

- The way of overlapping does affect the cushioning performance of the material composed EPE and honeycomb cardboard. In usual case, the cushioning performance appears to be better when the cardboard is placed below.
- No linear relationship is found between the thickness of honeycomb cardboard and the cushioning performance.
- When  $\epsilon = 55.200\%$ , EPE thickness can't affect the cushioning performance of the material. Under other shape changes, the thickness of EPE is not in a linear relationship with the cushioning performance of the material.

**Acknowledgements.** The project is supported by the general research projects of Beijing Institute of Graphic Communication (Eb201701, Ed201804), the National Natural Science Foundation of China (51305038) and Bei Yin talent selection and development project of Beijing Institute of Graphics Communication (Byyc201316-016).



## References

1. Liu, Y., & Zhang, Y. (2011). Dropping simulation and design improvement of a washing machine based on FE analysis. *Journal of Vibration and Shock*, 30(2), 164–166.
2. Song, T., Liu, Y., & Zhu, R. (2006). Structure optimization design of cushion packaging based on dynamic property test and orthogonal design. *Packaging Engineering*, 27(5), 56–63.
3. Zhang, G., Wu, J., & Guo, F. (2011). Drop analysis of pop can based on ANSYS/LS-DYNA. *Packaging Engineering*, 32(5), 4–5.
4. Ye, B. (2010). A beautiful future of the wall materials made of honeycomb cardboard which is promoted by a low-carbon economy. *China Packaging Industry*, (5), 98–99.
5. Lu, F., Liu, X., & Gao, D. (2014). Review of constitutive model and its application of cellular cushioning material. *Journal of Zhejiang University (Engineering Science)*, 8(7), 1334–1336.
6. Lu, F., Gao, D., & Liang, A. (2002). Study of damage boundary curve of cubic non-linear double layer package under rectangular pulse. *Packaging Engineering*, 29(12), 7–10.
7. Lu, F., & Gao, D. (2014). Dynamic response of a functionally graded foam structure. *Journal of Vibration and Shock*, 33(15), 54–57.
8. GB/T 8168-2008. *Static compression for package cushioning materials experiment method*.
9. Guoxun, P. (2006). *Logistics and transport packaging design* (pp. 1–64). Beijing: Printing Industry Press.
10. Zhang, G. (2001). Study on the Buffering Property of the Honeycomb Board. *Packaging Engineering*, 22(5), 7–9.



# Study on Life Cycle Inventory Analysis of Folding Carton

Mengting Li, Guorong Cao<sup>(✉)</sup>, and Lizheng Zhang

School of Printing and Packaging Engineering, Beijing Institute of Graphic Communication, Beijing, China  
caogurong@bigc.edu.cn

**Abstract.** To study the folding carton production process of an enterprise in the material consumption, energy consumption and environmental impacts which provides a reference for improving the production process of folding carton and reducing environmental pollution. Methods According to the input and output data of the folding carton production process, using the rebalance life cycle assessment software, the life cycle inventory of folding carton production process was analyzed by the method of life cycle assessment. Results In the production processes of folding carton, the greatest impact on the environment is silk screen, followed by offset printing. The power consumption of offset printing machine is large. At the same time, the ink amount of offset printing and silk screen is consumed greatly which causes serious environmental pollution. Conclusion The effect of the folding carton production process on the environment is mainly from silk screen and offset printing, and the production process of offset printing and silk screen needs to be improved.

**Keywords:** Folding carton life cycle · Inventory analysis environment effects

## 1 Introduction

In recent years, due to the widespread use of green materials and the increasing awareness of environmental protection in enterprises, the environmental pollution caused by packaging waste has been improved. However, environmental issues caused by packaging production processes have attracted increasing attention [1].

At present, there are many studies on the environmental impact of packaging production processes in China, such as Environmental Impact Estimation of Al-PE-Pa Complex Package Using Life Cycle Assessment [2] and Case Study of Life Cycle Assessment for Paper Packaging of Ceramic Table ware [3], etc. These studies lay a foundation for the study of life cycle of packaging products. Applying LCA to the packaging and printing industry can guide companies to minimize pollution emissions and promote the coordinated development of the economy [4].

It includes four steps: the definition of target and scope, inventory analysis, life cycle impact assessment and life cycle interpretation. In these steps, the inventory analysis is the most important part which runs through the entire life cycle and provides a general overview of all system-related inputs and outputs [5]. The paper takes the folding carton as the research object and carries on the life cycle inventory analysis on

it using rebalance software, which provides the necessary data support for the optimization of the folding carton craft. Rebalance is leading Internet LCA software in the world that makes life cycle assessment more perfect.

## 2 Production Process of Plodding Carton

Flow chart of a folding carton production is shown in Fig. 1. The base paper enters the slitting machine and cuts according to certain specifications. The finished paper will enter the offset press to print graphic according to the requirement of the product. Then gilding to get the semi-finished product 1. The semi-finished product 2 is obtained by screen printing. The concave and convex mould is used to carry out concave convex processing, and the semi-finished product 3 is obtained. The printed board is slotted and impressed on the die cutting machine. Finally packing into storage.

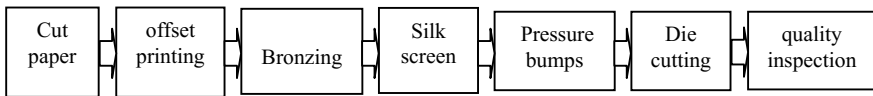


Fig. 1. Flow chart of folding carton production

## 3 Determination of Goals and Scope

This study analyzes the life cycle inventory of a folding carton production process and quantifies the environmental impact of each process. Since the modeling method of rebalance software is nested, each process is an independent unit. The product of the previous process is used as the raw material of the next process. As far as each process is concerned, the functional unit is the production of 1000 kg semi-finished product. The final functional unit is the production of one folding carton. The system boundary of folding carton is shown in Fig. 2. The system boundary is the entire production process from the supply of zinc supplied paper to the finished of folding carton. Zinc supplied paper, galvanized aluminum, screen printing inks and offset inks are raw materials in the production process of folding carton. Water and electricity are inputs. Waste solid, waste liquid and waste gas are outputs. Paper cutting, offset printing, Bronzing, silk screen, Pressure bumps, die cutting, quality inspection and transportation are Production Processes of folding carton. Their production and transportation are performed by other factories. So it considered without system boundaries. The production process data of folding carton used in the paper was obtained by researching on a folding carton production enterprise.

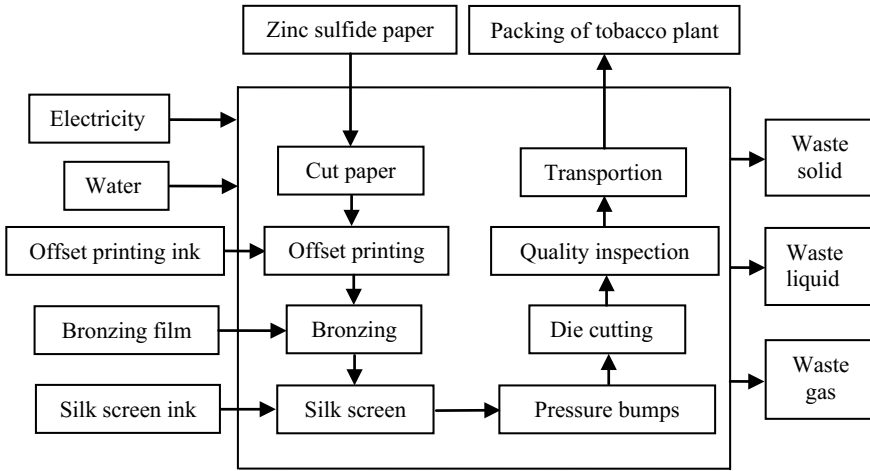


Fig. 2. System boundary of life cycle assessment of folding carton

### 4 Inventory Analysis and Impact Assessment

According to the actual production survey of a folding carton company in Shenzhen, the list of input and output data of folding carton is shown in Table 1. There are seven production processes in the system boundary. Every process is considered as an independent unit (Table 2).

Table 1. Inventory of inputs and outputs for one folding carton production

Process	Type	List name	Number	Unit
Cut paper	Product	Semi-finished product after cutting paper	1000	kg
	Consumption	Zinc sulfide paper	114.117	kg
	Consumption	Electrical energy	2.792	kWh
	Discharge	Waste paper	137.541	kg
	Product	Semi-finished product after offset printing	1000	kg
Offset printing	Consumption	Semi-finished product after cutting paper	992.404	kg
	Consumption	Offset printing ink	7.596	kg
	Consumption	Fountain solution	0.448	kg
	Consumption	UV water	0.149	kg
	Consumption	Propyl acetate	1.186	kg
	Consumption	CTP developer	0.215	kg
	Consumption	Water	50.784	kg
	Consumption	CTP plate	0.189	kg

(continued)

**Table 1.** (continued)

Process	Type	List name	Number	Unit
	Consumption	PE protection film	0.718	kg
	Consumption	Electrical energy	192.026	kWh
	Consumption	Ethanol	4.151	kg
	Discharge	Waste paper	56.933	kg
	Discharge	Waste plastic	0.718	kg
	Discharge	Old metal	0.189	kg
Bronzing	Product	Semi-finished product after bronzing	1000	kg
	Consumption	Paper tube	0.538	kg
	Consumption	PE protection film	0.683	kg
	Consumption	Electrified aluminum bronzing film	11.561	kg
	Consumption	Electrical energy	20.019	kWh
	Consumption	Semi-finished product after offset printing	1000	kg
	Discharge	Industrial waste	11.561	kg
	Discharge	Waste plastic	0.683	kg
Silk screen	Product	Semi-finished product after	1000	kg
	Consumption	Silk screen	39.701	kg
	Consumption	Semi-finished product after Bronzing	960.297	kg
	Consumption	Ethyl acetate	0.673	kg
	Consumption	Water	162.882	kg
	Consumption	Electrical energy	94.287	kWh
	Consumption	PE protection film	0.765	kg
	Discharge	Waste plastic	0.765	kg
	Discharge	Waste water	163.555	kg
Pressure bumps and die cutting	Product	Semi-finished product after pressure bumps and die cutting	1000	kg
	Consumption	PE protection film	0.663	kg
	Consumption	Electrical energy	15.736	kWh
	Consumption	Electric carving embossed version	0.102	kg
	Consumption	Semi-finished product after silk screen	1000	kg
	Discharge	Old metal	0.102	kg
	Discharge	Waste plastic	0.663	kg

(continued)

**Table 1.** (continued)

Process	Type	List name	Number	Unit
Quality inspection	Product	Quality testing	1000	kg
	Consumption	Electrical energy	44.106	kWh
	Consumption	Beige gum	0.379	kg
	Consumption	Self-adhesive	0.102	kg
	Consumption	Semi-finished product after pressure bumps and die cutting	1000	kg
	Consumption	Pitched kraft paper	0.337	kg
	Consumption	Big label	0.087	kg
	Consumption	PE protection film	0.241	kg
	Consumption	PE packing belt	1.259	kg
	Consumption	Stone kraft paper	40.087	kg
	Discharge	Waste paper	40.511	kg
	Discharge	Waste plastic	1.500	kg
	Discharge	Industrial waste	0.481	kg
	Product	Folding carton (after transportation)	1	Item(s)
	Transportation	Consumption	Cardboard	0.0000007
Consumption		Angle boards	0.0000007	kg
Consumption		Qualified carton	1	Item(s)
Consumption		Paperboard	0.000018	kg
Consumption		Carton transport	0.0062	t*km
Discharge		Waste paper	0.000032	kg

**Table 2.** Sensitivity analysis of GWP for one folding carton production

Process name	List name	Upstream data type	GWP (kg CO <sub>2</sub> eq) (%)
Zinc supplied paper	Base paper	Background AP	24.47
Cut paper	Zinc supplied paper	Foreground UP	22.88
Zinc supplied paper	Electricity	Background AP	11.16
Zinc supplied paper	PET film	Background AP	8.34
Silk screen	Screen printing ink	Background AP	3.35
Folding carton	Transportation	Background AP	2.86
Offset printing	Electricity	Background AP	2.45
Zinc supplied paper	Coating	Foreground UP	2.34
Bronzing	Anodized aluminum foil	Foreground UP	2.18

### 5 Results and Analysis

The results of the inventory analysis and impact assessment show that the main environmental impact of the folding cartons production process is Climate change (GWP), Primary energy demand (PED) and Resource depletion—water (WU). The numerical value of GWP, PDE and WU are 0.253, 7.223 and 0.398. Taking the effect of production processes of folding carton on climate change as an example. Figure 3 shows the effect of production processes of folding carton on climate change. It can be seen from Fig. 3 that Silk screen, offset printing and transportation have a great impact on climate change. Figure 4 shows the effect of inputs of screen printing on climate change. Figure 5 shows the effect of inputs of offset printing on climate change.

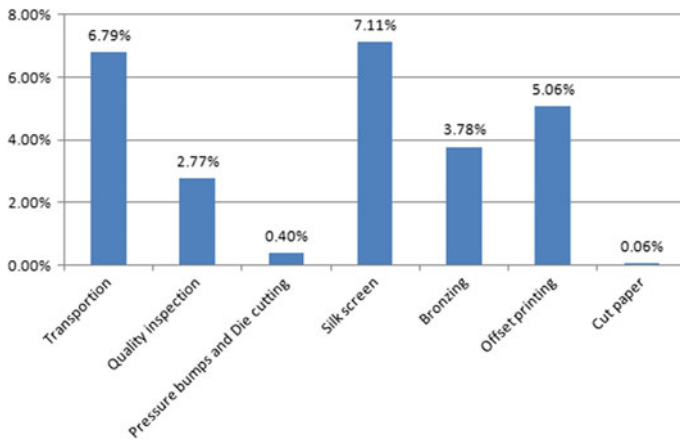


Fig. 3. The effect of various processes of folding carton on climate change (GWP)

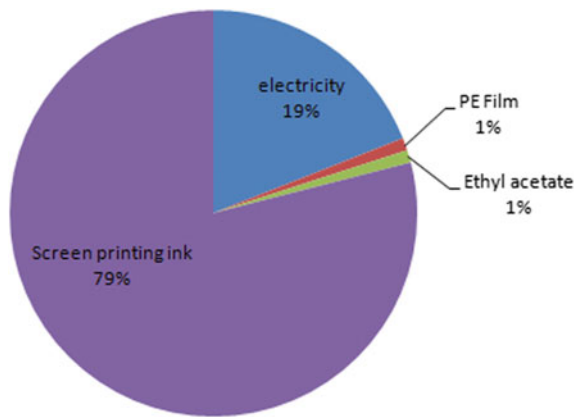
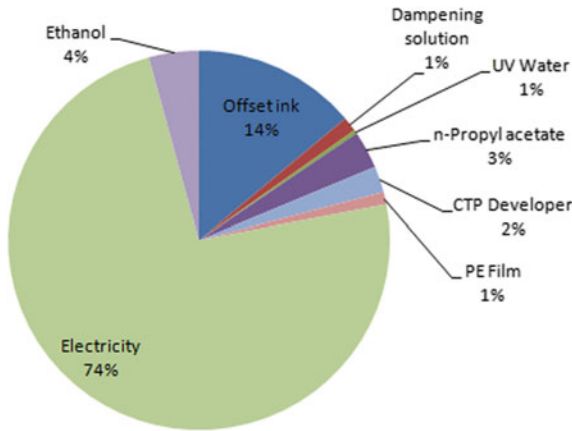


Fig. 4. The effect of screen printing materials on climate change



**Fig. 5.** The effect of offset printing materials on climate change

The impact assessment results show that the folding carton production process emits large amounts of greenhouse gases which cause global warming. The study mainly optimizes the folding carton production process. It does not consider the environmental impact brought by transport. In the production process of folding carton, screen printing is the most influential factor in climate change, the next is offset printing. Three conclusions have been drawn from the analysis that the environmental impact of offset printing and screen printing materials.

Firstly, screen printing ink has a great influence on climate change. The next, offset ink also has a certain impact on the global warming. Lastly, the offset printing consumes a lot of electricity which means that a large amount of greenhouse gases are emitted in Coal-fired power generation. Therefore, it is necessary to improve the choice of printing ink and the power consumption of the offset printing station.

Figure 2 is the sensitivity analysis of GWP for one folding carton production. There are material that the sensitivity more than 1%. Base paper has the greatest potential for improvement, followed by PET film, screen printing ink, Coating and anodized aluminum foil. These substances should be improved or replaced.

## 6 Conclusions and Suggestions

The study gives three suggestions to improve production proses of folding carton. First, there is little room for improvement in material utilization rate and qualification rate of each process. Therefore, it is important to take product design stage into consideration. The specific measures are appropriately reduce the number of processes and the input of major materials. We could convert end-of-pipe management into the green design of folding carton. Second, Screen and offset printing ink have a great influence on climate change. We should reduce the number of screen printing ink in the product design stage so as to reduce the environmental pollution. Last, it is imperative to save electricity in the offset printing stage. Strengthening the management of production processes can



also reduce the environmental impact of folding carton manufacturing. The power energy of the company is transported externally. Companies should rationally configure printing equipment, especially motors and transmission devices.

**Acknowledgements.** The general education reform project of Beijing Institute of Graphic Communication (22150116007/031), Packaging engineering teaching team (construction) of Beijing Institute of Graphic Communication (22150116006/017), Research on Certification and Evaluation Technology of Typical Air Pollutant Prevention and Control in Electric Power, Chemical Industry and Printing Industry (2017YFF0211803).

## References

1. Luo, G., & Yan, Z. (2004). Analysis on the green of the paper and plastic materials. *China Packaging Industry. Packaging engineering, 12(7)*, 217–231.
2. Xie, M., L, L., & H, Zechun. (2009). Environmental impact estimation of Al-PE-Pa complex package using life cycle assessment. *China Environmental Science, 29(7)*, 773–779.
3. Kong, C., & Liang, Y. (2013). Case study of life cycle assessment for paper packaging of ceramic table ware. *Packaging Engineering, 34(21)*, 43–48.
4. Ren, X., & Huo, L. (2008). Progres of application research of life cycle assessment in printing and packaging field. *Packaging Engineering, 29(10)*, 217–219.
5. Ren, H., Cao, L., & Qin, F. (2015). List analysis of life cycle in beer brewing. *Liquor-Making Science and Technology, 9*, 52–54.



# A Survey of the Most Acceptable Handle for Express Boxes

Yingzhe Xiao and Huiwen Meng<sup>(✉)</sup>

School of Packaging and Materials Engineering,  
Hunan University of Technology, Zhuzhou, Hunan, China  
840874024@qq.com

**Abstract.** Packages with handles are friendlier to workers than packages without handles. The optimal handle can greatly improve the safety and efficiency of manual material handling. This study aimed to assess the extent to which the worker's psychological and physiological stress was reduced by four different handles in manual handling tasks. 12 participants performed two manual tasks (load lifting (LIFT), carrying (CARRY)) using four handles (A, B, C, D), and the heart rate (HR), maximum acceptable weight of load (MAWL), body parts discomfort (BPD) and overall preference were recorded. In both tasks, there was no significant difference in the amount of heart rate when using four boxes, so was the BPD of wrist. The BPD of palm was significantly higher for the C than others. In LIFT, the MAWL and overall preference rating of handle C was the significant highest. In CARRY, the MAWL and overall preference rating of box B was the significant highest. Therefore, we demonstrate that for load lifting, handles on upper position were preferred. For carrying, handles on lower position were preferred. Furthermore, a space for hands to easily grip the handle was very important for enhancing the comfort. And the smoother and larger contact area could decrease the palm discomfort.

**Keywords:** Ergonomic manual materials · Handling · Package express

## 1 Introduction

MMH is widely found in daily life and in some labor intensive industries including express. The handle as a characteristic of an object is an important factor affecting worker's psychological and physiological load in MMH [1]. The musculoskeletal disorders, especially the low back pain, caused by the MMH have troubled a lot of workers and caused huge economic losses. The injuries have been the leading cause of years lived with disability (YLDs), and increased disability-adjusted life years (DALYs) in the world-wide [2]. Moreover the primary care (13%), inpatient services (17%) and physical therapy (17%) were the main parts of the direct costs of economic losses, in addition there were other indirect costs. The majority of indirect costs were because of the lost work productivity. In Sweden, the total cost of LBP were 1860 million EUR in 2001, 84% was the indirect costs [3]. Although the development of technology has substituted mechanism for human in many MMH tasks, the studies in the United States and Brazil have shown that the prevalence of MSD and the number of

people had some form of arthritis has increased and will become higher as the aged tendency of population. In China, there was a lack of relevant statistics. However, we believed that there were many express workers suffered from the MSD in such a huge express industry relying on high-intensity manual work. Therefore, how to reduce the worker's physical load in MMH requires study.

Previous studies have indicated that handles helped workers make tasks easier and safer [1]. Drury [4, 5] pointed out that handles' diameter and texture, work habit of workers could affect the working performance. Snook [6] reported that the workers' MAWL of box with handles was 15% higher than the box without handles. And he found that the position of handles could affect the workers' physiological load. The handles which have both horizontal and vertical stability are the best for workers. Jung [7] studied the worker's preference for different box sizes, handle positions, MMH tasks. Wu [8] compared the both two person carrying task and single person carrying task with handles and without handles. It showed that the both HR change and MAWL were affected by whether there were handles.

## 2 Methods

### 2.1 Participants

Twelve college students (mean age = 20.12, SD = 1.26) without back or shoulder pathologies volunteered to participate in this study, including seven males ( $169.7 \pm 5.3$  cm,  $63.3 \pm 10.6$  kg), five females ( $161 \pm 4.4$  cm,  $46.2 \pm 4.1$  kg). They were informed that experiment procedures, and trained to perform the experiment tasks before the test began. Each volunteer got same payments after performing each experiment.

### 2.2 Prototypes Development

In this study, the four prototypes were four corrugated express boxes of the same size and different handles, numbered A, B, C, D. Prototype A was the box commonly used in express delivery without handles as the blank control group. Prototype B's handles were new designed, and they were two indentations on the bottom of the both sides of box. Its advantage is to provide space for hands when workers need to carry, lift and move it from a flat. Prototype C was a box with improved handles which have  $20^\circ$  oblique from the horizontal in order to relieve the ulnar deviation of workers' hands when they handle it. Prototype D was the box with existing handles which were proposed by someone. There was a notch in the corner of the box that provides space for the fingers, as Prototype B did.

The size of prototype box was 365 mm  $\times$  243 mm  $\times$  243 mm (L  $\times$  W  $\times$  H). 365 mm was the most people's (50%) shoulder width of china, and 243 mm was calculated by the best scale (1.5:1:1) for 0201 corrugated box. The size of the prototype B handles was 72 mm  $\times$  82 mm  $\times$  20 mm, determined by most Chinese finger size, length  $\times$  width  $\times$  thickness as Fig. 1 shows. Prototype D's handle was a triangular pyramid, each side of it was 55 mm. All boxes were made of BE five-layer corrugated paper, and the bottom of box was sealed with glue, but the top wasn't.

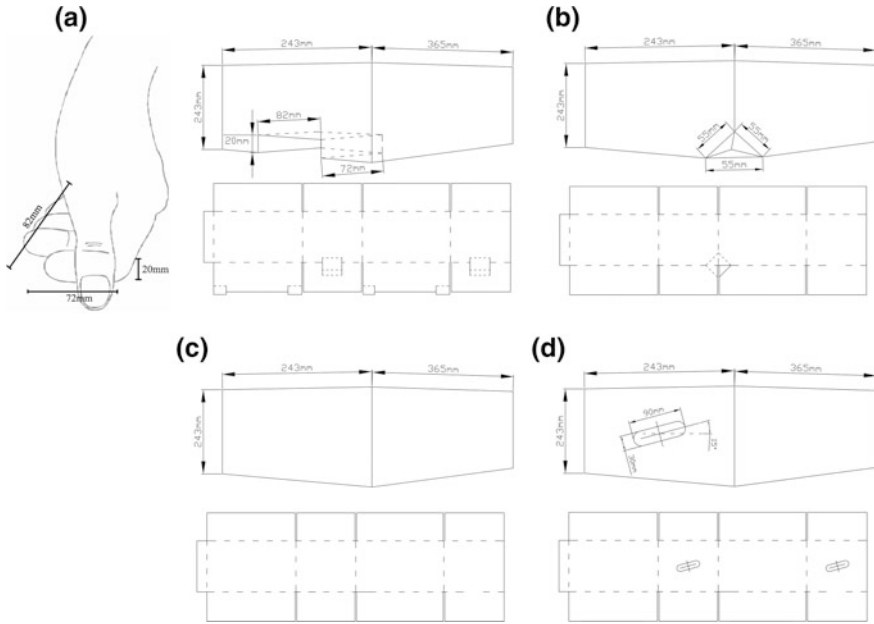


**Fig. 1.** The four prototypes have the same size and the size of handles was according to people hand size

### 2.3 Experimental Tasks

They were required to perform two modalities of handling tasks, LIFT and CARRY, according to the simulation of actual delivery process. The LIFT was that participants lifted load in the sagittal plane. The CARRY was that participants walked while carrying a load. In each task, participants need to do two tests. One was fixed-weight test that the participants operate in a fixed weight in order to measuring the amount of heart rate change before and after the action and body parts discomfort (BPD), overall preference. The other was change-weight test that the weight of load was continuously adjusted until the maximum acceptable weight (MAWL) of the subject for a handle was obtained. Every volunteer has a recovery period of 15 min after a task finished. There are altogether  $8(4 \times 2)$  tasks for one volunteer.

In the LIFT, the participants lifted boxes from the ground to a 100 mm platform, and then the volunteers lowered boxed to ground. One task included 48 times load lifting, costing 8 min in a fixed frequency, 6 times per minute. After a participant finished one task, he/she had 15 min to recover, and then started the next.

In the CARRY, The participants carried the boxes to go upstairs second floors, 5.94 m height, and then went downstairs. One task included two repetitions, lasting above 5 min. The participant had been suggested the most appropriate posture and speed, so the times they took was almost 5 min. After a participant finished the task, he/she had 15 min to recover, and then tested the next task. Then, the participant was asked to stand 35 cm away from the platform. The box was in front of him/her on ground.

The initial weight was 15 kg for female and 20 kg for male. At the break, the participant has been asked if the load was too heavy. If the load was too light (overweight), increase (decrease) 1 kg for the next test, until the subject agreed that was the weight that can be carried for a long time, and we record the value. After a participant finished the task, he/she had 30 min to recover, and then tested the next prototype.

## 2.4 Data Recording

Before the experimental began, the participants have been informed about the content of the experiment and its procedures and precautions to follow. And some physical dates were collected. A pre-test was conducted to find out the weight range of load used for the experiment.

### 2.4.1 Oxygen-Consumption

The HR could Heart rate can be used to estimate the oxygen consumption. In this study, 6 kg was acceptable for both male and female to handle in a long time.

First, we putted the load into the boxes and sealed the top. Then, the participants were asked to put on the heart rate Tester (PolarH10, Polar, Finland). Heart rate (HR) was continuously recorded during the experimental. When participants were seated and relaxed, before the task started, resting heart rate was recorded in a period (30 s). Every participant completed the tasks as required. Work HR was the average value calculated from the Heart rate at the three time points, which was 10 s before the end of task, the end of the task, 10 s after the end of task. The change value, work HR minus resting HR, characterized the energy consumption to complete tasks. Measurements were performed under normal temperature and relative humidity conditions ( $23 \pm 1.2$  °C and  $55 \pm 4\%$ , respectively).

### 2.4.2 Mawl

The maximum acceptable weight of load (MAWL) was an indicator of physiological load in MMH tasks [9]. At the beginning, the load was a bit overweight (15 kg for female, 20 kg for male) so that some participants maybe couldn't complete tasks. If the participant couldn't finish the task by standard or felt too tired after completed task, the weight of load would be reduced by 1 kg each task. After a recovery time, the next same process was conducted. The weight was adjusted constantly until the participant agreed that weight was the maximum weight they can deal without any uncomfortable, tired feeling and out of breath.

### 2.4.3 Subjective Assess

Body parts discomfort (BPD) [10] for palm and twist was recorded by questionnaire after participants finished CARRY and LIFT. The pain feeling was divided from 0 = no feelings to 10 = extremely painful. And the overall preference for every prototype was recorded by questionnaire considering the comfort, convenience or personal reason, grading from 1 = hate to 10 = love.

### 3 Results

Heart rate increment of four boxes was showed in Fig. 2. There was no statistical difference between them in both LIFT and CARRY (Fig. 3).

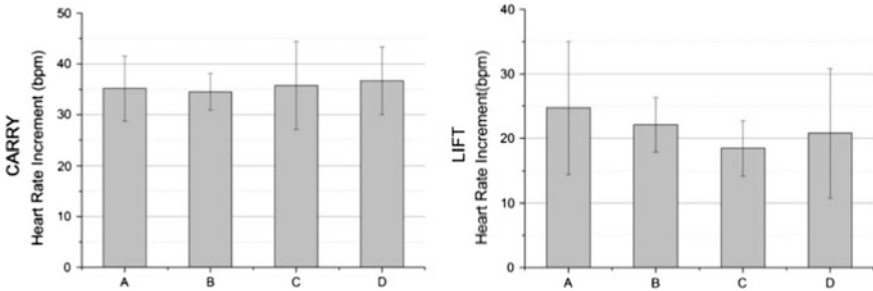


Fig. 2. Heart rate increment. In all picture, “\*\*” means significantly ( $p < 0.05$ )

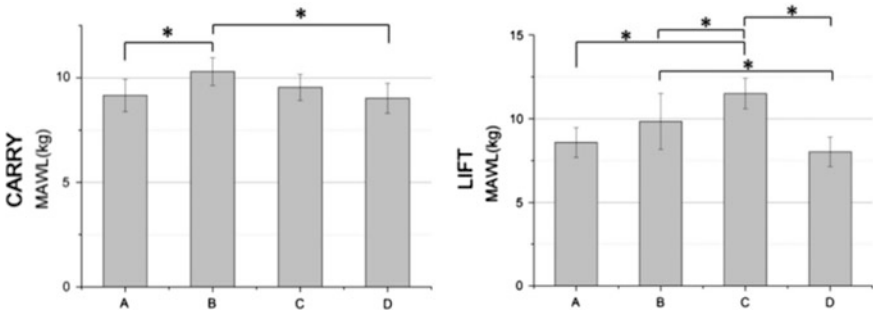


Fig. 3. Maximum acceptable weight of load in CARRY and LIFT

In CARRY, The MAWL for B was the highest and was significantly ( $P < 0.05$ ) higher than A and D, followed by C, which had no significant relationship with others. Otherwise, C has the significantly higher MAWL in LIFT, then the B significantly higher than D, strongly higher than A ( $P = 0.069$ ).

Subjects presented significant palm pain when using Prototype C, compared to other types of boxes in both CARRY and LIFT. The other three boxes didn't have much difference. There was no significant difference between in wrist pain when the subjects used the four boxes in both tasks as Fig. 4 shows. Prototype C didn't have the expected advantage of improving wrist comfort. In LIFT the most preferred box is prototype B. however, in CARRY the most preferred is prototype C as Fig. 5 shows.

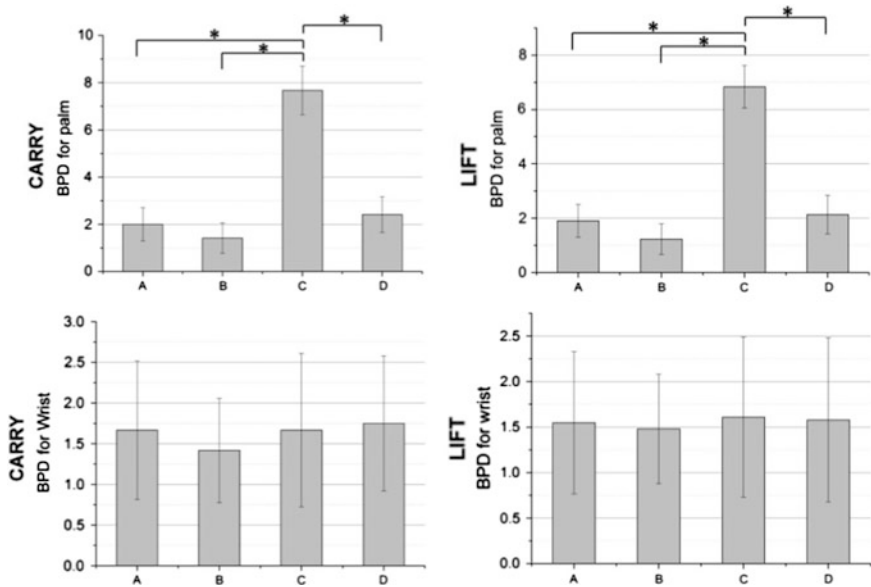


Fig. 4. Body part discomfort for palm and wrist in both tasks

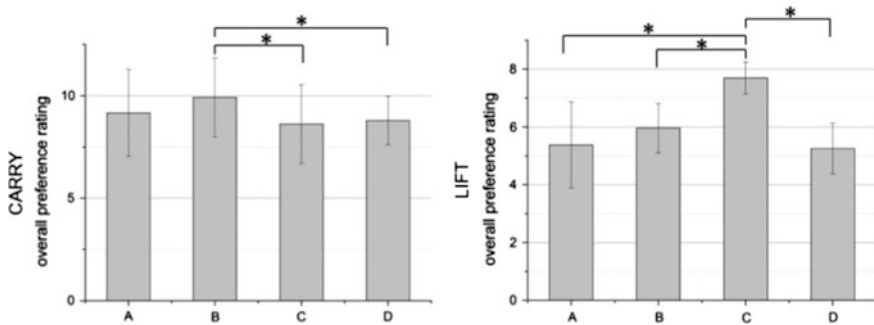


Fig. 5. Overall preference rating for four prototypes

## 4 Discussions

The present research aimed to evaluate the impact of four different handles on physiological and psychological responses during common MMH tasks. We can find that subjects preferred different handles in different tasks.

In LIFT, C was the most favorite handle corresponding to the largest MAWL. These consequences were in accordance with HWA-S JUNG's study that reported upper handle for box has the lower total numbers of BPD than lower handle [7]. Comparing the four handles in this study, the order from the lowest to the highest position at the beginning of the LIFT task is A, D, B, C. Most Participants (95%)

unconsciously choose the self-squat technique posture to lift the prototypes. With knee flexion angle fixed, the angle between the upper body and the ground decreased as the handle position lower. The more Upper limb flexion, the higher the shear force applied on L5-S1 vertebrae lumbar is [11]. Moreover, it is obvious that the prototype C has the highest palm BPD because it has the smallest contact area with the palm. Cut corrugated cardboard's cross section was consisted of five paper cross section, so sharp that made obvious impressions on participants' palm after completing the tasks. Other prototypes contacted with hands by the surface paper, and the contact areas were larger than C.

In CARRY, the prototype B has the highest MAWL and preference. In this study, all the participants choose the same position to carry boxes, consistent with Philippe Corbel's study [12]. When participants carry the box they hold it close to the body with waist forward. And they keep the elbow degree as large as possible. This gesture that the subjects consciously choose can be combined with the lifting force to balance the box gravity by increasing the friction between abdomen and box. The elbow angles when they carry box was more than  $90^\circ$ . The more the angle is, the less the force the upper limb need to apply [13]. The Boxes have upper position handles would block leg activity. So the B is more preferred. The carry task includes picking up box from plat and walking with box. The first stage affects the MAWL and whole preference like in the lift task. In the second stage, participants hold the box for a lasting time, the oppression for hand is more obvious than in lift task. So the BDP for palm is similar to that in lift task. The heart rate change was not affected by boxes, different from the SP Wu's [8] conclusion. The test time may result in this difference.

## 5 Conclusions

After comparing the current handle, redesigned handles and new designed handle, we can found that an appropriate handle could reduce physiological load and increased the comfort for courier. The improvements for handle confirmed in this study are: (1) an upper position for lift task, a lower position for carries task; (2) uncut palm contact surface; (3) a space for hand to insert before tasks start. Future studies are required to confirm the research findings through controlled experimental testing. Using the EMG to test the related muscle activity to research how these handles affect the work performance.

**Compliance with Ethical Standards. Funding:** This study is funded by the “creative packaging advertising base's special research projects” of Hunan (No. 17JDXMB04) and Hunan Province Education Department Ordinary University Teaching Reform Research Project (No. [2017]452–276).

**Conflict of Interest:** The authors declare that they have no conflict of interest.

**Ethical approval:** All procedures performed in studies involving human participants were in accordance with the ethical standards of the school of packaging and material engineering, Hunan University of Technology and with the 1964 Helsinki declaration and its later amendments or comparable ethical standards.

**Informed consent:** Informed consent was obtained from all individual participants included in the study.



## References

1. Garg, A., & Saxena, U. (1980). Container characteristics and maximum acceptable weight of lift. *Human Factors the Journal of the Human Factors & Ergonomics Society*, 22(4), 487–495.
2. Collaborators, I. P. (2017). Global, regional, and national incidence, prevalence, and years lived with disability for 328 diseases and injuries for 195 countries, 1990–2016: a systematic analysis for the Global Burden of Disease Study 2016. *Lancet*, 390(10100), 1211–1259.
3. Ekman, M., Johnell, O., & Lidgren, L. (2005). The economic cost of low back pain in Sweden in 2001. *Acta Orthopaedica*, 76(2), 275.
4. Coury, B. G., & Drury, C. G. (1983). Optimum handle positions in a box-holding task: *Ergonomics*. *Applied Ergonomics*, 14(4), 311–311.
5. Drury, C. G. (1980). Handles for manual materials handling. *Applied Ergonomics*, 11(1), 35–42.
6. Snook, S., & Ciriello, V. (1991). The design of manual handling tasks: Revised tables of maximum acceptable weights and forces. *Ergonomics*, 34(9), 17.
7. Jung, H. S., & Jung, H. S. (2010). A survey of the optimal handle position for boxes with different sizes and manual handling positions. *Applied Ergonomics*, 41(1), 115–122.
8. Wu, S. P., & Chang, S. Y. (2010). Effects of carrying methods and box handles on two-person team carrying capacity for females. *Applied Ergonomics*, 41(4), 615–619.
9. Ayoub, M., M. (1989). Manual materials handling.
10. Corlett, E. N., & Bishop, R. P. (1976). A technique for assessing postural discomfort. *Ergonomics*, 19(2), 175–182.
11. El Ouaid, Z., & Shirazi-Adl, A., Plamondon A. (2017). Trunk response and stability in standing under sagittal-symmetric pull-push forces at different orientations, elevations and magnitudes. *J Biomech*, <https://doi.org/10.1016/j.jbiomech.2017/10.008>.
12. Corbeil, P., Plamondon, A., Handrigan, G., Vallée-Marcotte, J., Laurendeau, S., Ten Have, J., & Manzerolle, N. (2019). Biomechanical analysis of manual material handling movement in healthy weight and obese workers. *Applied Ergonomics*. <https://doi.org/10.1016/j.apergo.2018.08.018>.
13. Hunsicker, P. A. (1955). Arm strength at selected degrees of elbow flexion. *Technical Report*, No, WADC-TR-54-548.



# Automated Box Buckling Strength Analyses with Finite Element Modeling

Shane Johnson<sup>1,2</sup>, Liping Kang<sup>3(✉)</sup>, Haihua Ou<sup>1</sup>, Zeeshan Kaiser<sup>1</sup>,  
and Jorge Macort<sup>4</sup>

<sup>1</sup> University of Michigan and Shanghai Jiao Tong University Joint Institute,  
Shanghai Jiao Tong University, Shanghai, China

<sup>2</sup> State Key Laboratory of Mechanical Systems and Vibration, Shanghai Jiao  
Tong University, Shanghai, China

<sup>3</sup> Shanghai WeBuild Smart Technology Co. Ltd., Shanghai, China  
kangliping2018@163.com

<sup>4</sup> The Chamberlain Group, Oak Brook, IL, USA

**Abstract.** Finite element analysis (FEA) provides valuable information for buckling/stacking analyses of corrugated boxes. However, FEA requires time consuming custom geometric analysis and specialized structural engineering personnel with background in modeling of nonlinear anisotropic viscoelastic material like paper products. This research studies a systematic approach by which simple geometric and paper properties are input and buckling strength/deformed box shapes are output. All the analyses will be conducted in a FEA software (ABAQUS) including geometric modeling and auto-meshing, material nonlinear anisotropic homogenization of corrugated board, and automated outputs. The systematic approach provides a rapid analyses tool for non-specialized personnel to achieve accurate buckling/stacking analysis of corrugated box.

**Keywords:** Corrugated board buckling strength · Auto-meshing algorithm · Homogenization · Finite element modeling

## 1 Introduction

Corrugated boxes are widely used in food packaging, horticulture packaging, electronics packaging, daily necessities packaging and other industry packaging etc. [1, 2] because of various attributes including low cost, high versatility, easy handling process, and short recycle period etc. [3]. However, mechanical behavior of the corrugated paperboard is complex due to its time dependent characteristics with reference to manufacturing, moisture dependence, load, and temperature etc. [4, 5]. Thus, extensive and time consuming analyses and experiments are needed to design corrugated boxes against environmental impact and loadings such as compression during stacking, vibration during transportation, impact, temperature and moisture effects etc. [6–10] especially for expensive and/or fragile products like eggs, fruit, and electronics, etc. However, most packaging outfits lack the expensive/complicated equipment for extensive experiments and/or lack specialized personnel (e.g. structural engineers) for

the analyses of the corrugated boxes. This leads to a lack of understanding and/or analyses of corrugated boxes against environmental impact and loadings, and eventually leads to damage of the corrugated boxes during transportation, stacking, and handling process etc. Thus, there is a great need for developing an easy and accurate approach for non-specialized personnel/company to conduct the performance analyses of the corrugated boxes.

This paper will first give a brief introduction of the traditional method being used for analyses of corrugated boxes and then a new computational framework will be introduced for providing efficient and accurate analyses of corrugated boxes with easy interface.

## **2 Traditional Method for Analyzing Corrugated Boxes**

Traditional methods for analyzing the strength and failure of corrugated boxes include experiments, analytical models, and computational software. A thorough detailed introduction of these methods was previously discussed by Frank [11].

Experiments are the most direct way to analyze corrugated boxes. They provide strength, failure modes, and stress and strain information etc. of the corrugated boxes. However, professional personnel with structural engineering expertise are needed to analyze complexed geometry and complicated material properties of the paper in addition to expensive equipment (such as Universal Material Testing Systems and environmental chambers) and time consuming test cycle needed for the test.

Several researchers have developed analytical models [12–18] for analyses of corrugated box such as the McKee equation. These are semi empirical models for box buckling analyses which require heavy and costly experimentation through fabrication and testing of ECT, bending, and box specimens for model calibration. Urbanik and Frank later developed the Generalized McKee Equation. However, all these analytical models are limited to vertically loaded regular slotted containers (RSC). These model are not suitable for boxes with other styles and loading conditions.

Commercial software [19–22] based on these models were also developed to predict box compression strength or stacking strength. The models are easy to implement and thus widely used in industry. However, only a limited number of them can predict box performance based on paper properties [12, 14, 21, 22], so extra characterization of corrugated boards such as edge crush tests (ECTs) have to be conducted before using the models. Also, they are limited to a specific box type such as tubes [13] or regular slotted containers (RSCs) [14, 21]. Furthermore, box features such as slots as often seen in vented fruit box or inserts are difficult to be accounted for in these models.

## **3 Proposed Computing Framework**

The objective of this computing framework is to provide a general analyses tool for efficient and accurate analyses of corrugated boxes with cloud computing option. This framework includes four modules named geometry module, material module,

boundary/loading module and analysis module. Users only need to define the geometry of the box (length, width, height, folds, cut-outs, scoring, and staples information etc.), material property of the paper (liner and medium paper properties) and to specify the output results needed (BCT, failure or yield zones, stress fields, load vs. displacement, etc.) in the user interface page. The job will be submitted to and conducted in a computing platform through a cloud computing option and the output (BCT, Stacking strength, etc.) report will be sent back to users after the job is done.

Finite element analyses of the corrugated boxes will be conducted in ABAQUS including: automeshing of CAD model, automatic FEA model construction (including: material homogenization of the paper, boundary application, etc.), and nonlinear analysis of corrugated boxes. Riks method with imperfections is used in nonlinear analysis for prediction of buckling mode for corrugated boxes as shown in Fig. 1. The buckling modes of the box are obtained by Eigen mode buckling analysis and then the linear combination of the buckling modes with a scaling factor is used as imperfections for the nonlinear Riks analysis. Since model convergence is not guaranteed for a particular analysis, a convergence analysis is conducted with various levels of imperfection to automatically determine the BCT.

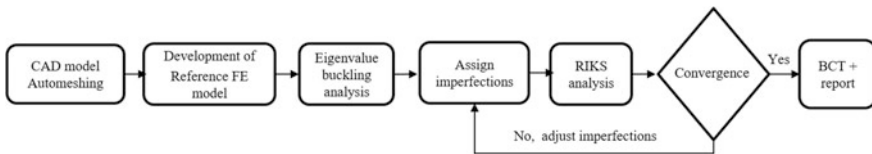


**Fig. 1.** Nonlinear analysis using Riks method with imperfections

Compared with analytical/empirical models and commercial software, the framework developed in this study has the advantages of (1) predicting box performance based on paper properties; (2) for different box types including RSC, EFOL, TFOL etc.; (3) with special design features such as scores, hand holds, ventilation holes, staples, etc. Compared with traditional finite element models, this framework has the advantage of predicting BCT for different box types without the requirement of professional structural engineers.

## 4 Case Study and Experimental Validations

For demonstration, three corrugated boxes with different box types (RSC, TFOL, and EFOL), sizes, corrugated board combinations, fluting types and relative humidity were modeled for the maximum box compression test strength values (BCT) predictions and compared with experimental results. Details of the boxes are shown in Table 1. These corrugated boxes were first conditioned (ASTM D685), and then kept in humidity chamber for 72 h under a set humidity level, and then compression tested (ASTM D642-15) in a Material Testing System (MTS) with a floating upper compression platen and fixed lower platen.

**Table 1.** Information of the corrugated boxes being analyzed

Box model	Outer dimension (mm)	Liner-medium-liner basis weight combination ( $\text{g/m}^2$ )	Fluting	Relative humidity (%)	Number of specimens
RSC	$304.8 \times 304.8 \times 304.8$	66.6-38.5-66.6	C	50	2
TFOL	$673.1 \times 198.4 \times 320.5$	51.8-48.8-51.8	B	85	4
EFOL	$282.4 \times 236.5 \times 487.4$	62.2-59.2-82.9	B	65	3

BCT from FE predictions and experiment are shown in Fig. 2. The prediction error varies from 3.6 to 14.4% for different boxes. The error for EFOL is larger than that of RSC and TFOL, and this is likely because of more details including hand holds and staples that are simulated in the FE models of EFOL. These details largely affect the side panel bending stiffness since 4 panels are partially bonded with the staples and with the stress concentration of the hand holds, these accumulate errors in the simulations.

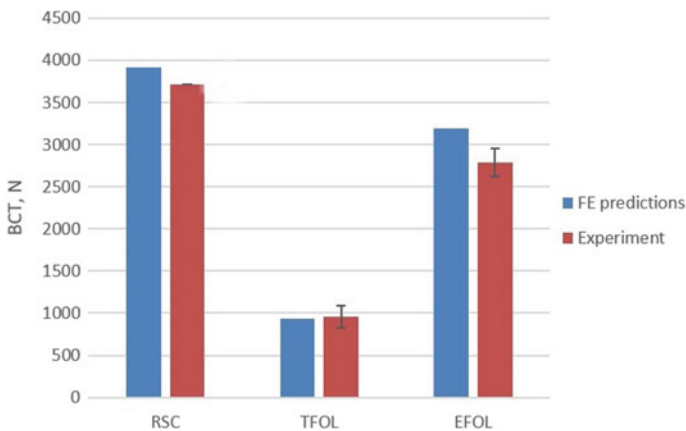


**Fig. 2.** Model predictions and experimental results for box BCT of 3 different box types. Note that the error bar for RSC's are not shown due to limited number of samples tested

## 5 Conclusions

This paper gives a brief introduction of the analysis methods of corrugated boxes and discusses the pros and cons of these approaches. Then, a new efficient and accurate computing framework is proposed with a cloud computing option for users without specialized background in structural/material/mechanical engineering. Users can easily define the inputs, and the job will be sent to the platform through the cloud computing option. Finite element models of corrugated boxes will be generated automatically in ABAQUS and the analyses will be done automatically. The report will be sent back to the users automatically after the job is done. This framework can analyze corrugated

boxes (1) with different sizes; (2) with different box types and geometries; (3) with material property directly from paper; (4) rapidly with acceptable accuracy; (5) without the need for specialized personnel (e.g. structural engineers). Thus, this framework enables users/packaging companies to optimize the design/logistics of the corrugated boxes rapidly and cost effectively as compared with other approaches available in the literature and/or market.

**Acknowledgements.** The authors are very thankful for the donation of kraft paper and corrugated box specimens from the Chamberlain Group in Oakbrook, Illinois. This research is funded by National Natural Science Foundation of China under grant No. 51505282 and No. 51750410692.

## References

1. Chamberlian, D., & Kirwan, M. J. (2013). Paper and paperboard-raw materials. In *Processing and Properties. Handbook of Paper and Paperboard Packaging Technology*. New York: Wiley, Ltd.
2. Opara, U. L., & Mditshwa, A. (2013). A review on the role of packaging in securing food system: Adding value to food products and reducing losses and waste. *African Journal of Agricultural Research*, 8, 2621–2630.
3. Kaushal, M. C., Sirohiya, V. K., & Rathore, R. K. (2015). Corrugated board structure: A review. *International Journal of Application of Engineering and Technology*, 2, 228–234.
4. Haslach, H. W. (2009). Time-dependent mechanisms in fracture of paper. *Mechanics of Time-dependent Materials*, 13, 11–35.
5. Johnson, S., & Popil, R. (2015). Corrugated board bonding defect visualization and characterization. *International Journal of Adhesion and Adhesives*, 59, 105–114.
6. Fadiji, T., Berry, T. M., Coetzee, C. J., & Opara, U. L. (2018). Mechanical design and performance testing of corrugated paperboard packaging for the postharvest handling of horticultural produce. *Biosystems Engineering*, 171, 220–244.
7. Pascall, M. A. (2010). *Packaging for fresh vegetables and vegetable products. Handbook of vegetables and vegetable processing*. Oxford: Wiley-Blackwell.
8. Rhim, J. W. (2010). Effect of moisture content on tensile properties of paper-based food packaging materials. *Food Science and Biotechnology*, 19, 243–247.
9. Navaranjan, N., & Johnson, B. (2006). *Modelling and experimental study of creep behaviour of corrugated paperboard*. Melbourne, Australia: Publisher.
10. Pathare, P. B., & Opara, U. L. (2016). Changes in moisture content and compression strength during storage of ventilated corrugated packaging used for handling apples. *Packaging Research*, 1, 1–6.
11. Frank, B. (2014). Corrugated box compression—a literature survey. *Packaging Technology and Science*, 105–128.
12. Katsuoki, K. (1989). Estimation of the compression strength of corrugated fibreboard boxes and its application to box design using a personal computer. *Packaging Technology and Science*, 2, 29–39.
13. Kellicutt, K. Q., & Landt, E. F. (1951). Safe stacking life of corrugated boxes. *Fibre Containers*, 36, 28–38.
14. Maltenfort, G.G. (1956). Compression strength of corrugated container. *Fibre Containers*, 41.

15. McKee, R. C., Gander, J. W., & Wachuta, J. R. (1961). Edgewise compressive strength of corrugated board. *Paperboard Packaging*, 46, 70–76.
16. Schramper, K. E., Whitsitt W. J., & Baum G. A. (1987). *Combined board edge crush (ECT) technology*. Appleton: Institute of Paper Chemistry.
17. Urbanik, T. J., & Frank, B. (2006). Box compression analysis of world-wide data spanning 46 years. *Wood and Fiber Science*, 38, 399–416.
18. Whitsitt, W. J., Gander, J. W., & McKee, R. C. (1968). *Effect of box dimensions and combined board creep life on box creep life*. Appleton: Institute of Paper Chemistry.
19. Sohrabpour, V., & Hellstrom, D. (2011). *Models and Software for Corrugated Board and Box Design*. Publisher.
20. Biancolini, M. E., & Brutti, C. (2003). Numerical and experimental investigation of the strength of corrugated board packages. *Packaging Technology and Science*, 16, 47–60.
21. Fadiji, T., Coetzee, C., & Opara, U. L. (2016). Compression strength of ventilated corrugated paperboard packages: Numerical modelling, experimental validation and effects of vent geometric design. *Biosystems Engineering*, 151, 231–247.
22. Han, J., & Park, J. M. (2007). Finite element analysis of vent/hand hole designs for corrugated fibreboard boxes. *Packaging Technology and Science*, 20, 39–47.



# Experimental Study on Material Matching for Corrugated Board Box of Lithium Battery

Chenyang Liu, Lijiang Huo<sup>(✉)</sup>, Wanping Zhan, and Yizhe Tian

School of Light Industry and Chemical Engineering, Dalian Polytechnic University, Liaoning, China  
lijianghuo@163.com

**Abstract.** Material matching for corrugated board box of lithium battery was carried out in this paper. Four-layer corrugated board (250 g/170 g/100 g/250g C stare blankly, match material g weight from left to right in order to face paper, corrugated paper and inside paper, the following is the same) and five-layer corrugated board (200 g/120 g/120 g/120 g/200g BA stare blankly) with the same quantity and size were selected as materials of the corrugated board box, and the changes of physical and mechanical properties of these two kinds of corrugated boards and their packaging cartons under different transportation environment conditions were tested and analyzed. The results show that the four-layer corrugated cardboard and its cartons are better than the five-layer corrugated cardboard and its cartons in transport protection performance under various temperature and humidity conditions selected in the experimental study.

**Keywords:** Lithium battery · Transport packaging · Corrugated board box · Material matching

## 1 Introduction

Lithium batteries, as a clean, efficient, energy-intensive and memory-free energy source, are increasingly used in our daily life. Lithium battery is a kind of dangerous chemicals. In the more severe transportation environment, it is easy to cause the damage of lithium batteries due to unqualified transportation packaging, and ultimately lead to irreparable consequences. Especially in recent years, the regional circulation of lithium batteries has increased rapidly, which puts forward higher requirements for the safety performance of lithium battery transport packaging protection. Therefore, through simulating the common transportation environment, the comprehensive protection performance of lithium battery transportation packaging box was tested and analyzed. The purpose of this paper is to explore the influence of different transportation environment conditions on the transportation safety performance of packaging carton, and then put forward scientific improvement measures and more reasonable lithium battery packaging scheme, and comprehensively improve its transportation protection performance.



## 2 Material Matching and Performance Testing for Corrugated Board Box of Lithium Battery

### 2.1 Material Matching for Corrugated Board Box of Lithium Battery

In the experimental study, the style of the corrugated board box is 0201. Its inside size are  $L = 300$  mm,  $B = 250$  mm,  $H = 310$  mm. The weight of lithium batteries in the carton is 20 kg. According to GB/T 6543-2008 [1] and GB/T 6544-2008 [2], four-layer corrugated board (250 g/170 g/100 g/250g C stare blankly, match material g weight from left to right in order to face paper, corrugated paper and inside paper, the following is the same) and five-layer corrugated board (200 g/120 g/120 g/120 g/200g BA stare blankly) with the same quantity and size were selected as materials of the corrugated board box.

### 2.2 Performance Testing for Corrugated Board Box of Lithium Battery

According to GB/T4857.2-2005 [3] and actual situation of transportation, ten kinds of experimental environment conditions were design, such as 20°/RH30%, 30°/RH30%, 38°/RH30%, 23°/RH50%, 20°/RH65%, 30°/RH65%, 38°/RH65%, 20°/RH90%, 30°/RH90%, 38°/RH90%. The reference standards and test items in the study are listed in Table 1 [4–8].

**Table 1.** The reference standards and test items

Test items	National standards
Compressive strength	GB/T 4857.4
Edge compressive strength	GB/T6546
Breaking strength	GB/T 6545
Puncture strength	GB/T 2679.7
Rate of water content	GB/T 462

The samples were prepressed 72 h in climatic chamber, then performance testing were taken.

## 3 Results and Discussion

The testing results of compressive strength, edge compressive strength, breaking strength, puncture strength and rate of water content were shown in Figs. 1, 2, 3, 4 and 5. The two kinds of samples in the experiments were indicated as B47B and S555S.

The results show that the four-layer corrugated cardboard and its cartons are better than the five-layer corrugated cardboard and its cartons in transport protection per-

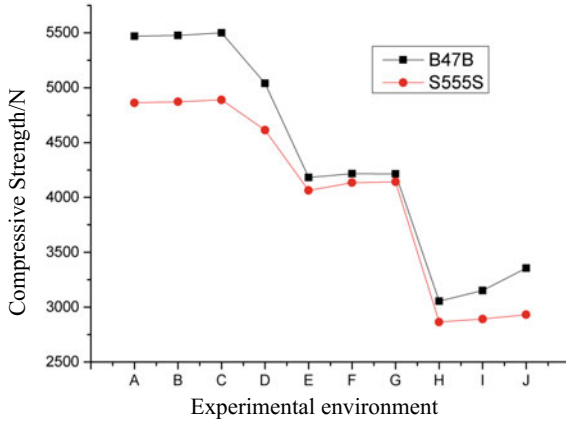


Fig. 1. The comparison of compressive strength of carton

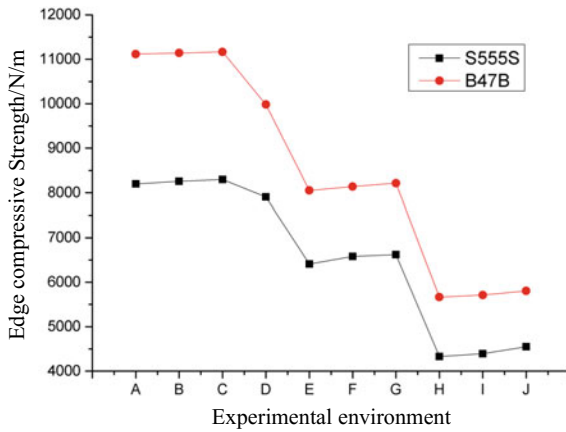


Fig. 2. The comparison of edge compressive strength of paperboard

formance under various temperature and humidity conditions selected in the experimental study. The comprehensive physical properties of corrugated board box reached the highest under the conditions of 23 °C and RH50%. It can be seen that the influence of ambient temperature on the physical and mechanical properties of corrugated board and corrugated board box is relatively small under the same humidity condition.

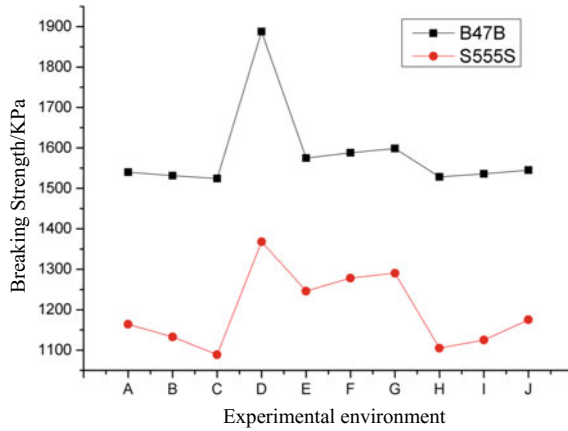


Fig. 3. The comparison of breaking strength of paperboard

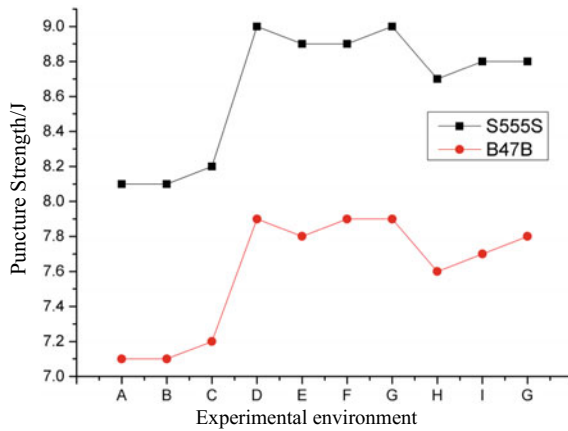


Fig. 4. The comparison of puncture strength of paperboard

### 4 Conclusions

Though the experiments of material matching for corrugated board box, the results show that corrugated board box can be used for packaging lithium batteries. Comparatively, the four-layer corrugated board (250 g/170 g/100 g/250g C stare blankly) has advantage in combination property for matching material in corrugated board box design and manufacture for packaging lithium batteries.

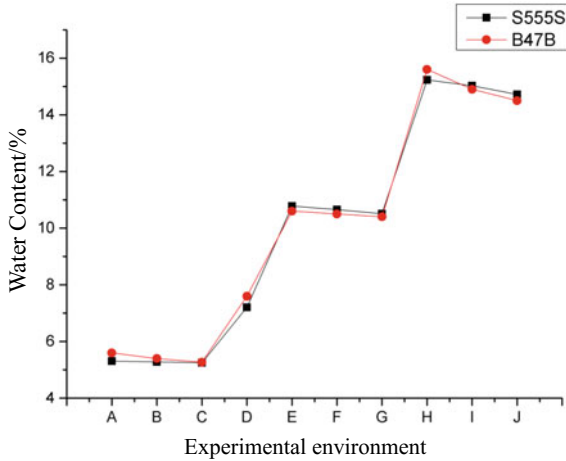


Fig. 5. The comparison of rate of water content of paperboard

### References

- Huang, Y. (2010). GB/T6543-2008 Standard application to corrugated board box used in transport packaging. *Printing Technology*, 6, 50–51.
- Huang, Y. (2010). GB/T6544-2008 Standard of corrugated board. *Printing Technology*, 4, 34–35.
- State Administration for Quality Supervision and Inspection and Quarantine of China, the National Standards Administration Commission of China, GB/T4857.2-2005, State Standard of the People’s Republic of China, transport packaging test, the second part: Temperature and humidity control.
- State Administration for Quality Supervision and Inspection and Quarantine of China, the National Standards Administration Commission of China, GB/T 4857.4-2008, State Standard of the People’s Republic of China.
- State Administration for Quality Supervision and Inspection and Quarantine of China, the National Standards Administration Commission of China, GB/T 6546–1998, State Standard of the People’s Republic of China.
- State Administration for Quality Supervision and Inspection and Quarantine of China, the National Standards Administration Commission of China, GB/T 6545–1998, State Standard of the People’s Republic of China.
- State Administration for Quality Supervision and Inspection and Quarantine of China, the National Standards Administration Commission of China, GB/T 2679.7-2005, State Standard of the People’s Republic of China.
- State Administration for Quality Supervision and Inspection and Quarantine of China, the National Standards Administration Commission of China, GB/T 462-2003, State Standard of the People’s Republic of China.



# Stress Analysis of the Glass Cup in the Process of Falling Based on the Finite Element Method

Xiaoli Song<sup>(✉)</sup>, Gaimei Zhang, Lizheng Zhang, Yue Cao,  
and Changhe Li

School of Printing and Packaging Engineering, Beijing Institute of Graphic  
Communication, Beijing, China  
songxiaoli09@163.com

**Abstract.** In order to study the stress distribution and the maximum stress of the glass cup in different drop heights and different drop ways, the mechanical properties of glass during falling process was analyzed based on the finite element method. The results show that as the drop height increases, the stress of the glass cup will gradually increase and the stress distribution area will broaden. When the stress reaches the maximum, the glass cups will be broken. Due to diverse drop ways, the stress and the stress distribution area of the glass cup is different, and the stress distribution area is not proportional to the drop angle of the glass cup.

**Keywords:** Finite element method · Stress glass

## 1 Introduction

During the process of transportation, products are damaged mainly by dropping. Therefore, it is of great value to study dynamic characteristics. The damage of objects due to the drop is not only related to their fragility, but also to drop heights and drop ways [1–3]. Most of traditional researches are based on theoretical analysis or experimental test. Theoretical researches are expensive. Moreover, measured physical data is very limited, making it difficult to acquire continuous spatial and temporal results and unable to completely display the structural response and structural deformation mechanism during dropping [4]. However, dynamic simulation of the dropping can clearly analyze the dynamic response of packages under shock and vibration excavate, obtain the test data which cannot be gained from physical experiments. Then main factor is analyzed based on the simulation results. Reasonable elastic elements are designed based on the results. The R&D speed of products is significantly improved. Thus, it is with obvious superiorities and embraces some application significance in transport packaging [5–7].

Glassware is featured by favorable appearance, high chemical stability and corrosion prevention, so it is widely applied to various fields. However, glass is fragile and is likely to be broken due to external vibration, collision and drop during transportation and use. In this Paper, the simulation test is conducted for the drop of glasses based on finite element method in order to study the mechanical property of glasses under different drop heights and in different drop ways [8].

## 2 Modeling and Analysis Process

In the analysis of the glass cup with the finite element method, a 2D glass cup model is built, as shown in Fig. 1. The 2D model is rotated to a 3D model with variable shell, as shown in Fig. 2 [9].

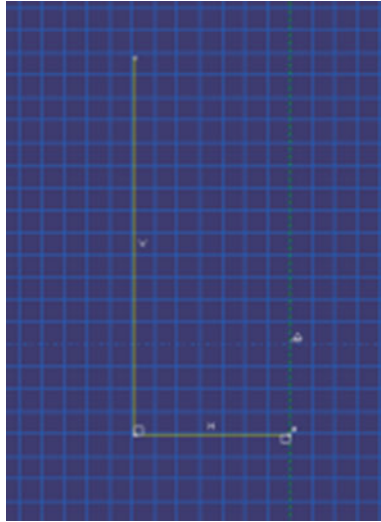


**Fig. 1.** A two-dimensional model of the glass cup

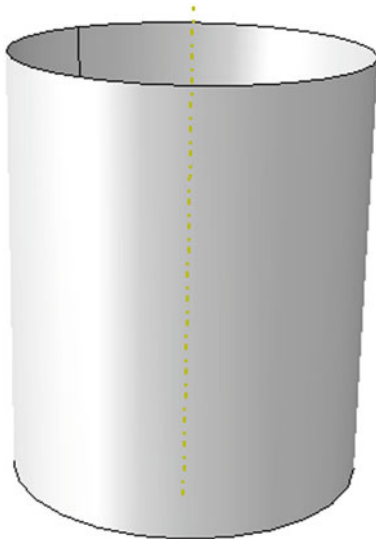


**Fig. 2.** A three-dimensional model of the glass cup

Overall specifications of the glass cup are those of Luminarc 200 ml straight glass cups with round rim. Overall dimensions of the glass cup are shown in Table 1. The material parameters of glass are shown Table 2 [10].

**Table 1.** Parameters of the glass cup (mm)

Body height	Bottom thickness	Wall thickness	Inside diameter of cup rim	Outside diameter of cup rim	Bottom radian
65.800	18.420	7.440	55.140	69.020	45.000

**Table 2.** Material parameters of glass

Material	Density/(g/cm <sup>3</sup> )	Elastic modulus/(GPa)	Poisson's ratio
Glass	2.400	67.000	0.0245

In the analysis, if the motion with gravity impact is calculated by ABAQUS/Explicit, it will take plenty of time to simulate freely falling parts. And it is easy to cause a mistake. So in order to simplify the process, we specify the velocity (m/s) to simulate the initial speed from  $H$  (m) high, namely the  $V$ (m/s) of impact speed on the glass cup, which can be calculated by Eq. (1) [11]. The  $\theta$  is the angle between the ground and the normal of the glass cup, which is shown in Fig. 3.

$$V = \sqrt{2gh} \quad (1)$$

Here,  $g$  is 9.810 (m/s<sup>2</sup>).

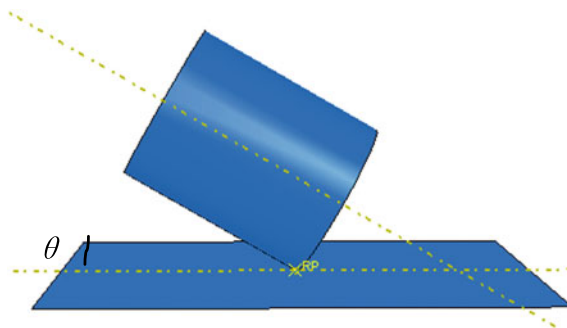


**Fig. 3.** The figure of the model about the  $\theta$

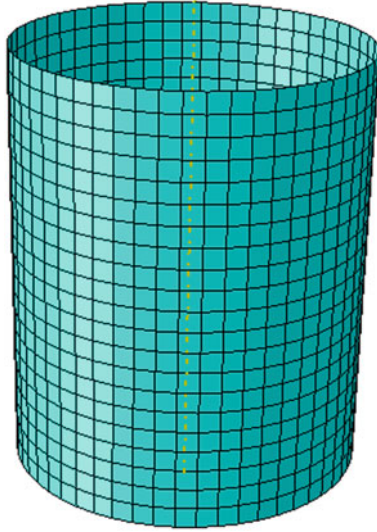


**Fig. 4.** The model of the glass cup after grid division

To produce accurate analysis results, Quad mapping partitioning technology and S4R are adopted to divide the grids, as shown in Fig. 4. The simulation is calculated by Dynamic/Explicit. The outer surface of the glass cup and the ground are both considered to be smooth with no friction resulting from the contact of the two.

### 3 Results and Analysis

#### 3.1 Effect of Drop Height on the Stress Distribution of the Glass Cup

When the  $\theta$  is set as  $30^\circ$ , the stress distribution figure of the glass cup is drawn in different drop heights, as shown in Fig. 5.

It can be discovered from Fig. 5 that the stress is mainly concentrated on the contact between the glass cup and the ground. As the drop height increases, the stress gradually increases and the stress distribution area broadens along with upward delivery. The glass cup is broken when the drop height is 1.600 m. The maximum stress can be queried from the tool create x, y data in the process of dropping. The stress in different drop heights is shown in Table 3.

It can be discovered from Fig. 5 and Table 3 that as the drop height increases, the maximum stress of the glass cup will gradually increase.



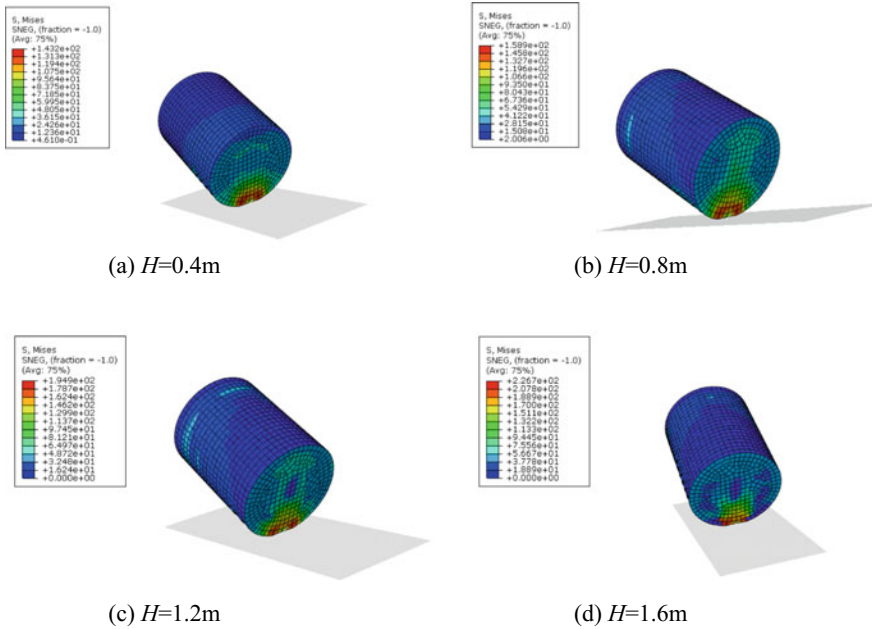


Fig. 5. Stress distribution figure of the glass cup under different drop heights

Table 3. Stress of the glass cup under different drop heights

H/m	0.4 m	0.8 m	1.2 m	1.6 m
$\sigma_{max}/MPa$	69.705	105.734	115.835	193.898

### 3.2 Effect of Different Drop Ways on the Stress Distribution of the Glass Cup

At the drop height  $H = 1.200$  m, the  $\theta$  is respectively set as  $0^\circ$ ,  $30^\circ$ ,  $60^\circ$  and  $90^\circ$ . The stress distribution of the glass cup is shown in Fig. 6.

It can be discovered from Fig. 6 that when  $\theta = 90^\circ$ , the biggest stress distribution area of the glass cup is formed. And the stress distribution area is not proportional to the angle. When  $\theta = 60^\circ$ , the glass cup is broken. Whether the glass cup is broken is much related to their location of contact with the ground. The maximum stress can be queried from the tool create xy data. The maximum stress of the glass cup in different drop ways is shown in Table 4.

It can be discovered from Fig. 6 and Table 4 that when  $\theta = 60^\circ$ , the glass cup is broken, and the instantaneous maximum stress is biggest.

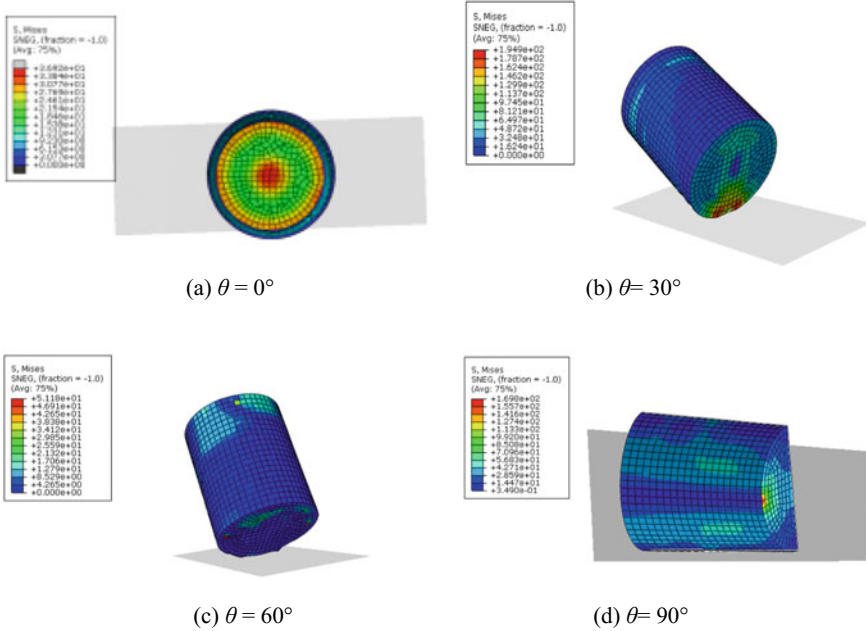


Fig. 6. The stress distribution of the glass cup in different drop ways

Table 4. Maximum stress of the glass cup in different drop ways

$\theta/^\circ$	0	30	60	90
$\sigma_{\max}/\text{MPa}$	124.204	115.835	228.632	193.898

### 4 Conclusions

Comparing the results, the conclusion can be obtained:

- As the drop height increases, the stress of the glass cup will gradually increase and the stress distribution area will broaden. When the stress reaches the maximum, the glass cups will be broken.
- Due to diverse drop ways, the stress and the stress distribution area of the glass cup is different, and the stress distribution area is not proportional to the drop angle of the glass cup.

**Acknowledgments.** The project is supported by the general research projects of Beijing Institute of Graphic Communication (Eb201701, Ed201804), the National Natural Science Foundation of China (51305038) and Bei Yin talent selection and development project of Beijing Institute of Graphics Communication (Byyc201316-016).

## References

1. Zhen, Y., Wencai, X., & Dai, H. (1999). Simulation software based on transportation package. *China Packaging*, 4(19), 101–102.
2. Xia, L., Huan, Q., & Ying-chun, C. (2005). Simulation of the impact response of airdropping cargo. *China Packaging*, 26(5):28–30.
3. Duan, L. (2009). *The Research on drop test of mobile telephone and its' CAE technology*. JiNan: Shandong University.
4. Hua, L. (2008). *Dropping simulation and reliability discussion of washing machine's transport package*. Wuxi: Jiangnan University.
5. Hicks B. J., Mullineux G., & Sirkett, D. (2009). A finite element-based approach for whole-system simulation of packaging systems for their improved design and operation. *Packaging Technology and Science*, 10(12), 84–87.
6. He, T., Yang, J., & Jin, X. (2007). *The example tutorial of nonlinear finite element based on ANSYS/LS-DYNA*. BEIJING: China Machine Press.
7. Zhang, W., & Zhang, A. (2006). Research on static properties of honeycomb paperboard based on ANSYS8.0. *Packaging Engineering*, 27(2), 57–58.
8. Liao, D., & Feng, Y. (2012). Composite packaging's innovation and transformation of glass cup. *China Packaging*, 4, 13–17.
9. Liu, X. (2011). Finite element analysis of dynamic properties of expanded polyethylene cushion packaging system. *Packaging Engineering*, 32(13), 11–13.
10. Zhang, G., Wu, J., & Guo, F. (2011). Drop analysis of pop can based on ANSYS/LS-DYNA. *Packaging Engineering*, 32(5), 4–5.
11. Gao, D., Dong, J., & Li, J. (2006). Research on simulation of dynamic response of corrugated board with nonlinear finite element. *Packaging Engineering*, 27(5), 1–3.



# Analysis on Stress of Laptop and Cushion During Drop Using Finite Element Method

Gaimei Zhang<sup>(✉)</sup>, Xiaoli Song, Fan Su, Yue Shi, Yue Cao, Yi Jiang,  
and Xue Han

School of Printing and Packaging Engineer, Beijing Institute of Graphic  
Communication, Beijing, China  
zhang\_gaimei@163.com

**Abstract.** In order to reduce the damage of laptop during drop experiment and protect the laptop, the finite element simulation is used to analyze the force of the laptop during the drop. Using finite element software ABAQUS, the model of the laptop and cushion packaging are built and the material parameters, drop height and drop types are set. The laptop is built as two parts including top and bottom. The acceleration, stress, strain and other information are obtained. Comparing acceleration and stress, the influence of different cushion on the stress of laptop and cushion during drop are analyzed. The results show that the cushion has a protective effect on the product and absorbs most of the force, and the stress of top and bottom is different during the drop.

**Keywords:** Finite element method · Simulation analysis · Stress · Cushion

## 1 Introduction

The laptop and its package will be impacted by the environment during its distribution. Dropping is one of the key factors leading to product breakage [1]. In order to obtain the property parameters of laptop and evaluate the reliability of the packaging, the test of impact for products in distribution is carried using the traditional method [2]. But it is not only expensive using this method, but also the result is affected by sensors, and only a part of the stress can be obtained [3]. Based on finite element method (FEM), the object is seen as the combination of some finite elements and the unit is simulated and the response of the unit under the load is obtained [4]. Liu et al. [5] studied the influence of different drop ways on liquor packaging based on the finite element method by simulating the dropping experiment with Ansys/LS-DYNA. Shen [6] analyzed the drop for the polyethylene foam buffer system. The simulation results are consistent with the falling curve obtained by the experiment, and the error is within the range of acceptance. Zhang et al. [7] simulated the stress of dangerous goods by changing the drop height and predicted the location of leakage. Liu [8] simulated the drop of the washing machine, the simulation results are in good agreement with the test results. Shi [9] simulated the drop of laptop to study the damage about the structure of laptop during the drop, based on software ABAQUS. Zhang [10] also analyzed the drop of laptop, but the system using cushion wasn't studied. Zhang [11] analyzed the stress of laptop effected by the structure of the cushion, the model is built as a

whole. The model of this paper is divided into two parts. Using finite element software ABAQUS, the model of the laptop and cushion packaging are established and material parameters, drop height and drop types are set. The laptop is built as two parts including top and bottom. The information of acceleration, stress, strain and others are obtained. Comparing acceleration and stress, the influence of different cushion on the stress of laptop and cushion during drop are analyzed. The results show that the cushion has a protective effect on the product and absorbs most of the force.

## 2 Model of Drop for Laptop and Cushion

### 2.1 Model Building and Parameters Setting

The model of laptop is set. The length and width of the laptop are 345 mm and 239 mm respectively, and the thickness is 32.8 mm, and the whole is divided into two parts. The thickness of the top part is 12.8 mm and the bottom part is with 20 mm thickness. The cushion pad is shown in Fig. 1a. The individual parts are assembled in assembly. After assembling, the model of laptop is shown in Fig. 1b. The computer model with cushion is shown in Fig. 1c.

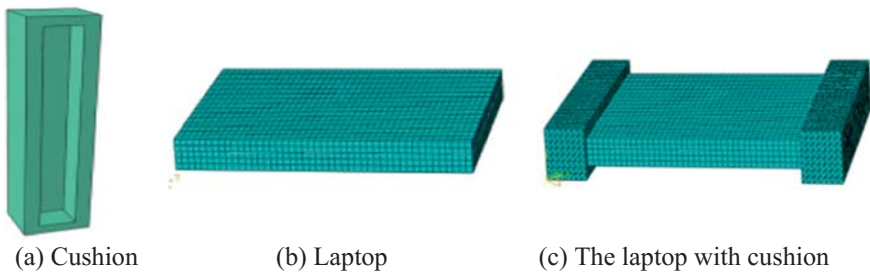


Fig. 1. Model of the laptop and its cushion

Table 1 lists the properties of the laptop and cushion and Tables 2 and 3 show the stress-plastic strain of cushion including EPS and EPE.

Table 1. The property parameters of materials [1–3]

Part	Elastic modulus (MPa)	Poisson ratio	Density (kg/m <sup>3</sup> )	Yield stress (MPa)
Laptop	200	0.394	1.260	57.5
EPS	0.55	0.3	20	
EPE	0.654	0.1	22	

Table 2. Stress-plastic strain data of EPS material [2]

Plastic strain	0	0.02	0.04	0.06	0.08	0.10	0.12	0.14	0.16	0.18	0.20
Stress/MPa	0.08	0.10	0.11	0.18	0.12	0.13	0.14	0.42	0.16	0.16	0.17

**Table 3.** Stress-plastic strain data of EPE material [3]

Plastic strain	0	0.08	0.16	0.24	0.32	0.40	0.48	0.56	0.7	0.78
Stress/MPa	0	0.02	0.03	0.04	0.05	0.06	0.09	0.12	0.20	0.30

The contact between the two parts and connection with tie are set. The restraint and initial speed on laptop and cushion was set. The laptop drops from the 1 m to the ground and its speed is equivalent to 4427 mm/s when it touches the ground.

### 3 Stress Analysis of Laptop During Drop

#### 3.1 Stress Nephogram of Laptop

Figure 2 is the stress nephogram of bottom part of laptop without cushion. Figure 2a shows the state of laptop beginning to drop, Fig. 2b shows the laptop beginning to contact the ground, Fig. 2c show the state of the maximum stress. Figure 2d shows that the laptop begins to move upward, and the stress begins to spread. Figure 3 shows the three dimensions stress nephogram of laptop, it can be found the maximum stress is located at the drop surface.

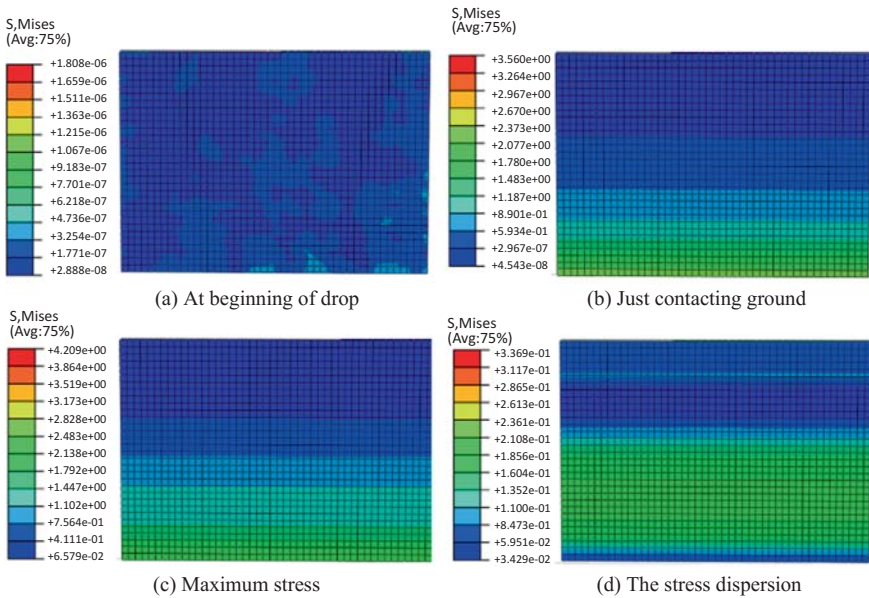


**Fig. 2.** The stress nephogram of laptop during the drop

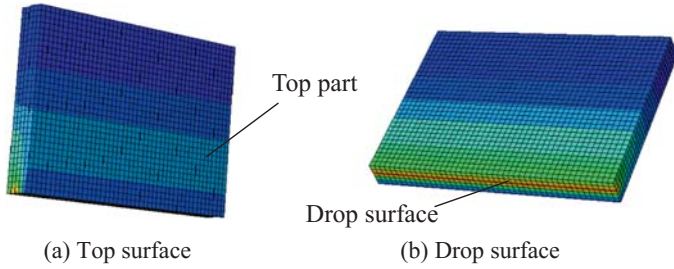


Fig. 3. The three dimensions stress nephogram of laptop at maximum stress state

Figure 4 shows the nephogram of bottom part for laptop with EPS, Fig. 4a shows that the stress is very small at the beginning of drop. Figure 4b shows the compression deformation of cushion, which absorbs most of the stress and reduces the stress on the laptop. The stress nephogram of the cushion packaging is shown in Fig. 5. It can be found that the maximum stress happens at the corner of the cushion, which is consisted with the laptop as Fig. 4b.

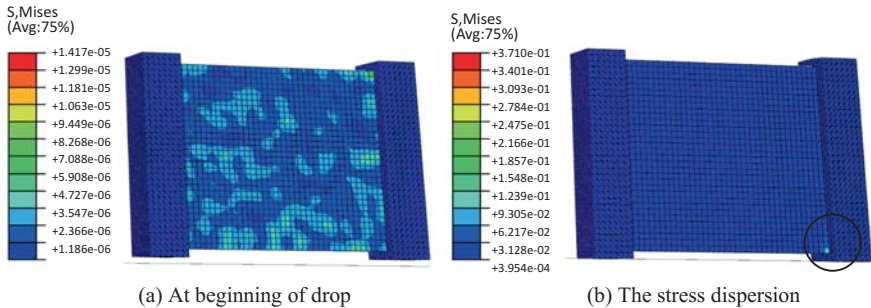


Fig. 4. The stress nephogram of the laptop with EPS

### 3.2 Stress-Strain Curve of Laptop

#### 3.2.1 No Cushion

The laptop is divided into two parts: the top part is thin, the bottom part is relatively thick, the stress and displacement curves are shown in Figs. 6 and 7. In contrast to the stress and displacement of the two parts, the maximum stress in the top part is 2.410 MPa, and the maximum stress in the bottom part is 0.566 Mpa, which indicates that the stress of top part with the same cushion is more than the other. The stress in the two parts is less than the yield stress 57.5 Mpa, and the displacements are 20.317 mm and 20.881 mm for the thin part and thick part. It shows that the deformation of the two parts is not obvious, and there is no dislocation and other phenomena.

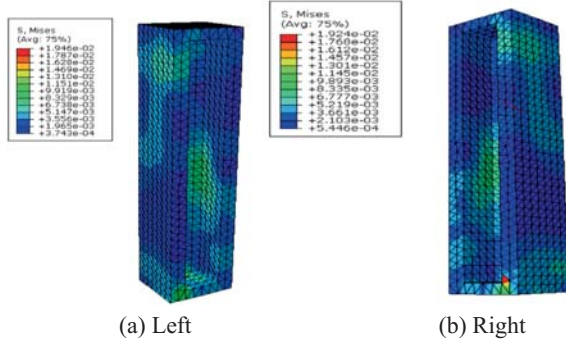


Fig. 5. The stress of the cushion

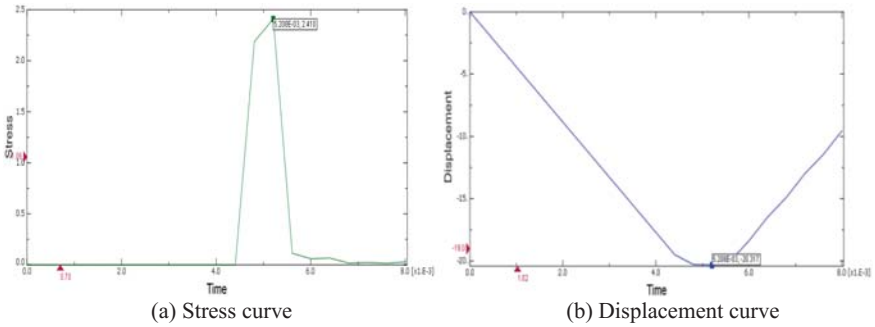


Fig. 6. The stress and displacement curves of the top part

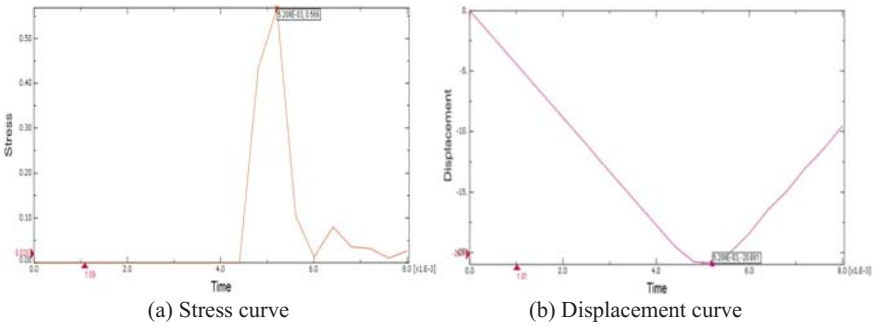
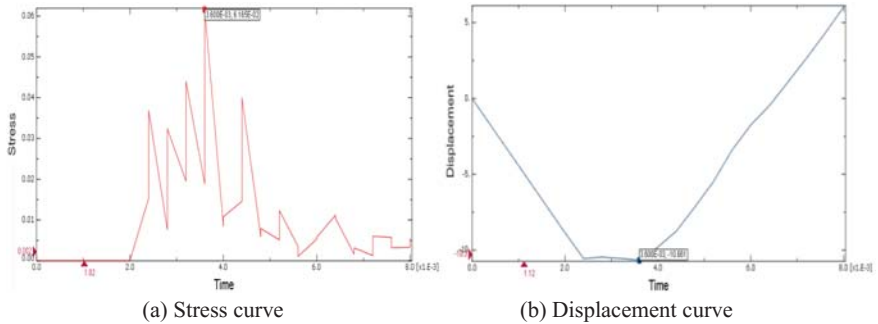


Fig. 7. The stress and displacement curves of the top part without cushion



### 3.2.2 Using Cushion

Figures 8 and 9 show the stress curve and displacement curve of the top part with EPS and EPE cushion respectively. The maximum stress of the top part of laptop using the EPE cushion is 0.05 MPa, less than 0.06 MPa using the EPS, which indicates that the EPS can absorb less stress and leads to more stress on the laptop. The cushioning property of the EPE is better than EPS. It can be seen from Figs. 9b and 8b that the displacement of the laptop is 10.69 mm and 10.66 mm for EPE and EPS.



**Fig. 8.** The stress and displacement curves of the top part with EPS cushion

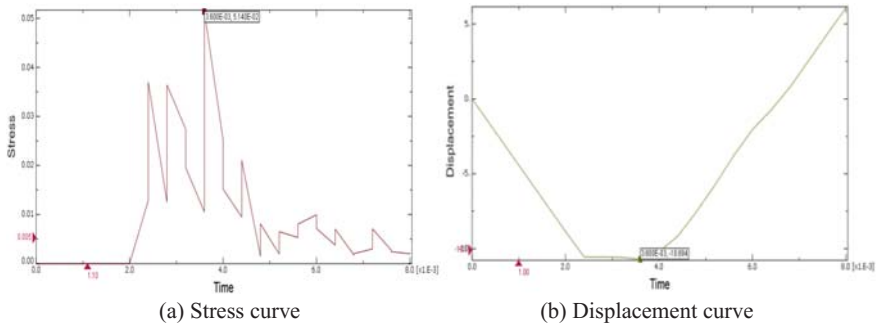


**Fig. 9.** The stress and displacement curves of the top part with EPE cushion

### 3.3 Maximum Acceleration

The acceleration curve during drop of laptop is obtained, shown in Fig. 10. The maximum acceleration of the laptop without cushion is  $69,150 \text{ m/s}^2$ , and it is  $28,410 \text{ m/s}^2$  for using cushion. It can be found that it is effective to protect the laptop using cushion.

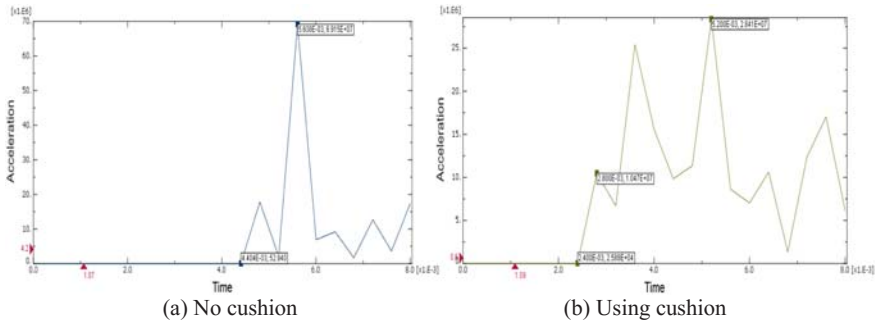


Fig. 10. Maximum acceleration

## 4 Conclusions

Through the analysis of laptop model by ABAQUS, the stress nephogram and the stress curve can be obtained. The protective effect of the cushion packaging on the laptop can be explained from the stress and acceleration, and the stress of the top part of the laptop can also be known. The results show that the cushion has a protective effect on the product and absorbs most of the force.

**Acknowledgements.** This research was supported by the National Natural Science Foundation of China (No. 51305038) and Science and Technology Research Projects of Beijing Institute of Graphic Communication (Ed201804, Eb201701).

## References

1. Peng, G. (2006). *Logistics and transport packaging design*. Beijing: Printing Industry Press.
2. Zhang, S., & Qian, Y. (2012). Simulation analysis of vibration characteristics of induction cookerpackage. *Packaging Engineering*, 33(23), 56–60.
3. Yang, X. (2015). *Numerical simulation of the drop impact of LCD TV package based on ANSYS Workbench*. Shandong: Shandong University.
4. Hao, H., Hu, R., & Kang, S. (2010). *ANSYS 12.0 LS-DYNA nonlinear finite element analysis from entry to the essence*. Beijing: Mechanical Industry Press.
5. Liu, A., Zhao, Y., Wang, Y., et al. (2014). The drop finite element analysis and optimization design of white wine packaging. *Packaging Engineering*, 35(17), 22–26.
6. Shen, Z., Chen, D., & Luo, J. (2016). Simulation and analysis of dropping impact acceleration of polyethylene foam buffer system. *Packaging Engineering*, 37(19), 128–131.
7. Zhang, X., Ren, C., Ji, H., et al. (2016). Dropping simulation analysis of dangerous goods packaging buckets. *Packaging Engineering*, 39(19), 116–120.
8. Liu, Y., & Zhang, Y. (2011). Dropping simulation and design improvement of a washing machine based on FE analysis. *Journal of Vibration and Shock*, 30(2), 164–166.
9. Shi, R., Liu, C., & Yuan, C. (2015). Laptop drop simulation analysis and optimization. *Manufacturing Automation*, 17, 41–43.

10. Zhang, B., & Gao, Q. (2014). Simulation analysis of drop test of notebook based on ANSYS. *Science and Technology Innovation Report*, 11(4), 75–76.
11. Zhang, G., Song, X., Shi, Y., et al. (2018). Evaluation on cushioning packaging system of laptop during drop based on ABAQUS. *Electrical Engineering*, 477, 437–442.

**Part VI**  
**Paper and Related Technology**



# Influence of Nano-silica on Inkjet Paper Coating

Huanmei Wang, Yunzhi Chen<sup>(✉)</sup>, and Zhengjian Zhang

China Light Industry Key Laboratory of Food Packaging Materials and Technology, Tianjin University of Science and Technology, Tianjin, China  
yzchen@tust.edu.cn

**Abstract.** The influence of nano-silica with different particle sizes on inkjet paper coating was investigated. Laboratory self-made silica sol with particle size of 16 and 100 nm was employed as the pigment, and Polyvinyl Alcohol (PVA) was used as the binder. In order to study how nano-silica influences the properties of the inkjet paper coating, four groups of coating were prepared by variation of the dosage for two types of silica sol particle sizes. The viscosity of coating, the microstructure, physical properties, inkjet printing quality and dynamic permeability were characterized. The results showed that 16 nm silica sol could increase the viscosity of coating and reduce coating liquidity. Meanwhile, it did not contribute to the improvement of the physical properties and permeability of the coated paper. When the ratio between 16 and 100 nm silica sol was 30:70, the coated paper exhibited the best glossiness, smoothness and the solid density. In addition, it was found that the microstructure of the coating demonstrated good correlation with the performance of the coated paper.

**Keywords:** Nano-silica · Inkjet printing · Coating · Microstructure · Permeability

## 1 Introduction

The inkjet market shows an increasing growth, which necessitates the use for the inkjet printing process more developed strategy by taking small-scale color printing and low-cost variable data printing into consideration [1]. Inkjet printing is a non-contact technique with remarkable performances such as versatility, excellent long-term fastness, sharp detail rendering, and large color gamut [2, 3]. Inkjet print is demonstrated its potential application in electronics, 3D printing and biological materials [2, 4, 5]. Inkjet printing quality is dependent on the performances of inkjet recording materials, such as penetration and wettability, can primarily govern the setting and drying of the liquid ink on the surface of the material [5].

In recent years, silica-based nano-particles adsorbents have generated more interests due to their large specific surfaces area, high hydrophilicity and high porosity properties [5, 6]. However, silica particles aggregate easily, which leads to low solid content, weak stability of coating, and having low micro-porosity [7]. These structures affected the physical properties and inkjet printing quality. Therefore, in order to make inkjet printing's lofty standards of flexible and reliable performance, the micro-porosity

and dispersity of SiO<sub>2</sub> particles have been studied [7, 8]. Wu prepared SiO<sub>2</sub> coating modified by silicon coupling agent. It was found that the wettability and ink absorbcency of modified silica coating was improved [8]. The properties of the coatings are greatly influenced by the particle size and pore structure of the coatings [9, 10].

However, there are few studies on the effect of nano-silica and its particle size on inkjet print coatings. In order to improve inkjet printing performance of the coating, silica sol of 16 and 100 nm were used as pigments. The influence of nano-silica on inkjet paper coating was researched by analyzing the viscosity of coating, the microstructure, physical properties, inkjet printing quality and dynamic permeability.

## 2 Experimental

In the experiment, the PVA was used as adhesive, and two kinds of silica sol (laboratory self-made) were used as pigments. The particle polydispersities of 16 and 100 nm silica sol were 0.132 and 0.101, respectively. According to the different proportions of nano-silica, 4 groups of coatings were prepared according to the experimental formulations. Table 1 showed the absolute mass ratio and number of each component.

**Table 1.** The coating formulations

Number	C1	C2	C3	C4
silica sol of 100 nm (pph)	100	70	30	0
silica sol of 16 nm (pph)	0	30	70	100
PVA (pph)	15	15	15	15

The viscosity of coatings was measured by the viscometer (CAP2000 + , by Bokefei Corporation, USA). A scanning electron microscope (SEM, by Hitachi, Japan) was used to observe the microstructure of the coatings. The permeability of coated papers was measured by Dynamic Permeation Analyzer. The coating amount, smoothness, whiteness and glossiness were measured according to GB/T451.2-2002, GB/T 22363-2008, GB/T 7974-2013 and GB/T 8941-2007. The coating amount of papers was 6–7 g/m<sup>2</sup>. The solid density of inkjet printing was measured by density meter (518, X-Rite, America).

## 3 Results and Discussion

### 3.1 Viscosity of Coatings

As shown in Fig. 1, the viscosity of coatings was increasing greatly with the increase of 16 nm silica sol dosage. Therefore, too much 16 nm silica sol was not conducive to the preparation and pumping of coating materials. This behavior is possible because the

16 nm silica sol with smaller particle size, higher specific surface area and more silica alcohol groups than the 100 nm silica sol, the binding force between particles increasing, and the coating viscosity increase.

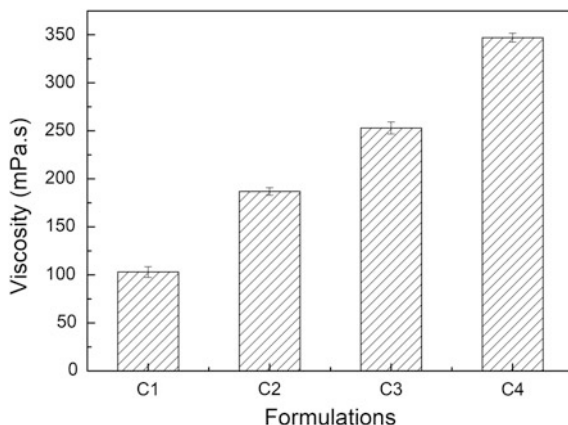


Fig. 1. The viscosity of different coatings

### 3.2 Microstructure of Coated Papers

The microstructure of coated papers from the SEM images was showed in Fig. 2. As shown in Fig. 2, C1 coated paper surface had relatively uniform pore structure formed by the coating, because the coating of 100 nm silica sol had good dispersion. C3 coated paper surface had non-uniform pore structure, and there were plenty of agglomerates on the coating. Since the 16 nm silica sol was filled in the pores between fibers, the uniform pore structure was hindered, and non-uniformity was formed due to the agglomeration of the 16 nm silica sol. The pores on the surface of C4 coated paper was large and uneven, because the 16 nm silica sol particles were too small to enter the fiber pores of the paper, and could not form a uniform coating.

### 3.3 Dynamic Permeability of Coated Papers

The dynamic permeation curves and permeation parameters of coated papers were showed in Figs. 3 and 4. The test liquid for dynamic penetration was water.

As shown in Fig. 3, dynamic permeation curves of C1, C2 and C3 coated papers showed an upward trend of obvious. The result indicated that the surface of the paper was uniform. The energy curve of C4 coated paper was upward trend of weak, which indicating that the paper surface was nonuniform.

$C_i$  refers to the difference between the ultrasonic energy value from the 100% to the energy value, when the testing liquid penetrates the coating. Higher of  $C_i$  value means the more coarse-pored the coating, covering possibly worse.  $C_t$  refers to the time that the testing liquid strikes through the coating, start of the penetration into the base paper. The higher of  $C_t$  value means the thicker of the coating thickness.

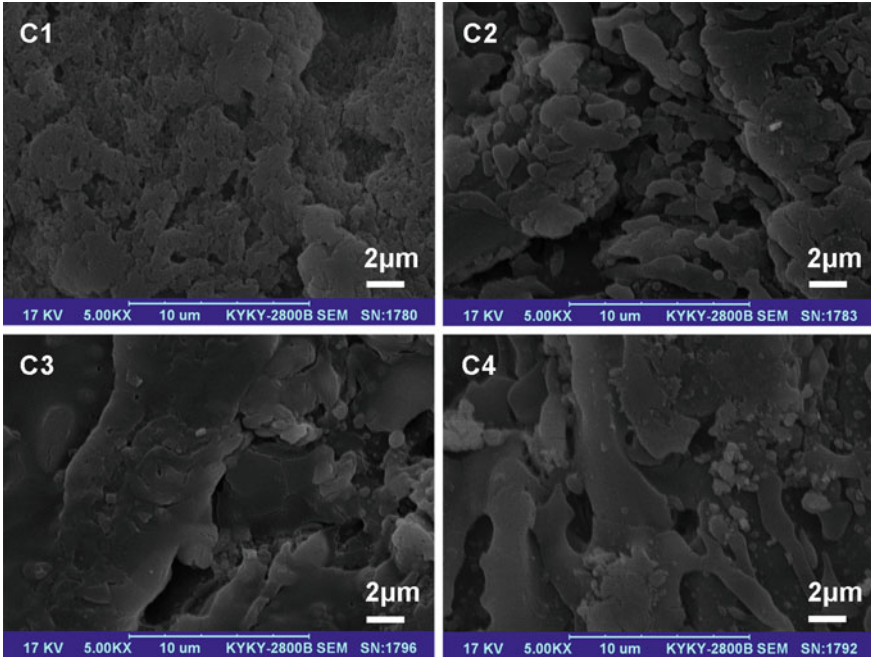


Fig. 2. SEM of coated papers

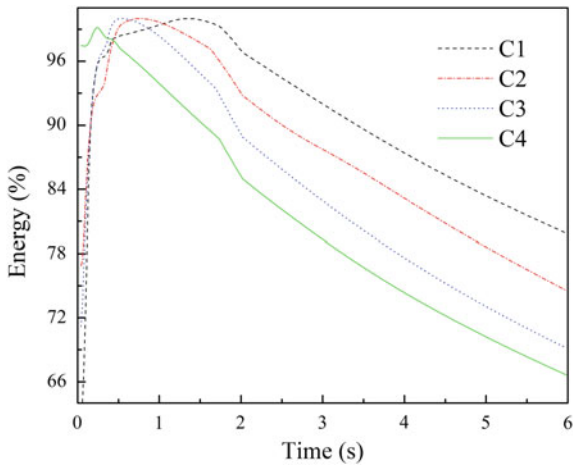


Fig. 3. Dynamic penetration curve

As shown in Fig. 4, the value of  $C_i$  indicated that the pore size of the coating increases as the amount of 16 nm silica sol increases. The value of  $C_1$  indicated that the coating thickness of the C1 and C2 coated papers was thicker, and the C4 coated paper



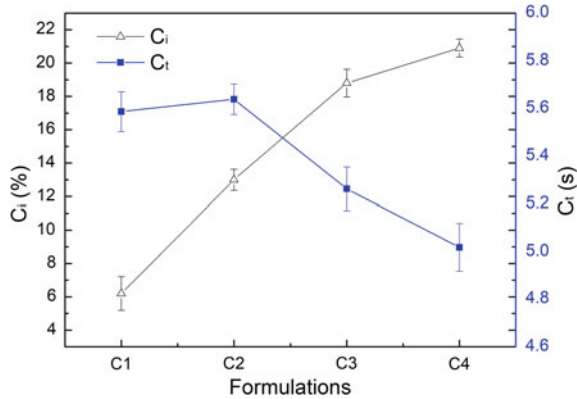


Fig. 4. Dynamic permeability parameters

had the thinnest coating. Because the 16 nm silica sol would penetrate into the fibrous pores of the paper, and the smaller particle size silica sol was more hydrophilic.

### 3.4 Physical Properties of Coated Papers

The whiteness, glossiness, and smoothness of the coated papers were presented in Figs. 5 and 6.

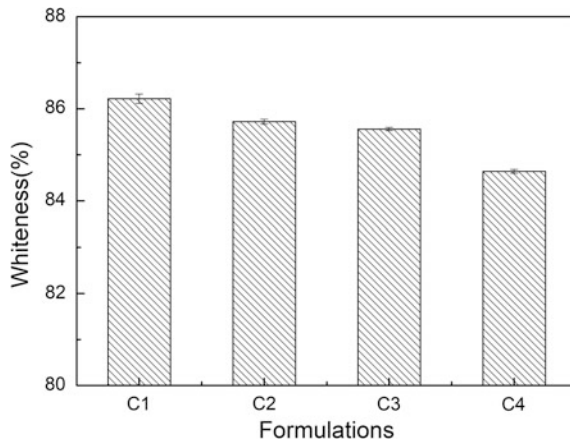


Fig. 5. Whiteness of coated papers

As shown in Fig. 5, the whiteness of coated paper had a tendency to decrease, with the increase in the amount of 16 nm silica sol. The result indicated that the small particle size silica sol had a low whiteness, and the small particle size silica sol could not cover raw paper well. As shown in Fig. 6, the glossiness and smoothness of coated paper showed the

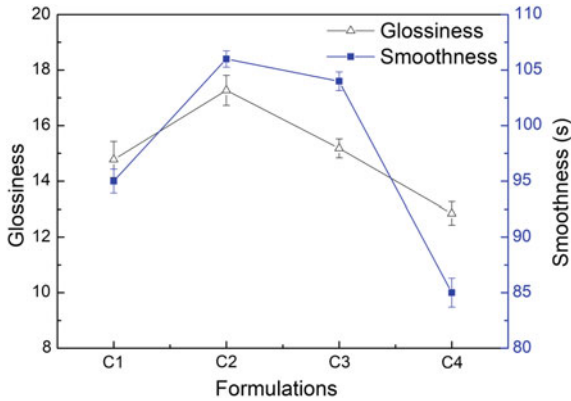


Fig. 6. Glossiness and smoothness of coated papers

same tendency, due to the correlation between glossiness and smoothness. C2 coated paper had the best glossiness and smoothness, while C4 coated paper was worst.

### 3.5 Inkjet Printing Performances of Coated Papers

As shown in Figs. 7 and 8, C2 coated paper had the best solid density, the solid density of C1 coated paper was better than C3 and C4. The result indicated that the inkjet printing quality of C2 coated paper was the best. Because C1 and C2 coated papers had uniform pore structure, which could fix the ink on the coating surface well. The coated paper, which was prepared by 16 nm silica sol, could not fix the ink on the coating surface well. Due to the 16 nm silica sol was filled in the pores between fibers, it was impossible to form a uniform microstructure.

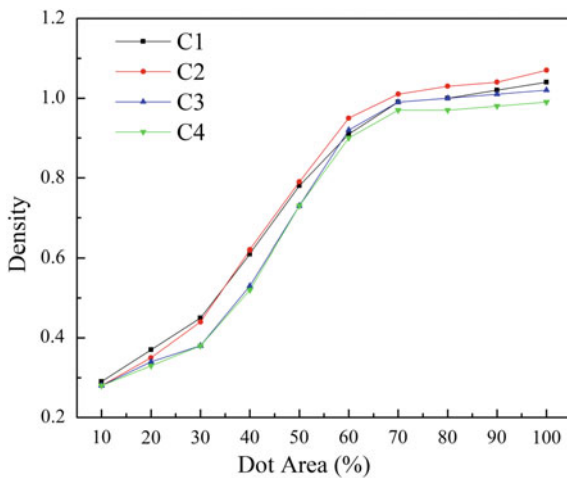


Fig. 7. Inkjet printing reproduction of Cyan

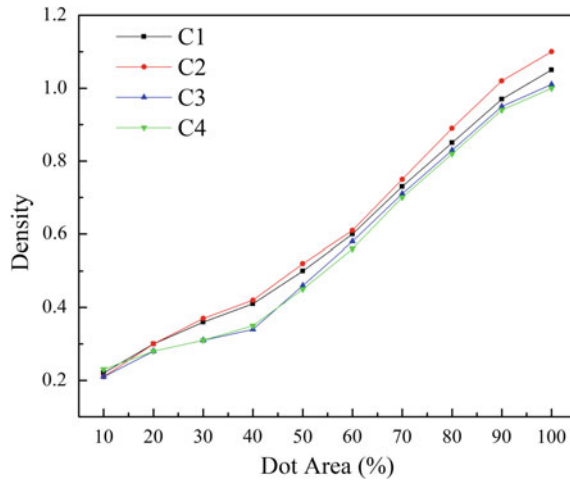


Fig. 8. Inkjet printing reproduction of Magenta

## 4 Conclusions

The combination of 16 and 100 nm silica sol significantly improved the coating viscosity. The viscosity of the coating was increased by 16 nm silica sol, and the fluidity of the coating was reduced.

The combination of 16 and 100 nm silica sol had a significant influence on the microstructure, physical properties and permeability of the coated paper. The surface of coated paper prepared by 16 nm silica sol failed to form a uniform pore structure. Therefore, its physical properties and printing performance were the poorest. The coated paper prepared by compounding 16 and 100 nm silica sol with ratio of 30:70 showed the best printing performances in terms of glossiness and smoothness.

In conclusion, the well-constructed microstructure can improve the physical properties, printability and permeability of the coated paper.

## References

- Li, J., Ye, F., Vaziri, S., Muhammed, M., Lemme, M. C., & Östling, M. (2013). Efficient inkjet printing of graphene. *Advanced Materials*, 25(29), 3985–3992.
- Singh, M., Haverinen, H. M., Dhagat, P., & Jabbour, G. E. (2010). Inkjet printing-process and its applications. *Advanced Materials*, 22(6), 673–685.
- Badalov, S., & Oren, Y. (2015). Ink-jet printing assisted fabrication of patterned thin film composite membranes. *Journal of Membrane Science*, 493(12), 508–514.
- Xu, T., Zhao, W., Zhu, J. M., Albanna, M. Z., Yoo, J. J., & Atala, A. (2013). Complex heterogeneous tissue constructs containing multiple cell types prepared by inkjet printing technology. *Biomaterials*, 34(1), 130–139.
- Kettle, J., Lamminmäki, T., & Gane, P. (2010). A review for high speed inkjet coating. *Surface & Coatings Technology*, 24(12), 2103–2109.

6. Wu, J., & Jiang, B. (2012). A coating of silane modified silica nanoparticles on PET substrate film for inkjet printing. *Applied Surface Science*, 258(2012), 5131–5134.
7. Sowade, E., Mitra, K. Y., Ramon, E., et al. (2016). Up-scaling of the manufacturing of all-inkjet-printed organic thin-film transistors: device performance and manufacturing yield of transistor arrays. *Organic Electronics*, 30, 237–246.
8. Jiang, B., & Tao, P. H. (2014). Study of the adsorption performance and preparation of functional nano-silica pigment particles. *Dyes and Pigments*, 104(104), 169–174.
9. Liu, X., Chen, Y., & Zhang, Z. (2017). Influence of silica pigments with different sizes on the performances of coated ink-jet printing paper. *Advanced graphic communications and media technologies, Lecture Notes in Electrical Engineering 417*, [https://doi.org/10.1007/978-981-10-3530-2\\_124](https://doi.org/10.1007/978-981-10-3530-2_124).
10. Wang, Q. (2012). Effect of different particle sizes of silica on the microstructure of color ink-jet printing paper coating layer. *Light industry science and technology*, 28(03), 32–34.



# Study of the Influence of Styrene-Acrylic Emulsion for Advanced Calligraphy Paper Performance

Xiaoxiu Hao<sup>1(✉)</sup>, Ziyu Xing<sup>1,2</sup>, Tong Wang<sup>1,2</sup>, and Changhong Liu<sup>1,2</sup>

<sup>1</sup> Tianjin Vocational Institute, Tianjin, China  
768182753@qq.com

<sup>2</sup> Tianjin University of Science and Technology, Tianjin, China

**Abstract.** On the basis of cooked rice paper coated with a good ink-absorbing and no ink paint, the advanced calligraphy paper uses cooked rice paper as the body paper. This thesis sets styrene-acrylic emulsion as binder, porcelain clay and zinc oxide as pigments. Firstly, it discusses effect on the performance of senior calligraphy paper writing caused by the two kinds of pigment preparation in different proportion and adhesion-filling ratio of different coating. Secondly, it implores the impact of different coatings on paper performance, such as tear, tensile strength, smoothness, and gloss. The result shows that when the styrene acrylic emulsion used as binder, ink absorption increased gradually with the increase of adhesion-filling ratio; tear, tension and gloss increased with the increase of clay and the decrease of zinc oxide, the decrease of smoothness; when the porcelain clay: zinc oxide is 2:3 and adhesion-filling ratio is 1:4.5, the whiteness, smoothness, and gloss of the Xuan paper are significantly enhanced after coating of the sample. The ink is not scattered during writing, the lines are neat, delicate, unbreakable, no ink paint, dense and bright surface, and with good writing performance.

**Keywords:** PiMade Xuan paper · Xuan paper coating · Advanced calligraphy paper

## 1 Introduction

Xuan paper is a traditional paper for Chinese painting and calligraphy. It can be divided into three types: Raw Xuan paper, Sized Xuan paper, and PiMade Xuan. Raw Xuan paper has strong water absorption, therefore ink seeps quickly. It is appropriate for ink painting. PiMade Xuan is made of Raw Xuan paper with a certain percentage of alum water. This kind of paper is harder than Raw Xuan paper. The water absorption capacity is weak, so that the ink and color will not spread when using. It is appropriate to paint elaborate-style painting. Sized Xuan paper is also made from Raw Xuan paper. The water absorption capacity is between the former two [1–3]. The advanced calligraphy paper can improve paper properties by coating processing. Porcelain clay pigment has strong plasticity and strong adhesion. Mixed with other coating proportion, it can improve the whiteness, smoothness and gloss of the paper. Zinc oxide has good color performance and cover performance, as white pigment can play the role on

moisturizing. The fluidity of styrene-acrylic emulsion is good. It can be used to adhere to the paper surface, making the paper surface smoother. It also has a certain viscosity, which will make the coated paper with a certain toughness [4–7]. In this experiment, styrene-acrylic emulsion was used as adhesives to study the effects of their tearing degree, tensile strength, smoothness, gloss and writing performance under different porcelain and zinc oxide ratios.

## 2 Experimental

### 2.1 Experimental Materials and Equipment

PiMade Xuan (Anhui Jingxian County Xuan paper factory); Porcelain clay (Shijiazhuang ground mountain mineral products trade Co., Ltd); Zinc oxide (Weifang Hengfeng Chemical Co., Ltd.); Styrene-acrylic emulsion (Shandong baoda professional Co., Ltd.); Sodium polyethylenate (Shanghai Rongchuang biotechnology Co., Ltd.).

QSM-2 type grinding machine (Tianjin material testing machine factory); JJ-IA type digital display electric agitator (Jintan medical instrument factory); D-DLY50 type paper and cardboard quantitative measuring instrument (Sichuan Changjiang paper making Instrument Co., Ltd.); DRK108B type electronic tearing tester (Ji'nan drick Instrument Co., Ltd.); DCP-KZ1000 type computer measurement and control anti-tension testing machine (Sichuan Changjiang paper making Instrument Co., Ltd.); YT-BST type smoothness tester (Hangzhou YanTe Technology Co., Ltd.); type YT-GM glossiness measuring instrument (Hangzhou YanTe Technology Co., Ltd.).

### 2.2 Experimental Methods

#### 2.2.1 The Advanced Calligraphy Paper Trial Production

Mix the different proportions of porcelain and zinc oxide. Add distilled water. Pour into the grinding machine for 40 min. After filtering, add different proportions of styrene-acrylic emulsion adhesive and additives. After coating, the Xuan paper is made into advanced calligraphy paper.

#### 2.2.2 Determination of the Tearing Degree of Xuan Paper

According to GB/T 455 Paper and Paper Tearability Measurement, firstly prepare a paper sample to cut out 5 pieces of each rectangle of 63 mm \* 50 mm in vertical and horizontal directions, and then use the DRK108B type electronic tearing tester to take measurements, average the measurement results. The tearing index should be calculated according to formula (1)

$$X = F/G \quad (1)$$

where, X—tear index, mN·m<sup>2</sup>/g; F—tearing degree, m N; G—quantitative, g/m<sup>2</sup>.

### 2.2.3 Determination of Tensile Strength of Xuan Paper

Firstly, prepare the coated paper test pieces, cut out 5 pieces of each rectangle of 15 mm \* 200 mm in vertical and horizontal directions, and then use the DCP-KZ1000 type computer measurement and control anti-tension testing machine to take measurements, and average the measurement results.

### 2.2.4 Measurement of Smoothness of Xuan Paper

According to GB/T 456-2002 paper and board smoothness measurement (Buick method), first prepare paper samples of Xuan paper, cut out five 50 mm \* 50 mm diameter samples, and then use YT-BST type smoothness tester to take measurements, and average the measurement results.

### 2.2.5 Determination of Gloss of Xuan Paper

According to the standard GB8941-2007 paper and board specular gloss measurement 75° angle determination method, clamp the sample, select the angle of 70° and then take five vertical and horizontal samples of Xuan paper. Taking measurements, and average the measurement results.

## 3 Results and Discussion

### 3.1 Effect of Different Porcelain Clay, Zinc Oxide Proportioning and Different Adhesion-Filling Ratio on the Ink Absorption Performance of Advanced Calligraphy Paper

As shown in Fig. 1, compared with different ratio porcelain clays and zinc oxide pigments, mixed and then made of the advanced calligraphy paper, made can be seen: In the case of a certain ratio of porcelain clay and zinc oxide, as the adhesion-filling ratio (proportion of porcelain clay to zinc oxide) gradually decreases, the ink absorbcency gradually increases. Because the viscosity of the mixed solution tends to be moderate, the adhesion state gradually tends to be good, so the absorption of ink increases. After coating the paper, the whiteness enhancement is especially obvious. The coating adhesion condition is good, so that the ink does not spread out. The line is neat, fine. The writing performance has improved.

### 3.2 Effect of Different Porcelain Clay, Zinc Oxide Proportioning and Different Adhesion-Filling Ratio on the Performance of Advanced Calligraphy Paper Tearing Degree

As shown in Fig. 2, cross direction refers to the direction perpendicular to the operating direction of the paper machine in the process of paper transcription, and machine direction refers to the direction parallel to the operating direction of the paper machine in the process of paper transcription. Compared with horizontal and vertical Xuan paper tearing indexes, it can be seen that the horizontal tearing degree of the coated Xuan paper is greater than that of the longitudinal tearing.

With the increase of the content of porcelain clay, the content of zinc oxide decreased, and the tear of coating paper showed an upward trend.

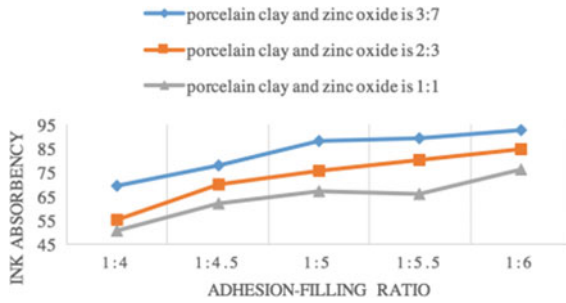


**Fig. 1.** Effect of different mixture ratios of porcelain clay and zinc oxide and different adhesion-filling ratio

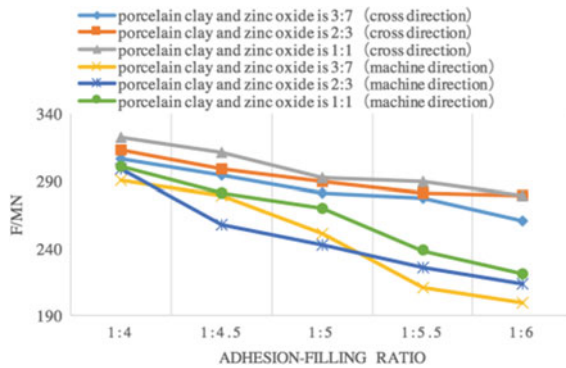


**Fig. 2.** Effect of different porcelain clay, zinc oxide proportioning and different adhesion-filling ratio on the performance of advanced calligraphy paper tearing degree

In the interval of the adhesion-filling ratio of 1:4–1:6, the tear degree of the coated paper is gradually decreased with the decrease of the paint adhesion-filling ratio. Because of styrene acrylic emulsion has certain viscosity, after coating can make coated paper has certain toughness. Therefore, styrene-acrylic emulsion can enhance the tearing degree of Xuan paper. After repeated rubbing with the pen, the paper surface will not break.

**3.3 Effect of Different Porcelain Clays, Zinc Oxide Proportioning, and Different Adhesion-Filling Ratio on the Tensile Properties of Advanced Calligraphy Paper**

As shown in Fig. 3, with the increase of clay content and the decrease of zinc oxide content, and the tension of the paper coating is obviously enlarged. Because porcelain clay is more conducive to improving the anti-tension of the coated paper, it is more tenacious than the original paper, and it is not easy to be broken, thus affecting the quality of the paper. In the interval of the adhesion-filling ratio of 1:4–1:6, with the



decrease of the paint adhesion-filling ratio, the anti-tension of the coated paper is gradually decrease. Using styrene-acrylic emulsion as adhesive can improve the tensile properties and waterproof properties of paper also improve the quality of paper. After coating the paper ink levels and a sense of richness are improved.

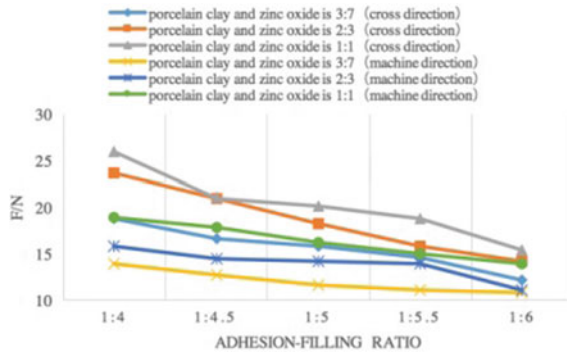


**Fig. 3.** Effect of different porcelain clay, zinc oxide proportioning and different adhesion-filling ratio on the tensile properties of advanced calligraphy paper

### 3.4 Effect of Different Porcelain Clays, Zinc Oxide Proportioning and Different Adhesion-Filling Ratio on the Smoothness of Advanced Calligraphy Paper

As shown in Fig. 4, with the increase of clay content and the decrease of zinc oxide content, and the smoothness of coated paper is gradually reduced. In the interval of the adhesion-filling ratio of 1:4–1:6, with the decrease of the paint adhesion-filling ratio, the smoothness of coated paper increases gradually. When the ratio is 1:6, the smoothness is the best. Because the fibers constituting the interleaved multi-gap structure of Xuan paper, the closer the Xuan paper fibers, the smaller the gap, the higher the smoothness. In addition to the properties of the plant fibers that are interwoven with the Xuan paper, the paper adds porcelain clay and zinc oxide fillers, and the particles of the filler are dispersed between the fibers, filling the gap between the fibers, thus improving the softness of the paper and making the surface of the paper more smooth, improving the performance of the coated paper. When writing, Xuan paper is smooth and has a good color. There will not be the phenomenon of Qin ink, but also can keep the works for a long time.

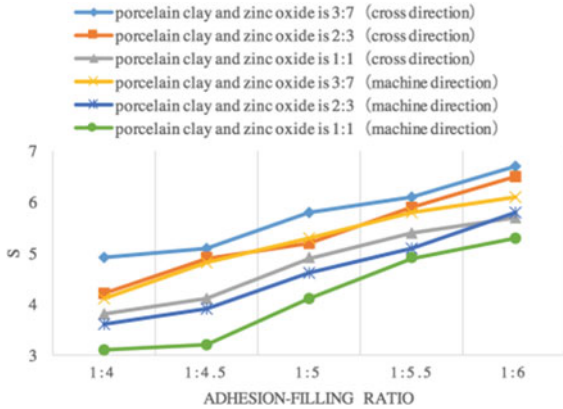


Fig. 4. Effect of different porcelain clay, zinc oxide proportioning and different adhesion-filling ratio on the smoothness performance of advanced calligraphy paper

### 3.5 Effect of Different Porcelain Clays, Zinc Oxide Proportioning and Different Adhesion-Filling Ratio on the Performance of Advanced Calligraphy Paper Gloss

As shown in Fig. 5, with the increase of clay content and the decrease of zinc oxide content, the gloss becomes gradually higher. Because the porcelain clay has a higher specific area, choose porcelain clay pigments with a small particle size to form a uniform and smooth coating on the surface of the Xuan paper makes the gloss of the Xuan paper increase gradually, and the gloss of the paper rises significantly. In the interval of the adhesion-filling ratio of 1:4–1:6, with the decrease of the paint adhesion-filling ratio, the gloss of the paper was gradually increased. Due to some changes in the pore structure of the surface coating, the light scattering changes. Because of the effect of the emulsion adhesive, the film can provide smooth and smooth coating surface, the gloss of the paper is improved, the surface becomes dense and bright, and the writing effect is improved.

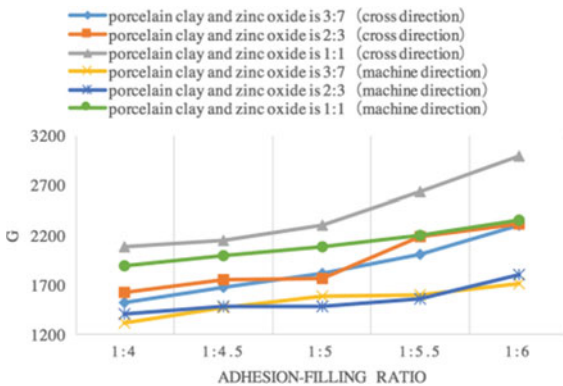


Fig. 5. Effect of different porcelain clay, zinc oxide proportioning and different adhesion-filling ratio on the performance of advanced calligraphy paper gloss

## 4 Conclusions

1. When the styrene-acrylic emulsion is used as a binder, under the condition that the ratio of the two pigments of porcelain clay and zinc oxide is fixed, the ink-absorbing property gradually increases as the adhesion-filling ratio gradually decreases. The whiteness of the Xuan paper is particularly enhanced after coating, and the coating is in a good state of adhesion and does not spread.
2. With the increase of porcelain clay, the decrease of zinc oxide, the tear degree, tensile strength and luster increased; after coating, the paper is not easy to be damaged, and the layers and richness of the ink are enhanced.
3. When the porcelain clay: zinc oxide is 2:3 and adhesion-filling ratio is 1:4.5, the whiteness, smoothness, and gloss of the Xuan paper are significantly enhanced after coating of the sample. The ink is not scattered during writing. The lines are neat, delicate, unbreakable, no ink paint. The surface is dense and bright, with good writing performance.

## References

1. Zhu, J. (2013). The characteristics, application and innovation of Chinese Xuan paper. *Journal of Taizhou Polytechnic College*, 05, 22–24.
2. Cao, T. (2012). One hundred years in research on Chinese Xuan paper. *Journal of Hefei Normal University*, 01, 45–56.
3. Liu, R. (2015). Xuan paper science knowledge question and answer (part 2). *Paper and Paper Making*, 12, 94–98.
4. Zhang, L. (2015). *Synthesis and research of core-shell styrene-acrylic emulsion through reactive emulsifier*. Hunan University.
5. Qiao, L., Cao, Jin, Rui, S., Liu, B., & Shen, G. (2015). Application of SAE emulsion on paper relics and its anti-aging performance. *Paper and Paper Making*, 10, 40–43.
6. Gao, T., & An, Q. (2014). Preparation of organosilicone-modified styrene-acrylate emulsion and its application on surface sizing. *Paper and Paper Making*, 04, 33–38.
7. Xiaolong, F., Zhang, G., Li, J., & Guixia, W. (2014). Preparation and characterization of soap-free styrene-acrylate emulsion surface sizing agent. *Paper and Paper Making*, 01, 40–44.



# Preparation of a Surface Sizing Agent of Dialdehyde Chitosan/Cationic Starch and Barrier Property

Yong Lv<sup>1,2(✉)</sup>, Ci Song<sup>1</sup>, Qiuqian Xu<sup>1</sup>, and Yusheng Yu<sup>1,3</sup>

<sup>1</sup> School of Engineering and Information, Yiwu Industrial and Commercial College, Yiwu, Zhejiang, China

lv Yong1225@gmail.com

<sup>2</sup> Key Laboratory of Eco-Textile, Ministry of Education, Jiangnan University, Wuxi, China

<sup>3</sup> Shenzhen Zhencai Yali Technology Co., Ltd., Shenzhen, China

**Abstract.** To improve the green environmental performance and barrier property of the food packaging paper materials, the dialdehyde chitosan (D-CTS) was prepared from the selective oxidation of chitosan by sodium periodate. A surface sizing agent was obtained through complexes of D-CTS and cationic starch (CS). The barrier properties for water vapor of paper-sheet coated by the complex sizing agent of D-CTS/CS were measured. Attenuated total reflectance-fourier transform infrared spectroscopy (ATR-FTIR) was used to explain the mechanism of the improved barrier properties. The results indicate: while the oxidation degree and concentration of D-CTS is 32.3% and 0.3 wt%, the optimum barrier property for water vapor was obtained. While the coating weight increased from 0 to 3.5 g/m<sup>2</sup>, the barrier property for water vapor (WVP) was reduced from  $2.73 \times 10^{-11} \text{ g cm}^{-1} \text{ s}^{-1} \text{ Pa}^{-1}$  to  $0.81 \times 10^{-11} \text{ g cm}^{-1} \text{ s}^{-1} \text{ Pa}^{-1}$ , reduced by 70.33%. Analyzed by ATR-FTIR, the degree of cross linking between D-CTS, CS and fibers increased. A smooth film formed on the surface can improve the WVP significantly.

**Keywords:** Dialdehyde chitosan · Cationic starch · Coated paper · Barrier property

## 1 Introduction

Paper packaging materials has the advantages of abundance, biodegradability, regeneration, low cost and so on. It is very suitable for food packaging materials [1, 2]. A low water vapor permeability is a crucial requirement for many food packaging materials and a low water vapor transmission rate is one of the main requirement [3, 4]. While paper packaging materials laminated with aluminum or extrusion-coated with synthetic polymers, the barrier resistance for water vapor could be improved significantly. However, these packaging materials produced by the above process are not environmentally friendly and difficult to be recycled. It is a very promising method to

dissolve biodegradable polymers in water, and then coating on the surface of paper. A barrier layer can be formed on the surface of paper to improve the barrier property. Cationic starch has low production cost and can be widely used as paper surface sizing agent to improve the mechanical properties and surface smoothness of paper. When the cationic starch is used for coating and sizing, the surface coating is loose and porous. It cannot meet the requirements of barrier property of food packaging [5]. Chitosan is the product of deacetylation of chitin, which is widely distributed in nature. Meanwhile, chitosan has cationic amino group, compact molecular chain, high crystallinity, good antibacterial property and barrier property, which are very suitable for food packaging [6]. Compared with other natural organic compounds such as starch, the production cost of chitosan is relatively high. It limited its extensive promotion and application in the field of food packaging.

The D-CTS prepared by selective oxidation of chitosan with sodium periodate, has an aldehyde group which can improve the cross linking and recombination performance of chitosan. Dialdehyde-chitosan/cationic starch sizing agent (D-CTS/CS) was prepared by mixing dialdehyde chitosan with cationic starch. It can reduce the cost of chitosan and improve the barrier property for water vapor, which can meet the requirements of general food packaging.

## 2 Experimental

### 2.1 Materials and Methods

Chitosan (Mw. 235 KDa) was purchased from Qingdao Shengyang Chemistry Industry Co. LTD (Shandong, China). The degree of deacetylation is 91% determined by potential titration method. Sodium periodate, NaOH, hydrochloric acid and so on are all analytically pure, which are provided by Sinopharm chemical reagent Co. LTD (Shanghai, China). Cationic starch with degree of substitution 0.037 is provided by National starch industry (Shanghai, China) Co. LTD. Paper pulp is Beimu bleached conifer pulp, importing from Canada.

### 2.2 Preparation of D-CTS/CS Sizing Agent

The preparation of dialdehyde chitosan was mainly based on the modified method of Vold et al. [7]. The prepared 2 g dialdehyde chitosan [with different oxidation degree determined by Combustion analysis (C, N)] were poured into 198 g water, stirred slowly until completely dissolved. The cationic starch gelatinization solution is poured into the 500 ml three mouth flask, adding different volume of dialdehyde chitosan solution. The pH value of the mixture was adjusted through the NaOH of 0.1 mol/l and HCl of 0.1 mol/l. Deionized water was added into the flask. D-CTS/CS sizing agent was obtained through stirring 1 H at the constant temperature of water bath. Paper sheets were made from the pulp according to TAPPI T 205 [8]. It was coated by D-CTS/CS Sizing agent under different conditions on the basis of GB/T 10335.1-2017.

### 2.3 Determination of Water Vapor Transmittance (WVP) of Paper-Sheet

$$WVP = (\Delta W \cdot X) / A \cdot T \cdot (P_1 - P_2)$$

Where  $\Delta W$  represents the weight gain of weighing bottle(g),  $X$  is thickness of the paper-sheet (mm),  $A$  represents area of paper-sheet ( $\text{mm}^2$ ),  $T$  means time intervals(h),  $(P_1 - P_2)$  means Pressure difference of water vapor inside and outside of weighing bottle (Kpa).

## 3 Results and Discussions

### 3.1 Effects on WVP of Different Oxidation Degree of D-CTS in Compound Sizing Agent

The shelf life of products can be effectively analyzed by testing the barrier properties for water vapor. Figure 1 shows the effect of different degree of oxidation in D-CTS in compound sizing agents on WVP. When the degree of oxidation increased from 0 to 32.3%, WVP of the paper-sheet reduced from  $1.03 \times 10^{-11} \text{ g cm}^{-1} \text{ s}^{-1} \text{ Pa}^{-1}$  to  $0.81 \times 10^{-11} \text{ g cm}^{-1} \text{ s}^{-1} \text{ Pa}^{-1}$ , reduced by 24.36%. This may due to that D-CTS with higher degree of oxidation can improve the performance of the cross linking between D-CTS, CS and fibers.

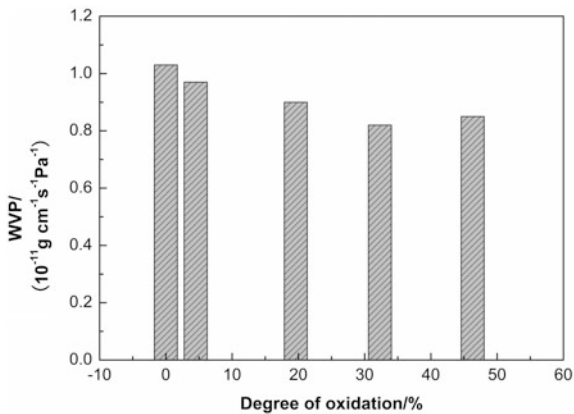
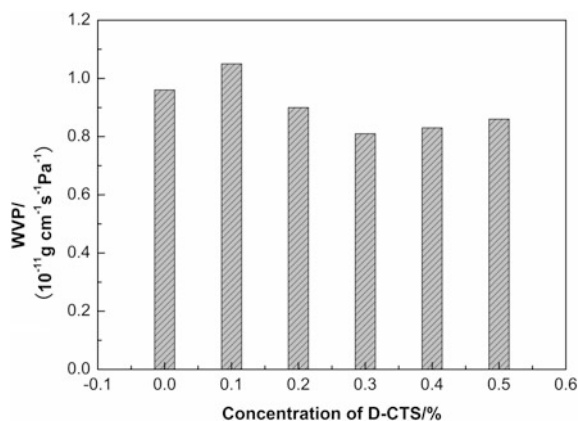


Fig. 1. Effect on WVP of different degree of oxidation in D-CTS in complex sizing agents

### 3.2 Effects on WVP of Different Contents of D-CTS in Compound Sizing Agent

It can be seen from Fig. 2 that the WVP of the paper decreases with the increase of the content of dialdehyde chitosan. The degree of oxidation of D-CTS was 32.3%. The WVP was risen up firstly due to the lower molecular weight of D-CTS. When the

content of D-CTS increased from 0 to 0.3%, the WVP decreased from  $0.98 \times 10^{-11} \text{ g cm}^{-1} \text{ s}^{-1} \text{ Pa}^{-1}$  to  $0.81 \times 10^{-11} \text{ g cm}^{-1} \text{ s}^{-1} \text{ Pa}^{-1}$ , which decreased 17.35%. This is mainly due to that the addition of D-CTS. The aldehyde group in the D-CTS has cross linking property, which can improve the film forming performance of cationic starch and D-CTS, thus make the water vapor transmittance lower.



**Fig. 2.** Effect on WVP of different contents of D-CTS in complex sizing agents

### 3.3 Effect on WVP of Coating Weight of Complex Sizing Agent

Figure 3 shows the effect of different coating weigh on WVP of paper-sheet. The oxidation degree of D-CTS used in complex sizing agent was 32.3% and the content was 0.3%. It can be seen from the curves that the coating weight has a great influence on the water vapor transmittance of paper-sheet. As the coating weight of sizing agent increased, the WVP of paper-sheet decreased. When the coating weight increased from 0 to  $3.5 \text{ g/m}^2$ , the WVP decreased from  $2.73 \times 10^{-11} \text{ g cm}^{-1} \text{ s}^{-1} \text{ Pa}^{-1}$  to  $0.81 \times 10^{-11} \text{ g cm}^{-1} \text{ s}^{-1} \text{ Pa}^{-1}$ , and decreased by 70.33%. The results show that the surface sizing agent can greatly reduce the water vapor transmittance and improve the packaging barrier performance of the coated paper-sheet. However, when the coating weight continues to increase, the WVP increases slowly. This due to that a more even film layer has been formed. Meantime, the increasing of the coating weight t has little effect on the barrier performance of the film.

### 3.4 Analysis of ATR-FTIR of the Paper-Sheet Coated by D-CTS/CS Sizing Agent

In order to better analyze the fingerprint region of the functional group, the range of the ATR-FTIR was ranged from  $2000\text{--}500 \text{ cm}^{-1}$ . As can be seen from Fig. 4, when the content of D-CTS reached 0.3%, the absorption peaks of  $1650 \text{ cm}^{-1}$  and  $1570 \text{ cm}^{-1}$  of the compound gradually became prominent [9]. The characteristic absorption peaks of C-ONR<sub>2</sub> and amide bonds are respectively  $1650$  and  $1570 \text{ cm}^{-1}$  [10].

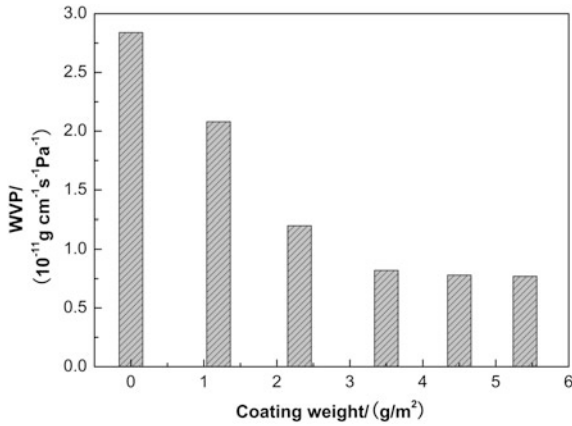


**Fig. 3.** Effect of different coating weight on WVP

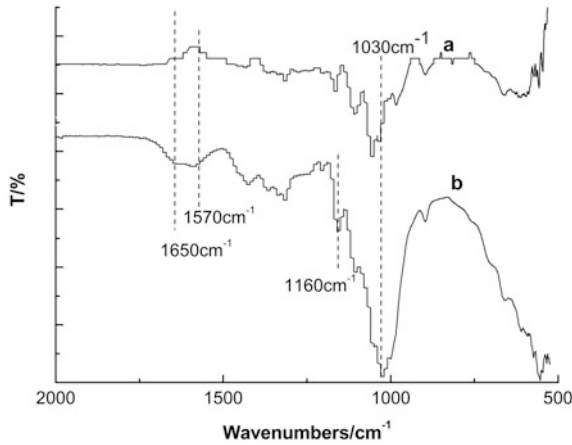


**Fig. 4.** ATR-FTIR spectra of coating paper with the different content of D-CTS in D-CTS/CS sizing agents (a: 0%, b: 0.3%)

With the increase of the proportion of D-CTS, the absorption peak of 1160 m<sup>-1</sup> and 1030 cm<sup>-1</sup> was significantly increased. It means that the content of c-o-c in D-CTS, CS and cellulose increased. The results show that the cross-linking degree between D-CTS and CS and cellulose increased. The compatibility between cationic starch and D-CTS was raised. The interaction force between paper fibers was enhanced, thus improving the barrier properties of paper.



## 4 Conclusions

In the preparation of D-CTS/CS sizing agents, the optimum oxidation degree and concentration of D-CTS is 32.3% and 0.3 wt%, respectively. While the coating weight was raised from 0 to 3.5 g/m<sup>2</sup>, the WVP was reduced from  $2.73 \times 10^{-11}$  g cm<sup>-1</sup> s<sup>-1</sup> Pa<sup>-1</sup> to  $0.81 \times 10^{-11}$  g cm<sup>-1</sup> s<sup>-1</sup> Pa<sup>-1</sup>, reduced by 70.33%. The curves of ATR-FTIR spectra showed that the degree of the cross linking between D-CTS, CS and fibers increased. Addition of D-CTS can improve the performance of the surface film forming property. A smooth film was formed on the surface by adsorbing polymers on the fibers or diffusing them into the fiber pores, which can improve the barrier property of the paper-sheet for water vapor.

**Acknowledgments.** This research was financially supported by university students' science and technology innovation program in Zhejiang (new talent plan)—Preparation of grease-proof and biomass-based paper for food package, the Pre-research Project of Yiwu Industrial and Commercial College (No. YY-SJ-201704), the research of Yiwu Industrial & Commercial College (No.2019JD305), the joint development project of printing media technology research center at YWICC and Yiwu printing and packaging industry innovative platform, and the 2018 Visiting Engineer Program of colleges of universities in Zhejiang (No. FG2018153).

## References

1. Wang, S., & Jing, Y. (2017). Effects of formation and penetration properties of biodegradable montmorillonite/chitosan nanocomposite film on the barrier of package paper. *Applied Clay Science*, 138, 74–80.
2. Fortunati, E. (2016). Multifunctional films, blends, and nanocomposites based on chitosan: Use in antimicrobial packaging. *Antimicrobial Food Packaging*, 467–477.
3. Maleki, G., Sedaghat, N., Woltering, E. J., et al. (2018). Chitosan-limonene coating in combination with modified atmosphere packaging preserve postharvest quality of cucumber during storage. *Journal of Food Measurement and Characterization*, 1–12.
4. Yong, L. (2014). *Preparation of selective oxidation chitosan derivatives and applications in paper making* (pp. 56–58). Wuxi: Jiangnan University.
5. Shen, J., Fatehi, P., & Ni, Y. (2014). Biopolymers for surface engineering of paper-based products. *Cellulose*, 21(5), 3145–3160.
6. Davidovich-Pinhas, M., Danin-Poleg, Y., Kashi, Y., et al. (2014). Modified chitosan: A step toward improving the properties of antibacterial food packages. *Food Packaging and Shelf Life*, 1(2), 160–169.
7. Vold, I. M. N., & Christensen, B. E. (2005). Periodate oxidation of chitosans with different chemical compositions. *Carbohydrate Research*, 340, 679–684.
8. Yong, L., Ci, S., Zhu, L., et al. (2013). Study on preparation of Chitosan with different D. D. *Value and Package Performance of Coated Paper*, 34(11), 1–4.
9. Khwaldia, K., Arab-Tehrany, E., & Desobry, S. (2010). Biopolymer coatings on paper packaging materials. *Comprehensive Reviews in Food Science and Food Safety*, 9(1), 82–91.
10. Lawrie, G., Keen, I., Drew, B., et al. (2007). Interactions between alginate and chitosan biopolymers characterized using FTIR and XPS. *Biomacromolecules*, 8(8), 2533–2541.



# Study on the Correlation Between Surface Properties of Paper and Printing Tonal Gradation by Grey Correlation Method

Li Cheng<sup>(✉)</sup>

Electronic and Information Engineering Institute,  
Jingchu University of Technology, Hubei, China  
284881546@qq.com

**Abstract.** With the expansion of the printing market and the need of industry restructuring, the improvement of printing product quality can be a key to the industry development. What's more, the pros and cons of paper surface properties is the important measure of its quality. Researching the correlation between surface properties of paper, such as whiteness, smoothness, gloss, ink absorption, and printing tonal gradation is particularly significant for the improvement of paper quality. Through the test and analysis on the surface properties of different types of paper, the research on the influence of paper surface properties to the printing tonal gradation, and the use of gray relational analysis method, we calculate the influence degree of the surface properties such as surface gloss, whiteness, and efficiency factors to the printing tonal gradation. After a series of experiment and data processing, we draw the conclusion that in the digital printing machine case, for offset paper, as for the influence degree of paper surface properties to printing tonal gradation, the comprehensive ranking from highest to lowest is gloss, whiteness, ink absorption, surface efficiency and smoothness. However, for coated paper, the comprehensive ranking is surface efficiency, gloss, whiteness, ink absorption and smoothness.

**Keywords:** Paper surface properties · Printed matter tone level · Correlation · Gray correlation analysis · Comprehensive ranking

## 1 Introduction

Printing paper is the main printing stock. The pros and cons of paper surface properties is the important measure of its quality [1, 2]. There are many differences between different paper in gloss, surface efficiency, whiteness, ink absorption, smoothness and many other aspects [3]. Even the same toner printed on different paper can get different printing tonal gradation [4, 5]. The surface properties of paper directly restrict printing tonal gradation and influence the final effect of printing products [6, 7]. Therefore, it is important to research on the influence of paper surface properties to the printing tonal gradation. Through the test and analysis on the surface properties of different types of paper (whiteness, smoothness, gloss, ink absorption and surface efficiency), the research on the influence of paper surface properties to the printing tonal gradation, and the use of gray relational analysis method, we calculate the influence degree of the

surface properties such as surface gloss, whiteness, and efficiency factors to the printing tonal gradation, rank them to suggest their relevance and provide references for practical production.

## 2 Experiment

### 2.1 Materials

UPM128, 157, 250 g/m<sup>2</sup> coated paper, 80, 100 g/m<sup>2</sup> offset paper; Absorbe facient paper printing ink of Tianjin Tianshi (K&N value).

### 2.2 Instruments

YT-GM Gloss Tester, YT-BST Smoothness Tester, XT-48A Whiteness Tester, X-Rite Spectrophotometer, Kemei C6000 Digital Printer.

### 2.3 Methods

#### 2.3.1 Testing of Surface Properties of Paper

- (1) Test whiteness of paper through GB7974-87 method.
- (2) Test smoothness of paper through GB456-2002 method.
- (3) Test specular glossiness of paper (75° measurement angle) through GB8941-2007 method.
- (4) Test ink absorption of paper through ink stain test method (TAPPI Standard RC-9). Use XT-48A to test whiteness of paper. The calculation formula (1) for ink absorption of paper (K&N value):

$$K\&N = \frac{R_{\infty} - R_F}{R_{\infty}} \times 100\% \quad (1)$$

In the formula,

$R_F$  Reflectivity of ink stain area;

$R_{\infty}$  Reflectivity of thick blank paper

- (5) Calculation of paper surface properties

Surface properties of paper are physical measurements including paper gloss and ink absorption, related with optical properties and printing eligibility indexes which influence quality of printing product [8]. The calculation formula (2) of paper surface properties is as followed:

$$PSE(\%) = \frac{100 - A(\%) + G(\%)}{2} \quad (2)$$

In the formula:

A Ink absorption of paper (K&N value)

G Paper gloss (specular gloss in 75° angle)

### 2.3.2 Testing of Printing Tonal Gradation

To reflect reproduction effect of printing tonal gradation, under the same printing technology, we test reflection solid ink density of cyan (C), magenta (M), yellow (Y), Black (K) as well as expansion rate of dots in 40 and 80%, and take the average of each data items [9].

## 3 Experiment Results and Discussions

### 3.1 Experiment Results

The test results of paper surface properties are shown in Table 1, the calculation results of paper surface efficiency are shown in Table 2 and results of printing tonal gradation can be referred to Table 3.

**Table 1.** Test results of paper surface properties

Paper type	Basis weight (g/m <sup>2</sup> )	Whiteness (%)	Gloss (%)	Smoothness (s)	Ink Absorption (%)
Offset paper	80	94.99	6.26	26.84	50.54
	100	92.45	6.46	32.72	52.589
Coated paper	128	88.76	64.48	320.74	14.14
	157	85.72	68.26	431.86	12.64
	250	86.99	66.98	385.84	13.64

**Table 2.** Calculation results of paper surface efficiency

Paper type	Basis weight (g/m <sup>2</sup> )	Ink absorption (%)	Gloss (%)	Surface efficiency (%)
Offset paper	80	54.94	6.26	25.66
	100	56.99	6.46	24.74
Coated paper	128	18.54	64.48	72.97
	157	17.03	68.26	75.62
	250	18.04	66.98	74.47

### 3.2 Grey Correlation Analysis

#### 3.2.1 Calculation of Grey Correlation Value

We calculate grey calculation value by referring to numerical methods and steps of grey relational analysis, which generally set the dependent variable as reference

**Table 3.** Test results of printing tonal gradation

Paper type	Basis weight (g/m <sup>2</sup> )	SID of C	SID of M	SID of Y	SID of K	Expansion rate of dots in 40% (%)	Expansion rate of dots in 80% (%)
Offset paper	80	1.3	1.2	0.95	1.73	16	13
	100	1.28	1.22	0.93	1.65	17	13
Coated paper	128	1.62	1.65	1.03	2.54	18	14
	157	1.63	1.68	1.03	2.56	20	15
	250	1.68	1.72	1.05	2.62	16	15

sequence and the independent variable as comparison sequence, therefore we set reflection solid ink density of four colors' printing product as well as expansion rate of dots in 40 and 80% as reference sequence and paper properties as comparison sequence.

For convenience, we can make use of Grey Modeling Software (seventh edition) to calculate correlation value [7]. The specific steps are:

Step 1: Use Excel to deal with test data.

Step 2: Open Grey Modeling Software and choose Dengshi Correlation lik.

Step 3: Import Excel file, push the calculation button of Dengshi Correlation and get the results.

Finally, we classify and count the results and get Tables 4 and 5.

**Table 4.** Grey correlation data of offset paper

Paper properties	Correlation					
	SID of C	SID of M	SID of Y	SID of K	Expansion rate of dots in 40%	Expansion rate of dots in 80%
Whiteness	0.9574	0.8514	0.979	0.935	0.7351	0.9034
Smoothness	0.6667	0.6667	0.6667	0.6667	0.6667	0.6667
Gloss	0.999	0.8795	0.9785	0.9065	0.7511	0.9378
Ink absorption	0.8454	0.9157	0.8369	0.8073	0.8789	0.8734
Surface Efficiency	0.9254	0.8294	0.9447	0.9645	0.7222	0.8767

### 3.2.2 Comparison of Grey Correlation Degree and Correlation

According to principle of grey correlation analysis, correlation degree is the measure of the correlation between the factors and the system behavior characteristics. It can only measure the relative size of the closely degree between factors, and its numerical absolute size often makes little sense. The key point is to reflect the correlation degree between each comparison consequence and the same reference consequence. If the comparison

**Table 5.** Grey correlation data of coated paper

Paper properties	Correlation					
	SID of C	SID of M	SID of Y	SID of K	Expansion rate of dots in 40%	Expansion rate of dots in 80%
Whiteness	0.851	0.8262	0.8817	0.8544	0.7181	0.721
Smoothness	0.6132	0.6129	0.6063	0.61	0.5779	0.6148
Gloss	0.8226	0.8364	0.7999	0.8169	0.77	0.9421
Ink absorption	0.7956	0.775	0.823	0.7993	0.7001	0.6855
Surface efficiency	0.9205	0.9278	0.9401	0.9319	0.7404	0.8421

consequence have greater correlation degree, its development tendency and change speed are closer to reference consequence, which means that the greater the correlation degree, the two consequences have closer correlation, the influence degree are greater.

**3.2.3 Grey Correlation Analysis of Paper Surface Properties**

From the grey correlation ranking in Table 6, we can find that different paper surface properties have different influences on its printing tonal gradation, for example, for solid ink density of Y of offset paper, the importance ranking of paper surface properties form large to small are: whiteness, gloss, surface efficiency, ink absorption and smoothness. Besides, even for the same surface property such as smoothness of offset paper, its contributions to the measurement of each printing tonal gradation are different. Therefore, when discussing the influence relationship between paper surface

**Table 6.** Comparison and ranking of grey correlation for paper properties

Paper type	Paper properties	Ranking						Ranking
		SID of C	SID of M	SID of Y	SID of K	Expansion rate of dots in 40%	Expansion rate of dots in 80%	
Offset paper	Whiteness	2	3	1	2	3	2	2
	Smoothness	5	5	5	5	5	5	5
	Gloss	1	2	2	3	2	1	1
	Ink absorption	4	1	4	4	1	4	3
	Surface efficiency	3	4	3	1	4	3	4
Coated paper	Whiteness	2	3	2	2	3	3	3
	Smoothness	5	5	5	5	5	5	5
	Gloss	3	2	4	3	1	1	2
	Ink absorption	4	4	3	4	4	4	4
	Surface efficiency	1	1	1	1	2	2	1

properties and printing tonal gradation, we should make suitable choices according to different properties.

For offset paper, no matter from horizontal comparison or longitudinal comparison, the influence degree of gloss and whiteness on each index of printing tonal gradation are relatively higher than that of ink absorption, surface efficiency and smoothness. From the ranking above, it is not difficult to find that the influence degree ranking of paper surface properties on solid ink density of C, M, Y, K and expansion rate of dots in 40 and 80% from large to small are gloss, ink absorption, whiteness, surface efficiency and smoothness.

For coated paper, the comprehensive ranking of influence degree is surface efficiency, gloss, whiteness, ink absorption and smoothness. The approaching degree of surface efficiency and gloss to each index of printing tonal gradation are higher than that of ink absorption, whiteness and smoothness. From the ranking, we can conclude that the surface property which has the greatest influence on solid ink density of C, M, Y, and K is surface efficiency, and on expansion rate of dots in 40 and 80% is gloss.

What's more, we find that smoothness is not a sensitive paper performance indicator and it is not the main factor leading to the differences between printing tonal gradations. As for the reason, during the printing process, smoothness only makes sense when being considered with ink absorption and other paper surface properties. It is not practical to decide the printing condition when we only determine the smoothness and even there will be great errors.

## 4 Conclusions

Through the grey correlation analysis, we can conclude that:

Under the condition of digital printing, for offset paper, the influence degree ranking of paper surface properties on printing tonal gradation from large to small are gloss, ink absorption, whiteness, surface efficiency and smoothness. However, for coated paper, the comprehensive ranking of influence degree is surface efficiency, gloss, whiteness, ink absorption and smoothness.

For digital printers, no matter for offset paper or coated paper, gloss and whiteness are surface properties which have relatively great influence on printing tonal gradation. Besides, smoothness is not a sensitive paper performance indicator and has least correlation degree with printing tonal gradation. Therefore; it is not the main factor leading to the differences between printing half toning levels.

Due to the limited number of samples and other conditions are insufficient, there may be inaccuracy when using grey correlation analysis to suggest the relevance between paper properties and printing tonal gradation. However, a major character of the gray model is that it needs only a few data to establish model. Although there are not many samples in the study, there will not be great gap in results to use the method in qualitative and quantitative analysis.

## References

1. Zifen, H. (2005). *Research on the relationship between properties of printing paper of printed matter quality*. Dissertation for Doctor's degree: Xi'an University of Technology.
2. Ru, Z. (2004). Introduction to the influence of paper features on the quality of the printing. *Print Today*, 2004(7), 68–70.
3. Xiaochun, L. (2001). *Research on the relationship between paper surface properties and printing halftoning levels as well as color reproduction*. Henan: The PLA Information Engineering University.
4. Qingtao, C. (2011). The study on paper surface properties. *Tianjin Paper Making*, 2011(2), 15–17.
5. Jinlin, X., & Haoxue, L. (2012). *Introduction to printing engineering*. Beijing: Chemical Industry Press.
6. Lin, Z. (2013). *Study on the correlation between paper printability and printing quality*. Dissertation for Doctor's degree, Shanxi University of Science and Technology.
7. Sifeng, L, Yingjie, Y., & Lifeng, W., etc. (2014). *The grey system theory and its application*. Beijing: Science Press.
8. Xiaokun, Q., Wenhua, Z., & Yonggang, Y. (2008). *Printing materials and eligibility*. Beijing: Printing Industry Press.
9. Yuanlin, Z. (2010). *Print quality test and control technology*. Beijing: Chemical Industry Press, 2010.01.





# Facile Strategy for the Fabrication of Superhydrophobic Coatings on the Surface of Paper

Qing Wang<sup>1</sup>, Guangxue Chen<sup>1</sup>(✉), Zhaohui Yu<sup>2</sup>, and Mingguang Yu<sup>3</sup>

<sup>1</sup> State Key Laboratory of Pulp and Paper Engineering, South China University of Technology, Guangzhou, China

chengx@scut.edu.cn

<sup>2</sup> Shenzhen YUTO Packaging Technology Co., Ltd., Shenzhen, China

<sup>3</sup> School of Materials Science and Energy Engineering, Foshan University, Foshan, China

**Abstract.** Inspired in nature, the fabrication of superhydrophobic surfaces without using fluoroderivates which are harmful to both environments and humans is nowadays a major object of study. This study aimed at building dual-scale multistructure using low coat, green-based coatings to prepare superhydrophobic paper surface. Specifically, castor oil based biothiol which can be self-initiated under UV irradiation was used as the matrix resin. After mixed the resin with fumed silica nanoparticle at certain weight ratio, spray coating the mixture on the surface of papers. Then the coated paper was cured under UV irradiation. The obtained surfaces showed a multi-scale rough texture and an apparent water contact angle of  $157.6 \pm 1.3$ . Moreover, the coatings are able to withstand 5 cycles of abrasion without an apparent decrease of superhydrophobicity.

**Keywords:** Superhydrophobic · Dual-scale · Green-based · Coating paper

## 1 Introduction

Recently, much attention has been paid for the preparation of superhydrophobic surface due to their potential application in combatting bacteria [1], self-cleaning [2], separation of liquids [3, 4], printing and reprography [5], etc. It is well known that a non-wetting surface is governed by a specific nano-micro structured surface topography and low surface energy.

Paper product is widely used in food and liquid packaging. Water resistance is one of important properties of paper-based packages. Traditionally, polymer barrier coated papers has been used to provide high degree of water resistance and are commonly considered as recyclable papers. Unfortunately, the cost of polymer barrier coating largely limits the actual application in packaging materials.

Herein, we reported a castor oil based superhydrophobic coating which could be cured under UV irradiation that could be prepared on paper surface. The surface showed good superhydrophobicity and excellent durability. Compared with above

approaches, our superhydrophobic coating could be simply applied on paper surface without any complex pretreatments of substrates, or the limitations of environmental humidity and temperatures during the fabrication process.

## 2 Experimental

### 2.1 Materials

3-Mercaptopropionic acid (MPA, 99%), p-toluene sulfonic acid (99%) and fumed nano silica ( $\sim 25$  nm) were obtained from Aladdin-reagent (Shanghai, China). Castor oil (CO, 98%) was supplied by Guangdong Guanghua Chemical Factory (Shantou, China). All materials were used as received.

### 2.2 Synthesis of UV Curable Castor Oil Based Biothiol

UV curable castor oil based biothiol was prepared by the method reported previously [6]. Specifically, CO (10 g), p-toluene sulfonic acid (0.2 g) were thoroughly mixed in a round-bottomed flask. MPA (3.4 g) was added dropwise at 110 °C, and the mixture was vigorously stirred for 3 h. The product was diluted by dichloromethane, washed thrice successively with water, dried over anhydrous  $\text{MgSO}_4$ , and evaporated to give CO-SH.

### 2.3 Fabrication of Superhydrophobic Polymer-Particle Solution

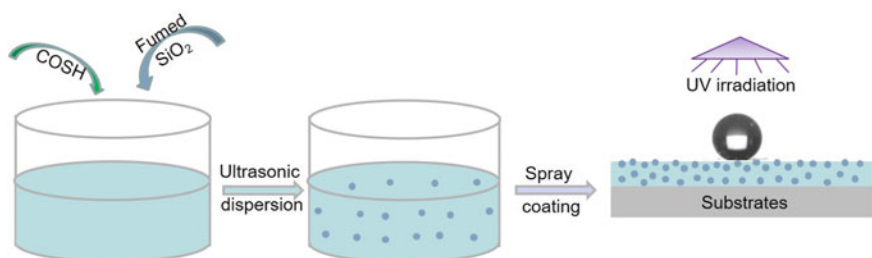
In an optimal preparing process, different amount of fumed silica nanoparticles (0.25, 0.5, 0.75 and 1 g) was added into 50 mL of acetone and ultrasonic dispersed for at least 1 h. To the resulting solution, 1.0 g of castor oil based biothiol was added and the solution was mechanically stirred for another 1 h to obtain superhydrophobic polymer-particle solution. After that, the resulting suspension was sprayed on filter paper surface from a 20 cm working distance and cured under UV irradiation for 120 s (irradiation intensity of 50  $\text{mW}/\text{cm}^2$ ).

### 2.4 Characterization

Morphology of the surfaces were measured out on a thermal field-emission scanning electron microscope (FESEM, Quanta 400F) at 15 kV. The transmittance of the coating on glass slides was obtained on a Pgeneral TU-1901 UV-visible spectrophotometer in the wavelength range of 400–800 nm. Water contact angles (WCAs) were measured on a Dataphysics OCA20 Contract-Angle System with liquid droplets of 5  $\mu\text{L}$ . The average water contact angle value was obtained by measuring at least 5 different positions on the same sample.

### 3 Results and Discussion

The procedure for fabricating superhydrophobic coating is depicted in Scheme 1. During the preparation of coating solution, the influences of weight ratio of CO-SH resin and fumed silica on the hydrophobicity of the as-prepared film were investigated, shown in Fig. 1. The water contact angle of the pristine cured film was  $94.3^\circ$ . With the addition of  $\text{SiO}_2$  nanoparticles, such as 20 wt%, the water contact angle of the as-prepared film increased to  $101.4^\circ$ . When the amount of  $\text{SiO}_2$  increased from 33.3, 42.9 to 50 wt%, the surface roughness of the corresponding film increased accordingly, which can amplify hydrophobicity into superhydrophobicity. As a result, the water contact angle increased to  $122.9^\circ$ ,  $135.8^\circ$  and  $155.6^\circ$ , respectively.



**Scheme 1.** Schematic illustration of procedure for preparation of CO-SH- $\text{SiO}_2$  films

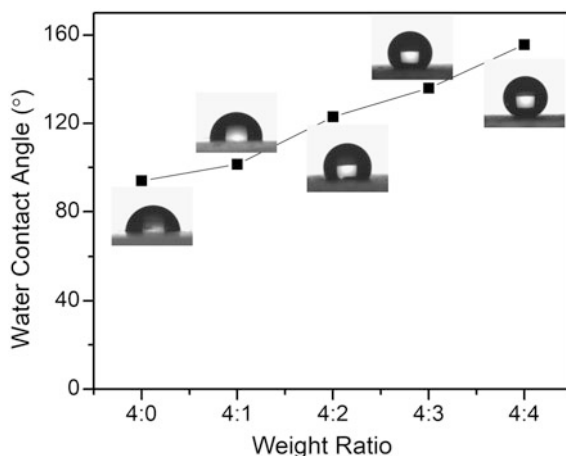


**Fig. 1.** Influence of weight ratio of CO-SH and  $\text{SiO}_2$  on the hydrophobicity of the UV cured coating

The surface morphology of pristine cured film and SiO<sub>2</sub> modified film were measured, shown in Fig. 3. The surface of UV cured film was smooth. After surface modification with silica nanoparticles (Fig. 3), a rough surface formed by accumulating SiO<sub>2</sub> nanoparticles being reasonably monodisperse in the coating surface. In Fig. 2c, the surface of coated paper was covered with by the resin and silica nanoparticles. Higher magnification SEM images (Fig. 2d) showed that silica nanoparticles were densely and uniformly distributed on the paper surface, which roughen the paper surface. The paper modified with special micro/nano rough structures was expected to improve hydrophobicity ability.

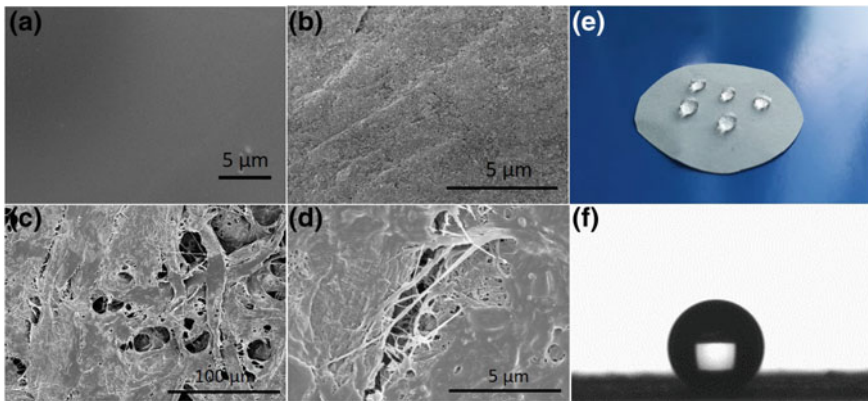


**Fig. 2.** SEM images of surface morphologies of COSH film (a), COSH-SiO<sub>2</sub> (b), surface morphologies of coated paper with different magnification (c, d). Optical image (e) and water contact angle of the as-prepared paper (f)

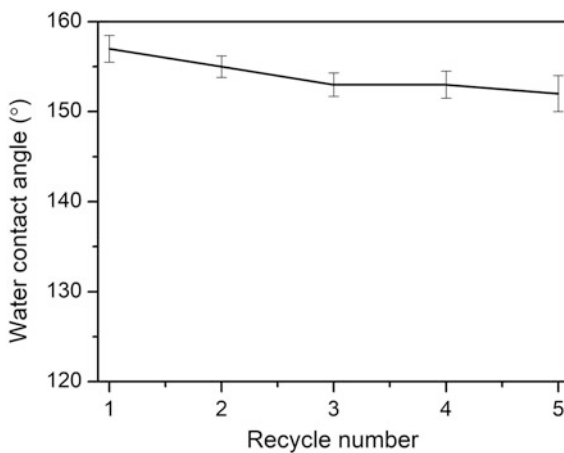


**Fig. 3.** Plots of WCAs after each friction cycle

The as-prepared paper displays superhydrophobicity property, as shown in Fig. 2e. Water droplets that are dropped onto the paper surface can stand on the surface and maintain their spherical shapes. As shown in Fig. 2f, the apparent water contact angle (WCA) of the as-prepared paper is  $157.6^\circ$ , which proved the excellent superhydrophobicity property of the paper.

As important criteria for practical applications, the durability of the obtained paper was evaluated. Sandpaper-abrasion test was performed to check the robustness of the paper against mechanical forces. The as-prepared paper was placed on 400 mesh sandpaper under a weight of 50 g and moved back and forth with abrasion length of about 10 cm. As shown in Fig. 3, there was a slight decrease of the WCA after 5 separation cycles, and the WCA also maintained above  $150^\circ$ . The results demonstrated that the prepared paper performed excellent durability.

## 4 Conclusions

A convenient and environmentally friendly approach to prepare UV curable superhydrophobic coating was demonstrated. The coating can be applied to different paper surfaces. The surface showed good superhydrophobicity with WCA higher than  $157.6^\circ$ . Besides, the surface retained excellent superior water repellency after 5 friction cycles. The procedure was carried out in a mild environment, with no intricate instruments or toxic reagents. The results suggest that these papers are promising sustainable and highly effective materials for large-scale packaging materials.

**Acknowledgements.** This work is supported by the Science and Technology Planning Project of Guangdong Province (No. 2017B090901064), the Science and Technology Project of Guangzhou City (No. 2016070220045), China Postdoctoral Science Foundation (2018M633054), the High-Level Talent Start-Up Research Project of Foshan University (gg040945), Shenzhen development and Reform Commission's strategic emerging industries and special funds for future industrial development (No. 2016.939) and the 2018 discipline construction fund of the School of Light Industry and Engineering, South China University and Technology.

## References

1. Shen, L., Wang, B., Wang, J., Fu, J., Picart, C., & Ji, J. (2012). Asymmetric free-standing film with multifunctional anti-bacterial and self-cleaning properties. *ACS Applied Materials and Interface*, 4, 4476–4483.
2. Ding, X., Zhou, S., Gu, G., & Wu, L. (2011). A facile and large-area fabrication method of superhydrophobic self-cleaning fluorinated polysiloxane/TiO<sub>2</sub> nanocomposite coatings with long-term durability. *Journal of Materials Chemistry*, 21, 6161–6164.
3. Wang, Q., Yu, M., Chen, G., Chen, Q., & Tian, J. (2017). Robust fabrication of fluorine-free superhydrophobic steel mesh for efficient oil/water separation. *Journal Materials Science*, 52, 2549–2559.
4. Yu, M., Wang, Q., Zhang, M., Deng, Q., & Chen, D. (2017). Facile fabrication of raspberry-like composite microspheres for the construction of superhydrophobic films and applications in highly efficient oil-water separation. *RSC Advances*, 7, 39471–39479.

5. Wang, Y., Li, X., Hu, H., Liu, G., & Rabnawaz, M. (2014). Hydrophilically patterned superhydrophobic cotton fabrics and their use in ink printing. *Journal of Materials Chemistry A*, 2, 8094–8102.
6. Wang, Q., Chen, G., Cui, Y., Tian, J., He, M., & Yang, J. (2017). Castor Oil Based Biothiol as a Highly Stable and Self-Initiated Oligomer for Photoinitiator-Free UV Coatings. *ACS Sustainable Chemistry & Engineering*, 5, 376–381.



# Research on the Influence of Optical Properties of Paper on the Ink-Jet Printing Color

Yonghong Qi<sup>(✉)</sup> and Boqi Wu

The Academy of Print Packaging and Digital Media, Xi'an University of Technology, Xi'an, Shaanxi, China  
yonghongqi@163.com

**Abstract.** There are many factors that affect the printing color. This paper researches how the whiteness and glossiness of paper produce an effect on the printing color. Six kinds of ink-jet paper are studied and the whiteness and glossiness are measured. A tested image is printed on the six kinds of paper with the same amount ink in turns. The solid density, color gamut, the color difference (CIE 1976) that the tested image to the standard G7 are measured and analyzed. According to the software IBM SPSS Statistics 20.0, the whiteness and glossiness of paper are positive to the solid density and color gamut, and negative to the CIE 1976 color differences to the G7. The formulas describing the effect of paper whiteness and gloss on the parameters are obtained.

**Keywords:** Whiteness · Glossiness · Digital printing paper · Printing color

## 1 Introduction

Paper is one of the important factors that can influence the print color. The whiteness, glossiness and the color of paper are the important properties of paper [1]. A lot of people have researched how the properties of paper take effect on the printing, such as Jiang [2], Li [3], Liu [4] etc. This paper researches on the whiteness and glossiness of the ink-jet printing paper, and the further goal expects to tell us how the whiteness and glossiness affect the printing color.

## 2 Experimental

### 2.1 Design the Experiment

There are six kinds of paper selected in the experiment. The whiteness and glossiness of every paper are measured. A test image designed by Adobe Illustrator is printed on the paper with the same amount ink. The data of the density and chromatic value of the product are measured by the spectrophotometer (X-Rite exact). The software, IBM SPSS Statistics 20.0 provides the connection that the whiteness and glossiness of the paper have an influence on the printing color.

### 2.2 Measure the Whiteness and Glossiness of the Six Kinds of Paper

The whiteness is measured by the whiteness meter (Type: PN-488, made by Hangzhou Pinxiang technology co.LTD, China). The glossiness is measured by the vancometer (Type: AcuGloss, made by X-Rite co.LTD, USA).

### 2.3 Design the Tested Image and Printing

A tested image including the yellow, magenta, cyan, black solid and tone, Ugra Fogra-Media Wedge V3.0 is designed with the software Adobe Illustrator. Figure 1 is followed.



Fig. 1. The standard test figure

The figure map and the color blocks of the right contained in Fig. 1 are quoted from the G7 test chart by the GRACoL.



Figure 1 is printed on the six kinds of paper in turns with the same amount ink by Epson Stylus PRO 9910 inkjet printer. After the printing products are dry, density values and chromatic values are measured by X-Rite iLiO and X-Rite exact.

### 3 Results and Discussion

#### 3.1 How Whiteness and Glossiness of Paper Affect on the Solid Density of Printing Product

Solid density is the density of 100% dot area and it is also one of important factors that determine the printing color. The three average solid density values are given of four printing color, yellow, magenta, cyan and black by the X-Rite exact spectrophotometer. Table 2 is shown.

**Table 1.** The whiteness and glossiness of paper

Paper types	Whiteness	Glossiness (85°)
matte paper (190 g/m <sup>2</sup> )	106.53	31.5
Fine color spray paper (100 g/m <sup>2</sup> )	111.73	5.2
Semi-matte paper (180 g/m <sup>2</sup> )	108.20	30.8
gloss photo paper (260 g/m <sup>2</sup> )	112.27	96.3
Matte paper (230 g/m <sup>2</sup> )	99.83	40.4
Typing paper of Epson (160 g/m <sup>2</sup> )	105.47	60.2

**Table 2.** Solid density values of every paper

The kinds of paper	D <sub>C</sub>	D <sub>M</sub>	D <sub>Y</sub>	D <sub>V</sub>
Matte paper (190 g/m <sup>2</sup> )	1.5	1.64	1.05	1.69
Fine color spray paper (100 g/m <sup>2</sup> )	1.06	1.13	0.83	1.07
Semi-matte paper (180 g/m <sup>2</sup> )	1.48	1.68	0.99	1.65
Gloss photo paper (260 g/m <sup>2</sup> )	1.54	1.71	0.99	1.73
Matte paper (230 g/m <sup>2</sup> )	1.06	1.31	0.88	1.13
Typing paper of Epson (160 g/m <sup>2</sup> )	1.49	1.69	1.02	1.63

According to Tables 1 and 2, the lower solid density values are given from the 100 g/m<sup>2</sup> fine color spray paper and the 230 g/m<sup>2</sup> matte paper because they are lower whiteness and glossiness values.

Formulas 3.1–3.4 are given by the software IBM SPSS Statistics 20.0. The formulas demonstrate the relationship between the whiteness, glossiness and the solid density.

$$D_C = -0.093 + 0.012x_1 + 0.004x_2 \quad (3.1)$$

$$D_k = -0.050 + 0.012x_1 + 0.005x_2 \quad (3.2)$$

$$D_M = 1.229 + 0.001x_1 + 0.005x_2 \quad (3.3)$$

$$D_Y = 0.995 + 0.0x_1 + 0.001x_2 \quad (3.4)$$

$D_C, D_K, D_M, D_Y$  is respectively the solid density of cyan, black, magenta and yellow ink;

$x_1$  replaces the value of whiteness of paper;

$x_2$  replaces the value of glossiness of paper.

According to the formulas 3.1–3.4, the whiteness and glossiness of paper are positively related to the solid density of every color. The whiteness value has much more influence than the glossiness to the dark ink, such as black and cyan ink. While, the glossiness value has much more influence than the whiteness value for yellow and magenta ink.

### 3.2 Whiteness and Glossiness Values Effect on the Color Gamut

Figure 2 is the color gamut of the six kinds of paper due to the EFI verifier software and the measured data by the spectrophotometer.

The larger color gamut comes from the bigger whiteness and glossiness. The relative areas that the CIE1976  $a^* - b^*$  color gamut are given by the Auto CAD software (Table 3).

The regression equation with two dependent variables, the whiteness and glossiness to the area of color gamut is obtained by the software IBM SPSS Statistics

$$S = 85.775 + 2.967x_1 + 2.422x_2 \quad (3.5)$$

$S$  the area of color gamut

$x_1$  the whiteness of paper

$x_2$  the glossiness of paper.

There is obvious that the whiteness and glossiness are positive to the color gamut.

When the whiteness values are adjacent, according to Table 1, the whiteness value of 260 g/m<sup>2</sup> gloss photo paper is close to the whiteness value of 100 g/m<sup>2</sup> fine color spray paper, the bigger glossiness value will produce the bigger color gamut, such as Fig. 3.

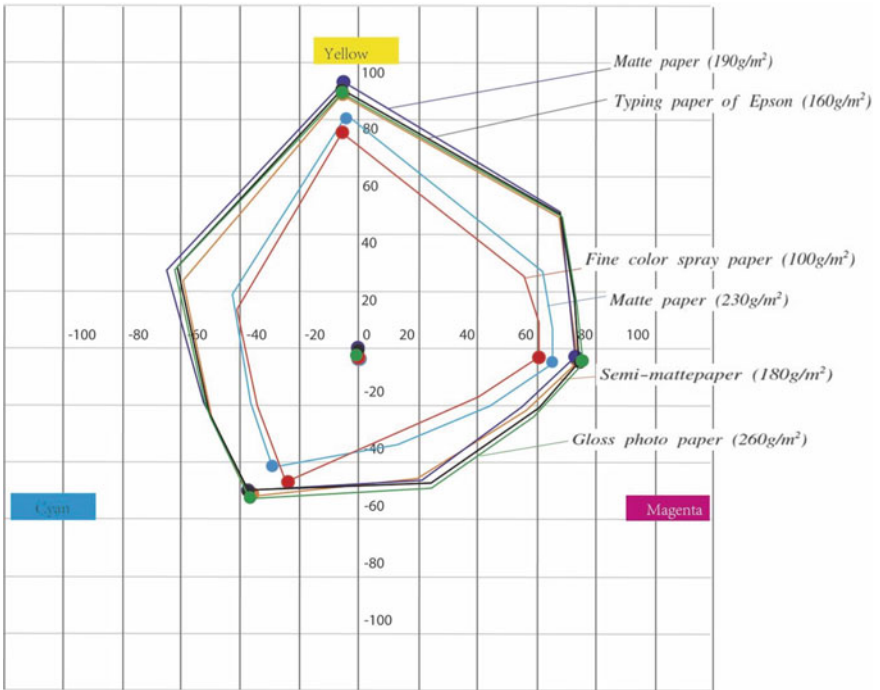


Fig. 2. The color gamut of six kinds of paper

Table 3. The relative area of six kinds of paper

The kind of paper	Relative area
Matte paper (190 g/m <sup>2</sup> )	599.40
Fine color spray paper (100 g/m <sup>2</sup> )	328.10
Semi-matte paper (180 g/m <sup>2</sup> )	566.40
Gloss photo paper (260 g/m <sup>2</sup> )	604.00
Matte paper (230 g/m <sup>2</sup> )	372.80
Typing paper of Epson (160 g/m <sup>2</sup> )	595.10

### 3.3 Whiteness and Glossiness Affect on the Color Difference

Color difference is one of important parameters when we evaluate the quality of the printing production. Table 4 gives the largest color difference that the six kinds of paper to the standard sample G7 by the software EFI Verifier.

According to Table 4, the smaller whiteness and glossiness will produce the larger color difference. That means the whiteness and glossiness are negative to color difference. In the same way, the regression equation, formula 3.6 is given.

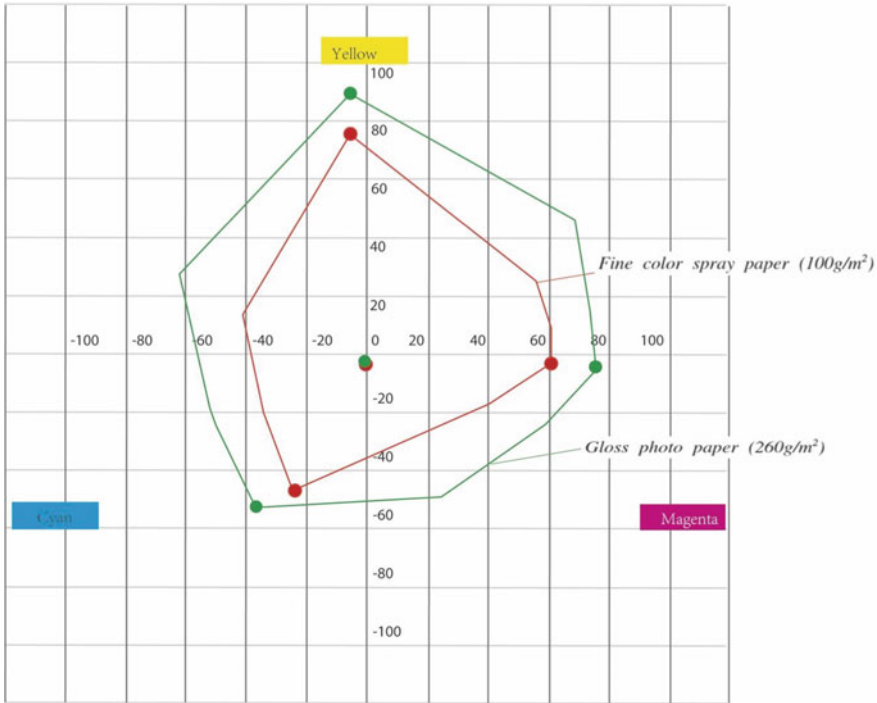


**Fig. 3.** The color gamut of the 260 g/m<sup>2</sup> paper and the 100 g/m<sup>2</sup> paper

**Table 4.** The largest color difference that every paper to the standard sample G7

The kinds of paper	The largest color difference
Matte paper (190 g/m <sup>2</sup> )	3
Fine color spray paper (100 g/m <sup>2</sup> )	30.7
Semi-matte paper (180 g/m <sup>2</sup> )	9.2
Gloss photo paper (260 g/m <sup>2</sup> )	9.2
Matte paper (230 g/m <sup>2</sup> )	26.4
Typing paper of Epson (160 g/m <sup>2</sup> )	7.8

$$\Delta E = 35.083 - 0.122x_1 - 0.172x_2 \tag{3.6}$$

$\Delta E$  the largest CIE1976 color difference,  
 $x_1$  the whiteness value,  
 $x_2$  the glossiness value.

Formula 3.6 illustrates that if we want to reduce the color difference to the standard sample G7, we should enhance the whiteness and glossiness of paper.

## 4 Conclusions

In terms of the discussion of above, some conclusions are obtained:

- (1) The whiteness and glossiness of paper is positive to the solid density of printing production. The whiteness value has much more influence than the glossiness to the black and cyan ink. While, the glossiness value has much more influence than the whiteness value for yellow and magenta ink.
- (2) The whiteness and glossiness of paper is positive to the color gamut.
- (3) The whiteness and glossiness are negative to the CIE1976 color differences that the tested samples to G7.

That's mean, whiteness and gloss of paper cannot be ignored when the high quality printing products are expected.

## References

1. (English) Thompson, B. (2006). *Printing Materials*. Beijing: Printing Industry Press.
2. Jiang, L., etc. (2008). The influence of the whiteness of paper on the printing quality. *Package engineering* 3:66–67.
3. Li, Y. (2016). The influence of the paper's optical characteristic on the image reproduction. *Printing technology*, 17, 41–44.
4. Liu, X. (2017). The effect of paper properties on printing quality. *Chemical enterprise management*, 32, 181–183.



# Standard Test Analysis of Edgewise Crush Resistance and Bursting Strength of Corrugated Board

Yafang Feng, Guorong Cao<sup>(✉)</sup>, Lizheng Zhang, Meiqi Yang,  
and Mengting Li

School of Printing and Packaging Engineering, Beijing Institute of Graphic  
Communication, Beijing, China  
caogurong@bigc.edu.cn

**Abstract.** Check whether the edgewise crush resistance and bursting strength specified in GB/T6544-2008 meet the two performance indexes of corrugated board produced by Yifeng Weiye Group, which provide the basis for the standard revision. Experiments were carried out to test the edgewise crush resistance and bursting strength of single and double corrugated board, and comparative analysis of these two performance indicators with standard superior products and qualified products. The results show that the proportion of samples with minimum comprehensive quantitative of corrugated board below the standard value is larger. Under the same weight, the edgewise crush resistance is higher than the standard superior products, and the bursting strength is basically between the standard superior products and qualified products. Corrugated board produced by Yifeng Weiye Group develops to low weight and high strength. The minimum comprehensive quantitative range of GB/T6544-2008 is narrow, and the performance indicators are low. Therefore, it is necessary to revise the GB/T6544-2008 to improve the quality of corrugated board.

**Keywords:** Corrugated board · Edgewise crush resistance · Bursting strength

## 1 Introduction

Corrugated board has many advantages such as rich raw materials, environmental protection, excellent protection and shockproof function, and it is widely used, which is in line with the trend of packaging development [1]. With the development of economy, the replacement of corrugated board production equipment, the advancement of process technology, the standardization of production management, and the high-strength and low-weight quality requirements of corrugated board, the performance of corrugated board has been greatly improved [2–4]. The GB/T6544-2008 has been implemented for 10 years. According to some enterprises who produce corrugated board and users, the edgewise crush resistance and bursting strength specified by national standard are low for the corrugated board currently produced. Therefore, the experimental data of this paper provides a basis for the revision of the two performance indexes of the edgewise crush resistance and bursting strength of single and double corrugated board in GB/T6544-2008.

## 2 Experiments

### 2.1 Experimental Materials, Instruments and Conditions

The corrugated board used in the experiment was provided by Yifeng Weiye Group, four batches of different weights produced in different periods, different types single and double corrugated board were used as experimental materials. The main instruments of the experiment have constant temperature and humidity test chamber, edgewise crush cutter, compression tester and bursting strength meter. The sample is cut, processed and tested according to the atmospheric conditions specified in GB/T10739-2002.

### 2.2 Edgewise Crush Resistance Experiment

The edgewise crush resistance test was carried out according to the GB/T6546-1998 assay. (1) Preparation of the sample, numbering and cutting the sample. Rectangular specimen has a size of  $(25 \pm 0.5) \text{ mm} \times (100 \pm 0.5) \text{ mm}$  was cut with knife and edgewise crush cutter. Cut at least 10 specimens for every kind of corrugated board, and the specimen shall not have indentation, abrasion, etc. (2) Pretreatment of the sample, the prepared sample was pretreated in constant temperature and humidity test chamber, temperature is  $(23 \pm 1) ^\circ\text{C}$  and humidity is  $(50 \pm 2)\%$  for 24 h. (3) Test, the sample is placed in the middle of the lower platen, so that the short side of the sample is perpendicular to the two platens, and then the sample is clamped by the guide block. Start the tester and apply pressure. When the pressure value is close to 50 N, remove the guide block until the sample is crushed and record the maximum pressure. Repeat the test.

### 2.3 Bursting Strength Experiment

Bursting strength was measured by GB/T6545-1998. (1) Sample preparation, each sample area is larger than bursting strength meter chuck area can be. At least 20 samples are removed from every kinds of corrugated board. (2) The instruments and conditions adopted in the pretreatment of the sample are the same as those under the edgewise crush resistance sample. (3) Test, the sample clamped in the middle of the two sample chucks, start the tester, in the sample explosion, record the value. Repeat test, 10 measurements on each side of each sample. Note that the data should be abandoned when the value of the sample increases significantly after blasting. The bursting strength of each test was taken as the average of 20 data of the front and back of the measurement.

## 3 Experimental Data Processing Analysis

### 3.1 Test Results and Analysis of Edgewise Crush Resistance

The minimum comprehensive quantification of corrugated board refers to the quantitative sum of other layers of paper except corrugated paper. Among them, the company

provided the model of corrugated board used in the experiment and the quantification of each layer of corrugated board. The minimum comprehensive quantification can be obtained by the quantitative calculation provided. Calculate the average value of the maximum pressure values of 10 samples of each corrugated board tested in the experiment. The experimental test data of the side pressure strength of single corrugated board and the double corrugated board are shown in Table 1. In the table, G represents the minimum comprehensive quantification and unit  $g/m^2$ ; ECT represents the edgewise crush resistance and unit KN/m.

**Table 1.** Experimental data of the edgewise crush resistance of single and double corrugated board

Corrugated board type		First batch of samples		Second batch of samples		Third batch of samples		Fourth batch of samples	
		G	ECT	G	ECT	G	ECT	G	ECT
Single corrugated board		280	3.90	320	4.53	220	3.09	200	4.20
		320	4.67	240	2.65	360	4.07	200	2.94
		280	4.11	220	2.72	320	3.95	280	3.90
		400	4.97	280	3.25	–	–	320	4.04
		360	4.94	–	–	–	–	220	3.34
		260	3.85	–	–	–	–	280	4.40
Corrugated board type	First batch of samples	Second batch of samples	Third batch of samples	Fourth batch of samples	Corrugated board type	First batch of samples	Second batch of samples	Third batch of samples	
	G	ECT	G	ECT		G	ECT	G	
Double corrugated board	460	6.96	420	6.87	420	5.84	280	5.10	
	340	5.33	440	7.62	300	5.91	300	5.59	
	380	5.47	280	6.17	340	6.29	470	7.64	
	260	3.58	300	7.91	280	4.65	340	6.55	
	300	5.13	320	6.57	320	5.14	260	5.12	
	380	6.95	460	6.06	–	–	440	7.07	
	–	–	380	7.20	–	–	380	6.40	

Using the method of linear regression analysis, the experimental data of the four batches of single-double corrugated board of Table 1 and the grades of the superior and the qualified grades of the single-double corrugated board of GB/T6544-2008 are plotted, as shown in Figs. 1 and 2.

It can be seen from Fig. 1 that the minimum comprehensive quantitative range of single corrugated board made by the experiment is 200–400  $g/m^2$ . Under the same weight condition, the edgewise crush resistance of most samples is higher than that of the national standard. It can be seen from Fig. 2 that the minimum comprehensive quantitative value of the sample is less than half of the original national standard value



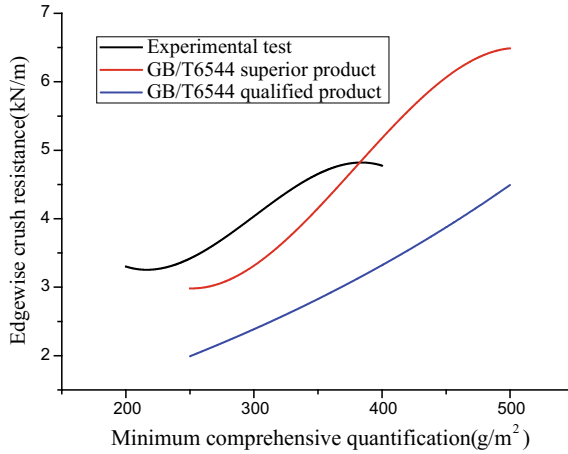


Fig. 1. Single corrugated board edgewise crush resistance

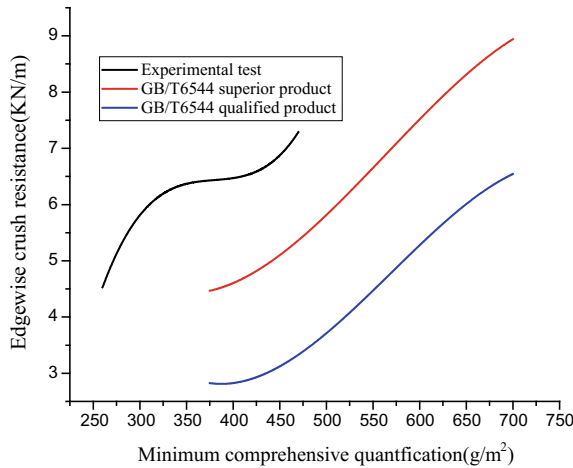


Fig. 2. Double corrugated board edgewise crush resistance

of 375 g/m<sup>2</sup>, and these samples have higher edgewise crush resistance than the minimum comprehensive quantitative standard of 375 g/m<sup>2</sup> in the standard. It can be explained that the edgewise crush resistance of single and double corrugated cardboard produced by enterprises providing experimental materials is very good.

### 3.2 Test Results and Analysis of Bursting Strength

The experimental data of the bursting strength of the single and double corrugated board is shown in Table 2. In the table G represents the minimum comprehensive quantification and unit g/m<sup>2</sup>, the unit of bursting strength is kpa.

**Table 2.** Experimental data of bursting strength of single and double corrugated board

Corrugated board type	First batch of samples		Second batch of samples		Third batch of samples		Fourth batch of samples	
	G	Bursting strength	G	Bursting strength	G	Bursting strength	G	Bursting strength
Single corrugated board	280	729	320	769	220	578	200	668
	320	743	240	608	360	812	200	625
	280	690	220	596	320	756	280	627
	400	950	280	653	–	–	320	780
	360	881	–	–	–	–	220	615
	260	753	–	–	–	–	280	826
Double corrugated board	1020	420	829	420	942	280	672	1020
	880	440	1108	300	910	300	843	880
	902	280	712	340	775	470	947	902
	718	300	891	280	741	340	758	718
	741	320	825	320	805	260	680	741
	943	460	948	–	–	440	1092	943
	–	380	822	–	–	380	816	–

Using the method of linear regression analysis, the experimental data of the four batches of single and double corrugated board of Table 2 and the grades of the superior and the qualified grades of the single and double corrugated board of GB/T6544-2008 are plotted, as shown in Figs. 3 and 4.

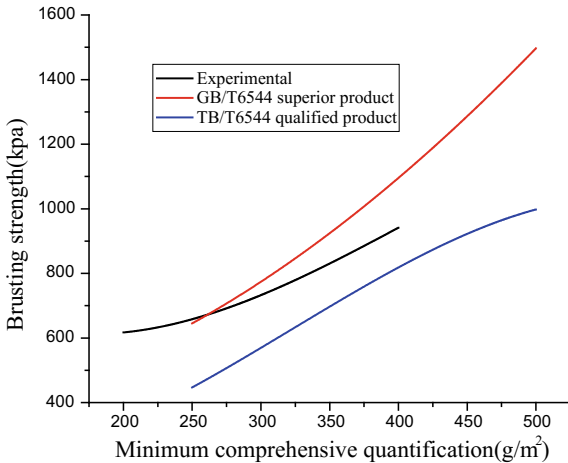


**Fig. 3.** Single corrugated board bursting strength

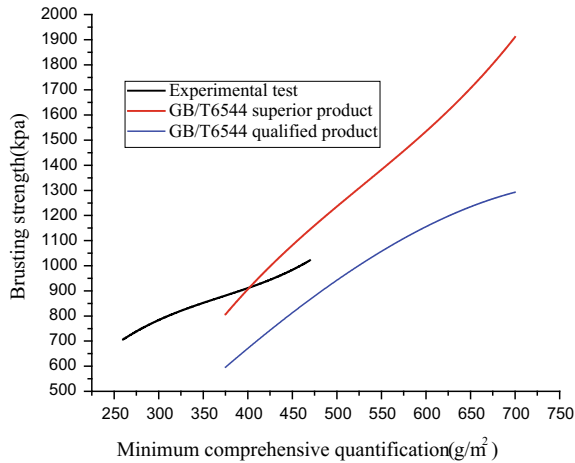


**Fig. 4.** Double corrugated board bursting strength

According to Fig. 3, under the same weight condition, the bursting strength of single corrugated board is between the national standard superior and qualified product, but the proportion of the sample with the minimum comprehensive quantitative lower than the national standard value of  $250 \text{ g/m}^2$  is larger. According to Fig. 4, the double corrugated board sample is less than the original national standard of  $375 \text{ g/m}^2$ , accounting for the majority; under the same weight condition, the bursting strength is between the superior product and the qualified product.

## 4 Conclusions

This paper, through the test of the edgewise crush resistance and bursting strength of single-double corrugated board, can draw the following conclusions:

- (1) The minimum comprehensive quantitative decline trend of corrugated cardboard tested in the experiment is obvious.
- (2) Under the same weight condition, the measured value of the edge crush test is higher than the standard superior value, and the bursting strength is between the standard superior product and the qualified product. It reflects that the paper materials provided by the company tend to be low in weight and high in strength.

In summary, it is necessary to test the products of the domestic mainstream corrugated board enterprises, and comprehensively evaluate whether to start the revision of the GB/T6544-2008 standard work.

**Acknowledgements.** This study is supported by the General Education Reform Project of Beijing Institute of Graphic Communication (22150116007/031), Packaging Engineering

Teaching Team (construction) of Beijing Institute of Graphic Communication (22150116006/017) and Research on certification and evaluation technology of typical air pollutant prevention and control in electric power, chemical industry and printing industry (2017YFF0211803).

## References

1. Wei, J. (2012). Performance research and development trend of corrugated cardboard for packaging. *China Packaging Industry*, 19, 9–11.
2. Zhu, Y. H. (2017). Process control and standardization of corrugated board production line. *Printing Techniques*, 7, 51–53.
3. Chen, G. Q. (2010). *Technical transformation and practice of corrugated board production line*. Zhejiang University of Technology.
4. Qin, L. J., & Liu, T. Z., et al. (2005). New technology, new equipment and new methods to increase the strength of corrugated paper. *Heilongjiang Paper*, 33(1), 22–24.

**Part VII**  
**Ink and Related Technology**



# Application of Anthracene-Based Fluorescent Materials on Green Fluorescent Inkjet Ink

Wan Zhang<sup>1(✉)</sup>, Hui Kuang<sup>2(✉)</sup>, Yingjie Xu<sup>1,2</sup>, Hui Wang<sup>1,2</sup>,  
Beiqing Huang<sup>1,2</sup>, and Xianfu Wei<sup>1,2</sup>

<sup>1</sup> School of Printing and Packaging Engineering, Beijing Institute of Graphic Communication, Beijing, China

22722234@qq.com

<sup>2</sup> Beijing Zhong Biao Fang Yuan Anti-counterfeiting Technology Co. Ltd., Beijing, China

16172352@qq.com

**Abstract.** Presently, the existing green fluorescent materials are rare earth luminescent material, which cannot reach the requirement of inkjet ink on dispersion and stability because of the inferior solubleness. In this paper, the fluorescent inkjet inks were prepared by anthracene-based derivatives, ink's printability was tested and the relationship between molecular structure and ink's printability was researched systematically. Finally, the optimal formula of green fluorescent inkjet ink was obtained. The results showed the photophysical properties of proofs a–c had obvious change comparing with inks a–c and the contact angle of ink d was the biggest of all due to the planar construction of fluorescent material with large conjugate degree. The green fluorescent material: 9, 10-bis (4-methoxyphenylethynyl) anthracene with 0.5% and crylic acid B817 with 12% formed the optimal formula. The printing quality of ink prepared by the optimal formula can accord with the demand of digital printing quality.

**Keywords:** Anthracene-based fluorescent materials · Fluorescent inkjet ink · Photophysical properties · Ink's printability

## 1 Introduction

Fluorescent inks have been extensively applied in the authentication of security, highlighting markers, toys, upholstery and so on owing to fluorescent colorant [1–3]. To date, because of the inferior solubleness, most of fluorescent colorants are utilized to prepare the traditional printing inks, such as offset printing inks [4], screen printing inks [5], etc. However, the traditional printing methods cannot meet the requirements of various users with the increasing market demand of fluorescent ink. As one of digital printing methods, inkjet printing which has personalized and instant features can improve the application with fluorescent ink, such as on the anti-counterfeiting code of packaging products, certificate, wallpaper and so on [6–14].

The selection of fluorescent materials for fluorescent inkjet ink is very important. At present, rare earth has many applications in fluorescent ink, but mainly in the traditional printing way, because this kind of materials are insoluble in inkjet ink system, and the

particle size and dispersion stability are also difficult to meet the requirements of inkjet ink. In addition, rare earth belongs to the rare product, which often needs to carry on the processing at high temperatures and large energy consumption. Peter D. and co-workers synthesized nanoparticles of ZnS doped with Mn which were stably dispersed into water based inkjet ink [15]. However, the particles of rare earth material are easy to gather with the increase of time, which would lead to the jam of nozzle. One strategy to suppress the gather of fluorescent colorants is the development of excellent soluble fluorescent colorants. Compared with rare earth fluorescence materials, organic luminescent materials are more suitable as a colorant for inkjet ink because of their excellent solubility and high quantum efficiency [16, 17]. Kim et al. developed four perylene and four phthalocyanine dyes of high thermal stability which were used to fabricate color filters by inkjet printing [18]. Maryam Ataeefard with co-workers incorporated three benzoxazolyl and benzimidazolyl coumarin derivative dyes used as fluorescent dyes into poly(styrene-co-acrylic acid) by using eco-friendly emulsion aggregation (EA) approaches in several amounts with final application of fluorescent laser printing ink called toner [19].

There are red and blue luminescent materials can be used in the current domestic existing inkjet inks system, for example, a kind of glowing red europium coordination polymer [20] and a blue heterocyclic organic matter [21], but also did not see green light-emitting materials can be dissolved in solvent ink system, which has become a research hot spot. Anthracene belongs to a family of polycyclic aromatic compounds, which possesses excellent photoluminescence (PL) quantum yields and solubleness as well as high thermal stability [22, 23]. Based on these ideas, we recently used the anthracene derivatives synthesized previously to prepared fluorescent inkjet ink [24]. In order to satisfy the requirement of inkjet printing, the four inks were prepared with four anthracene derivatives and the properties of inks were tested. Meanwhile, the relationship between the molecular structure of anthracene derivatives and the various properties of inks were studied systematically by using experimental and theoretical methods.

## 2 Experimental

### 2.1 Materials and Instruments

Dichloromethane (A.R./S.P.), ethanol (A.R.), acrylic resin (AZ-5391, B817, Atoz, Tianjin), polyvinyl alkanone resin (Xinkaiyuan, Henan), mengken paper, anthracene-based fluorescent materials [24] (9-(4-formylphenyl) anthracene, 9-(4-phenylethynyl) anthracene, 9-(4-methoxyphenylethynyl) anthracene and 9, 10-bis (4-methoxyphenylethynyl) anthracene).

Magnetic stirring apparatus (HJ-6A, Jintanronghua instrument manufacturing co. LTD, Jiangsu), coating machine (AUTOMATIC 18112), fluorescence spectrophotometer (RF-5301PC, Shimadzu, Japan), UV-Vis spectrophotometer (UV-2501PC, Shimadzu, Japan), static surface tension meter (K100, KRUSS, Germany), rheometer (AR2000, TA, USA), contact angle meter (DSA100, KRUSS, Germany), climatic chamber (Xenotest Alpha LM High Energy, Atlas Ltd. USA).

## 2.2 Experimental Methods

### 2.2.1 Synthesis of Anthracene-Based Derivatives

Figures 1 and 2 are the synthesis routes of anthracene-based derivatives. Compound 9-(4-formylphenyl) anthracene (**a**) was synthesized in good yield from 9-bromoanthracene and the corresponding arylboronic acid by a Suzuki cross-coupling reaction [25]. 9-(4-phenylethynyl) anthracene (**b**), 9-(4-methoxyphenylethynyl) anthracene (**c**) and 9, 10-bis (4-methoxyphenylethynyl) anthracene (**d**) were synthesized in yields of 26–65% from 9-bromoanthracene and 9,10-bromoanthracene respectively and the corresponding phenylacetylene by a Sonogashira cross-coupling reaction [26].

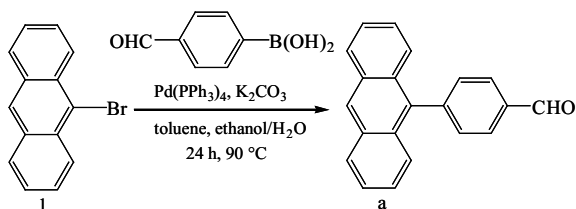


Fig. 1. Synthesis of anthracene-based derivatives **a**

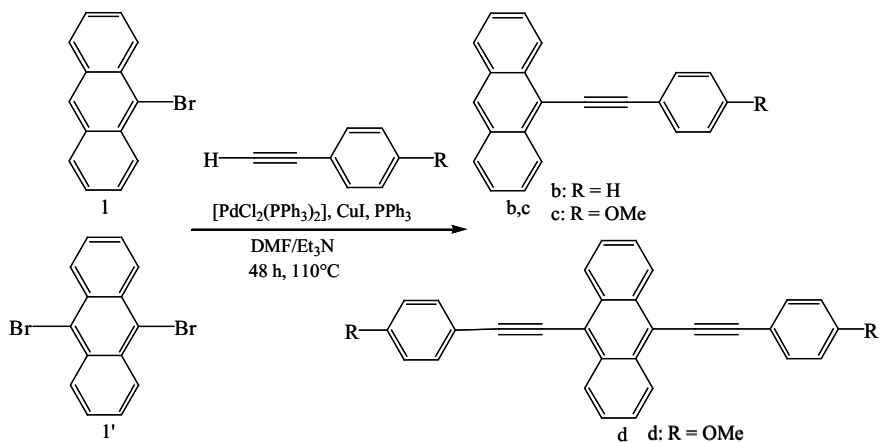


Fig. 2. Synthesis of anthracene-based derivatives **b**, **c**, **d**

### 2.2.2 Preparation Method of Fluorescent Inkjet Inks

The preparation method of fluorescent inkjet ink mainly includes the following three steps:

- (1) The anthracene-based fluorescent materials (0.5%) and ethanol (25%) were mixed and stirred at room temperature for 5–10 min to obtain component A.



- (2) The resin (18%) was mixed with ethanol (55%), 30–50 °C, the mixing time was 30–40 min, to get part B.
- (3) The part A and part B were mixed and stirred to completely transparent solution, time for 20–30 min, then the additive (1.5%) was added and stirred again, time for 10–25 min, to get the ink.

### 2.2.3 Tested Method of Proof'S Photophysical Properties

The coating proofs were obtained by using the coating machine on mengken paper which do not contain fluorescent whitening agent, and then, the proofs will be cut into 2 cm diameter circle. When measuring, the sample clipped was clamped between the circular holes, and the holes of the circular holes must be covered in order to avoid light leakage from the excitation light source. The parameter setting is the same as that of liquid measurement.

## 3 Result and Discussion

### 3.1 Photophysical Properties of Fluorescent Inkjet Inks

#### 3.1.1 Influences of Anthracene-Based Derivatives on Ink'S Photophysical Properties

The photophysical properties of inks **a–d** and proofs **a–d** were measured by UV-vis absorption and FL spectroscopy in dilute  $\text{CH}_2\text{Cl}_2$  solutions, as shown in Fig. 3. All spectral data are summarized in Table 1. It is obvious that the UV-vis and FL emission spectrum of inks **a–d** had almost no change compared with compounds **a–d** [24]. It illustrates that ink system has a little effect on the photophysical properties of fluorescent materials.

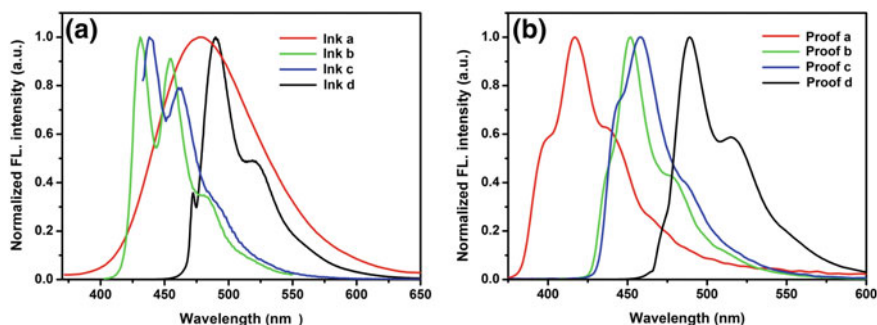


Fig. 3. The FL spectra of inks **a–d** (a) and proofs **a–d** (b)

Nevertheless, the normalized FL emission spectra of proofs **a–c** had huge change compared with inks **a–c**. A larger blue shift of 60 nm was observed from the normalized FL emission spectra of proof **a** (417 nm) in comparison with ink **a** (480 nm) because of its strongest electron-accepting group  $-\text{CHO}$ , which is not easy to enlarge

**Table 1.** Photophysical properties of inks **a–d** and proofs **a–d**

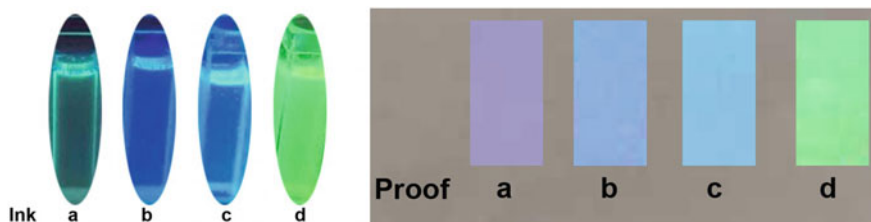
–		$\lambda_{\max}^{\text{abs}}^{\text{a}}$ (nm)	$\lambda_{\max}^{\text{PL}}^{\text{a}}$ (nm)	$\Phi_{\text{f}}^{\text{b}}$	$\tau^{\text{b}}$ (ns)	$L^{*\text{b}}$	$a^{*\text{b}}$	$b^{*\text{b}}$	$\Delta E^{\text{c}}$
Inks	a	349,367,387	480 (387)	0.18	3.05	75.19	−28.04	−12.25	53.69358
	b	399,420	431,455 (424)	0.52	4.72	41.64	40.81	−105.68	29.87086
	c	404,424	438,461 (428)	0.67	4.24	53.52	30.74	−99.31	23.60755
	d	449,472	490 (470)	0.50	2.19	70.7	−69.87	47.08	15.90597
Proofs	a	–	417 (385)	0.10	2.98	79.99	24.77	−20.68	–
	b	–	452 (423)	0.39	4.25	67.48	30.38	−94.92	–
	c	–	458 (456)	0.56	4.01	74.64	28.81	−109.68	–
	d	–	489 (471)	0.49	2.18	80.7	−66.87	35.08	–

<sup>a</sup>The maximum absorption and PL wavelength of compounds **a–d** and inks **a–d** respectively measured in  $\text{CH}_2\text{Cl}_2$  and ethanol at room temperature and. <sup>b</sup>Measured by spectroradiometer (PR-655, Photo Research Inc.). <sup>c</sup>Values calculated from the empirical formula

$$\sqrt{\left(L_{\text{ink}}^* - L_{\text{proof}}^*\right)^2 + \left(a_{\text{ink}}^* - a_{\text{proof}}^*\right)^2 + \left(b_{\text{ink}}^* - b_{\text{proof}}^*\right)^2}$$

the length of  $\pi$ -conjugation and reduce the HOMO-LUMO energy gap under solid state compared with liquid state. Meanwhile, proofs **b** and **c** possessed two peaks, and inks **b** and **c** exhibited single peak. However, it is interesting that the peak value and shape of proof **d** were according with ink **d** due to a stable flat structure of compound **d**.

The fluorescent impact of inks **a–d** and proofs **a–d** were observed by spectroradiometer (PR-655, Photo Research Inc.) under UV light, as shown in Fig. 4. The color data are listed in Table 1. Obviously, there are some changes of color between inks and proofs, especially the color of the proof **a**, which has presented a violet and great change compared to the light green of ink **a**, mainly in hue and saturation. Compared to other proofs **b**, **c** and **d**, inks **b**, **c** and **d** have a little change in hue, and just have a larger change in saturation. The  $\Delta E$  significantly in Table 1 shows the difference, consistent with the change of the fluorescence spectrum above, which illustrates the physical properties of fluorescent materials under the solid and liquid are different. In particular, the electron-accepting group can limit the ability of electron-accepting in solid state.

**Fig. 4.** The fluorescent impact of inks **a–d** printed on paper and proofs **a–d** under UV light

### 3.1.2 Effect of the Content of Fluorescent Materials on Ink'S Photophysical Properties

The inks were prepared by 9, 10-bis (4-methoxyphenylethynyl) anthracene and the contents were 0.1, 0.3, 0.5, 0.7, 0.9%. The fluorescent spectrum of ink was measured, as shown in Fig. 5. Obviously, the peak shapes and the emission peak maximum of five contents have no change, but the luminescent intensity is increasing with the increase of content. When the content is above 0.5%, the increase of luminescent intensity is drastically reduced. If the content continues to increase, the fluorescent material will be precipitated and the luminescence intensity will decrease. Therefore, the optimal fluorescent material content is 0.5%.

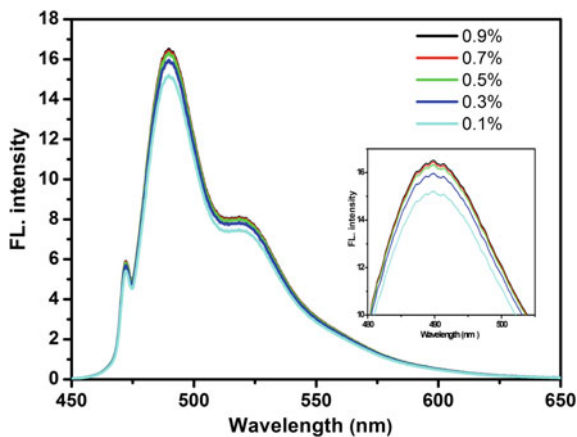


Fig. 5. Effect of fluorescent material's content on luminescent intensity

### 3.1.3 Effect of the Type of Fluorescent Materials on Ink'S Photophysical Properties

The inks were prepared by 9, 10-bis (4-methoxyphenylethynyl) anthracene and the acrylic resin AZ-5391, B817 and polyvinyl alkanone C21. The fluorescent spectrum of ink was measured, as shown in Fig. 6. It is obvious that the luminescent intensity of B817 is the highest of all and the C21 is the lowest, because the heterocyclic pyrrole can limit the fluorescent emission. In addition, acrylic resin containing  $-\text{COOH}$ , belongs to the basement group [27], also affects the fluorescent radiation of fluorescent material. The effect of B817 on the fluorescent radiation of ink is less than AZ-5391 because of the better wettability and solubility in the ethanol system.

## 3.2 Rheological Behavior of Fluorescent Inkjet Inks

### 3.2.1 Effect of Fluorescent Materials on Rheological Behavior

The steady rheological behaviors of inks **a–d** were determined with the shear rate 0.1–100(1/s) at room temperature, as shown in Fig. 7. The dynamic rheological behaviors

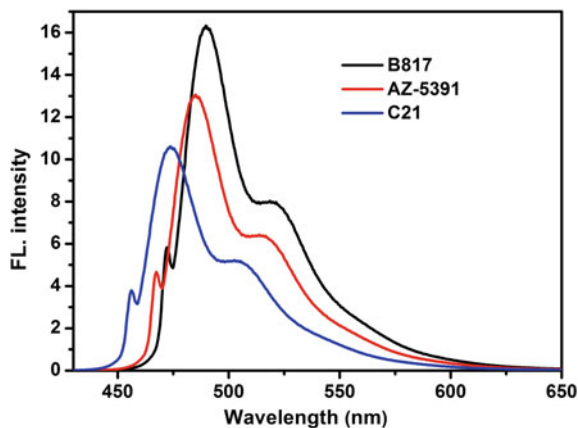


Fig. 6. Effect of resin's type on luminescent intensity

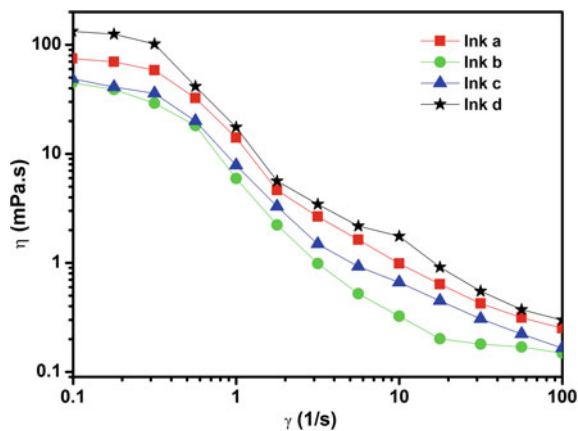


Fig. 7. The flow curves of inks a–d

of inks **a–d** were measured with the smaller strain (1%) at room temperature, as shown in Fig. 8.

From Fig. 7, all inks exhibited typical Non-newtonian rheological behavior (shear thinning): the viscosity decreases with shear rate increases. Although the inks **a–d** showed the same trend of steady rheological behavior, the viscosities of inks were different, 14.10 mPa.s for ink a, 5.94 mPa.s for ink b, 7.83 mPa.s for ink c and 17.57 mPa.s for ink d. Because the difference among inks **a–d** is only the compound, the molecular structure of compound affected largely the steady rheological behavior of ink. The viscosity of ink **d** is highest of all inks due to the largest molecular weight of compound **d**, which can lead to the difficulty of molecular motions and the decrease of the viscosity [28]. In addition, the viscosities of inks are inside the range indicated as

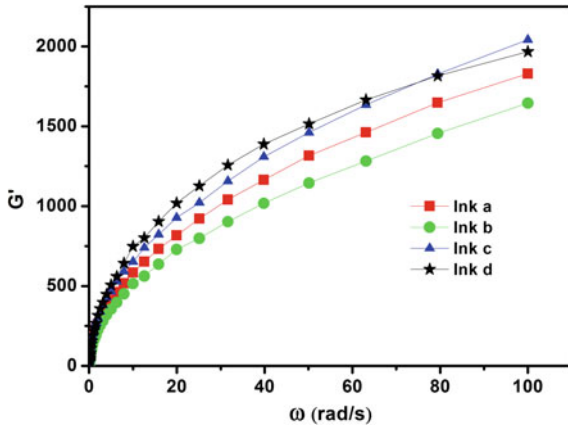


Fig. 8. The relationship between  $G'$  and  $\omega$

optimal for inkjet ink (4–40 mPa.s) could make the ink droplet be jetted from the nozzles fluently [29].

Figure 8 showed different inks exhibit the different relationships between stored elastic ration  $G'$  and angular frequency  $\omega$ . The  $G'$  of all inks increased with the increase of angular frequency under the smaller strain (1%), which illustrated the internal structure of this ink system are stable. However, the increased scope were different, the ink **c** and **d** have the larger increase owing to the OME group which can benefit the improvement of stability.

### 3.2.2 Effect of the Content of Resin on Ink’S Viscosity

The inks were prepared by 9, 10-bis (4-methoxyphenylethynyl) anthracene and the content of acrylic resinB817 10, 12, 14, 16, 18%. The viscosity of ink was measured, as shown in Fig. 9. With the decrease of resin’s content, the viscosity of ink decrease. As

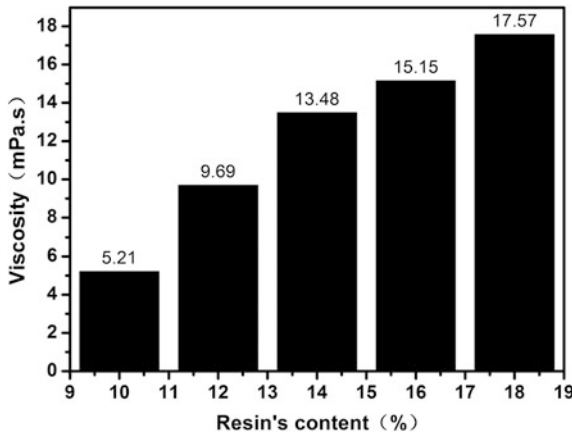


Fig. 9. Effect of resin’s content on viscosity

the highest viscosity component in ink system, resin can significantly affect the flow of ink system. In order to make the ink meet the inkjet requirements of desktop printer, the viscosity is generally around 10 mPa.s, therefore, the optimal resin content is 12%.

### 3.3 Surface Property of Fluorescent Inkjet Inks

#### 3.3.1 Effect of the Type of Fluorescent Materials on Ink'S Surface Property

The surface property is not only affect the inkjet fluency of ink from the nozzles, and affect the wetting state of ink droplet on the surface of the substrate. Thus, the surface property plays an important role on the printing quality. The contact angles of inks were measured by drop shape analyzer (DSA100, kruss, Germany) and the surface tension of inks were determined by tensiometer (k100, kruss, Germany) at room temperature.

From Fig. 10, it was obvious that the contact angles of inks are different in the range  $28.8^{\circ}$ – $44.1^{\circ}$  with the order is ink **d**>ink **c**>ink **a**>ink **b**, which illustrated all inks has favorable wettability on the surface of paper. Meanwhile, the contact angle of ink **d** is the largest of all inks for  $44.1^{\circ}$  and the wettability is worse. The variation trend of surface tension in Table 1 is similar to the contact angle. The maximum surface tension of ink **d** is 26.87 mN/m. The main reason is 9, 10-substituted anthracene derivative **d** has larger flat structure and higher degree of conjugation. Therefore, the molecular structure of compound is also the significant factor for the spreading wetting of ink on the surface of substrate.

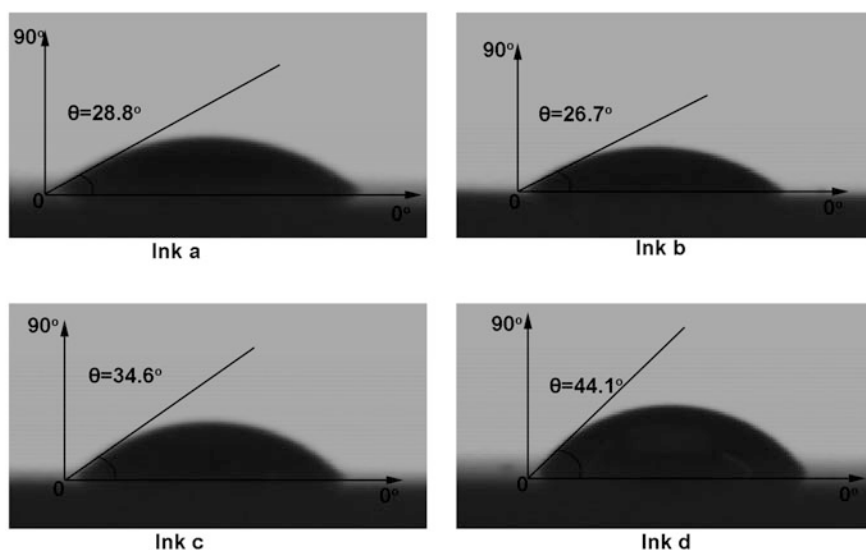
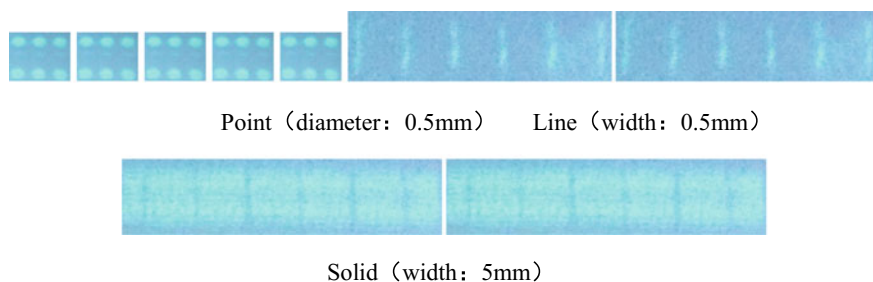


Fig. 10. Contact angles of inks a–d

### 3.4 Optimal Formula and Printing Proof

According to the above research results, the green fluorescent material: 9, 10-bis (4-methoxyphenylethynyl) anthracene with 0.5% and acrylic acid B817 with 12% formed the optimal formula. The proof was printing by the optimal formula and desktop printer Epson Me35, as shown in Fig. 11. The point with a diameter of 0.5 mm, the line with a width of 0.5 mm and the field block with a width of 5 mm were printed. From Fig. 11, the quality of point with better roundness and sharp edge is the best of all, the solid is full and lack of a slight line. But, the quality of lines is relatively poor, the edges are not clear, and the printing quality of lines needs to be further improved.



**Fig. 11.** Printing proof

## 4 Conclusions

- (1) The UV-vis and FL emission absorption spectrum of inks **a–d** had almost no change compared with compounds **a–d**. It illustrates that ink system has little effect on the photophysical properties of fluorescent materials. The normalized FL emission spectra of proofs **a–c** had huge change compared with inks **a–c**. A larger blue shift of 60 nm was observed from the normalized FL emission spectra of proof **a** (417 nm) in comparison with ink **a** (480 nm) because of its strongest electron-accepting group  $-\text{CHO}$ . There are some changes of color between inks and proofs, especially the color of the proof **a**, which has presented a violet and great change compared to the light green of ink **a**, mainly in hue and saturation.
- (2) All inks exhibited typical Non-newtonian rheological behavior (shear thinning). The viscosity of ink **d** is highest of all inks due to the largest molecular weight of compound **d**. The  $G'$  of all inks increased with the increase of angular frequency  $\omega$  under the smaller strain (1%), which illustrated the internal structure of this ink system are stable.
- (3) It was obvious that the contact angles of inks are different in the range  $28.8^\circ$ – $44.1^\circ$  with the order is ink **d**>ink **c**>ink **a**>ink **b**, which illustrated all inks has favorable wettability on the surface of paper. The contact angle and surface tension of ink **d** both are the largest of all inks for  $44.1^\circ$  and 26.87 mN/m.

- (4) The green fluorescent material: 9, 10-bis (4-methoxyphenylethynyl) anthracene with 0.5% and acrylic acid B817 with 12% formed the optimal formula. The printing quality of the ink prepared according to the optimal formula meets the requirements of digital printing quality, but the quality of line printing needs to be further improved.

**Acknowledgements.** This study is funded by the Scientific Research Common Program of Beijing Municipal Commission of Education of China (Nos. KM201810015012, KM201810015003).

## References

1. Hersch, R. D., Douzé, P., & Chosson S. (2007). Color images visible under UV light. In *International Conference on Computer Graphics and Interactive Techniques*, August 5, United states.
2. Rossier, R., & Hersch, R. D. (2011). *Hiding patterns with daylight fluorescent inks*. Switzerland: 19th Color Imaging Conference.
3. van Rensse, R. L. (2005). *Printing inks and printing techniques*. London: Optical Document Security.
4. Fatemeh, T., Farahnaz, N., & Saeed, B. (2014). Development of novel fluorescent offset ink based on coumarin dyes: Synthesis and properties. *Progress in Organic Coatings*, 77, 1351–1359.
5. Coudray, M. A. (2004). Boosting process-color ink gamut with fluorescents. *Screen Printing*, 94(6), 28–32.
6. Lai, H. Y., Chen, T. H., & Chen, C. H. (2011). Optical and electrical properties of ink-jet printed indium–tin-oxide nanoparticle films. *Materials Letters*, 65, 3336–3339.
7. Liu, H. M., Xu, W., Tan, W. Y., Zhu, X. H., Wang, J., Peng, J. B., & Cao, Y. (2016). Line printing solution-processable small molecules with uniform surface profile via ink-jet printer. *Journal of Colloid and Interface Science*, 465, 106–111.
8. Jafarifarid, S., Bastani, S., Atasheh, S. G., & Morteza, G. S. (2016). The chemo-rheological behavior of an acrylic based UV-curable inkjetink: Effect of surface chemistry for hyperbranched polymers. *Progress in Organic Coatings*, 90, 399–406.
9. Chang, C. J., Lin, Y. H., & Tsai, H. Y. (2011). Synthesis and properties of UV-curable hyperbranched polymers for ink-jet printing of color micropatterns on glass. *Thin Solid Films*, 519, 5243–5248.
10. Park, J. Y., Hirata, Y. C., & Hamada, K. (2012). Relationship between the dye/additive interaction and inkjet ink droplet formation. *Dyes and Pigments*, 95, 502–511.
11. Pan, Z. D., Wang, Y. M., Huang, H. N., Ling, Z. Y., Dai, Y. G., & Ke, S. J. (2015). Recent development on preparation of ceramic inks in ink-jet printing. *Ceramics International*, 41, 12515–12528.
12. Karanikas, E. K., Nikolaidis, N. F., & Tsatsaroni, E. G. (2012). Novel digital printing ink-jet inks with “antifraud markers” used as additives. *Progress in Organic Coatings*, 75, 1–7.
13. Stempien, Z., Rybicki, E., Rybicki, T., & Lesnikowski, J. (2016). Inkjet-printing deposition of silver electro-conductive layers on textile substrates at low sintering temperature by using an aqueous silver ions-containing ink for textronic applications. *Sensors and Actuators B*, 224, 714–725.



14. Ahn, S., Kim, W. K., Ryu, S. H., Kim, K. J., Lee, S. E., Kim, S. H., et al. (2012). OLED with a controlled molecular weight of the PVK (poly(9-vinylcarbazole)) formed by a reactive ink-jet process. *Organic Electronics*, *13*, 980–984.
15. Peter, D., Rosanna, K., & Ramin, R. F. (2013). Synthesis and inkjet printing of aqueous ZnS: Mn nanoparticles. *Journal of Luminescence*, *136*, 100–108.
16. Cui, R. Z., Tang, Y. R., Ma, Y. Q., Yang, X. Y., Geng, L. H., & Li, Y. H. (2015). Research progress of investigation on organic blue-light-emitting materials and diodes. *Chinese Journal of Applied Chemistry*, *32*(8), 855–872.
17. Lu, T. H., Huo, Y. P., Fang, X. M., & Ouyang, X. H. (2013). Progress of solution-processable organic small molecular for light emitting materials. *Chinese Journal of Organic Chemistry*, *33*, 2063–2079.
18. Kim, Y. D., Kim, J. P., Kwon, O. S., & Cho, I. H. (2009). The synthesis and application of thermally stable dyes for ink-jet printed LCD color filters. *Dyes and Pigments*, *81*, 45–52.
19. Maryam, A., & Farahnaz, N. (2015). Producing fluorescent digital printing ink: Investigating the effect of type and amount of coumarin derivative dyes on the quality of ink. *Journal of Luminescence*, *167*, 254–260.
20. Huang, B. Q., Zhang, W., & Wei, X. F. (2014). The preparation of red fluorescent inkjet ink Used in the additive method: ZL201210408556.5.
21. Wei, X. F., Zhang, W., & Huang, B. Q. (2014). The preparation of blue fluorescent inkjet ink Used in the additive method: ZL201210410173.1.
22. Ogi, D., Fujita, Y., Mori, S., Shirahata, T., & Misaki, Y. (2016). Bis- and tris-fused tetrathiafulvalenes extended with Anthracene-9,10-diylidene. *Organic Letters*, *18*(22), 5868–5871.
23. Peng, Z., Wang, Z., Tong, B., Ji, Y. C., Shi, J. B., Zhi, J. G., & Dong Y. P. (2016). Anthracene Modified by Aldehyde Groups Exhibiting Aggregation-Induced Emission Properties. *Chinese Journal of Chemistry*, *34*(11), 1071–1075.
24. Zhang, W., Wang, Q., Feng, X., Yang, L., Wu, Y. K., & Wei, X. F. (2017). Anthracene-based derivatives: Synthesis, photophysical properties and electrochemical properties. *Chemical Research in Chinese Universities*, *33*(4), 603–610.
25. Miyaura, N., & Suzuki, A. (1995). Palladium-catalyzed cross-coupling reactions of organoboron compounds. *Chemical Reviews*, *95*(9), 2457–2483.
26. Chinchilla, R., & Nájera, C. (2007). The sonogashira reaction: a booming methodology in synthetic organic chemistry. *Chemical Reviews*, *107*(3), 874–922.
27. Yang, L., Wei, X. F., & Huang, B. Q. (2014). The preparation of infrared fluorescent ink and the research of luminous performance. *Printing technology*, *1*, 54–56.
28. Sara, P., Silva, M. D., Silva Lima, P., & Oliveira, J. M. (2016). Rheological behaviour of cork-polymer composites for injection moulding. *Composites: Part B*, *90*, 172–178.
29. Güngör, G. L., Kara, A., Gardini, D., Blosi, M., Dondi, M., & Zanelli, C. (2016). Ink-jet printability of aqueous ceramic inks for digital decoration of ceramic tiles. *Dyes and Pigments*, *127*, 148–154.



# Preparation of Low Temperature Sintered Graphene/Silver Nanocomposite-Based Conductive Ink

Qingqing Zou, Congjun Cao<sup>(✉)</sup>, Huayang Zhu, and Chengmin Hou

Faculty of Printing, Packaging Engineering and Digital Media Technology,  
Xi'an University of Technology, Xi'an, China

caocongjun@sina.com, caocongjun@xaut.edu.cn

**Abstract.** At present, most silver nanoparticles (AgNPs) conductive inks on the market are in high-temperature sintering modes. In order to increase the application range of printed electronics, it is necessary to prepare conductive inks with low-temperature sintering and good conductivity. In this study, AgNPs and RGO/AgNPs nanocomposites were prepared with glucose as the green reducing agent. The morphology and structural characteristics of the material were analyzed by XRD, SEM and TEM, which were shown that the average particle size of AgNPs was about 30 nm, and when the mass ratio of graphene oxide(GO)and silver nitrate is 1:3, the average particle size of AgNPs loaded on RGO was about 18 nm. The conductive ink was prepared by mixing RGO/AgNPs nanocomposite and AgNPs as conductive filler. After sintering at 100 °C at low temperature, the conductive property was excellent, and its resistivity could reach to 2.4  $\mu\Omega$  cm.

**Keywords:** Low-temperature sintering · RGO/AgNPs nanocomposite · Conductive ink · Glucose

## 1 Introduction

Conductive inks are the essential material for Printed electronics. As silver has good electrical conductivity and oxidation resistance, it is reported that silver conductive inks are the most widely used in the market [1, 2]. However, at present, most silver-based conductive inks are metallized by high-temperature sintering and drying mode [3, 4], which restricts the application of the ink at low temperatures such as PET, coated paper, and other printing substrates [5, 6]. The properties of nanomaterials are highly dependent on the size [7], and some scholars have ever reduced the sintering temperature by preparing small-sized nanosilver particles. For example, Moon et al. [8] used silver nanoparticle with an average particle size of 50 nm to prepare a conductive ink. After sintering at 150 °C, the resistivity of the coating reached 18.4  $\mu\Omega$  cm. Although the sintering temperature of the ink is related to the melting point of the particles, the melting point depends on the size of the particles: the smaller the particle size, the lower the melting point [9]. However, when the particle size is less than 10–15 nm, that is, the particle size is smaller than the mean free path of electrons, diffuse

reflection of electrons occurs on the surface, and the resistivity suddenly rises and metal characteristics are lost. Therefore, the nano-silver metal characteristics cannot be lost while preparing small-size nano-silver.

Graphene has been widely used as a printed electronics field [10] due to its excellent performances, such as unique mechanical rigidity and excellent electrical properties. Comparing with the single structure of graphene or AgNP, their composites show new synergistic properties [11] such as excellent conductivity, optical transparency and good stability [12, 13]. Therefore, the RGO/AgNPs nanocomposite material can have a strong market application prospect in the low-temperature sintering conductive ink.

This article uses a simple and rapid method to prepare a conductive ink with low temperature sintering and good conductivity, as shown in Fig. 1. First, AgNPs with the small particle size was prepared. Secondly, the mass ratio of GO to silver nitrate during the initial reaction was studied (1:1, 1:2, 1:3, 1:4, 1:5). The effect of AgNPs size on graphene was studied, and RGO/AgNPs nanocomposite with smaller diameters were prepared. Finally, RGO/AgNPs nanocomposite and AgNPs were mixed to prepare RGO/AgNPs nanocomposite conductive ink which has excellent electrical conductivity after sintering at low temperatures.

## 2 Experimental

### 2.1 Materials

Absolute ethanol ( $C_2H_6O$ , AR, Tianjing in Fuyu), ammonia ( $NH_3 \cdot H_2O$ , AR, Tianjing in Fuyu), polyvinylpyrrolidone (PVP, K30, AR, Shanghai in Lanji), glucose ( $C_6H_{12}O_7$ , AR, Tianjing in Kermel), and silver nitrate ( $AgNO_3$ , AR,  $\geq 99.8\%$ , Tianjing in Yingda) are all analytically pure and can be directly use, Graphene oxide [14], waterborne polyurethane/polyacrylate [15] and deionized water were all made in the laboratory.

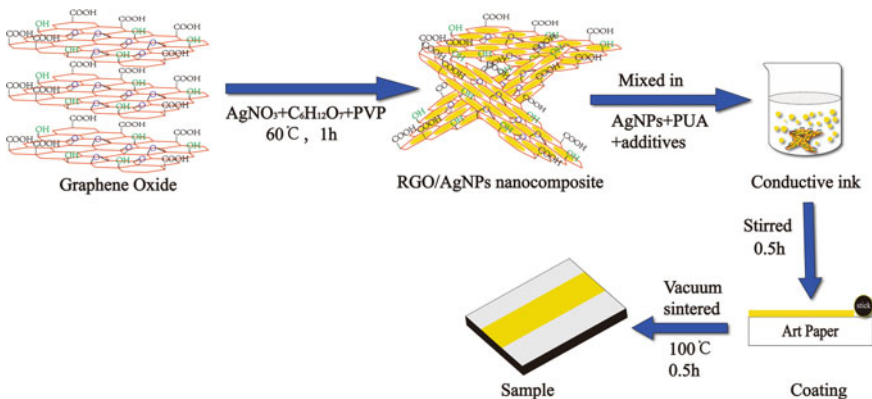
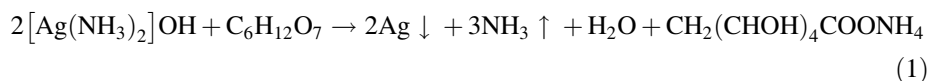


Fig. 1. RGO/ANPs conductive ink printing process

## 2.2 Synthesis of AgNPs

Under dark conditions, 0.1 M silver nitrate ethanol solution was formulated into a silver ammonia solution with pH = 10. A certain amount of PVP (mPVP: mAgNO<sub>3</sub> = 1.5:1) was added to the silver ammonia solution and stirred at 60 °C for 0.5 h when the solution brownish yellow. Using a constant pressure separatory funnel, the configured 1 M glucose-ethanol solution was slowly added dropwise to the brown-yellow solution and incubated at a constant temperature of 60 °C for 1 h. Centrifuge with ethanol, 10,000 rpm, 10 min, repeat 4–5 times. Removing the lower colloid and adding anhydrous ethanol to re-disperse ultrasonically to obtain a pure nano silver colloid.



## 2.3 Synthesis of RGO/AgNPs

A certain amount of silver nitrate was formulated into a silver ammonia solution having a pH = 9 and mixed with a 1 mg/mL graphene oxide dispersion. 0.1 g of polyvinylpyrrolidone was added and ultrasonically dispersed for 0.5 h. A 0.3 M solution of glucose in ethanol was added dropwise to the mixed solution, and the mixture was heated and stirred for 1 h. After cooling to room temperature, the mixture was centrifuged with deionized water at 8000 rpm for 10 min, centrifuged three times, and centrifuged three times with ethanol to obtain a stable graphene/nano-silver composite material dispersed in ethanol. The RGO/AgNPs nanocomposite named as A1, A2, A3, A4, and A5 correspond respectively to a mass ratio of graphene oxide to silver nitrate of 1:1, 1:2, 1:3, 1:4, 1:5.

## 2.4 Preparation of Conductive Ink

A1, A2, A3, A4, A5 RGO/AgNPs nanocomposite and AgNPs were dispersed in 1:4 ratio in deionized water, glycerol solvent, and absolute ethanol in a volume ratio of 1:2:3 and ensured that the conductive filler content was 60%. In addition, 10% waterborne polyurethane/polyacrylate was added, ultrasonic dispersion was performed for 30 min, and the conductive ink was prepared after 0.5 h of stirring. The ink was evenly coated on the coated paper. Each long coated sample was printed on the coated paper and vacuum heat treated at 100 °C for 0.5 h.

## 2.5 Characterization

The X-ray diffraction (XRD) of GO, RGO/AgNPs nanocomposite and AgNPs was characterized by XRD-7000 diffractometer. The SEM images of the graphene/nano-silver composite and the conductive ink after sintering at low temperature were obtained with a SU-8010 scanning electron microscope. The JEM-3001 transmission electron microscope characterizes the A1–A5 graphene/nano-silver composites. The conductivity of the conductive ink was measured with an RTS-9 digital four-probe tester.

### 3 Results and Discussion

#### 3.1 Characterization of AgNPs

The XRD of preparing AgNPs at low temperature using glucose as a reducing agent and PVP as a protective agent is shown in Fig. 2a. The four diffraction peaks with  $2\theta$  of  $38.10^\circ$ ,  $44.28^\circ$ ,  $64.42^\circ$ , and  $77.38^\circ$  correspond to the (111), (200), (220), and (311) crystal plane diffraction in the face centered cubic system [16]. According to Scherrer's equation [17], the average crystal size of AgNPs is about 28 nm. After analyzing the XRD of AgNPs, it was shown that the nanoparticle with small particle size was successfully prepared. In general, the lens directly measures the diameter of the particles. It is greater than or equal to the XRD pattern. The calculated crystal size is also accurate. Therefore, the size is obtained by the TEM of AgNPs as shown in Fig. 2b. From the figure, it can be seen that using glucose as a reducing agent and PVP as a protective agent, the particle size distribution of AgNPs prepared at a low temperature is relatively uniform, indicating that AgNPs with a small particle diameter and an average particle diameter of 30 nm are successfully prepared.

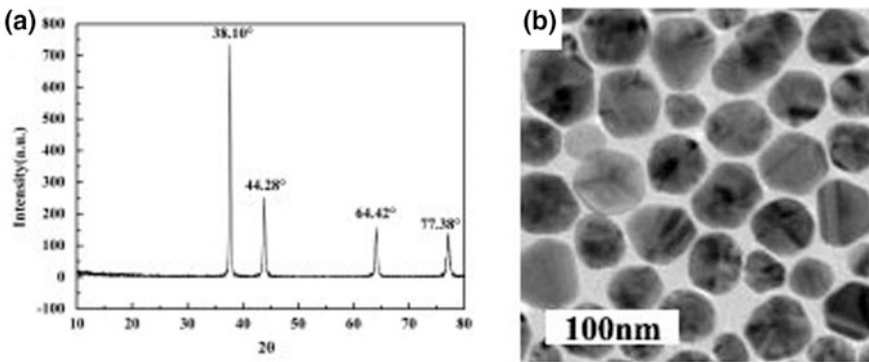
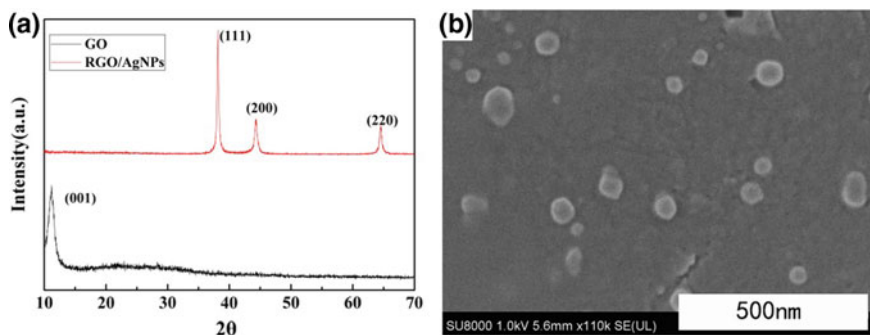


Fig. 2. a XRD pattern of AgNPs and b TEM image of AgNPs

#### 3.2 Characterization of RGO/AgNPs Nanocomposite

The XRD of GO and RGO/AgNPs nanocomposite is shown in Fig. 3a. The RGO/AgNPs nanocomposite has no diffraction peak (001) of GO, indicating that GO is successfully reduced to graphene. It can be clearly seen from the figure that XRD patterns of RGO/AgNPs nanocomposite have three well-defined diffraction peaks at  $38.14^\circ$ ,  $44.33^\circ$ , and  $64.45^\circ$  at  $2\theta$ , corresponding to the three diffraction peaks of nanosilver (111), (200) and (220). This also shows that nanosilver is successfully loaded on the surface of graphene. From the SEM of the RGO/AgNPs nanocomposite material, the graphene surface is flat and less wrinkled as shown in Fig. 3b. This is because nanosilver is successfully loaded on the surface of graphene, preventing agglomeration of graphene. This also shows that the morphology of the RGO/AgNPs nanocomposite produced by glucose reduction is good.



**Fig. 3.** **a** XRD patterns of GO and RGO/AgNPs nanocomposite and **b** SEM images of RGO/AgNPs nanocomposite

The TEM of the composite prepared by GO and silver nitrate at different mass ratios is shown in Fig. 4. From Figure a, the transparent lamellar structure of graphene can be seen without obvious agglomeration. However, there is a large difference in the size and distribution of AgNPs loaded on the graphene sheet, which is influenced by the mass ratio of GO and silver nitrate during the initial reaction. With the increase of the mass ratio, AgNPs loaded on the graphene increase and the particle size decreases. When the mass ratio of GO and silver nitrate is 1:3, AgNPs loaded on the graphene

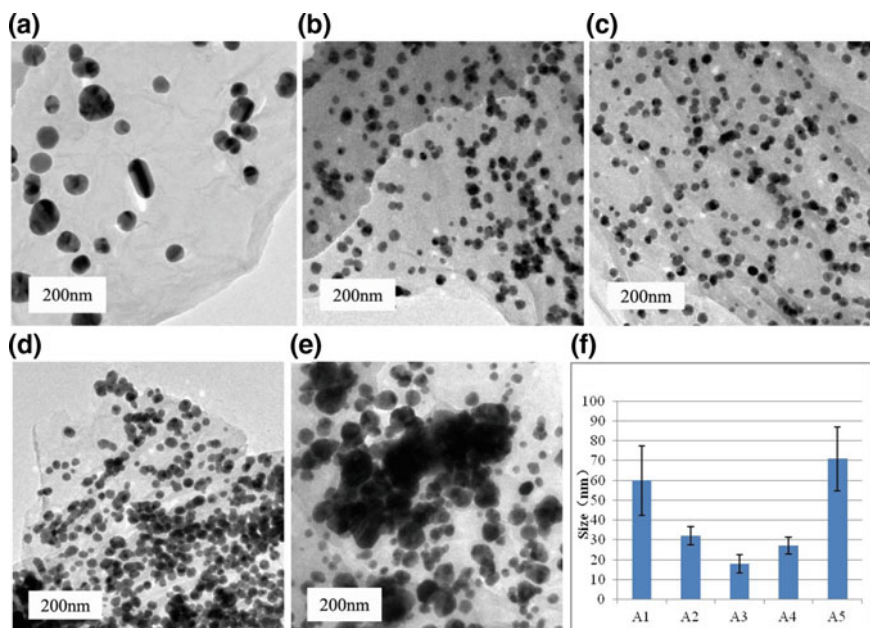


**Fig. 4.** **a** TEM images of A1 **b** A2 **c** A3 **d** A4 **e** A5 and **f** average particle size of AgNPs in different groups

have the best morphology, the average particle size is 18 nm, and the distribution is uniform. However, as the mass ratio increases, AgNPs aggregate with each other, making the particle size larger and the distribution uneven. Therefore, the increase in the mass ratio of GO and silver nitrate will tend to produce AgNPs with smaller particle sizes with in a certain range. If the mass ratio exceeds a certain range, agglomerates will occur between particles, and the particle size will increase.

### 3.3 Resistivity of Conductive Ink

The results of using A1-A5 RGO/AgNPs nanocomposite materials and AgNPs mixed as conductive fillers for the resistivity of the conductive ink are shown in Fig. 5. Because the resistivity of the A5 group conductive ink is too large, it does not appear in the figure. The third set of conductive inks had the lowest resistance and the resistivity reached  $2.4 \mu\Omega \cdot \text{cm}$ . This is because in the A5 group of conductive inks have a large particle size of AgNPs loaded on the graphene, and the sintering temperature is too low to form a network of conductive paths. The conductive ink of group A3 was heat-treated and cured at a temperature of  $100 \text{ }^\circ\text{C}$ . After SEM analysis, the results are shown in Fig. 6. It can be seen that the solvent of the ink volatilized after sintering, the conductive fillers melt and contacted with each other to form a dense conductive channel, so that the ink has conductivity.

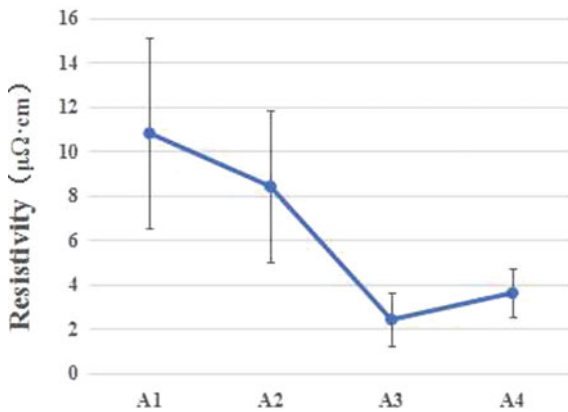
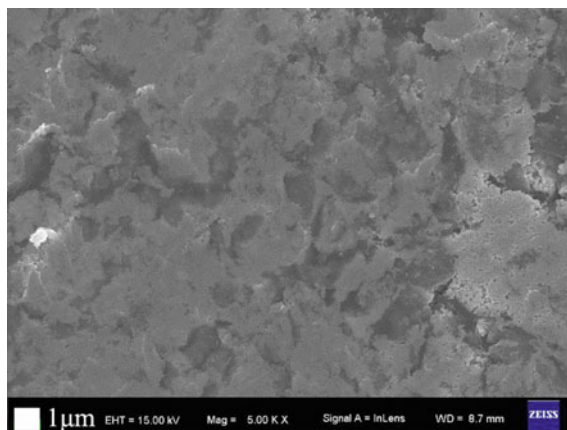


Fig. 5. The resistivity of conductive ink



**Fig. 6.** SEM image of A3 conductive ink after sintering at 100 °C

## 4 Conclusions

In this paper, low-temperature sintering conductive inks are prepared by preparing AgNPss with small particle diameters. Using glucose as a green reducing agent, AgNPs with an average particle size of 30 nm were prepared at a low temperature. When the mass ratio of GO and silver nitrate is 1:3, AgNPs supported on the graphene is uniformly distributed and the particles are small (average particle size is 18 nm). RGO/AgNPs nanocomposite and AgNPs were mixed as conductive filler. RGO/AgNPs nanocomposite-based conductive ink was prepared by adding binder and organic solvent. The coating resistance after sintering at 100 °C was 2.4  $\mu\Omega$  cm. Replacing part of the nanosilver with graphene/silver nanocomposites not only reduces the cost of the nanosilver ink, but also expands the application range of printed electronics.

**Acknowledgements.** This work was supported key laboratory project of Shaanxi provincial department of education (No.16JS082).

## References

1. Stewart, I. E., Kim, M. J., & Wiley, B. J. (2017). Effect of morphology on the electrical resistivity of silver nanostructure films. *ACS Applied Materials & Interfaces*, 9(2), 1870–1876.
2. Wang, F., Mao, P., & He, H. (2016). Dispensing of high concentration ag nano-particles ink for ultra-low resistivity paper-based writing electronics. *Scientific Reports*, 6, 21398.
3. Nie, X., Wang, H., & Zou, J. (2012). Inkjet printing of silver citrate conductive ink on pet substrate. *Applied Surface Science*, 261(8), 554–560.
4. Zhang, Z., Zhang, X., Xin, Z., Deng, M., Wen, Y., & Song, Y. (2011). Synthesis of monodisperse silver nanoparticles for ink-jet printed flexible electronics. *Nanotechnology*, 22(42), 425601.



5. Yu, H., Li, L., & Zhang, Y. (2012). Silver nanoparticle-based thermal interface materials with ultra-low thermal resistance for power electronics applications. *Scripta Materialia*, 66(11), 931–934.
6. Ogura, H., Maruyama, M., Matsubayashi, R., Ogawa, T., Nakamura, S., Komatsu, T., et al. (2010). Carboxylate-passivated silver nanoparticles and their application to sintered interconnection: a replacement for high temperature lead-rich solders. *Journal of Electronic Materials*, 39(8), 1233–1240.
7. Hornyak, G. L., Tibbals, H. F., & Dutta, J. (2008). *Introduction to nanoscience*. Introduction to nanoscience: CRC Press.
8. Moon, Y. J., Kang, H., Kang, K., Moon, S. J., & Hwang, J. Y. (2015). Effect of thickness on surface morphology of silver nanoparticle layer during furnace sintering. *Journal of Electronic Materials*, 44(4), 1192–1199.
9. Amp, P. R. C., & Jesser, W. A. (1977). Thermodynamic theory of size dependence of melting temperature in metals. *Nature*, 269(5628), 481–483.
10. Majee, S., Liu, C., Wu, B., Zhang, S. L., & Zhang, Z. B. (2017). Ink-jet printed highly conductive pristine graphene patterns achieved with water-based ink and aqueous doping processing. *Carbon*, 114, 77–83.
11. Zhang, Z., Xu, F., Yang, W., Guo, M., Wang, X., Zhang, B., et al. (2011). A facile one-pot method to high-quality Ag-graphene composite nanosheets for efficient surface-enhanced raman scattering. *Chemical Communications*, 47(22), 6440–6442.
12. Myekhlai, M., Lee, S., Lee, T., Chung, H., & Jeong, H. (2015). A facile and eco-friendly synthesis of graphene–silver hybrid materials for transparent conductive films. *Ceramics International*, 41(1), 983–989.
13. Chamoli, P., Das, M. K., & Kar, K. K. (2017). Green synthesis of silver-graphene nanocomposite-based transparent conducting film. *Physica E: Low-dimensional Systems and Nanostructures*, 90, 76–84.
14. Neto, A. H. C. (2010). The electronic properties of graphene. *Physica Status Solidi*, 244(11), 4106–4111.
15. Wang, X., Shen, Y., & Lai, X. (2014). Micromorphology and mechanism of polyurethane/polyacrylate membranes modified with epoxide group. *Progress in Organic Coatings*, 77(1), 268–276.
16. Yang, J., Zang, C., Sun, L., Zhao, N., & Cheng, X. (2011). Synthesis of graphene/ag nanocomposite with good dispersibility and electroconductibility via solvothermal method. *Materials Chemistry and Physics*, 129(1), 270–274.
17. Shen, J., Shi, M., Yan, B., Ma, H., Li, N., & Ye, M. (2011). One-pot hydrothermal synthesis of ag-reduced graphene oxide composite with ionic liquid. *Journal of Materials Chemistry*, 21(21), 7795–7801.



# Research of Inkjet Printing of Water-Based Inkjet Ink for the Curved Surface

Pengfei Zhao<sup>1,2</sup>, Pingping Zhang<sup>1,2</sup>, Xiaoli Liu<sup>1,2</sup>, Kai Huang<sup>1,2</sup>,  
Zhuangzhi Ye<sup>1,2</sup>, and Yanan Liu<sup>1,2</sup>(✉)

<sup>1</sup> Key Laboratory of Environmental Protection Technology for Printing Industry, China Academy of Printing Technology, Beijing, China  
liuyanana@keyin.cn

<sup>2</sup> Beijing Key Laboratory of New Technology of Packaging and Printing, China Academy of Printing Technology, Beijing, China

**Abstract.** Products with various shapes and curvature have been attracted a lot of attention with the improvement of individual requirements and the development of 3D printing technology. Traditional methods of printing are applied to decorate products with regular surface. However, it is difficult to realize the decoration of products with complex curved surface. There is no doubt that inkjet printing technology is the best way to decorate products with curved surface. The development of environmentally friendly water-based ink is important for applications of inkjet printing. Water-based ink, has anti-clogging capability and suitable properties such as viscosity and surface tension, is suitable for inkjet printing. In this paper, preparation and properties of water-based soft ink and hard ink were analyzed and discussed. Then, water-based inkjet ink with environmental protection and well printability was obtained through the selection of type and content of water-based resin, water-based color paste and other additives. The water-based inkjet ink can be used to decorate products with complex curved surface by inkjet printing technology.

**Keywords:** Inkjet printing · Water-based inkjet ink · Curved surface

## 1 Introduction

With the development of individualized and diversified requirements, 3D printing technology has been applied to mold manufacturing, medical engineering, electronic device manufacturing, creative design and tourism product manufacturing. It is necessary to give 3D products information such as images and texts.

Traditional methods of printing are mainly divided into screen printing and water transfer printing [1]. These traditional methods of printing are only applied to decorate products with regular surface.

Ink-jet printing is a non-contact digital printing technology (Fig. 1), which can deposit various materials, as droplets, on pre-determined points of a substrate under the control of a computer program [2–7]. As a promising technique, ink-jet printing is suitable to produce complex patterns. Inkjet printing has many advantages such as non-contact printing, faster printing speed [8], smaller footprints [9–11], lower amounts of

materials, free designs of mask and higher resolutions [12, 13]. There are four major types of ink-jet inks including phase-change, solvent-based, water-based and UV-curable [14–22]. Water-based inkjet ink is environmentally friendly, and it is non-flammable so that it can eliminate the hidden danger of flammability and explosibility.

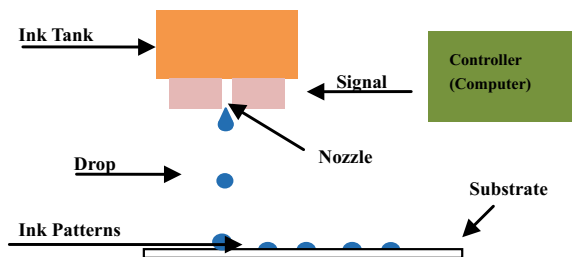


Fig. 1. Schematic of the inkjet printing process

The process of preparation of water-based inkjet ink is complicated because of the high performance requirement of inkjet ink. In addition, particle size, surface tension, viscosity, stability, pH, electrolyte and solid content should be considered [23, 24]. More importantly, water-based inkjet ink should have good redissolution to avoid clogging the inkjet printer head.

Environmentally friendly water-based ink will be a new trend in the future. Water-based ink is mainly composed of water-based resin, water-based color paste and other additives [25]. In this paper, the cyan, magenta, yellow and black (CMYK) of the hard inkjet ink and soft inkjet ink were prepared. The proportion of water-based resin, water-based color paste and water was adjusted and appropriate additives were added. Water-based inkjet ink with good adaptability has been obtained, and it has excellent properties such as suitable viscosity, surface tension and anti-clogging. Inkjet printing technology can be used to decorate products with complex curved surface.

## 2 Experiments

### 2.1 Experimental Materials and Instruments

#### 2.1.1 Experimental Materials

RU1, RU2, RU3 and RU4 were provided by Hangzhou Dijing Chemical Co., Ltd., Jining Hua Kai resin co., Ltd., Guangzhou maiTurui chemical co., Ltd. and Hefei Hengtian New material Technology Co., Ltd., respectively. S-70 was provided by Dongguan Wen Bo chemical material Co., Ltd. WE17 and WE1 was provided by Shenzhen Grayson Chemical New material Co., Ltd. D607 was provided by Guangzhou maiTurui chemical co., Ltd. Deionized water was provided by Watsons. Color paste was provided by Dongguan Youmeng color paste co., Ltd.

### 2.1.2 Experimental Instruments

Densitometer (X-Rite) was provided by U.S.A. Friction-resistance meter (MCJ-01) was provided by PARAM. Rotational viscosimeter (NDJ-9S) was provided by Shanghai Fangrui instrument Co., Ltd. Surface tension meter (BZY-1) was provided by Shanghai Pingxuan Scientific Instruments Co., Ltd. Vibrator (HT-30C) was provided by Shanghai Modern Environmental Engineering Technology Co., Ltd.

## 2.2 Characterization

1. Adhesion. Inkjet ink was coated on the substrate with No. 0 wire rod, and then the ink layer was dried under hot air. 3 M tape was affixed on the surface of the printed sample and then the tape was peeled off. It was evaluated from level 0 to level 5, according to the desquamate degree of ink on the surface of printed substrate. The level 0 represents the maximum value of adhesion, and the level 5 represents the minimum value of adhesion.
2. Wear resistance. The MCJ-01 wear-resistant test machine was used to test wear resistance.
3. Viscosity. A rotary viscometer was used to test the rotational viscosity of ink.
4. Fineness. Fineness was tested by the grind gauges.
5. Surface tension. BZY-1 automatic interface tension meter is used to measure and record data.
6. Stability of the water-based inkjet ink. Water-based inkjet ink is placed in an electricity heat drum wind drying oven at 50 °C. Test the performance of the water-based inkjet ink two days later.

## 3 Experiment Results and Discussion

### 3.1 Preparation of Water-Based Inkjet Ink

Compared with other printing processes, ink-jet printing offers many benefits such as non-contact printing, smaller footprints, and lower amounts of materials, free designs of mask and high resolutions. Environmentally friendly water-based inkjet ink belongs to the category of green printing material, and the development of water-based inkjet ink is the trend of ink-jet printing technology. Preparation of water-based inkjet ink was shown in Fig. 2.

### 3.2 Research of Soft Inkjet Ink

Soft inkjet ink that was required to have good flexibility is used for soft materials such as leather. Types and contents of water-based resin, water-based color pastes, water and additives of water-based inkjet ink, and properties of ink such as adhesion, scratch resistance, friction resistance, viscosity, fineness, stability, wettability and clogging nozzle were discussed. The formula of water-based soft inkjet ink CMYK is shown in Table 1.

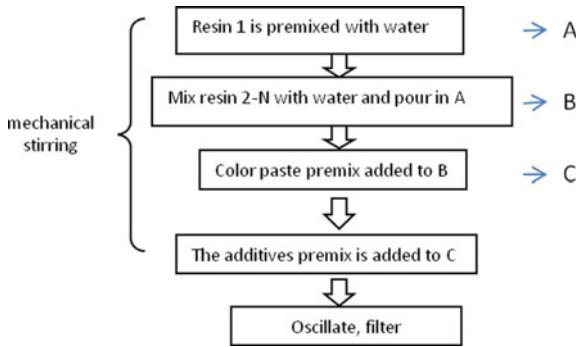


**Fig. 2.** Schematic of preparation of Water-based ink-jet ink process

**Table 1.** Formula of water-based soft inkjet ink (CMYK)

Soft inkjet ink	RU1 + RU4 + RU3/g	Water/g	Color paste/g	D607/g	Wax additives/g	Other additive
C	7.5 + 7.5 + 6	15	7.5-C	0.4	4	0.35
M	7.5 + 7.5 + 6	15	7.5-M	0.4	4	0.35
Y	7.5 + 7.5 + 6	15	7.5-Y	0.4	4	0.35
K	7.5 + 7.5 + 6	15	7.5-K	0.4	4	0.35

First, the ratio of water-based resins of the soft ink was studied, as shown in Table 3. The cyan water-based ink was taken as an example. Adhesion on the substrate printed soft inkjet ink is provided by the water-based resin RU1. The water-based resin PVA and RU3 would dissolve in the water to avoiding clog the nozzle within 30 min (Table 2). However, water-based inkjet ink with the PVA was unstability. Therefore, RU3 was added to the water-based inkjet ink to prevent clogging. The water-based resin RU4 provides flexibility, so that no matter how the leather bent, the water-based inkjet ink can be applied well without breaking or cracking. When the ratio of the three water-based resins was RU1: RU4: RU3 = 1: 1:0.8, the anti-clogging nozzle, adhesion and stability of water-based soft inkjet ink is excellent.

**Table 2.** Impact of the kind of resin on the water-based soft inkjet ink performance

RU1:RU4:RU3/PVA	Clog the nozzle	Adhesion	Stability
10:0	10 min	0	√
1:1:0	10 min	0	√
1:1:0.8 (PVA)	>2 h	0	×
0:0:1 (RU3)	>2 h	/	√
1:1:0.8 (RU3)	>30 min	0	√

Secondly, the ratio of water-based color paste was studied. The color density of the ink-jet printing inks was set as  $C \geq 0.8$ ,  $M \geq 0.8$ ,  $Y \geq 0.6$ , and  $K \geq 0.8$ . The influence of water-based color paste content on color density is shown in Fig. 3. The color density of inkjet ink increased with the increasing of color paste content. It meets the standard for inkjet printing with 12% color paste content.

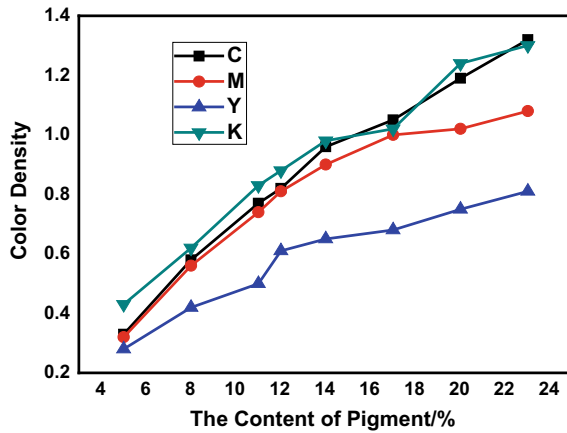


Fig. 3. Change in color density with water-based color paste content

Thirdly, content of water was studied. Viscosity of the inkjet ink was determined by adjusting the content of water (water-based inkjet ink C was taken as an example). The influence of the content of water was shown in Fig. 4. It showed that the viscosity of the inkjet ink decreased as the deionized water content increased. The viscosity was 23.9 mPa.s without adding water and it is 4.6 mPa.s when the content of water reached fifty percent. The suitable viscosity of water-based soft inkjet ink is within 5–6 mPa.s. Therefore, the water-based soft inkjet ink with 30% water content was determined.

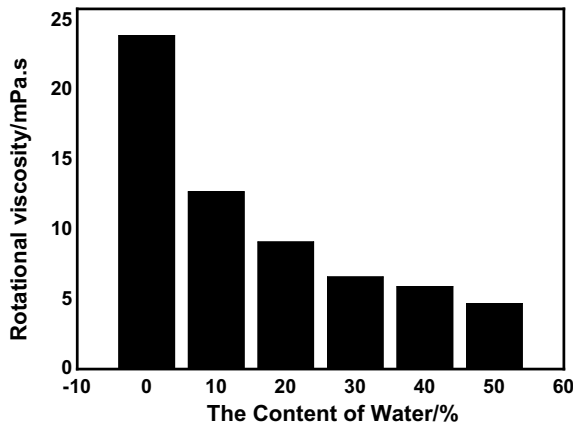


Fig. 4. Impact of the content of water on the rotational viscosity of water-based soft inkjet ink

Finally, increasing the amount of wetting agent D607 could improve the wettability of the water-based soft inkjet ink. It is found that the wettability of the water-based inkjet ink became better on the leather surface with the increase of content of D607. When 0.5% D607 was added, wettability was reached optimal condition. In order to improve the scratch resistance and friction resistance of ink layer, the wax additives were added. Water-based wax additives WE17, WE1 and S-70 with mass fraction of 5% were added, respectively, and the ink layer obtained good resistance. However, because of poor compatibility between wax additives and resins, delamination occurred. Excellent scratch resistance, rub resistance and stability of the sample with S-70 was obtained.

### 3.3 Research of Water-Based Hard Inkjet Ink

Hard inkjet ink used for hard materials (photosensitive resins, polylactic acid-PLA) was studied. In addition, the plastic surface is very smooth. Ink was hard to be immobilized on substrate. Thus, the speed of drying and adhesion must be considered. The formula of hard inkjet ink CMYK is shown in Table 3.

**Table 3.** Formula of water-based hard inkjet ink

Hard inkjet ink	RU1:RU2:RU3/g	Water/g	Color paste/g	D607/g	Wax additives/g
C	16 + 2+2	9.6	6.6-C	0.25	2.5
M	16 + 2+2	9.6	6.6-M	0.25	2.5
Y	16 + 2+2	9.6	6.6-Y	0.25	2.5
K	16 + 2+2	9.6	6.6-K	0.25	2.5

First, water-based resins directly determine the drying and adhesion properties of the ink. Table 4 shows the effect of individual resins on the water-based hard inkjet ink. Adhesion on the substrate printed soft inkjet ink is provided by the water-based resin RU1, and anti-clogging performance is provided by the water-based resin RU3. The water-based resin RU2 can be used to adjust the dryness of the water-based hard inkjet ink. When RU1 and RU3 mixture is sprayed on the PLA, the ink layer will not dry out, which will not provide the ink layer with adhesion property. So the water-based resin RU2 is added to ensure that the surface is dry in addition to without clogging the nozzle. The mass ratio of resin RU1: RU2: RU3 was 8:1:1 and water-based hard inkjet ink with excellent drying performance and anti-clogging inkjet printer nozzle was obtained.

Secondly, viscosity of the ink was adjusted by the content of water, and influence of the content of water on rotational viscosity was shown in Fig. 5. Viscosity of water-based hard inkjet ink is controlled in range of 7–8 mPa.s. Therefore, the content of water is determined to be 20%.

**Table 4.** Impact of the kind of resin on the water-based hard inkjet ink performance

RU1:RU2:RU3	Clog the nozzle	Drying property
1:0:0	10 min	Dry
0:1:0	3 min	Dry
0:0:1	>2 h	Wet
2:0:1	>30 min	Wet
4:0:1	>30 min	Wet
8:0:1	>30 min	Wet
9:0:1	25 min	Wet
8:1:1	>30 min	Dry

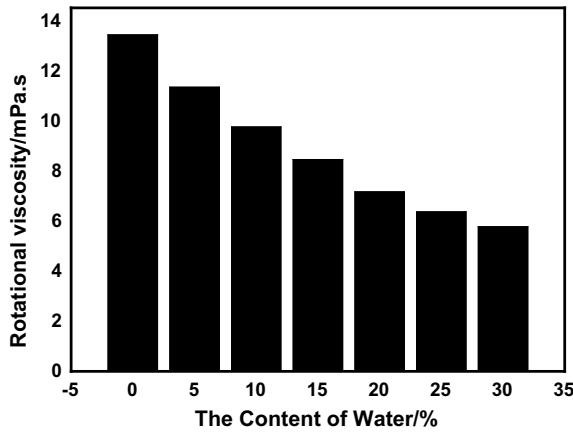


**Fig. 5.** Impact of the content of water on the rotational viscosity of water-based hard inkjet ink

### 3.4 Performance and Application of Water-Based Soft Inkjet Ink and Hard Inkjet Ink

The performance data of water-based inkjet soft ink and hard ink are shown in Tables 5 and 6. It showed that soft ink had fineness of 0 μm, viscosity of 5–6 mPa.s, and surface

**Table 5.** The performance of water-based soft inkjet ink (SF) (CMYK)

Soft inkjet ink	Viscosity/mPa.s	Fineness/μm	Surface tension mN/m	Clog the nozzle/min (min)	Stability	Adhesion	Scratch resistance	Friction resistance
C	5.9	0	27.1	>30	√	0	5	√
M	5.1	0	27.5	>30	√	0	5	√
Y	5.8	0	29.3	>30	√	0	5	√
K	5.4	0	28.5	>30	√	0	5	√



**Table 6.** The performance of water-based hard inkjet ink (CMYK)

Hard inkjet ink	Viscosity/mPa.s	Fineness/ $\mu\text{m}$	Surface tension mN/m	Clog the nozzle/min (min)	Stability	Adhesion	Scratch resistance	Friction resistance
C	8.3	0	26.9	>30	√	0	5	√
M	7.6	0	25.1	>30	√	0	5	√
Y	7.4	0	25.8	>30	√	0	5	√
K	8.0	0	27.0	>30	√	0	5	√

tension of 27–29 mN/m, and the corresponding parameters of hard ink were 0  $\mu\text{m}$ , 7–8 mPa.s and 25–27 mN/m respectively. The soft and hard inks possessed excellent stability, adhesion and scratch resistance. They also ensured that the nozzle will be anti-clogged when it was stopped during ink jet printing for half an hour.

## 4 Conclusion

Inkjet printing shows unique advantages compared with other printing processes. Multicolor curved printing products with high resolution and outstanding performance were obtained by the combination of inkjet printing technology and water-based inkjet ink, which are environmentally friendly and economical. In this paper, effect on water-based inkjet ink by different content of resin was analyzed and discussed. Water-based resin RU3 could effectively achieve good anti-clogging, adhesion and surface dryness properties. The content of resin, water-based color paste and additives was adjusted. A water-based inkjet ink with good properties, such as suitable viscosity, surface tension and anti-clogging has been obtained.

## References

1. Xiao, J. J., Cheng, G. Y., Zhai, N. J., Zhang, R., & Ma, T. Y. (2016). *Curved surface product color printing method*. Print Today 2016.2.
2. Zori, M. H., & Soleimani-Gorgani, A. (2012). Ink-jet printing of micro-emulsion  $\text{TiO}_2$ , nano-particles ink on the surface of glass. *Journal of the European Ceramic Society*, 32(16), 4271–4277.
3. Soleimani-Gorgani, A., Ghahari, M., & Peymannia, M. (2015). In situ production of nano- $\text{CoAl}_2\text{O}_4$ , on a ceramic surface by ink-jet printing. *Journal of the European Ceramic Society*, 35(2), 779–786.
4. Zhao, X., Evans, J. R. G., Edirisinghe, M. J., et al. (2003). Formulation of a ceramic ink for a wide-array drop-on-demand ink-jet printer. *Ceramics International*, 29(8), 887–892.
5. Grau, J., Cima, M., & Sachs, E. (1996). Fabricating alumina molds for slip casting and 3-D printing. *Ceramic Industry*.
6. Teng, W. D., & Edirisinghe, M. J. (1998). Development of continuous direct ink jet printing of ceramics. *British Ceramic Transactions*, 97(4), 169–173.
7. Magdassi, S. (2010). *The Chemistry of Inkjet Inks*. Singapore: World Scientific Pub.
8. Tortorich, R., & Choi, J. W. (2013). Inkjet printing of carbon nanotubes. *Nanomaterials*, 3(3), 453–468.
9. Hutchings, I. (2010). Ink-jet printing for the decoration of ceramic tiles: Technology and opportunities. *Proceedings of the Qualicer World Congress on Ceramic Tile Quality*.
10. Kim, J. H., Noh, H. G., Kim, U. S., et al. (2013). Recent advances in the ink-jet printing ceramic tile using colorant ceramic-ink. *Journal of the Korean Ceramic Society*, 50(6), 498–503.
11. Tay, B. Y., Rashid, H., & Edirisinghe, M. J. (2000). On the preparation of ceramic ink for continuous jet printing. *Journal of Materials Science Letters*, 19(13), 1151–1154.
12. Neville, S., & Fuller, S. (2004). A fast flexible ink-jet printing method for patterning dissociated neurons in culture. *Journal of Neuroscience Methods*, 136(2), 151–163.

13. Singh, M., Haverinen, H. M., Dhagat, P., et al. (2010). Inkjet printing—process and its applications. *Advanced Materials*, 22(6), 673–685.
14. Magdassi, S. (2009). *The chemistry of inkjet inks*. World Scientific.
15. Zhao, X., Evans, J. R. G., Edirisinghe, M. J., et al. (2002). Direct ink-jet printing of vertical walls. *Journal of the American Ceramic Society*, 85(8), 2113–2115.
16. Seerden, K. A. M., Reis, N., Evans, J. R. G., et al. (2010). Ink-jet printing of wax-based alumina suspensions. *Journal of the American Ceramic Society*, 84(11), 2514–2520.
17. Wang, T., & Derby, B. (2005). Ink-jet printing and sintering of PZT. *Journal of the American Ceramic Society*, 88(8), 2053–2058.
18. Sukeshini, M. A., Cummins, R., Reitz, T. L., et al. (2009). Ink-jet printing: a versatile method for multilayer solid oxide fuel cells fabrication. *Journal of the American Ceramic Society*, 92(12), 2913–2919.
19. Tomov, R. I., Krauz, M., Jewulski, J., et al. (2010). Direct ceramic inkjet printing of yttria-stabilized zirconia electrolyte layers for anode-supported solid oxide fuel cells. *Journal of Power Sources*, 195(21), 7160–7167.
20. Tseng, W. J., Lin, S. Y., & Wang, S. R. (2006). Particulate dispersion and freeform fabrication of BaTiO<sub>3</sub> thick films via direct inkjet printing. *Journal of Electroceramics*, 16(4), 537–540.
21. Darsono, D. S., Marsongko. (2008). UV-curing of titanium dioxide pigmented epoxy acrylate coating on ceramic tiles. *Journal- Ceramic Society Japan*, 116(1356), 896–903.
22. Halloran, J. W., Tomeckova, V., Gentry, S., et al. (2011). Photopolymerization of powder suspensions for shaping ceramics. *Journal of the European Ceramic Society*, 31(14), 2613–2619.
23. Hoath, S. D. (2016). Fundamentals of inkjet printing: the science of inkjet and droplets.
24. Piccinini, I., & Piccinini F. (2014). Technology for digital inks in ceramic tiles Manufacturing. In: *CFI-Ceramic Forum International*. Aschmattstrasse 8, D-76532 Baden Baden (pp. E1–E3) Germany: GollerVerlag GMBH.
25. Peng, X., Zhang, Q., Cheng, J., et al. (2017). Preparation and characterization of a stable nano-sized Zn<sub>x</sub>Co<sub>1-x</sub>Al<sub>2</sub>O<sub>4</sub> ink for glass decoration by ink-jet printing. *Glass Physics and Chemistry*, 43(3), 246–256.



# Preparation and Photopolymerization Kinetics of UV-Curable Fluorescent Inks Doped with Quantum Dots

Hui Wang<sup>(✉)</sup>, Le Ma, Bin Yang, Wan Zhang, Beiqing Huang, and Xianfu Wei

School of Printing and Packaging Engineering, Beijing Institute of Graphic Communication, Beijing 102600, China  
wanghui@bigc.edu.cn

**Abstract.** In order to prepare UV-curable fluorescent inks and investigate the UV-curing performance, we report the preparation and photopolymerization process of fluorescent quantum dots (QDs) doped UV-curable ink systems. The ink system is composed of fluorescent QDs, photoinitiators, prepolymers and diluting monomers. Conversion rates of double-bonds are characterized by real-time Fourier transform infrared (RT-FTIR) spectroscopy to investigate influencing factors on the photopolymerization kinetics, including UV radiation conditions and system components. Experimental results show that radiation energy density of the UV light source, type and concentration of the photoinitiator, and concentration of QDs have a significant influence on UV-curing process of the ink system. Due to strong absorption effect of QDs in specific wavelengths, appropriate matching of the UV light source, photoinitiators and spectral characteristics of fluorescent QDs is essential to improve UV-curing performance of the ink system. This study provides guidance for the development of formulation and printing technology of new types of fluorescent inks.

**Keywords:** Photopolymerization kinetics · UV-curing · Fluorescent inks · Quantum dot

## 1 Introduction

Quantum dots (QDs) have attracted considerable interest in recent years due to the exceptional optical properties [1], especially the tunability of luminescence emission, which has been widely studied in optical devices, such as displays [2], lasing [3] and illumination [4]. In these application fields, the printed electronics technology has gradually become an important approach to bypass traditional expensive silicon-based electronics to fabricate devices on flexible substrates [5]. With this method, the printing of QDs functional devices are usually carried out by using QDs-doped inks [6]. Therefore, the dispersion and coating of QDs-doped inks could be considered as a primary problem in the manufacturing of QDs functional devices by the means of printed electronics.

In the past decades, ultraviolet (UV)-assisted curing, which is considered as an efficiency and economical manufacturing technique, has been widely applied in

printing, coating, electronics, etc. [7]. In this research, we report the preparation of UV-curable QDs-doped inks with photoluminescence properties. Photopolymerization kinetics was characterized by real-time Fourier transform infrared (RT-FTIR) technique to investigate the UV-curing performance. Patterns with photoluminescence effect were successfully printed using the prepared QD-doped ink, showing potential values in further applications.

## 2 Experimental

### 2.1 Materials

Waterborne resin UCECOAT 7177 was purchased from Allnex Resins Co. (Shanghai, China). 4-acryloylmorpholine (ACMO), photoinitiator (PI) diphenyl (2, 4, 6-trimethylbenzoyl) phosphine oxide (TPO) and 2-hydroxy-2-methylpropiophenone (1173) were purchased from Tianjin Jiuri New Materials Co., Ltd. (Tianjin, China). QDs with a CdSe core and a ZnS shell structure were purchased from Xingshuo Nanotech Co. Ltd. (Suzhou, China) and suspended in deionized water with a concentration of 10 nmol/mL. All reagents were used as received.

### 2.2 Preparation of QDs-Doped UV-Curable Inks

A typical procedure for the preparation of QDs-doped UV-curable inks includes two steps: preparation of pre-polymer resin and doping of QDs. First, different amounts of PI TPO and 1173 were completely dissolved in dilute monomer ACMO with mechanical stirring. Then base polymer UCECOAT 7177 was added into the system to make pre-polymer resin, in which the mass ratio of ACMO to UCECOAT 7177 was maintained at 3:7 while the amount of PI was 3–7 wt% relative to the total mass of UCECOAT 7177 and ACMO. Second, different volumes of QDs suspension with a concentration of 10 nmol/mL was added into the pre-polymer resin. Mechanical stirring and sonication were carried out alternately for 6 h to form a uniform QDs-doped ink. Concentration of QDs doped in the ink could be calculated from the volume ratio of QDs suspension relative to the total system. The composition of inks was listed in Table 1.

### 2.3 Characterization

Ultraviolet-visible (UV-Vis) absorption spectra were characterized by a UV-2700 spectrophotometer (Shimadzu, Japan) at room temperature. UV-Vis absorption spectra of QDs and PIs at wavelengths of 250–700 nm were recorded using deionized water and ethanol as solvent, respectively.

An OmniCure Series 1000 UV spot light source (Lumen Dynamics, Canada) at the wavelength of 365 nm with a 5 mm quartz fiber was used to induce the photopolymerization. The power density of irradiation was measured by a UV-A light radiometer (Photoelectric Instrument Factory of Beijing Normal University, China).

**Table 1.** Composition of QDs-doped UV-curable inks

No.	Pre-polymer resin		Photoinitiator <sup>a</sup>		QDs <sup>b</sup> (nmol/mL)
	ACMO (wt%)	UCECOAT 7177 (wt%)	TPO (wt%)	1173 (wt%)	
Sample 1	30	70	5.0	0	0
Sample 2			5.0	0	0.1
Sample 3			5.0	0	0.2
Sample 4			5.0	0	0.5
Sample 5			3.0	0	0.5
Sample 6			7.0	0	0.5
Sample 7			0	5.0	0.5
Sample 8			2.5	2.5	0.5

<sup>a</sup>The content of PIs was against the total mass of UCECOAT 7177 and ACMO

<sup>b</sup>The concentration of QDs was against the total volume of the ink

Fourier transform infrared spectra (FTIR) of UV-curable inks coated on a ZnSe slide were scanned over the range of 650–4000 cm<sup>-1</sup> on a Nicolet iS50 spectrometer (Thermo Fisher, USA) equipped with a KBr beam splitter and a MCT/A detector cooled by liquid nitrogen. The spectrometer was operated in the absorbance mode and real-time signals of samples during the UV-assisted polymerization process were recorded at a collection rate of 4 scans/s with a resolution of 4 cm<sup>-1</sup>. The photopolymerization kinetics was determined by the decrease of absorption peak around 850–810 cm<sup>-1</sup> which was ascribed to the twisting vibration mode of double-bond in vinyl group [8]. Degree of conversion (*DC*) of double-bond was calculated from Eq. 1 [9, 10]:

$$DC\% = \frac{A_0 - A_t}{A_t} \times 100\% \quad (1)$$

$A_0$  is the initial peak area before the irradiation while  $A_t$  is the peak area at irradiation time  $t$  during the polymerization, respectively.

### 3 Results and Discussion

#### 3.1 Absorption of Photoinitiators and QDs

Absorption spectra were characterized to select appropriate PIs for the formulation design of UV-curable inks. As shown in Fig. 1, PI TPO and QDs have strong absorbance at the wavelength of 365 nm. In the contrast, PI 1173 has little absorbance at the same wavelength. It could be speculated that PI TPO might generate higher photoinitiated efficiency than PI 1173 while high loading of QDs might affect the curing performance of inks in the UV-irradiation with a wavelength of 365 nm. These assumptions would be examined in the following experiments for the studies of photopolymerization kinetics.

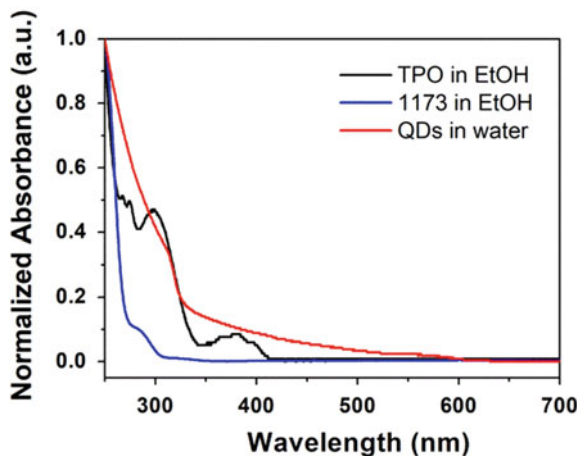


Fig. 1. Absorbance spectra of photoinitiators and QDs

## 3.2 Photopolymerization Kinetics of Inks

Photopolymerization kinetics is a strategy to investigate UV-curing rate by monitoring concentration variations of functional groups in reactants or resultants. To confirm the photopolymerization of the prepared QD-doped inks, RT-FTIR was employed to evaluate the conversion of reactive double-bonds. Effects of radiation power, species of PIs, concentration of PIs and loading amount of QDs on DC during the UV-curing process were discussed.

### 3.2.1 Effect of Radiation Power on Photopolymerization Kinetics of Inks

In order to investigate the effect of radiation power on the photopolymerization kinetics, we prepared a sample in which the mass ratio of PI TPO is 5 wt% and the concentration of QDs is 0.5 nmol/mL, as shown in Table 1. The recorded RT-FTIR polymerization profiles of the sample in UV-irradiation with different power densities are illustrated in Fig. 2.

As illustrated in Fig. 2, in the UV-radiation with a power density of 24 mW/cm<sup>2</sup>, DC of the sample increased rapidly in the first 1–10 s and finally reached to nearly 70%. With the increase of radiation power, more free-radicals were generated to induce a faster polymerization rate and a higher DC. When the radiation power reached 32 mW/cm<sup>2</sup>, the concentration of free-radicals was saturated while the DC reached its peak and no longer increased.

### 3.2.2 Effect of Concentration of Photoinitiators on Photopolymerization Kinetics of Inks

According to the analysis of absorption spectra of PIs and QDs, TPO was selected as an appropriate photoinitiator for QDs-doped inks in this research. Thus, a series samples with different concentrations of PI TPO were prepared to investigate the effect of PI concentration on DC. The recorded RT-FTIR polymerization profiles in the UV-irradiation with a power density of 24 mW/cm<sup>2</sup> are illustrated in Fig. 3.

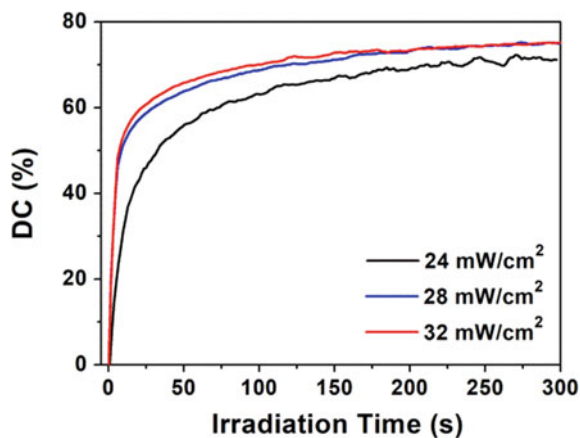


**Fig. 2.** Photopolymerization profiles of sample 4 in different power densities of UV-irradiation monitored by RT-FTIR

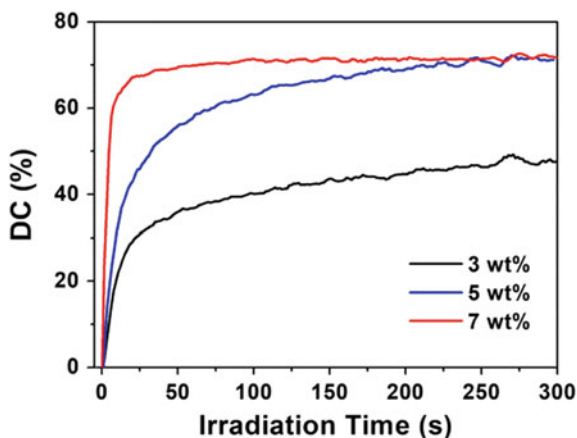


**Fig. 3.** Photopolymerization profiles of sample 4–6 with different concentrations of PI TPO monitored by RT-FTIR. The power density of UV-irradiation is 24 mW/cm<sup>2</sup>

As illustrated in Fig. 3, when the concentration of PI TPO increased from 3 to 5 wt%, the DC was increased from 48 to 72%. It is worth noting that when the concentration of the initiator continued to increase to 7%, the DC reached the maximum in a shorter period of time but the final conversion rate of double-bonds would not continue to increase. This is because the high concentration of PIs would generate large amount of free-radicals on the upper surface of the sample, which leading to a strong absorbance and scattering of irradiation light. Therefore, the UV-irradiation power inside the sample was weakened and the DC could not be further increased [11].



### 3.2.3 Effect of Species of Photoinitiators on Photopolymerization Kinetics of Inks

In order to investigate the effect of species of PIs on the UV-curing performance, samples with 5 wt% of PI TPO, PI 1173 and mixed PIs was prepared, as listed in Table 1. The recorded RT-FTIR polymerization profiles in the UV-irradiation with a power density of 24 mW/cm<sup>2</sup> are illustrated in Fig. 4. Obviously, in the first 100 s, the DC of samples prepared with PI TPO was higher than that prepared with PI 1173, which could be attributed to the stronger absorbance at the wavelength of 365 nm. However, the final conversion rate of double-bonds in sample prepared with PI TPO and PI 1173 tended to be the same, which could be explained by the gel effect. In addition, samples prepared with 5 wt% of mix PIs consisted of PI TPO and PI 1173 with the weight ratio of 1:1 generated an 80% final conversion rate of double-bonds, which was much higher than the single PI initiating system.

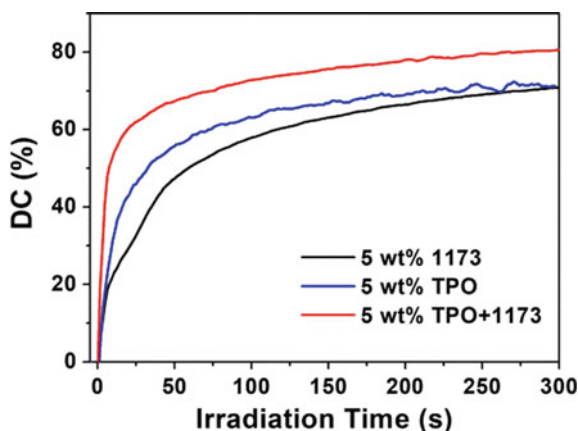


**Fig. 4.** Photopolymerization profiles of sample 4, sample 7 and sample 8 with different species of PIs monitored by RT-FTIR. The power density of UV-irradiation is 24 mW/cm<sup>2</sup> and the total amount of PIs is 5 wt% relative to the weight of pre-polymer resin for each sample

### 3.2.4 Effect of Concentration of QDs on Photopolymerization Kinetics of Inks

According to the analysis of absorption spectra, QDs used in this research had significant absorbance at the wavelength of 365 nm, which was predicted to lead to a competition with the generation of free-radicals. Thus, a series samples with different doping concentrations of QDs were prepared to investigate the photopolymerization kinetics. The recorded RT-FTIR polymerization profiles in the UV-irradiation with a power density of 24 mW/cm<sup>2</sup> are illustrated in Fig. 5.

As illustrated in Fig. 5, comparing with a pure pre-polymer resin, the doping of QDs significantly reduced the UV-curing rate and the DC, as the absorbance of irradiation light from higher loadings of QDs induced the inhibition of UV curing depth. Fortunately, a 71% final conversion rate of double-bonds could still be achieved with a

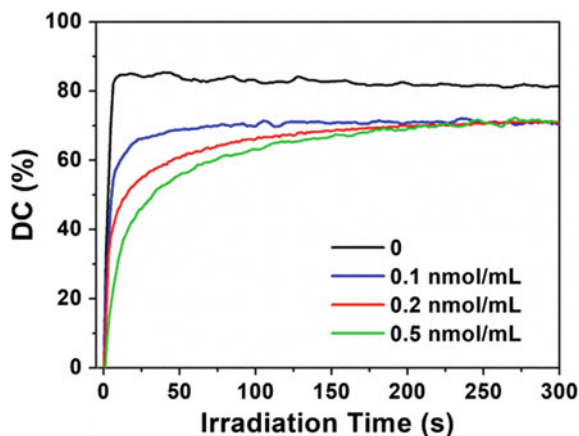


**Fig. 5.** Photopolymerization profiles of sample 1–4 with different concentrations of QDs monitored by RT-FTIR. The power density of UV-irradiation is  $24 \text{ mW/cm}^2$

0.5 nmol/mL concentration of QDs, which was enabled to provide completely cured coatings with visible photoluminescence emission. The photoluminescence property is reported in the next section.

### 3.3 Photoluminescence Property of the Printed QDs-Doped Ink

An ink sample doped with red emission QDs was prepared according to the composition in Table 1. The logo of Beijing Institute of Graphic Communication was printed on a plastic film by a rubber stamp using UV-curable QD-doped ink with the formulation of Sample 8 in Table 1. The pattern was cured by UV-irradiation with a power density of  $28 \text{ mW/cm}^2$  at the wavelength of 365 nm for 3 min. As shown in Fig. 6, there was almost nothing visible under ambient light while a clear red pattern could be observed under the UV light, which indicated that the prepared ink doped with

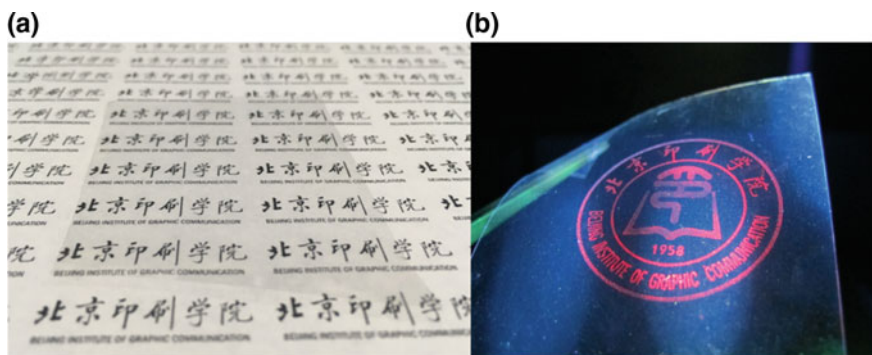


**Fig. 6.** A pattern printed from the prepared UV-curable ink doped with red emission QDs under **a** ambient light and **b** UV light. The diameter of the pattern is 3 cm

red light emission QDs showed perfect photoluminescence effect, which possesses potential application values in anti-counterfeit printings, optical sensors, biological probes, display devices and other fields.

## 4 Conclusions

In this research, we prepared a series of UV-curable waterborne fluorescent inks by doping QDs into pre-polymer resins. Experimental results of RT-FTIR analysis indicated that the UV-curing performance of inks was significantly affected by the concentration and species of PIs, the power density of UV-irradiation and the concentration of QDs. The prepared inks were successfully applied to the printing on a flexible substrate and patterns with visible photoluminescence emission were achieved. This research will promote the development and application of new types of special ink.

**Acknowledgement.** This study is funded by Science and Technology Program of Beijing Municipal Education Commission (No. KM201710015012, No. KM201810015012), Key Program of Beijing Institute of Graphic Communication (No. Ea201602), College Students Research Program of Beijing Institute of Graphic Communication “Preparation and Photopolymerization Properties of UV-Curing Fluorescent Inks” and “Research of Color Inks for 3D Printing”.

## References

1. Shirasaki, Y., Supran, J. G., Bawendi, M. G., et al. (2013). Emergence of colloidal quantum-dot light-emitting technologies. *Nature Photonics*, 7, 13–23.
2. Kim, T. H., Cho, K. S., Lee, E. K., et al. (2011). Full-colour quantum dot displays fabricated by transfer printing. *Nature Photonics*, 5, 176–182.
3. Wang, Y., Ta, V. D., & Gao, Y. (2014). Stimulated emission and lasing from CdSe/CdS/ZnS core-multi-shell quantum dots by simultaneous three-photon absorption. *Advanced Materials*, 26(18), 2954–2961.
4. Li, X. M., Wu, Y., Zhang, S. L., et al. (2016). CsPbX<sub>3</sub> quantum dots for lighting and displays: Room-temperature synthesis, photoluminescence superiorities, underlying origins and white light-emitting diodes. *Advanced Functional Materials*, 26(15), 2435–2445.
5. Perelaer, J., Smith, J. P., Mager, D., et al. (2010). Printed electronics: The challenges involved in printing devices, interconnects, and contacts based on inorganic materials. *Journal of Materials Chemistry*, 20, 8446–8453.
6. Wei, W. J., Xu, H., You, Q., Liu, C., et al. (2016). Preparation of quantum dot luminescent materials through the ink approach. *Materials and Design*, 91, 165–170.
7. Jin, Y. Z. (2010). *Light curing material performance and application manual*. Beijing: Chemical Industry Press.
8. Ling, J. J., Wang, K. M., Nie, J., et al. (2016). Synthesis and characterization of highly reactive poly methyl methacrylate monomers with photopolymerization. *Polymer Materials Science and Engineering*, 32(12), 7–12.
9. Decker, C., & Moussa, K. (1989). Real time kinetic study of lase induced polymerization. *Macromolecules*, 22, 4455–4461.

10. Avens, H. J., & Bowman, C. N. (2009). Mechanism of cyclic dye regeneration during eosin-sensitized photoinitiation in the presence of polymerization inhibitors. *Journal of Polymer Science Part A-Polymer Chemistry*, 47, 6083–6094.
11. Huang, D., Duan, Y. X., Liang, Z. Y., et al. (2003). Study on curing technology of UV-Cured up resin: Photoinitiator concentration and cure time. *Fiber Reinforced Plastics and Composite*, 3, 19–23.



# Preparation and Research of Acrylate Latex

Yingying Li, Xiulan Xin<sup>(✉)</sup>, and Xitong Mao

Beijing Technology and Business University, Beijing, China  
xinxl2007@126.com

**Abstract.** With the development of economy, people pay more and more attention to environmental protection. The proportion of water-based ink in the ink industry is increasing due to its good environmental friendliness. Water-based acrylate latex has been widely used in water-based inks due to its good film formation, printing adaptability, light resistance, and corrosion resistance. In this paper, a series of acrylate latexes were prepared by non-pre-emulsification semi-continuous emulsion polymerization by compounding small-molecule emulsifiers (LS: SDS & OP-10) with macromolecular emulsifiers (acrylic resins). And the effect of additive amounts of small molecule emulsifier and macromolecular emulsifier on the properties of acrylate latex was investigated. When the additive amount of the small molecule emulsifier was 1.5 wt% and the macromolecular emulsifier was 30 wt%, the acrylate latex with a small particle size, moderate viscosity, and good stability could be prepared.

**Keywords:** Acrylic resins · Acrylate latex · Small molecule emulsifier · Macromolecular emulsifiers

## 1 Introduction

The level of development in the printing industry is one of the indicators of the degree of industrialization and modernization of a country. The VOCs emissions and pollution brought by it have gradually attracted attention [1]. VOCs can chemically react with ammonium oxide in the atmospheric ozone layer to produce organic compounds [2]. And the combination of VOCs with fine particles and other substances in the air creates fine particulate matter (PM<sub>2.5</sub>), and the resulting haze threatens the health of humans and other plants and animals [3]. At present, China's flexible packaging printing industry mainly adopts gravure printing, and the large amount of solvent-based ink used in the printing process will bring huge VOCs emissions. Compared with solvent-based ink, water-based ink has the advantages of green environmental protection, non-toxic safety, and low VOCs emissions.

Waterborne binder has always been the focus of research in water-based ink. Waterborne acrylic resin is one of the most used binder resins in water-based inks due to its excellent printing adaptability, friction resistance, stability, heat resistance, and compatibility with pigments. The molecular weight and acid value of waterborne acrylic resin have a certain influence on the performance of the synthesized acrylate latex. Pedraza [4] studied the effect of pH on the film formation of acidic acrylic resin latex, the location of either or both acids will catalyze the cross-linking reaction of the

latex, which typically contains carboxylic acid groups as reactive moieties (especially hydroxyls) and strong acids as catalysts.

In this paper, a waterborne acrylic resin with the molecular weight  $M_w$  of 8000 and the degree of neutralization of 90% was used as macromolecular emulsifier. It was considered to combine macromolecular emulsifier with small-molecule emulsifier. And the effects of additive amounts of small molecule emulsifier and macromolecular emulsifier on the properties of acrylate latex were investigated.

## 2 Experimental

### 2.1 Materials

Methyl Methacrylate (MMA), n-Butyl Acrylate (BA): Chemically Pure, Sinopharm Group Chemical Reagent Co., Ltd.; Sodium Dodecyl Sulfate (SDS): Chemical Pure, Tianjin Chemical Reagent Factory No. 6; Polyphenol Ethers (OP-10): Chemically Pure, Tianjin Institute of Chemical Reagents; Macromolecular Emulsifier (SR679): Industrial Grade, Qingdao Linke Co., Ltd.

### 2.2 Apparatus

Nano particle size analyzer: Malvern, UK; Viscometer: Brookfield, American. Almost all-infrared stability analyzer: formulation, France Co., Ltd.

### 2.3 Procedure

A certain amount of deionized water, emulsifier, and sodium bicarbonate were weighed and added to a four-necked flask. The mixture was stirred at room temperature for 30 min to ensure that the emulsifier system was uniformly dispersed. Nitrogen flowed for 2 min. 1/10 of the mixed monomers were added during increasing the temperature. When the temperature rose to 80 °C, 1/10 initiator solution was added. The remaining monomer and initiator solution were added dropwise after 15 min, and was added within 3 h. Increase the temperature to 85 °C and last for 2 h. Add redox initiator when it cooling down to 50 °C, and last for 30 min. Then the pH of latex was adjusted to 8.5–9.

### 2.4 Measurements

#### 2.4.1 Solid Content

1.5–2 g of latex was weighed in the aluminum box with constant weight, dry the aluminum box and sample at 55 °C for 24 h. The solid content was calculated by the following formula (1):

$$W_d/\% = m_1/m_0 \times 100 \quad (1)$$

$m_0$ -original quality of the sample, g;  $m_1$ -quality of the dry sample, g.

### 2.4.2 Particle Size and Distribution

Nano-ZS dynamic light scattering particle size (DLS) was used to test the size and particle size distribution coefficient of the latex.

### 2.4.3 Stability

#### 2.4.3.1 Storage stability

The latex was sealed and stored at room temperature for 6 months. The storage stability of the latex was observed.

#### 2.4.3.2 Centrifugal stability

The appropriate amount of latex was put into the centrifuge tube, and centrifuged at 3000 r/min for 30 min. The centrifugal stability of the latex was observed.

#### 2.4.3.3 Dynamic stability

The dynamic stability of the latex was measured by a stability analyzer. The temperature was 25 °C.

### 2.4.4 Viscosity

The viscosity was measured by viscometer from American Brookfield Company.

## 3 Results

### 3.1 Effect of Small Molecular Emulsifier

In the experiment, when the additive amount of macromolecular emulsifier was 30 wt%, compound small molecule emulsifier with macromolecular emulsifier SR 679. The effect of changes in the amount of small-molecule emulsifier on the performance of the prepared acrylate latex was investigated. The addition of small molecule emulsifiers are 0, 0.5, 1.0, 1.5, 2.0, 2.5 wt% of the total monomer.

As it is shown in Table 1, when the macromolecular emulsifier was used alone, the prepared acrylate latex particles had a large particle size, the viscosity of the latex was low, and the system was unstable. The use of a latex prepared in combination with small-molecule emulsifier significantly improved particle size and stability. When the amount of small molecule emulsifier in the composite emulsifier was less than 2.0%, the latex particle size became smaller and the latex viscosity increased accordingly. Due to the increase of electrostatic repulsion and steric hindrance, the latex centrifugal stability and storage stability also increased. As the amount of small-molecule emulsifier continues to increase, the viscosity decreased and the average diameter of the latex particles increased. Because of the increase of the amount of free water in the system, the viscosity began to decrease and tended to a gentle trend of change.

**Table 1.** Effect of additive amount of small molecular emulsifier (LS)

Addition of LS (%)	Particle size (nm)	PDI	Zeta (mv)	Viscosity (mPa s)	Centrifugal stability	Storage stability
0	148.5	0.055	-47.6	20.7	Failed	Unstable
0.5	125.5	0.104	-61.6	21.6	Failed	Unstable
1.0	102.4	0.053	-56.4	26.1	Qualified	Stable
1.5	89.8	0.061	-54.6	31.0	Qualified	Stable
2.0	129.6	0.138	-66.6	21.2	Qualified	Stable
2.5	134.9	0.080	-59.9	20.9	Qualified	Stable

### 3.2 Effect of Macromolecular Emulsifier

According to the research of 3.1, based on 1.5 wt% of small molecule emulsifier, the effect of the addition of a macromolecular emulsifier at 15, 20, 25, 30, 35 wt% on the properties of the prepared acrylate latex was examined.

It can be seen from Table 2, with the increase of the amount of macromolecular emulsifier, latex particle size became smaller. Repulsive forces between particles and steric hindrance increased and also stability increased. When the amount of macromolecular emulsifier increased to 30 wt%, one high-quality polymer latex could be obtained, but if we continue to increase the amount of macromolecular emulsifier, the latex particle size became larger. It is because that the amount of monomer and water added in the medium was constant, and the maximum amount of latex particles that can be formed by the added emulsifier was certain. Redundant emulsifier covered the latex particles, and the average particle size increased.

**Table 2.** Effect of additive amount of macromolecular emulsifier

Addition of SR679 (%)	Particle size (nm)	PDI	Zeta (mv)	Centrifugal stability	Storage stability
15	124.2	0.015	-53.8	Qualified	Stable
20	105.5	0.037	-61.1	Qualified	Stable
25	104.6	0.021	-63.0	Qualified	Stable
30	89.8	0.061	-54.6	Qualified	Stable
35	128.8	0.072	-60.5	Qualified	Stable

### 3.3 Dynamic Stability Testing of Acrylate Latex

As it is shown in Fig. 1, the unstable parameters (TSI) of the latex prepared by the different additive amount of macromolecule emulsifiers were obtained. And the smaller change of TSI, the better stability of the latex. It also can be concluded that as the amount of macromolecule emulsifier increased, change of TSI became smaller, and the stability was better. It may be due to the aggregation of macromolecule emulsifiers between the spherical latex particles that formed a cross-linked structure, which played a role in stabilizing the latex particles.



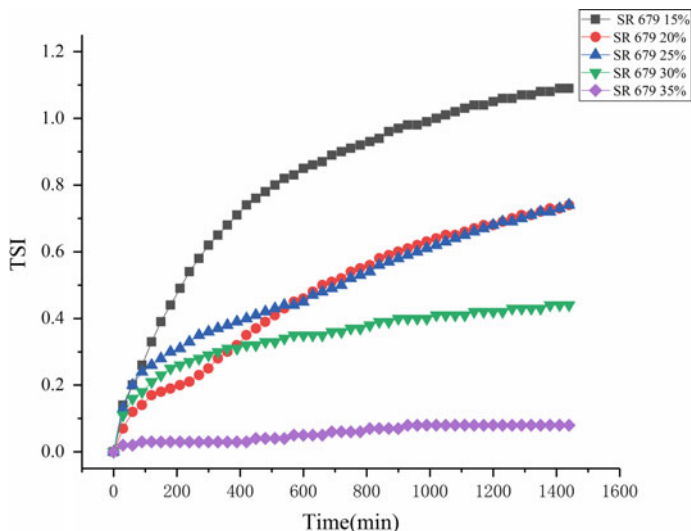


**Fig. 1.** Influence of amount of macromolecule emulsifier on TSI index of acrylate latex

## 4 Conclusions

In this paper, non-pre-emulsification semi-continuous emulsion polymerization was used to prepare the poly acrylate latex with 40% solids, small particle size, and good stability. The effects of the additive amount of small-molecule emulsifier and macromolecule emulsifier on the performance of acrylate latex were investigated when the neutralization degree of acrylate resin was 90%. It was found that, when the additive amount of the small molecule emulsifier was 1.5 wt% and the additive amount of the macromolecular emulsifier was 30 wt%, the acrylate latex with a small particle size, moderate viscosity, and good stability could be prepared.

**Acknowledgements.** This study was funded by a National Natural Science Foundation of China (21376008)—Design, Synthesis and Structure-Activity Relationship of Novel Emulsions for Water-based Inks.

## References

1. Zhou, X., Li, Y., Fang, C., et al. (2015). Recent advances in synthesis of waterborne polyurethane and their application in water-based ink: A review. *Journal of Materials Science and Technology*, 31(7), 708–722.
2. Atkinson, R. (2000). Atmospheric chemistry of VOCs and NO<sub>x</sub> (review). *Atmospheric Environment*, 34(12–14), 2063–2101.
3. Liu, N. (2013). On the relationship of industrial coatings VOC emissions and PM2.5. *Science & Technology Innovation Herald*.
4. Pedraza, E. P., & Soucek, M. D. (2008). Influence of acid–base pairs on film formation and catalysis for acidic acrylic latexes. *Progress in Organic Coatings*, 62(4), 417–424.



# Study on Performance of Nano-silver Conductive Inkjet Printed Circuits

Kaiyang Sang, Maohai Lin<sup>(✉)</sup>, Chenhang Zhang,  
Ben Liu, Zhijin Li, and Meiqi Lin

School of Printing and Packing Engineering,  
Qilu University of Technology, Jinan, China  
mhlin@qlu.edu.cn

**Abstract.** With the rapid development of printing electronics, conductive ink as an important part of printing electronics, the electrical conductivity of which printed on different substrates has become the focus of research. In this paper, the printed circuit of different patterns and thickness of ink layer were printed on photo paper and PET film by using the nano-silver conductive ink with the particle size of 30 nm and solid content of 5–10%, and its conductivity was tested under different sintering temperature. The experimental results showed that the circuit could still maintain good electrical conductivity with the change of printing pattern. As the thickness of the ink layer increases, the circuit width becomes wider, the conductivity of the circuit gradually increased and it decreased after reaching a certain number of layers. The conductivity increased rapidly with the increase of sintering temperature and it tended to be stable after slowing down when reaching a certain temperature. As the sintering time going by, the electrical conductivity of the circuit increased swiftly first and the growth trend became slower.

**Keywords:** Nano-silver conductive ink · Ink thickness · Sintering temperature · Sintering time · Conductivity

## 1 Introduction

In recent years, with the fast pace of life in modern society, printing technology has opened up a new industry model—printed electronics industry. Because of its remarkable advantages in many aspects, it has become a key industry in many fields. The core of printed electronics is to transfer functional inks with electrical properties to substrate through traditional printing methods or inkjet printing, so as to have corresponding electrical properties, thereby realizing the production of electronic components. The modern society with a higher and higher degree has a great and very promising development prospect, which has attracted great attention at home and abroad [1].

With the continuous innovation of technology, conductive inks have made great progress. Nano-silver inks developed by Pchem Associates have been used to print high-frequency RFID tags. Bayer made micro-wires with BayInk<sup>®</sup> nano-silver inks, the

thickness of which is no more than 20  $\mu\text{m}$ . Epoxies Etc in the United States has announced a new type of ink for screen printing and printing processes, which can be deposited on a variety of substrates such as polyimide film, polyester film, glass and ceramics [2].

In this paper, inkjet method was used to print conductive ink on a variety of substrates. By changing various physical environmental conditions, the electrical properties of circuits printed on the substrates were characterized to explore different factors, and to explore the electrical conductivity of lines with different factors.

## 2 Nano-silver Conductive Inkjet Printing Experiment

### 2.1 Photo Paper Base Printing Experiment

There is ink-absorbing coating on the surface of photo paper after surface treatment in production, so that conductive ink has good film-forming property on its surface. Therefore, photo paper does not need surface modification and can be directly spray-printed experiment [3].

#### 2.1.1 Effect of Print Layers on Printed Circuits and Their Conductivity

Nano-silver conductive ink with a particle size of 30 nm and a solids content of 10% was used for inkjet printing with an inkjet printer to ensure that the parameters of the inkjet printer remained the same and that the pattern of each print was consistent, that is, the line width was 200  $\mu\text{m}$  and the line length was 5 cm. Then the printing experiment was carried out. In this section, the number of printed layers was used as an experimental variable, and the number of printed layers was designed to be 1 layer, 3 layers, 5 layers, 7 layers, and 9 layers, with 5 layers as a group. Based on the reliability principle of the experiment, three groups of the same experiments, experiment a, experiment b, and experiment c, were analyzed to compare the line appearance of the jet printing experiment to explore whether the number of printed layers had an effect on the line appearance [4]. Through visual observation and instrument measurement, it can be clearly found that obvious burrs appear on the line and its edges become unsmoothed, and the line width changes obviously (Table 1).

**Table 1.** Line width

No.	Print layers	Width a/mm	Width b/mm	Width c/mm
1	1	202	203	200
2	3	206	207	204
3	5	212	213	209
4	7	225	223	225
5	9	230	228	231

### 2.1.2 Influence of Sintering Temperature and Time on Printed Circuit Conductivity

In this section, sintering temperature and sintering time were taken as experimental variables, four different sintering temperatures (90, 110, 130, and 150 °C) were designed and three different sintering time (10, 20, 30 min) was also set according to the time gradient. These experiments were used to investigate the effects of sintering temperature and time on the conductivity of the conductive traces [5].

One set of lines from different layers before the printing experiment was selected and placed in a vacuum drying oven, and three time gradients of 10, 20, and 30 min were set to sinter at four different temperatures until the operation was completed. The resistivity was measured with a four-probe instrument and their conductivity was analyzed (Fig. 1).

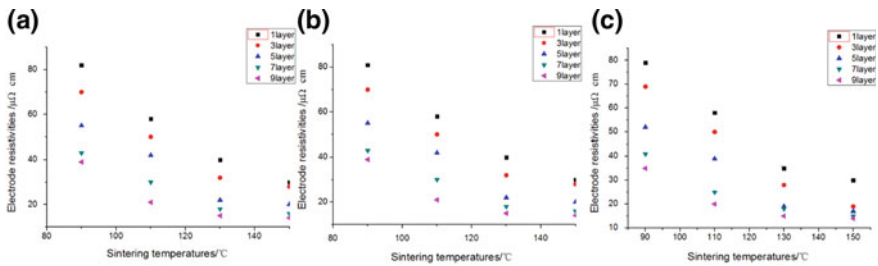


**Fig. 1.** Based on photo paper, the sintering time is 10 min (a), 20 min (b), and 30 min (c), and the relationship between resistivity and temperature

## 2.2 Transparent PET Film Substrate Printing Experiment

The other substrate chosen in this article is a transparent PET film, but the surface of the PET film is too smooth to directly perform the printing experiment. Therefore, the surface of the PET film must be firstly modified to change the hydrophilicity of the surface, and then the printing experiment is performed [6]. The characteristics of the surface modification of the material can be used to treat the surface of the PET film. The surface morphology, surface chemical composition and properties of the PET film can be idealized by changing the properties such as wettability and adhesion [7].

By measuring the contact angle of the ink droplets to detect the hydrophilicity of the ink droplets and the substrate, if the contact angle is large, it means that the hydrophilicity of the ink droplets and the substrate is poor, the exhibition of the ink droplets is difficult, and the circuit pattern may occur. Open circuit; if the contact angle is small, it means that the hydrophilicity of the ink droplet and the substrate is too good, the exhibition of ink droplets is very wide, and the wiring pattern is likely to cause a short circuit because they are connected together [8].

Using a transparent PET film as a substrate, the electrical conductivity of the circuit was explored by varying the number of print layers, sintering temperature and time, and measuring the resistivity of the conductive lines with a four-probe instrument (Fig. 2).

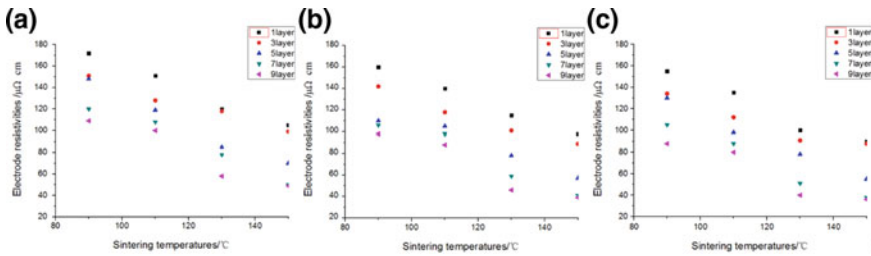


**Fig. 2.** Based on PET film, the sintering time is 10 min (a), 20 min (b), and 30 min (c) and the relationship between resistivity and temperature

By observing the data in the graph, it can be clearly seen that as the temperature and time continue to increase, the resistivity decreases, and the electrical conductivity of the circuit becomes better and better.

### 2.3 Analysis and Discussion

It can be seen from the above diagram that with the layer-by-layer superposition of the circuit layers, the resistivity of the line is reduced, which means that the conductivity of the line is getting better and better. The reason for this is that as the number of layers increases, the thickness of the film layer also increases, the number of nano-silver particles in the circuit increases, and the internal space remains the same, resulting in smaller and smaller gaps between the particles. More importantly, the surface of the nano-silver particles in the ink is coated with a protective agent. As the temperature rises, the protective agent loses its function due to thermal decomposition or denaturation, and the nano-silver particles are gradually exposed from the protective agent and tightly bound together to form a compact interworking structure, which can improve the conductivity of circuit.

In addition, the film-forming property of conductive ink on pet film is not as good as that of conductive ink on photo paper, which causes the difference of line resistivity. It appears that the conductivity of line on photo paper is better than that of pet film [9].

## 3 Conclusions

Nano-silver conductive ink was printed on different substrates by inkjet printing, and the conductive properties of the printed circuit were explored under the condition that the number of printed layers, sintering temperature, sintering time and other factors changed. When the number of printing layers was 5, the circuit was the most regular and clear. When the sintering temperature was 150 °C and the sintering time was 30 min, the protective agent in the conductive ink could be volatilized more effectively, which made the connection between silver particles closer and the conductivity of the circuit better.

Certainly, for the sintering temperature could be further reduced to achieve a lower temperature sintering, and the less time could be controlled in the sintering time to improve efficiency.

**Acknowledgements.** This work was supported by Shaanxi Key Laboratory of printing and packaging engineering (Project number: 2017KFKT-02).

## References

1. Wang, Y. (2017). *Low-temperature sintering of nano-silver conductive ink and its inkjet printing performance*. Nanjing University of Posts and Telecommunications.
2. Cheng, F. (2016). *Preparation and optical properties of nanosilver*. Hubei Normal University.
3. Shen, Y. K. (2015). *Synthesis of conductive silver and IGZO ink and preparation of thin films*. Guangdong University of Technology.
4. Yang, Y. (2015). *Preparation and properties of paper-based nanosilver inkjet ink*. South China University of Technology.
5. Hu, X. W. (2014). Recent advances in nano-conductive inks and their applications. *Printing Technology*, 11, 54–57.
6. Gao, Z. Q. (2013). *Preparation of nano silver conductive ink based on RFID inkjet printing*. Tianjin University of Science and Technology.
7. Jeong, S., Song, H. C., Lee, W. W., et al. (2011). Stable aqueous based Cu nanoparticle ink for printing well-defined highly conductive features on a plastic substrate. *Langmuir*, 27(6), 3144–3149.
8. Lin, J. J. (2008). Application of inkjet printing technology in PCB (Part 2). *Printed Circuit Information*, 08, 10–20.
9. Kamyshny, A., & Magdassi, S. (2014). Conductive nanomaterials for printed electronics. *Small*, 10(17), 3515–3535.



# Research on Electrophoretic Display Ink and Its Microencapsulation

Aijing Gao, Meijuan Cao, Jia Yan, Luhai Li<sup>(✉)</sup>, Xi Li, Shouzheng Jiao, and Tianshu Zhao

School of Printing and Packaging Engineering, Beijing Engineering Research Center of Printed Electronics, Beijing Institute of Graphic Communication, Institute of Printing and Packaging Engineering, Beijing, China  
liluhai@bigc.edu.cn

**Abstract.** Herein, the benzidine yellow PY14 (background color) and the red metal complex dye (developing particles) are dispersed in a mixed solvent of tetrachloroethylene and xylene without adding a charge control agent to prepare an electrophoresis liquid. The electrophoresis liquid is coated into microcapsules by a complex coacervation method, and the capsule wall material is gelatin and gum arabic. Observe the morphology of the microcapsules, test the reflection density, particle size distribution and test the performance index. Finally, an electrophoretic display principle device was fabricated using indium tin oxide (ITO) conductive glass. The results showed that when the particle size of benzidine yellow was dispersed to 1400 nm and the dispersion time was 120 min, the reflection density was the highest, which was the most favorable for display. The coated microcapsules were made into electronic devices and then electrophoresed structure of the cross-linked sample was better.

**Keywords:** Benzidine yellow · Reflection density · Particle size distribution · Microcapsule · Complex coacervation

## 1 Introduction

Microcapsules are widely used in electronic paper. At present, there are mainly four types of electronic paper: electrophoretic display technology [1], electronic powder fluid display technology [2], cholesterol liquid crystal display technology [3], and bistable nematic liquid crystal display technology [4]. Microcapsule technology [5] refers to dispersing a liquid substance such as a liquid, a solid or a gas into droplets or particles, and then depositing a polymer film-forming material (wall material) on the droplets or particles to form a film, the capsule droplets or particles are coated. This process is called microencapsulation. In the field of electrophoretic display, the capsule wall is a transparent polymer film material, and the capsule core is an electrophoretic particle dispersion. The electrophoretic particle dispersion may be selected from any one or more particles having a charge or a charge easily obtained on the surface, such as inorganic or organic pigment particles, inorganic-organic composite particles coated with organic substances, and the like [6]. Because all components of the electrophoretic ink can affect the electrophoresis performance. Since the electrophoretic display has

become the research content of people, the particle size control, reflection density value, and display contrast and contrast have been the direction of the researchers [7].

Most of the reported literatures have used benzidine yellow PY14 as a color-developing particle and tetrachloroethylene as a dispersing agent to prepare microcapsules. In this paper, the benzidine yellow particles are large and stable, and they are dispersed without the advantage of adding a charge control agent. The dispersed particle size and reflection density were then tested by a particle size zeta potential resistance tester and a reflection densitometer (X-rite 310). Finally, the particle size and dispersion time which are favorable for improving contrast and contrast are found, and then the microcapsules are coated under this formulation, and it is observed whether the microcapsules are electrophoresed.

## 2 Experimental

### 2.1 Materials

Industrial grade benzidine yellow PY14, red metal complex purchased from SIGMA (Germany), analysis of pure tetrachloroethylene (CCl<sub>4</sub>, 98%), xylene, sodium hydroxide, formaldehyde, acetic acid, hydrochloric acid purchased in Beijing Chemical Plant (China), industrial grade gum arabic and gelatin were purchased from ROUSSELOT (France), and indium tin oxide (ITO) conductive film was purchased from Beijing Chemical Plant (China).

### 2.2 Preparation of Electrophoretic Ink

#### 2.2.1 Dispersion of Benzidine Yellow

Dissolve benzidine yellow PY14, tetrachloroethylene, KD6 in a beaker at a mass ratio of 1.66:50:1, then add zirconium beads (500 g), and adjust the high speed mixer to 3000 r/min for 120 min, the mixed solution (100 mL) was taken every half hour, and then the mass ratio of the benzidine yellow to the zirconium beads was 3.32, 2.66, 1.99, 1.66, and 1.33 wt%, respectively.

Add benzidine yellow PY14 pigment (4 g), KD6 dispersant (10 mL) to tetrachloroethylene solvent (200 mL), add zirconium beads (200 g). The high speed mixer was adjusted to 3000 r/min for 2 h, and samples were taken every 0.5 h (5 mL).

#### 2.2.2 A Mixture of Red and Yellow Colors

The red metal complex (0.46 g) was uniformly dispersed in xylene (50 mL). The dispersed benzidine yellow PY14 and the red metal complex dye dissolved in xylene were then mixed in a ratio of 1:1 to form an electronic ink.

### 2.3 Microcapsules Prepared by Complex Coacervation

The gum arabic (3 g) and gelatin (3 g) were dissolved in deionized water (200 mL), and the gelatin solution was added to the gum arabic solution after standing for 5 h, set the stirring speed to 550 r/min at 40 °C, and add electronic ink (10 mL) after stirring for 10 min. After 15 min, adjust to 400 r/min and add acetic acid solution (10%) to pH



4. Stirring was continued for 15 min, then deionized water (140 mL) was added and stirring was continued for 2 h. After the mixture was cooled to room temperature, the formaldehyde solution (15%, 10 mL) was added. Stirring at low speed for 20 min, the NaOH solution was added dropwise, and the pH was slowly adjusted to 7–8. After repeated washing and drying, then standing for 24 h, the supernatant was removed and the remaining liquid was centrifuged for 10 min at a speed of 1000 r/min. Electronic ink microcapsules can be obtained.

## 2.4 Principle Device Fabrication and Ablation

The image portion of the ITO conductive film was sealed with a tape and completely immersed in a mixed solution of hydrochloric acid and water at a ratio of 1:3 for 10 min. The microcapsules were mixed with ZY-B-1 adhesive at 5:1, uniformly coated on the ablated ITO conductive glass, controlled to a thickness of about 200  $\mu\text{m}$ , and placed in a drying oven at 40  $^{\circ}\text{C}$  for drying. When the adhesive is dried quickly, another ITO glass is covered to form an electrophoretic device.

## 2.5 Characterization

The particle size distribution and reflection density of the following two samples were tested using a particle size zeta potential resistance tester and a reflection densitometer (X-rite 310): samples with different ratios of pigments and zirconium beads, samples taken at different times.

# 3 Results and Discussion

## 3.1 Particle Size Distribution and Reflection Density of Benzidine Yellow Under Different Mixing Ratios and Different Dispersion Times

When benzidine yellow is used as the background color, in order to improve the contrast and contrast with the color-developing particles, the brightness of benzidine yellow should be minimized, so samples with higher reflection density values should be used in the experimental data. As shown in Fig. 1, when the ratio is 1.33 wt%, the particle size distribution is the widest, the particle size is 1400 nm, and the reflection density value is the highest at 1400 nm. Therefore, the proportion of benzidine yellow is decreasing, and the proportion of zirconium beads is increasing, which is conducive to increasing contrast and contrast. As shown in Fig. 2, the dispersion of benzidine yellow is 1400 nm when dispersed for 120 min, and the reflection density value of the dispersed benzidine yellow particle size of 1400 nm at 120 min under the condition of 120 min can also be found, which is compared with the color-developing particles.

## 3.2 Microcapsule Morphology Observation and Changes in Principle Device After Power-on

Observe the microcapsules under a Leica microscope to obtain Fig. 3, when the electric field is not applied, the color of the microcapsules is uniform orange. When the voltage

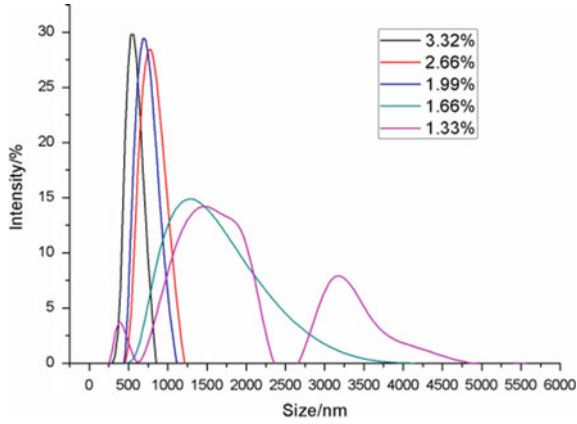


**Fig. 1.** Comparison of particle size peaks under different ratios of benzidine yellow PY14 and zirconium beads

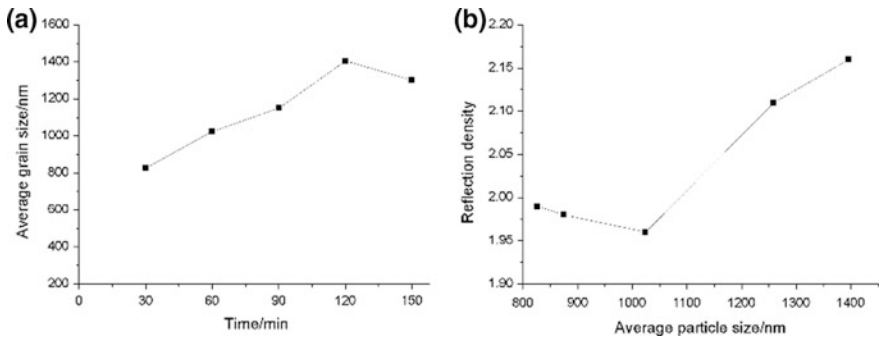


**Fig. 2.** Dispersed particle size at different times (a) and reflection density at different particle sizes (b)

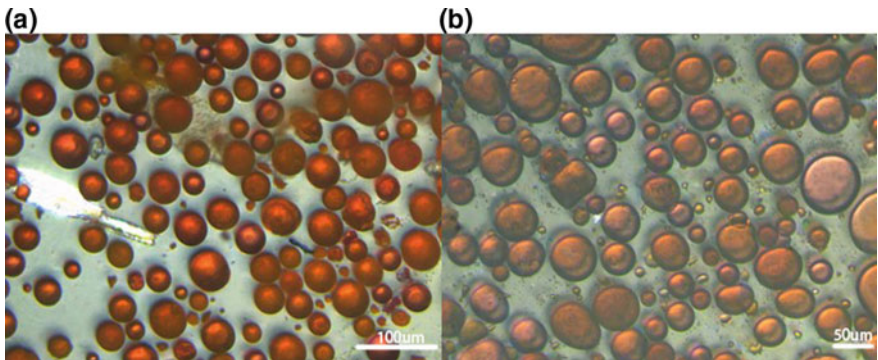


**Fig. 3.** Color change in microcapsules before and after power-on: a before power-on; b after power-on

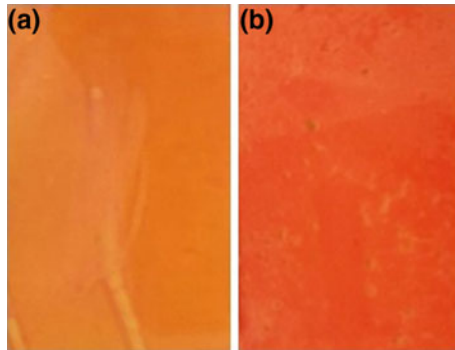


**Fig. 4.** The principle changes of the device before and after power-on: **a** before power-on; **b** after power-on

of 3 V is applied to the electrodes at both ends, the color of the microcapsules becomes red, and the color does not change after the power is turned off. It is proved that the microcapsules have bistable characteristics and electrophoresis can occur.

As shown in Fig. 4, after a voltage is applied to the device, the device is discolored, and the color does not change after the application of the voltage is stopped, thereby realizing a bi-stable display. It is proved that the electronic ink can be displayed repeatedly, and the whole surface is discolored by 5–6 s, and the response time is about 4 s.

## 4 Conclusions

In this experiment, it was found that benzidine yellow PY14 was dispersed as background color for 120 min. When dispersed to 1400 nm, the brightness was low, the reflection density was high, and the contrast with the color of the color-developing particles was obvious, which was favorable for microcapsule coating. The phenomenon of coagulation is prone to occur after the dispersion of benzidine yellow PY14. The coated microcapsules are made into an electronic device that can be electrophoresed after being energized, and can realize bistable display with a response time of 4 s.

**Acknowledgements.** This work was supported by the Youth Projects of National Natural Science of China (Grant No. 21706016), the Key Project of Beijing Institute of Graphic Communication (Ea201603), the Talent Project of Beijing Institute of Graphic Communication, the Beijing Municipal Education Commission (No. SQKM201710015005).

## References

1. Comisky, B., & Albert, J. D., Yoshizawa, H., et al. (1998). An electrophoretic ink for all-printed reflective electronic displays. *Nature*, 394(6690), 253–255.
2. Bridgestone Corp. (2003). Electrostatic liquid crystal display device for e.g. Mobile telephone, has powder fluid formed between ball-shaped spacer having adhesive agent, arranged at periphery portions of substrate. JP2003322883-A.
3. Lee, N. S., & Choi, W. S. (2004). Development of 3+2 dynamic drive scheme for cholesteric liquid crystal displays. *Display*, 25(5), 201–205.
4. Jianxin, G., & Haicheng, G. (2000). High performance transmissive bistable twisted nematic liquid crystal display. *Modern Display*, 3, 23–24.
5. Song J., Chen, L., Li, X. (2001). Microencapsulation technology and application (1), 25–29.
6. Whitesides, T. H., Zhou, Q. Y., & Wilcox, R. J. (2007). Electrophoretic media and processes for the production thereof. US 230750.
7. Li, L. (2003). Investigation on composition and properties of microencapsulated electrophoretic display ink, 63.



# Preparation and Characterization of Nano-TiO<sub>2</sub>/SiO<sub>2</sub> Composite Particles

Bin Du<sup>1</sup>, Kenan Yang<sup>1</sup>, Rubai Luo<sup>1,2</sup>(✉), Qiqi Li<sup>1</sup>, Feng Chen<sup>1</sup>,  
Haibin Li<sup>1</sup>, Ying Yang<sup>1</sup>, and Shisheng Zhou<sup>1</sup>

<sup>1</sup> Faculty of Printing, Packing Engineering and Digital Media Technology,  
Xi'an University of Technology, Xi'an, China

luorubai@xaut.edu.cn

<sup>2</sup> Shaanxi Key Laboratory of Printing and Packing Engineering, Xi'an  
University of Technology, Xi'an, China

**Abstract.** Nano-TiO<sub>2</sub> can be used as ink connecting materials to improve the UV resistance due to the ability to absorb ultraviolet light of the nano-TiO<sub>2</sub>. However, the photocatalytic action of TiO<sub>2</sub> will reduce the application performance of the ink. The nano-SiO<sub>2</sub> coating of nano-TiO<sub>2</sub> can block the direct contact between nano-TiO<sub>2</sub> and the resin, which not only reduces the photocatalytic performance but also retains the ultraviolet absorption. Therefore, nano-TiO<sub>2</sub>/SiO<sub>2</sub> composite particles were prepared using polyvinyl pyrrolidone (PVP) and 4-vinylpyridine (4VP) as dispersants. The results were shown by SEM, FT-IR, and XRD analysis. The results show that nano-SiO<sub>2</sub> can better encapsulate nano-TiO<sub>2</sub> when the PVP amount is 2 g, the 4VP amount is 2 ml, the titanium and silicon ratio is 1:2, and the ammonia amount is 5 ml. This study plays an active role in improving the UV resistance of inks.

**Keywords:** Nano-TiO<sub>2</sub>/SiO<sub>2</sub> · PVP · 4VP · UV resistance

## 1 Introduction

Nano-TiO<sub>2</sub> is a wide bandgap semiconductor material that can absorb ultraviolet light and produce photocatalytic action [1, 2]. Due to this unique physicochemical property, nano-TiO<sub>2</sub> can be used as ink connecting materials to improve the UV resistance of the ink. However, if nano-TiO<sub>2</sub> is added directly into the resin, the organic substrate which is in contact with nano-TiO<sub>2</sub> is decomposed because of the photocatalytic action of TiO<sub>2</sub>. The application performance of the ink is decreased.

For this reason, nano-SiO<sub>2</sub> can be coated on the surface of nano-TiO<sub>2</sub>. Since nano-SiO<sub>2</sub> has a good light permeability, the coating of nano-TiO<sub>2</sub> by nano-SiO<sub>2</sub> can prevent the direct contact between nano-TiO<sub>2</sub> and the resin, and reduce the photocatalytic performance [3, 4]. At the same time, it has a good absorption of ultraviolet light absorption.

## 2 Experimental

### (1) Materials

Tetraethyl orthosilicate (TEOS), Polyvinyl pyrrolidone (PVP), 4-vinylpyridine (4VP), Anhydrous ethanol, and ammonia are all of A.R. grade. Nano-TiO<sub>2</sub> is of Technical grade.

### (2) Experimental methods

The experiment was designed with a single factor control method. 1.5 g nano-TiO<sub>2</sub> powder was ultrasonically dispersed in 150 ml anhydrous ethanol for 30 min. A certain amount of PVP/4VP was added and ultrasonic dispersion was continued for 30 min. Then they were transferred to a three-necked flask and dispersed by ultrasound at 35 ° C. A certain amount of TEOS and 30 ml anhydrous ethanol mixture were dropped while a certain amount of ammonia was added in four batches within 3 h. Ultrasonic dispersion reaction was continued for 2 h. After the reaction, the samples were washed by centrifugation, dried and ground to obtain the nano-TiO<sub>2</sub>/SiO<sub>2</sub> composite particles.

## 3 Results and Discussion

### 3.1 SEM Analysis

The basic formulation is shown in Tables 1, 2 and 3. Hitachi SU-8010 Scanning Electron Microscope was used to analyze the prepared nano-TiO<sub>2</sub>/SiO<sub>2</sub> composite particles.

**Table 1.** Different PVP/4VP concentrations prepared nano-TiO<sub>2</sub>/SiO<sub>2</sub> composite particles

group No.	TiO <sub>2</sub> /g	PVP/g	4VP/ml	Ammonia/ml	TEOS/g	TEMP/°C
1	1.5	1	1	5	7.5	35
2	1.5	2	2	5	7.5	35
3	1.5	3	3	5	7.5	35
4	1.5	4	4	5	7.5	35

**Table 2.** Different titanium to silicon molar ratio prepared nano-TiO<sub>2</sub>/SiO<sub>2</sub> composite particles

group No.	Ti:Si	PVP/g	4VP/ml	Ammonia/ml	TEOS/g	TEMP/°C
5	2:1	1	1	5	7.5	35
6	1:1	2	2	5	7.5	35
7	1:2	3	3	5	7.5	35
8	1:3	4	4	5	7.5	35

**Table 3.** Different concentration of ammonia prepared nano-TiO<sub>2</sub>/SiO<sub>2</sub> composite particles

group No.	TiO <sub>2</sub> /g	PVP/g	4VP/ml	Ammonia/ml	TEOS/g	TEMP/°C
9	1.5	2	2	3	7.5	35
10	1.5	2	2	4	7.5	35
11	1.5	2	2	5	7.5	35
12	1.5	2	2	6	7.5	35

In group 1-4, with the increase of PVP/4VP concentration, the effect of the coating becomes better first and then becomes weaker, and group 2 has better effect. This is due to the fact that when the amount of PVP is 2 g, 4VP is 2 ml (the PVP/4VP concentration is 0.25%), PVP/4VP can guide the SiO<sub>2</sub> precursor and hydrolysis intermediates to the surface of nano-TiO<sub>2</sub> and coat the nano-TiO<sub>2</sub> well. When the amount of PVP/4VP exceeds 0.25%, the excess PVP is dispersed in the solution. In the process, TEOS is hydrolyzed and exists directly in the solution, and the nano-TiO<sub>2</sub> cannot be coated.

In group 5-8, with the decrease of the molar ratio of titanium to silicon, the effect of coating becomes better first and then becomes weaker, and group 7 has better effect. This is due to the fact that when the proportion of titanium to silicon is large, the amount of TEOS is small and the generated nano-SiO<sub>2</sub> cannot be completely coated on the surface of nano-TiO<sub>2</sub>. Nano-SiO<sub>2</sub> can form a relatively complete coating of nano-TiO<sub>2</sub> when the ratio of titanium to silicon is 1:2. But agglomeration is also more serious. When the proportion of titanium and silicon decrease, TEOS tends to nucleate and cannot be generated on the surface of nano-TiO<sub>2</sub> which makes it cannot produce a good coating effect on nano-TiO<sub>2</sub>.

In group 9-12, the reaction system was basically neutral and the hydrolysis of TEOS was extremely slow. When the amount of ammonia increased, the hydrolysis rate of TEOS increased and polycondensates formed gradually. These polycondensates, guided by PVP, were gradually reacted with hydroxyl groups on the surface of nano-TiO<sub>2</sub>. Polycondensates nucleated and grew around the surface of nano-TiO<sub>2</sub> particles, making SiO<sub>2</sub> generate on the surface of TiO<sub>2</sub>. When the amount of ammonia water exceeds 5 ml, TEOS hydrolyzes very quickly, and many active species of SiO<sub>2</sub> are produced in the system. These active species will grow up by itself, resulting in the phenomenon of homogeneous nucleation. This situation causes a large number of free SiO<sub>2</sub> particles in the system, so it cannot effectively coat TiO<sub>2</sub> [5].

According to the scanning electron microscope images of each group, the surface morphology and particle size of the nano-TiO<sub>2</sub>/SiO<sub>2</sub> composite particles prepared under different conditions are quite different. It shows that the coating has a good effect and the micro-nanostructures with a particle size of 200–300 nm. Among them, group 2 has the best effect (Fig. 1).

### 3.2 FT-IR Analysis

Figure 2 shows the FT-IR spectra of the nano-TiO<sub>2</sub> and the TiO<sub>2</sub>/SiO<sub>2</sub> composite particles of group 2.

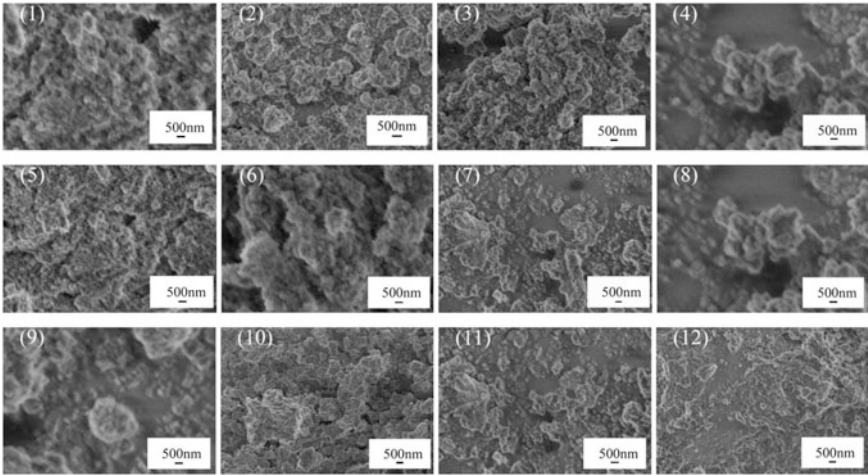


**Fig. 1.** Scanning electron micrographs of each group of nano-TiO<sub>2</sub>/SiO<sub>2</sub>

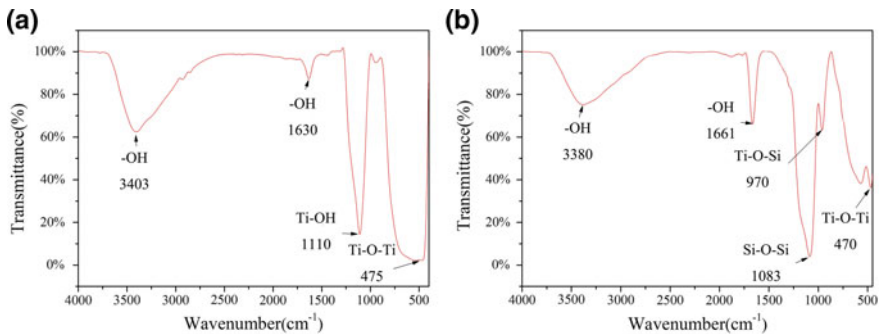


**Fig. 2.** FT-IR: a is TiO<sub>2</sub>, b is TiO<sub>2</sub>/SiO<sub>2</sub>

In Fig. 2a, the strong characteristic absorption peaks near 3403 and 1630 cm<sup>-1</sup> are the bending vibration peaks of -OH groups adsorbed on the surface of nano-TiO<sub>2</sub> particles. In Fig. 2b, the strong characteristic absorption peaks at 3380 and 1661 cm<sup>-1</sup> are the bending vibration peaks of -OH groups adsorbed on the surface of nano-TiO<sub>2</sub>/SiO<sub>2</sub> composite particles. In Fig. 2a, the vicinity of 1110 cm<sup>-1</sup> is Ti-OH bending vibration peak. In Fig. 2a, b, the characteristic absorption peak near 475 and 470 cm<sup>-1</sup> is the absorption peak of Ti-O-Ti bond. In Fig. 2b, there is a new peak of stretching vibration at 1083 cm<sup>-1</sup> with a strong absorption peak of Si-O-Si bond [6, 7]. And a new vibrational absorption peak of Ti-O-Si has appeared at 970 cm<sup>-1</sup>. And there are no absorption peaks in these two places in Fig. 2a. From this analysis, the nano-SiO<sub>2</sub> formed molecular bonding on the surface of nano-TiO<sub>2</sub>, resulting in the formation of Ti-O-Si bonds.



### 3.3 XRD Analysis

The prepared nano-TiO<sub>2</sub>/SiO<sub>2</sub> composite particles and pure TiO<sub>2</sub> samples were tested on an X-ray diffractometer. The test conditions were Cu/K ray at  $\lambda = 0.15406$  nm, scanning range was 20°–80°, step size was 0.02, tube voltage was 40 kV, and tube current was 200 mA. Figure 3 shows the X-ray diffraction pattern of nano-TiO<sub>2</sub> and nano-TiO<sub>2</sub>/SiO<sub>2</sub>.

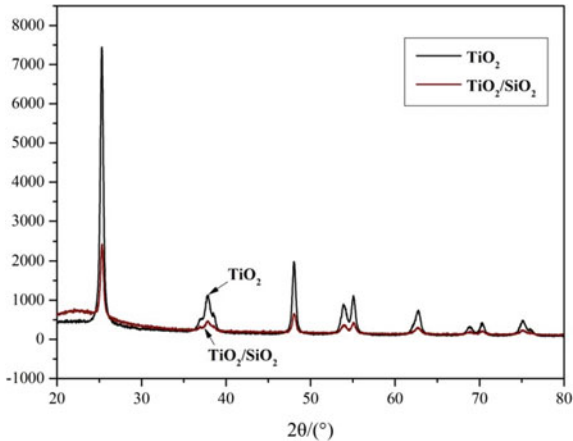


**Fig. 3.** X-ray diffraction pattern of nano-TiO<sub>2</sub> and TiO<sub>2</sub>/SiO<sub>2</sub>

It was found that the pure TiO<sub>2</sub> crystal is anatase by comparing the obtained diffraction spectra with the standard spectra. The XRD pattern of the TiO<sub>2</sub>/SiO<sub>2</sub> composite particles shows that the diffraction peaks of the coated TiO<sub>2</sub>/SiO<sub>2</sub> composite particles are reduced. However, there are still significant diffraction peaks at  $2\theta$  of 25.3°, 37.9°, and 48°, indicating that it also belongs to anatase nano-TiO<sub>2</sub>. These results show that the crystal structure and performance of the nano-TiO<sub>2</sub> are not affected by the nano-SiO<sub>2</sub> coating. At the same time, it shows that the coating of nano-SiO<sub>2</sub> on the surface of nano-TiO<sub>2</sub> is not completely dense, which is also beneficial to the absorption of ultraviolet light by nanocomposite particles.

## 4 Conclusions

In this paper, PVP and 4VP were used as dispersants for nano-TiO<sub>2</sub> and structure-guided agents for nanocomposites. TEOS was used as a precursor for nano-SiO<sub>2</sub>. A number of nano-TiO<sub>2</sub>/SiO<sub>2</sub> composite particles were prepared by coating nano-SiO<sub>2</sub> on the surface of nano-TiO<sub>2</sub> particles. The effect of different mixing conditions on the preparation of nano-TiO<sub>2</sub>/SiO<sub>2</sub> composite particles was analyzed through SEM. The FT-IR analysis showed that the composite particles exhibited unique Ti–O–Si vibration absorption peaks. The XRD analysis showed no change in the crystal structure of TiO<sub>2</sub>

after coating. The results show that when the PVP amount was 2 g, 4VP amount was 2 ml, the titanium and silicon ratio was 1:2, and the ammonia amount was 5 ml, nano-SiO<sub>2</sub> can encapsulate nano-TiO<sub>2</sub> better. This study provides new ideas for improving the UV resistance of inks.

**Acknowledgements.** This work was supported in part by NSF of the Science and Technology Department of Shaanxi Province under Grant Nos. 2016JM5068, NSF of the Science and Technology Department of Shaanxi Province under Grant Nos. 2018JQ5100, NSF of the Key Laboratory of Shaanxi Provincial Department of Education under Grant Nos. 15JS075 and Shaanxi Collaborative Innovation Center of Green Intelligent Printing and Packaging.

## References

1. Zhao, W., & Zhang, Q. (2007). XPS study on the surface of Fe/SiO<sub>2</sub> core shell composite particles. *Bulletin of the Chinese Ceramic Society*, 26(1), 38–42.
2. Abidi, N., & Cabrales, L. (2009). Functionalization of a cotton fabric surface with titania nanosols: Applications for self-cleaning and UV-protection properties. *ACS Applied Materials & Interfaces*, 1(10), 2141–2143.
3. Bai, C. (2014). *Fabrication of raspberry-like particles toward superhydrophobic surface* (pp. 35–46). Qilu University of Technology.
4. Zou, H., & Wu, S. (2008). Polymer/silica nanocomposites: Preparation, characterization, properties, and applications. *Cheminform*, 39(52), 3893–3957.
5. Qian, L. (2016). *Preparation of TiO<sub>2</sub>/SiO<sub>2</sub> composite nanoparticles and the application on anti-ultraviolet and superhydrophobic multifunctional cotton fabrics* (pp. 14–30). Shanghai University of Engineering Science.
6. Feng, C. (2005). *Study on assembly of functionalized nano-silica sol with polymers* (pp. 77–79). Nanjing University of Technology.
7. Shashikala, S., Jurgen, W., & Klaus, A. (2002). Variable temperature FT-IR studies of n-alkyl modified silica gels. *Journal of Physical Chemistry B*, 106(4), 878–888.



# Study on Storage Stability of Waterborne Gravure Ink and Adhesion on PET/BOPP Film Surface

Wei Sun, Ying Du, Xiaoyu Li, and Haiqiao Wang<sup>(✉)</sup>

Key Laboratory of Carbon Fiber and Functional Polymers, Ministry of Education, Beijing University of Chemical Technology, Beijing, China  
wanghaiqiao@mail.buct.edu.cn

**Abstract.** Water-based gravure printing ink is a very promising environmental-friendly ink for the application in the plastic substrates. This contribution aims to improve the storage stability, adhesion on non-polar plastic substrates, such as BOPP etc., of the water-based gravure printing ink. A core-shell polyacrylate resin emulsion was synthesized, and used as a binder to prepare water-based plastic gravure ink. The effects of location of the crosslinking groups on the storage stability and adhesion of the ink were studied, and the formulation of the ink was optimized. It was found that, when the cross-linking groups were located on the inner layer of the latex particles, the storage stability of the relative ink, especially of the yellow ink, was improved greatly whereas the adhesion and other properties of the ink were not changed significantly. The adhesion of ink on PET film, especially on the surface of BOPP film, can be increased effectively with addition of adhesion accelerator. With the reduction of emulsion T<sub>g</sub>, VOC content of ink is decreased, and film-forming rate and film-forming quality are improved, which improves adhesion of the ink. However, the adhesion of ink is decreased with the increase of wet film thickness.

**Keywords:** Waterborne gravure ink · Plastic film · Storage stability · Adhesion

## 1 Introduction

With the development of people's living standard and enhancement of the healthy consciousness, requirements for waterborne, non-toxic, green and healthy products are constantly increasing. Water-based ink attracts increasing attention due to its environmentally friendly nature, and has gradually become an essential aspect and inexorable trend in ink industry [1].

Water-based ink has already been adopted as plastic film printing ink by more and more western developed countries. About 35% of domestic flexible packaging printing also adopts water-based ink, which is mostly used gravure printing [2]. Therefore, the plastic gravure water-based ink would have wide application prospect.

During the storage of the water-based ink, some phenomena may be observed, such as decrease of flowability, pig skin, precipitation and losing efficacy, etc., due to the poor storage stability, which results the degradation of ink quality. Thus, the water-based ink should have good storage stability to ensure the effectiveness during the

period of use. The adhesion force of water-based ink is the ability that bond and attract each other through physical and chemical interactions between water-based ink and the surface of substrate [3], which is one of the important performance indices to evaluate water-based gravure ink [4]. Therefore, study on the effects on the storage stability and adhesion force of the water-based gravure printing ink is highly necessary.

In this contribution, a core-shell polyacrylate resin latex was synthesized and used as binder to prepare water-based plastic gravure ink. The effects of location of the crosslinking groups in the latex particles on the storage stability, and the effects of the adhesion force promoter,  $T_g$  of the latex and the wet film thickness on the adhesion of the ink on the PET and BOPP films were studied, which provides a certain reference value for the further promotion and application of plastic water-based gravure ink.

## 2 Experimental

### 2.1 Materials

The core-shell polyacrylate resin latex used in this experiment was made by the laboratory. The blue and yellow pastes were supplied by Beijing Xin Nuoan Powder Polymer Co., Ltd. Sp360 was purchased from Tianjin Safi Chemical Technology Development Co., Ltd. and used as a wetting agent. BYK333 is purchased from BYK Chemical as a leveling agent. Adhesion promoter FZ3667-C was provided by Beijing Hanyuan Chemical; Wax26 was supplied as a wax emulsion from the Shengli plastic material factory. De-ionized water was used throughout the work.

### 2.2 Methods

1. Latex preparation: Four kinds of core-shell polyacrylate latexes were synthesized by pre-emulsification method [5]. The latexes of the cross-linking group in the shell or core layer of the latex particles are named as  $M_1$  or  $M_2$ , respectively. The  $T_g$  of the shell or core layer of the  $M_2$  was designed to reduce by 5 °C to obtain the  $M_3$  or  $M_4$  latex, respectively.
2. Ink preparation: 1%BYK333, 1%Sp360, 1%Wax26 and 2% water were added to each group of ink formulations, the other components were shown in Table 1. Various additives were sequentially added to the latex under stirring, and continued to stir about 10 min after each addition. Then the color paste was slowly added to the above system and continued to stir for about 30 min with a proper increase in stirring speed. Water based ink is obtained after filtering 200 mesh filter cloth.

### 2.3 Characteristic

1. Storage stability: The viscosity of the ink after baked 0 h/6 h/12 h/18 h/24 h in the oven at 50 °C is measured using a rotational viscometer. The ink fineness when baking 0 h/48 h at 50 °C was tested using QXD-50 scraper fineness meter. The test was averaged 3 times.

**Table 1.** Ink formulations

	Emulsion/%				Paste/%			FZ3667-C/%
	M <sub>1</sub>	M <sub>2</sub>	M <sub>3</sub>	M <sub>4</sub>	Blue1#	Blue2#	Yellow	
I	65	–	–	–	–	–	25	1
II	–	65	–	–	–	–	25	1
III	65	–	–	–	25	–	–	1
IV	–	65	–	–	25	–	–	1
A	–	65	–	–	–	25	–	–
B	–	65	–	–	–	25	–	1
C	–	–	65	–	–	25	–	–
D	–	–	–	65	–	25	–	–

2. Adhesion: 3M tape was used to cover the ink spline, and a 10 mm × 10 mm square paper was placed under the spline. After the adhesive was adhered, the tape was quickly peeled off from the plastic surface at 90° to calculate the remaining ink. The number of grids occupied by the film was used as an evaluation criterion for adhesion. The adhesion of the film was tested in an oven at 50 °C for 10 min and at room temperature for 48 h.

### 3 Results and Discussion

#### 3.1 Effect of Cross-Linking Groups Position in Latex on Storage Stability of Ink

Figures 1 and 2 depicted the curves of ink viscosity and fineness change with baking (50 °C) time.

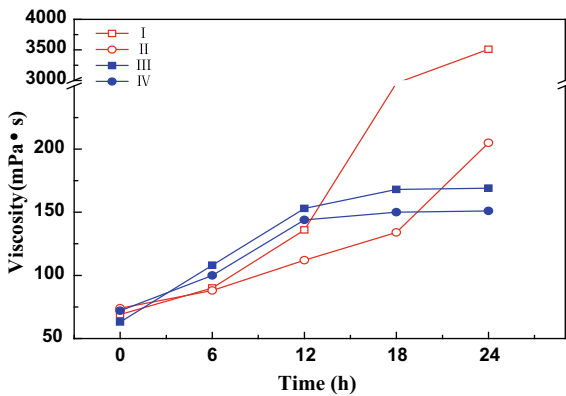


**Fig. 1.** The viscosity changes of I, II, III and IV samples

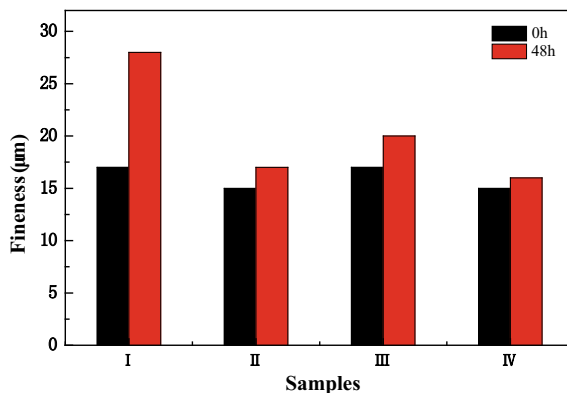


Fig. 2. The fineness changes of I, II, III and IV samples

From Fig. 1, it is found that, with the extension of baking time, the viscosity of the four inks all increased. Among them, the added value in the viscosity of ink I is the largest, reached 3510 m Pa s after 24 h, indicating that the yellow ink has the worst long-term storage stability. Compared III and IV, it is found that the viscosity change of ink IV is smaller, indicating that the long-term storage stability of ink IV is better than that of ink III.

Figure 2 shows that the fineness of Ink I increased significantly from 17 to 28  $\mu\text{m}$  after baking at 50  $^{\circ}\text{C}$  for 48 h, which indicates that a severe flocculation occurred in the ink I; while the fineness of ink II, III and IV increased by 2, 3 and 1  $\mu\text{m}$  respectively, suggesting that these inks are more stable.

In a word, the long-term storage stability of the ink  $M_2$  is better than that of the ink  $M_1$ , that is, when the crosslinking group is in the core layer of the latex particles, the storage stability of the ink can be significantly increased. This is due to the fact that when the cross-linking groups are located on the inner layers of the latex particles, crosslinkable groups are separated by the shell layer and cannot take place crosslinking reactions during the storage process, therefore relative ink demonstrates a better long-term storage stability.

### 3.2 Effect of Adhesion Promoter and Emulsion Tg on Adhesion

Table 2 describes the adhesion test results of ink A, B, C and D. Compared A with B, one can observe that the addition of FZ3667-C significantly improves the adhesion of the ink on the surface of BOPP film, increasing by 65% after 24 h. This is because the adhesion promoter migrates to the interface between the substrate and the ink after coating, forming a strong adhesive force, thereby improving the adhesion of the ink system. In addition, it can significantly reduce the surface tension and improve the wettability of the ink system, making ink better spread on the surface of plastic film, which further improves the adhesion of the ink.

Comparing A, C and D, it can be seen that lowering the Tg of the shell or the core layer of the latexes can increase adhesion of the ink and shorten the time for the ink

**Table 2.** Ink adhesion test results

	Adhesion/% (PET)			Adhesion/% (BOPP)		
	0 h	24 h	48 h	0 h	24 h	48 h
A	97	97	98	1	20	40
B	98	99	99	20	85	90
C	99	100	100	20	80	90
D	100	100	100	20	80	90

film acquiring maximum adhesion. Since the lowest film-forming temperature of the ink reduces with the decrease in the Tg of the latex. Under certain conditions, the ink made from the latex with low Tg is easier to form film, which not only accelerates the film-forming speed but also improves the performance of the relative film, thus the adhesion of the ink is improved accordingly.

**3.3 Effect of Thickness of Wet Film on Adhesion of Ink**

The films with wet film thickness of 4, 6.9, 20 and 25 μm, respectively, on PET and BOPP substrates were prepared using Ink IV by linear applicator, and the adhesion of the ink was measured after the films were baked at 50 °C for 5 min. The results are shown in Fig. 3. It can be seen that the adhesion of the ink on PET films is 99, 97, 60 and 40% while on BOPP films is 92, 85, 40 and 20%, respectively. The adhesion force of ink decreases with the increase of thickness of wet film, which can be explained by the cohesive force existed in intermolecular of the ink. The molecular number in the ink increases with the increase of thickness of wet film, which improves the cohesive force of the printing layer. The greater the cohesive force of the printing layer, the smaller the adhesion force [6]. Therefore, the thicker film is easier to be stripped from the film surface when it is subjected to external force.

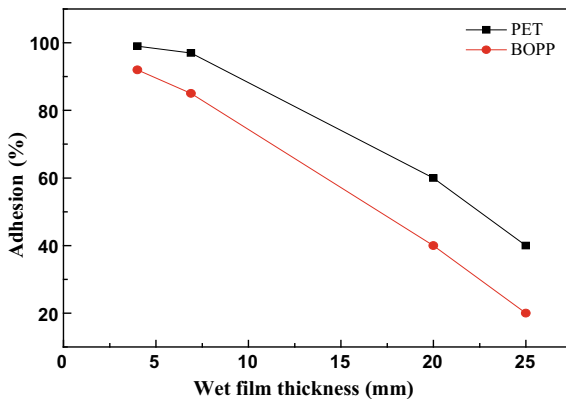


**Fig. 3.** Effect of wet film thickness on ink adhesion

## 4 Conclusions

The position of the cross-linking groups in the core-shell type of latexes has a great influence on the storage stability of the ink: when the cross-linking groups were located on the inner layer of the latex particles, the viscosity and fineness of the ink increase slowly with baking time, and no obvious thickening and pig skin. The storage stability of the ink, especially of the yellow ink, was improved greatly.

Adhesion promoter FZ3667-C can effectively improve the adhesion of ink on BOPP film surface, increased by 65% at 24 h. When  $T_g$  of the core or shell layer were decreased by 5 °C, the film formation rate of the ink was accelerated, the adhesion on the PET reached 100% and on the BOPP increased by 60% after 24 h. In addition, the adhesion of ink decreases with the increase of wet film thickness. The adhesion, when the thickness of the wet film increases from 4 to 25  $\mu\text{m}$ , decreases from 99 to 40% on the PET film, and is clearly reduced from 92 to 20% on the BOPP film.

## References

1. Xin, X. L., & Wei, Y. N. (2011). Research progress of waterborne ink. *Research on Printing and Packaging in China*, 03(3), 1–8.
2. He, L. (2017). Analysis of current situation and development of waterborne ink. *Paper and Papermaking*, 36(5), 47–49.
3. Hong, X. L., & Feng, H. B. (2005). *Coating chemistry*, 2nd ed. (pp. 88–90). Science Press.
4. Hong, L. L. (2007). Analyze of property and application of water-based ink. *Screen Printing Industry*, 3, 24–27.
5. Yin, C., Li, X., & Wang, H. (2016). Study of factors on ethanol resistance stability of water-based acrylic resin emulsion. In *China Academic Conference on Printing & Packaging and Media Technology*. [https://doi.org/10.1007/978-981-10-3530-2\\_106](https://doi.org/10.1007/978-981-10-3530-2_106).
6. Wang, N. Y. (2005). Test of ink adhesion. *Screen printing*, 1, 22–23.





# Preparation and Application in Ink of Aromatic Microspheres

Shouzheng Jiao, Zhicheng Sun<sup>(✉)</sup>, Dongsheng Li, Furong Li,  
Qian Li, Nan Yang, Xiaoliang Zhang, and Luhai Li

School of Printing and Packaging Engineering, Beijing Engineering Research  
Center of Printed Electronics, Beijing Institute of Graphic Communication,  
Beijing 102600, China  
sunzhicheng@bigc.edu.cn

**Abstract.** Aromatic microspheres have a wide range of applications due to their superior stability and slow release period. Specially, aromatic microspheres are of regular spherical structures with a uniform particle size distribution, most of which is between 40 and 100  $\mu\text{m}$ . After the aromatic microspheres were inked, the screen printing technology was used to transfer ink to the substrates, such as coated paper, cardboard, non-woven fabrics and cotton cloth. In this study, aromatic microspheres were prepared by in situ polymerization with citral as core materials and melamine-formaldehyde resin (MF) as shell material. Meanwhile, the surface morphology, particle size and heat resistance of aromatic microspheres were investigated in detail. The morphology and adhesive property of aromatic ink were tested and more types of substrates can be used after the ink is formed. The finally obtained aromatic microspheres have a compact surface and a uniform particle size distribution and can maintain a complete structure at a temperature of 317 °C or lower.

**Keywords:** In situ polymerization · Aromatic microspheres · Ink · Screen printing

## 1 Introduction

The health care effects of aromatic essential oils have received more and more attention with the development of the time. However, aromatic oils are composed of volatile compounds such as ester, ketone and aldehyde, which are easily lost during the processing and storage [1]. But happily, the appearance of microcapsule technology has greatly reduced unnecessary losses. It is a technology that requires a material with a specific function as a core material and can be coated with a film-forming material [2], so as to achieve the purpose of protecting the core material and changing the releasing speed of the core material. At the same time, the encapsulation can protect the essence or perfume, so that it can be degenerated without affecting the environment and its stability can be enhanced [3, 4].

Aromatic microspheres are under a wide range of applications in human life because of their longevity, good stability and many other advantages [5]. Aromatic microspheres are often applied to socks, insoles, sheets, and other textiles, releasing

fragrances through friction and other actions to deodorize, sterilize, and soothe the nerves [6, 7]. The dip-molding method is usually used to combine the aromatic microspheres and textiles [8]. However, the dip-molding process is more complex and the microspheres are easy to fall off. In the 1980s, the United States began to study the inking of aromatic microcapsules [9], but the adaptation of aromatic inks has not been reported, and the research of aromatic inks in China is still in its infancy. Moreover, the substrate is only suitable for a single and simple application, which is not sufficient for the large-scale production. Therefore, the preparation and ink application of aromatic microspheres were investigated in this paper. Specially, the screen printing technology was used to realize the transfer of aromatic microsphere inks with different substrate surfaces, which not only solved the disadvantages of the dip-molding method, but also widened the application of the aromatic microsphere inks.

## 2 Experiments

### 2.1 Experimental Materials

Unless otherwise noted, the reagents were obtained from commercial suppliers and were used without further purification. Poly(styrene-co-maleic anhydride) (>99%), Maclean Biotechnology Co., Ltd.; Formaldehyde (37% solution in H<sub>2</sub>O), Innochem Technology Co., Ltd.; Citral (cis + trans) (>95%), Sigma Chemical Reagent Co., Ltd.; Melamine (AR), Triethanolamine (AR), Sinopharm Chemical Reagent Co., Ltd.; Citric acid anhydrous(AR), Sodium hydroxide (AR), Aladdin Biotechnology Co., Ltd.

### 2.2 Instruments and Equipments

Scanning electron microscope (SEM), SU8020, Japan; Laser particle size analyzer, S3500, United States; Laser confocal microscope, VHX-5000, Japan; Thermal expansion instrument, DIL 402 PC, German; Principle of DSC, DSC214, German; Silk screen version and 100 mesh; Screen printing machines, OS-500FB.

### 2.3 Preparation of Aromatic Microspheres

Preparation of emulsifier: poly(styrene-co-maleic anhydride) (15 g), sodium hydroxide (4.5 g) and distilled water (130 mL) were added into the flask and mixed with magnetic stirring at 50 °C.

Preparation of essence lotion: citral (10.44 g) and emulsifier (10 g) were added into 50 mL of distilled water at 70 °C of water bath. After that, it was emulsified with an electric stirrer at an emulsifying speed of 500 rpm for 30 min fully for use.

Preparation of MF prepolymer: formaldehyde solution (12 mL), melamine (6 g) and distilled water (25 mL) were added into the flask and mixed. After that, the pH was adjusted to 8–9 with 10 wt% triethanolamine solutions. Finally, the reaction was stirred at 300 rpm for 30 min at 70 °C of water bath to obtain a transparent prepolymer solution.

Preparation of aromatic microspheres: the pH of essence lotion was adjusted to 8–9 with 10 wt% of citric acid solution. Next, the prepolymer solution was slowly added into the essential lotion and reacted at 70 °C for 2 h. After the reaction, the materials were washed, filtered and dried in vacuum. Accordingly, the final aromatic microcapsules were obtained.

## 2.4 Preparation of Aromatic Microspheres Ink and Printing Applications

The preparation of aromatic microspheres and ink process were showed in Fig. 1. The aromatic inks were prepared in a certain proportion of the printed protoplasmic (50%), water-based acrylic resin (25%), water (5%), paste (9%), aromatic microcapsules (10%), defoaming agents (0.2%) and flattening agents (0.8%). After that, the different coated papers such as aluminum foil paper, non-woven fabric and kraft paper were used as the substrates to transfer the ink.

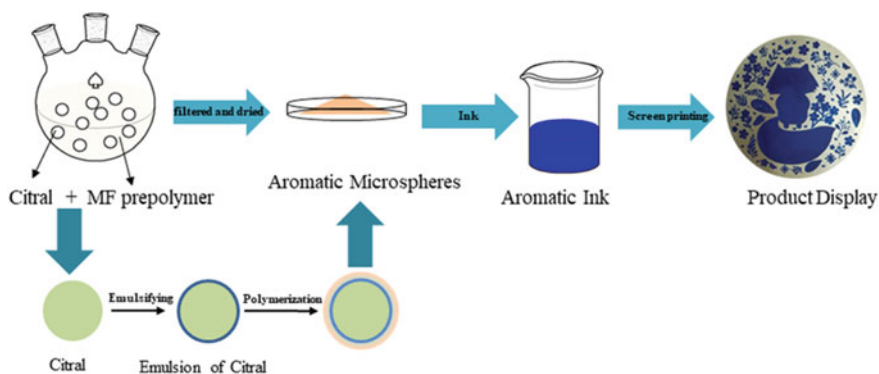


Fig. 1. Synthesis and ink process of aromatic microspheres

## 2.5 Characterization

Aromatic microspheres were added into the distilled water and dispersed by ultrasonic for 5 min. The distribution of particle size was obtained by laser particle size analyzer and the degree of dispersion was calculated. The surface morphology of the aromatic microspheres was observed through SEM.

DSC was utilized to characterize the glass transition temperature ( $T_g$ ) of aromatic microspheres. The degree of deformation of the heated shell material was analyzed by DIL to determine the temperature range in which the microspheres can maintain a definite morphology.

### 3 Results and Discussion

#### 3.1 Analysis of Surface Morphology and Particle Size Distribution of Microspheres

As shown in Fig. 2, the microspheres have a regular spherical shape, and the melamine resin shell densely covers the core material citral to provide a good sustained release effect. The obtained aromatic microspheres were tested for particle size distribution and the results are presented in Fig. 3 and Table 1. The average particle diameter (also called the median particle size) of the microspheres was 52.09  $\mu\text{m}$ , and the volume average particle size (MV) was 64.10  $\mu\text{m}$ . The particle size dispersion  $\text{PDI} = (\text{D90} - \text{D10})/\text{D50} = 1.36$  was calculated. It is shown that the particle size distribution of microspheres is narrower.

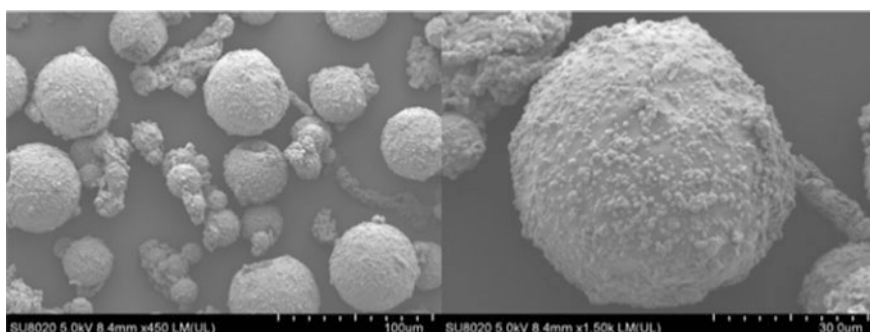


Fig. 2. SEM pictures of aromatic microspheres

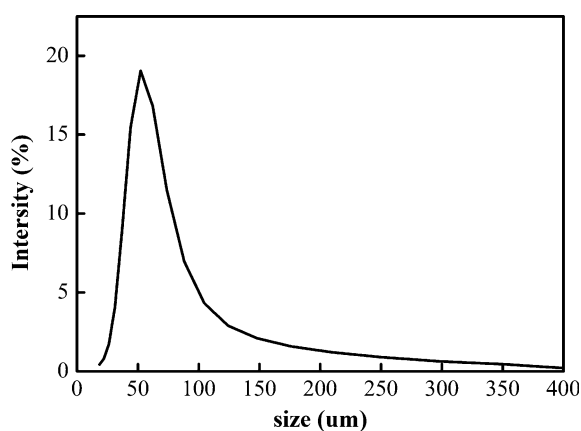


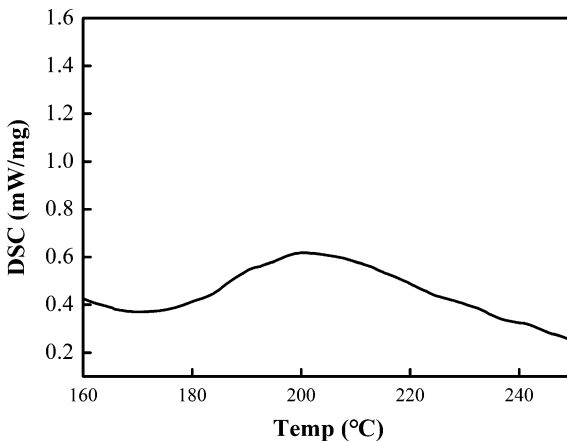
Fig. 3. Particle diameter distribution of aromatic microspheres

**Table 1.** Particle size characteristics parameters of microspheres

Particle diameter	D10	D20	D30	D40	D50	D60	D70	D80	D90	D95
Size $\mu\text{m}$	33.39	38.96	43.38	47.60	52.09	57.39	64.42	75.92	104.3	147.1

### 3.2 Thermal Analysis of Microcapsules

The DSC thermograms of microcapsules were displayed in Fig. 4. As shown in Fig. 4, the aromatic microsphere-coated citral vaporized from the melamine resin shell to the outside at 182 °C and the enthalpy change was 14.18 J/g. In addition, the heat resistance of the aromatic microspheres was tested by the DIL and Fig. 5 showed the changes of aromas at different temperatures. Before 317 °C, the structural morphology can be maintained at a relatively high temperature due to the excellent heat resistance of the melamine resin. However, when the temperature was higher than 317 °C, i.e. the melting point of melamine resin, the microspheres began to get damaged due to deform and collapse rapidly.

**Fig. 4.** DSC curve of aromatic microspheres

### 3.3 Aromatic Microsphere Ink Adhesion Test

As shown in Table 2, the cross-cut method with a spacing of 2 mm was used to test the adhesion and was graded according to the ISO 12944 international standard. Figure 6 showed that the texture surfaces of the cardboard, non-woven fabric and cotton cloth were relatively rough relative to the aluminum foil paper and coated paper substrate. The above phenomena resulted in a certain influences on the uniformity and planarity of the ink after heating. But then, more voids improved the contacting area between the ink and the substrates and were more favorable for the adhesion of aromatic inks.

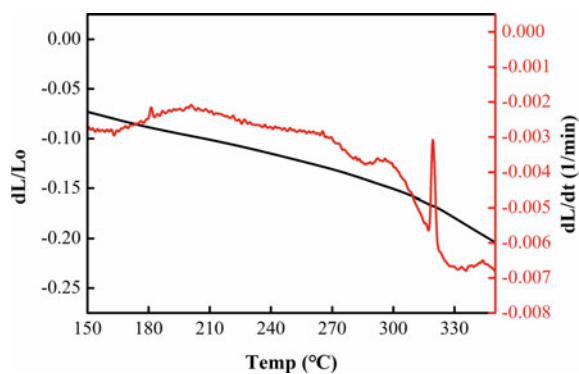


**Fig. 5.** DIL and First-order differential curve of aromatic microspheres

**Table 2.** Adhesion grade of aromatic microsphere inks on different substrates

Base material	Card paper	Coated paper	Copper foil	Aluminum foil	Non-woven	Cotton cloth
Adhesion level	0	2	3	3	0	0

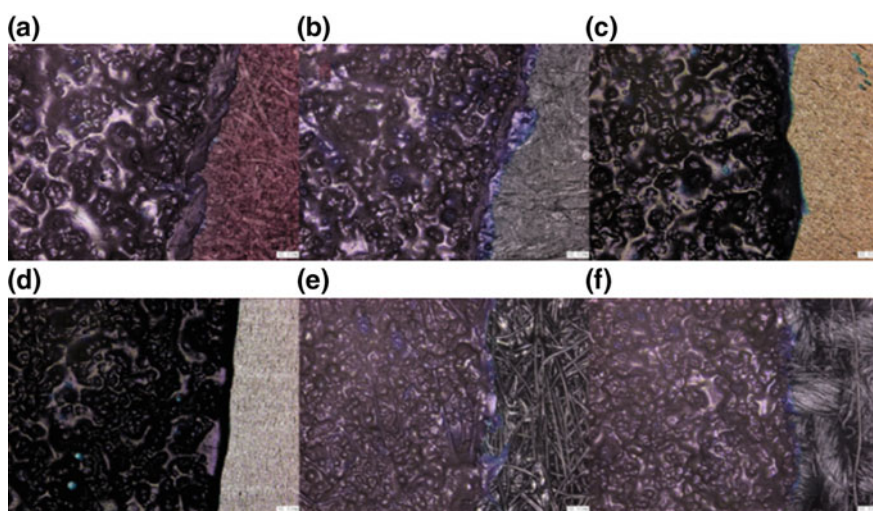


**Fig. 6.** Aromatic microspheres ink on different base material through screen printing. **a** card paper; **b** coated paper; **c** copper foil paper; **d** aluminum foil paper; **e** non-woven; **f** cotton cloth

## 4 Conclusions

In this study, the microspheres with melamine-formaldehyde resin embedding citral were prepared by in situ polymerization. The aromatic microspheres have a complete spherical structure with uniform surface and narrow particle size distribution, most of which are between 40 and 100  $\mu\text{m}$ . The microspheres at the temperature of below 317  $^{\circ}\text{C}$  can still maintain a certain structural shape, but the ink prepared from the perfume microspheres can be deformed at a relatively high temperature. The aromatic microspheres after drying still have the fragrance of the core material after a long time storage. In the future research work, the aromatic microspheres can be quantitatively tested by GC-MS. After the aromatic microspheres are inked, they can be moved to different substrates and have a good adhesion. By studying the inking of aromatic microspheres, it is possible to print large-area fragrance inks with specific functions on flexible and rigid substrates. Finally, the fragrance oil would be released by destroying the shell-core structure of the aromatic microspheres to apply to the medical adjuvant therapy.

**Acknowledgements.** This work was supported by the National Natural Science Foundation of China (21776021, 21646013), BIGC Key Project (Ea 201701, Ec201801), 2011 collaborative Innovation Center of Green Printing & Publishing Technology (No. 04190118003/002) and the Cross training Plan for High Level Talents in Beijing.

## References

1. Xiao, Z., Liu, W., Zhu, G., Zhou, R., & Niu, Y. (2014). A review of the preparation and application of flavour and essential oils microcapsules based on complex coacervation technology. *Journal of the Science of Food and Agriculture*, *94*(8), 1482–1494.
2. Tai, I. T., & Sun, A. M. (1993). Microencapsulation of recombinant cells: A new delivery system for genetherapy. *FASEB*, *54*(7), 1061–1063.
3. Wong, M. S., Cha, J. N., Choi, K. S., Deming, T. J., & Stucky, G. D. (2002). Assembly of nanoparticles into hollow spheres using block copolypeptides. *NanoLetter*, *2*(6), 583–588.
4. Shchukin, D. G., Ustinovich, E. A., Sukhorukov, G. B., Möhwald, H., & Sviridov, D. V. (2005). Metallized polyelectrolyte microcapsules. *Advanced Materials*, *17*(4), 468–472.
5. Chung, H., & Cho, G. (2003). Thermal properties and physiological responses of vapor-permeable water-repellent fabrics treated with microcapsule-containing PCMs. *Textile Research Journal*, *74*(7), 571–575.
6. Sukhorukov, G., Fery, A., & Möhwald, H. (2005). Intelligent micro- and nanocapsules. *Progress in Polymer Science*, *41*(30), 885–897.
7. Baranauskienė, R., Venskutonis, P. R., Galdikas, A., Senulienė, D., & Šetkus, A. (2005). Testing of microencapsulated flavours by electronic nose and SPM E-GC. *Food Chemistry*, *76*(92), 45–54.
8. Hong, K., & Park, S. (2000). Preparation of poly(L-lactide) microcapsules for fragrant fiber and their characteristics. *Polymer*, *32*(41), 4567–4572.
9. Maekawa, Y., Miyano, S., Yazawa, K., & Kondo, A. (1975). Aqueous printing ink containing perfume-containing microcapsules. US, US 3888689 A.



# Effect of 2,2-Bis(Hydroxymethyl) Propionic Acid Content on the Properties of Aqueous Polyurethane

Nan Song, Xiulan Xin<sup>(✉)</sup>, and Bin Li

Beijing Technology and Business University, Beijing, China  
xinxl2007@126.com

**Abstract.** As a multi-functional environmental protection material, waterborne polyurethanes (WPU) has received increasing attention due to their excellent elasticity, such as wear resistance, flexibility and wide range of substrate suitability. In the field of ink printing, waterborne polyurethane materials have become an effective alternative to solvent-based polyurethane adhesives. However, the performance of WPU still needs to be improved. In this paper, acetone-dilution method was used to synthesize the required waterborne polyurethane with different amount of DMPA. The particle size of the synthetic polyurethane emulsion is determined by the particle size distribution (PSD). Transmission electron microscopy (TEM) was used to confirm that the synthesized emulsion had a spherical structure. By comparing the solids content, the water absorption test and the adhesion test, it was confirmed that the content of DMPA has a great influence on the polyurethane system. As the DMPA content increases, the average particle size of the polyurethane can be reduced, and the adhesion of the emulsion to the substrate can be improved, but the water resistance decreases due to the increase of the hydrophilicity. Therefore, the comprehensive effect is best when the added amount of DMPA is 5%.

**Keywords:** Waterborne polyurethane · Macrodiol · DMPA · Water absorption

## 1 Introduction

Traditional polyurethane contains a lot of organic solvents and some harmful substances. Environmental concerns have forced the polyurethane industry to shift to water systems. Waterborne polyurethane has attracted wide attention due to its low solvent content [1–3]. Saalah S, Abdullah L C, Min M A, etc. The effects of different OH values on the properties of polyurethane [4] are discussed. In addition, the type and dosage of emulsifiers also have a great impact on the properties of polyurethane. The performance of waterborne polyurethane is improved by the combination of ionic emulsifier and non-ionic emulsifier. Polyurethane dispersions can be formed in water without additional emulsifiers by the introduction of hydrophilic components (mainly –COOH) by using raw materials containing specific groups or by adding extenders containing characteristic groups. Dispersion synthesis method has been widely used in industrial production, and it is also the main research method of waterborne



polyurethane, among which DMPA is the most used [5]. This paper discusses the effect of DMPA content differences on the properties of polyurethane to determine the formulation more suitable for use in future studies.

## 2 Experimental Section

### 2.1 Materials

Isophorone diisocyanate (IPDI, 99%) and N-methyl-2-pyrrolidone (NMP) were supplied by Shangdong Xiya Chemical Industry Co. Ltd. Poly-1, 4-butylene adipate glycol (PBA,  $M_n = 2000$ ; PEG,  $M_n = 400$ ), supplied by Chengdu Huaxia reagent Corporation. Dimethylol propionic acid (DMPA, 99%) was purchased from USA New Jersey. Dibutyltin didodecylate (DBTDL) was supplied by Sinopharm Chemical Regent Co. Ltd. Acetone (99.5%), 1, 4-butanediol (BDO, 99%) and triethyl amine (TEA, 99%) were received from Tianjin Guangfu Fine Chemical Research Institute.

### 2.2 Synthesis of Waterborne Polyurethanes with Different Macrodiols as Soft Segments

The reaction was carried out in a 250 mL four neck jacketed reactor with a thermometer. The reactor was equipped with a mechanical stirrer. The synthesis was performed under nitrogen atmosphere. Macrodiols, IPDI, and DBTDL were added to the reactor under the condition of 80 °C. After that, acetone was added for decreasing the viscosity of PUs prepolymer, and then DPMA was added to the container to react for three hours. Next BDO was added into the system for 1 h. When the reaction mixture was cooled down to 40 °C, TEA (It was added in 95% DMPA molar amount) was added into the reactor for 0.5 h. Then deionized water was added into the flask under the mechanical stirring with the stirring rate of 550 rpm for 1 h to obtain polyurethane dispersion (PUD). The whole recipe of WPU is listed in Table 1.

**Table 1.** The formula of WPU

Designation	Molar composition (mmol)				
	PBA	IPDI	PEG	DMPA	BDO
PUa	11.7	40.49	1	7.83	12.78
PUb	11.58	40.49	1	13.05	7.78
PUc	11.47	40.49	1	18.27	2.44

## 3 Testing and Characterization

Characterize of the particle size and the particle distribution of emulsion with Malvern Zetasizer Nano-ZS instrument.

The solid content of the WPU dispersions were detected by drying some emulsion (about 2.50 g) at 55 °C for more than 24 h and calculating the weight ratio of residue to the whole mass.

Transmission electron microscopy (TEM) images of the WPU dispersions were obtained from a JEM-2100 Microscope.

Water absorption of the cast films was assessed according to the standard method. Dry films cast from emulsion (original weight designated as  $w_1$ ) were immersed in water for 24 h at 25 °C. After the residual water was wiped from the films using filter paper, the weight ( $w_2$ ) was measured. Water absorption was calculated by the equation:

$$W(\%) = (W_2 - W_1)/W_1 \times 100\% \quad (1)$$

The adhesion tests on packaging films (PVC, OPP, PA, PE, PET) were tested according to ASTM standards D 3359-09. A lattice pattern with eleven cuts in each direction was made in the emulsion film to the substrate, pressure-sensitive tape was applied over the lattice and then removed, and adhesion was evaluated by comparison with descriptions and illustrations.

## 4 Results and Discussion

### 4.1 Particle Size and TEM of WPUs

The polyurethane dispersion with DMPA addition amount was designed and prepared to investigate the effect of DMPA addition on the average particle size of PU dispersion. The experimental results are shown in Fig. 1.

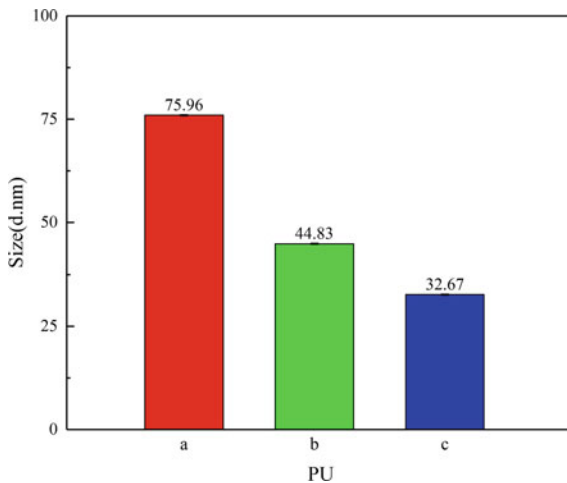


**Fig. 1.** Effect of DMPA amount on PU average particle size

According to the data in Fig. 1, the average particle size of the polyurethane dispersion decreases with the increase in the amount of DMPA, and the introduction of the hydrophilic group chain extender DMPA increases the content of ions in the polyurethane chain, making it more hydrophilic. The ability of the polyurethane

molecules to disperse in water is enhanced, which is advantageous for the formation of micelle particles. Adding more DMPA will increase the number of latex particles in the system, and the corresponding particle size will decrease. Conversely, the number of latex particles in the system will decrease and the particle size will increase accordingly.

As shown in Fig. 2 through the TEM results, it was found that the polyurethane was dispersed as uniform spherical particles in water. The measured particle size range is consistent with the results in Fig. 1.

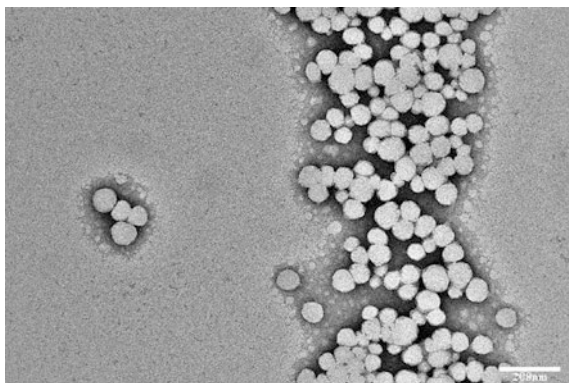


**Fig. 2.** TEM of PU1000re

#### 4.2 Solid Content and Potential of Polyurethane Dispersion

When the content of DMPA was high, the particle beam on the surface of the polyurethane micelle increases due to the increase in the amount of DMPA, and the electrostatic repulsion between the particles was large, so that the particles were not easily coalesced together and the stability of the polyurethane dispersion can be improved.

Table 2 shows the actual solid content, water absorption and potential of the PU. The theoretical solid content of all samples was 40%, and the actual solid content was close to the theoretical value. The absolute value of the potential was more than 40 mV, indicating that the synthesized polyurethane dispersion had good storage stability at 25 °C.

**Table 2.** The actual solid content, potential and water absorption of polyurethane dispersion

Sample	Actual solid content (%)	Potential (mV)	Water absorption (%)
PUa	39.95	-59.63	7.30
PUb	38.94	-60.35	10.51
PUc	40.02	-63.52	15.38

The more DMPA content was introduced into the chain, the greater the water absorption of the PU dries film. The reason was that the introduction of more DMPA means that the amount of carboxyl groups in the hydrophilic group increases in the segment, which directly leads to an increase in the water absorption of the dry film.

#### 4.3 Effect of DMPA Content on Polyurethane Adhesion

From Table 3, the adhesion force of PU on the film substrate except OPP can reached 5B, but the adhesion on OPP film was poor, because the polarity of OPP surface was small and the surface free energy was lower, was not conducive to the adhesion of the dispersion on its surface. However, with the increase in the amount of DMPA used, the adhesion of PU to the surface of OPP film was enhanced, and it was not possible to increase the adhesion to 1B. Because the increase in DMPA caused more carboxyl groups to be introduced into the polyurethane chain and the polarity of the dispersion was greater. It facilitates its attachment to the substrate.

**Table 3.** Effect of DMPA content on polyurethane adhesion

Sample	Adhesion (B)				
	PVC	OPP	PA	PE	PET
PUa	5	0	5	5	5
PUb	5	1	5	5	5
PUc	5	1	5	5	5

## 5 Conclusions

As the DMPA content increased, the particle size of the polyurethane became smaller, accompanied by a decrease in water resistance. Through the study of the comprehensive particle size and adhesion properties, it was found that when the DMPA content was 5%, waterborne polyurethanes with relatively small particle diameters and superior water absorption and adhesion could be obtained. There is a certain degree of storage stability.

**Acknowledgements.** This study was funded by a National Natural Science Foundation of China (21376008)—Design, Synthesis and Structure-Activity Relationship of Novel Emulsions for Water-based Inks.

## References

1. Wang, Y., Lue, A., & Zhang, L. (2009). Rheological behavior of waterborne polyurethane/starch aqueous dispersions during cure. *Polymer*, 50(23), 5474–5481.
2. Zhang, J., Li, X., Shi, X., et al. (2012). Synthesis of core-shell acrylic-polyurethane hybrid latex as binder of aqueous pigment inks for digital inkjet printing. *Progress in Natural Science: Materials International*, 22(1), 71–78.

3. Chen, G., & Chen, K. (1997). Self-curing behaviors of single pack aqueous-based polyurethane system. *Journal of Applied Polymer Science*, 63(12), 1–6.
4. Li, R., & Shan, Z. (2018). Enhancement of thermal conductivity of PEG-PPG-based waterborne polyurethane coating by incorporating ordered polyethylene glycol fragment. *Polymer Testing*.
5. Hou, L., Ding, Y., Zhang, Z., et al. (2015). Synergistic effect of anionic and nonionic monomers on the synthesis of high solid content waterborne polyurethane. *Colloids and Surfaces A: Physicochemical and Engineering Aspects*, 467(467), 46–56.



# A New Synthesis Method of Hyperbranched Polyurethane Acrylate for Conductive Ink

Xinya Du, Qifeng Chen, and Guangxue Chen<sup>(✉)</sup>

State Key Laboratory of Pulp and Paper Engineering,  
South China University of Technology, Guangzhou, China  
Chengx@scut.edu.cn

**Abstract.** Hyperbranched polyester polyols (HBPE) of second, third and fourth generation were synthesized by procedures involving one step (HBPE-2), step by step (HBPE-3, HBPE-4). Based on the hyperbranched polymer chain extension method, a new type of hyperbranched polyurethane acrylate (HPUA) was obtained by the end-capping of HBPE with the obtained UA which was synthesized isophorone diisocyanate (IPDI), hydroxyethyl methacrylate (HEMA) and dibutyltin dilaurate (DBTL) at the reaction temperature of 70 °C. The characterization of the polyesters was done by fourier transform infrared spectroscopy (FTIR), acid value, differential scanning calorimeter (DSC), isocyanate on solution, thermogravimetry (TG) and nuclear magnetic resonance (NMR). The results of DSC and TG showed that the glass transition temperature ( $T_g$ ) of HBPE-3 and HPUA-3 were respectively 56.13 and 35.56 °C. The cold crystallization temperature ( $T_c$ ) of HPUA-3 was 110.92 °C and melting temperature ( $T_m$ ) was 134.74 °C. Therefore, both of them can be achieved under low temperature melting. Moreover, the introduction of a large number of unsaturated units in the end of HPUA can provide new ideas to UV curing resin. Finally, it gained good conductivity (8405 S/m) when it was applied to conductive inks.

**Keywords:** HBPE · HPUA · Conductive ink · Resistivity

## 1 Introduction

There are two kinds of hyperbranched polymer, dendrimer and hyperbranched polymer. Dendrimer is regular and controllable. Its molecular size, shape, and functionality can be added and altered. Therefore, its molecular weight distribution was monodisperse. However, there are some inevitable problems, the complexity of the production process, purify is needed in each step and the mass production was limited and expensive. Hyperbranched polymer can be obtained conveniently by direct polymerization without separation and purification. But its molecular branching structure was so monotonous that the reaction process and the product structures were difficult to control under the same conditions. Fortunately, their physical and chemical properties are very close.

Hyperbranched polymers can be synthesized in many ways. The most common one was one-step synthesis method. This method polycondensated the  $AB_x$  ( $x > 2$ )

monomer with multifunctional monomer and the monomer with by functional group into hyperbranched polyester [1, 2] to gain hyperbranched polymers when by are used as core molecular. However, in recent years, it has been found that this method would be gelation when using high functional monomers as reactants [3]. In order to solve this problem, a quasi-one-step method was introduced in which AB<sub>x</sub> monomer was continuously added slowly during the reaction and B<sub>v</sub> monomer as the central core was added at the initial stage of the reaction. This method can not only control the molecular weight of the product, reduce the dispersion [4, 5], but also can get a higher degree of branching products [6].

The highly branched structure of hyperbranched polymer increases its molecular weight. When the concentration increased, due to the large molecular chain without entanglement, it can not only maintain the low viscosity and reduce the use of organic solvents, but also it has good film-forming property, unique rheological properties and chemical resistance. Moreover, the presence of a large number of polar groups gives excellent adhesion to the film, so it can be used as an ideal film forming resin in conductive ink.

## 2 Experimental Section

### 2.1 Chemicals and Materials

Chemicals: IPDI, DBTL, HEMA, PER, DMPA, acetone, ethy acetate, Di-n-butylamine, toluene diamine solution, ethanol were all purchased from Kermel Chemical Reagent Co., Ltd. (Tianjin, China). TsOH was supplied by Chemical reagent engineering technology research and Development Center (Guangdong, China). The above reagents were of analytical purity and were used without further purification. AgNPs was homemade with silver nitrate, glucose, and polyvinylpyrrolidone (PVP) were used as silver precursor, reducing agent, and capping agent, respectively.

Materials: DF-101S-type collective heating thermostatic magnetic stirrer, Spectrum 2000 fourier transform infrared spectroscopy (FTIR), Q2000 Differential Scanning calorimeter (DSC), BOMEX acid burette, SHZ-D water cycle vacuum pump, DHG-9140A electrothermal constant temperature blast dryer, AL204-type Electronic balance, TA Q500 thermogravimetric analyzer (TG) and nuclear magnetic resonance instrument (NMR, 600 MHz).

### 2.2 Reaction Mechanism

In this thesis, UV-curing HPUA was prepared based on hyperbranched polyurethane chain extension method. This method used hyperbranched polyurethane as the core molecular and introduced UV curing group on the end of HPUA. In this paper, the first step was to obtaining UA with the reaction of IPDI and HEMA under the condition of DBTL as the catalyst shown in formula (1). The second step was to synthesize HBPB with PER and DMPA shown in formula (2). The third step was to synthesis HPUA by mixing the obtained UA and HBPB shown in formula (3). The products of each step were characterized by FTIR and NMR. And the structures of different hyperbranched





## 2.3 Experimental Procedure

### 2.3.1 Synthesis of HPUA

The UA was obtained by the reaction of IPDI (6.6680 g) with HEMA (3.9005 g) using DBTL as a catalyst stirred (1200 RPM) at 70 °C till the content of -NCO reached the theoretically value (12.60%). A certain amount of TsOH, 8.5239 g PER and 10.7034 g DMPA were added into a flask with three necks. When the reaction temperature reached 140 °C, placed it in the oil bath with flowing nitrogen until the acid value of the solution was less than 10. After continued 40 min, obtained product was placed in the vacuum drying oven for 55 °C overnight under 0.1 MPa and HBPE was obtained. HPUA was synthesized through obtained UA and HBPE (the molar ratio of 1:1) reacted at 70 °C after steamed to remove residual solvents.

### 2.3.2 Preparation of Conductive Ink

AgNPs powder (0.5 g) was blended with HPUA and photoinitiator (0.1 wt%) in accordance with the proportion of silver accounting for the conductive ink of 30, 40, 50, 60, 70, and 80 wt%. The mixture was dispersed by ultrasonic cleaner. Finally, a new type of UV conductive ink was generated.

## 3 Results and Discussion

### 3.1 Optimum Reaction Time of UA

Figure 2 was the change of isocyanate on the condition of 0.1% catalyst and 40 °C. As time goes on, the reaction rate becomes slower and slower. The content of isocyanate was determined by toluene diamine solution. After carefully analyzed, the shortest time was defined as 100 min.

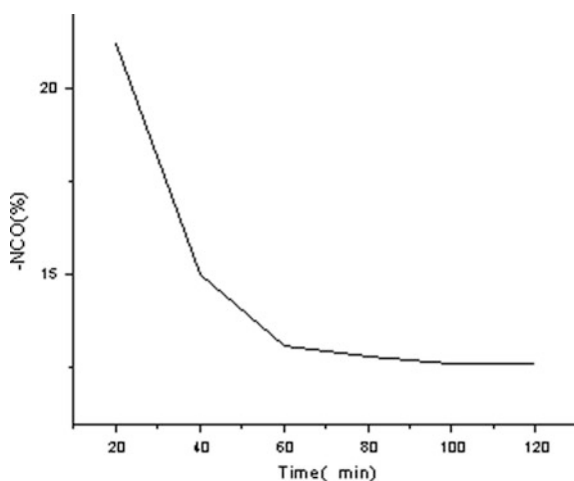


Fig. 2. Change of isocyanate content in the reaction

### 3.2 Characterization of HBPEs

Figure 3 was the chart of acid values in the synthesis reaction of HBPE-3. Based on the figure, we can find that the synthesis experiments of HBPE completed after 4 h. The reason for high reaction rate has been guessed that there was a large contact area for the reactants. However, with the shrinking of contact area, the reaction rate decreased slowly. Because it was esterification reaction, the raw material cannot be utilized completely.

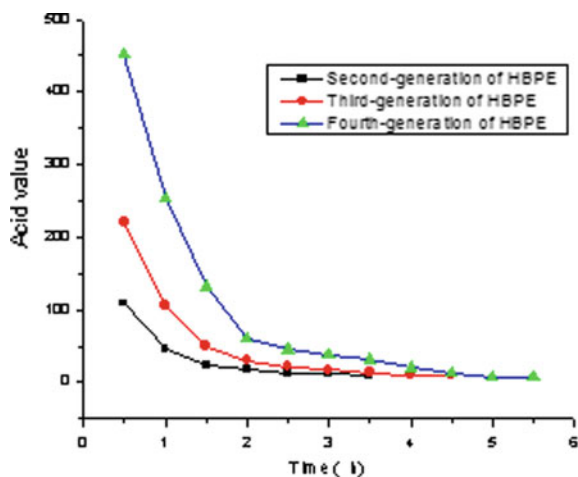


Fig. 3. Chart of acid values in the synthesis reaction of HBPE

Figure 4a, b showed the results of  $^1\text{H}$  NMR and  $^{13}\text{C}$  NMR of HBPE, respectively. The integral calculation found that  $D = 1.00$ ,  $L = 9.52$ ,  $T = 12.17$ , the degree of branching of the hyperbranched polyester was 0.46 and the melt viscosity was low.

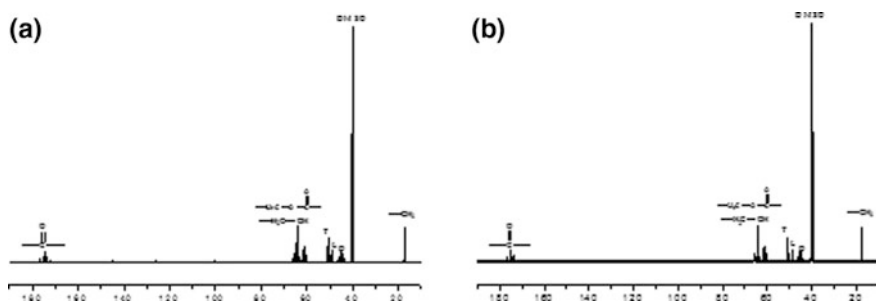


Fig. 4. **a** The hydrogen spectrum of HBPE; **b** the carbon spectrum of HBPE

### 3.3 Synthesis and Characterization of HPUA

Figure 5 showed the infrared spectra of HPUA and UA. It can be seen that UA had an  $-NCO$  absorption peak at  $2266\text{ cm}^{-1}$ . Whereas this peak was absent in the infrared curve of HPUA, indicating that the  $-NCO$  reacted completely.

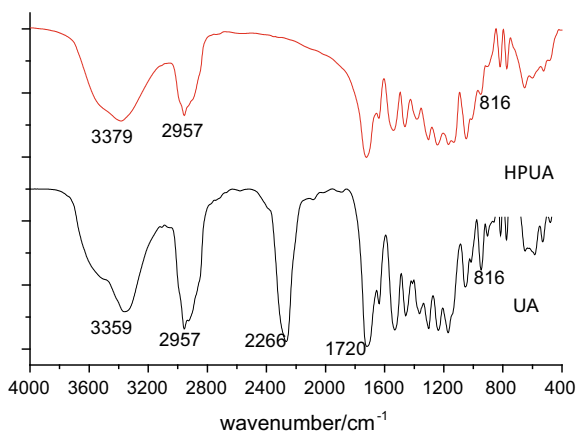


Fig. 5. Infrared spectra of HPUA and UA

Figure 6a, b showed the thermogravimetric analysis of HBPE and HPUA at a heating rate of  $10\text{ }^{\circ}\text{C}/\text{min}$ . As what can be seen from the figure, both products showed good thermal stability. The initial decomposition temperature of HPUA was  $214\text{ }^{\circ}\text{C}$  low than HBPE ( $238\text{ }^{\circ}\text{C}$ ). The final decomposition temperature ( $450\text{ }^{\circ}\text{C}$ ) was significantly higher than HBPE ( $350\text{ }^{\circ}\text{C}$ ). Because the modified hyperbranched polyesters introduced small molecular linear ester chains at the end of the branched chain, the difference of the molecular structures led to a significant change of the chain thermal motion.

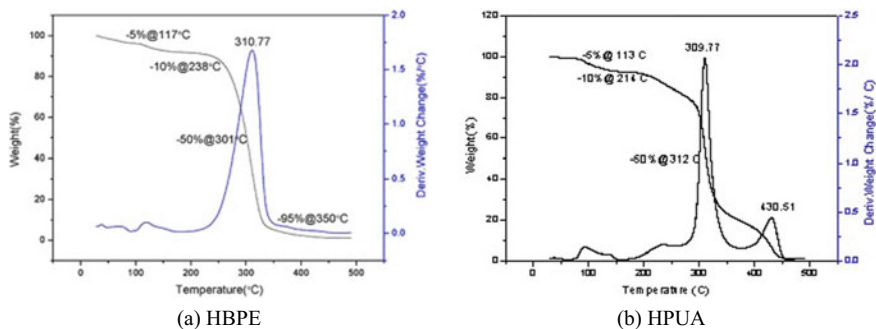


Fig. 6. Thermogravimetry analysis

Figure 7a, b showed DSC curves of HBPE and HPUA, respectively. It was showed  $T_g$  of HBPE, HPUA were 56.13 and 35.56 °C respectively. And the curve showed a small transition which suggested a small amount of endothermic.

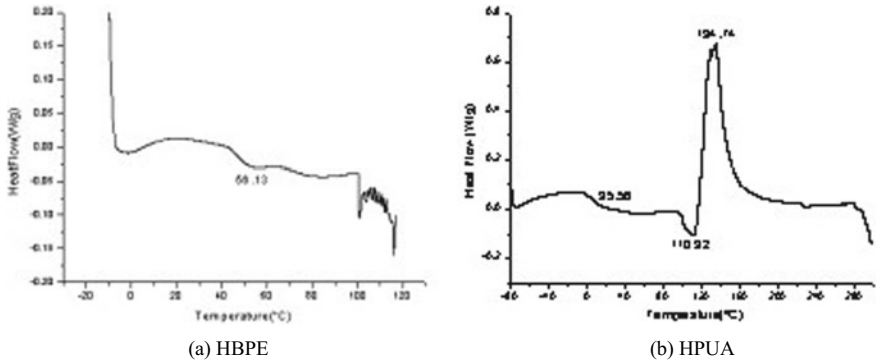


Fig. 7. The DSC chart

### 3.4 Conductivity of Conductive Ink

Table 1 lists the resistance, resistivity, and conductivity of ink with different silver content under a certain depth of ink layer (20  $\mu\text{m}$ ) and UV light (365 nm and 10  $\text{MW}/\text{cm}^2$ ) for 3 min. From the table we can see that the sample conductivity was significantly increased with the silver content increasing. When the silver content reached 70 wt%, the conductivity of the sample was so great that can be used as a printing ink.

Table 1. Resistance, resistivity and conductivity of ink with different silver contents

Nanosilver content (wt%)	Resistance ( $\Omega$ )	Resistivity ( $\Omega \text{ m}$ )	Conductivity (S/m)
30	$1.2 \times 10^9$	177,620	$3.1273 \times 10^{-5}$
40	$3.6 \times 10^8$	28,498	$3.5092 \times 10^{-5}$
50	582.3	0.016	68
60	19.712	$1.2032 \times 10^{-3}$	811.688
70	1.55	$2.4 \times 10^{-5}$	35,543
80	0.2762	$1.2203 \times 10^{-5}$	$8.2 \times 10^5$

## 4 Conclusions

UA was prepared from HEPA and IPDI. The results of solution titration showed that the reaction time was at least 100 min when the reaction temperature was 40 °C. Moreover, the introduction of a large number of unsaturated units at the end of HPUA can provide new ideas for developing new UV curing resin. The conductive ink with different silver powder content was prepared by mixing obtained HPUA with the nano-

silver powder. The resistivity and resistivity were measured by curing 20  $\mu\text{m}$  ink layer. Finally, when the content of silver reached 70%, it reached to  $2.4 \times 10^{-5} \Omega/\text{m}$  and had good electrical conductivity.

**Acknowledgements.** This work was supported by the independent research project of state key laboratory of pulp and paper engineering, Guangzhou Science and Technology Plan Project (201607020045), the Science and Technology Project of Guangdong Province (No. 2017B090901064), school of Light Industry Science and Engineering Funding for Discipline Construction in 2018.

## References

1. Malkoch, M., Claesson, H., Löwenhielm, P., Malmström, E., & Hult, A. (2004). Synthesis and characterization of 2, 2-bis (methylol) propionic acid dendrimers with different cores and terminal groups. *Journal of Polymer Science Part A: Polymer Chemistry*, 42(07), 1758–1767.
2. Murillo, E., Vallejo, P., Sierra, L., & López, B. (2009). Characterization of hyperbranched polyol polyesters based on 2, 2-bis (methylol propionic acid) and pentaerythritol. *Journal of Applied Polymer Science*, 112(01), 200–207.
3. Tan, H. M., & Luo, Y. J. (2004). *Hyperbranched polymers*. Beijing, China: Chemical Industry Press.
4. Huang, W. G., Su, L. J., & Bo, Z. S. (2009). Hyperbranched polymers with a degree of branching of 100% prepared by catalyst transfer Suzuki–Miyaura Polycondensation. *Journal of the American Society*, 131(30), 10348–10349.
5. Scherf, U., & List, E. J. W. (2002). Semiconducting polyfluorenes—Towards reliable structure-property relationships. *Advance Materials*, 14(07), 477–487.
6. Cheng, K. C., Don, T. M., Guo, W. J., & Chuang, T. (2002). Kinetic model of hyperbranched polymers formed by the polymerization of AB<sub>2</sub> monomer with a substitution effect. *Polymer*, 43(23), 6315–6322.



# Research on Printing and Prototyping Performance of Three-Dimensional Printing Materials for UV-Curing Ink-Jet

Beiqing Huang, Yueqiu Lü, Le Ma, Xianfu Wei, and Hui Wang<sup>(✉)</sup>

School of Printing and Packaging Engineering, Beijing Institute  
of Graphic Communication, Beijing, China  
wanghui@bigc.edu.cn

**Abstract.** In order to prepare color three-dimensional (3D) printing materials with good performance, magenta 3D printing material for UV-curing ink-jet is prepared by using magenta color paste, prepolymer, monomer and photoinitiator. Surface tension, viscosity, curing rate and volume shrinkage are characterized to investigate the effect of reactive components on the printing and prototyping performance. Composition of the 3D printing material was determined by formulation experiments. The results show that species of prepolymers and monomers have great influence on viscosity, curing rate and volume shrinkage of 3D printing materials. As volume shrinkage and expansion exist in free-radical and cationic UV-curing systems, respectively, a free-radical-cationic hybrid UV-curing system can provide the optimal printing and prototyping performance due to the minimizing of volume deformation. Species and contents of photoinitiators have significant influences on the UV-curing performance and an appropriate amount of photoinitiators can maximize the curing rate of 3D printing materials. This study is of great help for the research and development of true color 3D printing technology.

**Keywords:** UV-curing · 3D printing · Printing performance · Prototyping performance

## 1 Introduction

In recent years, three-dimensional (3D) printing [1] has been developing rapidly as an additive manufacturing technology. However, little research has been focused on the color reproduction of objects fabricated by color 3D printing. Usually, the color reproduction is executed with a colorizing procedure following the prototyping procedure. Although breakthrough [2] has been made in color 3D printing, the true color 3D printing technique is still in the research and development stage. Ink-jet assisted with ultraviolet (UV) radiation has been recognized as an effective means to fabricate 3D objects by accurate placement and solidification of fluid drops [3], providing a foundation for true color 3D printing. With this method, the implement of true color 3D printing requires the UV-curable prototyping materials prepared from ink-jetable color paste possess not only superior color effect but also excellent printing and prototyping performance: (i) appropriate viscosity and surface tension to make the printing material

could be smoothly ejected from the nozzle; (ii) high curing rate to improve the manufacturing efficiency and (iii) low volume shrinkage to ensure the fabrication precision [4].

In this research, preparation of 3D printing materials and the printing and prototyping performance for UV-curing ink-jet were reported. This research will provide a foundation for the high-quality color 3D printing materials and promote the development of true color 3D printing technology.

## 2 Experimental

### 2.1 Materials

Prepolymers: EB870, EB270, V400 and V100 (Allnex). Monomers: EOEOEA, HDDA, TPGDA, NPGDA, DPGDA and ACOMO (Tianjin Jiuri New Materials Co., Ltd.); TTA-15, TTA-21, TTA-22 and TTA-26 (Jiangsu Tetra New Material Technology Co., Ltd.); OXT-1 and OXT-3 (Hubei Gurun Technology Co., Ltd.). Photo initiators: 898, 2671, 2773, 2776 and 2777 (Tianjin Jiuri New Materials Co., Ltd.); 819 and 389 (IGM). Active amines: EHA (IGM). Pigment: Quinacridone Magenta RTS (DIC).

### 2.2 Equipments

Mechanical agitator (JJ-I, Changzhou Guohua Electric Appliance Co., Ltd., China); high-speed grinding machine (GJ-2S, Qingdao Haitongda Specialized Instrument Co., Ltd., China); UV-LED curing illuminator (UVATA Precision Optoelectronics Co., Ltd., China) with an irradiation power density of  $4 \text{ W/cm}^2$  at the wavelength of 385 nm; Surface tensiometer (K100, Krüss GmbH, Germany); Rheometer (AR2000ex, TA Instruments, USA); Spectral photometer (X-528, X-Rite Incorporated, USA); Electronic balance (CP153, Ohaus Instrument Co., Ltd., USA); Pycnometers (10 mL capacity, Bomex Glass Co., Ltd., China).

### 2.3 Preparation of 3D Printing Materials

The mixture of magenta color paste, prepolymer, monomer, photo initiator and additives was well stirred for 30 min and filtered to prepare 3D printing materials.

### 2.4 Performance Tests of 3D Printing Materials

#### 2.4.1 Viscosity

Viscosity was tested on the rheometer with a 60 mm aluminum rotor plate at  $25 \text{ }^\circ\text{C}$  to record the value of viscosity when the shear rate is  $1 \text{ s}^{-1}$ .

#### 2.4.2 Volume Shrinkage

The measurement method of volume shrinkage ratio (SR) refers to the international standard ISO 3521 [5]. SR of UV-curable 3D printing materials was calculated according to Eq. 1:

$$SR = \frac{\rho_2 - \rho_1}{\rho_2} \times 100\% \quad (1)$$

$\rho_1$  is the density of liquid samples measured by a pycnometer while  $\rho_2$  is the density of UV-cured solid samples measured by a specific gravity balance, respectively.

### 2.4.3 Curing Rate

Curing degree of samples was checked with finger-touch method. Samples were coated onto PET films by 0<sup>#</sup> wire rod at room temperature and cured by the UV-LED curing illuminator. For most samples in this research, the irradiation power was set as a maintained value and the conveyor speed was adjusted to make the sample to be cured, and the corresponding maximum speed (cm/min) of conveyor was recorded as the curing rate of each sample. For samples with cationic monomers in this research, both the irradiation power and the conveyor speed were set as maintained values, and the corresponding minimum number of curing times was recorded as the curing rate of each sample.

### 2.4.4 Surface Tension

Surface tensiometer was used to test the surface tension of each sample.

### 2.4.5 Color Density

Samples were coated onto PET films by 0<sup>#</sup> wire rod at room temperature and cured by the UV-LED curing illuminator. Color density of the coating was measured by a spectral photometer at five different locations and an average was applied.

## 3 Results and Discussion

### 3.1 Effect of Monomers on Printing and Prototyping Performance of 3D Printing Materials

#### 3.1.1 Species of Monomers

As a basic component of 3D printing materials, monomer not only plays a role in dilution but also participates in UV-curing reaction, which has a great influence on printing and prototyping performance. Monomer species with different molecular structures have different effects on material properties. According to the photopolymerization mechanism, monomers are classified into two types [6]: free-radical monomer and cationic monomer.

#### (1) Species of Free-Radical Monomers

3D printing materials were prepared using different species of free-radical monomers and the corresponding printing and prototyping performances of UV-curing for each sample were tested, as illustrated in Fig. 1.

As shown in Fig. 1a, surface tensions of 3D printing materials prepared with different monomers were in the range of 22–24 mN/m. The difference between the surface tension of each sample was relatively small.



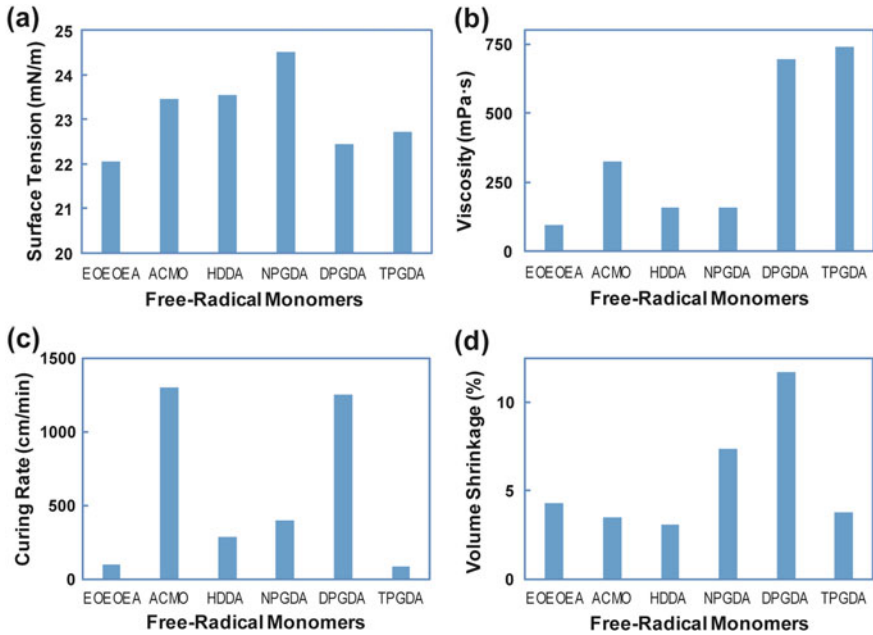


**Fig. 1.** **a** Surface tension, **b** viscosity, **c** curing rate in the UV-irradiation with a power of 20% and **d** volume shrinkage of 3D printing materials with different free-radical monomers

As shown in Fig. 1b, there exist significant differences between viscosities of samples prepared with different monomers. The sample prepared with EOEOEA, a monofunctional monomer, has the lowest viscosity than other samples prepared with bifunctional monomers. As the functionality of monomers increased, the intermolecular forces within the UV-curing system enhanced with the increasing molecular weight, leading to the raise of viscosity.

As shown in Fig. 1c, 3D printing materials prepared with different free-radical photoinitiators have different curing rates. The sample prepared with EOEOEA had the lowest curing rate, as the monofunctionality leads to the lowest reactivity. As an acrylamide compound with a tertiary amine group, monofunctional monomer ACMO produced higher curing rate than EOEOEA and any other bifunctional monomers. Meanwhile, the sample prepared with bifunctional monomer DPGDA also had a fast curing rate.

As shown in Fig. 1d, all of 3D printing materials prepared with different kinds of free-radical monomers have large volume shrinkage. Monomers with less side-chains in a linear molecular structure, for example, EOEOEA and HDDA, could produce a lower ratio of volume shrinkage. On the contrary, a higher ratio of volume shrinkage would be obtained when a multifunctional monomer with more side-chains is used, for example, DPGDA etc.

## (2) Species of Cationic Monomers

3D printing materials were prepared using different species of cationic monomers and the corresponding printing and prototyping performances of UV-curing for each sample were tested, as illustrated in Fig. 2.

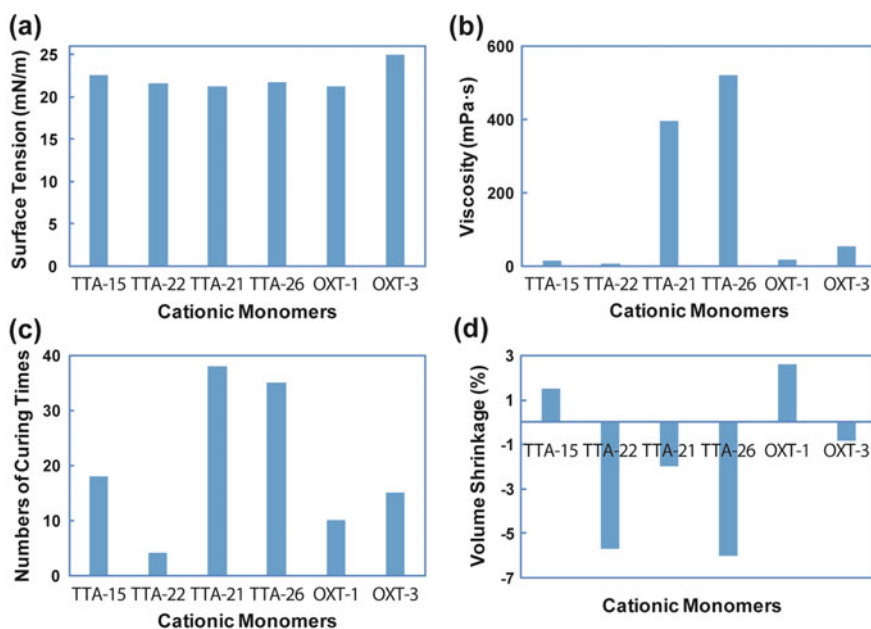


**Fig. 2.** **a** Surface tension, **b** viscosity, **c** numbers of curing times in the UV-irradiation with a power of 100% and a conveyor speed of 60 cm/min and **d** volume shrinkage of 3D printing materials with different cationic monomers

As shown in Fig. 2a, due to the larger molecular polarity, the dioxetane cationic monomer OXT-3 could produce a higher surface tension than others. Other cationic monomers have less effect on the surface tension, which was in the range of 21–22 mN/m, as there was little differences between the polarities of epoxy and oxidized cyclobutane molecular structures.

As shown in Fig. 2b, for samples prepared with TTA series epoxy monomers, TTA-21 and TTA-26 with larger molecular weight produced higher viscosity than TTA-15 and TTA-22. Similarly, the sample prepared with OXT-3 had a higher viscosity than samples prepared with OXT-1.

As shown in Fig. 2c, the 3D printing materials prepared with cationic monomers had a lower curing rate, which is significantly affected by the species of monomers. Reaction rate of ring opening polymerization in TTA-22 is much faster than other monomers especially TTA-21 and TTA-26, which owning two 3, 4-epoxycyclohexyl groups in each molecule. Therefore, a less curing times and a higher curing rate could be produced by TTA-22 comparing with TTA-21 and TTA-26.

As shown in Fig. 2d, 3D printing materials prepared with cationic monomers have less volume shrinkage. In addition, volume expansion was detected in samples prepared with epoxy and oxetane compounds TTA-21, TTA-22 and TTA-26, in which volume shrinkage was neutralized by the expansion effect associated with the progress of ring opening polymerization. In detail, the largest volume expansion was achieved by TTA-26 with two 3,4-epoxycyclohexyl groups. Similarly, OXT-3 with two oxetane groups generated a more obvious volume expansion than OXT-1 with only one oxetane group.

### 3.1.2 Formulation Design of Mixed Monomers

According to the previous experimental results, as various monomers show advantages in different aspects of printing and prototyping performances, it could be an efficient process to prepare 3D printing materials with excellent comprehensive performances by using mixed monomers. Thus, free-radical monomers EOEOEA, ACMO and DPGDA were selected to design a three-order simplex centroid formulation experiment, in which  $X_1$ ,  $X_2$  and  $X_3$  represented the weight fraction of EOEOEA, ACMO and DPGDA, respectively [7]. Data of 3D printing performance are listed in Table 1.

**Table 1.** Data of 3D printing performance for formulation design experiments by using mixed free-radical monomers

No.	Surface tension (mN/m)	Viscosity (mPa s)	Curing rate <sup>a</sup> (cm/min)	SR (%)
1	22.04	1.53	100	4.30
2	23.46	3.92	1360	3.40
3	22.12	13.30	740	8.60
4	22.66	8.22	1360	4.20
5	22.51	5.19	355	2.10
6	22.10	6.17	320	4.70
7	22.35	0.925	1010	0.20

<sup>a</sup>The UV-irradiation power was 20%

According to impacts of each indicator on 3D printing materials, the weight of viscosity, surface tension, curing rate and SR was valued as 0.2, 0.1, 0.35 and 0.35, respectively. By the means of programming solution, when  $X_1 = 0.25$ ,  $X_2 = 0.36$  and  $X_3 = 0.39$ , the regression equation had a maximum value of 91.01, which means the best performance could be achieved when the mass ratio of EOEOEA, ACMO and DPGDA is 25:36:39. Accordingly, the same proportion of mixed free-radical monomers was applied to prepare 3D printing materials and favorable performances were achieved, as shown in Table 2.

**Table 2.** Performance data of 3D print materials prepared from the optimal formulation using mixed free-radical monomers

Surface tension (mN/m)	Viscosity (mPa s)	Curing rate <sup>a</sup> (cm/min)	SR (%)
22.24	6.93	940	3.60

<sup>a</sup>The UV-irradiation power was 20%

Likewise, cationic monomers OXT-1 and TTA-22 were selected to design a two-order simplex centroid formulation experiment [7]. According to the programming solution, using TTA-22 as the single cationic monomer could produce favorable 3D printing performance, as shown in Table 3.

**Table 3.** Performance data of 3D print materials prepared from the optimal formulation using TTA-22 as the single cationic monomer

Surface tension (mN/m)	Viscosity (mPa s)	Numbers of curing times <sup>a</sup>	SR (%)
22.97	10.01	8	-5.70

<sup>a</sup>The UV-irradiation power was 100% and the conveyor speed was 60 cm/min

### 3.2 Effect of Prepolymers on Printing and Prototyping Performance of 3D Printing Materials

As the basic skeleton of 3D printing materials, prepolymers with different molecular structures lead to different properties and performances. In this research, 3D printing materials were prepared with different species of prepolymers and various performances were tested, as illustrated in Fig. 3.

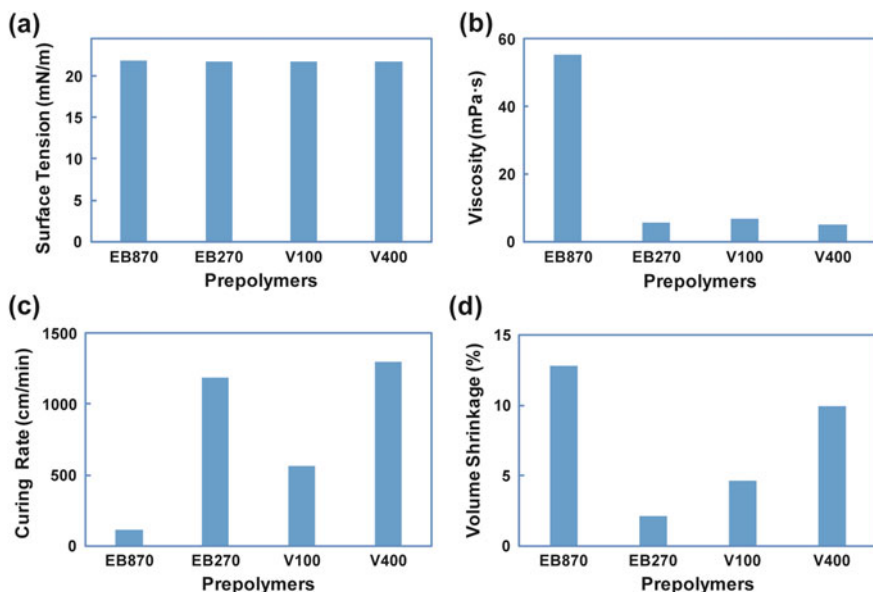


**Fig. 3.** a Surface tension, b viscosity, c curing rate in the UV-irradiation with a power of 20% and d volume shrinkage of 3D printing materials with different prepolymers

As shown in Fig. 3a, all of surface tensions of 3D printing materials prepared from different prepolymers were almost the same and close to 22 mN/m. The negligible differences of surface tension among different formulations could be attributed to not only the identical acrylate group in prepolymers, but also the addition of surfactants.

As shown in Fig. 3b, viscosities of samples prepared with different species of prepolymers show significant differences. Samples prepared with hyper branched polyester acrylate resin V400 and V100 have lower viscosity than samples prepared with aliphatic polyurethane acrylate EB870, as spherical structure of hyper branched polymer could effectively hinder the entangling of chain segments among molecules [6].

As shown in Fig. 3c, curing rate of samples prepared with different species of prepolymers show significant differences. When the irradiation power is maintained at 20%, samples prepared with EB270, V400 and V100 could be cured faster than the sample prepared with EB870. Due to the high functionality of hyper branched prepolymer and the rare occurrence of chain-transfer reaction, long-chain polymers could be generated in a shorter time with the presence of hyper branched prepolymers [6].

As shown in Fig. 3d, 3D printing materials with different prepolymers have different ratios of volume shrinkage. The minimum volume shrinkage which was only 2.1% was achieved by using EB270, benefiting from a minimum functionality of 2 comparing with other prepolymers.

Similarly with the strategy of using mixed monomers, in order to prepare 3D printing materials with excellent comprehensive performance, it is necessary to use mixed prepolymers in the UV-curing system. V400, V100 and EB270 were selected to design a three-order simplex centroid formulation experiment [7]. By the means of programming solution, the best performance could be achieved when the mass ratio of V400 to EB270 is about 1:1. Thus, the same proportion of mixed prepolymers was applied to prepare 3D printing materials and favorable performances were achieved, as shown in Table 4.

**Table 4.** Performance of 3D printing materials prepared from the optimal formulation with mixed prepolymers

Surface tension (mN/m)	Viscosity (mPa s)	Curing rate <sup>a</sup> (cm/min)	SR (%)
23.46	13.30	535	3.40

<sup>a</sup>The UV-irradiation power was 20%

### 3.3 Research of Hybrid UV-Curing System

According to the experimental date in Tables 2 and 3, it could be observed that free-radical polymerization system generated a higher ratio of volume shrinkage while cationic polymerization system lead to the expansion of volume with a slower curing rate. Therefore, it could be assumed that a low volume deformation together with high prototyping efficiency could be achieved at the same time through a free-radical-cationic hybrid UV-curing system. Consequently, a two-order simplex centroid formulation experiment [7] was designed to investigate the optimal ratio of free-radical

system and cationic system, weights of which were represented as  $X_1$  and  $X_2$ , respectively. By the means of programming solution, the best performance could be achieved by using a hybrid UV-curing system when the proportion of free-radical photopolymerization relative to cationic photopolymerization is about 9:1. Table 5 showed the 3D printing performance of materials prepared from the corresponding free-radical-cationic hybrid UV-curing system.

**Table 5.** Performance data of 3D print materials prepared from the optimal formulation using free-radical-cationic hybrid UV-curing system

Surface tension (mN/m)	Viscosity (mPa s)	Numbers of curing times <sup>a</sup>	SR (%)
22.65	10.71	9	-2

<sup>a</sup>The UV-irradiation power was 100% and the conveyor speed was 940 cm/min

### 3.4 Effect of Photo Initiators on Curing Rate of 3D Printing Materials

#### 3.4.1 Species of Photoinitiators

As the key component in a UV-curing system, the photoinitiator is related to the efficiency of initiating during the UV-assisted crosslinking polymerization between prepolymers and monomers, which plays a decisive role in the photocuring speed of UV-curable materials [6]. Currently, most of light sources employed in UV ink-jet are UV-LED lights, which are classified as a type of light source with a single wavelength, requiring the adaptation of absorption wavelengths of photoinitiators. As a result, the correct selection of photoinitiator would determine the curing rate of UV-curable materials [8]. Figure 4 illustrated curing rates of 3D printing materials prepared with different species of free-radical photoinitiators.

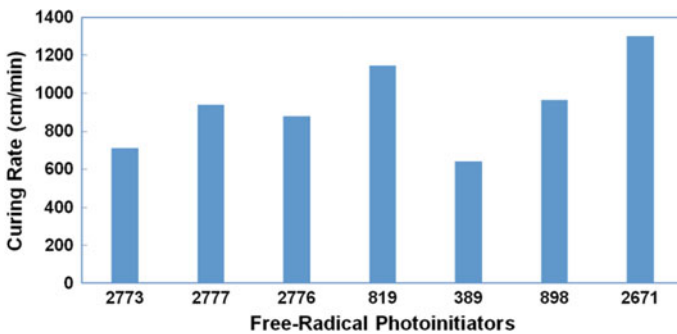


**Fig. 4.** Curing rates of materials prepared with different species of free-radical photoinitiators in the UV-irradiation with a power of 30%

As illustrated in Fig. 4, the curing rate of the materials prepared with different free-radical photoinitiators varied greatly. The curing rate of the material prepared with photoinitiator 389 is the slowest, which could be explained by the absence of absorbance at the irradiation wavelength of 385 nm. However, although other photoinitiators

have strong absorption effect at 385 nm, there were still differences among the 3D printing materials because of the different efficiency of photoinitiating.

### 3.4.2 Formulation Design of Mixed Photoinitiators

Curing rate of UV-curable materials could be effectively improved by using mixed photoinitiators through a fully absorbance of UV light irradiated from the light source. In this research, photoinitiator 898, 819, 2671 and 2777 were selected to design a four-order simplex centroid formulation experiment [7], in which  $X_1$ ,  $X_2$ ,  $X_3$  and  $X_4$  represented the weight fraction of 898, 819, 2671 and 2777, respectively. The curing rate of each sample was measured and the corresponding value of equation for the formulation design experiment was evaluated. By the means of programming solution, when  $X_1 = 0.20$ ,  $X_2 = 0$ ,  $X_3 = 0.50$  and  $X_4 = 0.30$ , the regression equation had a maximum value of 100.79, which means the highest curing rate could be achieved when the mass ratio of 898, 2671 and 2777 is 2:5:3. With this proportion, a 960 cm/min curing rate has been achieved in the UV-radiation power of 20%, showing an extraordinary curing performance.

### 3.4.3 Concentration of Photo Initiators

The photoinitiator content has a great influence on the photopolymerization rate of UV-curable materials and determines the amount of active intermediates (free-radicals or cations) produced in the process of photoinitiating.

According to active intermediates produced during the reaction, photoinitiators are divided into two types: free-radical photoinitiator and cationic photoinitiator [9]. In this research, 3D printing materials with different concentrations of free-radical photoinitiators and cationic photoinitiators were separately prepared and the corresponding curing rate was measured, as illustrated in Fig. 5.

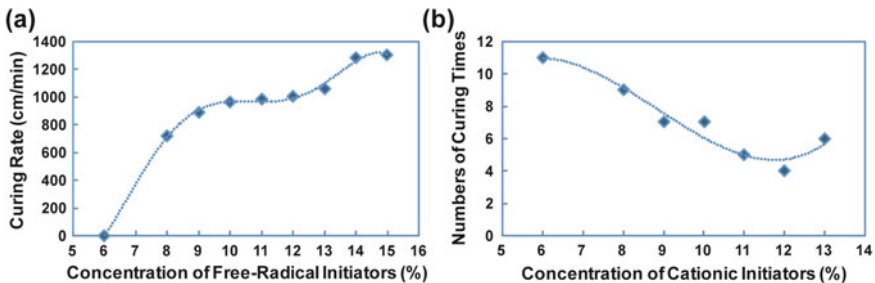


**Fig. 5.** Effect of photoinitiator concentration on the curing performance. **a** Curing rate of 3D printing material prepared with different concentrations of free-radical photoinitiators in the UV-irradiation with a power of 30%. **b** Numbers of curing times of 3D printing materials prepared with different concentrations of cationic photoinitiators in the UV-irradiation with a power of 100% and a conveyor speed of 60 cm/min

As illustrated in Fig. 5, for both free-radical and cationic UV-curing system, along with the increase of photoinitiator concentration, the curing rate first increased rapidly

and then tend to increase slowly, even decrease. This phenomenon could be explained as that the increasing photoinitiator concentration within a certain range increased the amount of active intermediates, which promoted more prepolymers and monomers to participate in the polymerization and accelerated the curing rate. When the photoinitiator concentration reached a certain value, most of the prepolymer and monomer had been initiated by active intermediates to participate in the polymerization. As a result, the chance of initiating new prepolymer and monomer to participate in the polymerization reaction is reduced and the polymerization rate slowed down. However, when the photoinitiator concentration continued to increase, too much active intermediate had been produced and the high concentration of active intermediate in the system caused side reactions such as coupling termination, which slowing down the photopolymerization rate the UV-curable material.

Therefore, for free-radical and cationic UV-curing system, the highest curing rate could be achieved by using photoinitiators with the concentration of 14% and 12%, respectively.

### 3.5 Comprehensive Performance of Magenta 3D Printing Materials

According to the experimental results above, an optimal formulation of 3D printing materials was achieved. Based on this formulation, a kind of magenta 3D printing material was prepared by using 20% magenta color paste, and the comprehensive performances were listed in Table 6.

**Table 6.** Performance of magenta 3D printing materials

Surface tension (mN/m)	Viscosity (mPa s)	Numbers of curing rate <sup>a</sup> (cm/min)	SR (%)	Color density
22.34	12.99	880	1.2	0.7

<sup>a</sup>The UV-irradiation power was 30%

As shown in Table 6, the prepared magenta 3D printing material provided a color density up to 0.7, which was far higher than a commercial available product. Besides, small volume shrinkage, fast curing rate and perfect printability were achieved, which guaranteed the printing performance and the prototyping efficiency.

## 4 Conclusions

We report the preparation and performance of color UV-curable 3D printing materials consisted of color paste, prepolymers, monomers and photoinitiators. According to the experimental results, conclusions of this research are as follows:

1. Fundamental properties of UV-curable 3D printing materials were determined by prepolymers. Lower viscosity and less volume shrinkage could be achieved by using V100 or EB270 while higher curing rate could be achieved by using EB270



- or V400, respectively. The optimal comprehensive performance could be achieved by using mixed prepolymers consisted of EB270 and V400 with a mass ratio of 1:1.
2. Molecular structure of the monomer greatly affected the viscosity, curing rate and volume shrinkage of 3D print materials. Viscosity of materials prepared with EOEOEA was smaller. Curing speed of materials prepared with ACMO and DPGDADE was faster. Volume shrinkage of materials prepared with ACMO and HDDA is smaller. Viscosity of materials prepared by cationic monomer TTA-22 is lower and there exist a certain degree of volume expansion during the photo-curing process. The optimal comprehensive performance could be achieved by using mixed free-radical monomers consisted of EOEOEA, ACMO and DPGDA with a mass ratio of 25:36:39, or cationic monomer TTA-22.
  3. Ratio of volume shrinkage is larger in free-radical photopolymerization systems. Benefiting from the volume expansion effect and a slower curing rate, the optimal comprehensive performance could be achieved by using a free-radical-cationic hybrid photo-curing system, in which the ratio of free-radical system relative to cationic system is 9:1.
  4. Absorption wavelength and photo-initiate efficiency of photoinitiators have great influences on the curing rate of UV-curable 3D printing materials. For the free-radical photopolymerization system with single type of photoinitiator, the highest curing rate could be achieved by using photoinitiator 2671. A higher curing rate could be achieved by using mixed free-radical photoinitiators consisted of 2777, 2671 and 898 with a mass ratio of 3:5:2. Along with the increase in the concentration of photoinitiator, curing rate was first promoted and then tended to be gentle even decreased after a certain value. The curing rate of both free-radical and cationic system could be the highest when the concentration of free-radical and cationic photoinitiator reached 14% and 12%, respectively.
  5. The prepared magenta 3D printing material appeared excellent printing and prototyping performance and provided a color density up to 0.7, which was far higher than a commercial available product.

**Acknowledgements.** This study is funded by Science and Technology Program of Beijing Municipal Education Commission (No. KM201710015012), Key Program of Beijing Institute of Graphic Communication (No. Ea201602), Research and Development Program of Beijing Institute of Graphic Communication (No. Ec201805), and College Students Research Program of Beijing Institute of Graphic Communication “Research of Color Inks for 3D Printing”.

## References

1. Gibson, I., Rosen, D., & Stucker, B. (2014). *Additive manufacturing technologies: 3D printing, rapid prototyping, and direct digital manufacturing* (2nd ed.). New York: Springer.
2. Brunton, A., Arikan, C. A., & Urban, P. (2015). Pushing the limits of 3D color printing: Error diffusion with translucent materials. *ACM Transactions on Graphics*, 35(1), 1–13.
3. Derby, B. (2010). Inkjet printing of functional and structural materials: Fluid property requirements, feature stability, and resolution. *Annual Review of Materials Research*, 40, 395–414.

4. Guo, C. L., Huang, B. Q., Wei, X. F., et al. (2015). Application of hybrid UV curing system in flexographic production through 3D printing. *Applied Mechanics and Materials*, 731, 277–282.
5. Wang, Z. T., Sun, T., Jing, L. L., et al. (2011). Study on volume shrinkage ratio of solvent-free epoxy coatings. *Paint & Coatings Industry*, 41(2), 53–56.
6. Jin, Y. Z. (2010). *Light curing material performance and application manual*. Beijing: Chemical Industry Press.
7. Li, Y. Y., & Hu, C. R. (2005). *Experiment design and data processing*. Beijing: Chemical Industry Press.
8. Yi, Q., Wei, X. F., Huang, B. Q., et al. (2013). Research on photoinitiator and illuminant of UV-LED ink. *Journal of Beijing Institute of Graphic Communication*, 21(6), 42–44.
9. Wei, J., & Jin, Y. Z. (2013). *Light curing coatings*. Beijing: Chemical Industry Press.



# Preparation of High Performance Poly (3,4-Ethylenedioxythiophene) Nanoparticles Ink and Its Inkjet Printability

Ting Chen<sup>1(✉)</sup>, Linjuan Yan<sup>2</sup>, Rong Liu<sup>1</sup>, Wei Zhong<sup>3</sup>,  
and Guangxue Chen<sup>2(✉)</sup>

<sup>1</sup> Guangdong CAILE Packaging Technology Co., Ltd., Zhongshan, China  
chen-scud@foxmail.com

<sup>2</sup> State Key Laboratory of Pulp & Paper Engineering, South China University  
of Technology, Guangzhou, China  
chengx@scut.edu.cn

<sup>3</sup> Shenzhen Yutong Packaging Technology Co., Ltd., Guangdong, China

**Abstract.** In this paper, Nano-poly(3,4-ethylenedioxythiophene) (PEDOT) particles with different morphologies and different degrees of oxidation were prepared by reverse interface method. Nano-PEDOT materials with different morphologies were configured as ink-jet printing inks. The printability of the ink was determined by the analysis of ink dispensability and stability, rheological properties, droplet flight speed, the volume of ink droplets ejected. The results found that nanoparticles with higher degree of polymerization, larger aspect ratio and specific surface area had better dispersion. The best surface tension of ink was 30–40 mN/m and the best viscosity was 8–20 mPa s. The piezoelectric frequency didn't exceed 10 kHz with the best printability. Good ink-jet printability effectively solved the production failures and product defects by the traditional metal nano-ink, which had been reunited and clogging. The ink application could reduce the complexity of processing methods by using the precursor printing. So the nanoparticles ink could be used in the patterning of transparent electrodes and functional layers of electronic devices. And full play to the advantages of printed electronics and products.

**Keywords:** Conducting polymer · Ink-jet printing · Nanoparticle

## 1 Introduction

Conductive polymers have been intensively researched and continuously made breakthroughs in applications such as sensors and biosensors, batteries, supercapacitors, drug delivery, artificial muscles and photovoltaic devices [1–4]. In addition to the similar properties of metals, conductive polymers also have the characteristics of polymers, such as light weight, flexibility, easy processing, and good mechanical stability [5]. Conjugated structure conductive polymers are insoluble and infusible in most solvents. Therefore, electronic devices are prepared by using conductive polymers to obtain functional film layers by electrochemical, vapor deposition, spray coating, etc. And then are patterned and functionalized by photolithography and the like. These are

typical subtractive manufacturing, which will cause cost waste, complicated process, environmental pollution and many other problems. As a classic additive manufacturing method, inkjet printing is an ideal choice for the development of large-area flexible electronics due to its low cost, simple process, environmental friendliness and wide adaptability [6, 7]. The problems that conductive polymers are insoluble and difficult to process restricts their application in the field of printed electronics [8].

In this paper, several kinds of PEDOT particles with different morphology and degree of polymerization were synthesized by reverse-interface polymerization [9, 10]. The nano-functional inks were prepared and their dispersion stability was observed. Inkjet printing was used to study the effect of ink-related parameters on printability. The effects of ink rheology, viscoelasticity, inkjet parameters of the nozzle on ink dynamics and adhesion on the substrate were analyzed by observing and testing the volume of the inkjet ink droplets, the flying speed of the ink droplets, the flight pattern, and the like. The innovation of this paper is that the stable and dispersed nano PEDOT can meet the technical requirements of inkjet printing. In particular, conductive polymers with a single electrical stability, such as conductive and semi-conductive properties, are obtained by controlling the degree of oxidation and the control of different morphologies, which greatly avoids the various complexities caused by doping (such as PEDOT:PSS) problem.

## 2 Experimental

### 2.1 Materials

3,4-ethylenedioxythiophene (EDOT), Analytical grade, was purchased from Aldrich Chemical Co., Inc. An aqueous poly(sodium 4-styrenesulfonate) (PSSNa) solution (content 23 wt%) was purchased from Shanghai Herochem Co., Ltd. Fluorosurfactant (Zonyl FS-30) was purchased from Du Pont China Holding Co., Ltd. Other materials were purchased from Aladdin Biochemical Technology Co., Ltd., including ammonium anhydrous ferric chloride ( $\text{FeCl}_3$ , analytical grade), bis(2-ethylhexyl) sulfosuccinate sodium salt (AOT, 99 wt%), n-hexane (analytical grade), absolute ethyl alcohol (analytical grade), hydrochloric acid (36 wt%).

### 2.2 Synthesis of Nanoparticles

Sodium bis(2-ethylhexyl) sulfosuccinate (AOT) with two-tailed structure was used as an anionic surfactant to form reverse micelles. N-hexane was used as the oil phase. The lotion is wrapped in AOT micelles. The 3,4-ethylenedioxythiophene (EDOT) monomer can be well dissolved in n-hexane, and the oxidant reacts at the oil-water interface to form poly 3,4-ethylenedioxythiophene (PEDOT). PEDOT nanoparticles with different morphologies and polymerization degrees were obtained by changing the ratio of oil to water, oxidation and dosage. Specific steps are as follows: (1) 3.5 g of AOT is dissolved in 20 mL of n-hexane, added to a 100 mL flask for magnetic stirring to form a uniform light yellow solution; (2) the temperature rises to 50 °C, different moles (1, 2, 3 mmol) and different Volume (0.35, 0.45, 1 mL)  $\text{FeCl}_3$  solution was added dropwise

to the system, stirring was continued for 4 h to form a stable microemulsion; (3) 1 mmol of EDOT monomer was added dropwise to the system, and the reaction continued for 8 h, the solution appeared dark blue precipitate; (4) The reaction solution was centrifuged to remove the upper yellow solution, and repeatedly washed with ethanol and deionized water; (5) The polymer solid was transferred to a vacuum drying oven and vacuum dried at 50 °C for 24 h. After the end, move to the dryer for storage.

### 2.3 Preparation of Inks

The preparation of the inkjet printing ink from the synthesized conductive polymer utilizes the macromolecular long-chain PSS as a dispersing agent and a dopant in the system, and also functions to adjust the viscosity of the dispersion liquid to suit the nozzle requirements. Ultrasonic dispersion of conductive polymer nanoparticles, multiple stages of ultrasonic treatment to avoid excessive temperature. The surface tension and leveling of the dispersion are adjusted using a nonionic surfactant. (1) Mixing 0.06 g of nanoparticles with a certain amount of sodium polystyrene sulfonate (PSSNa) solution and deionized water to prepare 0.6 wt% PEDOT dispersion; (2) Ultrasonic rod ultrasonic ultrasonic 5 times using ultrasonic pulverizer 5 min each time, 30 min apart; (3) Add a certain amount of DuPont fluorine nonionic surfactant FS-30 to the system, stir at low speed for 3 min; (4) Static defamer and observe the stability of the suspension.

## 3 Results and Discussion

### 3.1 Morphologies of Nanoparticles

Figure 1 shows PEDOT nanoparticles synthesized by the inverse emulsion method. By changing the volume ratio of different oil-water terms, the volume and shape of the conductive polymer nanoparticles can be well controlled. The EDOT monomer polymerizes at the interface under the action of the oxidant  $\text{FeCl}_3$  to form nanoparticles related to the morphology of the microemulsion, as shown in Fig. 1, under different conditions. Nanoparticles (a), nanospheres (b), worms (c), and nanorods (d) were obtained. A less aqueous solution can form a stable microemulsion and a spherical interface in the n-hexane oil phase. The PEDOT generated by the oxidative polymerization reaction is relatively regular.

The emulsion formed by more aqueous solution in n-hexane is not uniform. There are large and small droplets of different sizes in the emulsion resulting in irregular morphology. The size of oxidation and concentration directly affects the rate of oxidative polymerization of the monomer, leading to different production speed and morphology of the crystal face. In addition, when the amount of oxidant changes, the polymerization degree of the monomer is different, the molecular chain length changes, and the appearance color is also differently different, which will directly affect the conductivity and optical properties of the polymer.

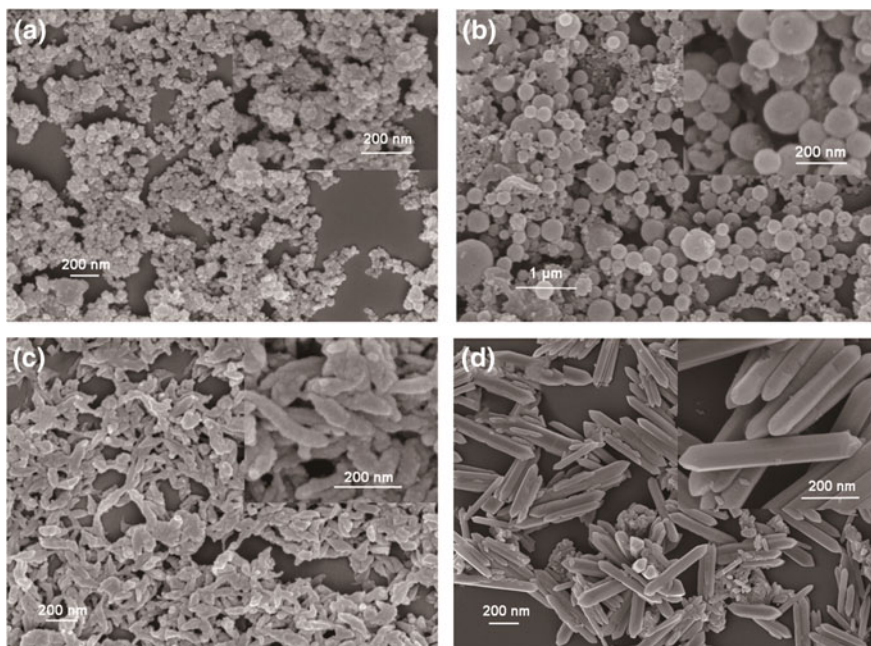


**Fig. 1.** FESEM image of PEDOT nanoparticles prepared by adding different conditions

### 3.2 Conductivity of Nanoparticles

The square resistance was as shown in Fig. 2. The samples all have high electrical conductivity and the square resistance is relatively small. From the data with a higher degree of polymerization (the darker the color), its conductivity is better. From the topography, the nano-particles with smaller structure are also better in conductivity. The nano-materials with larger aspect ratio have higher conductivity. Some PEDOT samples have nanotopography. If the material itself is less polymerized, the polymer backbone has a smaller number of conjugated  $\pi$  bonds and does not necessarily have conductive metal properties.

### 3.3 Surface Tension and Viscosity of Inks

The viscosity of the ink determines the kinetic energy of the jet. If the viscosity is too long, the surface tension of the ink allows the fluid to be continuously necked at the nozzle to form a uniform ink droplet. Therefore, it is necessary to strictly control the surface tension and viscosity of the ink during the ink arranging process. In this paper, the contents of PSS and FS-30 are used to control the viscosity and surface tension of the ink respectively. The effect is shown in Fig. 3.

A small amount of FS-30 added to the ink of the mixing system will greatly reduce the surface tension of the ink, as shown in Fig. 3a. When the FS-30 content was 0.06 wt%, the surface tension decreased by 72 mN/m by nearly half to 36.2 mN/m. However, as the content is further increased, the decrease in surface tension is

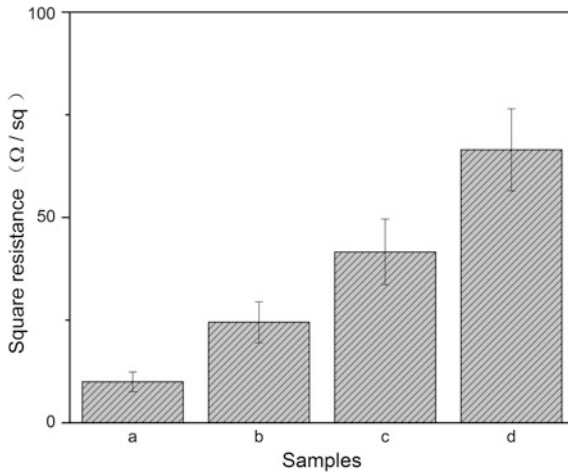


**Fig. 2.** Square resistance of sample a, b, c and d

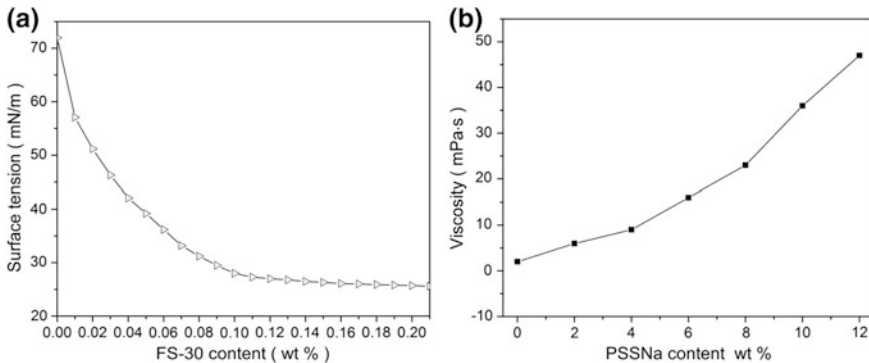


**Fig. 3.** The relationship between FS-30 content and the surface tension of the ink (a), PSSNa content and ink viscosity (b)

gradually slowed down. The surface tension affects the formation of ink droplets on the one hand and the wettability of the ink to the ink jet channels and the substrate on the other hand. In practice, the optimum viscosity and tension of the ink should be determined. This value also varies with nozzle type, piezoelectric frequency, ink jet pressure, nozzle material surface properties, ink type, and other parameters. As can be seen from Fig. 3b, with the addition of the polymer macromolecular PSS having a long chain, the viscosity of the dispersion is continuously increased. The increased viscosity is beneficial to increase the viscosity of the liquid and the cohesive work of the ink. So that the ejection time is shortened, the ink filament is shorter and the probability that the ink is broken at multiple places to form a satellite ink dot is reduced. However, if the viscosity is too large, the elasticity of the ink is lowered, the ink filament is likely to be too long, and the ink droplet ejection is difficult. The optimum viscosity range of the

SE-128 AA nozzle used in this experiment is 8–20 mPa s, and the surface tension is between 20 and 40 mN/m. Therefore, the content of PSSNa is controlled between 4 and 8 wt%, and the amount of FS-30 is between 0.04 and 0.1 wt%.

### 3.4 Dispersibility of Inks

According to the above formula range, the four inks configured to stand and observe the dispersion stability of the ink are shown in Fig. 4. The four inks from left to right in the figure are blue black a (nanoparticle), dark blue b (Nano-microspheres), blue-gray c (worm), and yellow-green d (nanorod) after grinding, sonication, and standing for 7 days respectively. The four inks are allowed to stand after treatment and remain in a stable suspension state throughout the first day. From the second day, blue-grey c and yellow-green d gradually appeared to precipitate more, and some solid nanoparticles were deposited at the bottom. By the seventh day, the two ink samples were thoroughly layered, the upper layer was a clear solution, and the lower layer was a precipitate, which is shown that the dispersion of the two nanoparticles was poor. Blue-black a<sub>3</sub> and deep blue b<sub>1</sub> can maintain a stable and stable suspension state for 7 days of rest time, and have good dispersion stability. Since all samples can be uniformly dispersed in an aqueous solution throughout the day, the stability is greater than that of the general metal particle type ink.

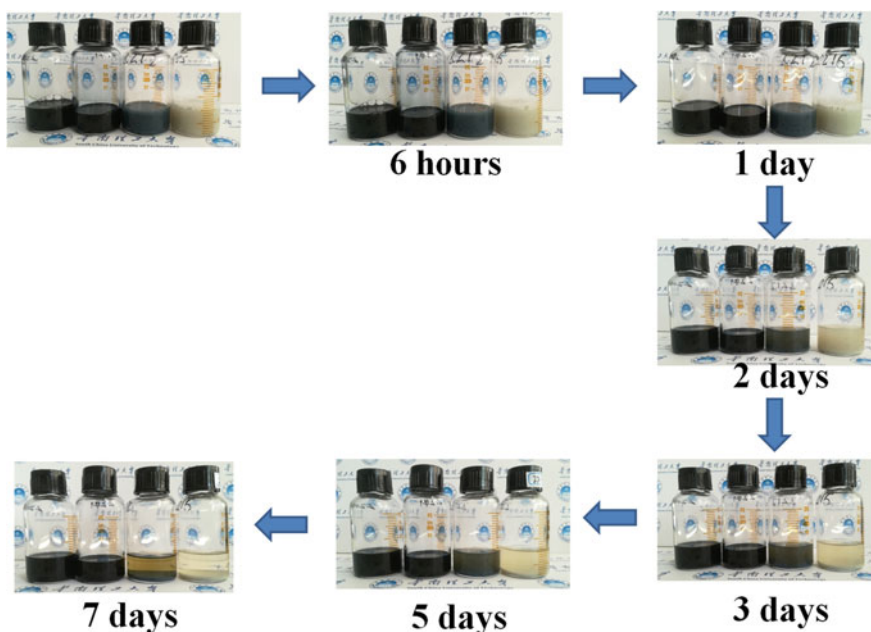


Fig. 4. Ink dispersion stability

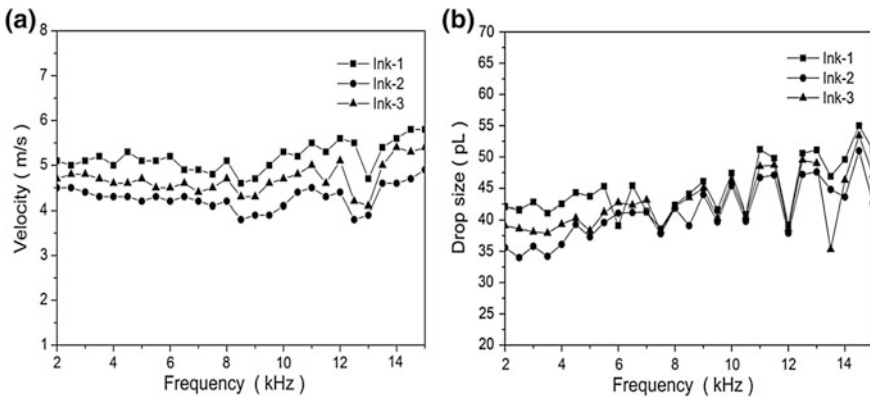


### 3.5 Parameters and Morphology of Droplet Flight

According to the above research results and the characteristics of SE-128 AA nozzle, dark blue nanospheres b with better dispersibility and conductivity were selected as testing inks, and a certain amount of PSSNa and FS-30 were added to prepare aqueous dispersion for inkjet printing. The testing inks are shown in Table 1. During the test, nozzles with excellent inkjet state were chosen, and the flight speed and droplet volume of the three inks were tested and recorded from the frequency of 2–15 kHz. The step frequency amplitude was 500 Hz, and the corresponding test data flight speed and ink droplets. The volume is shown in Fig. 5, and the flight profile is shown in Fig. 6.

**Table 1.** Three kinds of ink formulation and performance parameters

Number	PEDOT (wt%)	PSSNa (wt %)	FS-30 (wt %)	Surface tension (mN/m)	viscosity (mPa s)
Ink-1	0.6	2	0.06	35	6.1
Ink-2	0.6	8	0.06	35	16.2
Ink-3	0.6	8	0.1	28.1	15.9



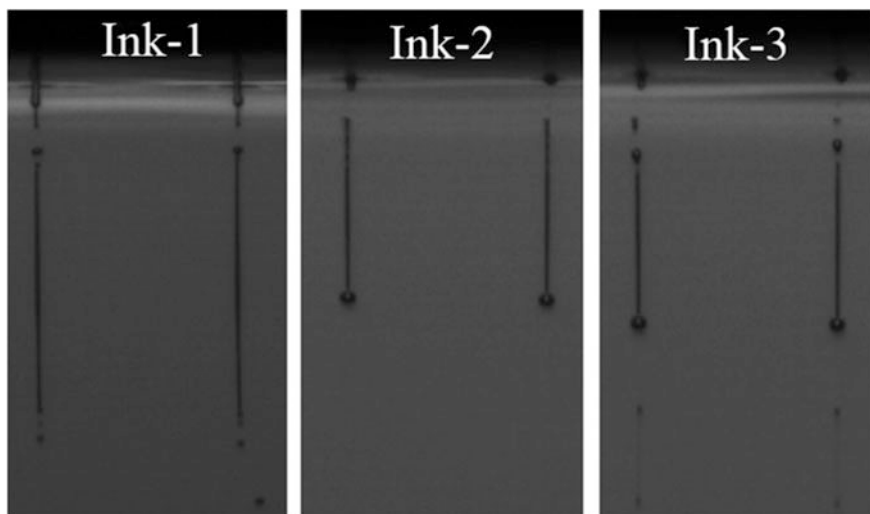
**Fig. 5.** Droplet velocity (a) and volumes (b) at different piezoelectric frequencies

Figure 5a shows the change in flight velocity of the three inks at frequencies between 2 and 15 kHz. On the whole, the flight speed in the low frequency region (<12 kHz) is basically stable, and there is a large fluctuation in the high frequency region. The higher frequency external voltage changes the negative pressure caused by the ink chamber faster, the injection action is completed within a few microseconds. Ink-1 and Ink-2 have the same surface tension, but the viscosity of Ink-1 is significantly lower than the latter, and the lower viscosity is more likely to break under the same external pressure stimulus to produce a larger initial velocity. Ink-2 has a large cohesive force in a relatively large viscosity state, and the work done by the pressure overcomes the cohesive force to consume more energy, resulting in a smaller initial velocity of the

ink. There is a small difference in the viscosity of Ink-2 and Ink-3, but Ink-2 has a high surface tension. As can be seen from the figure, the flying speed of Ink-2 is slightly lower than that of Ink-3. When the surface tension is large, the ink droplets need to be ejected to form an ink column, which increases the new surface energy and consumes more pressure. The work of the kinetic energy is reduced, and only a small initial velocity can be obtained. The surface tension of the Ink-3 is small, and the kinetic energy obtained at the nozzle not only satisfies the ink to create a new surface to produce a droplet, but also obtains more flying motion energy and has a higher speed during flight.

Figure 5b shows the volume change of the ink droplets of the three inks at a frequency between 2 and 15 kHz. Similar to the previous velocity analysis, there is a relatively stable droplet volume in the smaller frequency interval, and the ink droplets in the larger frequency interval fluctuate more, which is the combination of the piezoelectric frequency and the rheological properties of the ink. Due to the difference in viscosity, Ink-2 is more viscous than Ink-1. Under the action of cohesive work, the ink is not easily ejected, resulting in more ink remaining in the ink chamber, resulting in a smaller volume. Ink drops Ink-2 has a larger surface tension than Ink-3. The formation of ink droplets needs to overcome the new surface energy. The smaller the volume, the less the surface energy increases. So the surface area of Ink-2 is smaller and the volume is smaller. It is usually necessary to combine speed and volume for comprehensive analysis. The magnitude of kinetic energy is related to speed and mass. When density is certain, mass is determined by volume. The speed and volume are affected by the kinetic energy of ink droplets, whether it is to overcome ink splitting. Cohesive work, or to overcome the free energy of the new surface, will consume the initial kinetic energy of the ink, resulting in a certain degree of decline in flight speed and volume.

Figure 6 shows the flight patterns of the three inks. In the figure, since Ink-1 has a lower viscosity than the other two inks, the ink has a small cohesive work and is easily squeezed out of the nozzle under pressure and in an initial state with a large trailing length. When the viscosity of the ink is large, it has a large cohesive work and takes a long time to overcome the cohesive work pressure. The ejection time becomes shorter, and the tail of the ink droplet is shorter. At the end of the detachment of the ink, the ink will have a tendency to shrink into droplets under the combined action of surface tension and the like. On the one hand, it is easy to break at multiple places, increasing the probability of forming satellite ink dots. And on the other hand, it is difficult to completely shrinking into spherical droplets under surface tension. From the lower end of the ink-1 in Fig. 6, it can be seen that the satellite dots left by the last ink drop. At the tail, because of the small viscosity, the excess ink is brought out, and eventually the excess satellite dots are formed. In addition, the satellite dot at the lower end has a deflection phenomenon, which is extremely harmful to inkjet printing, which seriously affects the print quality. The main reason for this phenomenon is that the satellite ink dot breaks out and is the same as the charge of the main ink droplet. Since Ink-2 and Ink-3 have a large viscosity at the same time, the ink droplets have a short tail. However, Ink-2 has a relatively standard initial flight morphology of the ink droplets. Finally the ideal ink droplets will be formed under the action of surface tension. Because Ink-3 has less surface tension, the pressure work is less expensive in overcoming the new surface tension with faster initial speed and shorter ejection time.



**Fig. 6.** Three kinds of ink flight status

## 4 Conclusions

The reverse interfacial polymerization method can well control the morphology of the conductive polymer. By changing the amount of the oxidant, the degree of polymerization of the monomer can be effectively controlled. The number of conjugated  $\pi$  bonds in the molecular chain is increased, thereby further increasing the conductivity. Passing macromolecular long chain PSS and the nonionic surfactant FS-30 regulates the viscosity and surface tension of the dispersion system, which can guide the nano-conductive polymer ink with good dispersibility, and has no obvious agglomeration phenomenon for a long time. It is obviously superior to the metal nano-particle system. The surface tension is 30–40 mN/m, and the viscosity is 8–20 mPa s. It is suitable for inkjet printing of granular nano-PEDOT ink by SE-128 AA nozzle. The ink has good printing in inkjet printing process. A lower or moderate piezoelectric frequency (<10 kHz) keeps the droplet speed and volume stable.

**Acknowledgements.** This research work was funded by the 2018 discipline construction fund of the School of Light Industry and Engineering, South China University of Technology and the Guangdong Science and Technology Plan Project (2017B090901064) and the Guangzhou Science and Technology Plan Project (201607020045). At the same time, it is also the research content of “Research and application of printing process of conductive and luminescent materials” by Guangdong Caille Packaging Technology Co., Ltd. Thanks to Shenzhen Yutong Technology Co., Ltd. for providing research equipment in the special fund of Shenzhen development and reform commission (No. 939, 2016).

## References

1. Ebisawa, F., Kurokawa, T., & Nara, S. (1983). Electrical properties of polyacetylene/polysiloxane interface. *Journal of Applied Physics*, 54(6), 3255–3259.
2. Wolfart, F., Hryniewicz, B. M., Góes, M. S., et al. (2017). Conducting polymers revisited: applications in energy, electrochromism and molecular recognition. *Journal of Solid State Electrochemistry*, 21(9), 2489–2515.
3. Tang, C. (1986). Two-layer organic photovoltaic cell. *Applied Physics Letter*, 48(2), 183–185.
4. Tang, C. W., & Vanslyke, S. A. (1987). Organic electroluminescent diodes. *Applied Physics Letter*, 51, 913.
5. Chang, J. S., Facchetti, A. F., & Reuss, R. (2017). A circuits and systems perspective of organic/printed electronics: Review, challenges, and contemporary and emerging design approaches. *IEEE Journal on Emerging and Selected Topics in Circuits and Systems*, 7(1), 7–26.
6. Bao, Z., et al. (1997). High-performance plastic transistors fabricated by printing techniques. *Chemistry Materials*, 9, 1299–1301.
7. Jung, M., Kim J., Noh, J., et al. (2010). All-printed and roll-to-roll-printable 13.56-MHz-operated 1-bit RF tag on plastic foils. *IEEE Transactions on Electron Devices*, 57(3), 571–580.
8. Lebovka, N. I., Gigiberiya, V. A., Lytvyn, O. S., et al. (2014). Drying of sessile droplets of laponite-based aqueous nanofluids. *Colloids and Surfaces A: Physicochemical and Engineering Aspects*, 462.
9. Zheng, H., Jiang, Y., Xu, J., et al. (2010). The characteristic properties of PEDOT nano-particle based on reversed micelle method. *Science China Technological Sciences*, 53(9), 2355–2362.
10. Zheng, H., Jiang, Y., Xu, J., et al. (2011). Analysis on the characteristic properties of PEDOT nano-particle based on reversed micelle method. *Journal of Wuhan University of Technology-Material Science Education* 26(3), 422–428.



# Evaluation of Monomer Performance for UV-LED Inkjet Inks

Rongxia Bu, Shiyong Luo<sup>(✉)</sup>, and Xiao Liu

School of Printing and Packaging Engineering, Beijing Institute  
of Graphic Communication, Beijing, China  
luoshiyong@bigc.edu.cn

**Abstract.** UV-LED curing has the advantages of energy-saving, ozone-free, and mercury-pollution emissions, becoming one of the recently developed green printing technologies. Inkjet ink is the key material for digital printing. In order to prevent clogging of the nozzle, under the premise of ensuring high-speed solidification of inkjet inks, the lower the viscosity, the better. In this paper, five commonly used low viscosity monomers, HDDA, ACOMO, DPGDA, EOEOEA and DMAA, were investigated. TPO is used as an initiator, separately formulated UV-LED inkjet ink binders and inks, the infrared and visible light transmission spectra were used to characterize the curing speed of the binder and the color of the cured film. The UV-LED inkjet ink samples were tested for viscosity, curing degree. The low viscosity and curing degree are the assessment criteria, the monomers applicability are in order: ACOMO, HDDA, DPGDA, EOEOEA, DMAA.

**Keywords:** UV-LED inkjet ink · Monomer · Viscosity

## 1 Introduction

UV-LED curing is developed on the basis of UV curing, which is a technology that can be quickly cured at the center wavelength of 385 or 395 nm light emitted by the LED, and has the advantages of energy saving, no ozone, and mercury pollution [1]. Monomers, prepolymers, photoinitiators, additives, pigments, etc. are the main components of UV-LED inkjet inks. Monomers, also known as reactive diluents, contain photo-curing reactive groups and are an important component of photocuring systems [2]. In order to prevent clogging nozzles, monomers used in UV-LED inkjet inks generally require less viscosity, which are mainly used to adjust the viscosity of the system and dissolve other components of the inkjet inks. In addition, the monomer can also participate in the photo-curing reaction, thereby affecting the curing speed of the ink and various properties of the cured film [3]. The principle of monomer selection generally is: low viscosity, strong dilution ability, easy to dissolve. Under the premise of ensuring solidification, the lower the viscosity is, the higher the pigment content has. Generally, the monomers used in UV-LED inkjet inks should have low viscosity, have a strong dilution capacity for the ink system, and are dissolved easily in the system [4], toxic and volatile. The monomer selected generally has no toxic effect on the human body and does not pollute the environment [5]. Functionality, under normal

circumstances, with the increase of functionality and molecular weight, the interaction force between molecules increases, the viscosity increases; with the increase of functional groups participating in light curing reaction, the activity of light curing reaction is increased and the curing speed is improved [6]. In this article, we used five low-viscosity monomers: HDDA, ACOMO, DPGDA, EOEOEA, DMAA to formulate UV-LED inkjet ink binders and inks. In order to evaluate the effect of several common low-viscosity monomers on the performance of UV-LED inkjet inks, their viscosity, transparency, infrared spectrum, and other related properties were tested.

## 2 Experiments

### 2.1 Experimental Materials

Materials used in this experiment were purchased from Shanghai Guangyi Chemical Co., Ltd., Shanghai Kaiyin Chemical Co., Ltd., and others. Photoinitiators: 819, TPO; Monomers: ACOMO, HDDA, DPGDA, DMAA, EOEOEA; Pigment: Carbon black; Additives.

### 2.2 Preparation and Viscosity Testing of Inkjet Ink Binders

Inkjet ink binders, the other components are the same except the different types of monomers, the specific formula is shown in Table 1. The total amount of the materials in Table 1 is 95%, the remaining 5% is the pigment, and the unit of measurement is the mass percentage.

**Table 1.** Binder formula

Monomers	Other components				
	TPO	Dispersant	Prepolymer (resin)	Active amine	Leveling agent
70	4	8	7	3	0.4

Viscosity refers to a property that prevents fluid flow, also known as the internal friction force [7]. Viscosity has an important influence on the quality of UV-LED inkjet inks and also affects the quality of printing. Therefore, the viscosity of UV-LED inkjet inks needs to be controlled within a certain range. In general, UV-LED inkjet inks have a viscosity in the range of 15–30 mPa s. The viscosity is measured at room temperature using the Iwata No. 2 Viscosity Cup and the unit is s.

### 2.3 Visible Light Transmission Testing

Visible light transmission is the characterization of transparency of the cured film for UV-LED inkjet inks, the greater the transmittance, the higher the transparency of the tested substances [8]. The UV-LED ink-jet ink binder sample was coated on the glass slide using a hand-coated wire rod at room temperature. After being cured by UV-LED

light source, the cured film was scraped off using a utility knife, and the transparency of the cured film was measured with an ultraviolet-visible spectrophotometer. Thereby, the color of the cured film was characterized.

## 2.4 IR Spectroscopy Testing

The UV-LED ink-jet ink binder sample was coated on the glass slide with a hand-coated wire rod at room temperature. After being cured by UV-LED light source, the cured film was scraped off with a utility knife to test its infrared absorption spectrum curve, and at the same time, the infrared absorption spectrum curve of the connecting material for the UV-LED inkjet ink was tested [9]. Compared infrared spectrum curves, the curing degree of the binder for inkjet ink was judged by observing how much the characteristic absorption band area of C=C was reduced at  $810\text{ cm}^{-1}$ . The more the band area is reduced, the greater the curing degree [10].

## 3 Results and Discussions

### 3.1 Viscosity Testing Results

UV-LED inkjet ink was prepared with five kinds of monomers such as ACMO and HDDA respectively. Pigment is carbon black, add other additives, etc. Except for different types of monomers, the other components are the same. The viscosity of several UV-LED inkjet inks were tested by the Iwata No. 2 viscosity cup in the laboratory, the experimental results are shown in Fig. 1.

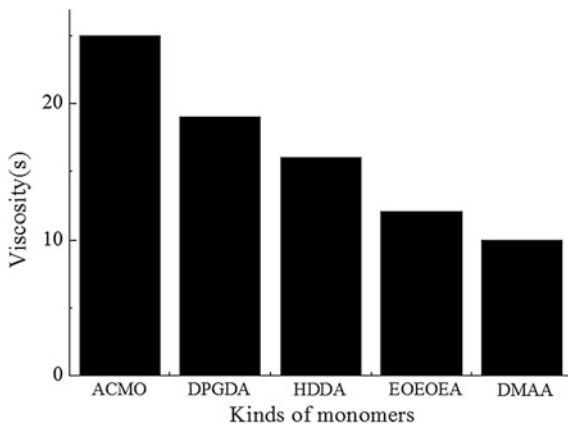


**Fig. 1.** Effect of different monomers on viscosity of UV-LED inkjet inks

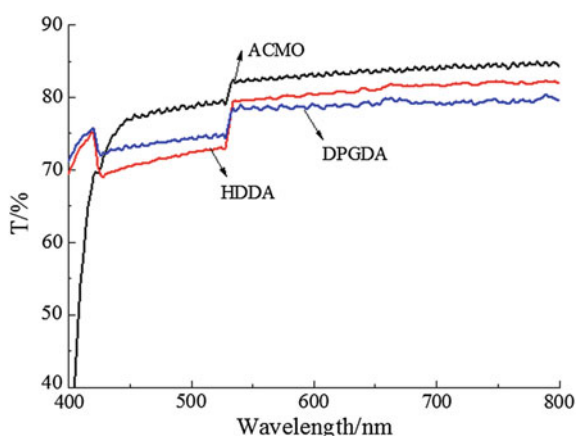
It can be seen from Fig. 1 that the viscosity of UV-LED inkjet inks containing ACMO, DPGDA, HDDA, EOEOEA, DMAA decreases in turn.

**Table 2.** Reduced proportion of area after curing

Monomer	Area before curing	Area after curing	Reduced proportion
HDDA	800	8	100
ACMO	346	10	35
DPGDA	678	24	30

### 3.2 Visible Light Transmittance Testing Results

UV-visible spectrophotometer was used to test the transparency of UV-LED inkjet inks which consisted of ACMO, HDDA and DPGDA, respectively. Due to the poor film-forming properties of ink-jet inks composed of DMAA and EOEOEA when cured on glass slides, their transparency cannot be tested. Therefore, the experimental results are shown in Fig. 2.

**Fig. 2.** Effect of different monomers on the transparency of UV-LED inkjet inks

As can be seen from Fig. 2, the visible light transmission spectrum curves of ACMO, HDDA, and DPGDA have similar trends. The relationship of visible light transmittance is  $ACMO > HDDA > DPGDA$ . The greater the transmittance, the higher the transparency of the tested material, so the UV-LED inkjet ink containing ACMO has the best transparency.

### 3.3 Infrared Spectrum Testing Results

For several kinds of monomers, the infrared spectrum curve of the connecting material and cured film of the composition was tested. The experimental results are shown in Fig. 3.

As can be seen from the above figures, the trends of the infrared spectrum of the UV-LED inkjet inks of different monomers are generally similar. As can be seen from



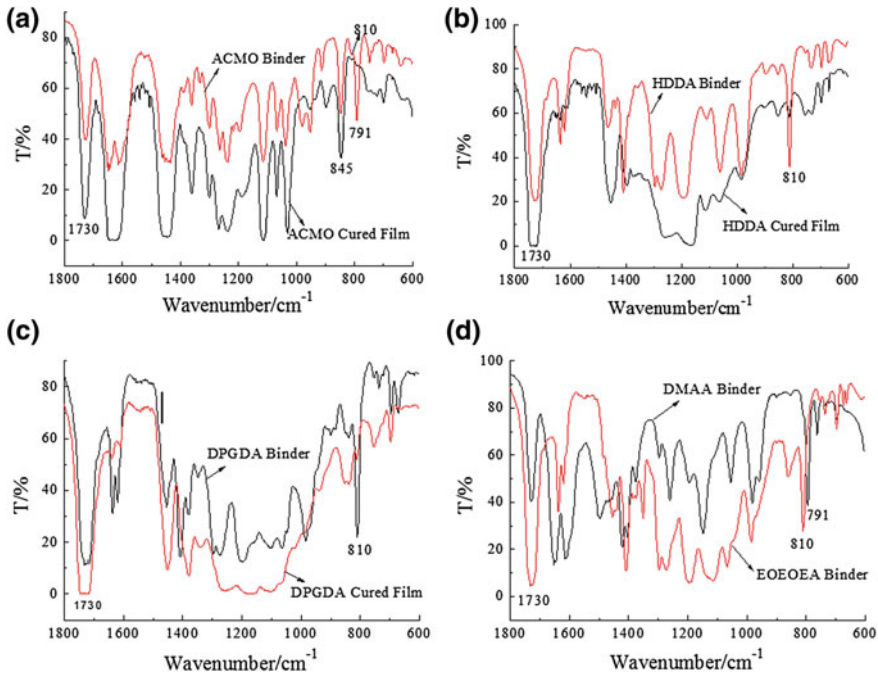


**Fig. 3.** Infrared spectrum curve of the connecting material and cured film of the composition. **a** Infrared contrast diagram of the binder and cured film containing ACMO. **b** Infrared contrast of HDDA-containing binder and cured film. **c** Infrared contrast diagram of binder and cured film containing DPGDA. **d** Infrared contrast of the binder containing DMAA and EOEOEA

the Table 2, the band area of the UV-LED inkjet ink binder containing HDDA is reduced by approximately 100 times. The UV-LED inkjet ink binder containing ACMO has a 35-fold reduction in the band area. The band area of UV-LED inkjet ink binder containing DPGDA is reduced by approximately 30 times. The IR spectra of the UV-LED inkjet inks containing DMAA and EOEOEA are similar, and therefore the curing degree is similar.

## 4 Conclusions

Inkjet ink is one of the important fields of UV-LED curing technology. In order to prevent clogging of the nozzles, inkjet inks are required to be rapidly cured at low viscosity. For the monomers used in inkjet inks, they were evaluated for their performance, and they were formulated into UV-LED inkjet ink binders and inkjet inks to test their relative performance respectively. Based on the above experimental results, comprehensive analysis and comparison, the monomers are in order: ACMO, HDDA, DPGDA, EOEOEA, DMAA.

**Acknowledgements.** This study is funded by the Key Science and Technology Project of Beijing Municipal Education Commission (KZ201610015015), and by the Research & Development Program Project of Beijing Institute of Graphic Communication (EC201804).

## References

1. Siegel, S. B. (2005). UV Commercialization of LED curing. *Proceedings of Rad Tech Asia*, 339–356.
2. Tong, Z. (2015). UV ink curing properties and composition. *Printing Today*, 8, 57–60.
3. Qing, Y., Qi, W., Xian, F. W., & Pei, Q. H. (2014). Effect of monomer on the performance of UV-LED inkjet inks. *Packaging Engineering*, 35(7), 127–132.
4. Hong, B. W. (2017). The selection of solvents in UV monomer production. *Chemical Engineering and Equipment*, 7, 40–43.
5. Xiang, L. H. (2009). Detection and control of volatile organic compounds in tobacco package. *Printing Technology*, 2, 28–32.
6. Zheng, J. Z., Ru, Q. H., Yun, Z. C., et al. (2015). Preparation of coated paper printing UV varnish. *Packaging Engineering*, 36(9), 144–149.
7. Qing, Y. (2014). Research on UV-LED inkjet inks. *Nanjing Forestry University*, 4, 56.
8. Wen, J. L., Ai, J. G., Guo, Z. L., & Li, Y. (2012). New high performance transparent UV-curable poly(methyl methacrylate) grafted ZnO/silicone-acrylate resin composites with simultaneously improved integrated performance. *Colloids and Surfaces A: Physicochemical and Engineering Aspects*, 396.
9. Yang, Z. J. (2010). *Light-cured material properties and application manual* (pp. 309–330). Beijing: Chemical Industry Publisher.
10. Dong, F., Maganty, S., Meschter, S. J., et al. (2018). Effects of curing conditions on structural evolution and mechanical properties of UV-curable polyurethane acrylate coatings. *Progress in Organic Coatings*, 114, 58–67.



# Study on Curing Rate of Color 3D Printing Materials

Le Ma, Beiqing Huang, Bin Yang, Yidong Zhao, Kangshi Qin,  
and Xianfu Wei<sup>(✉)</sup>

School of Printing and Packaging Engineering, Beijing Institute  
of Graphic Communication, Beijing, China  
weixianfu@bigc.edu.cn

**Abstract.** The absorption of photoinitiator and the curing rate of the photoinitiator will be affected by the color substance in the color 3D printing material. In order to improve the curing speed of color 3D printing materials, the influence of dyes on the curing speed of 3D printing materials was first explored. Different kinds of dyes were selected under the same color conditions, and the ink was prepared and UV spectrum was carried out. Test and analysis of curing speed. The types of dyes were controlled to change the types of monomer, prepolymer and photoinitiator respectively, prepare the ink, and test its curing speed, etc. Conclusion: the UV absorption of dyes has a great influence on the curing properties; the higher the functional degree of the active monomer, the faster the curing speed; the higher the activity of the prepolymer is, the less the chain transfer occurs, the better the curing property of the prepolymer is. The higher the UV absorption is in the wavelength range of UV-LED, the higher the initiation efficiency is, and the better the photoinitiator is.

**Keywords:** Dye · Photoinitiator · Curing rate · 3D printing

## 1 Introduction

With the development and progress of technology, color 3D printing technology will be one of the important trends in the future. In 2007, Object geometries corporation released a solojet 3D printing technology that uses an array nozzle to spray light-cured resin onto a substrate and then solidify it with ultraviolet light. This technique is the best all-color 3D printing scheme in the world at present, which can realize voxel level 3D printing results. The trend of color 3D printing in China is just beginning. Polyjet 3D printing technology is mainly realized by color rendering and light curing of materials. At present, the cost of this color material is still relatively expensive [1]. The development of color 3D printing ink with dye as color material will reduce the cost of color 3D printing, and expand the application and applicability of light-curing materials. The UV photopolymerization technology has the characteristics of fast, high efficiency and environmental protection [2]. It is widely used in the curing of various inks. UV color ink contains dyes, so the effect of dye addition on curing properties of UV curing materials is studied. The effects of the kinds of dyes, active monomers, prepolymer and photoinitiators on the curing properties were investigated.

## 2 Experimental Raw Materials and Instruments

### 2.1 Experimental Raw Material

Dye: 1# brilliant red (Shandong Hongfu Chemical Co., Ltd.), 2# brilliant red (Auterley Chemical Co., Ltd.), 3# 311 Peach Red (Wen zhou Autelai Chemical Co., Ltd.), 4# Peach Red (Zhongshan Hengtai Technology material Co., Ltd.), 236# brilliant red and 237# brilliant red (Kunshan Wanfukai Chemical Co., Ltd.) [3, 4].

Prepolymer: V100 Hyperbranched Acrylate (cyanide), EB270 Aliphatic Polyurethane Acrylate (Guangdong, China), EB150, EB870 Hyperbranched Polyester Acrylate (Zhan Xin Resin Shanghai Co., Ltd), LED01 Mixtures of polyhydroxyacrylic resins and thio derivatives (Zhan Xin Resin Shanghai Co., Ltd.) [5].

Active monomer

- (1) Mono-functional monomer: ethoxyethyl acrylate EOEOEA, Acryloyl morpholine ACMO;
- (2) Difunctional monomer: 1,6 hexanediol diacrylate HDDA, dipropylene glycol diacrylate DPGDA, neopentyl glycol diester NPGDA, tripropylene glycol diacrylate TPGDA;
- (3) Trifunctional monomer: trimethylolpropane triacrylate TMPTA (Tianjin Tianjiao Chemical Industry).

Free radical photoinitiator: 1-hydroxycyclohexylphenyl ketone 184, phenyl bis (2, 4, 6-trimethylbenzoyl) phosphine oxide 819, thiophenyl benzoxy cyclic acetone 907N, 2-isopropyl azantronone ITX, 2, 4, 6-trimethylbenzoyl-diphenyl phosphate oxide TPO, 1508, DETX; oxygen inhibitor: ammonia EHA.

### 2.2 Laboratory Apparatus

Electronic balance (Orhaus instrument (Changzhou) Co., Ltd.) HJ-6 Multi-head Magnetic heating Mixer (Jintan Jinnan instrument Manufacturing Co., Ltd.) UV-2700 UV-2700 UV-visible Spectrophotometer (Japan Shimadzu Company) UV-LED curing Machine (Ivata) Shanghai) Precision Optoelectronic Co., Ltd.

## 3 Ink Preparation

### 3.1 Determination of UV Absorption of Dyestuffs

The dye solution is prepared according to the concentration of the general ultraviolet test solution. First, take a certain amount of monomer, add dye, stir evenly with glass rod, put it in HJ-6 magnetic agitator for 5 min, and continue to prepare different concentration dilution solution with the same monomer. Then the dilute solution of dye was tested by UV-LED- ultraviolet spectrophotometer, and the absorption of ultraviolet spectrum of each dye was tested.

### 3.2 Preparation of Dye Inks

According to the content of each component in the formula, we first add monomer, dye, prepolymer, photoinitiator and so on to the beaker. Then the 20 min is heated on the HJ-6 multi-head magnetic heating agitator, and then the heating button is closed and the 10 min is stirred continuously.

## 4 Curing Property Test

At room temperature, 10 cm long and wide 5 cm films were cut, and then coated with hand-coated filament rods (12  $\mu\text{m}$ ). UV-LED curing light sources (385 and 395 nm, power 60 W) were used to solidify the films. The intensity of the fixed light sources remained constant and the speed of the conveyor belt was adjusted. With the fastest can make ink surface and inner layer solidification at the same time conveyor speed for the ink curing speed [6].

## 5 Analysis of Test Results

### 5.1 Selection of Dyes

#### 5.1.1 UV Absorption Analysis of Dyes

The absorption of different kinds of dyes in the homograft is different. The wavelength of the curing machine used in this experiment is 385 and 395 nm. In order to avoid the curing wavelength, the UV absorption test must be carried out to find the appropriate 'light transmittance window'.

Obviously, the less the dye absorbs at this wavelength, the better the curing performance of the ink is. Moreover, considering the color effect, the larger the absorption in the 500–600 nm ranges, the better. In this experiment, six dyes were selected to dissolve in monomeric EOEOEA. The results are as follows.

The UV absorption peak of fuchsin dye is 530–580 nm. It can be seen from Fig. 1 that the absorption peak of 3 # dye is more suitable for this experiment under the same monomer concentration. The 3# dye and 4# dye in the 385–395 nm ranges are the two dyes with the lowest absorption intensity in the 385–395 nm ranges, and the two dyes coincide in this range.

#### 5.1.2 Analysis of Curing Properties of Dyes

In order to measure the curing rate, six dyes were mixed into ink and cured on UV-LED curing machine. The test results are shown in Fig. 2.

As can be seen from Fig. 2, the 3 # dye and the 4 # dye have the lowest absorption at 385–395 nm, and the curing speed is the fastest; 2 #, 3 # and 4 # dyes have strong absorption at 385–395 nm, and the curing speed is also particularly slow. According to the experimental results, the types of dyes have a great influence on the curing performance of the ink.

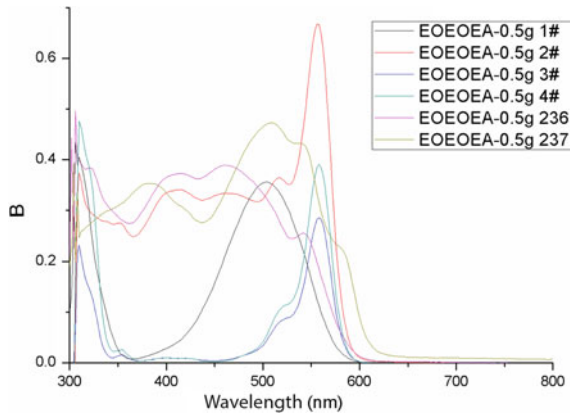


Fig. 1. UV absorption spectra of different dyes in the same monomer

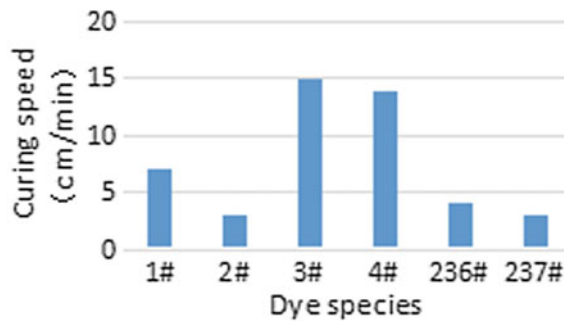


Fig. 2. Curing rate of different dyes in the same monomer

From Figs. 1 and 2, it is analyzed that the dye has the lowest absorbance and the fastest curing speed in the range of 385–395 nm, so the dye is selected in this experiment.

## 5.2 Effects of Active Monomer Types on Curing Properties

Active monomer, also called diluent, not only dilutes the prepolymer in the reaction, but also is used as dye solvent [6]. Therefore, the effect of its kind on the curing speed of three-dimensional photocuring materials is obvious. The types of prepolymer, photoinitiators and dyes in the fixed materials, changing the types of monomers, preparing dye inks, and testing the curing rate of dyes, as shown in Fig. 3.

As can be seen from Fig. 3, the curing speed of the monofunctional monomer EOEOEA is slower than 5 m/min, because the reactive group content of the monofunctional reactive monomer is low resulting in a lower photocuring speed, however, the curing speed of the monofunctional monomer ACMO is relatively fast to 35 m/min because the nitrogen atom contained in the molecule can reduce oxygen resistance.

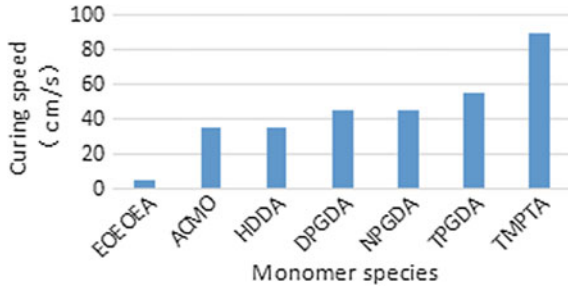


Fig. 3. Effect of monomer type on curing rate

There are two active groups in each molecule of DPGDAN, NPGDA and TPGDA which can take part in the reaction, so the photocuring rate is faster than that of single functional group. In the same way, the ratio of active group of trifunctional group is more than that of bifunctional group, so the curing speed of trifunctional group is faster. As shown in Fig. 3, the monomer TMPTA has the fastest curing speed.

### 5.3 Effect of Prepolymer Types on Curing Properties

The prepolymer is the basic skeleton of the three-dimensional printing light-curing material. In order to investigate the influence of the type of prepolymer on the curing rate of the material, the type of fixed active monomer, the type of photoinitiator and the type of dye, the type of prepolymer can be changed. Dye ink was prepared and its curing rate was measured. The experimental results are shown in Fig. 4.

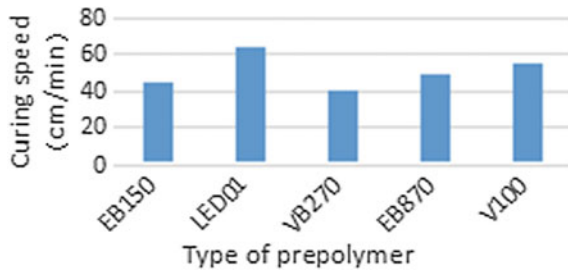


Fig. 4. Effect of type of prepolymer on curing properties

According to Fig. 4, it is easy to see that different kinds of prepolymer have different effects on curing properties. The curing rate of aliphatic polyurethane acrylate EB270 prepolymer was relatively low because of its low activity and the difficulty of forming long chain polymers in a short time. The curing rate of LED01 prepolymer is 65 cm/min, which is a mixture of polyhydroxyacrylic resin and Sulfur derivative, because of its high activity and low chain transfer, it can form long chain polymer in a short time.

#### 5.4 Effect of Photoinitiator on Curing Rate

The curing properties of color 3D printing materials are mainly determined by photoinitiator. Photoinitiator is the fundamental reason for the prepolymer and active monomer solidification, so the correct selection of photoinitiator is of great significance to this experiment. In this experiment, 7 kinds of photoinitiators were selected, the other components were fixed, the dye ink was prepared, and the curing rate was measured. The experimental results are shown in Fig. 5.

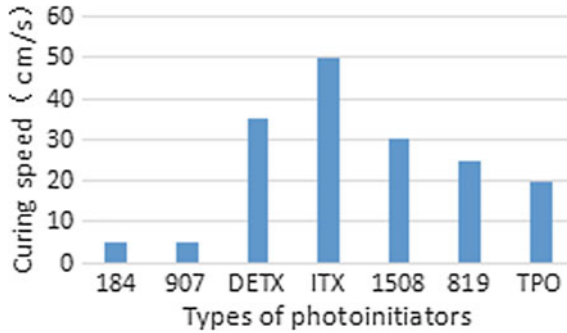


Fig. 5. Effect of photoinitiator on curing rate

The most important principle of choosing photoinitiator is that the absorption peak of photoinitiator should coincide with the spectral band of the UV source used [7]. As can be seen from Fig. 5, when curing with a fixed light source, the curing rate of ink prepared with different photoinitiators varies greatly; the fastest initiator is ITX, which is because the effective absorption peak of photoinitiator ITX is at 382 nm. The initiator efficiency is relatively high, so the curing speed of the dye ink prepared by it is faster; However, the curing rate of photoinitiator 184 and photoinitiator 907 is the smallest, mainly because the effective absorption peak of 184 is at 246 and 278 nm, and the absorption at 385–395 nm is weaker [8], so the curing rate is relatively slow.

## 6 Conclusions

Based on the study of the curing properties of dye ink, the following conclusions are drawn: the absorption of the dye is the lowest in the wavelength range of light source, the curing speed is the fastest, the curing speed of the three-functional group active monomer TMPTA is the fastest; the prepolymer LED01 of polyhydroxy acrylic resin and sulfur based derivatives has the best curing effect, and the fastest curing rate of the photoinitiator ITX at the effective absorption peak at 382 nm.

**Acknowledgements.** This study is funded by the program “Research on the Key Technologies of True Color 3D Printing” (No. KM: Ec201805), College Student Research Program of Beijing Institute of Graphic Communication ‘Research on the Solidification Speed of Color 3D Printing Materials’ and ‘Preparation and Photopolymerization Properties of UV-Curing Fluorescent Inks’.



## References

1. Shi, Y. S., Zhang, L. C., Bai, Y., & Zhao, Z. Y. (2015). The development of 3D printing technology and its software implementation. *Journal of Chinese Science*, 45(2), 197–198.
2. He, Y. X., & Chen, G. X. (2015). Study on color 3D printing based on UV ink-jet. *Packaging Engineering Inc.* 36(9), 134–135.
3. Xia, X. G., Xu, L. L., Han, W. P., Zhu, Z., & Wu, G. D. (2017). Research progress of reactive fluorescent dyes. *Dyes and Dyeing*, 54(6), 3–5.
4. Song, H. (2005). Study on waterborne dye ink for color inkjet printer 5, 27–32.
5. Zhang, W., Wei, X. F., Huang, B. Q., & Feng, Y. (2008). Effects of monomers and prepolymer on the performance of UV inkjet. *Information Recording Material*, 9(1), 3–4.
6. Guo, C. L. (2015). Study on UV photocuring material for flexo printing materials. *Journal of Beijing Institute of Graphic Communication*.
7. (2018). *What are the principles for the selection of initiators?* <http://m.xuzhi.net/m25/1105163.html>. Accessed 11 July.
8. Li, Y. R. (2016). UV-LED inkjet ink dispersion and curing study. *Journal of Beijing Institute of Graphic Communication*.



# Study on Pretreatment of Non-permeable Substrate Used for Printing Conductive-Ink

Rui Zhou, Zhiqiang Gao<sup>(✉)</sup>, Xintang Liu, and Rui Niu

Printing and Packaging Engineering, Shanghai Publishing and Printing College,  
Shanghai, China  
gaozq@sppc.edu.cn

**Abstract.** Apart from a high requirement for the precision of graphics, the refinement of printing electronics ink needs to involve functional printing ink. The pretreatment of substrate, especially non-permeable substrate, holds the key to ensure printing accuracy without compromising the performance of printing ink. Therefore, the topic deserves more efforts to investigate the feasibility of enhanced printing ink and mass production. In this study, PET was first pretreated through the process including plasma, coating (PVA and PVP) and then both particle-type and non-particle type (silver ammonia complex) nano silver ink were printed and sintered. The final findings indicated that particle-type nano silver ink achieved a better electrical property on PET with PVA coating while non-particle type nano silver ink advanced its electrical property on PET pretreated by plasma.

**Keywords:** Non-permeable substrates · Conductive-ink · PVP · PVA · Coating

## 1 Introduction

Different from traditional printing, printing electronics technology has a strict requirement for both graphics accuracy and material performance. To ensure neat edges for higher graphics accuracy, and even and smooth spreading of internal materials for functional stability while electrical conducting functional material is in middle of sedimentation, the researchers dedicated themselves to optimization of printing process, optimization of ink materials and pretreatment of substrates [1]. Ink materials and substrates were given special consideration in the study. Substrate is technically categorized into two types, which are permeable substrate, represented by paper and textile, and non-permeable substrate, including plastic film and glass. Coffee-ring effect, a key to ink spreading, is mostly influential on non-permeable substrate. To advance graphics precision, two approaches are adopted to pretreat non-permeable substrate such as plasma and coating [2, 3]. Functional ink material is usually present in two forms, particle-type functional ink and non-particle type functional ink. To manufacture particle-type functional ink, the researchers need to first turn functional filler into micron-level or nano-level particle, nanowire or sheet, and semi-products are dispersed into solution after macromolecule encapsulation [4]. That is where ink comes from. Once the printing is done, solution evaporates into gas, and nanometer materials

are connected to form functional layers through sintering [5]. The manufacturing process of non-particle type functional ink is a different story. Ink originates from solution with functional materials or ones in a form of complex. Functional materials precipitate gradually, and functional layers come into being during a high-temperature pretreatment.

For the sake of coffee-ring effect, drops leave layers of uneven sediments on unpretreated PET film after evaporation and drying. In the study, unpretreated PET film is not considered. PET film is applied as non-permeable substrate and later pretreated by plasma and coating (PVP and PVA resin). Sedimentary particle-type and non-particle type nano silver ink are sintered to form conductive layers. Four-probe method is employed to measure resistance and analyze the impact of different inks on electric conductivity, therefore investigating how different pretreatments of on-permeable substrates influence functional layers.

## 2 Experiment

### 2.1 Materials (Substrate/Ink) Preparation

PET films with a thickness of 0.1 mm were tailored into  $100 * 100 \text{ mm}^2$ , followed by plasma radiation pretreatment for 20 s or coating pretreatment. There were two types of coating liquids used in the study: (a) PVA resin blended with nano  $\text{SiO}_2$  powder; (b) PVP liquid. Liquids were separately applied to PET films. The reason why the PVP did not add  $\text{SiO}_2$  is that when applied  $\text{SiO}_2$  with high concentration PVP, will cause agglomeration. Current experimental conditions cannot solve this problem. PET films with coating were placed in the oven for 24 h at a temperature of  $80^\circ$ . Silver particles with a size of between 50 and 80 nm were dispersed into 40% diethylene glycol monomethylether aqueous solution by ultrasonic machine, to develop 30 wt% particle-type nano silver ink. 12 wt% silver complex ink was prepared with silver oxalate as a silver source, ethylenediamine as a complexing agent as well as isopropyl alcohol as solution.

### 2.2 Printing Pretreatment

Dimatix 2831 printer was employed to match two types of ink with three substrates. The substrate with particle-type ink was first tested by SEM for morphological characteristics. All samples were sintered in the oven at a temperature of  $120^\circ$ . Then the morphology of substrate with non-particle type ink was observed through SEM (ZEISS Sigma 500). In the end, four-point probe was used to measure sheet resistance of all samples.

## 3 Results and Discussion

Clear graphics margins of three pretreated substrates were observed in SEM images. That means the pretreatment has improved the accuracy of all graphics. However, morphology and conductivity varied in various substrates, which would be discussed in detail.

### 3.1 PET Printing Pretreated with Plasma

The drawing shows that particle-type ink is well arrayed on the substrate pretreated with plasma in general, but cracks are observed in some areas, because plasma breaks down macromolecule chains of PET substrate, leading to an enhanced surface energy for an effective control over ink spreading. In addition, ink mobility decreases and thus suspended particles are more likely to adhere to PET with high surface energy, while ink is being dried. However, it is not strong enough to restrict the ink motion, causing the crack. By contrast, non-particle type ink acquires a compact and even surface after sintering. The possible explanation is that non-particle type ink has been already spread evenly before the high-temperature pretreatment. When it is placed in the oven, solvent vaporizes with a growing viscosity and a decreasing mobility. Therefore, the motion is disabled while silver element is separate. As time goes by, silver element turns into an even silver film. Partial flaws and stacking are caused by PET surface defect (Figs. 1 and 2).

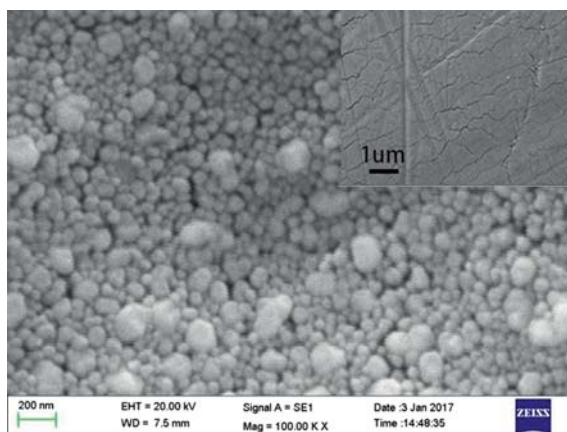


**Fig. 1.** Particle-type ink on PET

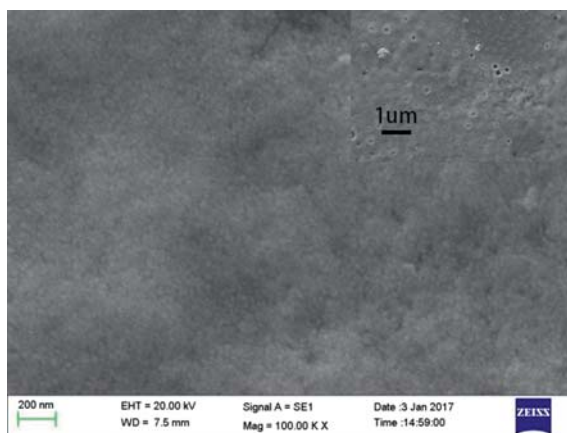


**Fig. 2.** Non-particle type ink on PET

### 3.2 PVP Coating

After particle-type ink is printed on PET substrate with PVP coating, there is a remarkable distribution defect of microstructure. Even fractures occur regularly on the macro level. The main reason lies in PVP coating swells while absorbing ink solution, along with an uneven shrinkage during the drying. As a result, nano silver particles may migrate with PVP macromolecule chains which they adhere to, which is finished within dozens of microseconds. Given that the regularity is consistent with the interval of two successive ink droplet printings, it is the sequence of droplet during the deposition which leads to the regular swelling and shrinkage (Figs. 3 and 4).

For non-particle type ink, there is a sheet-like microstructure with voids in-between sheet structures. On the macro level, the surface looks rough, loose and even, mainly

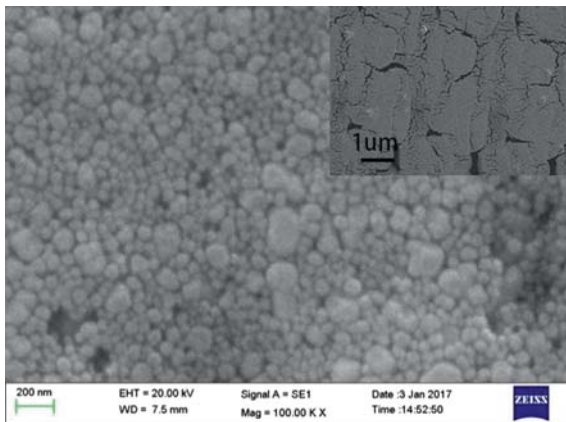


Fig. 3. Particle-type ink on PVP coating PET

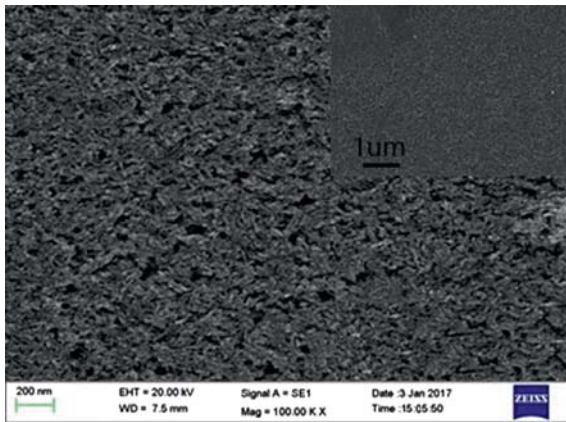
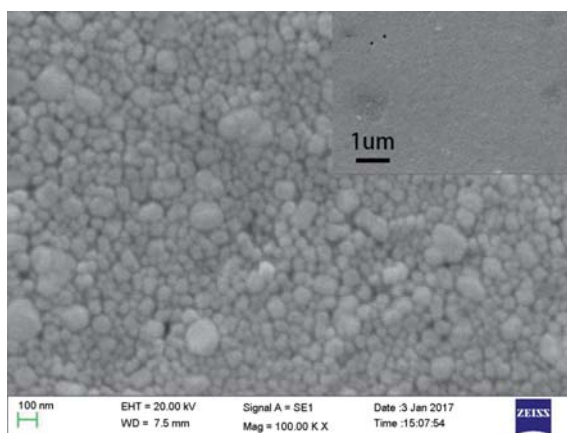


Fig. 4. Non particle-type ink on PVP coating PET

because silver element has precipitated and PVP molecular chains have been intertwined during sintering and curing. Also, PVP intermolecular binding force is not strong, causing the shrinkage of sheet structures connected by silver elements.

### 3.3 PVA Resin Blended with Silicon Dioxide Coating

Particle-type nano silver Ink is well spread on PET with PVA resin coating. It looks perfect as well on the macro level. PVA resin combined with silicon dioxide nano particles are empowered with fine water absorption. With water-absorbing resin covering silicon dioxide, the coating surface acquires a microstructure with more surface areas. In addition, silicon dioxide acts as a coating stent to effectively prevent swelling during the wetting or shrinkage during the drying, therefore creating a steady coating. Non particle-type ink shows a rod-like structure on such a substrate. The macrostructure is comparatively even with porosities, which is caused by penetration of non particle-type Ink into coating. After sintering, the structure is more like an original one (Figs. 5, 6 and 7).



**Fig. 5.** Particle-type ink on PVA resin blended with silicon dioxide coating PET

It indicates that the elementary structure of PVA coating is characterized by a rod-like shape, stacking and porosity. The structure increases surface areas and controls the ink spreading. Nano silver ink particles accumulate on the coating. Especially, small nano particles gather inside the conductive pattern within the range of 2 and 5  $\mu\text{m}$ , since there is a restricted motion on droplet margin during the drying. In general, the regularity of droplet margin is ensured and the overall homogeneity of conductive layers is guaranteed because of microstructure absorption.

### 3.4 Conductivity

Conductivities of various samples after sintering are listed in Table 1.

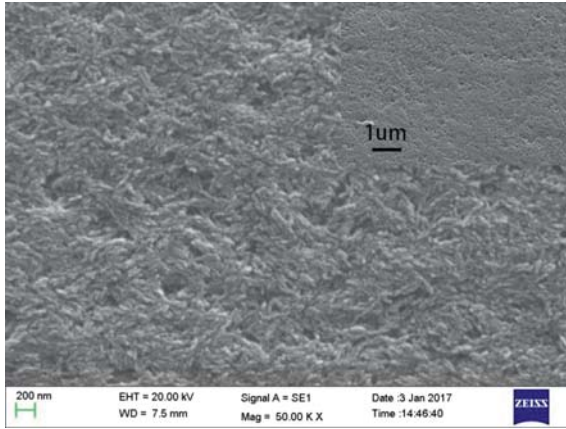


**Fig. 6.** Non particle-type ink on PVA resin blended with silicon dioxide coating PET

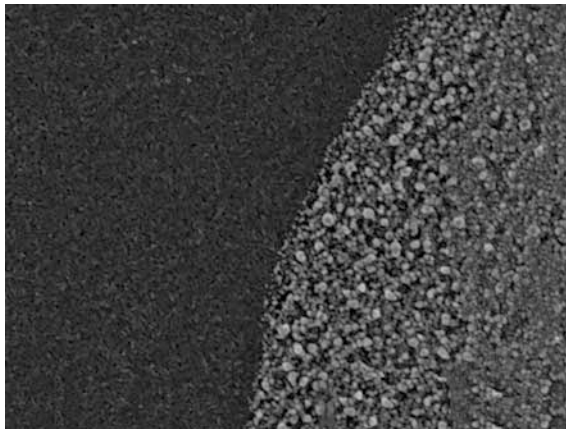


**Fig. 7.** The border between PVA coating and nano silver particle layer

**Table 1.** Square resistance of particle-type and non particle-type nano silver-ink on PET treat with plasma or coating

Nano silverink type	Square resistance (mΩ/Sq)		
	Plasma	PVP	PVA
Particle	112.50	–	12.65
Non-particle	80.21	–	–

Because of swelling, particle-type conductive-ink is disconnected on PVP coating and fails to form connected and effective conductive layers. After plasma pretreatment, PVA coating is given a higher homogeneity. That is because surface microstructure

decreases the motion of silver particles inside ink. In particular, PVA's fast absorption of solution reduces the motion time of nano silver particles. By contrast, non particle-type ink is dissolved in the coating and later precipitates along with coating structure during the heating, so it is impossible to form silver films.

## 4 Conclusions

Given microstructure and forming process of functional materials, different surface pretreatment specific to ink types can enhance the performance of functional materials.

PVA water-absorbing resin coating mixed with silicon dioxide may absorb ink solution quickly, reduce the evaporation duration and prevent shrinkage of polymer coating during the drying, eventually leading to conductive layers with sheet resistance of up to  $12.65/\text{m}^2$ . By contrast, non particle-type conductive-ink penetrates into coating and silver element cannot be connected after precipitation. Therefore, conductive layers with sheet resistance of  $80.21/\text{m}^2$  can only be achieved while substrate without coating is pretreated.

**Acknowledgements.** This study is supported by Lab of Green Platemaking and Standardization for Flexographic Printing.

## References

1. Yin, Z. P., Huang, Y. A., & Bu, N. B., et al. (2010). Inkjet printing for flexible electronics: Materials, processes and equipments. *Chinese Science Bulletin*, 55(30), 3383.
2. Liu, X., Yunzhi, C., & Si, Z. (2005). Effect of silica and alumina on coating structure and printing quality of inkjet paper. *International Paper*, 24(3), 10–13.
3. He, J., Lv, L., & Wang, H. (2013). The influence of photo paper substrate structure on the performance of spray printed conductive patterns. *Materials Herald*, 27(22), 69–71.
4. Yue, D., Li, X., Mu, Z., & Sun, X. (2016). Preparation, properties and applications of particle-free silver-based conductive inks. *Precious Metals*, 37(B11), 69–74.
5. Denneulin, A., Blayo, A., Neuman, C., et al. (2011). Infra-red assisted sintering of inkjet printed silver tracks on paper substrates. *Journal Nanoparticle Research*, 13(9), 3815.



**Part VIII**  
**Film and Related Material Technology**



# Preparation and Characterization of Non-woven Blend Membrane from CA and PES in DMAc/LiCl

Aiai Wang<sup>1,2</sup> and Zhonghua Sun<sup>1,2</sup>(✉)

<sup>1</sup> College of Engineering, Qufu Normal University, Rizhao, Shandong, China  
sun.zhonghua@163.com

<sup>2</sup> Tianjin Key Laboratory of Pulp & Paper, Tianjin University of Science & Technology, Tianjin, China

**Abstract.** In this article, in order to improve the hydrophilicity and anti-fouling ability of the pure PES membranes, CA was introduced in N,N-dimethylacetamide/lithium chloride with non-woven fabric as support. The influence on *PIF* was studied, and the preparation condition was optimized as follow: PES, 18 wt%; PVP K30, 4 wt%; CA, 3 wt%; Evaporation time, 20 s. The characteristics of membranes were studied by means of SEM, anti-fouling performance and compatibility. The compatibility results showed CA/PES membrane was a semi-compatibility system. The results indicated that the performances such as hydrophilicity and anti-fouling ability were improved remarkably with the addition of cellulose acetate.

**Keywords:** Cellulose acetate · Anti-fouling property · Membrane · N, N-dimethylacetamide/lithium chloride · Non-woven

## 1 Introduction

PES has excellent mechanical properties, high thermal stability, good chemical resistance and film formation [1, 2]. However, the membrane flux and anti-fouling performance of PES membrane were not ideal due to its inherent hydrophobicity and PES film easy to be adsorbed by fouling agent [3].

The cellulose esters have showed excellent biocompatibility, fouling resistance and processability, which have attracted extensive attention of researchers. Moreover, it is a kind of environment-friendly material and inexhaustible resource [4]. However, cellulose esters have defects in mechanical strength, oxidation degree, thermal chemistry and chemical resistance, which limit their application [5]. Cellulose acetate (CA), which has good hydrophilicity, is widely used, and many studies have shown that CA can be mixed with suitable polymers to meet new performance requirements [6, 7].

In membrane separation processes, excellent permeability and strong chemical resistance to feed flow of the porous membranes are needed. In the process of membrane usage, both its separation performance and service life are affected by membrane pollution. And membrane is limited by its hydrophilicity, but this can be improved by changing the components and proportion.

In this study, DMAc/LiCl (N, N-dimethylacetamide/lithium chloride) was used as the solvent and PVP (polyvinylpyrrolidone) was used as the pore-forming agent to form a uniform and stable casting solution, which was then scraped onto the non-woven fabric to form a film. The optimum preparation conditions were studied and discussed in detail.

## 2 Experimental

### 2.1 Materials and Methods

Cellulose acetate ( $M_w = 61,000$ ) was supplied by Sinopharm Chemical Reagent Co., Ltd and dried under vacuum at  $50\text{ }^\circ\text{C}$  for 24 h at least. Bovine serum albumin (BSA,  $M_w = 67,000$ ) was supplied by Beijing Aoboxing Biological Technology Co., Ltd. All other chemicals were of analytical grade and were used as received. The microstructures of the membrane were observed by SEM images, which were shot by JSM-6700F scanning microscope.

### 2.2 Preparation of Membranes

The separation membranes were prepared by phase inversion method [8]. A certain amount of PVP and CA were dissolved in DMAc/LiCl solvent, and a certain amount of PES were added to form the casting solution, then which was placed to take off the bubbles for 24 h.

The casting solution was scraped onto the non-woven fabric surface. After the solvent evaporated at room temperature for some time, the regenerated film was then put into the coagulation bath of deionized water for the removal of the residual solvent. Before the characterization, the membrane was placed in deionized water. Since thermodynamic influence factor, similar casting conditions should be ensured in the experimental process. Figure 1 illustrated the above process in a simplified sequence flow diagram.

### 2.3 Anti-fouling Filtration Experiments

The illustration of the filtration experiments was shown in Fig. 2. The pure water flux (*PWF*) was measured under 0.1 MPa pressure, and calculated according to the following equation [9]:

$$PWF = Q/(A \cdot t) \quad (1)$$

where  $Q$  is the permeation amount (L);  $A$  is the membrane area ( $\text{m}^2$ );  $t$  is the time (h).

The BSA solution (1 g/L) was used as the model to test the antifouling property. The shaking table adsorption method was used to evaluate the antifouling performance of membranes.

The membranes were placed into BSA solutions and shook for 1 h at  $25\text{ }^\circ\text{C}$ . The adsorption fouling under zero pressure was expressed with *FD* and the adsorption fouling under pressure was expressed with *FA*.

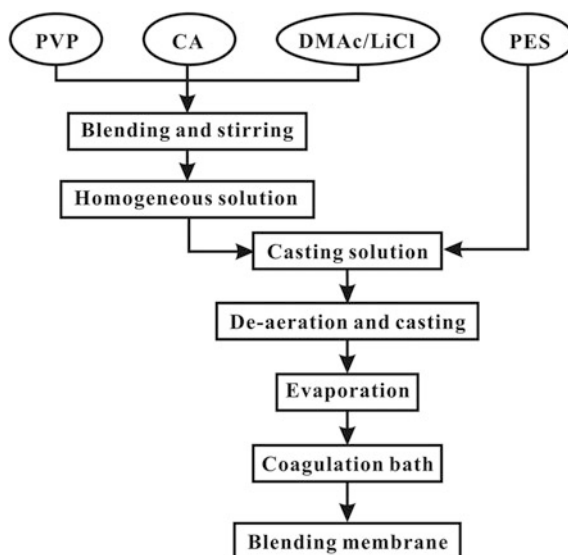


Fig. 1. Preparation process of blend membranes

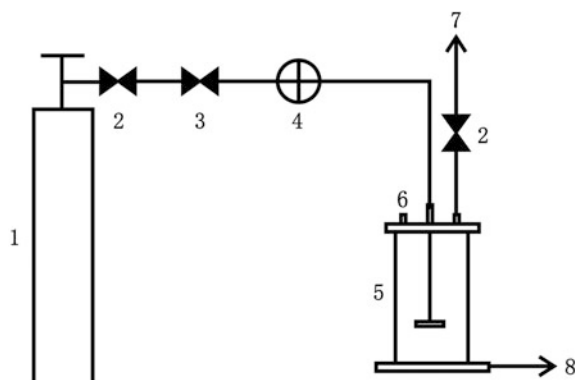


Fig. 2. Schematic diagram of the filtration apparatus 1-nitrogen cylinder, 2-cut-off valve, 3-relief valve, 4-regulator valve, 5-MSC300 Ultrafiltration cup (Shanghai Mosu, China), 6-feed inlet, 7-blowdown, 8-discharging outlet

$$FD = (T_0 - T_w)/T_0 \times 100\% \quad (2)$$

where  $T_w$ , is the  $PWF$  after adsorption;  $T_0$ , is the  $PWF$  before adsorption.

The BSA solution (1 g/L) was used as the feed solution and a new filtration experiment was done for 1 h at 25 °C.

$$FA = (F_0 - F_w)/F_0 \times 100\% \quad (3)$$

where  $F_w$ , is the *PWF* after experiment;  $F_0$ , is the *PWF* before experiment.

### 3 Results and Discussion

#### 3.1 The Water Flux

The effects of concentration and evaporation time on *PWF* were shown in Fig. 3. It could be found from Fig. 3a that *PWF* of the membrane showed a downward trend when PES concentration ranged from 12 to 22 wt%. This may be caused by the fact that, the increase of PES concentration led to the increase of solution viscosity, and the molecular chains intertwining, making the membrane surface denser, and thus limiting the free flow of polymer molecules. In the process of phase transformation, the solvent system including solvent and nonsolvent was impeded, resulting in smaller pore size and lower porosity. Thus, when PES concentration increased over 18 wt%, the *PWF* decreased significantly.

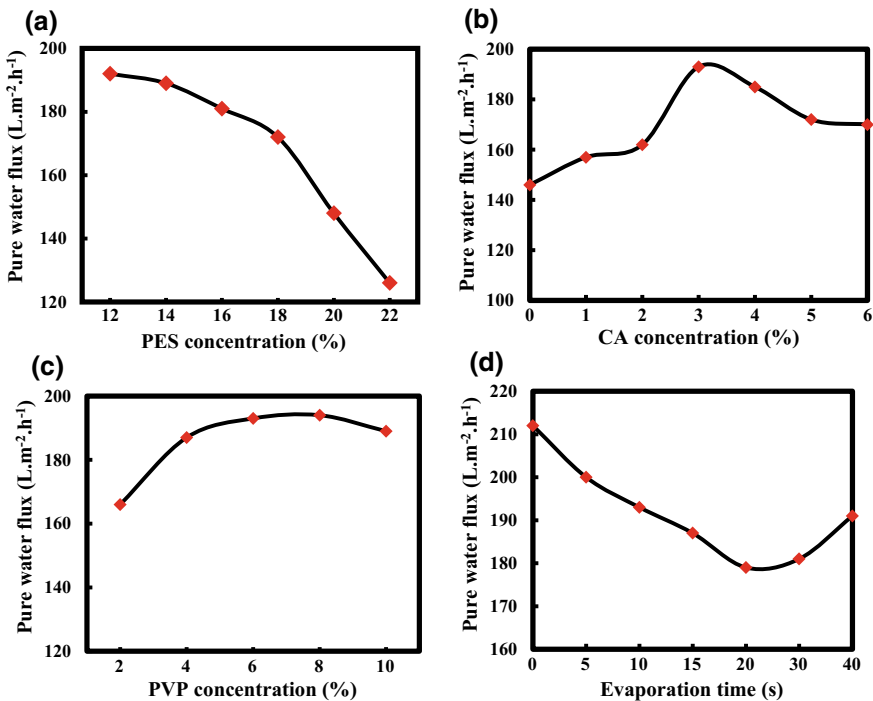


Fig. 3. Effects of concentration and evaporation time on *PWF*

It could be found from Fig. 3b that the *PWF* increased first and then decreased when CA was added to the casting solution. When CA concentration changed from 0 to 3 wt%, the *PWF* of the film increased, and the maximum value was reached when CA concentration was 3 wt%. The *PWF* of the film began to decrease when the amount of CA continued to increase. The hydrophobicity, porosity and pore connectivity of the porous membrane were improved by adding CA into the casting solution, so that *PWF* of the membrane was improved. When the content of CA was relatively low, the increase of *PWF* was mainly affected by the hydrophilic porosity and pore connectivity. However, when CA content was too high, the *PWF* of the membrane began to decrease, which was caused by excessive CA starting to aggregate in the membrane, resulting in the reduction in porosity and pore connectivity [10].

PVP is a hydrophilic additive that can be dissolved by water. After the initial polymer film was immersed in water, the part occupied by PVP would become microspores, so the porosity would increase with more PVP contained in the casting solution. Therefore, the *PWF* could be improved by adding CA. However, because of the reaction between PVP and CA, the porosity and *PWF* could be reduced if overmuch CA was added. Therefore, 3 wt% was the appropriate CA amount.

It could be found from Fig. 3c that the *PWF* increased slowly with the amount of PVP was further increased, and then appeared in a slightly phase downtrend. PVP moved from polymer solution into solidification bath.

When the concentration of PVP was low, the demixing process was mainly affected by the thermodynamic properties, so that the phase separation of the solution was improved. However, with the further increase of the concentration of PVP, viscosity buildup was higher than thermodynamic factors, which delayed the solution demixing. The increase of the solution viscosities made the *PWF* appear slight decrease.

It could be found from Fig. 3d that the *PWF* decreased firstly and then increased. With the evaporation of solvent, the membrane surface concentration increased, providing the foundation for forming a dense surface layer, which may hinder the exchange of the solvent and non-solvent in the course of immersion, so immersion in the water bath was greatly prevented for PVP [10]. The holes on the membrane surface became smaller over time, and the surface was getting denser and denser, thus the *PWF* reduced. In addition, since DMAc had strong water absorption capacity. As the time going, the water absorption of membrane was further improved, which indicated the membrane structure would be looser and the pore would be too large.

Take all factors into account, the preparation condition was optimized as follow: PES, 18 wt%; PVP K30, 4 wt%; CA, 3 wt%; Evaporation time, 20 s.

### 3.2 Anti-fouling Property

It could be found from Fig. 4 that the hydrophilicity and the anti-fouling property were enhanced with the CA added. The hydrophilic CA promoted the exchange of solvent and non-solvent in the course of phase separation. The hydrophilic group moved towards the membrane surface, reducing the free energy, forming more hydrogen bonds.

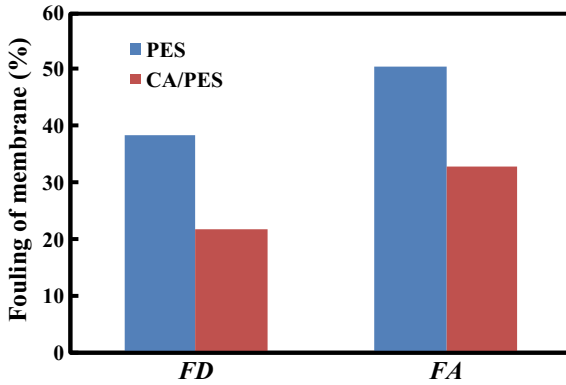


Fig. 4. Anti-fouling property of membranes

### 3.3 Compatibility

The compatibility of blends has been studied by using viscosity method [11]. For compatible mixtures, the viscosity change is linear and indicates a single-phase system. An incompatible system may appear an S-type viscosity curve, representing two opposite phases. The semi-compatible system may appear a non-linear (not S-type) curve. The curve properties of semi-compatible blends systems are completely different from those of the above two systems, the curves of it are non-linear at most concentrations.

It could be seen from Fig. 5 that the viscosity diagram of the mixed solution was non-linear (not S-type) with the increase of CA concentration, which indicated that CA/PES solution was semi-compatibility.

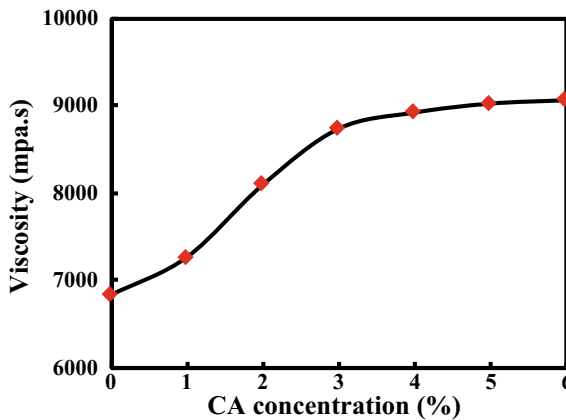
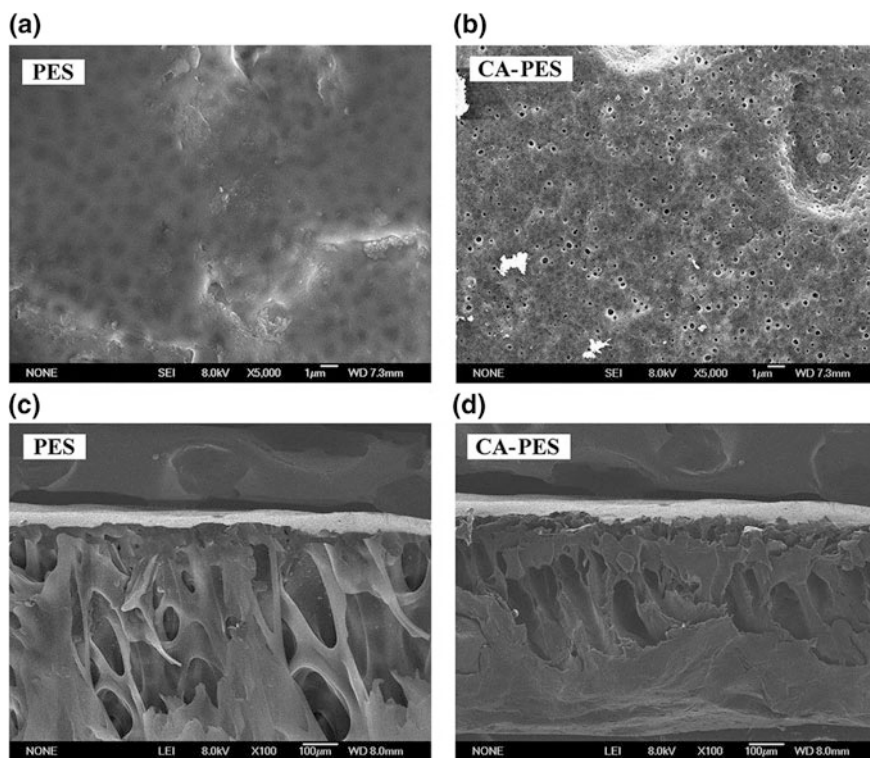


Fig. 5. Compatibility of CA/PES solution

### 3.4 Morphology

Figure 6 showed the surface and cross-sectional SEM images of membranes. It was found that numbers of micropores occurred on the surface of the blend film. The incorporation of CA and PVP led to a better hydrophilicity, which accelerated the diffusion of solvent and nonsolvent.



**Fig. 6.** Surface SEM images (a, b) and cross-sectional SEM images (c, d)

The results showed that CA and PVP had greatly changed the porous structure from sponge-like structure to finger-like structure. The addition of hydrophilic CA promoted the exchange of solvent and non-solvent in the course of immersion and formed a large pore and finger-like structure [12].

In summary, it could be concluded that CA/PES membranes had better *PWF* and anti-pollution performance. Furthermore, the CA/PES membranes had a flat surface in Fig. 7.



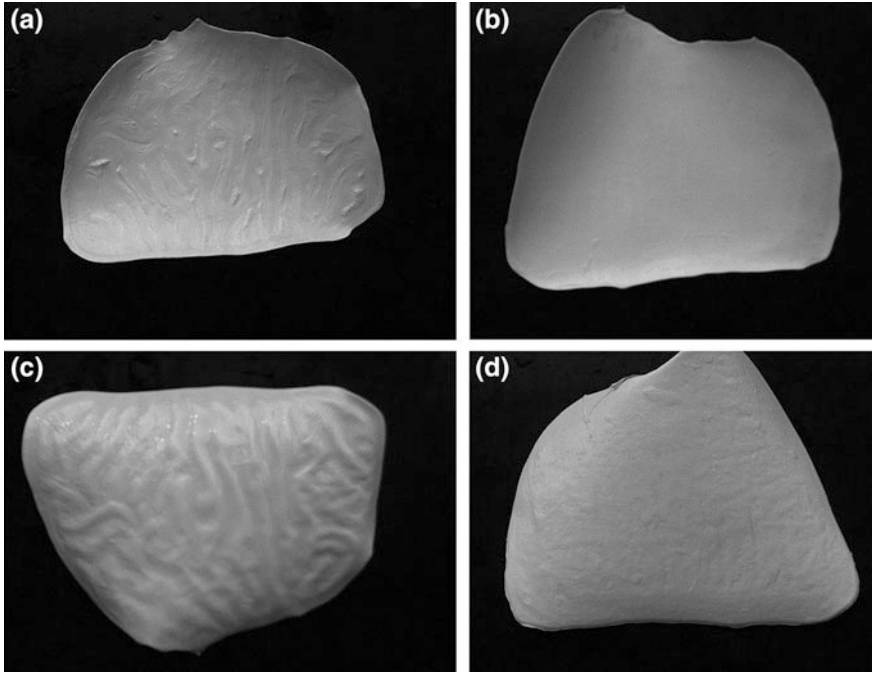


Fig. 7. The membrane photographs of PES (a, c) and CA/PES (b, d)

## 4 Conclusions

The hydrophilic materials had greatly changed the membrane structure from spongy to finger-like structure, which made the *PF* and anti-fouling performance get better.

**Acknowledgements.** The authors would like to acknowledge the financial supports from Shandong Provincial Natural Science Foundation, China (Grant No. ZR2017MB040) and A Project of Shandong Province Higher Educational Science and Technology Program, China (Grant No. J15LC03). The authors are also grateful for the project supported by the Foundation (Grant No. 201604) of Tianjin Key Laboratory of Pulp & Paper (Tianjin University of Science & Technology), China.

## References

1. Yi, Z., Zhu, L. P., Xu, Y. Y., et al. (2010). Polysulfone-based amphiphilic polymer for hydrophilicity and fouling-resistant modification of polyethersulfone membranes. *Journal Membrane Science*, 365(1), 25–33.
2. Ananth, A., Arthanareeswaran, G., & Wang, H. (2012). The influence of tetraethylorthosilicate and polyethyleneimine on the performance of polyethersulfone membranes. *Desalination*, 287(8), 61–70.

3. Mousavi, S. M., Dehghan, F., Saljoughi, E., et al. (2012). Preparation of modified polyethersulfone membranes using variation in coagulation bath temperature and addition of hydrophilic surfactant. *Journal of Polymer Research*, 19(7), 9861.
4. Rajesh, S., Shobana, K. H., Anitharaj, S., et al. (2011). Preparation, morphology, performance, and hydrophilicity studies of poly(amide-imide) incorporated cellulose acetate ultrafiltration membranes. *Industrial and Engineering Chemistry Research*, 50(9), 5550–5564.
5. Maheswari, P., Barghava, P., & Mohan, D. (2013). Preparation, morphology, hydrophilicity and performance of poly (ether-ether-sulfone) incorporated cellulose acetate ultrafiltration membranes. *Journal of Polymer Research*, 20(2), 1–17.
6. Sivakumar, M., Mohan, D. R., & Rangarajan, R. (2006). Studies on cellulose acetate-polysulfone ultrafiltration membranes: II. Effect of additive concentration. *Journal of Membrane Science*, 268(2), 208–219.
7. Nagendran, A., & Mohan, D. R. (2008). Cellulose acetate and polyetherimide blend ultrafiltration membranes: II. Effect of additive. *Polymers Advance Technology*, 19(1), 24–35.
8. Rahimpour, A., Madaeni, S. S., Shockravi, A., et al. (2009). Preparation and characterization of hydrophile nano-porous polyethersulfone membranes using synthesized poly(sulfoxide-amide) as additive in the casting solution. *Journal Membrane Science*, 334(1), 64–73.
9. Fushan, C., & Zhonghua, S. (2013). Preparation of homogeneous grafting cellulose and partial substitution for polyethersulfone membrane material. *Carbohydrate Polymers*, 95(1), 85–90.
10. Li, G., Tang, B., & Wu, P. (2009). An experimental investigation of evaporation time and the relative humidity on a novel positively charged ultrafiltration membrane via dry-wet phase inversion. *Journal Membrane Science*, 326(1), 168–177.
11. Chattopadhyay, S. (2000). Compatibility studies on solution of polymer blends by viscometric and phase-separation technique. *Journal of Applied Polymer Science*, 77(4), 880–889.
12. Blanco, J. F., Nguyen, Q. T., & Schaetzel, P. (2002). Sulfonation of polysulfones: Suitability of the sulfonated materials for asymmetric membrane preparation. *Journal of Applied Polymer Science*, 84(13), 2461–2473.



# Nanocellulose Prepared from Cassava Residues by Mechanochemical Method and Its Hydrophobic Modification

Yinghan Shi<sup>1</sup>, Guangxue Chen<sup>1(✉)</sup>, Qifeng Chen<sup>1</sup>, and Lijie Huang<sup>2</sup>

<sup>1</sup> State Key Laboratory of Pulp and Paper Engineering,  
South China University of Technology, Guangzhou, China  
chengx@scut.edu.cn

<sup>2</sup> Light Industry and Food Engineering College, Guangxi University,  
Nanning, China

**Abstract.** This study prepared nanocellulose from cassava residues by the mechanochemical method which adopted phosphoric acid as aids and used high-speed dispersion to offer mechanical force, aiming to improve the properties of such biodegradable materials as PLA, PHA and PVA and make full use of cassava residues. Stearic acid is used to improve the dispersity of the prepared nanocellulose, so that it can be well dispersed into some biodegradable materials with small polarity. In addition, these materials may also be hydrophobic after the addition of the modified nanocellulose. Nano Particle Analyzer, SEM and FTIR were applied to characterize the properties of the nanocellulose and the modified nanocellulose, and the dispersity of modified nanocellulose was characterized by the dispersity test. The results show that the size of the nanocellulose is between 15.1 and 18.1 nm, and there are a lot of small holes on its surface that leads to the increase of specific surface area. This modified method belongs to that of surface modification which can reduce the surface polarity of the nanocellulose and make it dispersed into the polar solvents.

**Keywords:** Mechanochemical · Cassava residues · Nanocellulose · Hydrophobic modification

## 1 Introduction

Cellulose synthesized by the photosynthesis of plants is one kind of organic high-molecular polymer. The annual production of newly produced cellulose on the earth exceeds  $15 \times 10^{12}$  tons by now [1]. Cellulose belongs to one kind of extensive renewable resource. As the world is now faced with severe challenges in environment and resource shortages. Therefore, people pay more attention to the basic research and practical application of renewable resources such as cellulose. For example, many studies use cellulose as raw materials to prepare nanocellulose expecting to replace petroleum raw materials has become one of the current research hotspots [2].

People have begun to develop nanoscale materials with the development of new materials' preparation. They find that nanomaterials have effects of small volume,

surface, interface, and quantum tunneling which leads to its optical, electrical, and chemical properties are more excellent compared with common micron-scale materials [3].

Nanocellulose prepared from cellulose is defined as a material which diameter is less than 1000 nm in a broad sense. According to the specific morphology, nanocellulose can be classified into needle-like nanocrystalline cellulose (NCC), fibrillar cellulose nanofiber (CNF) and network micro fibrillated cellulose (MFC) [4]. As a kind of nanoscale material extracted from natural cellulose, nanocellulose is not only abundant, renewable and degradable, but also has high elastic modulus, tensile strength and crystallinity. Also, nanocellulose features in large aspect ratio, external hydroxyl group, specific chemical modification and good biocompatibility [5], and it is also characterized by large specific surface area, high reactivity and good small size effect.

In this paper, cassava residues were used as raw material to prepare nanocellulose by mechanochemical method. To improve its dispersibility, this paper attempts to carry out hydrophobic modification with stearic acid, expecting to use it in the field of biodegradable packaging materials in the future.

## 2 Materials and Methods

### 2.1 Materials

Cassava residues cellulose (self-made); Phosphoric acid ( $H_3PO_4$ ) (Chemical Reagent Co., Ltd. Guangzhou, China); Anhydrous ethanol (Zhiyuan Chemical Reagent Co., Ltd. Tianjin, China); Stearic acid ( $C_{18}H_{36}O_2$ ) (Sanyuan Fine Chemical Co., Ltd. Wujiang, China).

High-Speed Disperser (LSFS400, Changzhou Lianbao Mechanical Equipment Co., Ltd.); Ultrasonic cleaner (YL-A, Wenzhou Ouhai Ultrasonic Equipment Co., Ltd.); Electric thermostatic blast drying oven (DGG-9053AF, Shanghai Senxin Experimental Instrument Co., Ltd.); Refrigerated speed centrifuge (HemaTGL, Hunan Wanda Equipment Co., Ltd.).

### 2.2 Preparation of Samples

#### 2.2.1 Preparation of Nanocellulose Suspension

First, 6 g of cassava residues cellulose was weighed, and then 120 ml of 98% phosphoric acid was poured into a beaker, then mixing them. The mixed solution was poured into a high-speed disperser at a speed of 900 r/min, and stirred at room temperature for 120 min. After the reaction, the solution was centrifuged over and over again with distilled water until its PH was neutral. Next, the solution was diluted with distilled water and the suspension was maintained at 60 °C for 60 min in an ultrasonic environment of 20 kHz and 40 W. Finally, after leaving to rest for some minutes, a nanocellulose suspension was obtained.

#### 2.2.2 Hydrophobic Modification of Nanocellulose

First, 20 ml of the above-prepared nanocellulose suspension was taken, and after stirring, 15 ml of absolute ethanol was added to the beaker. The solution was then

placed in an ultrasonic environment for 30 min. After sonication, the solution was placed in a constant temperature magnetic stirrer at 78 °C for 10 h. Finally, the solution was centrifuged with absolute ethanol. The Supernatant was discarded, and the precipitate was dried with the freeze dryer.

## 2.3 Characterization

### 2.3.1 Nanoparticle Size Analysis

0.5 ml of the nanocellulose suspension was pipetted into a 250 ml volumetric flask and allowed to stand for a period of time to stabilize the formulation solution to a certain concentration. Once a day, the particle size was measured by using the Malvern Nano Particle Size Analyzer.

### 2.3.2 Scanning Electron Microscope

First, the nanocellulose suspension and modified nanocellulose were dried with a freeze dryer. And a certain amount of cassava residues cellulose was dried to constant weight at 40 °C. A small number of dried samples were adhered to a conductive adhesive and sprayed with gold. The Scanning Electron Microscope was used to observe the morphologies of different samples.

### 2.3.3 Fourier Infrared Spectrometer Analysis

First, a certain amount of potassium bromide was weighed in an oven at 40 °C, and then the samples were ground after drying. 200 mg of treated potassium bromide powder was accurately weighed into a sampler tank, pressed it into uniform transparent flakes. Then it was measured on a Fourier infrared spectrometer as a blank background; after that, 2 mg of cassava residues cellulose, 2 mg of nanocellulose, and 200 mg potassium bromide were weighed and mixed them uniformly. The tablets were evenly pressed and a tablet machine was used to make it as transparent as possible. Finally, measurements were made on a Fourier infrared spectrometer.

### 2.3.4 Dispersion Experiment

The modified nanocellulose was dried in an oven at 40 °C in advance. The selected three sets of solvent combinations were observed as shown in Table 1.

**Table 1.** The solvent's combination in dispersion test

Sample	Solvent's combination	Polarity size
A	Ethyl acetate/distilled water (under)	4.3/10.2
B	Dichloromethane/distilled water (on)	3.4/10.2
C	Toluene/distilled water (under)	2.4/10.2

The experimental samples were all dispersed into the solvent's combinations at 4 mg/ml.

### 3 Results and Discussion

#### 3.1 Particle Size Analysis

The particle sizes of the three measurements are shown in Table 2. As can be seen from Table 2, we see that the nanocellulose prepared by this method mainly has a length from 229.5 to 248.4 nm and a diameter from 15.1 to 18.1 nm. A small particle size at 17.8% with a length of 10.59 nm and a diameter of 0.3321 nm appeared in the first measurement, but it doesn't appear in the latter two measurements. This may be because that the distribution of the prepared nanocellulose has a large size range when it is just prepared, and the nanocellulose with small size agglomerates every other day. According to the relevant literature, the number average length of individual fibers in cassava residues is around 0.6 mm, and the fiber's diameter is around 0.02 mm [6]. The results show that mechanochemical force reduces the length and the diameter of the cellulose in the cassava residues, wherein the cellulose produced is nanosized.

**Table 2.** The results of particle sizes by Malvern nanoparticle size analyzer

Times	Peak	Length (nm)	Diameter (nm)	Distribution (%)
First	Peak1	248.4	18.1	82.2
	Peak2	10.59	0.3321	17.8
Second	Peak1	229.5	18.34	100
Third	Peak1	246.4	15.1	100

#### 3.2 Surface Morphology

Figure 1a shows the SEM image of the cassava residues cellulose. It can be observed that the cassava residues cellulose is mainly composed of good sheet-like fiber bundles. The image of nanocellulose prepared by mechanochemical method is shown in Fig. 1b. What can be seen is that the surface of cellulose is further exfoliated and the fibrous tissue is exposed more, which indicates that under the effect of phosphoric acid and high-speed disperser, the structure of cellulose is still maintained. From the analysis of 3.1 above, we can see that the particle size of nanocellulose is pretty small. There are many small pores on the surface of the cellulose with the effect of mechanochemical force. The specific surface area of the cellulose is increased so much because of so many active hydroxyl groups on the cellulose surface. Therefore, it is very easy to form molecules. Inter-hydrogen bonds and van der Waals forces between the nanoparticles will also increase, so the nanocellulose will still agglomerate after freeze-drying.

The SEM images of modified nanocellulose are shown as Fig. 1c, d. From Fig. 1c, it can be observed that most of the nanocellulose is modified successfully by stearic acid. This is because the addition of stearic acid increases the barrier between nanoparticles, and to a certain extent, inhibits the trend of interparticle collisions that leads to the agglomerates [7]. There is also a small portion of nanofibrillar cellulose which is not wrapped, but gathers tightly together. Figure 1d shows a partial enlarged view of a representative bulk of modified nanocellulose. What can be seen is that the

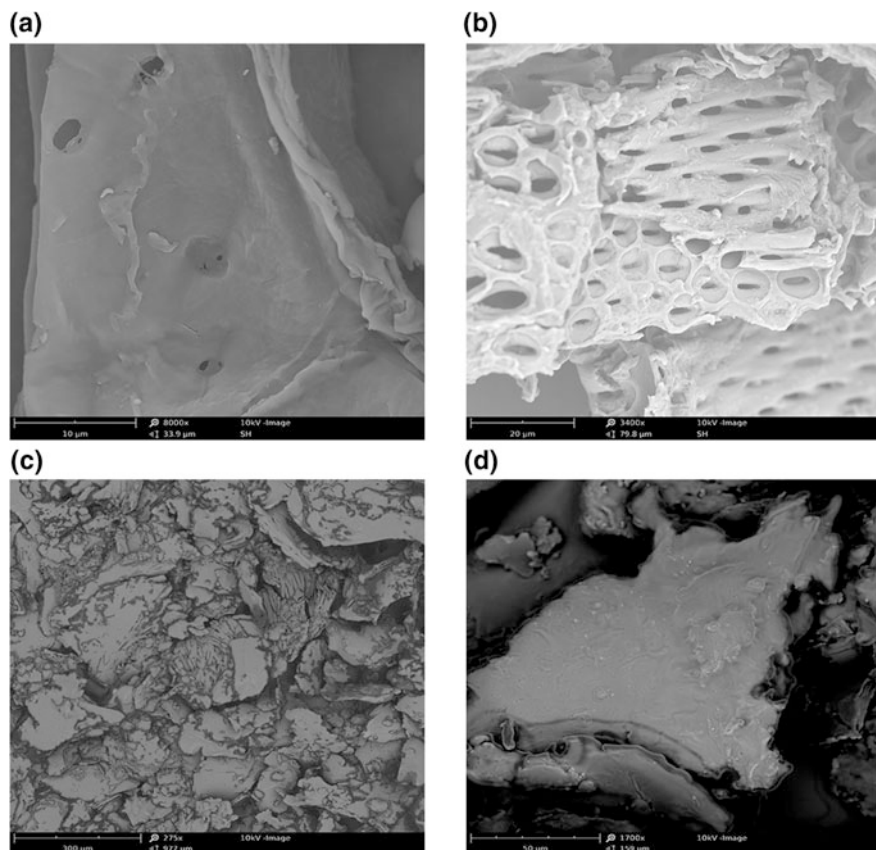


**Fig. 1.** SEM images of cassava residues cellulose (a), nanocellulose (b) and hydrophobically modified nanocellulose (c, d)

surface of the modified nanocellulose is somewhat rough. Because of the introduction of low surface energy stearic acid, a similar rough structure with a hydrophobic surface is formed just like the lotus leaf.

### 3.3 Fourier Infrared Spectrometer Analysis

The FTIR results of cassava residues cellulose, nanocellulose and modified nanocellulose are just shown in Fig. 2a–c respectively. The cassava residues cellulose and nanocellulose were observed from Fig. 2a, b. They all have the characteristic absorption peak from  $2926$  to  $3230\text{ cm}^{-1}$ , which belongs to multi-associative stretching vibration of intermolecular hydrogen bonding. There is the  $-\text{OH}$  vibration of crystal water in cellulose at  $1655\text{ cm}^{-1}$  [8]. Stretching vibration of  $-\text{C}-\text{O}-\text{C}$  and  $-\text{OH}$  deformation vibration in cellulose appears at around  $1030\text{ cm}^{-1}$ . There is small peak absorption at around  $898\text{ cm}^{-1}$  that belongs to the  $-\text{CH}$  rocking vibration of  $\beta$ -1,4-glycosidic bond in cellulose [9, 10]. We can conclude that the structure of cellulose is

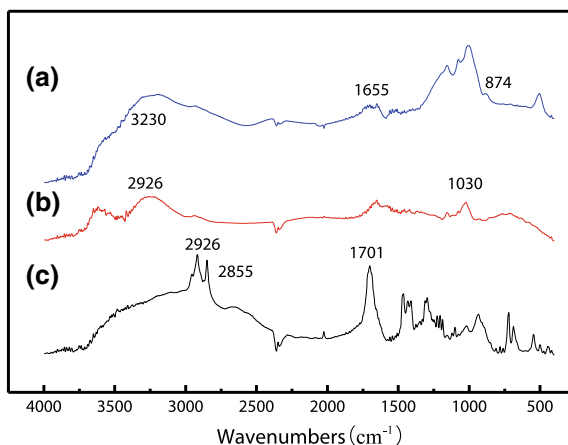


**Fig. 2.** FTIR spectra of cassava residues cellulose (a), nanocellulose (b) and modified nanocellulose (c)

still remained after mechanochemical force. From Fig. 2c, we can see that there are two absorption peaks at 2926 and 2855  $\text{cm}^{-1}$ . Compared with Fig. 2a, b, it may be the collective effect of moderate-strength symmetrical vibration for the  $-\text{CH}$  bond of  $-\text{CH}_3$  in stearic acid and the  $-\text{CH}_3$  of methyl and  $-\text{CH}_2$  of methylene in nanocellulose leads to the  $-\text{CH}_3$  in stearic acid grafted on the surface of nanocellulose. With a peak at around 1701  $\text{cm}^{-1}$ , the vibration of the  $-\text{C}=\text{O}$  bond in the modified nanocellulose is strong. This peak is attributed to esters, which is the occurrence of  $-\text{COOH}$  in stearic acid and  $-\text{OH}$  in modified nanocellulose. The result of esterification reaction in the chemical reaction happens between stearic acid and nanocellulose. Through a comprehensive analysis, what can be found is that the modification by using stearic acid belongs to one kind of surface modifications, and there is an esterification reaction between  $-\text{COOH}$  in stearic acid and  $-\text{OH}$  in nanocellulose while hydrophobic group  $-\text{CH}_3$  is grafted on the nanocellulose's surface.

### 3.4 Dispersion Experiment

The dispersive results of samples are shown in Fig. 3. The polarities of distilled water, ethyl acetate, dichloromethane and toluene are 10.2, 4.3, 3.4 and 2.4 respectively. From the solution with ethyl acetate/distilled water (under) in group A, we can see that the modified nanocellulose could not be dispersed in water, but could be dispersed in ethyl acetate with a small amount. There is a little modified nanocellulose at the interface between ethyl acetate and distilled water. In the combination of distilled water/dichloromethane (B, water on), the modified nanocellulose is more dispersed in methylene chloride. The modified nanocellulose is almost dispersed in toluene from the combination of toluene/water (C, water down). It can be concluded that the smaller the polarity of the solvent is, the more dispersive modified nanocellulose is. This is due to the fact that a large amount of  $-\text{COOH}$  in stearic acid is condensed with  $-\text{OH}$  in nanocellulose and a hydrophobic group  $-\text{CH}_3$  is introduced for reducing the surface



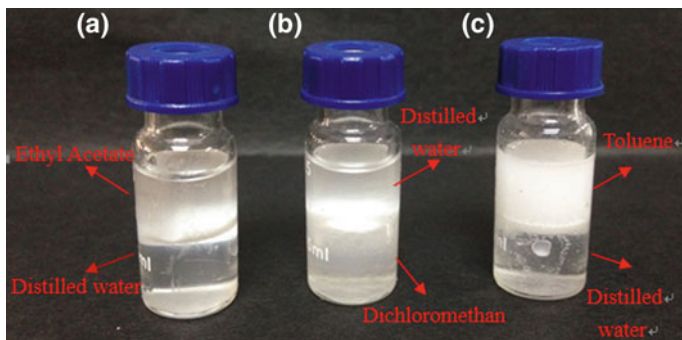


**Fig. 3.** Results of dispersive test

polarity of nanocellulose. Dispersion experiments show that stearic acid modifies the polarity of nanocellulose's surface, improving the dispersion of nanocellulose in non-polar solutions. It can be also concluded that the modified nanocrystals have a certain degree of hydrophobicity.

## 4 Conclusions

This study used cassava residues cellulose as raw materials to prepare nanocellulose by mechanochemical method which used high-speed disperser to offer mechanical force and adopted phosphoric acid as a chemical agent. The prepared nanocellulose has a small particle size with the length being mainly between 229.5 and 248.1 nm and the width being between 15.1 and 18.1 nm. SEM results show that the prepared nanocellulose has more reticular fiber structures, and its surface has many small pores with large specific surface area, which is conducive to the occurrence of graft copolymerization. From the infrared spectrum results, the nanocellulose still has the basic structure of cellulose, indicating that the preparation of this method doesn't destroy the structure of cellulose. During the entire preparation process, there are little damages of equipment and cassava residues cellulose. The preparation time is short and the process is less polluting.

This modification with stearic acid of nanocellulose belongs to that of surface graft. The esterification reacts between  $-OH$  in nanocellulose and  $-COOH$  in stearic acid, which also introduces the hydrophobic group of  $-CH_3$  on the surface of nanocellulose. The results of the dispersive test show that after the modification with stearic acid, the nanocellulose's polarity becomes smaller and can be well dispersed in solvent with a small polarity. The smaller the polarity is, the more modified nanocellulose is dispersed. In the future, we can try to add this modified nanocellulose with a small polarity into biodegradable materials, with an expectation of preparing green packaging materials which has excellent properties.

**Acknowledgements.** Thanks for the support given to this work by the Science and Technology Project of Guangdong Province (No. 2017B090901064), the Science and Technology Project of Guangzhou (No. 201607020045) and the Fundamental Research Funds for the Central Universities (Nos. D2154620).

## References

1. Klemm, D., Heublein, B., Fink, H. P., et al. (2005). Cellulose: Fascinating biopolymer and sustainable raw material. *Angewandte Chemie International Edition*, 544(22), 3358–3393.
2. Li, J. (2014). *Hydrophobic modification of nanocellulose and its application in pulp and papermaking*. Jinan: Qilu University of Technology.
3. Cao, G. (2004). *Nanostructures & nanomaterials: Synthesis, properties & applications*. Imperial College Press.
4. Dufresne, A. (2013). Nanocellulose: A new ageless bionanomaterial. *Materials Today*, 16(6), 220–227.
5. Salas, C., Nypelö, T., Rodriguez-Abreu, C., et al. (2014). Nanocellulose properties and applications in colloids and interfaces. *Current Opinion in Colloid & Interface Science*, 19(5), 383–396.
6. Tao, Z. (2012). *Synthesis, characterization, retention and aiding properties of functional derivatives of Cassava residue*. Guangzhou: South China University of Technology.
7. Cao, K., Wu Y., et al. (2016). Preparation and characterization of stearic acid modified nanofibrillated cellulose. *Technological Innovation and Application*, 28, 32–33.
8. Xiong, L., & Yu, W. (2013). Microscopic infrared spectroscopic analysis of cellulose molecular structure after acid treatment. *Cellulose Science and Technology*, 02, 59–62.
9. Fan, H., Wang, X., & Wang, Y. (2014). Rapid determination of wood cellulose content by Fourier Transform infrared spectroscopy. *Wood Processing Machinery*, 04, 33–37.
10. Liu, Y., Shao, G., & Xu, T. (2010). Infrared spectra analysis and comparison of bamboo fiber and other natural cellulose fibers. *Bamboo Research Journal*, 03, 42–46.



# Effects of Lignin on Properties of Hemicellulose/Methyl-Cellulose Composite Films

Lingxiao Liu, Maohai Lin<sup>(✉)</sup>, Guichun Hu, Meiqi Lin,  
and Zhengpeng Wu

School of Printing and Packing Engineering, Qilu University of Technology,  
Jinan, China  
mhlin@qlu.edu.cn

**Abstract.** In this paper, in order to explore the effect of lignin on properties of hemicellulose/methyl-cellulose composite film, hemicellulose/lignin/methyl-cellulose composite films which were with different mass fraction of lignin successfully were prepared by using solution blending method. The morphology of the composite films was characterized. The composite films were tested for its absorbency, hydrophilicity, and tensile strength. The results showed that there was a strong interaction and good compatibility between the lignin, hemicellulose and methyl-cellulose in the composite films; the addition of lignin reduces the absorbance of the composite films and improves the water resistance of the composite films. With the increase of lignin, the tensile strength of the composite films first increases and then decreases. When the lignin content is 10%, the tensile strength of the composite film is as high as 40.95 Mpa, which is 77% higher than that without lignin.

**Keywords:** Methyl-cellulose · Lignin · Composite film · Properties

## 1 Introduction

With people's attention to physical health, food safety has become indispensable, and the edible packaging composite film has emerged. A healthy and environmentally friendly packaging film is urgently needed to replace those traditional packaging films that are harmful to us. Among them, methyl-cellulose has good water solubility, rich raw materials and good film-forming properties, and its membrane is transparent and bright, which is an ideal new edible film [1]. However, it also has shortcomings such as poor water resistance and low tensile strength. The composite films can improve the performance of the film, however, the composite film of lignin, hemicellulose and methyl-cellulose has not been reported. In this experiment, a series of composite film was prepared by adding lignin with different contents to hemicellulose/methyl-cellulose. The relationship between the ratio of the film-forming liquid and the films performance was studied [2]. Through testing the performance of several composite film and screening the best ones, it is expected that the composite film will have the

best comprehensive properties and provide basic theoretical basis for optimizing the selection of edible composite film.

## 2 Experimental

### 2.1 Materials and Instruments

Main materials: methyl-cellulose; hemicellulose (self-made); alkali lignin (self-made); hydrochloric acid; sodium hydroxide; pH test paper. Main instruments: Digital thermostatic water bath, Changzhou Boyuan Experimental Analytical Instrument Factory; Optical contact angle measuring instrument, Germany KRUSS; X-Rite I5 spectrophotometer; Intelligent electronic tensile testing machine, Jinan Language Electromechanical Technology Co., Ltd.

### 2.2 Preparation of Samples

#### 2.2.1 Preparation of Lignin/Methyl-Cellulose/Hemicellulose Composite Films

Preparation of methyl-cellulose solution, hemicellulose solution, and lignin solution: mix the three in different proportions to obtain a composite film solution in which the total mass of three solute was 0.6 g and the ratio of methyl-cellulose to hemicellulose was 7:3 (Previous experiments have concluded that the performance of such composite membranes is best). The scale is shown in Table 1. HCl was added to a well-prepared solution till it turned to neutral that pH is 6 or 7 when it was measured with a pH test paper. After fully mixing, the final solution was transferred to the petri dish with a liquid shifter and dried for 5 days to form 6 homogeneous composite films [3].

**Table 1.** Solution measurement of methyl-cellulose/hemicellulose/lignin composite films

Sample name	MC mass fraction/%	Hemi mass fraction/%	Lignin mass fraction/%
Sample 1	70.0	30.0	0
Sample 2	66.5	28.5	5.0
Sample 3	63.0	27.0	10.0
Sample 4	59.5	25.5	15.0
Sample 5	56.0	24.0	20.0
Sample 6	52.5	22.5	25.0

### 2.3 Characterization

#### 2.3.1 Absorbance

The absorbance was measured with color i5 spectrophotometer [4]. During the measurement, the spectral absorption from 360 to 750 nm of the composite films were measured by irradiating the composite films with D65 standard light. Average of experimental results is made.

### 2.3.2 Hydrophilicity

The contact angle test was performed with an optical contact angle meter. Uniform, flat composite films without defects were selected and cut into 30 mm × 8 mm film samples. The prepared films were attached to the sample stage with double-sided adhesive and tested for contact angle. Average of experimental results.

### 2.3.3 Tensile Strength

A smart electronic tensile tester is used. The uniform, clean, flawless samples were selected. And they would be cut into 10 mm wide rectangles, with a pitch of 50 mm and a speed of 5 mm/min. Average of experimental results.

## 3 Results and Discussion

### 3.1 Effect of Lignin on Film Form of Composite Films

In Fig. 1, with the increase of lignin, the composite film gradually becomes yellow from a transparent color. According to the naked eye observation and the physical properties of the film itself, the film forming property is not very good, for example, it is too brittle and soft to remove from the film-forming petri dish; when the lignin content increases, the possibility of films formation are greatly increased, and the films

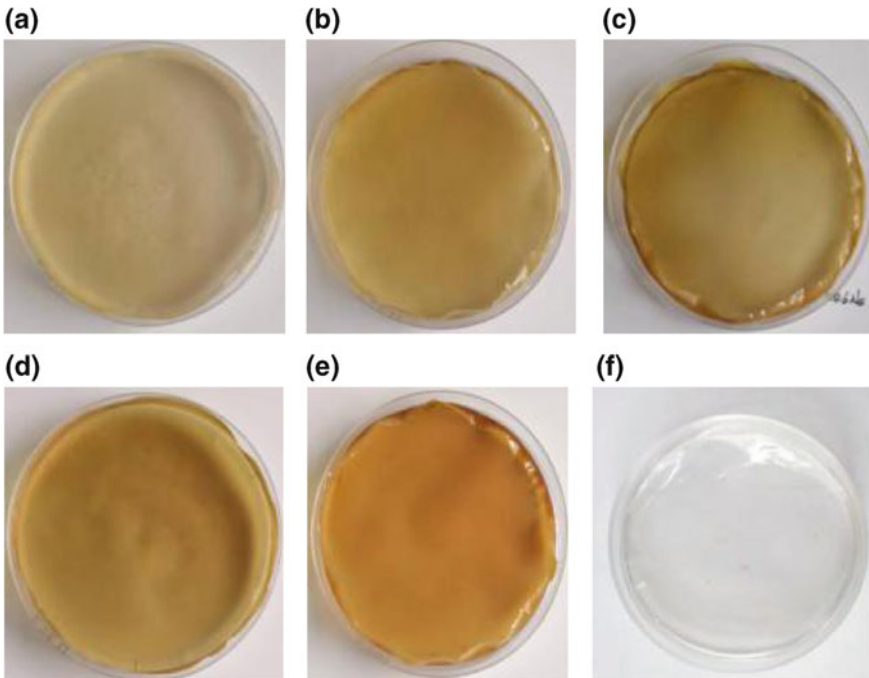


**Fig. 1.** Effect of lignin content on film formation of composite films: **a** 0% lignin; **b** 5% lignin; **c** 10% lignin; **d** 15% lignin; **e** 20% lignin; **f** 25% lignin

are less likely to break and are easily peeled off on the film-forming vessel [5]. When the lignin content was from 10 to 25%, the film surface began to wrinkle, and the appearance effect gradually decreased.

### 3.2 Effect of Lignin Content on Absorbance of Composite Films

As shown in Fig. 2, with the increase of lignin content, the absorbance of the composite films basically increased. The main reason may be due to the heterogeneous polymer blended in the formation of the film matrix, the particle size is not the same, the sedimentation velocity is inconsistent, resulting in a larger and uneven particle size in the resulting film leading to a slight decrease in the transmittance of the composite film [6]. Another reason may be due to poor miscibility of the molecules in the blend film, which results in a decrease in the transparency of the film due to scattering or reflection of light at the interface and enhanced light absorption [7].

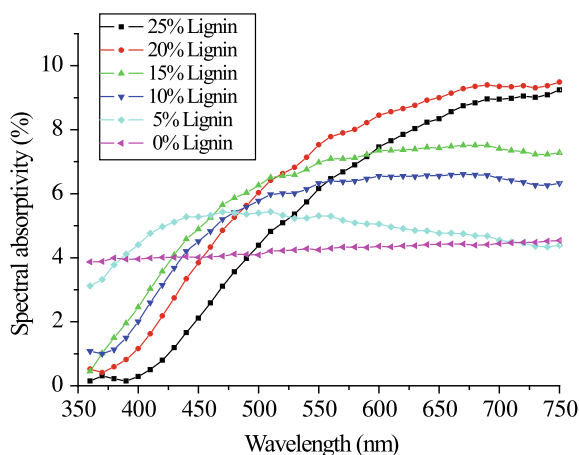
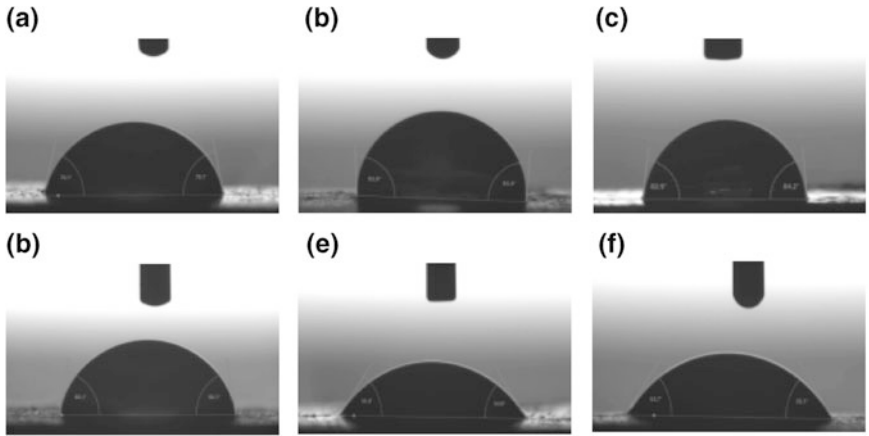


Fig. 2. Effect of lignin content on absorbance of composite films

### 3.3 Effect of Lignin Content on Hydrophilicity of Composite Films

Figure 3 shows that as the lignin content increases, the hydrophilicity of the composite films gradually decreases. When the lignin content is 25%, the hydrophilicity of the composite film is the smallest (In order to verify the accuracy of the results, lignin was added to 30% and the hydrophilicity was still reduced). Hemicellulose and methyl-cellulose are hydrophilic polymer materials, both containing hydrophilic groups [8]. But alkaline lignin is hydrophobic. It can be seen that the hydrophilicity of the composite films is reduced, mainly due to the fact that the alkaline lignin is insoluble in water while the methyl-cellulose and hemicellulose are dissolved in water.



**Fig. 3.** Contact angle of composite films with different lignin content: **a** 0% lignin; **b** 5% lignin; **c** 10% lignin; **d** 15% lignin; **e** 20% lignin; **f** 25% lignin

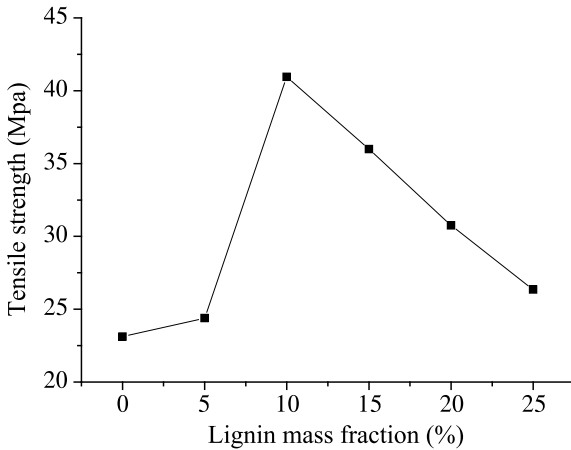


**Fig. 4.** Effect of lignin content on tensile strength of composite films

### 3.4 Effect of Lignin Content on Tensile Strength of Composite Film

As shown in Fig. 4, with the increase of lignin content, the tensile strength of the composite films increases at first and then decreases gradually. And the tensile strength of the composite film is the strongest when the lignin content is 10%. In general, the addition of lignin enhances the strength properties of composite film.

The main reason for this phenomenon may be that hydrogen bonding and van der Waals forces exist between the hemicellulose and the cellulose in the film formation process, and the hemicellulose and lignin may also be connected in the form of benzyl ether to form a Lignin-carbohydrate complex. However, as the lignin content continues to increase, the tensile strength of the composite films decreases. This is due to the fact

that the excessive lignin molecules cannot be combined with the other two molecules, and can only play a filling role, which may lead to a decrease in the tensile strength of the composite films.

## 4 Conclusions

1. With the addition of lignin, the transparency of the composite film is reduced, and the absorption rate of the composite film increases with the increase of lignin.
2. The addition of lignin can effectively improve the hydrophilicity of the composite films. Adding lignin can effectively increase the tensile strength of the composite films. When the lignin content is 10%, the tensile strength of the composite film is as high as 40.95 Mpa, which is 77% higher than that without lignin.
3. It can be concluded that the addition of lignin can effectively improve the overall performance of the composite film. The conclusions will help us to control the ratio of lignin and hemicellulose and methyl-cellulose, so as to obtain an edible packaging composite film that is more helpful to people.

**Acknowledgements.** Shaanxi Key Laboratory of printing and packaging engineering (Project number: 2017KFKT-02).

## References

1. Tong, Z., Han, D., Dachuan, L. I., et al. (2013). Effect of methyl-cellulose on the properties of silica film. *Film Science & Technology*.
2. Luo, Q., Huang, Y., Tang, K., et al. (2013). Methyl-cellulose edible film synthesis and the effect of plasticizer on the mechanical properties. *Journal of Chinese Institute of Food Science & Technology*, 13(10), 8–12.
3. Carrier, M., Windt, M., Ziegler, B., et al. (2017). Quantitative insights into the fast pyrolysis of extracted cellulose, hemicelluloses and Lignin. *Chemsuschem*, 10(16), 3212.
4. Ciolacu, D. E., & Darie, R. N. (2016). *Nanocomposites based on cellulose, hemicelluloses, and lignin. Nanomaterials and nanocomposites: Zero- to three-dimensional materials and their composites. Wiley VCH Verlag GmbH & Co. KGaA*.
5. Zhao, C., Jiang, E., & Chen, A. (2016). Volatile production from pyrolysis of cellulose, hemicellulose and lignin. *Journal of the Energy Institute*, 90(6).
6. Deng, J., Xiong, T., Wang, H., et al. (2016). Effects of cellulose, hemicellulose, and lignin on the structure and morphology of porous carbons. *Acs Sustainable Chemistry & Engineering*, 4 (7).
7. Huang, Y., Wang, L., Chao, Y., et al. (2016). Relationships between hemicellulose composition and lignin structure in woods. *Journal of Wood Chemistry and Technology*, 36 (1), 9–15.
8. Jiang, S. N., Chen-Yu, H. E., Jiang, S. J., et al. (2017). Preparation and properties of hydroxypropyl methyl-cellulose-whey protein concentrates composite film. *Food Science & Technology*.





# A Comparison Study on Thermal Degradation of Two Different Poly (Lactic Acid)/Metal Oxide Hybrids

Xiaojie Wang and Zhen Huang<sup>(✉)</sup>

Department of Packaging Engineering, Tianjin University of Commerce, Tianjin  
300134, People's Republic of China  
huangzhen50@yahoo.com

**Abstract.** A comparison investigation was made on thermal decomposition behaviors of poly (lactic acid) (PLA) hybrids with two different metal oxides of  $\text{TiO}_2$  and  $\text{ZnO}$  by means of thermogravimetric analysis. Experimental measurements were conducted with a scanning rate of 5–20 K/min in nitrogen. Abstracted from non-isothermal decomposition data, thermal degradation temperatures of PLA/metal oxide hybrids were obtained and compared so as to investigate the effects of two metal oxides. The activation energy  $E_a$  for PLA thermal decomposition was calculated by using the Kissinger method and the results implied that the metal oxide added had greatly changed the PLA thermal stability and the service lifespan was predicted based on the  $E_a$  values.

**Keywords:** Poly (lactic acid) · Metal oxide · Thermo gravimetric analysis · Activation energy · Non-isothermal decomposition

## 1 Introduction

Nowadays, biopolymers such as soy protein isolate [1], alginate [2], chitosan [3] and poly (lactic acid) (PLA) [4] have gained great attention because they are biodegradable and demonstrated appreciated properties. PLA has been extensively investigated for the purpose of possibly replacing those synthetic polymers of fossil fuel resources in the near future [4, 5]. For thermally manufacturing various plastic products and handling plastic wastes, thermal properties of PLA must be better understood for such purpose. Therefore, a number of thermal stability studies have been performed in recent years by means of non-isothermal methods and kinetic analyses [6–9]. In this work, we have selected  $\text{ZnO}$  and  $\text{TiO}_2$  because of their possible catalytic effects [10, 11] and investigated their influences on thermal degradation properties of PLA. The activation energies of two PLA hybrids are calculated along with the lifetime estimations for comparison purpose.

## 2 Experimental

### 2.1 Materials

Pristine PLA material was bought from Jinan Daigang Co., Ltd, China whereas  $\text{TiO}_2$  powder (chemical purity, >99.5%),  $\text{ZnO}$  (chemical purity, >99.5%) and  $\text{CHCl}_3$  (analytical purity, >99%) were all purchased from Tianjin Kaitong Chemical Reagent Co. Ltd., China.

### 2.2 Sample Preparation

The metal oxide-filled PLA samples were fabricated by firstly measuring certain amount of oxide powder and then dispersing it into  $\text{CHCl}_3$  in a round-bottom flask under stirring for 30 min, followed by feeding the PLA sample and agitating for 1 h. The resultant PLA suspension was flatted onto a clean glass for evaporating  $\text{CHCl}_3$  in a fume hood. The dried hybrid sample was then heated at 120 °C in an oven for 1 h to completely remove any solvent residual. The samples at a filler loading of 10 wt% were named as T-PLA for  $\text{TiO}_2$  and Z-PLA for  $\text{ZnO}$ , respectively. It should be noted that using such method could render the metal oxide particles generally homogenously distributed in the PLA matrix regardless of the sample thickness.

### 2.3 Thermogravimetric Analysis (TGA)

TGA analysis was conducted on various PLA hybrid samples by means of a Shimadzu DTG-60 analyzer. For each experiment, approximately 8 mg of the sample was loaded and heated from ambient to 750 K in a non-isothermal mode. The heating rate was set to be a constant of 5, 10, 15 or 20 K/min and the purge gas employed was inert nitrogen with a purging rate of 30 ml/min. For each heating rate, the measurement was repeated twice and no variation was observed in the temperature-dependent mass-loss curves.

## 3 Results and Discussion

### 3.1 Thermal Properties of PLA/Metal Oxide Hybrids

TGA spectra results of two different PLA hybrid samples are graphically demonstrated in Fig. 1 for the case of 5 K/min, along with those of pristine counterpart. It can be clearly observed that the overall mass loss is nearly 90% for two hybrid samples at the end of thermal degradation experiment, which is consistent with the same 10 wt% loading of two metal oxides of inorganic nature that were thermally stable under present experimental conditions. As a comparison, the pristine PLA sample is observed to completely burn off. Figure 1 shows that two metal oxides have exhibited similar effects on thermal stabilities of PLA. The addition of  $\text{TiO}_2$  is observed to have rendered PLA thermally degrade at a little lower temperature range than pure PLA while the  $\text{ZnO}$ -added hybrid sample is observed to thermally degrade at very low temperature span than pristine PLA. These findings suggest that adding  $\text{TiO}_2$  and  $\text{ZnO}$  has

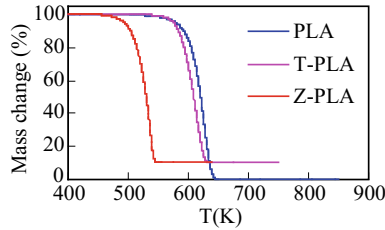


**Fig. 1.** TGA results of PLA and its two hybrid samples obtained at 5 K/min

decreased PLA thermal stability but at different extents. Similar observations are also applied to the other heating rates and these results are not shown here for simplicity purpose.

For better knowing how much two metal oxides to influence the thermal stability of PLA, some specific thermal temperatures are tabulated in Table 1 for PLA hybrids and its pristine sample at a heating rate of 5 K/min. These parameters are abstracted from TGA results shown in Fig. 1 and they are the temperatures at 5 mass% conversions ( $T_5$ ), 10 mass% conversions ( $T_{10}$ ), 50 mass% conversions ( $T_{50}$ ) and 90 mass% conversions ( $T_{90}$ ). The incorporation of  $\text{TiO}_2$  into PLA has boosted these specific temperatures to higher values as compared with pristine PLA. As shown in Table 1, the  $T_5$  and  $T_{10}$  of PLA are 579.47 and 592.32 K, respectively, and they are considerably decreased to 573.71 and 582.29 K, correspondently, after filling the  $\text{TiO}_2$ . Similarly, the  $T_{50}$  and  $T_{90}$  of PLA are seen to go up from 620.50 and 635.34 K to 606.67 and 622.49 K, respectively, for the T-PLA sample. These temperature decrements indicate that filling  $\text{TiO}_2$  into PLA has substantially worsened its thermal stability. Even further, the PLA/ZnO hybrid has greatly lower  $T_5$ ,  $T_{20}$ ,  $T_{50}$  and  $T_{90}$  values than its pure counterpart, and these parameters are respectively 491.01, 501.76, 527.75 and 539.65 K as seen in Table 1. These data have demonstrated that the filled ZnO has rendered the thermal stability of PLA significantly deteriorated. Overall, after adding ZnO or  $\text{TiO}_2$  PLA turns to become less thermally stable than the unfilled one. In the meanwhile, ZnO is observed to exhibit stronger effect than  $\text{TiO}_2$  to deteriorate PLA thermal degradation.

**Table 1.** Some specific temperatures of PLA hybrid samples at 5 K/min

Sample	$T_5$ (K)	$T_{10}$ (K)	$T_{50}$ (K)	$T_{90}$ (K)
PLA	579.47	592.32	620.50	635.34
T-PLA	573.71	582.29	606.67	622.49
Z-PLA	491.01	501.76	527.75	539.65

### 3.2 Thermal Degradation Kinetics of PLA Hybrids

For the purpose of understanding thermal degradation processes, kinetic analysis of TGA experimental results should be made and useful information about the accurate kinetic triplet may be thus resulted in terms of activation energy ( $E_a$ ), pre-exponential factor ( $A$ ), and mass conversion function ( $f(\alpha)$ ). Following the suggestions given by the ICTAC Kinetics Committee for kinetic analysis of thermal degradation of various solid matrices [12], a model-free Kissinger method can be easily employed to accurately estimate  $E_a$ . This method may be given as below [13],

$$\ln\left(\frac{\beta}{T_p^2}\right) = \ln\left(-\frac{AR}{E_a}f'(\alpha_p)\right) - \frac{E_a}{RT_p} \tag{1}$$

where  $R$  is universal gas constant (8.314 J/mol K),  $T_p$  is the temperature (K) at a maximum mass loss rate,  $\beta$  is the constant heating rate (K/min),  $f'(\alpha_p)$  is the first derivative of the reaction conversion function  $f(\alpha)$ ,  $a$  is the extent of mass conversion at any temperature and  $\alpha_p$  is the extent of mass conversion at  $T_p$ . Usually, the first term of the right side can be approximated to be a constant and the first order reaction mechanism is assumed behind. Figure 2 shows the Kissinger plots of  $\ln\left(\beta/T_p^2\right)$  against  $1/T_p$  for three PLA samples and the  $E_a$  value is then estimated from the slope of the Kissinger's line according to Eq. (1). As seen from Fig. 2, the  $E_a$  values are 148.60, 128.24 and 100.34 kJ/mol for pristine PLA, T-PLA and Z-PLA, respectively. Undoubtedly, these data are consistent with previous TGA results, that is to say, the two fillers of  $\text{TiO}_2$  and  $\text{ZnO}$  has made PLA become less thermally stable.

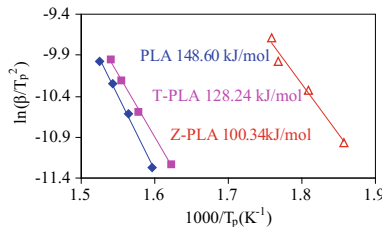


**Fig. 2.** The Kissinger's plots of  $\ln\left(\beta/T_p^2\right) \sim 1/T_p$  for thermal degradation of PLA samples

Since the  $E_a$  is available from the Kissinger method as above, the service lifespan of PLA,  $t_p$ , may be estimated with the aid of the following equation [14]:

$$t_p = \frac{-\ln(1 - \alpha)}{\beta(E_a/RT_p^2)} \tag{2}$$

Figures 3 and 4 present the life time results predicted for two different cases according to Eq. (2). Figure 3 presents the shelf life predictions for three PLA samples

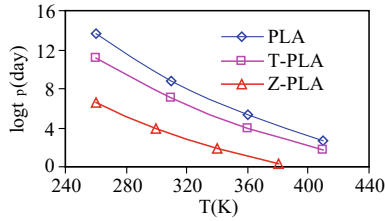


**Fig. 3.** The lifespan dependence on working temperature at 5% mass loss for three PLA samples

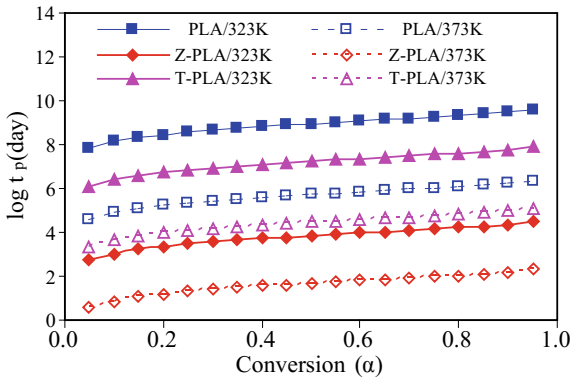


**Fig. 4.** The lifespan dependence on  $\alpha$  of two working temperatures for three PLA samples

supposed that they thermally fail if 5% mass conversion ( $\alpha = 0.05$ ) is occurred. Clearly, it can be observed from Fig. 3 that the PLA shelf life is strongly dependent on working temperature and it goes down exponentially with the increment of the working temperature. Moreover, the shelf lifespan of PLA is seen to become shorten after filling ZnO or TiO<sub>2</sub>. Similarly, the different lifespan predictions as a function of mass conversion for two metal oxide hybrids is also observed under isothermal conditions, as seen in Fig. 4. According to such predictions, it may be interestingly noted that PLA, T-PLA and Z-PLA require about  $6.53 \times 10^7$ ,  $1.30 \times 10^6$ , or 524 days for 5% mass loss at 323 K, and 39,211, 2158 or 3.5 days at 373 K for the same mass loss, respectively. Therefore, the life period estimation is meaningful to provide helpful thermal stability information for involved polymers. But it may be noticed that the prediction given here may possibly result in large errors as the first order reaction assumption is involved.

### 4 Conclusions

The influences of two different metal oxides on PLA thermal degradation are studied in present work. TGA data demonstrate that the thermal stability of PLA has become greatly deteriorated after filling TiO<sub>2</sub> or ZnO. Using the Kissinger method, the

activation energy  $E_a$  values calculated for pristine PLA, T-PLA and Z-PLA are 148.60, 128.24 and 100.34 kJ/mol, respectively. The service lifetimes for isothermal and non-isothermal conditions are also calculated for three PLA samples and the lifespan of PLA has shortened the addition of  $\text{TiO}_2$  or ZnO. With such information, the working temperature range may be properly selected for any subsequent application.

**Acknowledgements.** The authors would like to thank National Students' Innovation and Entrepreneurship Training Program (No. 201710069009) for funding this project.

## References

1. Koshy, R. R., Mary, S. K., Thomas, S., et al. (2015). Environment friendly green composites based on soy protein isolate—A review. *Food Hydrocolloids*, *50*, 174–192.
2. Reakasame, S., & Boccaccini, A. R. (2018). Oxidized alginate-based hydrogels for tissue engineering applications: A review. *Biomacromolecules*, *19*, 3–21.
3. Li, H. J., Hu, C., Yu, H. J., et al. (2018). Chitosan composite scaffolds for articular cartilage defect repair: A review. *RSC Advances*, *8*, 3736–3749.
4. Sangeetha, V. H., Deka, H., Varghese, T. O., et al. (2018). State of the art and future prospectives of poly(lactic acid) based blends and composites. *Polymer Composites*, *39*, 81–101.
5. Koh, J. J., Zhang, X. W., & He, C. B. (2018). Fully biodegradable poly(lactic acid)/Starch blends: A review of toughening strategies. *International Journal of Biological Macromolecules*, *109*, 99–113.
6. Huang, Z., Ye, Q. Q., & Teng, L. J. (2015). A comparison study on thermal decomposition behavior of poly (L-lactide) with different kinetic methods. *Journal of Thermal Analysis and Calorimetry*, *119*, 2015–2027.
7. Ye, Q. Q., Huang, Z., Hao, Y. H., et al. (2016). Kinetic study of thermal degradation of poly (L-lactide) filled with  $\beta$ -zeolite. *Journal of Thermal Analysis and Calorimetry*, *124*, 1471–1484.
8. Hao, Y. H., Huang, Z., Wang, J. W., et al. (2016). Improved thermal stability of poly (L-lactide) with the incorporation of zeolite ZSM-5. *Polymer Testing*, *49*, 46–56.
9. Das, P., & Tiwari, P. (2017). Thermal degradation kinetics of plastics and model selection. *Thermochimica Acta*, *654*, 191–202.
10. Laachachi, A., Ferriol, M., Cochez, M., et al. (2008). The catalytic role of oxide in the thermooxidative degradation of poly(methyl methacrylate)– $\text{TiO}_2$  nanocomposites. *Polymer Degradation and Stability*, *93*, 1131–1137.
11. Japic, D., Marinsek, M., & Orel, Z. C. (2016). Effect of ZnO on the thermal degradation behavior of poly(methyl methacrylate) nanocomposites. *Acta Chimica Slovenica*, *63*, 535–543.
12. Vyazovkin, S., Burnham, A. K., Criado, J. M., et al. (2011). ICTAC kinetics committee recommendations for performing kinetic computations on thermal analysis data. *Thermochimica Acta*, *520*, 1–19.
13. Kissinger, H. E. (1967). Variation of peak temperature with heating rate in differential thermal analysis. *Journal of Research of the National Bureau of Standards*, *57*, 217–221.
14. Georgieva, V., Zvezdova, D., & Vlaev, L. (2012). Non-isothermal kinetics of thermal degradation of chitosan. *Chemistry Central Journal*, *6*, 81–91.



# Preparation and Properties of PET/PE Solvent-Free Laminated Packaging Films

Pengfei Guo<sup>1</sup>, Yabo Fu<sup>1(✉)</sup>, Xijin Cui<sup>1</sup>, Jinjin Zuo<sup>2</sup>,  
Youzhong Zhao<sup>3</sup>, and Wencai Xu<sup>1</sup>

<sup>1</sup> Beijing Key Laboratory of Printing & Packaging Materials and Technology,  
Beijing Institute of Graphic Communication, Beijing, China

fuyabo@126.com

<sup>2</sup> Guangzhou Sinomech Co., Ltd., Guangzhou, China

<sup>3</sup> Shanghai KangDa New Materials Co., Ltd., Shanghai, China

**Abstract.** In flexible packaging solvent-free laminating process, in addition to the quality of the solvent-free adhesive itself, the peeling strength of the laminated product is also determined by many factors. In this experiment, through the control of conditions in the solvent-free laminating process, PET/PE solvent-free laminated film samples were prepared. This work studied the influence of coating weight of adhesive and laminating speed on the quality of laminated films. The results show that the peeling strength increase with the increasing of coating weight and decrease with the increasing of laminating speed, and the coating weight has great influence on peeling strength. The heat-sealing strength and dart impact strength of the sample can also meet the requirements of the national standard.

**Keywords:** Solvent-free laminating · Laminating speed · Coating weight · Peeling strength

## 1 Introduction

Solvent-free laminating is the process of bonding films and other materials through solvent-free adhesives with solids content close to 100% [1, 2]. Compared with the dry laminating process, solvent-free laminating process does not use organic solvents, which not only reduces the production costs, but also effectively reduces the environmental pollution [3, 4]. The solvent-free laminating technology originated in Germany in 1974 and was subsequently promoted in Europe [5]. After continuous development, Nordmeccanica Group of Italy has become a leader in the industry. The company invented a number of patents to improve solvent-free laminating equipment and promoted the development of solvent-free laminating [6, 7]. With the development of flexible packaging industry and the increase of environmental pollution in recent years, solvent-free laminating has also appeared a rapid development in China [8].

The difficulty of solvent-free laminating process lies in the reasonable matching between equipment, materials, adhesives, and process parameters [9, 10]. This work aims to prepare solvent-free laminated film samples under different experimental

conditions (substrate type, coating weight, and laminating speed) and to test their quality. Through the analysis of the results, the effects of laminating speed and coating weight on the quality of solvent-free laminated film were studied.

## 2 Experimental

### 2.1 Materials

This experiment selected the PET/PE substrate combinations commonly used in food flexible packaging as the experimental materials, shown in Table 1. Adhesive brands are represented by A, B, C.

**Table 1.** Experimental materials and groups

Name	Thick ( $\mu\text{m}$ )	Width (cm)	Manufacturer
PET	12	82	Guangzhou Yiyang Plastic Products Co., Ltd.
PE	60	80	Guangzhou Yiyang Plastic Products Co., Ltd.

### 2.2 Equipments

Experimental equipments used in the test are shown in Table 2.

**Table 2.** Experimental equipments

Name	Manufacturer	Type
Solvent-free laminating machine	Sinomech Co., Ltd.	SLF1000
Automatic glue mixer	Sinomech Co., Ltd.	SM-1-40
Film curing chamber	Luyangzhou Co., Ltd.	CX-105
Tensile testing machine	GBP packaging test instruments Co., Ltd.	GBH-1
Sealing gradiometer	Labthink Instruments Co., Ltd.	RTD-R1
Dart impact tester	Labthink Instruments Co., Ltd.	BMC-B1

### 2.3 Sample Preparation

Figure 1 is the flow chart of solvent-free laminating process. The gap between the metering roller and the transfer roller is adjusted to 70–90  $\mu\text{m}$  to control the coating uniformity. The sample can be prepared when coating weight and laminating speed required for the experiments are set correctly.

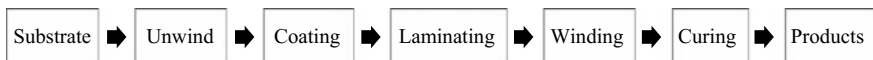


**Fig. 1.** Solvent-free laminating process



In this experiment, 10 samples were prepared with a coating weight of 0.6, 0.8, 1.0, 1.2, 1.5 g/m<sup>2</sup>, and a laminating speed of 100, 200, 300, 400, and 450 m/min. The prepared samples were placed in a film curing chamber at 40 °C for 24 h.

### 2.4 Test Methods

In this experiment, the peeling strength, heat sealing strength, and dart impact strength of the samples were tested. Peeling strength was tested according to the national standard GB/T 8808-1988: the method for peel force of flexible laminated plastics. The heat sealing was tested refers to QB/T 2358-1998: test method for heat sealing strength of plastic film packaging bags. The dart impact was tested according to the national standard GB/T 9639-1988: plastics film and sheeting determination of impact resistance—free falling dart method.

## 3 Results and Discussion

### 3.1 Peeling Strength

The following results are obtained by testing the peeling strength of samples with different coating weight and different laminating speed of PET/PE. From Fig. 2a, the peeling strength gradually increases with the increase of the coating weight in a certain range, and the peeling strength of the three adhesives increases significantly when the coating weight is greater than 1.0 g/m<sup>2</sup>. From Fig. 3b, it can be seen that the laminating speed has very little effect on the PET/PE laminated film, and the peeling strength does not change significantly in the range of 100–450 m/min. According to requirements of the peeling strength ≥ 2.0 N/15 mm on the Chinese national standard GB/T 10004-2008, the conditions of coating weight ≥ 1.0 g/m<sup>2</sup> can meet the requirements. The laminating speed has little influence and can be determined according to the actual situation.

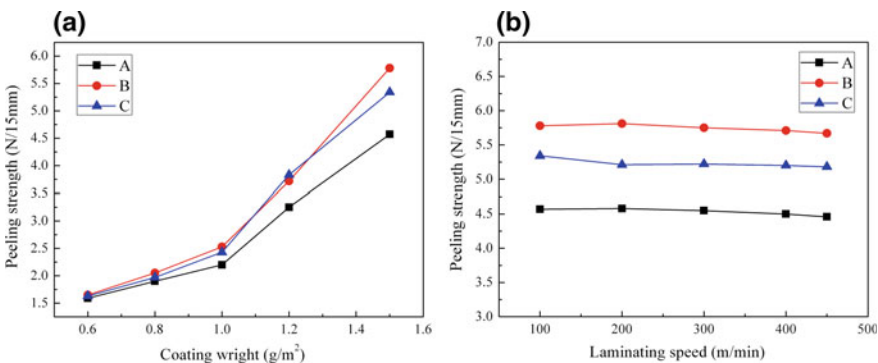


**Fig. 2.** **a** The effect of coating weight on the peeling strength of PET/PE when the laminating speed is 200 m/min; **b** the effect of laminating speed on the peeling strength of PET/PE when the coating weight is 1.5 g/m<sup>2</sup>

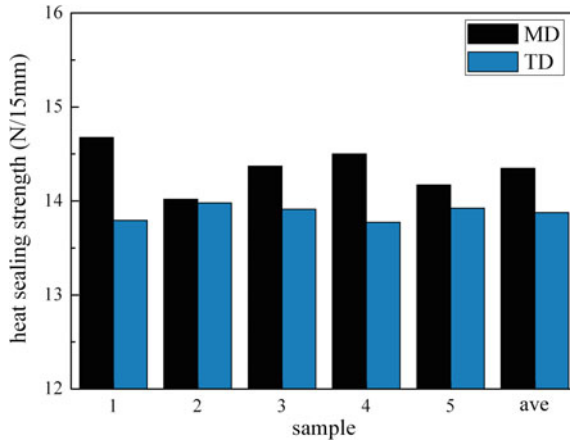


Fig. 3. Heat sealing strength (unit: N/15 mm)

### 3.2 Heat Sealing Strength

Based on the peeling strength results, sample of  $1.2 \text{ g/m}^2$ , 200 m/min, adhesive A was selected to test the heat-sealing strength. During the experiment, it was found that the heat-sealing strength at  $130 \text{ }^\circ\text{C}$  was too low and could be easily torn by hand. The heat-sealing sample had obvious wrinkles at  $150 \text{ }^\circ\text{C}$ , which affected the appearance, so the heat-sealing temperature was chosen to be  $140 \text{ }^\circ\text{C}$ . Heat sealing with a sealing gradiometer for 10 s, and then tested for heat sealing strength with the tensile testing machine. The results are shown in Fig. 3. It can be seen from the table that the heat-sealing strength of the sample at  $140 \text{ }^\circ\text{C}$  has reached the requirement of 13 N/15 mm in the national standard, and the heat-sealing strength is larger in MD direction than in TD direction.

### 3.3 Dart Impact Strength

According to the test results, we selected the same sample to test its dart impact strength. Drop weight gradually increased from 90, 120, 150 and 180 g. As a result, it was found that the sample was broken when the dart mass was 180 g, and no breakage occurred below 170 g. Repeated tests at 170 and 175 g, it can be seen that the dart impact strength of the sample is 170 g, shown in Table 3.

Table 3. Dart impact test results ( $\checkmark$  indicates sample damage,  $\times$  indicates no damage)

Number	1	2	3	4	5	6	7	8	9	10
Dart weight (g)	90	120	150	180	170	175	170	175	170	175
Result	$\checkmark$	$\checkmark$	$\checkmark$	$\times$	$\checkmark$	$\times$	$\checkmark$	$\times$	$\checkmark$	$\times$

## 4 Conclusions

In this experiment, plastic flexible packaging films were prepared by solvent-free laminating method, and the lamination quality of the samples was performed. The variation of peeling strength, heat sealing strength and dart impact strength of laminated films at different coating weight and various laminating speed were studied. With the increase of coating weight, the peeling strength of the laminated film samples will gradually increase under low-quantity coating conditions; and with the increase of laminating speed, the peeling strength gradually decreased or remained basically unchanged. The effect of the coating weight on the peeling strength is significantly greater than laminating speed. Moreover, the heat-sealing strength and dart impact strength of the sample can also meet the requirements of the national standard at low adhesive amount conditions. The result of this work indicates that solvent-less lamination is a feasible and promising technique to substitute for dry and other high pollution lamination process in flexible packaging.

**Acknowledgements.** This work was supported by the National Key R&D Program (No. 2016YFC0204200), National College Students Innovation and Entrepreneurship Training Program (22150118022/126), and the Coordinative Innovation Project of Beijing Municipal Commission of Education (No. 04190117019).

## References

1. Jia, C. (2013). Present and future situation of solvent-free composite technology. *China Packaging Industry*, 11, 88–89.
2. Chen, S., Chen, G., Chen, Q., Jia, C., & Wang, Q. (2012). The preparation of solvent-free polyurethane laminating adhesive with mixed-polyols. *Advanced Materials Research*, 549, 177–182.
3. Lv, L., Gao, D., Xu, W., & Zuo, G. (2010). Characteristics of solventless lamination technology and structure of equipment associated with it. *China Plastics*, 10, 9–16.
4. Venkatesh, R., & Jayachandran, S. (2008). Globalization and industry competitiveness in healthcare services and marketing. *Journal of Marketing Management*, 7(1), 15–24.
5. Guo, P., Fu, Y., He, H., et al. (2018). Research progress of solvent-free laminating technology in flexible packaging. *Packaging Engineering*, 9, 44–50.
6. Cerciello A. (2010) Adhesive-spreading unit, in particular for bonding machines. *U.S. 7814860*.
7. Cerciello A. (2013) Adhesive spreading unit provided with a roller-cleaning device. *WO, EP 2804702 A1*.
8. Chen, C. (2008). Interpretation of solvent-free composite. *Plastics Packaging*, 18(5), 27–32.
9. Yu, Y. (2014). Solvent-free composite process critical control point. *Printing Technology*, 6, 49–51.
10. Zhao Y. (2014). Superiorities and recent research advances of solventless lamination. 35 (10), 88–91.



# Transparency Research of Poly(L-lactide) Films and Its Modified Films

Xiaohui Zhang<sup>1</sup>(✉) and Wenjuan Gu<sup>2</sup>

<sup>1</sup> School of Media and Design, Hangzhou Dianzi University, Hangzhou, Zhejiang, China

zhang\_xiao\_hui2014@126.com

<sup>2</sup> Faculty of Mechanical and Electrical Engineering, Kunming University of Science and Technology, Kunming, Yunnan, China

**Abstract.** Using polyhedral oligomeric silsesquioxanes (POSS) to modify Poly (L-lactide) (PLLA) had been studied to improve the properties in recent years. In the paper, the transparency of PLLA films and modified PLLA films was studied. First, PLLA films and a series of modified PLLA films were prepared. Star-shaped POSS-g-PLLA was prepared by using L-lactic acid and POSS-NH<sub>3</sub>Cl in the presence of stannous (II) octanoate (Sn (Otc)<sub>2</sub>) catalyst. A series of modified films were prepared by using octa(γ-chloroammoniumpropyl) octasilsesquioxane (POSS-NH<sub>3</sub>Cl) and POSS-g-PLLA. Meanwhile, the reaction was characterized by Fourier Transform Infrared spectrometry (FTIR). Secondly, transparency of PLLA films, PLLA/POSS-NH<sub>3</sub>Cl films, PLLA/POSS-g-PLLA films and POSS-g-PLLA films were investigated, respectively. The conclusions were as follows: (1) the transparency of PLLA/POSS-NH<sub>3</sub>Cl, PLLA/POSS-g-PLLA and POSS-g-PLLA films was improved. (2) The transparency of POSS-g-PLLA films was the best, and the transparency of PLLA/POSS-g-PLLA films was better than that of PLLA/POSS-NH<sub>3</sub>Cl films. (3) The transparency of POSS-g-PLLA films was significantly improved. In the visible spectral range (400–800 nm), the transparency of POSS-g-PLLA films was increased with the increase of POSS-NH<sub>3</sub>Cl, and the transparency of the films improves even 58% in some wavelength. These phenomena were explained theoretically.

**Keywords:** PLLA · Modified PLLA films · Transparency

## 1 Introduction

Poly (L-lactic acid) or poly(L-lactide) (PLLA) has attracted increasing attention in medical, agricultural, packaging, and general plastic because of its non-toxicity, bio-renewability, biodegradability and good processability [1–7]. The characters of PLLA have been studied in many articles, and the transparency properties of PLLA have also been researched. Compared to low density polyethylene (LDPE), PLLA films have better ultraviolet light barrier properties [6]. But ultraviolet light barrier properties of PLLA films are little worse than those of cellophane and poly (ethylene terephthalate) (PET) [6]. PLLA films have transparency properties comparable to polystyrene

(PS) [7]. However, its defects such as the stiff and brittle characteristics, hydrophobicity, thermal stability, the difficult controlled degradation period and etc. have limited its further application. Therefore, not only organic polymers and inorganic substances [8] but also nanocomposites [9–11] have been used to modify PLLA in recent years. Carbon nanotubes (CNT) has been used to modified PLLA by blending of PLLA and CNT [10], not only the crystallization rate and the hydrolytic degradation of PLLA have been accelerated, but also the mechanical, electrical and thermal properties of PLLA have been improved. However, the transparency properties of these modified PLLA films have been debased.

Recently, polyhedral oligomeric silsesquioxanes (POSS) has been widely used as a new nanofiller to improve the comprehensive properties of PLLA. And the comprehensive properties of PLLA composites have been greatly improved by using POSS [11–15]. Up to present, researches blending PLLA with POSS have been studied which can improve the thermal, mechanical, oxidation resistance, gas permeability, pressure resistance properties [11–15].

However, PLLA grafting with POSS have rarely been reported [15]. In the Ref. [14], POSS-PLA (polylactide tethered with POSS) was synthesized by using the ring-opening polymerization of L-lactide with 3-hydroxypropylheptaisobutyl POSS, and PLLA/POSS-PLA (blending PLLA with POSS-PLA) was prepared and its properties were studied. The results showed that the mechanical properties of the blending materials could be improved, but the reinforced properties of the blending materials were limited. The simple blending of inorganic materials with organic materials is thermodynamically immiscible because that the inorganic materials is not immiscible in the organic materials.

The paper was studied based on the previous studies [16]. Firstly, the star-shaped polymer, POSS-g-PLLA was synthesized. Secondly, the modified PLLA films were prepared. Finally, the transparency properties of these modified PLLA films were characterized by UV-visible light transmittance analyzer.

## 2 Experimental

### 2.1 Materials

L-LA bought from Shenzhen Bright china Industry Co. Ltd. was pretreated based on the method described in the Ref. [16]. Polyethylene glycol (PEG) ( $M_w = 600$ , C.R.), Ethanol (A.R) and Sn (Oct)<sub>2</sub> (A.R) were supplied from Chemical Reagent Co. Ltd.. Chloroform (A.R) was purchased from Shanghai Experiment Reagent Co. Ltd. And these materials were used without further purification. Octa( $\gamma$ -chloroammoniumpropyl) octasilsesquioxane (POSS-NH<sub>3</sub>Cl) was prepared according as the method described in the Ref. [17]. Deionized water was self-prepared in the laboratories.

## 2.2 Preparations of PLLA, POSS-g-PLLA, PLLA Films, PLLA/POSS-NH<sub>3</sub>Cl Films, PLLA/POSS-g-PLLA Films, POSS-g-PLLA Films

PLLA and POSS-g-PLLA were synthesized according as Ref. [16]. The preparation procedure of the POSS-g-PLLA films was as follows: firstly, a certain proportion of POSS-g-PLLA and chloroform were charged into a flask with a magnetic stirrer until the mixture fully dissolved, a certain percentage of TDI [16] and dibutyltin were added into the mixture, then the mixture was stirred at 80 °C for 5 h by magnetic stirrer. Secondly, a certain percentage of PEG, TDI and dibutyltin were charged into the reactants, and the mixture was stirred at 80 °C for 5 h by magnetic stirrer. Finally, the reactants were poured into a Teflon mould, and retained for about 24 h at room temperature to give an about 0.5 mm thick sheet of films with smooth surface. The reaction between the preparations of POSS-g-PLLA films was presented in Fig. 1.

## 3 Characterizations

FTIR were performed on Nicolet AVATAR 360FT infrared analyzer, and KBr powder was used as a nonabsorbent medium. Firstly, samples were ground with KBr which were made 0.5 wt% mixtures and then the mixtures were pressed into disks. Secondly, the spectral analysis of sample was collected from 4000 to 400 cm<sup>-1</sup>.

The transparency of the films was tested by UV-visible light transmittance analyzer (WD-9403C) with the test range of 200–800 nm.

## 4 Results and Discussion

### 4.1 Structure of POSS-g-PLLA Film

FTIR for the POSS-g-PLLA film was shown in Fig. 2. Peaks at 1760 cm<sup>-1</sup> (–OH), 1460 cm<sup>-1</sup> (–CH<sub>3</sub>), 1190 and 1090 cm<sup>-1</sup> (C–O–C), 1604 cm<sup>-1</sup> (N–H) were found. 1380 cm<sup>-1</sup> was the peak assigned to the methane groups. 1647 and 1544 cm<sup>-1</sup>, newly emerged peaks, could show the existence of NH–C=O. The peak at 1090, 809 and 457 cm<sup>-1</sup> was assigned to the Si–O–Si stretching vibration [18, 19], and 1090 cm<sup>-1</sup> was the LO and TO of Si–O–Si vibration [20], 3030, 1604, 1540, 1460 and 760 cm<sup>-1</sup> was the benzene and CH<sub>2</sub>.

### 4.2 Transparency Properties of Films

In order to study the optical properties of PLLA, PLLA/POSS-NH<sub>3</sub>Cl, PLLA/POSS-g-PLLA and POSS-g-PLLA films, these films were characterized on UV-visible light analyzer. The results were shown in Figs. 3 and 4.

The effect on the light transmittance was not studied because of little effect on the light transmittance of PEG content in the films [21]. All the films were high transparent in the visible spectral range from the results. However, the transmittance of PLLA/POSS-NH<sub>3</sub>Cl, PLLA/POSS-g-PLLA and POSS-g-PLLA films was different. As can be seen From Fig. 3, the transparency of PLLA/POSS-g-PLLA was higher than

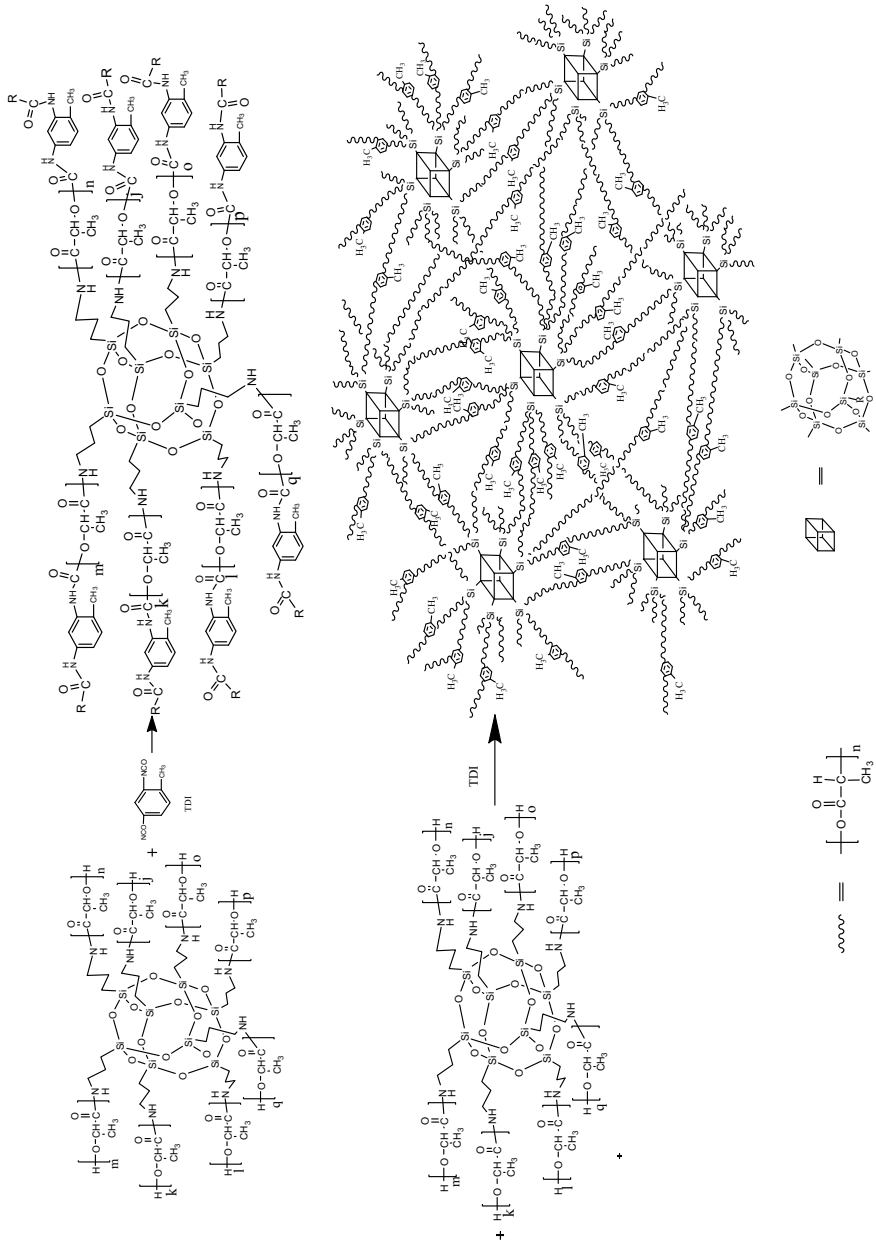
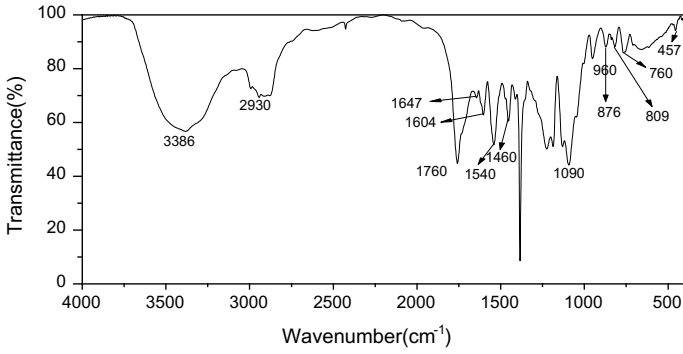
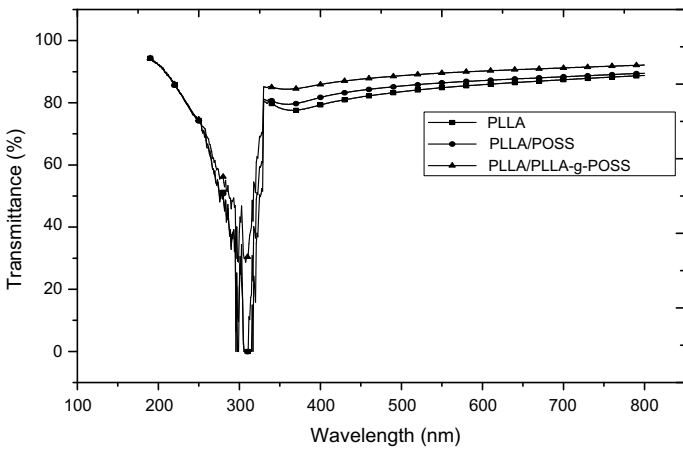


Fig. 1. Reaction between the preparations of POSS-g-PLLA films



**Fig. 2.** FTIR spectrum of POSS-g-PLLA film



**Fig. 3.** Transparency properties of PLLA, PLLA/POSS-NH<sub>3</sub>Cl and PLLA/POSS-g-PLLA films

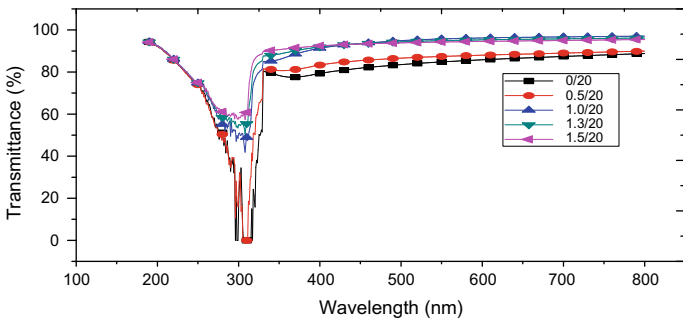


**Fig. 4.** Transparency properties of POSS-g-PLLA films



that of PLLA/POSS-NH<sub>3</sub>Cl, and the transparency of PLLA was the lowest among them. The phenomena could be explained as follows [6]: since the transmittance of polymer was mainly affected on their crystalline, structures, and so on. The transparency of not only PLLA/POSS-NH<sub>3</sub>Cl but also PLLA/POSS-g-PLLA was higher than that of PLLA because of the nano-structure of POSS [6]. The dispersed properties of POSS-g-PLLA in PLLA/POSS-g-PLLA was much better than that of POSS-NH<sub>3</sub>Cl in PLLA/POSS-NH<sub>3</sub>Cl, so the transparency of PLLA/POSS-g-PLLA was higher than that of PLLA/POSS-NH<sub>3</sub>Cl. From Fig. 4 it can be seen that the transparency of POSS-g-PLLA films was significantly improved with the increasing percentage of POSS-NH<sub>3</sub>Cl. The transmittance improved even 58% during the 250–330 nm. The phenomena could be explained as follows [22]: POSS-NH<sub>3</sub>Cl nanoscale material was existed in POSS-g-PLLA, and the POSS-g-PLLA films, synthesized with POSS-g-PLLA and PEG, possesses cage-type structure. Therefore, the light could easily pass, thus the transparency of POSS-g-PLLA films was increased with the increase of POSS-NH<sub>3</sub>Cl.

## 5 Conclusions

In this study, PLLA films, PLLA/POSS-NH<sub>3</sub>Cl films, PLLA/POSS-g-PLLA films and POSS-g-PLLA films have been prepared and the transparency of the films has been studied. It was found that, the transparency of these films was increased with the accession of POSS-NH<sub>3</sub>Cl, and the transparency of PLLA/POSS-g-PLLA was the best among PLLA films, PLLA/POSS-NH<sub>3</sub>Cl films. Above all, the transparency of POSS-g-PLLA films was increased with the increase of POSS-NH<sub>3</sub>Cl in the star-shaped POSS-g-PLLA, and improved even 58% during the 250–330 nm.

## References

1. Cinelli, P., & Chiellini, E. (2006). Foamed articles based on potato starch, corn fibers and poly(vinyl alcohol). *Polymer Degradation Stability*, 91, 1147–1155.
2. Vargas, L. F., Welt, B. A., Pullammanappallil, P., et al. (2009). Effect of electron beam treatments on degradation kinetics of polylactic acid (PLA) plastic iste under backyard composting conditions. *Packaging Technology and Science*, 22(2), 97–106.
3. Rahman, M., & Opaprakasit, P. (2018). Effects of UV/photo-initiator treatments on enhancement of crystallinity of polylactide films and their physicochemical properties. *Journal of Polymers and the Environment*, 26(7), 2793–2802.
4. Deplaine, H., Lebourg, M., & Ripalda, P. (2013). Biomimetic hydroxyapatite coating on pore walls improves osteointegration of poly(L-lactic acid) scaffolds. *Journal of Biomedical Materials Research. Part B, Applied Biomaterials*, 101(1), 173–186.
5. Petisco-Ferrero, S., Álvarez, L. P., et al. (2018). Plasma poly(acrylic acid) compatibilized hydroxyapatite-poly lactide biocomposites for their use as body-absorbable osteosynthesis devices. *Composites Science and Technology*, 161(16), 66–73.
6. Auras, R., Harte, B., et al. (2004). An overview of polylactides as packaging materials. *Macromolecular Bioscience*, 4, 835–864.

7. Auras, R. A., Singh, S. P., et al. (2005). Evaluation of orientated poly(lactide) polymers versus existing PET and oriented PS for fresh food service containers. *Packaging Technology and Science*, 18, 207–216.
8. Kondratowicz, F. Q., & Ukielski, R. (2009). Synthesis and hydrolytic degradation of poly(ethylene succinate) and poly(ethylene terephthalate) copolymers. *Polymer Degradation Stability*, 94, 375–382.
9. Huang, B. R., Saravanan, A., et al. (2018). Role of conductive nitrogen incorporated diamond nanowires for enhancing the UV detection and field emission properties of ZnO nanotubes. *Materials and Design*, 154, 130–139.
10. Chen, H. M., Chen, J., & Shao, L. N. (2013). Comparative study of poly(L-lactide) nanocomposites with organic montmorillonite and carbon nanotubes. *Journal of Polymer Science Part B: Polymer Physics*, 51, 183–196.
11. Markovic, E., & Matison, J. (2007). Poly(ethylene glycol) octa functionalized polyhedral oligomeric silsesquioxane: WAXD and rheological studies. *Macromolecules*, 40(13), 4530–4534.
12. Lee, K. M., & Knight, P. T. (2008). Polycaprolactone-POSS chemical/physical double networks. *Macromolecules*, 41, 4730–4738.
13. Kai, W., & Hua, L. (2008). Polyhedral oligomeric silsesquioxane and fullerene-end-capped poly( $\epsilon$ -caprolactone). *Macromolecular Chemistry and Physics*, 209, 1191–1197.
14. Lee, J. H., & Jeong, Y. G. (2010). Preparation and characterization of nanocomposites based on polylactides tethered with polyhedral oligomeric silsesquioxane. *Journal of Applied Polymer Science*, 115, 1039–1046.
15. Pan, H., & Qiu, Z. B. (2010). Biodegradable poly(L-lactide)/polyhedral oligomeric silsesquioxanes nanocomposites: enhanced crystallization, mechanical properties, and hydrolytic degradation. *Macromolecules*, 43, 1499–1506.
16. Zhang, X. H., Gu, W. J., & Li, H. B. (2012). Synthesis and characterization of star-shaped polylactic acid with polyhedral oligomeric silsesquioxanes. *Applied Mechanics and Materials*, 200, 397–400.
17. Gravel, M. C., Zhang, C., et al. (1999). Octa(3-chloroammoniumpropyl) octasilsesquioxane. *Applied Organometallic Chemistry*, 13, 329–336.
18. Koh-ichi, U., Satoshi, S., et al. (1999). Preparation and properties of silica films with higher-alkyl groups. *Journal of Non-Crystalline Solids*, 260(2), 199–207.
19. Capozzi, C. A., Pye, L. D., et al. (1992). Vibrational spectral/structural changes from the hydrolysis/polycondensation of methyl-modified silicates. *Materials Letters*, 15(2), 130–136.
20. Que, W., & Hua, X. (2003). Sol-gel derived titania/ $\gamma$ -glycidoxypropyltri-methoxysilane and methyltrimethoxy-silane hybrid materials for optical waveguides. *Journal of Sol-Gel Science and Technology*, 28(3), 319–325.
21. Gu, W. J., He, Z. F., & Zhang, X. H. (2014). POSS modified poly(lactide) acid film. *Chinese Journal of Lasers*, 41(4), s1060071–s1060074.
22. Mitsubishi, M., Zhao, F., & Kim, Y. (2008). Preparation of ultrathin silsesquioxane nanofilms via polymer Langmuir-Biodgett films. *Chemistry of Material*, 20(13), 4310–4316.



# Study on Physical Properties of Degradable Polylactic Acid Packaging Film

Yingying Qin and Hongge Guo<sup>(✉)</sup>

School of Printing and Packaging Engineering, Qilu University of Technology  
(Shandong Academy of Sciences), Shandong, China  
ghg@qlu.edu.cn

**Abstract.** In this paper, we chose the PLA resin of Ingeo 4032D from Nature Works (USA) as the research object, focusing on PLA modification by using starch and carbon black and mechanical and optical properties after modification. Study state showed that when the mass ratio of PLA and starch is 100:1, tensile strength decreased by 13.57%, tear strength dropped by 5.08%, light transmittance fell by 0.032%. With the mass ratio of PLA, starch and carbon black reaches 100:1:0.5, tensile strength increased by 3.21%, tear strength grew by 4.32%, and light transmittance went down by 54.6%. Therefore, the performance of the starch/PLA modified films fall short while the performance of the starch/PLA/carbon black modified films were optimized. the PLA/starch/carbon black modified films are more suitable for improving properties of PLA resin.

**Keywords:** Polylactic acid (PLA) · Modified · Physical properties

## 1 Introduction

Polylactic (PLA) resin is a biodegradable polymer material prepared by polycondensation reaction using lactic acid as the main raw material [1], which can be extracted from natural renewable resources such as corn and wheat. The production process has no pollution and the production energy consumption is only equivalent to 20–50% of the traditional petrochemical products while the carbon dioxide gas produced is only 50%, which can get rid of the dependence on oil resources [2]. After being discarded, PLA products can be decomposed in the natural environment and eventually degraded into water and carbon dioxide, without any pollution to the environment and realizing its circulation in the natural world. It is considered to be the most widely used type of biodegradable polymer material and has received wide attention in recent years (Fig. 1).

PLA resin is a thermoplastic aliphatic polyester, whose glass transition temperature and melting point are about 60 and 175 °C, respectively [3] while the processing temperature is generally controlled between 170 and 230 °C which Suitable for extrusion, blow molding, Stretching and other processing processes. In food packaging, PLA film has physical properties equivalent to other films such as polyethylene, good crystal transparency, moisture resistance, and similar anti-permeation properties to polyester. In addition, polylactic acid film has good solvent resistance, insoluble in

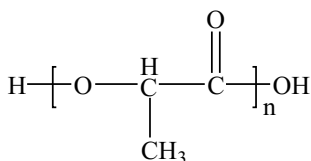


**Fig. 1.** Structural formula of PLA

alcohols, fats, hydrocarbons, edible oils, and mechanical oils [4]. Moreover, there is a lower temperature heat sealing ability, better printability than polyolefins and good ink retention, which can retain the flavor and package aesthetics of foods to a greater extent.

PLA resin also has certain drawbacks inevitably. The disadvantages including lower processing temperature, high glass transition temperature, slow crystallizing rate, low crystallinity, difficulty in controlling the degradation cycle and expensive price limit its scope of application as a film packaging material [5].

## 2 Experimental

### 2.1 Materials

See Table 1.

**Table 1.** Materials

Name	Type	Manufacturer
PLA	Ingeo4032D	Nature Works Corp. of the US
Starch	Analytical purity	Tianjin Beichen Founder Reagent Factory
Carbon black	MF-6	Tianjin Lihujin Chemical Corp. of China

### 2.2 Manufacturing Methods

**Pretreatment:** At first, PLA resin was put into vacuum drying oven at 80 °C, the starch was put into it at 60 °C and the carbon black was put into it at 105 °C. Every two hours, it was taken out for weighing, until the sample weight was not change, it was finished for drying.

**Mixed granulation:** PLA/starch and PLA/starch/carbon black were mixed respectively in proportion to the mass of 100:1, 100:2, 100:3 and 100:1:0.5, 100:1:1, 100:1:1.5, and the granular resin that could be used for blowing film was produced by using the extrusion granulator of torque rheometer.

**Film sample preparation:** the granular resin was added to blown film auxiliary of torque rheometer. The processing temperatures of the samples were shown in Table 2.

**Table 2.** The processing temperatures of the samples

Sample	1 zone/°C	2 zone/°C	3 zone/°C	4 zone/°C
PLA	155	165	175	180
PLA/starch	155	165	175	180
PLA/starch/carbon black	155	165	175	180

### 3 Results and Discussion

#### 3.1 Effect of Blending on Mechanical Properties of PLA Film

PLA has high rigidity, low softness and low impact resistance, and is a hard and brittle material at room temperature. The PLA must be toughened and modified if it is used in situations where toughness is high or to make films as soft as PE.

Polymer blending is a more economical way to modify polymer properties. PLA also has the advantages of high mechanical strength, stable chemical performance and easy processing [6], it can be mixed with elastomers, tough polymers, fillers or plasticizers [7, 8]. Starch and carbon black make two fillers commonly used in modification studies.

##### 3.1.1 Effect of Blending on Tensile and Tear Properties of PLA Film

Both the tensile tests and tear strength tests were tested at the tensile speed of 200 mm/min (Figs. 2 and 3).

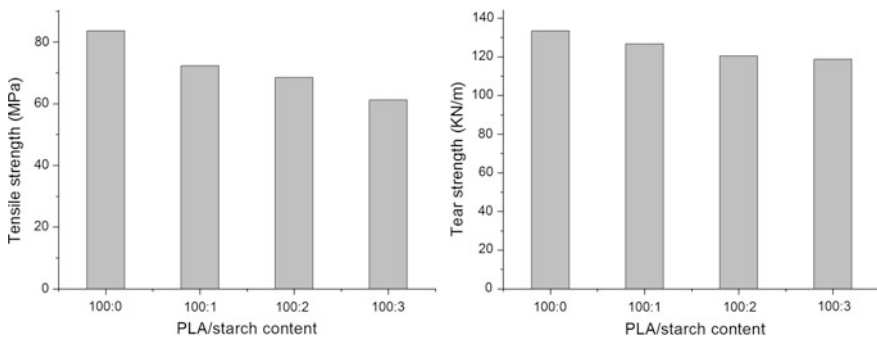


**Fig. 2.** Tensile strength and tear strength of PLA/starch composite films

The results showed that the tensile and tear strength of PLA/starch modified films decreased with the increasing of the content of starch, and the tensile tear and strength of carbon black modified PLA films increased with the increasing of the content of carbon black. The reason is that both polylactic acid and starch are rigid molecules, the intermolecular compatibility is poor, and voids are formed between the two interfaces, so that the tensile and tear strength of the modified films were lowered. The carbon

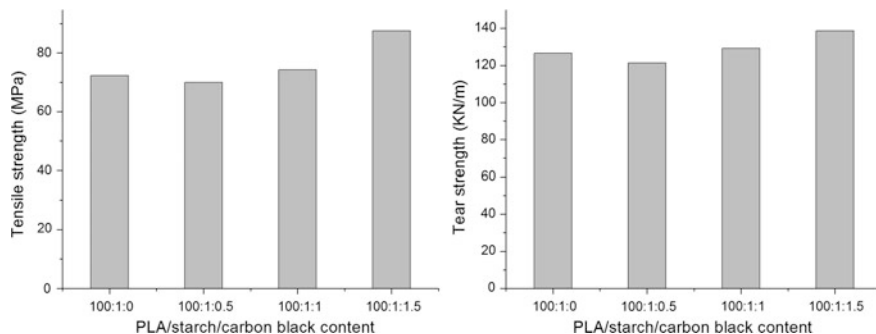


**Fig. 3.** Tensile strength and tear strength of PLA/starch/carbon black composite films

black with small particle size was added, the nucleation effect of the film was good, the crystallinity was perfect, the tensile and tear strength of the modified films increased.

### 3.1.2 Effect of Blending on Friction Coefficient of PLA Film

The results showed that the internal friction coefficient was larger than the external friction coefficient, and the friction coefficient of PLA modified films increased with the increasing of starch and carbon black content. The inner friction coefficient of the films was higher than the outer side. The reason for this phenomenon is that there was a wind ring on the outside during the film blowing process, the film was quenched, and the crystal was generated less, and the inner side of the film was hot air, and the crystal was generated, so the inner friction was higher than the outer side (Tables 3 and 4).

**Table 3.** Friction coefficient of PLA/starch composite films

Material	Static friction		Dynamic friction	
	Inner to inner	Outer to outer	Inner to inner	Outer to outer
PLA/starch 100:1	0.277	0.241	0.246	0.220
PLA/starch 100:2	0.323	0.311	0.291	0.281
PLA/starch 100:3	0.363	0.321	0.306	0.294

### 3.2 Effect of Blending on Optical Properties of PLA Film

Light transmittance is the percentage of the luminous flux that passes through a transparent or translucent body and its incident light flux.

Haze is the turbid or hazy appearance of the interior or surface of a transparent or translucent material. It is expressed as a percentage of the ratio of the diffused light flux to the transmitted material luminous flux (Figs. 4 and 5).

The results showed that when the starch was added, the light transmittance of the films changed little and the haze increased. When the carbon black was added, the light transmittance of the modified films decreased rapidly with the increasing of carbon

**Table 4.** Friction coefficient of PLA/starch/carbon black composite films

Material	Static friction		Dynamic friction	
	Inner to inner	Outer to outer	Inner to inner	Outer to outer
PLA/starch/carbon black 100:1:0.5	0.263	0.242	0.259	0.219
PLA/starch/carbon black 100:1:1	0.320	0.309	0.292	0.277
PLA/starch/carbon black 100:1:1.5	0.369	0.323	0.312	0.288

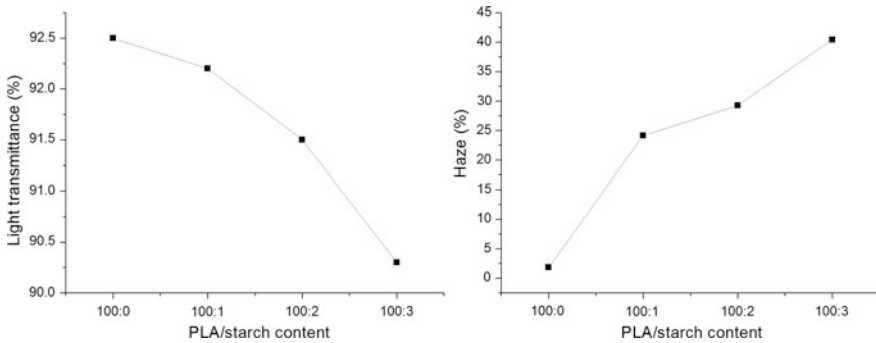


**Fig. 4.** Optical characteristics of PLA/starch

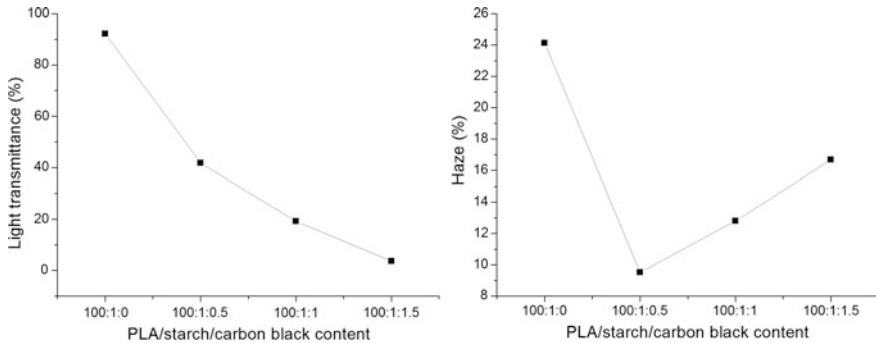


**Fig. 5.** Optical characteristics of PLA/starch/carbon black

black content, and the haze increased. The reason is that as the content of carbon black increases, the crystallinity of the films increases, and light scattering occurred between the crystal and the amorphous, so that the light transmittance is reduced and the haze is increased.

## 4 Conclusions

From the above experiments, we can draw the following conclusions:

1. The tensile and tear properties of the starch modified PLA films are reduced, while the tensile and tear properties of the carbon black modified PLA films are enhanced. The friction coefficient of the modified films is increases with the addition amount, and the internal the friction is greater than the external friction.
2. The light transmittance of the starch-modified film is reduced while the haze is increased. On the basis of this, carbon black modification is added, the light transmittance of the films is drastically decreased.
3. The performance of the PLA/starch modified films were worse than that of PLA, and the performance of the starch/PLA/carbon black modified films were optimized. Therefore, the PLA/starch/carbon black modified films are more suitable for food packaging.

## References

1. Sodergard, A., & Stolt, M. (2002). Properties of lactic acid-based polymers and their correlation with composition. *Progress in Polymer Science*, 27(6), 1123–1163.
2. Zhang, X. (2014). *Toughening modification of polylactic acid*. Changchun: Changchun University of Technology.
3. Zhou, P. (2014). *Poly lactide modification and supercritical carbon dioxide foaming*. Hangzhou: Zhejiang University of Technology.
4. Xu, Z. (2002). Synthesis and application of a novel biodegradable plastic-polylactic acid. *Hangzhou Chemical Industry*, 32(2), 9–11.
5. Xu, Z. (2003). A new biodegradable plastic-polylactic acid with promising prospects. *Synthesis and Application of Synthetic Materials*, 32(2), 39–43.
6. Tsuji, H., & Ikada, Y. (1995). Properties and morphologies of poly(l-lactide): 1. Annealing condition effects on properties and morphologies of poly(l-lactide). *Polymer*, 36(14), 2709–2716.
7. Jun, W. P., Seung, S. I., & Soo, H. K., et al. (2010). Biodegradable polymer blends of poly(l-lactic acid) and gelatinized starch. *Polymer Engineering & Science*, 40(12), 2539–2550.
8. Liu S. Q., Gai-Hong W. U., & Guo H. X., et al. (2015). Preparation and properties of polylactic acid (PLA)/nano-SiO<sub>2</sub> composite master batch with good thermal properties. *Journal of Donghua University (English Edition)*, 32(1), 97–102.





# Preparation and Characterization of Conductive Films Based on Nanocrystalline Cellulose

Hao Zhang<sup>(✉)</sup> and Liang Hong

Department of Materials and Chemical Engineering,  
Henan University of Engineering, Henan, China  
zhanghaobjfu@126.com

**Abstract.** In order to prepare the conductive films based on nanocrystalline cellulose (NCC), multi-walled carbon nanotubes (MWCNTs) modified by 3-glycidoxypropyltrimethoxysilane (GPTMS) were used. The modified MWCNTs were added into the NCC substrate. The effects of modification on the compatibility of MWCNTs were investigated with contact angles (CA). The conductive films were characterized using the scanning electron microscope (SEM), Fourier transform infrared spectroscopy (FT-IR), X-ray diffraction (XRD), and four-point probes. The results showed that the optimal concentration of GPTMS was 8 wt% and the CA of modified MWCNTs with substrate was 61.9°. According to the FT-IR spectrum, hydroxyl groups and C–H groups were introduced into the conductive films. The XRD patterns of the conductive films were influenced by surface-modified MWCNTs limitedly. The electrical resistivity of the conductive film was  $1.37 \times 10^{-3} \Omega \text{ cm}$  when the content of modified MWCNTs was 10 wt%.

**Keywords:** Nanocrystalline cellulose · Carbon nanotube · Conductive film · Preparation · Characterization

## 1 Introduction

As a kind of material which could be used as the main component of electronic elements, the conductive films are widely distributed in many regions of the industrial world. In addition to the electric conductivity, attention has been paid to the environmental performance and degradability of the conductive films [1].

In recent years, extensive efforts have been put on the research of the conductive films. One type of conductive films made of ZnO was found to favor the electrical current flow with an electrical resistivity of  $4.62 \times 10^{-4} \Omega \text{ cm}$  [2]. In order to improve the environmental performance of conductive composites, the degradable fibers made from cellulose materials (e.g. bacterial cellulose) were used as the main substrate of the composites [3]. Silver nanowire was added into the aqueous suspension of bamboo cellulose and chitosan. The mixture was filtrated and dried at 70 °C in a vacuum drying chamber. The fabricated composite had a sheet resistance of  $4.32 \Omega/\text{m}^2$  [4].

Compared with the traditional cellulose fiber, nano crystalline cellulose (NCC) can be regarded as a promising substrate to improve the properties of conductive films [5]. This study investigated the conductive films consisted of NCC substrate and surface-modified MWCNTs.

## 2 Experimental

### 2.1 Materials

The MWCNTs were purchased from the Chengdu Organic Chemicals Co. Ltd. The average length of the MWCNTs was between 10 and 50 nm, and the diameter was from 8 to 15 nm. The content of surface hydroxyl groups was 1.85 wt%. GPTMS was a kind of coupling agent and was used as the surface modifier of MWCNTs. The Larch was the substrate for NCC and was purchased from Hebei province in China. The NCC powder was prepared with 25 wt% sulfuric acid and the acid hydrolysis was operated at 60 °C for 3 h. The length of NCC particles was at the range of 150–300 nm, and the diameter was between 30 and 60 nm.

### 2.2 Methods

#### 2.2.1 Hydrolysis of GPTMS and Pretreatment of MWCNTs

GPTMS was treated as the modifier to adjust the chemical structure of MWCNTs. The modifier was dissolved in ethanol at the contents of 2, 4, 6, 8, and 10 wt%. In order to complete the hydrolysis of GPTMS, the pH of the ethanol was adjusted to the range of 3–3.5 with hydrochloric acid. The hydrolysis process of the surface modifier was terminated when the solution turned pellucid. One gram of MWCNTs was modified with 100 mL of hydrolyzed GPTMS solution. The modification was conducted at 65 °C for 2 h.

#### 2.2.2 Synthesis of Conductive Films

The NCC substrate (10 g) for each piece of conductive film was dissolved in a mixture of NaOH (6.25 wt%) and urea (12 wt%), and the temperature of which was dropped to –12 °C in advance. The surface-modified MWCNTs was added into the NCC substrate with the contents of 2, 4, 6, 8, 10 wt%, and the film without modified MWCNTs was treated as the control group. To fully disperse the modified MWCNTs, the composites were homogenized at a pressure of 120 MPa 5 times by a homogenizer from GEA NIRO SOAVI (Italy). Then the films were formed by freeze-drying at –50 °C for 48 h.

#### 2.2.3 Characterizations of Modified MWCNTs and Conductive Films

The CA between the modified MWCNTs and NCC substrate was measured using an optical contact angle-measuring instrument from DATAPHYSICS (Germany). The reported CA for each sample was the average value of five measurements made on different areas of the sample surface. The disperse state of the MWCNTs modified by GPTMS in the conductive films was analyzed with the SEM from HITACHI (Japan). Samples were mounted on a conductive adhesive tape, sputter coated with gold, and

observed using a voltage of 18 kV. The chemical structures of the conductive films were characterized by a BRUKER (Germany) FT-IR. The scan was operated from 4000 to 600  $\text{cm}^{-1}$  with an accumulation of 64 scans at a resolution of 4  $\text{cm}^{-1}$ . The crystal structure of the conductive films was examined with the XRD purchased from SHIMADZU (Japan) and the scan speed was  $2^\circ/\text{min}$ . The diffraction patterns of the conductive samples were obtained within a  $7\text{--}45^\circ$   $2\theta$  angular interval with  $0.05^\circ$  step. The electrical resistivity was tested with a four-point probes (M-2) produced by Suzhou Jingge Electronic Co. Ltd. The results represent the average value of four measurements.

### 3 Results and Discussion

#### 3.1 Modification and Compatibility of Surface-Modified MWCNTs

The effects of modification were estimated by CA between modified MWCNTs and NCC substrate. The alkyl-oxygen groups of GPTMS were converted to alcoholic hydroxyl groups through the hydrolysis. The surface of raw MWCNTs was covered with hydroxyl groups, which were substituted by the hydrolyzed GPTMS with the formation of stable hydrogen bonds during the modification process. The procedures of surface modification were illustrated in Fig. 1.

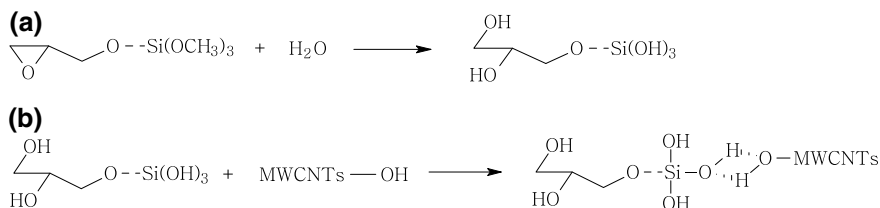


**Fig. 1.** Surface modification of MWCNTs with GPTMS: **a** hydrolysis of GPTMS; **b** surface modification of MWCNTs

As shown in Fig. 2, the CA between MWCNTs and NCC substrate declined with the increase of GPTMS. The hydrogen bonds were generated between GPTMS and MWCNTs while the hydroxyl groups of MWCNTs were replaced with the modifier. The molecular structure of modifier was filled with C–O–Si groups, which led to the reduction of the surface energy of modified MWCNTs [6]. Consequently, the compatibility of modified MWCNTs with NCC substrate was enhanced significantly. CA of original MWCNTs with NCC was  $87.2^\circ$ . When the content of modifier was 4 wt%, the CA was decreased by 23.7%. The decline of the CA slowed down with the further addition of GPTMS. Compared with the control group, CA between the MWCNTs modified by 8 wt% GPTMS and substrate was decreased by 29.1%. The enhancement of compatibility was very limited when the concentration of GPTMS was beyond 8 wt%. Therefore, the following studies focused on the MWCNTs modified by 8 wt% GPTMS.

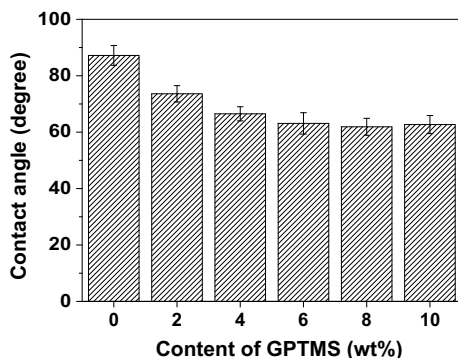


Fig. 2. CA between surface-modified MWCNTs and NCC substrate

### 3.2 Characterizations of the Conductive Films Based on NCC

#### 3.2.1 Disperse State of the Modified MWCNTs in the Conductive Film

The hydrophilic groups of original MWCNTs were replaced by the hydrolyzed GPTMS during the modification and then the disperse state of the modified MWCNTs in the substrate was improved significantly. A structural schematic mechanism of the conductive films based on NCC was presented in Fig. 3.

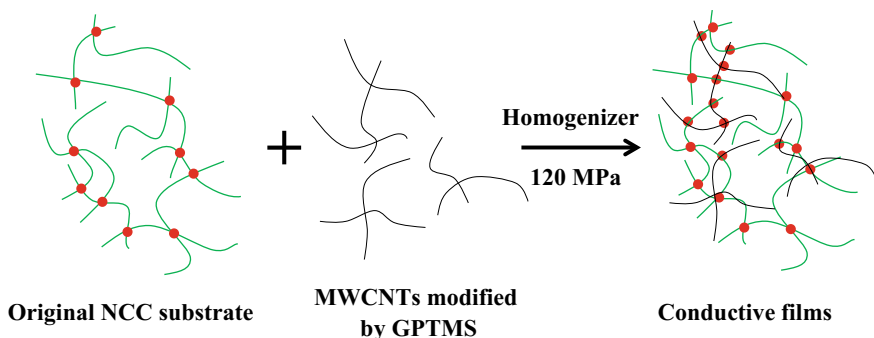
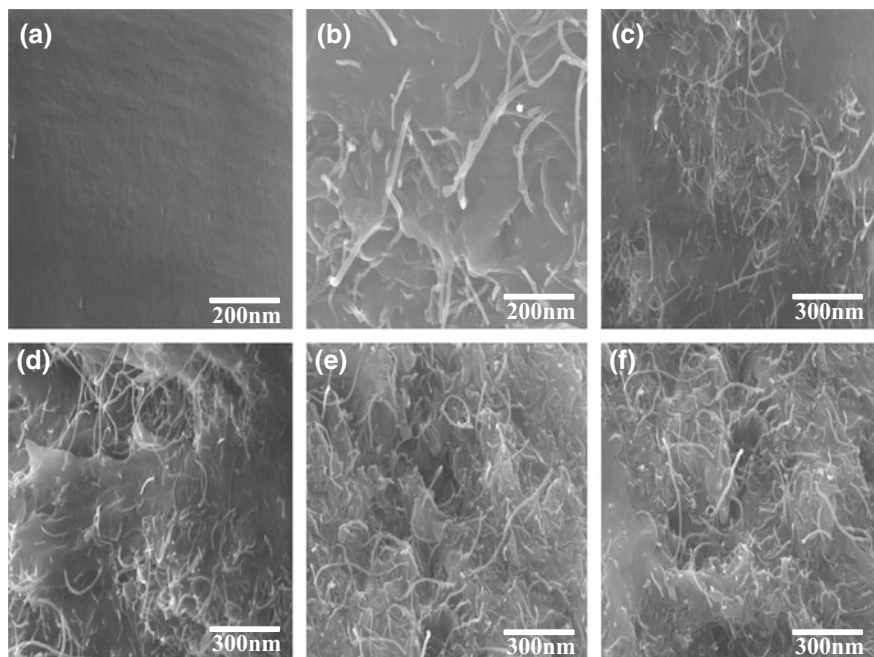


Fig. 3. Structural schematic mechanism of the conductive films based on NCC substrate

The disperse state of the modified MWCNTs in the conductive films was analyzed with SEM at different scales. Noticeably in Fig. 4, the dispersion in the substrate was related to the concentration of surface-modified MWCNTs.

Figure 4a showed the smooth morphology of substrate without modified MWCNTs. When the content of modified MWCNTs was 2 wt%, the dispersion of the nanotubes in the conductive films was uniform (as shown in Fig. 4b). The morphology of the composites was changed obviously with the addition of modified MWCNTs. As shown in Fig. 4d, the entanglement was visible in the conductive films synthesized with 6 wt% modified MWCNTs. In addition, some agglomerations of nanotubes were



**Fig. 4.** SEM micrographs of conductive films with different contents of surface-modified MWCNTs: **a** 0 wt%; **b** 2 wt%; **c** 4 wt%; **d** 6 wt%; **e** 8 wt%; (**f**): 10 wt%

observed in the conductive films when the contents of modified MWCNTs were 8 and 10 wt% (shown in Fig. 4e, f).

### 3.2.2 FT-IR Spectra of the Conductive Films

The chemical structures of NCC substrate and conductive films were confirmed by FT-IR, as shown in Fig. 5. The FT-IR spectrum of NCC substrate (indicated in Fig. 5a) showed a blunt peak at  $3430\text{ cm}^{-1}$ , which corresponded to the surface hydroxyl groups. The peak at  $2890\text{ cm}^{-1}$  belonged to the asymmetrically stretching vibration of C–H. The absorption peaks at  $2260$  and  $1755\text{ cm}^{-1}$  were related to the unsaturated structure such as carbonyl groups.

With the addition of modified MWCNTs, the characteristic peaks at  $3430$  and  $2890\text{ cm}^{-1}$  were enhanced significantly, as seen in Fig. 5d–f. And the reinforcement of these peaks showed the introduction of surface hydroxyl groups and C–H groups into the conductive films. As indicated in Fig. 5, the absorption peaks at  $2260$  and  $1755\text{ cm}^{-1}$  of the conductive films were relatively steady. This phenomenon showed that the content of carbonyl groups in the conductive films was affected by the modified MWCNTs indistinctively.

### 3.2.3 Crystal Structure of Conductive Films

The XRD patterns of NCC substrate and conductive films were indicated in Fig. 6. The characteristic diffraction peak at  $2\theta = 20.8^\circ$ , as the typical pattern of cellulose type II,

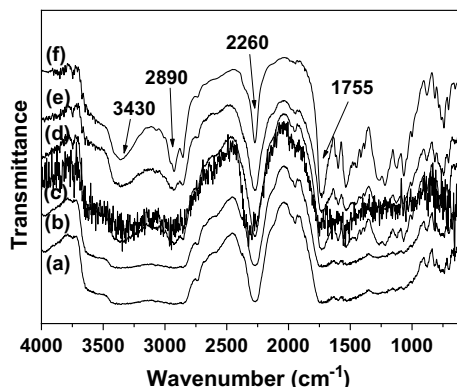


**Fig. 5.** FT-IR spectra of conductive films with different contents of surface-modified MWCNTs: **a** 0 wt%; **b** 2 wt%; **c** 4 wt%; **d** 6 wt%; **e** 8 wt%; **f** 10 wt%

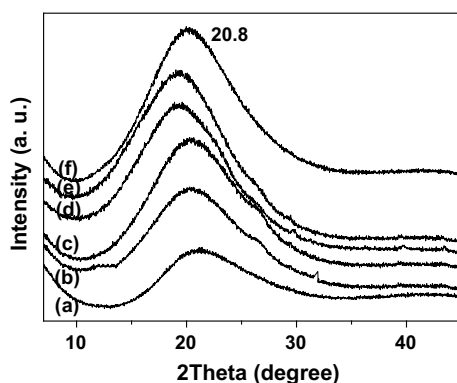


**Fig. 6.** XRD patterns of conductive films with different contents of surface-modified MWCNTs: **a** 0 wt%; **b** 2 wt%; **c** 4 wt%; **d** 6 wt%; **e** 8 wt%; **f** 10 wt%

was shown because the natural crystalline region of substrate was destroyed during the acid hydrolysis.

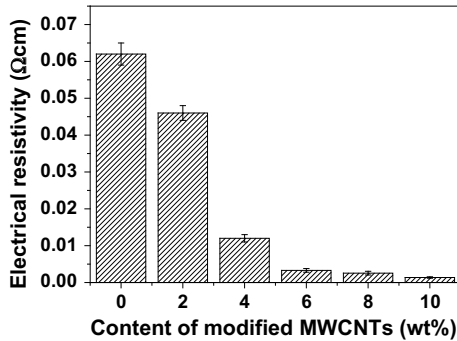
The diffraction position of conductive films was steady while the diffraction intensity of the peak at  $2\theta = 20.8^\circ$  was increased with the addition of modified MWCNTs (shown in Fig. 6). This is because the introduction of hydroxyl groups resulted in the compact arrangement of cellulose chains such that the ratio of crystalline region in the substrate was higher. The crystallinity of conductive films showed a slight rise with the enhancement of MWCNTs (indicated in Table 1).

### 3.2.4 Conductivity of NCC Films with Modified MWCNTs

The resistance of the films to flow of electrical current was associated with the disperse state of conductive additives. The concentrations affected the dispersion of modified

**Table 1.** Crystallinity of conductive films with different contents of surface-modified MWCNTs: (a) 0 wt%; (b) 2 wt%; (c) 4 wt%; (d) 6 wt%; (e) 8 wt%; (f) 10 wt%

Sample	a	b	c	d	e	f
Crystallinity (%)	41.6	42.2	42.7	44.2	45.8	46.5

**Fig. 7.** Electrical resistivity of conductive films with different contents of surface-modified MWCNTs

MWCNTs in substrate significantly. The relationship between the amount of modified MWCNTs and the conductivity was shown in Fig. 7.

Compared with the control group, the electrical resistivity of the conductive film decreased by 25.6% when the content of modified MWCNTs was 2 wt%. The electrical resistivity of the conductive films synthesized with 4 wt% modified MWCNTs was  $1.20 \times 10^{-2} \Omega \text{ cm}$ ; and the resistivity declined to  $3.30 \times 10^{-3} \Omega \text{ cm}$  with 6 wt% modified MWCNTs. It was obvious that the incremental contribution to the conductivity decreased when the content of modified MWCNTs was more than 8 wt%. When the content of surface-modified MWCNTs was 10 wt%, the electrical resistivity of the conductive films was  $1.37 \times 10^{-3} \Omega \text{ cm}$ . According to the SEM micrographs (Fig. 4), the aggregated disperse state of 8 and 10 wt% modified MWCNTs can be one of the main limitations for the conductivity.

## 4 Conclusions

In this study, GPTMS was treated as the surface modifier of MWCNTs. When the content of modifier was 8 wt%, the CA between modified MWCNTs and NCC substrate was  $61.9^\circ$ , which was 29.1% less than that of the original MWCNTs. According to the SEM micrographs, it can be concluded that the disperse state of modified MWCNTs was related to the concentration significantly. The homogeneous disperse state was visible when the contents of modified MWCNTs were less than 6 wt%. The FT-IR spectra indicated the effects of modified MWCNTs on the chemical structure of the conductive films. Hydroxyl groups and C-H groups were introduced into the NCC

substrate by modified MWCNTs. The XRD diffraction position of conductive films was steady, while the crystallinity increased from 41.6 to 46.5% when the content of MWCNTs was 10 wt%. The growth rate of the conductivity slowed down when the concentration of modified MWCNTs was more than 8 wt% and the electrical resistivity of the films synthesized with 10 wt% modified MWCNTs was  $1.37 \times 10^{-3} \Omega \text{ cm}$ .

**Acknowledgements.** The authors are grateful for the support of the Doctoral Foundation of the Henan University of Engineering (D2015016).

## References

1. Im, H. G., Jin, J., Ko, J. H., et al. (2013). Flexible transparent conducting composite films using a monolithically embedded AgNW electrode with robust performance stability. *Nanoscale*, 6(2), 711–715.
2. Yang, W. F., Liu, Z. G., Peng, D. L., et al. (2009). Room-temperature deposition of transparent conducting Al-doped ZnO films by RF magnetron sputtering method. *Applied Surface Science*, 255(11), 5669–5673.
3. Du, X., Zhang, Z., Liu, W., et al. (2017). Nanocellulose-based conductive materials and their emerging applications in energy devices—A review. *Nano Energy*, 35, 299–320.
4. Zhang, H. Y., Shi, L. L., & Feng, X. (2018). Use of chitosan to reinforce transparent conductive cellulose nanopaper. *Journal of Materials Chemistry C*, 6(2), 242–248.
5. Luo, X. G., Liu, S. L., Zhou, J. P., et al. (2009). In situ synthesis of Fe<sub>3</sub>O<sub>4</sub>/cellulose microspheres with magnetic-induced protein delivery. *Journal of Materials Chemistry*, 19(21), 3538–3545.
6. Zhang, H., Chen, H. Y., She, Y., et al. (2014). Anti-yellowing property of polyurethane improved by the use of surface-modified nanocrystalline cellulose. *BioResources*, 9(1), 673–684.





# Study on Preparation and Properties of Paper Plastic Laminatings Based on PVP and PVA

Meiqi Yang, Guorong Cao (✉), Peiyu Fu, and Lizheng Zhang

School of Printing and Packaging Engineering, Beijing Institute of Graphic Communication, Beijing, China  
caogurong@bigc.edu.cn

**Abstract.** To study a new type of paper plastic film laminating product based on PVP and PVA and its related properties.  $L_9 (3^3)$  orthogonal test was used to prepare PVP adhesives, in which three factors (levels) were PVP (10, 12, 14%), potassium stearate (1, 2, 3%) and glycerol concentration (8, 10, 12%). With the peel strength of PVP and PVA laminating products as the evaluation index, the optimal amount of PVP adhesive raw materials could be obtained. At the same time, the solid content and infrared spectrum of the adhesive and the thermal shrinkage rate of the laminating product were measured. The optimal amount of PVP adhesive for laminating was: 10% for PVP, 3% for potassium stearate and 12% for glycerin. The solid content of 10, 12, and 14% PVP adhesives were 55, 67 and 75%, respectively, satisfying the requirements for adhesives for laminating. Infrared spectroscopy analysis showed that there were interactions between the PVP molecules and glycerol hydrogen bonds, and the addition of potassium stearate and glycerin improved the performance of the PVP adhesive and enhanced its stability. With being tested by constant temperature and humidity and heat shrinkage, the samples showed no separation, shrinkage, blistering, wrinkling, warping and discoloration, and had excellent stability. In this paper, the optimum raw material dosage of PVP adhesive for laminating was obtained, and paper plastic laminatings based on PVP adhesive and PVA film were prepared.

**Keywords:** Paper plastic laminating · Adhesives · Peel strength · Heat shrinkage

## 1 Introduction

The laminating of paper printing is a type of post-printing surface decoration process, which refers to the surface of the paper printing with a laminating machine coated with a layer of plastic film, forming a paper-plastic product [1]. This process includes coating the plastic film with adhesive, drying it, and pressurizing and heating it with the paper printings into a whole, and finally forming a kind of waterproof, anti-fouling, folding-resistant, wear-resistant, and beautiful appearance with high value-added printing products [2] such as publications, folding cartons, bags, labels, etc. At present, most of the plastic film substrates used in the paper and plastic laminating on the market are BOPP and BOPET [3]. During the recycling of the laminating products, it is

necessary to mechanically separate the paper and plastic films, increasing the cost of recycling and making them lose their commercial value, which causes great waste of resources. Adhesives for paper and plastic laminating are mainly solvent-based adhesives, water-based adhesives, and hot-melt adhesives. Solvent adhesives generate a large amount of volatile organic solvents during use, polluting the environment; water-based adhesives and hot melt adhesives are insoluble in water and cannot separate paper-based and plastic films in water.

Polyvinyl alcohol (PVA) is a synthetic, non-toxic and harmless water-soluble polymer with a large number of hydroxyl groups in its molecular chain [4]. Hydrogen bonds are easily formed between molecules and molecules, molecules and water molecules. Therefore, PVA has good water solubility. At the same time, PVA film has excellent mechanical properties and surface tension and other properties [5, 6], which are in line with the relevant standards of paper-plastic laminating products. Polyvinylpyrrolidone (PVP) is a water-soluble polymer product [7], with the ability of polar groups in molecular chain and good compatibility with polyvinyl alcohol. In this paper, PVA film was used as the plastic substrate. PVP adhesives were prepared by orthogonal design scheme. Post-printing copper plate paper was used for laminating. PVP adhesives were tested for solid content and infrared, and the laminating samples were tested to measure the peel strength, which was taken as the only parameter to optimize the PVP adhesive formulae.

## 2 Experiments

### 2.1 Sample Preparation

#### 2.1.1 Preparation of PVP Adhesive

Establish Orthogonal Test Design: According to literature reports, the concentration of PVP, potassium stearate and glycerol concentration can influence the peel strength of PVP-PVA laminating materials, thus an orthogonal test design was considered for PVP adhesives, and a  $L_9(3^3)$  orthogonal test sheet was established as shown in Table 1. The peeling force of each sample after laminating is determined as the inspection index, and visual analysis is performed to determine the order of influence of the adhesive and the optimum process parameters.

**Table 1.** Orthogonal factor—levels of preparation of PVP adhesive

Levels	Factors		
	A PVP (%)	B $C_{18}H_{35}KO_2$ (%)	C Glycerol (%)
1	10	1	8
2	12	2	10
3	14	3	12

The orthogonal test group is shown in Table 2.

Preparation of PVP Adhesives: Self-made demonized water was heated to 85 °C to prepare a certain concentration of  $C_{18}H_{35}KO_2$  solution, stirring at a rate of 300 r/min

**Table 2.** Orthogonal test of preparation of PVP adhesive

Number	A (%)	B (%)	C (%)
1	1(10)	1(1)	1(8)
2	1	2(2)	2(10)
3	1	3(3)	3(12)
4	2(12)	3	2
5	2	1	3
6	2	2	1
7	3(14)	1	3
8	3	2	1
9	3	3	2

until completely dissolved. Then prepare a certain concentration of PVP solution on the same conditions. After the solution is completely dissolved, add the corresponding  $C_{18}H_{35}KO_2$ , add a certain amount of glycerin, and stir at 300 r/min until a uniform and stable adhesive solution is formed.

### 2.1.2 Preparation of PVP-PVA Film Laminating Samples

The prepared PVP adhesive was evenly coated on the PVA film with a 12  $\mu\text{m}$  wire rod. The film coating temperature was set at 90  $^{\circ}\text{C}$ , speed was 10 m/min, and the film pressure was 5 MPa. The laminating conditions of the experimental group were set the same. Each set of samples was placed in a temperature of  $23 \pm 2$   $^{\circ}\text{C}$ . and a relative humidity of 40–50% for more than 4 h [8] for test the peeling force.

## 2.2 Performance Test Method

### 2.2.1 Solid Content Test of PVP Adhesive

The solid content affects the product's use and production costs. Under normal circumstances, the adhesive solid content between 30 and 50% can meet the requirements of laminating products. Refer to “GB/T 2793-1995 Determination of Non-Volatile Content of Adhesive” to measure non-volatile content.

### 2.2.2 Film Laminating Peel Strength Test

The paper uses the electronic tensile machine to detect the peel strength of paper and plastic to evaluate the firmness of the bonded film product [9]. The specific method refers to “GB/T 8808-1988 soft composite plastic material peel test method”.

### 2.2.3 PVP Adhesive Infrared Spectrum Test

The chemical structures of PVP powder and PVP adhesive samples were measured by Fourier infrared spectrometer and compared.

### 3 Results and Discussion

#### 3.1 Solid Content Detection Results

The PVP adhesives were tested at concentrations of 10, 12, and 14%, respectively, and the solid contents were about 55, 67, and 75%, respectively. All of them satisfied the requirements of adhesives for laminating. The higher solids content of the PVP adhesive is beneficial to the control of the lamination process and the guarantee of the performance of the laminating product.

#### 3.2 Orthogonal Experimental Analysis of PVP Adhesive

Visual Analysis: The orthogonal test results of the peel strength of PVP adhesives and laminating samples are shown in Table 3.

**Table 3.** Orthogonal test and result of PVP adhesives

Number	A (%)	B (%)	C (%)	Peel strength(N/cm)
1	1(10)	1(1)	1(8)	0.44
2	1	2(2)	2(10)	0.55
3	1	3(3)	3(12)	1.00
4	2(12)	3	2	0.48
5	2	1	3	0.75
6	2	2	1	0.50
7	3(14)	1	3	0.56
8	3	2	1	0.29
9	3	3	2	0.36
K <sub>1j</sub>	0.660	0.493	0.410	
K <sub>2j</sub>	0.577	0.528	0.462	
K <sub>3j</sub>	0.403	0.618	0.768	
R	0.257	0.125	0.358	

From Table 3, the primary and secondary factors affecting the peel strength of PVP adhesives and laminating samples are: glycerin, PVP and potassium stearate. Within the scope of the experimental design, the optimal conditions for the preparation of the adhesive are  $A_1B_3C_3$ , i.e., PVP of 10%, potassium stearate of 3% and glycerin of 12%.

According to the experimental group  $A_1B_3C_3$ , three verification experiments were conducted to prepare PVP adhesives, and the average peel strength of the samples was 1.12 N/cm, which was greater than the value of each test set in Table 3. Therefore,  $A_1B_3C_3$  was used as the optimum conditions for laminating PVP adhesive preparation.

Variance Analysis: The visual analysis of the orthogonal test cannot estimate the experimental error. In order to distinguish the difference of the test result due to the change of the level of each factor or the random fluctuation of the test well, the variance analysis of the test result can be performed [10]. Variance analysis is shown in Table 4.

**Table 4.** Analysis of variance

Factors	Sum of square deviation	Degree of freedom	F value	Significance
PVP (%)	0.103	2	12.875	Obvious significance
C <sub>18</sub> H <sub>35</sub> KO <sub>2</sub> (%)	0.025	3	3.125	Has a certain significance
Glycerinum (%)	0.225	2	28.125	Highly significant
Error	0.01	2		

$F_{0.25}(2,2) = 3.0$ ,  $F_{0.10}(2,2) = 9.0$ ,  $F_{0.05}(2,2) = 19.0$ ,  $F_{0.01}(2,2) = 99.0$

According to Table 4, F value of glycerol >  $F_{0.05}(2,2)$ , that is, concentration of glycerol has a very significant effect on the test results, PVP has a significant effect on the test results, potassium stearate has a certain effect. According to the method of variance analysis, the factors that have significant influence can be selected to select the best level, and the factors that have smaller impact can be selected according to the actual needs. Selecting PVP of 10%, potassium stearate of 3%, and glycerin of 12%, i.e., A<sub>1</sub>B<sub>3</sub>C<sub>3</sub> is the best condition for preparing laminating PVP adhesive, which is consistent with the visual analysis method.

### 3.3 Infrared Spectroscopic Analysis of PVP Adhesives

The PVP infrared spectra measured by various methods are similar, and when there are molecules interacting with PVP, the PVP infrared spectra may show significant differences [11]. Infrared spectra of PVP and PVP adhesives are shown in Figs. 1 and 2.

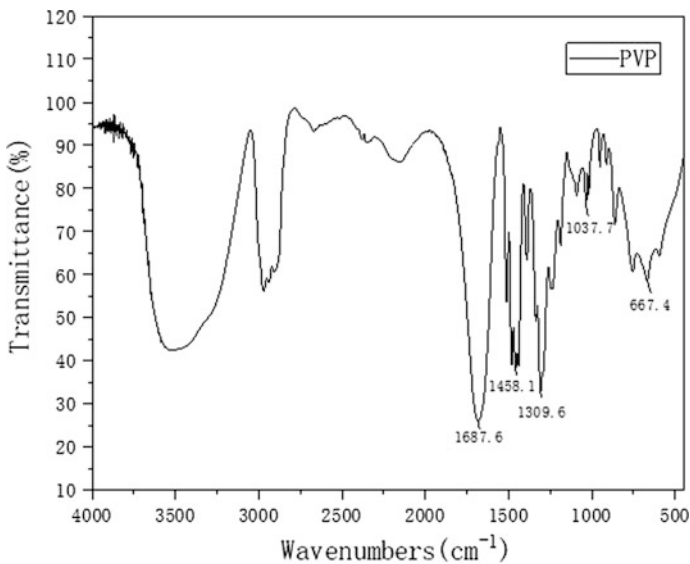


**Fig. 1.** Infrared spectra of PVP

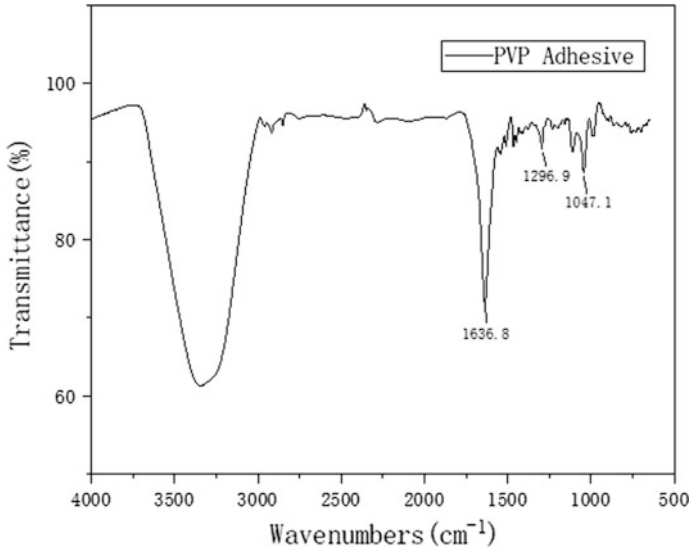


Fig. 2. Infrared spectra of PVP adhesives

As shown in Fig. 1, the characteristic absorption band in the range of 1660–1680  $\text{cm}^{-1}$  is generated by the  $-\text{C}=\text{O}$  stretching vibration of the PVP molecule, and the spectrum band is broad, indicating that there is a strong interaction between  $-\text{C}=\text{O}$  double bond and  $-\text{C}-\text{N}-$ , in which a coupling effect occurs. 1458  $\text{cm}^{-1}$  is the in-plane and out-of-plane bending vibration of the  $-\text{C}-\text{H}$  bond. 1309  $\text{cm}^{-1}$  is the  $-\text{C}-\text{N}$  bond vibration. From Fig. 2, the stretching vibrational absorption peak of  $-\text{C}=\text{O}$  in PVP molecule moves from 1687 to 1636  $\text{cm}^{-1}$ , indicating that there is a hydrogen bonding interaction between PVP molecule and glycerin. The decrease or even disappearance of 1458 and 1309  $\text{cm}^{-1}$  may be due to the entrapment of potassium stearate molecule on the PVP micelles. The  $-\text{OH}$  vibration of glycerol shows at 1047  $\text{cm}^{-1}$ . The addition of potassium stearate and glycerin improved the performance of the PVP adhesive and enhanced its stability.

## 4 Conclusions

In conclusion, a new type of paper plastic laminating can be prepared based on PVP and PVA. By designing the  $L_9(3^3)$  orthogonal test to formulate the PVP adhesive, the solid content of the adhesive and the infrared spectrum, the peeling strength of the laminating products, the following conclusions were obtained:

- (1) The solid content of 10, 12, and 14% PVP adhesives were about 55, 67, and 75%, respectively, which all met the requirements of adhesives for laminating.
- (2) After analyzing the orthogonal test of PVP adhesive by visual analysis and analysis of variance, the optimal condition for preparation of laminating products PVP adhesive is PVP of 10%, potassium stearate of 3%, glycerol concentration of 12%.

- (3) Infrared spectroscopy analysis showed that there were interactions between the PVP molecules and glycerol hydrogen bonds, and the addition of potassium stearate and glycerin improved the performance of the PVP adhesive and enhanced its stability.

**Acknowledgements.** This study is supported by Research on certification and evaluation technology of typical air pollutant prevention and control in electric power, chemical industry and printing industry (2017YFF0211803), the General Education Reform Project of Beijing Institute of Graphic Communication (22150116007/031) and Packaging Engineering Teaching Team (construction) of Beijing Institute of Graphic Communication (22150116006/017).

## References

1. GB/T 27934.1-2011. Paper film coating process control and detection methods Part 1: Basic requirements.
2. Xiaofeng, C. (2010). The choice of paper plastic coating process and adhesive. *China Packaging News*.
3. Shouyi, S. (2012). DeChang inaugurates a new era of global paper-plastic laminating technology—an interview with the general manager of Guangdong Deguan Film New Material Co., Ltd. marketing company SuGuihai. *China Packaging Industry*, 2012(10), 83–84.
4. Jiaming F., & Xuehua, Z. (2017). A review of patented technology of water-soluble polyvinyl alcohol films for packaging and agriculture. *Science & Technology Innovation and Application*, 2017(09), 45.
5. Zhiyong, K., & Aimin, X. (2003). Research progress of polyvinyl alcohol packaging film. *Plastics*, 2003(05), 65–69.
6. Baolin, W. (2014). Study on structure and properties of polyvinyl alcohol. *China Adhesives*, 23(03), 30–36.
7. Tingfang, M., & Tiejun, S. (2002). Properties, synthesis and applications of polyvinylpyrrolidone. *Applied Chemicals*, 03, 16–19.
8. GB/T 8808-1988. Soft composite plastic material peel test method.
9. Xinting, W. (2018). Preparation and properties of film and tape based on PVA film. *Beijing Institute of Graphic Communication*.
10. Haiying T., Guoqiang Z., Ping H., & Pei L. (2008). Analysis of an example of orthogonal experiment design. *Pharmacy Services and Research*, 2008(01), 75–76.
11. Yingde, C., Guobin, Y., & Lewen, L. (2001). *Synthesis and application of polyvinylpyrrolidone*. Beijing: China Science Press.



# Research on Migration of Butylated Hydroxytoluene from Polyethylene Packaging Materials

Yan Zhang<sup>1,2</sup>, Meng Tao<sup>1</sup>, and Qingbao Wei<sup>1</sup>(✉)

<sup>1</sup> Henan University of Animal Husbandry and Economy, Zhengzhou, China  
yanzhang12@yeah.net, zzmzwqb@163.com

<sup>2</sup> Zhengzhou Sanquan Foods Co., Ltd., Zhengzhou, China

**Abstract.** The migration of the antioxidant, butylated hydroxytoluene (BHT), from the high-density PE materials is researched by the GC-MS method. The initial BHT concentration is obtained through the ultrasonic hexane abstraction. This paper researches the rule of migration of BHT into fatty food simulacrum at 60 °C (the high temperature for short-time sterilization), 30 °C (the normal temperature for storage) and 4 °C (the low temperature for refrigeration).

**Keywords:** BHT · Migration rate · GC-MS

## 1 Introduction

PE material is widely used in food packages. The antioxidant, plasticizer, heat stabilizer and other reagents are often used as additives added in PE package materials for the purpose of improving the processing performance of PE or making up for the deficiency of resin performance. The migration of additives from the package materials has become the focus of attention [1]. The antioxidant, butylated hydroxytoluene (BHT), added in PE food package can inhibit and slow down the oxidation and degradation of PE. However, the BHT can permeate and migrate into food during contacting the food and influence the taste of food. Besides, the excessive BHT is toxic to the physical health of consumers.

## 2 Material and Method

### 2.1 Material and Reagent

BHT with the purity higher than 98.5% was purchased from Zhengzhou Huafeng Reagent Co., Ltd. The high density PE barrel was purchased from a supermarket.

### 2.2 Instrument and Equipment

American Agilent GC-MS was used for test of BHT migration quantity.



## 2.3 Method

### 2.3.1 Chromatographic Conditions

Chromatographic column (HP-5MS Agilent, 30 m × 250 μm × 0.25 μm) [2]; temperature rise procedure: keep for 2 min at 60 °C, rise to 180 °C at the speed of 20 °C/min and rise to 195 °C at the speed of 5 °C/min; carrier gas (N<sub>2</sub>) flow rate: 1.5 mL/min; pressure: 13.385 Ψ; sample volume: 1 μL.

### 2.3.2 Mass Spectrometry Conditions

Electron bombardment ion source; electron energy: 70 eV; transmission line temperature: 275 °C; ion source temperature: 230 °C; parent ion: m/z 205; activation voltage: 1.5 V; mass scan range: m/z 35–500.

## 2.4 Calculation of Migration Rate

$$\text{Migration rate} = A_1/A_2 \quad (2.1)$$

where  $A_1$  is the concentration of BHT in simulated food solution in a balanced state after migration;  $A_2$  is the initial BHT concentration in package materials.

## 3 Result and Analysis

### 3.1 Preparation of Standard Sample and Drawing of Standard Curve

Prepare the BHT standard solution with the BHT concentration of 500, 250, 62.5, 31.25, 15.625 and 0 ng/ml. Test with the spectrometer. Draw the standard curve based on data shown in Fig. 1. If the relativity  $R^2$  is 0.99976702, it indicates that the standard curve is valid.

### 3.2 Determination Method for Initial BHT Content in Sample

Cut the sample into 0.1 cm \* 0.15 cm granules. Weigh a certain amount of sample and place the sample in a 50 ml colorimetric tube with plug. Add 20 ml hexane in the tube and extract in ultrasonic state at 40 °C for 2 h. Measure 1 ml solution and filter the solution. Measure the BHT concentration  $T_1$  with the spectrometer. Then, pour out the remaining solution from the tube and add 20 ml hexane. Extract in ultrasonic at 40 °C for 1 h. Measure 1 ml solution and filter the solution. Measure the BHT concentration  $T_2$  with the spectrometer. When the proportion of  $T_2$  to  $T_1$  is less than 3%, it can be deemed that all BHT migrates from the package materials. Otherwise, BHT shall be extracted in ultrasonic again. Three parallel samples shall be experimented at the same time.

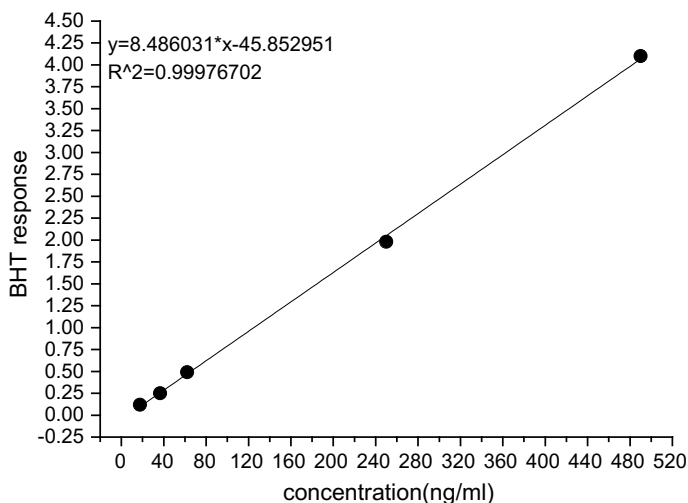


Fig. 1. Standard curve

### 3.3 Migration Experiment

#### 3.3.1 Experiment of Migration of BHT to Fatty Food Simulacrum at 60 °C

Hexane is used as the fatty food simulacrum [3]. Cut the sample into 1.5 cm \* 5 cm rectangular sheets. After weighing, place the rectangular sheets in a reagent bottle with plug, add 100 ml hexane in the bottle and place the bottle in a constant temperature incubator at 60 °C. Take 1 ml sample, filter and feed the sample every 1 h. Three parallel samples shall be experimented at the same time.

#### 3.3.2 Experiment of Migration of BHT to Fatty Food Simulacrum at 30 °C

The experiment method is same with that in Sect. 3.3.1. The difference is that the bottle is placed in a constant temperature incubator at 30 °C (Table 1).

Table 1. Determination of initial BHT content: hexane extraction

Item	Sample 1	Sample 2	Sample 3	Mean value
The 1st extraction	51.63064833	49.78557505	50.79802956	50.73808431
The 2nd extraction	0.847642436	0.847758285	0.905714286	0.867038335
The 3rd extraction	0.670039293	0.690935673	0.692807882	0.684594282

#### 3.3.3 Experiment of Migration of BHT to Hexane at 4 °C

The experiment method is same with that in Sect. 3.3.2. The difference is that the bottle is placed in a constant temperature incubator at 4 °C.

### 3.4 Initial BHT Content

It can be seen that relative deviation of three parallel samples in the ultrasonic hexane extraction is 0.12–1.88% and the parallelism is good. The proportion of average extraction value at the 2nd time to average extraction value at first two times is 1.68%, less than 2%. Therefore, it can be regarded that the extraction is complete [4]. The extraction capacity at the 1st time is far higher than that at last two times. The extraction capacities at last two times are basically the same. It indicates that the method can extract most BHT from sample [5].

### 3.5 Influence of Temperature on BHT Migration

The migration rate of BHT into hexane within 1 h at 60 °C is up to 45%, as shown in Fig. 2. The migration rate in the next 2–7 h is kept within 45–49%. It indicates that the migration rate mainly grows in the first 1 h. Then, the migration is kept in dynamic balance.

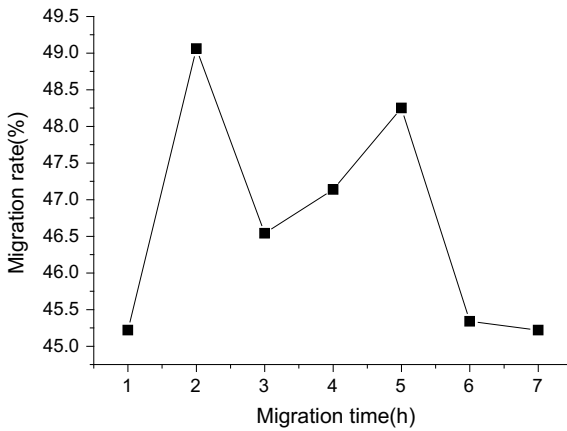


**Fig. 2.** Rate of migration of BHT into the food simulacrum-hexane (60 °C)

It can be seen from Fig. 3 that the migration rate of BHT at 30 °C in 2 h is up to 44% and reaches the balance with value 51–58% after 5 h.

It can be seen from Fig. 4 that the migration rate of BHT at 4 °C is up to 48% after 9 h and then is kept in the dynamic balance with the value 41.71–52.12%. The migration rate rapidly grows in early period and is basically stable in late period.

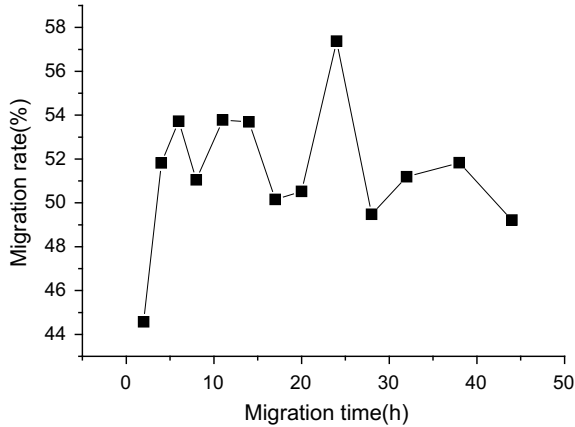


Fig. 3. Rate of migration of BHT into the food simulacrum-hexane (30 °C)

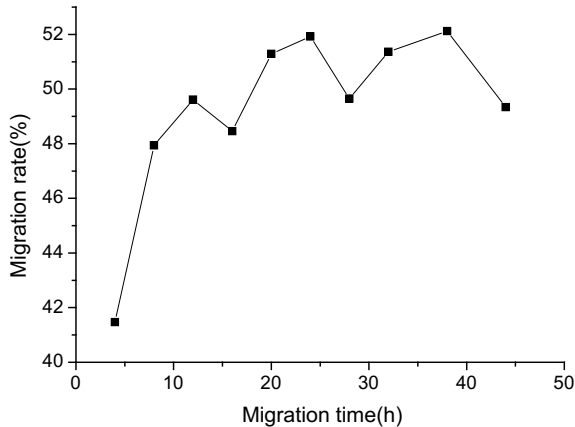


Fig. 4. Rate of migration of BHT into the food simulacrum-hexane (4 °C)

## 4 Conclusions

This paper researches the abstraction and determination method of initial BHT concentration in PE and abstracts BHT with hexane in ultrasonic with high efficiency, good repeatability and accurate determination of initial BHT concentration in PE. Furthermore, this paper compares the migration of BHT into hexane at 60, 30 and 4 °C. The result shows that the influence of temperature on migration rate isn't obvious because the migration rates at three temperature conditions are stable at 50%, which indicates that half BHT migrates. Temperature influences the time of reaching the migration stability, i.e. at 60 °C, BHT migration is balanced after about 1 h, at 30 °C, about 5 h, and at 4 °C, about 10 h. It proves that the temperature can increase the migration rate.

## References

1. Leda-Coltro, J. B. P., Paulo, A. C., et al. (2014). Migration of conventional and new plasticizers from PVC films into food simulants: a comparative study. *Food Control*, *44*(10), 118–129.
2. Albert-Guart, M. W., Mezquid, A., Lacorte, S., et al. (2013). Migration of plasticisers from Tritan™ and polycarbonate bottles and toxicological evaluation. *Food Chemistry*, *141*(3), 373–380.
3. Yining, X., & Maria, R. (2016). Effect of cut edge area on the migration of BHT from polypropylene film into a food Simulant Effect of cut edge area on the migration of BHT from polypropylene film into a food simulant. *Polymer Testing*, *51*, 190–194.
4. Cristina, N., Julio, G., et al. (2013). Determination of partition and diffusion coefficients of components of two rubber adhesives in different multilayer materials. *International Journal of Adhesion & Adhesives*, *40*, 56–63.
5. Yolanda, E., & Cristina, N. (2013). Nanoparticle release from nano-silver antimicrobial food containers. *Food and Chemical Toxicology*, *62*, 16–22.

**Part IX**  
**Novel Functional Material Technology**



# Synthesis of 6-[3,6,7,10,11-Pentakis(pentyloxy)triphenylen-2-yloxy]-hexyl Methacrylate and Its Mesophases Study

Yuwen Feng, Jingze Bi, Huanzhi Yang, Zhenhu Zhang, Chunxiu Zhang<sup>(✉)</sup>, and Jialing Pu

Beijing Institute of Graphic Communication, Beijing, China  
1691123024@qq.com, zhangchunxiu@bigc.edu.cn

**Abstract.** A novel triphenylene-based discotic liquid crystal 6-[3,6,7,10,11-Pentakis(pentyloxy)triphenylen-2-yloxy]-hexyl methacrylate. Chemical structure of this compound has determined by <sup>1</sup>HNMR and FT-IR spectrum, and its mesophase was investigated by differential scanning calorimeter (DSC) and polarizing optical microscopy (POM) methods. This new compound has the unique optical properties of discotic liquid crystals because of their remarkable photoconductivity and high charge carrier mobility. Columnar discotic liquid crystals based on triphenylene show great potential as molecular organic materials for optoelectronic devices.

**Keywords:** Triphenylene discotic · Liquid crystalline · Columnar phase

## 1 Introduction

Liquid crystals are the fourth state of matter except gas, liquid and solid. As a unique functional soft substance, it not only has the fluidity of the liquid, but also has the crystal anisotropy, which is considered as a kind of thermodynamic stability.

According to the different geometries of the liquid crystal molecules, we classify them into rod-shaped liquid crystals and discotic liquid crystals. Among them, the rigid aromatic core of the rod-shaped liquid crystal molecule shows a long rod shape, and several flexible side chains are connected along the long axis direction thereof, and the liquid crystal performance is exhibited when the aspect ratio is greater than 4. The discotic liquid crystal molecules are formed by a rigid central core. And the outer edge of a number of flexible side chains. The discotic liquid crystal molecules form an ordered columnar structure through molecular self-assembly and have certain carrier transport properties.

The first discovery of benzene hexamer was in 1977 by Chandrasekhar et al. [1]. In 1977, Indian scientists discovered that in the study of homohexene esters, it was found that discotic molecules have liquid crystal properties capable of forming columnar phases, and there is a strong interaction in the rigid cores of discotic molecules, and the mobility of molecules is due to the flexible side chains at the edges of the discotic molecules are formed by the relatively weak van der Waals forces. In this way, the balance between the rigid core and the flexible side chain determines the liquid

crystal properties of the material. At the same time, its balance performance also affects the self-aggregation behavior of the molecule. The discotic molecules can form an ordered nematic phase as well as ordered and positionally ordered columnar phases.

The rigid inner core of the self-assembled disc-shaped molecules tends to accumulate under the action, and the side chains of the edges are more likely to pile up together, and molecular-level micro-dissociation will occur, thereby forming a columnar phase. Ordered stacking of discotic molecules in the column facilitates orbital stacking of the discotic molecules, giving them excellent carrier transport performance in one dimension along the axis of the column [2]. The mobility in the direction along the axis of the column is more than 100 times along the vertical axis. The triphenylene molecules that we studied are typical liquid crystal molecules in the discotic liquid crystals [3]. They have a variety of structures, are easy to synthesize and purify, have a low melting point, and have good thermal stability. These excellent properties make them as we have always been one of the fine materials for in-depth study [4].

In this paper, the synthesis and processing of the novel triphenylene disc-shaped liquid crystal 6-[3,6,7,10,11-penta(pentyloxy)benzophen-2-yl]-hexane methacrylate and its application properties are studied. The derivatives of triphenylene have many optimized properties. The self-assembly properties of a result in stable photochemical properties and a high degree of order in its spatial structure.

## 2 Experimental

Chemicals used in the synthesis if not specified were all analytic reagents (Beijing Chemical Reagents Co). The chemical structure was characterized by measuring on a Bruker DMX-300 300 MHz NMR spectrometer and FTIR-8400.

### 2.1 Synthesis of 6-[3,6,7,10,11-Penta(Pentoxo)Benzophen-2-Yloxy]-Hexane Methacrylate

The target compound was synthesized according to the route shown in Fig. 1.

The synthesis of the target compound is mainly based on the literature. Using catechol as base material to synthesis compound 1. The synthesis of compound 1 was prepared by reference to the Williamson reaction. Then, according to the mechanism of Scholl reaction, compound 1 was catalyzed by iron trichloride and trimerized to give 2,3,6,7,10,11-hexamethoxy triphenylene [5]. In order to get 2-hydroxy-3,6,7,10,11-penta-pentoxotriphenylene (compound 3), the B-type bromate-cholesterol was selected because it has slightly lower of the activity than boron tribromide. Etherification reaction, Adding 2-hydroxy-3,6,7,10,11-pentapentyloxytriphenylene [6] to a 250 ml three-necked flask (800 mg, 1.185 mmol), Potassium carbonate (980 mg, 7.1 mmol), Acetonitrile (25 ml), stir for 15 min, Then 1,6-dibromoethane (3 g, 12 mmol) was added, this reaction was refluxed on a nitrogen gas shielded balloon at 75 °C for 12 h. The product (compound 4) was chromatographed with petroleum ether-dichloromethane-ethyl acetate as eluent. Recrystallization from ethanol gave the product 2-(6-bromohexyloxy)-3,6,7,10,11-pentapentyloxytriphenylene. The product (4.5 g, 5.3 mmol), methacrylic acid (0.93 g, 10.8 mmol), potassium hydrogen



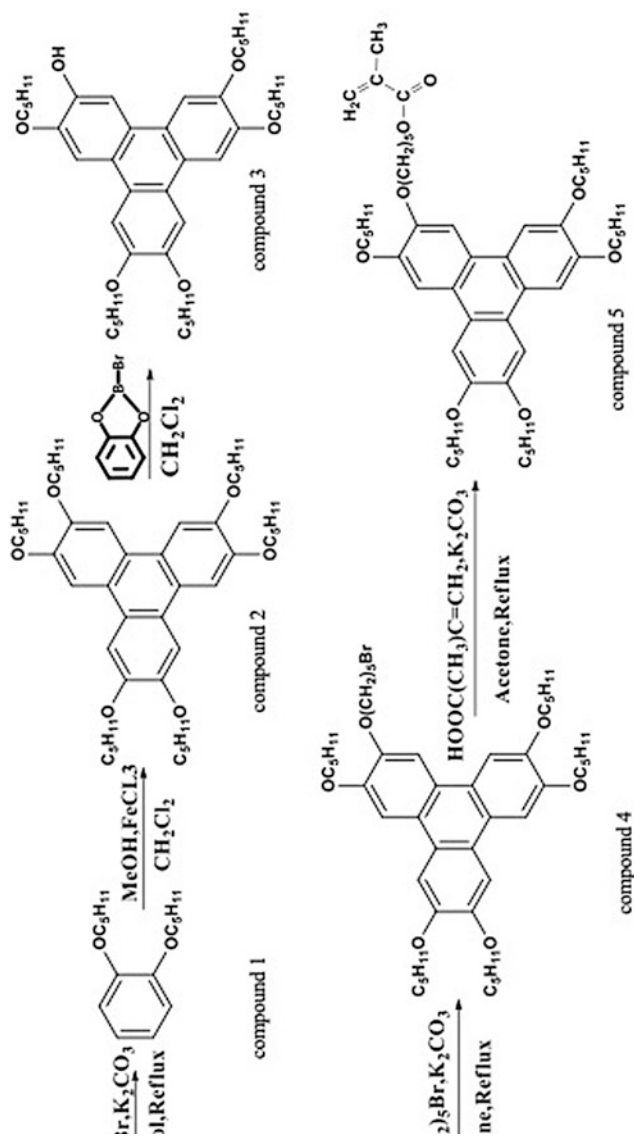


Fig. 1. Synthesized route of compound

carbonate (1.3 g, 13 mmol) was added in succession to 50 ml of N,N-dimethylformamide (25 ml). In the three-necked flask, reaction was carried out in nitrogen protection at 120 °C for 24 h. The product (compound 5) was chromatographed with petroleum ether-dichloromethane-ethyl acetate as eluent. And recrystallize in ethanol, a white solid was obtained as the final target product 6-[3,6,7,10,11-penta(pentyloxy)benzophen-2-yl]-hexane methacrylate [7].

## 2.2 Characterization

The thermal and optical properties of the synthesized material were observed using a Lecia polarized light microscope (POM) equipped with a Linkam LC600 hot stage and a Netzsch differential scanning calorimeter DSC (Thermal Analysis DSC 2010). The heating rates of both POM and DSC are 10 °C min<sup>-1</sup>. The DSC was used to calculate the phase transition from 0 to 155 °C and the associated enthalpy.

Characterization of liquid crystal properties. The relationship between the optical structure and the thermal stage was investigated using a polarizing microscope (POM). The sample was heated (10 °C/min) to 90 °C (isotropic phase), then cooled (10 °C/min) to room temperature, and the in-process liquid crystal texture was observed. Differential scanning calorimetry (DSC) was used to determine the change in phase transition temperature and related enthalpy at a scanning rate of 10 °C min<sup>-1</sup> at 0 °C.

To characterize the liquid crystal properties, we used a polarization microscope equipped with a Linkam LC600 hot stage to study the relationship between its optical structure and temperature changes. The sample was heated (10 °C/min) to 90 °C (isotropic phase) and then cooled (10 °C/min) to room temperature, during which time the change in the liquid crystal structure was observed. The thermal properties of the liquid crystals were observed using a NETZSCH differential scanning calorimeter DSC (thermal analysis DSC 2010). When the scanning speed was 10 °C min<sup>-1</sup> at 0 °C, the phase transition temperature and the associated enthalpy change were measured.

## 3 Results and Discussion

### 3.1 FT-IR and <sup>1</sup>H-NMR

See Fig. 2.

### 3.2 DSC

There is only one endothermic peak throughout the temperature increase. The temperature is 45.7 °C and the enthalpy value is 42.38 J/g, which means that only one phase change occurs during the heating process. According to the POM pattern obtained at 40 °C (as shown in Fig. 3), it can be inferred that after 45.7 °C, the target product turns from liquid crystal state to isotropic state. The red curve is the first temperature drops curve. The observation curve can show that there is only one exothermic peak. The temperature is 15 °C and the enthalpy value is 15.6 J/g.

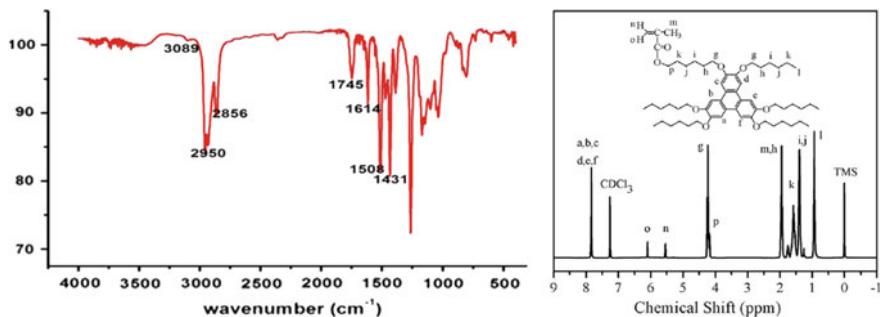


**Fig. 2.** FT-IR and  $^1\text{H-NMR}$  of final compound FT-IR(KBr):  $\nu_{\text{max}}$  ( $\text{cm}^{-1}$ ):3089(=C–H); 2950,2856( $-\text{CH}_3/-\text{CH}_2-$ );1745( $-\text{C}=\text{O}$ );1614 ( $-\text{C}=\text{C}-$ ); 1614,1508,1431 ( $\text{C}_6\text{H}_6$ )  $^1\text{H-NMR}$ :H (300 MHz,  $\text{CDCl}_3$ ): 7.80–7.86 (m,6H), 6.15–6.25 (s,1H), 5.40–5.50 (s,1H), 4.1–4.3 (m,14H), 2.0–1.5(m,43H)

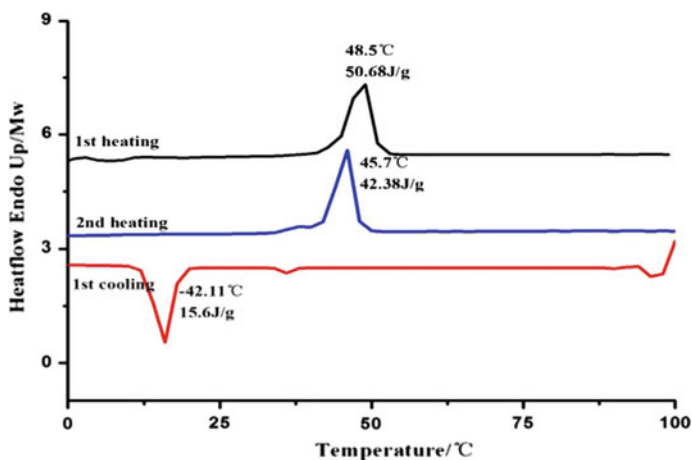


**Fig. 3.** DSC thermogram of compound 5

### 3.3 POM

At 20 °C a small amount of focal conic texture appears, as shown in Fig. 4. At 15 °C, the texture obtained is a linear defect texture, and the linear defect texture is a typical texture of a hexagonal columnar phase. Therefore, we can initially determine that the compound forms a hexagonal columnar phase at 15 °C.

## 4 Conclusions

As a result, the compound 6-[3,6,7,10,11-penta(pentyloxy)benzophen-2-yloxy]-hex-anemethacrylate was prepared and subjected to a series of characterizations [8]. The chemical structure was confirmed by measuring  $^1\text{H-NMR}$  and FT-IR spectra.

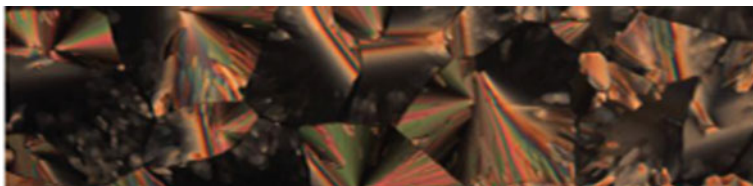


**Fig. 4.** Textures observed at 20 °C during cooling process

By combining the test results of the DSC, POM was used to observe the columnar phase structure of the target compound. The compound exhibits good liquid crystal columnar phase characteristics and liquid crystal range [9], which provides the basis for subsequent synthesis of organic semiconductor devices. It is also proved that the introduction of the composite matrix into the discotic liquid crystal can suppress the crystallization, expand the mesophase range, increase the clearing temperature and stabilize the columnar phase.

**Acknowledgements.** This work is supported by state Key Laboratory for Mechanical Behavior of Materials, the Natural Science Foundation of China (No. 51702019). National Natural Science Foundation of China (21604005) and the Beijing Municipal Education Commission Project under Grant (No. KM201210015008).

## References

1. Chandrasekhar, S., Sadashiva, B. K., & Suresh, K. A. (1977). Liquid crystals of disk-like molecules. *Pramana*, 7, 471–480.
2. Mu, B., Wu, B., Pan, S., et al. (2015). Hierarchical self-organization and uniaxial alignment of well synthesized side-chain discotic liquid crystalline polymers. *Macromolecules*, 48(8), 2388–2398.
3. Heppke, G., Krueker, D., et al. (2000). *Liquid Crystals*, 27, 643.
4. Yang, C. C., Chen, L., Zhong, K. L., et al. (2011). Various columnar nano-structures from self-assembly of triphenylene discotic liquid crystalline molecules. *Chemical Journal of Chinese Universities*, 32(12), 2777–2781.
5. Kim, J. K., Thébault, F., Heo, M. Y., et al. (2012). 2,3,6,7,10,11-Hexamethoxytriphenylene (HMTP): A new organic cathode material for lithium batteries. *Electrochemistry Communications*, 21(1), 50–53.
6. Zhang, M. X., Zhang, C. X., Pu, J. L., et al. (2012). Synthesis and mesophases study on 2-(8-bromooctanoic acid ester)-3,6,7,10,11-penta-pentyloxytriphenylene. *Solid State Phenomena*, 181–182, 156–159.
7. Boden, N., Bushby, R. J., Clements, J., et al. (1999). Device applications of charge transport in discotic liquid crystals. *Journal of Materials Chemistry*, 9, 2081–2086.
8. Zhang Z., Yang H., Zhang W., et al. (2018). Synthesis and property study of 2-undecenoic acid ester-3,6,7,10,11-penta-pentyloxytri-phenylene. *Applied Sciences in Graphic Communication and Packaging*
9. Boden, N., Borner, R. C., Bushby, R. J., Cammidge, A. N., & Jesudason, M. V. (1993). The synthesis of triphenylene-based discotic mesogens new and improved routes. *Liquid Crystals*, 15(6), 851–858.



# Effect of Lignin Content on the Degradation of the Composite Material Prepared from Thermoplastic Starch and Sugarcane Pith

Yali Wu<sup>1</sup>, Yanna Lv<sup>2(✉)</sup>, Maocheng Deng<sup>1(✉)</sup>, and Beihai He<sup>3</sup>

<sup>1</sup> School of Food and Biotechnology, Guangdong Industry Polytechnic, Centre of Guangdong Higher Education for Engineering and Technological Development of Speciality Condiments, Guangzhou, China

2003102018@gdip.edu.cn

<sup>2</sup> School of Light Industry & Chemical Engineering, Dalian Polytechnic University, Dalian, China

lvyn@dlpu.edu.cn

<sup>3</sup> State Key Lab of Pulp and Paper Engineering, National Engineering Research Center of Papermaking & Pollution Control, South China University of Technology, Guangzhou, China

**Abstract.** To investigate the effect of lignin content on the material prepared from thermoplastic starch and sugarcane pith (TPS/BP), individual alkaline and combined acid and alkaline pretreatments were employed to obtain BP with different contents of lignin for preparation of TPS/BP. Degradation by microbial organisms using shaking flask and observation of morphology by using SEM were investigated. The deepen scratch-like structure on the surface of BP was observed, which is possibly due to the removal of lignin. Lignin content was decreased by 15% after pretreatment at 100 °C using 5% NaOH solution. The biodegradability of the resultant TPS/BP was improved by 61.76% after 10 days' digestion at 30 °C with a rotatory speed of 150 rpm. The biodegradability of TPS/BP with lower lignin content of 4–5% was significantly enhanced, with complete degradation after 10 days' digestion in shaking flask.

**Keywords:** Lignin · Thermoplastic starch/sugarcane pith · Composite material · Microbial degradation

## 1 Introduction

Sugarcane bagasse is the main by product from sugarcane industry. It is one of the best feedstock for paper making. However, 30–40% are composed of soft, short and thin cell wall, namely, bagasse pith (BP). BP will hold a large amount of chemicals during pulping, which increases the viscosity of the waste liquid and reduces the pulping efficiency [1]. The strength of the resultant paper will also be reduced significantly [2]. Therefore, removal of BP ahead of pulping is a prerequisite for paper-making factories.

BP is now being used as energy source for heat and electricity through combustion, which is not the best way to make full use of it [3].

Preparation of biodegradable composite materials by blending starch and BP would not only dramatically increase the mechanical strength of thermoplastic starch (TPS) but would also decrease the cost for making TPS. This is a higher value-adding process to utilize BP [4]. Biodegradability is the main characteristic of the thermoplastic starch/BP (TPS/BP). Therefore, investigation of the influence of factors like the ratio, lignin content, etc. on the biodegradability would benefit the following manufacture.

The main components in BP are cellulose, hemicellulose and lignin. Lignin is bonded with cellulose and hemicellulose by either covalent bonds or hydrogen bonds. This structure restricts the materials from being degraded by microorganisms in a short period [5]. Therefore, pretreatments which will partially decompose the structure are usually required for better biodegradability [6, 7]. Acid, alkaline, and organic solvent pretreatments are able to increase the biodegradability mainly because of their delignification effect [8]. Delignification could also be achieved by hot water and dilute acid pretreatment [8].

Based on the above, in this work, the effect of conditions of alkaline pretreatment on lignin content was studied. BP with different lignin contents was used to prepare TPS/BP. Thereafter, biodegradability was tested using the prepared TPS/BP as sole carbon source. The influence of lignin content on the biodegradability was summarized afterwards.

## 2 Materials and Methods

### 2.1 Materials

BP was provided by Jiangmen sugarcane factory. The crude BP was fractionated by mesh sieves and the fraction between 40 and 60 mesh was collected and sealed in plastic bag for further use. The chemical compositions of bagasse pith were determined by following Chinese standards. The results and corresponding standards are shown in Table 1. Food grade corn starch was obtained from Changchun Dacheng corn company. Glycerol, urea, stearic acid, concentrated  $H_2SO_4$ , NaOH, and acetic acid are of analytical grade.

The microorganism strain which was used for biodegradation test was screened and stored in our own laboratory. The strain was identified and belonged to *Aspergillus* [9].

**Table 1.** Chemical analysis of bagasse pith

Ash content (%)	Extract content (%)			Klason lignin (%)	Acid soluble lignin (%)	Total lignin (%)	Holocellulose (%)	Pentosan (%)
	Hot water	Benzene-alcohol	1% sodium hydroxide					
9.21	4.43	2.85	46.11	19.61	1.54	21.15	63.21	21.83

## 2.2 Pretreatment of BP

### 2.2.1 Alkaline Pretreatment

The un-sieved BP was added into solutions with 1, 5, and 15% (w/v) NaOH, respectively, and placed at  $30 \pm 2$  °C. Another pretreatment was performed under reflux condition with 5% NaOH. After pretreatment, BP was filtrated and washed by acetic acid (acetic acid:water = 1:3, v/v), and finally washed by deionized water until pH 7. The solid residue was then placed in an 80 °C oven for 10 h. The 40–60 mesh fraction was collected for further use.

### 2.2.2 Combined Acid and Alkaline Pretreatment

The un-sieved BP was mixed with 0.5% H<sub>2</sub>SO<sub>4</sub> (w/w) and cooked at 120 °C for 60 min. The filtrated solid residue was washed by deionized water until pH 7 and dried at 80 °C for 10 h. Subsequently, a portion of the dried sample was added to 5% NaOH solution and placed at  $30 \pm 2$  °C for 100 min. Another portion was cooked with reflux at 100 °C for 100 min. The solid residue was filtrated and washed by acetic acid aqueous solution (1:3, v/v) and finally washed by deionized water until pH 7. The drying and sieving fractionation processes were the same as described before.

## 2.3 Preparation of TPS/BP

BP with different contents of lignin (10%) was blended with corn starch, glycerol/urea plasticizer, and lubricant. The mixture was subjected to a torque rheometer to prepare the composite material.

## 2.4 Characterization of Pretreated BP

### 2.4.1 Determination of Klason Lignin Content

The Klason lignin content was measured according to Official Standard Method of China (GB/T 2677. 8-1994). When 3% sulfuric acid was hydrolyzed, no reflux was carried out, but continuously added deionized water to maintain the total volume of the solution [10].

### 2.4.2 Determination of Acid Soluble Lignin Content

Klason lignin was filtrated and the solution was diluted by 3% H<sub>2</sub>SO<sub>4</sub> to certain concentration so that the absorbance was within the valid range. Thereafter, the absorbance at 205 nm was measured with 3% H<sub>2</sub>SO<sub>4</sub> as blank using a UV-2450 (Shimazu, Japan). Calculation of acid soluble lignin content was performed following the Ref. [10].

## 2.5 Scanning Electron Microscopy (SEM)

The surface of the pretreated samples was sprayed with gold and observed by S-3700N scanning electron microscope (Hitachi, Japan).

## 2.6 Biodegradation Tests

The medium was composed of TPS/BP 10%,  $(\text{NH}_4)_2\text{SO}_4$  0.25%,  $\text{K}_2\text{HPO}_4 \cdot 3\text{H}_2\text{O}$ , 0.25%. After autoclaved at 121 °C for 30 min, the activated culture (1%) was inoculated to 50 mL medium with TPS/BP as the sole carbon source. All cultures were placed at 30 °C with rotary speed at 150 rpm. Measurements of degradation degree were performed after 10 and 15 days, respectively. All experiments were run in triplicate. The biodegradation degree was calculated as follows [11].

$$\text{Bio degradation degree} = \frac{m_1 - m_2}{m_1} \times 100\%$$

where  $m_1$  is the weight of TPS/BP before degradation;  $m_2$  is the weight of TPS/BP after degradation.

## 3 Results and Discussion

### 3.1 Effect of Pretreatment Time

Compared with sugarcane bagasse, BP contains more Klason lignin, xylan, ash, and benzene-alcohol extracts [12]. Alkaline pretreatment was performed by using 5% NaOH aqueous solution at 30 °C. UV/Vis spectrophotometry method was employed to monitor the dissolved lignin content in liquid phase.

Figure 1 shows the spectra of liquid phase obtained from different time points during the pretreatment. Two peaks appeared at 290 and 320 nm, respectively. According to the characteristic UV/Vis spectrum of lignin [13, 14], these two peaks indicate the content of lignin in a solution. Kinetics of lignin extraction was plotted based on the absorbance at 290 and 320 nm, respectively and the results are shown in Fig. 2. The lignin content remained constant after extraction of 100 min, indicating the equilibrium was reached after 100 min. In order to prevent too much glucan and xylan from being dissolved by NaOH solution, 100 min was considered as the optimal extraction time.

### 3.2 Effect of NaOH Pretreatment Conditions on the Lignin Content

Table 2 shows the content of Kason lignin, acid soluble lignin and total lignin in BP resulting from different pretreatment conditions. Compared with the untreated BP, all the pretreated BP contained less lignin. Comparison among LF1, LF2, and LF3 indicated that delignification increased by 3.27% with increasing NaOH concentration from 1 to 5% with a fixed temperature. However, further increase of NaOH to 15% did not increase the delignification significantly. Therefore, 5% NaOH was the optimal concentration for delignification.

The effects of temperature (LF2, LF4) and the combination of acid and alkaline (LF5, LF6) were further investigated. The results show that higher temperature enhanced the delignification by 7.96%. Acid soluble lignin content decreased by 30% if acid pretreatment was performed prior to alkaline pretreatment. However, acid



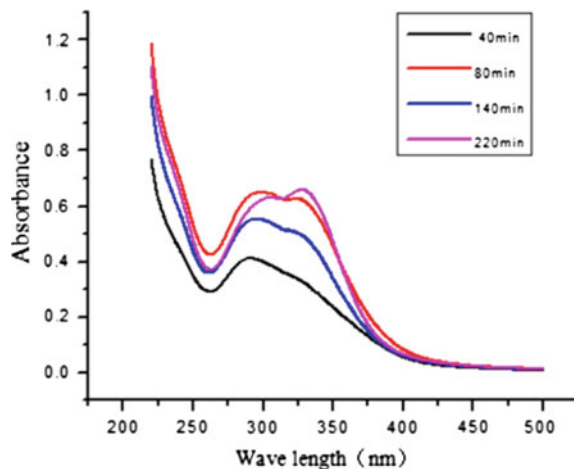


Fig. 1. UV absorption spectra recorded after different extraction times (Note 5% NaOH, 30 °C)

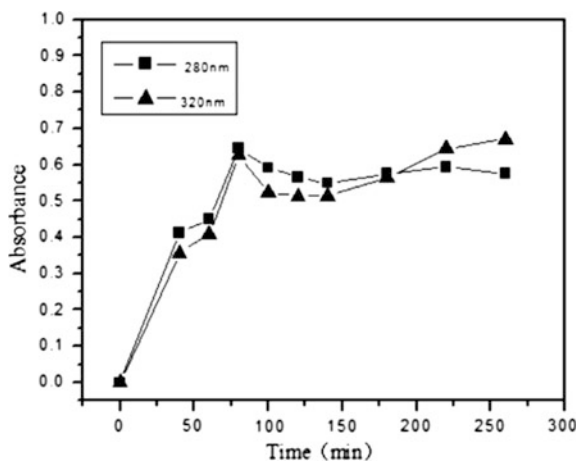


Fig. 2. Kinetics of lignin extraction by UV absorbance spectra at 290 and 320 nm

Table 2. Lignin contents the bagasse piths resulting from different pretreatments

BP sample	Klason lignin (%)	Acid soluble lignin (%)	Total lignin (%)
Untreated BP	19.61	1.54	21.15
LF1	15.33	1.53	16.86
LF2	12.06	1.28	13.34
LF3	11.47	1.23	12.70
LF4	4.63	0.75	5.38
LF5	12.81	0.87	13.68
LF6	3.47	0.49	3.96

pretreatment was not as efficient as alkaline pretreatment for Klason lignin removal. Lignin content decreased significantly from 21.15 to 3.96% after chemical pretreatment.

Delignification by alkaline pretreatment is achieved by destroying the ester bond between lignin and xylan [15]. Harsher conditions result in better delignification. Therefore, increases of temperature and NaOH concentration enhance the delignification. However, the temperature is more influential than NaOH loading because the delignification is a saponification reaction.

Morphology of the untreated and pretreated BPs was studied by SEM and the results are shown in Fig. 3. More particle-like impurities were observed on the surface of the untreated BP (Fig. 3a). These particle-like impurities were removed by 5% NaOH, 30 °C pretreatment (LF2) and combined pretreatment (LF5). Furthermore, scratches-like shape appeared after pretreatment due to alkaline extraction of lignin and other solubles. More surface cracks were observed on the surface of LF5 and the layer structure was destroyed. Pretreatment by 5% NaOH under reflux condition resulted in dramatical morphological alteration of BP (LF4). BP structure was loosened and partially resulted in debris. Taken together, with the same concentration of NaOH, reflux conditions gave rise to significant delignification, which further led to the destroyed BP structure.

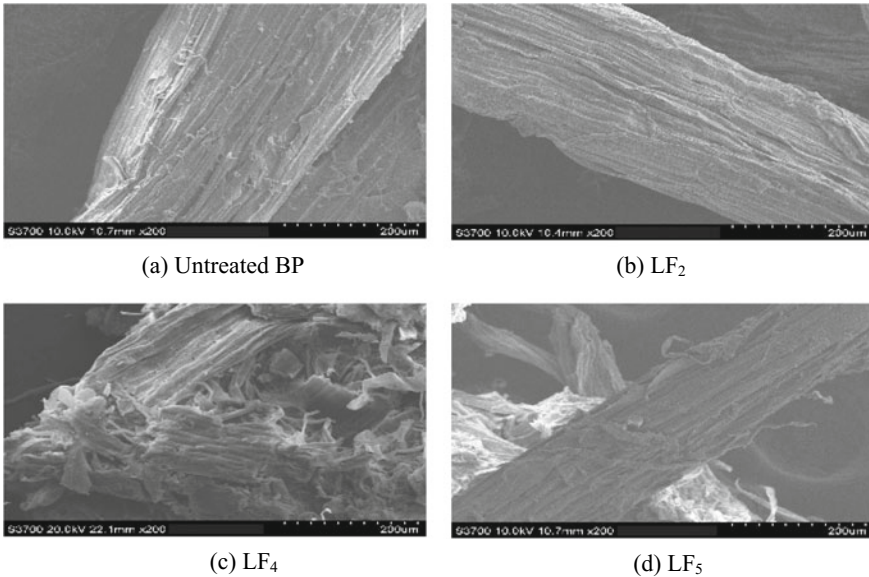


**Fig. 3.** SEM micrographs of Bagasse pith (200× magnification). For abbreviations, please refer to Table 2

### 3.3 Biodegradability of TPS/BP with Different Lignin Contents

Five TPS/BP composite materials, namely, A–E, were prepared using different pretreated BPs [16]. The biodegradability was investigated by using shake flask experiment. The degradation degree was detected on 10th and 15th day, respectively and the results are shown in Table 3. The degradation degree of all composite materials reached more than 90% after 15 days digestion. However, the degradation rate was significantly different. For instance, materials A, B, and D showed much slower degradation rate. Only 20–30% were degraded after 10 days. On the contrary, materials C and E were degraded very fast and reached more than 90% after 10 days.

**Table 3.** Degradability of treated BP based packaging materials

Materials	BP with different lignin content	10 day degradation degree (%)	15 day degradation degree (%)
A	Untreated BP	24.94	91.92
B	LF2	31.48	92.20
C	LF4	94.14	94.82
D	LF5	23.00	92.20
E	LF6	93.24	94.52

*LF1* 30 °C, 1% NaOH pretreated; *LF2* 30 °C, 5% NaOH pretreated; *LF3* 30 °C, 15% NaOH pretreated; *LF4* 5% NaOH, 100 °C with reflux pretreated; *LF5* 0.5% H<sub>2</sub>SO<sub>4</sub> cooked, followed by 5% NaOH, 30 °C pretreatment; *LF6* 0.5% H<sub>2</sub>SO<sub>4</sub> cooked, followed by 5% NaOH, 100 °C with reflux pretreatment

As expected, the materials with slower degradation rate contained more lignin (B and D); correspondingly, less lignin content resulted in higher degradation rate (C and E). The lignin content in LF4 was decreased by 8% compared to LF2, which corresponds to 61.67% increase in biodegradation after 10 days of their respective TPS/BP.

The structure of lignin is very complicated, and lignin is closely bonded to cellulose and hemicellulose [6], which makes it impossible to be degraded by microorganism directly. Delignification destroys the structure of BP as shown in Fig. 3. Deepen scratch-like shape, more debris, and increased surface area were observed in samples with higher degree of delignification. These morphologically changes increased the accessibility of water and enzymes [17], and further improved the biodegradability of the corresponding TPS/BP. These are in line with previous findings [18–20].

## 4 Conclusions

This work investigated the effects of pretreatment conditions on the lignin content and the influence of lignin content on the biodegradability of the resultant TPS/BP.

- (1) By comparison of different chemical pretreatment methods, increase in pretreatment temperature could effectively reduce the lignin content. Acid pretreatment was not as efficient as alkaline pretreatment in removing Klason lignin, but more

effective for acid soluble lignin removal. Lignin content decreased from 21.14 to 5.38% by pretreatment with 5% NaOH with 100 °C reflux for 100 min.

- (2) The morphology analyses showed that delignification altered the surface by deepening the scratch-like shape. In addition, delignification decreased the load capacity.
- (3) Biodegradable experiments showed that decreased lignin content significantly improved the biodegradability of the TPS/BP. TPS/BP biodegradable degree of higher than 93% after 10 days was achieved with lower lignin content of 4–5%. In addition, lignin content decreased by 8% gave rise to 61.76% increase in biodegradability after 10 days.

Taken together, lower content of lignin resulted in significantly higher biodegradability of the TPS/BP, paving the way for developing new degradable composite materials.

**Acknowledgements.** The work was supported by grants from Guangdong Soft Science Research Projects (No. 2015A020224045), the Ph.D. Program of Research Projects for Scientific Research and Initiation (201601279), State Key Laboratory of Pulp and Paper Engineering (201802), Guangzhou Science and Technology Plan Project of (201607010331), Program for the Excellent Talents in the University of 2014 (RC2016-002), and Funds for Guangdong Higher School Zhujiang Scholar Distinguished Professor of 2016.

## References

1. Jahan, M. S., Saeed, A., Ni, Y., et al. (2009). Pre-extraction and its impact on the alkaline pulping of bagasse. *Journal of Biobased Materials and Bioenergy*, 3(4), 380–385.
2. Wang, R. (1984). The effect on the paper properties of Bagasse pith and cooking methods. *World Pulp and Paper*, 3, 31–45.
3. Zhan, H., Fu, S., & Li, H. (2011). The development overview and technical progress for non-wood fiber pulping of bagasse, reed and cotton stalk. *China Pulp & Paper Industry*, 32(10), 6–9.
4. Prachayawarakorn, J., Sangnitdej, P., & Boonpasith, P. (2010). Properties of thermoplastic rice starch composites reinforced by cotton fiber or low-density polyethylene. *Carbohydrate Polymers*, 81(2), 425–433.
5. Lagaert, S., Belien, T., & Volckaert, G. (2009). Plant cell walls: Protecting the barrier from degradation by microbial enzymes. *Seminars in Cell & Developmental Biology*, 20(9), 1064–1073.
6. Yang, J., Yu, C., & Ma, Y., et al. (2014). The effect of ILs-H2O system pretreatment on the composition and structure of straw. *Journal of Dalian Polytechnic University*, 33(6), 427–430.
7. Ioelovich, M., & Morag, E. (2012). Study of enzymatic hydrolysis of mild pretreated lignocellulosic biomasses. *BioResources*, 7(1), 1040–1052.
8. Hu, F., & Ragauskas, A. (2012). Pretreatment and lignocellulosic chemistry. *Bioenergy Research*, 5(4), 1043–1066.
9. Wu, Y., Liao, Y., & Lv, Y. (2015). Screening and Identification of BPCPMs degrading microorganisms in soil. *Journal of Cellulose Science and Technology*, 23(1), 71–76.

10. Shi, S. F. H. (2009). *Analysis and testing of pulp and paper* (pp. 44–51). China Light Industry Press.
11. Li, F., Yang, H., Guo, Z., et al. (2011). Isolation and characterization of *Aspergillus versicolor* DS0503—a that degrades poly(butylene succinate)(PBS). *Journal of Normal University (Natural Science Edition)*, 43(1), 127–131.
12. Tu, Q., Fu, S., Zhan, H., & CHAI, X. (2008). Organosolv pulping of bagasse with formic acid. *Transactions of China Pulp and Paper*, 23(2), 15–18.
13. Li, Z., Sun, R., & Jin, Y. (2012). *Plant fiber resource chemistry* (pp. 73–113). China Light Industry Press.
14. Dintcheva, N. T., La Mantia, F. P (2007). Durability of a starch-based biodegradable polymer. *Polymer Degradation and Stability*, 92(4), 630–634.
15. Yang, J., Jiang, J., Zhang, N., et al. (2014). Effect of thin alkali pretreatment on enzymatic hydrolysis of Oak shell. *Renewable Energy Resources*, 32(6), 876–880.
16. Lv, Y., Ping, K., Jianzhi, O., et al. (2014). Studies on preparation and properties of biodegradable thermoplastic starch/bagasse pith composites. *Plastics Science and Technology*, 42(8), 95–98.
17. Dien, B. S., Sarath, G., Pedersen, J. F., et al. (2009). Improved sugar conversion and ethanol yield for forage sorghum (*sorghum bicolor* L. Moench) lines with reduced lignin contents. *Bioenergy Research*, 2(3), 153–164.
18. Studer, M. H., Demartini, J. D., Davis, M. F., et al. (2011). Lignin content in natural populus variants affects sugar release. *Proceedings of the National Academy of Sciences of the United States of America*, 108(15), 6300–6305.
19. Demartini, J. D., & Wyman, C. E. (2011). Changes in composition and sugar release across the annual rings of populus wood and implications on recalcitrance. *Bioresource Technology*, 102(2), 1352–1358.
20. Zhang, Y., Culhaoglu, T., Pollet, B., et al. (2011). Impact of lignin structure and cell wall reticulation on maize cell wall degradability. *Journal of Agricultural and Food Chemistry*, 59(18), 10129–10135.



# Fabrication of High Conductivity Polyurethane/Polyaniline Composite Coating Based on In-Situ Polymerization

Xuekai Gao and Fuqiang Chu<sup>(✉)</sup>

Key Laboratory of Green Printing & Packaging Materials and Technology  
in Universities of Shandong, School of Light Industry and Engineering,  
Qilu University of Technology, Jinan, China  
fqchu@126.com

**Abstract.** A novel water-based polyurethane (WPU)/polyaniline (PANI) composite coating with high electrical conductivity was fabricated by in-situ polymerization in this paper. The conductive PANI doped with dodecyl benzenesulfonic acid (DBSA) was synthesized from aniline salt through in-situ polymerization in a well-dispersed aqueous solution of WPU. The morphology of composite films, particles size and the electrical conductivity with the effect of different amount of PANI (varies from 1 to 7 wt%) were discussed. The results indicate that, the electrical conductivity of the WPU/PANI film increases with the increasing of the PANI content. Meanwhile, due to the formation of hydrogen bonds between  $-NH$  of PANI and  $-C=O$  of WPU, the stability and mechanical properties of the composites have been improved. The composite coatings with excellent conductivity have offered a pathway for the different applications in antistatic, electrostatic discharge (ESD), and electromagnetic interference (EMI) shielding materials.

**Keywords:** In-situ polymerization · Dodecyl benzenesulfonic acid · Water based polyurethane · Polyaniline

## 1 Introduction

In recent decades, as a new type of functional polymer material, conductive polyaniline (PANI) has been widely investigated due to its ease of synthesis, good environmental stability and controllable conductivity [1]. The conductive PANI can be prepared directly by chemical method or doping the emeraldine base (EB). However, doped PANI is almost insoluble in most common solvents, which largely limits its application. Most scientists recognize that this disadvantage can be overcome by two means: one is to modify the PANI by compatibilizers, another is to insert counter ions [2, 3]. Up till now, many composite methods have been explored extensively including simple solution mixing method [4], in-situ polymerization method [5] and impregnation adsorption polymerization method ect. Relatively speaking, the in-situ polymerization of aniline in the presence of a well-dispersed polymer emulsion is an excellent choice. Conducting core-shell latex nanoparticles have been synthesized through in-situ chemical polymerization [6, 7].

In this study, based on the previous studies, a WPU/PANI composite coating with high electrical conductivity was fabricated by in-situ polymerization. The composite coating combines the excellent mechanical properties of WPU and the electrical conductivity of PANI. Meanwhile, the PANI doped by DBSA, rather than other strong acid, can effectively prevent the destruction of polyurethane emulsion. Moreover, the resulting WPU/PANI conducting composite coating can be applied as anti-static packaging materials [8], electromagnetic interference (EMI) shielding materials and corrosion protection for metals by simply spraying.

## 2 Experimental

### 2.1 Materials

Polycarbonate diol (PCDL,  $M_r = 1000$ ) were purchased from Asahi KASEI in Japan, Isophorone diisocyanate (IPDI), 2,2-Dimethylol Propionic Acid (DMPA), polydimethylsiloxane (PDMS), Hydroxyethyl acrylate (HEA), Triethylamine (TEA), Polyvinyl Pyrrolidone (PVP), Aniline (An), Ammonium Persulphate (APS), Dodecyl benzenesulfonic acid (DBSA,  $MW = 326.49$ ) were purchased from macklin. All aqueous solutions were prepared by using deionized water.

### 2.2 Preparation of WPU

The prepolymer of urethane was prepared from PCDL and IPDI with a little catalyst in a three-necked round-bottomed flask under nitrogen gas purge. After that, the DMPA as hydrophilic chain extender, PDMS as modifiers, HEA as blocking agent, TEA as neutralizer, all these reagents were added in turn. The reaction was carried out at 80 °C with continuous stirring for 10 h until the  $N=C=O$  functional group being used up. Finally, the reactants were stirred at high speed in aqueous solution to form a WPU emulsion. Acetone was used to adjust the reaction concentration during the reaction.

### 2.3 Preparation of WPU/PANI Composite Coating by In-Situ Polymerization

1.5 wt% PVP was dissolved in deionized water and poured into a beaker containing WPU emulsion. After mixing for 1 h, a certain amount of An was added and mixed thoroughly. The solution was cooled to the temperature range of 0–5 °C. Meanwhile, a certain concentration of DBSA solution was prepared, and APS was dissolved in DBSA solution. Next, the APS/DBSA solution was added into An/WPU solution drop by drop. The reaction was kept for 8 h to complete the polymerization of An. Finally, the excellent coating was prepared by the addition of some additives.

### 2.4 Characterization

The chemical structures of pure WPU film, WPU/PANI film and conducting PANI were characterized by the Attenuated total reflectance-Fourier-transform infrared (ATR-FTIR). The microscopic morphology of PANI and WPU/PANI coating was

observed by scanning electron microscopy (SEM) and optical microscope. The electrical parameters of PANI and WPU/PANI coating were measured using Four-Point Probes. The particle size analysis was performed on a Nano ZS Malvern Zetasizer.

### 3 Results and Discussion

#### 3.1 Microstructure of Composite Coating

Figure 1 shows the ATR-FTIR spectra of pure WPU film, PANI/WPU conducting coating film and pure PANI. For pure WPU film (Fig. 1a), the characteristic absorption peak at  $3328\text{ cm}^{-1}$  is the  $\text{-N-H}$  stretching vibration absorption peak of the polyurethane chain segment. There are no absorptive peaks appearing from  $2280$  to  $2240\text{ cm}^{-1}$ , which indicates that the  $\text{-NCO}$  in the system had completely reacted. The appearance of  $1534$  and  $1725\text{ cm}^{-1}$  means that the synthesis of urethane groups ( $\text{-NHCOO}$ ) is successful. For pure PANI (Fig. 1c), the characteristic absorption peak appearing at  $2915\text{ cm}^{-1}$  belongs to the  $\text{N-H}$  extensional vibration in the imine structure. The characteristic absorption peak at  $1572$  and  $1495\text{ cm}^{-1}$  is attributed to the stretching vibration of the  $\text{N=Q=N}$  ring and  $\text{N-B-N}$  ring structure after doped with the DBSA. For PANI/WPU conducting coating film (Fig. 1b), the absorption peaks at  $3328$  and  $1725\text{ cm}^{-1}$  are migrated to  $3325$  and  $1720\text{ cm}^{-1}$  compared with pure PU. This is attributed to the formation of hydrogen bonds between  $\text{-C=O}$  in the main chain of the WPU and  $\text{-N-H}$  in the PANI, which reduces the interaction between the  $\text{-N-H}$  and  $\text{-C=O}$  groups in the P U.

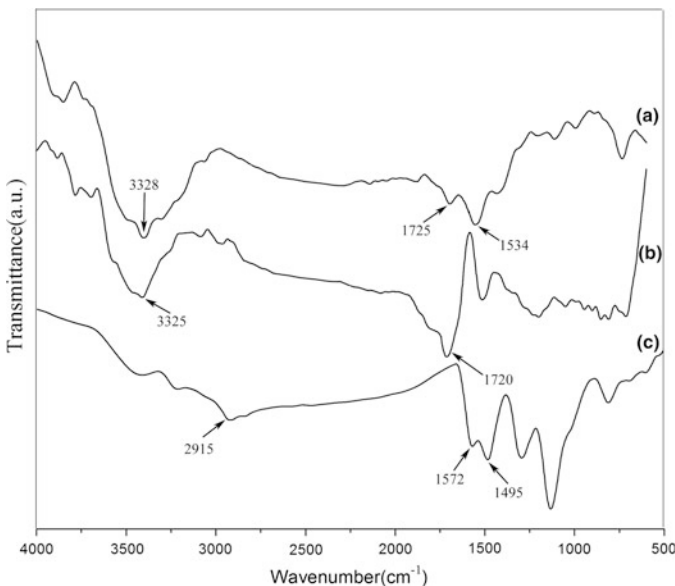


**Fig. 1.** The ATR-FTIR spectra of **a** pure WPU film, **b** PANI/WPU conducting coating film, **c** pure PANI



### 3.2 Particle Size Analysis of Composite Coating

In this experiment, the core-shell structure of PANI/WPU was prepared by the in-situ polymerization method. From the Table 1, it can be observed that the amount of PANI growing on the polyurethane particles increases with the content of PANI increasing. At the same time, more aggregates were formed in the composite coating as the molar ratio of APS/An. However, as increases of the molar ratio of APS/An, due to the redundant PANI was deposited on the agglomerates of the WPU emulsion, which caused the emulsion particles to fail to crosslink together, it can seriously affect the formation of conducting blend film. Hence, after a series of research, it can be concluded that the PANI/WPU blend coating with good film formation can be fabricated, when the content of PANI was controlled within 3% and the molar ratio of APS/An lower than 1.0.

**Table 1.** The average size of PANI/WPU particles in the mixtures of various weight of An and molar ratio of APS/An

An (wt%)	Average size (nm)	APS/An	Average size (nm)
0	~ 98	0.7	~ 108
1	~ 109	0.8	~ 117
2	~ 127	0.9	~ 129
3	~ 143	1.0	~ 136
5	~ 159	1.2	~ 149
7	~ 171	1.5	~ 182

### 3.3 Microscopic Morphology of PANI/WPU

Figure 2 displays the morphology of PANI coating and composite film. The optical micrograph (Fig. 2a) exhibit a homogeneous composite coating under 100 $\times$  magnification, and almost no agglomerate of PANI can be observed. The SEM micrograph (Fig. 2b) shows the surface microstructure of PANI/WPU. It can be found from the SEM that the two polymers are well combined together. These mean that the fabrication of APNI/WPU composite coating based on in-situ polymerization is achieved perfectly.

### 3.4 Electrical Properties of Composite Coating

The variation of the electrical conductivity of PANI/WPU composite coating film with different concentration of DBSA is depicted in Fig. 3. As illustrated in the graph, the electrical conductivity of conducting blend films increase with increasing the DBSA concentration (0.02–0.06 mol/L). When the concentration of DBSA added was 0.02 mol/L, the electrical conductivity value reached  $2.86 \times 10^{-2}$  S/cm. However, when the acid concentration is higher than 0.07 mol/L, the stability of the WPU emulsion will be impaired and the mechanical property of the blend film will reduced rastically.

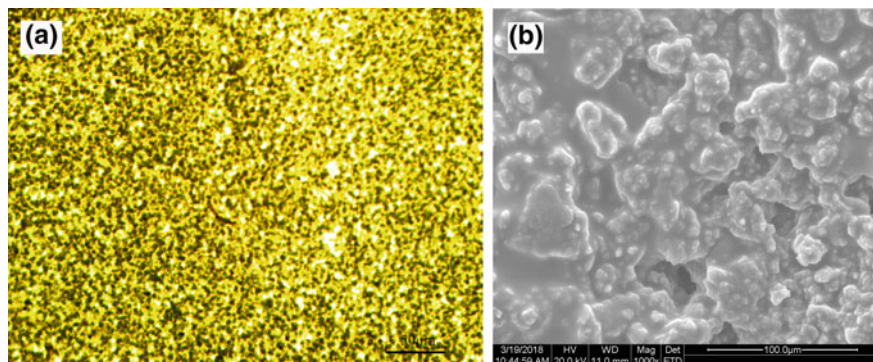


**Fig. 2.** Microscopic morphology: **a** optical micrograph (100 $\times$  magnification) of PANI/WPU coating, **b** the SEM micrograph of PANI/WPU composite film (PANI accounts for 5 wt% in dry composite)

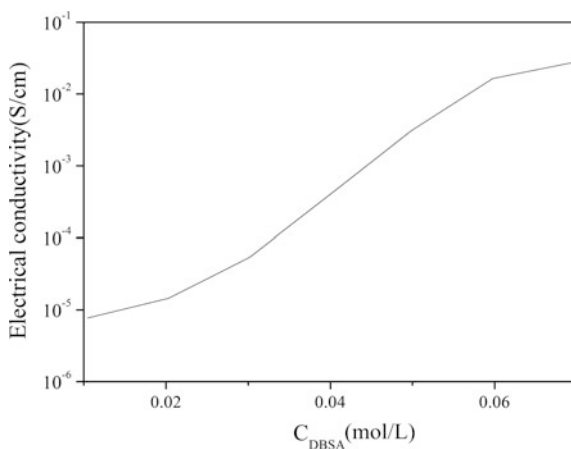


**Fig. 3.** The electrical conductivity of composite coating film by casting

## 4 Conclusions

Conducting PANI/WPU composite coatings have been prepared by in-situ polymerization of aniline in the WPU emulsion and its property was discussed in this paper. Significant hydrogen bonding is formed between the  $\text{-N-H}$  bond of PANI and the  $\text{-C=O}$  bond of WPU. Due to the above effect of hydrogen bonding, the WPU/PANI core-shell structure was well prepared in microscopic form. Within a certain degree, the particle size of composite coatings can be controlled by adjusting the molar ratio of APS/An and the An content. Meanwhile, the electrical conductivity of PANI/WPU blend film increases with increasing the concentration of DBSA.

**Acknowledgements.** This work is financially supported by the Government of Shandong Province (No. 2017GGX80105), which is gratefully acknowledged.

## References

1. Chen, C. H., Kan, Y. T., Mao, C. F., et al. (2013). Fabrication and characterization of water-based polyurethane/polyaniline conducting blend films. *Surface & Coatings Technology*, 231 (7), 71–76.
2. Masillamani, A. M., Peřinka, N., Hajná, M., et al. (2016). Charge transport and contact resistance in coplanar devices based on colloidal polyaniline dispersion. *Journal of Polymer Science B Polymer Physics*, 54(17), 1710–1716.
3. Vicentini, D. S., Guilherme, M. O., et al. (2007). Polyaniline/thermoplastic polyurethane blends: Preparation and evaluation of electrical conductivity. *European Polymer Journal*, 43 (10), 4565–4572.
4. Song B., Tuan C. C., Li L., et al. (2016). Highly conductive polyurethane/polyaniline-based composites for wearable electronic applications. In *Electronic Components and Technology Conference* (pp. 2424–2429). IEEE.
5. Chwang, C. P., Liu, C. D., Huang, S. W., et al. (2004). Synthesis and characterization of high dielectric constant polyaniline/polyurethane blends. *Synthetic Metals*, 142(1), 275–281.
6. Avadhanam, V., Thanasamy, D., Mathad, J. K., et al. (2017). Single walled carbon nano tube-polyaniline core-shell/polyurethane polymer composite for electromagnetic interference shielding. *Polymer Composites*, 39, 4104–4114.
7. Zhang, T. L., & Qin, Z. Y. (2011). Water-based polyurethanepolyaniline conductive core-shell latex nanoparticles. *Advanced Materials Research*, 306–307, 1296–1299.
8. Karmakar, H. S., Arukula, R., Thota, A., et al. (2017). Polyaniline-grafted polyurethane coatings for corrosion protection of mild steel surfaces. *Journal of Applied Polymer Science*, 135(6), 45806.



# Study of Extinction Characteristics of Au–Ag Nanosphere Periodic Array

Jun Wang<sup>1,2</sup>, Chunyu Chen<sup>1</sup>, Yabin Shao<sup>1</sup>, Jing Han<sup>1</sup>, Xin Zhao<sup>1</sup>,  
Jijuan Jiang<sup>1</sup>, and Yachen Gao<sup>1(✉)</sup>

<sup>1</sup> College of Electronic Engineering,  
Heilongjiang University, Heilongjiang, China  
{wangjun1003, C\_CY2009, shao\_yabin, hanjing1980}  
@163.com, xinzhiguisu@sina.com, 935109559@qq.com,  
gaoyachen@hlju.edu.cn

<sup>2</sup> College of Light Industry, Harbin University of Commerce,  
Heilongjiang, China

**Abstract.** In order to study the extinction characteristics of the periodic structures of Au and Ag nanospheres, an Au–Ag nanosphere periodic array structure has been established. Firstly, the geometry structure and research methods of Au–Ag structure are introduced. Secondly, the LSPR absorption spectra of Au–Ag nanospheres periodic array and Au and Ag nanospheres periodic array were compared by the finite difference time domain method. Then, the simulation and analysis of periodic array of Au–Ag nanospheres with different sizes and spacings are carried out. Finally, the Au–Ag nanosphere periodic array structures in different media environments are simulated and analyzed, and the refractive index sensitivity is obtained. The simulation results show that Au–Ag nanoparticles periodic array structure has two LSPR absorption peaks, and the two peaks position relative to the separate Au and Ag nanoparticles periodic arrays of LSPR absorption peak showed blueshift; in the same spacing condition, with the increase of radius  $r$ , the absorption peak wavelength of the double peak showed redshift firstly and then blueshift; when the radius  $r$  is constant, the LSPR peak wavelength showed redshift with the increase of the spacing  $L$ ; owing to Au nanospheres contribution in Au–Ag nanoparticles, the refraction absorption peak with the refractive index of the fitting rate sensitivity is 101.11 nm/RIU, refractive index sensitivity of 82.985 nm/RIU is higher than that of Au nanoparticles periodic array alone; and the contribution by Ag nanospheres in Au–Ag nanoparticles resulted in refraction absorption peak with the refractive index of the fitting rate sensitivity of 130.3 nm/RIU is lower than that of Ag nanoparticles periodic array of individual Refractive index sensitivity 154.23 nm/RIU. The structure basically meets the requirements of optical sensing accuracy and can be applied to filters.

**Keywords:** LSPR Au–Ag nanosphere · Absorption peak · Curve fitting · Refractive index sensitivity

## 1 Introduction

Metal nanostructures exhibit significant localized surface plasmon resonance (LSPR) effect [1–5], which has become a hot topic of research. When the light wave is incident to the metal nanostructures, the incident photon resonates with the oscillation of the free electron conduction on the surface of the nanoparticles at a certain wavelength, and shows an obvious LSPR absorption peak on the absorption spectrum [6, 7]. The study shows that the location of the absorption peak is not only related to the type of precious metal materials and the shape, size and spacing of nanoparticles, but also very sensitive to the surrounding medium, so it can be used in the sensing field. The sensor based on LSPR phenomenon can be used for drug research, biological detection, cell marking, fixed-point diagnosis, molecular dynamics research and disease diagnosis [8]. In recent years, the optical properties of different shapes of metal nanoparticles have attracted the attention of researchers, such as nanospheres [9], nanodisks [10], nanotubes [11]. The optical properties of heterostructure nanomaterials are obviously different from those of homogenous structures [12]. However, there are few reports on the optical properties of the periodic structure of Au–Ag nanospheres. In this paper, the LSPR characteristics of the Au–Ag nanospheres periodic array are simulated by the finite difference time domain (FDTD) method [13], and the LSPR absorption spectrum of the nanoparticles with different sizes and distances is carried out. Simulation analysis is carried out to explore the rule of LSPR phenomenon in the structures.

## 2 Array Structure and Research Method

### 2.1 Geometric Structure of Nanoparticles

Figure 1 shows the schematic diagram of the square array of Au–Ag nanospheres periodic array. The radius of Au and Ag nanospheres is  $r$ , and the horizontal and vertical distances of the two spheres are all  $L$ , that is, the Au and Ag nanospheres are uniformly arranged on the glass with thickness of 1  $\mu\text{m}$ .

### 2.2 Research Method

In recent years, the theory of Maxwell's equations based on the discrete dipole approximation (DDA), the theory of strictly coupled wave (Rigorous Coupled-Wave Analysis, RCWA), and the theory of finite difference time domain (FDTD) have emerged, and are widely used in the theoretical analysis of the LSPR phenomenon of metal nanoparticles [8]. Because the FDTD method can simulate the nanostructures of arbitrary shape, it is a numerical method to solve the vector Maxwell equation. With this method, the space and time distribution of electromagnetic fields interacting with light, arbitrary shape and multi particle nanostructures can be quickly obtained. Therefore, the FDTD method is used in the simulation study. The software used is FDTD Solutions. The light source adopted in the simulation is plane wave (wavelength range: 300–700 nm), the size of the grid is 1 nm, the optical constants of Ag are derived from the Palik (0–2  $\mu\text{m}$ ) model, and the optical constants of Au are taken from the CRC model.

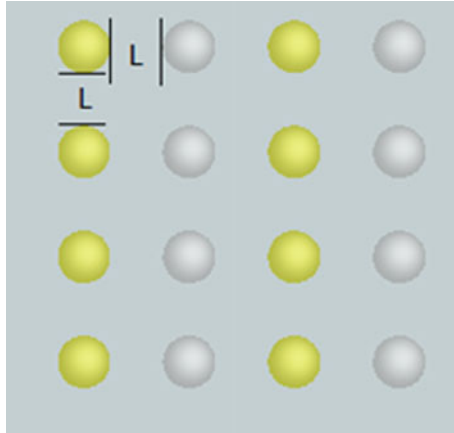


**Fig. 1.** Schematic diagram of periodic array of Au–Ag nanospheres

### 3 Simulation and Results Analysis

#### 3.1 Comparative Analysis of LSPR Absorption Spectra of Au–Ag Nanospheres and Au and Ag Nanospheres Periodic Arrays

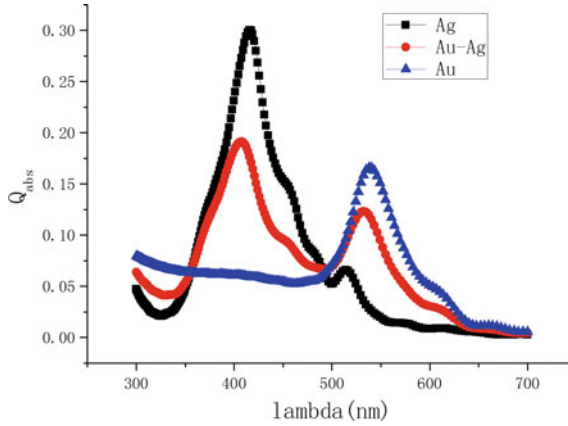
The extinction characteristics of the Au–Ag nanospheres periodic array with radius of 5 nm and spacing of 10 nm were simulated and analyzed. The medium environment is water with refractive index of 1.33. For comparison, the Au and Ag nanospheres periodic arrays with the same size and interval were simulated. The LSPR absorption spectra of the obtained Au–Ag nanospheres, Au and Ag nanospheres periodic arrays are shown in Fig. 2.

Figure 2 shows that with the same size, interval, and medium, there are two LSPR absorption peaks in the periodic array of Au–Ag nanospheres, which is caused by LSPR phenomena of both Au and Ag nanospheres. The positions of the two absorption peaks show blueshift compared to those of the Au and Ag nanospheres periodic arrays. Moreover, the absorption peak intensity of the structure is equivalent to that of Au and Ag alone.

#### 3.2 Simulation Analysis of Size Influence on Extinction Characteristics of Au–Ag Nanospheres Periodic Array

The simulation analysis of the extinction characteristics of Au–Ag nanospheres with different sizes is carried out. Figure 3a–c are their simulated extinction spectra, absorption spectra, and scattering spectra.

Figure 3a shows that with the constant spacing of  $L$ , with the increase of the radius  $r$ , the peak wavelength of the extinction rate of bimodal peak has a redshift, in which the redshift of the right peak is obvious, and the peak intensity of the corresponding extinction rate increases with the increase of the radius  $r$ . This is due to the increase in the number of particles participating in the surface plasmon resonance, which leads to



**Fig. 2.** Comparison of absorption spectra of Au–Ag composite nanospheres with Au and Ag nanospheres by periodic array LSPR ( $r = 5 \text{ nm}$ ,  $L = 10 \text{ nm}$ ,  $n = 1.33$ )

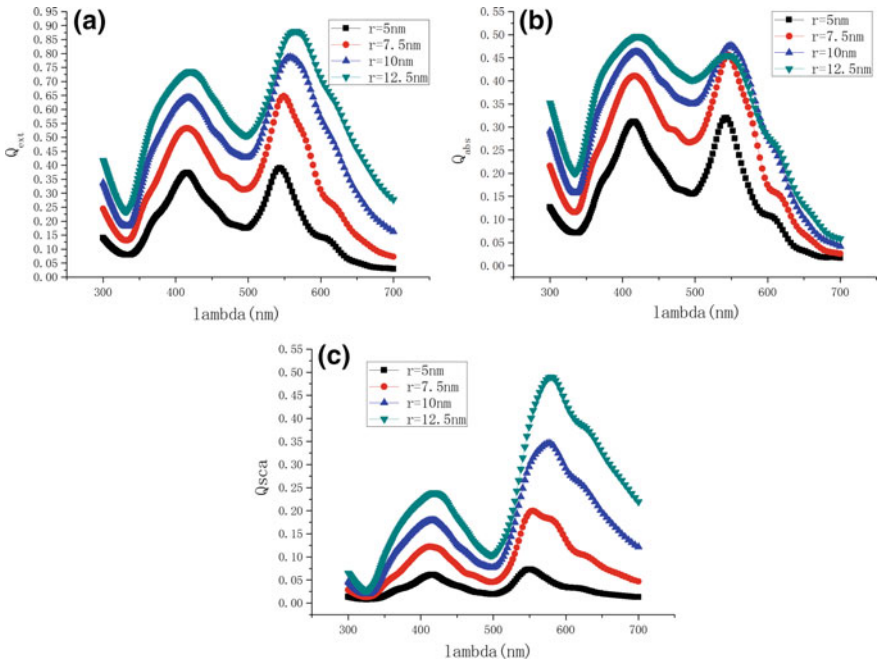


**Fig. 3.** Normalized optical characteristics of periodic arrays of Au–Ag composite nanospheres with different radius ( $L = 4 \text{ nm}$ ,  $n = 1.33$ ): **a** extinction spectrum; **b** absorption spectrum; **c** scattering spectrum

the absorption and scattering caused by the enhancement. As shown in Fig. 3b, with the increase of radius  $r$ , the bimodal peak wavelength of absorption shifts first red and then blue. Figure 3c shows that the peak intensity of scattering rate increases with the increase of radius  $r$ , which is due to the increase of scattering area per unit volume of nanoparticles.

### 3.3 Simulation Analysis of Periodic Arrays of Au–Ag Nanospheres with Different Spacing

The simulation analysis of the extinction characteristics of Au–Ag nanospheres with different spacing is carried out. Figure 4a–c are their simulated extinction spectra, absorption spectra, and scattering spectra.

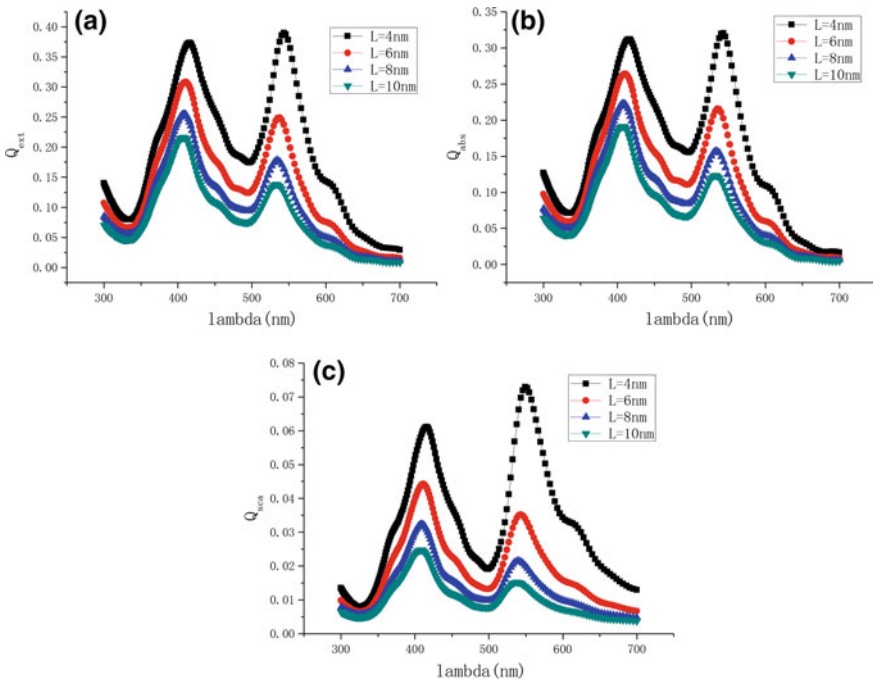


**Fig. 4.** Normalized optical characteristics of periodic array of Au–Ag composite nanospheres with different spacings ( $r = 5 \text{ nm}$ ,  $n = 1.33$ ): **a** extinction spectrum; **b** absorption spectrum; **c** scattering spectrum

Figure 4a, b shows that when the radius  $r$  is a constant value, the peak wavelength of the extinction rate and absorptivity of bimodal peak has a redshift with the increase of the spacing  $L$ , and the corresponding extinction rate and the peak absorbance intensity decreases with the increase of  $L$ , which is due to the weakening of the coupling effect between the nanospheres. From Fig 4c, we can see that the peak



intensity of scattering decreases with the increase of  $L$ , which is due to the decrease of the scattering area of nanoparticles in the unit volume.

### 3.4 Simulation Analysis of Medium Environment Influence on Extinction Characteristics of Au–Ag Nanospheres Periodic Array

In order to verify the LSPR characteristics of the periodic array of Au–Ag nanospheres with the same size in different media (the refractive index of medium is 1.33, 1.36, 1.43, 1.50 respectively), the extinction characteristics of Au–Ag nanosphere periodic arrays with radius of 5 nm and spacing of 10 nm were simulated and analyzed, so as to detect the sensitivity of the LSPR phenomena of Au–Ag nanosphere periodic arrays to the environmental changes of the media. For comparison, the Au and Ag nanospheres periodic arrays with the same size and interval were simulated. The obtained LSPR absorption spectra of Au–Ag nanosphere periodic arrays are shown in Fig. 5a. From Fig. 5a, the two absorption peaks in different refractive index media show redshift with the increase of the refractive index  $n$ ; the wavelengths of the absorption peaks caused by the contribution of the Ag sphere in the Au–Ag nanospheres are 407.707, 410.914, 420.846, 429.496 nm, and its linear fitting relation to the refractive index is shown in Fig. 5b, the absorption peak wavelength (nm)  $\lambda = 130.3n + 234.18$ , and the corresponding refractive index sensitivity is 130.3 nm/RIU. The wavelengths of absorption peaks caused by the contribution of Au balls in the Au–Ag nanospheres are 532.357, 535.083, 543.433, 549.146 nm. The linear fitting relationship with the refractive index is shown in Fig. 5c, and the wavelength of absorption peak (nm)  $\lambda = 101.11n + 397.95$ , thus the sensitivity of its corresponding refractive index is 101.11 nm/RIU.

With the same conditions, the LSPR absorption spectrum of the Au nanospheres periodic array is shown in Fig. 6a. In the four media of  $n = 1.33, 1.36, 1.43$  and  $1.50$ , the absorption peak wavelengths of Au nanospheres are 537.838, 540.621 nm, 546.275 and 552.048 nm respectively. The linear fitting relationship between the peak wavelength of absorption peak and the refractive index is shown in Fig. 6b, and the absorption peak wavelength (nm)  $\lambda = 82.985n + 427.6$ , thus the sensitivity of its corresponding refractive index is 82.985 nm/RIU.

With the same conditions, the LSPR absorption spectrum of the Ag nanospheres periodic array is shown in Fig. 7a. In the four media of  $n = 1.33, 1.36, 1.43$  and  $1.50$ , the absorption peak wavelengths of Au nanospheres are 415.821, 420.846, 431.269 and 442.222 nm respectively. The linear fitting relationship between the peak wavelength of absorption peak and the refractive index is as shown in Fig. 7b, and the absorption peak wavelength (nm)  $\lambda = 154.23n + 210.85$ , thus the sensitivity of its corresponding refractive index is 154.23 nm/RIU.

By comparing the LSPR absorption spectra and the refractive index sensitivity curves of Au–Ag nanospheres with Au nanospheres and Ag nanospheres in different media, it is found that the refractive index sensitivity of the absorption peak and the refractive index of the Au–Ag nanospheres is 101.11 nm/RIU, which is higher than that of single Au nanospheres. The refractive index sensitivity 82.985 nm/RIU indi-

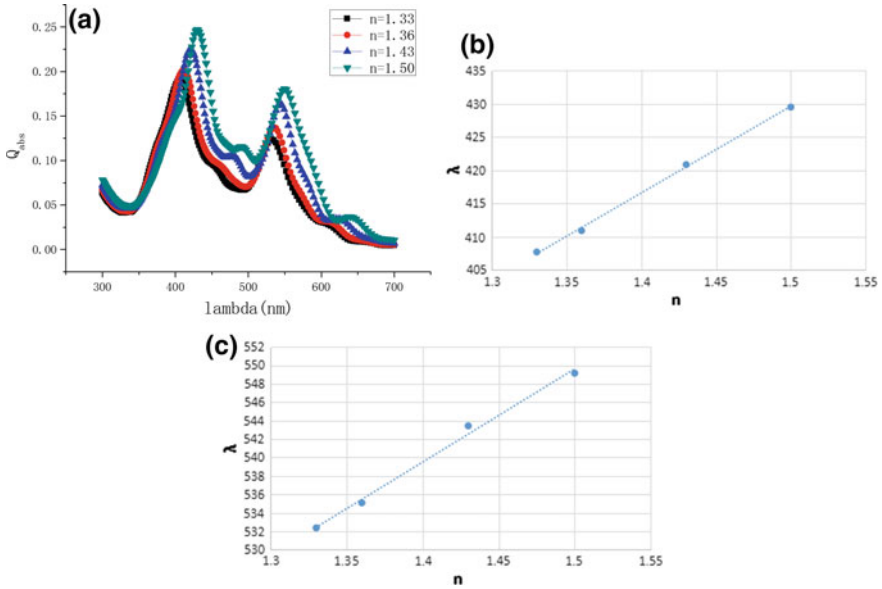


**Fig. 5.** Absorption spectra of Au–Ag composite nanosphere periodic arrays in different media environments (a), fitting curve between Ag absorption peak wavelength and refractive index of medium (b); fitting curve between Ag absorption peak wavelength and refractive index of medium (c) ( $r = 5$  nm,  $L = 10$  nm)

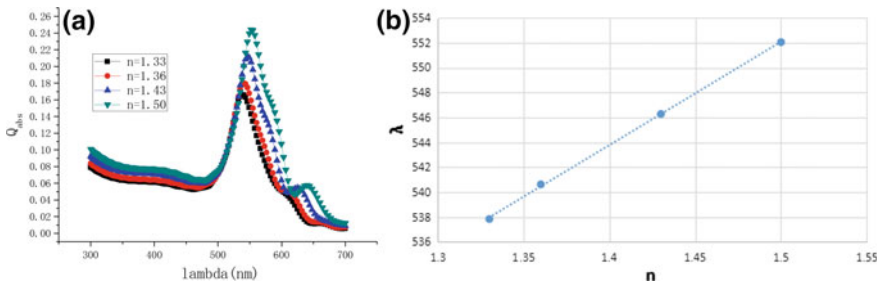


**Fig. 6.** Absorption spectra of Au nanosphere periodic arrays in different media environments (a); fitting curve between Au absorption peak wavelength and refractive index of medium (b) ( $r = 5$  nm,  $L = 10$  nm)

cates that the Au–Ag nanospheres periodic array structure can be used to improve the sensitivity of optical sensors based on micro nano structures. The sensitivity of the refractive index obtained by the fitting of the absorption peak and the refractive index in the Au–Ag nanospheres is 130.3 nm/RIU, which is lower than that of single Ag nanospheres with 154.23 nm/RIU. In addition, the Au–Ag nanospheres periodic array structures can be used for multi band filter design because of its two absorption peaks.

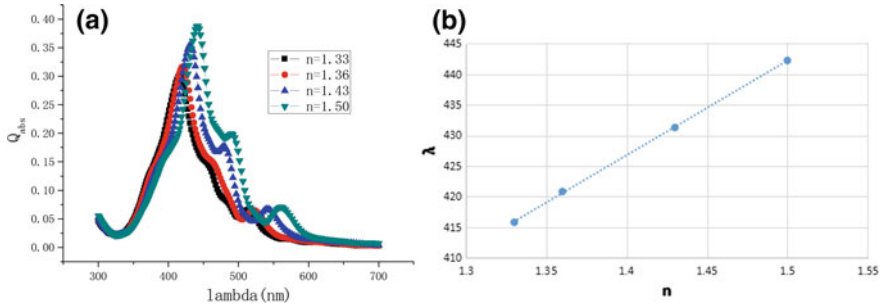


**Fig. 7.** Absorption spectra of Ag nanosphere periodic arrays in different media environments (a); fitting curve between Ag absorption peak wavelength and refractive index of medium (b) ( $r = 5$  nm,  $L = 10$  nm)

## 4 Conclusions

In this paper, the LSPR optical properties of Au and Ag nanospheres periodic structures have been studied by the finite difference time domain method, and the Au–Ag nanospheres periodic array structure has been established. The LSPR characteristics of periodic arrays of Au–Ag nanospheres with different sizes and spacings were simulated and analyzed. Finally, the Au–Ag nanospheres periodic array structure in different medium environment is simulated and analyzed, and the sensitivity of refractive index is obtained. The experimental results show that two LSPR absorption peaks appear in the periodic array structure of Au–Ag nanospheres, and the position of the two absorption peaks appears blueshift relative to the LSPR absorption peak of the single Au and Ag nanospheres. With the increase of the radius  $r$ , the peak wavelength of the absorption rate is first redshift and then blueshift. When the radius  $r$  is constant, with the increase of the distance  $L$ , the peak wavelength of the absorption rate of LSPR bimodal peaks has a redshift, and the refractive index sensitivity of the absorption peak and the refractive index of the Au–Ag nanospheres is 101.11 nm/RIU, which is higher than the refractive index sensitivity 82.985 nm/RIU of the single Au nanospheres. The Au–Ag nanospheres periodic array structure can be used to improve the sensitivity of the optical sensor based on micro nano structures. The sensitivity of the refractive index obtained by the fitting of the absorption peak and the refractive index in the Au–Ag nanospheres is 130.3 nm/RIU, which is lower than the refractive index sensitivity 154.23 nm/RIU of the single Ag nanospheres. The Au–Ag nanospheres periodic array structure can be used for multi band filter design because of its two absorption peaks.

**Acknowledgements.** This study is funded by the ‘Youth Project’ of Harbin University of Commerce (No. 17XN035).

## References

1. Zou, R. X., Zhang, Q., Zhao, Q., et al. (2010). Thermal stability of gold nanorods in an aqueous solution. *Colloids and Surfaces A: Physicochemical and Engineering Aspects*, 372(1), 177–181.
2. Huang, X. H., Neretina, S., & Ei-Sayed, M. A. (2009). Gold nanorods: From synthesis and properties to biological and biomedical applications. *Advanced Materials*, 21(48), 4880–4910.
3. Liang, H. P., Wan, L. J., Bai, C. L., et al. (2005). Gold hollow nano-sphere: Tunable surface plasmon resonance controlled by inter-or- cavity sizes. *Journal of Physical Chemistry B*, 109(16), 7795–7800.
4. Camden, J. P., Dieringer, J. A., Zhao, J., et al. (2008). Controlled plasmonic nanostructures for surface -enhanced spectroscopy and sensing. *Accounts of Chemical Research*, 41(12), 1653–1661.
5. Zhang, X. F., Zhang, L. M., Fan, Q. F., et al. (2011). The local surface plasmon resonance tuning characteristics of Gold nanoparticles core-shell structure. *Chinese Journal of Lasers*, 38(9), 0910001-1–0910001-5.
6. Kelly, K. L., Coronado, E., Zhao, L. L., et al. (2003). The optical properties of metal nanoparticles: The influence of size, shape, and dielectric environment. *Journal of Physical Chemistry B*, 107(3), 668–677.
7. Yan, Q. Q., Qin, W. J., Wang, C., et al. (2011). Plasmon-enhanced polymer bulk heterojunction solar cells with solution-processable Ag nanoparticles. *Optoelectronics Letters*, 7(6), 410–414.
8. Zhou, W., Zhang, W., Wang, C., et al. (2010). The analysis of noble metal nanoparticles LSPR Phenomena. *Chinese Journal of Sensors and Actuators*, 23(5), 630–634.
9. Zhnag, W., Sun, H., Liu, R. P., et al. (2012). Analysis of LSPR extinction properties of two-dimensional Au nanoparticles arrays. *Journal of Optoelectronics Laser*, 23(5), 1005–1010.
10. Fang, Z., Cai, J., Yan, Z., et al. (2011). Removing a wedge from a metallic nanodisk reveals a Fano resonance. *Nano Letters*, 11(10), 4475.
11. Cong, C., Wu, D. J., Liu, X. J., et al. (2012). Study on the localized surface plasmon resonance properties of bimetallic gold and silver three-layered nanotubes. *Acta Physica Sinica*, 61(3), 03701-1–03701-7.
12. Cheng, L., Jiang, Y. G., Huang, L. Q., et al. (2016). Optical properties of Ag–Al nanosphere heterodimer. *Spectroscopy and Spectral Analysis*, 36(11), 3470–3475.
13. Ge, D. B., & Yan, Y. B. (2011). *Finite-difference time-domain method for electromagnetic waves* (3rd ed.). Xi'an: Xi'an Electronic and Science University Press.



# Synthesis of 5-3,6,7,10,11-pentakis(pentyloxy)triphenylen-2-yloxy-pentyl Methacrylate and Its Mesomorphism Study

Jingze Bi, Yuwen Feng, Zhenhu Zhang, Huanzhi Yang,  
Chunxiu Zhang<sup>(✉)</sup>, and Jialing Pu

Beijing Institute of Graphic Communication, Beijing, China  
bjingze@hotmail.com, zhangchunxiu@bigc.edu.cn

**Abstract.** A novel triphenylene-based discotic liquid crystal 5-3,6,7,10,11-pentakis(pentyloxy)triphenylen-2-yloxy-pentyl methacrylate was successfully synthesized. Chemical structure of this compound was determined by <sup>1</sup>H-NMR and FT-IR spectrum, and its mesomorphism was investigated under the guidance of differential scanning calorimeter (DSC) and polarizing optical microscopy (POM) method. This compound apparently exhibited a classical texture of columnar phase in the mesophase temperature. The double bond on the side chain made it possible for this compound to be a candidate of designing and synthesizing liquid crystal polymer.

**Keywords:** Liquid crystal · Columnar phase · Mesomorphism · Triphenylene

## 1 Introduction

Discotic liquid crystals (DLCs) containing a rigid aromatic core and several flexible aliphatic side chains tended to self-assemble into columnar mesophases spontaneously [1]. As it had been discovered by Chandrasekhar in the year 1977, more and more scientists showed a great interest on synthesizing and researching of such a material. As the work-horse of discotic liquid crystals, discotic liquid crystals based on triphenylene core are widely used. The columns forming from the stacking of discs via  $\pi$ - $\pi$  interactions allowed for one-dimensional charge carrier transport with high efficiency which can be used as molecular organic materials in information recording materials, photoelectric materials, organic solar cells, organic light-emitting diodes and so on.

The Triphenylene derivatives which composed of a disk-like core and branches of peripheral flexible side chains are easily to synthesis and purify. At the same time, some of them have a low melting point and show an excellent thermal stability. Due to these advantages, the Triphenylene derivatives have a great potential to the best discotic liquid crystal materials.

In this paper, the synthesis process and performance of the new triphenylene-based discotic liquid crystal 5-3,6,7,10,11-pentakis(pentyloxy)triphenylen-2-yloxy-pentyl methacrylate and analyzed. Its structure is confirmed by <sup>1</sup>H-NMR and FT-IR

spectrum, and its thermal properties and optical properties were characterized by differential scanning calorimeter (DSC) and polarizing optical microscopy (POM). The structure of the triphenylene derivative is shown in Fig. 1.

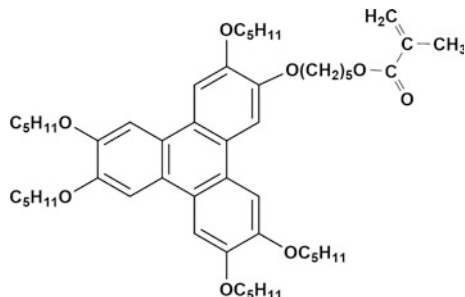


**Fig. 1.** Chemical structure of 5-3,6,7,10,11-pentakis(pentyloxy)triphenylen-2-yloxy-pentyl methacrylate

## 2 Experimental

All chemicals were purchased from Aladdin, and all solvents from Aldrich. All chemicals and solvents were used without further purification.  $^1\text{H-NMR}$  spectra were recorded in  $\text{CDCl}_3$  on Bruker NMR spectrometers, chemical shifts were given in parts per million ( $\delta$ ) and were referenced from tetramethylsilane (TMS). Fourier transform infrared spectroscopy (FT-IR) was carried out on a Shimadzu FTIR-8400 spectrometer using KBr pellets. Differential scanning calorimetry (DSC) was performed on a Netzsch DSC 214. Sealed about 5 mg sample in aluminum crucibles and scanned by  $5\text{ }^\circ\text{C min}^{-1}$  in nitrogen atmosphere. Polarizing optical microscopy (POM) was carried out on a Leica DM4500P microscope equipped with a Linkam TMS94 hot stage.

### 2.1 Synthesis of 5-3,6,7,10,11-pentakis(pentyloxy)triphenylen-2-yloxy-pentyl Methacrylate

Figure 2 shows the synthesis route of target compound 4.

The synthesis method of the target compound is mainly based on literature [2–5]. The synthesis of compound 1 was prepared by Williamson reaction. Then, according to the reaction mechanism of Scholl, compound 2 was synthesized by catalytor, iron trichloride and trimerized [6]. After that 2-hydroxyl-3,6,7,10,11-penta-pentoxytriphenylene (compound 3) was successfully synthesized by using B-type bromate-cholesterol according to slightly lower activity than boron tribromide. In the last, 5-3,6,7,10,11-pentakis(pentyloxy)triphenylen-2-yloxy-pentyl methacrylate (compound 4) was produced *n,n*-dimethyl-formicaci (DMF) was used as solvent and compound 3, 2-Methyl-2-propenoic acid, potassium bicarbonate, hydroquinone into a 250 ml three-necked flask as reactive material. This reaction lasted about one day in  $120\text{ }^\circ\text{C}$  of reflux in an oil bath. After completion of reaction, the product was washed with water and

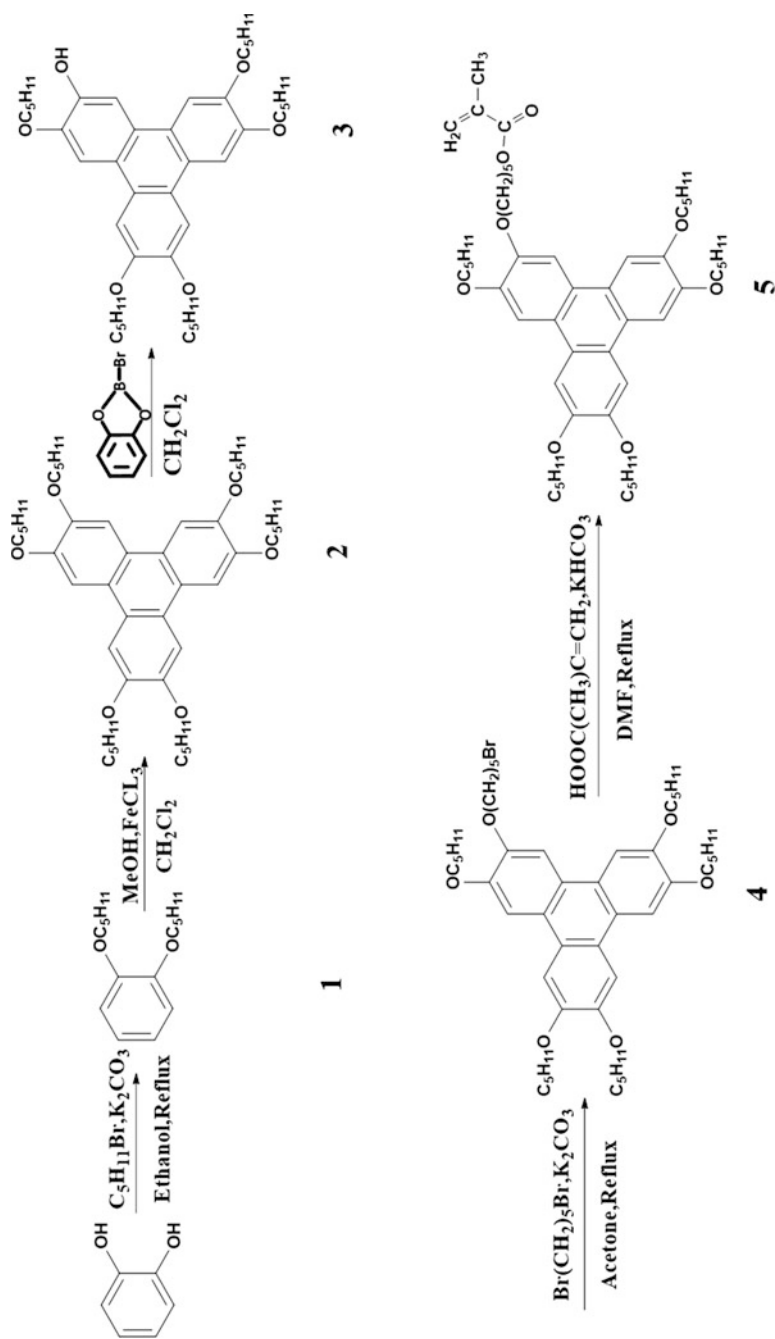
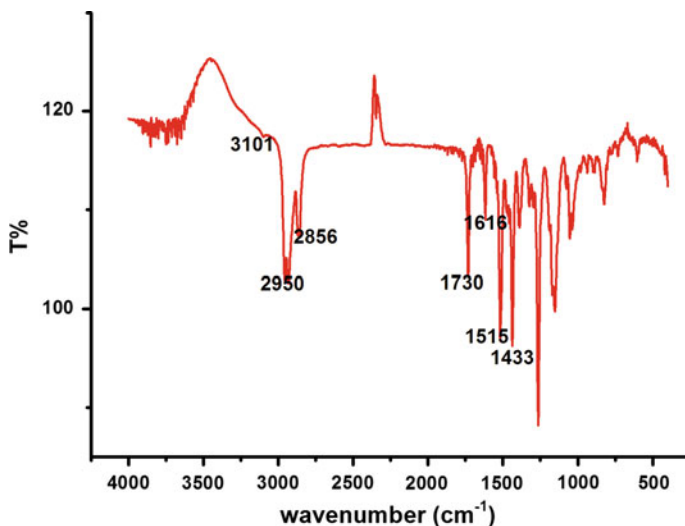


Fig. 2. Synthesized route of 5-3,6,7,10,11-pentakis(pentyloxy)triphenylene-2-yloxyacrylate methacrylate



**Fig. 3.** FT-IR spectrum of 5-3,6,7,10,11-pentakispentyloxytriphenylen-2-yloxypropyl methacrylate

alkaline solution. After dried and purified by chromatography, compound 4 was recrystallized from ethanol, the yield of compound 4 was 83.2%. The results of FT-IR and  $^1\text{H-NMR}$  are shown in Figs. 3 and 4.

## 2.2 Characteristics of Liquid Crystal

By using polarizing optical microscopy with temperature controller, optical texture of this liquid crystal was confirmed. Purified compound 4 was placed under microscope and heated from room temperature to 100 °C at a rate of 10 °C/min and then dropped to 0 °C at a rate of 5 °C/min. After finished the cooling process, we observed the change of texture. After that, this compound was tested by DSC for more specific phase transition temperatures and exact enthalpy changes.

## 3 Results and Discussion

### 3.1 POM

We can easily notice a classical pyramidal texture during the cooling process under the polarizing optical microscopy. This compound exhibited a birefringence phenomenon at room temperature and no crystal phase was observed. The detail texture pictures were shown in Fig. 5.



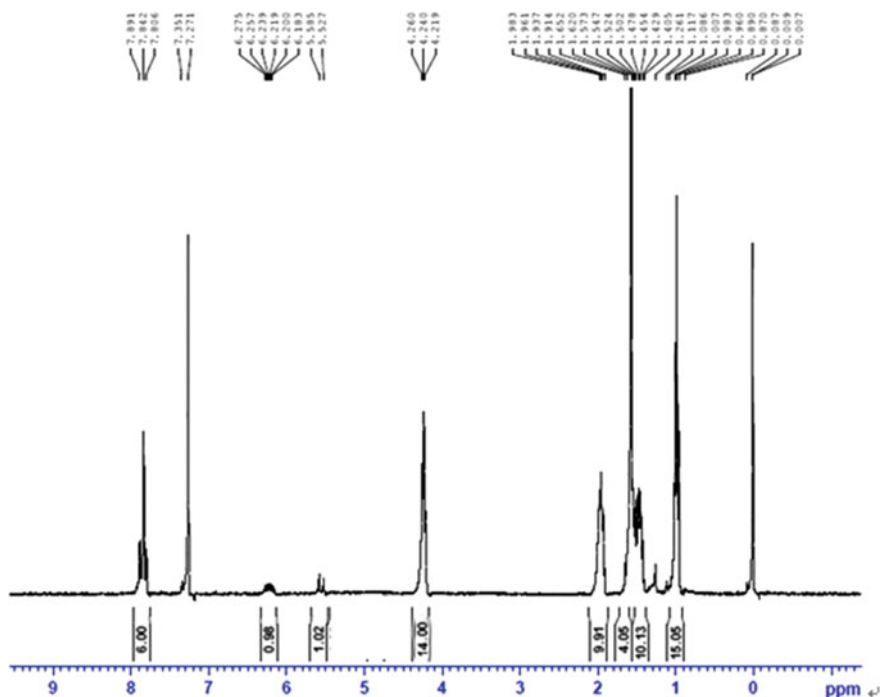


**Fig. 4.**  $^1\text{H-NMR}$  spectrum of 5-3,6,7,10,11-pentakispendtyloxytriphenylen-2-yloxypropyl methacrylate FT-IR(KBr): $V_{\text{max}}(\text{cm}^{-1})$ :3101( $-\text{CH}=\text{CH}_2$ ); 2950, 2856( $-\text{CH}_3/-\text{CH}_2$ ); 1730 ( $-\text{C}=\text{O}$ ); 1616, 1515, 1433 ( $-\text{C}=\text{C}-$ );  $^1\text{H-NMR:H}$  (300 MHz,  $\text{CDCl}_3$ ): 7.80–7.90 (t, 6H), 6.10–6.32 (m, 1H), 5.47–5.70 (m, 1H), 4.18–4.38 (m, 14H), 0.9–2.1(m, 41H)

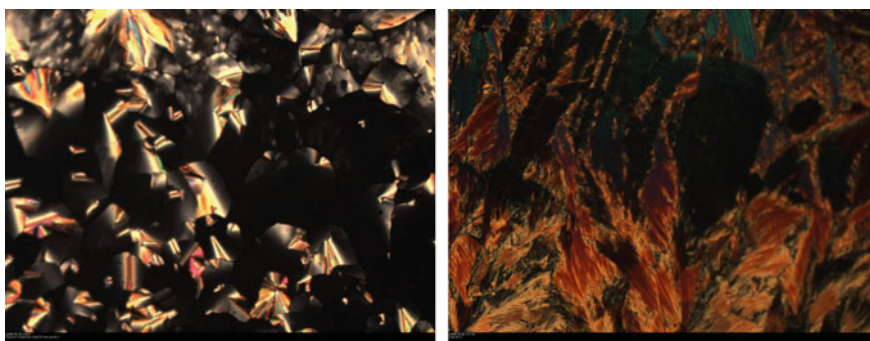


**Fig. 5.** Textures observed at 50 °C (left), and 10 °C (right) during cooling process

### 3.2 DSC

As shown in Fig. 6, we observed the first endothermic peak at 42.2 °C and the second endothermic peak at 56.7 °C during heating process from 0 to 100 °C. Combined with polarizing microscope image change from fecculent liquid to transparent liquid we can

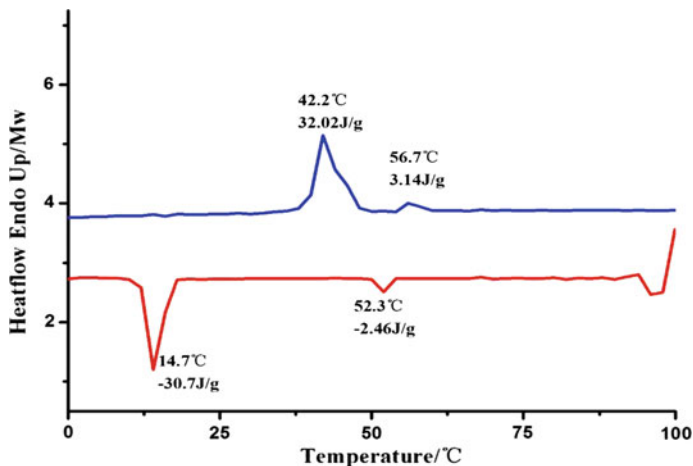


**Fig. 6.** DSC thermogram of 5-3,6,7,10,11-pentakis(pentyloxy)triphenylen-2-yloxy-pentyl methacrylate

draw a conclusion that the compound got into isotropic phase at 56.7 °C. In cooling process, we can also observed two exothermic peaks at 14.7 and 52.3 °C. Compared to the texture, we can get from 52.3 to 14.7 °C. This compound transformed into liquid crystal state at 52.3 °C and changed into crystal state at 14.7 °C. Endothermic heat and release process described throughout the DSC in good agreement with the phase transition observed by the polarizing microscope. The DSC curve of Compound 4 is shown in Fig. 4.

## 4 Conclusions

In this study, a novel 5-3,6,7,10,11-pentakis(pentyloxy)triphenylen-2-yloxy-pentyl methacrylate contained multiple flexible spacers between triphenylene and double bonds were successfully synthesized and characterized. The structures of the compounds were determined by both  $^1\text{H}$ NMR and FT-IR spectra. Liquid crystal properties of compounds were characterized by POM and DSC method. By all these means, we can draw a conclusion that 5-3,6,7,10,11-pentakis(pentyloxy)triphenylen-2-yloxy-pentyl methacrylate exhibits columnar mesophase between 14.7 and 56.7 °C, which can be discotic liquid crystal material as charge transport used in information recording materials, photoelectric materials, organic solar cells, organic light-emitting diodes and so on.

**Acknowledgements.** This work is supported by fund from Beijing Municipal Education Commission Project (Grant no. 23190115024, Grant no. 25000115006, no. Byyc201316-007), the Importation and Development of High Caliber Talents Project of Beijing Municipal Institutions (CIT&TCD201304123), NSFC (21174016).

## References

1. Chandrasekhar, S., Sadashiva, B. K., & Suresh, K. A. (1977). Liquid crystals of disk-like molecules. *Pramana*, 7, 471–480.
2. Mu, B., Wu, B., Pan, S., et al. (2015). Hierarchical self-organization and uniaxial alignment of well synthesized side-chain discotic liquid crystalline polymers. *Macromolecules*, 48(8), 2388–2398.
3. Kumar, S., & Manickam, M. (1998). Synthesis of functionalized triphenylenes by selective ether cleavage with B-bromocatecholboane. *Synthesis*, 8, 1119–1122.
4. Bushby, R. J., & Lozman, O. R. (2002). Discotic liquid crystals 25 years on. *Current Opinion in Colloid & Interface Science*, 7, 342–354.
5. Kumar, S. (2004). Recent developments in the chemistry of triphenylene -based discotic liquid crystals. *Liquid Crystals*, 31(8), 1037–1059.
6. Boden, N., Borner, R. C., Bushby, R. J., et al. (1993). The synthesis of triphenylene-based discotic mesogens new and improved routes. *Liquid Crystals*, 15(6), 851–858.



# Preparation of Durable Superhydrophobic Surface Material and Its Application in Packaging

Xiao Liu, Shiyong Luo<sup>(✉)</sup>, and Rongxia Bu

School of Printing and Packaging Engineering, Beijing Institute of Graphic Communication, Beijing, China  
luoshiyong@bigc.edu.com

**Abstract.** To study the technical principle of superhydrophobic surface preparation, research progress and application prospect in durability performance. This article reviews and proposes four types of technical methods to improve the durability of superhydrophobic: superhydrophobic surface with self-healing function, SLIPS surface, micro-nano structure with shape memory and mechanical strength of surface micro-nano structure itself, and the application prospect of its use as packaging material is analyzed. The superhydrophobic properties of the surface depend on the surface composition and surface micro-nano multistage structure. The low mechanical strength of the micro-nano multistage structure leads to poor durability of the superhydrophobic performance. Enhancing the durability of superhydrophobic properties on the surface is the prerequisite for the application of superhydrophobic materials on the surface, and it has great application prospects in terms of packaging materials.

**Keywords:** Superhydrophobic surface material · Durability · Preparation process · Packaging materials

## 1 Introduction

Surface wettability refers to the spreading behavior of a liquid on a solid surface and is a very important property of a solid surface [1]. Wetting control is extremely important in applications such as self-cleaning, anti-icing, antibacterial and anti-reflection. Most of the early researches focused on the preparation of micro- and nano-structures with new geometric shapes and geometries, or modified with different low surface energy substances, and used surface micro-nano-multi-level structures and low surface energy to achieve superhydrophobic performance. Although research on superhydrophobic surfaces has achieved certain results, few superhydrophobic surfaces that are considered to be resistant to various externally applied stresses are rare [2]. Because of its small size and low mechanical strength, it can easily be destroyed by external forces and lose its superhydrophobic properties.

The durability problem of superhydrophobic performance refers to the failure of the surface micro-nano structure or the failure of the low surface energy coating or both of them [3]. The schematic diagram is shown in Fig. 1. Therefore, it is necessary to resolve the problem of durability when superhydrophobic surfaces are used in industrial applications, including solvents with different acid and alkali solvents, external force damage (abrasion, indentation), ultraviolet (UV) irradiation, temperature and humidity effects [4].

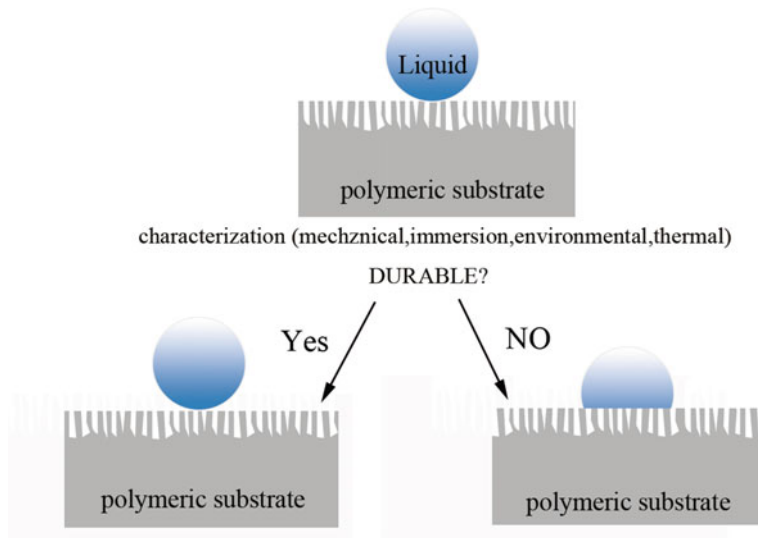


**Fig. 1.** Superhydrophobic surface durability

## 2 Definition of Superhydrophobic Surface

Surface wettability is typically characterized by the static contact angle (CA) of a liquid on a solid surface and the resulting roll angle (CAH) on a tilted solid surface. The principle of static contact angle is shown in Fig. 2a. The solid and liquid surfaces are tangent to the solid-liquid-gas three-phase boundary. The angle formed between the two tangents is the static contact angle. When the static contact angle is larger than  $150^\circ$ , the liquid can be assumed an almost circular shape on the solid surface [5]. Rolling angle refers to the minimum inclination angle of the solid surface that can roll off the inclined surface when the liquid is on the inclined surface. The principle is shown in Fig. 2b. When the static contact angle is greater than  $150^\circ$  and the dynamic contact angle is less than  $10^\circ$ , the surface has superhydrophobic properties [6].

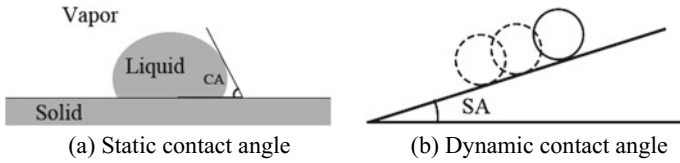


Fig. 2. Contact angle

### 3 Technical Approaches to Improve Surface Superhydrophobic Performance Durability

#### 3.1 Superhydrophobic Surface with Self-healing Function

Self-healing materials are emerging smart materials that can repair their damage spontaneously or irritably under external stimuli (e.g. heat, light, solvents, etc.) [7]. The construction of a superhydrophobic surface with self-healing means that the surface of the material is self-repaired by adding a repair agent or self-healing material, thereby enhancing the durability.

Haibao et al. [8] soaked the fabrics in polytetrafluoromethane and fluorinated graphite mixed dispersions and heat-cured to prepare superhydrophobic materials, and the water contact angle can reach  $157.7^\circ$ . The surface after being subjected to severe mechanical damage, the superhydrophobic property can be transferred to the surface to regenerate the superhydrophobic surface by heating, thereby achieving rapid self-repair. Zhanjian et al. [9] coated a silane-based carrier prepared a self-repairing polytetrafluoroethylene/polyester superhydrophobic coating. After ten rubbing or acid-base attack or ultraviolet irradiation for 14 days, the hydrophobic properties of the coating remain unchanged, and the surface energy is reduced by the migration of POTS to the surface to achieve the purpose of self-repair.

Most self-healing methods require certain stimuli to stimulate self-healing performance. Therefore, the invention of a surface that can be self-rough or self-healing without stimulation will be a big challenge in the future.

#### 3.2 SLIPS Surface

The preparation of the SLIPS surface is contrary to the principle that the lotus leaf relies on the micro-nano size mastoid structure to envelop the air to achieve superhydrophobicity. Porous materials with micro-nanometer-sized pores are first soaked in a liquid that is immiscible with the sparse fluid, and capillaries are used during the process to make the slippery liquid in the micro-nano pores migrate to the surface to enhance durability [10].

Shillingford and Wong [11] reported in detail the principle of SLIPS. The article points out that SLIPS is composed of a lubricating fluid film that is locked in place by a micro/nano porous substrate to form a stable, defect-free and inert “smooth” interface. Wong et al. [12] reported that a slippery liquid is stored in porous micro-nano

materials, and when the superhydrophobic property of the surface was destroyed, the stored repair liquid is wicked to the surface by capillary action to maintain the superhydrophobic performance.

Studies have shown that SLIPS constructs a superficially sparse surface that virtually eliminates liquid contact lines of high surface tension liquids and low surface tension liquids, minimizing the pressure-induced penetration of porous structures [13]. However, this method is still defective, and the slippery repair liquid during the preparation process will contaminate the contacted liquid, limiting its application in certain special aspects.

### 3.3 Micro-nanostructures with Shape Memory

The preparation of shape memory micro/nanostructures refers to the use of shape memory polymers in the preparation process to make the surface structure damaged by external forces, and then to restore its original shape and maintain its superhydrophobic through the environment of heating or light irradiation performance [14].

Chen and Yang [15] used the template method to prepare superhydrophobic surface of epoxy microcolumn arrays. After stress deformation and loss of ultra-hydrophobicity, after 80 °C heat treatment, the surface micro-nanostructures had shape memory function, and super-sparse performance was regained. Wang et al. [16] also prepared a shape memory surface structure. With the deformation of the surface structure, the contact angle of hexadecane ranges from 146° to 10°. After heating, the shape recovers and the contact angle changes again to 147°. But materials with shape memory are currently rare.

### 3.4 Improve the Mechanical Strength of the Surface Micro-nano Structure Itself

Increasing the mechanical strength of the surface micro-nano structure itself to enhance the durability of the super-hydrophobic surface is the most direct method, but the selection of the preparation material in this method is extremely demanding. Scarratt et al. [17] reported a composite PTFE film on the surface of polystyrene and polyolefin coextruded film. After cooling at 160 °C for 2 min, the former shrinks by 30% while the latter shrinks by 10%. The membrane surface is formed with two layers of pleated structure with long-lasting hydrophobic properties. Deng et al. [18] dispersed lauric acid-modified  $\text{Cu}(\text{OH})_2$  powder in ethanol, and after spraying on the surface of the glass slide, a powder coating was applied on the glass slide by immersion pulling method to make the surface superhydrophobic. The experiment used 30 g of sand to impact the surface of the coating, and the surface was tested by NaCl and NaOH aqueous solution, the surface was still superhydrophobic.

Although the superhydrophobicity mentioned in this type of literature can be regarded as a method of improving durability, it is only an increase in the durability of superhydrophobic properties compared with the early stage. Some literatures even consider the preparation of a superhydrophobic surface at room temperature for a period of time, which is considered to be durability.

## 4 Application and Prospect of Superhydrophobic Surface on Packaging Materials

With the development of the times and people's demand for packaging functions, packaging materials with superhydrophobic properties have gradually become a research hotspot. Japan developed a non-stick yoghurt aluminum-plastic packaging heat seal cover. The static contact angle can reach more than  $150^\circ$  [19]. From the scanning electron microscopy (SEM) test, as shown in Fig. 3, it can be observed that unlike other superhydrophobic surface morphologies, the morphology formed by this superhydrophobic surface is a cluster of micro- and nano-particles formed by stacking.

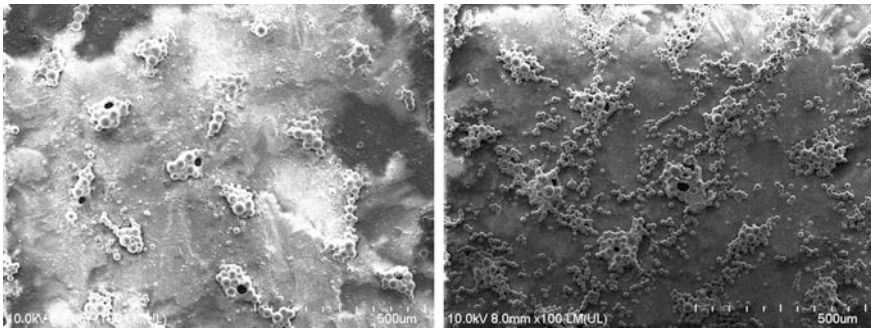


**Fig. 3.** Scanning Electron Microscope (SEM) photographs of yoghurt cover with superhydrophobic property

Although there is research on the application of domestic superhydrophobic surfaces on packaging, there are few packaging items on the market for food. In the future, the domestic superhydrophobic surface packaging material can be used for the packaging of liquid (paste) products, including grease, yogurt, toothpaste, jam, chili sauce and pastes, etc. Therefore, the packaged goods do not adhere to the packaging materials, which reduces the waste of the packaged goods and facilitates the recycling of the packaging materials. These packaging substrates are related to paper, plastics, aluminum-plastics and paper-plastic composites, and metals. The surface of these substrates is constructed with a surface with durable superhydrophobic properties, which will promote the advancement of packaging materials technology, with important application prospects and economic benefits.

## 5 Conclusions

The durability of the superhydrophobic surface is the premise of its application, how to use the superhydrophobic surface with self-repairing function, the surface of the SLIPS, the micro-nano structure with shape memory, and the technical method for improving the mechanical strength of the surface micro-nano structure itself. On the basis of or



developing new methods to improve durability is the key to the application of superhydrophobic surface materials, and durable superhydrophobic surface materials have important application prospects in the packaging of liquid (paste)-like products.

**Acknowledgements.** This study is funded by the Key Science and Technology Project of Beijing Municipal Education Commission (KZ201610015015), and by the Research and Development Program Project of Beijing Institute of Graphic Communication (EC201804).

## References

1. Shan, P. (2015). Preparation and properties of superhydrophobic/supersorbent materials. *South China University of Technology*.
2. Bengt, K. B. (2016). The hydrophobic effect. *Current Opinion in Colloid & Interface Science*, 22, 14–22.
3. Ellinas, K., Tserepi, A., & Gogolides, E. (2017). Durable superhydrophobic and superamphiphobic polymeric surfaces and their applications: A review. *Advances in Colloid and Interface Science*, 250, 132.
4. Verho, T., Bower, C., Andrew, P., et al. (2011). Mechanically durable superhydrophobic surfaces. *Advanced Materials*, 23, 673–678.
5. Mengchun, W. (2017). *Construction and function of self-repairing superhydrophobic membrane*. Jilin University.
6. Penghui, Z., Gang, C., & Zhicheng, W. (2017). Research progress on preparation and application of super-hydrophobic paper. *Paper Science & Technology*, 36, 40–45.
7. Wu, D. Y., Meure, S., & Solomon, D. (2008). Self-healing polymeric materials: A review of recent developments. *Progress in Polymer Science*, 33, 479–522.
8. Haibao, H., Jun, W., Luyao, B., et al. (2017). Significant and stable drag reduction with air rings confined by alternated superhydrophobic and hydrophilic trips. *Science Advances*, 3, 160–288.
9. Zhanjian, L., et al. (2017). Durable and self-healing superhydrophobic polyvinylidene fluoride (PVDF) composite coating with in-situ gas compensation function. *Surface & Coatings Technology*, 327, 18–24.
10. Manna, U., & Lynn, D. M. (2013). Restoration of superhydrophobicity in crushed polymer films by treatment with water: Self-healing and recovery of damaged topographic features aided by an unlikely source. *Advanced Materials*, 25, 104–108.
11. Shillingford, C., & Wong, T. S. (2014). Fabrics coated with lubricated nanostructures display robust omniphobicity. *Nanotechnology*, 25, 014019.
12. Wong, T. S., Kang, S. H., et al. (2011). Bioinspired self-repairing slippery surfaces with pressure-stable omniphobicity. *Nature*, 477, 443–447.
13. Wang, X. L., & Liu, X. J. (2011). Self-healing superamphiphobicity. *Chemical Communications*, 47, 2324–2326.
14. Athanasios, M., Eric, L., & Bayer, I. S. (2016). Recent advances in the mechanical durability of superhydrophobic materials. *Advances in Colloid and Interface Science*, 229, 57–79.
15. Chen, C. M., & Yang, S. (2014). Directed water shedding on high-aspect-ratio shape memory polymer micropillar arrays. *Advanced Materials*, 26, 1283–1288.
16. Wang, W., et al. (2017). Metamorphic superomniphobic surfaces. *Advanced Materials*, 2, 95.
17. Scarratt, L. R. J., Hoatson, B. S., et al. (2016). *ACS Appl Mater Interfaces*, 8, 6743–6750.

18. Den, W., et al. (2017). Eco-friendly preparation of robust superhydrophobic  $\text{Cu}(\text{OH})_2$  coating for self-cleaning, oil-water separation and oil sorption. *Surface & Coatings Technology*, 325, 14–21.
19. Zhijie, W. (2016). Preparation and superhydrophobic surface of alumina-based nanomaterials. *Donghua University*.



# Surface Structure Design and Performance Test of 3D Printing Microwave Absorbing Material

Yingjie Xu<sup>1</sup> (✉), Lai Peng<sup>1</sup>, X. Han<sup>1</sup>, You Zhao<sup>1</sup>, Chenyang Yuan<sup>1</sup>,  
Wan Zhang<sup>1</sup>, Xianfu Wei<sup>1</sup>, Beiqing Huang<sup>1</sup>, and Qi Wang<sup>2</sup>

<sup>1</sup> Beijing Institute of Graphic Communication, Beijing, China  
xuyingjie@bigc.edu.cn

<sup>2</sup> Nanjing Forestry University, Nanjing, Jiangsu Province, China

**Abstract.** In order to study the effect of surface structure on absorption properties of microwave absorbing materials. Methods Four models of microwave absorbing materials with blackbody structure are established using 3D modeling software. Then, microwave absorbing inkjet ink was prepared, and microwave absorbing materials with blackbody structure are prepared using 3D printer. The microwave absorbing properties of different materials in 6–40 GHz are tested according to GJB2038A-2011 for square flat materials: 180 mm × 180 mm × 4 mm. Results the maximum reflection loss of solid plates is only -1.45 dB. The maximum reflection loss of conical cavity is -1.48 dB, the maximum reflection loss of inverted cone cavity is -2.78 dB, the maximum reflection loss of swallow tail cavity is -3.84 dB, the absorption performances of these models are greatly improved at more than 30 GHz. The maximum reflection loss of fishtail cavity is up to -5.92 dB, which have the better absorption performances at more than 20 GHz. Conclusion The opening diameter of blackbody cavity in microwave absorbing material is 2.5 mm, when the 1/8 of the incident electromagnetic wave length is less than 2.5 mm (the electromagnetic wave frequency is greater than 15 GHz), the waveguide effect will be obvious. At this time, the wave impedance of the material decreases, the electromagnetic wave entering the material increases, which is finally absorbed in the blackbody cavity after being reflected many times. Through the design of the blackbody cavity structure, increasing the reflection times of the electromagnetic wave in the blackbody can improve the absorption intensity and the absorption bandwidth of the material.

**Keywords:** Microwave absorption · Ink-jet ink · Surface structure · 3D printing

## 1 Introduction

The application of electromagnetic absorption materials can efficiently solve the electromagnetic pollution problem that caused by electric equipment in human's production and life [1–4]. Furthermore, electromagnetic absorption technology has

become the most significant technology in research and development of military equipment all over the world [5–8].

3D printing technology is also called 3D rapid prototyping technology, which is a kind of additive manufacturing technology. Firstly, the model structure was designed by the 3D modeling software in the computer, and then the 3D objects with complex structures are produced rapidly by precise 3D piling and forming in different technologies. UV curable inkjet 3D printer can achieve fine resolution of 600 dpi at 0.01 mm single layer thickness [9, 10]. Using 3D printing technology can create complex micro-structure which is beneficial to increase the electromagnetic wave absorption efficiency. The 3D model of microwave absorbing material surface structure was designed at first, in order to prepare the magnetic absorbing materials by 3D printing technology [10, 11].

The pore structure can be formed, when making microwave absorbing materials, and the electromagnetic wave absorptivity can be greatly improved by the blackbody effect. In order to make full use of the surface area of the material, the diameter of the hole can't be too small. The cavity of the black body should be designed so that the incident light can be refracted and absorbed many times in the cavity. Professor Xuequan Li in Kunming Institute of Physics has carried out a great deal of research on the design of the black body cavities which were consulted in this paper.

## 2 Experimental

### 2.1 Experiment Materials

Hyperbranched acrylate V100 (Cytec Industry, USA), Methyl benzoylformate MBF (ShangyuHerun, China), different proportion of grapheneoxide/ferroferric oxide composite nanomaterials (GO/Fe<sub>3</sub>O<sub>4</sub>) [12].

### 2.2 Preparation of Samples

A certain proportion of UV light curing resin, photoinitiator and different amounts of electromagnetic absorber are mixed, which was add to the beaker, and stired for 30 min at room temperature by the magnetic stirrer. Then the pre-dispersed ink is added to the grinder, adding suitable amount of zirconium beads, the speed of the grinder at 2000 r/min, the grinding time is 120 min, the absorbent is fully wetted and dispersed in the UV curing resin, and UV electromagnetic absorption inkjet ink is prepared. In the end, the conical cavity model, the inverted cone cavity model, the swallow-tailed cavity model and the fishtail cavity model were designed by Rhinoceros software. Then, the microwave absorber material with blackbody structure was fabricated by 3D printer (Objet Connex 260, stratasys, USA).

### 2.3 Microwave Absorbing Properties Test

According to national standard GJB 2038A-2011, 180 mm × 180 mm × 4 mm square plate material test method, test the microwave absorbing performance of the

different material in the 6–40 GHz band. The effects of different blackbody structures on microwave absorbing properties of materials were compared.

### 3 Results and Discussion

#### 3.1 Structural Design and Absorptive Performance Test of Conical Cavity Model

Single model size: 3 mm × 3 mm × 4 mm; Cylinder: diameter 2.5 mm, height 2.5 mm; Frustum of cone: diameter of upper surface 2.5 mm, diameter of lower surface 1.25 mm, height 1.00 mm; Cone: diameter 1.25 mm, height 2.8 mm (Fig. 1a, b).

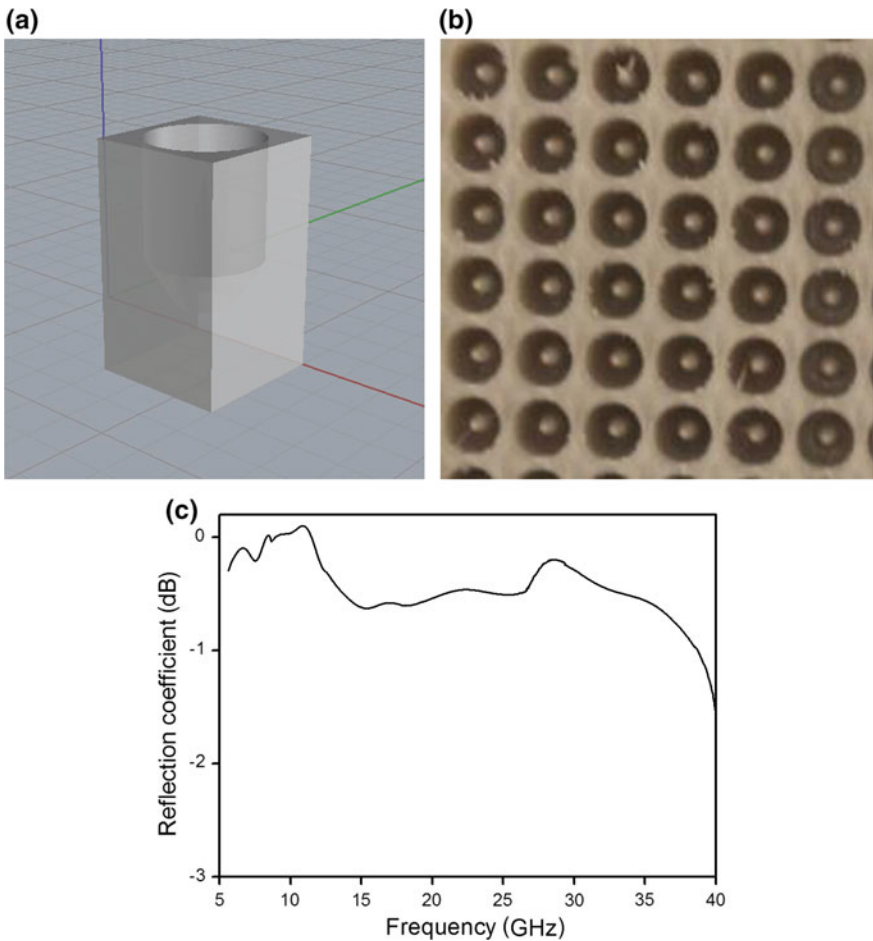


**Fig. 1.** **a** Minimum cell structure drawing of the conical cavity model; **b** practicality picture of the conical cavity model after print; **c** reflection coefficient of the conical cavity model

According to national standard GJB 2038A-2011, 180 mm × 180 mm × 4 mm square plate material test method, testing material's microwave absorption performance in the frequency band ranging from 6.0 to 40.0 GHz. As can be seen from Fig. 1c, the reflection loss rate of material decreased from -0.25 to -0.08 dB in the range of 6–6.8 GHz; Increased from -0.08 to -0.22 dB in the range of 6.8–7.5 GHz; Decreased from -0.22 to 0.11 dB in the range of 7.5–12.1 GHz; Increased from 0.11 to -0.72 dB in the range of 12.1–15.2 GHz; Basically remain unchanged in the range of 15.2–26.5 GHz; Decreased from -0.69 to -0.26 dB in the range of 26.5–28.9 GHz; Increased from -0.26 to -1.48 dB in the range of 28.9–40 GHz.

### 3.2 Structural Design and Absorptive Performance Test of Inverted Cone Cavity Model

Single model size: 3 mm × 3 mm × 4 mm; Internal structure size: Cylinder: diameter 2.50 mm, height 2.50 mm; Cone: diameter 1.50 mm, height 1.0 mm (Fig. 2a, b).

Testing material's microwave absorption performance in the frequency band ranging from 6.0 to 40.0 GHz. As can be seen from Fig. 2c, the reflection loss rate of material decreased from -0.49 to -0.30 dB in the range of 6.0–6.9 GHz; Increased from -0.30 to -0.47 dB in the range of 6.9–7.4 GHz; Decreased from -0.47 to -0.14 dB in the range of 7.4–10.8 GHz; Increased from -0.14 to -0.76 dB in the range of 10.8–15.4 GHz; Basically remain unchanged in the range of 15.4–26.9 GHz; Decreased from -0.74 to -0.29 dB in the range of 26.9–29.1 GHz; Increased from -0.29 to -2.78 dB in the range of 29.1–40 GHz.

### 3.3 Structural Design and Absorptive Performance Test of Swallow-Tailed Cavity Model

Single model size: 3 mm × 3 mm × 4 mm; Internal structure size: Cylinder diameter 2.50 mm, height 2.50 mm; Frustum of cone: diameter of upper surface 1.50 mm, diameter of lower surface 2.50 mm, height 1.0 mm; Cone: diameter 2.50 mm, height 0.33 mm (Fig. 3a, b).

Testing material's microwave absorption performance in the frequency band ranging from 6.0 to 40.0 GHz. As can be seen from Fig. 3c, the reflection loss rate of material decreased from -0.13 to -0.02 dB in the range of 6.0–6.8 GHz; Increased from -0.02 to -0.12 dB in the range of 6.8–7.4 GHz; Decreased from -0.12 to -0.02 dB in the range of 7.4–10.6 GHz; Increased from -0.02 to -1.43 dB in the range of 10.6–17.8 GHz; Decreased from -1.43 to -0.96 dB in the range of 17.8–29.8 GHz; Increased from -0.96 to -3.84 dB in the range of 29.8–40 GHz.

### 3.4 Structural Design and Absorptive Performance Test of Fishtail Cavity Model

Single model size: 3 mm × 3 mm × 4 mm; Rotating body: the diameter of upper and lower surface is 2.50 mm, the diameter of the middle axis is 1.38 mm, the height is 3.50 mm; The cone: length 1.11 mm, diameter 2.50 mm (Fig. 4a, b).

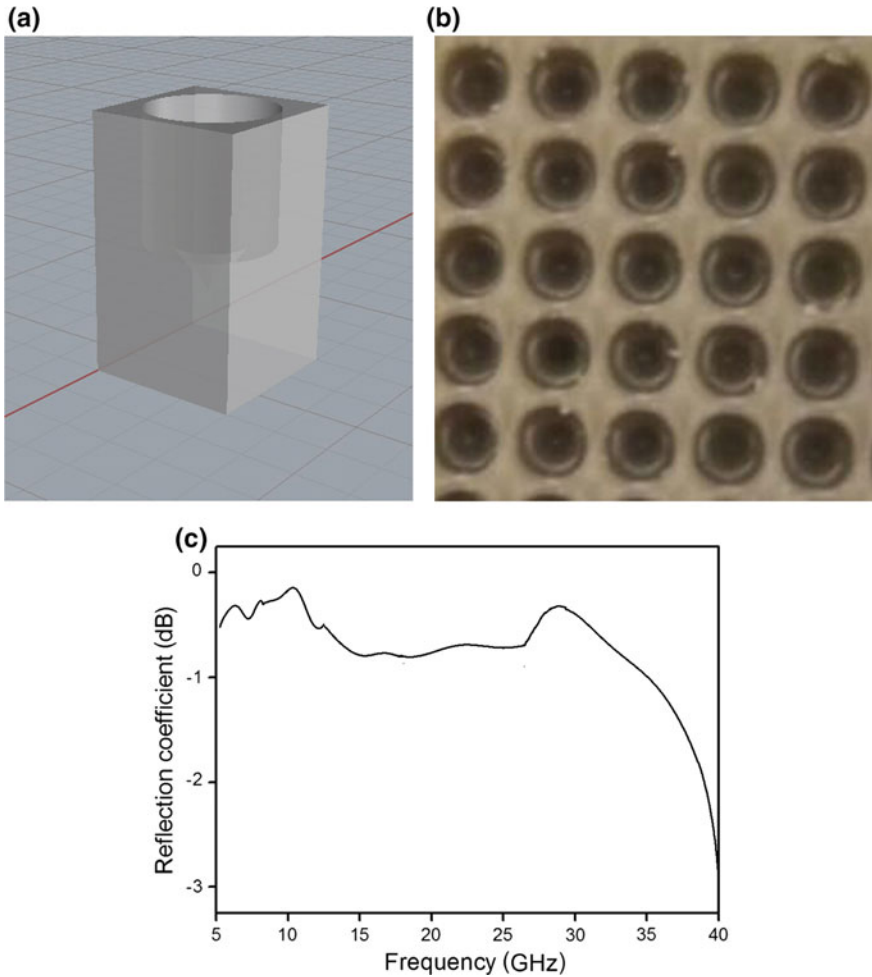


**Fig. 2.** **a** Minimum cell structure drawing of the inverted cone cavity model; **b** practicality picture of the inverted cone cavity model after print; **c** reflection coefficient of the inverted cone cavity model

Testing material's microwave absorption performance in the frequency band ranging from 6.0 to 40.0 GHz. As can be seen from Fig. 4c, the reflection loss rate of material decreased from  $-1.41$  to  $-1.01$  dB in the range of 6.0–6.7 GHz; Increased from  $-1.01$  to  $-1.40$  dB in the range of 6.7–7.1 GHz; Decreased from  $-1.40$  to  $-1.19$  dB in the range of 7.1–7.4 GHz; Increased from  $-1.19$  to  $-2.08$  dB in the range of 7.4–11.3 GHz; Decreased from  $-2.08$  to  $-1.49$  dB in the range of 11.3–17.3 GHz; Increased from  $-1.49$  to  $-5.92$  dB in the range of 17.3–40 GHz.

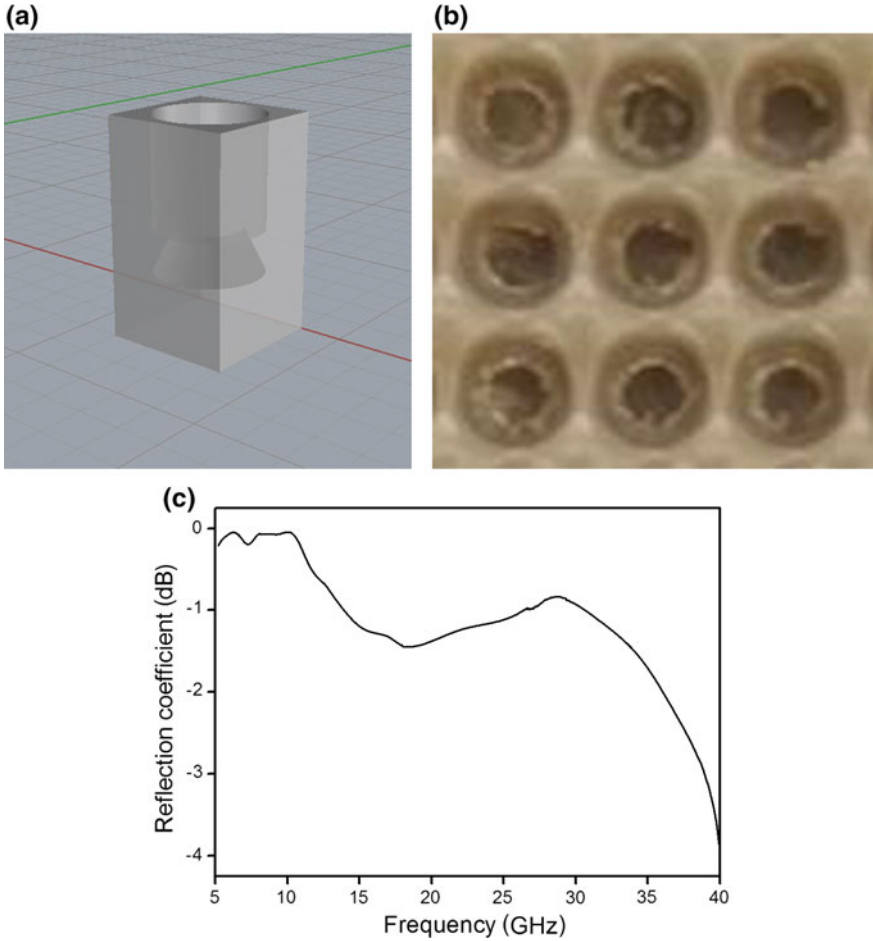


**Fig. 3.** **a** Minimum cell structure drawing of the swallow tailed cavity model; **b** practicality picture of the swallow tailed cavity model after print; **c** reflection coefficient of the swallow tailed cavity model

### 3.5 Absorptive Performance Test of Solid Plate

Testing microwave absorptive performance of the solid plate. In the frequency band ranging from 6.0 to 40.0 GHz. As can be seen from Fig. 5, the reflection loss rate of material decreased from  $-1.09$  to  $-0.91$  dB in the range of 6.0 to 6.9 GHz; Increased from  $-0.91$  to  $-0.99$  dB in the range of 6.9–7.2 GHz; Decreased from  $-0.99$  to  $-0.76$  dB in the range of 7.2–7.5 GHz; Increased from  $-0.76$  to  $-0.80$  dB in the range of 7.5–8.1 GHz; Decreased from  $-0.80$  to  $-0.75$  dB in the range of 8.1–10.1 GHz; Increased from  $-0.75$  to  $-1.45$  dB in the range of 10.1–12.2 GHz. Decreased from  $-1.45$  to 0 dB in the range of 12.2–17.1 GHz; Basically remain unchanged in the range



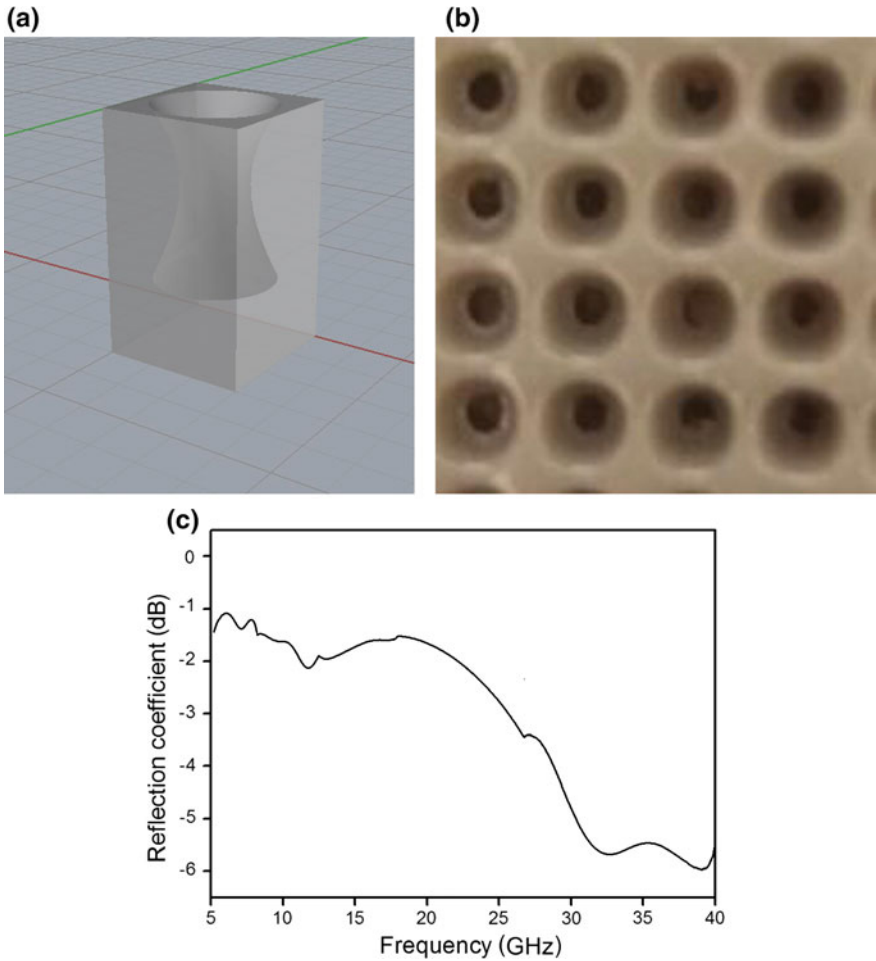


**Fig. 4.** **a** Minimum cell structure drawing of the fishtail cavity model; **b** practicality picture of the fishtail cavity model after print; **c** reflection coefficient of the fishtail cavity model

of 17.1–24.9 GHz; Increased from 0.04 to  $-0.32$  dB in the range of 24.9–27.4 GHz. Decreased from  $-0.32$  to  $1.87$  dB in the range of 27.4–39.1 GHz; Increased from  $1.87$  to  $1.81$  dB in the range of 39.1–40.0 GHz.

## 4 Conclusions

The opening diameter of blackbody cavity in microwave absorbing material is 2.5 mm, when the  $1/8$  of the incident electromagnetic wave length is less than 2.5 mm (the electromagnetic wave frequency is greater than 15 GHz), the waveguide effect will be obvious. At this time, the wave impedance of the material decreases, the electromagnetic wave entering the material increases, which is finally absorbed in the blackbody

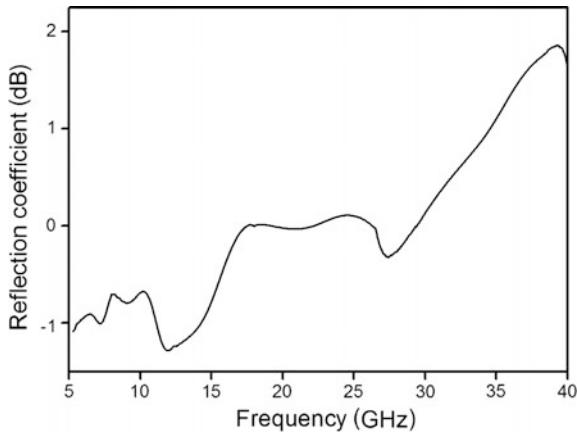


**Fig. 5.** Reflection coefficient of the solid plate

cavity after being reflected many times. Through the design of the blackbody cavity structure, increasing the reflection times of the electromagnetic wave in the blackbody can improve the absorption intensity and the absorption bandwidth of the material. The maximum reflection loss of solid plates is only  $-1.45$  dB. The maximum reflection loss of conical cavity is  $-1.48$  dB, the maximum reflection loss of inverted cone cavity is  $-2.78$  dB, the maximum reflection loss of swallow tail cavity is  $-3.84$  dB, the absorption performances of these models are greatly improved at more than 30 GHz. The maximum reflection loss of fishtail cavity is up to  $-5.92$  dB, which have the better absorption performances at more than 20 GHz.

**Acknowledgements.** This study is funded by Scientific Research Project of Beijing Educational Committee (KM201810015003, KM201810015012) and BIGC Project.

## References

1. Jin, L., Zhao, X., Xu, J., et al. (2018). The synergistic effect of a grapheme nanoplate/ $\text{Fe}_3\text{O}_4$ @ $\text{BaTiO}_3$  hybrid and MWCNTs on enhancing broadband electromagnetic interference shielding performance. *RSC Advances*, 8(4), 2065–2071.
2. Zhao, H., Fu, Z., Chen, H., et al. (2016). Excellent electromagnetic absorption capability of Ni/Carbon based conductive and magnetic foams synthesized via a green one pot route. *ACS Applied Materials & Interfaces*, 8, 1468–1477.
3. Wang, X., Zhang, M., Zhao, J., et al. (2017).  $\text{Fe}_3\text{O}_4$ @polyaniline yolk-shell micro/nanospheres as bifunctional materials for lithium storage and electromagnetic wave absorption. *Applied Surface Science*, 427, 1054–1063.
4. Zhao, S., Gao, Z., Chen, C., et al. (2016). Alternate nonmagnetic and magnetic multilayer nanofilms deposited on carbon nanocoils by atomic layer deposition to tune microwave absorption property. *Carbon*, 98, 196–203.

5. Pan, H., Yin, X., Xue, J., et al. (2016). In-situ synthesis of hierarchically porous and polycrystalline carbon nanowires with excellent microwave absorption performance. *Carbon*, 107, 36–45.
6. Shao, Y., Lu, W., Chen, H., et al. (2018). Flexible ultra-thin Fe<sub>3</sub>O<sub>4</sub>/MnO<sub>2</sub> core-shell decorated CNT composite with enhanced electromagnetic wave absorption performance. *Composites Part B Engineering*, 144, 111–117.
7. Li, J., Xie, Y., Lu, W., et al. (2018). Flexible electromagnetic wave absorbing composite based on 3D RGO-CNT-Fe<sub>3</sub>O<sub>4</sub> ternary films. *Carbon*, 129, 76–84.
8. Liu, J., Cao, W., Jin, H., Yuan, J., et al. (2015). Enhanced permittivity and multi-region microwave absorption of nanoneedle-like ZnO in the X-band at elevated temperature. *Materials Chemistry C*, 3, 4670–4677.
9. Jiang, H., & Kang, X. (2013). Analysis of the development of 3D printing technology. *Advanced Materials Industry*, 10, 30–35.
10. Zhang, X., Tang, S., Zhao, H., et al. (2016). Research status and key technology of 3D printing technology. *Journal of Materials Engineering*, 44, 122–128.
11. Shi, J., Yang, J., Li, J., et al. (2012). Modeling of heterogeneous materials and research on digital micro droplet spray technology. *Journal of Nanjing Normal University (Engineering and Technology Edition)*, 1, 10.
12. Xu, Y., Wand, Q., Cao, Y., et al. (2017). Preparation of a reduced graphene Oxide/SiO<sub>2</sub>/Fe<sub>3</sub>O<sub>4</sub> UV-curing material and its excellent microwave absorption properties. *RSC Advances*, 7, 18172–18177.



# Preparation and Study of HA-CS-Mineralized Collagen Gel

Miaomiao Hu<sup>1,2</sup>, Kun Hu<sup>1,2,3(✉)</sup>, Yuzhu Cui<sup>1,2</sup>, Jia Yan<sup>1,2</sup>,  
Guijuan Yang<sup>1,2</sup>, Lin Zhu<sup>1,2</sup>, Min Yan<sup>1,2</sup>, Yen Wei<sup>4</sup>, Luhai Li<sup>1,2</sup>,  
and Fan Zhang<sup>5</sup>

<sup>1</sup> Institute of Printing and Packaging Engineering, Beijing Institute of Graphic Communication, Beijing, China  
kunhu@139.com

<sup>2</sup> Beijing Engineering Research Center of Printed Electronics, Beijing, China

<sup>3</sup> College of Biological Science and Engineering, Fuzhou University, Fujian, China

<sup>4</sup> Department of Chemistry and Tsinghua Center for Frontier Polymer Research, Tsinghua University, Beijing, China

<sup>5</sup> The First Hospital of Fuzhou Medical Association, Fujian, China

**Abstract.** A hydrogel is a novel high molecular polymer that forms a three-dimensional network structure by polymer chemical or physical cross-linking. In this experimental study, a chitosan-hyaluronic acid gel was used as a carrier, and nano-hydroxyapatite/collagen was composited to prepare a gel-based composite for 3D bio-printing. The properties of the composite gel were analyzed by in vitro gel test, rheological analysis, infrared spectroscopy and scanning electron microscopy. The results showed that the chitosan-hyaluronic acid gel with different mineralized collagen concentrations could be gelled rapidly at 37 °C for 5 min. Rheology experiments show that CS-HA mineralized collagen has shear thinning characteristics suitable for 3D bio-printing. The hydrogel was observed to have a cross-linked morphology by scanning electron microscopy, and the porous structure was good. Has a high biomedical re-research value and use value.

**Keywords:** Chitosan · Hyaluronic acid · Rheology · Hydrogel · 3D bioprinting

## 1 Introduction

Hydrogels are polymers that swell in water and retain a large amount of water without being dissolved [1]. Chitosan (CS) is a biomaterial that naturally adsorbs cationic biopolysaccharides. It has good biocompatibility and biodegradability, but the chitosan gel has large brittleness, weak viscoelasticity, insufficient mechanical properties and weak water holding capacity [2–4]. Hyaluronic acid (HA) is a high molecular polysaccharide composed of D-glucuronic acid and N-acetylglucosamine. It is one of the best moisturizing ingredients recognized so far and has high biocompatibility [5–7].

Lei et al. [8] introduced (HA) into CS by glutaraldehyde cross-linking method, which solved the shortcomings of chitosan, but its viscosity is low, which seriously affects its application in the field of soft tissue repair.

Therefore, a composite material suitable for three-dimensional bioprinting was prepared by using CS-HA gel as carrier composite mineralized collagen material. The mineralized collagen composite used in the experiment is a new and effective bone graft material developed on the basis of long-term study of bone defect regeneration and repair [9–11]. By optimizing the formulation and preparation process of CS-HA mineralized collagen composite gel, the biocompatibility of the material is improved to a certain extent, and the viscosity and gelation time of the composite gel are greatly improved, and the surface structure thereof is improved. It is more regular with the potential to apply to medical fields such as soft tissue repair.

## 2 Experimental

### 2.1 Materials

Chitosan (CS) and Hyaluronic acid (HA, 97%) were purchased from Macklin (China). Acetic acid, glutaraldehyde, and other reagents were bought from Sinopharm Chemical Reagent Co., Ltd. (China).

### 2.2 Preparation of Chitosan-Hyaluronic Acid-Mineralized Collagen Gel by Glutaraldehyde Cross-Linking

Chitosan and hyaluronic acid are dissolved in deionized water (pH 7–7.8). After stirring, a certain amount of acetic acid (2%, mass fraction) is slowly added to fully dissolve the chitosan. Through pre-experiment, the experiment of 1–20% mineralized collagen concentration gradient was carried out. According to the gel obtained by the experiment, 1–6% was weak and liquid, and 11–20% was brittle. It was solid, so the mineralized collagen added by 7–11% (% by mass of CS-HA) was weighed and dissolved, and 0% was used as a control group. Then, the cross-linking agent glutaraldehyde was added, stirred uniformly, and then refrigerated at 4 °C for 24 h.

### 2.3 Measurement and Statistical Data Analysis

Due to the prepared CS-HA mineralized collagen sol has a high viscosity, the gel has a solid property. In order to study the structural influence of the composite gel added with mineralized collagen on the original composite gel, the gels of different concentrations of freeze-dried gel were subjected to infrared test. In order to verify its gel-forming ability and injectability at body temperature, the samples were tested for gelation, printing and rheology; in order to understand the morphology of the gel sample, the initial gel Sampling and freeze drying were performed. The microscopic morphology was observed by scanning electron microscopy (SEM).

### 3 Results and Discussion

As shown in Table 1, under the condition of 37 °C, the gelation time of the six groups of samples was basically the same, and the average value was 5–6 min. It can be basically determined that the concentration of mineralized collagen does not have much influence on the gelation time of the CS-HA composite sol. And the gelation phenomenon of the sol can be concluded that the composite gel can be used in biomedical applications to provide support for the repair of soft tissues.

**Table 1.** Qualitative study on the gel temperature of CS-HA mineralized collagen composite sol

Mineralized collagen concentration (w/w)	0%	7%	8%	9%	10%	11%
Observation time (min)	5.5	6	6	5.5	6	6
Observation time (min)	5.5	5.5	5.5	6	6	6
Observation time (min)	6	5.5	6	6	6	6
Gelation time average	5.67	5.67	5.83	5.83	6	6
Gelation time variance	0.06	0.06	0.08	0.08	0	0

From the rheological test results of Fig. 1, the rate of change of the viscosity of the composite gel also decreases with increasing shear rate. It is a non-Newtonian fluid. In addition, the viscosity of the hydrogel depends primarily on its molecular weight and concentration. At a mineralized collagen concentration of 10%, the viscosity of the composite gel is highest due to the large intermolecular force. Viscosity is an important physical property in 3D printing and implant restoration. The influence of viscosity is important for printing and repair.

The CS-HA mineralized collagen gel was subjected to infrared test, and the results are shown in Fig. 2. It can be seen that most places are basically coincident. It can be judged by the infrared spectrum of the control group that the mineralized collagen does not affect or participate in the cross-linking reaction of CS-glutaraldehyde-HA. When the mineralized collagen concentration is 10%, the atomic electronegativity at the two ends of the bond The difference is large and the absorbance is maximum. Therefore, it has great application prospects in tissue engineering.

Figure 3 is a scanning electron micrograph of the CS-HA mineralized collagen composite gel after lyophilization. The composite gel obtained after crosslinking is kept in a entangled form, and its fibers are entangled with each other. As the concentration of mineralized collagen increases, the degree of physical entanglement of the molecular chains increases, and the arrangement between the molecules is more staggered and the mechanical strength is also improved.

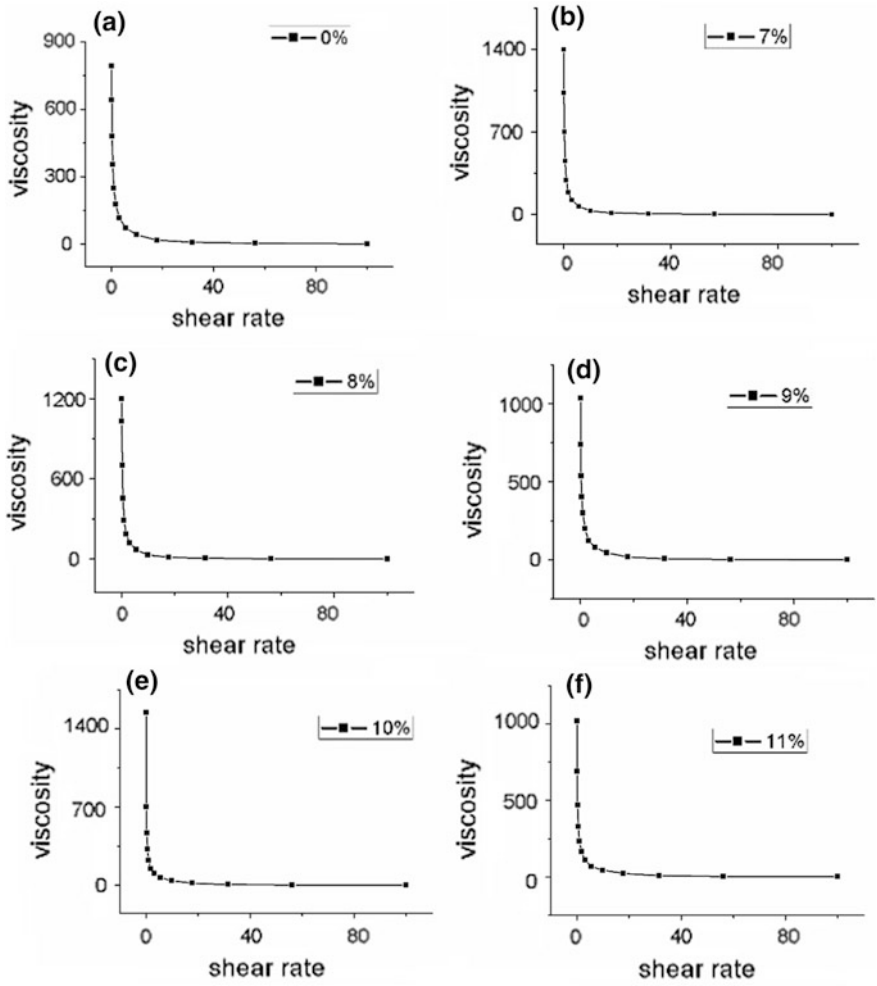


**Fig. 1.** Rheological properties of CS-HA composite gel with different mineralized collagen concentrations: **a** 0%, **b** 7%, **c** 8%, **d** 9%, **e** 10%, **f** 11%

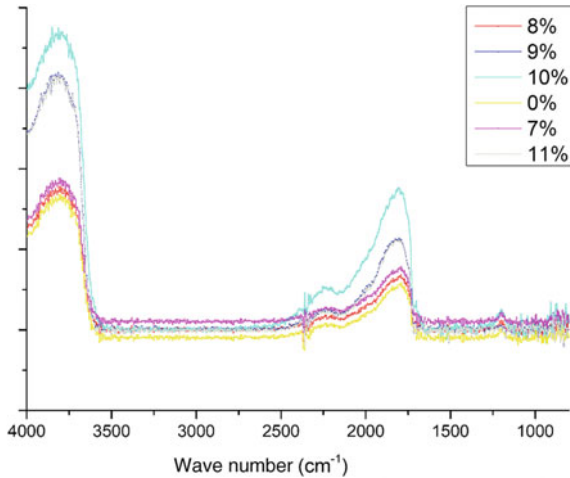


**Fig. 2.** Infrared spectroscopy of CS-HA gel with different mineralized collagen concentrations

## 4 Conclusions

In this work, CS-HA mineralized collagen composite gel was prepared (CS: 15 g/L, HA: 1.0 g/L, the amount of cross-linking glutaraldehyde was 10% of the mass of CS-HA, and the amount of mineralized collagen was concentration gradient. The temperature is room temperature), and chitosan has good compatibility with hyaluronic acid. In the sol-gel process, the gel was rapidly formed at 37 °C. No other new absorption peaks were observed in the infrared spectrum, indicating that no new bonds were formed, and the mineralized collagen did not change the properties of the gel matrix. The prepared hydrogel belongs to a pseudoplastic fluid and has the characteristics of shear thinning. It can be observed in the scanning electron micrograph that the composite gel maintains a crosslinked morphology in which the fibers are intertwined. Compared with CS-HA gel, CS-HA mineralized collagen gel has potential application value in biomaterials.

**Acknowledgements.** Financial support from the Science and Technology Major Project Foundation of Fujian Province (No. 2015YZ0003), Special project of the education committee—practical training plan Study on a novel temperature-sensitive hyaluronic acid/mineralized collagen composite gel material (Grant No. 03150118005/002/011), Research Project of 3D Printing Mineralized Collagen-based Child Mandible (Grant No. 04190118002/050), Undergraduate Research Training Program—A Preparation for 3D Bioprinting Composite Gel Materials (Grant No. 22150118022/083).



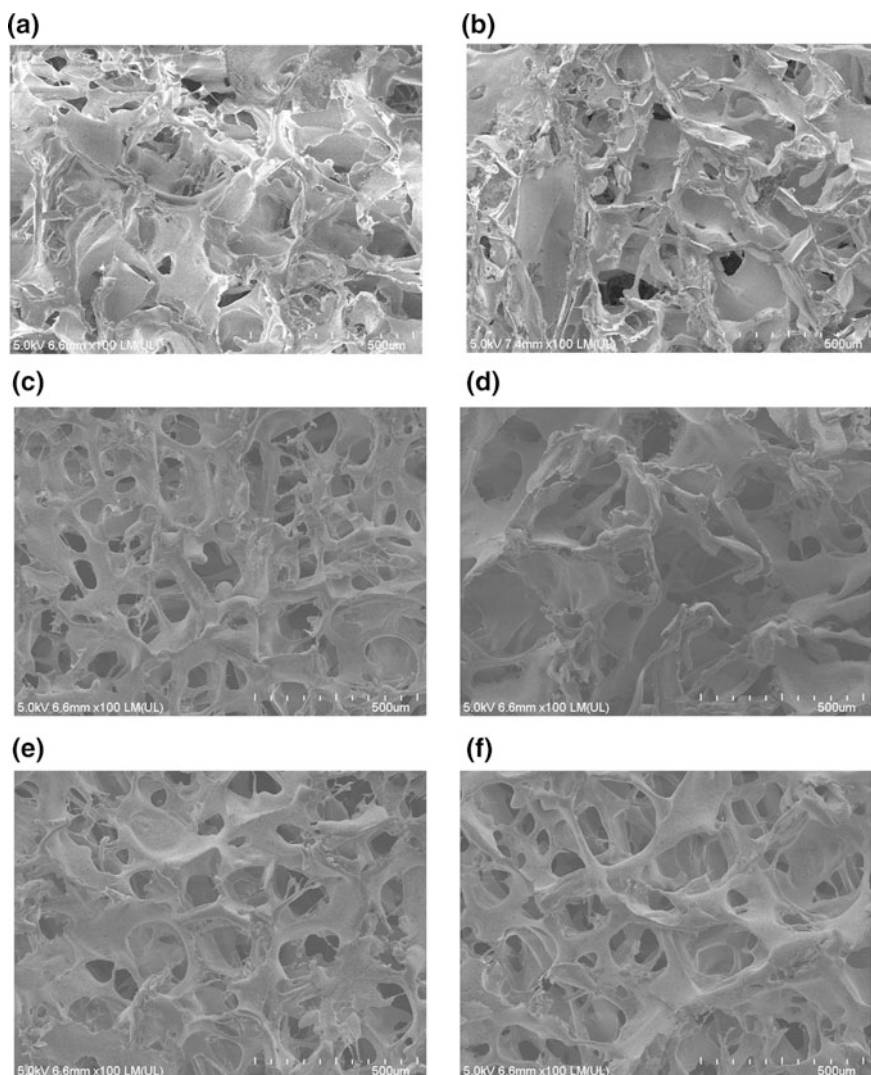


**Fig. 3.** SEM pictures of composite gels of different concentrations of mineralized collagen: **a** 0%, **b** 7%, **c** 8%, **d** 9%, **e** 10%, **f** 11%

## References

1. Ji, C., Khademhosseini, A., & Deghani, F. (2011). Enhancing cell penetration and proliferation in chitosan hydrogels for tissue engineering applications. *Biomaterials*, 32, 9718–9730.
2. Varaprasad, K., Vimala, K., et al. (2012). Biodegradable chitosan hydrogels for in vitro drug release studies of 5-fluorouracil an anticancer drug. *Journal of Polymers and the Environment*, 20(2), 573–580.

3. Park, Y., Lee, Y. S., Sheen, S., et al. (2000). Platelet derived growth factor releasing chitosan sponge for periodontal bone regeneration. *Biomaterials*, *21*(2), 153–159.
4. Ladet, S. G., Tahiri, K., et al. (2011). Multi-membrane chitosan hydrogels as chondrocytic cell bioreactors. *Biomaterials*, *32*(23), 5354–5364.
5. Yang, Y., Sun, C., et al. (2011). Influence of chondroitin sulfate and hyaluronic acid on structure, mechanical properties, and glioma invasion of collagen I gels. *Biomaterials*, *32* (31), 7932–7940.
6. Kong, M., Park, H., Feng, C., et al. (2013). Construction of hyaluronic acid noisome as functional transdermal nanocarrier for tumor therapy. *Carbohydrate Polymers*, *94*(1), 635–640.
7. Cui, F., & Feng, Q. L. (2004). *Biomaterials science* (2nd ed.). China: Tsinghua University Publication.
8. Lei, H. Y., Fan, X. R., et al. (2014). Preparation of chitosan-hyaluronic acid composite hydrogel. *Chemical Industry and Engineering Progress*, *33*(9), 2398–2406.
9. Collins, M. N., & Birkinshaw, C. (2006). Comparison of the effectiveness of four different crosslinking agents with hyaluronic acid hydrogel films for tissue—culture applications. *Journal of Applied Polymer Science*, *104*(5), 3183–3191.
10. WuX Liu, S., Yeung, K. W. K., Liu, C., & Yang, X. (2014). Biomimetic porous scaffolds for bone tissue engineering. *Materials Science & Engineering R Reports*, *80*(1), 1–36.
11. Sionkowska, A., Kaczmarek, B. et al. (2017). Preparation and characterization of collagen/chitosan/hyaluronic acid thin films for application in hair care cosmetics. *Pure and Applied Chemistry*, *89*(12), 1829–1839.



# An Integrated Film Sensor for Measuring Force and Temperature for Artificial Skin Applications

Xiaoyu Wang, Yue Shi, Fenlan Xu, Ruping Liu, Wei Wang<sup>(✉)</sup>,  
and Luhai Li

Beijing Engineering Research Center of Printed Electronics, Beijing Institute  
of Graphic Communication, Beijing, China  
18900616029@189.cn, liluhai@bigc.edu.cn

**Abstract.** Artificial skin is an important research direction in artificial intelligence and robotics. Response of artificial skin to stimuli in the external environment is multifunctional, including temperature, pressure and so on. In this paper, the integrated film sensor measuring force and temperature can simultaneously sense the external pressure and the temperature stimulation. To build the sensor, the integration of strain and temperature measurement materials is on a PET film. This integrated film sensor then has a good scalability and mechanical performance, and can according to the specific application of environment to carry on various design and application measurement. Thus, such kind of force and temperature integrated thin film sensor can be widely used, especially in artificial skin, intelligent robot, artificial limb, medical examination and so on.

**Keywords:** Artificial skin · Measuring force · Measuring temperature · Film sensor

## 1 Introduction

With the continuous improvement of the scientific level and the continuous innovation of technology, new research areas such as artificial intelligence, the Internet of things, semiconductor materials and other fields have developed rapidly [1]. One important research direction is to make artificial skin for robotics and other applications. In an environment where people can't contact or inconvenient for people to contact, artificial skin on a robotic arm can replace human inductor tubes and help humans to feel the external environment [2–4].

This research will be of great significance to our future production and life. As shown in Fig. 1, we can see the different applications of artificial skin in wearable equipment. As shown in Fig. 1a, Sheng Xu et al. showed that a sensor can be used for ECG detection [5]. As shown in Fig. 1b, Brenna D Argall et al. showed that a robot has tactile sensors all over its body [6]. As shown in Fig. 1c, Pedro Silva Girao et al. showed a manipulator with a tactile sensor [7]. As shown in Fig. 1d, Lijia Pan et al. showed a board that detects the weight of a piece [8]. As shown in Fig. 1e, Zheng Lou et al. used a pressure sensor to detect vocal cord vibration [9]. As shown in Fig. 1f, Lucie Viry et al.

showed tiny sensor electrodes [10]. Most of the electronic skin currently studied is based on temperature sensors or pressure sensors. When sensing the external environment, the feeling of human skin is not only to measure temperature or pressure, but to measure simultaneously temperature and pressure. In order to prepare electronic skin which is closer to human skin, we propose a thin film sensor for simultaneous measurement of pressure and temperature.

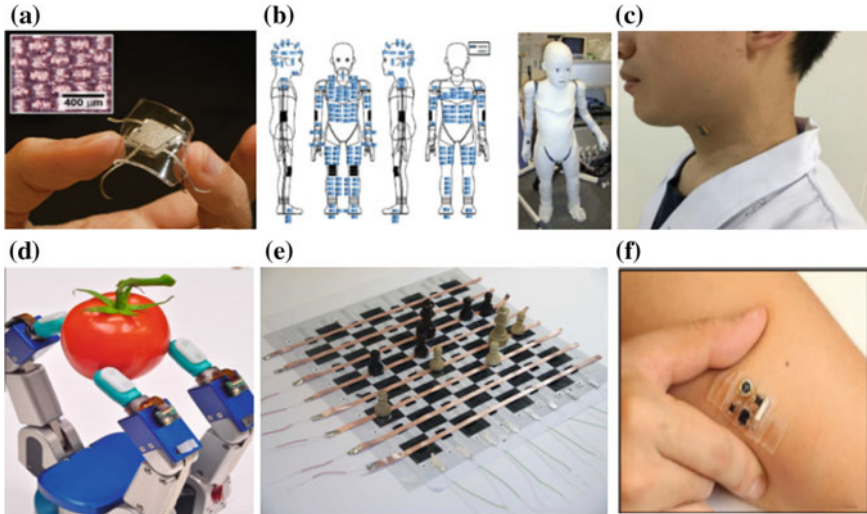


**Fig. 1.** The application of artificial skin in wearable equipment

## 2 Structures and Composition of Sensor

At present, most of the sensors can only measure only temperature or only pressure. Such monotonous measurement limits the application of sensors. If we need to measure the pressure and temperature at the same time, we need to install at least two sensors, a temperature sensor and a pressure sensor. The superposition of temperature sensors and pressure sensors to measure temperature and pressure simultaneously increases the complexity of the measurement devices and increases the cost of measurement, and the staff are laborious at installation, and the arrangement of the lines will be very complex. In order to measure two factors of temperature and pressure at the same time through a device, we try to integrate the temperature and pressure sensors on a substrate so that we measure both temperature and pressure at the same time. Pressure sensors have special structures. The bottom layer is the base material. A silver electrode is printed on the substrate. A pressure sensing layer is printed on the silver electrode. The upper layer of the pressure sensing layer is a substrate with silver electrodes. One side of the silver electrode is to the pressure sensing layer. A temperature sensing layer is deposited on one side of the silver electrode. The upper layer of the temperature

sensing layer is the substrate. Finally, the sensor is encapsulated by 3M glue. A schematic diagram of the structure of the sensor is shown in Fig. 2.

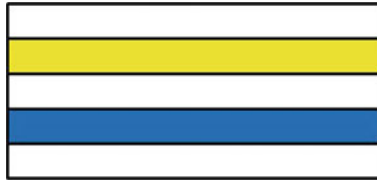


**Fig. 2.** A schematic diagram of the structure of a sensor. The white area represents the base material. Blue region represents pressure sensing layer. The Yellow region represents the temperature sensing layer

## 2.1 Base Material

The base material we choose is polyphenol oxygen resin. Polyphenol oxygen resin, also known as polyphenol oxygen, also being called linear epoxy resin, polyhydroxy ether and phenoxy resin, is a kind of sticky and soft thermoplastic material, with high cohesion and impact resistance. Polyphenols have excellent mechanical strength and toughness. At higher load speeds, it can still exhibit good ductility, low creep and shrinkage [11]. The main stem of polyphenolics is composed of ethers and hydroxyl groups. This structure can promote the ability of wetting and bonding with polar substances and fillers. Polyphenols resin has no reactive epoxy end group, and is a raw material with long thermal stability and long storage life. Polyphenols resin has good adhesion to high polar materials. Therefore, polyphenols resin is chosen as the base material in this paper.

## 2.2 Electrode

The electrode material we use is the conductive silver pulp. At present, the electrode has copper electrode, silver electrode and gold electrode, but because the conductivity of copper electrode is not good, and the price of gold electrode is more expensive, we choose the silver electrode with better price and better wire performance [12, 13]. The silver electrode of the film sensor is prepared by printing conductive silver pulp on the thin film screen. The silver electrode prepared in this way is excellent in electrical conductivity, accurate in size, and can be produced in large quantities, greatly improving the quality of the product and production efficiency, and greatly saving the life, production cost and manpower, material and financial resources. Such a preparation method can help to measure the industrialization of devices and provide a possibility for mass production of measuring devices in the future.

## 2.3 Pressure Sensing Layer

The pressure sensing layer we use is functional conductive ink. The functional conductive ink we use is composed of resins, solvents, auxiliaries and nano-carbon black.

The resin used for this time is polyhydroxy ether. The average molecular weight range of polyhydroxy ether is about 25,000–60,000. Because each molecule averages 40 or more regular intervals of hydroxyl groups, it is very suitable for thermosetting crosslinking, especially when the temperature increases. The solvent is ethylene glycol butyl ether acetate. Ethylene glycol butyl ether acetate is a high boiling point, multi-functional, two component alcohol ether ester solvent. It has excellent solubility for many substances. Carbon black is the most common form of carbon materials [14]. The preparation process of carbon black is simple and the production cost is low. Carbon black filler has a large difference in morphology and structure [15]. Because of its low price, simple process and strengthening of polymer substrate, it is gradually becoming the first choice for the preparation of flexible conductive materials [16]. Porous conductive materials with larger specific surface area can obtain better conductive composite materials more easily. The conductivity of carbon filled polymer is largely dependent on its structure, specific surface area, particle size and surface polar groups. In general, the more complex the structure of carbon black particles is, the easier it is to form aggregates between carbon black particles. The smaller the impediment, the more is the conductive.

## 2.4 Temperature Sensing Layer

The temperature sensors we use are platinum and platinum, which are highly sensitive to temperature. Platinum is deposited on a thin film substrate to form a thin film temperature sensor [17]. With the change of temperature, platinum resistance will change significantly. Our encapsulation method is to use 3 M adhesive force bonding. Such a package is convenient and cheap. The encapsulation effect is also good. It can encapsulate the sensor to prevent the sensor from receiving external interference and prevent wear.

## 3 Conclusions

The film sensors that measure the pressure and temperature at the same time can simultaneously correspond temperature and pressure, which will greatly improve the integration of the device and the working efficiency, and also reduce the measurement cost. The film sensor is composed of flexible film substrate and film functional layer. Therefore, it is flexible and stretchable, and can be applied to unevenness surface, which will extend the measurement range of the device. Such a device is useful to artificial skin applications. In view of the six human senses, such as temperature, pressure, humidity, and so on, we will further optimize our sensors to make artificial skin more similar to human skin.

**Acknowledgements.** This work was supported by the Beijing Municipal Education Commission (KM201710015005), the Research and Development Program of BIGC (Ec201808).

## References

1. Tegin, J., & Wikander, J. (2005). Tactile sensing in intelligent robotic manipulation a review. *Industrial Robot*, 32(1), 64–70.
2. Hoshi T., & Shinoda H. (2006). A large area robot skin based on cell-bridge system. *Sensors*, <https://doi.org/10.1109/icsens.2007.355595>.
3. Wang, G., Chen, D., Chen, K., et al. (2015). The current reach status and development strategy on biomimetic robot. *Journal of Mechanical Engineering*, 51(31), 27–44.
4. Srdjan, M., Masashi, N., et al. (2014). Epidermal merkel cells are mechanosensory cells that tune mammalian touch receptors. *HHS Public Access*, 509(7502), 617–621.
5. Xu, S., et al. (2014). Soft microfluidic assemblies of sensors, circuits, and radios for the skin. *Science*, 344(6179), 70–74.
6. Brenna, D. A., Aude, G., et al. (2010). A survey of tactile human-robot interactions. *Robotics and Autonomous Systems*, 58(10), 1159–1176.
7. Girao, P. S., et al. (2013). Tactile sensors for robotic application. *Measurement Journal of the International Measurement confederation*, 46(3), 1257–1271.
8. Pan L., et al. (2014). An ultra-sensitive resistive pressure sensor based on hollow-sphere microstructure induced elasticity in conducting polymer film. *Nature Communications*, <https://doi.org/10.1038/ncomms4002>.
9. Zheng, L., et al. (2016). An ultra-sensitive and rapid response speed graphene pressure sensor for electronic skin and health monitoring. *Nano Energy*, 23, 7–14.
10. Lucie, V., et al. (2014). Flexible three-axial force sensor for soft and highly sensitive artificial touch. *Advanced Materials*, 26(17), 2659–2664.
11. Lei, H., Willam, G. P., Lucas, K. M., et al. (2007). Modeling carbon black/polymer composite sensors. *Sensors and Actuators B*, 125(2), 396–407.
12. Lee, H., Chang, S., Yoon, E., et al. (2006). A flexible polymer tactile sensor: fabrication and modular expandability for large area deployment. *Journal of Microelectromechanical Systems*, 15(6), 1681–1686.
13. Zhu, B., Niu, Z., Chen, X., et al. (2014). Micro-structured graphene arrays for highly sensitive flexible tactile sensors. *Small*, 10(18), 3594.
14. Wang, X., Yang, G. U., Zhang, T., et al. (2014). Silk-molded flexible, ultrasensitive, and highly stable electronic skin for monitoring human physiological signals. *Advanced Materials*, 26(9), 1336–1342.
15. Jiang, M. J., Dang, Z. M., Yao, S. H., et al. (2008). Effects of surface modification of carbon nanotubes on the microstructure and electrical properties of carbon nanotubes/rubber nanocomposites. *Chemical Physics Letters*, 457(4–6), 352–356.
16. Li, Q., Xue, Q., Hao, L., et al. (2008). Large dielectric constant of the chemically functionalized carbon nanotube/polymer composites. *Composites Science and Technology*, 62(26), 4229–4231.
17. Karasek, L., & Sumita, M. (1995). Characterization of dispersion state of filler and polymer-filler interactions in rubber-carbon black composites. *Journal of Materials Science*, 31(2), 281–289.



# Application of NIR Analysis Technology in Determining the Freshness Grade of Eggs

Liwei Chen, Wenguang Wei, Xiujuan Zhi, and Bin Du<sup>(✉)</sup>

Beijing Laboratory of Food Quality and Safety, Food Science and Engineering College, Beijing University of Agriculture, Beijing, China  
{2384357871, 38534891}@qq.com, 13522951554@163.com,  
{2384357871

**Abstract.** Eggs are rich in high-quality protein and nutrients. The quality and nutritional value of eggs with different freshness grades are quite different. In this paper, the near-infrared analysis technique was used to detect 180 eggs samples stored within 50 d under the condition of 25 °C temperature and 60% humidity. According to the change of freshness index under different storage time, the eggs were classified and the qualitative classification model was established. The results showed that the near infrared analysis technique was an effective method for fast prediction of eggs in the fields of freshness and edible condition.

**Keywords:** NIR analysis technology · Freshness grade · Eggs

## 1 Introduction

Eggs containing rich nutrients are considered as an important source of high quality protein and vitamin B. The freshness of eggs is the core index to measure the internal quality of eggs. The results showed that great differences in the quality and the nutritional value appeared in eggs under the different freshness grades [1–3]. According to the relevant standards of the Ministry of Agriculture, eggs with freshness below B level are unsuitable for consumption. A rapid and nondestructive testing method for quality supervision and market classification can ensure the consumers to get the high-quality eggs. It was time-consuming and destructive for conventional methods to obtain the evaluation indexes of egg freshness such as weightlessness rate, Hough unit, egg pH value, gas chamber diameter, egg yolk index, and protein index. For a big country of egg production and consumption, the study in detecting egg freshness quickly, accurately and nondestructively to ensure the storage, processing and circulation of eggs is an important research topic [4].

As a green, pollution-free, fast and nondestructive testing technology, near infrared spectroscopy (NIR) has recently attracted much attention in the study of egg freshness and quality prediction [4–8]. In this paper, 180 fresh eggs of postpartum 24 h were taken as samples, and their NIR spectral data, the changes in the weight, Haff unit and the thick protein height under the storage of 50 d were systematically measured and analyzed. The freshness of the samples was graded and the qualitative classification



model of the freshness grade was established with the change of the near infrared spectrum. It is used to predict the freshness and edible condition of eggs quickly.

## 2 Materials and Methods

### 2.1 Materials and Instruments

Eggs: fresh eggs in postnatal 24 h, were purchased from Beijing Hao Yi animal husbandry Co., Ltd.

Test instruments: Nicolet 6700 Fourier Transform Near Infrared Spectroscopy Analyzer, Thermo Nicolet company; EA-01 egg quality analyzer, Israeli ORKA company; YP1002N electronic balance, Shanghai Precision Scientific Instrument Co., Ltd.

### 2.2 Sample Treatment

180 fresh eggs after postpartum 24 h, were randomly selected as samples containing the similar color and size with no cracks on the surface of eggshell. The eggs were cleaned and sterilized with distilled water and anhydrous ethanol. They were divided into 12 groups (A, B, C, D, E, F, G, H, I, J, K, L), and each group contained 15 eggs. The initial egg weight was evaluated at 25 °C and stored at room temperature with the humidity of ca. 60%.

### 2.3 Determination of Evaluation Index of Freshness of Eggs

#### 2.3.1 Determination of Hover Unit and Protein Height

The EA-01 multi-function egg quality analyzer was utilized to measure the Hough unit which is the index of the inspection of the American Department of Agriculture in the freshness of the egg. The calculation formula is as follows:

$$Haugh = 100lg(H + 7.57 - 1.7m^{0.37})$$

In the formula, H is egg heavy protein height (mm) and m is egg quality (g).

The classification standards are as follows:  $Haugh > 72$ , AA grade;  $60 < Haugh < 71$ , A grade;  $31 < Haugh < 59$ , B grade;  $Haugh < 30$ , C grade.

#### 2.3.2 Determination of the Weight Loss Rate

The rate of weightlessness is the ratio of weight loss to fresh shell eggs after storage for a period of time. The formula is as follows:

Weightlessness rate =  $[(m_0 - m_t)/m_0] \times 100\%$ , where  $m_0$  represents the quality of fresh shell eggs, and  $m_t$  represents the quality of shell eggs after a period of storage.

### 2.4 Spectral Collection and Data Processing

The Nicolet 6700 Fourier Transform Near Infrared Spectroscopy Analyzer produced by Thermo Scientific was used in the experiment. The NIR spectrum was collected by the

integral sphere diffuse reflectance sampling system. The sampling interval was  $7.714\text{ cm}^{-1}$  and the detector was InGaAs. The instrument should be preheated at least 30 min in advance. The data acquisition parameters of NIR spectrum are set to the scanning range of  $10,000\text{--}4000\text{ cm}^{-1}$ , the scanning times of 32 times, the resolution of  $16\text{ cm}^{-1}$ , the room scanning temperature and automatic deduction of atmospheric background. Each egg is put at 5 different positions with 3 times of scanning, and the average spectrum was obtained. The software for spectral data acquisition and processing is Omnic 8.1.11 and TQ Analyst 8.5.28, and the experimental data analysis software is IBM SPSS Statistics 22.

## 2.5 Discriminant Analysis

Discriminant analysis, known as “resolution method”, is a multivariable statistical analysis method, which is based on the various eigenvalues of a certain research object to determine its type attribution under the condition of classification. The principal component analysis (PCA) method provided by TQ Analyst was used for discriminant analysis in this experiment. PCA method is used to extract the feature information in the group sample, further identifying the main factors that can affect the system, simplifying the dimension of a large number of variables, and summing up the complex factors into several main components, and make the problem simple while ensuring the complete data structure.

## 3 Results and Analysis

### 3.1 Changes in Freshness Index of Eggs Under Different Storage Time

The thick protein height, Haff unit and weightlessness rate of eggs under different storage days were detected, as shown in Table 1.

**Table 1.** Changes in freshness index of eggs under different storage time

Storage time (d)	Measurement index		
	Thick protein height (mm)	Haff unit	Weightlessness rate (%)
0	$6.063 \pm 0.880^a$	$79.20 \pm 3.435^a$	$0.0 \pm 0.0^a$
3	$4.967 \pm 0.455^b$	$67.42 \pm 4.475^b$	$1.2 \pm 0.1^a$
6	$4.383 \pm 0.591^{b,c}$	$66.25 \pm 5.272^{b,c}$	$3.0 \pm 0.5^b$
9	$3.867 \pm 0.641^{c,d}$	$59.12 \pm 6.514^{c,d}$	$3.8 \pm 0.7^b$
12	$4.617 \pm 0.264^b$	$65.35 \pm 2.683^{b,c}$	$5.6 \pm 1.6^c$
15	$3.633 \pm 0.242^{d,e}$	$54.72 \pm 3.330^{d,e}$	$6.1 \pm 1.2^c$
18	$3.017 \pm 0.454^{e,f}$	$49.25 \pm 6.238^e$	$7.8 \pm 2.8^d$
21	$3.300 \pm 0.237^{d,e,f}$	$55.13 \pm 2.828^{d,e}$	$8.4 \pm 1.3^d$
33	$2.833 \pm 0.455^f$	$51.08 \pm 6.352^{d,e}$	$13.6 \pm 3.1^e$
49	$2.573 \pm 0.486^f$	$46.74 \pm 8.044^e$	$16.7 \pm 1.5^f$

*Note* Indicators with different letters in the same column (a, b, c, d, e, f) represent significant statistical differences in different storage days ( $p < 0.05$ ),  $n = 15$

The results showed that there were significant differences in the height of egg protein, HU and weight loss in different storage days. With the increase of storage time, the thick protein gradually became thinner, the protein height decreased, the Haff unit decreased obviously, the weight loss rate increased significantly and the egg quality deteriorated. The quality of the egg is deteriorated, which is probably assigned to the escape of the moisture and the CO<sub>2</sub> through the stomata. In addition, the water diffusion in the egg white weakened the yolk membrane and the yolk liquefied, with the prolongation of storage time. The phenomenon of dispersing yellow and the appearance of water-like state of thick protein were closely related to the protein denaturation.

The Hough value of the egg is the index for the inspection of the egg standard and the freshness of the egg, which is related to the height and quality of the egg's thick protein. The eggs after the postpartum 24 h can be considered as the AA level eggs, as shown in Table 1. However, the eggs with storage time during 9–12 d located in class A. After 15 d, all the experimental samples were declined to B grade until the end of the experiment. The quality change was consistent with the conclusions provided by Liu Yande et al. [6].

### 3.2 Spectral Analysis

The near infrared diffuse reflectance spectra of eggs which were selected at random with three different storage time of 0 d, 6 d and 18 d, respectively, were shown in Fig. 1. The transverse coordinate was wavenumber, and the longitudinal coordinate was absorbance, with the scanning range of 10,000–4000 cm<sup>-1</sup>. It is found that the spectra of eggs with different freshness grades have obvious differences. Data analysis in Table 1 showed that the thick protein in egg, the thickness of egg yolk film, the concentration of yolk, and the water of egg yolk, have changed irreversibly with the prolongation of storage time. The NIR spectroscopy mainly produced by molecular vibration frequency within the group absorption and frequency absorption harmony, and only hydrogen-containing functional groups such as C–H, N–H, S–H, and O–H' stretching vibration can be detected.

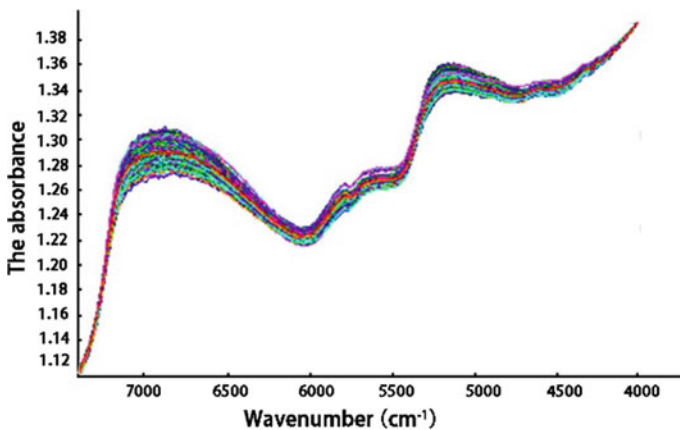


Fig. 1. NIR spectra of egg samples with different storage time

The change of the internal composition will inevitably lead to the change of its near infrared diffuse reflectance spectrum. The difference of the spectrum of egg samples in different storage period provided the possibility on the quality evaluation of the egg. In this model analysis, the selection of spectral range 4065.21–7335.89  $\text{cm}^{-1}$  is automatically optimized by TQ Analyst software.

### 3.3 The Effect of Different Spectral Pretreatment Methods on the Qualitative Discrimination Model of Eggs

Spectral preprocessing is usually very effective and necessary in NIR spectroscopy. The derivative, filter noise and baseline correction of the spectrum can be pretreated to reduce the spectral drift caused by the influence of the instrument state, sampling environment and sample uniformity, which is more conducive to the extraction of useful information in modeling.

Different pretreatment methods are used to analyze and compare the NIR spectra of egg samples collected in the experiment. The results showed that the untreated original spectrum is the best in modeling. After reducing the dimension of principal component analysis, the two models can well identify the spectral differences of unknown samples, and the accuracy of prediction results is greater than or equal to 98.2%. Table 2 compared the models using different preprocessing methods. The results showed that if the quality of the sample is high, it usually does not need to be pretreated, which can make the modeling achieve the ideal effect. So, in the process of collecting the spectrum, we should avoid the influence of the factors such as the state of the instrument, the sampling environment, the uniformity of the sample and so on.

**Table 2.** Effect of different spectral pretreatment methods on the qualitative discrimination model of eggs

Preprocessing type a–b	Model index			
	Misclassified	Principal components used	Percent of variability	Cumulative contribution rate (%)
1–1	16	10	99.6	98.9950
1–2	16	10	99.7	99.0712
2–1	59	10	34.5	48.0091
2–2	62	10	40.7	55.1462
2–3	43	10	93.5	95.1623
3–1	174	10	23.8	21.6355
3–2	185	10	34.9	32.2522
3–3	47	10	80.7	99.7009

Note a: 1:Spectrum, 2:First derivative, 3:Second derivative

Note b: 1:No smoothing, 2:Savitzky-Golay filter, 3:Norris derivative file

The spectra of samples stored within 50 d were qualitatively analyzed according to the three freshness grades of grade AA, A and B, as shown in Fig. 2. Based on the second principal component scores obtained from the first principal component scores,

the distribution of NIR diffuse reflectance in the principal component space of the samples of three different freshness grades has obvious clustering characteristics. When storage time increased, the eggs of the different freshness levels of AA, A and B showed distinct discreteness and classification. The results showed that it is feasible to establish a qualitative discriminant model for 3 fresh grade samples. In addition, the information showed that there are some overlapped regions between the A and B-class egg samples, which may be related to the individual differences in the eggs in the experiment, and the characteristics of the samples is not significant near the boundary conditions. Based on this, the qualitative discriminant model of eggs can be established to classify the freshness of the sold eggs, and the corresponding 3D discriminant analysis model is shown in Fig. 3. Obviously, the 3D model can express its classification characteristics more intuitively.

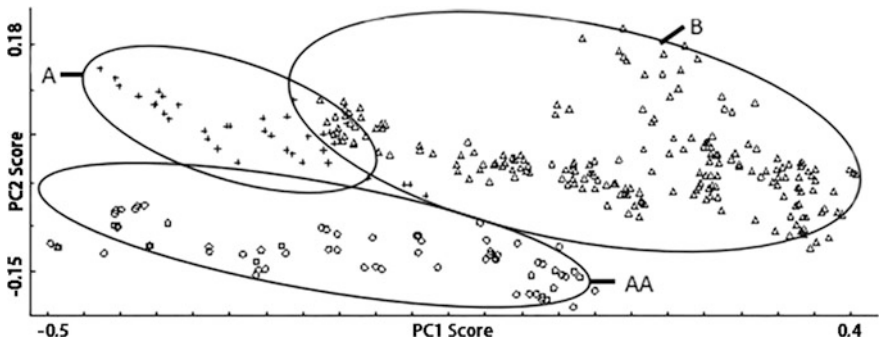


**Fig. 2.** Discriminant analysis of NIR spectra of shell eggs with different grades

The cumulative contribution rate is the degree of interpretation of the variation factors, that is, the calibration model is used to identify the spectral differences of the external samples. With the change of the main fraction, the recognition degree of the spectral variation in the calibration model is shown in Fig. 4. The greater the main fraction of the main fraction, the higher the recognition degree of the model for the spectral variation. In this experiment, the threshold of variability was set to 95%, and the primary score was 2. It can be seen from Fig. 4 that the cumulative contribution rate can reach 99.2% when the main fraction is 2, indicating that the first two principal components can explain 99.2% of the amount of information of the original wavelength, and the two principal components are the main factors affecting the freshness of the eggs, with statistical significance, and the results are accurate and reliable.

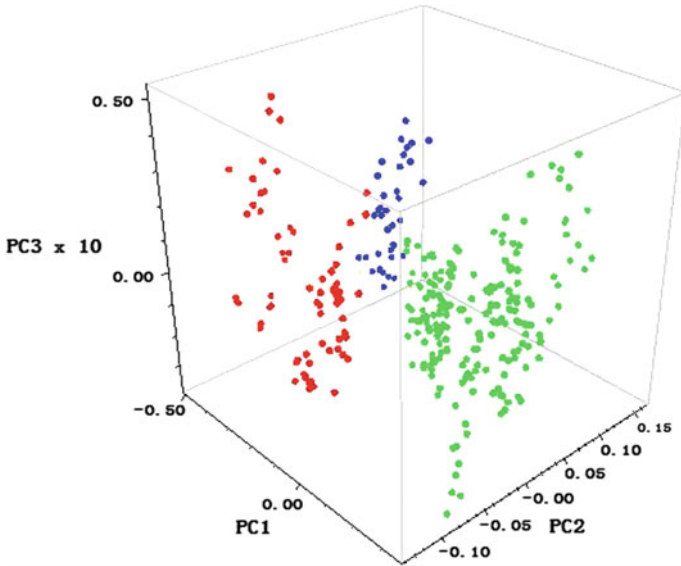


Fig. 3. 3D discriminant model of egg freshness grade

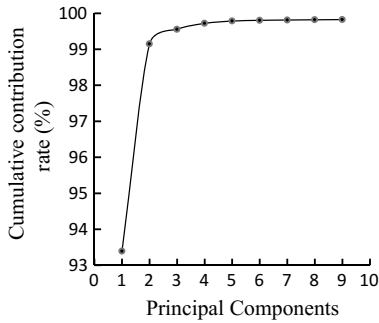


Fig. 4. The change of cumulative contribution rate with the principal components

## 4 Conclusions

In this experiment, 180 eggs samples stored within 50 d were analyzed by principal component analysis. The clustering effect of the eggs of different quality levels (AA, A and B) in the experimental collection spectrum can construct the quality classification model of eggs, to realize the rapid classification of the eggs sold in the market, and to guarantee the consumers to buy the price qualitatively.

## References

1. Li, X. M. (2017). Online detection of egg freshness by visible near infrared spectroscopy. *Huazhong Agricultural University*.
2. Du, D., Wang, F. N., Wang, S. P. (2014). Study on the change rule of egg freshness with storage conditions. *Food Technology*, 39(05), 26–29+33.
3. Xue, Y. R., Mao W., Zhao, R. S., et al. (2017). Study on the changes of microorganism and egg quality during the storage of eggs. *Animal and Feed Science*, 38(08), 67–69+72.
4. Bi, X. K., Zhao, J. W., Lin, H., Sun, L., et al. (2013). Portable near-infrared spectrometer for distinguishing the storage time of eggs. *Food Science*, 34(22), 281–285.
5. Tang, D. (2012). Egg quality detection method based on near infrared transmission spectroscopy. *China Jiliang University*.
6. Zhao, J. W., Bi, X. K., Lin, H., Sun, L., Guan, B. B. (2013). *Visible-near-infrared transmission spectra for rapid analysis of the freshness of eggs*, *laser & optoelectronics Progress*, 50, 053003.
7. Hou, Z. C., Yang, N., Li, J. Y., & Xu, G. Y. (2009). Study on the application of Fourier transform near infrared reflectance to the quality of egg and egg. *Spectroscopy and Spectroscopic Analysis*, 29(08), 2063–2066.
8. Li, J. F. (2009). Study on the detection of egg freshness based on near infrared diffuse reflectance technology. *Huazhong Agricultural University*.



# Study on the Degradation Property of nHAC/PLA Composite Wire Material

Yuzhu Cui<sup>1,2</sup>, Miaomiao Hu<sup>1,2</sup>, Kun Hu<sup>1,2,3(✉)</sup>, Jia Yan<sup>1,2</sup>,  
Guijuan Yang<sup>1,2</sup>, Chunyang Zhang<sup>1,2</sup>, Xinyu Wang<sup>1,2</sup>, Panpan Xue<sup>1,2</sup>,  
Yen Wei<sup>4</sup>, Luhai Li<sup>1,2</sup>, and Fan Zhang<sup>5</sup>

<sup>1</sup> Institute of Printing and Packaging Engineering, Beijing Institute of Graphic Communication, Beijing, China

kunhu@139.com

<sup>2</sup> Beijing Engineering Research Center of Printed Electronics, Beijing, China

<sup>3</sup> College of Biological Science and Engineering, Fuzhou University, Fujian, China

<sup>4</sup> Department of Chemistry and Tsinghua Center for Frontier Polymer Research, Tsinghua University, Beijing, China

<sup>5</sup> The First Hospital of Fuzhou Medical Association, Fujian, China

**Abstract.** Nano-crystal hydroxyapatite/collagen (nHAC) composites have good biological properties, and polylactic acid is a kind of polymer with good biocompatibility, both of which have been widely used in the field of bone repair. The nHAC/PLA composite wires studied in this paper were prepared from the combination of polylactic acid and nanocrystal hydroxyapatite/collagen, which was used as the raw material of 3D printed bone prosthesis, and the degradation performance of nHAC/PLA composite wires was studied. The experiment was carried out by in vitro degradation method, and the weight loss rate of the material in different periods was analyzed. The surface topography of the material was observed by laser confocal microscopy. FTIR and DSC were used to characterize the material before and after degradation. The results show that the material degradation occurs during the experiment, which is the decrease of tensile property, the reduction of material weight and the change of surface topography. In addition, no changes in molecular structure and other substances were produced during the degradation process.

**Keywords:** Nano-hydroxyapatite · Polylactic acid · 3D printing · Degradation

## 1 Introduction

Polymer with good biocompatibility and biodegradability has become a common material in biomedical applications [1–4]. 3D printing is a rapid additive manufacturing technology [5, 6]. Currently, research on the application of 3D printing in medicine is underway [7, 8]. Xiao et al. [9] has written another article explains the research on



material performance of 3D printing. Polylactic acid has the disadvantages of poor toughness, long degradation cycle under natural conditions, and high product price, which limits its application range. In response to these shortcomings, Liu et al. [10] used a compound having a reactive group as a toughening agent or an interfacial modifier to prepare a super-tough polylactic acid composite material. No research has been done on its biodegradability. The rate of degradation of materials affects the response of many cells [11]. The unique composition and structural characteristics of nHAC/PLA composites make it uniquely biodegradable.

## 2 Materials and Methods

The mineralized collagen powder and the polylactic acid material are doped and mixed at a ratio of 0%, 3%, and 7%, and after ultrasonic vibration mixing, the mixture is stirred and dissolved to uniformity using chloroform, and then dried by a freeze dryer to obtain a solvent. Rapid evaporation, using a plastic crusher for material crushing, and then through the extruder to prepare a wire ( $\Phi = 1.75$  mm) that can be used in FDM printers.

Solid works was used for modeling. The surface of the model was designed as a digital pattern, which was labeled as 1-1, 1-2, 1-3, etc. The files was imported into the Cura software for slicing and exporting into the gcode file, and finally the Gcode file was input into the FDM 3D printer for printing.

The prepared models was placed in a Petri dish and 10 ml degradation solution was added. The degradation solution was SBF solution. Then it was placed in a sterile box at 37 °C. Replace the liquid in the bottle every week for fresh degradation solution. Three samples were taken from each observation point, then filtered with double distilled water and then dried at low temperature. The dry weight of the sample is ( $W_t$ ) and the weightlessness rate is calculated. The surface morphology was observed by laser confocal analysis, and then subjected to FTIR and DSC characterization and the tensile properties were tested by universal tensile machine  $\text{Weight loss (\%)} = (W_o - W_t)/W_o * 100\%$  .

## 3 Results and Discussion

It can be seen from Fig. 1 that the degradation rate decreases with the increase of degradation days, and the quality of the material changes more and more with the change of time. The weight loss rate (degradation rate) is the amount of degraded material divided by the total amount of material. With the increase of days, the weight lost gradually becomes more and more, showing an upward trend. Therefore, it can be concluded that: at different weeks, different proportions of mineralized collagen/PLA composite wires have degradation, but the degradation rate is different, which is not stable degradation (Fig. 2).

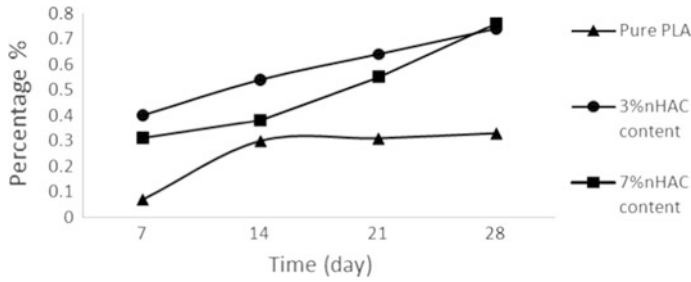


**Fig. 1.** Weight loss (%) of nHAC/PLA wires

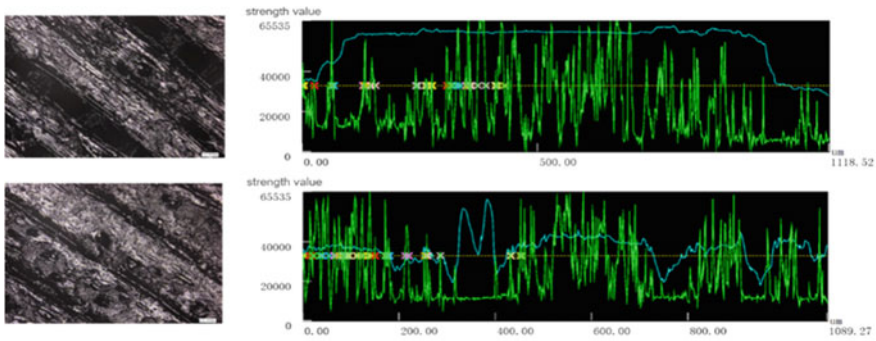


**Fig. 2.** Laser confocal images before and after degradation

The confocal pattern of the laser before and after degradation changes, and the surface of the object can be observed from smooth to rough, indicating flaking during the experiment. The surface was rough, the pits were large, which also indicated that the degradation occurred during the experiment.

As shown in Fig. 3, the wave number trend of composite wire with different degradation weeks is basically the same, and the transmission rate is slightly different. The wavenumber peaks at 800, 900, 1000–1500, 1800, 3000. According to Fig. 3, the original groups can still be seen in the infrared spectrum of the composite wire under different degradation weeks, and the molecular structure did not change significantly after the degradation (Fig. 4).

DSC analysis showed that nHAC/PLA composite glass transition temperature of the wire between 35 and 40 °C, the polymer chain of oscillations, reduced strength, toughness, melting point is 180–183 °C, melting, all melt crystallization, polymer chain in irregular state, is a Newtonian flow (Table 1).

Tensile tests before and after degradation showed that the tensile strength, tensile fracture stress and elongation at break of the composites with different nHAC contents decreased after degradation, which may be related to the breakage of the molecular chain and the shortening of the chain length of PLA during the degradation experiment, further indicating that degradation occurred during the experiment. And the degradation of composite material will reduce its tensile properties.

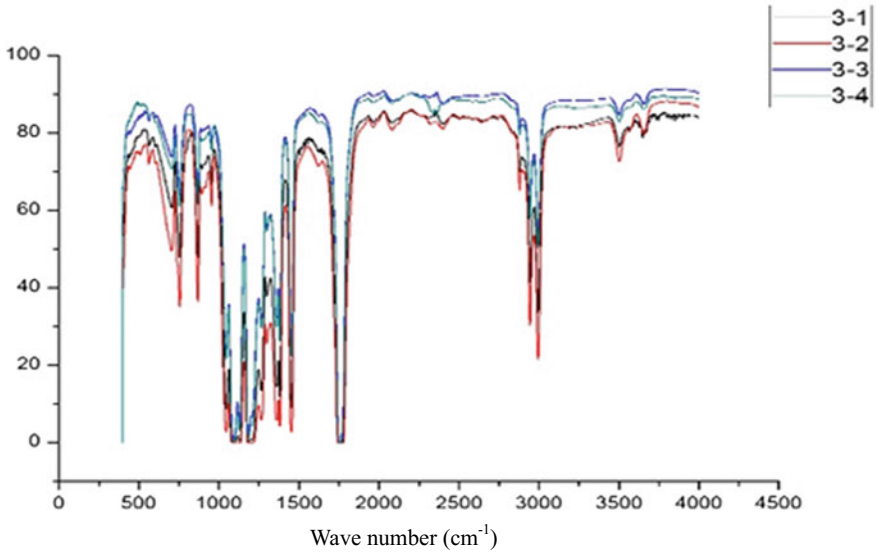


Fig. 3. FTIR curves at different degradation weeks

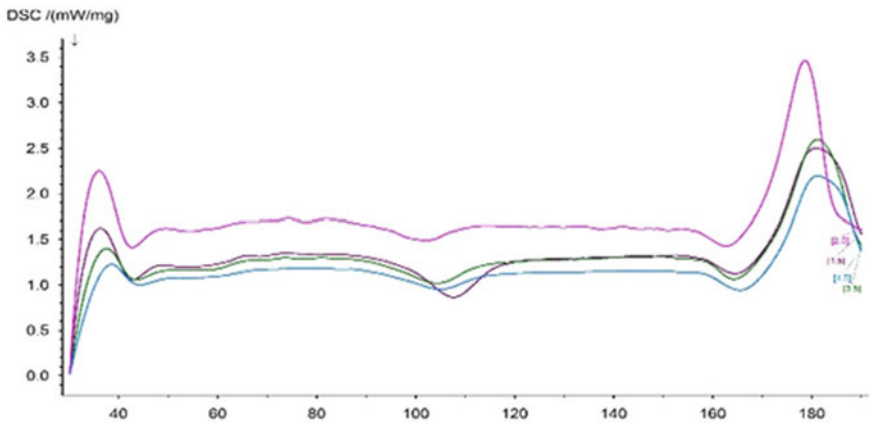


Fig. 4. DSC results of materials with nHAC content of 3% at different time points

**Table 1.** The mean values of mechanical strength of the tensile test for nHAC/PLA wires printed with different doping ratios before and after the degradation experiment

The content of nHAC in the sample (%)	The tensile strength (MPa)	Tensile fracture stress (MPa)	Elongation at break (%)
a. <i>Before</i>			
0	50.875	27.61	5.3
3	61.37	27.53	5.294
7	51.385	29.48	7.57
b. <i>After</i>			
0	47.575	14.55	3.905
3	57.225	16.665	3.935
7	46.125	12.5075	3.9275

## 4 Conclusions

The degradation rate of nHAC/PLA composite wires in simulated body fluid was studied by in vitro experiment. It was proved that nHAC/PLA composite wires degraded in simulated body fluid to a certain extent. The material degraded in different time and proportion, but the degradation rate was different. In laser confocal focusing, the surface of the object can be observed from smooth to rough, which indicates that there is flake spalling during the experiment. The surface is rough, the pit is more, and the trembling line is dense. Under different degradation cycles, the original groups can still be seen in infrared spectra, and the molecular structure of the composite wires has not changed greatly after degradation. The tensile test data of mechanical properties show that the tensile properties of the material after the test have decreased, indicating that the molecular chain of PLA has broken during the experiment, and the long chain has become a short chain. In summary, in vitro experiments showed that the nHAC/PLA composite was degraded, and the molecular structure did not change, and no other substances were produced. It was initially proved that this material can be applied to the biomedical field.

**Acknowledgements.** This study is funded by the Science and Technology Major Project Foundation of Fujian Province (No. 2015YZ0003), Special project of the education committee—practical training plan—study on the physical performance of 3D printed skull repair (Grant No. 03150118005/003/012), Research Project of 3D Printing Mineralized Collagen-based Child Mandible (Grant No. 04190118002/050), Undergraduate Research Training Program—Research on Artificial Bone Repair Wires for 3D Printing (Grant No. 22150118022/076).

## References

1. Woodruff, M. A., & Hutmacher, D. W. (2010). The return of a forgotten polymer—polycaprolactone in the 21st century. *Progress in Polymer Science*, 35(10), 1217–1256.
2. Woodruff, M. A., Lange, C., Reichert, J., et al. (2012). Bone tissue engineering: from bench to bedside. *Materials Today*, 15(10), 430–435.

3. Ulery, B. D., Nair, L. S., & Laurencin, C. T. (2011). Biomedical applications of biodegradable polymers. *Journal of Polymer Science Part B: Polymer Physics*, 49(12), 832.
4. Yang, X. B., Bhatnagar, R. S., Li, S., et al. (2004). Biomimetic collagen scaffolds for human bone cell growth and differentiation. *Tissue Engineering*, 10(7–8), 1148.
5. Zhai, Y., Lados, D. A., & Lagoy, J. L. (2014). Additive manufacturing: making imagination the major limitation. *JOM The Journal of the Minerals Metals & Materials Society*, 66(5), 808–816.
6. Satyanarayana, B., & Prakash, K. J. Component Replication Using 3D Printing Technology. *Procedia Materials Science*, 10, 263–269.
7. Scoggin, J., & Murray, T. A. (2016). Novel uses of 3D printing for in vitro biomedical research. In *Biomedical Engineering Conference* (pp. 29–30). IEEE.
8. Trappey, A. J. C., Trappey, C. V., & Lee, K. L. C. (2016). Tracing the evolution of biomedical 3D printing technology using ontology-based patent concept analysis. *Technology Analysis & Strategic Management*, 29(4), 1–14.
9. Xiao, Y., Yan, J., Hu, K., et al. (2016). Effect of high temperature on morphology and structure of a new composite as raw material of filament for fused deposition modeling processes. *China Academic Conference on Printing & Packaging and Media Technology*, 791–796.
10. Liu, H., Song, W., Chen, F., et al. (2011). Interaction of microstructure and interfacial adhesion on impact performance of polylactide (PLA) ternary blends. *Macromolecules*, 44(6), 1513–1522.
11. Fini, M., Giannini, S., Giardino, R., et al. (1995). Restorable device for fracture fixation: in vivo degradation and mechanical behaviour. *International Journal of Artificial Organs*, 18(12), 772–776.



# Application of NIR Analysis Technology in Quality Control of Tartary Buckwheat Products

Yan Cheng, Liang Zhuang, Xiujuan Zhi, and Bin Du<sup>(✉)</sup>

Beijing Laboratory of Food Quality and Safety,  
Food Science and Engineering College,  
Beijing University of Agriculture, Beijing, China  
{272514558, 847301566, 38534891}@qq.com,  
bindu80@bua.edu.cn

**Abstract.** Tartary buckwheat is rich in nutritive value, and can prevent modern civilization diseases. The survey found that the functional foods made by tartary buckwheat are generally favored by the three high- population. However, the related buckwheat products lack implementation standards and clear formulation. This paper established the quantitative analysis and discriminant model of buckwheat self-made products, and further explored the adulteration of buckwheat flour and the qualitative identification method of buckwheat noodles. The results showed that it is feasible to determine the adulteration of tartary buckwheat powder by NIR analysis, and determine the qualitative discrimination of the tartary buckwheat noodles. Due to the significant influence from the additives on Modeling and analysis, it is impossible to use a single model to analyze it quantitatively. Under the condition of knowing the formulation, it is possible to establish recognition model and apply this technique in market supervision.

**Keywords:** NIR analysis technology · Quality control · Tartary buckwheat

## 1 Introduction

Tartary buckwheat is recognized by the World Health Organization (WHO) as a therapeutic food for diabetes, hypertension, hyperlipidemia, coronary heart disease, stroke and so on. It has significant functions in hypoglycemic, blood lipid, and enhancement of human immunity. The buckwheat noodle as a kind of functional food in china, can meet the needs of the special consumers to the therapeutic food. At present, the price of buckwheat on the market is much higher than those of other grain crops such as wheat and rice. Some Unscrupulous merchants tend to adulterate to deceive the consumers. Therefore, the study in the adulteration identification technology for buckwheat flour and related products is considered to be necessary to ensure the consumer's consumption safety.

Near infrared spectroscopy (NIR) has been widely used in the composition and quality analysis of agricultural products, nutrient analysis, food safety, raw materials and identification of adulteration, and so on. NIR has been considered as a fast, convenient, environmentally friendly and nondestructive method [1–5]. In this paper, the

current situation of market for buckwheat flour products in china was investigated. In view of the existing problems, the adulteration identification method of buckwheat flour was explored by using NIR technology. The NIR analysis model of buckwheat noodle products was established for the self-made samples in the laboratory, and the effective technical way for the market supervision of buckwheat flour products was explored.

## 2 Materials and Methods

### 2.1 Materials and Instruments

Buckwheat flour, refined gluten powder, konjac fine powder, guar gum, xanthan gum and salt were purchased in the market. FW100 grinder: Tianjin City Tai site Instrument Co., Ltd.; MT140 series rolling machine: Hubei Juxin Machinery Co., Ltd; Nicolet 6700 Fourier Transform Near Infrared Spectroscopy Analyzer: Thermo Nicolet, USA.

### 2.2 The Formulation and Preparation Process of Buckwheat Noodles

Buckwheat noodle formulation: buckwheat flour noodle is prepared by blending buckwheat flour and wheat flour, in the range of 5–75% of tartary buckwheat powder, 25–95% of wheat flour, 3% of compound additive (konjac fine powder: guar gum: Xanthan Gum = 3:3:2), 3% of edible salt and alkali (salt:alkali = 5:1).

The production process of buckwheat noodles: 1. waking up the dough for 15 min in the fermenting box at  $25 \pm 1$  °C; 2. flaking the dough at first time; 3. waking up the flakes for 30 min in fermenting box at  $25 \pm 1$  °C; 4. flaking at second time; 5. cutting strips and drying.

### 2.3 Spectrometric Determination

It is necessary to preheat the machine at least 30 min, with  $7.714 \text{ cm}^{-1}$  of the sampling interval, the  $2.6 \mu\text{m}$  InGaAs detector, the CaF<sub>2</sub> beam splitter, the infrared light source, the scanning range of  $10,000\text{--}4000 \text{ cm}^{-1}$ , the scanning of 32 times, the resolution of  $16 \text{ cm}^{-1}$ , and the automatic atmospheric background deduction. The spectrum acquisition software Ominic and analysis software TQ analyst 8.528 were used to analyze collected data. In the spectrometric determination, the samples were placed in the rotary sampling cup, at  $23 \pm 2$  °C.

### 2.4 Sample Grouping

Group A: buckwheat flour was added into wheat flour powder with the weight ratios of 5, 10, 20, 30, 40, 50 and 75%, respectively; 5 parallel samples per ratio; scanning 5 times for each sample.

Group B: the additives and edible salt were added into the above mentioned samples in Group A. They were divided into non-additive group (I), saline-alkali group (II), salt-alkali and compound additive group (III); 5 parallel samples of each gradient; each sample was scanned 5 times.

Group C: The samples of the group B, according to the production process of the noodle, were made into buckwheat noodles in the laboratory, and the dried noodles were crushed and screened as the samples. The samples were divided into non-additive group (I), saline-alkali group (II), saline-alkali and thickener group (III); each gradient has 5 parallel samples, and each sample was scanned 5 times.

## **2.5 Experimental Design**

### **2.5.1 Identification and Quantitative Analysis of the Adulteration of Buckwheat Powder**

Partial least squares (PLS) is a regression modeling method of multivariate variable to independent variables. Using this method, the spectral data of samples in Group A are modeled to determine whether the raw buckwheat powder is doped by wheat flour and the actual doping amount.

### **2.5.2 Effect of Additives on Model Data of Buckwheat Flour**

Principal component analysis (PCA) can reduce the dimension of data and eliminate the overlapping parts of information. The effect of different additives on the original spectral data of buckwheat flour was determined by principal component analysis to determine the buckwheat noodles in different types of B.

### **2.5.3 Qualitative Discrimination of Buckwheat Noodles**

The NIR spectrum data is a high dimensional data matrix. The principal component analysis method is used to analyze the original spectral variables of the group C. Under the condition of no loss in useful information, the category of the buckwheat noodles (I, II, III) is identified by less new variables.

## **2.6 Cumulative Contribution Rate**

The cumulative contribution rate is the recognition degree of the calibration model for the spectral difference of the external samples. For spectral variation, the larger the principal score, the higher the calibration degree. Generally speaking, the cumulative contribution rate is above 70%. In this study, we set the threshold of variability which can be explained to be more than 95%.

## **3 Results and Analysis**

### **3.1 Analysis of Market Sales of Buckwheat Noodles**

The buckwheat noodles from 32 different brands were randomly selected and analyzed. In 93.75% of them, the proportion of ingredients in buckwheat flour was not marked. The thickening agent was added in 6.25% of the samples, the salt or edible alkaloids were labeled in 78.12% of the products, and 15.63% of the products marked no additives. Table 1 listed a small number of investigation data. It could not be verified whether the buckwheat powder was added to buckwheat noodle, and whether they used salt and alkali or thickening agent. In addition, the survey found that most of the



buckwheat noodles were executed by the standard LS/T3213 which was issued for color noodles in 1992. The state did not carry out the implementation standard of the buckwheat products, and some enterprises carried out their own enterprise standards, leading to the chaotic market of buckwheat noodle.

**Table 1.** Analysis on identification of dried buckwheat noodles on the market

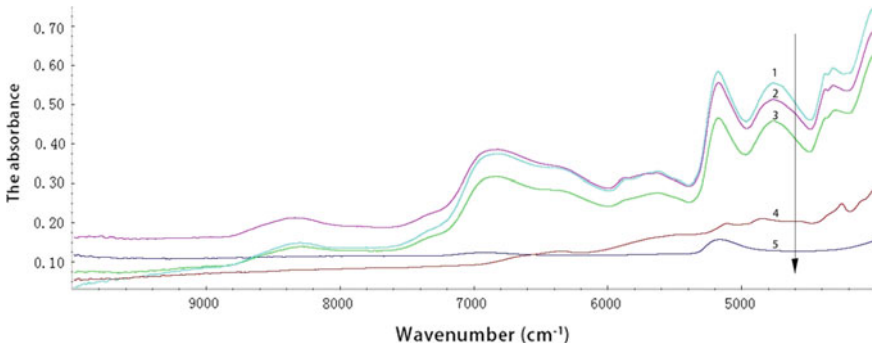
Brand	Place of origin	Batching table	Execution standard
Wujiabuckwheat flour	Wuchuan Inner Mongolia	Buckwheat flour 65%, wheat flour 35%	–
Huantai buckwheat flour	Liangshan, Sichuan	100% pure tartary buckwheat powder	Q/21301131-X.20
Wujia instant buckwheat noodle	Wuchuan Hohhot	Tartary buckwheat flour, wheat flour and iodized salt	Q/WJS06
Jindubuckwheat flour	Yanqing, Beijing	Wheat flour, buckwheat flour, starch, water, salt	LS/T3213
Gufu buckwheat flour	Jining, Shandong	Wheat flour, buckwheat flour, water, edible salt, alkali noodles	LS/T3213
Jinshun buckwheat flour	Daxing, Beijing	Wheat core snowflake powder, buckwheat powder, iodized salt, water	LS/T3213
Jinlongyu buckwheat noodle	Shijiazhuang, Hebei	High quality wheat flour, purified water, immature buckwheat flour, edible salt and edible alkali	Q/BAAK0015S

### 3.2 Near Infrared Diffuse Reflectance Spectra of Different Substances

In Fig. 1, the abscissa is the wave number and the ordinate is absorbance, with the scanning range of 10,000–4000  $\text{cm}^{-1}$ . In the NIR spectroscopy which was mainly produced by molecular vibration frequency within the group absorption and frequency absorption harmony, only hydrogen-containing functional groups such as C–H, N–H, S–H, and O–H' stretching vibration can be detected. The change of the internal composition will inevitably lead to the change of its near infrared diffuse reflectance spectrum. The spectrum of the diagram showed the difference of the spectrum of each material, especially in 4000–5400  $\text{cm}^{-1}$ , which provided a possibility for NIR Analysis of buckwheat products.

### 3.3 Identification and Quantitative Analysis of Buckwheat Flour Adulteration

TQ Analyst software was used to automatically select the spectral range of 4543.47–4828.88  $\text{cm}^{-1}$ , 5569.41–5885.68  $\text{cm}^{-1}$  and 5893.39–5947.39  $\text{cm}^{-1}$ . According to the modeling results of Fig. 2a, b, a fitting regression line ( $y = 1.001x - 0.046$ ) was



(1. buckwheat flour 2. wheat flour 3. composite additive 4. base 5. salt)

**Fig. 1.** Near infrared spectra of different material

obtained, with the calibration correlation coefficient  $R_c$  (0.999), the prediction correlation coefficient  $R_p$  (0.999), and the linear relationship was good. The mean square root error (RMSEP) of the model was 0.858, and the mean square root mean square error (RMSEC) was 0.827, leading to the 1.037 (RMSEC/RMSEP). The gap between the predicted value and the actual value was small. From Fig. 2c, d, it only need 4 main score to reach the above index, and the cross validation mean square variance of the correction set sample (RMSECV) is very small, and the cumulative contribution rate is close to 100%. So, the regression model under the principal component can be applied to the quantitative analysis of unknown samples, that is to say, for adulterated buckwheat powder, the model can determine the actual content of buckwheat flour to carry out effective market regulation.

### 3.4 Effect of Different Additives on Model Data of Buckwheat Flour

Some additives such as sodium carbonate and konjac powder can be added to the preparation and processing of tartary buckwheat noodles, which can prevent its broken bar. It not only can make the noodles of buckwheat golden yellow, increase appetite, but also increase the elasticity of tartary buckwheat noodle and reduce the loss rate of cooking [6–9]. In this experiment, the experimental data of group B after adding different additives were collected and the principal component analysis was carried out under the range of 4119.21–9881.46  $\text{cm}^{-1}$ . The analysis results of the discriminant model of buckwheat flour were found in Fig. 3a–c. The diagram (b) was a 3D model diagram corresponding to the (a) graph model, and the addition of salt and alkali could be found clearly. The compound additive group (III) was obviously deviated from groups (I, II), probably because the near infrared spectrum area was usually used to analyze the organic compounds containing C–H, N–H and O–H bonds, and the effect of the addition of inorganic salts and alkali components on the information extraction was very small. When the content of buckwheat is predicted, the effect of salt and alkali can be ignored, but the compound additive will obviously interfere with the prediction

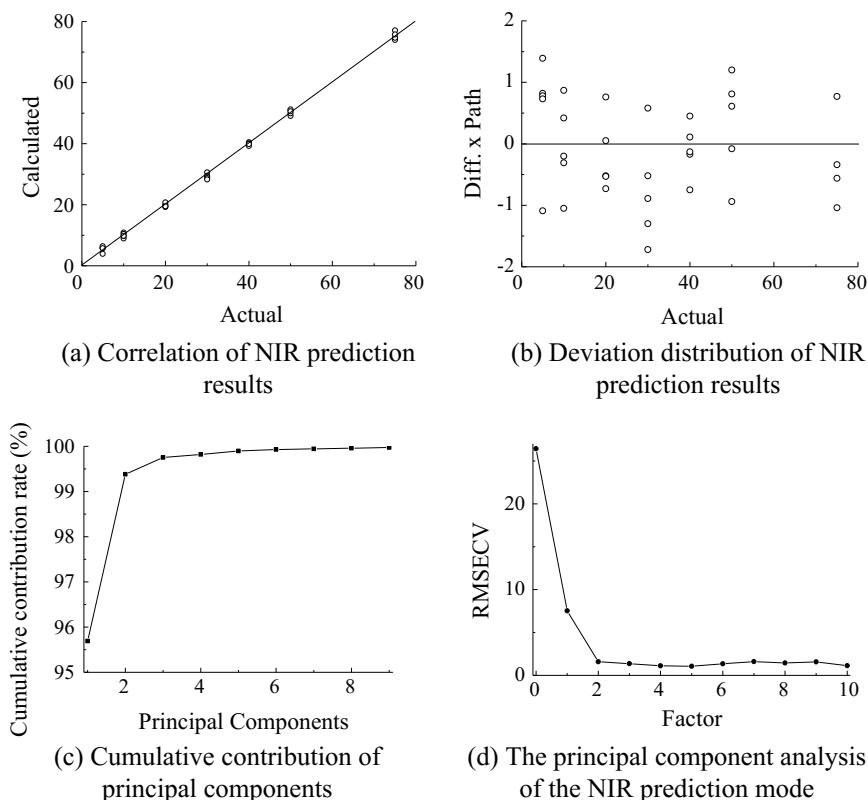
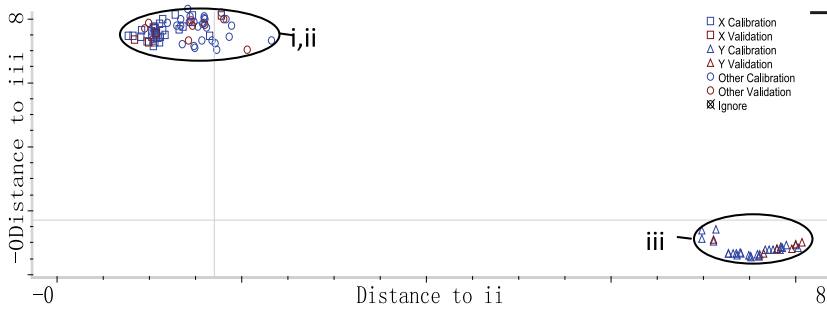


**Fig. 2.** Quantitative analysis model of buckwheat powder content

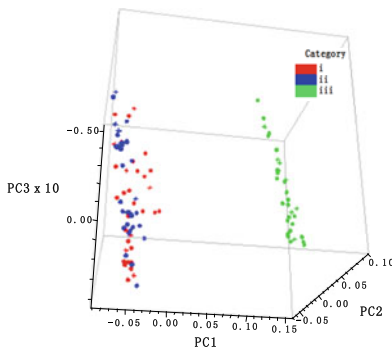
results. It is not feasible to carry out quantitative analysis of the three groups at the same time. The first 3 principal components of the model reflected 96.25% of the information, indicating that the discriminant analysis model under this principal component has statistical significance.

### 3.5 Qualitative Discrimination of Buckwheat Noodles

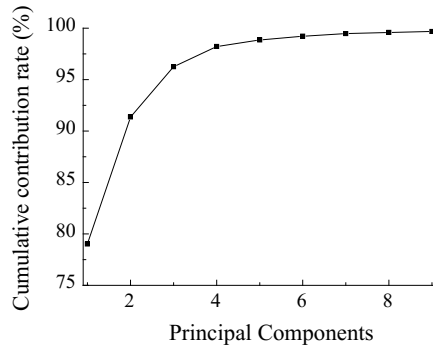
The principal component regression analysis of buckwheat noodle samples of group C in the range of  $4119.21\text{--}9881.46\text{ cm}^{-1}$  showed that the first 3 principal components reflected 100% information, and the discriminant analysis model had statistical significance. The 3D model of the analysis was established based on the results of the first, second and third principal components, as shown in Fig. 4b. The information showed that NIR diffuse reflectance information from different samples in the principal component space had obvious clustering characteristics, and the model could be used to accurately judge whether the homemade buckwheat noodles belong to the non-additive group (I), saline-alkali group (II) or the compound additive (III). The model showed that it is not feasible to make quantitative analysis of the three groups at the same time.



(a) Effects of different additives on the discriminant analysis model of buckwheat flour



(b) 3D graph of discriminant analysis model



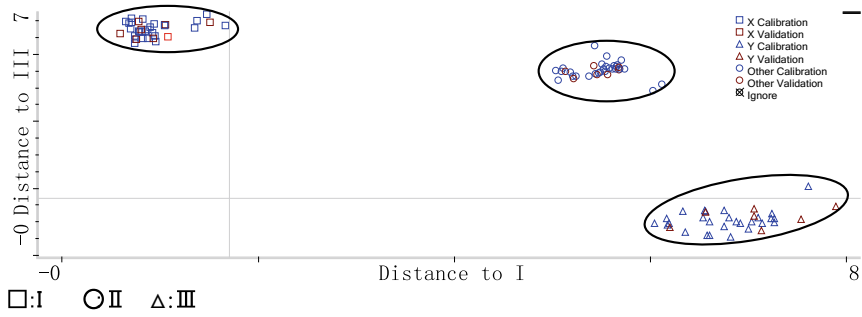
(c) Cumulative contribution rate of principal components

**Fig. 3.** The effects of salt, soda and thickener on the discriminant analysis model of buckwheat flour

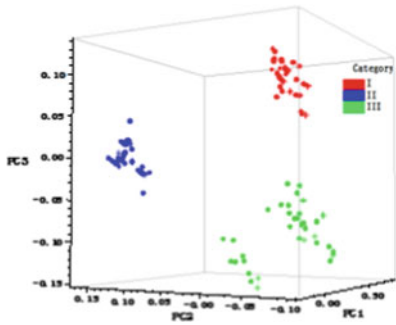
Under the condition of standardizing the standard, making clear the formula and classifying the model, it is possible to make use of the NIR analysis technique to make a more accurate quantitative analysis.

## 4 Conclusions

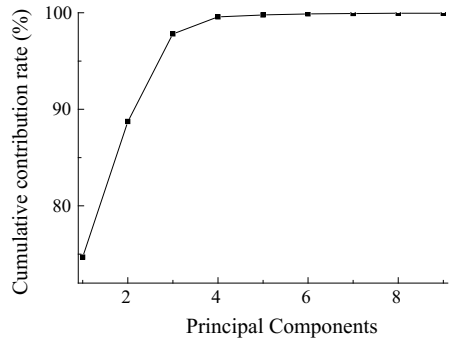
- (1) NIR technology was utilized to explore the adulteration identification of raw buckwheat flour and establish NIR analysis model for homemade samples. The results showed that this method can be used effectively for quantitative analysis of adulterated buckwheat flour and market.
- (2) Based on the principal component regression analysis of the spectra of samples, it was found that the qualitative analysis of the buckwheat noodle products is good.



(a) Discriminant analysis of buckwheat noodles in group I, II and III



(b) 3D graph of discriminant analysis model



(c) Cumulative contribution rate of principal components

**Fig. 4.** The discriminant analysis model of buckwheat hanging noodles

It can accurately determine whether the sample is pure buckwheat products and whether there are additives. However, it is possible to predict the content of buckwheat flour in the noodle products, only under the condition of knowing product standard, clear formula, and classification modeling.

## References

1. Chu, X. L., & Lu, W. Z. (2014). Research and application progress of near infrared spectroscopy technology in recent five years in China. *Spectroscopy and Spectral Analysis*, 34 (10), 2595–2605.
2. Wang, F., Yang, J., Xi, Z., & Zhu, H. (2013). Research on Rapid Identification Method of Buckwheat Varieties by Near-Infrared Spectroscopy Technique. In *Computer and Computing Technologies in Agriculture VII, CCTA 2013*. IFIP Advances in Information and Communication Technology, vol 419. Springer, Berlin, Heidelberg.
3. Liu, J. X. (2008). *Practical NIR spectroscopy technology*. Beijing: Science Press.
4. Zhu, X. R., Li, S. F., & Shan Y. (2010). Detection of adulterants such as sweeteners materials in honey using near-infrared spectroscopy. *Journal of Food Engineering*, 101, 92–97.

5. Kelly, J. D., Petisco, C., & Downey, G. (2006). Potential of near infrared transreflectance spectroscopy to detect adulteration of Irish honey by beet invert syrup and high fructose corn syrup. *Journal of Near Infrared Spectroscopy*, *14*(2), 139–146.
6. Gong, F. Y., Xiao, S. M., & Zhang, Z. (2011). Development of tartary buckwheat noodles. *Journal of Xichang College (Natural Science)*, *25*(3), 31–33.
7. Tian, X. H., Tan, B., Wang, L. P., et al. (2012). The effect of common food additives on the quality of tartary buckwheat noodle cooking. *Food and oil Food Technology*, *20*(5), 12–15.
8. Guo, X. N., Han, X. X., Zhang, H., et al. (2009). Research on Buckwheat nutritional health noodles. *Chinese Journal of Cereal and Oil*, *10*, 116–119.
9. Zhang, Z. (2013). Effect of adding sodium carbonate and konjac flour on the quality of tartary buckwheat noodle. *Jiangsu Agricultural Sciences*, *41*(04), 256–258.